CHEMICAL INDUSTRIES/119

Clathrate Hydrates of Natural Gases

Third Edition

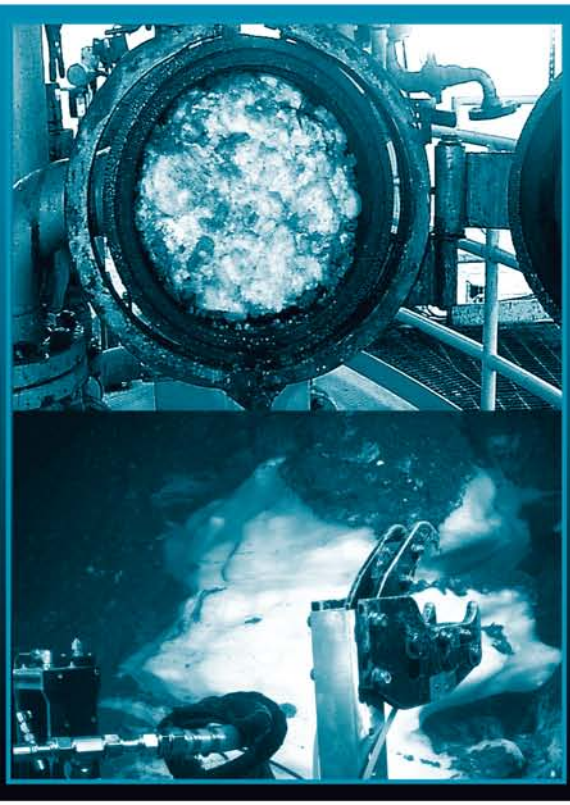

E. Dendy Sloan
Carolyn A. Koh

CRC Press
Taylor & Francis Group

Clathrate Hydrates of Natural Gases

Third Edition

CHEMICAL INDUSTRIES

A Series of Reference Books and Textbooks

Founding Editor

HEINZ HEINEMANN
Berkeley, California

Series Editor

JAMES G. SPEIGHT
Laramie, Wyoming

1. *Fluid Catalytic Cracking with Zeolite Catalysts,* Paul B. Venuto and E. Thomas Habib, Jr.
2. *Ethylene: Keystone to the Petrochemical Industry,* Ludwig Kniel, Olaf Winter, and Karl Stork
3. *The Chemistry and Technology of Petroleum,* James G. Speight
4. *The Desulfurization of Heavy Oils and Residua,* James G. Speight
5. *Catalysis of Organic Reactions,* edited by William R. Moser
6. *Acetylene-Based Chemicals from Coal and Other Natural Resources,* Robert J. Tedeschi
7. *Chemically Resistant Masonry,* Walter Lee Sheppard, Jr.
8. *Compressors and Expanders: Selection and Application for the Process Industry,* Heinz P. Bloch, Joseph A. Cameron, Frank M. Danowski, Jr., Ralph James, Jr., Judson S. Swearingen, and Marilyn E. Weightman
9. *Metering Pumps: Selection and Application,* James P. Poynton
10. *Hydrocarbons from Methanol,* Clarence D. Chang
11. *Form Flotation: Theory and Applications,* Ann N. Clarke and David J. Wilson
12. *The Chemistry and Technology of Coal,* James G. Speight
13. *Pneumatic and Hydraulic Conveying of Solids,* O. A. Williams

14. *Catalyst Manufacture: Laboratory and Commercial Preparations,* Alvin B. Stiles
15. *Characterization of Heterogeneous Catalysts,* edited by Francis Delannay
16. *BASIC Programs for Chemical Engineering Design,* James H. Weber
17. *Catalyst Poisoning,* L. Louis Hegedus and Robert W. McCabe
18. *Catalysis of Organic Reactions,* edited by John R. Kosak
19. *Adsorption Technology: A Step-by-Step Approach to Process Evaluation and Application,* edited by Frank L. Slejko
20. *Deactivation and Poisoning of Catalysts,* edited by Jacques Oudar and Henry Wise
21. *Catalysis and Surface Science: Developments in Chemicals from Methanol, Hydrotreating of Hydrocarbons, Catalyst Preparation, Monomers and Polymers, Photocatalysis and Photovoltaics,* edited by Heinz Heinemann and Gabor A. Somorjai
22. *Catalysis of Organic Reactions,* edited by Robert L. Augustine
23. *Modern Control Techniques for the Processing Industries,* T. H. Tsai, J. W. Lane, and C. S. Lin
24. *Temperature-Programmed Reduction for Solid Materials Characterization,* Alan Jones and Brian McNichol
25. *Catalytic Cracking: Catalysts, Chemistry, and Kinetics,* Bohdan W. Wojciechowski and Avelino Corma
26. *Chemical Reaction and Reactor Engineering,* edited by J. J. Carberry and A. Varma
27. *Filtration: Principles and Practices: Second Edition,* edited by Michael J. Matteson and Clyde Orr
28. *Corrosion Mechanisms,* edited by Florian Mansfeld
29. *Catalysis and Surface Properties of Liquid Metals and Alloys,* Yoshisada Ogino
30. *Catalyst Deactivation,* edited by Eugene E. Petersen and Alexis T. Bell
31. *Hydrogen Effects in Catalysis: Fundamentals and Practical Applications,* edited by Zoltán Paál and P. G. Menon
32. *Flow Management for Engineers and Scientists,* Nicholas P. Cheremisinoff and Paul N. Cheremisinoff
33. *Catalysis of Organic Reactions,* edited by Paul N. Rylander, Harold Greenfield, and Robert L. Augustine
34. *Powder and Bulk Solids Handling Processes: Instrumentation and Control,* Koichi Iinoya, Hiroaki Masuda, and Kinnosuke Watanabe
35. *Reverse Osmosis Technology: Applications for High-Purity-Water Production,* edited by Bipin S. Parekh
36. *Shape Selective Catalysis in Industrial Applications,* N. Y. Chen, William E. Garwood, and Frank G. Dwyer

37. *Alpha Olefins Applications Handbook,* edited by George R. Lappin and Joseph L. Sauer
38. *Process Modeling and Control in Chemical Industries,* edited by Kaddour Najim
39. *Clathrate Hydrates of Natural Gases,* E. Dendy Sloan, Jr.
40. *Catalysis of Organic Reactions,* edited by Dale W. Blackburn
41. *Fuel Science and Technology Handbook,* edited by James G. Speight
42. *Octane-Enhancing Zeolitic FCC Catalysts,* Julius Scherzer
43. Oxygen in Catalysis, Adam Bielanski and Jerzy Haber
44. *The Chemistry and Technology of Petroleum: Second Edition, Revised and Expanded,* James G. Speight
45. *Industrial Drying Equipment: Selection and Application,* C. M. van't Land
46. *Novel Production Methods for Ethylene, Light Hydrocarbons, and Aromatics*, edited by Lyle F. Albright, Billy L. Crynes, and Siegfried Nowak
47. *Catalysis of Organic Reactions*, edited by William E. Pascoe
48. *Synthetic Lubricants and High-Performance Functional Fluids*, edited by Ronald L. Shubkin
49. *Acetic Acid and Its Derivatives*, edited by Victor H. Agreda and Joseph R. Zoeller
50. *Properties and Applications of Perovskite-Type Oxides*, edited by L. G. Tejuca and J. L. G. Fierro
51. *Computer-Aided Design of Catalysts*, edited by E. Robert Becker and Carmo J. Pereira
52. *Models for Thermodynamic and Phase Equilibria Calculations*, edited by Stanley I. Sandler
53. *Catalysis of Organic Reactions*, edited by John R. Kosak and Thomas A. Johnson
54. *Composition and Analysis of Heavy Petroleum Fractions*, Klaus H. Altgelt and Mieczyslaw M. Boduszynski
55. *NMR Techniques in Catalysis,* edited by Alexis T. Bell and Alexander Pines
56. *Upgrading Petroleum Residues and Heavy Oils*, Murray R. Gray
57. *Methanol Production and Use*, edited by Wu-Hsun Cheng and Harold H. Kung
58. *Catalytic Hydroprocessing of Petroleum and Distillates*, edited by Michael C. Oballah and Stuart S. Shih
59. *The Chemistry and Technology of Coal: Second Edition, Revised and Expanded,* James G. Speight
60. *Lubricant Base Oil and Wax Processing*, Avilino Sequeira, Jr.
61. *Catalytic Naphtha Reforming: Science and Technology*, edited by George J. Antos, Abdullah M. Aitani, and José M. Parera

62. *Catalysis of Organic Reactions*, edited by Mike G. Scaros and Michael L. Prunier
63. *Catalyst Manufacture,* Alvin B. Stiles and Theodore A. Koch
64. *Handbook of Grignard Reagents,* edited by Gary S. Silverman and Philip E. Rakita
65. *Shape Selective Catalysis in Industrial Applications: Second Edition, Revised and Expanded*, N. Y. Chen, William E. Garwood, and Francis G. Dwyer
66. *Hydrocracking Science and Technology*, Julius Scherzer and A. J. Gruia
67. *Hydrotreating Technology for Pollution Control: Catalysts, Catalysis, and Processes*, edited by Mario L. Occelli and Russell Chianelli
68. *Catalysis of Organic Reactions*, edited by Russell E. Malz, Jr.
69. *Synthesis of Porous Materials: Zeolites, Clays, and Nanostructures,* edited by Mario L. Occelli and Henri Kessler
70. *Methane and Its Derivatives*, Sunggyu Lee
71. *Structured Catalysts and Reactors*, edited by Andrzej Cybulski and Jacob A. Moulijn
72. *Industrial Gases in Petrochemical Processing*, Harold Gunardson
73. *Clathrate Hydrates of Natural Gases: Second Edition, Revised and Expanded*, E. Dendy Sloan, Jr.
74. *Fluid Cracking Catalysts*, edited by Mario L. Occelli and Paul O'Connor
75. *Catalysis of Organic Reactions*, edited by Frank E. Herkes
76. *The Chemistry and Technology of Petroleum: Third Edition, Revised and Expanded*, James G. Speight
77. *Synthetic Lubricants and High-Performance Functional Fluids: Second Edition, Revised and Expanded,* Leslie R. Rudnick and Ronald L. Shubkin
78. *The Desulfurization of Heavy Oils and Residua, Second Edition, Revised and Expanded,* James G. Speight
79. *Reaction Kinetics and Reactor Design: Second Edition, Revised and Expanded,* John B. Butt
80. *Regulatory Chemicals Handbook*, Jennifer M. Spero, Bella Devito, and Louis Theodore
81. *Applied Parameter Estimation for Chemical Engineers*, Peter Englezos and Nicolas Kalogerakis
82. *Catalysis of Organic Reactions,* edited by Michael E. Ford
83. *The Chemical Process Industries Infrastructure: Function and Economics*, James R. Couper, O. Thomas Beasley, and W. Roy Penney
84. *Transport Phenomena Fundamentals*, Joel L. Plawsky

85. *Petroleum Refining Processes*, James G. Speight and Baki Özüm
86. *Health, Safety, and Accident Management in the Chemical Process Industries*, Ann Marie Flynn and Louis Theodore
87. *Plantwide Dynamic Simulators in Chemical Processing and Control*, William L. Luyben
88. *Chemical Reactor Design*, Peter Harriott
89. *Catalysis of Organic Reactions*, edited by Dennis G. Morrell
90. *Lubricant Additives: Chemistry and Applications*, edited by Leslie R. Rudnick
91. *Handbook of Fluidization and Fluid-Particle Systems*, edited by Wen-Ching Yang
92. *Conservation Equations and Modeling of Chemical and Biochemical Processes*, Said S. E. H. Elnashaie and Parag Garhyan
93. *Batch Fermentation: Modeling, Monitoring, and Control*, Ali Çinar, Gülnur Birol, Satish J. Parulekar, and Cenk Ündey
94. *Industrial Solvents Handbook, Second Edition*, Nicholas P. Cheremisinoff
95. *Petroleum and Gas Field Processing*, H. K. Abdel-Aal, Mohamed Aggour, and M. Fahim
96. *Chemical Process Engineering: Design and Economics*, Harry Silla
97. *Process Engineering Economics*, James R. Couper
98. *Re-Engineering the Chemical Processing Plant: Process Intensification*, edited by Andrzej Stankiewicz and Jacob A. Moulijn
99. *Thermodynamic Cycles: Computer-Aided Design and Optimization*, Chih Wu
100. *Catalytic Naphtha Reforming: Second Edition, Revised and Expanded*, edited by George T. Antos and Abdullah M. Aitani
101. *Handbook of MTBE and Other Gasoline Oxygenates*, edited by S. Halim Hamid and Mohammad Ashraf Ali
102. *Industrial Chemical Cresols and Downstream Derivatives*, Asim Kumar Mukhopadhyay
103. *Polymer Processing Instabilities: Control and Understanding*, edited by Savvas Hatzikiriakos and Kalman B. Migler
104. *Catalysis of Organic Reactions*, John Sowa
105. *Gasification Technologies: A Primer for Engineers and Scientists*, edited by John Rezaiyan and Nicholas P. Cheremisinoff
106. *Batch Processes*, edited by Ekaterini Korovessi and Andreas A. Linninger
107. *Introduction to Process Control*, Jose A. Romagnoli and Ahmet Palazoglu

108. *Metal Oxides: Chemistry and Applications*, edited by J. L. G. Fierro
109. *Molecular Modeling in Heavy Hydrocarbon Conversions*, Michael T. Klein, Ralph J. Bertolacini, Linda J. Broadbelt, Ankush Kumar and Gang Hou
110. *Structured Catalysts and Reactors, Second Edition*, edited by Andrzej Cybulski and Jacob A. Moulijn
111. *Synthetics, Mineral Oils, and Bio-Based Lubricants: Chemistry and Technology*, edited by Leslie R. Rudnick
112. *Alcoholic Fuels*, edited by Shelley Minteer
113. *Bubbles, Drops, and Particles in Non-Newtonian Fluids, Second Edition*, R. P. Chhabra
114. *The Chemistry and Technology of Petroleum, Fourth Edition*, James G. Speight
115. *Catalysis of Organic Reactions*, edited by Stephen R. Schmidt
116. *Process Chemistry of Lubricant Base Stocks*, Thomas R. Lynch
117. *Hydroprocessing of Heavy Oils and Residua*, edited by James G. Speight and Jorge Ancheyta
118. *Chemical Process Performance Evaluation*, Ali Cinar, Ahmet Palazoglu, and Ferhan Kayihan
119. *Clathrate Hydrates of Natural Gases, Third Edition*, E. Dendy Sloan and Carolyn A. Koh

Clathrate Hydrates of Natural Gases

Third Edition

E. Dendy Sloan
Colorado School of Mines
Golden, Colorado, U.S.A.

Carolyn A. Koh
Colorado School of Mines
Golden, Colorado, U.S.A.

CRC Press
Taylor & Francis Group
Boca Raton London New York

CRC Press is an imprint of the
Taylor & Francis Group, an **informa** business

CRC Press
Taylor & Francis Group
6000 Broken Sound Parkway NW, Suite 300
Boca Raton, FL 33487-2742

Printed in the United States of America on acid-free paper
10 9 8 7 6 5 4 3 2 1

International Standard Book Number-13: 978-0-8493-9078-4 (Hardcover)

Library of Congress Cataloging-in-Publication Data

Sloan, E. Dendy, 1944-
Clathrate hydrates of natural gases. -- 3rd ed. / E. Dendy Sloan and Carolyn Koh.
p. cm. -- (Chemical industries series ; 119)
Includes bibliographical references and index.
ISBN-13: 978-0-8493-9078-4 (alk. paper)
ISBN-10: 0-8493-9078-8 (alk. paper)
1. Natural gas--Hydrates. 2. Clathrate compounds. I. Koh, Carolyn. II. Title. III. Series.

TN884.S56 2007
665.7--dc22 2007008791

Visit the Taylor & Francis Web site at
http://www.taylorandfrancis.com

and the CRC Press Web site at
http://www.crcpress.com

Contents

Preface

Since each reader has a unique perspective, it is worthwhile to provide a guide for reading and an apologia for this book. The goal of writing this book was for it to be of use in practice and in research.

The third edition conforms to the Library of Congress dictum that a minimum of 33% new material is required to determine a new edition, rather than a new printing. In particular, the third edition includes new information on

- New fundamental information on structure, kinetics, and prediction methods
- Industrial transition from time-independence to time-dependence
- New phase equilibrium data and kinetic models
- A new computer program CSMGem, for hydrate thermodynamic calculations
- A new program CSMPlug to predict safety/dissociation times for plug removal
- A description of the paradigm change in flow assurance to risk management
- Conceptual pictures in flow assurance of oil- and gas-dominated flowlines
- Concepts and case studies on low dosage hydrate inhibitor prevention
- The paradigm change from hydrate reservoir assessment to reservoir production
- Eight summary *in situ* conditions for hydrates in the permafrost and oceans
- New case studies summarizing Hydrate Ridge and Mallik 2002 test drillings

Our primary objective was to update the hydrate knowledge base over the last decade—an explosion of knowledge with more than 4000 hydrate-related publications. These unique compounds are more properly called clathrate hydrates to distinguish them from the stoichiometric hydrates commonly found in inorganic chemistry. A modern, increased understanding of these compounds can provide a fresh perspective on past theories and data. It was hoped that such an overview would yield new insights for both the readers and the authors, and that directions might be suggested for future research and practical applications.

A second objective was to provide a balance between hydrate experimental and theoretical perspectives. The monograph was intended as a single record of the majority of hydrocarbon thermodynamic data obtained since 1934, the time of discovery of hydrates in pipelines. The third edition, in particular, shows the transition away from thermodynamics to kinetics, as mankind learns to study more sophisticated, time-dependent phenomena.

Often the comparative availability and low cost of computing causes the elevation of theory and simulation over experiment. In the field of hydrates, however, the most significant advances in knowledge have been made by researchers who have performed painstaking experiments guided by intuition, theory, and recently, simulation. Experiments have provided the physical foundation and correction of theories. In almost every case, the most marked theoretical advances, such as those of van der Waals and Platteeuw (1959), were founded upon significant experimental advances, such as the determination of the hydrate crystal structures by von Stackelberg and coworkers, Claussen, Pauling, and Marsh in the preceding two decades.

The final objective was to provide a complementary vehicle for the accompanying Windows + PC compatible computer programs. The principal program on the CD, CSMGem, is a complete Gibbs Energy Minimization revision of the program completed in this laboratory in 2002. Normally, such programs, based on fairly complex statistical thermodynamics, cannot be written precisely from the literature without substantial time and effort. It is not necessary to understand the theory (Chapter 5) in order to use the computer program to perform several hydrate calculations; the reader should follow the directions and examples in the User's Guide (Appendix A) and the User's Manual on the CD in this volume's end chapters. However, without the computer program, the theory would remain sterile. At the same time, the book provides a more thorough exposition of the program's principles than can be normally displayed in single papers accompanying a program.

A second major computer program, CSMPlug, also has a User's Guide in Appendix B and a User's Manual on the CD. This program enables the user to evaluate hydrate plug safety concerns and dissociation times. The safety aspects of plug dissociation should be a major concern in every hydrate situation, which sometimes results in damage to equipment and health. Often the plug dissociation times are much longer than intuition suggests and a prediction can help prevent "ineffective solutions" which sometimes worsen the problem. The program can be used to predict nonpressurized dissociation on core recovery, in addition to plug dissociation in a depressurized flowline.

Readers of different backgrounds will wish to follow different paths through the chapters. Both the engineer and the researcher may wish to read Chapter 1 that provides a historical overview of clathrate hydrates. One cannot deal with hydrates without some knowledge of the all-important crystal structures provided in Chapter 2. Chapter 3 on hydrate kinetics gives the current picture of hydrate time-dependence to supplement the time-independent phase equilibria in Chapter 4, the last chapter that should be of common interest to both the engineer and the

researcher. A recommendation summary for the book chapters is given in the following table:

A Suggestion on How to Read This Book

Reader's background	Engineer	Researcher
Chapter title	**Applicable sections**	
Chapter 1: Historical Overview	All sections	All sections
Chapter 2: Structures	All sections	All sections
Chapter 3: Kinetics	3.1.6, 3.2	All sections
Chapter 4: Phase Equilibria	4.1, 4.2, 4.4, 4.6	As needed
Chapter 5: Statistical Thermodynamics	None	All sections
Chapter 6: Experimental Methods and Data	6.1, 6.2 as needed	6.1, 6.2
Chapter 7: Hydrates in Nature	As needed	All sections
Chapter 8: Production, Transportation, and Processing	As needed	As needed
Appendices—Users Guide & Examples for CSMGem and CSMPlug	All sections	All sections

The initial limitations of the book are still largely present in the third edition. First the book applies primarily to clathrate hydrates of components in natural gases. Although other hydrate formers (such as olefins, hydrogen, and components larger than 9 Å) are largely excluded, the principles of crystal structure, thermodynamics, and kinetics in Chapters 2 through 5 will still apply.

Second, primarily due to language inability and literature access, the third edition has a Western Hemisphere perspective. Two translations (Schroeder, 1927 and Makogon, 1985) were made in preparation for the first edition manuscript. Discussions at length were held with Drs. Y.F. Makogon and Ginsburg, and with Professor Berecz and Ms. Balla-Achs, whose earlier hydrate monographs were initially published in Russian and in Hungarian. Yet as in all bi-author manuscripts, this book is the limited product of two individuals' perspectives, which were shaped by past workers and present colleagues.

Dr. John Ripmeester and his colleagues at the Steacie Institute of NRC Canada have led the world in hydrate science for the last several decades, and they have been gracious hosts to help CSM visitors learn. Drs. K.A. Kvenvolden and T.S. Collett of the U.S. Geological Survey and Scott Dallimore of the Canadian Geological Survey, have been generous with their publications and discussions regarding *in situ* hydrates. Our academic colleagues: Professor R.J. Bishnoi and colleagues Professors M. Pooladi-Darvish and M. Clarke (University of Calgary), Professor M. Adewumi (Penn State University), Professor P. Clancy (Cornell University), Dr. S.F. Dec (Colorado School of Mines), Professor K.D.M. Harris (Cardiff University), Professor J.-M. Herri (St. Etienne School of Mines), Professor W. Kuhs (University of Göttingen), Professor K.E. Gubbins (North Carolina State University), Professor K. Marsh (University of Canterbury), Professor

K.T. Miller (Colorado School of Mines), Professor Y.H. Mori (Keio University), Dr. G. Moridis (Lawrence Berkley National Laboratory), Professors C. Ruppel and C. Santamarina (Georgia Institute of Technology), Professor J. Sjöblom (Norwegian Technical National University), Professor A.K. Soper (Rutherford Appleton Laboratory), Professors A. Tréhu and M. Torres (Oregon State University), Professor B. Tohidi and Dr. R.E. Westacott (Heriot-Watt University), and Professor P. Englezos (University of British Columbia), have graciously shared their recent theoretical and experimental results that are of central importance to our current hydrate understanding.

Industrial collaborators provided some degree of balance to an academic perspective. Dr. W.R. Parrish of Phillips Petroleum Company (retired) encouraged and contributed to the work from our laboratory for two decades. Dr. J. Chitwood and Dr. J.L. Creek of Chevron, Dr. L. Talley of ExxonMobil, and Dr. T. Palermo of IFP, have also provided leading industrial perspectives on flow assurance. Two decades of consortium participation by the following companies provided industrial perspectives: BP, Chevron, ConocoPhillips, ExxonMobil, Halliburton, Petrobras, Shell, Schlumberger, and Statoil.

Our collaborators at the Colorado School of Mines have always been the major end product from our laboratory. The graduate students and postdoctoral fellows have done all of the experiments and much of the thinking that has evolved from this laboratory. These young minds preserved a fresh perspective for the authors: Dr. S. Adisasmito, Dr. B. Al-Ubaidi, M. Amer, Dr. G.B. Asher, Dr. A. Ballard, Dr. V. Bansal, Dr. P. Bollavaram, J. Boxall, M.S. Bourrie (deceased), Dr. D. Bruinsma, S.B. Cha, Dr. T.S. Collett, S. Davies, L. Dieker, Dr. P.B. Dharmawardhana, Y. Du, M. Eaton, Dr. D.D. Erickson, Dr. E. Freer, A. Giussani, D. Greaves, Dr. A. Gupta, Dr. K.C. Hester, A. Hughson, Dr. Z. Huo, Dr. A. Khokhar, Dr. R. Kini, D. Kleehammer, T. Kotkoskie, J. Ivanic, Dr. M. Jager, R. Johnson, J.J. Johnson, Dr. P. Kumar, J. Lachance, Dr. R. Larsen, Dr. J.P. Lederhos, Dr. J.P. Long, Dr. P. Long, E. Maas, Dr. T.Y. Makogon, S. Mann, P. Matthews, L. McClure, Dr. A.P. Mehta, P.D. Menten, Dr. M. Mooijer-van den Heuvel, B. Muller-Bongartz, Dr. A. Freitas-Mussemeci, J. Nicholas, T. Nguyen, Dr. H. Ohno, H. Ouar, Dr. V. Panchalingham, A. Papineau, Professor R. Pratt, P. Rensing, K. Rider, Dr. L. Rovetto, Dr. R.M. Rueff, B. Sikora, Dr. K.A. Sparks, T. Strobel, R. Sturgeon-Berg, Dr. S. Subramanian, Professor A.K.W. Sum, C. Taylor, C. Timm, Dr. D. Turner, J.W. Ullerich, M. Walsh, B.E. Weiler, Dr. S. Wierzchowski, S. Yamanlar, Dr. S.O. Yang, Dr. M.H. Yousif, and Dr. C.O. Zerpa. CAK also acknowledges the following graduate students and postdoctoral fellows from her former laboratory at King's College, London University: Dr. N. Aldiwan, Dr. V. Boissel, Dr. P. Buchanan, Dr. A. Carstensen, Dr. K. Hirachand, Dr. S. Klironomou, Dr. Y. Lui, Dr. R. Motie, Dr. R.I. Nooney, Dr. H. Thompson, Dr. R.E. Westacott, Dr. W. Zhang, Dr. M. Zugik. In this third edition we thank Simon Davies, Collin Timm, and Andrew Persichetti for their help with Appendices A, B, and the figures, respectively.

The intrinsic joy of learning about clathrate hydrates has in itself been a pleasure that we hope will be communicated through these pages to younger workers. The

survival of a research area, like that of a civilization, depends on whether the young see learning as a worthwhile goal. Noting that these pages doubtless contain several mistakes, the authors invoke the acute observation of Francis Bacon[1]: "Truth emerges more readily from error than from confusion."

The third edition is dedicated to her parents, Ann and Paul, and husband Ian by CAK, and to his wife Marjorie by EDS.

E. Dendy Sloan, Jr.
Carolyn A. Koh
Golden, Colorado

[1] "Novum Organum," Vol. VIII, *The Works of Francis Bacon* (J. Spedding, R.L. Ellis, and D.D. Heath, eds.) New York, p. 210 (1969).

Authors

Carolyn Ann Koh is an associate professor of chemical engineering and is the co-Director of the Center for Hydrate Research at the Colorado School of Mines. Previously, she was a reader in chemistry at King's College, London University. She received the Young Scientist Award in 2002 and is a Fellow of the Royal Society of Chemistry. She has been visiting professor of Cornell University, Penn State, and London University. She has over 55 refereed publications, and has given numerous invited lectures on hydrates. Dr. Koh holds degrees from the University of West London and conducted a postdoctoral fellowship at Cornell University, Ithaca, NY.

E. Dendy Sloan, Jr. holds the Weaver Chair in chemical engineering and is the Director of the Center for Hydrate Research at the Colorado School of Mines, where he co-directs a group of 20 researchers on natural gas hydrates. He has three degrees in chemical engineering from Clemson University and did postdoctoral work at Rice University. Prior to coming to the Colorado School of Mines, he was a senior engineer with E.I. DuPont deNemours, Inc.

Sloan chairs both the Federal Methane Hydrate Advisory Committee and the CODATA International Hydrate Database Task Group. He has over 150 refereed hydrates publications, including a second book, *Hydrate Engineering* published by the Society of Petroleum Engineers in 2000. Sloan was named the Donald M. Katz Research Awardee by the Gas Processors Association in 2000 and has been an SPE Distinguished Lecturer on hydrates. He is a Fellow of the American Institute of Chemical Engineers.

1 Overview and Historical Perspective

Natural gas hydrates are crystalline solids composed of water and gas. The gas molecules (guests) are trapped in water cavities (host) that are composed of hydrogen-bonded water molecules. Typical natural gas molecules include methane, ethane, propane, and carbon dioxide.

Historically, the research efforts on natural gas hydrates can be classified into three landmark phases that cover the following periods:

- The first period, from their discovery in 1810 until the present, includes gas hydrates as a scientific curiosity in which gas and water are transformed into a solid.
- The second period, continuing from 1934 until the present, predominantly concerns man-made gas hydrates as a hindrance to the natural gas industry.
- The third period, from the mid-1960s until the present, began with the discovery that nature predated man's fabrication of hydrates by millions of years, *in situ* in both the deep oceans and permafrost regions as well as in extraterrestrial environments.

As a result, the present is a culmination of three periods, representing the most fascinating and productive time in the history of natural gas hydrates. During the first century after their discovery, the number of hydrate publications totaled approximately 40; in modern times, the number of hydrate publications, both in the technical and in the popular press, has increased dramatically with over 400 publications in 2005 alone. The semilogarithmic plot of Figure 1.1 illustrates the exponential growth in the number of hydrate-related publications in the twentieth century. Table 1.1 lists reviews, chapters, and monographs on the subject of hydrates.

The purpose of this chapter is to review the three periods mentioned above, as an overview and historical perspective. The major concepts will be discussed briefly; detailed investigations are presented in the following chapters.

1.1 Hydrates as a Laboratory Curiosity

In 1778, Joseph Priestley performed cold experiments in his Birmingham laboratory by leaving the window open before departing on winter evenings, returning the next morning to observe the result. He observed that vitriolic air (SO_2) would impregnate water and cause it to freeze and refreeze, whereas marine acid air (HCl)

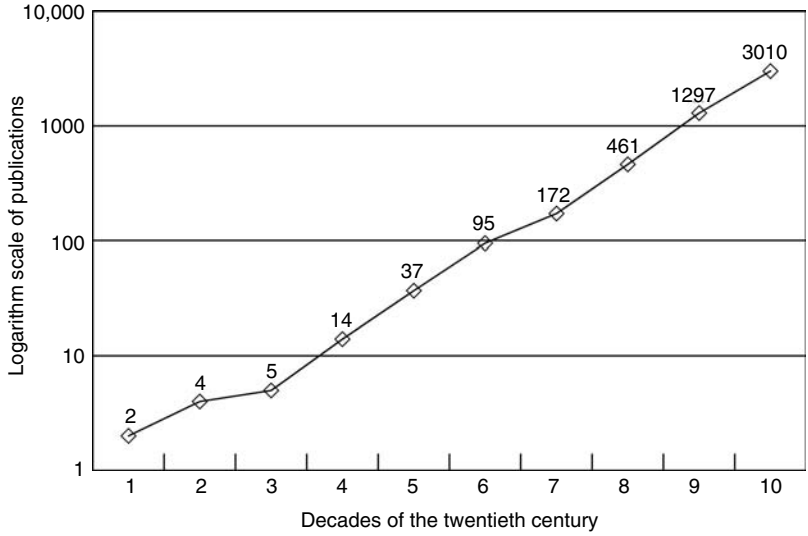

FIGURE 1.1 The growth of hydrate-related publications in the twentieth century by decade. (Reproduced from Sloan, E.D., *Am. Mineral.*, **89**, 1155 (2004). With permission from the Mineralogy Society of America.)

and fluor acid air (SiF_4) would not. With such experiments, Makogon and Gordejev (1992, unpublished data) suggest that Priestley might have discovered clathrate hydrates more than 30 years before Davy's discovery of clathrate hydrates.

> "It is water impregnated with vitriolic acid air that may be converted into ice, whereas water impregnated with fluor acid will not freeze .... I had observed that with respect to marine acid air and alkaline air (NH_3) that they dissolve ice, and that water impregnated with them is incapable of freezing, at least in such a degrees of cold as I had exposed them to. The same I find, is the case with fluor acid air, but it is not so at all with vitriolic acid air, which, entirely contrary to my expectation, I find to be altogether difficult .... But whereas water impregnated with fixed air discharges it when it is converted into ice, water impregnated with vitriolic acid air, and then frozen retains it as strongly as ever."

However, unlike Davy's experiments, Priestley's temperature (17°F) of the gas mixture was below the ice point, so there is no unequivocal evidence that the frozen system was hydrate. There is also no record of validation experiments by Priestley; consequently, Davy's independent discovery of chlorine hydrate is generally credited as the first observance.

Natural gas hydrates were first documented by Sir Humphrey Davy (1811), with these brief comments on chlorine (then called oxymuriatic gas) in the Bakerian lecture to the Royal Society in 1810.

> "It is generally stated in chemical books, that oxymuriatic gas is capable of being condensed and crystallized at low temperature; I have found by several experiments that this is not the case. The solution of oxymuriatic gas in water freezes more

TABLE 1.1
Reviews, Chapters, and Monographs on Clathrate Hydrates

1927	Schroeder: *Die Geschichte der Gas Hydrate*
1946	Deaton and Frost: *Gas Hydrates and Relation to the Operation of Natural-Gas Pipelines*
1959	Katz et al.: "Water–Hydrocarbon Systems" in *Handbook of Natural Gas Engineering*
1967	Jeffrey and McMullan: "The Clathrate Hydrates" in *Progress in Inorganic Chemistry*
1973	Davidson: "Clathrate Hydrates" in *Water: A Comprehensive Treatise* Vol. 2
1974	Makogan: *Hydrates of Natural Gas*
1977	Berecz and Balla-Achs: *Gas Hydrates*
1980	Kvenvolden and McMenamin: *Hydrates of Natural Gas: A Review of Their Geologic Occurrence*
1983	Cox, ed.: *Natural Gas Hydrates: Properties, Occurrence and Recovery*
1983	Lewin & Associates and Consultants: *Handbook of Gas Hydrate Properties and Occurrence*
1987	Krason and Ciesnik: *Geological Evolution and Analysis of Confirmed or Suspected Gas Hydrate Localities* (13 volumes)
1988	Holder et al.: "Phase Behavior in Systems Containing Clathrate Hydrates" *Rev. Chem. Eng.*
1990	Katz and Lee: "Gas Hydrates and Their Prevention" in *Natural Gas Engineering: Production and Storage*
1990	Sloan: *Clathrate Hydrates of Natural Gases*
1993	Englezos: "Clathrate Hydrates" *Ind. Eng. Chem. Res.*
1994	Sloan, Happel and Hnatow, eds.: *International Conference on Natural Gas Hydrates*, NY
1995	Kvenvolden, K.A.: *A Review of the Geochemistry of Methane in Natural Gas Hydrate*
1996	Monfort, ed.: *Second International Conference on Natural Gas Hydrates, Toulouse*
1997	Makogon: *Hydrates of Hydrocarbons*
1998	Henriet and Mienert, eds.: *Gas Hydrates: Relevance to World Margin Stability and Climate Change*
1998	Ginsburg and Soloviev: *Submarine Gas Hydrates*
2000	Holder and Bishnoi, eds.: *Third International Conference on Natural Gas Hydrates*, Salt Lake City
2000	Sloan: *Hydrate Engineering*
2000	Paull et al.: *Proc. Ocean Drilling Program, Science Results for Leg 164 (Blake Ridge)*
2001	Paull and Dillon, eds.: *Natural Gas Hydrates: Occurrence, Distribution and Detection*
2002	Mori, ed.: *Fourth International Conference on Natural Gas Hydrates*, Yokohama
2003	Kennett et al.: *Methane Hydrates in Quaternary Climate Change: The Clathrate Gun Hypothesis*
2003	Max, ed. *Natural Gas Hydrates in Oceanic and Permafrost Environments*
2004	Taylor and Kwan, eds.: *Advances in the Study of Gas Hydrates*
2004	Zhang and Lanoil, eds.: "Geomicrobiology and Biogeochemistry of Gas Hydrates and of Hydrocarbon Seeps" in *Chemical Geology*
2005	Austvik, ed.: *Fifth International Conference on Natural Gas Hydrates*, Trondheim
2005	Dallimore et al., eds.: "Report of the Mallik 5L International Field Experiment on Recovering *In Situ* Hydrates from Permafrost", *Geological Survey of Canada Report*.
2005	IODP: Preliminary Report Leg 311 (Northern Cascadia Margin)
2006	Johnson et al., eds.: *Economic Geology of Natural Gas Hydrates*
2006	Tréhu et al.: *Ocean Drilling Program Scientific Report Leg 204*

readily than pure water, but the pure gas dried by muriate of lime undergoes no change whatever at a temperature of 40 below 0° of Fahrenheit."

Over the following one and one-quarter centuries, researchers in the field had two major goals, namely, (1) to identify all the compounds that formed hydrates and (2) to quantitatively describe the compounds by their compositions and physical properties. Table 1.2 provides a summary of the research over this period.

TABLE 1.2
Hydrates from 1810 to 1934

Year	Event
1810	Chlorine hydrate discovery by Sir Humphrey Davy
1823	Corroboration by Faraday—formula $Cl_2 \cdot 10H_2O$
1882, 1883	Ditte and Mauméné disputed the composition of chlorine hydrates
1884	Roozeboom confirmed the composition as $Cl_2 \cdot 10H_2O$
1884	LeChatelier showed that the Cl hydrate P–T curve changes slope at 273 K
1828	Bromine hydrates discovered by Löwig
1876	Br_2 hydrates corroborated by Alexeyeff as ($Br_2 \cdot 10H_2O$)
1829	SO_2 hydrates found by de la Rive as $SO_2 \cdot 7H_2O$
1848	Pierre determined the formula of $SO_2 \cdot 11H_2O$
1855	Schoenfield measured the formula as $SO_2 \cdot 14H_2O$
1884, 1885	Roozeboom postulated upper/lower hydrate quadruple points using SO_2 as evidence; determined univariant dependence of P on T
1856–1858	CS_2 hydrate composition disputed by Berthelot (1856), Millon (1860), Duclaux (1867), Tanret (1878)
1877, 1882	Cailletet and Cailletet and Bordet first measured mixed gas hydrates from $CO_2 + PH_3$ and from $H_2S + PH_3$
1882	de Forcrand suggested $H_2S \cdot (12–16)H_2O$ and measured 30 binary hydrates of H_2S with a second component such as $CHCl_3$, CH_3Cl, C_2H_5Cl, C_2H_5Br, C_2H_3Cl. He indicated all compositions as $G \cdot 2H_2S \cdot 23H_2O$
1883	Wroblewski measured carbon dioxide hydrates
1885	Chancel and Parmentier determined chloroform hydrates
1888	Villard obtained the temperature dependence of H_2S hydrates
1888	de Forcrand and Villard independently measured the temperature dependence of CH_3Cl hydrate
1888	Villard measured hydrates of CH_4, C_2H_6, C_2H_4, C_2H_2, N_2O
1890	Villard measured hydrates of C_3H_8 and suggested that the temperature of the lower quadruple point is decreased by increasing the molecular mass of a guest; Villard suggested hydrates were regular crystals
1896	Villard measured hydrates of Ar, and proposed that N_2 and O_2 form hydrates; first to use heat of formation data to get the water/gas ratio
1897	deForcrand and Thomas sought double (w/H_2S or H_2Se) hydrates; found mixed (other than H_2S_x) hydrates of numerous halohydrocarbons mixed with C_2H_2, CO_2, C_2H_6
1902	de Forcrand first used Clausius–Clapeyron relation for ΔH and compositions; tabulated 15 hydrate conditions
1919	Scheffer and Meyer refined Clausius–Clapeyron technique
1923, 1925	de Forcrand measured hydrates of krypton and xenon

In Table 1.2, the following pattern was often repeated: (1) the discovery of a new hydrate was published by an investigator; (2) a second researcher disputed the composition proposed by the original investigator; and (3) a third (or more) investigator(s) refined the measurements made by the initial two investigators, and proposed slight extensions. As a typical example, in the case of chlorine hydrate after Davy's discovery in 1810, Faraday confirmed the hydrate (1823) but proposed that there were ten water molecules per molecule of chlorine. Then Ditte (1882), Mauméné (1883), and Roozeboom (1884) re-examined the ratio of water to chlorine.

The period from 1810 to 1900 is characterized by efforts of direct composition measurements with inorganic hydrate formers, especially bromine, inorganics containing sulfur, chlorine, and phosphorus, and carbon dioxide. Other notable work listed in Table 1.2 was done by Cailletet and Bordet (1882), who first measured hydrates with mixtures of two components. Cailletet (1877) was also the first to measure a decrease in gas pressure when hydrates were formed in a closed chamber, using a precursor of an apparatus still in use at the Technical University of Delft, the Netherlands.

1.1.1 Hydrates of Hydrocarbons Distinguished from Inorganic Hydrates and Ice

Two French workers, Villard and de Forcrand, were the most prolific researchers of the period before 1934, with over four decades each of heroic effort. Villard (1888) first determined the existence of methane, ethane, and propane hydrates. de Forcrand (1902) tabulated equilibrium temperatures at 1 atm for 15 components, including those of natural gas, with the exception of iso-butane, first measured by von Stackelberg and Müller (1954).

The early period of hydrate research is marked by a tendency to set an integral number of water molecules per guest molecule, due to the existing knowledge of inorganic stoichiometric hydrates that differed substantially from clathrate hydrates. For example, Villard's Rule (1895) states that "all crystallize regularly and have the same constitution that can be expressed by the formula $M + 6H_2O$." Schroeder (1927) noted that Villard's Rule was followed by 15 of the 17 known gas hydrate formers. Today, we know that too many exceptions are required for Villard's Rule to be a useful heuristic. Molecules approximated by Villard's Rule are small guests that occupy both cavities of structures I or II (see Chapter 2).

It gradually became clear that the clathrate hydrates distinguished themselves by being both nonstoichiometric and crystalline; at the same time, they differed from normal hexagonal ice because they had no effect on polarized light.

1.1.2 Methods to Determine the Hydrate Composition

The work in Table 1.2 illustrates one of the early research difficulties that is still present—namely, the direct measurement of the water to gas ratio in hydrates (hydration number, n = water molecules per guest). Whereas many solids

such as carbon dioxide precipitate in a relatively pure form, or a form of fixed composition, gas hydrate composition is variable with temperature, pressure, and the composition of associated fluid phases. Although the composition measurement of either the gas or the water phase is tractable (usually via chromatography), measurement of the hydrate composition is more challenging.

On a macroscopic basis, it is difficult to remove all excess water from the hydrate mass; this causes a substantial decrease in the accuracy of hydrate composition measurements. Hydrate formations often occlude water within the solid in a metastable configuration, thereby invalidating the composition obtained upon dissociation. Mixed guest compositions of the hydrate are also confounded by the concentration of heavy components in the hydrate phase. Unless the associated gas reservoir is large, preferential hydration may result in variable gas consumption and perhaps an inhomogeneous hydrate phase as discussed in Chapter 6.

Villard (1896) proposed an indirect macroscopic method to determine hydration number, which uses the heat of formation, both above and below the ice point. In his review, Schroeder (1927) indicates that after 1900, researchers abandoned direct measurement of hydrate phase composition, preferring Villard's method (see Section 4.6.2) that relies on easier measurements of pressure and temperature. Miller and Strong (1946) provided another thermodynamic method to determine hydration number, discussed in Section 4.6.2.2.

Circone et al. (2005) obtained hydration numbers from direct macroscopic measurements of the amount of gas released during dissociation. Their results were in close agreement with those obtained by Galloway et al. (1970) from measurements of gas uptake during synthesis and release during decomposition, and by Handa (1986e) from calorimetric measurements.

The advent of modern microscopic measurement tools and a means for bridging the microscopic and macroscopic domains (statistical thermodynamics) enable the direct determination of hydrate phase properties. The hydration number can be determined from single crystal or powder (using Rietveld refinement) x-ray and neutron diffraction. The hydration number can also be determined using Raman (Sum et al., 1997; Uchida et al., 1999) and NMR (Ripmeester and Ratcliffe, 1988) spectroscopy combined with statistical thermodynamics. Davidson et al. (1983) and Ripmeester and Ratcliffe (1988) first used NMR spectroscopy and Sum et al. (1997) first used Raman spectroscopy to determine the guest occupancies of each type of cage. Single crystal and powder x-ray and neutron diffraction (Udachin et al., 2002; Rawn et al., 2003) have also been applied to determine guest occupancies and hydrate composition. These methods are discussed in Chapter 6.

1.1.3 Phase Diagrams Provide Hydrate Classification

Roozeboom (1884, 1885) generated the first pressure–temperature plot for SO_2 hydrate, similar to that in Figure 1.2 for several components of natural gases. In the figure, H is used to denote hydrates, I for ice, V for vapor, and L_w and L_{HC} for aqueous and hydrocarbon liquid phases, respectively. For each component,

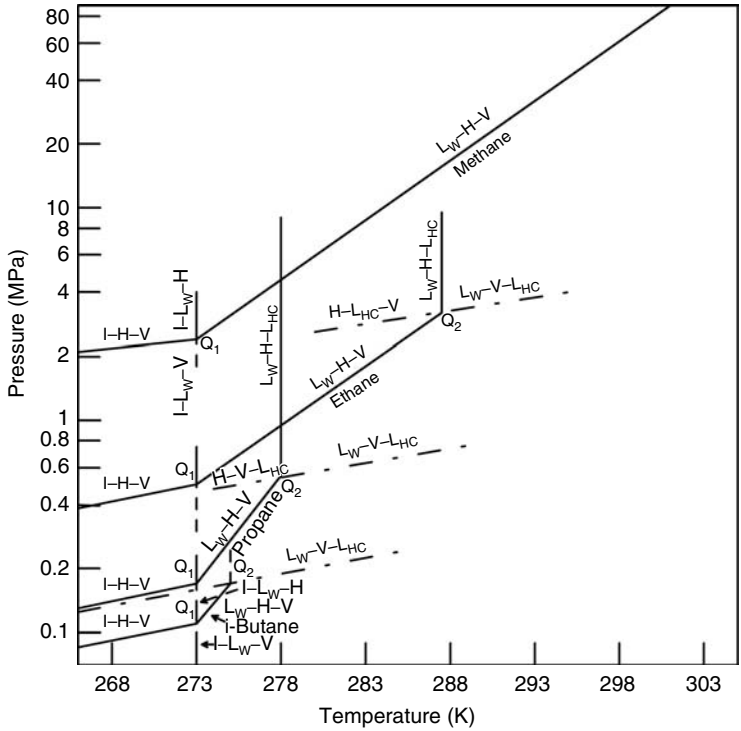

FIGURE 1.2 Phase diagrams for some simple natural gas hydrocarbons that form hydrates. Q_1: lower quadruple point; Q_2: upper quadruple point. (Modified from Katz, D.L., Cornell, D., Kobayashi, R., Poettmann, F.H., Vary, J.A., Elenbaas, J.R., Weinaug, C.F., *The Handbook of Natural Gas Engineering*, McGraw Hill Bk. Co. (1959). With permission.)

the hydrate region is to the left of the three phase lines (I–H–V), (L_w–H–V), (L_w–H–L_{HC}); to the right, phases exist for liquid water or ice and the guest component as vapor or liquid.

In Figure 1.2, the intersection of the above three phase lines defines both a lower hydrate quadruple point Q_1 (I–L_W–H–V) and an upper quadruple point Q_2 (L_W–H–V–L_{HC}). These quadruple points are unique for each hydrate former, providing a quantitative classification for hydrate components of natural gas.

Each quadruple point occurs at the intersection of four three-phase lines (Figure 1.2). The lower quadruple point is marked by the transition of L_W to I, so that with decreasing temperature, Q_1 denotes where hydrate formation ceases from vapor and liquid water, and where hydrate formation occurs from vapor and ice. Early researchers took Q_2 (approximately the point of intersection of line L_W–H–V with the vapor pressure of the hydrate guest) to represent an upper temperature limit for hydrate formation from that component. Since the vapor pressure at the critical temperature can be too low to allow such an intersection, some natural gas components such as methane and nitrogen have no upper quadruple point, Q_2, and

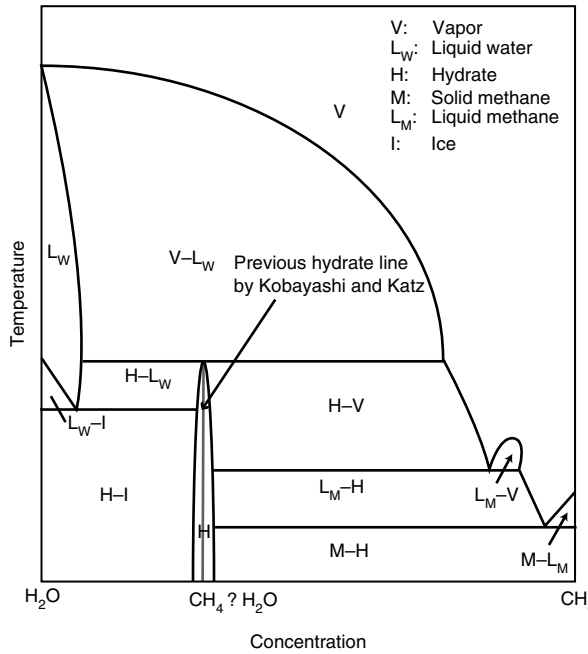

FIGURE 1.3 Proposed CH_4–H_2O T–x phase diagram with the solid solution range ($P \approx$ 5 MPa). Regions expanded for ease of viewing. (Reproduced from Huo, Z., Hester, K.E., Sloan, E.D., Miller, K.T., *AIChE. J.*, **49**, 1300 (2003). With permission.)

consequently they have no upper temperature limit for hydrate formation. Phase diagrams are discussed in detail in Chapter 4.

The isobaric methane–water phase diagram was produced by Kobayashi and Katz in 1949 (Figure 1.3). This classical phase diagram represents the hydrate composition as a vertical constant composition line. This assumes that the hydrate is stoichiometric and that cage occupancy is independent of temperature or system composition. Reassessment of this phase diagram was initiated by the authors' laboratory in 2002 (Huo et al., 2002, 2003). We revisited the largely overlooked work by Glew and Rath (1966). Glew and Rath (1966) found from density measurements of sI ethylene oxide that nonstoichiometry (with the minimum occupancy of the small cages varying from 19% to 40%) can occur depending on the solution composition. This work validated the earlier statistical thermodynamic calculations showing nonstoichiometry in clathrate hydrates (van der Waals and Platteeuw, 1959).

X-ray diffraction and Raman studies were performed to re-evaluate the relation between hydrate and overall composition (Huo et al., 2002, 2003). A modified methane–water phase diagram was proposed to include a small solid solution range of around 3% (Figure 1.3). [A solid solution is a solid-state solution of one or more solutes (guests) in a solvent (host framework). Generally, the crystal structure (of the clathrate hydrate) remains homogeneous and unchanged when substituting/

adding solutes (varying guest occupancies) to the solvent (host framework).] The solid solution range is represented by a parabolic hydrate region (attributed to incomplete filling of small cages of sI hydrate) in the isobaric methane–water phase diagram, which replaces the vertical stoichiometric hydrate line of Kobayashi and Katz (1949).

1.2 Hydrates in the Natural Gas Industry

In the mid-1930s Hammerschmidt studied the 1927 hydrate review of Schroeder (D.L. Katz, Personal Communication, November 14, 1983) to determine that natural gas hydrates were blocking gas transmission lines, frequently at temperatures above the ice point. This discovery was pivotal in causing a more pragmatic interest in gas hydrates and shortly thereafter led to the regulation of the water content in natural gas pipelines.

The detection of hydrates in pipelines is a milestone marking both the importance of hydrates to industry and the beginning of the modern research era. As a complement to the history prior to 1934 in Table 1.2, hydrate studies in more recent times are indicated in Table 1.3. The key scientific developments and applications to the natural gas industry are listed in Table 1.3. With this listing as an abstract, an introduction to modern research is provided in the next few pages, with more details and literature references in later chapters.

1.2.1 Initial Experiments on Natural Gas Hydrates

After Hammerschmidt's initial discovery, the American Gas Association commissioned a thorough study of hydrates at the U.S. Bureau of Mines. In an effort spanning World War II, Deaton and Frost (1946) experimentally investigated the formation of hydrates from pure components of methane, ethane, and propane, as well as their mixtures with heavier components in both simulated and real natural gases.

Predictive method results are still compared to the Deaton and Frost data. It should be remembered, however, that while this study was both painstaking and at the state-of-the-art, the data were of somewhat limited accuracy, particularly the measurements of gas composition. As will be seen in Chapters 4 and 5, small inaccuracies in gas composition can dramatically affect hydrate formation temperatures and pressures. For example, Deaton and Frost were unable to distinguish between normal butane and iso-butane using a Podbielniak distillation column, and so used the sum of the two component mole fractions. Accurate composition measurement techniques such as chromatography did not come into common usage until early in the 1960s.

Many workers including Hammerschmidt (1939), Deaton and Frost (1946), Bond and Russell (1949), Kobayashi et al. (1951), and Woolfolk (1952) investigated the effects of inhibitors on hydrates. In particular, many chloride salts such as those of calcium, sodium, and potassium, were considered along with methanol and monoethylene glycol. Methanol gradually became one of the

TABLE 1.3
Milestones in Hydrate Studies since 1934

1934	Hammerschmidt discovers hydrates as pipeline plugs; provides Hammerschmidt equation; discovers thermodynamic inhibitors
1941	Katz et al. begin K-values and gas gravity methods to predict hydrate mixtures
1946	Deaton and Frost present data summary on hydrates and their prevention
1949	von Stackelberg reports 20 years of diffraction data on hydrate crystals
1949	Kobayashi begins a 50 year hydrate research effort with study of binary systems
1951	Claussen proposes, and von Stackelberg and Müller confirm sII unit crystal
1952	Claussen and Polglase, Müller and von Stackelberg, and Pauling and Marsh confirm sI unit crystal
1954	von Stackelberg and Jahn measure sII hydrate formed from two sI guest molecules
1959	van der Waals and Platteeuw (vdWP) propose statistical theory based on structure
1960	Robinson begins 30 year hydrate research effort with study of paraffin/olefin hydrates
1963	McKoy and Sinanoglu apply Kihara potential to vdWP theory
1963	Davidson makes first dielectric measurements
1965	Kobayashi and coworkers apply vdWP theory to mixtures
1966	Davidson makes first broadline NMR measurements of hydrates
1972	Parrish and Prausnitz apply vdWP theory to natural gases
1975	Sloan begins measurements of two-phase hydrate equilibria
1976	Ng begins with three- and four-phase study of liquid hydrocarbons
1976	Holder et al. begin work with study of sI and sII coexistence and hydrates in earth
1979	Bishnoi and coworkers begin kinetic study with simulations of well blowouts
1980	Ripmeester and Davidson make first pulsed NMR measurements
1982	Tse and coworkers begin molecular dynamic (MD) simulation of hydrates
1984	Davidson et al. confirm Holder's suggestion that small, simple guests form sII
1984	Handa begins study of calorimetry and phase equilibria
1985	John and Holder determine effect of higher order coordination shells in vdWP theory
1986	Englezos begins study of kinetics of methane, ethane dissociation
1987	Ripmeester and coworkers discover new structure H (sH) hydrates
1988	Danesh, Todd, and coworkers begin four phase experiments with hydrates
1990a,b	Rodger studies relative stability using MD simulation
1991	Mehta obtains sH data, applied vdWP theory to CH_4 + large (>8 Å) guest(s)
1991	Behar et al. introduce water emulsification concept to control hydrate blockage
1991	Sloan proposes molecular mechanism with kinetic inhibition implications
1992	Kotkoskie et al. show that hydrates are controlled by drilling mud water activity
1996	Sum measures hydrate composition and hydration number using Raman spectroscopy
1997	Kuhs et al. publish first report of double occupancy of nitrogen molecules in large cage of sII hydrate at high pressures, exceeding several hundred bar
1997	Udachin et al. report first single crystal x-ray diffraction measurements of a sH gas hydrate
1997	Dyadin et al. discover a very high pressure phase of methane hydrate that is stable up to 600 MPa
1999	Dyadin et al. discover that H_2 forms a clathrate hydrate at high pressures up to 1.5 GPa
2004	Camargo et al. and BP/SINTEF introduce "cold flow" concept to prevent hydrate plug formation without the need of chemical additives

most popular inhibitors, due to its ability to concentrate in free water traps after being vaporized into the upstream gas. Effects of thermodynamic inhibitors such as methanol are quantified in Chapters 4, 5, 6, and 8.

1.2.2 Initial Correlation of Hydrate Phase Equilibria

When Hammerschmidt (1934) identified hydrates in pipelines, he published a correlation summary of over 100 hydrate formation data points. Shortly afterward, Professor D.L. Katz and his students at the University of Michigan began an experimental study. Because it was impractical to measure hydrate formation conditions for every gas composition, Katz determined two correlative methods.

The initial predictive method by Wilcox et al. (1941) was based on distribution coefficients (sometimes called K_{vsi} values) for hydrates on a water-free basis. With a substantial degree of intuition, Katz determined that hydrates were solid solutions that might be treated similar to an ideal liquid solution. Establishment of the K_{vsi} value (defined as the component mole fraction ratio in the gas to the hydrate phase) for each of a number of components enabled the user to determine the pressure and temperature of hydrate formation from mixtures. These K_{vsi} value charts were generated in advance of the determination of hydrate crystal structure. The method is discussed in detail in Section 4.2.2.

The second (and simplest available) method, generated by Professor Katz (1945) and students in a graduate class, is presented in Figure 1.4. The plot enabled the user to estimate a hydrate formation pressure, given a temperature and gas gravity (gas molecular weight divided by that of air). The original work also enabled the determination of the hydrate formation limits due to expansions of natural gases, as in throttling gas through a valve. This method and its limitations are discussed in detail in Section 4.2.1 as a useful first approximation for hydrate formation conditions.

Katz's two predictive techniques provided industry with acceptable predictions of mixture hydrate formation conditions, without the need for costly measurements. Subsequently, hydrate research centered on the determination of the hydrate crystal structure(s). Further refinements of the K_{vsi} values were determined by Katz and coworkers (especially Kobayashi) in Chapter 5 of the *Handbook of Natural Gas Engineering* (1959), by Robinson and coworkers (Jhaveri and Robinson, 1965; Robinson and Ng, 1976), and by Poettmann (1984).

1.2.3 Hydrate Crystal Structures and Hydrate Type Definitions

In the late 1940s and early 1950s, von Stackelberg and coworkers summarized two decades of x-ray hydrate crystal diffraction experiments at the University of Bonn. The interpretation of these early diffraction experiments by von Stackelberg (1949, 1954, 1956), von Stackelberg and Müller (1951a,b), Claussen (1951a,b), and Pauling and Marsh (1952) led to the determination of two hydrate crystal structures (sI and sII) shown in Figure 1.5.

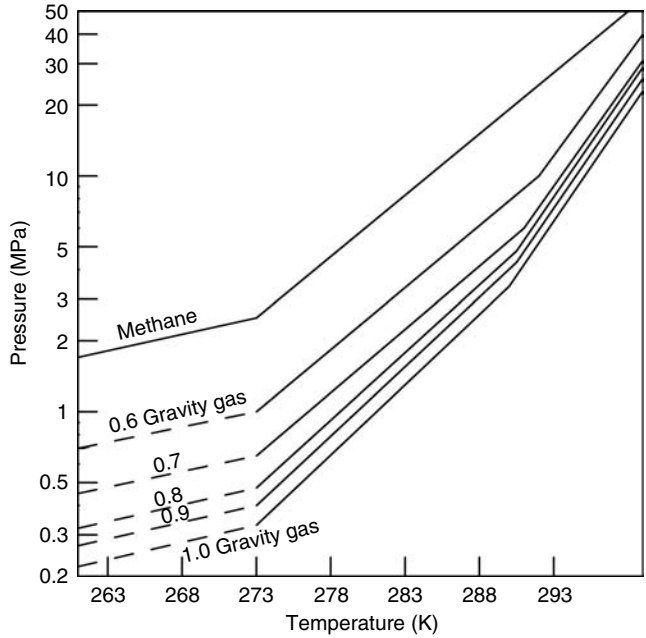

FIGURE 1.4 Gas gravity chart for prediction of three-phase (L_W–H–V) pressure and temperature. (Reproduced from Katz, D.L., *Transactions AIME*, **160**, 140 (1945). With permission.)

During the period from 1959 to 1967, an extensive series of crystallographic studies were performed on sI and sII clathrate hydrates by Jeffrey and coworkers (Mak and McMullan, 1965; McMullan and Jeffrey, 1965) resulting in summary reviews (Jeffrey and McMullan, 1967; Jeffrey, 1984). These studies showed hydrates to be members of the class of compounds labeled "clathrates" by Powell (1948)—after the Latin "clathratus" meaning "to encage."

The existence of a third hydrate structure, structure H (sH) was not discovered until 1987 (Ripmeester et al., 1987). The unit cell of sH is shown in Figure 1.5c. Details of all three unit cells and their constituent cages are given in Chapter 2. Structure H requires both a small molecule such as methane and larger molecules typical of a condensate or an oil fraction. Just after their discovery, Ripmeester et al. (1991) reported the formation of sH with components of gasoline and a light naptha fraction.

About the same time as the initial measurements of sH with methane and adamantane in the Colorado School of Mines (CSM) laboratory by Lederhos et al. (1992), Becke et al. (1992) surmised that they measured the sH equilibrium for methane + methylcyclohexane. Structure H phase equilibria data were reported for binary systems with methane as the help gas (Mehta and Sloan, 1993, 1994, 1996; Thomas and Behar, 1994), with methane and nitrogen as the help gas (Danesh et al., 1994), and binary systems with salt (Hutz and Englezos, 1995).

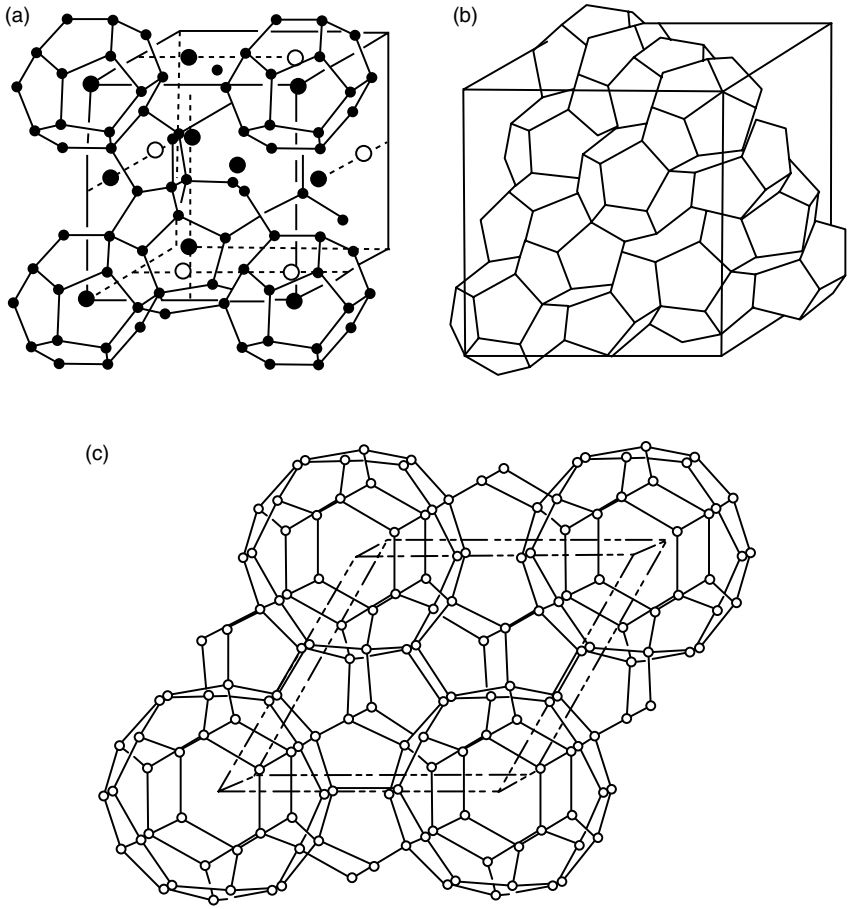

FIGURE 1.5 Hydrate crystal unit structures: (a) sI (McMullan and Jeffrey, 1965), (b) sII (Mak and McMullan, 1965), and (c) sH. (Both figures (a) and (b) were reproduced from the *J. Chem. Phys*. by the American Institute of Physics. With permission.)

A detailed summary of extant sH phase equilibria data and statistical predictions up to 1996 is in the doctoral dissertation of Mehta (1996). Since 1996, more than 30 new sH phase equilibria data sets have been reported, notably from the laboratories of Peters in Delft, the Netherlands; Tohidi in Edinburgh, Scotland; Mori in Yokohama, Japan; and Ohgaki in Osaka, Japan. The different components that form sH hydrate are given in Table 2.7.

All hydrate structures have repetitive crystal units, as shown in Figure 1.5, composed of asymmetric, spherical-like "cages" of hydrogen-bonded water molecules. Each cage typically contains at most one guest molecule, held within the cage by dispersion forces. The hydrate crystalline structures and mechanical properties are discussed in Chapter 2. Throughout this book the common name

"natural gas hydrate(s)" may be used interchangeably with the correct designation "clathrate hydrate(s) of natural gas."

Von Stackelberg and coworkers classified hydrates in a scheme that is still used:

- "Mixed" is the term reserved for hydrates of more than one component, in which cages of the same kind are occupied by two types of molecules, with the restriction of at most one molecule per cage.
- "Double" hydrates was initially reserved for structure II hydrates in which one component is hydrogen sulfide or hydrogen selenide. It has come to mean hydrates in which each size cage is primarily occupied by a different type of molecule. Von Stackelberg proposed that double hydrates were stoichiometric due to their almost invariant composition. Van der Waals and Platteeuw (1959) suggested this invariance was caused instead by azeotropic composition (i.e., hydrate and gas phase compositions are the same).
- A hilfgase or "help gas" hydrate is composed of small components such as nitrogen or methane that would aid in hydrate formation of a second larger component.
- To complete these common definitions, Davidson (1973) proposed that the term "simple" hydrate denote only one guest species.

While sI, sII, and sH are the most common clathrate hydrates, a few other clathrate hydrate phases have been identified. These other clathrate hydrates include new phases found at very high pressure conditions (i.e., at pressures of around 1 GPa and higher at ambient temperature conditions). Dyadin et al. (1997) first reported the existence of a new methane hydrate phase at very high pressures (500 MPa). This discovery was followed by a proliferation in molecular-level studies to identify the structure of the high pressure phases of methane hydrate (Chou et al., 2000; Hirai et al., 2001; Kurnosov et al., 2001; Loveday et al., 2001, 2003).

Up until 1997, it was considered that a maximum of one guest could occupy a hydrate cage. Kuhs et al. (1997) first reported that nitrogen doubly occupies the large cage of sII hydrate. Multiple occupancies were then subsequently reported for argon (Yu et al., 2002), oxygen (Chazallon and Kuhs, 2002), and hydrogen (Mao et al., 2002) in sII hydrate. Further details of the common hydrate structures, new hydrate structures, high pressure hydrate phases, and multiple guest occupancy are given in Chapter 2.

1.2.4 Basis for Current Thermodynamic Models

With the determination of hydrate structure, more rigorous predictive methods were formulated for hydrate thermodynamic property predictions. Barrer and Stuart (1957) initially suggested a statistical thermodynamic approach to determining gas hydrate properties. In a similar yet more successful approach,

van der Waals and Platteeuw (1959) proposed the foundation of the method currently used. This method is perhaps the best modern example for the use of statistical thermodynamics to predict macroscopic properties, such as temperature and pressure, using microscopic properties such as intermolecular potentials. It represents one of the few routine uses of statistical thermodynamics in industrial practice.

The advantage of the method in addition to accuracy is that, in principle, it enables the user to predict properties of mixtures from parameters of single hydrate formers. Since there are only eight natural gas components (yet an infinite number of natural gas mixtures) that form hydrates, the method represents a tremendous saving in experimental effort for the natural gas industry. The modified van der Waals and Platteeuw method is detailed in Chapter 5.

McKoy and Sinanoglu (1963) and Child (1964) refined the van der Waals and Platteeuw method using different intermolecular potentials such as the Kihara potential. Workers at Rice University, such as Marshall et al. (1964) and Nagata and Kobayashi (1966a,b), first fit simple hydrate parameters to experimental data for methane, nitrogen, and argon. Parrish and Prausnitz (1972) showed in detail how this method could be extended to all natural gases and mixed hydrates.

Efforts to improve the original assumptions by van der Waals and Platteeuw were detailed in a review by Holder et al. (1988). Erbar and coworkers (Wagner et al., 1985) and Anderson and Prausnitz (1986) presented improvements to inhibitor prediction. Robinson and coworkers introduced guest interaction parameters into their prediction scheme, as summarized by Nolte et al. (1985). At Heriot-Watt University, the group of Tohidi and Danesh generated another prediction extension, with emphasis on systems containing oil or condensate (Avlonitis et al., 1989; Avlonitis, 1994; Tohidi et al., 1994a).

The van der Waals and Platteeuw method has been extended to flash programs by a number of researchers (Bishnoi et al., 1989; Cole and Goodwin, 1990; Edmonds et al., 1994, 1995; Tohidi et al., 1995a; Ballard and Sloan, 2002). These flash calculations predict the equilibrium amount of the hydrate phase relative to associated fluid phases.

Several companies (D.B.R. Oilphase/Schlumberger, Infochem Computer Services, Ltd., Calsep) have commercially available computer programs (DBR hydrate, Multiflash, PVTSim) for the prediction of hydrate properties, and such methods are incorporated into process flowsheeting programs such as ASPEN™, HYPERCHEM™, and SIMCI™. Researchers in the CSM laboratory (Sloan and Parrish, 1983; Sloan et al., 1987; Mehta and Sloan, 1996) generated new parameters for the prediction of sI, sII, and sH hydrates, which were incorporated into the program, CSMHyd.

The next generation prediction tool to CSMHyd is the Gibbs energy minimization program, CSMGem (Ballard and Sloan, 2002). CSMGem accounts for the water nonideality in the hydrate phase because of volume expansion. A comparison of the absolute hydrate formation temperature error of five common prediction programs is given in Chapter 5, Figures 5.7 and 5.8. The average

absolute errors in temperature for all these prediction programs varied between 0.4 and 0.66 K, which is acceptable for engineering purposes. (The CSMGem program and User's guide are given in the attached CD accompanying this book and the Users' Examples are given in Appendix A.)

Further improvements to the van der Waals and Platteeuw model were to account for the experimental observations of lattice distortion by various guest molecules (von Stackelberg and Müller, 1954; Berecz and Balla-Achs, 1983). Westacott and Rodger (1996) removed the assumption that there is no lattice relaxation by calculating the free energy of the water lattice directly from the phonon properties of crystals. Zele et al. (1999) also accounted for the effect of lattice stretching due to guest size by calculating a new reference chemical potential using molecular dynamics simulations.

The formation of sII hydrate from two sI guests was first measured by von Stackelberg and Jahns in 1954. Detailed studies of the sI/sII transition with natural gas mixtures were performed by Subramanian (2000). Several models have been shown to successfully predict the sI/sII transition of two sI guests (Hendricks et al., 1996; Ballard and Sloan, 2000, 2001; Klauda and Sandler, 2003; Anderson et al., 2005).

The application of *ab initio* quantum mechanical calculations to determine the guest–host intermolecular potential parameters was performed in a parallel effort by the group of Sandler et al. (Klauda and Sandler, 2000, 2003) and the groups of Trout and Tester et al. (Anderson et al., 2004, 2005). Klauda and Sandler (2005) extended their model to predict in-place hydrate formation in nature.

Two heuristics of hydrate formation are as follows:

1. The guest molecule fit within each cavity determines the hydrate stability pressure and temperature.
2. Hydrate formation is a surface phenomenon, when formed on an artificial (laboratory) timescale.

Fundamentals of phase equilibria (i.e., phase diagrams, early predictive methods, etc.) are listed in Chapter 4, while Chapter 5 states the more accurate, extended van der Waals and Platteeuw predictive method. Chapter 6 is an effort to gather most of the thermodynamic data for comparison with the predictive techniques of Chapters 4 and 5. Chapter 7 shows phase equilibria applications to *in situ* hydrate deposits. Chapter 8 illustrates common applications of these fundamental data and predictions to gas- and oil-dominated pipelines.

1.2.5 Time-Dependent Studies of Hydrates

In the mid-1960s, driven by the promise of natural gas hydrates as a substantial energy resource in the USSR, a large experimental effort was begun in a research group led by Makogon (1965, 1981) at the Gubkin Petrochemical and Gas Industry Institute. The area of hydrate kinetics and thermodynamics had priority in the Soviet research program, because the same physics can be applied to problems of

hydrate formation in transmission/processing equipment as well as those of *in situ* hydrates, the third major area of hydrate study. The Russian studies from the 1960s are the first to place emphasis on the kinetics of hydrate formation, both in the bulk phases and in porous environments.

Up until around the mid-1990s, there were only a limited number of groups investigating the time-dependent properties of hydrates. These groups include:

- Lubas (1978) and Bernard et al. (1979) who investigated the formation of hydrates in gas wells.
- Bishnoi and coworkers, who have had the longest tenure in the Western Hemisphere for investigating macroscopic kinetics of hydrate growth and decomposition. The experiments were restricted to low hydrate concentrations in an attempt to avoid heat and mass transfer phenomena (Vysniauskas and Bishnoi, 1983a,b; Kim, 1985; Englezos et al., 1987a,b; Englezos and Bishnoi, 1988a,b; Parent, 1993; Natarajan et al., 1994; Malegaonkar et al., 1997).
- Holder et al. (Holder and Angert, 1982a,b; Holder and Godbole, 1982; Holder et al., 1984a,b).
- Sloan and coworkers (Selim and Sloan, 1985, 1987, 1989; Ullerich et al., 1987; Yousif et al., 1990; Long and Sloan, 1996; Long et al., 1994; Lederhos et al., 1996; Lekvam and Ruoff, 1997).

Since around the mid-1990s, there has been a proliferation of hydrate time-dependent studies. These include macroscopic, mesoscopic, and molecular-level measurements and modeling efforts. A proliferation of kinetic measurements marks the maturing of hydrates as a field of research. Typically, research efforts begin with the consideration of time-independent thermodynamic equilibrium properties due to relative ease of measurement. As an area matures and phase equilibrium thermodynamics becomes better defined, research generally turns to time-dependent measurements such as kinetics and transport properties.

This growth in activity, investigating the time-dependent hydrate properties, has also been largely driven by hydrate technology in oil/gas flowlines (flow assurance) shifting from hydrate avoidance to hydrate risk management. Hydrate avoidance involves preventing hydrates from forming by avoiding the hydrate thermodynamic stability zone. Hydrate risk management, however, involves the use of transient methods to delay hydrate formation or prevent hydrate particles from agglomerating, thus preventing pipeline blockages. A further motivation for performing time-dependent hydrate studies is the increasing interest in assessment and production of energy from natural hydrates in permafrost and oceanic deposits.

Measurement and modeling of time-dependent hydrate properties is clearly far more challenging than time-independent (thermodynamic) hydrate properties. Although significant advances have been achieved in measurement and modeling

of hydrate formation, there are still significant knowledge gaps in this area to be filled before a reliable transient hydrate model can be developed.

Macroscopic measurements that have been applied to hydrate formation and decomposition include light scattering and calorimetry. Light scattering has been applied to measure the hydrate particle size distribution during formation and decomposition (Nerheim et al., 1992, 1994; Monfort and Nzihou, 1993; Parent, 1993; Yousif et al., 1994; Parent and Bishnoi, 1996; Clarke and Bishnoi, 2000, 2001, 2004; Turner, 2005). Differential scanning calorimetry has been used to measure hydrate formation and hydrate particle agglomeration in water-in-oil emulsions (Dalmazzone et al., 2005; Lachance, J., unpublished results) and water-in-porous glasses (T. Varma-Nair, Personal Communication, March 23, 2006).

Mesoscale imaging techniques have been applied to hydrate formation and decomposition processes. Specifically, scanning electron microscopy (SEM) has been used to investigate the hydrate grain texture and pore structure recovered at different stages of hydrate formation (Staykova et al., 2003; Stern et al., 2005). Magnetic resonance microimaging has also been performed to obtain spatial, time-resolved images during hydrate formation (Moudrakovski et al., 2004). X-ray computed tomography (CT) has been applied to track the spatial progression of the dissociation front in hydrate samples and to characterize the heterogeneity of a hydrate core during formation and decomposition (Freifeld et al., 2002; Gupta et al., 2006).

Microscopic time-resolved measurements of the hydrate phase during gas hydrate formation, decomposition, and inhibition began only in the mid-1990s. These techniques include *in situ* synchrotron x-ray diffraction (Koh et al., 1996; Klapproth et al., 2003; Uchida et al., 2003), neutron diffraction (Henning et al., 2000; Koh et al., 2000; Halpern et al., 2001; Staykova et al., 2003), Raman spectroscopy (Subramanian and Sloan, 2002; Komai et al., 2004), and NMR spectroscopy (Moudrakovski et al., 2001; Kini et al., 2004; Gupta et al., 2007).

Computer simulations provide a means of examining the early stages of hydrate formation (nucleation) on a molecular level (Baez and Clancy, 1994; Radhakrishnan and Trout, 2002; Moon et al., 2003, 2005). Computer simulation has also been applied to study hydrate dissociation (Baez and Clancy, 1994; English and MacElroy, 2004) and the effects on dissociation kinetics of external electromagnetic fields (English and MacElroy, 2004).

The state-of-the-art of the fundamentals of hydrate formation and decomposition processes is reviewed in Chapter 3. Because many time-dependent data appear to be a function of different apparatuses, time-dependent data are not listed in a separate chapter analogous to Chapter 6 for thermodynamic data. However, applications of transient methods for preventing or remediating hydrate blockages in pipelines are discussed in Chapter 8. In addition, a computer program, CSMPlug, and a User's Guide are provided on the CD accompanying this book (with Users' Examples in Appendix B) to determine the time for plug removal in flowlines.

1.2.6 Work to Enable Gas Production, Transport, and Processing

Since 1970, hydrate research has been motivated by production and processing problems in unusual environments, such as the North Slope of Alaska, in Siberia, in the North Sea, and in deep ocean drilling. For example, problems of hydrate formation in drilling applications reported by Barker and Gomez (1989) stimulated measurements of hydrate formation in oil-based drilling fluids (Grigg and Lynes, 1992) and in water-based drilling fluids (Cha et al., 1988; Hale and Dewan, 1990; Kotkoskie et al., 1992; Ouar et al., 1992), resulting in a prediction method to prevent future occurrences.

Kobayashi and coworkers (Sloan et al., 1976; Song and Kobayashi, 1982, 1984) and workers in the CSM laboratory (Sloan et al., 1986, 1987) have measured concentrations of water in hydrate-forming fluid phases in equilibrium with hydrates (when there is no free-water phase present) for application in single phase pipelines in cold regions, such as the North Slope or subsea. The trend in deepwater pipelines appears to be toward multiphase transmission (Shoup and Shoham, 1990) and their inhibition.

In Scotland, Danesh, Todd, and coworkers measured the inhibition of multiphase systems with methanol (Avlonitis, 1994) and mixed electrolyte solutions (Tohidi et al., 1993, 1994a, 1995b,c). They also performed the most comprehensive study of systems with heavy hydrocarbons such as might be produced/transported in the North Sea (Avlonitis et al., 1989; Tohidi et al., 1993, 1994b, 1996) including systems with structure H hydrate formers.

In Canada, Ng and Robinson (1983, 1984) and Ng et al. (1985a,b, 1987) have performed the most comprehensive measurements of aqueous phase concentrations of methanol and glycols needed to inhibit hydrates formed from both the gas and condensed hydrocarbon phases. Ng and Chen (1995) have provided data for solubility of inhibitors in other phases. Inhibition of methane and carbon dioxide hydrates by mixed electrolytes has been studied by Englezos and Bishnoi (1988a,b) and Dholabhai et al. (1991), and separately in Bishnoi's laboratory (Dholabhai et al., 1993a,b, 1994, 1996; Tse and Bishnoi, 1994) and in Englezos' laboratory (Englezos, 1992a,b,c,d; Englezos and Ngan, 1993).

Bishnoi's laboratory has measured hydrate formation under shutdown conditions (Jamaluddin et al., 1991) and in gas and condensate pipelines (Dholabhai et al., 1993a,b). Norsk Hydro's experience with hydrate formation in pipeline design and operation is described by Stange et al. (1989), Lingelem and Majeed (1992), and Lingelem et al. (1994). Dorstewitz and Mewes (1993, 1995) present German experiences with hydrate formation in small flow loops. At the SINTEF multiphase flow facility, extensive measurements of hydrate formation and dissociation have been carried out by Austvik (1992), Lund et al. (1996a,b), and Lysne (1994, 1995). A comprehensive study of hydrate formation in pipelines involved the formation/dissociation of 17 hydrate plugs in the Tommeliten Field (Austvik et al., 1995). Hydrate blockage formation was also studied in the Werner–Bolley gas line (Hatton and Kruka, 2002). Conceptual models and case studies

of how industrial hydrate plugs are formed and how they can be prevented are described in Chapter 8.

In the 1990s, two types of chemical inhibitor technologies (antiagglomerants and kinetic inhibitors) were introduced, as a means of methanol replacement. The antiagglomerant method, for emulsifying the water phase internal to a liquid hydrocarbon phase using a surfactant, was pioneered by Behar et al. (1991). The second technology requires kinetic inhibition by preventing crystal growth for a period exceeding the free-water residence time in a pipeline, and was first proposed by the CSM laboratory (Sloan, 1991) with chemical inhibitors listed by Long et al. (1994) and Lederhos et al. (1996). Details of both methods are given in Chapter 8.

Hydrate formation is a substantial problem in deepwater production and flowlines. Pipelines that transport condensed hydrocarbon phases such as gas condensate or crude oil have limited possibilities for removing hydrates once the plugs have formed. Earlier work by Scauzillo (1956), indicating that formation may be inhibited by the input of hydrocarbon liquids, cannot be confirmed by thermodynamic calculations, and Skovborg (1993) has found counter-examples. Thus, the construction of large-scale pilot flow loops have been completed by large corporations such as ExxonMobil (Reed et al., 1994), Tulsa University, and Institut Francais du Petrole. Such experiments are discussed briefly in Chapter 6.

Subsea gas and oil production, processing, and transportation since the past decade are moving to deeper waters (e.g., 6500–7200 ft in the Canyon Express system). These deepwater conditions are associated with higher pressures and lower temperatures, which are well within the hydrate stability zone. For these deepwater facilities, traditional thermodynamic methods (heating, thermodynamic inhibitor injection, line burial) for preventing hydrate formation in pipelines and related industrial equipment are becoming increasingly uneconomic. Therefore, the industry is moving to risk management approaches that are based on time-dependent phenomena. The risk management tools for preventing hydrate blockages include kinetic inhibitors, antiagglomerants, cold slurry flow, or combinations of these tools. The application of these methods to pipelines is discussed in Chapter 8, along with a number of industrial case studies. The application of plug remediation methods, such as depressurization, is also described in Chapter 8. A fundamental requirement for risk management is the availability of reliable and accurate transient formation and decomposition models to predict when hydrates will form and decompose, respectively. Fundamental knowledge on hydrate formation and decomposition, which is needed to develop such models, is discussed in Chapter 3.

1.2.7 Hydrates in Mass and Energy Storage and Separation

Several researchers have studied hydrates as a means of separating gases and water, and as a means of storing mass and energy. Because many of these studies are not typically with natural gas components, they are only given cursory attention here. A few details of this section are to be found in Chapters 4 and 8.

The storage and transportation of natural gas in hydrate form was investigated by Benesh (1942), Miller and Strong (1946), Parent (1948), and Dubinin and Zhidenko (1979). Hydrate storage of gases has assets of lower storage space and low pressures for safety. Methane hydrate has an energy density equivalent to a highly compressed gas, but is less dense than liquefied natural gas (LNG).

In the 1990s, Gudmundsson et al. (1994, 1995) and Gudmundsson and Parlaktana (1992) showed favorable economics for gas in hydrates using higher storage temperatures and suggested that this was enabled by the ice barrier formed by dissociated hydrates. Gudmundsson and Borrehaug (1996) proposed to ship natural gas in hydrated form, rather than in liquefied natural gas (LNG) tankers and suggested that the economics were favorable. The basic concept proposed by Gudmundsson to transport stranded gas in hydrated form has been extended by researchers from Mitsui Shipbuilding in conjunction with the Japanese Maritime Research Institute (Nakajima et al., 2002; Shirota et al., 2002; Takaoki et al., 2005). The hydrated gas is stored in pellet form at low temperatures, with the stability of the pellets aided by the concept of anomalous preservation first reported by Stern and coworkers (2001).

Hydrates as a storage material for hydrogen have been explored by a number of research groups. Dyadin et al. (1999) were the first to discover that hydrogen can form a clathrate hydrate at high pressures (1.5 GPa). Structure confirmation of hydrogen hydrate was performed by Mao et al. (2002), where hydrogen was shown to multiply occupy the cavities of structure II hydrate at high pressures (300 MPa at 350 K). Florusse et al. (2004) demonstrated that hydrogen can be stabilized in the clathrate framework at pressures over two orders of magnitude lower than for pure hydrogen hydrate by using a second guest, tetrahydrofuran.

The first Soviet hydrate separation available in the Western literature was that of Nikitin (1936, 1937, 1939, 1940), who developed a method for separating rare gases by using SO_2 hydrates. Nikitin was also the first to suggest a guest/host lattice structure for hydrates. In his review, Davidson (1973) notes that the capacity of host lattices for guests is equivalent to the best activated carbons or zeolites. Barrer and Edge (1967) showed fractionation to be effective when aided in hydrate formation by chloroform. Tsarev and Savvin (1980) and Trofimuk et al. (1981, 1982) suggested other hydrate separations of light gas components.

Kang and Lee (2000) showed that carbon dioxide could be removed from flue gas using hydrate-based gas separation. A small amount of tetrahydrofuran (THF) was added to promote hydrate formation and hence this separation process. Hydrate formation has also been used to separate hydrogen sulfide (Yamamoto et al., 2002), HCFCs, and HFCs (Okano et al., 2002) from waste streams.

Hydrates as a means of cool energy storage have been extensively investigated in the United States (Ternes and Kedl, 1984; Carbajo, 1985a,b; Ternes, 1985) and in Japan (Mori and Mori, 1989a,b; Tanii et al., 1990; Akiya et al., 1991; Mori and Isobe, 1991; Nakazawa et al., 1992; Ogawa et al., 2005). Conceptually, electrical "peak shaving" requires the use of excess electrical capacity to generate hydrates during evening hours. The cool energy is recovered by endothermic melting of hydrates in daylight hours. Hydrates are useful for energy storage and recovery,

because (1) their heat of fusion approximates that of ice and (2) hydrates can be formed at temperatures above the ice point for a better refrigeration coefficient of performance.

Another separation application of hydrates is the desalination of seawater. The 15-year effort of Barduhn and coworkers is particularly notable (Barduhn et al., 1962; Barduhn, 1967, 1968, 1975; Barduhn and Rouher, 1969; Vlahakis et al., 1972). Most of the early desalination work has been reported in six Desalination Symposia Proceedings (Udall et al., 1965; Delyannis, 1967; Delyannis and Delyannis, 1970, 1973, 1976, 1978). These early attempts to use gas hydrates for seawater desalination involved mixing gas and seawater so that all the gas was consumed. As a result, a hydrate–brine slurry was formed that was essentially unwashable. Researchers at Marine Desalination Systems have attempted to circumvent this problem by increasing the mass to surface area of hydrate crystallites formed, such that adsorption of salt becomes insignificant (Max, 2001, 2002; Osegovic et al., 2005).

Englezos and coworkers (Gaarder et al., 1994; Gaarder and Englezos, 1995) have used hydrates of propane and carbon dioxide to remove water from aqueous paper mill effluents. The process seems technically viable and the contaminants in the aqueous stream did not inhibit hydrate formation significantly.

Hydrates have also been applied to foodstuffs in Fennema's laboratory (Huang et al., 1965, 1966; van Hulle et al., 1966; van Hulle and Fennema, 1971, 1972; Scanlon and Fennema, 1972). A process for producing edible hydrates of carbon dioxide was patented by Baker (1993).

Hydrates have further applications in bioengineering through the research of John and coworkers (Rao et al., 1990; Nguyen, 1991; Nguyen et al., 1991, 1993; Phillips et al., 1991). These workers have used hydrates in reversed micelles (water-in-oil emulsions) to dehydrate protein solutions for recovery and for optimization of enzyme activity, at nondestructive and low-energy conditions.

1.3 Hydrates as an Energy Resource

A world atlas, giving sites with evidence of hydrate deposits, both onshore and offshore, is presented in Chapter 7, Figure 7.2. Since each volume of hydrate can contain as much as 184 volumes of gas (STP), hydrates are currently considered a potential unconventional energy resource. Table 1.4 lists the milestones accomplished to further our knowledge on naturally occurring hydrates.

Estimates of world hydrate reserves, given in Chapter 7 are very high, but uncertain. This is reflected by the large variation in the estimated values over the period 1990–2005 (0.2×10^{15}–120×10^{15} m^3 of methane at STP). However, even with the most conservative estimates, it is clear that the energy in these hydrate deposits is likely to be significant compared to all other fossil fuel deposits. Chapter 7 presents the concepts for hydrates in Earth. These concepts are illustrated with field case studies involving the assessment of the hydrate resource (in the Blake Bahama Ridge and Hydrate Ridge) and the production of energy from hydrates (in the Messoyakha and Mallik 2002).

TABLE 1.4
Hydrate Milestones since 1965—*Hydrates in Nature*

1965	Makogon and coworkers announce hydrates in Siberian permafrost
1969	Ginsburg begins study of hydrates in geological environments
1969	Russians begin a decade of producing gas in Messoyakha, possibly from hydrates
1972	ARCO–Exxon recover hydrated core from Alaskan well
1974	Bily and Dick report hydrates in Canada's MacKenzie Delta
1980	Kvenvolden publishes survey of worldwide hydrates
1980	Dillon and Paull begin work on hydrates in Atlantic Ocean
1982	Brooks begins recovery of *in situ* biogenic and thermogenic hydrates from Gulf of Mexico
1983	Collet presents analysis of ARCO–Exxon drilling logs study for hydrated core
1988	Makogon and Kvenvolden separately estimate *in situ* hydrated gas at 10^{16} m^3
1988	Kvenvolden and Claypool estimate that hydrate decomposition does not contribute to greenhouse effect
1994	Sassen discovers *in situ* sH hydrates in Gulf of Mexico
1996	Microbiological study of 12 sites in Atlantic and Pacific Oceans and Mediterranean Sea from cores collected during 1986–1996 by Ocean Drilling Program (ODP) (Parkes et al., 2000)
1998	Pilot drilling, characterization, and production testing of hydrates began in permafrost regions (e.g., in Mallik 2L-38 well in Canada)
2000	Methane hydrate R&D Act of 2000 (U.S. Congress)
2002	Mallik 5L international permafrost field experiment on Richards island in MacKenzie Delta of Canada concluded that hydrates could be economically recovered at high concentrations
2002	ODP Leg 204 drilling off Hydrate Ridge in Oregon (Sahling et al., 2002, Tréhu et al., 2003, 2006a)
2005	IODP Expedition to Cascadia Margin (Riedel et al., 2006)
2006	First *in situ* ocean Raman measurements at Barkley Canyon off Vancouver Island (Hester 2007, Hester et al., 2007)
2006	Indian National Gas Hydrate Program (NGHP) expedition of ocean hydrates, recovering 493 core samples

The following are three general heuristics for naturally occurring ocean hydrates (Tréhu et al., 2006a,b):

1. Water depths of 300–800 m (depending on the local bottom water temperature) are sufficient to stabilize the hydrate.
2. Only a few sites contain thermogenic hydrates (containing CH_4 + higher hydrocarbons), such as in the Gulf of Mexico and in the Caspian Sea. These deposits tend to comprise large accumulations near the seafloor.
3. Hydrates are typically found where organic carbon accumulates rapidly, mainly in continental shelves and enclosed seas. These are biogenic hydrates (containing CH_4, formed from bacterial methanogenesis).

1.3.1 *In Situ* Hydrates

An overview of the Soviet hydrate literature, with particular emphasis on natural occurrences, was published by Krason and Ciesnik (1985). Later, Makogon (1994),

who has worked for five decades in hydrates, published a review of Soviet hydrates. He reported that the early Russian researchers hypothesized that hydrates existed in the northern permafrost, suggested *in situ* formation mechanisms, and discussed the possibility of hydrate formation associated with coals. A review of gas hydrates in the Okhotsk Sea in Russia proposes hydrate prone areas on the basis of seismic and core sampling measurements (Matveeva et al., 2004).

The work by Ginsburg and Soloviev (1995) has estimated worldwide hydrate reserves in amounts consistent with the most commonly cited Russian hydrate reserve estimations by Trofimuk et al. (1980); namely 5.7×10^{13} m^3 of gas in continental hydrates and 3×10^{15} m^3 of gas in hydrates in oceans. Note that, while both the estimated amounts are controversial, there are two orders of magnitude less hydrates on land than in the oceans.

In 1967, the Soviets discovered the first major hydrate deposit in the permafrost (Makogon, 1987). The hydrate deposit in the Messoyakha field has been estimated to involve at least one-third of the entire gas reservoir, with depths of hydrates as great as 900 m. During the decade beginning in 1969, more than 5×10^9 m^3 of gas were produced from hydrates in the Messoyakha field. The information in the Soviet literature on the production of gas from the Messoyakha field is discussed in Chapter 7. Table 7.4 in Chapter 7 also lists other locations in Russia, including the Black Sea, Caspian Sea, and Lake Baikal, where evidence for hydrates has been provided from sample recovery or BSR (bottom simulating reflectors) data.

The majority of the Soviet publications are by nine authors, listed here in decreasing order with respect to their number of publications: Y.F. Makogon, G.D. Ginsburg, N.V. Cherskii, V.P. Tsarev, A.A. Trofimuk, V.A. Khoroshilov, S. Byk, V.A. Fomina, and B.A. Nikitin. In a review of the Russian literature, Krason and Ciesnik (1985) indicate that other Soviet authors have only a small number (<5) of publications. Makogon (1994) notes that over ten monographs in Russian have been published on the topic; he has available a Soviet Bibliography (in Russian) that cites a number of hitherto unknown hydrate references.

In the Western Hemisphere, in 1972, a core of hydrates was recovered from the ARCO–Exxon Northwestern Eileen Well Number Two in West Prudhoe Bay, Alaska (Collett, 1983). Also in 1972, hydrates were found when drilling an Imperial well in Canada's MacKenzie Delta (Bily and Dick, 1974). Instances such as the above have caused further geologic investigations of permafrost hydrates in Russia, Canada, and Alaska. Using logs from the ARCO–Exxon well, Collett (1983) evaluated possible hydrate occurrences in 125 wells in the North Slope of Alaska. Weaver and Stewart (1982) and Franklin (1983) indicated well log responses in several wells in the Arctic Archipelago region. Judge (1982) and Collett (1995) summarized *in situ* hydrate resources in North America.

The Deep Sea Drilling Project (DSDP), currently the Integrated Ocean Drilling Program (IODP) of the National Science Foundation, has undertaken the most systematic evaluation of ocean hydrate deposits. The DSDP has recovered hydrate cores in the deep oceans from both coasts of the United States, from the Mid-America Trench off Guatemala, and off the coast of Peru. A total of 23 oceanic hydrate cores have been recovered, including the Gulf of Mexico and three Soviet

water bodies. Even with these core recoveries, most of the evidence of hydrates in oceans had been inferential. Bottom Simulating Reflectors (BSRs) have been used to infer the existence of hydrates in most of the locations shown in Figure 7.2. Much of the oceanic geochemical and geophysical research for these determinations has been done by Kvenvolden and McMenamin (1980), Kvenvolden and Claypool (1981), Kvenvolden (1982, 1983, 1985a,b, 1995), Kvenvolden et al. (1984, 1993a,b), Dillon et al. (1980, 1994), Dillon and Paull (1983), Paull and Dillon (1981), Paull et al. (1995, 1997, 2005), as well as extensive studies in the Gulf of Mexico by Brooks et al. (1984, 1985a,b, 1987).

Direct evidence of ocean hydrates has been obtained using *in situ* Raman measurements in Barkley Canyon, off Vancouver Island (Hester, 2007). The occurrence of sH in natural hydrate deposits has been inferred from gas analyses of recovered core samples from the Gulf of Mexico (Sassen and Macdonald, 1994; Yousuf et al., 2004) and confirmed by diffraction and NMR for samples from Barkley Canyon (Pohlman et al., 2005; Lu et al., 2007).

Drilling results in the Blake Bahama Ridge have given promise for recovery of energy from hydrate reserves. Hydrate recovery results from ODP Leg 164 in the Blake Bahama Ridge seem to confirm the large resource estimation (Paull et al., 1997, 2000; Lorenson and Collett, 2000).

Following on from the geochemical and geophysical work performed on ODP Leg 146 (Westbrook et al., 1994), Leg 204 focused on an area known as Hydrate Ridge, which is located in the southern Cascadia accretionary margin where the Juan de Fuca plate converges to the North American plate. Leg 204 was undertaken to help evaluate the economic potential of hydrates, the role of hydrates as a geohazard, and their impact on climate (Trehu et al., 2003). IODP Leg 311 then proceded with hydrates being explored in the northern Cascadia accretionary margin (Riedel et al., 2005) in a similar geological setting to Hydrate Ridge. The primary goal of the IODP Leg 311 expedition was to constrain geological models for the formation of the gas hydrates.

Starting in 1998, pilot drilling, characterization, and production testing were performed in permafrost regions in the Mallik well in Canada, with the international field experiment concluding in 2002. The Mallik 2002 well demonstrated proof of concept that it is possible to recover energy from permafrost hydrates combining dissociation techniques of depressurization and thermal stimulation. Further details of sample recovery and detection and inference of in-place hydrates from BSRs from the above-mentioned locations and other sites (including the Mackenzie Delta, Hydrate Ridge, Northern Cascadia Margin, and many more) are given in Chapter 7.

The Japanese initiated a National Project to drill hydrates in the Nankai Trough. This included coring and seismic work to assess the resource (Ministry of Economy, Trade and Industry, METI-sponsored project in 1999–2000; Japan National Oil Company, JNOC, and Japan Petroleum Exploration Corporation, JPEX, studies in 1997–2000). Remote operated vehicle and manned submarine explorations have been employed to perform the resource assessments (Marine Science and Technology, JAMSTEC). The energy potential of significant hydrate deposits in

the Okhotsk Sea and the Nankai Trough has led to the Japanese making substantial investments in hydrate research (JNOC, 2000).

The Indian National Gas Hydrate Program (NGHP) expedition of ocean hydrates was performed in 2006. During this expedition, over 494 cores were recovered at depths ranging from 952 to 2674 mbsf. The cores were distributed to a number of research laboratories (including USGS, GFZ, CSM, NRC) for meso- and molecular-level analysis on the hydrate samples (T. Collett and R. Boswell, Personal Communication, August 31, 2006).

1.3.2 Investigations Related to Hydrate Exploration and Recovery

The determination of *in situ* hydrates spawned a wave of research to measure hydrate properties needed for geological research and gas recovery. Several measurements were made of sonic velocity and thermal conductivity of hydrates in sediments (e.g., Stoll and Bryan, 1979; Pearson et al., 1984; Asher, 1987; Waite et al., 2005), while others measured the calorimetric properties (e.g., Rueff, 1985; Handa, 1986a,b,c,d; Rueff et al., 1988) needed to estimate dissociation energy. Davidson (1983) summarized hydrate properties as being similar to ice, with a few notable exceptions. Chapter 2 presents comparisons of physical property measurements of ice and hydrate.

Along with the measurements of hydrate properties came several studies to determine the recoverability of gas from hydrates beneath the permafrost. Kamath and coworkers, in a research effort spanning over more than a decade, studied hydrate drilling and recovery in Alaska (Kamath, 1984; Kamath et al., 1984; Kamath and Godbole, 1987; Kamath and Holder, 1987; Roadifer et al., 1987a,b; Godbole et al., 1988; Nadem et al., 1988; Sira et al., 1990; Kamath et al., 1991; Sharma et al., 1991, 1992).

Soviet researchers indicated that thermal stimulation from above the ground was not economically viable. Trofimuk et al. (1982) suggested alternatives of pressure reduction, inhibitor injection, geothermal stimulation, or *in situ* combustion techniques. Recovery techniques modeled in the Western Hemisphere were by either pressure reduction or thermal stimulation. The first of these was by McGuire (1982), followed by Holder et al. (1984a), Burshears et al. (1986), and workers in the CSM laboratory (Selim and Sloan, 1985, 1987, 1989; Yousif et al., 1988, 1990).

Hydrate dissociation models that were later developed to simulate hydrate recovery techniques include numerical models by Masuda et al. (1997), Moridis (2002), and Hong et al. (2003); analytical models by Makogon (1997) and Tsypkin (2000). The details of these models are given in Chapter 7.

There have been significant developments in logging and coring tools for assessing amounts of hydrated gas in permafrost and oceanic locations. Logging tools including calliper, γ-ray density, resistivity, neutron porosity, drilling logs, and NMR are used to determine the hydrate depth and the concentration of hydrate gas to some extent. Secondary tools including infrared temperature sensing, gas evolution from cores, pore water chlorinity decrease, and x-ray computed

tomography (CT) of cores provide the extent and concentration of the hydrate reservoir. The use of pressurized coring tools is becoming increasingly recognized as a key (Tréhu et al., 2006b) to help maintain the integrity of the recovered sample core compared to unpressurized coring tools. Further details of the use of these logging and coring tools are given in Chapter 7.

1.4 Environmental Aspects of Hydrates

Other "natural" hydrates have been suggested during the past few decades. Miller (1974) concluded that hydrates of carbon dioxide were on Mars, and Pang et al. (1983) indicated that the E rings of Saturn were hydrates. Delsemme and Miller (1970), Mendis (1974), and Makogon (1987) suggested that hydrates exist in comets; in particular, carbon dioxide and water in comets were combined in the form of hydrates.

Shoji and Langway (1982) described air hydrates found with ice cores off Greenland, while Tailleur and Bowsher (1981) indicated the presence of hydrates associated with coals in permafrost regions. Hondoh (1996) suggested that deep ice hydrates of air in Antarctica can be used to predict the Earth's ancient climate. Such hydrates are formed from air imbedded in snowfall and have been buried at pressure for hundreds of thousands of years. Rose and Pfannkuch (1982) have considered the applicability of the "Deep Gas Hypothesis" to the origin of methane in hydrates.

Kvenvolden (1988) provided the first estimates that hydrate decomposition should not contribute significantly to the greenhouse effect. Despite these estimates, there have been suggestions in the popular press (Leggett, 1990) that hydrates may contribute to an exponentially growing feedback loop for global warming. In 1996, a conference on hydrate decomposition and contribution to global warming (Henriet, 1996) indicated that the uncertainties in the existing climate models were significantly greater than the likely contribution of hydrates to global warming.

More recently, there has been renewed and increased interest in the role of methane hydrate as a potential source for climate change. Kennett et al. (2003) reported the somewhat controversial "clathrate gun" hypothesis (also known as the "late Quaternary climate change"), which suggests that methane released from methane hydrate around 15,000 years ago has resulted in immense global warming. Significant efforts have been initiated by German scientists to investigate the role of hydrates in climate change (Lovell, 2006). There are also ongoing investigations of the role of gas hydrates in the carbon cycle (Dickens, 2001, 2003; Milkov, 2004, 2005).

1.5 Safety Aspects of Hydrates

There are four safety aspects associated with hydrates that should be mentioned in order of decreasing importance:

1. When hydrates plug pipelines they are usually removed through depressurization, sometimes depressurizing only one side of the plug.

Chapter 8 gives the evidence that plugs dissociate first at the pipewall, thus becoming a projectile in a pipeline with substantial momentum, relative to the gas phase. Lysne (1995, p. 78) lists three such incidences in which hydrate projectiles erupted from pipelines at elbows and caused the loss of three lives and over US$7 million in capital costs. Where possible, depressurization from both sides of a plug is recommended.

2. In drilling through hydrates (Roadifer et al., 1987a) and in drilling normal wells, hydrates have jeopardized the safety of drillers and plugged blowout preventers (Barker and Gomez, 1989) necessitating the use of special drilling precautions and drilling muds.
3. In the past, hydrates have been associated with significant movement of earth (seafloor slumps) in deepwater ocean environments. Notably, Bugge et al. (1988), Schmuck and Paull (1993), MacDonald et al. (1994), and Paull and Dillon (2001) have described both large and small Earth movements associated with hydrates. Concerns have been expressed (Campbell, 1991) about the effect of hydrates on foundations of platforms and pipelines, as well as offshore drilling. Hydrates as geohazards are discussed in Section 7.8.
4. Hydrates have also been the source of speculation of long-range climate change and safety in the greenhouse effect (Leggett, 1990). Hydrates in climate change are discussed in Section 7.8.

Speculations about the role of hydrates in disasters such as the Piper Alpha platform (Boniface, 1990) or Lake Nyos (Rogers and Yevi, 1996) are characterized as hypotheses that are not discussed in this book.

1.6 Relationship of this Chapter to those that Follow

With the overview provided by the current chapter, the remainder of this book provides a detailed development of research conducted in the above areas, together with examples of industrial interest. A brief description of the following chapters is given as follows:

Chapter 2 presents a comprehensive description of the chemical structure of hydrates and, by inference, begins to consider molecular and macroscopic properties with emphasis on similarities and differences from ice. Discussion is also given to the transport properties of hydrates.

Chapter 3 presents the fundamentals of the time-dependent hydrate phenomena of nucleation, growth, and decomposition. These fundamentals are presented with an objective of understanding how hydrate formation and decomposition occur, such that this knowledge may be applied to a range of hydrate applications, such as flow assurance, storage, separation, or gas production from hydrate reservoirs.

Chapter 4 provides phase diagrams and simple prediction schemes for each of the hydrate phase diagram regions.

Chapter 5 details the modified statistical thermodynamic prediction method of van der Waals and Platteeuw (1959). The application of molecular simulation methods to hydrates is outlined in Section 5.3.

Chapter 6 provides a listing of the hydrate phase equilibria and transport property data since 1934 for natural gas pure components, mixtures, and inhibitors together with common measurement techniques. Details of hydrate phase measurements using spectroscopy and diffraction are also discussed.

Chapter 7 discusses *in situ* hydrates in the oceans and permafrost. Seven key concepts are presented for hydrates in nature. These concepts are illustrated in four field case studies for hydrate assessment (Blake Bahama Ridge, Hydrate Ridge) and production (Messoyakha and Mallik, 2002).

Finally, Chapter 8 considers some common industrial problems (and solutions) concerning hydrates in processing, transportation, and production. The phenomena of how hydrate plugs form and how they are prevented or simulated are illustrated by several industrial case studies.

The appendices and the computer programs (on the accompanying CD-ROM) deal with predictions of hydrate plug dissociation (CSMPlug) and hydrate phase equilibria and structure (CSMGem).

References

Akiya, T., Owa, M., Nakaiwa, M., Tanii, T., Nakazawa, K., Ando, Y., presented at *26th Annual IECEC*, Boston, MA, October 3–9 (1991).

Alexeyeff, W., *Ber.*, **9**, 1025 (1876).

Anderson, B.J., Bazant, M.Z., Tester, J.W., Trout, B.L., *J. Phys. Chem. B*, **109**, 8153 (2005).

Anderson, B.J., Tester, J.W., Trout, B.L., *J. Phys. Chem. B*, **108**, 18705 (2004).

Anderson, F.E., Prausnitz, J.M., *AIChE J.*, **32**, 1321 (1986).

Asher, G.B., *Development of a Computerized Thermal Conductivity Measurement System Utilizing the Transient Needle Probe Technique: An Application to Hydrates in Porous Media*, Dissertation, Colorado School of Mines, Golden, CO (1987).

Austvik, T., *Hydrate Formation and Behavior in Pipes*, D. Ing. Thesis, University of Trondheim, Trondheim, Norway (1992).

Austvik, T. (ed.), in *Proc. Fifth International Conference on Natural Gas Hydrates*, Trondheim, Norway, June 13–16 (2005).

Austvik, T., Hustvedt, E., Meland, B., Berge, L.I., Lysne, D., presented at *Seventh International Conference on Multiphase Production*, BHRA Group Conference Series Publication 14, Cannes, France, June 6–7 (1995).

Avlonitis, D.A., *Chem. Eng. Sci.*, **49**, 1161 (1994).

Avlonitis, D.A., Danesh, A., Todd, A.C., Baxter, T., presented at *Fourth BHRA International Conference on Multiphase Flow Offshore*, Nice, France, June 15 (1989).

Baez, L.A., Clancy, P., Annals of the New York Academy of Sciences, **713**, 177 (1994).

Baker, T.P., Intl. Patent Appl. PCT/EP93/01837 (1993).

Ballard, A.L., Sloan, E.D., *Chem. Eng. Sci.*, **55**, 5773 (2000).

Ballard, A.L., Sloan, E.D., *Chem. Eng. Sci.*, **56**, 6883 (2001).

Ballard, A.L., Sloan, E.D., *J. Supramol. Chem*., **2**, 385 (2002).
Barduhn, A.J., *Chem. Eng. Prog*., **63**, 98 (1967).
Barduhn, A.J., *Desalination*, **5**, 173 (1968).
Barduhn, A.J., *Chem. Eng. Prog*., **71**, 80 (1975).
Barduhn, A.J., Rouher, O.S., *Desalination*, **6**, 57 (1969).
Barduhn, A.J., Towlson, H.E., Hu, Y.C., *AIChE J*., **8**, 176 (1962).
Barker, J.W., Gomez, R.K., *J. Petrol. Technol.*, **41**, 297 (1989).
Barrer, R.M., Edge, A.V.J., in *Proc. Roy. Soc. Lond. A*, **300**, 1 (1967).
Barrer, R.M., Stuart, W.I., in *Proc. Roy. Soc. Lond. A*, **243**, 172 (1957).
Becke, P., Kessel, D., Rahimian, I., in *Proc. European Petroleum Conference*, Cannes, France, November 16–18, SPE 25032 (1992).
Behar, E., Bourmayer, P., Sugier, A., Thomas, M., in *Proc. 70th Gas Processors Association Conference*, San Antonio, TX, March 11–12 (1991).
Benesh, M.E., US Patent 2,270,016, 437 (1942).
Berecz, E., Balla-Achs, M., *Gas Hydrates, Studies in Inorganic Chemistry*, 411, Elsevier, New York, 343 pp (1977, English Translation 1983).
Bernard, W.R., Wilkie, D.I., Cooke, W.J., Can Patent 1,056,716, c.6/19/79 f. 7/29/77 (1979).
Berthelot, P.E.M., *Ann. Chim. Phys. Ser*., *3*, **46**, 490 (1856).
Bily, C., Dick, J.W.L., *Bull. Can. Petr. Geol*., **22**, 340 (1974).
Bishnoi, P.R., Gupta, A.K., Englezos, P., Kalogerakis, N., *Fluid Phase Equilib*., **53**, 97 (1989).
Bond, D.C., Russell, N.B., *Trans. AIME*, **179**, 192 (1949).
Boniface, A., *The Chemical Engineer (U.K.)*, I Chem E, London, p. 12, August 23 (1990).
Brooks, J.M., Jeffrey, A.W.A., McDonald, T.J., Pflaum, R.C., *Init. Repts. Deep Sea Drilling Project* (von Huene, R., Auboin, J., et al., eds.), Washington, U.S. Govt. Printing Office, **84**, 699 (1985a).
Brooks, J.M., Kennicutt, M.C., Bidigare, R.R., Fay, R.A., *EOS Trans. Amer. Geophys. Union*, **66**, 106 (1985b).
Brooks, J.M., Kennicutt, M.C., Bidigare, R.R., Wade, T.L., Powell, E.N., Denoux, G.J., Fay, R.R., Childress, J.J., Fisher, C.R., Rossman, I., Boland, G., *EOS Trans. Amer. Geophys. Union*, **68**, 498 (1987).
Brooks, J., Kennicutt, M.C., Fay, R.R., McDonald, T.J., Sassen, R., *Science*, **225**, 409 (1984).
Bugge, T., Benderson, R.H., Kenyon, N.H., *Phil. Trans. Roy. Soc. Lond. A*, **325**, 357 (1988).
Burshears, M., O'Brien, T.J., Malone, R.D., in *Proc. SPE Unconventional Gas Technology Symposium*, SPE 15246, Louisville, KY, May 18–21, p. 449 (1986).
Cailletet, L., *Compt. Rend*., **85**, 851 (1877).
Cailletet, L., Bordet, R., *Compt. Rend*., **95**, 58 (1882).
Camargo, R., Goncalves, M., in *Proc. Offshore Technology Conference 2004*, OTC 16687, Houston, TX, May 26 (2004).
Campbell, K.J., *Offshore*, **46**, October (1991).
Carbajo, J.J., *Mixed Clathrates for Cool Storage Applications*, ONRL/TM-9530, pp. 1–24 (1985a).
Carbajo, J.J., in *Proc. 20th International Energy Conference and Engineering Conference*, Miami, 6 (1985b).
Cha, S.B., Ouar, H., Wildeman, T.R., Sloan, E.D., *J. Phys. Chem*., **92**, 6492 (1988).
Chancel, G., Parmentier, F., *Compt. Rend.*, **100**, 27 (1885).
Chazallon, B., Kuhs, W.F., *J. Chem. Phys*., **117**, 308 (2002).

Child, W.C., *J. Phys. Chem*., **68**, 1834 (1964).
Chou, I.M., Sharma, A., Buruss, R.C., Shu, J., Mao, H.K., Hemley, R.J., Goncharov, A.F., Stern, L.A., Kirby, S.H., *Proc. Natl Acad. Sci. USA*, **97**, 13484 (2000).
Circone, S., Kirby, S.H., Stern, L.A., *J. Phys. Chem. B*, **109**, 9468 (2005).
Clarke, M.A., Bishnoi, P.R., *Chem. Eng. Sci*., **55**, 4869 (2000).
Clarke, M.A., Bishnoi, P.R., *Can. J. Chem. Eng*., **79**, 143 (2001).
Clarke, M.A., Bishnoi, P.R., *Chem. Eng. Sci.*, **59**, 2983 (2004).
Claussen, W.F., *J. Chem. Phys*., **19**, 662 (1951a).
Claussen, W.F., *J. Chem. Phys*., **19**, 1425 (1951b).
Claussen, W.F., *J. Chem. Phys*., **19**, 259 (1951c).
Claussen, W.F., Polglase, M.F., *J. Am. Chem. Soc*., **74**, 4817 (1952).
Cole, W.A., Goodwin, S.P., *Chem. Eng. Sci*., **45**, 569 (1990).
Collett, T.S., *Detection and Evaluation of Natural Gas Hydrates from Well Logs, Prudhoe Bay Alaska*, M.S. Thesis, University of Alaska (1983).
Collett, T.S., *National Assessment of U.S. Oil and Gas Resources on CD-ROM* (Gautier, D.L., Goldton, G.L., Takahishi, K.I., eds.), USGS Digital Data Series 30, Washington D.C. (1995).
Cox, J.L. (ed.), *Natural Gas Hydrates: Properties, Occurrence and Recovery*, Butterworths, Boston, MA (1983).
Dallimore, S.R., Collett, T.S. (eds.), "Scientific Results from the Mallik 2002 Gas Hydrate Production Research Well Program, Meckenzie Delta, Northwest Territories, Canada," *Geological Survey of Canada*, Bulletin 585, including CD (2005).
Dalmazzone, D., Hamed, N., Clausse, D., Fouconnier, B., Dalmazzone, C., Herzhaft, B., in *Proc. Fifth International Conference on Gas Hydrates*, Trondheim, Norway, June 13–16, Paper 5041 (2005).
Danesh, A., Tohidi, B., Burgass, R.W., Todd, A.C., *Chem. Eng. Res. Des*., **72**, 197 (1994).
Davidson, D.W., "Clathrate Hydrates," in *Water: A Comprehensive Treatise*, Plenum Press, New York, **2**, Chap. 3, 115 (1973).
Davidson, D.W., "Gas Hydrates as Clathrate Ices," in *Natural Gas Hydrates: Properties, Occurrence and Recovery* (Cox, J.L., ed.), Butterworths, Boston, MA (1983).
Davidson, D.W., Handa, Y.P., Ratcliffe, C.I., Tse, J.S., Powell, B.M., *Nature*, **311**, 142 (1984).
Davidson, D.W., Leaist, D.G., Hesse, R., *Geochim. Cosmochim. Acta*, **47**, 2293 (1983).
Davy, H., *Phil. Trans. Roy. Soc. Lond.*, **101**, 1 (1811).
de Forcrand, R., *Compt. Rend*., **95**, 129 (1882).
de Forcrand, R., *Compt. Rend*., **106**, 849 (1888).
de Forcrand, R., *Compt. Rend*., **135**, 959 (1902).
de Forcrand, R., *Compt. Rend*., **176**, 355 (1923).
de Forcrand, R., *Compt. Rend*., **181**, 15 (1925).
de Forcrand, R., Thomas, S., *Compt. Rend*., **124**, 109 (1897).
de la Rive, A., *Am. Chim. Phys. Ser. 2*, **40**, 405 (1829).
Deaton, W.M., Frost, E.M., *Gas Hydrates and Their Relation to the Operation of Natural-Gas Pipe Lines*, 101 pp, U.S. Bureau of Mines Monograph 8 (1946).
Delsemme, A.H., Miller, S.L., *Planet. Space Sci*., **18**, 709 (1970).
Delyannis, A. (ed.), in *Proc. Second European Symposium on Fresh Water Sea* Athens, Greece, May 9–12 (1967).
Delyannis, A., Delyannis, E. (eds.), in *Proc. Third European Symposium on Fresh Water Sea*, Dubrovnik, Yuguslavia, September 13–17, European Federation of Chemical Engineers (1970).

Delyannis, A., Delyannis, E. (eds.), in *Proc. Fourth European Symposium on Fresh Water Sea*, Heidelberg, Germany, September 9–14, European Federation of Chemical Engineers (1973).

Delyannis, A., Delyannis, E. (eds.), in *Proc. Fifth European Symposium on Fresh Water Sea*, Alghero, Sardinia, May 9–12, European Federation of Chemical Engineers (1976).

Delyannis, A., Delyannis, E. (eds.), in *Proc. Sixth European Symposium on Fresh Water Sea*, Las Palmas, Gran Canaria, Spain, September 17–22, European Federation of Chemical Engineers (1978).

Dholabhai, P.D., Englezos, P., Kalogerakis, N., Bishnoi, P.R., *Can. J. Chem. Eng*., **69**, 800 (1991).

Dholabhai, P.D., Kalogerakis, N., Bishnoi, P.R., *SPE Prod. Facil*., **185**, August (1993a).

Dholabhai, P.D., Kalogerakis, N., Bishnoi, P.R., *Can. J. Chem. Eng*., **71**, 68 (1993b).

Dholabhai, P.D., Pankaj, D., Bishnoi, P.R., *J. Chem. Eng. Data*, **39**, 191 (1994).

Dholabhai, P.D., Parent, J.S., Bishnoi, P.R., *Ind. Eng. Chem. Res*., **35**, 819 (1996).

Dickens, G.R., *Modeling the Global Carbon Cycle with a Gas Hydrate Capacitor: Significance for the Latest Paleocene Thermal Maximum. Natural Gas Hydrates: Occurrence, Distribution, and Detection* (Paull, C.K., Dillon, W.P., eds.), AGU, Washington, DC, Geophys. Monogr. Ser. 124, pp. 19–38 (2001).

Dickens, G.R., *Earth Planetary Sci. Lett. (Frontiers)*, **213**, 169 (2003).

Dillon, W.P., Grow, J.A., Paull, C.K., *Oil Gas J*., **78**, 124 (1980).

Dillon, W.P., Myung, W.L., Coleman, D.F., Annals of the New York Academy of Sciences, **715**, 364 (1994).

Dillon, W.P., Paull, C.K., *Natural Gas Hydrates: Properties, Occurrence and Recovery* (Cox, J.L., ed.), Butterworth Publishers, Boston, MA, p. 73 (1983).

Ditte, A., *Compt. Rend*., **95**, 1283 (1882).

Dorstewitz, F., Mewes, D., presented at *Sixth International Symposium on on Transport Phenomena in Thermal Engineering*, Seoul, Korea, May (1993).

Dorstewitz, F., Mewes, D., in *Proc. Fifth International Offshore and Polar Engineering Conference*, The Hague, June 11–15, 244 (1995).

Dubinin, V.M., Zhidenko, G.G., *Transp. Khranenie Gaza (Ref. Inf.)*, **6**, 20 (1979).

Duclaux, E., *Compt. Rend*., **64**, 1099 (1867).

Dyadin, Y.A., Aladko, E.Y., Larionov, E.G., *Mendeleev Commun*., 34 (1997).

Dyadin, Y.A., Larionov, E.G., Aladko, E.Y., Manakov, A.Y., Zhurko, F.V., Mikina, T.V., Komarov, V.Y., Grachev, E.V., *J. Struct. Chem*., **40**, 790 (1999).

Edmonds, B., Moorwood, R.A.S., Szcepanski, R., presented at *GPA European Chapter Meeting*, Aberdeen, Scotland, September 24 (1994).

Edmonds, B., Moorwood, R.A.S., Szcepanski, R., presented at *UK Inst. Chem. Eng. VLE '96*, University of Aston, Birmingham, U.K. (1995).

Englezos, P., *A Model for the Formation Kinetics of Gas Hydrates from Methane, Ethane, and Their Mixtures*, M.S. Thesis, University of Calgary, Alberta (1986).

Englezos, P., in *Proc. Second International Offshore and Polar Engineering Conference*, San Francisco, CA, June 14–19, 644 (1992a).

Englezos, P., *Chem. Eng. Res. Des*., **70**, 43 (1992b).

Englezos, P., *Ind. Eng. Chem. Res*., **31**, 2232 (1992c).

Englezos, P., *Trans. I. Chem. E*, **70**, 43 (1992d).

Englezos, P., *Ind. Eng. Chem. Res*., **32**, 1251 (1993).

Englezos, P., Bishnoi, P.R., *Fluid Phase Equilib*., **42**, 129 (1988a).

Englezos, P., Bishnoi, P.R., *AIChE J*., **34**, 1718 (1988b).

Englezos, P., Kalogerakis, N., Dholabhai, P.D., Pankaj, D., Bishnoi, P.R., *Chem. Eng. Sci*., **42**, 2647 (1987a).
Englezos, P., Kalogerakis, N., Dholabhai, P.D., Bishnoi, P.R., *Chem. Eng. Sci*., **42**, 2659 (1987b).
Englezos, P., Ngan, Y.T., *J. Chem. Eng. Data*, **38**, 250 (1993).
English, N.J., MacElroy, J.M.D., *J. Chem. Phys*., **120**, 10247 (2004).
Faraday, M., *Phil. Trans. Roy. Soc. Lond*., **113**, 160 (1823).
Florusse, L.J., Peters, C.J., Schoonman, J., Hester, K.C., Koh, C.A., Dec, S.F., Marsh, K.N., Sloan, E.D., *Science*, **306**, 469 (2004).
Franklin, L., in *Natural Gas Hydrates: Properties, Occurrence and Recovery* (Cox, J.L., ed.), Butterworth, Boston, MA, 115 (1983).
Freifeld, B.M., Kneafsey, T.J., Tomutsa, L., Stern, L., Kirby, S., in *Proc. Fourth International Conference on Gas Hydrates*, Yokohama, Japan, May 19–23, 750 (2002).
Gaarder, C., Englezos, P., *Nordic Pulp Paper Res. J*., **2**, 110 (1995).
Gaarder, C., Ngan, Y.T., Englezos, P., *Emerg. Tech. Hazrds. Waste Management* (Tedder, D.W. and Pohland, F.G., eds.), ACS Symposium Series 554, Atlanta GA (September 21–33, 1992), pp. 114–23, (1994).
Galloway, T.J., Ruska, W., Chappelear, P.S., Kobayashi, R., *Ind. Eng. Chem. Fund.*, **9**, 237 (1970).
Ginsburg, G.D., *Hydrogeology of the North Yenisei Region*, 109, Natural Gas Crystalline Hydrate Formation in the Interior of the Earth, Sbornik Statei po Gidrogeologii i Geothermii No. 1, 109–128 (1969).
Ginsburg, G.D., Soloviev, V.A., in *Proc. 27th Annual Offshore Technology Conference*, Houston, TX, May 1–4, OTC 7693 (1995).
Ginsburg, G.D., Soloviev, V.A., *Submarine Gas Hydrates*, VNIIOkeangeologgia, St. Petersburg (1998).
Glew, D.N., Rath, N.S., *J. Chem. Phys*., **44**, 1710 (1966).
Grigg, R.B., Lynes, G.L., *SPE Drilling Eng.*, **7**, 32 (1992).
Godbole, S.P., Kamath, V.A., Ehlig-Economides C., SPE Formation Evaluation, 263, March (1988).
Gudmundsson, J.S., Borrehaug, A., in *Proc. Second International Conference on Gas Hydrates* (Monfort, J.P., ed.), Toulouse, France, June 2–6, 415 (1996).
Gudmundsson, J.S., Hveding, F., Borrehaug, A., in *Proc. Fifth International Offshore & Polar Engineering Conference*, The Hague, June 11–16, 282 (1995).
Gudmundsson, J.S., Parlaktana, M., presented at *AIChE Spring National Meeting*, New Orleans, LA, March (1992).
Gudmundsson, J.S., Parlaktuna, M., Khokhar, A.A., *SPE Production and Facilities*, February, 69 (1994).
Gupta, A., Dec, S.F., Koh, C.A., Sloan, E.D., *J. Phys. Chem. C*, **111**, 2341 (2007).
Gupta, A., Kneafsey, T.J., Moridis, G.J., Seol, Y., Kowalsky, M.B., Sloan, E.D., *J. Phys. Chem. B*, **110**, 16384 (2006).
Hale, A.H., Dewan, A.K.R., *SPE Drilling Eng.*, June, 109 (1990).
Halpern, Y., Thieu, V., Henning, R.W., Wang, X.P., Schultz, A.J., *J. Am. Chem. Soc*., **123**, 12826 (2001).
Hammerschmidt, E.G., *Ind. Eng. Chem*., **26**, 851 (1934).
Hammerschmidt, E.G., *Gas*, **15**, 30 (1939).
Handa, Y.P., *Can. J. Chem*., **62**, 1659 (1984).
Handa, Y.P., *J. Chem. Thermodyn*., **18**, 891 (1986a).

Handa, Y.P., *J. Phys. Chem*., **90**, 5497 (1986b).
Handa, Y.P., *Calorimetric Studies of Laboratory Synthesized and Naturally Occurring Gas Hydrates*, paper presented at AIChE Annual Meeting, Miami Beach, November 2–7 (1986c).
Handa, Y.P., *J. Phys. Chem*., **90**, 5917 (1986d).
Handa, Y.P., *J. Chem. Thermodyn*., **18**, 915 (1986e).
Hatton, G.J., Kruka, V.R., *Hydrate Blockage Formation—Analysis of Werner Bolley Field Test Data*, DeepStar CTR 5209-1 (2002).
Hendricks, E.M., Edmonds, B., Moorwood, R.A.S., Szcepanski, R., *Fluid Phase Equilib*., **117**, 193 (1996).
Henning, R.W., Schutz, A.J., Thieu, V., Halpern, Y., *J. Phys. Chem*., **104**, 5066 (2000).
Henriet, J.P. (ed.), in *Proc. of Gas Hydrates: Relevance to World Margin Stability and Climate Change Conference* (Tutorial and Abstracts Vols.), Gent, Belgium, September 18–20 (1996).
Henriet, J.P., Mienert, J., *Geol. Soc. Special Publ.*, **137**, 338 (1998).
Hester, K.C., Probing Hydrate Stability and Structural Characterization of both Natural and Synthetic Clathrate Hydrates, Ph.D. Thesis, Colorado School of Mines, Golden, CO (2007).
Hester, K.C., Dunk, R.M., Walz, P.G., Peltzer, E.T., Sloan, E.D., Brewer, P.G., *Fluid Phase Equilibria*, in press (2007).
Hester, K.C., White, S.N., Peltzer, E.T., Brewer, P.G., Sloan, E.D., *Marine Chem*., **98**, 304 (2006).
Hirai, H.H., Uchihara, Y., Fujihisa, H., Sakashita, M., Katoh, E., Aoki, K., Nagashima, K., Yamamoto, Y., Yagi, T., *J. Chem. Phys*., **115**, 7066 (2001).
Holder, G.D., Angert, P.F., in *Proc. Society of Petroleum Engineers Meet*., New Orleans, LA, September 26–29, SPE 11105 (1982a).
Holder, G.D., Angert, P.F., in *Proc. 57th SPE Fall Technical Conference*, New Orleans, LA, September 26–29, SPE 11105 (1982b).
Holder, G.D., Bishnoi, P.R. (eds.), Annals of the New York Academy of Sciences, **912** (2000).
Holder, G.D., Godbole, S.P., *AIChE J*., **28**, 930 (1982).
Holder, G.D., Kamath, V.A., Godbole, S.P., *Ann Rev Energy*, Annual Reviews Inc., Palo Alto, CA, **9**, 427 (1984a).
Holder, G.D., Katz, D.L., Hand, J.H., *Am. Assn. Petrol. Geol. Bull*., **60**, 981 (1976).
Holder, G.D., Malekar, S.T., Sloan, E.D., *Ind. Eng. Chem. Fund*., **23**, 123 (1984b).
Holder, G.D., Zets, S.P., Pradhan, N., *Rev. Chem. Eng*., **5**, 1 (1988).
Hondoh, T., in *Proc. Second International Conference on Gas Hydrates* (Monfort, J.P., ed.), Toulouse, France, June 2–6, 131 (1996).
Hong, H., Pooladi-Darvish, M., Bishnoi, P.R., *J. Can. Petrol. Technol*., **42**, 45 (2003).
Huang, C.P., Fennema, O., Powrie, W.D., *Cryobiology*, **2**, 109 (1965).
Huang, C.P., Fennema, O., Powrie, W.D., *Cryobiology*, **2**, 240 (1966).
Huo, Z., Hester, K.E., Sloan, E.D., Miller, K.T., *AIChE J*., **49**, 1300 (2003).
Huo, Z., Jager, M.D., Miller, K.T., Sloan, E.D., *Chem. Eng. Sci*., **57**, 705 (2002).
Hutz, U., Englezos, P., in *Proc. Seventh International Conference on Fluid Phase Properties and Phase Equilibria for Chemical Process Design*, Snowmass, Colorado, May (1995).
IODP Expedition 311 Scientists, Cascadia Margin gas hydrates. *IODP Prel. Rept.*, 311.doi:10:2204/iodp.pr.311. (2005).
Jamaluddin, A.K.M., Kalogerakis, N., Bishnoi, P.R., *J. Petrol. Sci. Eng*., **5**, 323 (1991).

Jeffrey, G.A., *Inclusion Compounds* (Atwood, J.L., Davies, J.E.D., MacNichol, D.D., eds.), Academic Press, London, **1**, 135 (1984).
Jeffrey, G.A., McMullan, R.K., *Prog. Inorg. Chem*., **8**, 43 (1967).
Jhaveri, J., Robinson, D.B., *Can. J. Chem. Eng*., **43**, 75 (1965).
JNOC press release, Proof of the methane-hydrate-containing layer in the national wildcat, "Nankai Trough," based on the *National Domestic Petroleum Exploration Program*, Japan National Oil Corporation, January 20 (2000).
John, V.J., Holder, G.D., *J. Phys. Chem*., **89**, 3279 (1985).
Johnson, A.H., Max, M.D., Dillon, W.P., *Economic Geology of Natural Gas Hydrates*, Series: Coastal Systems and Continental Margins, **9**, Springer (2006).
Judge, A., in *Proc. Fourth Can. Permafrost Conference* (French, H.M., ed.), National Research Council of Canada, 320 (1982).
Kamath, V.A., *Study of Heat Transfer Characteristics during Dissociation of Gas Hydrates in Porous Media*, Ph.D. Dissertation, University of Pittsburgh, PA (1984).
Kamath, V.A., Godbole, S.P., *J. Petrol. Technol*., **39**, 1379 (1987).
Kamath, V.A., Holder, G.D., *J. Chem. Thermodyn*., **16**, 399 (1984).
Kamath, V.A., Holder, G.D., Angent, P.F., *Chem. Eng. Sci.*, **39**, 1435 (1984).
Kamath, V.A., Holder, G.D., *AIChE J*., **33**, 347 (1987).
Kamath, V.A., Mutalik, P.N., Sira, J.H., Patil, S.L., in *Proc. SPE International Symposium on Oilfield Chemistry: Formation Evaluation*, San Antonio, TX, October 8–11, SPE 19810 (1991).
Kang, S.-P., Lee, H., *Environ. Sci. Technol*., **34**, 4397 (2000).
Katz, D.L., *Trans. AIME*, **160**, 140 (1945).
Katz, D.L., Cornell, D., Kobayashi, R., Poettmann, F.H., Vary, J.A., Elenbaas, J.R., Weinaug, C.F., *Handbook of Natural Gas Engineering*, McGraw-Hill, New York, 802 (1959).
Katz, D.L., Lee, R.L., "Gas Hydrates and Their Prevention," *Natural Gas Engineering Production and Storage*, McGraw-Hill, New York, Chap. 5 (1990).
Kennett, J.P., Cannariato, G., Hendy, I.L., Behl, R.J., *Methane Hydrates in Quaternary Climate Change: The Clathrate Gun Hypothesis*, The American Geophysical Union, Washington, DC (2003).
Kim, H.C., *A Kinetic Study of Methane Hydrate Decomposition*, Ph.D. Thesis, University of Calgary, Alberta (1985).
Kini, R., Dec, S.F., Sloan, E.D., *J. Phys. Chem. A*, **108**, 9550 (2004).
Klapproth, A., Goreshnik, E., Staykova, D., Klein, H., Kuhs, W.F., *Can. J. Phys*., **81**, 503, (2003).
Klauda, J.B., Sandler, S.I., *Ind. Eng. Chem. Res*., **39**, 3377 (2000).
Klauda, J.B., Sandler, S.I., *Chem. Eng. Sci*., **58**, 27 (2003).
Klauda, J.B., Sandler, S.I., *Energy Fuels*, **19**, 459 (2005).
Kobayashi, R., Katz, D.L., *J. Petrol Technol*., **1**, 66 (1949).
Kobayashi, R., Withrow, H.J., Williams, G.B., Katz, D.L., in *Proc. Natural Gasoline Association of America*, 27, San Antonio, TX (1951).
Koh, C.A., Savidge, J.L., Tang, C.C., *J. Phys. Chem*., **228**, 239 (1996).
Koh, C.A., Wisbey, R.P., Wu, X.P., Westacott, R.E., Soper, A.K., *J. Chem. Phys*., **113**, 6390 (2000).
Komai, T., Kang, S.P., Yoon, J.H., Yamamoto, Y., Kawamura, T., Ohtake, M., *J. Phys. Chem. B*, **108**, 8062 (2004).
Kotkoskie, T.S., Al-Ubaidi, B., Wildeman, T.R., Sloan, E.D., *SPE Drilling Eng*., June, 130 (1992).

Krason, J., Ciesnik, M., *Geological Evolution and Analysis of Confirmed or Suspected Gas Hydrate Localities: Gas Hydrates in Russian Literature*, U.S. Department of Energy, DOE/MC/21181-1950, **5**, 164 (1985).

Krason, J., Ciesnik, M., *Geological Evolution and Analysis of Confirned or Suspected Gas Hydrate Locations: Basin Analysis, Formation and Stability of Gas Hydrates of the Aleutian Trench and the Bering Sea*, U.S. Department of Energy, DOE/MC/21181-1950, **10**, 152 (1987).

Kuhs, W.F., Chazallon, B., Radaelli, P.G., Pauer, F., *J. Inclusion Phenom. Mol. Recogn. Chem.*, **29**, 65 (1997).

Kurnosov, A.V., Manakov, A.Y., Komarov, V.Y., Voronin, V.I., Teplykh, A.E., Dyadin, Y.A., *Doklady Phys. Chem.*, **381**, 303 (2001).

Kvenvolden, K.A., in *Proc. Fourth Canadian Permafrost Conference R.J.E. Brown Memorial*, Calgary, Alberta, March 2–6, 1981, **305** (1982).

Kvenvolden, K.A., *Natural Gas Hydrates* (Cox, J.L., ed.), Butterworths, Boston, MA (1983).

Kvenvolden, K.A., *Marine and Petrol. Geol.*, **2**, 65 (1985a).

Kvenvolden, K.A., AAPG Bull., **69**, 276 (1985b).

Kvenvolden, K.A., Claypool, G.E., Threlkeld, C.N., Sloan, E.D., *Org. Geochem.*, **6**, 703 (1984).

Kvenvolden, K.A., *Chem. Geol.*, **71**, 41 (1988).

Kvenvolden, K.A., *Org. Geochem.*, **23**, 997 (1995).

Kvenvolden, K.A., Claypool, G.E., *Trans. Amer. Geophys. Union*, **62**, 900 (1981).

Kvenvolden, K.A., Claypool, G.E., *U.S. Geol. Survey Open File Report 88-216*, **1**, 50 p. (1988).

Kvenvolden, K.A., Collet, T.S., Lorenson, T.D., in *Biogeochemistry of Global Change*, (Oremland, R.S., ed.) Chapman Hall, NY, **487** (1993a).

Kvenvolden, K.A., Ginsburg, G.D., Soloviev, V.A., *Geo-Mar. Lett.*, **13**, 32 (1993b).

Kvenvolden, K.A., McMenamin, M.A., *U.S. Geol. Survey Circular*, 825 (1980).

Lederhos, J.P., Long, J.P., Sum, A., Christiansen, R.L., Sloan, E.D., *Chem. Eng. Sci.*, **51**, 1221 (1996).

Lederhos, J.P., Mehta, A.P., Nyberg, G.B., Warn, K.J., Sloan, E.D., *AIChE J.*, **38**, 1045 (1992).

Leggett, J., *Global Warming: The Greenpeace Report* (Leggett, J., ed.), Oxford University Press, Oxford, U.K. pp. 4–41 (1990).

Lekvam, K., Ruoff, P., *J. Cryst. Growth*, **179**, 618 (1997).

Lewin and Associates, Inc. and Consultants, *Handbook of Gas Hydrate Properties and Occurrence*, U.S. Department of Energy, DOE/MC/19239-1546 (1983).

Lingelem, M.N., Majeed, A.I., *Trans. Inst. Chem. Eng. Part A*, **70**, 38 (1992).

Lingelem, M.N., Majeed, A.I., Stange, E., Annals of the New York Academy of Sciences, **715**, 75 (1994).

Long, J., Lederhos, J., Sum, A., Christiansen, R., Sloan, E.D., in *Proc. 73rd Gas Processors Association Annual Convention*, New Orleans, LA, March 7–9, 85 (1994).

Long, J., Sloan, E.D., *Mol. Simul.*, **11**, 145 (1993).

Long, J., Sloan, E.D., *Int. J. Thermophys.*, **17**, 1 (1996).

Lorenson, T.D., Collett, T.S., Gas content and composition of gas hydrate from sediments of the southeastern North American continental margin, in *Proc. ODP, Sci. Results*, (Paull, C.K., Matsumoto, R., Wallace, P.J., and Dillon, W.P. eds.), College Station, TX (Ocean Drilling Program), **164**, 37–46 (2000).

Loveday, J.S., Nelmes, R.J., Guthrie, M., Belmonte, S.A., Allan, D.R., Klug, D.D., Tse, J.S., Handa, Y.P., *Nature*, **410**, 661 (2001).
Loveday, J.S., Nelmes, R.J., Klug, D.D., Tse, J.S., Desgreniers, S., *Can. J. Phys*., **81**, 539 (2003).
Lovell, M. (ed.), in *Proc. Sediment-Hosted Gas Hydrates: New Insights on Natural and Synthetic Systems*, Geological Soc. Meeting, London, January 25–26 (2006).
Löwig, G., *Mag. Pharm*., **23**, 12 (1928).
Lu, H., Seo, Y., Lee, J., Moudrakovski, I., Ripmeester, J.A., Chapman, N.R., Coffin, R.B., Gardner, G., Pohlman, J., *Nature*, **445**, 303 (2007).
Lubas, J., *Nafta (Pol)*, **34**, 380 (1978).
Lund, A., Urdahl, O., Gjertsem, L., Kirkhorn, S.S., Fadnes, F., in *Proc. Second International Conference on Natural Gas Hydrates* (Monfort, J.P., ed.), Toulouse, France, June 2–6, 407 (1996a).
Lund, A., Urdahl, O., Kirkhorn, S., *Chem. Eng. Sci*., **51**, 3449 (1996b).
Lysne, D., Annals of the New York Academy of Sciences, **715**, 514 (1994).
Lysne, D., *An Experimental Study of Hydrate Plug Dissociation by Pressure Reduction*, D. Ing. Thesis, Norwegian Institute of Technology, University of Trondheim, Trondheim, Norway (1995).
MacDonald, I.R., Guinasso, N.L., Sassen, R., Brooks, J.M., Lee, L., Scott, K.T., *Geology*, **22**, 699 (1994).
Mak, C.W., McMullan, R.K., *J. Chem. Phys*., **42**, 2732 (1965).
Makogon, Y.F., *Gazov. Promst*., **5**, 14 (1965).
Makogon, Y.F., *Hydrates of Natural Gas*, Moscow, Nedra, Izadatelstro, 208 (1974 in Russian). Translated by W.J. Cieslesicz, PennWell Books, Tulsa, Oklahoma, 237 (1981 in English).
Makogon, Y.F., *La Recherche*, **18**, 1192 (1987).
Makogon, Y.F., presented at *Proc. Third Chemical Congress of North America*, Toronto, Canada, June 5–10 (1988).
Makogan, Y.F., Annals of the New York Academy of Sciences, **715**, 119 (1994).
Makogon, Y.F., *Hydrates of Hydrocarbons*, PennWell Publishing Corp., Tulsa, OK, 237 pp (1997).
Malegaonkar, M.B., Dholabhai, P.D., Bishnoi, P.R., *Can. J. Chem. Eng*., **75**, 1090 (1997).
Mao, W.L., Mao, H.K., Goncharov, A.F., Struzhkin, V.V., Guo, Q.Z., Hu, J.Z., Shu, J.F., Hemley, R.J., Somayazulu, M., Zhao, Y.S., *Science*, **297**, 2247 (2002).
Marshall, D.R., Saito, S., Kobayaski, R., *AIChE J*., **10**, 723 (1964).
Masuda, Y., Naganawa, S., Nato, A., Sato, K., presented at *SPE Western Regional Meeting*, Long Beach, CA, June 23–27, SPE 38291 (1997).
Matveeva, T., Soloviev, V., Wallmann, K., Obzhirov, A., Biebow, N., Poort, J., Salomatin, A., Shoji, H., *Geo-Mar. Lett.*, **23**, 278 (2004).
Maumene, E., *Chem. N*., **47**, 154 (1883).
Max, M.D., *PCT Int. Appl*. (Marine Desalination Systems, L.L.C., USA), 114 (2001).
Max, M.D., *PCT Int. Appl*. (Marine Desalination Systems, L.L.C., USA), 78 (2002).
Max, M.D., (ed.) *Natural Gas Hydrates in Oceanic and Permafrost Environments*, Kluwer Academic Publishers, London, 422 pp (2003).
McGuire, P.L., in *Proc. Fourth Canadian Permafrost Conference* (H.M. French, ed.), Calgary, Alberta, March, 2–6, 1981; 356 (1982).
McKoy, V., Sinanoglu, O., *J. Chem. Phys*., **38**, 2946 (1963).
McMullan, R.K., Jeffrey, G.A., *J. Chem. Phys*., **42**, 2725 (1965).

Mehta, A.P., *A Thermodynamic Investigation of Structure H Clathrate Hydrates*, Ph.D. Thesis, Colorado School of Mines, Golden, CO (1996).
Mehta, A.P., Sloan, E.D., *J. Chem. Eng. Data*, **38**, 580 (1993).
Mehta, A.P., Sloan, E.D., *J. Chem. Eng. Data*, **39**, 887 (1994).
Mehta, A.P., Sloan, E.D., *AIChE J*., **42**, 2036 (1996).
Mendis, D.A., *Nature*, **249**, 536 (1974).
Milkov, A.V., *Earth-Sci. Rev.*, **66**, 183 (2004).
Milkov, A.V., *Organic Geochem.*, **36**, 681 (2005).
Miller, B., Strong, E.R., *Am. Gas Assn. Monthly*, **28**, 63 (1946).
Miller, S.L., *Marine Sci. Natural gases Marine Sediments*, **3**, 151 (1974).
Millon, H., *Compt. Rend*., **51**, 249 (1860).
Monfort, J.P. (ed.), in *Proc. Second International Conference on Gas Hydrates*, Toulouse, France, June 2–6 (1996).
Monfort, J.P., Nzihou, A., *J. Cryst. Growth*, **128**, 1182 (1993).
Moon, C., Hawtin, R.W., Rodger, P.M., in *Proc. Fifth International Conference on Gas Hydrates*, Trondheim, Norway, June 13–16, Paper 1017 (2005).
Moon, C., Taylor, P.C., Rodger, M.P., *Can. J. Phys*., **81**, 451 (2003).
Mori, T., Mori, Y.H., *Int. J. Refrig*., **12**, 259 (1989a).
Mori, T., Mori, Y.H., *AIChE J*., **35**, 1227 (1989b).
Mori, Y.H. (ed.), in *Proc. Fourth International Conference on Natural Gas Hydrates*, Yokohama, Japan, May 19–23 (2002).
Mori, Y.H., Isobe, F., *Int. Comm. Heat Mass Transfer*, **18**, 599 (1991).
Moridis, G.J., in *Proc. SPE Gas Technology Symposium*, Calgary, Alberta, April 30–May 2, SPE 75691 (2002).
Moudrakovski, I.L., McLaurin, G.E., Ratcliffe, C.I., Ripmeester, J.A., *J. Phys. Chem. B*, **108**, 17591 (2004).
Moudrakovski, I.L., Sanchez, A.A., Ratcliffe, C.I., Ripmeester, J.A., *J. Phys. Chem. B*, **105**, 12338 (2001).
Nadem, M., Patil, S.L., Mutalik, P.N., Kamath, V.A., Godbole, S.P., presented at *Third Chemical Congress of North America*, Toronto, Canada, June 5–10 (1988).
Nagata, I., Kobayashi, R., *Ind. Eng. Chem. Fund*., **5**, 344 (1966a).
Nagata, I., Kobayashi, R., *Ind. Eng. Chem. Fund*., **5**, 466 (1966b).
Nakajima, Y., Takaoki, T., Ohgaki, K., Ota, S., in *Proc. Fourth International Conference on Gas Hydrates*, Yokohama, Japan, May 19–23, 987 (2002).
Nakazawa, K., Kanzawa, A., Sato, M., Akiya, T., Ogawa, S., in *Proc. Second JSME-KSME Therml Engineering Conference*, Kitakyushu, Japan, October 19–21, 1–117 (1992).
Natarajan, V., Bishnoi, P.R., Kalogerakis, N., *Chem. Eng. Sci*., **49**, 2075 (1994).
Nerheim, A.R., Svartaas, T.M., Samuelsen, E.K., in *Proc. Second International Offshore and Polar Engineering Conference*, San Francisco, June, 620 (1992).
Nerheim, A.R., Svartaas, T.M., Samuelsen, E.K., in *Proc. Fourth International Offshore and Polar Engineering Conference*, Osaka, Japan, April, 323 (1994).
Ng, H.J., Chen, C.-J., *Gas Processors Association Research Report 149*, March (1995).
Ng, H.J., Chen, C.-J., Robinson, D.B., *Gas Processors Association Research Report 92*, September (1985a).
Ng, H.J., Chen, C.-J., Robinson, D.B., *Gas Processors Association Research Report 87*, March (1985b).
Ng, H.J., Chen, C.-J., Robinson, D.B., *Gas Processors Association Research Report 106*, April (1987).
Ng, H.J., Robinson, D.B., *Gas Processors Association Research Report 66*, April (1983).

Ng, H.J., Robinson, D.B., *Gas Processors Association Research Report 74*, March (1984).
Nguyen, H., Reed, W., John, V.T., *J. Phys. Chem.*, **95**, 1467 (1991).
Nguyen, H.T., *Clathrate Hydrate Formation and Protein Solubilization in Reversed Micelles*, Ph.D. Thesis, Tulane University, LA (1991).
Nguyen, H.T., Kommareddi, N., John, V.T., *J. Colloid Interf. Sci*., **155**, 482 (1993).
Nikitin, B.A., *Z. Anorg. Allq. Chem*., **227**, 81 (1936).
Nikitin, B.A., *Nature*, **140**, 643 (1937).
Nikitin, B.A., *Zh. Obshch. Khim*., **9**, 1167 (1939).
Nikitin, B.A., *Izv. Akad. Nauk SSSR, Ord. Khim. Nauk*, **I**, 39 (1940).
Nolte, F.W., Robinson, D.B., Ng, H.J., in *Proc. 64th Annual Convention Gas Processors Association*, Houston, Texas, March 18–20, 137 (1985).
Ogawa, T., Ito, T., Watanabe, K., Tahara, K., Hiraoka, R., Ochiai, J., Ohmura, R., Mori, Y.H., in *Proc. Fifth International Conference on Gas Hydrates*, Trondheim, Norway, June 13–16, Paper 4019 (2005).
Okano, T., Yamasaki, A., Kiyono, F., Fujii, M., Yanagisawa, Y., in *Proc. 4*th *Intl. Conf. Gas Hydrates*, Yokohama, Japan, May 19–23, 1012 (2002).
Osegovic, J.P., Holman, S.A., Tatro, S.R., Brazel, LA., Ames, A.L., Evans, M.C., Max, M.D., in *Proc. Fifth International Conference on Gas Hydrates*, Trondheim, Norway, June 13–16, Paper 4017 (2005).
Ouar, H., Cha, S.B., Wildeman, T.R., Sloan, E.D., *Trans. I Chem. E*, **70**, 48 (1992).
Pang, K.D., Voga, C.C., Rhoads, J.W., Ajello, J.M., in *Proc. 14th Lunar and Planet Science Conference*, Houston, TX, **14**, 592 (1983).
Parent, J.D., *Inst. Gas Techn. Res. Bull*., 1 (1948).
Parent, J.S., *Investigations into the Nucleation Behaviour of the Clathrate Hydrates of Natural Gas Components*, M.Sc. Thesis, University of Calgary, Alberta (1993).
Parent, J.S., Bishnoi, P.R., *Chem. Eng. Commun*., **144**, 51 (1996).
Parkes, R.J., Cragg, B.A., Wellsbury, P., *Hydrogeol. J*., **8**, 11 (2000).
Parrish, W.R., Prausnitz, J.M., *Ind. Eng. Chem. Proc. Des. Dev*., **11**, 26 (1972).
Pauling, L., Marsh, R.E., *Proc. Natl Acad. Sci. USA*, **38**, 112 (1952).
Paull, C.K., Dillon, W.P., U.S. Geological Survey, Miscellaneous Field Studies Map MF-1252, Washington, DC (1981).
Paull, C.K., Dillon, W.P., *Natural Gas Hydrates: Occurrence, Distribution and Detection*, American Geophysical Union Monograph 124 (2001).
Paull, C.K., Lorenson, T.D., Borowski, W.S., Ussler III, W., Olsen, K., and Rodriguez, N.M., Isotopic composition of CH_4, CO_2 species, and sedimentary organic matter within samples from the Blake Ridge: gas source implications, in *Proc. ODP, Sci.* Results (Paull, C.K., Matsumoto, R., Wallace, P.J., and Dillon, W.P. eds.), College Station, TX (Ocean Drilling Program), **164**, 67–78 (2000).
Paull, C.K., Matsumoto, R., Wallace, P.J., et al., in *Proc. Ocean Drilling Program Initial Reports*, **164** (1997) Leg 164 (Blake Ridge).
Paull, C.K., Ussler, W., Borowski, W.S., Spiess, F.N., *Geology*, **23**, 89 (1995).
Paull, C.K., Ussler, W., Lorenson, T., Winters, W., Dougherty, J., *Geo-Mar. Lett*., **25**, 273, November, DOI:10.1007/s00367-005-0001-3 (2005).
Pearson, C., Murphy, J.R., Mermes, R.E., Halleck, P.M., Los Alamos Scientific Laboratory Report LA-9972 MS, **9** (1984).
Phillips, J.B., Nguyen, H., John, V.T., *Biotech. Prog*., **7**, 43 (1991).
Pierre, J., *Ann Chim. Phys. Ser. 3*, **23**, 416 (1848).
Poettmann, F.H., *Hydrocarbon Processing*, **63**, 111 (1984).

Pohlman, J.W., Canuel, E.A., Chapman, N.R., Spence, G.D., Whiticar, M.J., Coffin, R.B., *Organic Geochem.*, **36**, 703 (2005).
Powell, H.M., *J. Chem. Soc. (London)*, **1948**, 61 (1948).
Priestley, J., *Experiments and Observations on Different Kinds of Air and Other Branches of Natural Philosophy Connected with the Subject* (in Three Volumes), T. Pearson, Birmingham, 359 (1790).
Radhakrishnan, R., Trout, B.L., *J. Chem. Phys*., **117**, 1786 (2002).
Rao, A.M., Nguyen, H., John, V.T., *Biotech. Prog*., **6**, 465 (1990).
Rawn, C.J., Rondinone, A.J., Chakoumakos, B.C., Circone, S., Stern, L.A., Kirby, S.H., Ishii, Y., *Can. J. Phys*., **81**, 431 (2003).
Reed, R.L., Kelley, L.R., Neumann, D.L., Oelfke, R.H.,Young, W.D., Annals of the New York Academy of Sciences, **715**, 430 (1994).
Riedel, M., Collett, T.S., Malone, M.J., and the Expedition 311 Scientists. Proc. IODP, **311**: Washington, DC (2006) (Integrated Ocean Drilling Program Management International, Inc.). "http://dx.doi.org/10.2204/iodp.proc.311.2006".
Ripmeester, J.A., Davidson, D.W., *Bull. Magn. Reson*., **2**, 139 (1980).
Ripmeester, J.A., Ratcliffe, C.I., *J. Phys. Chem*., **92**, 337 (1988).
Ripmeester, J.A., Ratcliffe, C.I., *Inclusion Compounds* (Atwood, J.L., Davies, J.E.D., McNichol, D.D., eds.), Oxford University Press, Oxford, U.K., **5** (1991).
Ripmeester, J.A., Ratcliffe, C.I., McLaurin, G.E., *AIChE Meeting*, Houston, TX, April 10 (1991).
Ripmeester, J.A., Tse, J.S., Ratcliffe, C.I., Powell, B.M., *Nature*, **325**, 135 (1987).
Roadifer, R.D., Godbole, S.P., Kamath, V.A., in *Proc. SPE California Regional Meeting*, Ventura, CA, April 8–10, SPE 16361 (1987a).
Roadifer, R.D., Godbole, S.P., Kamath, V.A., in *Proc. SPE 62nd Annual Technical Conference*, Dallas, TX, September 27–30, SPE 16671 (1987b).
Robinson, D.B., Hutton, J.M., *J. Can. Petr. Tech*., **6**, 6 (1967).
Robinson, D.B., Ng, J.-J., *Hydrocarbon Proc.*, 95 (December 1976).
Rodger, P.M., *Chemistry in Britain*, November, 1090 (1990a).
Rodger, P.M., *Mol. Simul*., **5**, 315 (1990b).
Rodger, P.M., *J. Phys. Chem*., **94**, 6080 (1991).
Rogers, R., Yevi, G., in *Proc. Second International Conference on Gas Hydrates* (Monfort, J.P., ed.), Toulouse, France, June 2–6, 477 (1996).
Roozeboom, H.W.B., *Rec. Trav. Chem. Pays-Bas*, **3**, 26 (1884).
Roozeboom, H.W.B., *Rec. Trav. Chem. Pays-Bas*, **4**, 65 (1885).
Rose, W., Pfannkuch, H.O., in *Proc. SPE/DOE Unconventional Gas Recov. Symposium*, Pittsburgh, PA, May 16–18, 417 (1982).
Rueff, R.M., *The Heat Capacity and Heat of Dissociation of Methane Hydrates: A New Approach*, Disssertation, Colorado School of Mines, Golden, CO (1985).
Rueff, R.M., Sloan, E.D., Yesavage, V.F., *AIChE J*., **34**, 1468 (1988).
Sahling, H., Rickert, D., Lee, R.W., Limke, P., Suess, E., *Marine Ecol. Prog. Sci.*, **231**, 121 (2002).
Sassen, R., Macdonald, I.R., *Organic Geochem*., **22**, 1029 (1994).
Scanlon, W.J., Fennema, O., *Cryobiology*, **8**, 249 (1972).
Scauzillo, F.R., *Chem. Eng. Prog.*, **52**, 324 (1956).
Scheffer, F.E.C., Meyer, G., *Proc. R. Acad. Sci. Amsterdam*, **21**, 1204, 1338 (1919).
Schmuck, E.A., Paull, C.K., *Geo-Mar. Lett*., **13**, 145 (1993).
Schoenfeld, F., *A. Ch. Neue Reihe*, **19**, 19 (1855).

Schroeder, W., *Die Geschichte der Gas Hydrate*, Sammlung. Chem. Tech. Vortrage, 29, F. Enke, Stuttgart, 98 (1927).
Selim, M.S., Sloan, E.D., in *Proc. 55th Ann. SPE California Regional Meeting*, Bakersfield, CA, March 27–29, SPE 13597, 75 (1985).
Selim, M.S., Sloan, E.D., in *Proc. 62nd SPE Ann. Tech. Conference*, Dallas, TX, September 27–30 (1987).
Selim, M.S., Sloan, E.D., *AIChE J*., **35**, 1049 (1989).
Sharma, G.D., Kamath, V.A., Patil, S.L., *Particle Technology and Surface Pohenomena in Minerals and Petroleum* (Sharma, M.K., Sharma, G.D., eds.), Plenum Press, New York, 135 (1991).
Sharma, G.D., Kamath, V.A., Patil, S.L., in *Proc. 1992 International Offshore and Polar Eng. Conference*, San Francisco, CA, June 14–19 (1992).
Shirota, H., Aya, I., Namie, S., Bollavaram, P., Turner, D.J., Sloan, E.D., in *Proc. Fourth International Conference on Gas Hydrates*, Yokohama, May 19–23, 972 (2002).
Shoji, H., Langway, C.C., *Nature*, **298**, 548 (1982).
Shoup, G.J., Shoham, O., in *Proc. SPE 22nd Ann. Offshore Tech. Conference*, Houston, TX, May 7–10, **22**, 609 (1990).
Sira, J.H., Patil, S.L., Kamath, V.A., in *Proc. SPE 65th Ann. Tech. Conference*, New Orleans, LA, September 23–26, SPE20770, 977 (1990).
Skovborg, P., *Gas Hydrate Kinetics*, Ph.D. Thesis, Institute for Kemiteknik, Danmarks Tekniske Hojskole, Lyngby, Denmark (1993).
Sloan, E.D., *J. Petrol. Technol*., December, 1414 (1991).
Sloan, E.D., *Hydrate Engineering*, Monograph 21, Society of Petroleum Engineers, Richardson, TX (2000).
Sloan, E.D., *Nature*, **426**, 353 (2003).
Sloan, E.D., *Am. Mineral*., **89**, 1155 (2004).
Sloan, E.D., Happel, J., Hnatow, M.A. (eds.), Annals of the New York Academy of Sciences, **715** (1994).
Sloan, E.D., Khoury, F.M., Kobayashi, R., *Ind. Eng. Chem. Fund*., **15**, 318 (1976).
Sloan, E.D., Parrish, W.R., *Natural Gas Hydrates: Properties, Occurrence, and Recovery* (Cox, J.L., ed.), Butterworth publishers, Boston, **17** (1983).
Sloan, E.D., Sparks, K.A., Johnson, J.J., *Ind. Eng. Chem. Res*., **26**, 1173 (1987).
Sloan, E.D., Sparks, K.A., Johnson, J.J., Bourrie, M.S., *Fluid Phase Equilib*., **29**, 233 (1986).
Song, K.Y., Kobayashi, R., *Ind. Eng. Chem. Fund*., **21**, 391 (1982).
Song, K.Y., Kobayashi, R., *Gas Proc. Assn. Rsch. Report 80*, Tulsa, OK, May (1984).
Stange, E., Majeed, A., Overa, S., presented at *68th Gas Proc. Assn. Ann. Convention*, San Antonio, TX, March 13–14 (1989).
Staykova, D.K., Kuhs, W.F., Salamatin, A.N., Hansen, T., *J. Phys. Chem*., **107**, 37 (2003).
Stern, L.A., Circone, S., Kirby, S.H., Durham, W.B., *J. Phys. Chem*., **105**, 1756 (2001).
Stern, L.A., Circone, S., Kirby, S.H., Durham, W.B., in *Proc. Fifth International Conference on Gas Hydrates*, Trondheim, Norway, June 13–16, Paper 1046 (2005).
Stoll, R.D., Bryan, G.M., *J. Geophys. Res*., **84**, 1629 (1979).
Subramanian, S., *Measurements of Clathrate Hydrates Containing Methane and Ethane Using Raman Spectroscopy*, Ph.D. Thesis, Colorado School of Mines, Golden, CO (2000).
Subramanian, S., Sloan, E.D., *J. Phys. Chem*., **106**, 4348 (2002).
Sum, A., *Measurements of Clathrate Hydrate Properties Via Raman Spectroscopy*, M.S. Thesis, Colorado School of Mines, Golden, CO (1996).

Sum, A.K., Burruss, R.C., Sloan, E.D., *J. Phys. Chem. B*, **101**, 7371 (1997).
Tailleur, I.L., Bowsher, A.L., *USGS Clathrates in the NPRA Workshop* (July 16–17, 1979), USGS Open File Report 81-1298 (1981).
Takaoki, T., Hirai, K., Kamei, M., Kanda, H., in *Proc. Fifth International Conference on Natural Gas Hydrates*, Trondheim, Norway, June 13–16, Paper 4021 (2005).
Tanii, T., Minemoto, M., Ando, Y., *Heat Pumps, Saving Energy & Environ. Challenges*, Pergammon, Tokyo, March 12–15, 807 (1990).
Tanret, C., *Compt. Rend.*, **86**, 765 (1878).
Taylor, C.E., Kwan, J.T. (eds.), *Advances in the Study of Gas Hydrates*, Springer, Berlin, 225 pp. (2004).
Ternes, M.P., *Results on the Characterization of Gas Hydrate Formation in a Direct Contact Heat Pump Cool Storage System*, DOE/Oak Ridge National Laboratory, July (1985).
Ternes, M.P., Kedl, R.J., US Patent 6,649,628 (1984).
Thomas, M., Behar, E., in *Proc. 73rd Gas Proc. Assn. Convention*, New Orleans, LA, March 7–9 (1994).
Tohidi, B., Burgass, R., Danesh, A., Todd, A., in *Proc. SPE Offshore European Conference*, Aberdeen, U.K., September 7–10, 255 (1993).
Tohidi, B., Burgass, R., Danesh, A., Todd, A., in *Proc. SPE 69th Ann. Tech. Conference*, New Orleans, LA, September 25–28, SPE 28478, 157 (1994a).
Tohidi, B., Burgass, R., Danesh, A., Todd, A., in *Proc. First International Conference on Natural Gas Hydrates*, (Sloan, E.D., Happel, J., Hnatow, M.A., eds.), Annals of the New York Academy of Sciences, **715**, 532 (1994b).
Tohidi, B., Danesh, A., Burgass, R.W., Todd, A.C., in *Proc. BHRA Group Conf.*, Multiphase '95, Cannes, France, June 7–9, 519 (1995a).
Tohidi, B., Danesh, A., Todd, A., *Chem. Eng. Res. Des.*, **73**, 464 (1995b).
Tohidi, B., Danesh, A., Burgass, R., Todd, A., in *Proc. Fifth International Offshore & Polar Eng. Conference*, The Hague, June 11–16, 263 (1995c).
Tohidi, B., Danesh, A., Burgass, R., Todd, A., in *Proc. Second International Conference on Gas Hydrates* (Monfort, J.P., ed.), Toulouse, France, June 2–6, 109 (1996).
Tréhu, M.A., Bohrmann, G., Rack, R.F., Torres, M.E., Bargs, N.L., et al., in *Proc. ODP (Ocean Drilling Program), Initial Repts. 204*, Texas A&M University, College Station, TX (2003). " http://dx.doi.org/10.2973/odp.proc.ir.204.2003".
Tréhu, A.M., Bohrmann, G., Torres, M.E., Colwell, F.S. (eds.), in *Proc. Ocean Drill. Program*, Scientific Results, TAMU, College Station, TX, **204** (2006a).
Tréhu, A.M., Ruppel, C., Holland, M., Dickens, G.R., Torres, M.E., Collett, T.S., Goldberg, D.S., Riedel, M., Schultheiss, P., *Oceanography*, **191**, 24 (2006b).
Trofimuk, A.A., Cherskii, N.V., Makogon, Y.F., Tsarev, V.P., presented at *11th ASA Conference on Conventional and Unconventional World Natural Gas Resources*, Laxenburg, Austria, June 3–4 (1980).
Trofimuk, A.A., Cherskii, N.V., Tsarev, V.P., Nikitin, S.P., *Geologiva i Geofizika*, **23**, 3 (1982).
Trofimuk, A.A., Makogon, Y.F., Tolkachev, M.V., *Geol. Nefti i Gaza*, **10**, 15 (1981).
Tsarev, V.P., Savvin, A.Z., *Gazov. Prom-st.*, **2**, 46 (1980).
Tse, C.W., Bishnoi, P.R., *Can. J. Chem. Eng.*, **72**, 119 (1994).
Tse, J.S., Davidson, D.W., in *Proc. Fourth Canadian Permafrost Conference*, Calgary, Alberta, National Research Council of Canada, Ottawa, March 2–6, 329 (1982).
Tsypkin, G.G., Annals New York Academy of Sciences, **912**, 428 (2000).

Turner, D., *Clathrate Hydrate Formation in Water-in-Oil Dispersions*, Golden, Colorado School of Mines, Golden, CO (2005).
Uchida, T., Hirano, T., Ebinuma, T., Narita, H., Gohara, K., Mae, S., Matsumoto, R., *AIChE J.*, **45**, 2641 (1999).
Uchida, T., Takeya, S., Kamata, Y., Ikeda, I.Y., Nagao, J., Ebinuma, T., Narita, H., Zatsepina, O., Buffett, B.A., *J. Phys. Chem. B*, **106**, 12426 (2002).
Uchida, T., Takeya, S., Wilson, L.D., Tulk, C.A., Ripmeester, J.A., Nagao, J., Ebinuma, T., Narita, H., *Can. J. Phys*., **81**, 351 (2003).
Udachin, K.A., Ratcliffe, C.I., Enright, G.D., Ripmeester, J.A., *Supramol. Chem*., **8**, 173 (1997).
Udachin, K.A., Ratcliffe, C.I., Ripmeester, J.A., in *Proc. Fourth International Conference on Gas Hydrates*, Yokohama, Japan, May 19–23, 604 (2002).
Udall, S.L., Holum, K., DiLuzio, F.C., in *Proc. International Symposium Water Desalination*, Washington, DC, October, 3–9 (1965).
Ullerich, J.W., Selim, M.S., Sloan, E.D., *AIChE J*., **33**, 747 (1987).
van der Waals, J.H., Platteeuw, J.C., *Adv. Chem. Phys*., **2**, 1 (1959).
van Hulle, G., Fennema, O., *Cryobiology*, **7**, 223 (1971).
van Hulle, G., Fennema, O., *Cryobiology*, **8**, 91 (1972).
van Hulle, G., Fennema, O., Powrie, W.D., *Cryobiology*, **2**, 246 (1966).
Villard, P., *Compt. Rend*., **106**, 1602 (1888).
Villard, P., *Compt. Rend*., **111**, 302 (1890).
Villard, P., *Compt. Rend*., **120**, 1262 (1895).
Villard, P., *Compt. Rend*., **123**, 337 (1896).
Vlahakis, J.G., Chen, H.-S., Suwandi, M.S., Barduhn, A.J., Syracuse U., *Research and Development Report 830*, prepared for the US DOE of the Interior, November (1972).
von Stackelberg, M., *Naturwiss*, **36**, 359 (1949).
von Stackelberg, M., *Z. Elektrochem*., **58**, 104 (1954).
von Stackelberg, M., *Rec. Trav. Chim. Pays-Bas*, **75**, 902 (1956).
von Stackelberg, M., Fruhbuss, H., *Z. Elektrochem*., **58**, 99 (1954).
von Stackelberg, M., Jahns, W., *Z. Elektrochem*., **58**, 162 (1954).
von Stackelberg, M., Meinhold, B., *Z. Elektrochem*., **58**, 40 (1954).
von Stackelberg, M., Müller, H.R., *Naturwiss*, **38**, 456 (1951a).
von Stackelberg, M., Müller, H.R., *J. Chem. Phys.*, **19**, 1319 (1951b).
von Stackelberg, M., Müller, H.R., *Z. Electrochem*., **58**, 25 (1954).
Vysniauskas, A., Bishnoi, P.R., *Chem. Eng. Sci*., **38**, 1061 (1983b).
Vysniauskas, A., Bishnoi, P.R., *Natural Gas Hydrates: Properties, Occurrence and Recovery* (Cox, J.L., ed.), Butterworths, Boston, MA (1983a).
Wagner, J., Erbar, R.C., Majeed, A., in *Proc. 64th Annual Gas Processors Association Convention*, Houston, TX, March 18–20, **64**, 129 (1985).
Waite, W.F., Gilbert, L.Y., Winters, W.J., Mason, D.H., in *Proc. Fifth International Conference on Natural Gas Hydrates*, Trondheim, Norway, June 13–16, Paper 5042 (2005).
Weaver, J.S., Stewart, J.M., in *Proc. Fourth Canadian Permafrost Conference* (French, H.M., ed.), National Research Council of Canada, 312 (1982).
Westbrook, G.K., Carson, B., Musgrave, R.J., et al., *Proc. Ocean Drill Prog. Leg*, **146**, 477 (1994).
Westacott, R.E., Rodger, P.M., *Chem. Phys. Lett.*, **262**, 47 (1996).
Wilcox, W.I., Carson, D.B., Katz, D.L., *Ind. Eng. Chem*., **33**, 662 (1941).

Wilson, L.D., Tulk, C.A., Ripmeester, J.A., in *Proc. Fourth International Conference on Gas Hydrates*, Yokohama, Japan, May 19–23, 614 (2002).
Woolfolk, R.M., *Oil Gas J*., **50**, 124 (1952).
Wroblewski, S.V., *Compt. Rend.*, **94**, 212, 1355 (1882).
Yamamoto, Y., Komai, T., Kawamura, T., Yoon, J.-H., Kang, S.-P., Okita, S., in *Proc. Fourth International Conference on Gas Hydrates*, Yokohama, Japan, May 19–23, 428 (2002).
Yousif, M.H., Abass, H.H., Selim, M.S., Sloan, E.D., in *Proc. 63rd SPE Annual Technical Conference*, Houston, TX, October 2–5, SPE 18320 (1988).
Yousif, M.H., Dorshow, R.B., Young, D.B., Annals of the New York Academy of Sciences, **715**, 330 (1994).
Yousif, M.H., Li, P.M., Selim, M.S., Sloan, E.D., *J. Inclusion Phenom*., D.W. Davidson Memorial Volume (Atwood, J.L., Davies, J.E.D., eds.), **8**, 71 (1990).
Yousuf, M., Qadri, S.B., Knies, D.L., Grabowski, K.S., Coffin, R.B., Pohlman, J.W., *Appl. Phys. A*, **78**, 925 (2004).
Yu, A., Manakov, A.Y., Voronin, V.I., Teplykh, A.E., Kurnosov, A.V., Goryainov, S.V., Ancharov, A.I., Likhacheva, A.Y., in *Proc. Fourth International Conference on Gas Hydrates*, Yokohama, Japan, May 19–23, 630 (2002).
Zele, S.R., Lee, S.Y., Holder, G.D., *J. Phys. Chem. B*, **103**, 10250 (1999).
Zhang, C.L., Lanoil, B. (eds.), *Chem. Geol.*, **205**, 187 (2004).

2 Molecular Structures and Similarities to Ice

All common natural gas hydrates belong to the three crystal structures, cubic structure I (sI), cubic structure II (sII), or hexagonal structure H (sH) shown in Figure 1.5. This chapter details the structures of these three types of hydrate and compares hydrates with the most common water solid, hexagonal ice Ih. The major contrast is that ice forms as a pure component, while hydrates will not form without guests of the proper size.

Structure I is formed with guest molecules having diameters between 4.2 and 6 Å, such as methane, ethane, carbon dioxide, and hydrogen sulfide. Nitrogen and small molecules including hydrogen ($d < 4.2$ Å) form structure II as single guests. Larger ($6\,\text{Å} < d < 7\,\text{Å}$) single guest molecules such as propane or iso-butane will form structure II. Still larger molecules (typically $7\,\text{Å} < d < 9\,\text{Å}$) such as iso-pentane or neohexane (2,2-dimethylbutane) can form structure H when accompanied by smaller molecules such as methane, hydrogen sulfide, or nitrogen.

Yet, because all three common hydrate structures consist of about 85% water on a molecular basis, many of the hydrate mechanical properties resemble those of ice Ih. Among the exceptions to this heuristic are yield strength, thermal expansivity, and thermal conductivity. The final portion of this chapter examines mechanical, electrical, and transport properties with emphasis on those properties that differ from ice.

Less common clathrate hydrates formed by compounds other than natural gas guests (such as Jeffrey's structures III–VII, structure T, complex layer structures) and high pressure hydrate phases are also briefly described to provide a comprehensive account of clathrate hydrate structural properties.

The purpose of this chapter is also to provide the reader with a source of reference of the structural properties of hydrates. A summary of the key tabulated data given in this chapter is as follows:

Tables 2.1 and 2.2a provide details of the geometry of the hydrate cages (number of cavities per unit cell, average cavity radius) and crystal cell structures (space group, lattice parameters, cell formula, atomic positions), respectively. Table 2.2b lists the atomic coordinates for structures I, II, and H.

Table 2.3 provides an overview of the properties of structures I–VII (cavity types, space group, lattice parameter, cell formula).

Table 2.4 shows the ratio of molecular diameter to cavity diameter for guests in structures I and II. The corresponding data for structure H is given in Table 2.7, and the data for cyclopropane and trimethylene oxide (which form both sI and sII) are also provided.
Tables 2.5a,b lists the different structure I and II guests, and the structure and properties of the hydrates they form.
Table 2.6 lists the small help guests for structure II, where all the large molecules listed will not stabilize the hydrate without the presence of a help guest.
Table 2.8 summarizes the spectroscopic features, and mechanical and thermal properties for ice and hydrates of structures I and II.

This chapter focuses on the question, "What are hydrates?" and Chapter 3 concerns the question, "How do hydrates form?" Although a few thermodynamic properties are discussed in this chapter, the phase equilibrium conditions are considered in Chapters 4, 5, and 6.

2.1 Crystal Structures of Ice Ih and Natural Gas Hydrates

In Section 2.1.1 molecular structures of ice, water, and the hydrogen bond are considered. With these knowledge bases of more common substances, the hydrate cavities are assembled in each hydrate unit crystal in Section 2.1.2. Characteristics of guest molecules in hydrate structures are detailed in Section 2.1.3, before a summary is presented in Section 2.1.4.

2.1.1 Ice, Water, Hydrogen Bonds, and Clusters

In this section, the structures of ice, water, and the hydrogen bond are based on the classical works of Bernal and Fowler (1933), Pauling (1935), and Bjerrum (1952), as well as the reviews of Frank (1970), and Stillinger (1980). These subjects are treated in comprehensive detail in the seven volume series edited by Franks (1972–1982), to which any student of water compounds will wish to refer. A second series of monographs on water, also edited by Franks (1985–1990), was published to update the earlier monograph series. Discussion on computer simulation studies of the structure and dynamics of water is largely based on the work of Debenedetti (1996, 2003).

2.1.1.1 Ice and Bjerrum defects

The most common solid form of water is known as ice Ih (hexagonal ice), with the molecular structure as shown in Figure 2.1 from Durrant and Durrant (1962). In ice each water molecule (shown as a circle) is hydrogen bonded (solid lines) to four others in essentially tetrahedral angles (Lonsdale, 1958). A description of

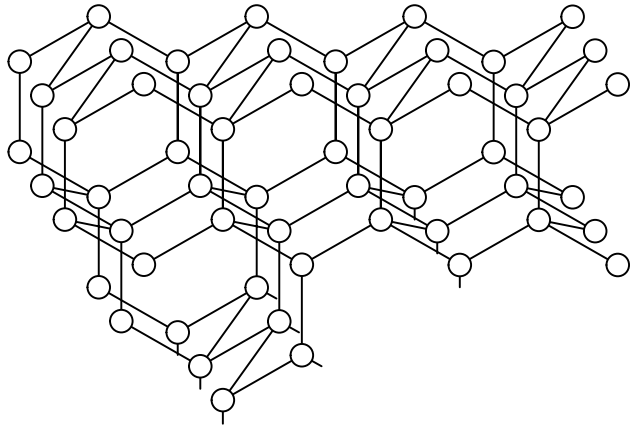

FIGURE 2.1 Basic crystal structure for ice Ih. (Reproduced from Durrant, P.J., Durrant, B., *Introduction to Advanced Inorganic Chemistry*, John Wiley & Sons, Inc., New York (1962). With permission.)

the hydrogen bond is provided in Section 2.1.1.3. The tetrahedral O─O─O angle of 109.5° in the most stable because there is almost no geometrical distortion. Stillinger (1980) suggests that tetrahedral coordination represents the most feasible way of packing molecules to permit fully developed hydrogen bonds.

In ice, the tetrahedrally hydrogen-bonded water molecules form nonplanar "puckered" hexagonal rings, rather than planar sheets. The typical distance between oxygen nuclei is 2.76 Å; covalently bonded protons are about 1 Å from an oxygen nucleus, and the hydrogen-bond length comprises the remaining 1.76 Å. Only one proton lies on each line connecting adjacent oxygen atoms in a hydrogen bond.

The ice crystal structure consists of water molecules hydrogen-bonded in a solid lattice. Since water molecules are similarly bonded in hydrates, both water molecules and hydrogen bonds are considered briefly in the following two sections. Many mechanical properties of ice are similar to hydrates, as detailed in Section 2.2.

Molecular dynamics and material transport in hexagonal ice (ice Ih) are closely related to the occurrence of ice-typical lattice defects. These defects include the Bjerrum defects (orientational defects) and ionic defects that coexist with other solid-state defects (interstitials and vacancies), and originate from distortions in the hydrogen-bond network (Figure 2.2). The Bjerrum crystal defects and their propagation are among the most frequently cited molecular properties. In his classic paper, Bjerrum (1952) considered possible reasons for low temperature disorder in the ice lattice. Normal electrostatic interactions caused by the orientations of the oxygens and the protons are necessary but insufficient to account for the total disorder. In addition, as shown in Figure 2.2, thermally excited water molecules cause two types of proton position faults, or defects, in the ice lattice.

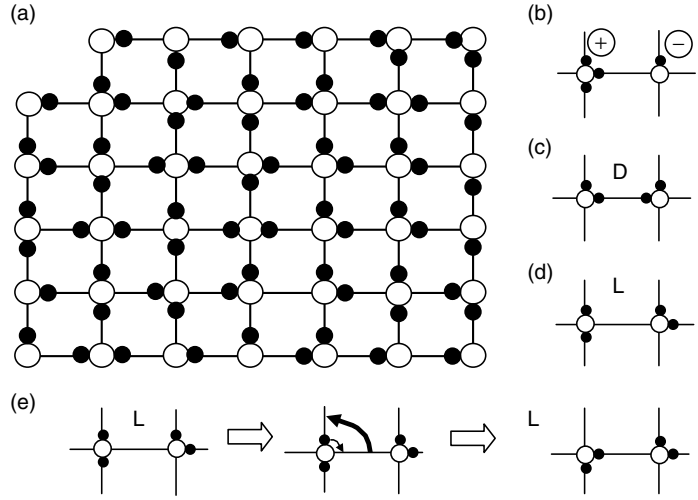

FIGURE 2.2 (a) Two-dimensional proton-disordered ice lattice (Bjerrum defect illustrated between molecules 4–5, in row 5). Open circles: oxygen atoms; closed circles: hydrogen atoms. (b) Ionic (H_3O^+ or OH^-) defects originate from a violation of the Bernal–Fowler (BF) Rule#1 (BF Rule#1: each oxygen atom is covalently bonded to exactly two hydrogen atoms). (c) Bjerrum defects violate the BF Rule#2 (BF Rule#2: there is exactly one hydrogen atom along each O─O vertex, which is covalently bonded to one oxygen and forms a hydrogen bridge to the other oxygen). Bjerrum D-defects (or D-faults), where the O─O vertex is occupied by two hydrogen atoms. (d) Bjerrum L-defects (or L-faults), where there are no hydrogen atoms at the O─O vertex. (e) Displacement (large curved arrow) of a Bjerrum L-defect induced by a tetrahedral (in three dimensions) reorientation of one water molecule (small arrow). (Redrawn from Geil, B., Kirschgen, T.M., Fujara, F., *Phys. Rev. B*, **72**, 014304 (2005). With permission from the American Physical Society.)

Normally, one proton exists between two oxygen nuclei (Figure 2.2a); yet the Bjerrum D-defect has two protons between oxygen nuclei in the ice lattice (Figure 2.2c), while the L-defect has none (Figure 2.2d). These defects cause the surrounding water molecules to pivot about the oxygen atom to provide one hydrogen bond between oxygen atoms thus resolving the unfavorable defect energy strain (Figure 2.2e).

Bjerrum defects act as catalysts to promote dipole turns, with one fault for every 10^6 molecules, corresponding to a turn rate of 10^{-12} s^{-1} at an orientation fault site. Devlin and coworkers (Wooldridge et al., 1987) suggested that Bjerrum defects are essential to the growth of hydrates from the vapor phase.

Molecular reorientations at Bjerrum fault sites are responsible for the dielectric properties of ice. A second type of fault (proton jumps from one molecule to a neighbor) accounts for the electrical conductivity of ice, but cannot account for the high dielectric constant of ice. Further discussion of such ice faults is provided by Franks (1973), Franks and Reid (1973), Onsager and Runnels (1969), and Geil et al. (2005), who note that interstitial migration is a likely self-diffusion mechanism.

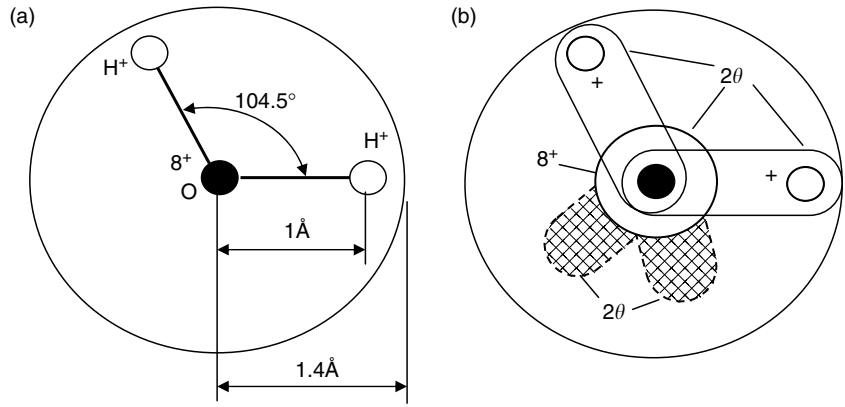

FIGURE 2.3 Water model of Bernal and Fowler (eight electrons on oxygen [8+] and one electron on each hydrogen [+]), indicating (a) the covalent O–H bond length and H–O–H bond angle, (b) the two lone pair orbitals on oxygen—hatched. (Reproduced from Makogon, Y.F., *Hydrates of Natural Gas*, Moscow, Nedra, Izadatelstro, p. 208 (1974 in Russian) Translated by W.J. Cieslesicz, PennWell Books, Tulsa, Oklahoma, pp. 237 (1981 in English). With permission.)

2.1.1.2 The water molecule

Figures 2.3a,b show the model of Bernal and Fowler (1933) for the water molecule. The molecular geometry is well known (Benedict et al., 1956) from rotational and vibrational spectra. The oxygen atom has eight electrons, and has the electronic configuration $1s^2 2s^2 2p^4$. Each hydrogen atom has a $1s^1$ electron; these electrons are shared with two bonding electrons of oxygen, to constitute the water molecule.

In water, four valence electrons form two "lone pair" orbitals that have been determined (Pople, 1951) to point above and below the plane formed by the three nuclei (H–O–H) of the molecule. The shared electrons with the protons give the molecule two positive charges, and the lone pair electrons give the molecule two negative charges. The result is a molecule with four charges and a permanent electric dipole (McCelland, 1963) of 1.84 Debye.

2.1.1.3 Hydrogen bonds

In 1920, two men in G.N. Lewis' laboratory at Berkeley proposed the hydrogen bond (Latimer and Rodebush, 1920) using a simplified electrostatic point charge model of the water molecule. The work by Kollman (1977) indicated that the simplified model remains acceptable because of a cancellation of two other energy components.

In the preceding section, the water molecule was described as having two positive and two negative poles. The water hydrogen bond, shown in Figure 2.4a, is caused by the attraction of the positive pole on one molecule to a negative pole on a neighboring water molecule. In ice and in hydrates, only one hydrogen (or proton)

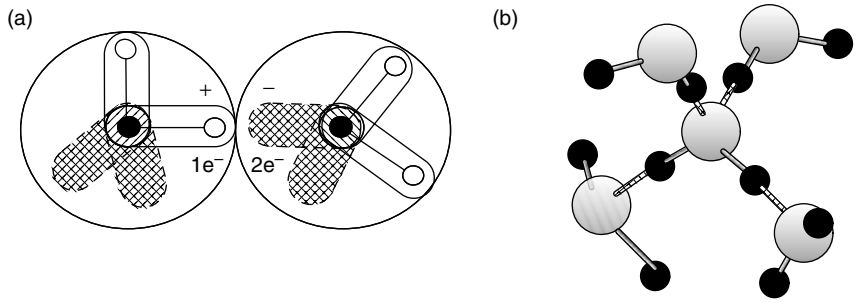

FIGURE 2.4 Hydrogen bonding (hydrogen bonds are crosshatched) (a) between two molecules (Reproduced and modified from Makogon, Y.F., *Hydrates of Natural Gas*, Moscow, Nedra, Izadatelstro, p. 208 (1974 in Russian) Translated by W.J. Cieslesicz, PennWell Books, Tulsa, Oklahoma, p. 237 (1981 in English). With permission), and (b) between four molecules. (Reproduced from Franks, F., Reid, D.S., in *Water: A Comprehensive Treatise* (Franks, F., ed.) Plenum Press, New York, **2**, Chap. 5 (1973). With permission.)

lies between two oxygen atoms with a distance between oxygen nuclei of 2.76 Å. The average O─O─O angle in ice and hydrates only departs a few degrees from the tetrahedral (109.5°) angle (Davidson, 1983).

Through this hydrogen bond, each water molecule is attached to four others, donating two and accepting two hydrogen bonds, as illustrated in Figure 2.4b. Each proton of the molecule is attracted to the negative pole of a neighboring molecule. Also, the two negative poles on the initial molecule attract the positive poles from two other water molecules. The four surrounding molecules are arranged tetrahedrally around the central molecule.

The energy required to break one hydrogen bond (ca. 5 kcal/mol) is more than an order of magnitude greater than a typical van der Waals bond (ca. 0.3 kcal/mol), such as the one that would attract two nonpolar molecules in a fluid. On the other hand, the hydrogen-bond energy is not nearly as large as that of a covalent chemical bond (102 kcal/mol), such as exists between hydrogen and oxygen within a water molecule (Cottrell, 1958).

2.1.1.4 Hydrogen bonds cause unusual water, ice, and hydrate properties

Along with the attraction of the hydrogen bond, the fact that these strong bonds separate the water molecules rigidly causes the solid density to be less than that of the liquid. In ice only 34% of the volume is occupied by water molecules, in contrast to 37% volume occupation in liquid water; this explains the unusual property of a decrease in density on freezing, accounting for the fact that ice floats.

Because the hydrogen bond is significantly weaker than the covalent bond, when hydrates form or dissociate, only hydrogen bonds are considered between neighboring molecules. Van der Waals forces are present, but are insignificant

relative to hydrogen bonds. When hydrates form or dissociate, chemical bonds do not need to be broken between hydrogen and oxygen within a water molecule.

Hydrogen bonds are also present to a large extent in liquid water. In a review, Luck (1973) notes that the hydrogen bonds inhibit the vaporization of liquid water, with the result that the boiling point of water at ambient pressure is 260 K higher than that of methane, a compound with a similar molecular weight. Hydrogen bonds provide a major exception to the heuristic that the vapor pressure of a substance is inversely proportional to molecular weight. Stillinger (1980) indicates that many of the unusual properties of water are caused by the hydrogen bond. These anomalous properties include the density maximum as a function of temperature, the increase in specific heat (C_p) as the temperature is reduced, and an increasing diffusion constant as the density is increased (Speedy and Angell, 1976; Prielmeier et al., 1987; Debenedetti, 2003). The breakdown in tetrahedral order (deviation from tetrahedral geometry) with increasing temperature or density is considered to cause the anomalous properties of liquid water. Molecular dynamics (MD) computer simulations also indicate that several properties of water (e.g., the translational diffusion coefficient and entropy) exhibit anomalous density dependence as a result of the breakdown of local tetrahedrality (Lynden-Bell and Debenedetti, 2005).

Only 15% of hydrogen bonds break when ice melts, as Pauling (1945, p. 304) calculated by comparing the heat of sublimation of ice with the heat of fusion of ice. This estimation supported the Frank and Evans (1945) "iceberg" model of liquid water molecules in a hydrogen-bonded network. The iceberg model comprises an equilibrium mixture of short-lived (10^{-10} s) hydrogen-bonded clusters, together with a nonhydrogen-bonded dense phase. Franks (1975) suggested that the term "iceberg" is often misused, since such short-lived or flickering clusters are not measurable on a macroscopic scale.

Stillinger (1980) suggested that disconnected icebergs should not be present, but that a more likely model is that of a random, three-dimensional network of hydrogen bonds, rather than long-lived clusters of molecules. Such networks of hydrogen-bonded water molecules and clusters are present when hydrates form or dissociate. These clusters are discussed relative to nucleation of hydrates in the following chapter.

The thermodynamic and structural processes that occur when water molecules are in the vicinity of hydrophobic entities (water fearing, insoluble in water) are referred to collectively as "hydrophobic hydration" (Tanford, 1973; Privalov and Gill, 1988; Blokzijl and Engberts, 1993; Chau and Mancera, 1999). Hydrophobic hydration is important in gas hydrate formation, which usually starts with hydrophobic gas molecules (e.g., methane) being introduced into liquid water.

In the Frank and Evans "iceberg" model, ice-like structures form around hydrophobic entities, such as methane. In this model, the hydrophobic molecules enhance the local water structure (greater tetrahedral order) compared with pure water. Ordering of the water hydration shell around hydrophobic molecules has been attributed to clathrate-like behavior, in which the water hydration shell is dominated by pentagons compared to bulk liquid water (Franks and Reid, 1973).

There have been numerous re-examinations of the "iceberg" model, and a considerable amount of controversy still exists. Molecular dynamics' computer simulations (Head-Gordon, 1995) suggest that although there are larger numbers of pentagons in the hydration shell compared to the bulk, the hydration shell also contains significant numbers of hexagons and larger polygons. Other computer studies indicate that the hydration shell around methane has a higher degree of tetrahedral bond-order than that in bulk water (Chau and Mancera, 1999). Hummer et al. (1996) calculated the potential of mean force between cavities in water and demonstrated that this has the properties expected of hydrophobic interactions. Conversely, Ashbaugh and Paulaitis (2001) presented a thermodynamic theory of hydrophobic hydration that does not invoke the concept of structure enhancement of water near a hydrophobic entity. Hydrophobic hydration has also been examined using neutron scattering (Bowron et al., 2001; Dixit et al., 2002; Buchanan et al., 2005) and surface-specific vibrational spectroscopy (Satana et al., 2001).

2.1.1.5 Pentamers and hexamers

The pentagonal and hexagonal faces are central to hydrate cavities, and therefore, their geometries are considered here. Small clusters, such as pentamers can be studied via geometric considerations, computer simulation, and more recently spectroscopy.

Computer simulation studies by Stillinger and Rahman (1974) suggest that the pentamer is the most likely structure to spontaneously arise in water at many temperatures, followed in frequency by hexamers, and squares. In a review of water, Frank (1970) noted that closed rings of bonds are always more stable than the most stable open chains of the same cluster number, due to the extra energy of the hydrogen bond. Through molecular dynamics studies of many five-molecule clusters, Plummer and Chen (1987) argued that the cyclic pentamer that comprises many hydrate cavities is the only stable five-member cluster above 230 K.

Molecular dynamics studies of liquid water by Ohmine and coworkers have shown that five- and six-membered rings, and even seven-membered rings dominate the topology in the hydrogen-bond network. (Ohmine, 1995; Matsumoto et al., 2002). Stacked pentamer rings have also been shown to be prevalent in the global minima energy structures of larger water clusters (Wales and Hodges, 1998). The global minimum pentamer ring structure was shown to form readily even at 4 K (Burnham et al., 2002).

Recent advances in spectroscopic methods have enabled the water pentamer to be studied experimentally. Infrared cavity ringdown spectroscopy has been used to examine the intramolecular absorption features of the gas-phase water pentamer, which match the spectral features of the pentamer rings in liquid water and amorphous ice (Paul et al., 1999; Burnham et al., 2002). Vibration Rotation Tunnelling (VRT) spectroscopy has been used to provide a more direct probe of the water pentamer intermolecular vibrations and fine structure in liquid water (Liu et al., 1997; Harker et al., 2005). The water pentamer was found to average out

to a symmetric quasiplanar structure on the timescale of the experiments (Harker et al., 2005).

In planar rings, water molecules in solid hydrogen-bonded pentagons have O─O─O angles (108°) only a little different from either the normal water angle (104.5°) or the tetrahedral angle (109.5°). However, the O─O─O angles of square faces (90°) and the hexagonal faces (120°) indicate almost similar strains on the bonds. Such strains may be reflected in thermodynamic properties or kinetic phenomena associated with these faces and cavities. Heptagons (128.6°) and octagons (135°) have still higher strained angles of O─O─O bonds and so occur infrequently in water structures.

2.1.2 Hydrate Crystalline Cavities and Structures

The information on hydrate structures I and II in this section is derived in large part from the excellent reviews of Jeffrey and McMullan (1967), Davidson (1973), and Jeffrey (1984), with the addition of substantial work on molecular motions reviewed by Davidson and Ripmeester (1984). The structure H material was excerpted from Ripmeester et al. (1987, 1988, 1991, 1994), Udachin et al. (1997b, 2002), Mehta (1996), and Mooijer-van den Heuvel et al. (2001, 2002).

Of more than 130 compounds that are known to form clathrate hydrates with water molecules, the majority form either sI, sII, or sH, with exceptions such as (1) bromine (Allen and Jeffrey, 1963; Dyadin et al., 1991), (2) dimethyl ether (Gough et al., 1974, 1975; Udachin et al., 2001a), (3) ethanol (Brownstein et al., 1967; Calvert and Srivastava, 1967), and (4) very high pressure hydrate phases (Dyadin et al., 1997; Loveday et al., 2001b, 2003b; Kursonov et al., 2004). Detailed emphasis is given to sI, sII, and sH hydrates since these are by far the most common natural gas hydrate structures.

The above (1)–(3) exceptions do not involve natural gas compounds and therefore are not described in any detail, but rather just mentioned in passing. The reader is referred to reviews by Davidson (1973), Davidson and Ripmeester (1978), and the papers of Jeffrey (1984), Dyadin et al. (1991), Udachin and Ripmeester (1999) and Udachin et al. (2001a) for further details on the less common hydrate structures of other compounds. The relevance of other compound structures is becoming increasingly of interest in areas of refrigeration, gas storage, and gas separation using clathrate hydrates.

2.1.2.1 The cavities in hydrates

The hydrate structures (Figure 1.5) are composed of five polyhedra formed by hydrogen-bonded water molecules shown in Figure 2.5, with properties tabulated in Table 2.1. Jeffrey (1984) suggested the nomenclature description (n_i^{mi}), for these polyhedra, where n_i is the number of edges in face type "i," and m_i is the number of faces with n_i edges.

The pentagonal dodecahedron (12-sided cavity) of Figure 2.5 is labeled 5^{12} because it has 12 pentagonal faces ($n_i = 5$, $m_i = 12$) with equal edge lengths and

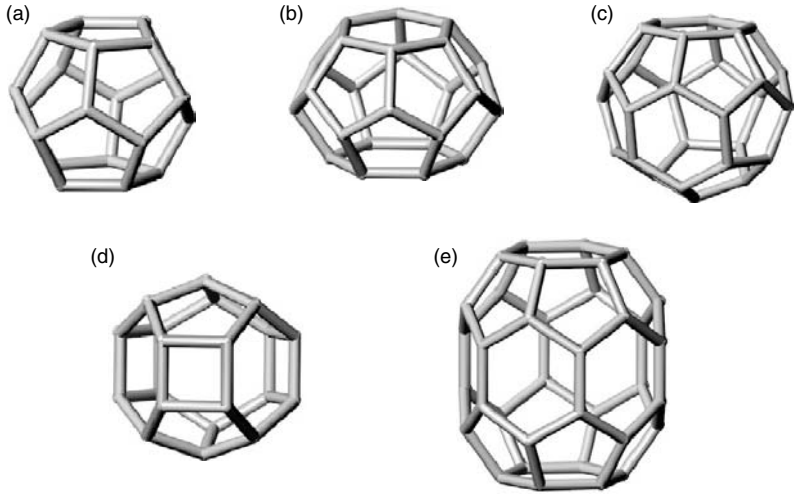

FIGURE 2.5 Three cavities in gas clathrate hydrates: (a) pentagonal dodecahedron (5^{12}), (b) tetrakaidecahedron ($5^{12}6^2$), (c) hexakaidecahedron ($5^{12}6^4$), (d) irregular dodecahedron ($4^35^66^3$), and (e) icosahedron ($5^{12}6^8$).

equal angles. The 14-sided cavity (tetrakaidecahedron) is called $5^{12}6^2$ because it has 12 pentagonal and 2 hexagonal faces. The 16-hedron (hexakaidecahedral cavity) is denoted $5^{12}6^4$ because in addition to 12 pentagonal faces, it contains 4 hexagonal faces. The irregular dodecahedron cavity ($4^35^66^3$) has three square faces and six pentagonal faces, in addition to three hexagonal faces. The largest icosahedron cavity ($5^{12}6^8$) has 12 pentagonal faces, as well as a girdle of 6 hexagonal faces and a hexagonal face each at the cavity crown and foot.

Tabushi et al. (1981) suggested that the 15-hedron ($5^{12}6^3$) is absent from Figure 2.5 and in all clathrates except bromine due to an unfavorable strain relative to the other cavities in sI and sII. In their review of simple and combined cavities, Dyadin et al. (1991) suggested that in addition to the cavities found in sI, sII, and sH, there are 4^25^8 and $5^{12}6^3$ cavities. In Jeffrey's (1984) list of a series of seven hydrate crystal structures (Table 2.3), additional cavities to those found in sI, sII, and sH are $5^{12}6^3$, 4^45^4, $4^35^96^27^3$, 4^66^8.

Since the cavities are expanded relative to ice, hydrate cavities are prevented from collapse by the repulsive presence of guest molecules, either in the cavity itself or in a large percentage of the neighboring cavities. Rodger (1990a,b) indicates that guest repulsion is more important than attraction to maintain cavity expansion. The mean polyhedral volume of the 12-, 14-, and 16-hedral cavities has been shown to vary with temperature and guest size and shape (Chakoumakos et al., 2003).

Jeffrey noted that the 12-, 14-, and 16-hedra are not stable in a pure water structure. However, some studies have suggested that liquid water is structured as cavities (Sorensen, 1994; Walrafen and Chu, 1995). Pauling (1959) proposed that water was composed of complexes of 5^{12} cavities with a water molecule as

TABLE 2.1
Geometry of Cages

Hydrate crystal structure	I		II		H		
Cavity	**Small**	**Large**	**Small**	**Large**	**Small**	**Medium**	**Large**
Description	5^{12}	$5^{12}6^2$	5^{12}	$5^{12}6^4$	5^{12}	$4^35^66^3$	$5^{12}6^8$
Number of cavities/unit cell	2	6	16	8	3	2	1
Average cavity radius[a] (Å)	3.95	4.33	3.91	4.73	3.94[b]	4.04[b]	5.79[b]
Variation in radius[c] (%)	3.4	14.4	5.5	1.73	4.0*	8.5*	15.1*
No. of water molecules/cavity[d]	20	24	20	28	20	20	36

[a] The average cavity radius will vary with temperature, pressure, and guest composition.
[b] From the atomic coordinates measured using single crystal x-ray diffraction on 2,2-dimethylpentane · 5(Xe,H_2S)-34H_2O at 173 K (from Udachin et al., 1997b). The Rietveld refinement package, GSAS was used to determine the atomic distances for each cage oxygen to the cage center.
[c] Variation in distance of oxygen atoms from the center of a cage. A smaller variation in radius reflects a more symmetric cage.
[d] Number of oxygen atoms at the periphery of each cavity.

Asterisks represent the variation in radius taken by dividing the difference between the largest and smallest distances by the largest distance.

the guest. On the basis of computer simulations, anomalies observed in the water cluster distributions determined by mass spectrometry were proposed to be due to a pentagonal dodecahedron with a mobile surface proton in the cage structure (Holland and Castleman, 1980).

The first direct experimental evidence for a stable clathrate structure of $(H_2O)_{21}H^+$, where the H_3O^+ ion is encaged inside the clathrate structure of $(H_2O)_{20}$ came from time-of-flight mass spectrometry (Wei et al., 1991). It is worth noting that evidence for the so-called magic number (21) water clusters found by Castleman and coworkers is restricted to the vapor phase (Holland and Castleman, 1980; Wei et al., 1991). More recently Dec et al. (2006) have used nuclear magnetic resonance (NMR) spectroscopy to obtain direct evidence of long-lived hydration shells around methane in the aqueous phase, which have a hydration number of 20. This corresponds to the magic number of 21, where similar to H_3O^+, methane is encaged inside a $(H_2O)_{20}$ hydration shell. Computer simulations indicated that the enhanced stability of the "magic number" (21) water cluster is due to the strong Coulombic interaction between the encaged H_3O^+ ion and surrounding 20 water molecules that form a deformed pentagonal dodecahedral cage (Nagashima et al., 1986).

Many hydrate cavities have analogs: (1) in the clathrasils in which SiO_2 replaces water as a host molecule (Gerke and Gies, 1984) and (2) in the Buckminsterfullerene (covalently bonded carbon cavities) family (Curl and Smalley, 1991). Even with these analogous structures providing estimates of other cavities, for hydrate unit crystals there is the additional restriction that the cavities must be packed to fill space.

With the exceptions of cavities containing square faces, all hydrate cavities (as well as clathrasil and Buckyball family cavities) follow Euler's theorem (Lyusternik, 1963) for convex polyhedra, stated as $(F + V = E + 2)$. The number of faces (F) plus the vertices (V) equals the edges (E) plus 2. Euler's theorem is easily fulfilled in cavities having exactly 12 pentagonal faces and any number of hexagonal faces except one.

Pentagonal Dodecahedra. The basic building block, present as the small cavity in all known natural gas hydrate structures, is the 5^{12} pentagonal dodecahedron of Figure 2.5a. When 12 pentagons are combined, the 5^{12} structure results. All 60 of the molecules in the 12 pentagons are not required for the structure; because pentagons share sides, only 20 molecules are required to make a 5^{12} cavity.

Euclid (fl.c. 300 BC) proved that the 5^{12} structure is the largest of the five strictly regular convex polyhedra. That is, it is the only hydrate cavity, which has planar faces that have both equal edges and O–O–O angles. In the 5^{12} structure there is only 1.5° departure of the O–O–O angles from the tetrahedral angles of ice Ih, and only 3.5° departure from the free water angle; the O–O bond lengths exceed those in ice by only 1%. Angell (1982) suggested that unstrained 5^{12} polyhedra arise naturally within the random hydrogen-bonded network in highly supercooled water.

The 5^{12} cavity geometry (faces, $F = 12$; vertices, $V = 20$; edges, $E = 30$) follows Euler's theorem of $F + V = E + 2$. Chen (1980, p. 109) suggested that the 5^{12} cavity seems geometrically favored by nature because it maximizes the number of bonds (30) to molecules (20) along the surface, when compared to similar cavities. Holland and Castleman (1980) studied a number of clusters and determined that the 5^{12} cluster had a hydrogen bond advantage over ice, and that it was less strained than other clathrate clusters.

Note that Figure 2.5a, for simplicity, does not display the hydrogen atoms that protrude from the 5^{12} cavity. Because there are 20 water molecules with 30 bonds, 10 water molecules have hydrogen atoms pointing away from the cavity, as potential points of attachment to other molecules or cavities. Thus the 5^{12} cavity, with ten protruding hydrogen atoms, has the appearance of a "dandelion" rather than a sphere. Similarly, the other cavities also have protruding hydrogen atoms.

As shown in Table 2.1, the 5^{12} cavity is almost spherical (showing a low percentage variation in radius, that is, a low variation in oxygen atom distances from the cavity center) with a radius of 3.95 and 3.91 Å in structures I and II, respectively. This small dimensional difference determines the size of the occupant. Until recently, it was thought (Davidson, 1973) that the smallest hydrate guest molecules stabilized the 5^{12} cavity of structure I.

Davidson et al. (1984a) crystallographically confirmed the suggestion of Holder and Manganiello (1982) that guest molecules of pure argon (3.83 Å diameter) or krypton (4.04 Å diameter) occupy the 5^{12} cavities of structure II. More recently, Davidson et al. (1986a) and Tse et al. (1986) determined that nitrogen and oxygen, respectively, occupied the 5^{12} cavity of structure II. Methane and hydrogen sulfide, with diameters of 4.36 Å and 4.58 Å, respectively, occupy the 5^{12} cavity of structure I. Helium, hydrogen, and neon, the smallest molecules with diameters less than 3.0 Å were considered too small to stabilize any cage. More recently, these small molecules have been shown to multiply and singly occupy large and small cages, respectively, of structure II at very high pressures (Manakov et al., 2002; Mao et al., 2002; Lokshin et al., 2005a,b). See Section 2.1.2.2.5 on high pressure hydrate phases for more details.

Tetrakaidecahedron. The geometries of the 14-hedra ($5^{12}6^2$) and the 16-hedra ($5^{12}6^4$) are detailed by Allen (1964), who presented Schlegel diagrams of these cavities, to complement the diagrams of Figures 2.5b,c. In these two-dimensional diagrams, shown in Figures 2.6a,b for the $5^{12}6^2$ and $5^{12}6^4$ cavities, one has the perspective of placing one's eye at a hexagonal face and looking into the cavity interior. The periphery of each figure is hexagonal, and the placement of other hexagonal faces serve to locate the pentagonal faces.

The $5^{12}6^2$ cavity also follows Euler's theorem, with 14 faces plus 24 vertices to give 36 edges plus 2. Figure 2.6a shows the 14-hedra to be formed by 2 facing hexagons, with 12 connecting pentagons. Each hexagon has six pentagons attached to its edges, resulting in two "cups," each formed by a hexagon at the base with six pentagons at the hexagon sides. The two cups join at the periphery to form the $5^{12}6^2$ cavity.

The orthogonal view of the $5^{12}6^2$ cavity, in Figure 2.5b, shows it to be the most nonspherical cavity in sI or sII. The four crystallographically different types of oxygen sites are 4.25, 4.47, 4.06, and 4.64 Å from the 14-hedra cavity center, giving a 14% variation from sphericity (Table 2.1), resembling an oblate ellipsoid. This cavity also has the largest O─O─O angle variation (5.1°) from the tetrahedral angle preferred by water.

With an average radius of 4.33 Å, the $5^{12}6^2$ cavity is large enough to contain molecules smaller than 6.0 Å in diameter. Ripmeester (Personal Communication, May 2, 1988) indicates that the 14-hedron is the preferred cage for almost all structure I hydrates, in which it plays the main stabilizing role. The oblate nature of the $5^{12}6^2$ cage causes the shape of the guest molecule to play a role in cavity stability.

Hexakaidecahedron. Figures 2.5c and 2.6b provide the orthogonal view and the Schlegel diagram for the $5^{12}6^4$structure, respectively. The latter diagram allows Euler's theorem to be verified: 16 faces plus 28 vertices equals 42 edges plus 2. The $5^{12}6^4$ notation for this cavity indicates four hexagonal faces.

The hexagonal faces are symmetrically arranged so that normals to hexagonal face centers form the vertices of a tetrahedron. Each hexagonal face is surrounded entirely by pentagonal faces. No two hexagons share a common edge. The radii from the cavity center to the crystallographically different oxygen sites do not vary

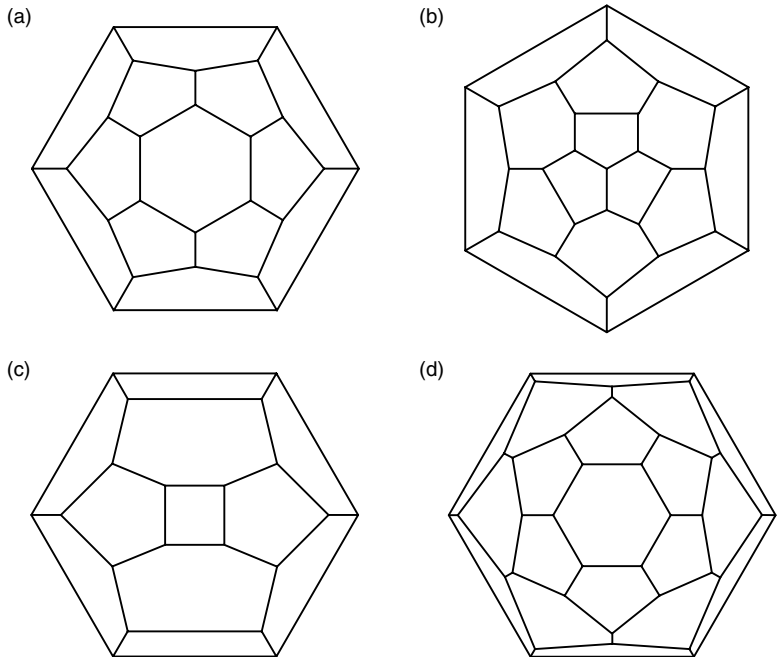

FIGURE 2.6 Schlegel diagrams for (a) tetrakaidecahedron ($5^{12}6^2$), (b) hexakaidecahedron ($5^{12}6^4$), (c) irregular dodecahedron ($4^3 5^6 6^3$), (d) icosahedron ($5^{12}6^8$). (Reproduced from Allen, K.W., *J. Chem. Phys*., **41**, 840 (1964). With permission from the American Institute of Physics.)

more than 1.7% (Table 2.1); therefore, the 16-hedron is the most spherical cavity of the five types.

The $5^{12}6^4$ cavity can contain molecules as large as 6.6 Å. Consequently, when the larger components of natural gas such as propane or iso-butane form simple (single guest) hydrates, they stabilize this cavity alone in structure II but the smaller cavities remain vacant.

Trimethylene oxide (Hawkins and Davidson, 1966), cyclopropane (Hafemann and Miller, 1969; Majid et al., 1969), and ethylene sulfide (Ripmeester, Personal Communication, May 2, 1988) are three molecules that can form in either the $5^{12}6^2$ of structure I or the $5^{12}6^4$ of structure II as simple hydrates. Raman spectroscopy measurements suggest that a low fraction of 5^{12} cages may also be occupied by cyclopropane at high pressures (Suzuki et al., 2001). Such compounds change structures depending on the temperature and pressure of formation, and guest composition in the aqueous phase as discussed in Section 2.1.3.

The Irregular Dodecahedron ($4^3 5^6 6^3$) and the Icosahedron ($5^{12}6^8$). Single crystal diffraction data for sizes of structure H cavities ($4^3 5^6 6^3$ and the $5^{12}6^8$ shown in Figures 2.5d,e) have been performed by Udachin and coworkers (Udachin and Lipkowski, 1996; Udachin et al., 1997b; Kirchner et al., 2004). The radii of the $4^3 5^6 6^3$ and $5^{12}6^8$ cavities were determined to be 4.04 and 5.79 Å, based on single crystal x-ray diffraction data (Udachin et al., 1997b), as indicated in Table 2.1.

The irregular dodecahedron ($4^3 5^6 6^3$) has the unusual property of following Euler's theorem ($F = 12$, $V = 20$, $E = 30$, so that $F + V = E + 2$) without having 12 pentagonal faces. The geometry of the cavity is remarkable due to the three square and three hexagonal faces that contain a considerable amount of bond strain. A Schlegel diagram is shown in Figure 2.6c for the $4^3 5^6 6^3$ cage, with the perspective first discussed for the $5^{12}6^2$ cavity.

The size of the $4^3 5^6 6^3$ cavity can be estimated using the correlation of Ripmeester et al. (1988) for the NMR measurements of chemical shift of isotopic ^{129}Xe as a function of the free radius available to the xenon atom inside each cage. Using this correlation and adding the van der Waals radius of water (1.4 Å), the radius of the $4^3 5^6 6^3$ cage was estimated as 4.06 Å. This estimated value was verified using single crystal x-ray diffraction.

The $5^{12}6^8$ cavity also follows Euler's theorem ($F = 20$, $V = 36$, $E = 54$), but it has a more usual geometry with 12 pentagonal and 8 hexagonal faces. The girdle of hexagonal faces, plus those at the crown and foot, provide a greatly expanded cage, allowing for occupants over 1 Å larger than those of any other cage. A Schlegel diagram is drawn for the $5^{12}6^8$ cage in Figure 2.6d.

Two points should be noted about both the $4^3 5^6 6^3$ and $5^{12}6^8$ cages: (1) the square and hexagonal faces are highly strained and (2) they are significantly less spherical than the 5^{12} cavity. In Figure 2.5, the two free-standing cavities are shown as having approximately planar sides; however, when they are connected in a sH model of the unit structure, both the strains and nonsphericity become apparent. (See discussion of the next section related to sH, Figures 2.9a,b.)

The fraction of strained angles in each of the five cavities may be estimated by considering pentagonal O–O–O angles to be approximately unstrained (3.5°) relative to free water (H–O–H angle of 104.5°) with cubic and hexagonal angles having essentially the same strain (15°). The fraction of strained angles in each cavity increases in order of $5^{12}6^2 < 5^{12}6^4 < 5^{12}6^8 < 4^3 5^6 6^3$ (16.7% < 28.6% < 44.4% < 50%, respectively). The two unusual cavity types in sH each have almost half their angles strained. Such strains may be reflected in a slow kinetics of formation.

A visual inspection of the cavities in Figure 2.5 shows b, d, and e to be nonspherical. The $5^{12}6^8$ is the most oblate of all five cavities; consequently, the shape of the occupying molecule is more significant than other cages. Ripmeester and Ratcliffe (1990a) note that, in contrast to the criteria for all other hydrate cages, size alone does not seem to be sufficient for a molecule to be a suitable guest in the $5^{12}6^8$. As indicated in Section 2.1.3.2, efficient space filling of the cage is necessary to optimize the van der Waals contact between the guest and the cage walls.

2.1.2.2 Hydrate crystal cells—structures I, II, and H

Crystal properties of sI, sII, and sH are given in Table 2.2a. Table 2.2b lists the atomic coordinates for these structures, which will enable the advanced reader to generate computer models of the hydrate crystals. The contrast of sI and sII structures is obtained by linking the basic 5^{12} cavity in two different ways to achieve fourfold hydrogen bonds. All modes of associating pentagonal

TABLE 2.2a
Hydrate Crystal Cell Structures

Structure	I		II		H	
Crystal system	Cubic		Cubic		Hexagonal	
Space group	Pm3n (No. 223)[c]		Fd3m (No. 227)[c]		P6/mmm (No. 191)[c]	
Lattice description	Primitive		Face centered		Hexagonal	
Lattice parameters[a]	$a = 12$ Å $\alpha = \beta = \gamma = 90°$		$a = 17.3$ Å $\alpha = \beta = \gamma = 90°$		$a = 12.2$ Å $c = 10.1$ Å $\alpha = \beta = 90°$, $\gamma = 120°$	
Ideal unit cell formula	$6(5^{12}6^2) \cdot 2(5^{12}) \cdot 46H_2O$		$8(5^{12}6^4) \cdot 16(5^{12}) \cdot 136H_2O$		$1(5^{12}6^8)$ $3(5^{12}) \cdot 2(4^3 5^6 6^3) \cdot 34H_2O$	
Number of faces[b]: hexagonal (H), pentagonal (P), square (S)	H = 6 P = 48		H = 16 P = 144		H = 7 P = 30 S = 3	
Atomic positions: number and symmetry	$5^{12}6^2$ (d) 5^{12} (a)	6, $\bar{4}$ 2 m 2, m3	$5^{12}6^4$ (b) 5^{12} (c)	8, $\bar{4}$ 3 m 16, $\bar{3}$ m	$5^{12}6^8$ 5^{12} (g) $4^3 5^6 6^3$	1, 6/mmm 3, mmm 2, $\bar{6}$ m2
	O (c) O (i) O (k)	6, $\bar{4}$ 2 m 16, 3 m 24, m	O (a) O (e) O (g)	8, $\bar{4}$ 3 m 32, 3 m 96, m	O (o), O (h) O (n) O (m)	12, m 4, 3 m 12, m 6, mm2
	(1/2 H) (i) 3(1/2 H) (k) 2(1/2 H) (l)	16, 3 24, m 48, 1	2(1/2 H) (e) 3(1/2 H) (g) (1/2 H) (i)	32, 3 m 96, m 192, m	X(1/2 H) X(1/2 H) X(1/2 H)	

[a] Lattice parameters are a function of temperature, pressure, and guest composition. Values given are typical average values.
[b] Number of faces accounting for face-sharing in the unit cell.
[c] Space group reference numbers from the International Tables for Crystallography.

Atomic positions indicate the Wyckoff letter in parentheses.

Table modified from Jeffrey (1984, p. 150).

dodecahedra lead to either fivefold or sixfold coordination of water molecules, except the following two, which yield fourfold hydrogen bonds (1) by linking the vertices of dodecahedra or (2) by sharing common faces of adjacent dodecahedra.

Structure I is an example of vertex-linking of the 5^{12} cavities in three dimensions, while structure II illustrates face-sharing of the 5^{12} cavities in three dimensions (see Figure 2.7). In structures I and II the spaces between the 5^{12} cavities form larger $5^{12}6^2$ or $5^{12}6^4$ cavities, respectively. Structure H illustrates

TABLE 2.2b
Atomic Coordinates and Isotropic Displacement Parameters for sI, sII, and sH Hydrates

sI Hydrate, $CH_4 \cdot 5 \cdot 75D_2O$[a]

Atom	*x*	*y*	*z*	Temperature factor (10^{-2} Å^2)
O1	0.1841(2)	0.1841(2)	0.1841(2)	0.92(7)
O2	0.0000	0.3100(2)	0.1154(2)	0.57(5)
O3	0.0000	0.5000	0.2500	0.76(9)
D7	0.2314(3)	0.2314(3)	0.2314(3)	1.7(1)
D8	0.0000	0.4305(5)	0.2007(5)	1.5(2)
D9	0.0000	0.3801(5)	0.1614(5)	1.2(2)
D10	0.0000	0.3157(5)	0.0349(4)	1.8(2)
D11	0.0673(4)	0.2662(4)	0.1373(4)	2.4(2)
D12	0.1177(4)	0.2257(4)	0.1582(4)	1.9(2)
5^{12} center	0	0	0	
$5^{12}6^2$ center	0	0.25	0.5	

sII Hydrate, $C_3H_8 \cdot 17D_2O$[b]

Atom	*x*	*y*	*z*	U(eq)
O1	0.1823(4)	0.1823(4)	0.3693(4)	1.52(9)
O2	0.2187(4)	0.2187(4)	0.2187(4)	1.52(9)
O3	1/8	1/8	1/8	1.52(9)
D4	−0.0613(1)	−0.021(1)	0.149(1)	4.2(2)
D5	0.1453(8)	0.1453(8)	0.369(2)	4.2(2)
D6	0.192(1)	0.192(1)	0.316(1)	4.2(2)
D7	0.208(1)	0.208(1)	0.270(1)	4.2(2)
D8	0.160(1)	0.160(1)	0.160(1)	4.2(2)
D9	0.183(1)	0.183(1)	0.183(1)	4.2(2)
5^{12} center	0	0	0	
$5^{12}6^4$ center	3/8	3/8	3/8	

sH Hydrate, 2,2-dimethylpentane.5(Xe,H_2S).34H_2O[c]

Atom	*x*	*y*	*z*	B_{iso}
O1	0.79099(6)	0.20901	0.27765(13)	2.27(4)
O2	0.66667	0.33333	0.36433(23)	2.17(7)
O3	0.61389(12)	0.61389	0.13726(13)	2.39(5)
O4	0.86798(8)	0.13202	0.50000	2.26(7)
5^{12} center	0.66667	0.33333	0.00000	1.99(3)
$4^3 5^6 6^3$ center	0.50000	0.50000	0.50000	1.99(3)
$5^{12}6^8$ center	0.00000	0.00000	0.00000	

[a] Gutt et al. (2000) from Rietveld refinement of high-resolution neutron powder diffraction at 2 K.
[b] Rawn et al. (2003) from Rietveld refinement of neutron powder diffraction at 17 K.
[c] Udachin et al. (1997b), from single crystal x-ray diffraction at 193 K. B_{iso} is the mean of the principal axes of the thermal ellipsoid.

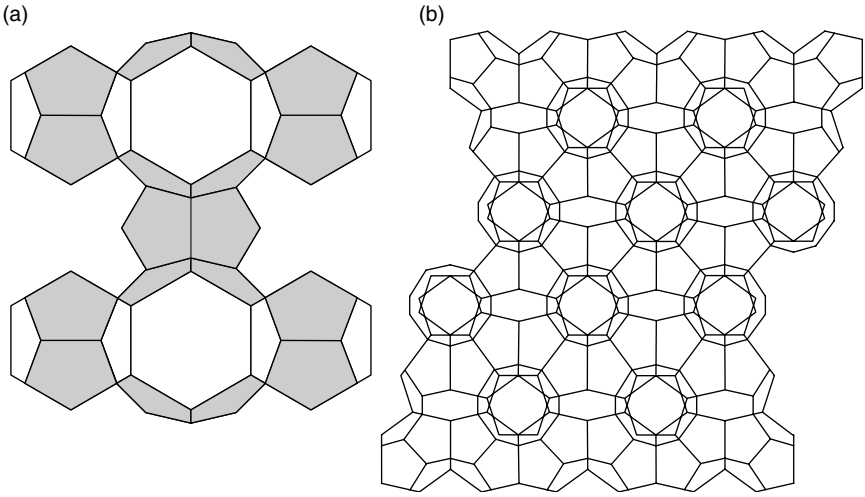

FIGURE 2.7 (a) Linking five 5^{12} polyhedra by two $5^{12}6^2$ polyhedra to form structure I. (b) Two-dimensional view of face-sharing of 5^{12} polyhedra to form $5^{12}6^4$ polyhedra voids for structure II. (Reproduced from Jeffrey, G.A., McMullan, R.K., *Prog. Inorg. Chem.*, **8**, 43 (1967), John Wiley & Sons. With permission.)

face-sharing in two dimensions, so that a layer of 5^{12} cavities connects a layer of $5^{12}6^8$ and $4^3 5^6 6^3$ cavities.

Davidson and Ripmeester (1984) discuss the mobility of water molecules in the host lattices, on the basis of NMR and dielectric experiments. Water mobility comes from molecular reorientation and diffusion, with the former being substantially faster than the water mobility in ice. Dielectric relaxation data suggest that Bjerrum defects in the hydrate lattice, caused by guest dipoles, may enhance water diffusion rates.

Jeffrey's (1984) list of a series of seven hydrate crystals (structures I–VII) are summarized in Table 2.3. These seven hydrate crystals are formed by polyhedra such as those in the last section. He noted, however, that a "study of all the possible three-dimensional four-connected structures based on polyhedra with twelve or more vertices is a formidable topological problem," inferring that some structures may have been overlooked. Indeed, structure H is not one of the seven structures listed by Jeffrey. Although only two of these structures (sI and sII) have been identified so far with hydrocarbon gas components, Jeffrey's list of seven hydrate structures for the true clathrate hydrates are given here for completeness. Exploring new and less common hydrate structures is becoming of increasing interest for a range of technological applications of hydrates. Dyadin et al. (1991) have also proposed seven structures, including the three listed in natural gas hydrates (sI, sII, sH); the others have yet to be found with hydrocarbons such as natural gas components.

TABLE 2.3
Jeffrey's (1984) List of a Series of Seven Hydrate Crystal Structures

I	II	III	IV	V	VI	VII
12-Hedra (5^{12})	12-Hedra (5^{12})	12-Hedra (5^{12})	12-Hedra (5^{12})	12-Hedra (5^{12})	8-Hedra ($4^4 5^4$)	
14-Hedra ($5^{12}6^2$)	16-Hedra ($5^{12}6^4$)	14-Hedra ($5^{12}6^2$) 15-Hedra ($5^{12}6^3$)	14-Hedra ($5^{12}6^2$) 15-Hedra ($5^{12}6^3$)	16-Hedra ($5^{12}6^4$)	17-Hedra ($4^3 5^9 6^2 7^3$)	14-Hedra ($4^6 6^8$)
Cubic (sI) Pm3n $a = 12$ Å	Cubic (sII) Fd3m $a = 17.3$ Å	Tetragonal* $P4_2/mnm$ $c \sim 12.4$, $a \sim 23.5$ Å	Hexagonal P6/mmm $c \sim 12.5$, $a \sim 12.5$ Å	Hexagonal $P6_3/mmc$ $c \sim 19$, $a \sim 12$ Å	Cubic $I\bar{4}3d$ $a = 18.8(2)$ Å	Cubic Im3m $a = 7.7$ Å
6X.2Y. $46H_2O$	8X.16Y. $136H_2O$	20X.10Y. $172H_2O$	8X.6Y. $80H_2O$	4X.8Y. $68H_2O$	16X $156H_2O$	$2X.12H_2O$
Gas hydrates	Gas hydrates	Bromine hydrate	None known	None known	Me_3CNH_2 hydrate	HPF_6 hydrate

Note: X refers to guest molecules in 14-hedra or larger voids, Y refers to guests in 12-hedra.

2.1.2.2.1 Structure I

Definitive x-ray diffraction data on structure I was obtained by McMullan and Jeffrey (1965) for ethylene oxide (EO) hydrate, as presented in Table 2.2a. The crystal consists of a primitive cubic lattice, with parameters as given in Table 2.2a. The common pictorial view of structure I is presented in Figure 1.5a. In that figure, the front face of a 12 Å cube is shown, with two complete $5^{12}6^2$ (emphasizing hydrogen bonds) connecting four 5^{12}.

An alternative, less frequent view is found in Figure 2.7a, which shows five 5^{12} connected by two $5^{12}6^2$; this is a primary illustration of linking 5^{12} through additional water molecules, which form $5^{12}6^2$. Jeffrey (1984, p. 153) suggests that the structure is defined by the $5^{12}6^2$ hedra, in the following description:

> "There is no direct face sharing between the 12-hedra (5^{12}). The structure can be constructed from the vertices of face-sharing 14-hedra ($5^{12}6^2$) arranged in columns with the 14-hedra sharing their opposing hexagonal faces. These columns are then placed in contact so as to share a pentagonal face between each pair of 14-hedra, with the column axes along (x, 1/2, 0) a 12 Å cubic cell. The remaining space is then the 12-hedra in a body centered cubic arrangement of their centers."

While Figure 1.5a appears to contain many water molecules, there are only 46 water molecules inside the structure I cubic cell and there are only eight polyhedra totally within the cube. Each of six cube faces contains two halves of a $5^{12}6^2$, for a total of six $5^{12}6^2$ within the cell. Each of the eight vertices of the

cube contains one-eighth of a 5^{12}, which, when added to the 5^{12} in the center of the cube, gives a total of two 5^{12} per cell.

2.1.2.2.2 Structure II

After crystal structure II was deduced, a definitive x-ray diffraction study of tetrahydrofuran/hydrogen sulfide hydrate was undertaken by Mak and McMullan (1965), two of Jeffrey's colleagues. The crystal consists of a face-centered cubic lattice, which fits within a cube of 17.3 Å on a side, with parameters as given in Table 2.2a and shown in Figure 1.5b. In direct contrast to the properties of structure I, this figure illustrates how a crystal structure may be completely defined by the vertices of the smaller 5^{12} cavities. Because the 5^{12} outnumber the $5^{12}6^4$ cavities in the ratio 16:8, only 5^{12} are clearly visible in Figure 1.5b.

A second view of a layer of structure II is presented in Figure 2.7b, which is a two-dimensional view of the way many face-sharing 5^{12} are arranged so that the residual voids are $5^{12}6^4$ (which share all the hexagonal faces). This is only a partial view of the crystal cell. These layers are stacked in a staggered pattern ABCABC so that the centers of the 16-hedra form a diamond lattice within a cube, with shared hexagonal faces. An alternative view of the packing in structure II is given in Figure 2.8 (in the {111} direction). Layers of face-sharing 5^{12} cavities alternate with layers consisting of $5^{12}6^4$ and 5^{12} cavities.

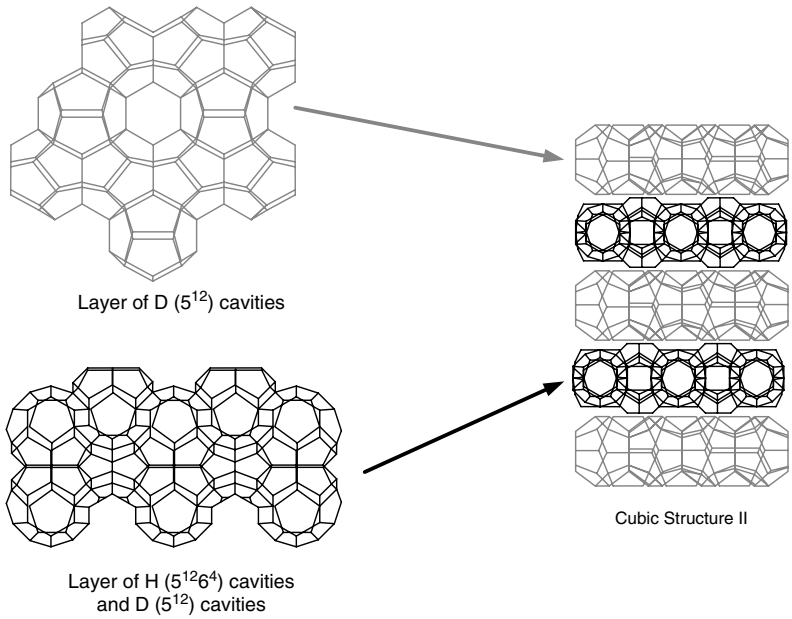

FIGURE 2.8 Schematic diagram showing structure II is built up of layers of 5^{12} cavities alternating with layers of $5^{12}6^4$ and 5^{12} cavities. (Reproduced from Udachin, K., Ripmeester, J.A., in *Proc. Fifth Int. Conf. on Gas Hydrates*, Trondheim, Norway, June 13–16, Paper 2024 (2005). With permission.)

Jeffrey (1984, p. 156) suggests that the voids formed by connecting 16-hedra could accommodate much larger guests (perhaps sharing voids) than those normally found in gas hydrates, but such clathrates have yet to be found. When the layer in Figure 2.7b forms the pattern ABABA, a hexagonal rather than cubic cell is formed; this structure is not found in natural gas hydrates, but is present with such molecules as isopropylamine, $(CH_3)_2CHNH_2 \cdot 8H_2O$ (Jeffrey's structure V).

2.1.2.2.3 Structure H

Ripmeester et al. (1987) reported structure H with evidence provided by NMR spectroscopy and x-ray powder diffraction. The structure was found to be isostructural with clathrasil dodecasil-1H, a clathrate formed with SiO_2 replacing H_2O as the host molecule (Gerke and Gies, 1984). It is likely that structure H was first prepared (but unrecognized) by de Forcrand in 1883, more than 100 years earlier than the structure was identified by Ripmeester et al. De Forcrand prepared binary (double) hydrates with iso-butyl chloride or bromide as the large guest, where these guests are similar in size to iso-pentane, now known to be an sH hydrate former.

Similar to Jeffrey's hypothetical structure IV, structure H is a hexagonal crystal of space group P6/mmm. However, in contrast to structure IV, structure H comprises $4^3 5^6 6^3$ and $5^{12} 6^8$ cavities in addition to 5^{12} cavities. On the basis of size considerations (including the relative size of the guests, the size of the cages in I–VII, and the unit cell parameters for sH), the structure was incompatible with Jeffrey's structures. Therefore, sH is not one of Jeffrey's (1984) known or hypothetical structures. Single crystal diffraction data for structure H have been obtained by Udachin et al. (1997b, 2002) and Kirchner et al. (2004).

The structure H unit cell, has a composition of $3(5^{12}) \cdot 2(4^3 5^6 6^3) \cdot 1(5^{12} 6^8) \cdot 34H_2O$. An orthogonal view is shown in Figure 1.5c. One important aspect of sH is that two sizes of molecules are required to stabilize the structure. Small molecules, such as methane or hydrogen sulfide, enter both small cavities (5^{12} and $4^3 5^6 6^3$) and large molecules typically larger than 7.3 Å, such as 2,2-dimethylbutane (neohexane), enter the $5^{12} 6^8$ cavity. In contrast to sI and sII, which generally form hydrates readily with single occupants of either the small and/or large cavity, no exception to the requirement of a double hydrate has been found for sH.

Figures 2.9a,b provide more enlightening perspectives of sH, as top and side views of the unit cell. Figure 2.9a is a top view of the unit cell rhombus (dark lines) with an edge length of 12.26 Å. Four $5^{12} 6^8$ cavities (labeled A, B, C, and D) are shown at the vertices of the unit cell; quarters of these cavities within the unit crystal combine to make one complete $5^{12} 6^8$ cavity contributing to the unit cell. The two $4^3 5^6 6^3$ cavities (labeled 1 and 2, each with three pentagonal faces showing) are within the unit cell connecting the $5^{12} 6^8$ cavities. Four other $4^3 5^6 6^3$ cavities (labeled 3, 4, 5, and 6—also showing three pentagonal faces each) are connected through square faces to the sides of the rhombus.

Figure 2.9a illustrates (bird's eye view) that on one layer, the $5^{12} 6^8$ cavities are connected by $4^3 5^6 6^3$ cavities, only by hexagonal faces. The $4^3 5^6 6^3$ cavities are connected to other $4^3 5^6 6^3$ cavities only by square faces. All pentagonal faces of each type of cavity serve to connect this layer of unusual cavities to layers of

5^{12} cavities (not shown). The figure also illustrates that the $4^3 5^6 6^3$ cavities are both strained and nonspherical in the unit cell, in contrast to the free standing cavities shown in Figure 2.5. No 5^{12} cavities are in this layer.

Figure 2.9b is an end-on, side view of the cell rhombus. In the figure, are outlines of three $5^{12}6^8$ cavities (labeled A, B, and C) are shown with the vertical borders of the rhombus at centroids of each $5^{12}6^8$. The fourth $5^{12}6^8$ of Figure 2.9a is aligned behind the middle $5^{12}6^8$ cavity in Figure 2.9b. This view shows both the nonspherical nature of the $5^{12}6^8$ cavities and their nonplanar, strained hexagonal faces in contrast to the almost planar hexagonal faces in sI and sII.

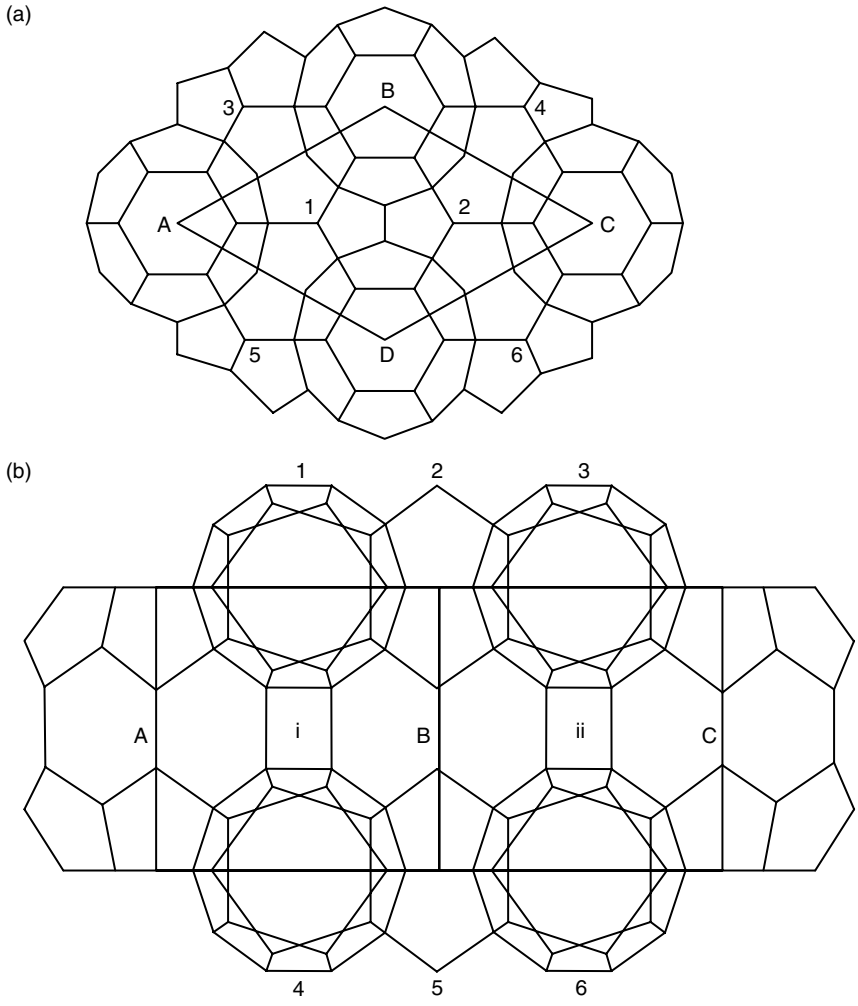

FIGURE 2.9 Top view (a) and side view (b) of a structure H hydrate unit cell. (Reproduced from Lederhos et al., *AIChE J.* (1992). With permission.)

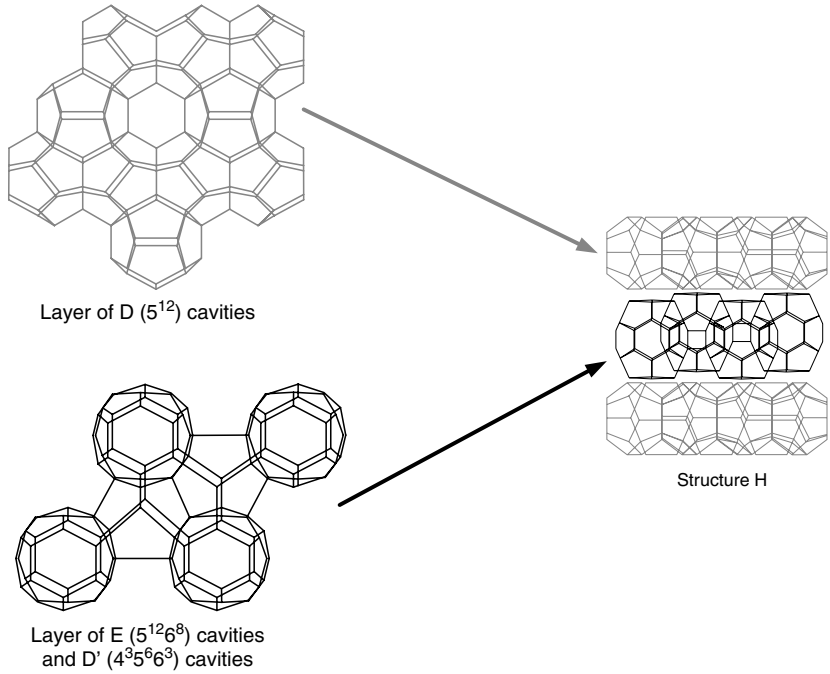

FIGURE 2.10 Schematic diagram showing structure H is built up of layers of 5^{12} (D) cavities and layers of $5^{12}6^8$ (E) and $4^35^66^3$ (D') cavities. (Reproduced from Udachin, K., Ripmeester, J.A., in *Proc. Fifth Int. Conf. on Gas Hydrates*, Trondheim, Norway, June 13–16, Paper 2024 (2005). With permission.)

Also in Figure 2.9b, six 5^{12} cavities (labeled 1 through 6) protrude from the top and bottom edges of the unit crystal, to illustrate the 5^{12} connecting role to layers composed of one $5^{12}6^8$ and two $4^35^66^3$ cavities within the unit crystal. The figure clearly shows one-half of each of six 5^{12} cavities (or three complete 5^{12} cavities) contained in the unit cell.

In Figure 2.9b, two square faces (labeled i and ii, connecting the three $5^{12}6^8$ cavities) each belong to $4^35^66^3$ cavities. Since the $4^35^66^3$ cavities alone possess square faces, these unusual cavities have only square face connections.

Another way of viewing the packing in structure H is shown in Figure 2.10 (in the {001} direction). Layers consisting of 5^{12} cavities alternate with layers consisting of large $5^{12}6^8$ and small $4^35^66^3$ cavities.

2.1.2.2.4 Jeffrey's structures III to VII, and other unusual structures

Jeffrey's structure III (given in Table 2.3) has been observed with Br_2 single guest molecules. Br_2 molecules occupy the larger polyhedra to give a stoichiometry of $20Br_2 \cdot 172H_2O$. This Br_2 hydrate tetragonal structure was revisited by Udachin et al. (1997a). Single crystal x-ray analysis was performed on crystals grown

from Br_2:H_2O solutions of composition 1:20 to 1:5, confirming the space group $P4_2/mnm$, where $a = 23.04$ Å, $c = 12.075$ Å. The unit cell is composed of two types of 5^{12} (D) cavities ($2D_A \cdot 8D_8$), two distinct $5^{12}6^2$ (T) cavities ($8T_A \cdot 8T_B$), and four ($5^{12}6^3$) cavities. Variable filling of large cages can occur, such that the hydration number varies (the minimum hydration number is 8.6). In this structure the large cages need not be full (this can also be the case for other hydrate structures). Guest–guest interactions could play a role in dictating the structure type. Particularly, in this case where the electron-rich bromine molecule has a sizeable molecular quadrupole moment.

Jeffrey's structure types IV and V are composed of known cavities 5^{12}, $5^{12}6^2$, $5^{12}6^3$, and $5^{12}6^4$. However, so far there are no "true" clathrate hydrates known for structures IV or V. These structures were extrapolated from semiclathrate hydrate structures of alkylamines (IV: Me_3N, $EtCH_2NH_2$, $(CH_3)_2CHNH_2$; V: Me_2CHNH_2). An analogous extrapolation is that for the structure I gas hydrate that forms the same primitive cubic structure as semiclathrate hydrates with $EtNH_2$ and Me_2NH guests. In semiclathrates, the host lattice consists of hydrogen-bonded water molecules and hydrogen-bonded functional groups of the guest molecules. The polyhedral voids are then occupied by the hydrophobic component of the guest molecules.

Structure IV (and also structures H and II) can be constructed by stacking two-dimensional sheets of 5^{12}cages, which are joined by sharing pentagonal faces (Udachin and Ripmeester, 1999a). Structure IV can be obtained by AA stacking of these two-dimensional sheets of 5^{12} cages.

The unusual cavities in Jeffrey's structure VI (4^45^4, $4^35^96^27^3$) and structure VII (4^66^8) have been observed only for single *tert*-butylamine guests and hexafluorophosphoric acid ($HPF_6 \cdot 6H_2O$) guests, respectively. *tert*-Butylamine, Me_3CNH_2 (Jeffrey and McMullan, 1967), is unique among amine hydrates since it forms a true clathrate rather than a semiclathrate.

Other unusual structures that are different to Jeffrey's structures III–VII are summarized as follows. Structure T is a trigonal structure (space group = P321, $a = 35$, $c = 12.4$ Å) that is formed from single dimethyl ether guests (Udachin et al., 2001a). Similar to Jeffrey's structure III (bromine hydrate; as mentioned above), structure T consists of $5^{12}6^3$ cavities. In addition to the known $5^{12}6^2$ and $5^{12}6^3$ cavities, structure T also contains some more unusual $4^25^86^1$ small cavities and $4^15^{10}6^3$ large cavities. A striking feature of structure T is the ratio of small/large cages in the unit structure is much smaller than any of the known hydrate structures. Therefore, in the absence of small guests, this structure is most efficient at minimizing vacant void space.

The complex hydrate structure, 1.67 choline hydroxide-tetra-*n*-propylammonium fluoride $30 \cdot 33H_2O$ (space group = R-3, $a = 12.533$, $c = 90.525$ Å) was discovered by Udachin and Ripmeester (1999b). It should be noted that the tetra-*n*-propylammonium salt will not form a hydrate on its own (Dyadin et al., 1988), even though other tetra-alkylammonium salts will form a variety of hydrate structures. Similar to structures II, H, and IV, this complex structure consists of stacked sequences of layers, CABBCAABCCABBCAAB. That is,

alternating layers of structure H and structure II pack together to form this structure. Choline is located in both the large cavities ($5^{12}6^8$ and $5^{12}6^4$) present in the lattice. However, as the choline molecule is too large to fully fit inside the $5^{12}6^4$ cavity, the guest hydroxyl displaces one of the water molecules in the host lattice and forms hydrogen bonds with the framework.

Udachin and Ripmeester (2005) proposed that several hypothetical structures can be formed by stacking layers of cubic structure II and structure H. Simulated x-ray powder diffraction patterns were calculated for these proposed structures, and atomic positions were also determined from these simulated x-ray patterns. For example, a closed cage version of the above complex structure was proposed. In this idealized structure, the guests do not hydrogen bond to the water cavities, and the 5^{12} and $4^3 5^6 6^3$ cavities are complete (space group = $R\bar{3}m$, $a = 5.533$, $c = 90.525$ Å). Also, a hypothetical hexagonal $P\bar{6}m2$ structure ($a = 12.16$, $c = 29.77$ Å) can be obtained from two layers of cubic structure II and one layer of structure H. Udachin and Ripmeester suggest this structure (consisting of 5^{12}, $4^3 5^6 6^3$, $5^{12}6^4$, and $5^{12}6^8$ cavities) may exist in nature and could accommodate guests such as methane, hydrogen sulfide, propane, butane, and isopentane. The simulated x-ray diffraction pattern for this structure can be indexed as a macroscopic mixture of phases of structure II and H, which the authors warn could result in misinterpretations of diffraction data. Also proposed were structures consisting of intergrowths of structure II, and the new closed cage complex structures, since all of these structures are based on stacking layers of 5^{12} cavities. The occurrence of these new structures would depend on their stability compared to the stability of the simpler hydrate structures.

Other unusual hydrate structures are formed by tetra-*n*-alkylammonium salts. The hydrates of these salts were first identified by Fowler et al. (1940), then later examined using x-ray diffraction by McMullan and Jeffrey (1959) and Dyadin et al. (1988). The tetra-*n*-butylammonium bromide (TBAB) hydrate is a semiclathrate, in which part of the hydrate cage is broken to accommodate the large TBAB molecule. The hydration number in TBAB hydrate $(C_4H_9)_4N^+Br^- \cdot nH_2O$ has been reported to vary from $n = 2.03$ to $n = 36$, which results in a range of crystal cell structures (Lipkowski et al., 2002; Shimada et al., 2005). For example, the hydrate crystal structure consists of a trigonal cell (space group R3c) for $n = 2.03$, or an orthorhombic cell (space group Pmma) for $n = 32$. Other studies have shown that small molecules (such as H_2S, H_2) can be encaged inside the 5^{12} dodecahedral cavities of TBAB hydrate (Oyama et al., 2003; Strobel et al., 2006a).

As this text is primarily concerned with natural gas hydrates, no further discussion will be given to Jeffrey's structures III–VII and the other unusual structures described above, since as stated previously these structures have yet to be found for natural gas components.

2.1.2.2.5 High pressure gas hydrate phases

At very high pressures (in the GPa range), gas hydrates can undergo structural transitions to hydrate phases and filled ice structures. Figure 2.11 illustrates the structural changes that have been reported for gas hydrates at very high pressures at

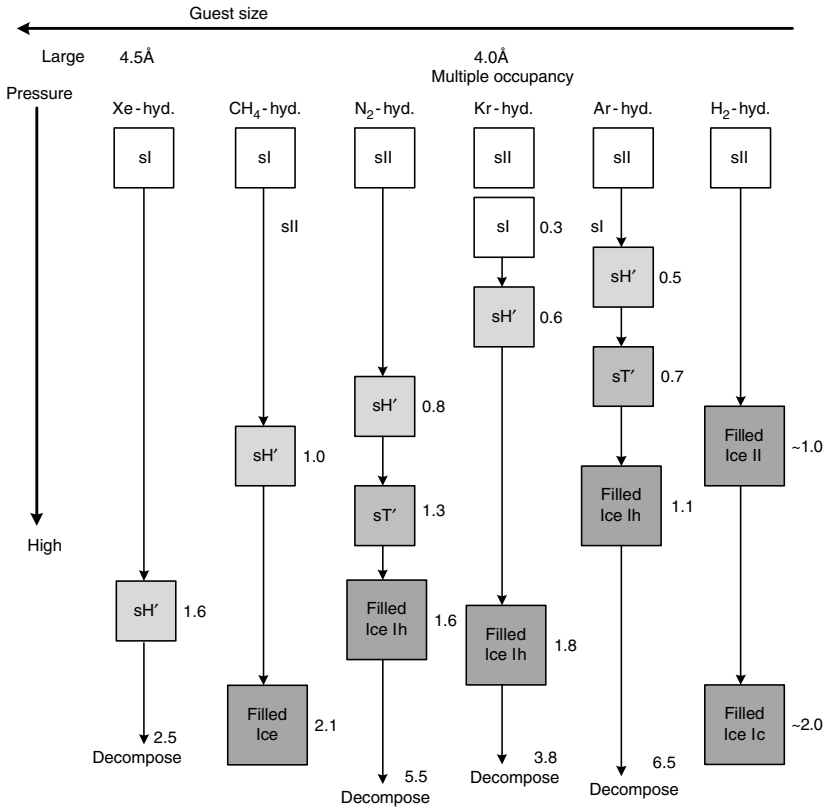

FIGURE 2.11 Very high pressure (0.3–2.1 GPa) structural changes of gas hydrates at room temperature. Numerical values (adjacent to square boxes) indicate transition pressures. Hexagonal (sH′) and tetragonal (sT′) hydrate phases are distinct from sH and sT hydrate structures found at normal pressures. (Modified and redrawn from Hirai, H., Tanaka, H., Kawamura, K., Yamamoto, Y., Yagi, T., *J. Phys. Chem. Solids*, **65**, 1555 (2004). With permission from Elsevier.)

room temperature (Hirai et al., 2004). The horizontal axis shows the guest size and the vertical axis indicates the pressure. The numerical values indicate the structural transition pressures in GPa. The hexagonal sH′ and tetragonal sT′ structures indicated in Figure 2.11 are distinct from sH and sT hydrate structures described in Sections 2.1.2.2.3 and 2.1.2.2.4, respectively.

As shown in Figure 2.11, hydrogen sII hydrate (stable at around 220 MPa at 249 K) transforms to a filled ice II structure as the pressure increases to around 1 GPa. On increasing the pressure further to around 2 GPa a filled cubic ice Ic structure forms (Vos et al., 1993). For argon, sII is the initial structure stable at normal pressures (<30 MPa). Increasing the pressure to about 0.5 GPa, a hexagonal hydrate phase is formed. Increasing the pressure further to around 0.7 GPa, a tetragonal hydrate structure is formed, and at even higher pressures,

a filled ice Ih structure is formed (Kurnosov et al., 2001; Hirai et al., 2002; Loveday et al., 2003).

Krypton forms sII hydrate at normal pressures and then transforms to sI hydrate at 0.3 GPa, to a hexagonal hydrate phase at 0.6 GPa, and then to a filled ice Ih structure at 1.8 GPa (Desgreniers et al., 2003). Nitrogen forms sII initially and then transforms to a hexagonal hydrate phase at 0.8 GPa, to a tetragonal hydrate structure at around 1.3 GPa, and finally to a filled ice Ih structure at 1.6 GPa (Loveday et al., 2003a; Sasaki et al., 2003). Methane sI hydrate transforms to a dense hexagonal hydrate phase at around 1.0 GPa, and then at 2.1 GPa to a filled-ice orthorhombic structure that has a H-bond network closely related to ice Ih (Hirai et al., 2001; Loveday et al., 2001a,b). Xenon sI hydrate transforms to a dense hexagonal hydrate phase at 1.6 GPa, and then with further increases in pressure decomposes without forming a filled ice structure (Desgreniers et al., 2003; Loveday et al., 2003).

At normal pressures, typically only one guest molecule is accommodated within each clathrate hydrate cage. However, diffraction measurements and computer calculations demonstrate that at very high pressures, clathrate hydrate structures can consist of water cages containing more than one guest molecule. Specifically, neutron diffraction measurements show that double occupancy of the large cage of sII hydrate can occur for both nitrogen hydrate and oxygen hydrate at higher pressures (Chazallon and Kuhs, 2002). Similar conclusions have been derived from molecular dynamics computer calculations (van Klaveren et al., 2001). Multiple occupancy has also been suggested for argon hydrate (Itoh et al., 2001).

Manakov et al. (2002) were able to fit their x-ray data with structure H hydrate by placing five argon molecules in the large cavities. Similarly, Loveday et al. (2003) were able to reconcile their diffraction data with a structure H hydrate structure containing five methane molecules in the large cavities and five methane molecules in two small cavities, giving a dense hydrate structure with a 3.5:1 methane/water ratio. However, Loveday et al. (2003) suggest that despite obtaining a good fit with structure H hydrate, to dispel "residual doubt" of the structure, confirmation from single crystal diffraction data is needed. Multiple cage occupancy has also been proposed in sI, sII, and sH argon hydrates from first principle and lattice dynamics calculations (Inerbaev et al., 2004).

In the case of pure hydrogen hydrate, sII hydrate is formed with multiple occupancy of the water cages. Initially, Mao et al. (2002, 2004,) suggested that pure hydrogen hydrate consists of double and quadruple occupancy of hydrogen molecules in the small and large cages of sII hydrate, respectively. However, more recently Lokshin et al. (2004) in collaboration with the Mao group reported that D_2 molecules only singly occupy the small cages of D_2 hydrate. The large cage occupancy was found to reversibly vary from two to four D_2 molecules per $5^{12}6^4$ cage over the temperature range of around 200 to 40 K (Lokshin et al., 2004; Lokshin, 2005b). Confirmation that H_2 can form a clathrate hydrate is especially noteworthy since it was previously assumed that small molecules such as H_2 and He are too small to stabilize a clathrate hydrate structure.

The pure H_2 hydrate structure is typically formed at very high pressures. However, the addition of a promoter molecule, for example, tetrahydrofuran (THF), to form a binary H_2/THF hydrate will stabilize H_2 within the sII framework (with THF occupying all large cavities) at pressures two orders of magnitude lower than that in pure hydrogen hydrates (Florusse et al., 2004). H_2 singly occupies the small cage of sII H_2/THF hydrate (Hester et al., 2006; Strobel et al., 2006b).

2.1.3 Characteristics of Guest Molecules

A second classification of hydrates is obtained through consideration of the guest molecules. Such a classification is a function of two factors: (1) the chemical nature of the guest molecule and (2) the size and shape (particularly in sH) of the guest. The size of the guest molecule is directly related to the hydration number and, in most cases, to its nonstoichiometric value.

2.1.3.1 Chemical nature of guest molecules

Two classifications of the chemical nature of the guest molecule have been proposed. The first scheme by von Stackelberg (1956) was a combination of both size and chemical nature as discussed in Section 1.2.3. The second scheme by Jeffrey and McMullan (1967) characterized the guest molecules in one of the following four groups: (1) hydrophobic compounds, (2) water-soluble acid gases, (3) water-soluble polar compounds, and (4) water-soluble ternary or quaternary alkylammonium salts.

Jeffrey (1984) clearly summarized chemical nature-based classification schemes by stating that the guest molecule must not contain either a single strong hydrogen-bond group or a number of moderately strong hydrogen-bonding groups. The molecules of natural gas components are not involved in hydrogen bonding, and so their chemical nature is not a delimiter. Most of the natural gas molecules that form hydrates are hydrophobic, with the notable exceptions of hydrogen sulfide and carbon dioxide, so that natural gas guests fall within the first two categories of Jeffrey and McMullan (1967).

In the third category, experimentalists have capitalized on the complete aqueous miscibility of the cyclic ethers, such as ethylene oxide (EO) for structure I and tetrahydrofuran(THF) for structure II, to provide easy access to hydrate crystal structures. With complete miscibility, an aqueous solution of EO or THF may be made at the hydrate composition of 24 wt% and 19 wt%, respectively (i.e., corresponding to stoichiometric amounts of water/EO = 7.7:1 and water/THF = 17:1, where EO and THF are assumed to occupy all the large cages of sI and sII, respectively; although EO will occupy some of the small cages (Huo, 2002)). Cyclic ether hydrates may thus be formed at atmospheric pressure (by cooling below 284.2 K [EO sI] or 277.5 K [THF sII]) without concern for mass transfer effects. However, the oxygen atoms that cause cyclic ethers to be miscible also promote a disproportionate number of Bjerrum defects in the hydrate (Davidson and Ripmeester, 1984) relative to natural gas guests.

Restrictions on Guest Motions. The physicochemical nature of the guest molecule, once enclathrated, has been studied in some detail. Dielectric constant and NMR techniques have been successfully applied by Davidson (1971) and Davidson and Ripmeester (1984). The translational degree of freedom of the guest is limited.

X-ray and neutron diffraction measurements indicate that the size of the guest and type of cage it occupies influences the guest position within a hydrate cage. Single crystal x-ray diffraction studies have shown that the center of ethane is 0.17 Å from the center of the large cage of structure I (Udachin et al., 2002). Likewise, propane occupies an off-center position in the large cage of structure II (Kirchner et al., 2004). For structure II benzene + xenon hydrate, xenon is located at the center of the small cage, while benzene is 0.27 Å from the center of the large cavity. For sH methylcyclohexane + methane hydrate, the carbon of methane is located at the center of both the 5^{12} and $4^3 5^6 6^3$ small cages, with methylcyclohexane in the favored chair conformation in the $5^{12}6^8$ cage (Udachin et al., 2002).

Davidson (1971) determined that the most important rotation inhibition interactions between guest molecules (in adjacent cages) were the dipole–dipole interactions, but even they were of minor importance. Within a single cage, both nonpolar and polar guest molecules such as EO, THF, and acetone have only small barriers to rotational freedom, which approximates that in the vapor phase. The rotational freedom is probably due to the fact that the sum of the cage water dipoles effectively cancel near the center of each cage, and even the quadrupolar fields are relatively small.

2.1.3.2 Geometry of the guest molecules

In a review of the motions of guest molecules in hydrates, Davidson (1971) indicated that all molecules between the sizes of argon (3.8 Å) and cyclobutanone (6.5 Å) can form sI and sII hydrates, if the above restrictions of chemical nature are obeyed. Ripmeester and coworkers note that the largest simple structure II former is tetrahydropyran (THP) ($C_5H_{10}O$) with a van der Waals diameter of 6.95 Å (Udachin et al., 2002). Closely following THP are *m*- and *p*-dioxane and carbon tetrachloride, each with a molecular diameter of 6.8 Å (Udachin et al., 2002). Molecules of size between around 7.1 and 9 Å can occupy sH, provided that the below shape restrictions are obeyed and a help gas molecule such as methane is included.

According to the work by von Stackelberg and Jahns (1954), the structure I and II water lattice parameters showed no significant distortion by any guest. However, Udachin et al. (2002) have shown from single crystal x-ray diffraction that there is a general trend of lattice size with guest size (although this trend is not completely regular). For example, trimethylene oxide, chloroform, THP, and benzene (with Xe as the second guest), which have increasing van der Waals diameters of 6.01, 6.50, 6.95, and 7.07 Å, exhibit increasing lattice parameters of 17.182, 17.236, 17.316, and 17.363 Å, respectively, at 263 K. As detailed in Chapter 5, Holder et al. (1994) and Zele et al. (1999) show that lattice stretches of

this order of magnitude can have a significant effect on thermodynamic parameters. Similar systematic studies on sH await single crystal diffraction measurements.

Increases in lattice parameter with guest size, and hence increasing unit cell volume, may have a significant effect on the free energy change (Tse, 1987). In addition, small changes in lattice parameter have been predicted to cause significant changes to the hydrate formation pressure (Kini et al., 2002). For example, a change of only 0.5% in lattice size may cause a change in predicted pressure of up to 15%, and even a 0.1% change in lattice size can change the predicted pressure by about 2%. The program CSMGem, included in the CD accompanying this book, has corrected the older theory of van der Waals and Platteeuw (1959).

The lattice parameter, and hence the average cavity diameter, is a function of temperature, pressure, and guest composition. The dependence of lattice parameter on guest composition and temperature is illustrated in Figures 2.12a (sI), b (sII).

Ratios of Guest Molecules to Host Cavities. To determine the size upper limit of each cavity available for a guest, Davidson suggested subtracting the van der Waals radius of the water molecule from the "average cage radius" values given in Table 2.1. To determine the upper and lower limits to guest size, it is instructive to consider the diameter ratios of the guest molecule to each cavity for simple (single guest) hydrate formers.

Table 2.4 presents the diameter ratios of natural gas components (and a few other compounds) relative to the diameter of each cavity in both structures. Also presented are two unusual molecules, cyclopropane and trimethylene oxide, which can form simple hydrates of either structure sI or sII; hydrates of these molecules are discussed in Section 2.1.3.3, in the subsection on structural changes in simple hydrates.

In Table 2.4 size ratios of guest diameter/cavity diameter denoted with the superscript "ζ" are those occupied by the simple hydrate formers. For example, in methane hydrate, methane occupies both the small and large cages of structure I. In propane hydrate, propane occupies only the large cages of structure II. The values in Table 2.4 demonstrate a size ratio lower bound of about 0.76, below which the molecular attractive forces contribute less to cavity stability. Above the upper bound ratio of about 1.0, the guest molecule cannot fit into a cavity without distortion. Simple hydrate species capable of occupying the 5^{12} cavity of either structure will also enter the large cavity of that structure.

For simple hydrate-forming components of natural gas, nitrogen was determined (Davidson et al., 1986a) to stabilize the 5^{12} cavities of structure II with a size ratio of 0.82 and it also occupies all the large $5^{12}6^4$ cavities. Nitrogen, being the smallest natural gas hydrate former, provides insignificant stability to the large cavity in either structure ($5^{12}6^2$ or $5^{12}6^4$), so nitrogen forms sII with a fractionally higher number of small cavities occupied in the unit cell. In Table 2.4, the size ratio of nitrogen in the 5^{12} cavity of structure II is 0.82; whereas the $5^{12}6^4$ cavity shows a size ratio of 0.62, which is less than the lower bound value of 0.76, hence indicating less significant cavity stability. Since nitrogen is so small, two molecules can occupy the $5^{12}6^4$ cavity at high pressures, as discussed in Section 2.1.2.2.5.

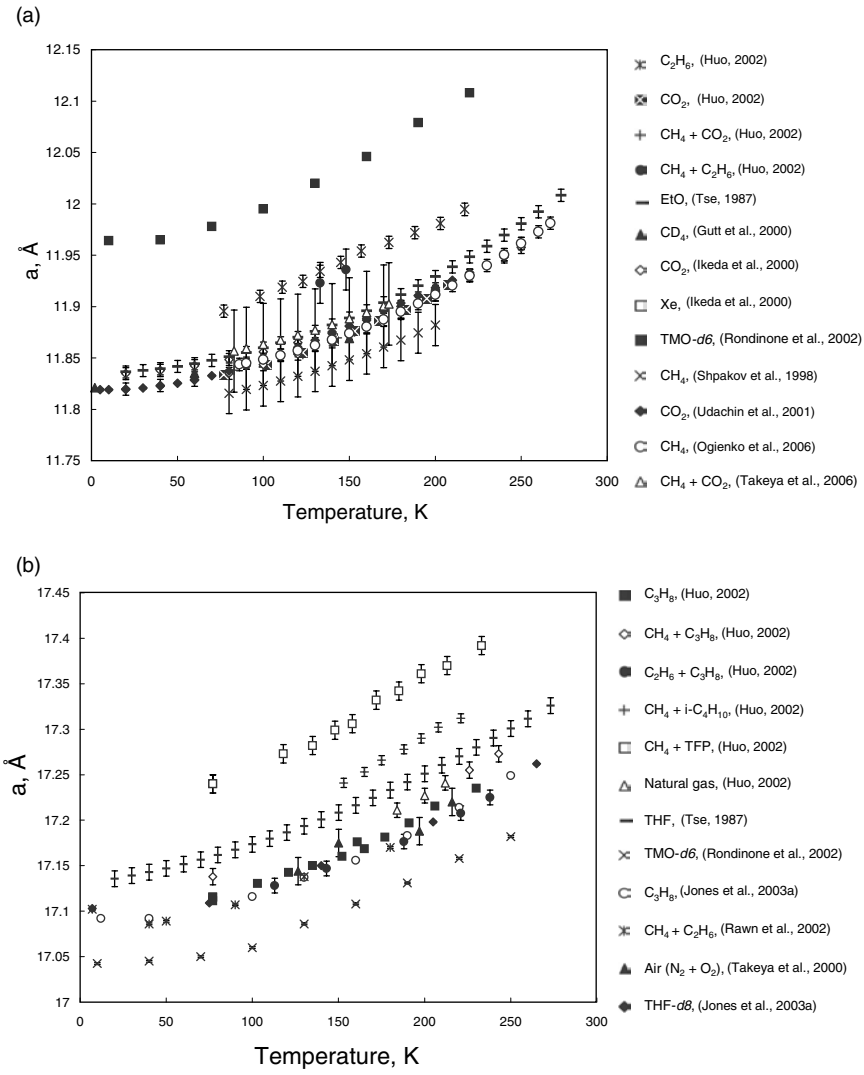

FIGURE 2.12 Lattice parameter vs. temperature plots for sI (a) and sII (b) hydrates.

As simple hydrates, methane, and hydrogen sulfide can stabilize the 5^{12} cavities of structure I (size ratios of 0.86 and 0.90, respectively) and they can occupy all the large $5^{12}6^2$ cavities of sI (size ratios of 0.74 and 0.78, respectively). Ethane occupies the $5^{12}6^2$ cavities of structure I with a ratio of 0.94. Propane and iso-butane each occupy the $5^{12}6^4$ cavities of structure II with a size ratio of 0.94 and 0.98, respectively.

n-Butane does not form a simple hydrate; the ratio of n-butane to the largest cavity of sII is almost 7% larger than the $5^{12}6^4$ free cavity diameter. However,

TABLE 2.4
Ratio of Molecular Diameters[b] to Cavity Diameters[c] for Natural Gas Hydrate Formers and a Few Others

		Molecular diameter/cavity diameter for cavity type			
Guest hydrate former		**Structure I**		**Structure II**	
Molecule	**Diameter[b] (Å)**	5^{12}	$5^{12}6^2$	5^{12}	$5^{12}6^4$
He	2.28	0.447	0.389	$0.454^{\zeta\phi}$	$0.342^{\zeta\phi}$
H_2	2.72	0.533	0.464	$0.542^{\zeta\phi}$	$0.408^{\zeta\phi}$
Ne	2.97	0.582	0.507	$0.592^{\zeta\phi}$	$0.446^{\zeta\phi}$
Ar	3.8	0.745	0.648	0.757^{ζ}	0.571^{ζ}
Kr	4.0	0.784	0.683	0.797^{ζ}	0.601^{ζ}
N_2	4.1	0.804	0.700	0.817^{ζ}	0.616^{ζ}
O_2	4.2	0.824	0.717	0.837^{ζ}	0.631^{ζ}
CH_4	4.36	0.855^{ζ}	0.744^{ζ}	0.868	0.655
Xe	4.58	0.898^{ζ}	0.782^{ζ}	0.912	0.687
H_2S	4.58	0.898^{ζ}	0.782^{ζ}	0.912	0.687
CO_2	5.12	1.00^{ζ}	0.834^{ζ}	1.02	0.769
C_2H_6[a]	5.5	1.08	0.939^{ζ}	1.10	0.826
c-C_3H_6	5.8	1.14	0.990	1.16	0.871^{ζ}
Trimethylene oxide, $(CH_2)_3O$[a]	6.1	1.20	1.04^{ζ}	1.22	0.916^{ζ}
C_3H_8	6.28	1.23	1.07	1.25	0.943^{ζ}
i-C_4H_{10}	6.5	1.27	1.11	1.29	0.976^{ζ}
n-C_4H_{10}	7.1	1.39	1.21	1.41	1.07

$^{\zeta}$ Indicates the cavity occupied by the simple hydrate former.
$^{\phi}$ Indicates that the simple hydrate is only formed at very high pressure.
[a] The structure has been confirmed by single crystal x-ray analysis (Udachin et al., 2002).
[b] Molecular diameters obtained from von Stackelberg and Muller (1954), Davidson (1973), Davidson et al. (1984a, 1986a), or Hafemann and Miller (1969).
[c] The cavity diameter is obtained from the cavity radius from Table 2.1 minus the diameter of water (2.8 Å).

a hydrate of sII can be formed from n-butane with the help of gases in the small cages, such as methane (Wu et al., 1976), hydrogen sulfide (Davidson et al., 1977a), or xenon (Ripmeester and Ratcliffe, 1990a; Udachin et al., 2002).

Of the natural gas components that form simple hydrates, nitrogen, propane, and iso-butane are known to form structure II. Methane, ethane, carbon dioxide, and hydrogen sulfide all form sI as simple hydrates. Yet, because the larger molecules of propane and iso-butane only fit into the large cavity of structure II, natural gas mixtures containing propane and iso-butane usually form structure II hydrate (see Section 2.1.3.3 in the subsection on structural changes in binary hydrate structure).

In Table 2.4 it is interesting to note that the simple hydrate of methane always occupies the small cavity of structure I (5^{12} diameter ratio is 0.86) while the diameter ratio of methane to the 5^{12} cavity of structure II is 0.87—apparently a very small difference. Ripmeester (1988) suggested that for such small, simple hydrate formers the transition from structure II to structure I is brought about by the additional stability gained by the guest occupying the $5^{12}6^2$ cavity. Yet for smaller molecules, such as nitrogen, sII forms because it has almost three times the number of 5^{12} cages per unit volume (0.0033/Å^3 in sII vs. 0.0012/Å^3 in sI) that stabilize sII.

Table 2.4 indicates the structures that have been confirmed by single crystal x-ray analysis by Udachin et al. (2002). In this work, Udachin et al. were able to obtain high-quality single crystals on these compounds and therefore obtained the absolute cage occupancies. For ethane sI hydrate, the large cages are filled with a very low fraction (0.058) of the small cages occupied.

Tables 2.5a,b provide a comprehensive list of guest molecules forming simple sI and sII clathrate hydrates. The type of structure formed and the measured lattice parameter, *a*, obtained from x-ray or neutron diffraction are listed. Unless indicated by a reference number, the cell dimension is the 0°C value given by von Stackelberg and Jahns (1954). Where no x-ray data exists, assignment of structure I or II is based on composition studies and/or the size of the guest molecule. Tables 2.5a,b also indicate the year the hydrate former was first reported, the temperature (°C) for the stable hydrate structure at 1 atm, and the temperatures (°C) and pressures (atm) of the invariant points (Q_1 and Q_2). Both cyclopropane and trimethylene oxide can form sI or sII hydrates. Much of the contents of these tables have been extracted from the excellent review article by Davidson (1973), with updated information from more recent sources (as indicated in the tables).

A principal theme of this text is the direct relation of macroscopic properties to molecular structure. In concluding the discussion on the sI and sII cavity size ratios, two examples are given of how macroscopic engineering properties (equilibrium pressure and temperature, and heat of dissociation) are determined by the size ratios in Table 2.4.

Example 2.1: Molecular Size Determines Structure and Equilibrium Pressure

When the restriction of a simple hydrate is removed, the addition of a small amount of a second, larger hydrocarbon sometimes has a dramatic effect on the hydrate formation pressure. Consider the hydrate formation pressure effect of adding a small amount of propane (C_3H_8) to methane (CH_4), and how such effects may be interpreted in terms of molecular structure.

In Chapter 6, the data of Deaton and Frost (1946) indicate that at 280.4 K, hydrates form from liquid water with pure CH_4 at 5.35 MPa, yet hydrates are formed at 3.12 MPa with 99% CH_4 + 1% C_3H_8. One might wonder

TABLE 2.5a
List of Simple sI and sII Hydrate Formers, and the Hydrate Structure and Properties

Guest molecule	Structure, *a* value (°C)	Year first reported	*T* (°C); *P* (atm) at Q_1	*T* (°C); *P* (atm) at Q_2	*T* (°C), *P* = 1 atm
Ar	II**, 17.07(173°)	1896	−0.8; 87	No Q_2	−124
Kr	II**, 17.08(173°)	1923	−0.1; 14.3	No Q_2	−49.8
Xe	I, 12.0	1925	0; 1.5	No Q_2	−10.4
H_2	II	1999			
N_2	II*	1960	−1.3; 141.5	No Q_2	—
O_2	II*	1960	−1.0; 109.2	No Q_2	—
Cl_2	I, 11.82[b] (0°)	1811	−0.22; 0.316	28.3; 8.4	9.7
BrCl	I, 12.07	1828	0; 0.165	25, 2.5	18
CO_2	I, 12.07	1882	0; 12.4	9.9, 44.4	−55
N_2O	I, 12.03	1888	0; 9.7	12, 41	—
H_2S	I, 12.02	1840	−0.4; 0.918	29.5; 22.1	0.4
H_2Se	I, 12.06	1882	0; 0.455	30, 11	8
SO_2	I, 11.97	1829	−2.6; 0.274	12.1; 2.33	6.8
COS	I, 12.14	1954	—	—	—
CH_4	I, 11.981[c]	1888	−0.2; 25.3	No Q_2	−78.7
C_2H_2	I, 12.00[d] (−156°)	1878	0; 5.75	15; 33	−40.2
C_2H_4	I	1888	−0.1; 5.44	No Q_2	−36.9
C_2H_6	I	1888	−0.03; 5.23	14.7; 33.5	−32
Propylene	II	1952	−0.134; 4.60	0.958; 5.93	—
Cyclopropane	I, 12.14	1960		16.21; 5.59	2.8
	II	1969	−0.05; 0.619		
C_3H_8	II, 17.40	1890	0; 1.74	5.7; 5.45	−11.6
iso-butane	II, 17.57	1954	0.00; 1.12	1.88; 1.653	−2.8
Cyclopentene	II	1950	—	3.2	—
Cyclopentane	II	1950	—	7.7	—
CH_3F	I	1890	0; 2.1	18.8; 32	—
CH_2F_2	I	1890	—	17.6	—
CHF_3	I, 12.05	1890	—	21.8	—
CF_4	I	1969	0; 41.5	—	—
C_2H_3F	I, 12.11	1954	—	—	—
C_2H_5F	I	1890	0; 0.7	22.8; 8	3.7
CH_3CHF_2	I, 12.12	1954	0; 0.54	14.9; 4.30	4.3
$(CH_3)_3CF$	II	1969	—	—	—

* O_2 (Tse et al., 1986) and N_2 (Davidson et al., 1984b) form sII hydrate.

**Ar, Kr (Davidson et al., 1984a) form sII hydrate.

Lattice parameter values determined by [a](Davidson et al., 1984a), [b](Pauliing and Marsh, 1952), [c](Ogienko et al., 2006), [d](Hou, 2002).

Note: Unless indicated, extracted from Davidson (1973, Table I). Guests requiring an additional small molecule to stabilize the hydrate structure are not included in this table.

TABLE 2.5b (Continued)

Guest molecule	Structure, *a* value (°C)	Year 1st reported	*T* (°C); *P* (atm) at Q_1	*T* (°C); *P* (atm) at Q_2	*T* (°C), *P* = 1 atm
CH_3Cl	I, 12.00	1856	0; 0.41	20.5; 4.9	7.5
CH_2Cl_2	II, 17.33	1897	0; 0.153	1.7; 0.211	—
$CHCl_3$	II, 17.236[e]	1885	−0.09; 0.065	1.7; 0.090	—
C_2H_3Cl	II	1897	—	1.15; 1.80	—
C_2H_5Cl	II, 17.30	1890	0; 0.265	4.8; 0.77	—
CH_3CHCl_2	II	1897	0; 0.072	1.5; 0.092	—
CH_2ClF	I	1960	−0.2; 0.222	17.88; 2.825	9.83
$CHClF_2$	I, 11.97 (2°)	1947	−0.2; 0.84	16.3; 7.6	0.9
$CHCl_2F$	II	1954	−0.13; 0.145	8.61; 0.998	—
CCl_2F_2	II, 17.37; 17.13 (2°)	1947	−0.1; 0.36	12.1; 4.27	5.2
CCl_3F	II, 17.29	1947	−0.1; 0.080	8.5; 0.65	—
CH_3CClF_2	II, 17.29	1954	−0.04; 0.136	13.09; 2.294	9.1
CH_3Br	I, 12.09	1856	−0.24; 0.238	14.73; 1.51	11.3
C_2H_5Br	II	1948	0; 0.2	1.4; 0.22	—
CH_3I	II, 17.14	1880	0; 0.097	4.3; 0.23	—
$CBrF_3$	II	1961	−0.1; 0.88	11	0.5
CBr_2F_2	II	1960	—	4.9; 0.501	—
$CBrClF_2$	II	1960	0.00; 0.189	9.96; 1.673	7.6
CH_3SH	I, 12.12	1887	0.00; 0.31	12.0; 1.25	10
Ethylene oxide	I, 12.1 (−10°) 12.03 (−25°)	1863	−2.1	11.1	—
Dimethyl ether	II, 17.47	1954	—	—	—
Propylene oxide	II, 17.124 (−138°)	1952	−4.7	−3.5	—
Trimethylene oxide	II, 17.095 (−138°); I, 12.11[f] (−52°)	1966	—	−13.1 −20.8	—
1,3-Dioxolane	II, 17.118 (−138°) 17.157[a]	1966	—	−3	—
Furan	II, 17.3 (−10°)	1950	—	4.6	—
2,5-Dihydrofuran	II, 17.166 (−138°)	1966	−3.3	−1.2	—
Tetrahydrofuran	II, 17.18 (−10°) 17.170 (−138°) 17.194[e]	1950	−1	4.4	4.4
Tetrahydropyran	II, 17.316[e] (−100°)	1995[g]	−0.8		
Acetone	II, 17.16 (−38°) 17.181[a]	1961	—	−19.8	—
Cyclobutanone	II, 17.161 (−138°)	1966	—	0	—

[e] Values determined by Udachin et al. (2002), [f] (Rawn et al., 2002), [g] (Dyadin et al., 1995)

Note: Unless indicated extracted from Davidson (1973, Table I). Guests requiring an additional small molecule to stabilize the hydrate structure are not included in this table.

how the addition of only 1% C_3H_8 caused a decrease in pressure by 42%. In Section 5.2, Figure 5.15 (at 277.6 K) shows that such a precipitous pressure decrease is caused by a hydrate crystal change from sI (with 100% CH_4) to sII (with 99% CH_4 + 1% C_3H_8). With a crystal structure change, it seems reasonable that a significantly different thermodynamic state (three-phase temperature and pressure) is required for stability.

We can interpret the 42% decrease in equilibrium pressure, caused by a 1% change in composition, in terms of cavity size ratios shown in Table 2.4. Propane only fits into the $5^{12}6^4$ cavity of structure II, C_3H_8 is too large to occupy any other cavity. For CH_4, diameter ratios in the 5^{12} cavities of sI (0.86) and sII (0.87) differ by 1.5%.

Pure methane is stabilized in sI only by the additional stability of the molecule in the $5^{12}6^2$ cavity. With only a small amount of propane to encourage the stability of sII, the similar size ratios of methane in the 5^{12} cavities and large degree of stability propane provides (0.94) to the sII large cage enable a structure transition.

In summary, the concept of guest to cavity size ratios (and hydrate structure change) can provide molecular comprehension of a substantial decrease in equilibrium pressure required for a small composition change. The sII stability by small amounts of propane results in the fact that most natural gases form sII, because most reservoirs contain small amounts of propane.

The second example of microscopic structure reflected in macroscopic properties is almost as important as determining phase equilibria conditions. After establishing that hydrates will form (or dissociate) at certain pressure and temperature conditions, engineers are often interested in the amount of energy required for the phase transition.

Example 2.2: Cavity Size Ratios Determine Heat of Dissociation

In Section 4.6.1 enthalpy evidence for structures I, II, and H is presented to suggest that guest size determines the approximate heat of dissociation by determining the cavity occupied.

The heat of dissociation (ΔH_d) is defined as the enthalpy change to dissociate the hydrate phase to a vapor and aqueous liquid, with values given at temperatures just above the ice point. To a fair engineering approximation ΔH_d is

1. a function not only of the hydrogen bonds in the crystal but also of cavity occupation, and
2. independent of guest components and mixtures of similar size components within a limited size range.

As one illustration, simple hydrates of C_3H_8 and i-C_4H_{10} have similar ΔH_d of 129 and 133 kJ/mol (Handa, 1986) because they both occupy the $5^{12}6^4$ cavity, although their size/cavity ratios are somewhat different (0.94 and 0.98). This similarity of ΔH_d is remarkable, but it is due principally to the occupation of the $5^{12}6^4$ cavity.

Similar statements could be made about the ΔH_d values for other simple hydrate formers that occupy similar size cavities, such as C_2H_6 (ΔH_d = 72 kJ/mol; Handa, 1986) and CO_2 (ΔH_d = 73 kJ/mol; Long, 1994) in the $5^{12}6^2$ cavity, or CH_4 and H_2S (ΔH_d within 3% of each other; Long, 1994) that occupy both 5^{12} and $5^{12}6^2$ as simple hydrates.

As a second illustration, mixtures of $C_3H_8 + CH_4$ have a value of ΔH_d = 79 kJ/mol over a wide range of composition. In such mixtures, C_3H_8 occupies most of the $5^{12}6^4$ cavities while CH_4 occupies only a small number of $5^{12}6^4$ and many 5^{12}. As shown in Section 4.6, most natural gases (which form structure II) have similar values of ΔH_d. Note that mixtures that fill both sII cavities have a lower value of ΔH_d (79 kJ/mol) than components such as C_3H_8 that fill only the $5^{12}6^4$ cavity (ΔH_d = 129 kJ/mol).

Similarly, over a wide range of composition for methane and ethane, ΔH_d values are similar (74 kJ/mol) for components entering both cavities of sI. Identical arguments may be used to explain similar ΔH_d values of 79.5 $\pm$ 7 kJ/mol (Mehta and Sloan, 1996) for sH binary mixtures with methane, since all three cavities are occupied.

The second illustration indicates that less energy is required to dissociate structures with both cavities filled, than those with one cavity filled. Tse (1994) suggests that collisions of a guest with the cavity wall weakens interactions between the hydrogen bonds, which is also reflected in a high value of thermal expansion.

Table 2.6 lists the help guests for sII hydrate and includes the works of Ripmeester and Ratcliffe (1990b), Udachin et al. (2002), and Davidson (1973, table VII) of stabilizing effects of help guests. The stabilizing effect of a second encageable component is particularly evident for structure II hydrates, in which the help gas may occupy the otherwise empty cages. In all the cases listed, the large molecule does not form a hydrate on its own and requires a help guest to stabilize the structure. For example, benzene and cyclohexane will not form a hydrate on their own, but are stabilized in structure II hydrate with Xe as the help gas (Ripmeester and Ratcliffe, 1990a). Similarly, cyclohexanone will not form a hydrate on its own, but in the presence of a help gas, such as hydrogen, will form sII hydrate (Strobel et al., 2007).

Pressure reductions have been observed for methane hydrate formation when organic components (that are very insoluble in water) are added to the water + methane system. These organic components include THP, cyclobutanone, methylcyclohexane, CHF_3, and CF_4 (Mooijer-van den Heuvel et al., 2000;

TABLE 2.6
List of Help Guests for sII Hydrate

Hydrate former	Hydrate structure	Help gas
Cyclohexanone[a]	sII	H_2
Benzene*	sII	Xe
Cyclohexane*	sII	Xe
Cyclohexene oxide*	sII	Xe
Isobutylene*	sII	Xe
cis-2-Butene*	sII	Xe
Allene*	sII	Xe
n-Butane*	sII	CH_4, H_2S, Xe
Norbornane*	sII	Xe
Bicycloheptadiene*	sII	Xe
Methyl formate*	sII	Xe
Acetonitrile*	sII	Xe
Neopentane*	sII	Xe
1,4-Dioxane	Assumed sII	CH_4
1,3-Dioxane	Assumed sII	CH_4
CCl_4		CO_2, N_2
C_2H_5I		N_2
CS_2		N_2, O_2
CH_2ClCH_2Cl		Air

[a] Confirmed from neutron diffraction data by Strobel et al. (2007).
* Hydrate structures containing hydrate former + Xe help gas have been confirmed by ^{129}Xe NMR spectroscopy by Ripmeester and Ratcliffe (1990a).

Hara et al., 2005). THP, cyclobutanone, and cyclohexane also showed pressure reductions for carbon dioxide hydrate formation (Mooijer-van den Heuvel et al., 2001). THP, cyclobutanone, cyclohexane, and methylcyclohexane all reduced not only the pressure for propane hydrate formation, but also shifted the $H–L_W–L_{C3H8}$ line to lower temperature (Mooijer-van den Heuvel et al., 2002).

Tohidi et al. (2001) also suggested that the stability of simple methane and nitrogen hydrates could be increased by using sH large guest formers. They suggested that the C_6—C_{10} fraction of real petroleum fluids are potential sH hydrate formers, though no evidence exists so far that real reservoir fluids are more likely to form structure H.

As a complement to Table 2.4, size ratios of sH formers are shown in Table 2.7. Although many large sH formers are known, only alkanes and cycloalkanes are of interest, because alkenes and alkynes do not occur in natural hydrocarbons due to their reactivity. A large number of branched alkanes, including methyl butane, all polymethyl butanes, and a number of polymethyl pentanes form sH hydrates.

TABLE 2.7
Structure H Size Ratios of Molecular Diameters[d] to Cavity Diameters[e] for Alkanes, Cycloalkanes with Methane, and Other Small Molecules in Both the Small Cavities

		Cavity type	Molecular diameter/cavity diameter[e]
Large molecule guest diameter[d] (Å)		**Small molecule**	$5^{12}6^8$
2-Methylbutane[a]	7.98	Xe	0.91
2,2-Dimethylbutane[a]	8.02	CH_4, Xe	0.91
2,3-Dimethylbutane[a]	7.44	CH_4, N_2, Xe	0.85
2,2,3-Trimethylbutane[a]	7.49	CH_4, Xe	0.85
2,2-Dimethylpentane[a,c]	9.20	CH_4, N_2, Xe, Xe/H_2S	1.05
3,3-Dimethylpentane[a]	9.24	CH_4, Xe	1.05
Methylcyclopentane[a]	7.33	CH_4, Xe	0.83
Ethylcyclopentane	9.15	CH_4	1.04
Methylcyclohexane[a,b]	8.37	CH_4, N_2, Xe	0.95
cis-1,2-Dimethyl-cyclohexane[a]	8.38	Xe	0.95
1,1-Dimethyl-cyclohexane	8.33	Xe	0.95
Ethylcyclohexane	9.82	CH_4	1.12
Cycloheptane	7.60	CH_4	0.87
Cyclooctane[a]	7.83	Xe	0.89
Adamantane[a]*	7.36	Xe	0.84
Hexamethylethane[a]	7.32	Xe	0.83
Cycloheptene[a]	7.51	Xe	0.85
cis-Cyclooctene[a]	7.75	Xe	0.88
Bicyclo[2,2,2]oct-2-ene[a]	7.17	Xe	0.82
2,3-Dimethyl-2-butene[a]	6.78	Xe	0.77
2,3-Dimethyl-1-butene[a]	7.87	Xe	0.90
3,3-Dimethyl-1-butene[a]	7.66	Xe	0.87
3,3-Dimethyl-1-butyne[a]	7.74	Xe	0.88
2-Adamantanone[a]	7.87	Xe	0.90
Hexachloroethane[a]	6.86	Xe	0.78
Tetramethylsilane[a]	7.32	Xe	0.83
tert-Butylmethylether[a]	7.72	Xe	0.88
Isoamyl alcohol[a]	8.96	Xe	1.02

[a] Large guest occupancy in the $5^{12}6^8$ cavity of sH hydrate confirmed by ^{129}Xe NMR spectroscopy (Ripmeester and Ratcliffe, 1990a).

[b] sH hydrate structure confirmed by single crystal x-ray data (Udachin et al., 2002).

[c] sH confirmed by single crystal x-ray diffraction with Xe, H_2S in small cages (Udachin, 1997b).

[d] Longest length of large guest molecules derived from DFT B3LYP computations using SPARTAN, coordinates exported to HyperChem, and H atom van der Waals diameter added.

[e] Cavity diameter determined from cavity radii from Table 2.1 (see note *d* of Table 2.1) minus the molecular diameter of water (2.8 Å).

Table 2.7 contains data for natural gas help gases (methane, hydrogen sulfide, and nitrogen) for sH (Ripmeester et al., 1987, 1991; Tse, 1990; Danesh et al., 1994; Udachin et al., 1997b, 2002). These help gases occupy both small cavities. Xe is also included in the list of help gases since this has been used for structure confirmation of the sH cavity occupancy of many of the large molecules (Ripmeester and Ratcliffe, 1990a).

In Table 2.7, $5^{12}6^8$cavity size ratios exceed unity for a few of the large guest components. Yet there is a substantial amount of data indicating that the compounds in Table 2.7 form sH hydrates, for example, isoamyl alcohol has a size ratio in the $5^{12}6^8$ cage of 1.02, yet has been confirmed by ^{129}Xe NMR to form sH hydrate. It is uncertain whether ratios exceeding unity are because of the overestimation of the sizes of the large guests or a slight underprediction of the $5^{12}6^8$ cavity, or perhaps the guest shape plays a significant role.

Shape of Guest Molecules. The shape of guest molecules plays a minor part in the hydrate structure and properties for sI and sII; however for structure H, guest shape does play a very significant role. Although spectroscopic evidence exists for the shape effect in sI and sII, most of the sH shape evidence relies upon phase equilibria of compound homologs of similar size, but slightly different shapes.

For sI and sII, Davidson et al. (1977a, 1981) performed NMR spectroscopy and dielectric relaxation measurements where applicable, in order to estimate the barriers to molecular reorientation for simple hydrates of natural gas components, except carbon dioxide. Substantial barriers to rotation should also affect such properties as hydrate heat capacity.

For structure I formers, essentially no barriers were found for methane and hydrogen sulfide, while the average barrier for ethane was 1.2 kcal/mol, indicating a rotational restriction due to its shape in the oblate 14-hedra. The average barriers for structure II formers were 0.6, 1.2, and 1.4 kcal/mol for propane, iso-butane, and n-butane (double hydrate with hydrogen sulfide), respectively (Davidson et al., 1977b). These barriers may be compared to a van der Waals interaction of 0.3 kcal/mol or a hydrogen bond of 5 kcal/mol. For example, using heat capacity measurements, White and MacLean (1985) determined that there was no barrier to rotation for hydrated THF molecules.

Due to shape restrictions, n-butane forms sII (with a small help gas) in the gauche isomer (Davidson et al., 1977b; Subramanian and Sloan, 2002)—rather than the *trans* isomer that is preferred in the gas phase. At most temperatures of interest to the natural gas processor above 100 K, sII guest molecules have only small restrictions to reorientation.

However, the "small rotation inhibition" heuristic for sI and sII may be flawed for guests at the upper size boundary of the large cavity. For guest molecules of intermediate sizes, such as cyclopropane and trimethylene oxide, small changes in size caused by thermal stimulation of rotational and vibrational energies may be sufficient to determine the occupied cavity as discussed in the following section.

For structure H, however, the shape of the large guest molecule is of considerable importance, perhaps because it is important to fill the available large cage efficiently. Ripmeester and Ratcliffe (1990a) indicate that, unlike sI and sII,

in sH size considerations are necessary but not sufficient, stating that *trans*-2-butene and the methyl butenes are of a size to fit into the $5^{12}6^8$, yet they do not form hydrates. Molecules of similar or larger sizes have been demonstrated to be sH guests. Efficient space filling of the available cage space is therefore also an important factor to establish whether a molecule will form sH hydrate. That is, the maximum van der Waals contact between the guest and cage walls is required for a large molecule to form sH hydrate. In contrast, this is not an important factor in sI or sII hydrates, where with very few exceptions all molecules of the correct size will stabilize these hydrate structures.

Recently, n-pentane and n-hexane, both previously thought not to form a hydrate, have been shown to occupy the sH lattice with CH_4 and 2,2-dimethylbutane, a known sH former (Lee et al., 2006).

The specifications for the small help gas molecules that fill the small cages of sH hydrate are less rigorous and all guests that adequately fill the small cages in sI and sII hydrate are thought to be suitable sH help gas molecules, for example, Ar, O_2, Kr, CO, Xe, CH_4, H_2S, and then to a lesser extent SO_2, CO_2, CH_3Cl, and acetylene. CH_4, Xe, H_2S, H_2 have been confirmed to be small sH help gas molecules by structural tools, such as NMR spectroscopy, x-ray, and neutron diffraction.

Molecular simulations (Rodger, 1990a,b; Tanaka and Kiyohara, 1993) and neutron scattering (Tse et al., 1993; Baumert et al., 2002) indicate that repulsions between guest and water molecules in sI and sII help stabilize the hydrate structure. A strained cage such as the $5^{12}6^8$ may require optimal filling to achieve the repulsion necessary to form easily at low pressures. Baumert and colleagues (2002) suggest that the repulsive interaction between the guest and cage could also be responsible for the effective energy transfer between the guest and host vibrations, which may cause the low glasslike thermal conductivity of the hydrates.

2.1.3.3 Filling the hydrate cages

In all three hydrate structures, at usual pressures, each cavity can contain at most one guest molecule. At very high pressures, nitrogen, hydrogen, methane, and argon can multiply occupy the large cavity of structure II. (Further discussion on high-pressure phases and multiple occupancy is given in Section 2.1.2.2.5.) Figure 2.13, a revision of a figure originally by von Stackelberg (1949) presents the sizes of simple gas hydrates relative to the size of each cavity.

Five points should be made about Figure 2.13:

1. At normal pressures (i.e., less than around 30 MPa at about 260–290 K), molecules below 3.5 Å become too small to stabilize any cavity, while above 7.5 Å molecules are too large to fit into any cavity of sI or sII.
2. Some molecules can only stabilize the large cavity of sII (e.g., propane and iso-butane only stabilize the $5^{12}6^4$).
3. When a molecule stabilizes the small cavities of a structure, it will also enter the large cavities of that structure.

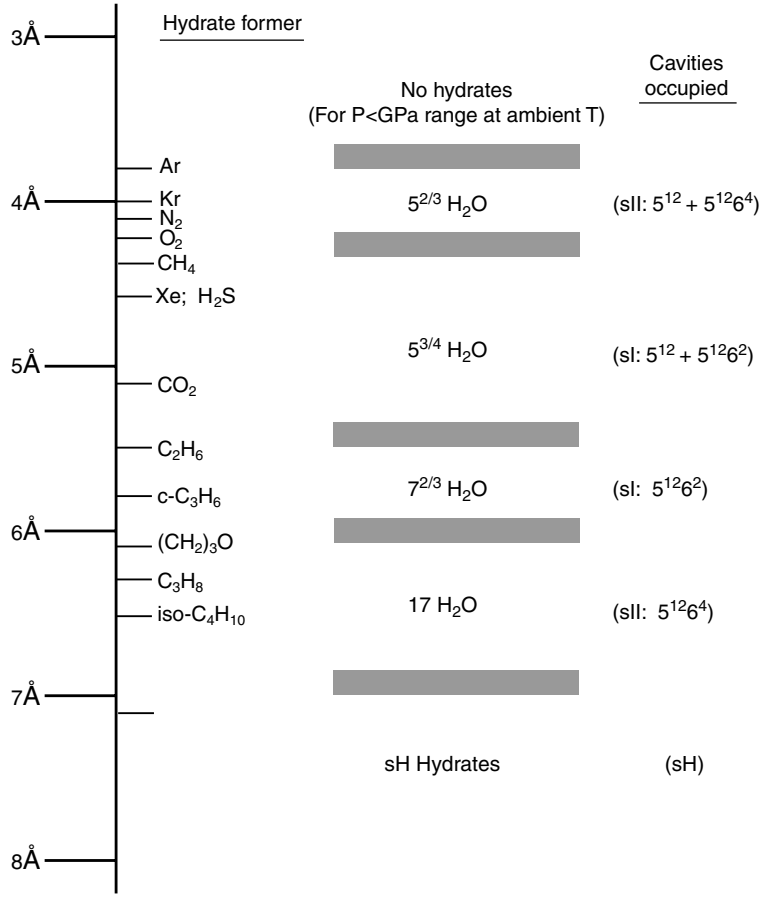

FIGURE 2.13 Comparison of guest molecule sizes and cavities occupied as simple hydrates. (Modified from von Stackelberg, M., *Naturwiss*, **36**, 359 (1949). With permission from Springer-Verlag.)

4. Since 1983, it has been known that the smallest guests (argon, krypton, nitrogen, and oxygen) form sII rather than sI.
5. Molecules of a size within the shaded boundaries exhibit the most nonstoichiometry.

Ideal Hydration Numbers. In Figure 2.13, x-ray and neutron results by Davidson et al. (1984a, 1986a) for argon, krypton, oxygen, and nitrogen indicate that these simple hydrates not only stabilize the 16 smaller cavities of the sII unit cell but also occupy the 8 larger cavities of that structure, for an ideal guest/water ratio of $24G \cdot 136H_2O$ or $G \cdot 5\ 2/3H_2O$. If guest molecule G can only fit the $5^{12}6^4$ of structure II, the ideal ratio will be $8G \cdot 136H_2O$ or $G \cdot 17H_2O$.

The ideal guest/water ratio is $G \cdot 5¾H_2O$ for molecules that can occupy both cavities of structure I, and $G \cdot 7(2/3)H_2O$ for occupants of only the $5^{12}6^2$ of structure I. As indicated in Figure 2.13 molecules of transitional size (shaded region) such as cyclopropane (Majid et al., 1969) and trimethylene oxide (Hawkins and Davidson, 1966) with diameters of 5.8 and 6.1 Å, respectively, may form either structure.

Simple hydrates of sH do not form (at normal pressures), so the concept of an ideal hydrate number is only applicable to two or more guests. In the simplest case, with type X guests fully occupying the smallest two cavity types (5^{12} and $4^35^66^3$) and molecule Y occupying the $5^{12}6^8$ cavity, the ideal hydrate number is $5X \cdot 1Y \cdot 34H_2O$.

Ideal hydrate numbers validate the notion that a substantial amount of hydrocarbon is present in the hydrate. For example, if all cavities of structure II are filled, each volume of hydrate may contain 182 volumes of gas at standard temperature and pressure. This ratio shows the hydrated gas density to be equivalent to a highly compressed gas, but somewhat less than the density of a liquid hydrocarbon. The similarity of hydrates to a highly compressed gas suggests their use for storage, or as an unconventional gas resource, where they occur *in situ* in the deep oceans or permafrost.

Because it is impossible for all cavities to be occupied (an analog would be a perfect crystal) simple hydrates always have more water molecules than the ideal composition. Usually the ratios range from $G \cdot 5(3/4)\,H_2O$ to $G \cdot 19H_2O$, with typical fractional occupancies of the smaller cavities of 0.3–0.9, based on size restrictions. This variation causes clathrate hydrates to be called "nonstoichiometric hydrates," to distinguish them from stoichiometric salt hydrates.

Hydrate Nonstoichiometry. The cause of the nonstoichiometric properties of hydrates has been considered. Evidence for the view that only a fraction of the cavities need to be occupied is obtained from both the experimental observations of variation in composition, and the theoretical success of the statistical thermodynamic approach of van der Waals and Platteeuw (1959) in Chapter 5. Typical occupancies of large cavities are greater than 95%, while occupancy of small cavities vary widely depending on the guest composition, temperature, and pressure.

Davidson (1971) indicated that occupancy of the smaller cages is incomplete for molecules less than 5.0 Å in diameter, and that larger cages in each structure seem to be almost completely occupied. Via the use of NMR, Ripmeester and Davidson (1981) have determined that for ^{129}Xe, the occupancy of the small cages of structure I is 0.74 times that of the large cages.

Glew (1959) suggested that the most nonstoichiometric guest molecules are those for which the size of the guest approaches the upper limit of the free volume of a cavity. For two molecules that approach the size limit of cavities, Glew and Rath (1966) presented experimental evidence that hydrate nonstoichiometry for both chlorine and ethylene oxide was due to the composition of the phase in equilibrium with the hydrates.

A systematic determination of both hydration number (Cady, 1983) and relative cage occupancies (Davidson and Ripmeester, 1984) shows that molecules such as CH_3Cl and SO_2 are the most nonstoichiometric. Although theoretical calculations using the van der Waals and Platteeuw model provides some rationale for the nonstoichiometry, experimental quantification of nonstoichiometry as a function of guest/cavity size ratio has yet to be determined.

Structural Changes in Simple Hydrates. Of particular interest to the question of structure are the simple hydrates of cyclopropane and trimethylene oxide because they can form hydrates of either structure I or structure II as a function of formation conditions. These hydrates are unique examples of structural change of single guest species at different conditions of pressure and temperature.

Consider cyclopropane, first determined to form each structure by Hafemann and Miller (1969). Because trimethylene oxide is miscible, it has a very dissimilar phase diagram, confounding a comparable analysis.

Figure 2.14 is a corrected phase diagram by Majid et al. (1969). In Figure 2.14 most of the hydrate area is occupied by structure I, except for a smaller area between 257.1 and 274.6 K where structure II hydrate forms. This provides four quadrupole points:

1. The normal lower point Q_1 ($I–L_W–H_{II}–V$) at about the ice point.
2. The normal upper point Q_2 ($L_W–H_I–V–L_{CP}$) at 289.4 K.

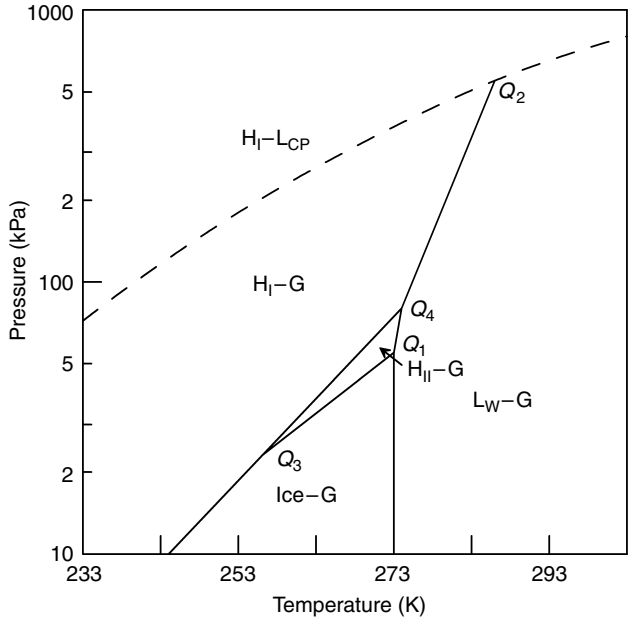

FIGURE 2.14 Pressure–temperature phase diagram for cyclopropane. (Reproduced from Majid, Y.A., Garg, S.K., Davidson, D.W., *Can. J. Chem.*, **47**, 4697 (1969). With permission from the National Research Council of Canada.)

3. The new lowest point Q_3 ($I–H_I–H_{II}–V$) at 257.1 K.
4. A new intermediate point Q_4 ($L_W–H_I–H_{II}–V$) at 274.6 K.

Quadrupole points Q_3 and Q_4 are unusual in that they have two coexisting hydrate phases. Between these two points is a line along which the two hydrate structures coexist with vapor, this line may be a unique example of the way guest size affects the cavity occupied and the pressure and temperature of hydrate formation.

Ohgaki and coworkers (Suzuki, 2001) suggest from Raman spectroscopy measurements that the small 5^{12} cavity of structure I, although vacant at pressures below 200 MPa, is occupied to a small extent by cyclopropane at pressures higher than 200 MPa. The small cage occupancy was also shown to increase with increasing pressures of up to 400 MPa (reaching a small cage/large cage occupancy ratio of around 0.08). The corresponding vibrational energy for cyclopropane in the large cage showed no pressure dependence. Examination of the O─O vibrational modes of the hydrate lattice showed no significant shifts with pressure, unlike that observed for carbon dioxide or methane hydrate. Therefore, these measurements suggest that the cavities of cyclopropane hydrate do not easily contract.

The above findings are analogous to those reported by the same research group for ethane (Morita et al., 2000) and ethylene (Sugahara et al., 2000) hydrates. Based on Raman spectroscopy, ethane or ethylene occupancy of the small cavities of structure I increases with increasing pressure. The low small cage occupancy of ethane in structure I hydrate was also detected from single crystal x-ray diffraction measurements (Udachin et al., 2002).

Structural Changes in Binary (Double) Hydrates. Although CH_4 and C_2H_6 are both sI hydrate formers, Subramanian et al. (2000) showed that a binary CH_4/C_2H_6 mixture can exhibit sI/sII transitions with varying pressure and/or composition. In contrast, a binary CH_4/CO_2 mixture, where again both pure components are sI hydrate formers, forms only sI hydrate.

The sI/sII structural transition of CH_4/C_2H_6 was predicted in 1996 by Hendricks et al. (1996). sI/sII structural transitions were first discovered in the mid-1950s. Von Stackelberg showed from x-ray data that guest combinations of H_2S with CH_3Br, COS, and CH_3CHF_2 form sII hydrates, even though all these guests individually are structure I formers (von Stackelberg and Jahns, 1954). Ripmeester suggested that all small sI guests (occupying the small cavity to a significant extent) when combined with large structure I guests (which do not occupy the small cavity) may form sII hydrate under certain circumstances (Ripmeester, 2000). The formation of sI vs. sII for methane–ethane hydrate has significant effects on the phase equilibria data for this system.

Figure 2.15 (Ripmeester, 2000) correlates the observations of double hydrates and demonstrates the complexity of the structure–size relationship for hydrates containing two types of guest molecules. The combinations of two different types of guests forming sII and sH double hydrates are also listed in Tables 2.6 and 2.7, respectively.

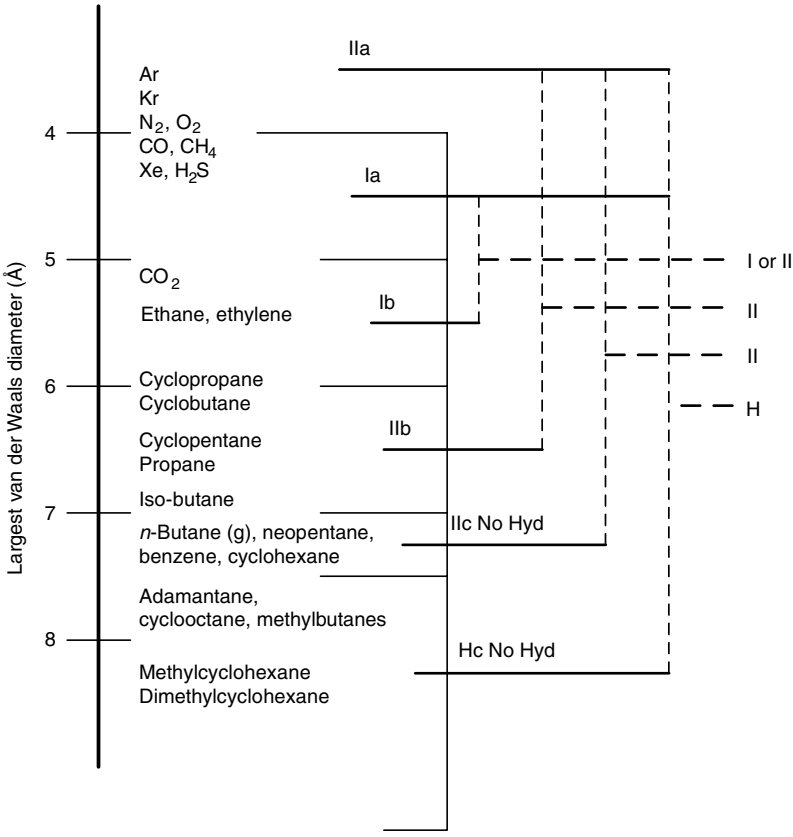

FIGURE 2.15 Correlations of single and double H hydrates. Demonstrating the complexity in guest size–structure correlations for hydrates containing two types of guests. Molecules are classified by how they would behave as single guests. (For example, structure II guests can be divided into three size ranges: [a] occupy 5^{12} cages, [b] only/mostly occupy $5^{12}6^4$ cages, and [c] do not occupy either cage.) The following combinations are known to form double hydrates, although some of the boundaries may not be firmly established: Ia + Ib → structure I or II; IIa or Ia + IIb → structure II; Ia or IIa + IIc → structure II; and Ia or IIa + Hc → structure H. (Redrawn from Ripmeester, J., in *Proc. Third Int. Conf. on Gas Hydrates* (Holder, G.D. and Bishnoi, P.R., eds.), Salt Lake City, UT, Annals of the New York Academy of Sciences, **912**, 1 (2000). With permission.)

Hester and Sloan (2005) extended the size–structure correlations for double hydrates. A simple scheme of guest size–structure boundaries was proposed to predict the sI/sII structural transitions for double hydrates consisting of sI hydrate formers (Figure 2.16). Raman spectroscopy and neutron diffraction measurements were performed to test the limits of these structural transitions.

In agreement with this simple scheme, Ohgaki and coworkers (Makino et al., 2005) used Raman spectroscopy to confirm that a mixture of methane + cyclopropane (one of the largest sI formers) exhibits a sI/sII transition depending

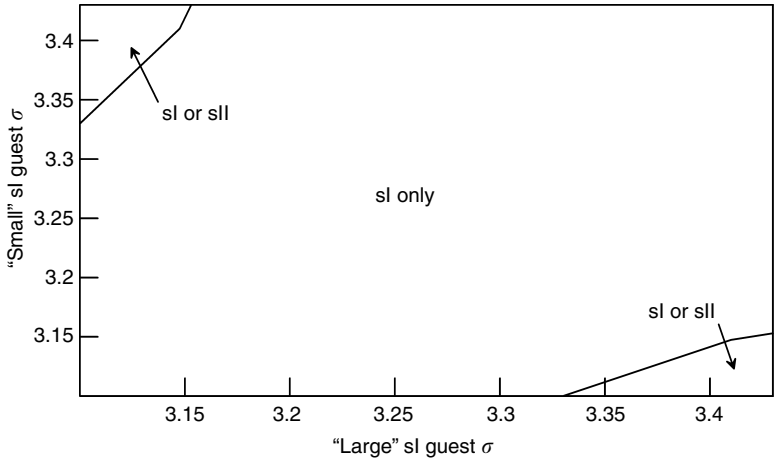

FIGURE 2.16 Qualitative schematic diagram showing predicted sigma (σ) ranges (sigma is effectively the size of the molecule), where a sI to sII transition occurs in a binary system of two sI formers (Hester, 2007).

on the guest composition. Both methane and cyclopropane are sI formers at the experimental conditions of 2.35 MPa, 291.1 K. Conversely, methane + ethylene (a relatively small sI former) mixtures do not undergo a sI/sII structural transition (Makino et al., 2005; Hester, 2007). The relatively small size of ethylene compared to ethane would place it outside of the sI + sII region in Figure 2.16.

2.1.4 Summary Statements for Hydrate Structure

On the basis of the analyses presented in Section 2.1, the following statements represent a summary of hydrate structures:

1. Natural gas clathrate hydrates normally form either in the primitive cubic structure I, in the face-centered cubic structure II, or in the hexagonal structure H.
2. The hydrogen bond is the basis for the interactions of the water molecules bonding in tetrahedral structures similar to that of ice. Pentagonal and hexagonal water clusters formed by hydrogen bonds are frequently found in water, square clusters exist at less frequent intervals.
3. A common cavity to hydrate structures is the pentagonal dodecahedron (5^{12}), which is connected through its vertices to form structure I, through face-sharing in three dimensions to form structure II, or through face-sharing in two dimensions to form connecting layers in structure H.
4. Spaces between the 5^{12} cavities are the larger, oblate $5^{12}6^2$ cavities in structure I, or the spherical $5^{12}6^4$ cavities in structure II. In structure H, both large ($5^{12}6^8$) and small ($4^3 5^6 6^3$) cavities form between layers of 5^{12} cavities.

5. Small molecules that occupy the small cavities, also occupy the large cavities. Large molecules can stabilize sI or sII by only occupying the large cavity, leaving the smaller cavity vacant. Structure H requires that both large and small cavities be occupied.
6. Occupation of hydrate cavities and the hydrate structure is determined to a large degree by the guest size in structures I and II. In structure H both size and shape considerations are necessary for a guest molecule. The repulsive interactions between guests and hosts stabilize the hydrate structure.
7. Hydrate nonstoichiometry appears to be related to the ratio of the guest molecule diameter to the free cavity diameter. Nonstoichiometry increases as that ratio approaches unity.
8. The size ratio of the guest to cavity, is a general guide to determining crystal structures and cage occupancy. In turn, crystal structure determines equilibrium pressures and temperatures for the hydrate phase, as shown in Example 2.1.
9. The combination of structure I guests in a binary hydrate can result in a structural transition (sI/sII), when one guest is small (occupying the small cages to a significant extent) and the other guest is large (only occupying the large cages).
10. Heats of dissociation for all three structures are largely determined by hydrogen bonding and the cavity occupation, as shown in Example 2.2. When similar cavities are occupied, the heats of dissociation are similar (regardless of the guest) within the restrictions listed. Detailed evidence for heats of dissociation effects is presented in Chapter 4.6.1.1.
11. At very high pressures (0.3–2.1 GPa), gas hydrates undergo structural transitions to other hydrate phases and filled ice phases. Guests can multiply occupy the large cages of these high-pressure hydrate phases.
12. The less common structures, Jeffrey's structures III–VII, structure T, and complex layer structures have so far only been found for compounds other than natural gas. These compounds form tetragonal (sIII), hexagonal (sIV, sV), cubic (sVI, sVII), trigonal (sT), and alternating sI/sH layer structures.

2.2 Comparison of Properties of Hydrates and Ice

If all the cavities of structure I or structure II were occupied as a simple hydrate, for example, with xenon or argon, the minimum number of water molecules (5.75 and 5.67, respectively) would be obtained per guest molecule. Both these values yield a structure that is 85 mol.% water. If all three cavity types were completely filled in structure H with two guests, the water mole fraction would be 0.85 as well. As discussed in Section 2.1, due to the nonstoichiometric nature of hydrates, the mole fraction of water is invariably higher than 0.85.

With such high water contents, it is useful as a first approximation to consider some properties of hydrates as variations from those of ice. Davidson (1973)

provides a second microscopic rationale for this comparison by noting that hydrate hydrogen bonds average only 1% longer than those in ice and the O─O─O angles differ from the ice tetrahedral angles by 3.7° and 3.0° in structures I and II, respectively.

Section 2.2.1 summarizes the spectroscopic measurements that have been performed to examine the dynamics of water molecules in hydrate versus ice networks. Sections 2.2.2 and 2.2.3 provide a brief overview of the mechanical and thermal properties, respectively, of hydrates compared to ice. Characterization of these properties will aid in facilitating the accurate interpretation of data obtained from *in situ* detection measurements of natural hydrates. These natural hydrates occur in sediments in permafrost and marine environments. The hydrate mechanical and thermal properties are also important in the evaluation of the location and distribution of natural hydrates in sediments. (Further details are given in Chapter 7—Hydrates in the Earth.)

Table 2.8 is a slight modification of a microscopic and macroscopic property summary by Davidson (1983) for ice and hydrate structures I and II. Although the values in the table were generally measured or estimated for methane or propane hydrates, the contribution of the guest molecule (other than causing the structure to exist) may be considered small for these properties, to a first approximation.

One might anticipate similar results for structures I and II in the absence of measurements. In many of the properties that are derived from structure, the differences between the hydrate crystal structures are not appreciable. One might intuitively expect properties on the basis of the water crystal structure to exhibit less variation between hydrate structures than between hydrate and ice properties, in view of the fact that the 5^{12} cavity is common to each hydrate structure.

2.2.1 Spectroscopic Implications

Via NMR and Raman spectroscopy, we can measure the solid hydrate phase. Although an overview of such spectroscopy measurements is provided in Section 6.2, some of the important results for hydrate properties in comparison to ice are provided here.

Proton NMR spectroscopy and dielectic constant measurements provide evidence about the motion of the water molecules in crystal structures, as reviewed by Davidson and Ripmeester (1984). At very low temperatures (<50 K) molecular motion is "frozen in" so that hydrate lattices become rigid. The hydrate proton NMR analysis suggests that the first-order contribution to motion is due to reorientation of water molecules in the structure; the second-order contribution is due to translational diffusion at these low temperatures.

This is one distinguishing feature between hydrates and ice; water molecules diffuse two orders of magnitude slower in hydrates than in ice. As shown in Table 2.8, ice water molecules diffuse almost an order of magnitude faster than they reorient about a fixed position in the crystal structure. In direct contrast, hydrate water molecules reorient 20 times faster than they diffuse. As for all

TABLE 2.8
Comparison of Properties of Ice, sI, and sII Hydrates*

Property	Ice	Structure I	Structure II
Structure and dynamics			
Crystallographic unit cell space group	$P6_3/mmc$	Pm3n	Fd3m
No. of H_2O molecules	4	46	136
Lattice parameters at 273 K (Å)	$a = 4.52$, $c = 7.36$	12.0	17.3
Dielectric constant at 273 K	94	~58	~58
Far infrared spectrum	Peak at 229.3 cm^{-1}	Peak at 229.3 cm^{-1} with others	
H_2O reorientation time at 273 K (μs)	21	~10	~10
H_2O diffusion jump time (μs)	2.7	>200	>200
Mechanical properties			
Isothermal Young's modulus at 268 K (10^9 Pa)	9.5	8.4[est]	8.2[est]
Poisson's ratio	0.3301[a]	0.31403[a]	0.31119[e]
Bulk modulus (GPa)	8.8; 9.097[a]	5.6; 8.762[a]	8.482[a]
Shear modulus (GPa)	3.9; 3.488[a]	2.4; 3.574[a]	3.6663[a]
Compressional velocity, V_P (m/s)	3870.1[a]	3778[a,b]	3821.8[a]
Shear velocity, V_S (m/s)	1949[a]	1963.6	2001.14[b]
Velocity ratio (comp/shear)	1.99	1.92	1.91
Thermal properties			
Linear thermal expansion at 200 K (K^{-1})	56×10^{-6}	77×10^{-6}	52×10^{-6}
Thermal conductivity ($Wm^{-1}\,K^{-1}$)	2.23	0.49 ± 0.02;	0.51 ± 0.02
at 263 K	2.18 ± 0.01[c]	0.51 ± 0.01[c] 0.587[d]	0.50 ± 0.01[c]
Adiabatic bulk compression at 273 K (GPa)	12	14[est]	14[est]
Heat capacity ($Jkg^{-1}K^{-1}$)	1700 ± 200[c]	2080	2130 ± 40[c]
Refractive index (632.8 nm, −3°C)	1.3082[e]	1.346[e]	1.350[e]
Density (g/cm^3)	0.91[f]	0.94 also see Example 5.2	1.291[g]

* *Note:* Unless indicated, values are from Davidson (1983), Davidson et al. (1986b) and Ripmeester et al. (1994).

[a] Helgerud et al. (2002) at 253–268 K, 22.4–32.8 MPa (ice, Ih), 258–288 K, 27.6–62.1 MPa (CH_4,sI), 258–288 K, 30.5–91.6 MPa (CH_4–C_2H_6, sII).
[b] Helgerud et al. (2003) at 258–288 K, 26.6–62.1 MPa.
[c] Waite et al. (2005) at 248–268 K (ice Ih), 253–288 K (CH_4, sI), 248–265.5 K (THF, sII).
[d] Huang and Fan (2004) for CH_4, sI.
[e] Bylov and Rasmussen (1997).
[f] Fractional occupancy (calculated from a theoretical model) in small (S) and large (L) cavities: sI = CH_4: 0.87 (S) and CH_4: 0.973 (L); sII = CH_4: 0.672 (S), 0.057 (L); C_2H_6: 0.096 (L) only; C_3H_8: 0.84 (L) only.
[g] Calculated for 2,2-dimethylpentane $5(Xe,H_2S)\cdot 34H_2O$ (Udachin et al., 1997b); est = estimated.

solids, however, water diffusion rates in either solid structure is still several orders of magnitude slower than that of a vapor or liquid.

The dielectric constant values in Table 2.8 also suggest that, while hydrate water molecules reorient rapidly compared to molecules in other solids, reorientation rates are only one-half those in ice. The hydrate value is lower than that of ice due to the lower density of hydrogen-bonded water molecules.

Far infrared spectral data by Bertie et al. (1975) and Bertie and Jacobs (1978) indicate that the strength of the hydrogen bonds in hydrates is very similar to that in ice. The far infrared peak at around 229 cm^{-1}, assigned to the lattice modes (translational vibrations) of water molecules, is not significantly shifted in H_2O ice Ih compared to the hydrates. However, the lattice mode peak is different in the deuterated hydrate compared to D_2O ice (Bertie, 1972). Inelastic neutron scattering studies indicate that the water (D_2O) lattice vibrations are coupled to the guest vibrations (Tse et al., 2001; Gutt et al., 2002). Dielectric and NMR measurements also show that the water lattice dynamics are strongly coupled to the guest motions (Ripmeester et al., 2004).

2.2.2 Mechanical Properties

2.2.2.1 Mechanical strength

Compression deformation measurements at constant applied stress (creep) of methane hydrate (Stern et al., 1996) and of gas-hydrate-bearing sediment (Parameswaran et al., 1989; Cameron et al., 1990) suggested that the strength of hydrate is roughly comparable to that of ice. However, in 2003, Durham and coworkers (2003) suggested that these previous creep measurements may have been influenced by impurities, such as liquid water or ice in the sample, a secondary ice layer formed during compaction/deformation, or by a lack of sufficient confining pressure to suppress fracture. Indeed, in 2003, Durham and coworkers determined from compression deformation experiments (at 260–273 K) that methane hydrate is more than 20 times stronger (creep resistant) than ice Ih. That is, under the same applied stress, ice will deform significantly faster by several orders of magnitude than pure methane hydrate. It is known that ice deforms by the coordinated motion of crystalline defects, which are generally diffusion limited (Poirier, 1985). Therefore, the higher mechanical strength of methane hydrate compared to ice may be related to the rate of diffusion of water in methane hydrate being two orders of magnitude slower than ice (Durham et al., 2003). Hence, hydrate should be more creep resistant than ice.

Winters et al. (2000) showed that the compressive strength of a core containing methane hydrate in the pore space is greater than that without hydrate in the pore space. Ebinuma and coworkers (2005) recently performed compression tests on samples consisting of different saturations (48–52%) of methane hydrate filling the pores of silica sand. Methane hydrate saturation is the ratio of the hydrate volume to pore volume. The mechanical strength of the silica sand was found to increase with increasing methane hydrate saturation. The mechanical strength of hydrate samples prepared from sand/ice/gas was shown to remain

constant until the methane hydrate saturation reached up to 25%. Conversely, the mechanical strength of hydrate samples prepared from water-wet sand/gas increased monotonically with methane hydrate saturation.

Hydrate formation in sediment pores depends on the the wettability of the sediment, phase saturations of free water and gas in the pores, the size of the pores, etc. The growth habit of hydrate in sediment pores has been described by Dvorkin et al. (2000) as: (1) hydrate floating in the pore fluid, (2) hydrate as a load-bearing part of the solid phase, (3) hydrate cementing grain contacts, or (4) hydrate acting as a cement forming only at grain contacts. Winters et al. (Winters et al., 2004, Pecher, et al., 2004) suggested that the sediment strength is much lower in the pore filling model than in the cementing model. They showed that laboratory hydrates made from Ottawa sand exhibited strong cementing behavior, while a natural gas hydrate sample from the Mallik 2L-38 well was pore filling.

2.2.2.2 Elastic properties

There is a paucity of reliable, consistent data for hydrate elastic properties. Since these properties depend on crystal structures, many of them can be estimated reliably. However, since 1998, there have been significant efforts to perform accurate measurements of these properties in order to help facilitate correct interpretation of sonic or seismic velocity field data obtained on hydrates in the natural environments.

Whalley (1980) presented a theoretical argument to suggest that both the thermal expansivity and Poisson's ratio should be similar to that of ice. With the above two estimates, Whalley calculated the compressional velocity of sound in hydrates with a value of 3.8 km/s, a value later confirmed by Whiffen et al. (1982) via Brillouin spectroscopy. Kiefte et al. (1985) performed similar measurements on simple hydrates to obtain values for methane, propane, and hydrogen sulfide of 3.3, 3.7, and 3.35 km/s, respectively, in substantial agreement with calculations by Pearson et al. (1984).

Pandit and King (1982) and Bathe et al. (1984) presented measurements using transducer techniques, which are somewhat different from the accepted values of Kiefte et al. (1985). The reason for the discrepancy of the sonic velocity values from those in Table 2.8 and above is not fully understood. It should be noted that compressional velocity values can vary significantly depending on the hydrate composition and occupancy. This has been demonstrated by lattice-dynamics calculations, which showed that the adiabatic elastic moduli of methane hydrate is larger than that of a hypothetical empty hydrate lattice (Shpakov et al., 1998).

Shimizu et al. (2002) extended the previous Brillouin spectroscopy measurements by performing *in situ* measurements on a single crystal methane hydrate. They examined the effect of pressure on shear (TA) and compressional (LA) velocities, and compared these results to that for ice. The shear velocities of methane hydrate and ice were very similar, showing a slight decrease (about 2 to 1.85 km/s) with increasing pressure (0.02–0.6 GPa). Conversely, the compressional velocities of ice and methane hydrate were different. The

compressional velocity of methane hydrate varied from about 3.76 to about 4 km/s, starting at pressures of 0.02–0.6 GPa. The compressional velocity of ice varied from about 3.9 to 4.0 as the pressure was increased from 0.02 to 0.3 GPa. Similar compressional (3.65 km/s) and shear (1.89 km/s) velocities of methane hydrate were measured by Waite et al. (2000).

Pandit and King (1982) also presented values for the bulk modulus, the shear modulus, and the ratio of compressional to shear velocity, with comparisons to ice values as given in Table 2.8. Shimizu et al. (2002) used Brillion spectroscopy to determine the elastic anisotropy, bulk modulus, and elastic modulus, based on velocity measurements for methane hydrate at high pressures (0.02–0.6 GPa). Methane hydrate was found to exhibit almost isotropic elasticity. This is in contrast to cubic crystals (e.g., pressure-induced solid CO_2, CH_4, ice VII), which, although they are optically isotropic, generally show substantial anisotropy. The isotropic elasticity of methane hydrate was attributed to its void-rich network of cavities and larger deviations from an ideal tetrahedral geometry. The adiabatic elastic moduli and bulk modulus values for methane hydrate were found to increase almost linearly with pressure. Shimizu (2002) indicated, based on the evaluation of the compressional components of elastic moduli, that methane hydrate is significantly more compressible than ice.

Lee and Collett (2001) measured the compressional (P-wave) and shear (S-wave) velocities of natural hydrates in sediments (33% average total porosity) at the Mallik 2L-38 well. The P-wave velocity of nongas-hydrate-bearing sediment with 33% porosity was found to be about 2.2 km/s. The compressional velocity of gas-hydrate-bearing sediments with 30% gas hydrate concentration (water-filled porosity of 23%) was found to be about 2.7 km/s, and 3.3 km/s at 60% concentration (water-filled porosity of 13%), that is, about a 20% or 50% increase to nongas-hydrate-bearing sediment. The shear velocity was found to increase from 0.81 to 1.23 km/s.

2.2.3 Thermal Properties

2.2.3.1 Thermal conductivity of hydrates

Stoll and Bryan (1979) first measured the thermal conductivity of propane hydrates (0.393 $Wm^{-1}K^{-1}$ at $T = 215.15$ K) to be a factor of 5 less than that of ice (2.23 $Wm^{-1}K^{-1}$). The low thermal conductivity of hydrates, as well as similarities of the values for each structure (shown in Table 2.8) have been confirmed from numerous studies (Cook and Leaist, 1983 [0.45 $Wm^{-1}K^{-1}$ for methane hydrate at 216.2 K]; Cook and Laubitz, 1981; Ross et al., 1981; Ross and Andersson, 1982; Asher et al., 1986; Huang and Fan, 2004; Waite et al., 2005). The thermal conductivity of the solid hydrate (0.50–0.58 W m^{-1} K^{-1}) more closely resembles that of liquid water (0.605 W m^{-1} K^{-1}).

A pictorial summary of the relative thermal conductivities of water structures (water, ice, and hydrate), including those in sediment is presented in Figure 2.17 (Gupta, 2007). The large variation in composite thermal conductivity for water

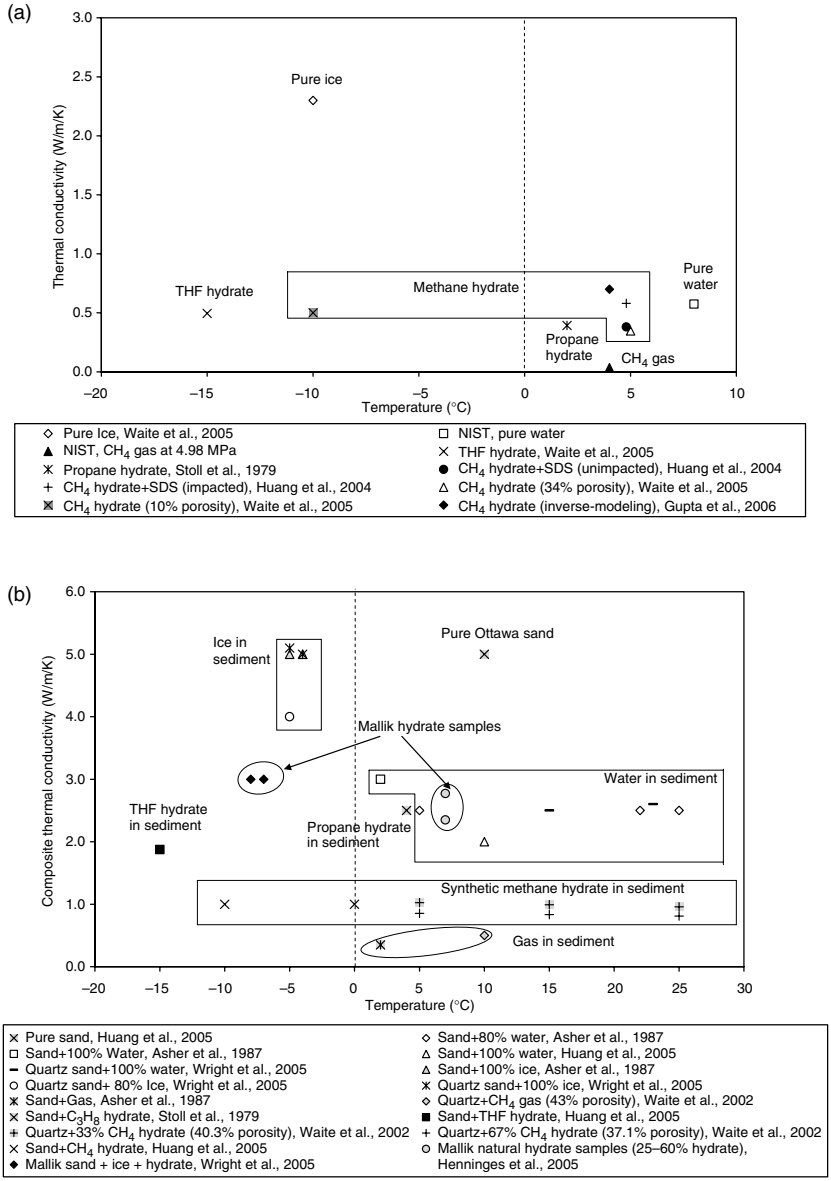

FIGURE 2.17 Thermal conductivity of gas, water, ice, and hydrates: (a) without and (b) with unconsolidated sediment (Gupta, 2007).

structures in sediment can be attributed to different phase saturations and types of sediment.

Ross et al. (1981) also determined that the THF hydrate thermal conductivity was proportionally dependent on temperatures, but had no pressure dependence.

Ross and Andersson (1982) suggested that this behavior, which was never before reported for crystalline organic materials, was associated with the properties of glassy solids. Waite et al. (2005) measured the temperature dependence of porous methane hydrate thermal conductivity. Early work on this anomalous property led to the development of a thermal conductivity needle probe (Asher et al., 1986) as a possible means of *in situ* discrimination of hydrates from ice in the permafrost.

Most of the thermal conductivity measurements have been performed using THF hydrate since this hydrate is fully miscible with water, is stable at atmospheric pressure, and will form a uniform hydrate (with all the large cages occupied by THF). Conversely, methane hydrate samples can contain gas, water, or ice, and hence exhibit variable densities that are interrelated to the thermal conductivity (Waite et al., 2005). Also, unlike THF hydrate, it is difficult to synthesize a nonporous methane hydrate sample in the laboratory. The thermal conductivity of methane hydrate increases from 0.50 to 0.587 on decreasing the sample porosity from 34% to about 5% (by compacting the hydrate sample with an external pressure; Huang and Fan, 2004; Waite et al., 2005). The use of THF hydrate as a model for methane hydrate would at first thought seem reasonable considering that the thermal conductivity has been reported to be independent of hydrate structure and type (Cook and Laubitz, 1981; Ross and Andersson, 1982; Cook and Leaist, 1983). However, there are increasing concerns that THF hydrate may not be a suitable thermal property analog to methane hydrate.

Waite et al. (2005) showed that the thermal conductivity of THF hydrate (0.50 $W\,m^{-1}\,K^{-1}$) is similar to that of methane hydrate (0.50 and 0.51 $W\,m^{-1}\,K^{-1}$ for porous and compacted samples, respectively) below $-7.5°C$. However, above $-7.5°C$, there are significant discrepancies between the thermal properties of these hydrates. THF hydrate exhibited a sharp increase in thermal conductivity to around 0.7 $W\,m^{-1}\,K^{-1}$ when the temperature was changed from $-7.5°C$ to around $3°C$. Thereby indicating that THF hydrate is not a suitable thermal property analog of methane hydrate above $-7.5°C$. Huang and Fan (2005) showed that the thermal conductivity values of THF hydrate measured over the temperature range $-10°C$ to $-2°C$ were similar to that of methane hydrate. (Variations in the temperature dependence range of THF hydrate may be due to THF hydrate + ice being formed.) At higher temperatures, the thermal conductivity of methane hydrate and THF hydrate can differ by about 20% (Huang and Fan, 2004), indicating that the guest molecule can affect the hydrate thermal conductivity.

Several models have been proposed to estimate the thermal conductivity of hydrate/gas/water or hydrate/gas/water/sediment systems. The most common are the classical mixing law models, which assume that the effective properties of multicomponent systems can be determined as the average value of the properties of the components and their saturation (volumetric fraction) of the bulk sample composition. The parallel (arithmetic), series (harmonic), or random (geometric) mixing law models (Beck and Mesiner, 1960) that can be used to calculate the composite thermal conductivity (k_θ) of a sample are given in Equations 2.1 through 2.3.

Parallel model:

$$k_\theta = k_H S_H + k_W S_W + k_G S_G \tag{2.1}$$

Series model:

$$k_\theta = (S_H/k_H + S_W/k_W + S_G/k_G)^{-1} \tag{2.2}$$

Random model:

$$k_\theta = k_H^{SH} * k_W^{SW} * k_G^{SG} \tag{2.3}$$

where S_H, S_W, and S_G are the saturations of hydrate, water, and gas, respectively, and k_H, k_W, and k_G are the thermal conductivities of hydrate, water, and gas, respectively.

Thermal conductivity can also be estimated from thermal response measurements of the test sample. A particularly powerful approach is the application of the inverse model, ITOUGH2 (Finsterle, 1997; Moridis, 2005b), to estimate the thermal conductivity of porous hydrate and hydrate-bearing sediment systems from thermal response data coupled with gas pressure and x-ray computed tomography (x-ray CT) measurements (Finsterle, 1997; Kneafsey et al., 2005; Gupta, 2007). Composite thermal conductivities of 2.380 and 3.145 $W\,m^{-1}\,K^{-1}$ were determined for a water/gas/sand system and a water/gas/hydrate/sand system, respectively (Kneafsey et al., 2005; Moridis, 2005a).

Henninges et al. (2005) estimated the composite thermal conductivities of hydrate-bearing sediments during the Mallik 2002 research program in the Mackenzie-Delta in the northwestern part of arctic Canada. Hydrate-bearing sand sediments with k_θ values in the range 2.35–2.77 $W\,m^{-1}\,K^{-1}$ were estimated from well-logging data obtained from fiber optic distributed temperature sensing cables. However, there were considerable uncertainties in the hydrate saturations in the natural sediments due to the heterogeneity of these systems. Therefore, controlled laboratory measurements (similar to the above CT x-ray measurements) as a function of hydrate composition, saturation, and microstructure would be valuable in aiding the interpretation of field data.

In the hydrate lattice structure, the water molecules are largely restricted from translation or rotation, but they do vibrate anharmonically about a fixed position. This anharmonicity provides a mechanism for the scattering of phonons (which normally transmit energy) providing a lower thermal conductivity. Tse et al. (1983, 1984) and Tse and Klein (1987) used molecular dynamics to show that frequencies of the guest molecule translational and rotational energies are similar to those of the low-frequency lattice (acoustic) modes. Tse and White (1988) indicate that a resonant coupling explains the low thermal conductivity.

The above molecular dynamics results have been confirmed by incoherent inelastic neutron scattering (IINS) measurements on xenon hydrate (Tse et al., 2001; Gutt et al., 2002). In earlier measurements on methane hydrate, the dominant

rotational motions of methane obscured any direct information on host–guest coupling. However, in the Xe hydrate measurements, the scattering intensity of xenon is negligible compared to water, and therefore the translational vibrations of the water lattice can be directly studied. It was suggested that thermal resistivity in a real solid is caused by scattering of the lattice phonons. Therefore, the coupling between guest and host vibrations or phonons may cause the anomalous temperature dependence of the thermal conductivity. This coupling between the guest and host lattice does not noticeably affect most structural thermodynamic and mechanical properties, but results in a marked decrease in the transport of heat.

2.2.3.2 Thermal expansion of hydrates and ice

Linear thermal expansion coefficients of hydrate structures I, II, and ice have been determined through dilatometry (Roberts et al., 1984) and through x-ray and neutron powder diffraction (Tse, 1987; Tse et al., 1987; Ikeda et al., 1999, 2000; Udachin et al., 2001b; Circone et al. 2003; Rawn et al., 2003). The values for sH hydrate at 200 K have been measured for hexamethylethane (HME) and 2,2-dimethylbutane (DMB) at 150 and 200 K by Tse (1990) who notes that cubic expansion values are similar to those of sI and sII, but there is a difference in the direction of linear expansion for structure H. At 200 K, linear thermal expansions for sI ($77\times10^{-6}\,K^{-1}$), sII ($52\times10^{-6}\,K^{-1}$), sH ($a = 67\times10^{-6}$, $c = 59\times10^{-6}\,K^{-1}$ for DMB), and ice ($a = 56\times10^{-6}$, $c = 57\times10^{-6}\,K^{-1}$) were listed. Figure 2.18 shows plots of linear thermal expansions vs. temperature for sI, sII, and ice Ih (Hester et al., 2007).

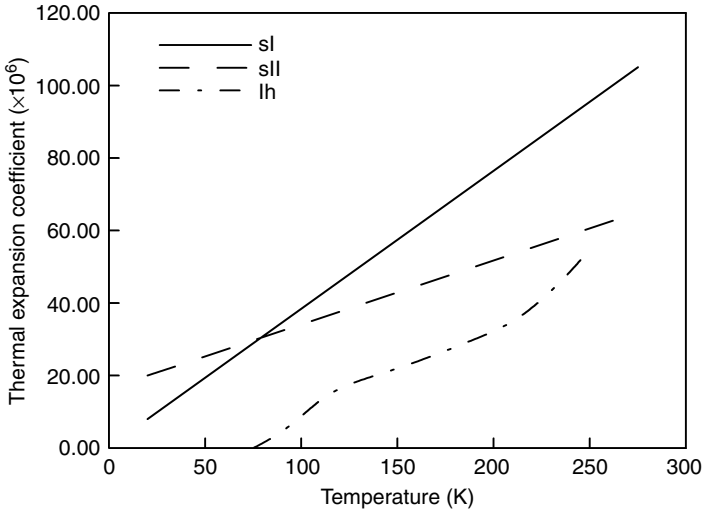

FIGURE 2.18 Linear thermal expansion coefficient vs. temperature for sI and sII hydrates, and ice Ih (Hester et al. 2007).

Through constant pressure molecular dynamics calculations for the thermal expansion of ice and of empty structure I, Tse et al. (1987) determined that the high hydrate thermal expansivity is due to anharmonic behavior in the water lattice. Tse (1994) suggests that this results from collisions of the guest molecule with the cage wall, which exerts an internal pressure to weaken the interaction between the water hydrogen bonds. Free energy calculations of several proton-disordered configurations of structure I hydrate and ice were performed over a wide range of temperatures to evaluate the cause of the high thermal expansion of hydrate compared to ice (Tanaka et al., 1997). In agreement with the work by Tse, the results indicated that the large thermal expansivity of hydrate is caused by the guest molecule, with the different arrangements of oxygen atoms in the hydrate and ice playing only a minor role.

2.3 The What and the How of Hydrate Structures

With the conclusion of the present chapter, the reader should have a firm notion of what the molecular structures are and how these structures compare and contrast to that of ice.

If water will normally form ice in the absence of a solute molecule, the question arises about the mechanism for forming a clathrate with an exact structure, when the solubility of hydrocarbon molecules in liquid water is known to be small (or negligible in ice), relative to the amount of hydrocarbon needed for hydrates. Thus, along with the definition of what the hydrate structures are, comes the logical question of how these structures form. During the past two decades, sophisticated experimental and modeling tools have been applied to address this question. The microscopic mechanism and the macroscopic kinetics of hydrate formation are the major considerations of Chapter 3.

References

Allen, K.W., *J. Chem. Phys*., **41**, 840 (1964).

Allen, K.W., Jeffrey, G.A., *J. Chem. Phys*., **38**, 2304 (1963).

Angell, C.A., *Water: A Comprehensive Treatise*, (Franks, F., ed.) Plenum Press, New York, **7,** 1 (1982).

Ashbaugh, H.S., Paulaitis, M.E., *J. Am. Chem. Soc*., **123**, 10721 (2001).

Asher, G.B., *Development of a Computerized Thermal Conductivity Measurement System Utilizing the Transient Needle Probe Technique: An Application to Hydrates in Porous Media*, Ph.D. Thesis, Colorado School of Mines, Golden, CO (1987).

Asher, G.B., Sloan, E.D., Graboski, M.S., *Int. J. Thermophys.*, **7**, 285 (1986).

Ballard, A., *A Non-Ideal Hydrate Solid Solution Model for a Multi-Phase Equilibria Program*, Ph.D. Thesis, Colorado School of Mines, Golden, CO (2002).

Bathe, M., Vagle, S., Saunders, G.A., Lambson, T.F., *J. Matl. Sci. Lett*., **3**, 904 (1984).

Baumert, J., Gutt, C., Press, W., Tse, J.S., Janssen, S., in *Proc. Fourth International Conference on Gas Hydrates*, Yokohama, Japan, May 19–23, 687, (2002).

Beck, A.E., Mesiner, A.D., in *Methods for Determining Thermal Conductivity and Thermal Diffusivity*, Interscience Publishers Inc., New York, **1**, 49, (1960).

Benedict, W.S., Gailar, N., Plyler, E.K., *J. Chem. Phys*., **24**, 1139 (1956).
Bernal, J.D., Fowler, R.H., *J. Chem. Phys*., **1**, 515 (1933).
Bertie, J.A., Bates, F.E., Hendricksen, D.K., *Can. J. Chem*., **53**, 71 (1975).
Bertie, J.A., Jacobs, S.M., *J. Chem. Phys*., **69**, 4105 (1978).
Bertie, J.A., Othen, D.A., *Can. J. Chem*., **50**, 3443 (1972).
Bjerrum, N., *Science*, **115**, 385 (1952).
Blokzijl, W., Engberts, J.B.F.N., *Angew. Chem.*, *Int. Ed*., **32**, 1545 (1993).
Bowron, D.T., Soper, A.K., Finney, J.L., *J. Chem. Phys*., **114**, 6203 (2001).
Brownstein, S., Davidson, D.W., Fiat, D., *J. Chem. Phys*., **46**, 1454 (1967).
Buchanan, P., Soper, A.K., Westacott, R.E., Creek, J.L., Koh, C.A., *J. Chem. Phys*., **123**, 164507 (2005).
Burnham, C.J., Xantheas, S.S., Miller, M.A., Applegate, B.E., Miller, R.E., *J. Chem. Phys*., **117**, 1109 (2002).
Bylov, M., Rasmussen, P., *Chem. Eng. Sci.*, **52**, 3295 (1997).
Cady, G.H., *J. Phys. Chem*., **85**, 4437 (1983).
Calvert, L.D., Srivastava, P., *Acta Crystallogr*., **A25**, S131 (1967).
Cameron, I., Handa, Y.P., Baker, T.H.W., *Can. Geotechnol. J.*, **27**, 255 (1990).
Chakoumakos, B.C., Rawn, C.J., Rondinone, A.J., Stern, L.A., Circone, S., Kirby, S.H., Ishii, Y., Jones, C.Y., Toby, B.H., *Can. J. Phys.*, **81**, 183 (2003).
Chau, P.L., Mancera, R.L., *Mol. Physics*, **96**, 109 (1999).
Chazallon, B., Kuhs, W.F., *J. Chem. Phys.*, **117**, 308 (2002).
Chen, T.S., *A Molecular Dynamics Study of the Stability of Small Prenucleation Water Clusters*, Dissertation, U. Missouri-Rolla, Univ. Microfilms No. 8108116, Ann Arbor, MI (1980).
Chou, I.M., Sharma, A., Burruss, R.C., Shu, J.F., Mao, H.K., Hemley, R.J., Goncharov, A.F., Stern, L.A., Kirby, S.H., in *Proc. National Academic Science USA*, **97**, 13484 (2000).
Circone, S., Stern, L.A., Kirby, S.H., Durham, W.B., Chakoumakos, B.C., Rawn, C.J., Rondinone, A.J., Ishii, Y., *J. Phys. Chem. B*, **107**, 5529 (2003).
Cook, J.G., Laubitz, M.J., in *17th Intl. Thermal Conductivity Conf.*, Gathersburg, Maryland, 13 pp (1981).
Cook, J.G., Leaist, D.G., *Geophys. Res. Lett*., **10**, 397 (1983).
Cottrell, T.L., *The Strengths of Chemical Bonds*, Butterworths, London (1958).
Curl, R.F., Smalley, R.E., *Scientific American*, 54 (1991).
Danesh, A., Tohidi, B., Burgass, R.W., Todd, A.C., *Trans. I. Chem. E*, **7(A)**, 197 (1994).
Davidson, D.W., *Can. J. Chem*., **49**, 1224 (1971).
Davidson, D.W., *Water: A Comprehensive Treatise*, Plenum, New York, (1973).
Davidson, D.W., *Natural Gas Hydrates* (Cox, J.L., ed.) Butterworths, Boston, 1 (1983).
Davidson, D.W., Garg, S.K., Gough, S.R., Hawkins, R.E., Ripmeester, J.A., *Can. J. Chem*., **55**, 3641 (1977a).
Davidson, D.W., Gough, S.R., Lee, F., Ripmeester, J.A., *Revue de Chimie Minerale*, **14**, 447 (1977b).
Davidson, D.W., Gough, S.R., Ripmeester, J.A., Nakayama, H., *Can. J. Chem*., **59**, 2587 (1981).
Davidson, D.W., Handa, Y.P., Ratcliffe, C.I., Tse, J.S., Powell, B.M., *Nature*, **311**, 142 (1984a).
Davidson, D.W., Garg, S.K., Gough, S.R., Handa, Y.P., Ratcliffe, C.I., Tse, J.S., Ripmeester, J.A., *J. Inclusion Phenom*., **2**, 231 (1984b).

Davidson, D.A., Handa, Y.P., Ratcliffe, C.I., Ripmeester, J.A., Tse, J.S., Dahn, J.R., Lee, F., Calert, L.D., *Mol. Cryst. Liq. Cryst*., **141**, 141 (1986a).
Davidson, D.W., Handa, Y.P., Ripmeester, J.A., *J. Phys. Chem*., **90**, 6549 (1986b).
Davidson, D.W., Ripmeester, J.A., *J. Glaciology*, **21**, 33 (1978).
Davidson, D.W., Ripmeester, J.A., *Inclusion Compounds*, (Atwood, J.L., Davies, J.E.D., MacNichol, D.D., eds.), Academic Press, **3**, Chapter 3, 69 (1984).
Deaton, W.M., Frost, E.M., Jr., *Oil Gas J*., **36**, 75 (1937).
Deaton, W.M., Frost, E.M., Jr., *Gas Hydrates and Their Relation to the Operation of Natural Gas Pipe Lines*, 101 pp. U.S. Bureau of Mines Monograph, 8 (1946).
De Forcrand, R., *Ann. Chim. Phys*., **28**, 5 (1883).
Debenedetti, P.G., *Metastable Liquids, Concepts and Principles*, Princeton University Press, NJ (1996).
Debenedetti, P.G., *J. Phys.: Condens. Matter*, **15**, R1669 (2003).
Dec, S.F., Bowler, K.E., Stadterman, L.L., Koh, C.A., Sloan, E.D., *J. Am. Chem. Soc*., **128**, 414 (2006).
Desgreniers, S., Flacau, R., Klug, D.D., Tse, J.S. in *Proc. Int. Conf. of CeSMEC*, Miami, FL (2003).
Dixit, S., Soper, A.K., Finney, J.L., Crain, J., *Europhys. Lett*., **59**, 377 (2002).
Durham, W.B., Stern, L.A., Kirby, S.H., *Can. J. Phys*., **81**, 373 (2003).
Durrant, P.J., Durrant, B., *Introduction to Advanced Inorganic Chemistry*, John Wiley and Sons, Inc., New York (1962).
Dvorkin, J., Helgerud, M.B., Waite, W.F., Kirby, S.H., Nur, A., Introduction to physical properties and elasticity models. *Natural Gas Hydrates in Oceanic and Permafrost Enviroments* (Max, M., ed.), 245 (2000).
Dyadin, Y.A., Aladko, E.Y., Larionov, E.G., *Mendeleev Commun*., **7**, 34 (1997).
Dyadin, Y.A., Bondaryuk, I.V., Shurko, F.V., *Inclusion Compounds,V5*, Edited by Atwood, Davies, MacNichol, Oxford University Press, **5**, 213 (1991).
Dyadin, Y., Bondaryuk, I.V., Zhurko, F.V., *Inorganics and Physical Aspects of Inclusion*, Oxford University Press, 213 (1991).
Dyadin, T., Larionov, E., Aladko, E., Yu, A., Manakov, F., *J. Structural Chem*., **40**, 790 (1999).
Dyadin, Y., Mikina, T., Zhurko, F., Mironov, Y., Msanuilov, A., Skripko, G., *Mendeleev Commun.*, **5**, 62 (1995).
Dyadin, Y.A., Udachin, K.A., Bogatyryova, S.V., Zhurko, F.V., *J. Inclusion Phenom*., **6**, 565 (1988).
Dyadin, Y.A., Zhurko, F.V., Bondaryuk, I.V., Zhurko, G.O., *J. Inclusion Phenom. Mol. Recognition Chem*., **10**, 39 (1991).
Ebinuma, T., Kamata, Y., Minagawa, H., Ohmura, R., Nagao, J., Narita, H., in *Proc. Fifth International Conference on Gas Hydrates*, Trondheim, Norway, June 13–16, Paper 3037 (2005).
Fan, S., *J. Chem. Eng. Data*, **49**, 1479 (2004).
Finsterle, S., *Laurence Berkeley National Laboratory Report* LBNL-40400 (1997).
Florusse, L.J., Peters, C.J., Schoonman, J., Hester, K.C., Koh, C.A., Dec, S.F., Marsh, K.N., Sloan, E.D., *Science*, **306**, 469 (2004).
Fowler, D.L., Loebenstein, W.A., Pall, D.B., Kraus, C.A., *J. Am. Chem. Soc.*, **62**, 15 (1940).
Frank, H.S., *Science*, **169**, 635 (1970).
Frank, H.S., Evans, M.W., *J. Chem. Phys*., **13**, 507 (1945).
Franks, F., *Water: A Comprehensive Treatise*, Plenum Press, New York, (1972–1982).
Franks, F., *Water: A Comprehensive Treatise*, Plenum Press, New York, **4** (1975).

Franks, F., *Water Science Reviews*, Cambridge University Press, New York (1985–1990).
Franks, F., Reid, D.S., *Water: A Comprehensive Treatise*, (Franks, F., ed.) Plenum Press, New York **1**, Chapter 5 (1973).
Geil, B., Kirschgen, T.M., Fujara, F., *Phys. Rev. B*., **72**, 014304 (2005).
Gerke, H., Gies, H., *Z. Kristallographie*, **166**, 11 (1984).
Glew, D.W., *Nature*, **184**, 545 (1959).
Glew, D.W., Rath, N.S., *J. Chem. Phys*., **44**, 1710 (1966).
Gough, S.R., Garg, S.K., Ripmeester, J.A., Davidson, D.W., *Can. J. Chem*., **52**, 3193 (1974).
Gough, S.R., Ripimeester, J.A., Davidson, D.W., *Can. J. Chem*., **53**, 2215 (1975).
Gupta, A., *Methane Hydrate Dissociation Measurements and Modeling: The Role of Heat Transfer and Reaction Kinetics*, Ph.D. Thesis, Colorado School of Mines, Golden, CO (2007).
Gupta, A., Sloan, E.D., Kneafsey, T.J., Tomutsa, L., Moridis, G., in *Proc. Fifth International Conference on Gas Hydrates*, Trondheim, Norway, June 13–16, Paper 2005 (2005).
Gutt, C., Asmussen, B., Press, W., Johnson, M.R., Handa, Y.P., Tse, J.S., *J. Chem. Phys.*, **113**, 4713 (2000).
Gutt, C., Baumert, J., Press, W., Tse, J.S., Janssen, S., *J. Chem. Phys*., **116**, 3795 (2002).
Hafemann, D.R., Miller, S.L., *J. Phys. Chem*., **73**, 1392 (1969).
Handa, Y.P., *J. Phys. Chem*., **90**, 5497 (1986).
Haenel, R., Stegena, L., Rybach, (eds.) *Handbook of Terrestrial Heat-Flow Density Determination*, Kluwer Academic Publishers, Dordrecht, Netherlands, 87 (1988).
Hara, T., Hashimoto, S., Sugahara, T., Ohgaki, K., *Chem. Eng. Sci*., **60**, 3117 (2005).
Harker, H.A., Viant, M.R., Keutsch, F.N., Michael, E.A., McLaughlin, R.P., Saykally, R.J., *J. Phys. Chem. A*, **109**, 6483 (2005).
Hawkins, R.E., Davidson, D.W., *J. Phys. Chem*., **70**, 1889 (1966).
Head-Gordon, T., in *Proc. National Academic Science U.S.A.*, **92**, 8308 (1995).
Helgerud, M.B., Circone, S., Stern, L., Kirby, S., Lorenson, T.D., in *Proc. Fourth International Conference on Gas Hydrates*, Yokohama May 19–23, 2002, 716 (2002).
Helgerud, M.B., Waite, W.F., Kirby, S.H., Nur, A., *Can. J. Phys*., **81**, 47 (2003).
Hendricks, E.M., Edmonds, B., Moorwood, R.A.S., Szcepanski, R., *Fluid Phase Equilib*., **117**, 193 (1996).
Henninges, J., Heunges, E., Buirkhardt, H., in *Proc. Fifth International Conference on Gas Hydrates*, Trondheim, Norway, June 13–16, Paper 3034 (2005).
Hester, K.C., *Probing Hydrate Stability and Structural Characterization of Both Natural and Synthetic Clathrate Hydrates*, Ph.D. Thesis, Colorado School of Mines, Golden, CO (2007).
Hester, K.C., Huo, Z., Ballard, A.L., Miller, K.T., Koh, C.A., Sloan, E.D., *J. Phys. Chem. B*, in press (2007).
Hester, K.C., Koh, C.A., Sloan, E.D., Schultz, A.J., in *Proc. Fifth International Conference on Gas Hydrates*, Trondheim, Norway, June 13–16, Paper 5038 (2005).
Hester, K.C., Sloan, E.D., *Intl. J. Thermophysics*, **26**, 95 (2005).
Hester, K.C., Strobel, T.A., Huq, A., Schultz, A.J., Sloan, E.D., Koh, C.A., *J. Phys. Chem. B*., **110**, 14024 (2006).
Hirai, H., Nishimura, Y., Kawamura, T., Yamamoto, Y., Yagi, T., *J. Phys. Chem. B*, **106**, 11089 (2002).
Hirai, H., Tanaka, H., Kawamura, K., Yamamoto, Y., Yagi, T., *J. Phys. Chem. Solids*, **65**, 1555 (2004).

Hirai, H.H., Uchihara, Y., Fujihisa, H., Sakashita, M., Katoh, E., Aoki, K., Nagashima, K., Yamamoto, Y., Yagi, T., *J. Chem. Phys*., **115**, 7066 (2001).
Holder, G.D., Manganiello, D.J., *Chem. Eng. Sci*., **37**, 9 (1982).
Holder, G.D., Zele, S., Enick, R., LeBlond, C., in *Proc. First International Conference on Natural Gas Hydrates*, (Sloan, E.D., Happel, J., Hnatow, M.A., eds.), Annals of the New York Academy of Sciences, **715**, 344 (1994).
Holland, P.M., Castleman, A.W., *J. Chem. Phys*., **72**, 5984 (1980).
Huo, Z., *Hydrate Phase Equilibria Measurements by X-Ray Diffraction and Raman Spectroscopy*, Ph.D. Thesis, Colorado School of Mines, Golden, CO (2002).
Huang, D., Fan, S., *J. Chem. Eng. Data*, **49**, 1479 (2004).
Huang, D., Fan, S., *J. Geophysical Research-Solid Earth*, **110**, B01311 (2005)
Huang, D.Z., Fan, S.S., *J. Chem. Eng. Data*, **49**, 1479 (2004).
Huang, D.Z., Fan, S.S., *J. Geophysical Research-Solid Earth*, **110**, B01311 (2005).
Hummer, G., Garde, S., Garcia, A.E., Pohorille, A., Pratt, L.R., in *Proc. National Academic Science U.S.A.,* **93**, 8951 (1996).
Ikeda, T., Mae, S., Yamamuro, O., Matsuo, T., Ikeda, S., Ibberson, R.M., *J. Phys. Chem. A*, **104**, 10623 (2000).
Ikeda, T., Yamamuro, O., Matsuo, T., Mori, K., Torii, M.S., *J. Phys. Chem. Solids*, **60**, 1527 (1999).
Inerbaev, T.M., Belosludov, V.R., Belosludov, R.V., Sluiter, M., Kawazoe, Y., Kudoh, J.I., *J. Inclusion Phenom. Macrocyclic Chem*., **48**, 55 (2004).
Itoh, H., Tse, J.S., Kawamura, K., *J. Chem. Phys*., **115**, 9414 (2001).
Jeffrey, G.A., *Inclusion Compounds*, (Atwood, J.L. Davies, J.E.D., MacNichol, D.D., eds.) Academic Press, pp. 135 (1984).
Jeffrey, G.A., McMullan, R.K., *Prog. Inorg. Chem*., **8**, 43 (1967).
Jones, C.Y., Marshall, S.L., Chakoumakos, B.C., Rawn, C.J., Ishii, Y. *J. Phys. Chem. B*, **107**, 6026 (2003).
Jones, C.A., Rondinone, A.J., Chakoumakos, B.C., Circone, S., Stern, L.A., Kirby, S.H., Ishii, Y., *Can. J. Phys.*, **81**, 431 (2000).
Kiefte, H., Clouter, M.J., Gagnon, R.E., *J. Phys. Chem*., **89**, 3103 (1985).
Kini, R.A., Huo, Z., Jager, M.D., Bollavaram, P., Ballad, A.L., Dec, S.F., Sloan, E.D., in. *Proc. Fourth International Conference on Gas Hydrates*, Yokohama, Japan, May 19–23, 867 (2002).
Kirchner, M.T., Boese, R., Billups, W.E., Norman, L.R., *J. Am. Chem. Soc.*, **126**, 9407 (2004).
Kirschgen, T.M., Zeidler, M.D., Geil, B., Fujara, F., *Phys. Chem. Chem. Phys*., **5**, 5247 (2003).
Kneafsey, T.J., Tomutsa, L., Moridis, G.J., Seol, Y., Freifeld, B., Taylor, C.E., Gupta, A., in *Proc. Fifth International Conference on Gas Hydrates*, Trondheim, Norway, June 13–16, Paper 1033 (2005).
Kollman, P., *J. Am. Chem. Soc*., **99**, 4875 (1977).
Kurnosov, A.V., Manakov, A.Y., Komarov, V.Y., Voronin, V.I., Teplykh, A.E., Dyadin, Y.A., *Doklady Phys. Chem.*, **381**, 303 (2001).
Kursonov, A.V., Komarov, V.Y., Voronin, V.I., Teplykh, A.E., Manakov, A.Y., *Angew. Chem. Intl. Ed.*, **43**, 2922 (2004).
Latimer, W.M., Rodebush, W.H., *J. Am. Chem. Soc.*, **42**, 1419 (1920).
Lederhos, J.P., Mehta, A.P., Nyberg, G.B., Warn, K.J., Sloan, E.D., *AIChE J.*, **38**, 1045 (1992).
Lee, J-W, Lu, H., Moudrakovski, I.L., Ratcliffe, C.I., Ripmeester, J.A., *Angew. Chem. Int. Ed.*, **118**, 2516 (2006).

Lee, M.W., Collett, T.S., *Geophysics*, **66**, 763 (2001).
Lipkowski, J., Yu, V., Rodionova, T.V., *J. Supramol. Chem.*, **2**, 435 (2002).
Liu, S., Welch, M., Klinowski, J., *J. Phys. Chem.*, **101**, 2811 (1997).
Lokshin, K.A., Zhao, Y.S., He, D.W., Mao, W.L., Mao, H.K., Hemley, R.J., Lobanov, M.V., Greenblatt, M., *Phys. Rev. Lett.*, **93**, 125503 (2004).
Lokshin, K.A., Zhao, Y., Lobanov, M.V., Greenblatt, M., in *Proc. Fifth International Conference on Gas Hydrates*, Trondheim, Norway, June 13–16, Paper 2005 (2005a).
Lokshin, K.A., Zhao, Y., Mao, W.L., Mao, H., Hemley, R.J., Lobanov, M.V., Greenblatt, M., in *Proc. Fifth International Conference on Gas Hydrates*, Trondheim, Norway, June 13–16, Paper 5024 (2005b).
Long, J.P., *Gas Hydrate Formation Mechanism and Kinetic Inhibition*, Ph.D. Thesis, Colorado School of Mines, Golden, CO (1994).
Lonsdale, H.K., in *Proc. Roy. Soc. Series A*, **247**, 424 (1958).
Lotz, H.T., Schouten, J.A., *J. Chem. Phys.*, **111**, 10242 (1999).
Loveday, J.S., Nelmes, R.J., Guthrie, M., Belmonte, S.A., Allan, D.R., Klug, D.D., Tse, J.S., Handa, Y.P., *Nature*, **410**, 661 (2001a).
Loveday, J.S., Nelmes, R.J., Guthrie, M., Klug, D.D., Tse, J.S., *Phy. Rev. Lett.*, **8721**, 215501 (2001b).
Loveday, J.S., Nelmes, R.J., Klug, D.D., Tse, J.S., Desgreniers, S., *Can. J. Phys.*, **81**, 539 (2003).
Luck, W.A.P., in *Water a Comprehensive Treatise*, (Franks, F., ed.) Plenum Press, New York, **2**, Chapter 4 (1973).
Lynden-Bell, R.M., Debenedetti, P.G., *J. Phys. Chem. B*, **109**, 6527 (2005).
Lyusternik, L.A., *Convex Figures and Polyhedra*, Dover, New York (1963).
Majid, Y.A., Garg, S.K., Davidson, D.W., *Can. J. Chem.*, **47**, 4697 (1969).
Mak, C.W., McMullan, R.K., *J. Chem. Phys.*, **42**(**8**), 2732 (1965).
Makino, T., Sugahara, S., Ohgaki, K., in *Proc. Fifth International Conference on Gas Hydrates*, Trondheim, Norway, June 13–16, Paper 5026 (2005).
Makogon, Y.F., *Hydrates of Natural Gas*, Moscow, Nedra, Izadatelstro, p. 208 (1974 in Russian) Trans. W.J. Cieslesicz, PennWell Books, Tulsa, Oklahoma, pp. 237 (1981 in English).
Manakov, A.Y., Voronin, V.I., Teplykh, A.E., Kurnosov, A.V., Goryainov, S.V., Ancharov, A.I., Likhacheva, A.Y., in *Proc. Fourth International Conference on Gas Hydrates*, Yokohama, Japan, May 19–23, 630 (2002).
Mao, H.K., Mao, W.L., *PNAS*, **101**, 708 (2004).
Mao, W.L., Mao, H.K., Goncharov, A.F., Struzhkin, V.V., Guo, Q.Z., Hu, J.Z., Shu, J.F., Hemley, R.J., Somayazulu, M., Zhao, Y.S., *Science*, **297**, 2247 (2002).
Matsumoto, M., Saito, S., Ohmine, I., *Nature*, **416**, 409 (2002).
McCelland, A.L., *Dipole Moments*, W.H. Freeman & Co., San Francisco, CA (1963).
McMullan, R., Jeffrey, G.A., *J. Chem. Phys.*, **31**, 1231 (1959).
McMullan, R.K., Jeffrey, G.A., *J. Chem. Phys.*, **42**, 2725 (1965).
Mehta, A.P., *A Thermodynamic Investigation of Structure-H-Type Clathrate Hydrates*, Ph.D. Thesis Colorado School of Mines, Golden, CO (1996).
Mehta, A.P., Sloan, E.D., *AIChE J.*, **40**, 312 (1994).
Mehta, A.P., Sloan, E.D., in *Proc. Second International Conference on Gas Hydrates*, (Monfort, J.P., ed.) Toulouse, France, June 2–6, 1 (1996).
Mooijer-van den Heuvel, M.M., Peters, C.J., Arons, J.D., *Fluid Phase Equilib.*, **172**, 73 (2000).

Mooijer-van den Heuvel, M.M., Peters, C.J., Arons, J.D., *Fluid Phase Equilib.*, **193**, 245 (2002).
Mooijer-van den Heuvel, M.M., Witteman, R., Peters, C.J., *Fluid Phase Equilib.*, **182**, 97 (2001).
Moridis, G.J., *Laurence Berkeley National Laboratory Report*, (2005b).
Moridis, G.J., Seol, Y., Kneafsey, T.J., in *Proc. Fifth International Conference on Gas Hydrates*, Trondheim, Norway, June 13–16, Paper 1004 (2005a).
Morita, K., Nakano, S., Ohgaki, K., *Fluid Phase Equilib.*, **169**, 167 (2000).
Nagashima, U., Shinohara, H., Nishi, N., Tanaka, H., *J. Chem. Phys.*, **84**, 209 (1986).
Ogienko, A.G., Kurnosov, A.V., Manakov, A.Y., Larionov, E.G., Ancharov, A.I., Sheromov, M.A., Nesterov, A.N., *J. Phys. Chem. B*, **110**, 2840 (2006).
Ohmine, I., *J. Phys. Chem.*, **99**, 6767 (1995).
Onsager, L., Runnels, L.K., *J. Chem. Phys.*, **50**, 1089 (1969).
Oyama, H., Ebinuma, T., Shimada, W., Takeya, S., Nagao, J., Uchida, T., Narita, H., *Can. J. Phys.*, **81**, 485 (2003).
Pandit, B.I., King, M.S., *Fourth Canadian Permafrost Conference* (French, H.M., ed.), Khangai Mountains, Mongolia, 335 (1982).
Parameswaran, V.R., Paradis, M., Handa, Y.P., *Can. Geotechnical J.*, **26**, 479 (1989).
Paul, J.B., Provencal, R.A., Chapo, C., Roth, K., Caseas, R., Saykally, R.J., *J. Phys. Chem.*, **103**, 2972 (1999).
Pauling, L., *J. Am. Chem. Soc.*, **57**, 2680 (1935).
Pauling, L., *The Nature of the Chemical Bond*, Cornell University. Press, Ithaca, New York (1945).
Pauling, L., *The Structure of Water*, Pergammon Press, New York 1 (1959).
Pauling, L., Marsh, R.E., *Proc. Nat. Acad. Sci.*, **38**, 112 (1952).
Pearson, C., Murphy, J.R., Mermes, R.E., Halleck, P.M., *Los Alamos Scientific Laboratory Report*, LA-9972 MS, **9** (1984).
Pecher, I.A., Waite, W.F., Winters, W.J., Mason, D.H., Physical properties and rock physics models of sediment containing natural and laboratory-formed methane gas hydrate. *Am. Mineral.*, **89**, 1221 (2004).
Plummer, P.L.M., Chen, T.S., *J. Chem. Phys.*, **86**, 7149 (1987).
Poirier, J.P., *Creep of Crystals*, Cambridge University Press, New York (1985).
Pople, J.A., in *Proc. Royal Society*, **205**, 163 (1951).
Prielmeier, F.X., Zang, E.W., Speedy, R.J., Ludemann, H-D. , *Phys. Rev. Lett.*, **59**, 1128 (1987).
Privalov, P.L., Gill, S.J., *Adv. Protein Chem.*, **39**, 191 (1988).
Rawn, C.J., Rondinone, A.J., Chakoumakos, B.C., Circone, S., Stern, L.A., Kirby, S.H., Ishii, Y., *Can. J. Phys.*, **81**, 431 (2003).
Rawn, C.J., Rondinone, A.J., Chakoumakos, B.C., Marshall, S.L., Stern, L.A., Circone, S., Kirby, S., Jones, C.Y., Toby, B.H., Ishii, Y., in *Proc. Fourth International Conference on Gas Hydrates*, Yokohama, Japan, May 19–23, **595** (2002).
Ripmeester, J., in *Proc. Third International Conference on Gas Hydrates*, (Holder, G.D., Bishnoi, P.R., eds.), Salt Lake City, UT, Annals of the New York Academy of Sciences, **912**, 1 (2000).
Ripmeester, J.A., in *Proc. Fifth International Conference on Gas Hydrates*, Trondheim, Norway, June 13–16, Paper 2008 (2005).
Ripmeester, J.A., Davidson, D.W., *J. Mol. Struct.*, **75**, 67 (1981).
Ripmeester, J.A., Ratcliffe, C.I., *J. Phys. Chem.*, **94**, 8773 (1990a).
Ripmeester, J.A., Ratcliffe, C.I., *J. Phys. Chem.*, **94**, 7652 (1990b).

Ripmeester, J.A., Ratcliffe, C.I., Cameron, I.G., *J. Phys. Chem. B*, **208**, 929 (2004).
Ripmeester, J.A., Ratcliffe, C.I., Klug, D.D., Tse, J.S., in *Proc. First International Conference on Natural Gas Hydrates*, (Sloan, E.D., Happel, J., Hnatow, M.A., eds.) Annals of the New York Academy of Sciences, **715**, 161 (1994).
Ripmeester, J.A., Ratcliffe, C.I., McLaurin, G.E., *AIChE Meeting in Houston Texas*, April 10 (1991).
Ripmeester, J.A., Ratcliffe, C.I., Tse, J.S., *J. Chem. Soc. Faraday Trans. I*, **84**, 3731 (1988).
Ripmeester, J.A., Tse, J.S., Ratcliffe, C.I., Powell, B.M., *Nature*, **325**, 135 (1987).
Roberts, R.B., Andrikidis, C., Tainish, R.J., White, G.K., in *Proc. Tenth International Cryogenic Engineering Conference*, Helsinki, 499 (1984).
Rodger, P.M., *J. Phys. Chem.*, **94**, 6080 (1990a).
Rodger, P.M., *Mol. Simulation*, **5**, 315 (1990b).
Rondinone, A.J., Chakoumakos, B.C., Rawn, C.J., Ishii, Y., in *Proc. Fourth International Conference on Gas Hydrates*, Yokohama, Japan, May 19–23, 625 (2002).
Ross, R.G., Andersson, P., *Can. J. Chem.*, **60**, 881 (1982).
Ross, R.G., Andersson, P., Backstrom, G., *Nature*, **290**, 322 (1981).
Sasaki, S., Hori, S., Kume, T., Shimizu, H., *J. Chem. Phys.*, **118**, 7892 (2003).
Satana, L.F., Brown, M.G., Richmond, G.L., *Science*, **292**, 908 (2001).
Shimada, W., Shiro, M., Kondo, H., Takeya, S., Oyama, H., Ebinuma, T., Marita, H., *Acta Crystallographica Section C, Crystal Structure Commun.*, **C61**, 065 (2005).
Shimizu, H., Kumazaki, T., Kume, T., Sasaki, S., *Phys. Rev. B: Condens. Matt. Mater. Phys.*, **65**, 212102/1 (2002).
Shpakov, V.P., Tse, J.S., Tulk, C.A., Kvamme, B., Belosludov, V.R., *Chem. Phys. Lett.*, **282**, 107 (1998).
Sluiter, M., Inerbaev, T.M., Belosludov, R.V., Kawazoe, Y., Subbotin, O.S., Belosludov, V.R., in *Proc. Fifth International Conference on Gas Hydrates*, Trondheim, Norway, June 13–16, Paper 5003 (2005).
Sorensen, C.M., "Clathrate Structures and the Anomalies of Supercooled Water," in *Proc. 12th Int. Conf. on Prop. of Water and Steam*, Orlando, FL, September (1994).
Speedy, R.J., Angell, C.A., *J. Chem. Phys.*, **65**, 851 (1976).
Stern, L.A., Kirby, S.H., Durham, W.B., *Science*, **273**, 1843 (1996).
Stillinger, F.H., in *Water in Polymers*, (Rowland, S.P., ed.) Washington DC, **1,** 11 (1980).
Stillinger, F.H., Rahman, A., *J. Chem. Phys.*, **60**, 1545 (1974).
Stoll, R.D., Bryan, G.M., *J. Geophys. Res.*, **84**, 1629 (1979).
Strobel, T., Hester, K.C., Koh, C.A., Dec, S.F., Miller, K.T., Sloan, E.D., *Hydrogen in Hydrates Workshop*, Kauai, Hawaii, March 5–9 (2006a).
Strobel, T.A., Hester, K.C., Sloan, E.D., Koh, C.A., *J. Am. Chem. Soc.*, in press (2007).
Strobel, T.A., Taylor, C.J., Hester, K.C., Dec, S.F., Koh, C.A., Miller, K.T., Sloan, E.D., *J. Phys. Chem. B*, **110**, 17121 (2006b).
Subramanian, S., Kini, R., Dec, S., Sloan, E., in *Proc. Gas hydrates, Challenges for the Future*, Annals of the New York Academy of Sciences, **912**, 873 (2000).
Subramanian, S., Sloan, E.D., *J. Phys. Chem. B*, **106**, 4348 (2002).
Sugahara, T., Morita, K., Ohgaki, K., *Chem. Eng. Sci.*, **55** 6015 (2000).
Suzuki, M., Tanaka, Y., Sugahara, T., Ohgaki, K., *Chem. Eng. Sci.*, **56**, 2063 (2001).
Tabushi, I., Kiyosuke, Y., Yamamura, K., *Bull. Chem. Soc. of Japan*, **54**, 2260 (1981).
Takeya, S., Kida, M., Minami, H., Sakagami, H., Hachikubo, A., Takahashi, N., Shoji, H., Soloviev, V., Wallmann, K., Biebow, N., Obzhirov, A., Saloatin, A., Poort, J., *Chem. Eng. Sci.*, **61**, 2670 (2006).
Takeya, S., Nagaya, H., Matsuyama, T., Hondoh, T., Lipenkov, V. Y., *J. Phys. Chem. B*, **104**, 668 (2000).

Tanaka, H., Kiyohara, K., *J. Chem. Phys*., **98**, 4098 (1993).
Tanaka, H., Tamai, Y., Koga, K., *J. Phys. Chem. B*, **101**, 6560 (1997).
Tanford, C., *The Hydrophobic Effect: Formation of Micelles and Biological Membranes*, Wiley, New York, (1973).
Tohidi, B., Østergaard, K.K., Danesh, A., Todd, A.C., Burgass, R.W., *Can. J. Chem. Eng.*, **79**, 384 (2001).
Tse, J.S., *J. De Physique*, **48**, 543 (1987).
Tse, J.S., *J. Inclusion Phenom. Mol. Recognition Chem*, **8**, 25 (1990).
Tse, J.S., in *Proc. First International Conference on Natural Gas Hydrates* (Sloan, E.D., Happel, J., Hnatow, M.A., eds.) Annals of the New York Academy of Sciences, **715**, 187 (1994).
Tse, J.S., Handa, Y.P., Ratcliffe, C.I., Powell, B.M., *J. Inclusion Phenom*., **4**, 235 (1986).
Tse, J.S., Klein, M.L., *J. Phys. Chem*., **91**, 5789 (1987).
Tse, J.S., Klein, M.L., McDonald, I.R., *J. Phys. Chem.*, **87**, 4198 (1983).
Tse, J.S., Klein, M.L., McDonald, I.R., *J. Chem. Phys.*, **81(12)**, 6146 (1984).
Tse, J.S., McKinnon, W.R., Marchi, M., *J. Phys. Chem.*, **91**, 4188 (1987).
Tse, J.S., Powell, B.M., Sears, V.F., Handa, Y.P., *Chem. Phys. Lett*., **215**, 383 (1993).
Tse, J.S., Shpakov, V.P., Belosludov, V.R., Trouw, F., Handa, Y.P., Press, W., *Europhys. Lett.*, **54**, 354 (2001).
Tse, J.S., White, M.A., *J. Phys. Chem.*, **92**, 5006 (1988).
Udachin, K., Lipkowski, J., *Supramol. Chem.*, **8**, 181 (1996).
Udachin, K., Ripmeester, J., *Nature*, **397**, 420 (1999).
Udachin, K., Ripmeester, J.A., in *Proc. Fifth International Conference on Gas Hydrates*, Trondheim, Norway, June 13–16, Paper 2024 (2005).
Udachin, K.A., Enright, G.D., Ratcliffe, C.I., Ripmeester, J.A., *J. Am. Chem. Soc.*, **119**, 11481 (1997a).
Udachin, K.A., Ratcliffe, C.I., Enright, G.D., Ripmeester, J.A., *Supramol. Chem.*, **8**, 173 (1997b).
Udachin, K.A., Ratcliffe, C.I., Ripmeester, J.A., *Angew. Chem. Int. Ed.*, **40**, 1303 (2001a).
Udachin, K.A., Ratcliffe, C.I., Ripmeester, J.A., *J. Phys. Chem. B*, **105**, 4200 (2001b).
Udachin, K.A., Ratcliffe, C.I., Ripmeester, J.A., in *Proc. Fourth International Conference on Gas Hydrates*, Yokohama, Japan, May 19–23, 604 (2002).
van der Waals, J.H., Platteeuw, J.C., *Adv. Chem. Phys.*, **2**, 1 (1959).
van Klaveren, E.P., Michels, J.P.J., Schouten, J.A., Klug, D.D., Tse, J.S., *J. Chem. Phys.*, **114**, 5745 (2001).
von Stackelberg, M., *Naturwiss*, **36**, 359 (1949).
von Stackelberg, M., *Rec. Trav. Chim. Pays-Bas*, **75**, 902 (1956).
von Stackelberg, M., Jahns, W., *Z. Elektrochem.*, **58**, 162 (1954).
von Stackelberg, M., Müller, H.R., *Z. Electrochem*., **58**, 25 (1954).
Vos, W.L., Finger, L.W., Hemley, R.J., Mao, H.K., *Phys. Rev. Lett.*, **71**, 3150 (1993).
Waite, W., Helgerud, M., Nur, A., Pinkston, J., Stern, L., Kirby, S., in *Proc. Gas Hydrates, Challenges for the Future*, Annals of the New York Academy of Sciences, **912**, 1003 (2000).
Waite, W.F., Gilbert, L.Y., Winters, W.J., Mason, D.H., in *Proc. Fifth International Conference on Gas Hydrates*, Trondheim, Norway, June 13–16, Paper 5042 (2005).
Wales, D.J., Hodges, M.P., *Chem. Phys. Lett.*, **286**, 65 (1998).
Walrafen, G.E., Chu, Y.C., *J. Phys. Chem*., **99**, 10635 (1995).
Wei, S., Shi, Z., Castleman, A.W., *J. Chem. Phys.*, **94**, 3268 (1991).

Whalley, E., *J. Geophys. Res*., **85**, 2539 (1980).
Whiffen, B.L., Kiefte, H., Clouter, M.J., *Geophys. Res. Lett*., **9**, 645 (1982).
White, M.A., MacLean, M.T., *J. Phys. Chem.*, **89**, 1380 (1985).
Winters, W., Dallimore, S., Collett, J.K., Katsube, J., Cranston, in *Proc. Gas Hydrates: Challenges for the Future*, **912**, 94 (2000).
Winters, W.J., Mason, D.H., Waite, W.F., Methane hydrate formation in partially-water saturated Ottawa sand. *Am. Mineral.*, **89**, 1202 (2004).
Wooldridge, P.J., Richardson, H.H., Devlin, J.P., *J. Chem. Phys.*, **87**, 4126 (1987).
Wright, J.F., Nixon, F.M., Dallimore, S.R., Henninges, J., Cote, M.M., *Geological Survey of Canada Bulletin*, **585**, 129 (2005).
Wu, B.J., Robinson, D.B., Ng, H.J., *J. Chem. Thermodyn*, **8**, 461 (1976).
Zele, S.R., Lee, S.Y., Holder, G.D., *J. Phys. Chem. B*, **103**, 10250 (1999).

3 Hydrate Formation and Dissociation Processes

The most challenging and intriguing questions regarding hydrates concern how hydrates form, dissociate, and are inhibited with time. The previous chapter provides the foundation required to understand these time-dependent processes. Time-dependent hydrate phenomena are substantially more challenging than time-independent phenomena of structure and thermodynamics. One can expect a decrease in accuracy of time-dependent measurements and models by at least one order of magnitude relative to their thermodynamic counterparts, as found in Chapters 4 through 6.

Due to the difficulty of quantifying time-dependent phenomena, the present chapter deals with hydrate formation and dissociation in laboratory systems. The principles are extended to hydrate formation/dissociation/inhibition in pipelines in Chapter 8 on hydrates in production, processing, and transportation. Dissociation in porous media, such as the assessment of gas evolution from *in situ* hydrate reserves using hydrate reservoir models is discussed in Chapter 7 on hydrates in the earth. The present chapter is also restricted mostly to the time-dependent properties of structures I and II due to the limited time-dependent data on structure H. The experimental tools that have been applied to measure hydrate time-dependent phenomena are presented in Chapter 6.

The purpose of this chapter is to provide the reader with an understanding of time-dependent phenomena for the following:

1. Hydrate nucleation (Section 3.1), which is a *stochastic process*, describing
   - the knowledge base for hydrate nucleation (Section 3.1.1)
   - conceptual pictures of hydrate nucleation (Section 3.1.2)
   - the stochastic nature of heterogeneous nucleation (HEN) (Section 3.1.3)
   - correlations of nucleation (Section 3.1.4)
   - the memory effect phenomenon (Section 3.1.5)
   - the state-of-the-art for hydrate nucleation (Section 3.1.6)
2. Hydrate growth (Section 3.2), which may be controlled by kinetic, heat, and mass transfer limitations, describing
   - the conceptual picture of hydrate growth (Section 3.2.1)
   - crystal growth processes (Section 3.2.2)
   - correlations of growth, including models for intrinsic kinetics, and mass and heat transfer (Section 3.2.3)
   - the state-of-the-art for hydrate growth (Section 3.2.4)

3. Dissociation (Section 3.3), which is typically heat transfer limited with hydrate plug/cores generally dissociating radially, describing
   - the conceptual picture of hydrate dissociation (Section 3.3.1)
   - correlations of dissociation (Section 3.3.2)
   - the anomalous self-preservation phenomenon (Section 3.3.3)
   - the state-of-the-art for hydrate dissociation (Section 3.3.4)

Two questions of hydrate time-dependent phenomena are essential to both industry and researcher: (1) When will hydrates nucleate? (2) Once nucleated, how rapidly will hydrates grow or dissociate?

As an example of hydrate nucleation and growth, consider the gas consumption versus time trace in Figure 3.1a for an agitated system operated at constant pressure and temperature. An autoclave cell (e.g., 300 cm^3) containing water (e.g., 150 cm^3) is pressurized with gas and brought to hydrate formation (P, T) conditions. The gas is added from a reservoir to maintain *constant pressure* as hydrates form with time. The rate of consumption of gas is the hydrate formation rate that can be controlled by kinetics, or heat or mass transfer.

The induction time is marked as 1 and includes the time taken for crystal nuclei to form which are not visible to macroscopic probes. The induction time is defined in practice as the time elapsed until the appearance of a detectable volume of hydrate phase or, equivalently, until the consumption of a detectable number of moles of hydrate former gas. The induction time is often also termed the hydrate nucleation or lag time (Section 3.1). (The induction or lag time is the time taken for hydrates to be detected macroscopically, after nucleation and onset of growth have occurred, whereas nucleation occurs on too small a size scale to be detected. Therefore, the term nucleation time will not be used in this context. Instead, the term induction time or induction period will be used. The induction time is most likely to be dominated by the nucleation period, but also includes growth up to the point at which hydrates are first detected.)

During the induction period, the temperature and pressure conditions are within the hydrate stable region. However, hydrate does not form within this period because of metastability (i.e., the ability of a nonequilibrium state to persist for a long period of time). The growth period (in region 2) is where very rapid hydrate growth occurs (Section 3.2). During the growth period, gas is being concentrated in the hydrate cages—hydrated gas molecules are more densely packed than those in the vapor. As the water is consumed by hydrate formation, the slope of the gas consumption trace eventually decreases with time (Points 3–4). Hydrate dissociation is not shown in the figure.

An alternative hydrate formation and dissociation experiment is shown in the temperature and pressure trace of Figure 3.1b. In this case, the volume is constant and the temperature is changed during the experiment. In the experimental apparatus an agitated autoclave cell (e.g., 300 cm^3) housing a sight glass window contains water (e.g., 150 cm^3) that is pressurized with methane gas to the upper

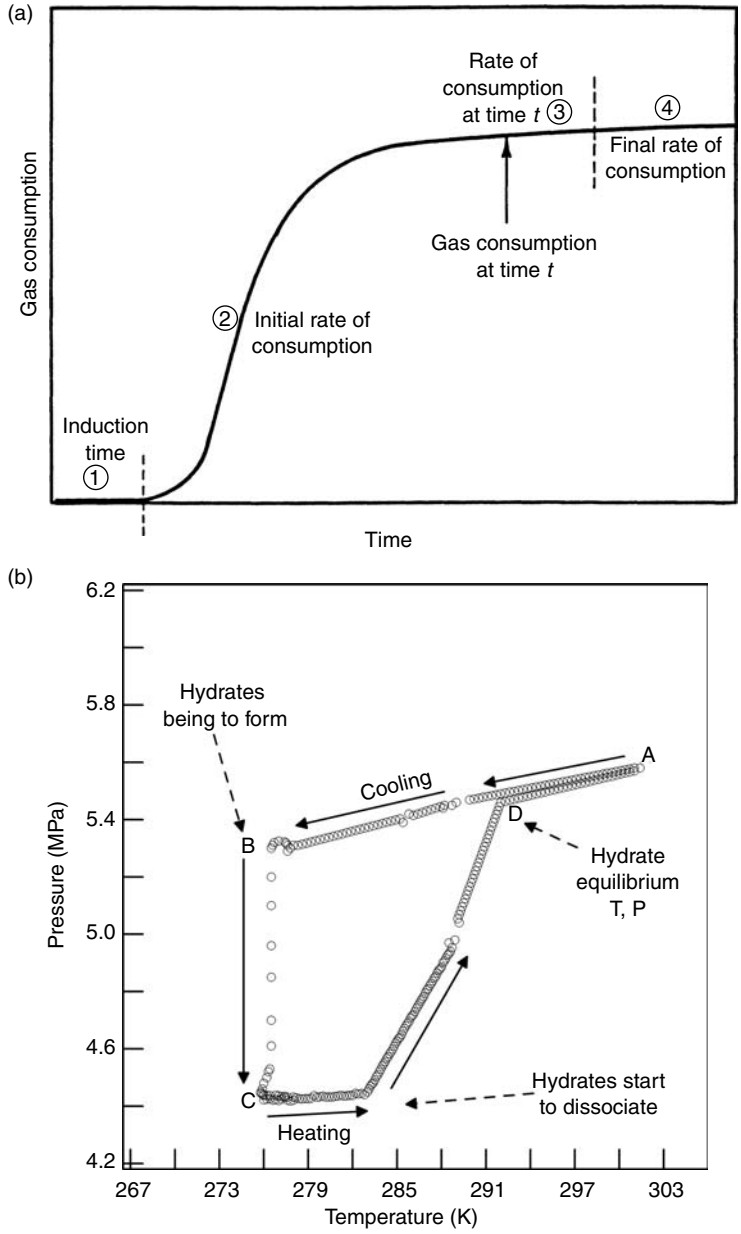

FIGURE 3.1 (a) Gas consumption vs. time for hydrate formation. (Reproduced from Lederhos, J.P., Long, J.P., Sum, A., Christiansen, R.L., Sloan, E.D., *Chem. Eng. Sci.*, **51**, 1221 (1996). With permission from Elsevier Science Ltd.) (b) Temperature and pressure trace for formation of simple methane hydrates. (Reproduced from Ouar, H., Cha, S.B., Wildeman, T.R., Sloan, E.D., *Trans I Chem. E.*, **70A**, 48 (1992). With permission from the American Chemical Society.)

rightmost temperature and pressure. As the cell temperature is lowered the pressure decreases, principally due to gas contraction as well as increased gas solubility upon cooling *at constant volume*. Neither gas nor water is added to the system during the experiment.

The metastability of the system prevents hydrate forming immediately at Point D (at the hydrate equilibrium temperature and pressure; Figure 3.1b). Instead the system pressure continues to decrease linearly with temperature for a number of hours, without hydrate formation occurring (A to B is the induction period, cf. 1 in Figure 3.1a). At Point B, hydrates begin to form. The pressure drops rapidly to Point C (about 1.01 MPa or 10 atm in 0.5 h). B to C is the catastrophic growth period (cf. 2 in Figure 3.1a).

Hydrate dissociation begins when the cell is heated from Point C in Figure 3.1b, so that the system pressure increases, at first slowly and then sharply along the steep dissociation line (between Points C and D). Finally at Point D, the hydrates are completely dissociated, as confirmed visually through the sight glass. The hydrate equilibrium condition (or hydrate dissociation temperature and pressure) is given by Point D (Section 3.3).

Usually 1–2 days (for reactors on this scale) of experimental effort are required to traverse the loop as shown in Figure 3.1b. In order to avoid obtaining an erroneous dissociation temperature and pressure, the dissociation part of the loop must be performed at a sufficiently slow heating rate (about 0.12 K/h) to allow the system to reach equilibrium (Tohidi et al., 2000; Rovetto et al., 2006). The temperature difference between the temperature at Point D to that at Point B is called the subcooling [more properly the supercooling, ΔT_{sub}, where $\Delta T_{\text{sub}} = T_{\text{eqm}}(\text{D}) - T(\text{B})$].

As illustrated in Figure 3.1b, there is a fundamental difference in hydrate initiation and dissociation due to the associated gas and liquid phases being disorderly on a molecular level, while the hydrate crystals are orderly in nature. Entropy favors disorder over order, so the initial hydrate formation is hindered by a long, metastable period (induction period). During this period, the disorderly gas and liquid water begin to rearrange into the orderly hydrate crystal structure. Conversely, dissociation begins relatively rapidly after the hydrate is removed from the temperature and pressure stability region.

3.1 Hydrate Nucleation

Hydrate nucleation is the process during which small clusters of water and gas (hydrate nuclei) grow and disperse in an attempt to achieve critical size for continued growth. The nucleation step is a microscopic phenomenon involving tens to thousands of molecules (Mullin, 1993, p. 173) and is difficult to observe experimentally. Current hypotheses for hydrate nucleation are based upon the better-known phenomena of water freezing, the dissolution of hydrocarbons in water, and computer simulations of both phenomena. Evidence from experiments shows that nucleation is a statistically probable (not deterministically certain; see Section 3.1.3) process.

3.1.1 Knowledge Base for Hydrate Nucleation

Nucleation thermodynamics were published by Ginns in 1928 based upon his work at the end of the last century. Volmer and Weber (1926) indicated that the growth and decay of clusters of molecules played a major role in nucleation kinetics. The most recent reviews of hydrate nucleation are by Kashchiev and Firoozabdi (2002a,b).

In order to achieve some understanding of the nucleation of hydrate crystals from supercooled water + gas systems, it is useful to briefly review the key properties of supercooled water (Section 3.1.1.1), hydrocarbon solubility in water (Section 3.1.1.2), and basic nucleation theory of ice, which can be applied to hydrates (since hydrate nucleation kinetics may be considered analogous, to some extent, to that of ice; Section 3.1.1.3). The three subsections of 3.1.1 (i.e., supercooled water, solubility of gas in water, and nucleation) are integral parts of conceptual pictures of nucleation detailed in Section 3.1.2.

3.1.1.1 Key properties of supercooled water

Water is considered to be supercooled when it exists as a liquid at lower temperatures than its melting point, for example, at less than 0°C at atmospheric pressure. In this state, the supercooled water is metastable. The properties of supercooled water have been examined in detail in excellent reviews by Angell (1982, 1983) and Debenedetti (1996, 2003). A brief review of the properties of supercooled pure liquid water and the different liquid water models are discussed in this section. These structures comprise hydrogen-bonded water networks and/or water clusters ("cages") that are the starting points to hydrate formation.

The anomalies of liquid water become more pronounced when it is supercooled. For example, the volume and entropy fluctuations of liquid water become more pronounced as the temperature decreases. This is in contrast to most other liquids, in which the volume and entropy fluctuations become smaller as the temperature is lowered. Furthermore, the volume and entropy fluctuations in water at less than 4°C are anticorrelated, that is, the increase in volume which occurs when water is cooled results in a decrease in entropy (Debenedetti, 2003).

The anticorrelation between entropy and volume for liquid water has been attributed to the formation of an open hydrogen-bonded network, in which a decrease in orientational entropy is accompanied by a volume increase (Debenedetti, 2003). This network is transient and short-ranged in liquid water (rather than being permanent and long-ranged in ice), and is the microscopic basis for water's negative thermal expansion. This open hydrogen-bonded network has a profound influence on the thermodynamics of liquid water (Debenedetti, 2003).

In order to understand the behavior of supercooled water it is useful to briefly review the different liquid water models:

1. The "hydrogen-bonded network" picture of Rahman and Stillinger (1973, 1974) is the most favored model. Stillinger (1980) also described water as a "macroscopically connected (three dimensional) random

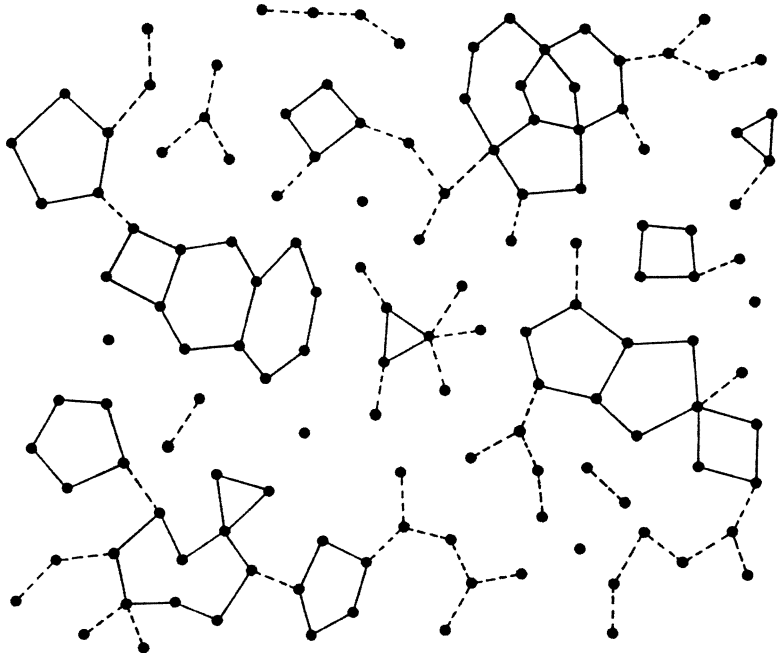

FIGURE 3.2 Networks of water molecules from molecular dynamics. (Reproduced from Rahman, A., Stillinger F.H., *J. Am. Chem. Soc.*, **95**, 7943 (1973). With permission from the American Chemical Society.)

network of hydrogen bonds, with frequent strained and broken bonds, that is continually undergoing topological reformation." A schematic of such a random network, which includes polygons (most commonly five and six member polygons), is provided in Figure 3.2.

2. The flickering "iceberg" theory of Frank and coworkers (1945, 1957, 1968, 1970) and Nemethy and Scheraga (1962): this model of water comprises an equilibrium mixture of short-lived (10^{-10} s) hydrogen-bonded clusters, together with a nonhydrogen-bonded dense phase (also see Section 2.1.1.4). Consistent with this flickering "iceberg" model is Pauling's (1959) model of water, consisting of a complex of 5^{12} cavities, in which the guest molecule is water.

The most favored model for supercooled water is based on model (1) for liquid water the "hydrogen-bonded network." The latter forms the basis of the open hydrogen-bonded network model mentioned previously for supercooled water. Support for this model is based on data and simulations of highly supercooled water (Speedy, 1987; Dore, 1988; Poole et al., 1993; Stanley et al., 1993; Sastry et al., 1996; Angell, 1999; Franzese and Stanley, 2002).

An alternative model of supercooled water comprises clathrate-like entities, which is consistent with model (2) for liquid water. Sorenson (1994) and Walrafen

and coworkers (1995, 1997) suggested support for this model on the basis of Raman spectroscopic measurements on supercooled water (at −33°C) and sII THF hydrate. It should be noted that the water scientific community refer to short-lived liquid cavities (not unit crystals sI, sII, or sH) as clathrate-like structures in water.

Measurements of the properties of highly supercooled water (Speedy, 1987; Speedy et al., 1987; Angell, 1999) indicated that the vital parameter was the concentration and spatial distribution of several unstrained hydrogen-bonded polyhedra (such as the 5^{12} cavity) embedded within the random network of molecules. The hydrogen-bond angles in these polyhedra make it thermodynamically favorable for them to share edges and faces without the introduction of strain. As a result unstrained polyhedra are shown to exhibit an attraction for each other. The sharing of polyhedral faces and edges in supercooled water is suggestive of prenucleation phenomena for hydrates. Further support for the so-called cage effect for supercooled water comes from Mode-Coupling Theory (Chen et al., 1997).

Truskett and Dill (2002) proposed a two-dimensional water-like model to interpret the thermodynamics of supercooled water. This model is consistent with model (1) for liquid water. Cage-like and dense fluid configurations correspond to transient structured and unstructured regions, observed in molecular simulations of water (Errington and Debenedetti, 2001). Truskett and Dill's model provides a microscopic theory for the global phase behavior of water, which predicts the liquid-phase anomalies and expansion upon freezing.

Makogon (1974) was the first to incorporate the above concepts into a hydrate nucleation mechanism, indicating that water molecules cluster with a decrease in temperature.

3.1.1.2 Solubility of natural gases in water

The solubility of nonpolar gases in liquid water is very small, at pressures both above and below the hydrate formation point. Miller and Hildebrand (1968) indicate that the solubility of nonpolar gases in water is at least an order of magnitude lower than the corresponding solubility of nonpolar gases in cyclohexane. Values for solubilities, as well as infinite dilution enthalpies, entropies, and heat capacities of solution at 298 K are given in Table 3.1. Examining the solubility and thermodynamics of nonpolar gases in liquid water can provide insight into why certain gases form more stable hydrates than others. These properties may also explain why hydration shells or cage-like clusters can form around the nonpolar molecule.

Since $\Delta G = \Delta H - T\Delta S$, a large negative (unfavorable) entropy of solution overcomes the negative (favorable) enthalpy of solution to yield a small positive value of ΔG of solution. Large negative entropy changes and large positive heat capacity changes are unique to aqueous solutions of nonpolar gases. Himmelblau (1959) noted a dramatic decrease in the entropy of solution for hydrate formers, in contrast to the small nonhydrate formers such as He, H_2, and Ne, is an indication of some special solubility phenomenon associated with size. It is now

TABLE 3.1
Solution Properties of Natural Gas Hydrate Components at 298 K

Component	Solubility[a] $10^5 x_2$	$-\Delta H_{soln}$[b] KJ/mol	$-\Delta S_{soln}$[c] J/(K mol)	ΔC_p[d] kJ/(K mol)
Methane	2.48	13.26	44.5	55
Ethane	3.10	16.99	57.0	66
Propane	2.73	21.17	71.0	70
Iso-butane[e]	1.69	25.87	86.8	NA
Nitrogen	1.19	10.46	35.1	112
Hydrogen sulfide[f]	177.9	26.35	88.4	36
Carbon dioxide[g]	60.8	19.43	65.2	34

[a] Solubility at 101.3 kPa from Miller and Hildebrand (1968) except i-C_4H_{10}, H_2S, and CO_2, as indicated below.
[b] $\overline{H}^o_{L2} - \overline{H}^*_G$, transfer from gas to infinite dilution liquid, from Franks and Reid (1973).
[c] $\overline{S}^o_{L2} - \overline{S}^*_G$, transfer from gas to liquid, standard state, fugacity = 101.3 kPa.
[d] C_p from Alexander et al. (1971) except CH_4, C_2H_6, and H_2S from D'Orazio and Wood (1963).
[e] i-C_4H_{10} properties calculated from Wetlaufer et al. (1964).
[f] H_2S properties calculated from Carroll (1990), Selleck et al. (1952), and hypothetical ΔH_{soln}, ΔS_{soln} extrapolated below Q_2 (302 K).
[g] CO_2 properties calculated from Alexander et al. (1971).

known that He, H_2, and Ne can form sII hydrate, albeit at very high pressures (Section 2.1.2.2.5).

Entropy is a measure of disorder. The largest negative entropy of solution in Table 3.1 is generally considered as evidence of the creation of structure (increased order) within the body of water. More recently it has been suggested that the creation of a cavity can explain the entropy decrease. Large heat capacity changes also indicate the structuring effect of the solute on the water molecules. The size of the solute molecule has a substantial effect on solubility.

In a review of the thermodynamics of water, Franks and Reid (1973) showed that the optimum molecular size range for maximum solubility was similar to hydrate stability. Franks and Reid noted, "this is not intended to imply that long-lived clathrate structures exist in solution—only that the stabilization of the water structure by the apolar solutes resembles the stabilization of water in a clathrate lattice." Glew (1962) noted that, within experimental error, the heat of solution for ten hydrate formers (including methane, ethane, propane, and hydrogen sulfide) was the same as the heat of hydrate formation from gas and ice, thereby suggesting the coordination of the aqueous solute with surrounding water molecules.

The most popular explanation of such changes in solubility stems from the hypothesis of Frank and Evans (1945), that the presence of the solute molecule causes an increase in the order of bulk water molecules, with the formation of water hydration shells around solute molecules. This is with the caution that such ordering

should not be considered as long-lived or complete in any sense. This hypothesis has been traditionally referred to as the "iceberg" model and has been reexamined and extended numerous times over the past decades (see Section 2.1.1.4 for more details).

The lifetimes of the cage-like water clusters in solution have been also investigated using molecular dynamics (MD) simulations (Guo et al., 2005). Statistical analyses were performed to determine the lifetimes of 5^{12} and $5^{12}6^2$ cage-like clusters, with 200 analyses performed for each cluster. Varying the hydrogen-bond topology of these cage-like clusters was found to have no significant effect on the lifetimes of these clusters that on average ranged from 24.7 to 27.9 picoseconds (ps).

Stillinger (1980) indicated that in the above cage-like clusters around solutes, any nonbonded hydrogens always point outward from the convex structure, thereby encouraging further bonding beyond the cage. This is illustrated in the stereographic pictures in Figure 3.3 of clathrate-like clusters. During the reorientation of water molecules to accommodate the solute molecule, the bonds are calculated to be stronger in the solvation cages compared to pure water, and possess many of the geometrical properties of the 5^{12} cavity (see Section 2.1.2.1).

The sharing of imperfect cluster faces of the clathrate-like clusters can be viewed as a thermodynamic tendency to minimize the negative entropies of solution. The tendency for face- or edge-sharing of individual solvation clusters, as Stillinger (1980) pointed out, is the same as the tendency for clustering of pure supercooled water.

3.1.1.3 Nucleation theory for ice and hydrates

Hydrate nucleation and growth may have direct analogies in crystallization processes such as the precipitation of salt from solution. Metastability in salt crystallization was hypothesized to occur through supersaturation by Ostwald (1900). (A supersaturated solution is one in which the liquid [solvent] contains more dissolved solute than can be ordinarily accommodated at that temperature; the greater the degree of supersaturation, the greater number of crystal nuclei that will form in solution.) Miers and Isaac (1907) experimentally proved metastability and postulated that for each solute–solvent pair, a concentration–temperature relationship exists that defines the metastable limit, formally called the thermodynamic spinodal.

Figure 3.4a shows a normal crystallization curve with the spinodal (supersaturation limit) curve (CD) and equilibrium curve (AB). At point P neither nuclei nor crystal growth will occur since the solution is superheated by the amount RP. Once the saturation line (AB) is crossed, either through cooling or increase in concentration, nuclei and crystals may or may not form in the metastable region. Metastable point Q is shown between point R and the crosshatched line CD.

The induction time or lag time is the period between cooling (i.e., supercooling as in 3.1.1.1) to the left of Point R in Figure 3.4a, until the time of solid formation.

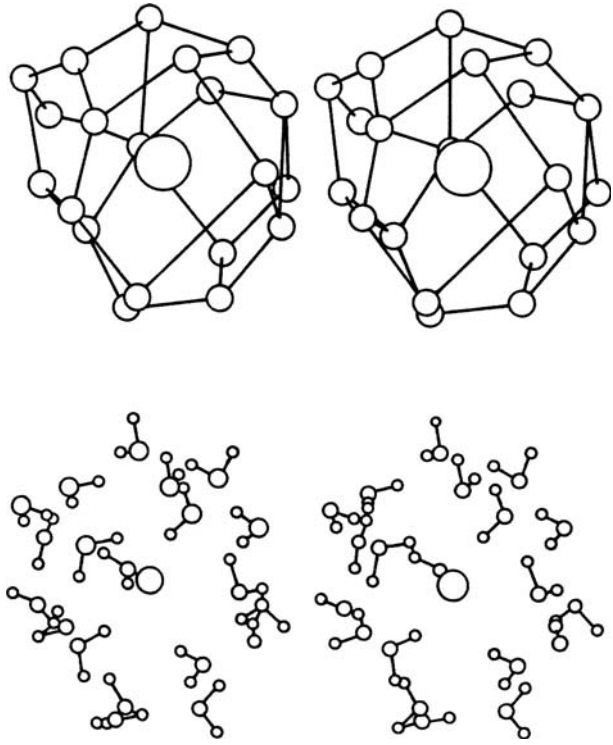

FIGURE 3.3 Stereographic view of water molecules cluster alignment by a dissolved apolar molecule (large circles) from Monte Carlo computer simulation studies. Top figure shown with lines connecting water. (Reproduced from Swaminathan, S., Harrison, S.W., Beveridge, D.L., *J. Am. Chem. Soc.*, **100**, 5705 (1978). With permission from the American Chemical Society.)

Typically, hydrate nucleation and growth will occur within the metastable region before entering the spinodal region. Cooling into the region to the left of line CD (into the spinodal region), nucleation will occur readily (Mullin and Jancic, 1979), due to the high degree of supersaturation, or driving force. Line CD is shown as a broad band, because it has been calculated (e.g., Englezos and Bishnoi, 1988), and only determined experimentally for some systems (e.g., for ice but not for hydrates).

Mullin (1993, p. 117) describes the crystallization regions in Figure 3.4a as the following:

1. The stable zone to the right of equilibrium line AB where crystallization is impossible.
2. The metastable (supersaturated) zone between lines AB and CD where spontaneous crystallization is improbable. However, if a crystal seed were placed in such a metastable solution, growth would occur on the seed.

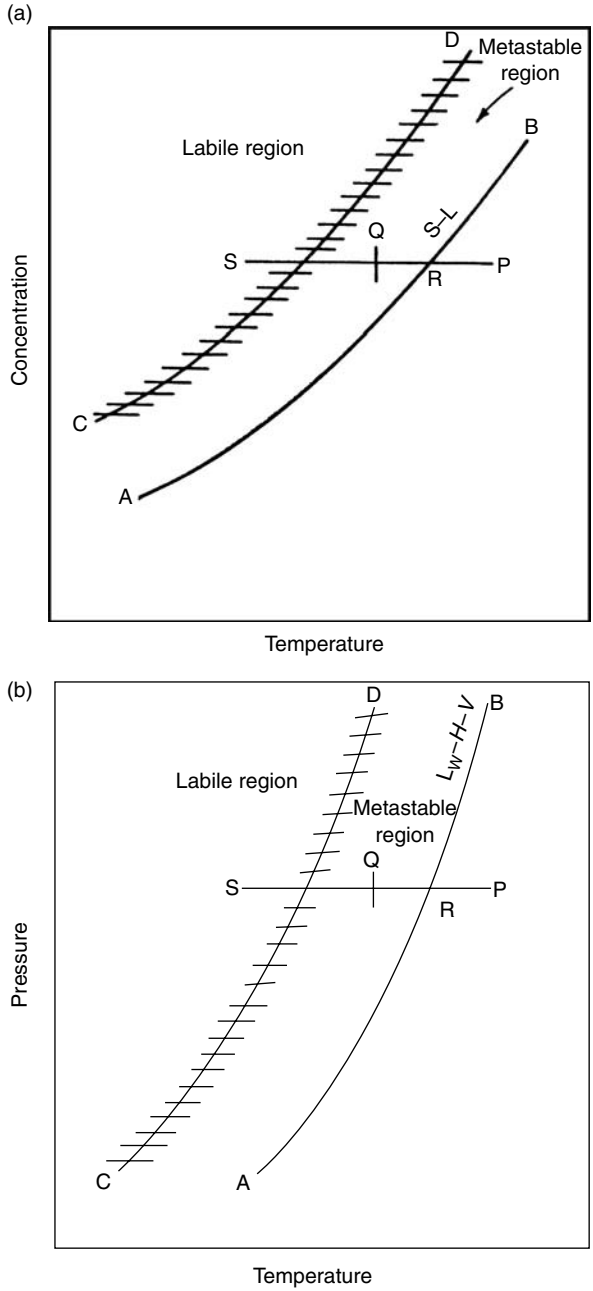

FIGURE 3.4 (a) Crystal and (b) hydrate formation as a function of subcooling relative to the equilibrium line (AB) and the spinodal line (CD; supersaturation limit).

3. The unstable or labile (supersaturated) zone to the left of line CD, where spontaneous crystallization occurs.

A direct analogy is shown in Figure 3.4b for hydrates if the concentration axis of Figure 3.4a is replaced by a logarithmic pressure axis. The lines CD and AB have effectively the same meaning in Figure 3.4b as in Figure 3.4a. However, it is not known where the spinodal line (CD) occurs for hydrates. To the left of line CD on a ln P versus T plot, nucleation will readily occur due to the fact that the driving force is very high (see Section 3.1.3). However, between lines AB and CD there is substantial evidence that the hydrate induction period is not subject to correlation or prediction at the lower driving forces of subcooling or overpressure.

To determine the relationship between hydrate nucleation (requiring three phases) and the more usual type (two-phase nucleation) consider the theory of homogeneous and heterogeneous nucleation in crystallization, as reviewed by Mullin (1993, p. 172) and Kashchiev and Firoozabadi (2002b), from which much of the below discussion has been excerpted.

3.1.1.3.1 Homogeneous nucleation

Homogeneous nucleation (HON) is rarely encountered in the real world. However, despite its shortcomings, the classical nucleation theory (first originating from the work of Volmer and Weber, 1926) still forms the basis of most modern treatments of nucleation. Therefore, only a brief discussion of the fundamental concepts of homogeneous nucleation is included here for completeness.

Homogeneous nucleation is a solidification process occurring in the absence of impurities. It involves many more molecules than could collide simultaneously, so a sequence of bimolecular collisions of an autocatalytic nature is more probable (see Figure 3.5). That is, there is a sequential formation of clusters (embryos) within the supercooled liquid of increasing cluster size (A_2 = cluster containing two molecules, A_3 = cluster containing three molecules, etc.), until the critical cluster size, A_n is reached. The critical cluster size (also called critical nucleus) is the cluster size that must be reached before nuclei/clusters can grow spontaneously (see Figure 3.5).

Before achieving the critical size, clusters (or embryos) of molecules form in the bulk metastable liquid, and these clusters may either grow or shrink as a result of density or composition fluctuations. When the cluster attains a critical size, monotonic growth occurs. Such a phenomenon of critical cluster size formation and spontaneous growth may be interpreted by the excess Gibbs free energy (ΔG) between a small solid particle of solute and the solute in solution. ΔG is equal to the sum of the surface excess free energy ΔG_s (for solute molecules becoming part of the surface of the crystal nuclei), and the volume excess free energy ΔG_v (for solute molecules ending up in the bulk/interior of the crystal nuclei).

$$\Delta G = \Delta G_s + G_v = 4\pi r^2\sigma + \tfrac{4}{3}\pi r^3 \Delta g_v \tag{3.1}$$

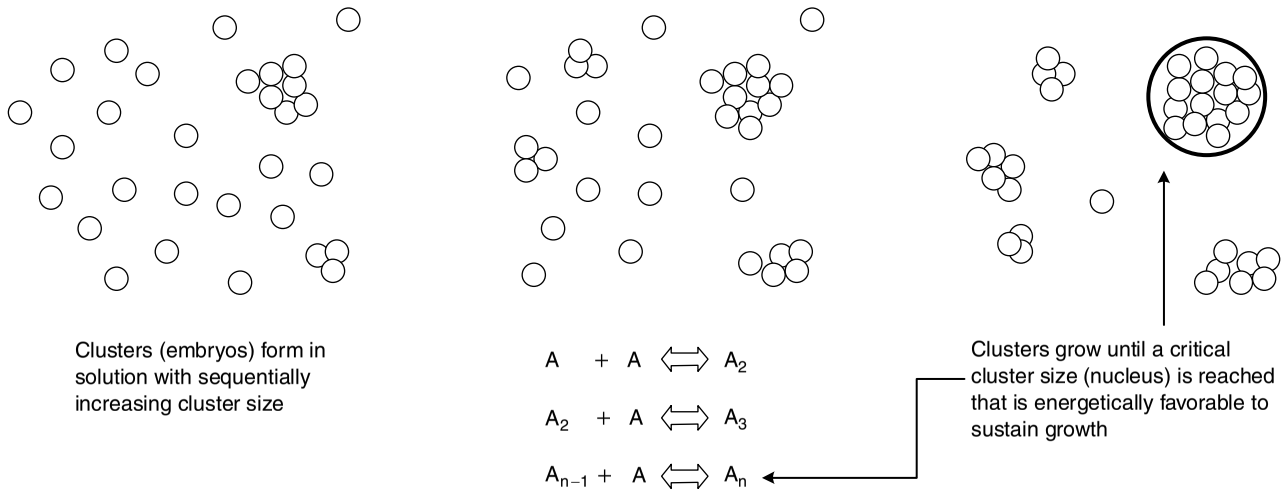

FIGURE 3.5 Schematic of the formation of a critical nucleus according to Classical Nucleation Theory. (T. Strobel, Personal Communication, October 24, 2006.)

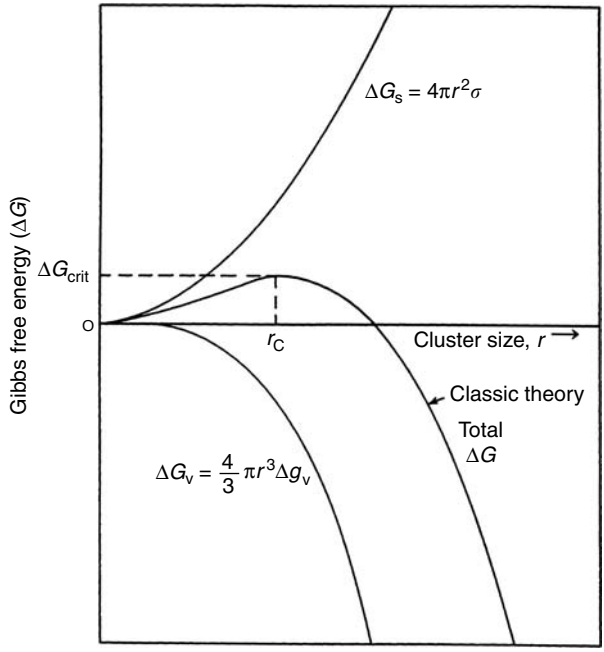

FIGURE 3.6 Comparison of surface excess free energy (ΔG_s) and volume excess free energy (ΔG_v) as functions of cluster size. (Reproduced and modified from Larson, M.A., Garside, J., *Chem. Eng. Sci.*, **41**, 1285 (1986). With permission from Elsevier.)

where Δg_v is the free energy change per unit volume and σ is the surface tension (of the crystal–liquid interface). As shown in Figure 3.6 because Δg_v is negative, ΔG_s and ΔG_v are of opposite sign and are different functions of r, the radius of the solid particle. The addition of the surface and volume effects causes a maximum (ΔG_{crit}) in the value of ΔG at the radius corresponding to the critical nucleus, r_c. That is, the free energy barrier, ΔG_{crit} must be surmounted to form a cluster of a critical size, beyond which the nuclei/clusters grow spontaneously.

The maximum value of ΔG and the critical radius are obtained by differentiating Equation (3.1) and setting the result to zero to obtain:

$$r_c = -2\sigma/\Delta g_v \tag{3.2a}$$

and

$$\Delta G_{crit} = 4\pi\sigma r_c^2/3 \tag{3.2b}$$

The rate at which critical sized clusters are formed is very sensitive to the height of the free energy barrier (ΔG), or equivalent to the extent of penetration into the metastable region. As the critical cluster size becomes smaller, so does the free energy barrier that must be overcome to form the critical cluster. With increasing

supersaturation, the free energy barrier eventually becomes small enough for nucleation to become spontaneous.

Englezos et al. (1987a) and Englezos and Bishnoi (1988) determined an expression for the radius of the hydrate critical nucleus using the Gibbs free energy per unit volume of hydrate formed (Δg_v) in a modification of Equations 3.2a and b as

$$r_c = \frac{-2\sigma}{\Delta g_v} \tag{3.3a}$$

$$(-\Delta g_v) = \frac{RT}{\nu_h}\left[\sum_1^2 \theta_j \ln\left(\frac{f_{b,j}}{f_{\infty,j}}\right) + \frac{n_w \nu_w (P - P_\infty)}{RT}\right] \tag{3.3b}$$

where the surface tension σ is the value of ice in water, ν_h and ν_w are the molar volumes of hydrate and water, respectively, θ_j is the fractional filling of the hydrate cages on a water free basis, $f_{b,j}$ and $f_{\infty,j}$ are the bulk phase experimental and equilibrium fugacities, respectively, of component j at temperature T, $(P - P_\infty)$ represents the overpressure, and n_w is the number of water molecules per gas molecule. The equation contains the assumption that the hydrate phase is at equilibrium, rather than at operating conditions. In Equation 3.3b the summation term on the right should be divided by the hydration number in order to make it dimensionally consistent.

Using Equations 3.3a and b, Englezos et al. (1987a) calculated the critical radius of methane hydrate to be 30–170 Å. In comparison, critical cluster sizes using classical nucleation theory are estimated at around 32 Å (Larson and Garside, 1986), while computer simulations predict critical sizes to be around 14.5 Å (Baez and Clancy, 1994; Westacott and Rodger, 1998; Radhakrishnan and Trout, 2002).

Chen (1980, p. 7) suggested that the use of bulk phase properties, such as those in Equations 3.1 through 3.3, may be satisfactory only in qualitative analyses. Microscopic critical clusters contain several tens to thousands of molecules, and as such have a spectrum of sizes and properties, which may be difficult to quantify with a single number on a macroscopic scale.

3.1.1.3.2 Heterogeneous nucleation

In practice, homogeneous nucleation is very difficult to achieve, unless very small droplets of ultrapure water are dispersed within an oil emulsion, or very small droplets are formed by expansion through a supersonic (Lavel) nozzle (Wyslouzil et al., 1997).

As also noted by Mullin (1993, pp. 182, 183):

> "homogeneous nucleation is not a common event. Aqueous solutions as normally prepared in the laboratory may contain more than 10^6 particles per cm^3. It is virtually impossible to achieve a solution completely free of foreign particles, although careful filtration can reduce the contaminants to less than 10^3 per cm^3 which may render the solution . . . immune to spontaneously nucleation."

In the more usual case, heterogeneous nucleation (HEN) occurs in the presence of a foreign body (e.g., dust microparticles) or surface (e.g., fluid interface, container, or pipe wall), at smaller supercoolings than that required for homogeneous nucleation. From a free energy standpoint, it is more probable to grow an ice or hydrate nucleus on a two-dimensional surface (container wall or dust) than in the three-dimensional surface-free volume of water. The angle of contact (θ) between the hydrate crystal and a surface is related to ϕ, a fraction that is multiplied by the value of ΔG_{crit} in homogeneous nucleation to obtain a smaller $\Delta G'_{\text{crit}}$ for heterogeneous nucleation:

$$\Delta G'_{\text{crit}} = \phi\, \Delta G_{\text{crit}} \tag{3.4a}$$

$$\phi = [(2 + \cos\theta)(1 - \cos\theta)^2]/4 \tag{3.4b}$$

When the angle of contact $\theta = 180°$ (complete nonwetting of the substrate) then $\Delta G'_{\text{crit}} = \Delta G_{\text{crit}}$ and when θ is 0° (complete wetting of the substrate) then $\Delta G_{\text{crit}} = 0$. The foreign surface effectively lowers the $\Delta G'_{\text{crit}}$ and critical radius (r_c) required for catastrophic growth, as shown in Equations 3.4a and b. Homogeneous nucleation of hydrates is an anomaly. Hence, heterogeneous nucleation occurs much more frequently.

The kinetics of nucleation of one-component gas hydrates in aqueous solution have been analyzed by Kashchiev and Firoozabadi (2002b). Expressions were derived for the stationary rate of hydrate nucleation, J, for heterogeneous nucleation at the solution–gas interface or on solid substrates, and also for the special case of homogeneous nucleation. Kashchiev and Firoozabadi's work on the kinetics of hydrate nucleation provides a detailed examination of the mechanisms and kinetic expressions for hydrate nucleation, which are based on classical nucleation theory. Kashchiev and Firoozabadi's (2002b) work is only briefly summarized here, and for more details the reader is referred to the original references.

Thus, the work, $W(J)$, to form a hydrate cluster of n building units can be determined using the classical theory of nucleation.

$$W(n) = -n\,\Delta\mu + C v_{\text{h}}^{2/3} \sigma_{\text{ef}} n^{2/3} \tag{3.5}$$

where $\Delta\mu$ is the supersaturation. Physically, this term represents the work gained on assembling n hydrate building units into an n-sized hydrate cluster (nucleation can only occur when $\Delta\mu > 0$). C is the shape factor. A spherical cluster is formed in homogeneous nucleation ($C = (36\pi)^{1/3}$; Figure 3.7a). In heterogeneous nucleation, a cap-shaped cluster is formed on a solid substrate, while a lens-shaped cluster is formed at the interface between the solution and gas phase (Figures 3.7b,c, respectively). The volume of the hydrate building unit, ν_{h} (m^3), is composed of one gas molecule and n_{w} (hydration number) water molecules. The effective specific surface energy, σ_{ef} (J/m^2), is the work done to create the interface between the cluster and the solution (in HON), or the solution and substrate (HEN), or solution and gas (HEN).

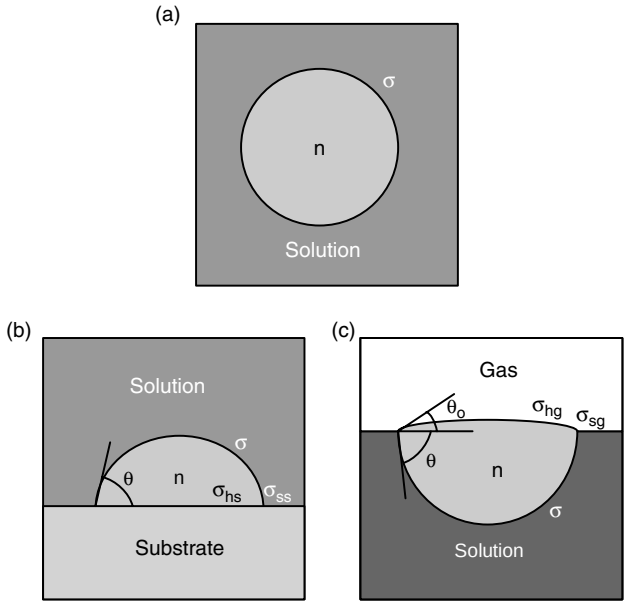

FIGURE 3.7 Schematic of (a) spherical cluster of n building units in HON; (b) cap-shaped cluster of n building units in 3D HEN on a substrate; (c) lens-shaped cluster of n building units in 3D HEN at the solution–gas interface. $\sigma_{ss}, \sigma_{hs}, \sigma_{sg}, \sigma_{hg}$ are specific energies of the solution–substrate, hydrate–substrate, solution–gas and hydrate–gas interfaces. (Reproduced from Kashchiev, D., Firoozabadi, A., *J. Cryst. Growth*, **243**, 476 (2002b). With permission from Elsevier.)

In Figure 3.7, the wetting angle is given by θ. The nonwetting case ($\theta = 180°$) is given by HON, which is the energetically limiting case of HEN. Kashchiev and Firoozabadi note that the HEN cap-shaped hydrate cluster on the hydrate-wetted solid surface in solution is thermodynamically favored over HON. The better the substrate/hydrate wetting (i.e., the smaller the wetting angle θ), the greater the probability of HEN.

The authors further note that although visual observations have shown that hydrate crystallizes at the solution–gas interface, this may also be because of nucleation and subsequent growth within a thin solution layer adjacent to the solution–gas interface. For kinetic reasons, the supersaturation in the thin solution layer can be locally high, and therefore hydrate nucleation and subsequent growth in this layer would in fact be more probable than in the bulk of the solution.

3.1.1.4 Site of hydrate nucleation

Long and Sloan (1996) performed a series of measurements to investigate the site of nucleation for natural gas and carbon dioxide hydrate initiation in a sapphire tube.

A hydrate nucleating agent (precipitated amorphous silica) and a quiescent surface inhibitor (sodium dodecyl sulfate) were used in an attempt to initiate hydrates in the bulk phase. While the induction time (for detectable hydrate formation) was not predictable, in every case hydrate was initiated at a surface—usually at the vapor–water interface, but infrequently along the sides of the sapphire tube in the gas phase, and at the metal end-plate below the liquid phase.

A number of other researchers have also confirmed that nucleation and subsequent growth typically occurs at the water–hydrocarbon interface: for methane hydrate (Huo et al., 2001; Østergaard et al., 2001; Taylor, 2006) and carbon dioxide hydrate (Kimuro et al., 1993; Fujioka et al., 1994; Hirai et al., 1995; Mori, 1998).

Molecular dynamics (MD) simulation studies also indicate that the initial formation of methane hydrate occurs preferentially near the water–methane interface where there is a significant concentration gradient (Moon et al., 2003).

Hydrate formation usually occurs at the vapor–liquid interface (or within a thin film located at the vapor–liquid interface; Kashchiev and Firoozabadi, 2002b), not only because the interface lowers the Gibbs free energy of nucleation, but also because the interface is the location of the required very high concentrations of host and guest molecules. The hydrate guest composition may be as high as 0.15 mole fraction, with the remainder being water. Yet the water mole fraction in the hydrocarbon phase is typically less than 0.05, while the mole fraction of hydrocarbon in the aqueous phase is never greater than 0.001.

With such low concentrations of components available to form critical nuclei, hydrate formation seems unlikely in the bulk phases. However, at an interface where higher concentrations exist through adsorption (particularly at the vapor–liquid interface where both phases appear in abundance) cluster growth to a supercritical size is a more likely event. High mixing rates may cause interfacial gas + liquid + crystal structures to be dispersed within the liquid, giving the appearance of bulk nucleation from a surface effect.

3.1.2 Conceptual Picture of Hydrate Nucleation at the Molecular Level

Since hydrate initiation usually occurs at the vapor–liquid interface, molecular models of hydrate nucleation have focused on that surface. The earliest conceptual picture for hydrate nucleation is the labile cluster mechanism. A labile cluster is an unstable entity that readily undergoes change. The labile clusters are composed of a guest molecule surrounded by 20 and 24 (cf. 5^{12}, $5^{12}6^2$ cages of sI) or 20 and 28 (cf. 5^{12}, $5^{12}6^4$ cages of sII) water molecules in the first solvation shell. This model considers nucleation to occur by the agglomeration of labile clusters either on the liquid or the vapor side of the interface (Figure 3.9). A modification of the labile cluster model is based on adsorption and clustering on the vapor side of the interface (Figure 3.11). An alternative more recent mechanism is the local structuring hypothesis that focuses on the development of guest molecules being arranged (ordered) in configurations similar to that in the hydrate and a

hydrogen-bonded water network (Figures 3.12 and 3.13). These three postulated mechanisms will be discussed in Sections 3.1.2.1 through 3.1.2.3.

It is plausible that hydrate nucleation proceeds via some combination of these mechanisms. The hydrate nucleation and growth processes may be analogous to the corresponding processes occurring during ice formation. This analogy may be suggested from the recent MD simulation of ice nucleation and growth resulting in water freezing (Matsumoto et al., 2002). These simulations were run for an extremely long time compared to typical simulations, capturing timescales of up to 500 ns (nanoseconds). Ice nucleation occurs when a sufficient number of relatively long-lived hydrogen bonds develop at the same location to form a compact initial nucleus. The initial nucleus, on reaching a critical size, expands rapidly resulting in the entire system freezing (Figure 3.8).

3.1.2.1 Labile cluster nucleation hypothesis

Using the fact that water clusters around dissolved gas molecules (Section 3.1.1.2), it was proposed that clusters may grow to achieve a critical radius, as shown schematically in Figure 3.9 (Sloan, 1990; Sloan and Fleyfel, 1991; Muller-Bongartz et al., 1992). Christiansen and Sloan (1994) extended the model, with the following key elements:

1. Pure water exists without guests, but with many transient, labile ring structures of pentamers and hexamers.
2. Water molecules form labile clusters around dissolved guest molecules. The cluster size depends on the dissolved guest size range. The number of water molecules in each cluster shell (i.e., coordination number of water molecules surrounding a guest molecule) for natural gas components are: methane (20), ethane (24), propane (28), iso-butane (28), nitrogen (20), hydrogen sulfide (20), and carbon dioxide (24).
3. Clusters of dissolved species combine to form unit cells. To form sI coordination numbers of 20 and 24 are required for 5^{12} and $5^{12}6^2$ cavities, while sII requires coordination numbers of 20 and 28 for the 5^{12} and $5^{12}6^4$ cavities. Nucleation is facilitated if labile clusters are available with both types of coordination numbers for either sI (e.g., $CH_4 + CO_2$ mixtures) or sII (e.g., $CH_4 + C_3H_8$ or most unprocessed natural gases). If the liquid phase has clusters of only one coordination number, nucleation is inhibited until the clusters can transform to the other size, by making and breaking hydrogen bonds.
4. An activation barrier is associated with the cluster transformation. If the dissolved gas is methane, the barrier for transforming the cluster coordination number from 20 (for the 5^{12}) to 24 (for the $5^{12}6^2$) is high, both because the guest cannot lend much stability to the larger cavity (see Section 2.1.3.2) and because the $5^{12}6^2$ cavities outnumber the 5^{12} in sI by a factor of 3. Transformation of methane–water clusters from

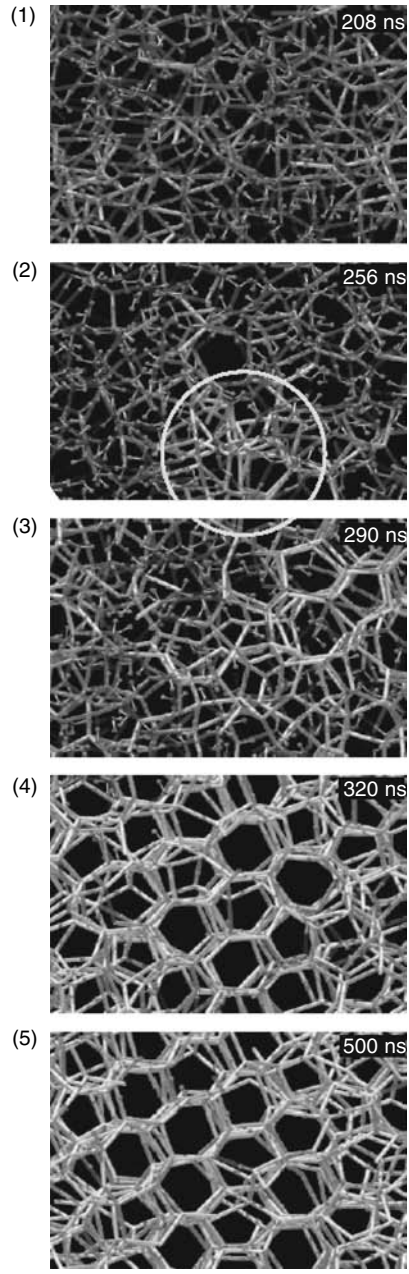

FIGURE 3.8 MD simulation of ice nucleation and growth showing the hydrogen-bond network structure of water at a given time. At time $t = 208$ ns (1), $t = 256$ ns (2), $t = 290$ ns (3), $t = 320$ ns (4), $t = 500$ ns (5). Lines indicate hydrogen bonds between water molecules. Bright white lines indicate long-lasting H-bonds (lifetimes >2 ns). An initial nucleus is formed in the circled region (in 2). (Reproduced from Matsumoto, M., Saito, S., Ohmine, I., *Nature*, **416**, 409 (2002). ©With permission.)

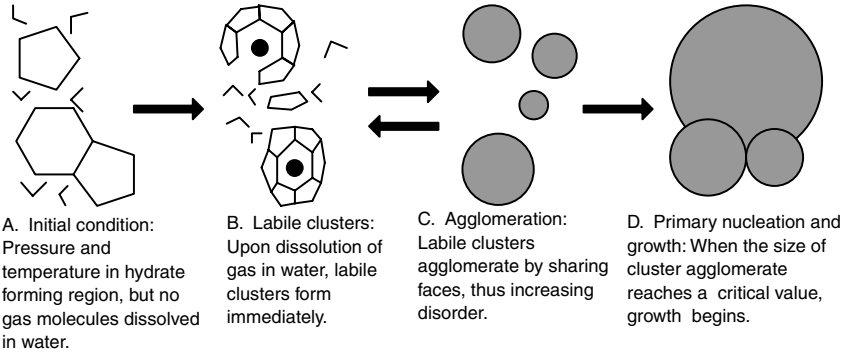

FIGURE 3.9 Schematic model of labile cluster growth. (Reproduced from Christiansen, R.L., Sloan, E.D., in *Proc. First International Conference on Natural Gas Hydrates* (1994) New York Academy of Sciences. With permission.)

20 to 28 has an even higher energy barrier, because methane is not large enough to stabilize the $5^{12}6^4$ cavity (unless at very high pressure).

5. If the dissolved gas is ethane with a water coordination number of 24, the transformation of empty cavities (with a coordination number of 20) is likely to be rapid, due to the high ratio (3:1) of $5^{12}6^2$ to 5^{12} cavities in sI. If the dissolved gas is propane with a coordination number of 28, transformation to sII is likely to be slow because $5^{12}6^4$ cavities are outnumbered by 5^{12} cavities by a factor of two.
6. Figure 3.10 shows the cluster mechanism imposed on the pressure–temperature trace presented in Figure 3.1b. At Point A after pressurization of the system, guest molecules are dissolved in water and short-lived cages have been formed. The linking of clusters to each other occurs after cooling from Point A until a critical radius cluster is formed at Point B, where catastrophic nucleation and growth occurs. On heating the system from Point C, the reaction is driven to dissociate the hydrate (to the right in Figure 3.10).
7. At temperatures higher than Point D (and at $T < 28°C$) in Figure 3.10, clusters continue to persist, so that the solid phase is not totally disrupted upon the transition to a liquid and vapor. Only after a matter of some hours or days will the clusters be dispersed to a more normal water distribution.
8. Alternative structures arise that provide parallel formation pathways and consequently slow nucleation kinetics.

In the hypothesis, Points 5 and 8 above (alternative structures) have come under criticism, first by Skovborg et al. (1992) and then by Natarajan et al. (1994). However, Skovborg noted that alternating structures may account for some of his nucleation data. A further criticism of the labile cluster hypothesis is that the energy barrier for agglomeration of clusters is far larger than cluster disintegration (Radhakrishnan and Trout, 2002).

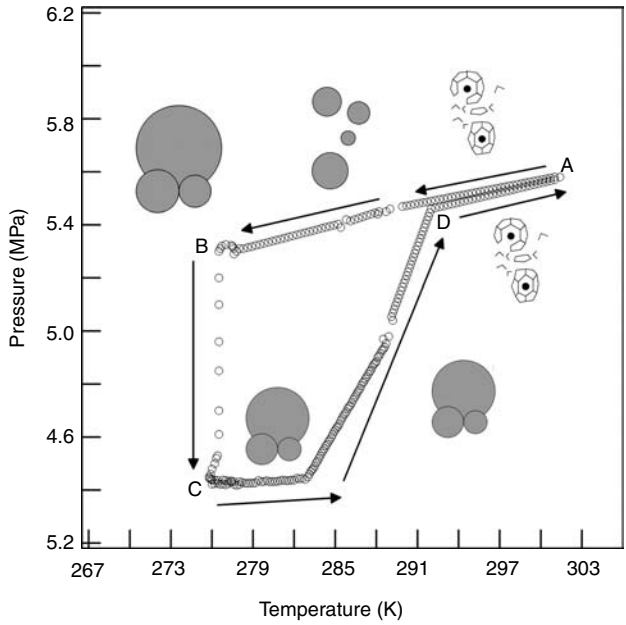

FIGURE 3.10 Hydrate labile cluster growth mechanism imposed on a pressure–temperature trace. (Reproduced from Christiansen, R.L., Sloan, E.D., in *Proc. First International Conference on Natural Gas Hydrates* (1994) New York Academy of Sciences. With permission.)

3.1.2.2 Nucleation at the interface hypothesis

Long (1994) and Kvamme (1996), suggested that nucleation arises on the vapor side of the interface. A conceptual picture is shown in Figure 3.11, with the following components for heterogeneous nucleation on the vapor side of the interface:

1. Gas molecules are transported to the interface. Long (1994) notes that the gas impingement rate is 10^{22} molecules/(cm^2s) at the normal temperatures and pressures of hydrate formation. Kvamme (1996) indicates this step is transport of molecules through a stagnant boundary.
2. Gas adsorbs on the aqueous surface. While both Long and Kvamme list adsorption as a separate step before either surface diffusion or clustering of the water, adsorption may occur in a partially completed cavity.
3. The gas migrates to a suitable location for adsorption through surface diffusion. At this location the water molecules form first partial, and then complete cages around the adsorbed species.
4. Labile clusters join and grow on the vapor side of the surface until a critical size is achieved. This can occur either by the addition of water and gas molecules to existing cavities, via the joining of cavities along the interface (as indicated in the cluster aggregation mechanism) or both.

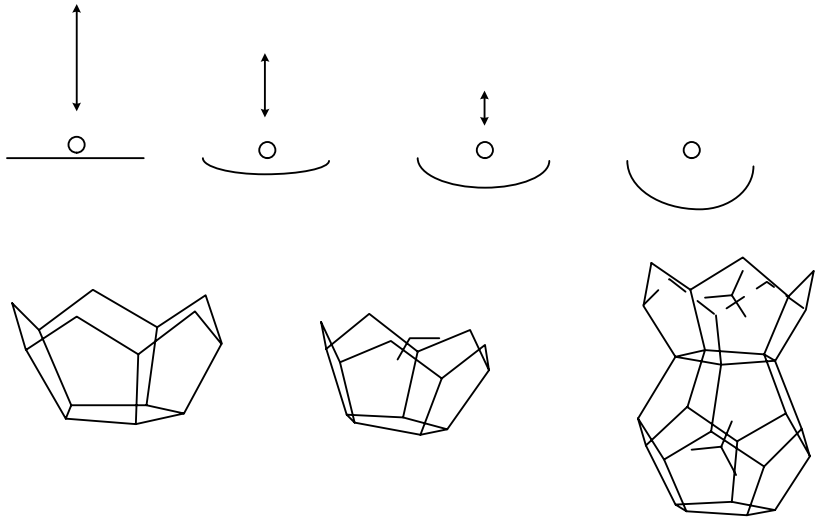

FIGURE 3.11 Adsorption of gas molecules onto labile hydrate cavities at gas–water interface. (From Long, J., *Gas Hydrate Formation Mechanism and Its Kinetic Inhibition*, Ph.D. Thesis, Colorado School of Mines, Golden, CO, 1994. With permission.)

As noted in Section 2.1.2.1, the outside of hydrate cavities are never smooth, but have hydrogen atoms pointing outward that serve as positive attractions for other molecules and cavities, just as the cavity oxygen atoms with no outwardly pointing hydrogen atoms serve as negative charges for further attachments.

The interfacial cluster hypothesis should not be viewed as an orderly progression from small water clusters to large hydrate masses. In contrast, one might envision every combination of hydrogen bonds possible, with some clusters growing, but other clusters shrinking. A better conception is a very large number of clusters at every instant—not just one or a few clusters progressing in time.

3.1.2.3 Local structuring nucleation hypothesis

Molecular simulation methods have been applied to investigate the nucleation mechanism of gas hydrates in the bulk water phase (Baez and Clancy, 1994), and more recently at the water–hydrocarbon interface (Radhakrishnan and Trout, 2002; Moon et al., 2003). The recent simulations performed at the water–hydrocarbon interface provide support for a local structuring nucleation hypothesis, rather than the previously described labile cluster model.

Radhakrishnan and Trout (2002) performed Landau free energy calculations to investigate the (homogeneous) nucleation mechanism of carbon dioxide hydrate at the liquid water–liquid carbon dioxide interface. These free energy calculations showed that it was thermodynamically more favorable for labile clusters to disintegrate than to agglomerate. The authors therefore suggested that it is highly

unlikely that carbon dioxide hydrate nucleation occurs via the labile cluster mechanism. Instead, they proposed the local structuring hypothesis, in which:

1. Thermal fluctuations cause a group of guest (CO_2) molecules to be arranged in a configuration similar to that in the clathrate hydrate phase. The structure of water molecules around locally ordered guest molecules is perturbed compared to that in the bulk. The thermodynamic perturbation of the liquid phase is due to the finite temperature of the system. This process is stochastic.
2. The number of guest molecules in a locally ordered arrangement exceeds that in the critical nucleus. Guest–guest and host–host cluster order parameters take on values that are very close to the clathrate hydrate phase, which results in formation of a critical nucleus.

Moon et al. (2003) also proposed a local order (or structure) model similar to that of Radhakrishnan and Trout (2002), on the basis of MD simulations of methane hydrate nucleation at a methane–water interface over a timescale of around 7 ns. Within this timescale, there is steady growth of water clusters of critical sizes comparable to previous reports (see Section 3.1.1.3). However, full crystallization cannot be seen on this timescale. Simulated radial distribution functions of the methane–methane distances as a function of time are shown in Figure 3.12. Initially, a strong peak at around 4 Å is present due to the methane–methane close contacts within water. As time progresses, this peak at 4 Å disappears and a strongly symmetric peak at 6.5 Å appears, which corresponds to the nearest inter-methane distance in methane hydrate, consistent with two methane molecules separated by a planar water ring. A third peak at 10.5 Å is shown to also grow throughout the simulation. The radial distribution functions up to 7 Å are qualitatively consistent with corresponding functions determined

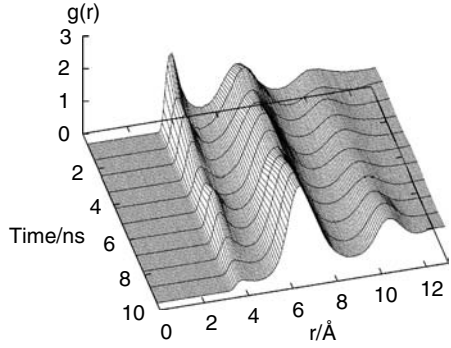

FIGURE 3.12 Methane–methane radial distribution functions calculated from successive 0.9 ns portions of the simulation, indicating ordering of the methane molecules during hydrate nucleation. (Reproduced from Moon, C., Taylor, P.C., Rodger, P.M., *J. Am. Chem. Soc.*, **125**, 4706 (2003). With permission from the American Chemical Society.)

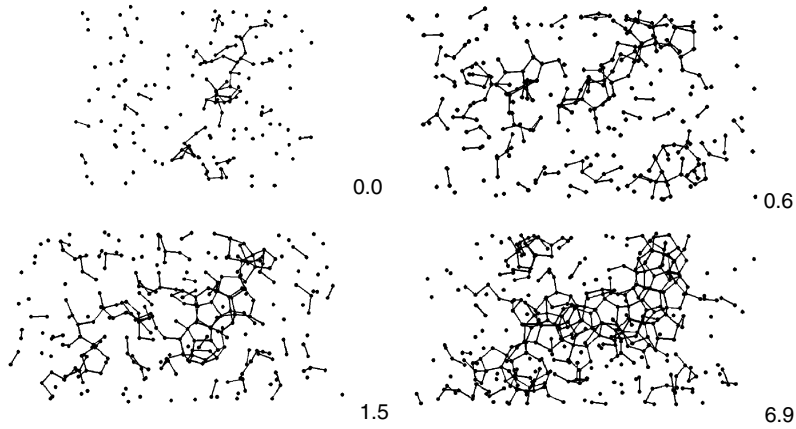

FIGURE 3.13 Snapshots of clathrate clusters at given times (ns). Only hydrate-like waters are shown; lines indicate the hydrogen-bond network. (Reproduced from Moon, C., Taylor, P.C., Rodger, P.M., *J. Am. Chem. Soc.*, **125**, 4706 (2003). With permission from the American Chemical Society.)

from neutron diffraction (Koh et al., 2000). Increasing structural order is also shown in the simulated water radial distribution functions.

Figure 3.13 shows snapshots of the hydrate nucleation simulations by Moon et al. (2003). Initially, there is no evidence of clustering, after 0.6 ns there is aggregation to form a two-dimensional sheet-like structure. The first complete clathrate cage (5^{12}) is formed after 0.8 ns, with numerous incomplete cages evident even earlier. After 7 ns a structured chain of clathrate cages (6 complete 5^{12} cages and another 20 incomplete/fluxional cages) is seen that spans the width of the simulation box; that is, unlike the case of the labile cluster hypothesis, which involves a buildup of individually solvated methane molecules, the simulation results showed a more concerted rearrangement of water over longer ranges than an individual solvation cage. The larger clusters formed contain long-range ordering of the guests, which therefore supports the local ordering hypothesis.

A further interesting feature of this simulation study is the identification of face-sharing doublets of 5^{12} cages at around 6 ns, which remain stable for the remainder of the simulation (Figure 3.14). Conversely, there was no evidence of water bridged 5^{12} cages. The 5^{12} cages pack by sharing faces in sII hydrate, while in sI hydrate 5^{12} cages are bridged by additional water molecules. This is consistent with experimental diffraction studies, which suggest that for the sI hydrate former, CO_2, a metastable sII hydrate phase can be formed prior to the formation of the more stable sI hydrate (Staykova and Kuhs, 2003).

Despite the formation of clathrate-like clusters and complete 5^{12} cages during these simulations, the increased ordering observed from the radial distribution functions and local phase assignments resulted in the authors concluding that their simulation results are consistent with a local order model of nucleation, and therefore do not support the labile cluster model.

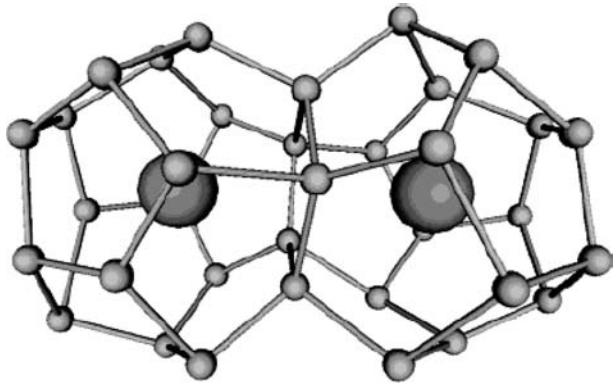

FIGURE 3.14 A stable face-sharing dimer of 5^{12} cages, formed by 6 ns. (Reproduced from Moon, C., Taylor, P.C., Rodger, P.M., *J. Am. Chem. Soc.*, **125**, 4706 (2003). With permission from the American Chemical Society.)

A number of studies have indicated that a labile cage-like (5^{12}) cluster of 20 water molecules around a hydrate guest former may not form preferentially at the initial stages of nucleation. MD simulations of xenon hydrate formation from a xenon–ice system showed that there is no preferential formation of cavities with 20 water molecules, which would be similar to the small hydrate cage. Rather, the statistical mean cage size distribution was found to be between 24 and 27 water molecules. Tse et al. (2002) suggest that this supports the experimental observation that sII SF_6 hydrate formation does not require occupation of small cages.

In order to verify which of the above nucleation mechanisms accurately represents hydrate nucleation, it is clear that experimental validation is required. This can then lead to such qualitative models being quantified. However, to date, there is very limited experimental verification of the above hypotheses (labile cluster or local structuring model, or some combination of both models), due to both their stochastic and microscopic nature, and the timescale resolution of most experimental techniques. Without experimental validation, these hypotheses should be considered as only conceptual aids. While the resolution of a nucleation theory is uncertain, the next step of hydrate growth has proved more tenable for experimental evidence, as discussed in Section 3.2.

3.1.3 Stochastic Nature of Heterogeneous Nucleation

As an example of the difference between stochastic and deterministic properties consider Figure 3.15. A deterministic property is illustrated by any common thermodynamic property, such as temperature, as illustrated by the vertical line in Figure 3.15. For a specific equilibrium state, the probability of observing a specific temperature is 1, that is, a certainty that is called deterministic.

However, for some properties, the probability of observation is distributed over a range of values, so that observation of a certain value (at the peak of the

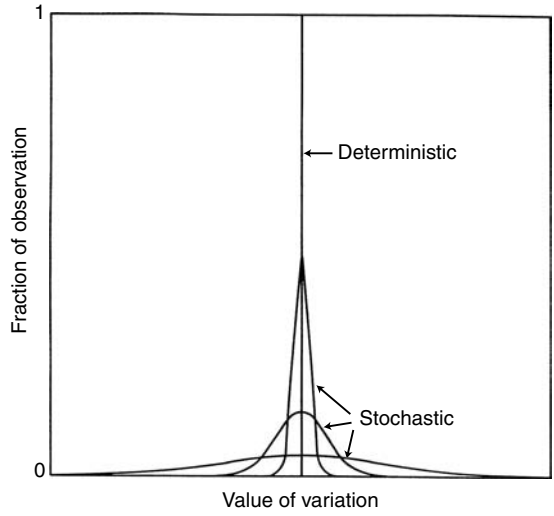

FIGURE 3.15 Comparison of stochastic and deterministic properties. (Reproduced from Rowley, J.L., *Statistical Mechanics for Thermophysical Property Calculations* (1994). With permission from Prentice Hall Inc.)

curve) is most likely but not certain. In such cases, normal distributions are shown in the lower three curves in Figure 3.15, for which the integral of each is unity. Ideally we hope to observe the mean value (the maximum in each curve), but there is a significant chance that other values (distributed about the mean) will be also observed. Distributions with uncertainty in the observed value, such as shown in the lower curves of Figure 3.15, are called stochastic.

Therefore, the key question arises: is hydrate nucleation stochastic or deterministic? The measurements performed to date (summarized in this section) indicate that the induction period (including hydrate nucleation and growth onset until hydrate formation is detected) is stochastic, particularly at low driving forces in the region such as shown between lines AB and CD in Figure 3.4b. However, with a higher driving force, the system becomes less stochastic, with a narrower distribution range.

Haymet and coworkers used an automated lag-time apparatus (ALTA) to obtain statistical data on the supercooling point (SCP, also known as freezing temperature) of water freezing to ice (Wilson et al., 2003) and water/tetrahydrofuran (THF) freezing to hydrate/ice (Wilson et al., 2005). The SCP is the temperature of spontaneous freezing of a solution (Zachariassen, 1982). A small sample (300 μL) was cooled linearly (at 4.5 K/min) until the sample froze. The frozen sample was melted, and then refrozen. This freezing–melting cycle was repeated over 300 times on the same sample.

Wilson et al. (2003, 2005) demonstrate the stochastic nature of the SCP, and that many measurements should be performed on a single sample in order to obtain statistically valid measurements of the SCP. However, a particularly

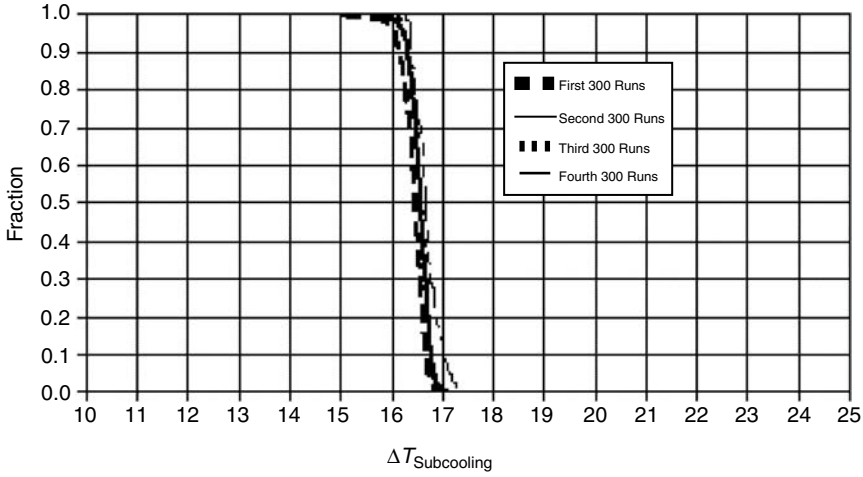

FIGURE 3.16 Survival curves for four back-to-back series of 300 runs each on the same THF/water (10 wt% THF) sample in the same tube. The nucleation temperature is not changed significantly between each data series. (Reproduced from Wilson, P.W., Lester, D., Haymet, A.D.J., *Chem. Eng. Sci.*, **60**, 2937 (2005). With permission from Elsevier.)

startling feature of the results is the narrow range of SCP values obtained from these measurements (i.e., within ±2.5 K).

In order to determine the SCP (or freezing temperature), a survival curve was constructed by plotting the fraction of unfrozen samples at a given temperature (or time) versus the degree of supercooling (Figure 3.16). That is, the same sample did not always freeze at the same temperature on each run, instead there was a distribution of freezing temperatures. To provide accurate statistics for the system, 300 runs were found to be sufficient, that is, the survival curve did not change magnitude or shape with further repeat measurements. The results of four back-to-back series of 300 runs on the same sample are shown in Figure 3.16 and show that the SCP temperature is not changed significantly when comparing these series of data.

Each survival curve clearly shows that at smaller supercooling temperatures (i.e., higher experimental temperatures) all runs remained unfrozen, while at larger supercooling temperatures (i.e., lower experimental temperatures) all runs were frozen. From these survival curves, Wilson et al. (2003, 2005) defined the nucleation temperature for a given sample, also called the SCP, or kinetic freezing point, as the temperature at which half the runs of the same sample have frozen (T50). The inherent width of each survival curve was considered as an indication of the stochastic nature of nucleation, with the "10–90" width (i.e., the range of temperature from 10% samples unfrozen to 90% samples frozen) to be an indicator of the error bars for the SCP.

One key question arises from the above results. That is, considering the measurement temperatures were well below the ice melting point, was ice formed

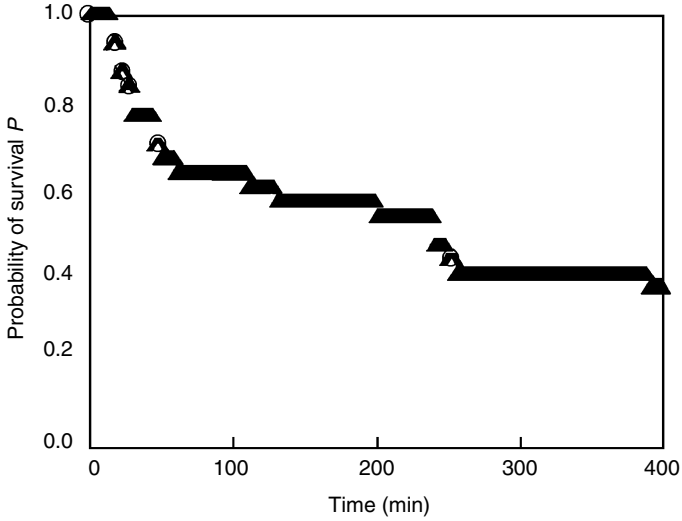

FIGURE 3.17 Probability of survival of CH_3CCl_2F hydrate free samples plotted vs. the induction time. The triple liquid–water/hydrate/liquid–CH_3CCl_2F equilibrium temperature is 281.6 K. The sample is cooled to 277.2 K (within 90 s), and held at this temperature until nucleation occurs and hydrate growth is detected. (Reproduced and modified from Ohmura, R., Ogawa, M., Yasuka, K., Mori, Y.J., *J. Phys. Chem. B*, **107**, 5289 (2003). With permission from the American Chemical Society.)

instead of, or in addition to hydrate? Also, would these results for a simple system of a miscible solution of tetrahydrofuran–water be transferable to the more complex system of a gas–water mixture? To address these questions, the freezing temperature (SCP) of xenon hydrate formed from a xenon gas–water mixture was measured repeatedly using differential scanning calorimetry (Hester, K.C., unpublished data). Twelve repeat samples were measured, with the preliminary results indicating that the scatter of the data was only within a 2°C range, which is a similar scatter range to that reported by Wilson et al. (2005). Therefore, repeated induction time–temperature measurements (at high driving force with a constant cooling rate) may vary only within a narrow range of values. This suggests that the induction time–SCP measured using a constant cooling rate may be a more probabalistic parameter.

In contrast, induction time measurements of CH_3CCl_2F hydrate performed at constant temperature (measuring hold times), demonstrated a much higher degree of stochastic or random behavior (Ohmura et al., 2003). In these experiments the induction time was detected, using video imaging, as the first change in morphology of the CH_3CCl_2F droplet that was immersed in water. The probability of survival curves tend to vary over a far wider distribution of nucleation times (Figure 3.17). These results show that the induction time in these cases (where the sample is held at constant temperature) can be more stochastic than those obtained during cooling.

Several other studies have been performed to measure hydrate induction times where the sample was held at constant temperature (e.g., Muller-Bongartz et al., 1992; Parent, 1993; Bansal, 1994; Nerheim et al., 1994; Cingotti et al., 1999; Kelland et al., 2000). In all these studies significant scatter in the induction time data were reported.

The above studies support the notion that nucleation is a very stochastic phenomenon when the sample is held at constant temperature, compared to when the sample was cooled at a constant cooling rate. As suggested previously, the magnitude of the driving force can affect the degree of stochastic or random behavior of nucleation. For example, on the basis of extensive induction time measurements of gas hydrates, Natarajan (1993) reported that hydrate induction times are far more reproducible at high pressures (>3.5 MPa) than at lower pressures. Natarajan formulated empirical expressions showing that the induction time was a function of the supersaturation ratio.

3.1.4 Correlations of the Nucleation Process

Data and correlations for the nucleation process should be used with extreme caution. One major conclusion of this section is that induction time correlations may be applied (if at all) under very restricted conditions for the following three reasons:

1. Induction times are very scattered and, particularly at low driving forces (under isothermal conditions), nucleation is stochastic and therefore unpredictable.
2. Induction times appear to be apparatus-dependent, for example, the times depend on the degree of agitation (cavitation or turbulency), surface area of the system, and the rate of heat or mass transfer.
3. Induction times appear to be also a function of time-dependent variables such as the history of the water, the gas composition, and the presence of foreign particles.

Despite 1–3 above, recent statistical measurements performed by Wilson et al. (2003, 2005) suggest that the freezing temperature for hydrate/ice nucleation varies only within around 2°C at high driving forces under continuous cooling. In essence, there is only a limited number of statistical data sets available in the literature, with varying reports of the extent of reproducibility of induction times from different groups. Statistical analyses are required in order for reliable induction times to be obtained for gas hydrate systems. To date, statistical analyses of hydrate induction times have not been performed for gas hydrate systems. Furthermore, there is a need for induction time measurements to be performed and correlated between different apparatus setups. In order to be able to assess whether the induction time–freezing temperature of gas hydrates can be predicted to an acceptable level of accuracy, much work still remains to be performed. It may be however, that such a task is intractable.

TABLE 3.2
Different Driving Forces Used for Nucleation

Investigators	Year	Driving force
Vysniauskas and Bishnoi	1983b	$T^{eq} - T^{exp}$
Skovborg and Rasmussen	1992	$\mu_{WH}^{exp} - \mu_{WL}^{exp}$
Natarajan et al.	1994	$f_i^{exp}/f_i^{eq} - 1$
Christiansen and Sloan	1995	Δg^{exp}
Kashchiev and Firoozabadi	2002	$\Delta\mu$, supersaturation
Anklam and Firoozabadi	2004	Δg
Arjmandi et al.	2005b	$T^{eq} - T^{exp}$

3.1.4.1 Driving force of nucleation

A number of driving forces for the nucleation process are used in the hydrate literature, as listed in Table 3.2. Apart from a few works (Sloan et al., 1998; Kashchiev and Firoozabadi, 2002a; Arjmandi et al., 2005a), limited justifications have been provided for these driving forces, based upon equilibrium or nonequilibrium thermodynamics. The purpose of this subsection is to provide a brief justification for a general nucleation driving force, and to show other driving forces to be special cases of the more general case. The driving force is the key component of a hydrate nucleation correlation. In essence, the general case driving force is shown below to incorporate all the driving forces proposed (Table 3.2), though the term ln (f_i^{eq}/f_i^{exp}) dominates (f_i^{eq} and f_i^{exp} are the fugacity of component i at the equilibrium and experimental pressure, respectively, that is, indicating overpressure). The subcooling driving force is shown to be the isobaric equivalent of the isothermal general case driving force.

Christiansen and Sloan (1995) presented the total molar change in Gibbs free energy of hydrate formation, Δg^{exp} as the driving force. The driving force derived by Christiansen and Sloan has been shown to be the general case for all driving forces for nucleation presented by previous researchers. Under constraints of constant temperature and pressure, processes move toward the minimum value of Gibbs free energy. Figure 3.18 illustrates an isothermal route for calculating such a state variable by devising a convenient calculable path between the two end points—the products (superscript "pr") and reactants (rx) at the operating temperature and pressure. In this system, only the gas and water converted to hydrate are considered as reactants while hydrate represents the product.

$$\Delta g^{exp} = \Delta g^{rx} - \Delta g^{pr} \tag{3.6a}$$

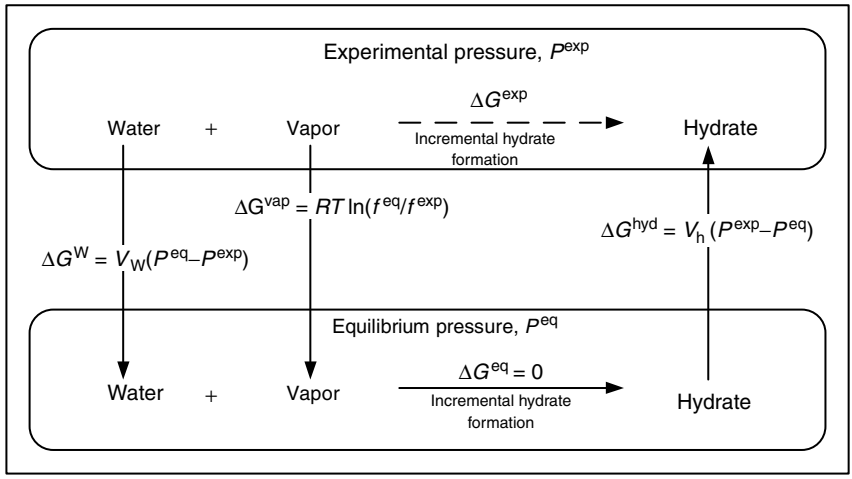

FIGURE 3.18 Isothermal path for calculating ΔG for hydrate formation from water and vapor. (Reproduced and modified from Christiansen, R.L., Sloan, E.D., Jr. in *Proc. 74th Gas Processors Association Annual Convention* (1995). With permission from the Gas Processors Association.)

with

$$\Delta g^{rx} = \sum_{i=1}^{N} x_i(\mu_i^{eq} - \mu_i^{exp}) \tag{3.6b}$$

and

$$\Delta g^{pr} = \sum_{i=1}^{N} x_i(\mu_i^{exp} - \mu_i^{eq}) \tag{3.6c}$$

The molar Gibbs free energy difference is obtained between the end points by adding five components of the path:

1. Separation of reactants (gas and liquid) at the experimental pressure ($\Delta g^{sep} = 0$).
2. Decreasing the pressure of each reactant to the equilibrium value.
3. Combining water and gas at equilibrium to hydrate ($\Delta g^{eq} = 0$).
4. Compression of product hydrate from equilibrium to experimental pressure.
5. Combining hydrate and unreacted gas and water at experimental pressure ($\Delta g^{comb} = 0$).

The above path only considers gas and water that react to hydrate. If the molar Gibbs free energy of (1) separation, (3) reaction at equilibrium, and (5)

recombination are all taken as zero, then the $\Delta g^{\exp}$ value is the sum of steps (2) and (4), as in Equation 3.7b.

$$\Delta g^{\exp} = \Delta g^1 + \Delta g^2 + \Delta g^3 + \Delta g^4 + \Delta g^5 \tag{3.7a}$$

$$\Delta g^{\exp} = 0 + \Delta g^2 + 0 + \Delta g^4 + 0 \tag{3.7b}$$

In Equations 3.7a and b, Δg^4 is the isothermal compression of hydrate from equilibrium to experimental pressure, in which the hydrate is assumed incompressible.

$$\mu_{\mathrm{H}}^{\exp} - \mu_{\mathrm{H}}^{\mathrm{eq}} = \nu_{\mathrm{H}}(P^{\exp} - P^{\mathrm{eq}}) \tag{3.8}$$

In Equations 3.6b and 3.7b in which reacting water and gas are taken from experimental to equilibrium conditions, Δg^2 is divided into two parts, one for the water and a second for the gas: (1) the water (L) value is similar to Equation 3.8, and (2) the gas phase uses a fugacity ratio for each component I:

For the water phase (assumed to be pure water):

$$\mu_{\mathrm{L}}^{\mathrm{eq}} - \mu_{\mathrm{L}}^{\exp} = \nu_{\mathrm{L}}(P^{\mathrm{eq}} - P^{\exp}) \tag{3.9a}$$

and for each component in the gas phase (assumed to contain no water) we obtain:

$$\mu_i^{\exp} - \mu_i^{\mathrm{eq}} = RT \ln(f_i^{\mathrm{eq}}/f_i^{\exp}) \tag{3.9b}$$

When Equations 3.8 and 3.9a and b are inserted into Equation 3.6, we obtain:

$$\Delta g = \nu_{\mathrm{L}}(P^{\mathrm{eq}} - P^{\exp}) + RT\Sigma x_i \ln(f_i^{\mathrm{eq}}/f_i^{\exp}) + \nu_{\mathrm{H}}(P^{\exp} - P^{\mathrm{eq}}) \tag{3.10}$$

Equation 3.10 is the general case for all driving forces shown in Table 3.2 for three reasons:

1. The $(\mu_{\mathrm{WH}}^{\exp} - \mu_{\mathrm{WL}}^{\exp})$ driving force of Skovborg and Rasmussen is a part of Equation 3.6), shown as the leftmost term in Equations 3.8 and 3.9a.
2. For all hydrates, the second term on the right dominates Equation 3.10, and the first and last terms effectively cancel, because the molar volume of water is within 15% of that of hydrates. The Natarajan et al. driving force of $[(f_i^{\exp}/f_i^{\mathrm{eq}}) - 1]$ is the first term in an infinite series expansion of the second term $[\ln(f_i^{\exp}/f_i^{\mathrm{eq}})$ in Equation 3.10—acceptable when $(f_i^{\exp}/f_i^{\mathrm{eq}}) < 1.3]$.
3. The ΔT driving force is the isobaric equivalent of the isothermal Δg in Equation (3.10). The Gibbs–Helmholtz relation may be applied to

obtain:

$$\Delta g = -(s)\Delta T \tag{3.10a}$$

where the $-(s)$ term relates the Gibbs free energy term to the temperature change.

Arjmandi et al. (2005b) reviewed the work by Christiansen and Sloan (1995) and Kashchiev and Firoozabadi (2002a,b). Arjmandi et al. (2005b) used these previously proposed driving force equations to investigate the effect of pressure on the driving force, and the relationship between driving force and subcooling. Using the equations derived by Christiansen and Sloan (1995) and Kashchiev and Firoozabadi (2002b), the driving force for hydrate formation in a methane–water system was found to be proportional to the degree of subcooling at isothermal and isobaric conditions. In general, at constant subcooling, the driving force decreased with increasing pressure, though the magnitude of the decreased driving force was not considerable above 20 MPa. Therefore, the authors noted that at normal operation conditions of above 20 MPa, subcooling could be used solely to represent the driving force for hydrate formation (see Figure 3.19).

However, for a multicomponent natural gas mixture, at 5–20 MPa, the subcooling was found to significantly underestimate the driving force (the pure methane–water system showed a far better match between driving force and subcooling). However, above 20 MPa, the driving force was matched well by

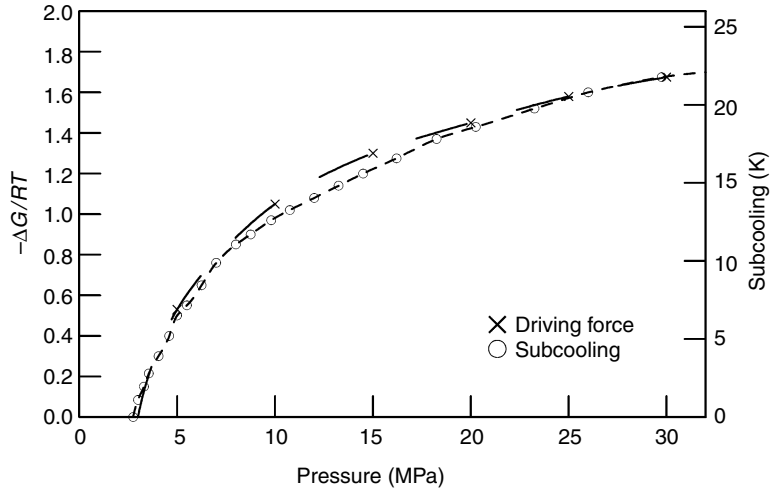

FIGURE 3.19 Variations in driving force and subcooling with pressure calculated at constant temperature, $T = 273.2$ K, for a methane–water hydrate system. (Reproduced from Arjamandi, M., Tohidi, B., Danesh, A., Todd, A.C., *Chem. Eng. Sci.*, **60**, 1313 (2005b). With permission from Elsevier.)

subcooling. Induction time measurements were also reported by Arjmandi et al. (2005b), indicating that the induction times were not a function of pressure for a natural gas–water system.

3.1.5 The "Memory Effect" Phenomenon

There has been a general consensus among hydrate researchers that hydrates retain a "memory" of their structure when melted at moderate temperatures. Consequently, hydrate forms more easily from gas and water obtained by melting hydrate, than from fresh water with no previous hydrate history. Conversely, if the hydrate system is heated sufficiently above the hydrate formation temperature at a given pressure, the "memory effect" will be destroyed. Some experimental observations of the memory effect phenomenon are summarized in Table 3.3.

The observations of the memory effect phenomenon summarized in Table 3.3 have been explained by two opposing hypotheses:

1. Hydrate structure (which is not visible to the naked eye) remains in solution (or on an ice surface) after hydrate dissociation in the following forms:
   - Residual structure (Makogon, 1974; Lederhos et al., 1996; Takeya et al., 2000; Ohmura et al., 2003) consisting of partial hydrate cages or polyhedral clusters (short-range ordered structure). For a significant

TABLE 3.3
Some Experimental Observations of the Memory Effect Phenomenon

Key observation	Researcher(s)
Hydrates form more readily from melted hydrate	Makogon (1974)
Thermal history of water affects hydrate induction times, that is, t_{ind} (hot/warm water) > t_{ind} (thawed ice or hydrate)	Vysniauskas and Bishnoi (1983); Lederhos (1996); Parent and Bishnoi (1996); Takeya et al. (2000); Ohmura et al. (2003)
Successive cooling curves S_1, S_2 and S_3 show decreased metastability from the vapor–liquid–hydrate line (Figure 3.20)	Schroeter et al. (1983)
Induction period is eliminated by re-forming hydrate on an ice surface preexposed to xenon	Moudrakovski et al. (2001b)
Induction times decrease when hydrate is reformed from hydrate decomposed for 1 h compared to 12 h	Lee et al. (2005)
Hydrate morphology depends on the dissociation conditions before reformation. A rough surface forms from hydrates decomposed for ≥24 h, while a smooth surface forms from hydrates decomposed for only 30 min	Servio and Englezos (2003a)

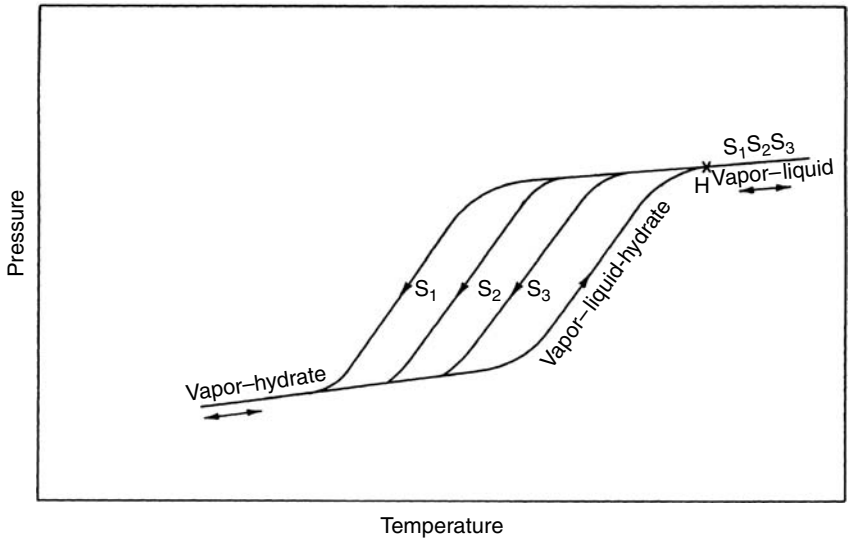

FIGURE 3.20 Successive cooling curves for hydrate formation with successive runs listed as $S_1 < S_2 < S_3$. Gas and liquid water were isochorically cooled into the metastable region until hydrates formed in the portion of the curve labeled S_i. The container was then heated and hydrates dissociated along the vapor–liquid water–hydrate (V–L_W–H) line until point H was reached, where dissociation of the last hydrate crystal was visually observed. (Reproduced from Schroeter, J.P., Kobayashi, R., Hildebrand, M.A., *Ind. Eng. Chem. Fundam.* **22**, 361 (1983). With permission from the American Chemical Society.)

period of time after hydrate dissociation a substantial amount of water structure remains, in a manner analogous to Bridgman's (1912) suggestion that "the disappearance of nuclei (dissociation of ice) is a matter of extraordinary slowness."

- Persistent hydrate crystallites (long-range ordered structure), which were shown from neutron scattering to remain in solution for several hours after increasing the temperature above the hydrate dissociation temperature (Buchanan et al., 2005).

2. Dissolved gas remains in solution after the hydrate has decomposed (Rodger, 2000).

Although the evidence of the memory effect phenomenon is plentiful, and clearly not in question, there have been only a limited number of direct molecular-level investigations to verify the above hypotheses. Furthermore, the results of these investigations have so far presented opposing conclusions on which hypothesis is correct.

For example, Chen's (1980) MD simulations seemed to confirm suggestions by Makogon (1974) and Long and Sloan (1996) that both the pentamer ring and the residual structure (short-range order) are stable up to 315 K (cf. simulations by Baez and Clancy, 1994). Conversely, Rodger suggests, based on MD simulations,

that the memory effect is due more to the persistence of a high concentration and retarded diffusion of methane in the melt, than it does to the persistence of metastable hydrate precursors.

The memory effect has important implications for the gas industry. For example, after hydrates initially form in a pipeline, hydrate dissociation should be accompanied by the removal of the water phase. If the water phase is not removed, the residual entity (i.e., residual structure, persistent crystallites, or dissolved gas) will enable rapid reformation of the hydrate plug. Conversely, if hydrate formation is desired, the memory effect suggests that hydrate formation can be promoted by multiple dissociation and reformation experiments (provided the melting temperature is not too high, or melting time is not too long).

3.1.6 State-of-the-Art for Hydrate Nucleation

Hydrate nucleation phenomena are qualitatively summarized with the following statements:

1. Induction times are stochastic, with limited predictability for hydrate onset, particularly at low driving forces, and tend to be apparatus-dependent.
2. At high driving forces and with constant cooling hydrate formation is less stochastic than that at a low driving force or at constant temperature.
3. Hydrate induction times from water are approximately proportional to the displacement from equilibrium conditions (e.g., subcooling). Other variables, which affect nucleation include guest size and composition, geometry, surface area, water contaminants and history, the degree of agitation or turbulence.
4. There are two hypotheses for hydrate nucleation, which are given below:
   - Labile cluster: liquid water molecules are arranged around a dissolved solute molecule in a "prehydrate" structure, with essentially the correct coordination number. A conceptual hypothesis exists for clusters growing to larger structures at an interface.
   - Local structuring: the "prehydrate" structure consists of a locally ordered water–guest structure rather than individual hydrate cavities.
5. Formation of hydrate nuclei (from aqueous liquid) occurs as heterogeneous nucleation, usually at an interface (either fluid + solid, gas + liquid, or liquid + liquid). When both a nonaqueous liquid and vapor are present with water, hydrates form at the liquid–liquid interface.
6. If the temperature for melting hydrate is close to the dissociation temperature, or insufficient time is given to melt hydrate, a memory effect is observed (attributed to residual structure, persistent hydrate crystallites remaining in solution, or dissolved gas) to promote future more rapid hydrate formation. This memory effect is destroyed at temperatures greater than 28°C, or after several hours of heating.

3.2 Hydrate Growth

After the stochastic nature of hydrate crystal nucleation, the quantification of the hydrate growth rate provides some relief for modeling hydrate formation. However, only a limited amount of accurate data exist for the crystal growth rate after nucleation. Most of the nucleation parameters (displacement from equilibrium conditions, surface area, agitation, water history, and gas composition) continue to be important in hydrate growth.

However, during the growth process mass and heat transfer become of major importance. In Figure 3.1b (the *P–T* schematic of hydrate growth from water and gas in a closed system) the growth regime is the period between points B and C, in which a significant amount of gas is incorporated into the hydrate phase. The analogous period is labeled "2" in Figure 3.1a. Because the hydrate contains up to 15 mol% gas (at least two orders of magnitude greater than the methane gas solubility) the mass transport of the gas to the hydrate surface is of major importance, and may dominate the process. In addition, the exothermic heat of hydrate formation can also control growth.

3.2.1 Conceptual Picture of Growth at the Molecular Level

On the molecular level, hydrate growth can be considered to be a combination of three factors: (1) the kinetics of crystal growth at the hydrate surface, (2) mass transfer of components to the growing crystal surface, and (3) heat transfer of the exothermic heat of hydrate formation away from the growing crystal surface (see Section 3.2.3 for heat transfer models).

3.2.1.1 Crystal growth molecular concepts

A hypothesis picture of hydrate growth at a crystal is shown in Figure 3.21, modified from Elwell and Scheel (1975). This conceptual picture for crystal growth may be combined with either the labile cluster or local structuring hypotheses for nucleation.

In the figure, step growth of the hydrate crystal is depicted with the following components:

(i) A guest in a temporal water cluster is transported to the growing crystal surface. Evidence for such clusters is provided in Section 3.1.1.2. The cluster is driven to the surface by the lower Gibbs free energy provided at the crystal surface.
(ii) The cluster adsorbs on the crystal surface. The solid crystal exerts a force field into the fluid which results in the cluster adhering to the surface. Upon adsorption, some of the water molecules detach from the cluster and diffuse away.

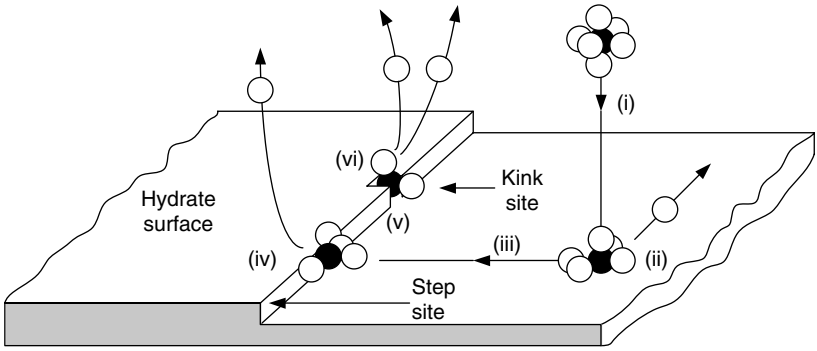

FIGURE 3.21 Hypothesis picture of hydrate growth at a crystal. (Reproduced and modified from Elwell, D., Scheel, H.J. *Crystal Growth from High Temperature Solution* (1975). With permission from Academic Press.)

(iii) The cluster diffuses over the surface to a step in the crystal. Since the solid force field is perpendicular to the crystal face, the adsorbed species can diffuse only in two dimensions along the surface.
(iv) The cluster attaches to a crystal step, releasing further solvent molecules. The step is an attractive site because two solid faces of the step exert a force (with two surface–reactant interactions) on the mobile species, in contrast to a single force field (with one surface–reactant interaction) on the flat surface.
(v) The cluster can now move only in a single dimension, along the step. The cluster diffuses along the step to a kink or defect point in the step.
(vi) The cluster adsorbs at the kink. The kink is an attractive site because three or more solid faces of the kink exert a larger force on the species than the two forces exerted by the step alone, and
(vii) The cluster is now immobilized in three dimensions (not shown).

At (ii), (iv), (vi) where the cluster is integrated into the crystal surface, the cluster rearranges itself into the proper cavity and excess solvent molecules are released. If the guest is too large for a cavity (e.g., C_3H_8 cannot fit into a 5^{12}) then some time is involved while the empty cavity rearrangement is completed. Water rearrangement into the proper cavity may be the rate-limiting kinetic step. Cavity bonds are completed with the final integration of the cluster into the kink. The final excess cluster molecules are released and the species loses any residual energy of mobility or translation along the crystal surface.

With Avogadro's number of molecules participating in the above process, it would be a mistake to suppose all molecules progress through the above steps in a deterministic manner. With so many particles in motion, every possible combination of attachment is tried. For example, some clusters adsorb directly at a kink without significant diffusion. Other clusters detach from the surface and diffuse away in contrast to our macroscopic observations of growth. However,

in hydrate growth the number of attaching particles (through any number of the above steps) exceed those detaching.

If all possible combinations were equally probably, we would observe stochastic behavior like primary nucleation, so that crystal growth kinetics would be virtually unpredictable. However, a few molecular paths for crystal growth are highly preferred over others, these paths combine in an ensemble to provide the macroscopic observations of crystal growth described in the next section.

The reader should be warned that the above conceptual picture has little supporting evidence from hydrate growth experiments, other than the few single crystal growth studies in Section 3.2.2.1. Nevertheless, it is hoped that such a conceptual picture can promote some understanding of the phenomena involved, if only to serve as a basis for improvement.

All seven steps require time, resulting in a rate of incorporating clusters into the growing crystal surface, which is called crystal growth kinetics. The following two sections consider translation of such a rate into a macroscopic equation for correlation and prediction. It is difficult to say which of the steps control the process, or even if the conceptual picture is valid. However, the first step—species transport to the solid surface—is well established and a brief description is given in Section 3.2.1.2.

3.2.1.2 The boundary layer

All modern pictures and models of hydrate crystal growth include mass transfer from the bulk phases to the hydrate. Unfortunately, some confusion arises due to the fact that two interfaces are usually considered, and the driving forces may not be intuitive for those not familiar with the area. In order to provide a basis for the modeling section, a brief overview of the diffusional boundary layer is given.

The following discussion is excerpted from Mullin (1993) and Elwell and Scheel (1975). Diffusional boundary theory is well-established (see e.g., Bird et al., 1960) and the concept of a boundary "unstirred" layer was introduced a century ago. Noyes and Whitney (1897) proposed that the change in the rate of crystal growth ($\mathrm{d}m/\mathrm{d}t$) was controlled by diffusion from the bulk concentration to the crystal (equilibrium) interface.

$$\mathrm{d}m/\mathrm{d}t = k_{\mathrm{d}} A (c - c^{\mathrm{eq}}) \tag{3.11}$$

where c and c^{eq} are the solution concentrations in supersaturated solution and at equilibrium respectively, A is the crystal surface area, and k_{d} is the coefficient of mass transfer. In his classical work on crystallization, Nernst (1904) stressed the importance of k_{d} that he equated to (D/δ), where D is the solute coefficient of diffusion, and δ represents the thickness of a stagnant boundary layer adjacent to the crystal.

Physical evidence for the existence of such a layer was established using interferometry by Berg (1938) and Bunn (1949). Berthoud (1912) and Valeton (1924) modified the concept to include two steps: (1) diffusion to the interface and (2) reaction at the interface. The diffusion step was represented by modifying the

driving force in Equation 3.11 for the solute concentration at the crystal–solution interface, c_i:

$$\mathrm{d}m/\mathrm{d}t = k_\mathrm{d}A(c - c_i) \tag{3.12}$$

The second (reaction) step was for incorporation of the substance into the crystal at the interface:

$$\mathrm{d}m/\mathrm{d}t = k_\mathrm{r}A(c_i - c^\mathrm{eq}) \tag{3.13}$$

where k_r is a rate constant for the surface reaction.

In this model (shown conceptually in Figure 3.22) a stagnant boundary layer exists on the fluid side of the crystal interface. Across this layer there exists a concentration gradient taken as the bulk fluid concentration (c) minus the interfacial concentration (c_i) in the fluid. Because the interfacial concentration (c_i) is difficult to measure, Equations 3.12 and 3.13 are usually combined by eliminating c_i to obtain:

$$\mathrm{d}m/\mathrm{d}t = K'A(c - c^\mathrm{eq}) \tag{3.14}$$

where the overall transfer coefficient K' is expressed in terms of the coefficients for diffusion k_d and reaction k_r as:

$$1/K' = 1/k_\mathrm{d} + 1/k_\mathrm{r} \tag{3.15}$$

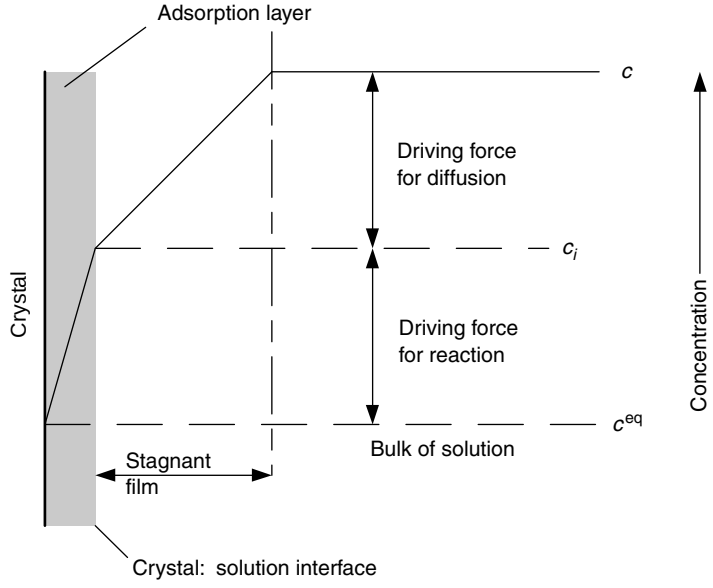

FIGURE 3.22 Conceptual model of mass transfer from bulk phases to hydrate.

Equations 3.12, 3.13, and the final Equation 3.14 are all forms of the classic engineering expression [Rate = (Driving force)/Resistance] where the driving force is expressed as concentration differences. The overall resistance ($1/K'$) can be controlled by a low value of either individual coefficient. The mass transfer coefficient (k_d) controls crystallization when the reaction is very rapid relative to diffusion, but the reaction coefficient (k_r) controls crystallization when diffusion is much more rapid than reaction. In such cases the overall coefficient K' may be approximated by the smaller k value. However, the concentrations in the driving force remain measurable (c) or calculable (c^{eq}) rather than non-measureable (c_i).

Three modifications are often made to the basic Equation 3.14:

1. The crystal growth rate (dm/dt) is represented as the rate of gas consumption,
2. The concentrations (c) are replaced with fugacities, and
3. The controlling process is sometimes considered to be neither reaction nor diffusion through the liquid–crystal boundary layer, but diffusion through the boundary layer at the vapor–liquid interface, as in the Skovborg–Rasmussen model.

When the hydrate growth rate (dm/dt) is measured by the rate of gas consumption (dn_i/dt) the pseudo-steady-state approximation is made. That is, at any instant the rate of gas consumption by the hydrate is assumed equal to the rate of gas consumption from the gas phase. Frequently, experimenters monitor the amount of gas needed to keep the pressure constant in the hydrate vessel so that the driving force remains constant. In such cases, the rate of gas consumption from a separate supply reservoir is measured.

In Equation 3.14, the liquid concentration may be replaced by fugacity if three assumptions are made: (a) constant temperature and pressure, (b) ideal liquid solutions, and (c) constant total molar concentration (c_{tot}). With these assumptions the fugacity (f_i) is related to the concentration (c_i) by the expression:

$$f_i = \left(\frac{\phi_i^L P}{c_{tot}} \right) c_i \tag{3.16}$$

where ϕ_i^L is the fugacity coefficient. With assumptions (a), (b), and (c), the bracketed term in Equation 3.16 is a constant, so that Equation 3.14 may be rewritten as

$$\frac{dn_i}{dt} = KA(f_i - f_i^{eq}) \tag{3.17}$$

where

$$K = \left(\frac{c_{tot}}{\phi_i^L P} \right) K' \tag{3.17a}$$

In the Skovborg and Rasmussen (1994) model discussed in Section 3.2.3.2, Equation 3.17 is replaced with the transfer of the component across the liquid side of the vapor–liquid interface, so that

$$\frac{\mathrm{d}n_i}{\mathrm{d}t} = k_{\mathrm{L}} A_{(g-l)} (x_i^{int} - x_i^{\mathrm{b}}) \tag{3.17b}$$

where k_{L} is mass transfer coefficient across the liquid boundary at the gas–liquid interface, $A_{(g-l)}$ is the area of the gas–liquid interface, and x_i^{int} and x_i^{b} are the interfacial (equilibrium) and bulk mole fractions of "i" at the system temperature and pressure.

Equation 3.17b may be regarded as the starting point for the models discussed in Section 3.2.3. In all hydrate growth models the coefficient K is a parameter fitted to kinetic data.

3.2.2 Hydrate Crystal Growth Processes

The different types of hydrate crystal growth processes may be divided into: (1) single crystal growth, (2) hydrate film/shell growth at the water–hydrocarbon interface, (3) multiple crystal growth in an agitated system, and (4) growth of metastable phases. Each of these different growth processes will be discussed in this section.

3.2.2.1 Single crystal growth

Hydrates can grow as single crystals in a water–hydrocarbon solution, particularly under low driving force conditions. Single crystal growth of hydrates is a useful method to investigate the effect of additives on hydrate crystal growth and morphology. Single crystal growth is also required for detailed structural analysis using x-ray and neutron diffraction (see Section 2.1.2.2). Single crystals of tetrahydrofuran and ethylene oxide hydrate, in which both hydrate formers are completely miscible in water, can be readily grown in the laboratory and isolated for structural analysis. Conversely, single crystals of gas hydrates are less easily obtained and isolated, and only a few studies have successfully obtained single crystals of gas hydrates for structural analysis (Udachin et al., 2002).

Figure 3.23 shows single hydrate crystals of structures I and II grown from stoichiometric solutions of ethylene oxide (b) and tetrahydrofuran (a) respectively in quiescent conditions (Larson et al., 1996). The single crystals shown in Figure 3.23 exhibit (110) and (111) crystal planes for structure I and II, respectively. In single crystal growth, it is important to realize that the slowest-growing planes are observed (Mullin, 1993, p. 203), while rapidly growing single crystal planes disappear. Smelik and King (1997) reported similar single crystal shapes from their high pressure single crystal system.

From such single crystal growth studies it is hypothesized that the (111) plane in sII grows slowest because it contains a predominance of hexagonal faces relative

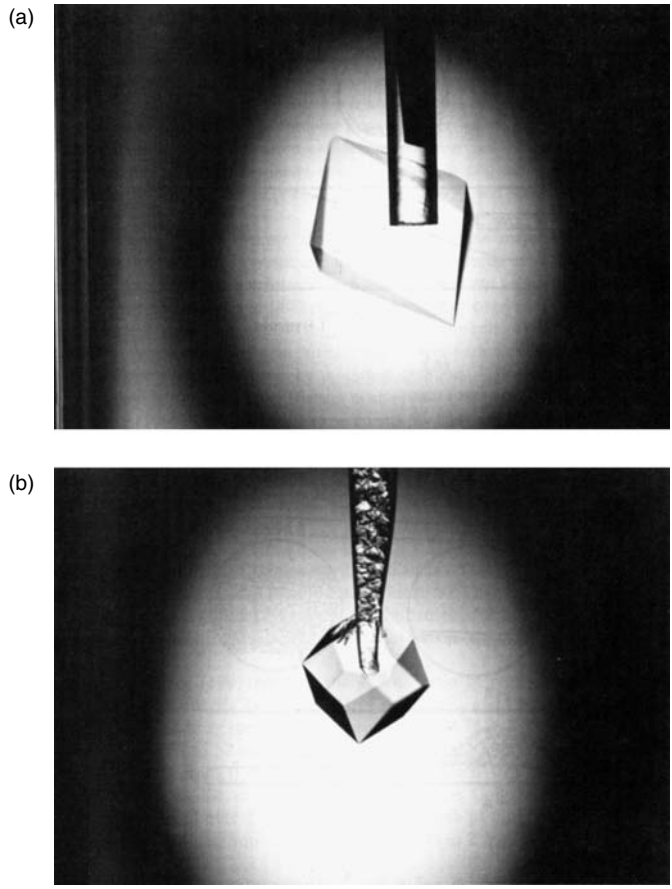

FIGURE 3.23 Photograph of single hydrate crystals of (a) tetrahydrofuran (sII); (b) ethylene oxide (sI). (Photographs by Larsen, 1996.)

to other crystal planes in sII. Crystal planes containing hexagonal faces may grow slowest because hexagonal faces are considerably more strained (120° between O–O–O angles) than are pentagonal faces (108°), relative to either the tetrahedral O–O–O angle (109°) or the water angle (H–O–H of 104.5°). A similar argument is made for the appearance of the (110) plane in sI.

3.2.2.2 Hydrate film/shell growth at the water–hydrocarbon interface

Hydrate growth is typically initiated at the water–hydrocarbon interface (as discussed in Section 3.1.1.4). Measurements of the growth of a hydrate film (or shell) at the water–hydrocarbon interface provides insight into the growth mechanism(s), which can be incorporated into realistic hydrate growth models.

TABLE 3.4
Experimental Studies of Film/Shell Growth at the Water–Hydrocarbon Interface

Hydrate film/shell measurement	Water–hydrocarbon interfacial system	Research group(s)
Film growth at liquid water–hydrate former interface	Water–methane	(Smelik and King, 1997; Makogon et al., 1998; Freer et al., 2001; Taylor, 2006)
Film growth at liquid water–hydrate former interface	Water–fluorocarbon	(Sugaya and Mori, 1996; Ohmura et al., 2000; Ito et al., 2003)
Film growth at liquid water–hydrate former interface	Water–carbon dioxide	(Uchida et al., 1999b; Hirai et al., 2000; Mori, 2001; Uchida et al., 2002; Hirai and Sanda, 2004)
Shell growth on gas (hydrate former) bubble surface	Natural gas bubble in salt water	(Maini and Bishnoi, 1981; Topham, 1984)
Shell growth on gas (hydrate former) bubble surface	Air bubble–ice interface	(Salamatin et al., 1998)
Shell growth on gas (hydrate former) bubble surface	Hydrofluorocarbon gas bubble in water	(Nojima and Mori, 1994)
Shell growth on liquid hydrate former droplet surface	Hydrofluorocarbon droplet in water	(Kato et al., 2000; Ohmura et al., 1999, 2003)
Shell growth on liquid hydrate former droplet surface	Cyclopentane droplet in water	(Taylor, 2006)
Shell growth on liquid hydrate former droplet surface	Liquid carbon dioxide droplet in water	(Shindo et al., 1993)
Shell growth on droplet surface of aqueous solution of hydrate former	Aqueous THF solution droplet in *n*-decane	(Taylor, 2006)
Shell growth on water droplet surface	Water droplet in methane or carbon dioxide gas	(Servio and Englezos, 2003a; Moudrakovski et al., 2004)
Shell growth on water droplet surface	Water droplet in fluorocarbon gas	(Fukumoto et al., 2001)

Table 3.4 summarizes the different studies that have been performed to measure the growth and morphology of a hydrate film/shell at the water–hydrocarbon interface (where the hydrocarbon can be gas or liquid).

Some common features arising from these studies suggest that the morphology changes are generally similar irrespective of the hydrate former, that is, the supersaturation (or driving force) affects morphology, and there are analogous features between growth behavior at a water–hydrate former planar interface and at the surface of a liquid droplet.

Servio and Englezos (2003a) examined the effect of pressure driving force on the morphology of methane and carbon dioxide hydrates grown from water droplets

(5 and 2.5 mm in diameter) immersed in a hydrate-forming gas atmosphere. The growth experiments were performed at 274.6 K and 2150 kPa (high driving force) or 1000 kPa (low driving force) above the corresponding three-phase hydrate equilibrium pressure ($P_{eq,CH4} = 2900$ kPa and $P_{eq,CO2} = 1386$ kPa at 274.6 K). The water droplets were placed on a Teflon-coated 316 stainless steel surface to prevent the water droplets from wetting the surface. Each experiment used two or three water droplets in the crystallizer tank. At high driving force, within 5 s after nucleation the surface of the droplet appeared roughened (and dull) with many fine needle-like crystals extruding away from the gas hydrate–water interface (see Figure 3.24a). This morphological development was the same for methane and carbon dioxide hydrate former gases.

At high driving force, Servio and Englezos suggested hydrate formation comprises three growth phases: (1) the appearance of a hydrate layer (shell) around the water droplet with needle-like crystals, and up to 10 h after nucleation the needle-like crystals grow in size and thickness, (2) the crystal needles collapse onto the hydrate layer covering the droplet, and (3) appearance of depressions in the hydrate layer surrounding the water droplet, which occurred within 10–15 h to a couple of days in some experiments. At a high driving force, hydrate is likely to nucleate and grow at many different locations, compared to a low driving force, where hydrates can form in a more regular manner and location.

Conversely, at low driving force conditions, there was no evidence of needle-like crystals on the droplet surface, which instead had a smooth and shiny texture (Figure 3.24b). This contrast in morphologies at high and low driving forces was suggested to be because of a larger number of nucleation sites being formed at high driving force compared to that at low driving force. This is consistent with Mullin's (2001) suggestion that the rate of nucleation (number of nuclei formed per unit time per unit volume) increases with the degree of supersaturation. The degree of supersaturation is proportional to the driving force. Therefore, at high driving force many nucleation sites are present with faster nucleation kinetics and therefore this may result in more random crystal growth and hence a rougher surface. Associated with this faster kinetics is the heat limited growth process, as indicated by the formation of needle-like dendritic crystals. In contrast, at low driving force there are fewer nucleation sites, with growth occurring more slowly and across the droplet surface until it is covered with a smooth hydrate layer.

The three growth phases suggested from the work of Servio and Englezos (2003b) above, are analogous to the results obtained by Taylor (2006) on the growth of cyclopentane hydrate on the surface of a water droplet immersed in cyclopentane. In these studies a water droplet was placed on a cantilever and submersed in cyclopentane, before being nucleated by another hydrate particle (Figure 3.25a). On contact, nucleation occurs, followed by the formation of a thin porous hydrate shell around the water droplet within a few minutes (Figure 3.25b). About 0.5 h after nucleation, depressions were observed on the droplet surface (Figure 3.25c).

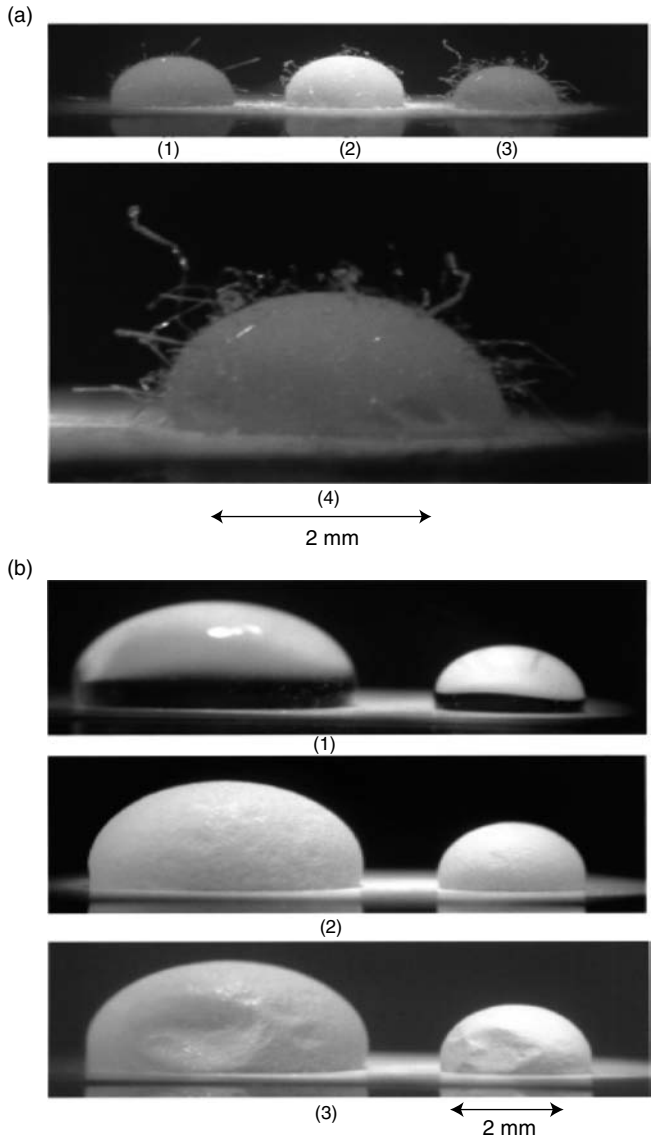

FIGURE 3.24 (a) Methane hydrate covering the surface of water droplets (1, 2, 3) under high driving force, 10 min after nucleation. Image (4) is a magnified view of droplet (3), and (b) methane hydrate covering two water droplets under low driving force at three different times: (1) at $t = 0$, (2) at $t = 10$ h where the water droplet is covered by hydrate, (3) at $t = 25$ h where the water droplet is covered by hydrate and depressions in the hydrate layer appear. (Reproduced from Servio, P., Englezos, P., *AIChE J.*, **49**, 269 (2003a). With permission from Wiley Interscience.)

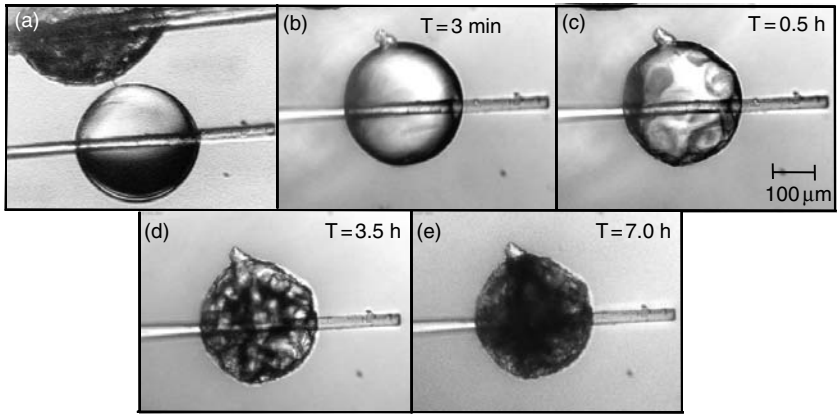

FIGURE 3.25 Cyclopentane hydrate formation from a water droplet: (a) initial contact, (b) hydrate shell formation around the water droplet, (c) depressions formed on the hydrate shell, (d) conversion of interior water to hydrate, indicated by darkening, (e) almost completely converted hydrate. (From Taylor, C.J., *Adhesion Force between Hydrate Particles and Macroscopic Investigation of Hydrate Film Growth at the Hydrocarbon/Water Interface*, Master's Thesis, Colorado School of Mines, Golden, CO, (2006). With permission.)

The depressions may be because of cyclopentane diffusing through the porous hydrate layer converting the interior of the shell into hydrate. The internal droplet volume is decreased as the water is converted to hydrate and part(s) of the droplet collapse. Alternatively, water may diffuse from the interior droplet to the outer shell surface to react with hydrate former, also resulting in a decrease in internal droplet volume. Staykova et al. (2003) suggest that both hydrate former and water mass transport should easily occur through the porous hydrate layer. Further hydrate conversion was indicated by darkening of the droplet (Figures 3.25d,e).

The above growth processes of the conversion of a water droplet to hydrate particle appear analogous to film growth occurring at a planar water-hydrocarbon surface. Growth studies at a planar interface show the hydrate film grows laterally across the entire interface. Over time, the hydrate layer thickens to a final thickness that depends on the degree of subcooling. The hydrate film thickness and growth rate have been determined using gas consumption coupled with video imaging (Freer et al., 2001; Taylor, 2006), or from measurements using a micrometer (Makogon et al., 1998). The hydrate film thickness is shown to increase with increasing subcooling (Figure 3.26). An initial film thickness of 12 and 6 μm was measured for cyclopentane hydrate and methane hydrate, respectively. A similar initial film thickness of 10 μm was measured using laser interferometry for a liquid hydrofluorocarbon (CH_2FCF_3)–liquid water interface (Ohmura et al., 2000).

Raman measurements and solubility predictions of the guest molecule concentration within the bulk aqueous phase suggest that the hydrate film thickens into the water phase (Makogon et al., 1998; Subramanian and Sloan, 2000; Subramanian, 2000). The Raman peak area for methane (C–H

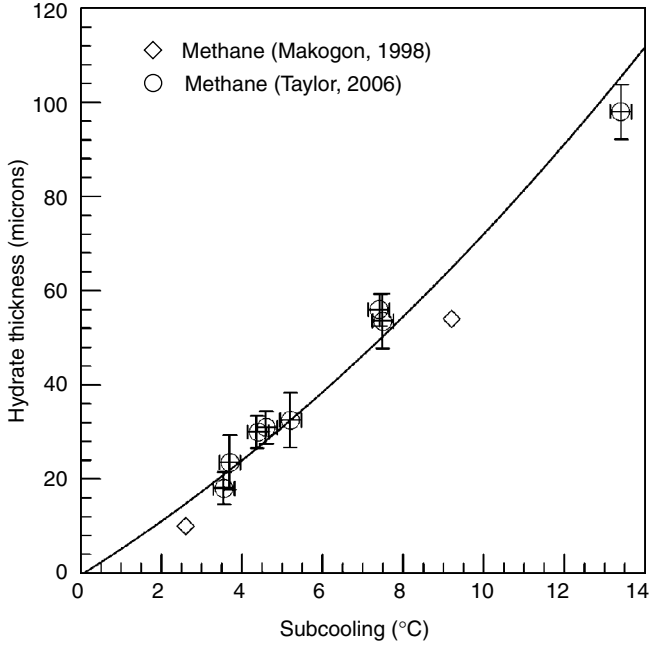

FIGURE 3.26 Final methane hydrate film thickness vs. subcooling. (From Taylor, C.J., *Adhesion Force between Hydrate Particles and Macroscopic Investigation of Hydrate Film Growth at the Hydrocarbon/Water Interface*, Masters Thesis, Colorado School of Mines, Golden, CO (2006). With permission.)

symmetric stretching vibration) dissolved in water is directly proportional to the concentration of dissolved methane. On decreasing the temperature below the hydrate equilibrium temperature (Points A to B, Figure 3.27a), the intensity of the dissolved methane peak increases slightly, indicating a slight increase in methane concentration in the aqueous phase. However, after hydrate formation occurs (Point C), the intensity of the dissolved methane peak decreases, indicating a decrease in the methane concentration. Upon further cooling (Points D and E), the intensity again decreases. This corresponds to the predicted decrease in methane concentration as the temperature is decreased along the C_{sh} curve (C_{sh} is the methane solubility curve with hydrate present; Figure 3.27b; dashed line). Throughout the cooling process, the methane concentration was qualitatively predicted from the solubility curves (C_s, without hydrate and C_{sh}, with hydrate; determined from CSMGem).

The trends shown from the predicted curves, C_{sh} and C_s, are in qualitative agreement with corresponding dissolved methane Raman peak intensities. Therefore, the Raman spectra (Figure 3.27a) support the proposed mechanism that hydrate growth occurs in part as a result of methane diffusing from the bulk aqueous phase to the hydrate film formed at the vapor–liquid interface. This decreases the methane concentration in the bulk water phase. Hydrate growth from an aqueous

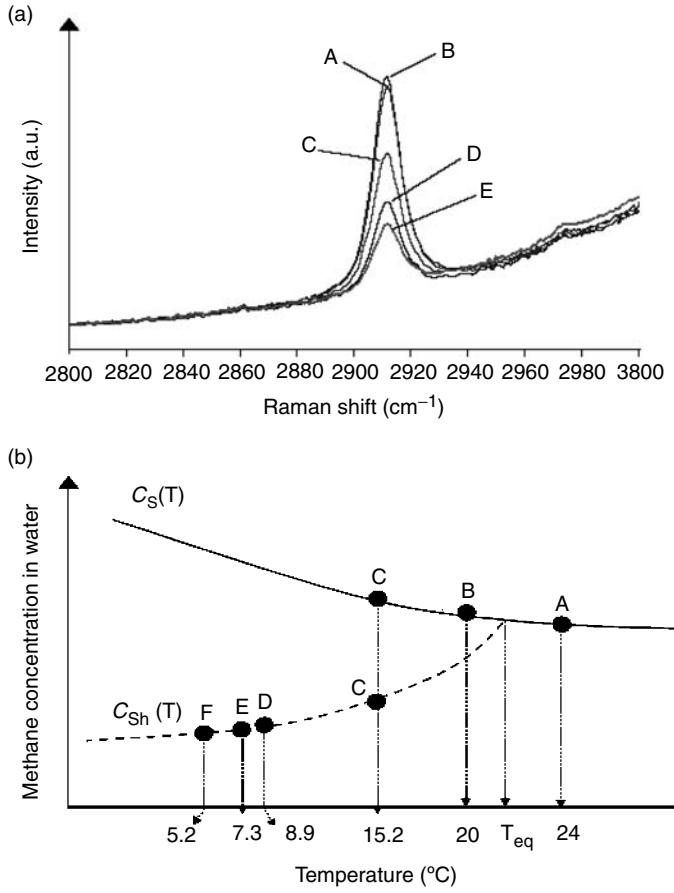

FIGURE 3.27 Methane hydrate film development at the water–methane interface from dissolved methane in the aqueous phase, as indicated from Raman spectroscopy (a) and methane solubility predictions (b). (a) A series of Raman spectra of dissolved methane collected at different temperatures during the continuous cooling process. Spectra marked A through E correspond to temperatures of 24°C, 20°C, 15.6°C, 10.2°C, and 2.8°C, respectively. (b) A schematic illustration of temperature dependencies of the equilibrium methane concentration in liquid water (C_S = without hydrate, C_{Sh} = with hydrate). The scale of the vertical axis is arbitrary, but the Raman peak area is proportional to methane dissolved in water. Points A through F correspond to different temperatures during the continuous cooling process. (From Subramanian, S., *Measurements of Clathrate Hydrates Containing Methane and Ethane Using Raman Spectroscopy*, Ph.D. Thesis, Colorado School of Mines, Golden, CO (2000). With permission.)

solution of water and dissolved methane has been also suggested by Tohidi et al. (2001, 2002) from glass micromodel experiments.

A conceptual picture of the proposed mechanism for hydrate film growth at the hydrocarbon–water interface based on the above experimental results is given

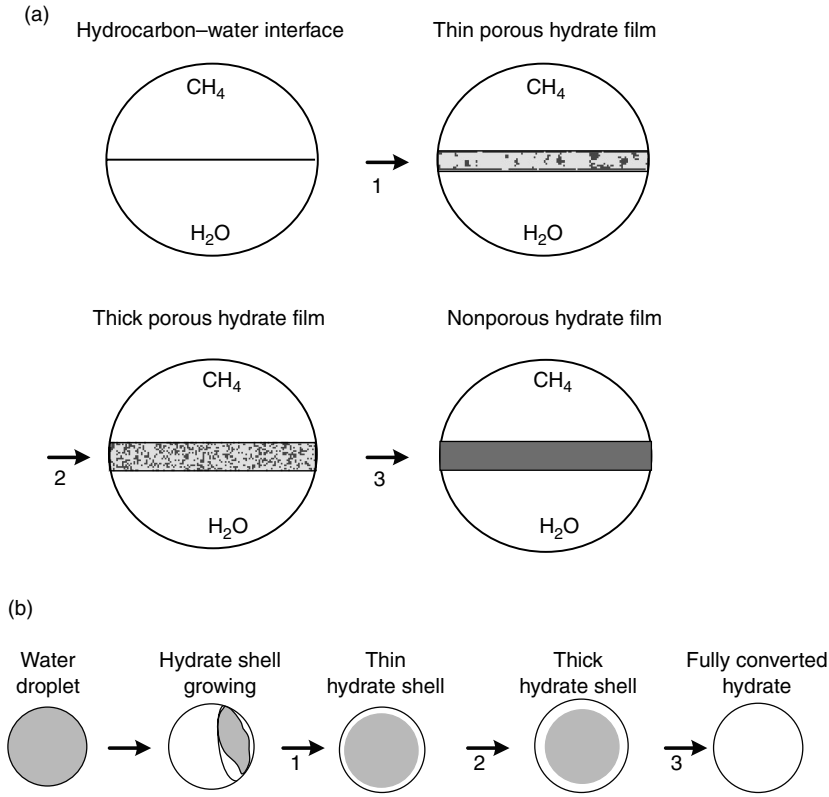

FIGURE 3.28 (a) Schematic of the proposed mechanism for hydrate film formation at a hydrocarbon–water interface. Step 1: Propagation of a thin porous hydrate film across the hydrocarbon–water interface. Step 2: Film development. Step 3: Hydrate film solidification (Taylor, 2006; Subramanian, 2000) and (b) Schematic of the proposed mechanism for hydrate formation from a water droplet. Step 1: Propagation of a thin porous hydrate shell (film) around the water droplet. Step 2: Shell development. Step 3: Bulk conversion of the droplet interior to hydrate (Taylor, 2006).

in Figure 3.28a. This model is extended to hydrate formation from the surface of a water droplet in Figure 3.28b. Figure 3.28b is based on both the film growth and droplet conversion experiments detailed above.

Information on the mesoscopic and microscopic processes occurring at the surface of ice particles during hydrate particle formation has been obtained from scanning electron microscopy (SEM; Staykova, 2003; Kuhs et al., 2005; Stern et al., 2005), nuclear magnetic resonance (NMR) microimaging (Moudrakovski et al., 2004), and neutron diffraction (Henning et al., 2000). Direct evidence for hydrate shell formation has been obtained from scanning electron micrographs recorded for methane hydrate samples (Stern et al., 2005). In these experiments, hydrate was formed from ice grains by cycling the temperature below and just

above the ice point. The authors suggest that the mesoporous structure (Figures 3.29c,d) of the hydrate surface (or shell around the melted ice/water droplet) allows liquid water from the interior of the shell to leak out of the shell, hence leaving hollow shells of hydrate (Figures 3.29a,b).

Figure 3.30 shows a field emission FE-SEM image of the porous structure of a typical methane hydrate single crystal formed from an ice particle (Staykova, 2003). Mean pore sizes on the order of several hundred nm (macropores) were determined from the FE-SEM images for single crystals of methane, argon and nitrogen hydrate. Pore sizes of several 10's of nm (mesopores) were identified for carbon dioxide hydrate. These pore channels would allow water and gas to be transported through the hydrate layers. As the permeability of the hydrate layer decreases, transport would become more difficult.

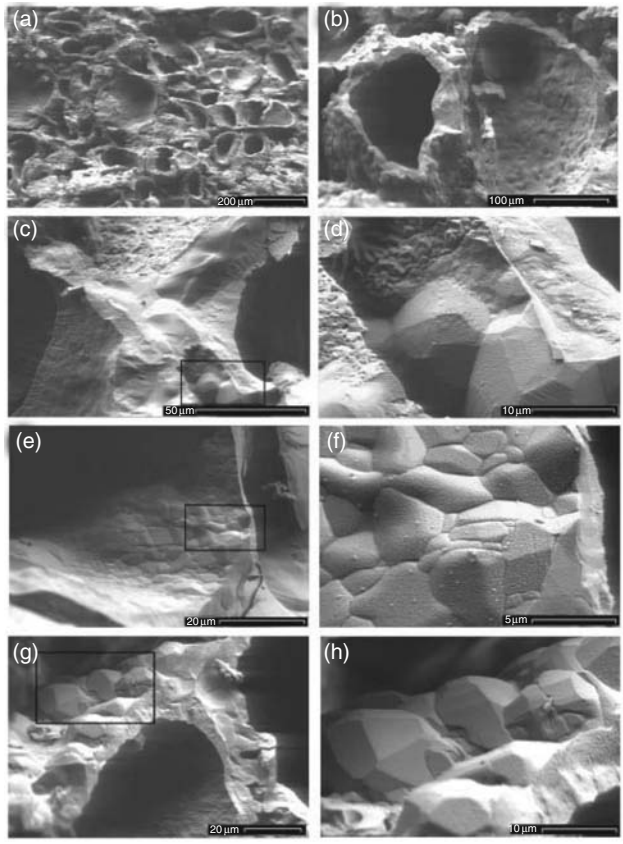

FIGURE 3.29 Scanning Electron Micrographs (SEM) of methane hydrate. (a, b) Hydrate shells; (c, d) mesoporous hydrate surface, (e, f) quenched hydrate, (g, h) hydrate crystal edges. (Reproduced from Stern, L., Circone, S., Kerby, S., Durham, W., in *Proc. Fifth International Conference on Gas Hydrates* (2005). With permission.)

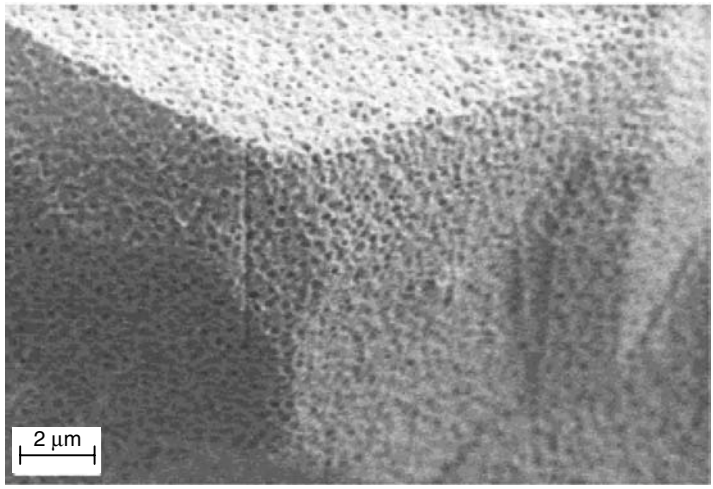

FIGURE 3.30 Field emission scanning electron microscopy image of the submicron porous structure of methane hydrate after 2 weeks of reaction at 60 bar, 265 K. (Reproduced from Staykova, D.K., Kuhs, *J. Phys. Chem. B*, **107**, 10299 (2003). With permission from the American Chemical Society.)

Similarly, hydrate shell formation has been observed directly using ^{1}H NMR microimaging (Moudrakovski et al., 2004). In these measurements ice particles were converted above the ice point to hydrate particles of methane (at 172 bar, 277 K) and carbon dioxide (58 bar, 275 K). The microimaging method was able to clearly detect hydrate shells around water droplets (Figure 3.31). The results also show that in less common cases, the thickness of the hydrate shells increases indicating the reaction is limited to gas diffusion through the hydrate shell. After some time the interior of the droplet then converts to hydrate. However, the most common observation was that on formation of the hydrate shell around the water droplet, rather than shell thickening, the bulk water of the droplet was converted to hydrate. Similar results were obtained for methane hydrate formation from water droplets suspended in iso-octane. The microimaging results also revealed the heterogeneous nature of the nucleation and growth of the water droplets to hydrate particles.

In summary, the microimaging technique provides a powerful tool to study directly the mechanism of converting water droplets to hydrate particles. The results reported indicate that provided the gas hydrate former can diffuse into the interior droplet, hydrate growth can proceed in the bulk interior droplet away from the hydrate shell–water interface, as well by growing out from the hydrate shell resulting in shell thickening.

In situ neutron diffraction studies have provided insight into the mechanism of surface conversion of ice particles to carbon dioxide hydrate particles (Henning et al., 2000). The experiments were performed at 230–276 K and around 6.2 MPa. It was proposed from these measurements that after the initial period of fast

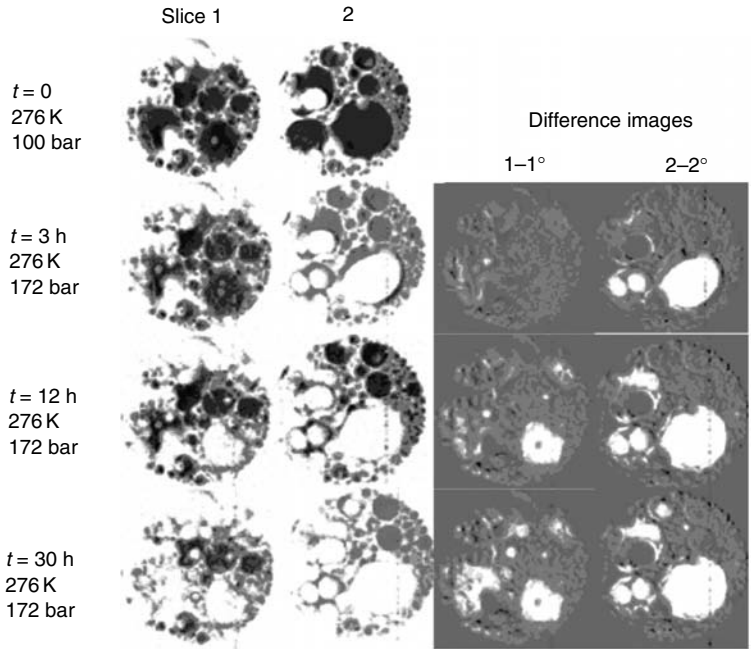

FIGURE 3.31 ^{1}H NMR microimages of methane hydrate formation as a function of time. Left: Images for two slices; right: difference images; in both, white represents hydrates. (Reproduced from Moudrakovski, I.L., McLaurin, G.E., Ratcliffe, C.I., Ripmeester, J.A., *J. Phys. Chem. B*, **108**, 17591 (2004). With permission from the American Chemical Society.)

conversion to hydrate on the surface of the ice particles, the process is controlled by diffusion of carbon dioxide molecules through the hydrate layer. After diffusion through the hydrate layer, hydrate formation proceeds from carbon dioxide and water molecules in a quasi-liquid layer (or premelting layer). This is in agreement with the findings of Stern et al. (1998) who reported enhanced methane hydrate formation at a liquid-like surface film on fine ice grains (about 200 micrometers) from optical cell experiments.

3.2.2.3 Crystal growth with interfacial agitation

Analysis of hydrate formation data can be obtained from a tabulation of gas consumption during hydrate formation as a function of time measured in stirred reactors. Formation data thus require either a table (or a plot) of individual experiments. Such a prospect is not viable in this monograph, since the literature hydrate formation data contain a large number of experiments with questionable transferability between apparatuses. Instead an overview of experimental conditions is presented below. The reader is referred to theses and subsequent publications of Englezos (1986), Dholobhai (1989), Skovborg (1993), Bansal (1994), and Turner (2005) for typical data.

As with most hydrate kinetic studies, multiple major works have come from Bishnoi's laboratory. In particular, the work of Englezos et al. (1987a,b) and Englezos and Bishnoi (1988) is a milestone in quantifying hydrate growth. Englezos' experiments were performed in a mixed (400 rpm) reactor held at constant pressure (0.6–8.9 MPa) and constant temperature (274–282 K). The growth of CH_4, C_2H_6, and $CH_4 + C_2H_6$ hydrates were measured for an initial linear growth period (<2 h) after appearance of the hydrate phase, indicated by a turbid solution. The data for these studies are summarized in two reports by Bishnoi et al. (1984–1985, 1986) and have been digitized by Skovborg (1993). A total of 17 experiments for CH_4 were performed by Englezos in the temperature range from 274 to 282 K and the pressure range of 2.3–9.3 MPa. For C_2H_6 a total of 9 experiments were done in the same temperature range, but at a pressure range from 0.7 to 2.2 MPa. For mixtures of $CH_4 + C_2H_6$ 23 kinetic data sets were measured; 8 sets for mixtures of $75\%CH_4 + 25\%C_2H_6$, 6 sets for equimolar mixtures, and 9 sets for $25\%CH_4 + 75\%C_2H_6$. Clarke and Bishnoi (2005) performed further measurements on CO_2 hydrate growth and found the intrinsic rate constant varied from 3.214×10^{-3} to 6.423×10^{-3} mol/(m^2Pa s) over the temperature range 274–279 K and pressure range 1.6–3.0 MPa.

Also in Bishnoi's laboratory, Dholabhai et al. (1993) studied the effect of electrolytes on methane hydrate formation kinetics. They found that after the equilibrium fugacity (or driving force) is adjusted for the presence of salt, hydrate growth kinetics are quantitatively described by the pure water kinetics model of Englezos.

Skovborg (1993) studied the growth rates of pure components of CH_4, C_2H_6, C_3H_8, and mixtures of $CH_4 + C_2H_6$, $CH_4 + C_2H_6 + C_7H_{16}$, and a North Sea fluid. Skovborg carried out 98 experiments at D.B. Robinson, Ltd. over a pressure range from 0.75 to 52 bars with subcooling ranging from 1.2°C to 7.5°C and hydrocarbon liquid volumes from 0% to 92%. It should be noted that the pressure (driving force) decreased during Skovborg's experiments. At the Colorado School of Mines, Bansal (1994) performed over 100 experiments on growth of C_2H_6 and $CH_4 + C_3H_8$ hydrates at temperatures ranging from 0°C to 4°C and pressures of up to 2.7 MPa.

Laser light scattering has been also applied to measure hydrate growth rates and particle size distributions in high pressure stirred reactors (Nerheim, 1993; Parent and Bishnoi 1996; Nesterov and Feklistov, 1999; Servio et al., 2000; Clarke and Bishnoi, 2000; Clarke and Bishnoi, 2001, 2005; Turner, 2005) and in a flow loop system (at the ExxonMobil facility). An *in situ* particle size analyzer (FBRM, focused beam reflectance measurement method; Lasentec) has been recently applied at CSM together with a particle video microscopy method (PVM, which visualizes particles illuminated with an array of near-infrared lasers; Lasentec) to measure hydrate particle formation and agglomeration.

3.2.2.4 Growth of metastable phases

The appearance of metastable phases during hydrate growth can provide valuable insight into the molecular mechanism of hydrate growth, as well as an increased

level of understanding of the possible origin of thermodynamic structural transitions. Molecular measuring tools such as Raman and NMR spectroscopy, and neutron and x-ray diffraction can be used to detect the appearance of metastable phases. That is, the characteristic spectroscopic or diffraction peak(s) for a hydrate structure that is not thermodynamically stable can be detected during hydrate growth.

Coexistence of sI and sII carbon dioxide hydrate has been detected from x-ray diffraction measurements during hydrate growth (Staykova and Kuhs, 2003). Similarly, metastable sII hydrate phases were detected using NMR spectroscopy during sI xenon hydrate formation (Moudrakovski et al., 2001a) and during sI methane/ethane hydrate formation (Bowler et al., 2005; Takeya et al., 2003).

Changes in the large-to-small cage occupancy during hydrate growth detected using NMR spectroscopy also suggest the presence of metastable phases. NMR studies showed that the large-to-small cage occupancy of sI xenon hydrate was around 1.0 initially and changed to a value of around 3–4 after rapid growth commenced. Therefore, during the induction period, the hydrate clusters were composed of a larger number of occupied small cages than large cages (Moudrakovski et al., 2001b). Similar results were found for methane hydrate using Raman spectroscopy (Subramanian, 2000).

3.2.3 Correlations of the Growth Process

Table 3.5 summarizes the different hydrate growth models that have been developed by various research groups. Three major correlations for hydrate growth exist:

1. Intrinsic growth kinetics
2. Mass transfer limited
3. Heat transfer limited

This section presents models from each of the correlations (1–3), with a brief critique. One should approach the use of any kinetic model with extreme caution for three reasons:

1. Hydrate nucleation (the initiation of growth, occuring during the induction period) is a stochastic process (with significant scatter in the data at low driving force under isothermal conditions).
2. Every model for hydrate formation may be apparatus-dependent. If the data for the model were generated in a high pressure reactor, there is no assurance that the data would be translatable to (for example) a natural gas pipeline.
3. Most of the data were determined for sI while natural gas typically forms sII; crystal structure is a significant factor in the rate of crystal growth.

TABLE 3.5
A Summary of the Different Hydrate Growth Models

Growth model	Driving force/model features	Researchers
Growth kinetics	$(f - f_{eq})$	(Englezos et al., 1987a,b)
Growth kinetics	$(f - f_{eq})$ Minor modification to Englezos' model	(Malegaonkar et al., 1997)
Mass transfer	$(x^i_{int} - x^i_b)$ Simplification/modification to Englezos' model	(Skovborg and Rasmussen, 1994)
Mass transfer	Based on phase field theory	(Svandal et al., 2005)
Mass transfer	Based on Monte Carlo cellular automata	(Buanes et al., 2005)
Heat transfer	Curved film front growth on water–hydrate former interface	(Uchida et al., 1999a)
Heat transfer	Curved film front growth on water–hydrate former fluid interface	(Mori, 2001)
Heat transfer	Straight film front growth on water side of water–hydrate former interface	(Freer et al., 2001; Mochizuki and Mori, 2005, 2006)

3.2.3.1 Growth kinetics—the Englezos–Bishnoi model

The role of hydrate intrinsic kinetics has been more recently suggested to play a smaller role in hydrate growth in real systems than heat and mass transfer effects. In view of this, the discussion on the kinetics models is only briefly presented here. For a more thorough treatment, the reader is referred to the original references (Englezos et al., 1987a,b; Malegaonkar et al., 1997).

Englezos et al. (1987a,b) generated a kinetic model for methane, ethane, and their mixtures to match hydrate growth data at times less than 200 min in a high pressure stirred reactor. Englezos assumed that hydrate formation is composed of three steps: (1) transport of gas from the vapor phase to the liquid bulk, (2) diffusion of gas from the liquid bulk through the boundary layer (laminar diffusion layer) around hydrate particles, and (3) an adsorption reaction whereby gas molecules are incorporated into the structured water framework at the hydrate interface.

Modifications to the model by Englezos et al. were later made to remove some minor inconsistencies and to account for the high solubility of carbon dioxide in water (Malegaonkar, et al., 1997). The last two steps are concepts with initial basic equations discussed in Section 3.2.1. Similarly to Equation 3.17, Englezos modeled steps (2) and (3) using Equation 3.18, where at steady state the rates of the two steps are assumed equal. Therefore, the rate of growth per particle is given by:

$$(\mathrm{d}n_i/\mathrm{d}t)_p = K^* A_p (f_i^b - f_i^{eq}) \tag{3.18}$$

with

$$1/K^* = 1/k_r + 1/k_d \tag{3.19}$$

where

$(dn_i/dt)_p$ = number of gas moles consumed per second by the hydrate
A_p = the surface area of each particle
f_i^b = fugacity of component i in the bulk liquid
f_i^{eq} = equilibrium fugacity of component i in the liquid at the hydrate interface
K^* = hydrate formation growth rate constant, representing a combined rate constant for diffusion (mass transfer) and adsorption (reaction) processes
k_r = reaction rate constant
k_d = mass transfer coefficient through the film around the particle
$(f_i^b - f_i^{eq})$ defines the overall driving force.

However, as with any model, it is well to recognize the limitations before attempting usage. Below are some inherent restrictions in the Englezos–Bishnoi–Malegoankar model:

1. The data were modeled with one fitted parameter (K^*) for hydrate growth of simple hydrate formers of methane, ethane, carbon dioxide. Since all these model components form sI hydrate, the model should be used with caution for sII and sH.
2. The model was for linear growth during the first 100 min after hydrate nucleation, starting from the time of visual observation of hydrates (the turbidity point). In their critique, Skovborg and Rasmussen (1994) note that, when the model is extrapolated by an order of magnitude, increasing growth (curvature) is observed with time, in contrast to long-time data.
3. The model is very sensitive to the number of moles consumed at the turbidity point, to which there is no easy access.
4. In calculating the critical radius it was assumed that the hydrate remains at the equilibrium pressure, not the system pressure. This assumption indicates a system force imbalance and ignores the final term in Δg.
5. From our current knowledge, it is suggested that intrinsic kinetics typically plays a minor role in hydrate formation in real systems (turbulent pipeline flow), and instead mass and heat transfer may play a larger role in determining the rate of hydrate formation.

Even with the above restrictions, the Englezos–Bishnoi model was a pioneering exercise that provided a foundation for further work. The data obtained were measured very carefully, and thus can be fit with all kinetic models. It is fair to say that other macroscopic kinetic experiments follow in the footsteps of the Englezos–Bishnoi work.

3.2.3.2 Mass transfer—the Skovborg–Rasmussen model

Skovborg and Rasmussen (1994) studied the Englezos–Bishnoi model and noted two restrictions in addition to limitations 2 and 3 in the last section:

1. The secondary nucleation constant was very low (10^{-3}) suggesting that no secondary nucleation exists, and that all particles were of the same size and grow at the same rate. Therefore, Skovborg and Rasmussen suggested that the crystallization population balance could be removed from the model.
2. The value of K^* may have been too high, caused by an error in the mass transfer coefficient through the liquid film, k_L. Skovborg suggests that values of k_L were obtained at solubility conditions without hydrate formation, perhaps leading to an error. (See Handa's solubility predictions in Section 4.1.6). Skovborg noted that a 50% error in k_L will result in an error of two orders of magnitude in K^*.

The above observations encouraged Skovborg and Rasmussen to simplify the Englezos–Bishnoi model. They assumed that the entire hydrate process could be modeled as a mass transfer restriction of the gas through the liquid film at the gas–liquid interface. As such, their model reduced the number of differential equations to a single equation:

$$dn/dt = k_L A_{(g-l)} c_{wo} (x_{int} - x_b) \tag{3.20}$$

where

$A_{(g-l)}$ = gas–liquid interface area, (79.3 cm^2 at 300 rpm in Englezos et al., 1987a)
c_{wo} = initial concentration of water
x_{int} = bulk liquid mole fraction of the component.

Skovborg re-analyzed the Englezos kinetic data and obtained mass transfer coefficients of 4.076×10^{-5} and 5.457×10^{-5} m/s for CH_4 and C_2H_6, respectively.

A Perspective on the Skovborg–Rasmussen Model. With its simplification, the Skovborg–Rasmussen model represents perhaps the most approachable mathematical treatment for mass transfer controlled growth. As with all models, it should be studied carefully and used with caution. There are several limitations to the model:

1. Absolute average deviations to the fit of the Englezos–Bishnoi data for CH_4, C_2H_6, and their mixtures, are 22%, 14%, and 30% respectively, relative to the experimental inaccuracies on the order of 10–20%. That is, the mixture predictions may be in error by ±30%. While many predictions work well, others failed for methane at long times.

2. There is no published evidence that the model parameters are apparatus-independent, or that the fit can be extended to other systems.
3. Surface area A deviations from 30% to 70% were calculated for identical runs of methane and ethane, suggesting a self-consistency problem.
4. The model is sensitive to errors in driving force, and the driving force errors are systematic in the model.
5. The model appears to be a data fit, rather than have theoretical significance.

3.2.3.3 Heat transfer models

Lateral growth of a hydrate film across the water–gas interface can be described by various models (Figures 3.32a through d). The Uchida et al. (1999a) model (Figure 3.32a) has been based on their experiments performed on a water droplet surface submerged in liquid carbon dioxide. In this model, hydrate crystals form only at the front of the hydrate film and the front is maintained at the three-phase (water–guest–hydrate) equilibrium temperature. Steady heat transfer from the front to the water and guest fluid is assumed. Assuming that heat removed from the front is balanced with heat generated by hydrate formation (exothermic process), Uchida et al. related the linear growth rate of the hydrate film along the interface (v_f) to the hydrate film thickness (δ), and the degree of subcooling (ΔT). δ was determined by fitting the calculated $v_f - \Delta T$ plot to the corresponding experimental data.

Mochizuki and Mori (2005, 2006) suggest that the major problem with the Uchida et al. (1999a) model is the formulation of the conductive heat transfer from the film front, which has little physical reasoning. Direct measurements of the hydrate film thickness under pressure are generally far more difficult than lateral film growth measurements. Therefore, it was recognized that the Uchida et al. (1999a) model provides a method of determining the hydrate film thickness.

An alternative model is that presented by Mori in 2001 (Figure 3.32b), which is again based on lateral growth of the hydrate film on the interface between a stagnant water pool and a guest fluid. However, in this model, there is a countercurrent flow that occurs at a velocity opposite in sign but equal in magnitude to the velocity of the film front. The heat of hydrate formation released at the film front is assumed to be removed away from the front to the liquid phases by steady convective heat transfer. The film front is semicircular in shape and held at the three-phase equilibrium temperature, as in the Uchida et al. (1999a) model. This second model gives better agreement with the experiments for the v_f–ΔT relations than the first model. However, Mochizuki and Mori (2005, 2006) suggest that the second model's countercurrent convection is unrealistic since the hydrate mass density is very similar to liquid water. Hence, lateral growth of the hydrate film should not displace the water in the front, but instead result in transformation of the water into hydrate almost at its location. Convection in the guest fluid should be small since the guest fluid has a far lower thermal conductivity than liquid water, and so would play no more than a minor role in heat removal.

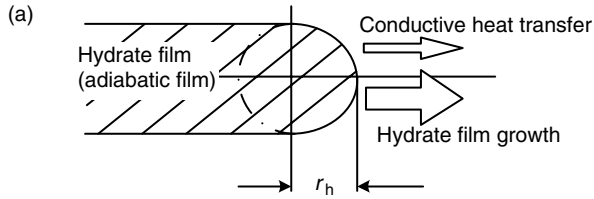

Hydrate film model by Uchida et al. (1999)

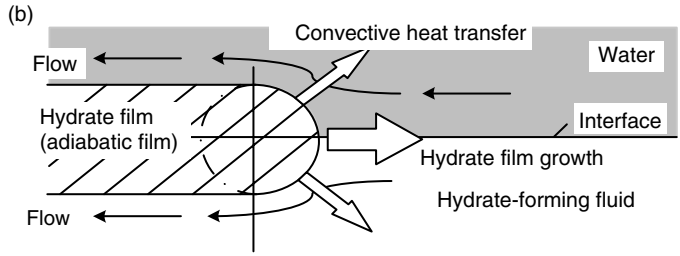

Hydrate film model by Mori (2001)

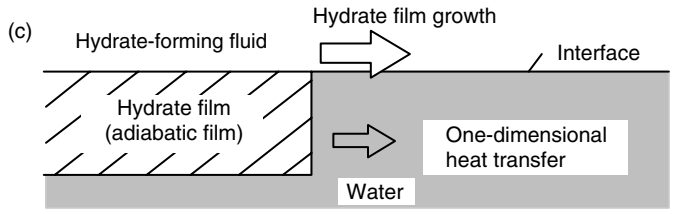

Hydrate film model by Freer et al. (2001)

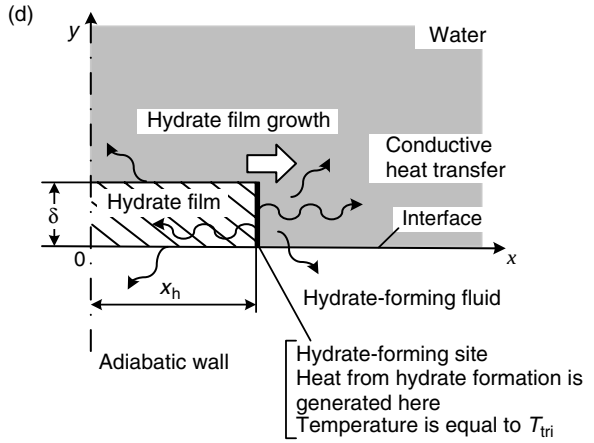

Hydrate film model by Mochizuki and Mori (2006)

FIGURE 3.32 Physical models of hydrate film growth along the water–hydrate former fluid interface. (Reproduced from Mochizuki, T., Mori, Y.H., *J. Cryst. Growth*, **290**, 642 (2006). With permission from Elsevier.)

The Freer et al. (2001) model (Figure 3.32c) was based on experimental data on methane hydrate film growth at the methane–water interface. The v_f of the film was modeled assuming one-dimensional conductive heat transfer from the front of the film to the water phase extending beyond the front. As the computed v_f was much lower than that from experiment, Freer et al. (2001) suggested that hydrate film growth may be controlled by kinetics of hydrate formation. Mochizuki and Mori suggest that since the hydrate films are initially very thin, the fronts are probably convex contours with strong curvatures, rather than straight-edged.

In the most recent model by Mochizuki and Mori (2006), transient two-dimensional conductive heat transfer from the film front to both the water and guest fluid phases and the hydrate film itself is assumed (Figure 3.32d). In this model, as that in the model of Freer et al. the hydrate film is assumed to exist on the water side of the water–guest fluid interface. The hydrate film is assumed homogeneous from a macroscopic scale. Water and guest phases extend infinitely. Lateral hydrate film growth is assumed to be faster than film thickening/thinning. Hydrate forms only on the front of the hydrate film and the temperature of the front is maintained at the three-phase equilibrium temperature. No guest or water movement occurs, and the rate of heat removal from the front is balanced by the rate of heat generation by hydrate formation.

The linear growth rate of the hydrate film along the water/hydrocarbon (hydrate former fluid) interface, $v_f\,(= \mathrm{d}x_h/\mathrm{d}t)$, is given in Equation 3.21:

$$\rho_h \delta \Delta h_H v_f = \int_0^{\delta} \left(\lambda_h \left.\frac{\partial T}{\partial x}\right|_{x=x_{h-}} - \lambda_w \left.\frac{\partial T}{\partial x}\right|_{x=x_{h+}} \right) \mathrm{d}y \tag{3.21}$$

where δ = hydrate film thickness; $\partial T/\partial x|_{x=x_{h-}}$ and $\partial T/\partial x|_{x=x_{h+}}$ are the hydrate-side and water-side temperature gradients, respectively, at $x = x_h$ (i.e., the x position of the hydrate-film front); Δh_H = heat of hydrate formation per unit mass of hydrate; λ_h and λ_w = thermal conductivity of hydrate and water, respectively.

The interfacial temperature must be higher than the system temperature because the solid molecules have less energy that those in the liquid and dissolved gas, so that heat is released as the molecules transform from fluid to solid. The heat raises the interfacial temperature to its equilibrium value, where it is limited by second law considerations.

Mochizuki and Mori (2005, 2006) indicate that experimentally observed hydrate film growth is typically radial rather than linear. However, reasonable agreement was obtained between the calculated and experimental v_f values using either the straight front or the semicircular-front models. Also, though the heat release rate of the semicircular-front was smaller than the straight-front, for order-of-magnitude estimations of δ, the straight-front model was acceptable. The heat released from hydrate formation was also assumed to be released to the water and guest fluid via the water–hydrate film interface and guest fluid–hydrate film interface within a short distance (about 0.1 mm) from the film front. Heat is

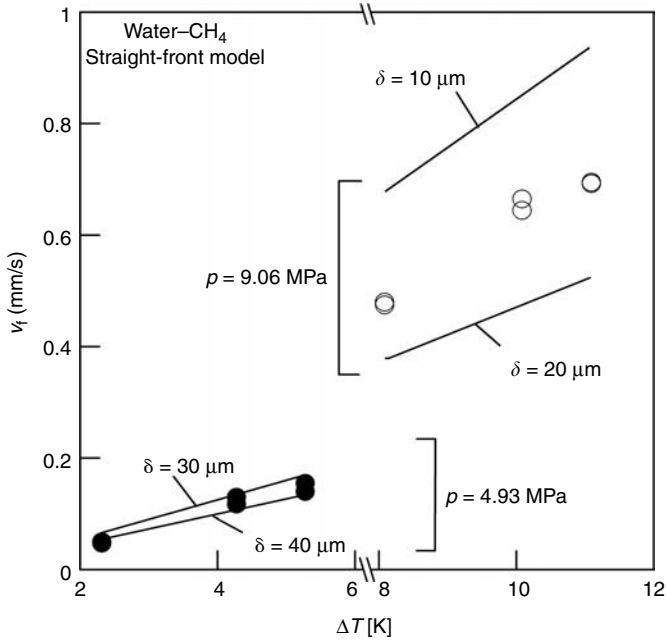

FIGURE 3.33 Comparison between calculated (lines by Mochizuki and Mori, 2006) and measured (points by Freer et al., 2001) hydrate film growth rates as a function of subcooling. (Reproduced from Mochizuki, T., Mori, Y.H., *J. Cryst. Growth*, **290**, 642 (2006). With permission from Elsevier.)

assumed to be directly transferred from the hydrate–water interface to the water phase, and transferred into the film and then diffused away into the water and guest fluid phases.

Comparison of the film growth rates calculated using the model by Mochizuki and Mori (2005, 2006) with experimental data by Freer et al. (2001) for methane hydrate is shown in Figure 3.33. The hydrate film thickness parameter, δ was fit to the experimental data. The δ values obtained from the model are within an order of magnitude agreement with experiment (Makogon et al., 1998; Taylor et al., 2006). However, the experiments suggest that the hydrate film thickness increases with increasing subcooling, which is the opposite trend to that suggested by the model.

Application of the planar hydrate film growth model to hydrate film growth on a water droplet was also tested by comparing Mochizuki and Mori's model (2006) with experiments by Uchida et al. (1999a) for carbon dioxide hydrate growth. The calculated and measured growth rates were again within an order of magnitude agreement. The film thickness obtained by fitting the model to the data was found to be significantly lower for carbon dioxide hydrate than methane hydrate. Mochizuki and Mori (2006) suggest that in the case of droplet conversion the limited system size in the experiment may have an effect on the results. That is, heat transfer from the film front to the surrounding liquid is around 1–3 mm, which is comparable

to the size of the water droplet. This may result in the film front being in close enough proximity to surfaces of the reactor cell to cause mechanical or thermal interactions between the surface and film front.

3.2.4 State-of-the-Art for Hydrate Growth

The state-of-the-art for hydrate growth may be summarized with only a few statements:

1. Hydrate growth data and modeling are more tenable than are nucleation phenomena. In particular, the growth data (after nucleation) appears to be linear for as much as 100 min in Englezos' data.
2. Any existing growth model has been shown to fit only the data on which its parameters were based. Most data were obtained in a high-pressure reactor and may not apply to formation rates in a pipeline. Limited flow loop data are available.
3. Most of the data on which the models are based are obtained for sI, while most pipeline hydrates are sII due to the propane (and higher) constituents of natural hydrocarbons.
4. Heat and mass transfer effects can be more significant than intrinsic kinetics in multiphase systems.
5. Metastable states can form during hydrate growth, which is not accounted for in the simulations or models.

3.3 Hydrate Dissociation

Hydrate dissociation is of key importance in gas production from natural hydrate reservoirs and in pipeline plug remediation. Hydrate dissociation is an endothermic process in which heat must be supplied externally to break the hydrogen bonds between water molecules and the van der Waals interaction forces between the guest and water molecules of the hydrate lattice to decompose the hydrate to water and gas (e.g., the methane hydrate heat of dissociation is 500 J/gm-water). The different methods that can be used to dissociate a hydrate plug (in the pipeline) or hydrate core (in oceanic or permafrost deposits) are: depressurization, thermal stimulation, thermodynamic inhibitor injection, or a combination of these methods. Thermal stimulation and depressurization have been well quantified using laboratory measurements and state-of-the-art models. Chapter 7 describes the application of hydrate dissociation to gas evolution from a hydrate reservoir, while Chapter 8 describes the industrial application of hydrate dissociation. Therefore in this section, discussion is limited to a brief review of the conceptual picture, correlations, and laboratory-scale phenomena of hydrate dissociation.

3.3.1 Conceptual Picture of Hydrate Dissociation

The modern conceptual picture of dissociation of a hydrate core/plug typically involves radial hydrate dissociation rather than the previously suggested axial

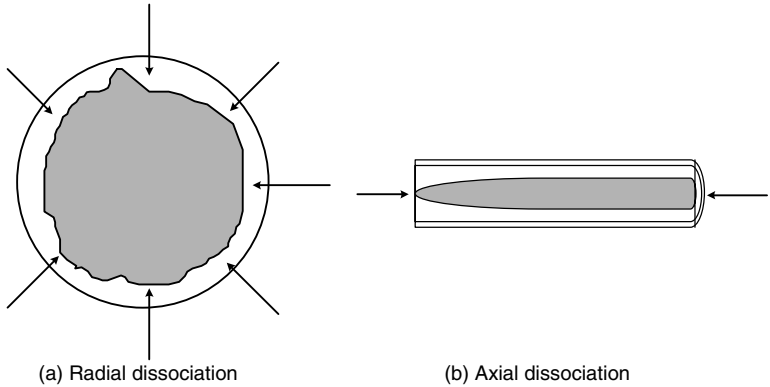

FIGURE 3.34 Current radial dissociation picture (a), compared to old axial dissociation picture (b).

hydrate dissociation (Figure 3.34). The most accurate picture is based on heat-transfer-limited hydrate dissociation, where the hydrate plug remains in the center of the pipe and is surrounded by a stationary water phase. This stationary water phase can conduct heat to the dissociating front of the hydrate (Davies et al., 2006). The nature of radial dissociation is a particularly fortuitous physical phenomenon since this leads to significantly more rapid hydrate plug dissociation than that for axial dissociation. This is due to (1) the radial plug dimensions being always smaller that the longitudinal dimensions and (2) the larger radial surface heat transfer area compared to the axial surface for heat transfer.

This radial dissociation model is supported by direct evidence obtained from x-ray computed tomography (CT) measurements of the dissociation of a methane hydrate core (Gupta, 2007). X-ray CT measurements capture images and density profiles of the hydrate core, showing that hydrate dissociates radially (Figure 3.35). At each time interval, different stages of radial dissociation of the hydrate plug were observed from the CT images, with the final step being water draining. No evidence of axial dissociation was observed (cf. Peters et al., 2000; Bollavaram and Sloan, 2002).

3.3.2 Correlations of Hydrate Dissociation

The different hydrate dissociation models that have been developed by various research groups are summarized in Table 7.10. The majority of these models are based on heat transfer limited dissociation. Some of the models have been developed to incorporate both heat transfer and kinetics.

On the basis of comparisons with experimental data on hydrate dissociation it has been shown by a number of research groups that heat transfer plays the dominant role in hydrate dissociation, rather than intrinsic kinetics (Moridis, 2002; Hong et al., 2003; Davies et al., 2006). This is analogous to studies showing that the ice melting process is controlled by heat transfer (Galwey and Brown, 2000). Hong et al. (2003) suggest that at the very early stage of hydrate dissociation, the

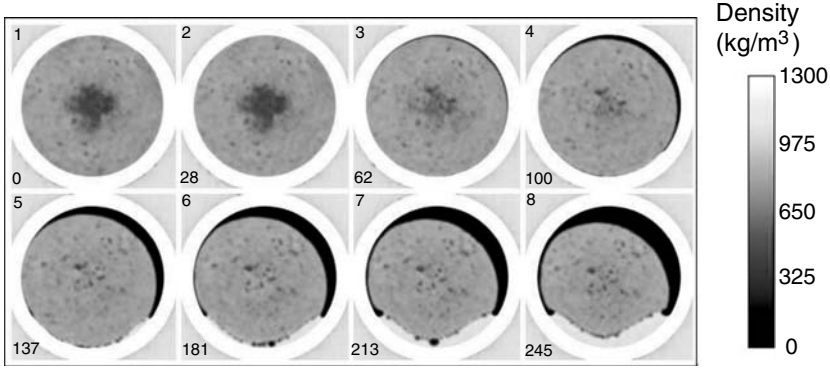

FIGURE 3.35 (See color insert following page 390.) X-ray CT imaging shows radial dissociation of a hydrate core. Image number 1–8 (top number on each image) recorded over 0–245 min (bottom number on each image). The cell pressure was decreased from 4.65 to 3.0 MPa over 248 min. The hydrate core temperature decreased from 277 to 274 K with time, following the three-phase methane hydrate equilibrium line. (From Gupta, A., *Methane Hydrate Dissociation Measurements and Modeling: The Role of Heat Transfer and Reaction Kinetics*, Ph.D. Thesis Colorado School of Mines, Golden, CO (2007). With permission.)

process can be controlled by intrinsic kinetics. Because heat is removed during decomposition, the temperature will quickly drop at the interface. Therefore, a temperature gradient is present in the hydrate zone, with heat being conducted from the hydrate zone to the interface. Hence, the dissociation process is controlled by heat transfer throughout the later stages.

From the extensive experimental and model development work performed at CSM (during a period of over 15 years), it has been demonstrated that a heat transfer controlled model is able to most accurately predict dissociation times (comparing to laboratory experiments) without any adjustable parameters. The current model (CSMPlug; see Appendix B for details and examples) is based on Fourier's Law of heat transfer in cylindrical coordinates for the water, ice, and hydrate layers, and is able to predict data for single- and two-sided depressurization, as well as for thermal stimulation using electrical heating (Davies et al., 2006). A heat transfer limited process is controlled by the rate of heat supplied to the system. Therefore, a measurable intermediate (cf. activated state) is not expected for heat transfer controlled dissociation (Gupta et al., 2006).

Rehder et al. (2004) measured the dissociation rates of methane and carbon dioxide hydrates in seawater during a seafloor experiment. The seafloor conditions provided constant temperature and pressure conditions, and enabled heat transfer limitations to be largely eliminated. Hydrate dissociation was caused by differences in concentration of the guest molecule in the hydrate surface and in the bulk solution. In this case, a solubility-controlled boundary layer model (mass transfer limited) was able to predict the dissociation data. The results showed that carbon dioxide hydrate dissociated much more rapidly than methane hydrate due to the higher solubility in water of carbon dioxide compared to methane.

Nuclear magnetic resonance studies of methane hydrate dissociation suggest that intrinsic kinetics is not likely to play a dominant role in the dissociation process (Gupta et al., 2006). Methane hydrate dissociation was shown to progress in the absence of an intermediate state (or activated state), with no preferential decay of large to small cavities. Similar measurements have been performed for Xe hydrate dissociation (Moudrakovski et al., 2001b).

3.3.3 Anomalous Self-Preservation

"Self-preservation" is the phenomenon where hydrates can remain stable for extended periods outside the hydrate stable region (Figure 3.36). Self-preservation or anomalous self-preservation has been experimentally observed by a numerous researchers (Davidson et al., 1986; Yakushev and Istomin, 1992; Stern et al., 2001a, 2001b, 2003; Takeya et al., 2002; Kuhs et al., 2005; Shimada et al.,, 2005). However, little is understood of this phenomenon. The ability to increase and prolong the stability of gas hydrates is desirable for gas storage applications.

As shown in Figure 3.36, the anomalous preservation region is observed over the temperature range 242–271 K on rapid depressurization to 0.1 MPa. This anomalous behavior has been also called "anomalous self-preservation." The latter consists of a short rapid dissociation phase with a release of 5–20 vol%

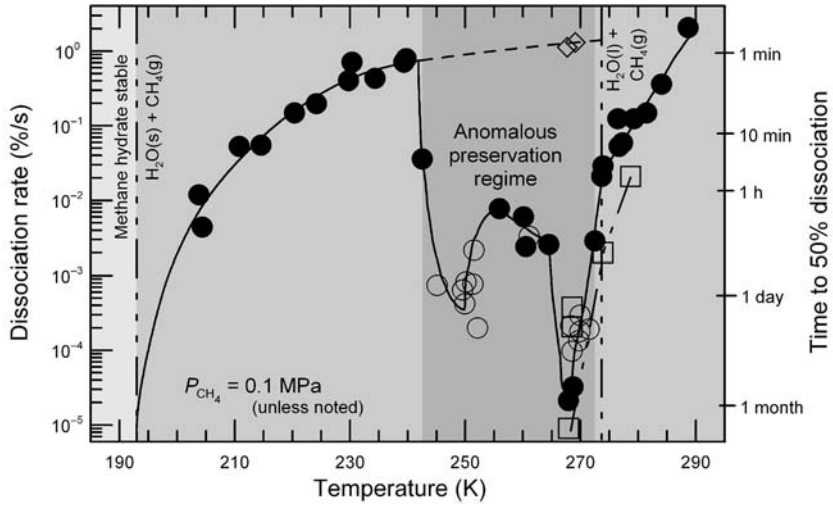

FIGURE 3.36 Average rates for methane hydrate samples reaching 50% dissociation at 0.1 MPa, following destabilization by rapid release of *P*. The anomalous preservation regime is between 242 and 271 K. Square symbols: experiments in which *P* is maintained at 2 MPa, Diamonds: 0.1 MPa rapid depressurization tests on sII methane–ethane hydrate, showing no comparable preservation behavior at 268 K. (Reproduced from Stern, L.A., Circone, S., Kirby, S.H., Durhan, W., *Can. J. Phys.*, **81**, 271 (2003). With permission from the National Research Council.)

of the total methane in the hydrate sample. During this gas release, adiabatic cooling of methane as well as general heat absorption occurs. After this rapid dissociation phase, the methane hydrate remains "metastably preserved" for up to 2–3 weeks depending on the dissociation temperature (Stern et al., 2003). Carbon dioxide hydrate (sI) also exhibits this anomalous self-preservation behavior (Stern et al., 2001a). Conversely, sII hydrates of ethane–methane (Stern et al., 2003) and propane (Stern et al., 2005) show no preservation effects.

The cause of the anomalous "self-preservation" behavior is not well-understood. Stern et al. (2003) acknowledge that ice-shielding could explain self-preservation of residual gas hydrate (<8%) in temperature-ramping tests and in low-temperature rapid-depressurization tests. However, they suggest such an ice protective rind cannot adequately explain anomalous preservation of methane hydrate at 242–271 K, particularly as sII hydrate does not exhibit anomalous preservation. Kuhs et al. (2005) suggest, from neutron diffraction and SEM data, that anomalous "self-preservation" could be due to significant annealing of ice stacking faults (ice defects) at around 240 K. They suggest that below 240 K, the ice covering the hydrate has gaps between ice crystallites, which allow gas diffusion.

3.3.4 State-of-the-Art for Hydrate Dissociation

The following summary statements are made about hydrate dissociation, based upon the previous subsections:

1. A hydrate plug or core dissociates radially, not axially.
2. X-ray CT provides a powerful means of imaging the hydrate core during the dissociation process, and obtaining real time density profiles of the core.
3. Hydrate dissociation is an endothermic process, typically controlled by heat transfer.
4. Using a heat transfer limited model based on Fourier's Law in cylindrical coordinates (developed at the Colorado School of Mines), hydrate dissociation under field conditions provides an order of magnitude (higher) prediction, which is acceptable in the industrial setting (see Chapter 8 and Appendix B for more details, including a description of CSMPlug to determine dissociation dimensions and times).
5. Anomalous self-preservation stabilizes methane hydrate and carbon dioxide hydrate particles at atmospheric pressure at 242–271 K for up to 2–3 weeks. This phenomenon can have implications for natural gas storage.

3.4 Summary

The time-dependent phenomena of hydrate nucleation and growth are challenging to both measure and model. This is in contrast to hydrate thermodynamics that

are well understood at typical industrial temperature and pressure conditions. The difficulties of measuring and correlating hydrate formation processes are largely because of the stochastic nature and apparatus dependence of the data. However, the state-of-the-art indicates that hydrate formation is controlled primarily by heat and mass transfer, with kinetics playing a more minor role in most cases. Hydrate decomposition on the other hand appears more tractable, and can be predicted in most cases using a heat transfer model. Sophisticated meso- and microscopic tools have been developed and applied to study the mechanisms of hydrate growth and decomposition.

References

Alexander, D.M., Hill, D.T., White, L.R., *Australian J. Chem.*, **24**, 1143 (1971).

Angell, C.A., in *Water: A Comprehensive Treatise*, Vol. 7 (Franks, F., ed.) Plenum Press, New York, p. 1 (1982).

Angell, C.A., *Ann. Rev. Phys. Chem.*, **34**, 593 (1983).

Angell, C.A., *J. Phys. Chem. B*, **103**, 3977 (1999).

Anklam, A.F., Firoozabadi, A., *J. Chem. Phys.*, **121**, 11867 (2004).

Arjmandi, M., Ren, S., Tohidi, B., in *Proc. Fifth International Conference on Gas Hydrates*, Trondheim, Norway, June 13–16, Paper 4011 (2005a).

Arjmandi, M., Tohidi, B., Danesh, A., Todd, A.C., *Chem. Eng. Sci.*, **60**, 1313 (2005b).

Baez, L.A., Clancy, P., in *Proc. First International Conference on Gas Hydrates*, (Sloan, E.D., Happel, J., Hnatow, M.A., eds) *Ann. N.Y. Acad. Sci*., **715**, 177 (1994).

Bansal, V., *Kinetic Study of Clathrate Hydrates*, M.S. Thesis, Colorado School of Mines, Golden, CO (1994).

Berg, W.F., *Proc. Roy. Soc. (London)*, **A164**, 79 (1938).

Berthoud, A., *J. de Chim. Phys.*, **10**, 624 (1912).

Bird, R.B., Stewart, W.E., Lightfoot, E.N., *Transport Phenomena,* Wiley & Sons Inc., New York, (1960).

Bishnoi, P.R., Kalogerakis, N.E., Jeje, A.A., Dholabhai, P.D., Englezos, P., in *Final Report to Department of Energy, Mines, and Resources, Earth Physics Branch,* Ottawa, Ontario K1A OX3, Canada, DSS File No.: 20SU.23235 (1986).

Bishnoi, P.R., Saeger, R.B., Kalogerakis, N.E., Jeje, A.A., in *Annual Report to Department of Energy, Mines, and Resources, Earth Physics Branch,* Ottawa, Ontario K1A OX3, Canada, pp. 2OSU.23235 (1984–1985).

Bollavaram, P., Sloan, E.D., in *Proc. Fourth International Conference on Gas Hydrates*, Yokohama, Japan, May 19–23, 947 (2002).

Bowler, K., Stadterman, L.L., Creek, J.L., Koh, C.A., Sloan, E.D., Dec, S.F., in *Proc. Fifth International Conference on Gas Hydrates*, Trondheim, Norway, June 13–16, Paper 5030 (2005).

Bridgman, P.W., in *Proc. American Academy of Arts and Sciences*, **XLVII, N13**, 530 (1912).

Buchanan, P., Soper, A.K., Westacott, R.E., Creek, J.L., Koh, C.A., *J. Chem. Phys.*, **123**, 164507 (2005).

Bunn, C.W., *Discussions Faraday Soc.*, **5**, 132 (1949).

Buanes, T., Kvamme, B., Svandal, A., *J. Cryst. Growth*, **287**, 491 (2006).

Carroll, J.J., *Phase Behavior in the System Water–Hydrogen Sulfide*, Ph.D. Thesis, University of Alberta, Edmonton, Canada (1990).

Chen, S.H., Gallo, P., Scioritino, F., Tartaglia, P., *Supercooled Liquids—Advances and Novel Applications,* ACS, Washington DC, p. 264 (1997).
Chen, T.-S., *A Molecular Dynamics Study of the Stability of Small Prenucleation Water Clusters*, Dissertation, U. Missouri-Rolla, University Microfilms No. 8108116, Ann Arbor, MI (1980).
Christiansen, R.L., Sloan, E.D., in *Proc. First International Conference Natural Gas Hydrates*, (Sloan, E.D., Happel, J., Hnatow, M.A., eds) *Ann. N.Y. Acad. Sci*., New Paltz, NY, June 13–16, 1993 (1994).
Christiansen, R.L., Sloan, E.D., Jr., in *Proc. Annual Convention of Gas Processors Association*, San Antonio, Tx, **74**, 15 (1995).
Cingotti, B., Sinquin, A., Pic, J.S., Herri, J.M., Cournil, M., in *Proc. SPE International Symposium on Oilfield Chemistry,* Houston, TX, Feb. 16–19, 549 (1999).
Clarke, M., Bishnoi, P.R., *Chem. Eng. Sci.*, **55**, 4869 (2000).
Clarke, M.A., Bishnoi, P.R., *Chem. Eng. Sci.*, **56**, 4715 (2001).
Clarke, M.A., Bishnoi, P.R., *Chem. Eng. Sci*., **60**, 695 (2005).
Comini, G., Guidice, S.D., Saro, O., *Intl. J. Numer. Methods Eng.*, **30**, 697 (1990).
Davidson, D.W., Garg, S.K., Gough, S.R., Handa, Y.P., Ratcliffe, C.I., Ripmeester, J.A., Tse, J.S., Lawson, W.F., *Geochim. Cosmochim. Acta*, **50**, 619 (1986).
Davies, S.R., Selim, M.S., Sloan, E.D., Bollavaram, P., Peters, D.J., *AIChE J.*, **52**, 4016 (2006).
Debenedetti, P.G., *Metastable Liquids, Concepts and Principles,* Princeton University Press, Princeton, NJ (1996).
Debenedetti, P.G., *J. Phys.: Condens. Matter*, **15**, R1669 (2003).
Dholabhai, P.D., *Incipient Equilibrium Conditions for Methane Hydrate Formation in Aqueous Mixed Electrolyte Solutions*, M.Sc. Thesis, University of Calgary, Calgary (1989).
Dholabhai, P.D., Kalogerakis, N., Bishnoi, P.R., *Can. J. Chem. Eng.*, **71**, 68 (1993).
D'Orazio, L.A., Wood, R.H., *J. Phys. Chem.*, **67**, 1435 (1963).
Dore, J., *Phys. World*, **1**, 25 (1988).
Elwell, D., Scheel, H.J., *Crystal Growth from High Temperature Solutions*, Academic Press, London (Chapters 4–6), 273 (1975).
Englezos, P., *A Model for the Formation Kinetics of Gas Hydrates from Methane, Ethane, and their Mixtures*, M.S. Thesis, University of Calgary, Alberta (1986).
Englezos, P., *Rev. IFP*, **51**, 789 (1996).
Englezos, P., Bishnoi, P.R., *Fluid Phase Equilib.*, **42**, 129 (1988).
Englezos, P., Kalogerakis, N., Dholabhai, P.D., Bishnoi, P.R., *Chem. Eng. Sci.*, **42**, 2647 (1987a).
Englezos, P., Kalogerakis, N., Dholabhai, P.D., Bishnoi, P.R., *Chem. Eng. Sci.*, **42**, 2659 (1987b).
Errington, J.R., Debenedetti, P.G., *Nature*, **409**, 318 (2001).
Frank, H.S., *Science*, **169**, 635 (1970).
Frank, H.S., Evans, M.W., *J. Chem. Phys.*, **13**, 507 (1945).
Frank, H.S., Franks, F., *J. Chem. Phys.*, **48**, 4746 (1968).
Frank, H.S., Wen, W.Y., *Discussions Faraday Soc.*, **24**, 133 (1957).
Franks, F., Reid, D.S., In *Water: A Comprehensive Treatise*, Vol. 2, Chapter 5 (Franks, F., ed.) Plenum Press, New York (1973).
Franzese, G., Stanley, H.E., *J. Phys.: Condens. Matter*, **14**, 2201 (2002).
Freer, E., Selim, M.S., Sloan, E.D., *Fluid Phase Equilib.*, **185**, 65 (2001).
Fukumoto, K., Tobe, J.-I., Ohmura, R., Mori, Y.H., *AIChE J.*, **47**, 1899 (2001).

Fujioka, Y., Takeuchi, K., Shindo, Y., Komiyama, H., *Intl. J. Energy Res.*, **19**, 765 (1994).
Galwey, A.K., Brown, M.E., *J. Therm. Anal. Calorimetry*, **60**, 863 (2000).
Glew, D.N., *Nature*, **195**, 698 (1962).
Guo, G.-J., Zhang, Y.-G., Refson, K., *J. Chem. Phys*, **413**, 415 (2005).
Gupta, A., *Methane Hydrate Dissociation Measurements and Modeling: The Role of Heat Transfer and Reaction Kinetics*, Ph.D. Thesis, Colorado School of Mines, Golden, CO (2007).
Gupta, A., Dec, S.F., Koh, C.A., Sloan, E.D., *J. Phys.Chem. C*, **111**, 2341 (2007).
Henning, R.W., Schultz, A.J., Thieu, V., Halpern, Y., *J. Phys. Chem. A*, **104**, 5066 (2000).
Himmelblau, D.M., *J. Phys. Chem.*, **63**, 1803 (1959).
Hirai, S., Okazaki, K., Araki, N., Yoshimoto, K., Ito, H., Hijikata, K., *Energy Convers. Manag*., **36**, 471 (1995).
Hirai, S., Tabe, Y., Kamijo, S., Okazaki, K., *Therm. Sci. Eng.*, **8**, 1 (2000).
Hirai, S., Sanda, H. , *Am. Mineral.*, **89**, 1260 (2004).
Holder, G.D., Angert, P.F., in *Proc. 57th SPE Annual Technical Conference and Exhibition*, New Orleans, September 26–29, pp. SPE 11105 (1982).
Hong, H., Pooladi-Darvish, M., Bishnoi, P.R., *J. Can. Petrol. Technol.*, **42**, 45 (2003).
Huo, Z., Freer, E., Lamar, M., Sannigrahi, B., Knauss, D.M., Sloan, E.D., *Chem. Eng. Sci.*, **56**, 4979 (2001).
Ito, Y., Kamakura, R., Obi, S., Mori, Y., *Chem. Eng. Sci*, **58**, 107 (2003).
Jamaluddin, A.K.M., Kalogerakis, N., Bishnoi, P.R., *Can. J. Chem. Eng.*, **67**, 948 (1989).
Kashchiev, D., Firoozabadi, A., *J. Cryst. Growth*, **241**, 220 (2002a).
Kashchiev, D., Firoozabadi, A., *J. Cryst. Growth*, **243**, 476 (2002b).
Kato, M., Iida, T., Mori, Y.H., *J. Fluid Mechanics*, **414**, 367 (2000).
Kelland, M., Svartaas, T., Ovsthus, J., Namba, T., in *Proc. Gas Hydrates: Challenges for the Future* (Holder, G.D., Bishnoi, P.R., eds), *Ann. N.Y. Acad. Sci.*, **912**, 281 (2000).
Kimuro, H., Yamaguchi, F., Ohtsubo, K., Kusayanagi, T., Morishita, M., *Energy Convers. Manag.*, **34**, 1089 (1993).
Kini, R., Dec, S.F., Sloan, E.D., *J. Phys. Chem. A*, **108**, 9550 (2004).
Koh, C.A., Savidge, J.L., Tang, C.C., *J. Phys. Chem.*, **100**, 6412 (1996).
Koh, C.A., Wisbey, R.P., Wu, X.P., Westacott, R.E., Soper, A.K., *J. Chem. Phys.*, **113**, 6390 (2000).
Kuhs, W.F., Genov, G., Staykova, D.K., Hansen, T., in *Proc. Fifth International Conference on Gas Hydrates*, Trondheim, Norway, June 13–16, Paper 1003 (2005).
Kvamme, B., in *Proc. Second International Conference on Gas Hydrates*, Toulouse, France, June 2–6, p. 139 (1996).
Larson, M.A., Garside, J., *Chem. Eng. Sci.*, **41**, 1285 (1986).
Larson, R., Makogan, T., Knight, C., Sloan, E.D., in *Proc. Second International Conference on Gas Hydrates* (Monfort, J.P., ed.) Toulouse, France, June 2–6 (1996).
Lederhos, J., *The Transferability of Hydrate Kinetic Inhibitor Results between Bench Scale Apparatuses and a Pilot Scale Flow Loop*, Ph.D. Thesis, Colorado School of Mines, Golden, CO (1996).
Lederhos, J.P., Long, J.P., Sum, A., Christiansen, R.L., Sloan, E.D., *Chem. Eng. Sci.*, **51**, 1221 (1996).
Lee, J.D., Susilo, R., Englezos, P., in *Proc. Fifth International Conference on Gas Hydrates*, Trondheim, Norway, June 13–16, Paper 1034 (2005).
Long, J., *Gas Hydrate Formation Mechanism and Its Kinetic Inhibition*, Ph.D. Thesis, Colorado School of Mines, Golden, CO (1994).

Long, J.P., Sloan, E.D., *Int. J. Thermophysics*, **17**, 1 (1996).
Maini, B.B., Bishnoi, P.R., *Chem. Eng. Sci.*, **36**, 183 (1981).
Makogan, Y.F., *Hydrates of Natural Gas, Moscow, Nedra, Izadatelstro,* PennWell Books, Tulsa, Oklahoma, p. 237 in Russian (1981 in English) (1974).
Makogon, Y., Makogan, T., Holditch, S., in *Proc. Japan National Oil Conference*, 259, Tokyo, (1998).
Malegaonkar, M.B., Dholabhai, P.D., Bishnoi, P.R., *Can. J. Chem. Eng.*, **75**, 1090 (1997).
Masuda, Y., Fujinaga, G.A., Naganawa, S., Fujita, K., Hayashi, Y., in *Proc. Third International Conference on Gas Hydrates*, Salt Lake City, UT, July 18–22 (1999).
Matsumoto, M., Saito, S., Ohmine, I., *Nature*, **416**, 409 (2002).
Miers, H.A., Isaac, F., *Proc. Roy. Soc. (London)*, **A79**, 322 (1907).
Miller, K.W., Hildebrand, J.H., *J. Am. Chem. Soc.*, **90**, 3001 (1968).
Mochizuki, T., Mori, Y.H., In *Proc. Fifth International Conference on Gas Hydrates*, Trondheim, Norway, June 13–16, Paper 1009 (2005).
Mochizuki, T., Mori, Y.H., *J. Cryst. Growth*, **290**, 642 (2006).
Moon, C., Taylor, P.C., Rodger, P.M., *J. Am. Chem. Soc.*, **125**, 4706 (2003).
Mori, Y.H., *Energy Convers. Manag.*, **39**, 1537 (1998).
Mori, Y.H., *J. Cryst. Growth*, **223**, 206 (2001).
Moridis, G.J., in *Proc. SPE Gas Technology Symposium*, Calgary, Alberta, April 30–May 2, p. 75691 (2002).
Moudrakovski, I.L., McLaurin, G.E., Ratcliffe, C.I., Ripmeester, J.A., *J. Phys. Chem. B*, **108**, 17591 (2004).
Moudrakovski, I.L., Ratcliffe, C.I., Ripmeester, J.A., *Angew. Chem. Intl. Ed.*, **40**, 3890 (2001a).
Moudrakovski, I.L., Sanchez, A.A., Ratcliffe, C.I., Ripmeester, J.A., *J. Phys. Chem. B*, **105**, 12338 (2001b).
Muller-Bongartz, B., Wildeman, T.R., E.D. Sloan, Jr., in *Proc. Second International Offshore and Polar Engineering Conference*, p. 628 (1992).
Mullin, J.W., *Crystallization, 3rd Edition,* Butterworth-Heinmann, Oxford, U.K. (1993).
Mullin, J.W., Jancic, S.J., *Trans. Chem. Eng.*, **57**, 188 (1979).
Mullin, J.W., *Crystallization, 4th Edition,* Elsevier Science & Technology Books, Amsterdam (2001).
Natarajan, V., *Thermodynamics and Nucleation Kinetics of Gas Hydrates*, Ph.D. Thesis, University of Calgary, Alberta (1993).
Natarajan, V., Bishnoi, P.R., Kalogerakis, N., *Chem. Eng. Sci.*, **49**, 2075 (1994).
Nemethy, G., Scheraga, H.A., *J. Chem. Phys.*, **36**, 3382 (1962).
Nerheim, A.R., *Investigation of Gas Hydrate Formation Kinetics by Laser Light Scattering*, D. Ing. Thesis, Norwegian Institute of Technology, Trondheim, Norway (1993).
Nerheim, A.R., Svartaas, T.M., Samuelsen, E.J., in *Proc. Fourth International Offshore and Polar Engineering Conference*, Osaka, p. 323 (1994).
Nernst, W., *Z. fur Physik. Chemie*, **47**, 52 (1904).
Nesterov, A.N., Feklistov, V.V., *Instruments and Experimental Techniques* (Translation of *Pribory i Tekhnika Eksperimenta*), **42**, 265 (1999).
Nojima, K., Mori, Y.H., in *Proc. Tenth International Heat Transfer Conference* (Hewitt, G.F., ed.) Brighton, UK, **3**, 377 (1994).
Noyes, A.A., Whitney, W.R., *J. Am. Chem. Soc.*, **19**, 930 (1897).
Ohmura, R., Kashiwazaki, S., Mori, Y.H., *J. Cryst. Growth*, **218**, 372 (2000).
Ohmura, R., Shigetomi, T., Mori, Y.H., *J. Cryst. Growth*, 196, 164 (1999).
Ohmura, R., Ogawa, M., Yasuka, K., Mori, Y.J., *J. Phys. Chem. B*, **107**, 5289 (2003).

Ostergaard, K.K., Tohidi, B., Burgass, R.W., Danesh, A., Todd, A.C., *J. Chem. Eng. Data*, **46**, 703 (2001).
Ostwald, W., *Zeit. fur Physik Chemie*, **34**, 495 (1900).
Ouar, H., Cha, S.B., Wildeman, T.R., Sloan, E.D., *Trans I Chem. E.*, **70A**, 48 (1992).
Parent, J.S., *Investigations into Nucleation Behavior of the Clathrate Hydrates of Natural Gases*, M.Sc. Thesis, University of Calgary, Alberta (1993).
Parent, J.S., Bishnoi, P., *Chem. Eng. Commun.*, **144**, 51 (1996).
Pauling, L., *The Structure of Water,* Pergammon Press, New York, p. 1 (1959).
Peters, D., Selim, S., Sloan, E., in *Proc. Challenges for the Future: Gas Hydrates* (Holder, G.D., Bishnoi, P.R., eds), *Ann. N.Y. Acad. Sci.*, **912**, 304 (2000).
Poole, P.H., Sciortina, F., Essmann, U., Stanley, H.E., *Nature*, **360**, 324 (1993).
Radhakrishnan, R., Trout, B.L., *J. Chem. Phys.*, **117**, 1786 (2002).
Rahman, A., Stillinger, F.H., *J. Am. Chem. Soc.*, **95**, 7943 (1973).
Rahman, A., Stillinger, F.H., *Phys. Rev.* A, **10**, 368 (1974).
Rehder, G., Kirby, S., Durham, B., Stern, L., Peltzer, E.T., Pinkston, J., Brewer, P., *Geochimica Cosmochimica Acta*, **68**, 285 (2004).
Rodger, M., in *Proc. Gas Hydrates: Challenges for the Future*, (Holder, G.D., Bishnoi, P.R., eds), *Ann. N.Y. Acad. Sci.*, **912**, 474 (2000).
Rovetto, L.R., Strobel, T.A., Koh, C.A., Sloan, E.D., *Fluid Phase Equilib.*, **247**, 84 (2006).
Rowley, J.L., *Statistical Mechanics for Thermophysical Property Calculations*. Prentice-Hall, Englewood, NJ (1994).
Salamatin, A.N., Hondoh, T., Uchida, T., Lipenkov, V.Y., *J. Cryst. Growth*, **193**, 197 (1998).
Sastry, S., Debenedetti, P.G., Scioritino, F., Stanley, H.E., *Phys. Rev. Lett.*, **53**, 6144 (1996).
Schicks, J.M., Naumann, R., Erzinger, J., Hester, K.C., Koh, C.A., Sloan, E.D., *J. Phys. Chem. B*, **110**, 11468 (2006).
Schroeter, J.P., Kobayashi, R., Hildebrand, M.A., *Ind. Eng. Chem. Fundam.*, **22**, 361 (1983).
Selleck, F.T., Carmichael, L.T., Sage, B.H., *Ind. Eng. Chem.*, **44**, 2219 (1952).
Servio, P., Englezos, P., *AIChE J.*, **49**, 269 (2003a).
Servio, P., Englezos, P., *Crystl. Growth Design*, **3**, 61 (2003b).
Servio, P., Englezos, P., Bishnoi, P.R., in *Proc. Gas Hydrates: Challenges for the Future*, (Holder, G.D., Bishnoi, P.R., eds), *Ann. N.Y. Acad. Sci.*, **912**, 576 (2000).
Shimada, W., Takeya, S., Kamata, Y., Uchida, T., Nagao, J., Ebinuma, T., Narita, H., *Proc. Fifth International Conference on Gas Hydrates*, Trondheim, Norway, June 13–16, Paper 1032 (2005).
Shindo, Y., Lund, P.C., Fujioka, Y., Komiyama, H., *Int. J. Chemical Kinetics*, **25**, 777 (1993).
Skovborg, P., Gas Hydrate Kinetics, Ph.D. Thesis, Institut for Kemiteknik, Danmarks Tekniske Hojskole, Lyngby, Denmark (1993).
Skovborg, P., Ng, H.J., Rasmussen, P., Mohn, U., *Chem. Eng. Sci.*, **48**, 445 (1992).
Skovborg, P., Rasmussen, P., *Chem. Eng. Sci.*, **49**, 1131 (1994).
Sloan, E.D., in *Proc. 69th Annual Gas Processors Convention*, Phoenix, 8 (1990).
Sloan, E.D., Fleyfel, F., *AIChE J.*, **37**, 1281 (1991).
Sloan, E.D., Subramanian, S., Matthews, P.N., Lederhos, J.P., Khokhar, A.A., *Ind. Eng. Chem. Res.*, **37**, 3124 (1998).
Smelik, E.A., King, H.E., *Am. Mineral.*, **82**, 88 (1997).
Sorensen, C.M., in *Proc. 12th Int. Conf. on Prop. of Water and Steam*, Orlando, Fl, September (1994).
Speedy, R.J., *J. Phys. Chem.*, **91**, 3354 (1987).

Speedy, R.J., Madura, J.D., Jorgensen, W.L., *J. Phys. Chem.*, **91**, 909 (1987).
Stanley, H.E., Coniglio, A., Havlin, S., Lee, J., Schwarzer, S., in *On Clusters and Clustering* (Reynolds, P.J., ed.) Elsevier, Amsterdam, pp. 345 (1993).
Staykova, D.K., Kuhs, *J. Phys. Chem. B.*, **107**, 10299 (2003).
Stern, L., Hogenboom, D.L., Durham, W.B., Kirby, S.H., Chou, I.M., *J. Phys. Chem.*, **102**, 2627 (1998).
Stern, L.A., Circone, S., Kirby, S.H., Durham, W.B., *J. Phys. Chem.* B, **105**, 1756 (2001a).
Stern, L.A., Circone, S., Kirby, S.H., Durham, W.B., *Energy Fuels*, **15**, 499 (2001b).
Stern, L.A., Circone, S., Kirby, S.H., Durham, W.B., *Can. J. Phys.*, **81**, 271 (2003).
Stern, L., Circone, S., Kirby, S., Durham, W., in *Proc. Fifth International Conference on Gas Hydrates*, Trondheim, Norway, June 13–16, Paper 1046, 300 (2005).
Stillinger, F.H., in *Water in Polymers*, Vol. 1 (Rowland, S.P., ed.) American Chemical Society, Washington DC, p. 11 (1980).
Subramanian, S., *Measurements of Clathrate Hydrates Containing Methane and Ethane Using Raman Spectroscopy*, Ph.D. Thesis, Colorado School of Mines, Golden, CO (2000).
Subramanian, S., Sloan, E.D., In *Proc. Gas Hydrates: Challenges for the Future*, 912 (Holder, G.D., Bishnoi, P.R., eds), *Ann. N.Y. Acad. Sci.*, **912**, 583 (2000).
Sugaya, M., Mori, Y.H., *Chem. Eng. Sci.*, **51**, 3505 (1996).
Svandal, A., Kvamme, B., Granasy, L., Pusztai, T., *J. Phase Equilib. Diffusion*, **26**, 534 (2005).
Swaminathan, S., Harrison, S.W., Beveridge, D.L., *J. Am. Chem. Soc.*, **100**, 5705 (1978).
Takeya, S., Ebinuma, T., Uchida, T., Nagao, J., Narita, H., *J. Crystal Growth*, **237**, 379 (2002).
Takeya, S., Hori, A., Hondoh, T., Uchida, T., *J. Phys. Chem. B*, **104**, 4164 (2000).
Taylor, C.J., Adhesion Force between Hydrate Particles and Macroscopic Investigation of Hydrate Film Growth at the Hydrocarbon/Water Interface, Masters Thesis, Colorado School of Mines, Golden, CO (2006).
Taylor, C.J., Dieker, L.D., Miller, K.T., Koh, C.A., Sloan, E.D., *J. Colloid Interface Sci.*, (2006).
Tohidi, B., Anderson, R., Clennell, B., Burgass, R.W., Biderkab, A.-B., *Geology*, **29**, 867 (2001).
Tohidi, B., Anderson, R., Clennell, B., Yang, J., Bashir, A., Burgass, R., in *Proc. Fourth International Conference on Gas Hydrates*, Yokohama, Japan, May 19–23, 761 (2002).
Tohidi, B., Burgass, R.W., Danesh, A., Østergaard, K.K., Todd, A.C., in *Proc. Gas Hydrates: Challenges for the Future*, (Holder, G.D., Bishnoi, P.R., eds), *Ann. N.Y. Acad. Sci.*, **912**, 924 (2000).
Topham, D.R., *Chem. Eng. Sci.*, **39**, 821 (1984).
Truskett, T.M., Dill, K.A., *J. Chem. Phys.*, **117**, 5101 (2002).
Tse, J.S., Klug, D.D., *J. Supramol. Chem.*, **2**, 467 (2002).
Tsypkin, G.G., in *Proc. Gas Hydrates: Challenges for the Future*, (Holder, G.D., Bishnoi, P.R., eds), *Ann. N.Y. Acad. Sci.*, **912**, 428 (2000).
Turner, D., *Clathrate Hydrate Formation in Water-in-Oil Dispersions*, Ph.D. Thesis, Colorado School of Mines, Golden, CO (2005).
Uchida, T., Ebinuma, T., Kawabata, J., Narita, H., *J. Cryst. Growth*, **204**, 348 (1999a).
Uchida, T., Ebinuma, T., Mae, S., *Formation Rate Measurements of CO_2 Hydrate Film Formed at Liquid CO_2 Water Interface, Greenhouse Gas Control Technologies*, (Riemer, P., Eliasson, B., Wokaun, A., eds.) Elsevier, 1073 (1999b).

Uchida, T., Ikeda, I.Y., Takeya, S., Ebinuma, T., Nagao, J., Narita, H., *J. Cryst. Growth*, **237–239**, 383 (2002).
Udachin, K.A., Ratcliffe, C.I., Ripmeester, J.A., *J. Supramol. Chemistry*, **2**, 405 (2002).
Valeton, J.J.P., *Zeit. fur Kristallog*, **59**, 483 (1924).
Voller, V., Swaminathan, C.R., Thomas, B.G., *Int. J. Numer. Methods Eng*, **30**, 875 (1990).
Volmer, M., Weber, A., *Z. Phys. Chem. (Leipzig)*, **119**, 277 (1926).
Vysniauskas, A., Bishnoi, P.R., *Chem. Eng. Sci.*, **38**, 1061 (1983).
Walrafen, G.E., Chu, Y.C., *J. Phys. Chem.*, **99**, 10635 (1995).
Walrafen, G.E., Yang, W.H., Chu, Y.C., *Supercooled Liquids*, **21**, 287 (1997).
Westacott, R.E., Rodger, P.M., *J. Chem. Soc., Faraday Transactions*, **94**, 3421 (1998).
Wetlaufer, D.B., Malik, S.K., Stoller, L., Coffin, R.L., *J. Am. Chem. Soc*, **86**, 508 (1964).
Wilson, P.W., Heneghan, A.F., Haymet, A.D.J., *Cryobiology*, **46**, 88 (2003).
Wilson, P.W., Lester, D., Haymet, A.D.J., *Chem. Eng. Sci*., **60**, 2937 (2005).
Wyslouzil, B.E., Cheung, J.L., Wilemski, G., Strey, R., *Phys. Rev. Lett.*, **79**, 431 (1997).
Yakushev, V.S., Istomin, V.A., in *Proc. Physics and Chemistry of Ice* (Maeno, N., Hondoh, T., eds) Hokkaido University Press, Sapporo, 136 (1992).
Zachariassen, K.E., *Ice Nucleating Agents in Cold-Hardy Insects,* Springer-Verlag, Berlin (1982).

4 Estimation Techniques for Phase Equilibria of Natural Gas Hydrates

Introduction

Substantially different from ice, the phase equilibria of natural gas hydrates represents the most important set of hydrate properties. In contrast to kinetic phenomena, hydrate phase equilibria are well defined and determine a boundary to the kinetic problem. This chapter addresses hydrate phase equilibria with approximate methods that provide an understanding of the phenomena involved.

Engineers may ask, "When I plan to use a simulation package such as ASPEN PLUS™, PRO II™, UNISIM™, or even the CD provided with this book, why should I be concerned with simpler, less accurate methods of phase equilibria and diagrams? If I'm concerned with accuracy, why not use two prediction packages and compare the result?"

The answer addresses one of the key modern engineering dilemmas, that of providing engineering judgment to evaluate calculations from "black-box" complex computer codes. Computer programs may provide a number that may not be a good model of physical reality. The simpler methods in this chapter are very valuable, first for intuitive understanding and second to provide both a first estimation and a check of more complex calculations.

As one step toward understanding phase equilibria, the rigorous phase diagrams of the first edition have been greatly simplified, and those of the second edition have been corrected via recent experiments. Those who deal with gas production, transportation, and high temperature processing should find greater utility in these diagrams, which are restricted to the region above 0°F. However, gas processors dealing with lower, cryogenic temperatures may wish to refer to the first edition (1989) [or to Harmens and Sloan, (1990) or to Wierzchowski and Monson, (2006)] for more comprehensive phase diagrams.

At the conclusion of this chapter, the engineer should be able to answer questions such as the following:

1. What are pressure–temperature–composition bounds on sI and sII hydrate formation?
2. What is a typical pressure–temperature phase diagram for sH hydrates?
3. What rapid calculations can be made to check the prediction of a computer simulation?

4. What is a quick estimate of the thermodynamic inhibitor effect?
5. What are the accuracy limits of hydrate hand calculation methods?
6. How much heat is necessary to dissociate hydrates?

Just as engineering is sometimes considered to be an applied science, the concepts of this chapter should provide for applications—to hydrates in the earth (Chapter 7) and to hydrate problems in production, transportation, and processing of oil and natural gas (Chapter 8). As an introduction to the chapter, consider an example of some typical hydrate calculations.

Example 4.1: Estimates of Hydrate Formation Conditions

An engineer (or researcher) wishes to predict hydrate formation pressures of single guests of methane (CH_4) and of propane (C_3H_8) at 278.2 K, and to determine how those pressures would be affected by changing the gas composition to 95.6 mol% CH_4 + 4.4% C_3H_8.

Some Solution Methods

1. For simple C_3H_8 hydrates, the engineer could review the P–T phase diagram such as that shown in Figure 4.1 (reproduced from Figure 1.2) and note the regions of hydrate formation. He might then draw a straight line between the lower and upper quadruple points (Q_1 and Q_2 in Table 4.2) to obtain a semilogarithmic plot of pressure versus the absolute temperature, as shown in Figure 4.1. The pressure may be semilogarithmically interpolated to obtain a pressure of 0.46 MPa at 278.2 K. For CH_4, however, there is no upper quadruple point on the P–T phase diagram, so this technique is not available.
2. For CH_4 hydrates, the engineer may turn to an Antoine-like relation ($\ln P = a + b/T$, with constants in Table 4.1) to calculate a hydrate formation pressure of 4.04 MPa. A corresponding value for C_3H_8 at 278.2 K is calculated as 0.54 MPa, slightly different from the value of 0.46 obtained in method 1. Note that solution methods 1 and 2 imply a semilogarithmic correlation for single guest hydrates.
3. These simple hydrate predictions compare well with the data of Thakore and Holder (1987) at 4.5 and 0.51 MPa for CH_4 and C_3H_8, respectively, at 278.2 K.
4. For the mixture of 95.6% CH_4 + 4.4% C_3H_8, a first approach would be a linear or semilogarithmic, compositional interpolation of the mixture formation pressure at 278.2 K, but those values are 4.3 and 4.1 MPa, respectively, both of which are in error by 300%.
5. For accurate mixture formation pressure estimation, a simple phase diagram or Antoine-like equation does not exist, but the engineer may use the gas gravity chart (Figure 1.4) to approximate the phase

equilibrium condition, as detailed in Section 4.2.1. The gas gravity is 0.596 and the formation pressure is predicted as 1.95 MPa. (See Section 4.2.1 for details and examples of this calculation.)

6. If a better estimate of the mixture formation pressure is needed, the engineer may use the K_{vsi} value method in Section 4.2.2 to obtain an estimated hydrate pressure of 1.26 MPa.
7. The engineer may finally turn to the computer simulation packages mentioned above to obtain a mixture hydrate dissociation pressure of 1.26 MPa.
8. The final test of such mixture calculations is comparison with data. In this case, the mixture hydrate formation pressure at 278.2 K was measured by Thakore and Holder (1987) as 1.30 MPa. Note that the small amount of C_3H_8 (4.4%) caused the mixture dissociation pressure (1.3 MPa) to be closer to that of simple C_3H_8 (0.50 MPa) than that of CH_4 (4.31 MPa). Note also that the K_{vsi} method generated in 1942 provides a result comparable to that of the modern computer method.

The above example illustrates that the determination of simple (one guest) hydrate formation from water and gas has been experimentally established with a high degree of certainty. However, an infinite number of mixture hydrate possibilities exist for the eight sI and sII hydrate formers in natural gas (CH_4, C_2H_6, C_3H_8, i-C_4H_{10}, n-C_4H_{10}, CO_2, H_2S, N_2). In the three-phase region, the prediction methods are easily justified by the large effort and expense to obtain hydrate data.

Hydrate phase diagrams for water–hydrocarbon systems provide a convenient overview of the calculation types. These diagrams differ substantially from the normal hydrocarbon phase diagrams primarily due to hydrates and the hydrogen bonds inherent in aqueous systems. The phase diagrams of Section 4.1 provide an overview for the calculation methods in this chapter and the next.

Section 4.2 deals with the most useful hydrate equilibria—calculations of temperatures and pressures at which hydrates form from gas and free water. In this section, two historical methods, namely, the gas gravity method (Section 4.2.1) and the K_{vsi} value method (Section 4.2.2), for calculating the pressure–temperature equilibrium of three phases (liquid water–hydrate–vapor, L_w–H–V)[1] are discussed. With the gas gravity method in Section 4.2.1.1, a method is given for limits to expansion, as for flow through a valve. In Section 4.2.2 a distribution coefficient (K_{vsi}) method is provided to determine whether a component prefers residing in the hydrate or the vapor phase. These methods provide initial estimates for the calculation and provide a qualitative understanding of the equilibria. A statistical

[1] Phase (and abbreviation) nomenclature given in order of decreasing water concentration in each phase.

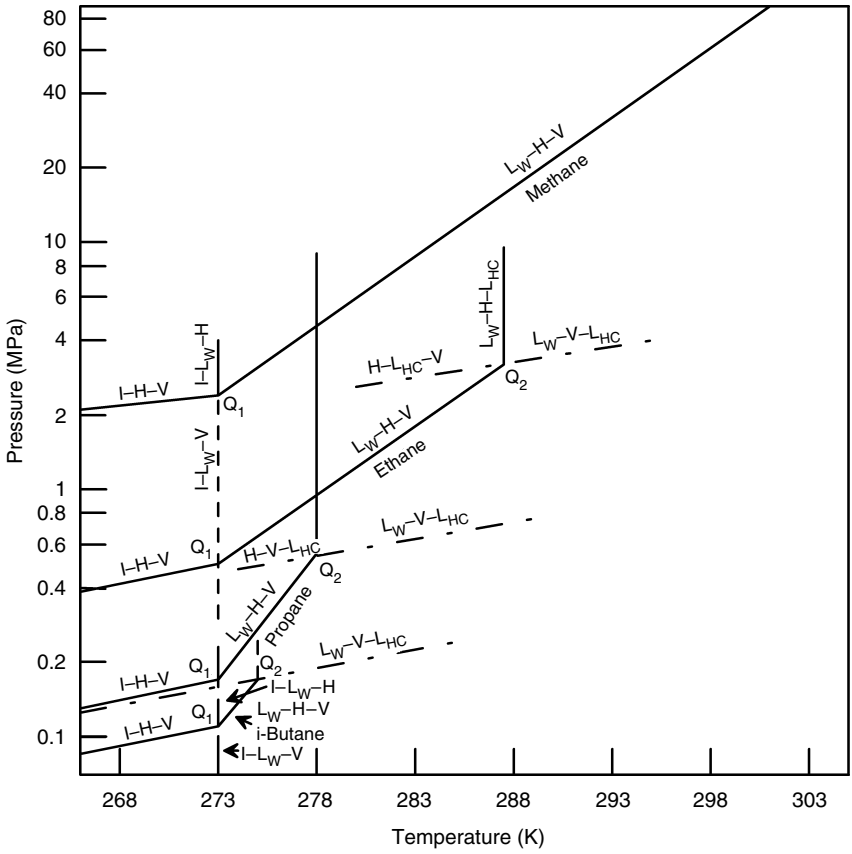

FIGURE 4.1 Phase diagrams for some simple natural gas hydrocarbons that form hydrates. Q_1: lower quadruple point, Q_2: upper quadruple point. (Modified, from Katz, D.L., Cornell, D., Kobayashi, R., Poettman, F.H., Vary, J.A., Elenbaas, J.R., Weinaug, C.F., *Handbook of Natural Gas Engineering* (1959). With permission from McGraw-Hill.)

thermodynamic method provides the best three-phase calculation; however, because it is both more comprehensive and detailed, it is relegated to Chapter 5. Because the discovery of structure H (Ripmeester et al., 1987) was more recent compared to sI/sII there are no approximate methods for pressure and temperature phase equilibrium in the current chapter, but the statistical mechanics method is applied to that structure in Chapter 5, obviating the approximate methods.

The two calculation methods in Section 4.2 enable prediction of the three-phase (L_W–H–V) gas mixture region extending between the two quadruple points Q_1 and Q_2 in Figure 4.1. Section 4.3 provides a method to use the techniques of Section 4.2 to locate both quadruple points on a pressure–temperature plot. Section 4.3 also discusses equilibrium of three condensed phases [aqueous liquid–hydrate–hydrocarbon liquid (L_W–H–L_{HC})]. Determination of equilibrium from condensed phases provides an answer to the question, "Given a liquid

TABLE 4.1
Hydrate Formation for Three-Phase Conditions of Single Natural Gas Components, Using P [kPa] = exp($a + b/T$ [K])

Component	Type	T range (°C)	a	b
Methane	L_W–H–V	0 to 25	38.980	−8533.80
Methane	I–H–V	−25 to 0	14.717	−1886.79
Ethane	L_W–H–V	0 to 14	44.273	−10424.25
Ethane	I–H–V	−25 to 0	17.511	−3104.54
Propane	L_W–H–V	0 to 5	67.130	−16921.84
Propane	I–H–V	−25 to 0	17.156	−3269.65
Isobutane	L_W–H–V	0 to 1.5	61.740	−15571.43
Isobutane	I–H–V	−25 to 0	18.950	−3887.32
Carbon dioxide	L_W–H–V	0 to 11	44.580	−10246.28
Carbon dioxide	I–H–V	−25 to 0	18.594	−3161.41
Nitrogen	L_W–H–V	0 to 25	37.808	−7688.63
Nitrogen	I–H–V	−25 to 0	15.129	−1504.28
Hydrogen sulfide	L_W–H–V	0 to 25	34.828	−8266.10
Hydrogen sulfide	I–H–V	−25 to 0	16.560	−3270.41

Source: From Kamath, V.A., *Study of Heat Transfer Characteristics During Dissociation of Gas Hydrates in Porous Media*, Ph.D. Dissertation University of Pittsburgh, University Microfilms No. 8417404, Ann Arbor, MI, 1984. With permission.

hydrocarbon, without gas, and a free water phase, at what pressure and temperature will hydrates form?" The structure H exception is considered in Chapter 5, because, as noted in Chapter 2, the large guest molecule required is a liquid, while the small molecule is a gas at ambient conditions.

The inhibition of three-phase hydrate formation is discussed in Section 4.4. These predictions enable answers to such questions as, "How much methanol (or other inhibitor) is required in the free water phase to prevent hydrates at the pressures and temperatures of operation?" Classical empirical techniques such as that of Hammerschmidt (1934) are suitable for hand calculation and provide a qualitative understanding of inhibitor effects. It should be noted that only thermodynamic inhibitors are considered here. The new low-dosage hydrate inhibitors [LDHIs, such as kinetic inhibitors (KIs) or antiagglomerants (AAs)] do not significantly affect the thermodynamics but the kinetics of hydrate formation; LDHIs are considered in Chapter 8.

The calculation of two-phase (hydrate and one other fluid phase) equilibrium is discussed in Section 4.5. The question, "To what degree should hydrocarbon gas or liquid be dried in order to prevent hydrate formation?" is addressed through these equilibria. Another question addressed in Section 4.5 is, "What mixture solubility in water is needed to form hydrates?"

Finally, Section 4.6 concerns the relationship of phase equilibrium to other hydrate properties. The hydrate application of the Clapeyron equation is discussed

with regard to calculating heats of formation and the hydrate number. Other techniques for determining the hydrate number are also discussed.

The calculation methods in this chapter and the next should be taken only as estimates, within the accuracy limits cited. Since predictions are only as good as available experimental data, when questions arise, the examined data should be taken as reliable and the calculation method questioned. If it were economical to obtain accurate data for each case, that would be preferred. However, at the time of writing this book, the typical cost is a week of effort and $2000/data point, once the apparatus is calibrated.

Measurable Variables and Gibbs' Phase Rule: How to Ask a Valid Phase Equilibrium Question

In phase equilibria there are five common types of variables:

1. Pressure
2. Temperature
3. Concentrations of the gas, liquid(s), or hydrate phases
4. Volume or density
5. Phase amounts

In the above list, the pressure and temperature are commonly measured in every process, so it is normal to discuss phase equilibrium in terms of those variables, as will be done in this chapter and the next.

However, engineers normally can access only the concentrations of the water-free hydrocarbon phase, and that of the hydrocarbon-free water/ice phase, rather than the total phase concentrations. Other concentrations are generally difficult to measure, except by unusual techniques. While the concentration of the water-free hydrocarbon phase is readily measured (via chromatography, for example) the water concentration of the hydrocarbon phase is generally so low (typically parts per thousand or less) that sophisticated techniques (dual chromatographic columns, etc.) are required for reliable measurement.

In addition, the water phase usually has very low concentrations of hydrocarbons (ice has none) so that sophisticated techniques are needed to measure the low concentrations of hydrocarbons in water, which are usually much less than 1 mol%. While some scientists may have these instruments available, engineers do not typically have access to such sophisticated measurement techniques.

Similarly, the last two variables in the above list (volume/density and phase amounts) are difficult to measure with commonly available instruments. As a result, hydrate phase equilibria are normally determined in terms of four variables: (1) pressure, (2) temperature, (3) water-free hydrocarbon phase composition, and (4) the free-water phase composition (excluding hydrocarbons but including salts, alcohols, and glycols).

The other variables such as the density, hydrate composition, and phase amounts may be predicted by phase equilibria, and confirmed by a few

measurements that are difficult to obtain and thus not common. For example, as shown in Chapter 6, spectroscopic devices such as NMR or Raman spectroscopy can be used to determine the hydrate composition or hydrocarbons dissolved in water; however, access to NMR or Raman methods are available only in a few laboratories. Similarly, the phase amounts (water, vapor, and hydrate) have only been measured a few times, notably in the laboratory of Tohidi et al. (1994).

Normally, the practicing engineer can specify the water-free hydrocarbon composition, and the amount of inhibitor (salts, alcohols, or glycols) in the free water phase, and would like to predict the three-phase (L_w–H–V) hydrate formation pressure, given the lowest temperature of the process (or predict the formation temperature, given the highest pressure in the process). Protection at the extreme conditions (lowest T and highest P) helps ensure hydrate protection at the other process conditions.

One essential question is, "How many variables must be specified to obtain a solution unique to the phase equilibrium calculation?" It is possible to have an infinite number of solutions to a problem if too few variables are specified—or no solution if too many variables are specified. One answer to this question is provided by Gibbs' Phase Rule (Gibbs, 1928, p. 96), simply stated for nonreacting systems by the equation:

$$F = C - P' + 2 \tag{4.0}$$

where

F = the number of intensive variables needed to specify the system
C = the number of components in the system
P' = the number of phases in the system.

An intensive variable [such as the temperature (T), pressure (P), or individual mole fractions of a single phase (x_{si}, x_i, or y_i of the hydrate, liquid, or vapor phases, respectively)] is defined as a measured value that is independent of the phase amount. For example, T, P, x_{si}, x_i, y_i or density are intensive variables, while phase masses, volumes, or amounts are extensive variables, and thus not addressed by Gibbs' Phase Rule.

Consider the potential for hydrate formation from methane gas and free water. One question would be, "At what temperature (T) will hydrates form for a given pressure (P)?" Before the calculation is done, one might wonder if there is a unique solution for the problem, or if the problem is under-specified (has an infinite number of solutions). Since the components are methane and water $C = 2$, and the phases are three (L_W–H–V) by the Gibbs' Phase Rule, one intensive variable ($F = 1$), such as either T or P must be specified in order to obtain a unique solution for the formation of hydrates.

Thus by specifying either T or P, there is a unique solution to determine the other intensive variables (such as the T or P that was not specified, as well as the other intensive variables listed above). Again, extensive variables such as the volumes or phase amounts are not considered in Gibbs' Phase Rule.

As a special case of this example, one might specify that a natural gas mixture is in very large excess relative to the water phase (as in a gas-dominated pipeline), so that the gas composition does not change upon hydrate formation. Effectively, $C = 1$ for the gas components, with an additional component for the water (total $C = 2$). With three phases (L_W–H–V), there must be one intensive variable ($F = 2 - 3 + 2$) for a constant gas mixture composition (in large excess) relative to the water phase, specifying that the highest pipeline pressure is sufficient to determine the temperature (and the other intensive variables) at which hydrates form with a gas of fixed composition.

On the other hand, if a pure methane (or fixed gas composition) pipeline has no free water but only dissolved water in the gas, an operator may ask, "What is the temperature for a pipeline pressure of 2150 psia, at which hydrates will form without a free water phase?" Because $C = 2$ (water and fixed gas composition) and $P' = 2$ (gas and hydrates), there are two intensive variables ($F = 2 - 2 + 2$) required to specify the system; so there is no unique solution, but an infinite number of temperatures can be obtained in the two-phase (H–V) region, when only pressure is specified. A better question would be, "For a methane (or fixed gas composition) pipeline operating at 2150 psia and a water content of 200 ppm what would be the temperature at which hydrates will form?" In this case, two intensive variables (P and y_W) are specified so there is a unique solution.

In the last common condition, for four phases in equilibrium (such as I–L_W–H–V) at the lower quadruple point, the number of intensive variables must equal the number of components minus two. For a mixture of methane and water (or for a gas mixture in large excess so that the composition does not change) no intensive variables are required—that is, the lower quadruple point is fixed at a unique pressure, temperature, as well as the composition of all the phases.

See Section 4.1.5 for other examples of how Gibbs' Phase Rule works in the methane + water phase diagram. Section 5.2 shows the application of the Gibbs' Phase Rule for hydrate guests of methane, ethane, propane, and their mixtures.

4.1 Hydrate Phase Diagrams for Water + Hydrocarbon Systems

The phase behavior of hydrocarbon + water mixtures differs significantly from that of normal hydrocarbon mixtures. Differences arise from two effects, both of which have their basis in hydrogen bonding. First, the hydrate phase is a significant part of all hydrocarbon + water phase diagrams for hydrocarbons with a molecular size lower than 9 Å. Second, water and hydrocarbon molecules are so different that, in the condensed state, two distinct liquid phases form, each with a very low solubility in the other.

For a rigorous discussion of phase diagrams, the reader is referred to Harmens and Sloan (1990) or to Huo et al. (2003), which represent an extension and in some cases a correction to those published earlier by Kobayashi (1951), by Kobayashi in Katz et al. (1959), by Bourrie and Sloan (1986), or in the earlier editions of this

monograph (also see Section 1.1.3). Recently, Wierzchowski and Monson (2006) provided a molecular simulation of the phase diagram, with an accompanying discussion. The remainder of Section 4.1 provides a qualitative understanding of phase diagrams. Quantitative predictions may be obtained by methods in later sections of this chapter and, most accurately, in Chapter 5.

While a first approach to phase diagrams is given here, Section 5.2 extends the phase diagrams in this portion of Chapter 4 to single, binary, and ternary mixtures of methane, ethane, and propane. The reader may wish to consult Section 5.2 for a more enlightening discussion that applies the van der Waals and Platteeuw method to the most common components of natural gases.

4.1.1 Pressure–Temperature Diagrams of the $CH_4 + H_2O$ (or $N_2 + H_2O$) System

Consider the pressure–temperature (P–T) diagram of Figure 4.2a, shown schematically for the methane + water system or the nitrogen + water system at conditions above and below the hydrate region. Since methane is the major component of natural gas, this diagram and the associated T–x diagram (Section 4.1.5) provide phase behavior understanding in the hydrate region for gas systems without a liquid hydrocarbon phase.

The structure of all such phase diagrams rests on experimental data for phase boundaries, and on the Gibbs' Phase Rule discussion of the previous section. The diagrams use symbols of I, L_W, H, V, and L_{HC} to represent ice, liquid water, hydrate, vapor, and liquid hydrocarbon, listed in order of decreasing water contents. By the Gibbs' Phase Rule a two-component system such as methane + water is represented on a pressure–temperature diagram as an area (for two phases), a line (three phases), or a point (four phases). In order to obtain nearly straight lines, in all of Section 4.1 semilogarithmic plots (ln P versus T) are used.

Consider quadruple point (Q_1) in Figure 4.2a where four phases (I–L_W–H–V) coexist. The quadruple point temperature approximates 273 K for all hydrate formers, yet the quadruple pressures vary widely (e.g., 0.0113 MPa for i-C_4H_{10}, 2.56 MPa for CH_4, and 14.3 MPa for N_2). Quadruple point (Q_1) is the starting point for four, three-phase lines:

1. The L_W–H–V line has pressure–temperature conditions of the most interest in natural gas systems.
2. The I–H–V line, which has a lower P–T slope than the L_W–H–V line. Note that there is a data paucity in the region below 273 K, which is avoided industrially (hence a lack of funding) due to problems with ice formation.
3. The I–L_W–H line rises vertically from the quadruple point, with very large pressure changes for small temperature changes, as typified by incompressible phases.
4. The I–L_W–V line that connects the quadruple point to the water triple point (I–L_W–V_W) (273.16 K, 0.62 kPa), denotes the transition between

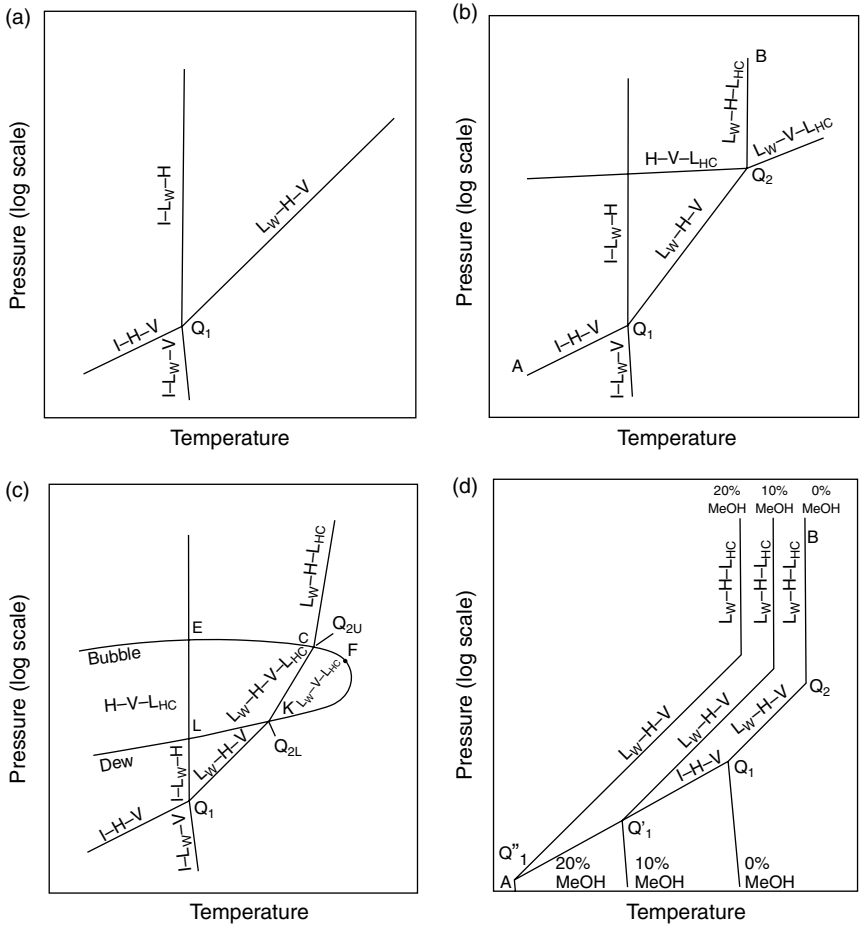

FIGURE 4.2 Pressure–temperature diagrams. (a) Methane + water or nitrogen + water system in the hydrate region. (b) Hydrocarbon + water systems with upper quadruple points. (c) Multicomponent natural gas + water systems. (d) Hydrocarbon + water systems with upper quadruple points and inhibitors.

water and ice without hydrate formation. Since Q_1 approximates 273 K for all natural gas systems, the I–L_W–V line extends almost vertically below Q_1 to 0.62 kPa.

In all of Figure 4.2 note that composition, a third dimension, has been compressed onto the two shown (pressure and temperature), so that the lines shown may project from or into the page.

The equation of Table 4.1 from Kamath (1984) enables prediction of the most common regions of interest of simple natural gas components—the pressure and temperature conditions for both L_W–H–V and I–H–V. When using the equation,

TABLE 4.2
Natural Gas Component Quadruple Points

Component	T (K), P (MPa) at Q_1	T (K), P (MPa) at Q_2
Methane	272.9, 2.563	No Q_2
Ethane	273.1, 0.530	287.8, 3.39
Propane	273.1, 0.172	278.8, 0.556
Isobutane	273.1, 0.113	275.0, 0.167
Carbon dioxide	273.1, 1.256	283.0, 4.499
Nitrogen	271.9, 14.338	No Q_2
Hydrogen sulfide	272.8, 0.093	302.7, 2.239

carefully note the temperature limits. It would be a mistake (for example) to extend the prediction of the L_W–H–V region beyond the temperature of either quadruple point Q_1 or Q_2 (given in Table 4.2), where those three phases cannot exist.

1. The pressures and temperatures of the L_W–H–V and the I–H–V lines mark the limits to hydrate formation. At higher temperatures or lower pressures of both lines, hydrate cannot form and the system will contain only aqueous and hydrocarbon fluid phases, while hydrate formation can occur to the left of L_W–H–V and I–H–V. Since ice and hydrates both cause flow problems, a gas pipeline rule of thumb is to keep the system temperature above the ice point and to the right of the L_W–H–V and the I–H–V lines, or to displace the L_W–H–V line below the pipeline operating conditions by injection of a thermodynamic inhibitor such as methanol.
2. The L_W–H–V line has no upper pressure or temperature limit because the pure methane (or nitrogen) vapor–liquid critical points (at 191 and 126 K respectively) are far below the quadruple point Q_1. Such low critical temperatures prevent intersection of the vapor pressure line with the L_W–H–V line above 273 K to produce an upper quadruple point.
3. Similarly, no upper pressure limit to the I–L_W–H line has been found. Note that these phases are all incompressible, so that a very large pressure change results from only a small temperature change, in a closed system.
4. The areas between the three-phase lines represent the two-phase region held in common with the bounding three-phase lines. For instance, the area between L_W–H–V and I–H–V is the H–V region in which hydrates are in equilibrium only with vapor (water saturated). Similarly, the L_W–H two-phase region exists between L_W–H–V and I–L_W–H lines, and the I–H two-phase region exists between the I–L_W–H and I–H–V lines. In this two-dimensional plot the two-phase regions overlap, indicating that the three-phase lines are not all in the plane of the page, but have been compressed into two dimensions, from three, with the third

dimension being composition. The compression of the composition axis onto the *P–T* plane causes the two-phase regions to overlap. Two-phase regions are discussed with *T–x* diagrams in Section 4.1.5.

5. The diagram schematic is the same for simple hydrate systems of sI ($CH_4 + H_2O$) and sII ($N_2 + H_2O$) as well as those of fixed natural gas mixture compositions, without a liquid hydrocarbon phase. Systems containing a liquid hydrocarbon are similar in behavior to the $C_3H_8 + H_2O$ diagram, discussed in Section 4.1.2.

It has been shown (Bansal et al., 1993) that curvature in the L_W–H–V line in Figure 4.2a results if the guest vapor–liquid critical temperature is slightly below the L_W–H–V conditions.

4.1.2 Systems (e.g., $H_2O + C_2H_6$, C_3H_8, or i-C_4H_{10}) with Upper Quadruple Points

Figure 4.2b shows the equivalent of Figure 4.2a to be slightly more complex for systems such as ethane + water, propane + water, isobutane + water, or water with the two common noncombustibles, carbon dioxide or hydrogen sulfide. These systems have a three-phase (L_W–V–L_{HC}) line at the upper right in the diagram. This line is very similar to the vapor pressure (V–L_{HC}) line of the pure hydrocarbon, because the presence of the almost pure water phase adds a very low vapor pressure (a few mmHg at ambient conditions) to the system.

Figure 4.2b shows that at the intersection of the L_W–V–L_{HC} line with the L_W–H–V line, a second quadruple point ($Q_2 = L_W$–H–V–L_{HC}) is formed. Measured upper quadruple points for simple natural gas components are shown in Table 4.2. Point Q_2 is the origin for two additional three-phase lines: (1) a L_W–H–L_{HC} line that is almost vertical due to the three incompressible phases and (2) a H–V–L_{HC} line, of less concern, because it exists within the L_W–H–L_{HC} and the L_W–H–V boundaries.

For systems with two quadruple points, the hydrate region is bounded by line I–H–V at conditions below Q_1, line L_W–H–V between Q_1 and Q_2, as well as line L_W–H–L_{HC} at conditions above Q_2. Hydrates can form at lower temperatures and higher pressures to the left of the region enclosed by the three lines in Figure 4.2b; to the right, no hydrates are possible. Upper quadruple point Q_2 is often approximated as the maximum temperature of hydrate formation, because line L_W–H–L_{HC} is almost vertical; however see data in Chapter 6 for exceptions.

In Figure 4.2b, the areas between the three-phase lines represent two-phase regions held in common with the three-phase lines. The area bound by three three-phase lines (I–L_W–H, L_W–H–V, and L_W–H–L_{HC}) is the L_W–H region in which hydrates are in equilibrium only with liquid water. Similarly, the H–V region is between the three three-phase lines (H–V–L_{HC}, L_W–H–V, and I–H–V). Finally, the H–L_{HC} two-phase region exists between L_W–H–L_{HC} and H–V–L_{HC} lines and the I–H two-phase region exists between the I–L_W–H and I–H–V lines.

See Section 4.1.5 for a T–x diagram with another perspective of these two-phase regions.

Note that the last paragraph contains two-phase regions (H–V, H–L_{HC}, and I–H) for hydrate equilibrium with a phase that is not liquid water. There is a common misconception that hydrates cannot form without a liquid water phase, a condition clearly possible in these diagrams. Professor Kobayashi's laboratory measured hydrate conditions without a free water phase from vapor or liquid systems from 1973 to 2000. Such equilibria are of interest for gas and gas condensate pipelines without a free water phase.

4.1.3 Pressure–Temperature Diagrams for Multicomponent Natural Gas Systems

In Figure 4.2c for natural gases without a liquid hydrocarbon (or when liquid hydrocarbons exist below 273 K), the lower portion of the pressure–temperature phase diagram is very similar to that shown in Figure 4.2a. Two changes are (1) the L_W–H–V line would be for a fixed composition mixture of hydrocarbons rather than for pure methane (predictions methods for mixtures are given in Section 4.2 and in Chapter 5) and (2) quadruple point Q_1 would be at the intersection of the L_W–H–V line and 273 K, at a pressure lower than that for methane. The other three-phase lines of Figure 4.2a (for I–L_W–H and I–H–V) have almost the same slope at Q_1. Otherwise, the same points in Section 4.1.1 apply.

However, for the case in which natural gases contain heavier components, the upper portion of the diagram is more like that shown in Figure 4.2b. A straight line labeled L_W–H–V represents the hydrate formation region equivalent to the region between quadruple point Q_1 (I–L_W–H–V) and the upper quadruple point Q_2 (L_W–H–V–L_{HC}) in Figure 4.2b. One significant change in Figure 4.2c is that quadruple point Q_2 becomes a line, as indicated in the next paragraph.

When a liquid hydrocarbon mixture is present, the L_W–V–L_{HC} line in Figure 4.2b broadens to become an area, such as that labeled CFK in Figure 4.2c. This area is caused by the fact that a single hydrocarbon is no longer present, so a combination of hydrocarbon (and water) vapor pressures creates a broader phase equilibrium envelope. Consequently, the upper quadruple point (Q_2) evolves into a line (KC) for the multicomponent hydrocarbon system.

Line KC may not be straight in the four-phase region but is drawn that way for illustration. The location of the lower point K is determined by the intersection point of the phase envelope ECFKL with the L_W–H–V line, determined by the methods of Section 4.2 or Chapter 5. To determine the upper point C, first a vapor–liquid equilibrium calculation is performed, assuming the liquid phase (exiting the envelope at point C) equals the vapor composition at point K. That liquid is used to calculate a vapor composition which is used in a vapor–liquid water–hydrate calculation to determine the upper intersection with the phase envelope ECFKL. A more thorough treatment of the calculation of multicomponent equilibrium with a condensed hydrocarbon phase is given in Sections 4.3.2.

4.1.4 Pressure–Temperature Diagrams for Systems with Inhibitors

The presence of thermodynamic inhibitors (e.g., salts, alcohols, or glycols) causes a change in the pressure–temperature diagram, as illustrated in Figure 4.2d. For simplicity the diagram only shows the hydrate bounding region (to the left of line AQ_1Q_2B) for a pure component system with upper and lower quadruple points (Q_1 and Q_2). Line AQ_1Q_2B in Figure 4.2d is equivalent to line AQ_1Q_2B in Figure 4.2b with three slopes that change at the quadruple points.

In Figure 4.2d, the presence of a thermodynamic inhibitor (e.g., methanol) shifts the upper two-thirds of the line Q_1Q_2B to the left, approximately parallel (on a semilogarithmic plot of ln P versus T) to the uninhibited line. With inhibitor, however, the transition temperature from water to ice (Q_1) is decreased, so that the inhibited L_W–H–V line intersects the I–H–V at a lower point (labeled Q_1' for 10 wt% methanol and Q_1'' for 20 wt% methanol). The inhibited three parallel lines represent L_W–H–V or L_W–H–L_{HC} equilibrium at methanol concentrations (marked 0%, 10%, and 20% MeOH) in the free water phase.

Each line in Figure 4.2d (except for the lower, almost vertical I–L_W–V lines) bounds hydrate formation conditions listed with a methanol concentration in the free water phase. To the left of each line with "H" in the label, hydrates will form with a water phase of the given methanol composition; to the right of the line hydrates will not form. For example, when the free water phase has 10% methanol, hydrates will not form at pressure–temperature conditions to the right of the line marked 10% MeOH. Yet if no methanol were present, the hydrates would form at pressures and temperatures between the two lines marked 10% and 0% MeOH. Similarly, for process pressure and temperature conditions between the lines marked 10% and 20%, at least 20% methanol in the free water phase would be required to prevent hydrate formation.

For clarity Figure 4.2d has omitted the lines analogous to three three-phase lines in Figure 4.2b (I–L_W–H that intersects vertically at Q_1 and L_W–V–L_{HC}, and H–V–L_{HC} that intersect at Q_2). Such lines are less important for hydrate formation, but join the diagram at the appropriate, shifted quadruple points. For systems without an upper quadruple point (as in Figure 4.2a) or systems with a liquid hydrocarbon region (as in Figure 4.2c) the hydrate boundary region is similarly shifted to the left of (and approximately parallel to) the uninhibited phase lines.

Other inhibitors such as monoethylene glycol (EG or MEG) and salts shift the hydrate lines similarly, but to a different degree. However, methanol is the most economical inhibitor on a weight basis. Quantitative predictions of inhibitor effects are provided in Sections 4.4 and 5.3.

4.1.5 Temperature–Composition Diagrams for Methane + Water

In the first edition (1989) of this monograph the details of all isobaric temperature–composition (T–x) diagrams were discussed, in a synopsis of

Harmens and Sloan (1990). The second edition (1998) simplified those diagrams further. This third edition corrects slight errors in the isobaric T–x diagram using the work of Huo et al. (2003) and the recent phase diagram simulations of Wierzchowski and Monson (2006). However, much of the value of such diagrams may be obtained from the discussion of a single figure. Consider Figure 4.3, the T–x diagram and accompanying discussion from Kobayashi and Katz (1949), as slightly corrected by Huo et al. (2003) for $CH_4 + H_2O$ at a pressure around 48 bar (about 700 psia), just above the critical pressure for methane, but a little lower than normal pipeline pressures.

Figure 4.3 is not drawn to scale. Some regions are expanded and are shown schematically due to the mutual immiscibility of liquid hydrocarbons and water. There are three single phase regions in the diagram: (1) the highest is the single vapor region (V), (2) at the upper left there is the liquid water (L_W) single phase

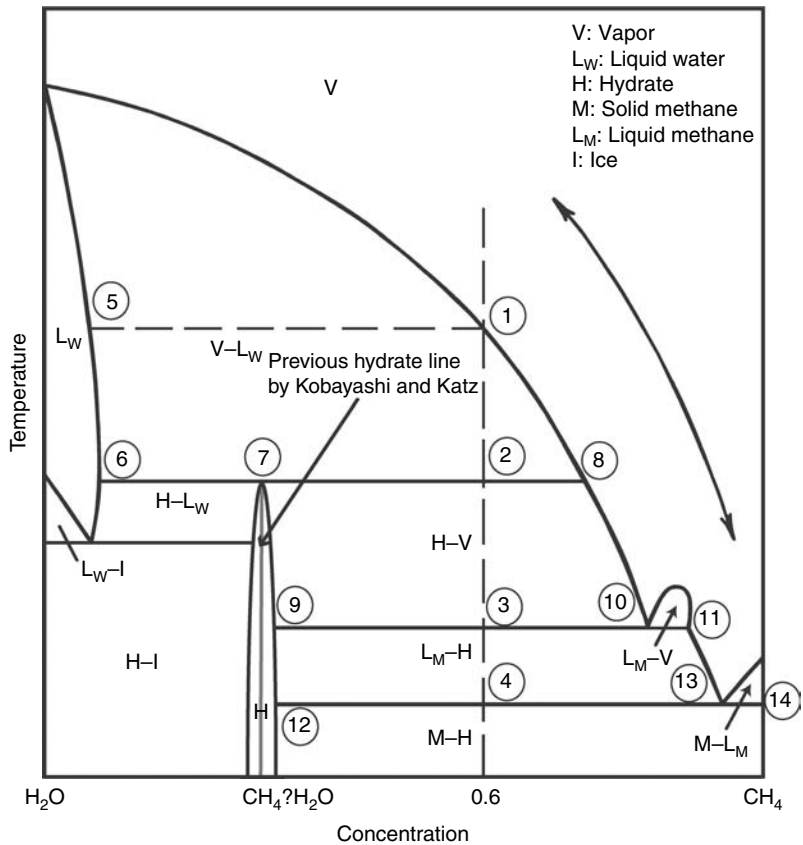

FIGURE 4.3 Temperature–composition diagrams for methane and water. (Reproduced from Huo, Z., Hester, K., Miller, K.T., Sloan, E.D., *AIChE J.*, **49**, 1300 (2003). With permission from the American Institute of Chemical Engineers.)

region that has less than 0.1 mol% dissolved methane, and (3) the hydrate region that is shown of small variable concentrations straddling the concentration marked $CH_4 \cdot ?H_2O$. Each area in Figure 4.3 is marked with the appropriate two-phase equilibrium. Horizontal solid lines represent three-phase equilibrium, all involving the hydrate phase.

To illustrate the phase transitions on a T–x diagram, consider the cooling of a 60 mol% $CH_4 + 40\%$ H_2O mixture from a high temperature at a constant pressure in the vapor region, shown as a dashed vertical line. The vapor exists as a single-phase until the water dew point (Point 1) is reached, where the composition of the equilibrium liquid water with a little methane dissolved is Point 5. Further cooling of the gas–liquid mixture causes the amount of the water phase to increase; note that by Gibbs' Phase Rule ($F = C - P' + 2$) two intensive variables (e.g., the P of the isobaric diagram and T) are required to specify each fluid composition at the two-phase borders.

Cooling the system is continued until the temperature of Point 2, where the hydrate phase (vertical area that begins at Point 7) forms from the vapor (Point 8) and liquid (Point 6). At Point 2 three phases (L_W–H–V) coexist for two components, so Gibbs' Phase Rule ($F = 2-3+2$) indicates that only the isobaric pressure of the entire diagram is necessary to obtain the temperature and the concentrations of the three phases (L_W, H, and V) in equilibrium.

At the three-phase condition, the calculated methane mole fractions in the aqueous, sI hydrate, and vapor phases are 0.0014 (Point 6), 0.14 (Point 7), and 0.9997 (Point 8) respectively, illustrating that the aqueous and vapor concentrations shown in Figure 4.3 are expanded for illustration purposes. Note that the isobaric three-phase temperature at Point 2 marks one P–T condition on the three-phase line (L_W–H–V) shown in Figure 4.2a, with prediction methods in Table 4.1 and Section 4.2. In both Figures 4.2a and 4.3, at temperatures above this line, hydrates cannot form at the specified pressure.

Further heat removal at constant temperature will result in the complete conversion of the free water phase to hydrate at the same initial overall composition of 60% methane. The system enters the two-phase hydrate–vapor (H–V) region just below the horizontal line at Point 2. By specifying the water composition of the vapor in the two-phase (H–V) region (along the negatively sloping line between Points 8 and 10), the gas processor determines how dry the gas must be to prevent the possibility of hydrate formation. The position of the vapor composition line determines, for example, whether a glycol drying column or a molecular sieve dessicant should be used to dehydrate the gas.

At still lower temperatures of the original mixture, some of the vapor condenses to liquid methane at the three-phase (H–V–L_M) boundary (Point 3). Again the three-phase temperature and phase compositions (Points 9, 10, and 11) are specified by the single variable of pressure ($F = C - P' + 2 = 2 - 3 + 2$). Below this three-phase line the vapor phase is totally condensed to a liquid resulting in a two-phase (H–L_M) region between Points 3 and 4.

Point 4 is at the temperature of the lowest three-phase line (H–L_M–M), which occurs just below the solidification point of pure methane (M). Below this line

(connecting Points 12, 4, 13, and 14) the liquid methane phase disappears and hydrate exists only with solid methane.

A comprehension of Figure 4.3 has value because a similar phase diagram could be drawn for a natural gas of fixed composition between the quadruple points (Q_1 and Q_{2L}). The same phase transitions and boundaries would qualitatively occur, with the artificial constraint that all hydrocarbon phases be of the same composition as the original gas. A second useful outcome of binary phase diagrams like Figure 4.3 is the use of the lever rule (Koretsky, 2004, p. 367) at constant temperature to determine relative phase amounts; note that the lever rule can be applied for quantitatively correct phase diagrams.

4.1.6 Solubility of Gases Near Hydrate Formation Conditions

The solubility of hydrocarbons in the aqueous phase determines the width of the region L_W marked on the T–x diagram of Figure 4.3. Section 3.1.1.2 provides numerical values of atmospheric solubilities, enthalpies, and entropies of solution. The solubility phenomena is that water molecules form networks with short-lived, partial hydrogen-bonded clusters around solute molecules, giving solubility maxima for molecules with hydrate guest diameters. In Section 3.1.2.1 it was suggested that clustering is related to hydrate metastability and nucleation.

There are only few data sets of aqueous solubility for systems with hydrates: (1) methane and ethane solubility in water as a function of temperature ramping rate (Song et al. 1997), (2) carbon dioxide solubility in water by Yamane and Aya (1995), (3) methane in water and in seawater (Besnard et al., 1997), (4) methane in water in L_w–H region [see Servio and Englezos (2002) and Chou and Burruss, Personal Communication, December 18, 2006, Chapter 6]. As a standard for comparison, Handa's (1990) calculations for aqueous methane solubility are reported in Table 4.3.

While Table 4.3 shows solubility both above and below the hydrate point, at the three-phase hydrate condition Handa's predictions show a sharp maximum in solubility with pressure at constant temperature. In Holder's laboratory, Toplak (1989) measured the solubility of gas in liquid water around the hydrate point, both in water that had formed hydrates and in water with no residual structure; his results show no dramatic change in pure component solubility at the three-phase (L_W–H–V) condition. Kobayashi and coworkers (Besnard et al., 1997) measured a significant solubility increase at the hydrate point beyond that calculated using Henry's law. However, comprehensive solubility measurements around the hydrate point await further experiments.

4.1.7 Pressure–Temperature Diagrams for Structure H Systems

The pressure–temperature diagram for structure H has both similarities and differences from those diagrams shown above. Because the new hydrate was discovered

TABLE 4.3
Calculations of Methane Solubility in Water and Seawater, at Conditions Above and Below the Hydrate Point

Temperature = 273.15 K			Temperature = 278.15 K		
P (bar)	Water $10^3\ x_{CH_4}$	Seawater $10^3\ x_{CH_4}$	P (bar)	Water $10^3\ x_{CH_4}$	Seawater $10^3\ x_{CH_4}$
1	0.04667	0.03587	1	0.04022	0.03133
26.29[a]	1.113	NA	42.73[a]	1.473	NA
28.95[b]	NA	0.9334	49.54[b]	NA	1.297
50	1.931	1.484	100	2.801	2.182
100	3.194	2.455	150	3.555	2.769
150	4.024	3.093	200	4.105	3.198
200	4.619	3.550	250	4.544	3.539
250	5.095	3.916	300	4.926	3.836
300	5.506	4.232	350	5.267	4.102
350	5.879	4.519	400	5.582	4.347
400	6.222	4.783	450	5.875	4.576
450	6.545	5.031	500	6.153	4.793
500	6.849	5.264			

[a] Three-phase hydrate formation pressure in water.
[b] Three-phase hydrate formation pressure in seawater.

Source: From Handa, Y.P., *J. Phys. Chem.*, **94**, 2652, 1990. With permission.

in 1987, few data have been determined and thus limit the discussion. For the most comprehensive treatment, the reader is referred to the thesis of Mehta (1996).

A phase diagram for xenon + neo-hexane is presented in Figure 4.4, because the best measurements are available for this system (Makogon et al., 1996). While xenon is not a component of natural gas (or condensate), and because the xenon diameter is only 0.2 Å larger than CH_4, the phase diagram for CH_4 + neo-hexane is similar, but at higher pressures. The schematic of Figure 4.4 is very similar for many structure H systems in natural gas and for hydrocarbon processing.

The following points should be noted regarding the structure H phase diagram shown in Figure 4.4:

1. The temperatures and pressures for the sH system are very similar to those found in sI and sII diagrams. If a hydrate forms in a pipeline with both gas and condensate/oil phases present, examining the pressure–temperature conditions may be insufficient to determine the hydrate crystal structure.
2. Two quintuple points (Q_1 and Q_2) fix the positions of the lines in Figure 4.4. Each point (Q_1 and Q_2) is the origin of five four-phase lines. However, only the two lines of central importance (discussed below) have been measured from each quintuple point.

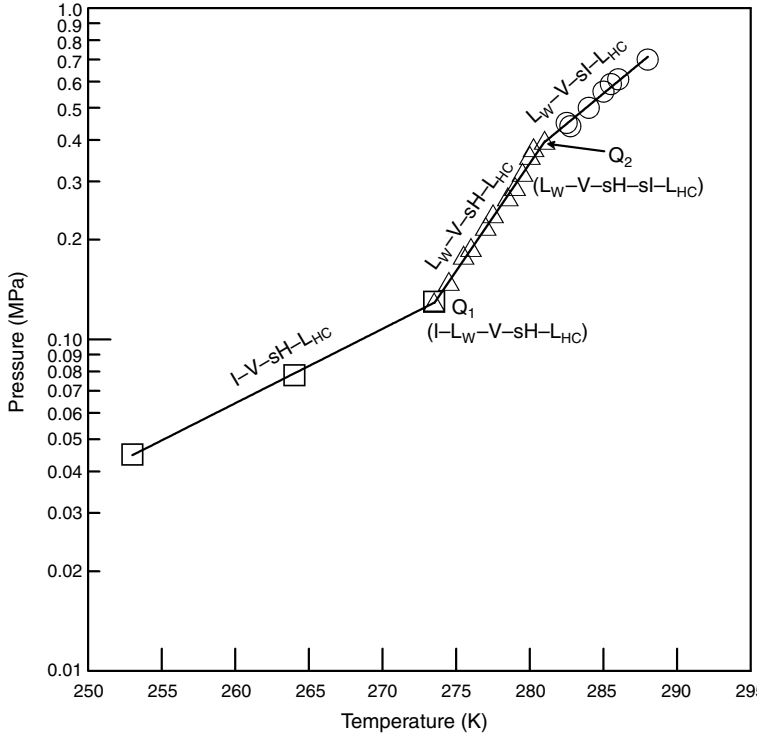

FIGURE 4.4 Pressure–temperature diagram for Xenon + Neo-hexane. (Reproduced from Makogon T.Y., Mehta, A.P., Sloan, E.D., *J. Chem. Eng. Data*, **41**, 315 (1996). With permission from the American Chemical Society.)

3. Structure H has only four-phase equilibrium lines (as opposed to the three-phase lines in Figure 4.2). Four-phase lines are required by Gibbs' Phase Rule, because a minimum of three components (a large and small guest, and water) are present. Structure H can only form with two guests (minimum)—one in both small cavities (5^{12} and $4^3 5^6 6^3$) and one in the large ($5^{12}6^8$) cavity; water must also be present. The large hydrate component is usually present as a liquid with a low vapor pressure. In unusual cases (e.g., adamantane) the large guest component may be present in the system as a solid.
4. The lower quintuple point (Q_1) is the location of five coexisting phases—namely, I–L_W–sH–V–L_{HC}. The position of Q_1 is determined by the intersection of the I–sH–V–L_{HC} line and the L_W–sH–V–L_{HC} line, close to the ice point temperature (273.15 K). However, the pressure of Q_1 is a function of the hydrate guests.
5. The upper quintuple point (Q_2) has a common line with Q_1 (L_W–sH–V–L_{HC}), but it also is the origin of a new line (L_W–sI–V–L_{HC}). At temperatures higher than Q_2 the hydrate phase is sI rather than sH.

Therefore Q_2 places an upper temperature limit on sH, while allowing for sI hydrate equilibrium at higher temperatures.

With the above beginning, much remains to be done with such a phase diagram, and this is an area of active research. Ripmeester and Ratcliffe (1991) noted that because structure H systems form with many hydrocarbon systems, there is the chance it may dominate as a hydrate type. Mehta and Sloan (1996a) discuss cases in which structure H forms in preference to sII in condensate systems. However, measurements by Tohidi et al. (2001), and Mehta and Ripmeester (2002) suggested that for most reservoir fluids, sII would be the common hydrate with sH as the exception. It should be noted that early workers (Becke et al., 1992) were surprised to find sH while investigating a liquid hydrocarbon system of interest to North Sea operations. On the strength of gas compositions Sassen and MacDonald (1994) and Pohlman et al. (2005) reason that sH hydrates were found in the Gulf of Mexico and the Cascadia Margin, respectively.

4.2 Three-Phase (L_W–H–V) Equilibrium Calculations

The conditions of three-phase (L_W–H–V) equilibrium are the most useful. In particular, methods to calculate the temperature and pressure at which hydrates form from a given gas composition and free water have both industrial and academic applications.

There are comparatively few measurements of the hydrate phase composition, due to experimental difficulty. Hydrate phase difficulties arise because water is often occluded in the hydrate mass, separation of hydrate and water is difficult, and the hydrate phase of mixtures is often inhomogeneous in experiments. Consequently, the ratio of water to hydrocarbon is often inaccurate. As discussed in Chapter 6, only over the last two decades have experimental techniques (e.g., diffraction and NMR and Raman spectroscopy) become accurate enough to determine the degree of filling of hydrate cavities with different types of molecules.

In this section two prediction techniques are discussed, namely, the gas gravity method and the K_{vsi} method. While both techniques enable the user to determine the pressure and temperature of hydrate formation from a gas, only the K_{vsi} method allows the hydrate composition calculation. Calculations via the statistical thermodynamics method combined with Gibbs energy minimization (Chapter 5) provide access to the hydrate composition and other hydrate properties, such as the fraction of each cavity filled by various molecule types and the phase amounts.

Because the two prediction techniques of this chapter were determined over half a century ago, they apply only to sI and sII hydrates, without consideration of the more recent sH, which always contains a heavier component. For structure H equilibrium, only the statistical thermodynamics method of Chapter 5 is available for prediction of hydrate pressure, temperature, and composition.

The two calculation techniques in this chapter may be regarded as successive approximations to hydrate phase equilibrium, increasing both in accuracy and in

sophistication. The first method, in Section 4.2.1, based upon the parameter of gas gravity, is a simple graphical technique that provides a first-order accuracy estimate of hydrate formation. The second prediction technique of Section 4.2.2, the K_{vsi}-value method, is both more accurate and slightly more complex than the gravity method. Both methods are suitable for hand calculation.

A third technique is based upon the statistical thermodynamics approach of van der Waals and Platteeuw (1959a) and provides the best approximation to hydrate phase equilibrium. It has the additional advantage of being extendable to all phase equilibrium regions discussed above. Unfortunately, this third method is too lengthy for inclusion in this chapter without disruption of presented concepts. The discussion of the third method is deferred until Chapter 5; a CSMGem computer program and User's Manual on the CD with this book provides access; the Appendix has a User's Guide—with examples of this program.

4.2.1 The Gas Gravity Method

The simplest method of determining the temperature and pressure of a gas mixture three-phase (L_W–H–V) conditions is available through the gas gravity charts of Katz (1945). Gas gravity is defined as the molecular mass of the gas divided by that of air. In order to use this chart, reproduced as Figure 4.5 from Figure 1.4,

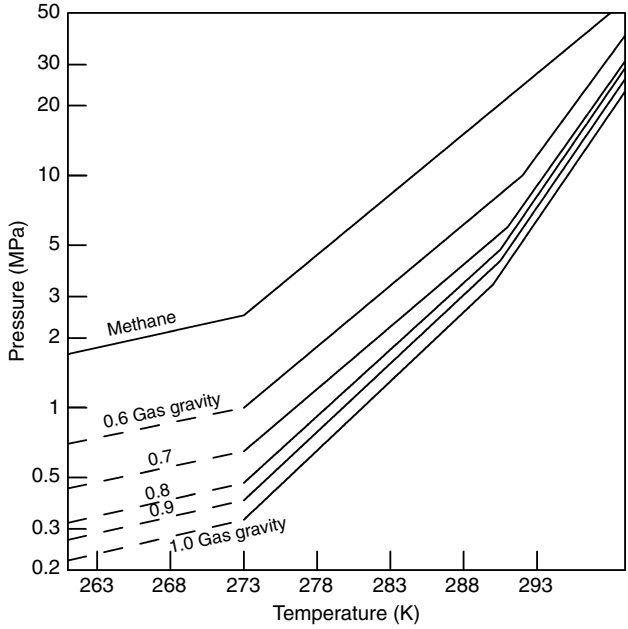

FIGURE 4.5 Gas gravity chart for prediction of three-phase (L_W–H–V) pressure and temperature. (Reproduced from Katz, D.L., *Trans. AIME*, **160**, 140 (1945). With permission from the American Institute of Mining, Metallurgical, and Petroleum Engineers.)

the gas gravity is calculated and either temperature or pressure is specified. The second intensive variable (either pressure or temperature) at which hydrates will form is read directly from the chart. The following example from the original work by Katz illustrates chart use.

Example 4.2: Calculating Hydrate Formation Using Gas Gravity Chart

Find the pressure at which a gas composed of 92.67 mol% methane, 5.29% ethane, 1.38% propane, 0.182% i-butane, 0.338% n-butane, and 0.14% pentane form hydrates from free water at a temperature of 283.2 K (50°F).

Solution

The gas gravity is calculated as 0.603 by the procedure below:

Component	Mol fraction y_i	Mol wt MW	Avg mol wt in mix $y_i \cdot$ MW
Methane	0.9267	16.043	14.867
Ethane	0.0529	30.070	1.591
Propane	0.0138	44.097	0.609
i-Butane	0.00182	58.124	0.106
n-Butane	0.00338	58.124	0.196
Pentane	0.0014	72.151	0.101
	1.000		17.470

$$\text{Gas Gravity} = \frac{\text{MW of Gas}}{\text{MW of Air}} = \frac{17.470}{28.966} = 0.603$$

At 283.2 K, the hydrate pressure is read as 3.1 MPa.

Similarly Example 4.1 used the gas gravity method to predict hydrate pressure of 1.95 MPa at 278.2 K for a mixture of 95.6% CH_4 + 4.4% C_3H_8 as compared to the experimental value of 1.3 MPa.

The purpose of the original chart was to enable the determination of the hydrate limits to adiabatic expansion of a gas, as detailed in Section 4.2.1.1. The hydrate formation lines on Figure 4.5 appear to be fairly linear at low temperatures with a slope change above 288 K for each gravity; this slope change is intentional and has been ascribed to a change in hydrate structure (Katz, D.L., Personal Communication, November 14, 1983).

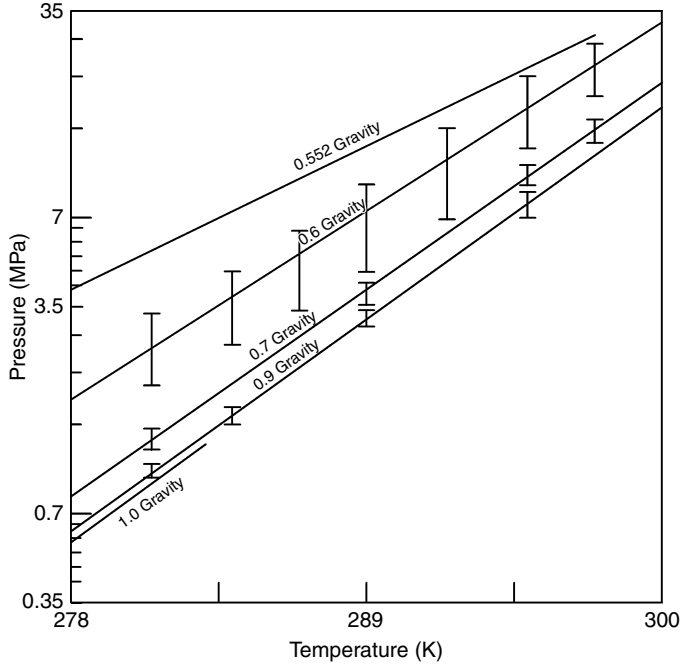

FIGURE 4.6 Gas gravity chart error bars. (Reproduced from Sloan, E.D., in *Proc. 63rd Annual Convention of Gas Processors Association*, **63**, 163 (1984). With permission from the Gas Processors Association.)

All of the qualitative trends shown in Figure 4.5 are correct and thus provide a valuable heuristic as a check for more sophisticated calculations. For example, the figure correctly indicates a logarithmic pressure increase with temperature over a short range. Over a wider temperature range the logarithmic pressure is more nearly linear with reciprocal absolute temperature. The figure also correctly shows that gases with heavier components cause hydrates to form at lower pressures for a given temperature (or at higher temperatures for a given pressure).

The gas gravity method to predict hydrate formation was generated from a limited amount of data as well as with calculations performed (and therefore the accuracy determined) via the K_{vsi}-value method of Section 4.2.2. Typical calculated error bars (Sloan, 1984) for the gas gravity chart are presented in Figure 4.6, compared against the statistical thermodynamic approach of Chapter 5. The original chart of Figure 4.5 was generated for gas containing only hydrocarbons, and so should be used with caution for those gases with substantial amounts of noncombustibles (i.e., CO_2, H_2S, N_2). While this method is very simple, it should be considered as approximate. In approximately 60 years since its conception, more hydrate data and prediction methods have caused the gravity method to be used as a first estimate, whose principal asset is ease of calculation.

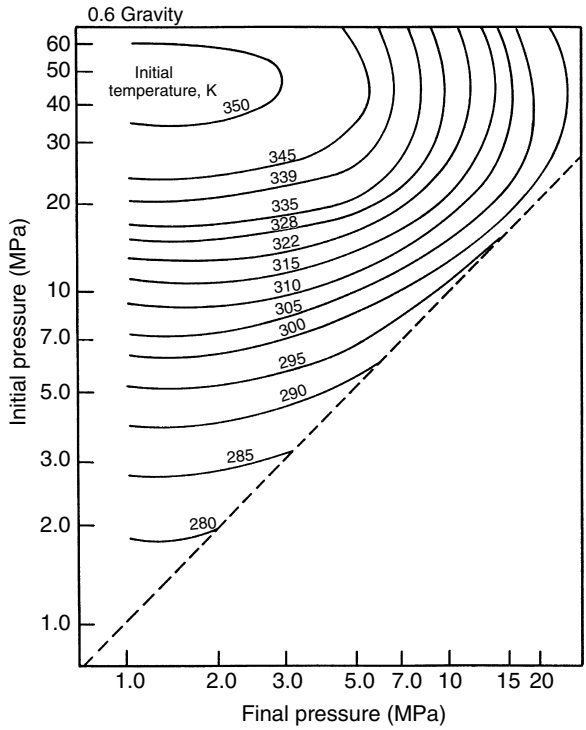

FIGURE 4.7 Joule–Thomson limits to 0.6 gravity gas expansion. (Reproduced from Katz, D.L., *Trans. AIME*, **160**, 140 (1945). With permission from the American Institute from Mining, Metallurgical, and Petroleum Engineers.)

4.2.1.1 Hydrate limits to gas expansion through a valve

The generation of the hydrate Joule–Thomson charts, such as Figure 4.7, for hydrate formation limits to gas adiabatic expansion was the original goal for construction of the hydrate gas gravity chart in Figure 4.5. A series of "expansion limits" or Joule–Thomson charts for gas gravities between 0.55 and 1.0 are available in the original article by Katz (1945). Figures 4.7 through 4.9 (for gas gravities of 0.6, 0.7, and 0.8, respectively) are presented as those of the highest utility. These Joule–Thomson charts were generated using the initial Mollier (enthalpy–entropy) charts for natural gas by Brown (1945), without accounting for the expansion of any free water present before the valve—assuming a single-phase expansion of natural gas, to the initiation limit of hydrates.

The pressure and temperature of the gas normally decreases upon expansion along an isenthalpic curve ($\Delta H = 0$) until the intersection with the hydrate boundary of Figure 4.5 is encountered, which provided one point on a figure such as Figure 4.7. Multiple points were calculated to construct each figure. The charts enabled the user to estimate the limits to adiabatic expansion before

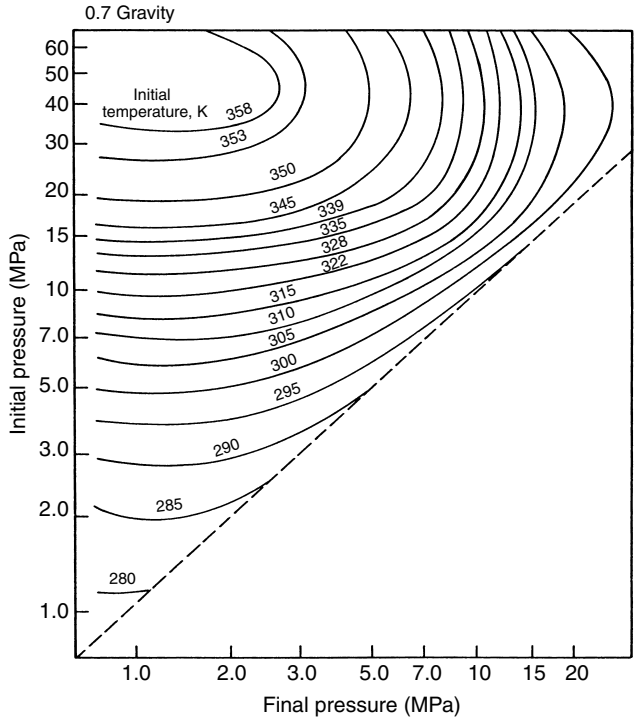

FIGURE 4.8 Joule–Thomson limits to 0.7 gravity gas expansion. (Reproduced from Katz, D.L., *Trans. AIME*, **160**, 140 (1945). With permission from the American Institute of Mining, Metallurgical, and Petroleum Engineers.)

hydrate formation occurred. The examples given below, of the use of Figure 4.7, were also taken from the original work by Katz (1945).

Example 4.3: Calculations of Hydrate Formation on Gas Expansion

1. To what pressure may a 0.6 gravity gas at 13.8 MPa (2000 psia) and 311 K (100°F) be expanded without danger of hydrate formation?

Solution

From Figure 4.7 read 7.24 MPa (1050 psia).

2. A 0.6 gravity gas is to be expanded from 10.34 MPa (1500 psia) to 3.45 MPa (500 psia). What is the minimum initial temperature that will permit the expansion without danger of hydrates?

Solution

From Figure 4.7 the answer is read as 310 K (99°F) or above.

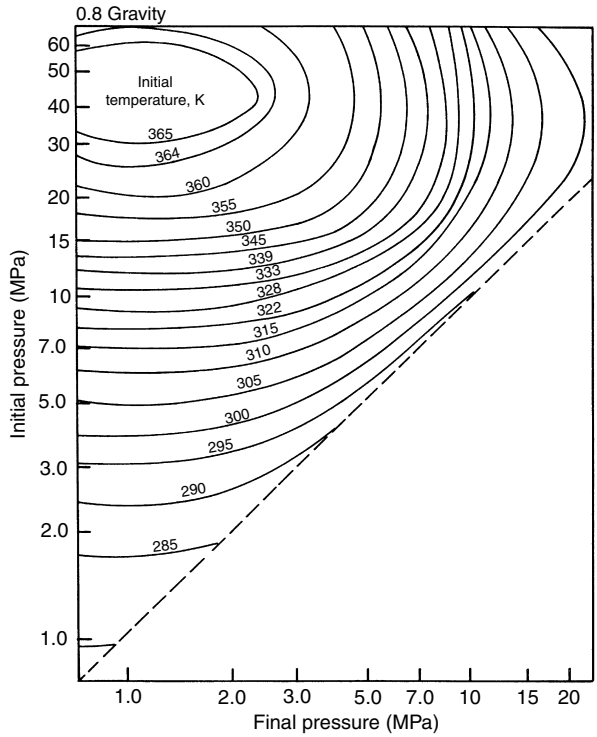

FIGURE 4.9 Joule–Thomson limits to 0.8 gravity gas expansion. (Reproduced from Katz, D.L., *Trans. AIME*, **160**, 140 (1945). With permission from the American Institute of Mining, Metallurgical, and Petroleum Engineers.)

Figures 4.7 through 4.9 are provided for hydrate limits to isenthalpic Joule–Thomson expansions, such as that which occurs when a gas with entrained free water droplets flows through a valve. A similar set of charts could in principle be determined for hydrate limits to isentropic ($\Delta S = 0$) expansions such as would occur when a gas flows through a perfect turboexpander of a modern gas processing plant. To date, however, no such charts have been generated.

The inaccuracies listed in the previous section for the gas gravity chart are inherent in the expansion charts of Figures 4.7 through 4.9 due to their method of derivation. Accuracy limits to these expansion curves have been determined by Loh et al. (1983) who found, for example, that the allowable 0.6 gravity gas expansion from 339 K and 24 MPa was 2.8 MPa rather than the value of 4.8 MPa, given in Figure 4.7.

The work of Loh et al. (1983) was done using the same principles as those used to generate Figure 4.7. That is, from the initial temperature and pressure, an isenthalpic cooling curve, and its intersection with the hydrate three-phase locus, was determined. However, the isenthalpic line was determined via the Soave–Redlich–Kwong equation-of-state rather than the Mollier charts of

Brown, and the statistical thermodynamic method of van der Waals and Platteeuw (1959a) was substituted for the three-phase hydrate line prediction by the gas gravity chart of Katz.

4.2.2 The Distribution Coefficient (K_{vsi}-Value) Method

The distribution coefficient method, often called the "K_{vsi}-value" method, was conceived by Wilcox et al. (1941) and finalized by Carson and Katz (1942). The best methane, ethane, and propane charts are from the latter reference. Updated charts are presented for carbon dioxide (Unruh and Katz, 1949), hydrogen sulfide (Noaker and Katz, 1954), nitrogen (Jhaveri and Robinson, 1965), isobutane (Wu et al., 1976), and n-butane (Poettmann, 1984), as well as for a method that is a function of hydrate structure (Mann et al., 1989).

Carson and Katz noted that their experimental hydrate composition changed at different temperatures and pressures in a manner indicative of a solid solution of mixtures, rather than segregated macroscopic quantities of pure hydrocarbons within the hydrate. The concept of a solid solution enabled the notion of the mole fraction of a guest component in the solid phase hydrate mixture, on a water-free basis. Carson and Katz defined a vapor–solid distribution coefficient (K_{vsi}) for each component as

$$K_{vsi} \equiv y_i / x_{si} \tag{4.1}$$

where

y_i = mole fraction of component i in the water-free vapor and
x_{si} = mole fraction of component i in the water-free, solid hydrate.

The K_{vsi} values for natural gas components are presented as a function of temperature and pressure in Figures 4.10 through 4.17. By viewing these charts one may quantitatively determine in which phase a component will concentrate. For example, components such as methane and nitrogen have K_{vsi} values always greater than unity, so they concentrate in the vapor rather than the hydrate; components such as propane or isobutane with K_{vsi} values normally less than unity are concentrated in the hydrate phase. Equation 4.2 was used to fit all of the K_{vsi} values in Figures 4.10 through 4.17.

$$\begin{aligned}\ln K_{vsi} = {} & A + B^*T + C^*\Pi + D^*T^{-1} + E^*\Pi^{-1} + F^*\Pi^*T + G^*T^2 + H^*\Pi^2 \\ & + I^*\Pi^*T^{-1} + J^*\ln(\Pi^*T^{-1}) + K^*(\Pi^{-2}) + L^*T^*\Pi^{-1} + M^*T^{2*}\Pi^{-1} \\ & + N^*\Pi^*T^{-2} + O^*T^*\Pi^{-3} + Q^*T^3 + R^*\Pi^{3*}T^{-2} + S^*T^4\end{aligned} \tag{4.2}$$

where

Π = pressure (psia) and
T = temperature (°F).

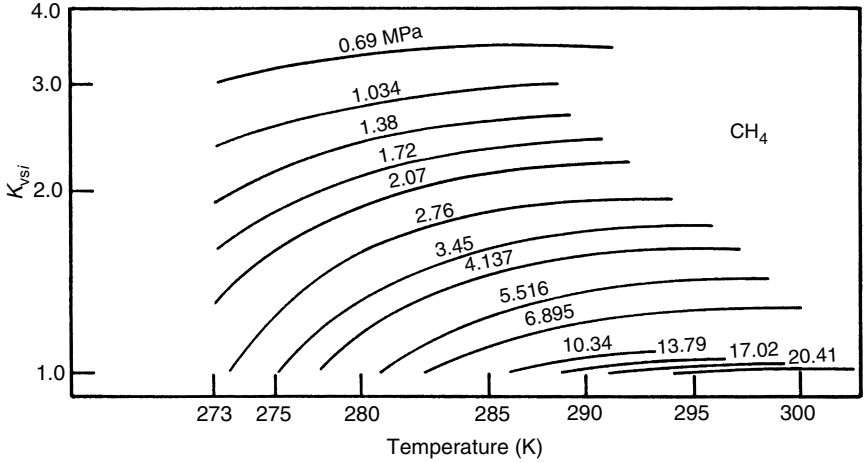

FIGURE 4.10 Methane K_{vsi} chart. (Reproduced from Carson, D.B., Katz, D.L., *Trans. AIME*, **146**, 150 (1942). With permission from the American Institute of Mining, Metallurgical, and Petroleum Engineers.)

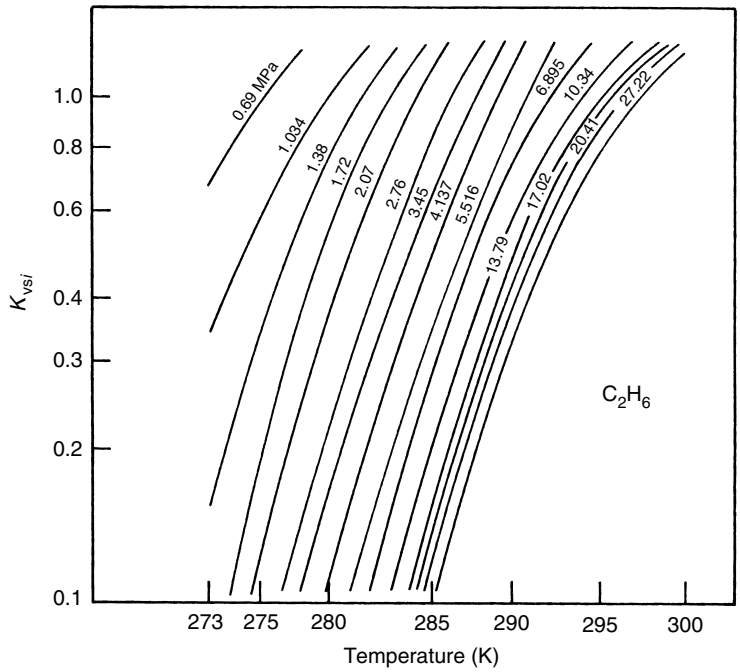

FIGURE 4.11 Ethane K_{vsi} chart. (Reproduced from Carson, D.B., Katz, D.L., *Trans. AIME*, **146**, 150 (1942). With permission from the American Institute of Mining, Metallurgical, and Petroleum Engineers.)

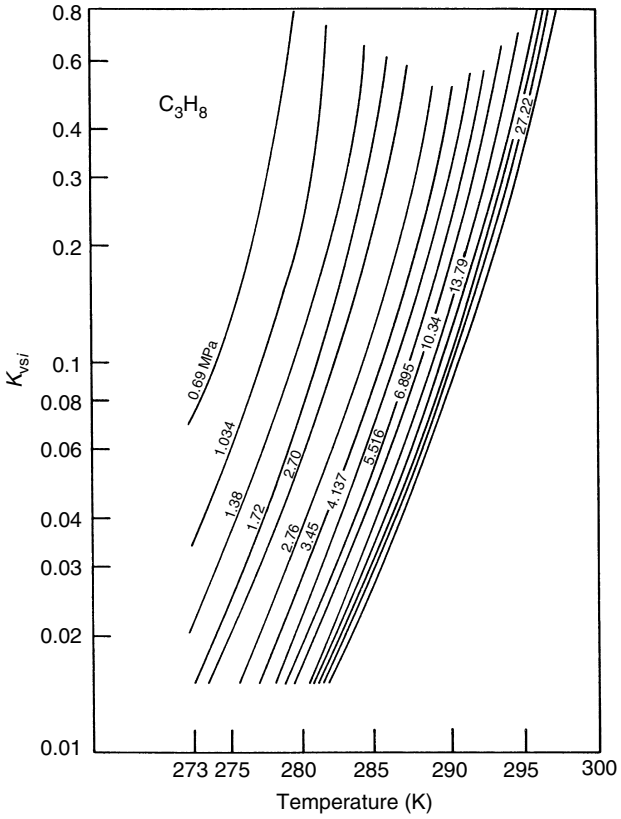

FIGURE 4.12 Propane K_{vsi} chart. (Reproduced from Carson, D.B., Katz, D.L., *Trans. AIME*, **146**, 150 (1942). With permission from the American Institute of Mining, Metallurgical, and Petroleum Engineers.)

Table 4.4a presents the parameters of Equation 4.2, with an indication of the correlation coefficient. The K_{vsi}-value charts or equations are used to determine the temperature or pressure of three-phase (L_W–H–V) hydrate formation. The condition for initial hydrate formation from free water and gas is calculated from an equation analogous to the dew point in vapor–liquid equilibrium, at the following condition:

$$\sum_{i=1}^{n} \frac{y_i}{K_{vsi}} = 1.0 \tag{4.3}$$

which is the requirement that the nonaqueous hydrate mole fractions sum to unity.

At the three-phase pressure for a given temperature and gas phase composition, the sum of the mole fraction of each component in the vapor phase divided by the K_{vsi} value of that component must equal unity. In order to have hydrates

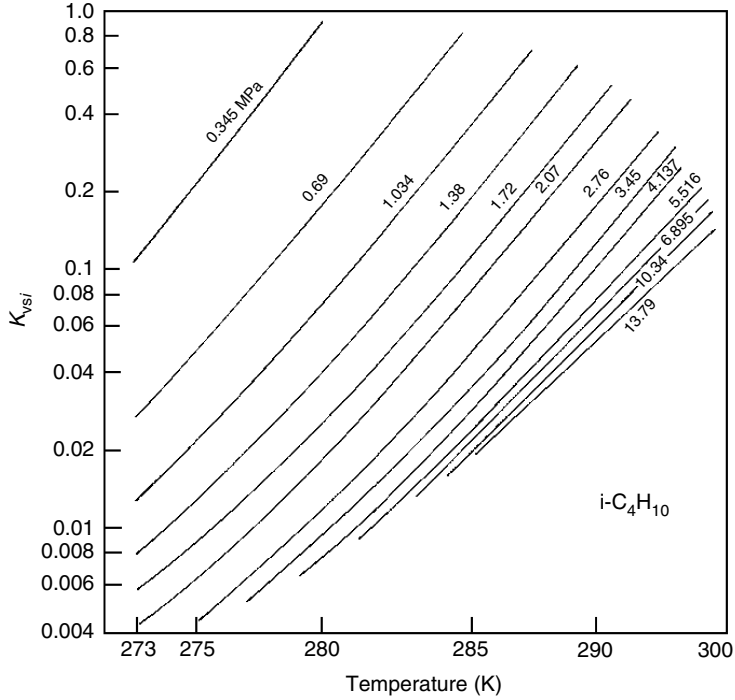

FIGURE 4.13 Isobutane K_{vsi} chart. (Reproduced from Wu, B.-J., Robinson, D.B., Ng, H.-J., *J. Chem. Thermodyn.*, **8**, 461 (1976). With permission from Academic Press, Ltd.)

present with a gas mixture, it is always necessary to have at least one K_{vsi} value greater than unity and at least one K_{vsi} value less than unity. Using interpolation and extrapolation, the pressure is changed in an iterative manner, and other K_{vsi} values are determined until the above sum ($\Sigma y_i/K_{vsi}$) equals one at the point of hydrate formation (or dissociation). A similar technique is followed to determine the three-phase temperature at a given pressure. The technique is illustrated with the following example from Carson and Katz (1942) for the calculation of the pressure for hydrate formation.

Example 4.4: Calculating Hydrate Formation Using K_{vsi} Method

Determine the pressure of hydrate formation at 283.2 K (50°F) from a gas with a composition of 78.4 mol% CH_4, 6.0% C_2H_6, 3.6% C_3H_8, 0.5% i-C_4H_{10}, 1.9% n-C_4H_{10}, 9.4% N_2, 0.2% CO_2.

Solution:

Guess two pressures (300 and 350 psia) as approximations to the condition at which $\Sigma y_i/K_{vsi} = 1.0$. Read the corresponding value of K_{vsi} for each

component at those pressures, to use in the table given below:

Component	y_i, Mole fraction	K_{vsi} at 2.07 MPa (300 psia)	y_i/K_{vsi}	K_{vsi} at 2.41 MPa (350 psia)	y_i/K_{vsi}
Methane	0.784	2.04	0.384	1.90	0.412
Ethane	0.060	0.79	0.076	0.63	0.0953
Propane	0.036	0.113	0.318	0.09	0.400
i-Butane	0.005	0.046	0.108	0.034	0.1471
n-Butane	0.019	∞	0.0	∞	0.0
Nitrogen	0.094	∞	0.0	∞	0.0
Carbon dioxide	0.002	3.0	0.0007	2.3	0.0009
Sum	1.000		0.8874		1.0553

Since the value of $\Sigma y_i/K_{vsi}$ is below unity at 300 psia, but above unity at 350 psia, the pressure at $\Sigma y_i/K_{vsi} = 1.0$ must lie between 300 and 350 psia. Interpolating linearly, the chart values yield $\Sigma y_i/K_{vsi} = 1.0$ at 2.3 MPa (333 psia). The experimental value of hydrate formation at 283.2 K (50°F) is 2.24 MPa (325 psia).

Similarly, in Example 4.1, the hydrate pressure for 95.6% CH_4 + 4.4% C_3H_8 was calculated as 1.26 MPa with an experimental value of 1.3 MPa.

Müller-Bongartz (Personal Communication, February 6, 1989) tested the accuracy of predictions from Equation 4.2 against the ternary and multicomponent data in Chapter 6 with the results given in Table 4.4b. From these comparisons, it can be seen that the polynomial fit of Equation 4.2 is not entirely satisfactory, but it will often serve as an acceptable estimate, which may be refined through use of Figures 4.10 through 4.17, or via the method given in Chapter 5, with the User's Examples in the Appendix.

The accuracy of the K_{vsi}-value method is impressive, considering the fact that the method preceded the knowledge of the crystal structure. Carson and Katz (1942) labeled their charts as tentative, yet the original methane, ethane, and propane charts continue to be useful. The K_{vsi} chart of methane was constructed from three data points at 4.14 MPa (600 psia), while the curves at other pressures were based on two data points and drawn symmetrically to the curve at 4.14 MPa (Katz, D.L. Personal Communication, November 14, 1983).

The K_{vsi} charts for components other than methane were derived from binary experimental data, with the K_{vsi} values for the second component based on that for methane. That is, at an experimental hydrate formation temperature, pressure, and binary gas composition, the values of y_i were fixed and the methane value of

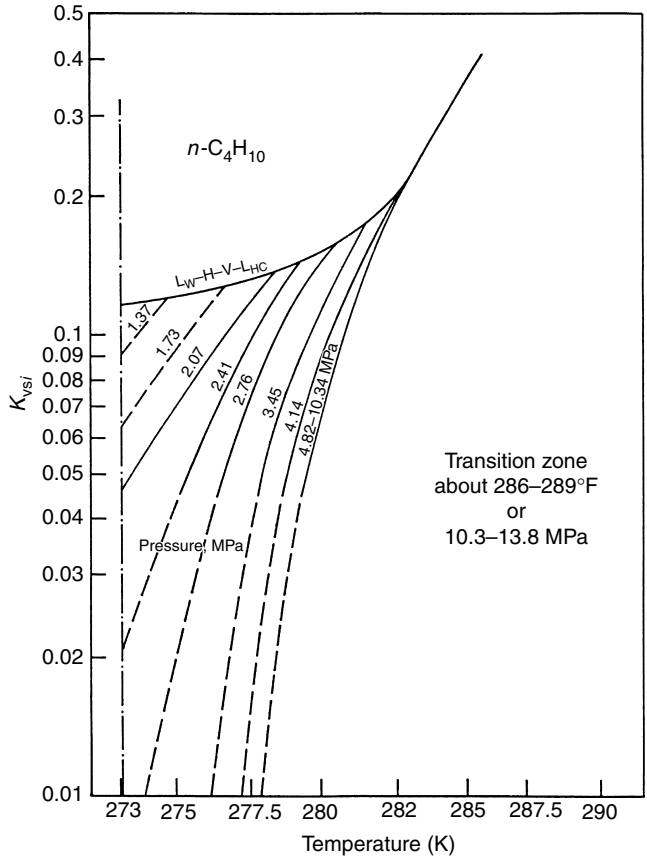

FIGURE 4.14 n-Butane K_{vsi} chart. (Reproduced from Poettmann, F.H., *Hydrocarbon Proc.*, **63**, 111 (1984). With permission from Gulf Publishing Co.)

K_{vsi} was found on the original methane chart. Then the only unknown, the K_{vsi} value of the second component was calculated, which satisfied Equation 4.3. With this calculation method one might expect K_{vsi} charts for other components to be less accurate than that for methane, because any inaccuracy in the methane chart is incorporated in succeeding charts.

In the discussion appendix of the original paper by Carson and Katz (1942), Hammerschmidt indicated that, while the method was acceptable for gases of "normal" natural gas composition, an unacceptable deviation was obtained for a gas rich in ethane, propane, and the butanes. More work is also required to revise the K_{vsi}-value charts for two components, namely, carbon dioxide and nitrogen. In three-phase hydrate data for binary mixtures of carbon dioxide and propane, Robinson and Mehta (1971) determined that the K_{vsi} method for carbon dioxide gave unsatisfactory results. The API Data Book shows the K_{vsi} values for nitrogen to be only a function of pressure, without regard for temperature; Daubert (Personal

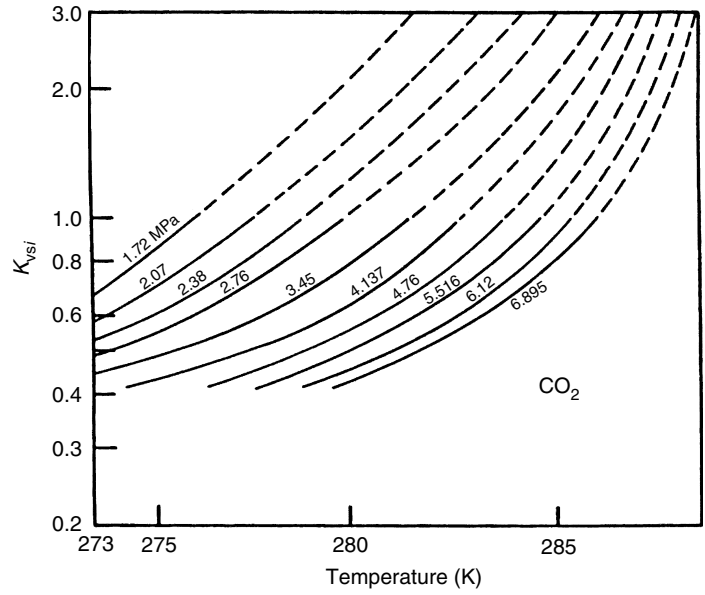

FIGURE 4.15 Carbon dioxide K_{vsi} chart. (Reproduced from Unruh, C.H., Katz, D.L., *Trans. AIME*, **186**, 83 (1949). With permission from the American Institute of Mining, Metallurgical, and Petroleum Engineers.)

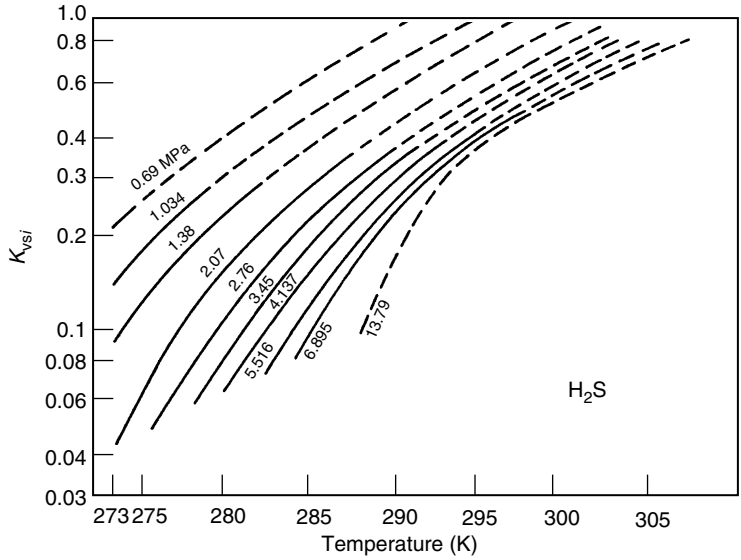

FIGURE 4.16 Hydrogen sulfide K_{vsi} chart. (Reproduced from Noaker, L.J., Katz, D.L., *Trans. AIME*, **201**, 237 (1954). With permission from the American Institute of Mining, Metallurgical, and Petroleum Engineers.)

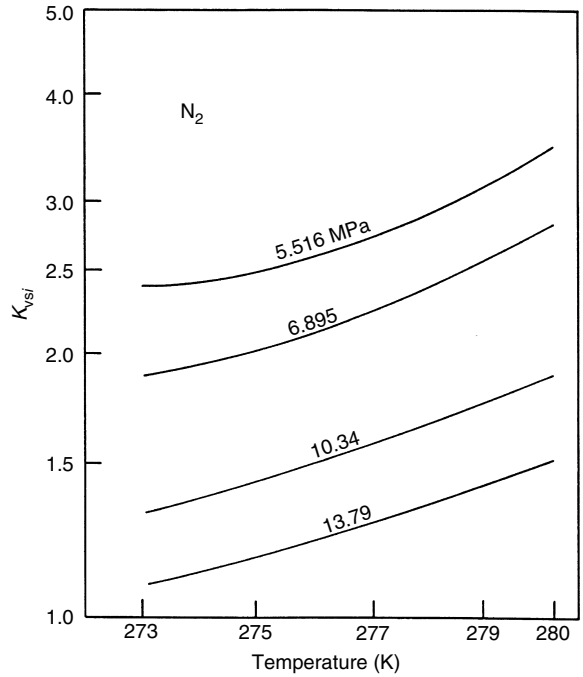

FIGURE 4.17 Nitrogen K_{vsi} chart. (Reproduced from Jhaveri, J., Robinson, D.B., *Can. J. Chem. Eng.*, **43**, 75 (1965). With permission from the Canadian Society for Chemical Engineering.)

Communication, June 8, 1987) indicated that data were insufficient for temperature dependence over a wide range of conditions.

It should be thermodynamically impossible for one set of K_{vsi} charts to serve both hydrate structures (sI and sII), due to different energies of formation. That is, the K_{vsi} at a given temperature for methane in a mixture of sI formers cannot be the same as that for methane in a mixture of sII formers because the crystal structures differ dramatically. Different crystal structures result in different x_{si} values that are the denominator of K_{vsi} ($\equiv y_i/x_{si}$). However, the Katz K_{vsi} charts do not allow for this possibility because they were generated before the two crystal structures were known. The inaccuracy may be lessened because, in addition to the major component methane, most natural gases contain small amounts of components such as ethane, propane, and isobutane, which cause sII to predominate in production/transportation/processing applications.

More properly a set of charts should be specified for each crystal structure, as was done by Mann et al. (1989). That work included a separate set of K_{vsi} charts for each of two (sI and sII) hydrate structures, but without a substantial increase in accuracy beyond the original charts.

Another estimation of accuracy may be obtained from Figures 4.18 and 4.19 that compare Katz's K_{vsi} values with K_{vsi} values obtained from the methods of

TABLE 4.4a
Parameters of Equation 4.2

Component	A	B	C	D	E
CH_4	1.63636	0.0	0.0	31.6621	−49.3534
C_2H_6	6.41934	0.0	0.0	−290.283	2629.10
C_3H_8	−7.8499	0.0	0.0	47.056	0.0
i-C_4H_{10}	−2.17137	0.0	0.0	0.0	0.0
n-C_4H_{10}	−37.211	0.86564	0.0	732.20	0.0
N_2	1.78857	0.0	−0.001356	−6.187	0.0
CO_2	9.0242	0.0	0.0	−207.033	0.0
H_2S	−4.7071	0.06192	0.0	82.627	0.0

Component	F	G	H	I
CH_4	−5.31E–6	0.0	0.0	0.128525
C_2H_6	0.0	0.0	−9.0E–8	0.129759
C_3H_8	−1.17E–6	7.145E–4	0.0	0.0
i-C_4H_{10}	0.0	1.251E–3	1.0E–8	0.166097
n-C_4H_{10}	0.0	0.0	9.37E–6	−1.07657
N_2	0.0	0.0	2.5E–7	0.0
CO_2	4.66E–5	−6.992E–3	−2.89E–6	−6.223E–3
H_2S	−7.39E–6	0.0	0.0	0.240869

Component	J	K	L	M	N
CH_4	−0.78338	0.0	0.0	0.0	−5.3569
C_2H_6	−1.19703	−8.46E4	−71.0352	0.596404	−4.7437
C_3H_8	0.12348	1.669E4	0.0	0.23319	0.0
i-C_4H_{10}	−2.75945	0.0	0.0	0.0	0.0
n-C_4H_{10}	0.0	0.0	−66.221	0.0	0.0
N_2	0.0	0.0	0.0	0.0	0.0
CO_2	0.0	0.0	0.0	0.27098	0.0
H_2S	−0.64405	0.0	0.0	0.0	−12.704

Component	O	Q	R	S	Correlation coefficient
CH_4	0.0	−2.3E–7	−2.0E–8	0.0	0.999
C_2H_6	7.82E4	0.0	0.0	0.0	0.998
C_3H_8	−4.48E4	5.5E–6	0.0	0.0	0.998
i-C_4H_{10}	−8.84E2	0.0	−5.4E–7	−1.0E–8	0.999
n-C_4H_{10}	9.17E5	0.0	4.98E–6	−1.26E–6	0.996
N_2	5.87E5	0.0	1.0E–8	1.1E–7	0.999
CO_2	0.0	8.82E–5	2.55E–6	0.0	0.996
H_2S	0.0	−1.3E–6	0.0	0.0	0.999

Note: The n-C_4H_{10} conditions should only be evaluated for formation with at least one, smaller guest component.

TABLE 4.4b
Accuracy of Predictions Using Equation 4.2

Prediction of hydrate	Temperature (K)	Pressure (kPa)
Number of data predicted	559	583
Percentage convergence, %	71.1	51.3
Absolute average deviation, %	8.13	17.2

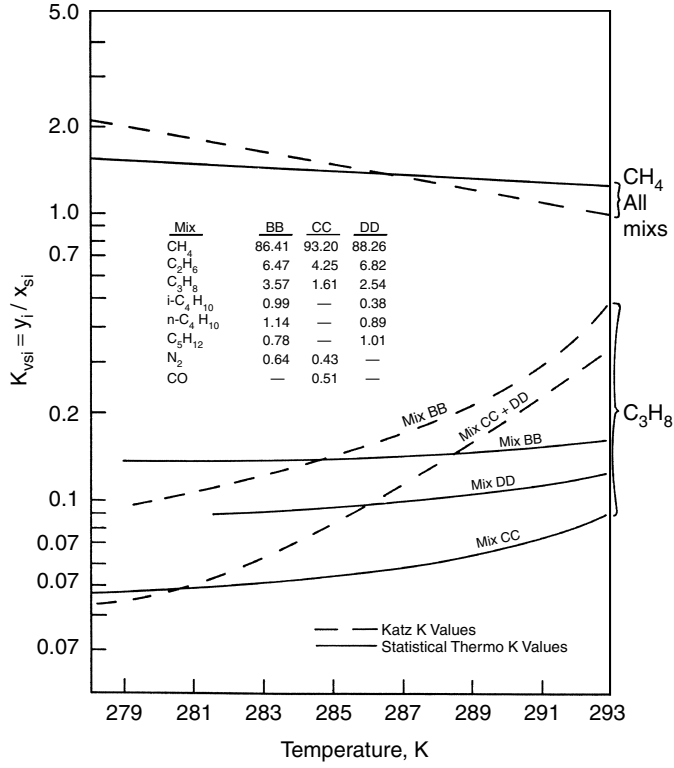

FIGURE 4.18 K_{vsi} values for methane and propane from Chapter 4 Katz charts (dashed lines) and Chapter 5 statistical method (solid lines). (Reproduced from Sloan, E.D., in *Proc. 63rd Annual Convention of Gas Processors Association*, **63**, 163 (1984). With permission from the Gas Processors Association.)

Chapter 5, for three natural gases studied by Deaton and Frost (1946). In the figures, the K_{vsi} values are presented as functions of temperature, with gas compositions as parameters. While both methods predict the three-phase pressure and temperature conditions acceptably, it is important to note that there are substantial differences in the K_{vsi} values by each method.

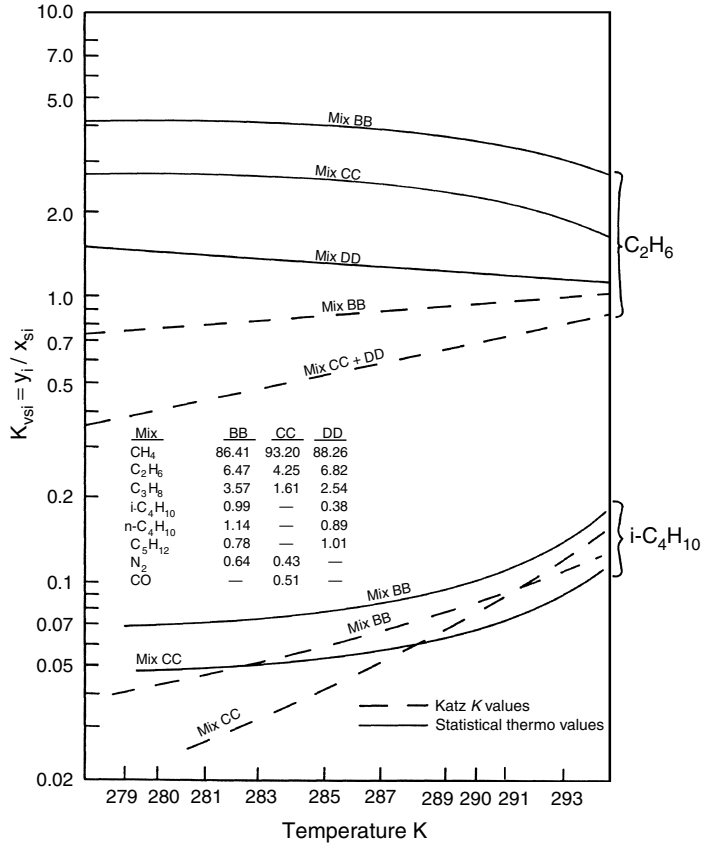

Mix	BB	CC	DD
CH_4	86.41	93.20	88.26
C_2H_6	6.47	4.25	6.82
C_3H_8	3.57	1.61	2.54
$i\text{-}C_4H_{10}$	0.99	—	0.38
$n\text{-}C_4H_{10}$	1.14	—	0.89
C_5H_{12}	0.78	—	1.01
N_2	0.64	0.43	—
CO	—	0.51	—

FIGURE 4.19 K_{vsi} values for ethane and isobutane from Chapter 4 Katz charts (dashed lines) and Chapter 5 statistical method (solid lines). (Reproduced from Sloan, E.D., in *Proc. 63rd Annual Convention of Gas Processors Association*, **63**, 163 (1984). With permission from the Gas Processors Association.)

In particular, the methane K_{vsi} values of Carson and Katz are more accurate than those of the other components, suggesting that the charts' longevity is because methane is the major component of a natural gas. The differences in the K_{vsi} values shown in Figures 4.18 and 4.19 suggest that the charts be used with caution, particularly for gases with significant amounts of either heavy or noncombustible components.

A second limitation to the K_{vsi}-value charts occurs in the limited range of temperatures above the ice point. Table 4.5 presents the results of a comparison of the experimental three-phase data for hydrates with the predictions of the K_{vsi} charts and the predictions from the statistical thermodynamics method in Chapter 5. In addition to the inaccuracies, it should be noted that 28% of the three-phase data could not be predicted via the K_{vsi} charts, principally due to chart temperature range limitations.

TABLE 4.5
Accuracy and Applicability of K_{vsi} Values Compared Against the Statistical Thermodynamic Method of Chapter 5

Total number of data points for 20 natural gases	141
Data points not predictable using the K_{vsi} charts	40 (28%)
Average error[a] comparing predictions to data	
Using the K_{vsi} charts	12.3%
Using the statistical thermodynamics method	5.8%

[a] Average error means average absolute error in pressure for a given temperature.

It should be noted that the use of the K_{vsi} charts implies that both the gas phase and the hydrate phase can be represented as ideal solutions. This means that the K_{vsi} of a given component is independent of the other components present, with no interaction between molecules. While the ideal solution model is approximately acceptable for hydrocarbons in the hydrate phase (perhaps because of a shielding effect by the host water cages), the ideal solution assumption is not accurate for a dense gas phase. Mann et al. (1989) indicated that gas gravity may be a viable way of including gas nonidealities as a composition variable.

Even with such limitations, the K_{vsi}-value method represented a significant advance in hydrate prediction ability. It was conceived prior to the determination of the hydrate crystal structures and it is a fine representation of the intuitive insight that characterizes much of Katz's work. The K_{vsi}-value method was the first predictive method, and it was used as the basis for the calculations in the gravity method, so it is logical that the K_{vsi}-value method should be more accurate.

4.3 Quadruple Points and Equilibrium of Three Condensed Phases (L_W–H–L_{HC})

Both the gas gravity method and the K_{vsi}-value method enable the estimation of three-phase (L_W–H–V) equilibrium between quadruple points Q_1 and Q_2 for mixtures as well as for simple natural gas hydrate formers such as those in Table 4.2.

4.3.1 The Location of the Quadruple Points

The lower quadruple point Q_1 (I–L_W–H–V) is located at the intersection of the three-phase L_W–H–V and the I–H–V pressure–temperature loci, usually within a degree of the ice point (273.15 K). The intersection temperature closely approximates the ice point because (with the exception of carbon dioxide and hydrogen sulfide) the solubility of hydrate formers in water is normally too small to change the freezing point of water significantly.

The approximate location of the upper quadruple point Q_2 (L_W–H–V–L_{HC}) is located by the intersection of the L_W–H–V line with the L_W–V–L_{HC} line. The termination of the three-phase (L_W–V–L_{HC}) line is the critical point that approximates the two-phase (V_{HC}–L_{HC}) critical point of the pure hydrocarbon vapor pressure. As a consequence, the intersection of the pure hydrocarbon vapor pressure with the L_W–H–V line (determined as in Section 4.2) provides the pressure and temperature of the upper quadruple point Q_2.

The three-phase (L_W–V–L_{HC}) pressure–temperature line is approximated by the vapor pressure (V_{HC}–L_{HC}) locus for the pure component due to two effects, both of which are caused by the hydrogen-bond phenomenon described in Chapter 2. First, hydrogen bonds cause almost complete immiscibility between the hydrocarbon liquid and the aqueous liquid, so that the total pressure may be closely approximated by the sum of the vapor pressures of the hydrocarbon phase and that of water. Second, hydrogen bonds cause such a self-attraction of the water molecules that the water vapor pressure is very low, composing only a small fraction of the total vapor pressure at any temperature. Because each immiscible liquid phase essentially exerts its own vapor pressure, and because the water vapor pressure is very small, the hydrocarbon vapor pressure is a very good approximation of the three-phase (L_W–V–L_{HC}) locus.

4.3.2 Condensed Three-Phase Equilibrium

Katz (1972) first noted that hydrates could form from heavy liquids such as crude oils that have dissolved gases suitable for hydrate formation. He suggested that the point of hydrate formation from water and a liquid hydrocarbon phase (no gas present) could be predicted using the vapor–hydrate distribution coefficient K_{vsi} of Equation 4.1 together with the more common vapor–liquid distribution coefficient $K_{v\ell i}$ ($\equiv y_i/x_{\ell i}$). In this case Equation 4.3 becomes:

$$\sum_{i=1}^{n} \frac{y_i}{K_{vsi}} = \sum_{i=1}^{n} \frac{x_{\ell i} K_{v\ell i}}{K_{vsi}} = 1.0 \tag{4.3a}$$

The substitution of $y_i = x_{\ell i} \cdot K_{v\ell i}$ in the numerator of Equation 4.3a suggests that this equation applies at the bubble point, or the quadruple point (L_W–H–V–L_{HC}) that marks the lowest pressure of a three-phase (L_W–H–L_{HC}) region (point C in Figure 4.2c). The P–T locus of the three-phase (L_W–H–L_{HC}) line is almost vertical, so Equation 4.3a is an approximation of both the lowest pressure and the highest temperature for the three phases in equilibrium. Katz noted that Scauzillo (1956) had measured systems that did not appear to conform to the above equation. Later measurements by Verma (1974) and Holder (1976) confirmed Katz's analysis for hydrate formation from crude oil reservoirs.

For condensed three-phase (L_W–H–L_{HC}) hydrate equilibrium, at pressures above the upper quadruple point, the pressure changes extremely rapidly with only a small change in temperature. This is because all three phases are relatively

incompressible, so that only a small temperature change is needed to cause a large pressure change. As a consequence, determination of a condensed phase P–T locus is a stringent test for even the most accurate equation-of-state to predict both density and mutual solubility of the hydrocarbon and the aqueous phases. As a first approximation, the incompressible three-phase (L_W–H–L_{HC}) condition can be estimated by a vertical line on the pressure–temperature plot. Figure 4.1 shows the condensed phase P–T plot above Q_2 to be almost vertical for simple hydrate formers of natural gas hydrocarbons. The fact that the three-phase (L_W–H–L_{HC}) equilibrium can be approximated by a line of infinite slope on a P–T diagram led nineteenth century investigators to suggest that the upper quadruple point Q_2 represented the maximum temperature of hydration formation.

As noted in Section 4.1.1, without an upper quadruple point methane and nitrogen hydrates are considered to have no upper temperature of formation. The pure component critical temperatures of methane and nitrogen (190.6 and 126.2 K, respectively) negate any possible intersection of their vapor pressures with the three-phase L_W–H–V loci. It should be noted that the above is a good rule of thumb at normally encountered temperature and pressures. At very high pressures (>500 bar) nitrogen has been determined to have unusual phase behavior. Schouten and coworkers (van Hinsberg et al., 1993, 1994) have measured a nitrogen phase transition (sII $\Rightarrow$ sI) at high pressures (to 2 GPa). Kuhs et al. (1996) indicate that at pressures above 500 bar nitrogen can doubly occupy the large cage of sII. Similarly, data compiled by Ballard and Sloan (2004) show that methane hydrates do have a maximum temperature of formation at 321 K.

However, the condensed three-phase P–T locus is not exactly vertical. Ng and Robinson (1977) measured the L_W–H–L_{HC} equilibrium for a number of structure II hydrate mixtures and suggested that a better estimation of the slope dP/dT might be obtained through the Clapeyron equation:

$$\frac{dP}{dT} = \frac{\Delta H}{T \Delta V} \tag{4.4}$$

where ΔH and ΔV represent the enthalpy and volume, respectively, accompanying the process of conversion of liquid water and liquid hydrocarbon into hydrate. The value of ΔH was found to be almost constant at 65.4 ± 2.1 kJ/mol for many gas mixtures. Therefore, to a good approximation, the temperature and volume change $[\Delta V \equiv V_H - (V_{LW} + V_{LHC})]$ at the quadruple point Q_2 determines the slope of the condensed phase equilibrium. Of 21 gas mixtures studied by Ng and Robinson in the L_W–H–L_{HC} region, the value for dP/dT ranged between 3.4 and 66.3 MPa/K, with an average value of 10.16 MPa/K (840 psig/°F); therefore the large value of ΔH causes the slope (dP/dT) to be very high in all cases.

For the upper temperature for hydrate formation, Makogon (1981) suggested a better criterion than the location of Q_2 is the P–T condition at which the density of the combined hydrocarbon and water is equal to that of the hydrate. He assumed

complete liquid immiscibility and used the inverted Clapeyron relation:

$$\frac{dT}{dP} = \frac{T\Delta V}{\Delta H_H} \tag{4.5}$$

where

ΔH_H = heat of hydrate formation from liquid water and liquid hydrocarbon[2]

ΔV = the molar volume of the hydrate less that of the hydrocarbon and liquid water ($\equiv V_H - V_{LHC} - V_{LW}$).

Since the value of ΔH_H remains constant over a large range of pressures, the maximum in T is determined by the point at which the molar volume change is zero. The volume comparison must be made between the pure liquid hydrocarbon, liquid water, and hydrate, since the hydrocarbon must exist as liquid at pressures between the vapor pressure and the critical pressure. Maxima in hydrate formation temperatures above Q_2 have been calculated, but they have yet to be measured.

4.4 Effect of Thermodynamic Inhibitors on Hydrate Formation

Several means of hydrate prevention and dissociation are discussed in detail in Chapter 8. In the present section we consider the lowering of the three-phase (L_W–H–V) temperature or the increase of the L_W–H–V pressure via an inhibitor. In this section we consider only thermodynamic inhibitors such as alcohols, glycols, or salts. For kinetic inhibition using LDHIs, such as KIs or AAs, the reader is referred to Chapter 8.

By Gibbs' Phase Rule illustrated in this chapter's introduction, a second intensive variable is needed (in addition to either temperature or pressure) to specify the three-phase binary system with an inhibitor ($F = 3 - 3 + 2$). Typically, the concentration of the inhibitor in the free water phase is specified as the second intensive variable. Substances that have considerable solubility in the aqueous phase, such as alcohols, glycols, and salts, normally act as inhibitors to hydrate formation. The colligative mechanism of formation inhibition is aided by increased competition for water molecules by the dissolved inhibitor molecule or ion through hydrogen bonding for alcohols or glycols, or via Coulombic forces (for salt ions).

As a first approximation, the temperature depression for hydrate inhibition might be considered to be similar to the depression of the freezing point of ice by an equivalent mass fraction of the inhibitor. However, Nielsen and Bucklin (1983) derived an equation indicating that the hydrate depression temperature will always be less than the ice depression temperature by a factor equal to [(heat of fusion of ice)/(heat of hydrate dissociation)], which has a numerical value between 0.6 and 0.7 as a function of the hydrate structure. This is illustrated in Figure 4.2d, by the fact that at constant pressure, the ice depression temperature (i.e., distance between

[2] The translation of Makogon's work indicates hydrocarbon vapor, but the condensed hydrocarbon phase is clearly required by the pressure and temperature conditions.

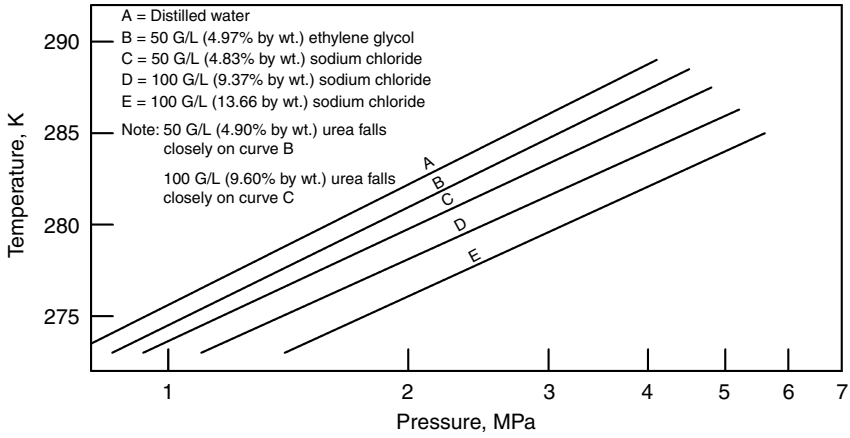

FIGURE 4.20 Hydrate equilibrium curves with various inhibitors. (Reproduced courtesy of the United States Bureau of Mines (Deaton and Frost, 1946).)

the lower, almost vertical lines) is always greater than the constant pressure distance between the slanted lines, for an equivalent amount of methanol.

Figure 4.20 shows the correlation of experimental data of Hammerschmidt (1939) with five inhibitors with the pressure and temperature axes reversed from their normal position. The striking feature of Figure 4.20 is the parallel nature of all experimental lines, for the inhibition effect of both alcohols and salts relative to pure water. The parallel solid lines provide some indication of the molecular nature of the inhibition. Normally a phase transformation is considered relative to the change in Gibbs free energy defined as:

$$\Delta G \equiv \Delta H - T\Delta S \tag{4.6}$$

The two components of ΔG are (1) an energetic part ΔH and (2) a structural part ΔS, for the equilibrium $(V + L_W \leftrightarrow H)$ at constant temperature and pressure. Upon addition of an inihbitor the Gibbs free energy is increased in order for a lower temperature (or higher pressure) to be required for hydrate formation. Using the Clapeyron equation with the data of Figure 4.20 to relate the slope $(\mathrm{d}\,\ell\mathrm{n}P/\mathrm{d}T)$ to the enthalpy of formation ΔH, one can determine that the value of ΔH is relatively constant. Therefore it appears that the energetic effects are not appreciably affected by the inhibitors. In order to increase the Gibbs free energy, the primary effect of the inhibitor is on the structure of the water phase. The inhibitor encourages nonrandomness (structures other than hydrate-like clusters) in the water, in order to be effective.

Several types of inhibitors have been tried, but the glycols and alcohols have proved to be the most successful. As an example, ammonia was initially determined to be twice as effective an inhibitor as methanol; however, over long periods, ammonia reacts with carbon dioxide and water to form ammonium carbonate and

ammonium carbamate through the reactions:

$$2NH_3 + H_2O + CO_2 \rightarrow (NH_4)_2CO_3$$
$$CO_2 + 2NH_3 \rightarrow NH_4CO_2NH_2$$

The solid ammonium carbonate and carbamate are much more difficult to remove than the hydrates (Townsend and Reid, 1978, p. 100). The natural gas industry has opted for methanol and glycols, which may be injected into pipelines and processes without undesirable side reactions.

4.4.1 Hydrate Inhibition via Alcohols and Glycols

The alcohols (in the homologous series beginning with methanol and ending with butanol) all hydrogen bond to water with their hydroxyl group. However, as summarized in Chapter 2, a substantial body of work [reviewed by Franks (1973) and Ben Naim (1980)] indicates that the hydrocarbon end of the alcohol molecule causes a clustering effect on water molecules similar to that of hydrate formers. Alcohols therefore have two effects on water that compete with dissolved apolar molecules for clusters: the hydroxyl group hydrogen bonds the water molecules (the major effect), and the hydrocarbon end of the alcohol tends to organize the water into solvent clusters (the lesser effect), in direct competition with the hydrate for guest and host molecules.

Makogon (1981, p. 134) and Berecz and Balla-Achs (1983, p. 102) indicated that methanol can increase the temperature of hydrate formation at concentrations less than 5 mass% (presumably due to the clustering effect), but higher concentrations inhibit formation. Nakayama and Hashimoto (1980) also suggested that several of the alcohols could form hydrates; yet further study by Nakayama et al. (1997) caused the opposite opinion. Further measurements by Svartas (1988) also indicated that small methanol amounts do not increase hydrate thermodynamic stability.

Wallqvist (1991, 1992) simulated methanol in hydrate cages at very short times (1 ns) and showed that a 4 wt% methanol solution was stable but a 7% solution melted. Koga (1995), Koga et al. (1994a,b), and Koga and Tanaka (1996) simulated hydrate hydrogen bonding of methylamine and methanol guests at times of 100 ps. The increase in the partial charge on the hydrogen atom causes methanol hydrates to be unstable, but methyl amine hydrates are stabilized.

Of alcohols, methanol has been the most popular inhibitor, due to its cost and its effectiveness. Katz et al. (1959, p. 218) indicated that the inhibition ability of alcohols increases with volatility, that is, methanol > ethanol > isopropanol. Typically methanol is vaporized into the gas stream of a transmission line, then dissolves in any free water accumulation(s) where hydrate formation is prevented. Makogon (1981, p. 133) noted that in 1972 the Soviet gas industry used 0.3 kg of methanol for every 1000 m^3 of gas extracted. Stange et al. (1989) indicated that North Sea methanol usage may surpass the ratio given by Makogon by an order

of magnitude. Nielsen and Bucklin (1983) present calculations to indicate that methanol injection in a gas processing turboexpander plant is less expensive than drying with either alumina or molecular sieves. Nevertheless, the use of methanol has become so expensive that methanol recovery and return lines are becoming more common. Some refiners have placed a surcharge of >$5/bbl on any liquids that have methanol contamination.

The glycols [EG or MEG, diethylene glycol (DEG), and triethylene glycol (TEG)] provide more hydrogen bonding opportunity with water through one more hydroxyl group than alcohols, as well as through oxygen atoms in the case of the larger glycols. The glycols generally have higher molecular weights with lower volatility, so they may be recovered and recycled more from processing/transmission equipment. For gas dominated systems, MEG is frequently preferred to methanol due to recovery.

In a comprehensive set of experimental studies, Ng and Robinson (1983) determined that methanol inhibited hydrate formation more than an equivalent mass fraction of glycol in the aqueous liquid. The preference for methanol versus glycol may also be determined by economic considerations (Nelson, 1973). However, in many North Sea applications ethylene glycol is the preferred inhibition method.

Techniques for hydrate inhibition deal with the methanol concentration in the aqueous liquid in equilibrium with hydrate at a given temperature and pressure. The user also must determine the amount of methanol to be injected in the vapor. This problem was addressed first by Jacoby (1953) and then by Nielsen and Bucklin (1983), who presented a revised methanol injection calculation. The most recent data are by Ng and Chen (1995) for distribution of methanol in three phases: (1) the vapor phase, (2) the aqueous phase, and (3) the liquid hydrocarbon phase.

To approximate the hydrate depression temperature for several inhibitors in the aqueous liquid, the natural gas industry uses the original Hammerschmidt (1939) expression to this day as a check:

$$\Delta T = \frac{2335W}{100M - MW} \tag{4.7}$$

where

ΔT = hydrate depression, °F
M = molecular weight of the alcohol or glycol
W = wt% of the inhibitor in the liquid.

Equation 4.7 was based on more than 100 experimental determinations of equilibrium temperature lowering in a given natural gas–water system in the inhibition concentration range of 5–25 wt% of the free water. The equation was used to correlate data for alcohols and ammonia inhibitors. Hammerschmidt (1939) provided for a modification of the molecular weight M when salts were used as inhibitors. Unfortunately, no information on the gas composition and no listing of the individual experimental data were provided. The assumption is normally made that the gases used by Hammerschmidt were methane-rich.

TABLE 4.6
Comparison of Two Simple Prediction Methods for Hydrate Inhibition by Methanol

Simple component	Wt% MeOH	Number of hydrate data points	Average % error in temperature by	
			Hammerschmidt Equation 4.7	Freezing point depression
Methane	10	4	3.98	4.21
Methane	20	3	7.56	15.3
Ethane	10	5	2.03	8.97
Ethane	20	2	1.26	23.5
Propane	5	3	1.62	3.13
Carbon dioxide	10	3	7.63	3.53

Pieroen (1955) and Nielsen and Bucklin (1983) presented derivations to show the theoretical validity of the Hammerschmidt equation. The latter work suggested that the equation applies only to typical natural gases, and to methanol concentrations less than 0.20 mole fraction (typically for system operation at temperatures above 250 K). It may easily be shown (Yamanlar et al., 1991) that the Hammerschmidt equation should not apply to high concentrations of an inhibitor that might vaporize. Nixdorf and Oellrich (1996) have shown that the Hammerschmidt equation under-predicts natural gas systems inhibited with TEG.

Due to a cancellation of errors, the equation (without modification) is applicable for aqueous ethylene glycol concentrations to about 0.40 mole fraction (typically for system operation to 233 K). A comparison of results from Hammerschmidt's equation, as well as the prediction by the freezing point depression of water for methanol inhibition is summarized in Table 4.6.

Nielsen and Bucklin (1983) presented an improved version of the Hammerschmidt equation which is accurate over a wider range, that is, to concentrations as large as 0.8 mole fraction. They suggested that Equation 4.8 may be effectively used to design methanol injection systems operating as low as 165 K

$$\Delta T = -129.6\,\ell\mathrm{n}(1 - x_{\mathrm{MeOH}}) \tag{4.8}$$

where ΔT is the hydrate temperature depression below the uninhibited condition, in °F. Makogon (1981, p. 134) indicated that the inhibition effect is a function (albeit much smaller) of pressure as well as that of temperature.

An important recent development is the consideration of under-inhibited systems, as reported by Austvik and coworkers, (Austvik et al., 1995; Gjertsen et al., 1996). Yousif et al. (1996) measured two adverse effects of small amounts of methanol on hydrate inhibition: (1) insufficient inhibition with methanol enhances the rate and amount of hydrates that form and (2) hydrates that form with

small amounts of methanol adhere to surfaces more than those formed in the absence of methanol. At under-inhibited amounts of methanol, MEG, and salt, hydrates coated the pipe wall more, both in field and in laboratory studies. This suggests that pipeline plugging may be worse in under-inhibited systems than if no thermodynamic inhibitor were added.

4.4.2 Hydrate Inhibition Using Salts

The action of salts as inhibitors is somewhat different than that of alcohols or glycols. The salt ionizes in solution and interacts with the dipoles of the water molecules with a much stronger Coulombic bond than either the hydrogen bond or the van der Waals forces that cause clustering around the apolar solute molecule. The stronger bonds of water with salt ions inhibit hydrate formation; water is attracted to ions more than water is attracted to the hydrate structure.

As a secondary effect, this clustering also causes a decrease in the solubility of potential hydrate guest molecules in water, a phenomenon known as "salting-out." Both ion clustering and salting out combine to require substantially more subcooling to overcome the structural changes and cause hydrates to form.

For an accurate estimate of salt effects, the computer program (enclosed with this monograph) should be used, incorporating the methods in Chapter 5, and in the User's Manual in the book's CD. However, a rapid estimate for the depression of salt on hydrate equilibrium may be obtained by knowledge of the depression of salt on ice equilibrium, using the method in this section.

Pieroen (1955) provided a theoretical foundation for the Hammerschmidt equation, showing that when the solubility of one phase in the other is neglected, a nonvaporizing inhibitor such as salt can be approximated as

$$\ln a_{\mathrm{w}} = \frac{\Delta H}{nR}\left[\frac{1}{T_{\mathrm{w}}} - \frac{1}{T_{\mathrm{s}}}\right] \tag{4.9}$$

where a_{w} is water activity, ΔH is the heat of dissociation of hydrate, n is the hydration number, and T_{w} and T_{s} are the hydrate formation temperatures in pure water and the salt solution. Menten et al. (1981) showed that the above equation can be incorporated directly into a hydrate calculation method. More recently, Dickens and Quinby-Hunt (1997) suggested that the above equation could be combined with a similar equation for the formation of ice:

$$\ln a_{\mathrm{w}} = \frac{\Delta H^{\mathrm{fus}}}{R}\left[\frac{1}{T_{\mathrm{f}}} - \frac{1}{T_{\mathrm{fs}}}\right] \tag{4.10}$$

where ΔH^{fus} is the heat of fusion of ice (6008 J/mol), T_{f} and T_{fs} are the freezing point temperatures of water (273.15 K) and water with a salt solution. Equating Equations 4.9 and 4.10 one obtains a simple relation to calculate T_{s}, the hydrate

formation temperature in the presence of salt

$$\left[\frac{1}{T_w} - \frac{1}{T_s}\right] = \frac{6008n}{\Delta H}\left[\frac{1}{273.15} - \frac{1}{T_{fs}}\right] \tag{4.11}$$

A procedure use of Equation 4.11 is shown in the example below.

Example 4.5: Short Cut Calculation of Hydrate Formation Conditions with Salt

Calculate the methane hydrate formation temperature at 2.69 MPa with 0.03936 mole fraction sodium chloride in the water phase.

Solution

1. At the specified salt concentration (0.03936 mole fraction), determine the freezing point of water (T_{fs}) from a handbook, such as the *Handbook of Chemistry and Physics*, as $T_{fs} = 268.9$ K.
2. Determine the enthalpy of hydrate dissociation to gas and pure water (ΔH) and the hydration number (n) at the ice point using the methods of Section 4.6. For methane, $\Delta H = 54{,}190$ J/(mol methane) and $n = 6.0$.
3. Calculate the coefficient ($6008n/\Delta H$) in Equation 4.11. For methane the value of the coefficient is 0.665.
4. Calculate the three-phase hydrate dissociation temperature, T_w (without salt), at the pressure of interest using either tabulated data, the equations in Table 4.1, or the K_{vsi} method. For example, the methane three-phase temperature at 2.69 MPa is 273.3 K, as measured by de Roo et al. (1983).
5. Calculate the hydrate dissociation temperature T_s in the presence of salt using Equation 4.11. Equation 4.11 predicts the dissociation temperature to be 270.45 K. De Roo et al. (1983) measured the dissociation temperature as 268.3 K.

While Equation 4.11 provides a simple accurate method to estimate the effects of salt, the following points should be noted:

1. Equation 4.11 does not contain pressure explicitly. If Equation 4.11 is recast as:

$$\frac{\Delta T^{hyd}}{T_w T_s} = K\frac{\Delta T^{fus}}{T_f T_{fs}} \tag{4.12}$$

then the ΔT^{hyd} may be constant over a wide range of pressures, because K is the constant shown in Equation 4.11.

2. The hydrate temperature depression will always be less than the ice temperature depression ΔT^{fus}, since the value of $\Delta H/n$ in Equation 4.9 is always greater than ΔH^{fus} in Equation 4.10. In the case of Example 4.5 the ΔT^{hyd} is 66.5% of the value of ΔT^{fus}.
3. The hydration number n and the heat of dissociation ΔH change as a function of the components, as indicated in Section 4.6.
4. The method can be extended to salt mixtures, if the freezing point depression of water is known for the mixture. Patwardhan and Kumar (1986) suggest a simple extension to determine water activities for mixed salts from single salt activities, such as in Equations 4.9 and 4.10.

4.5 Two-Phase Equilibrium: Hydrates with One Other Phase

Hydrates may also exist in equilibrium with only a fluid hydrocarbon phase (either vapor or liquid) when there is no aqueous phase present. Two-phase (H–V or H–L_{HC}) regions are shown in the T–x diagram of Figure 4.3. Similarly, Figure 4.3 shows the L_W–H region for hydrates in equilibrium with water containing a small amount of dissolved methane, as in the case for hydrate formation in oceans, as exemplified in Chapter 7.

By the Gibbs' Phase Rule illustrated in the introduction to this chapter, in the three-phase regions, of Sections 4.2 through 4.4, only one intensive variable is needed to specify a binary system; that is, specifying T determines P, and vice versa for a fixed gas composition. However, two variables are needed to specify a two-phase binary system; typically water concentration in the hydrocarbon fluid is specified as the second variable at a specified temperature or pressure. The determination of the equilibrium water concentration enables the engineer to maintain the hydrocarbon fluid in the single-phase region, without hydrate solid formation for fouling or flow obstruction. Similarly, for L_W–H equilibria, the methane solubility in water determines when hydrates will be stable, as shown in Section 7.3.3.

Two common misconceptions exist concerning the presence of water to form hydrates in pipelines, both of which are illustrated via the T–x phase equilibrium diagrams in Figure 4.3. The first and most common misconception is that a free water phase is absolutely necessary for the formation of hydrates. The upper three-phase (L_W–H–V) line temperature marks the condition of hydrate formation from free water and gas. Below that temperature and to the right of the hydrate line, however, are two-phase regions in which hydrates are in equilibrium only with hydrocarbon vapor or liquid containing a small (<1000 ppm) amount of water.

From a strict thermodynamic standpoint then, a vapor or liquid (with dissolved water) can form hydrates at the H–V or the H–L_{HC} boundaries without a free water phase. The question of the accumulation of a hydrate phase is a question of kinetics,

dependent upon the time necessary for hydrate nuclei to attain a critical size. This time may be in excess of that available for laboratory study, but may occur in processes that operate over extended periods of days, months, or years.

In addition there have been multiple studies (Sloan et al., 1976; Cady, 1983a,b; Kobayashi et al., 1987; Woolridge et al., 1987) that demonstrate that hydrate growth can occur from a hydrocarbon fluid phase if a hydrate nucleus is either already present, absorbed at sites on a wall, or on a third surface.

From an operator's perspective, if a dehydrator abnormality enables free water to enter a vessel or pipeline, then that free water can readily form hydrates, so that additional saturated vapor (without free water) will cause that initial hydrate mass to grow. Therefore, from a practical standpoint one should require that the hydrocarbon fluid be maintained in the thermodynamic single-phase region if hydrates are to be prevented.

The second misconception about two-phase hydrates concerns the dew point of the hydrocarbon phase. Bucklin et al. (1985) correctly indicate that the extrapolated points from the vapor–liquid water region at higher temperatures give metastable dew points. This effect is indicated in the *Gas Processors Association Handbook* (1981, Figure 15.14). However, it is also incorrect to determine the dew point, assuming that ice is the condensed water phase; such equilibrium occurs relatively rarely. Much more frequently, hydrate is the condensed water phase at low temperature or high pressure. Details of vapor–hydrate equilibrium are given in Section 4.5.1, while the liquid hydrocarbon–hydrate equilibrium is described in Section 4.5.2. Chapter 8 discusses production/transmission/processing implications of these equilibria.

4.5.1 Water Content of Vapor in Equilibrium with Hydrate

The water content of the vapor phase in (H–V) equilibrium is very small (typically less than 0.001 mole fraction) and therefore difficult to measure accurately. As a consequence, in the history of gas processing, semilogarithmic straight lines (gas water content versus reciprocal absolute temperature) from the L_W–V region were extrapolated into the H–V region with limited justification.

A typical chart for water content from this period is presented in Figure 4.21. In Figure 4.21 the water content chart at temperatures above the hydrate stability conditions is based primarily on the data of Olds et al. (1942) while the data of Skinner (1948) were the basis for extrapolations to temperatures below the hydrate formation point. A summary chart is given by McKetta and Wehe (1958). However, below the initial hydrate formation conditions, Figure 4.21 represents metastable values, as observed in gas field data by Records and Seely (1951). Kobayashi and Katz (1955) indicated that such concentration extrapolations across hydrate phase boundaries yield severe errors.

Laboratory confirmation that the water content of gas in equilibrium with hydrate should be much lower than the extrapolated values has been verified by Sloan et al. (1976) for methane hydrates, and by Song and Kobayashi (1982) for

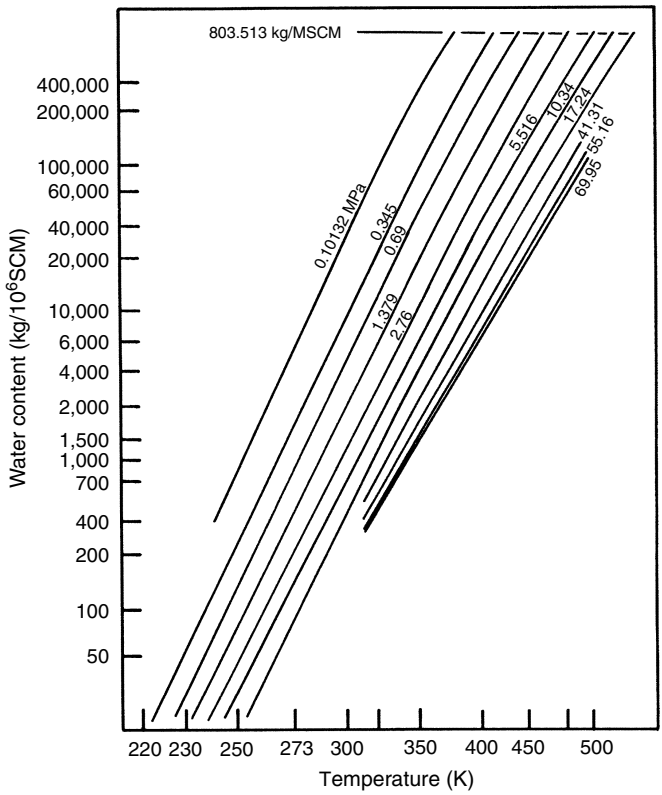

FIGURE 4.21 Metastable water content of gas. (Reproduced, from Kobayashi, R., Song, K.Y., Sloan, E.D., in *Petroleum Engineering Handbook* (1987). With permission from the Society of Petroleum Engineers.)

methane–propane hydrates. A typical replacement chart is shown in Figure 4.22. In this figure the high temperature L_W–V region is separated from the low temperature H–V region by a line representing the three-phase (L_W–H–V) boundary.

The isobaric data in the vapor–hydrate region of Figure 4.22 follow semilogarithmic straight lines when water content is plotted against reciprocal absolute temperature, but these lines have slopes different from the straight lines in the L_W–V region. In addition, the three-phase (L_W–H–V) point at which the slope change occurs is a function of gas composition. The change in the slope of an isobar from the L_W–V region occurs at different temperatures for differing compositions.

With the above complexities, a comprehensive water content chart (or series of charts) for gases of differing compositions would be problematic. Further, the data are so sparse that mathematical methods for determining the water content of gases in the V–H region should be considered to fit to a small amount

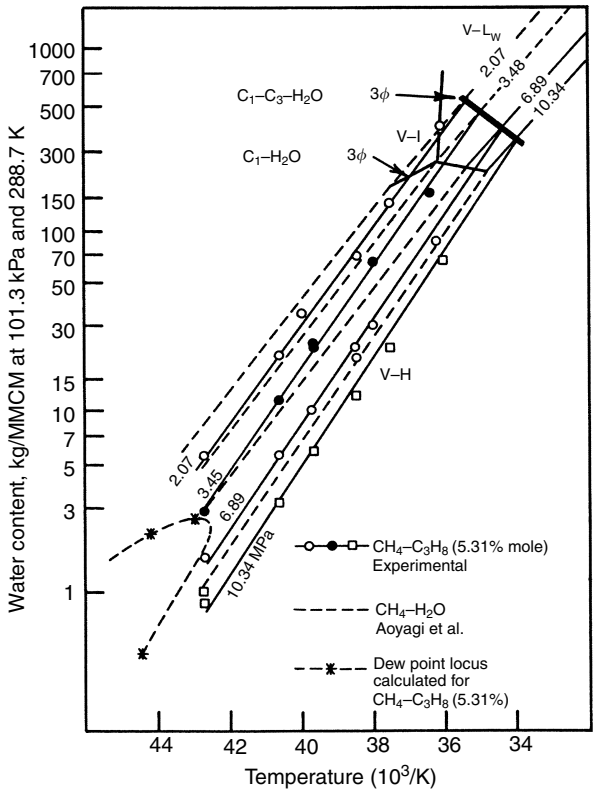

FIGURE 4.22 Equilibrium water content chart for methane (dashed) and for methane +5.31% propane (solid). (Reproduced from Song, K.Y., Kobayashi, R., *Ind. Eng. Chem. Fund.*, **21**, 391 (1982). With permission from the American Chemical Society.)

of data, and should be regarded with some suspicion. A more thermodynamically correct calculation method for interpolation of the available database is given in Chapter 5, and is available on the computer program CSMGem with this book's CD.

It is worthwhile to emphasize that all of the available data for V–H studies have been for methane-rich gases. For heavier gases, or for noncombustible gases, there are almost no data in the V–H two-phase region; the sole exception is the water content study of Song and Kobayashi (1987) for carbon dioxide.

4.5.2 Water Content of Liquid Hydrocarbon in Equilibrium with Hydrates

In the H–L_{HC} two-phase region there is a severe paucity of both data and a simple calculation scheme. These data find applications in condensate pipelines, which may have hydrates. The only data available are from this laboratory

[Sloan et al. (1986, 1987)] with corrections by Song and Kobayashi (1994). A prediction scheme is discussed in Chapter 5 using the statistical thermodynamics method and included in the program CSMGem.

Because there are so few data for water content of the fluid hydrocarbon in either of the two-phase (H–V or H–L_{HC}) regions, their accuracy cannot be determined. These data are very difficult to obtain due to the low concentrations (typically $<$100 ppm mol). The inaccuracies in normal experimental data in other phase regions are frequently greater than the absolute values of the water content in the H–L_{HC} region.

With low concentrations of water a substantial amount of time may be required before the water molecules can agglomerate into a hydrate structure. Experimental time to acquire each data point is normally on the order of days or weeks, rather than hours. Appreciable metastability is observed, and long times are required for the formation of critical hydrate nuclei. Nevertheless, the long time involved should not be taken as an indication that hydrates are not thermodynamically stable in the two-phase region. The phase diagram analyses presented in Section 4.1 indicate the thermodynamic validity of this region.

4.5.3 Methane Content of Water in Equilibrium with Hydrates

Data and predictions for methane dissolved in water, solely in equilibrium with hydrates (L_W–H without a vapor phase) find application in instances such as formation of hydrates in marine systems (Chapter 7). To date there are only few reliable hydrate data in equilibrium with water containing methane—the data of Servio and Englezos (2002) and Chou et al. (Personal Communication, December 18, 2006), as listed in Chapter 6.

Because there are so few data for the methane content of water in equilibrium with hydrate (L_W–H) regions, their accuracy cannot be determined. These data are very difficult to obtain due to the low methane concentrations (typically $<$100 ppm mol). The inaccuracies in normal experimental data in other phase regions are frequently greater than the absolute values of the water content in the L_W–H region.

As in the previous sections, it is worthwhile to compare these data against the predictions of CMSGem and User Manual, included on the CD in the endpapers, with examples in Appendix A.

4.6 Hydrate Enthalpy and Hydration Number from Phase Equilibrium

The enthalpy of hydrate formation of simple natural gas hydrate formers (from gas and water or ice) is given in Table 4.7 taken from the dissertation of Kamath (1984). Note that each component has two temperature regions, above and below the ice point, with a ΔH difference related by the heat of fusion at the ice point.

TABLE 4.7
Hydrate Formation Enthalpy for Three-Phase Conditions of Single Natural Gas Components Using ΔH [cal/gmol gas] = $a + b/T$ [K]

Component	Type	T range (°C)	$a \times 10^{-3}$	b
Methane	L_W–H–V	0 to 25	13.521	−4.02
Methane	I–H–V	−25 to 0	6.534	−11.97
Ethane	L_W–H–V	0 to 14	13.254	−15.00
Ethane	I–H–V	−25 to 0	8.458	−9.59
Propane	L_W–H–V	0 to 5	−37.752	250.09
Propane	I–H–V	−25 to 0	7.609	−4.90
Carbon dioxide	L_W–H–V	0 to 11	19.199	−14.95
Carbon dioxide	I–H–V	−25 to 0	9.290	−12.93
Nitrogen	L_W–H–V	0 to 25	6.188	18.37
Nitrogen	I–H–V	−25 to 0	4.934	−9.04
Hydrogen sulfide	L_W–H–V	0 to 25	6.782	31.45
Hydrogen sulfide	I–H–V	−25 to 0	8.488	−7.81

Source: From Kamath, V.A. *Study of Heat Transfer Characteristics During Dissociation of Gas Hydrates in Porous Media*, Ph.D. Dissertation, University of Pittsburgh, University Microfilms No. 8417404, Ann Arbor, MI, 1984. With permission.

The intention of this section is to relate these enthalpies both to the phase equilibrium values and to show how these values relate to microscopic structure and to hydration numbers at the ice point.

4.6.1 The Clausius–Clapeyron Equation and Hydrate Equilibrium

In the most common thermodynamic case, the Clapeyron equation is used with pure components to obtain the heat of vaporization from pure component two-phase (vapor pressure) data. The Clapeyron equation is one of the primary successes of thermodynamics, because it enables the calculation of ΔH, which is difficult to measure, from easily available properties of pressure and temperature.

In hydrate equilibrium, it may seem slightly unusual to apply it to binary systems (water and one guest component) of three-phase (L_W–H–V or I–H–V) equilibrium to obtain the heats of dissociation. As van der Waals and Platteeuw (1959b) point out, however, the application of the Clapeyron equation is thermodynamically correct, as long as the system is univariant, as is the case for simple hydrates.

If the volume of hydrate approximates that of water (or ice) in the hydrate formation reaction ($L_W + V \leftrightarrow H$), then to a good approximation, $\Delta V \approx V_g$ ($= zRT/P$, where z is compressibility). The substitution of this expression for ΔV

TABLE 4.8
Accuracy of the Clausius–Clapeyron Equation for Hydrate Heat of Dissociation to Vapor and Water

Component	ΔH calculated (kJ/mol gas)	ΔH measured (kJ/mol gas)
Methane	56.9	54.2
Ethane	71.1	71.8
Propane	126.0	129.2
Isobutane	130.4	133.2

in the Clapeyron equation (Equation 4.4) leads to a more useable form, namely, the Clausius–Clapeyron equation:

$$\frac{\mathrm{d}\,\ell\mathrm{n}\,P}{\mathrm{d}(1/T)} = -\frac{\Delta H}{zR} \tag{4.13}$$

Semilogarithmic plots of formation pressure versus reciprocal absolute temperature yield straight lines, over limited temperature ranges, for hydrate formation from either liquid water, or ice. From Equation 4.13 such linear plots either indicate (1) relatively constant values of the three factors: (a) heat of formation, ΔH, (b) compressibility factor, z, (c) stoichiometry ratios of water to guest or (2) cancellation of curvilinear behavior in these three factors.

The most recent confirmation of the validity of the Clausius–Clapeyron equation for hydrates was by Handa (1986a,b), who measured the heat of dissociation (via calorimetry) of the normal paraffins that form simple hydrates. Table 4.8 shows Handa's values for hydrate dissociation enthalpy compared to those calculated with the Clausius–Clapeyron equation by Sloan and Fleyfel (1992). The agreement appears to be very good for simple hydrates.

Roberts et al. (1940), Barrer and Edge (1967), Skovborg and Rasmussen (1994) present similar, detailed derivations to consider the use of the Clapeyron equation for hydrate binary and multicomponent systems. The reader is referred to the work of Barrer and Edge (1967) for the precise meaning of $\mathrm{d}P/\mathrm{d}T$ and the details of the derivation. Barrer and Stuart (1957) and Barrer (1959) point out that the problem in the use of the Clapeyron equation evolves from the nonstoichiometric nature of the hydrate phase. Fortunately, that problem is not substantial in the case of hydrate equilibrium, because the nonstoichiometry does not change significantly over small temperature ranges. At the ice point, where the hydrate number is usually calculated, the nonstoichiometry is essentially identical for each three-phase system at an infinitesimal departure on either side of the quadruple point.

4.6.1.1 Enthalpy of dissociation and cavity occupation

In this section, enthalpy evidence for structures I, II, and H is presented to suggest that guest size fixes the heat of dissociation. That is, heat of dissociation for the hydrate structure is determined by the cavity occupied. The initial work for sI and sII was presented by Sloan and Fleyfel (1992), with a critique by Skovborg and Rasmussen (1994) and a reply by Sloan and Fleyfel (1994). Similar results for sH are presented by Mehta and Sloan (1996b).

To a fair engineering approximation ΔH_d is not only a function of the hydrogen bonds in the crystal, but also a function of cavity occupation. Because the Clausius–Clapeyron equation determines the heat of hydrate formation by the slopes of plots of $\ln P$ versus $1/T$, one may easily determine relationships between heats of dissociation.

The evidence for such a relationship is as follows:

1. The slope of the hydrate dissociation line ($\ln P$ versus $1/T$) is directly related to the cavity size(s) occupied by the guests, as shown in Figure 4.23.
2. For mixed guests such as $CH_4 + C_2H_6$, Figure 4.24 shows that a superimposed identical slope fits all data over a wide range of mixed sI compositions for a value of $\Delta H = 74$ kJ/mol. Similarly, Figure 4.25 shows that mixtures of $CH_4 + C_3H_8$ have an identical superimposed

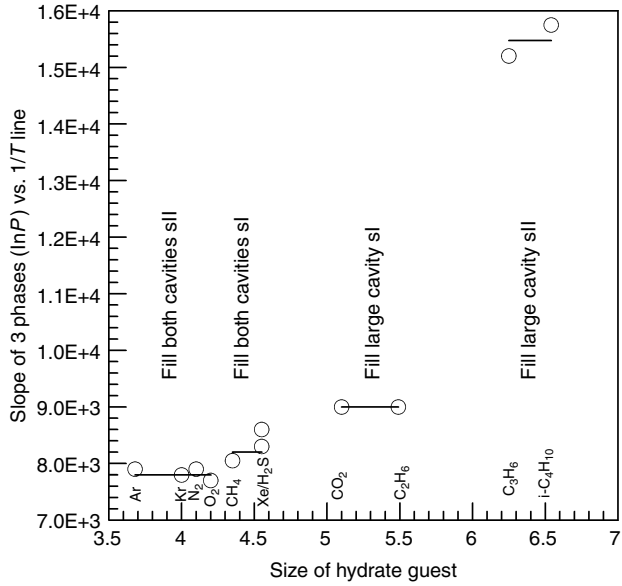

FIGURE 4.23 Relationship of the slope of the hydrate dissociation line ($\ln P$ vs. $1/T$) to the cavity size(s) occupied by guests. (Reproduced from Sloan, E.D., Fleyfel, F., *Fluid Phase Equilib.*, **96**, 233 (1994). With permission from Elsevier Science Publishers.)

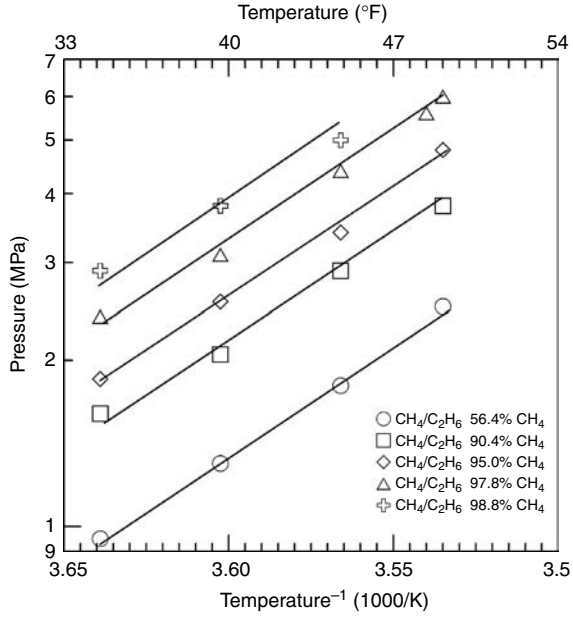

FIGURE 4.24 Hydrate dissociation lines for mixtures of methane and ethane. (Reproduced from Sloan, E.D., Fleyfel, F., *Fluid Phase Equilib.*, **76**, 123 (1992). With permission from Elsevier Science Publishers.)

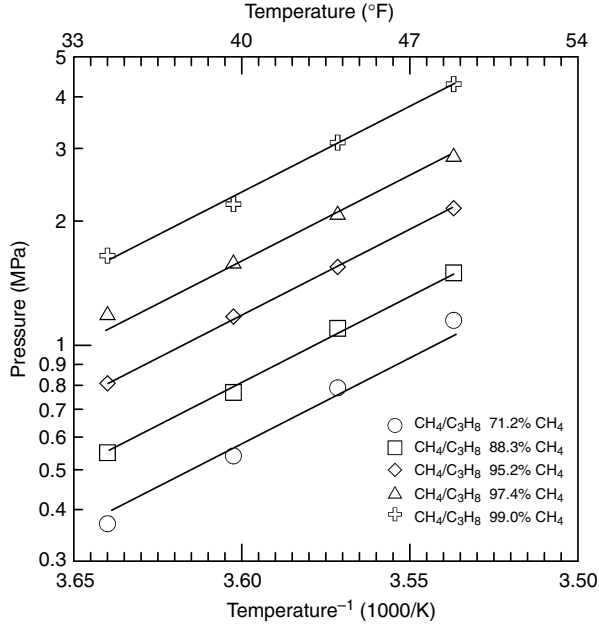

FIGURE 4.25 Hydrate dissociation lines for mixtures of methane and propane. (Reproduced from Sloan, E.D., Fleyfel, F., *Fluid Phase Equilib.*, **76**, 123 (1992). With permission from Elsevier Science Publishers.)

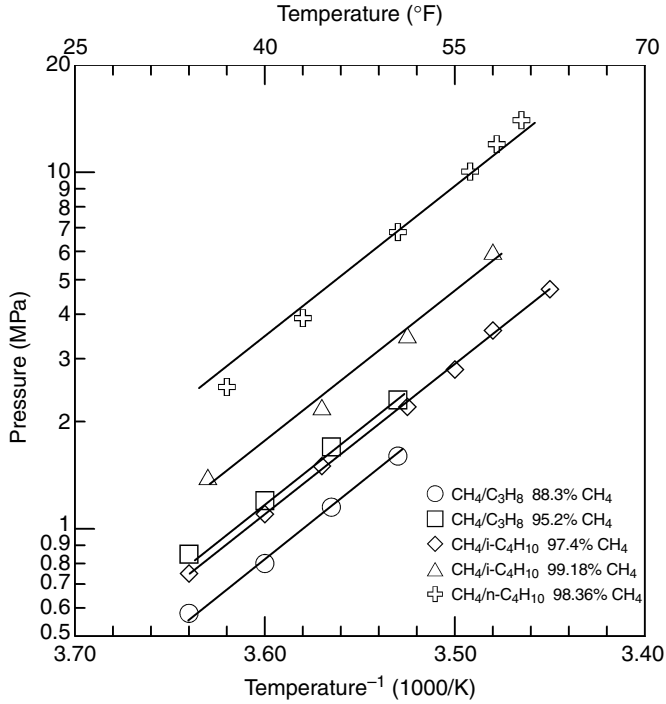

FIGURE 4.26 Hydrate dissociation lines for mixtures of methane with isobutane and methane with normal butane. (Reproduced from Sloan, E.D., Fleyfel, F., *Fluid Phase Equilib.*, **76**, 123 (1992). With permission from Elsevier Science Publishers.)

slope over a wide gas composition range for sII hydrate formation yielding a value of $\Delta H = 79.2$ kJ/mol. As indicated in Chapter 6, mixtures of $CH_4 + C_2H_6$ form sII hydrates over the concentration range 67–99% CH_4 even though CH_4 and C_2H_6 simple hydrates each form sI. The difference in the heats (5.2 kJ/mol) for these two mixtures may be within the experimental accuracy.

3. Figure 4.26 shows that semilogarithmic plots for several sII binary mixtures ($CH_4 + C_3H_8$, + n-C_4H_{10}, + i-C_4H_{10}) can be fit with a superimposed identical slope that is equal to the slope for $CH_4 + C_3H_8$ shown in Figure 4.25.
4. Figure 4.27 shows that the same slopes for sII hydrate in Figures 4.25 and 4.26 bracket the data for many natural gases.
5. Mehta and Sloan (1996b) present data in Table 4.9 for 19-structure H hydrates formers along univariant four-phase lines. With only three exceptions, the enthalpy of hydrate formation is 79.5 kJ/mol ±7%. In each case, methane occupies the 5^{12} and the $4^3 5^6 6^3$ cages while the larger guest occupies the $5^{12}6^8$ cage.

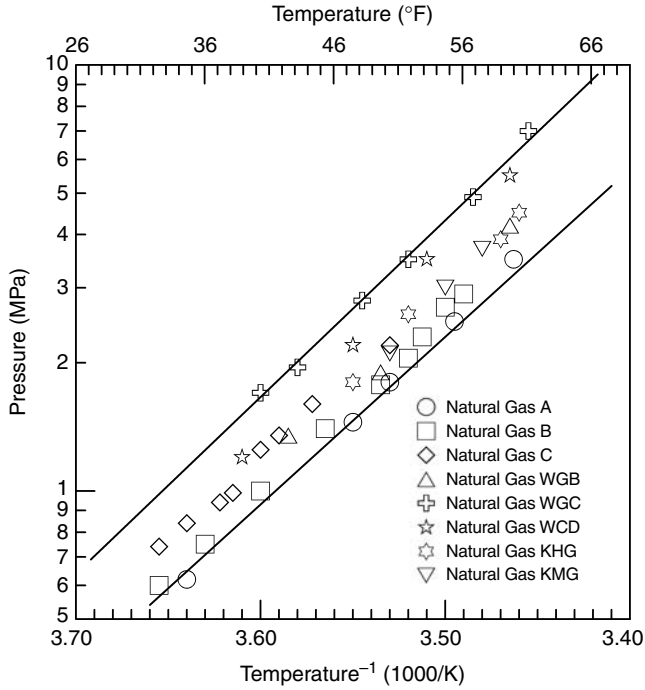

FIGURE 4.27 Hydrate dissociation lines for natural gases. (Reproduced from Sloan, E.D., Fleyfel, F., *Fluid Phase Equilib.*, **76**, 123 (1992). With permission from Elsevier Science Publishers.)

4.6.2 Determination of the Hydration Number

Historically, two periods occurred for the determination of the number of hydrate water molecules per guest molecule. In the first century (1778–1900) after the discovery of hydrates, the hydration number was determined directly. That is, the amounts of hydrated water and guest molecules were each measured via various methods. The encountered experimental difficulties stemmed from two facts: (1) the water phase could not be completely converted to hydrate without some occlusion and (2) the reproducible measurement of the inclusion of guest molecules was hindered by hydrate metastability. As a result, the hydrate numbers differed widely for each substance, with a general reduction in the ratio of water molecules per guest molecule as the methods became refined with time. After an extensive review of experiments of the period, Villard (1895) proposed "Villard's Rule" to summarize the work of that first century of hydrate research:

> The dissociable (hydrate) compounds, that form through the unification of water with different gases and that are only stable in the solid form, all crystallize regularly and have the same constitution that can be expressed by the formula $M + 6H_2O$, where M designates a molecule of the respective gas

TABLE 4.9
Structure H Heats of Dissociation (ΔH) at 273.15 K

Guest	−Slope (1/K)	Comp z_{CH_4}	ΔH (kJ/mol gas)
2-Methylbutane	9,333	0.9310	72.24
2,2-Dimethylbutane	10,118	0.9641	81.10
2,3-Dimethylbutane	10,324	0.9555	82.01
2,2,3-Trimethylbutane	9,289	0.9688	74.66
2,2-Dimethylpentane	8,006	0.9279	61.76
3,3-Dimethylpentane	9,906	0.9584	78.93
Methylcyclopentane	10,384	0.9578	82.68
Ethylcyclopentane	10,632	0.9595	84.81
Methylcyclohexane	10,173	0.9650	81.61
1,1-Dimethylcyclohexane	10,465	0.9750	84.83
cis-1,2-Dimethylcyclohexane	10,161	0.9624	81.30
Cycloheptane	10,568	0.9504	83.50
Cyclooctane	10,568	0.9641	84.70
Adamantane	7,899	0.9579	62.90
Cycloheptene	7,651	0.9508	60.48
cis-Cyclooctene	9,445	0.9616	75.51
2,3-Dimethyl-1-butene	9,709	0.9431	76.12
3,3-Dimethyl-1-butene	9,704	0.9529	76.87
3,3-Dimethyl-1-butyne	9,228	0.9246	70.93

While the above estimate may seem antiquated, Villard's Rule is a good rule of thumb in many cases. Note that if a guest fills all of both cavities in sI and sII, the hydration number would be 5.75 and 5.67, respectively, so a value of 6 allows for the possibility of empty cages, and is frequently taken as a good approximation to the hydration number for methane hydrates. However, Villard's Rule is not a good approximation for components that only fill the large cavity of either sI (e.g., ethane) or sII (e.g., propane).

4.6.2.1 Using the Clapeyron equation to obtain hydration number

After 1900 the direct determination of hydrate number was abandoned in favor of the second, indirect method. The indirect method is still in use today and is based on calculation of the enthalpies of formation of hydrate from gas and water, and from gas and ice. This method was originally proposed by de Forcrand (1902) who used the Clapeyron equation to obtain the heat of dissociation from three-phase, pressure–temperature data, as in the below paragraph. With this more accurate method many exceptions were found to Villard's Rule. The historical summary provided in Chapter 1 indicates that while the number of hydrated water molecules was commonly thought to be an integer, frequently that integer

was determined to differ from 6, particularly after de Forcrand had proposed his method.

The method considers the equilibrium of gas and n mol of liquid water (or ice) with hydrates on either side of the ice point:

$$\text{Gas} + n(\text{Liquid Water}) \leftrightarrow \text{Hydrate} \quad \Delta H_1 \tag{4.14}$$

$$\text{Gas} + n(\text{Ice}) \leftrightarrow \text{Hydrate} \quad \Delta H_2 \tag{4.15}$$

Equation 4.14 for L_W–H–V equilibrium may be subtracted from Equation 4.15 for I–H–V equilibrium at quadruple point Q_1 (approximately 273 K), with the result of the number of moles of liquid water converted to ice:

$$n(\text{Liquid water}) \leftrightarrow n(\text{Ice}) \quad \Delta H_3 \tag{4.16}$$

where $\Delta H_3 = \Delta H_1 - \Delta H_2$.

Because the enthalpy of fusion (ΔH_f) of water is well known, ΔH_3, the difference in the ΔH values of Equations 4.14 and 4.15, may be divided by the heat of fusion of ice (ΔH_f) to obtain n, the number of moles of water (or ice) converted to hydrates.

The de Forcrand method has been found to be much more accurate than Villard's Rule. One reason for its accuracy is related to the determination of ΔH_1 and ΔH_2 from three-phase (L_W–H–V or I–H–V) equilibrium measurements of pressure and temperature via the Clapeyron equation:

$$\frac{dP}{dT} = \frac{\Delta H}{T \Delta V} \tag{4.17}$$

where ΔH may be taken as the enthalpy change in either Equation 4.14 or 4.15, ΔV is the corresponding volume change, and P and T are the phase equilibrium points along the appropriate three-phase line.

Example 4.7: Hydration Number from Pressure–Temperature Data for L_W–H–V and I–H–V

Sortland and Robinson (1964) measured the formation conditions of sulfur hexafluoride hydrates from 264 to 297 K. Using the Clapeyron equation with their data they determined values of $\Delta H_1 = 29{,}570$ cal/gmol and $\Delta H_2 = -5140$ cal/gmol. When these two values are added and the result is divided by the molar heat of fusion of water (1435.3 cal/gmol) a value of 17.02 gmol H_2O per gmol SF_6 is obtained in the hydrate. This value is significantly different from that of Villard's Rule, and indicates that the SF_6 molecules essentially fill all of the large cavities in structure II hydrate. If each of the large cavities in structure II were filled, the ratio would be

exactly 17 (=136 water molecules/8 cavities). Note that most natural gases fill both cavities and thus have a lower hydration number that is approximated by Villard's Rule.

This indirect method avoids problems of metastability and occlusion in the direct method because the P–T measurements are at equilibrium and they are not dependent on the amounts of each phase present. The question about the validity of the method centers on the validity of the Clapeyron equation to the three-phase hydrate equilibrium, as discussed in the following section.

Table 4.10 shows the literature values for hydrate numbers, all obtained using de Forcrand's method of enthalpy differences around the ice point. However, Handa's values for the enthalpy differences were determined calorimetrically, while the other values listed were determined using phase equilibrium data and the Clausius–Clapeyron equation. The agreement appears to be very good for simple hydrates. Note also that hydrate filling is strongly dependent on

TABLE 4.10
Hydration Number ($M \cdot nH_2O$) for Simple Hydrates of Natural Gas Components from Handa (1986a,b)

Component	n	Reference
Methane	6.00	Handa (1986a,b)
	5.99	Circone et al. (2006)
	5.77	Glew (1962)
	7.00	Roberts et al. (1941)
	7.18	Deaton and Frost (1946)
	6.00	Galloway et al. (1970)
	7.4	de Roo et al. (1983)
	6.3	de Roo et al. (1983)
Ethane	7.67	Handa (1986a,b)
	7.00	Roberts et al. (1941)
	8.25	Deaton and Frost (1946)
	8.24	Galloway et al. (1970)
Propane	17.0	Handa (1986a,b)
	5.7	Miller and Strong (1946)
	17.95	Deaton and Frost (1946)
	18.0	Knox et al. (1961)
	17.0	Cady (1983a)
Isobutane	17.0	Handa (1986b)
	17.1	Uchida and Hayano (1964)
	17.5	Rouher and Barduhn (1969)

pressure and temperature, so exact comparisons can only be made at identical conditions.

4.6.2.2 Hydration numbers by the Miller and Strong method

After de Forcrand's Clapeyron, and Handa's methods, a third method for the determination of hydrate number, proposed by Miller and Strong (1946), was determined to be applicable when simple hydrates were formed from a solution with an inhibitor, such as a salt. They proposed that a thermodynamic equilibrium constant K be written for the physical reaction of Equation 4.14 to produce 1 mol of guest M, and n mol of water from 1 mol of hydrate. Writing the equilibrium constant K as multiple of the activity of each product over the activity of the reactant, each raised to its stoichiometric coefficient, one obtains:

$$\mathrm{M} \cdot (\mathrm{H_2O})_n \leftrightarrow \mathrm{M} + n\mathrm{H_2O} \tag{4.14a}$$

where $\mathrm{M} \cdot (\mathrm{H_2O})_n \equiv$ hydrate (H)

$$K = \frac{(a_{\mathrm{M}})(a_{\mathrm{W}})^n}{a_{\mathrm{H}}} \tag{4.18}$$

The thermodynamic reaction equilibrium constant K, is only a function of temperature. In Equation 4.18, a_{M}, the activity of the guest in the vapor phase, is equal to the fugacity of the pure component divided by that at the standard state, normally 1 atm. The fugacity of the pure vapor is a function of temperature and pressure, and may be determined through the use of a fugacity coefficient. The method also assumes that a_{H}, the activity of the hydrate, is essentially constant at a given temperature regardless of the other phases present.

The activity of water a_{W} in Equation 4.18 is normally taken as unity disregarding the solubility of the gas. At a given temperature, if an inhibitor such as a salt is present, the activity of the water decreases and the activity of the gas must increase in order to maintain a constant product $\mathrm{K} \cdot a_{\mathrm{H}}$ at that temperature. Thus writing a second equation for the formation of a hydrate from an inhibited liquid we get

$$a_{\mathrm{M}} \cdot a_{\mathrm{W}}^n = K \cdot a_{\mathrm{H}} \quad \text{without the inhibitor} \tag{4.18a}$$

and

$$a'_{\mathrm{M}} \cdot a'^n_{\mathrm{W}} = K \cdot a_{\mathrm{H}} \quad \text{with the inhibitor} \tag{4.19}$$

Subtracting Equation 4.19 from Equation 4.18a, with the right sides constant, one may replace the activity of the guest M with its fugacity (if the same standard

state fugacity is used for both activities) to obtain

$$f_M \cdot a_W^n = f_M' \cdot a_W'^n \tag{4.20}$$

Recalling that the (′) denotes the presence of an inhibitor, Equation 4.20 may be rearranged to obtain the hydrate number n as

$$n = \frac{\ell n(f/f')}{\ell n(a'/a)} \tag{4.21}$$

In Equation 4.21, the activity of pure water (a) is unity and the activity of the water with the inhibitor (a') is the product of the water concentration (x_W) and the activity coefficient (γ_W). The water concentration is known and the activity coefficient is easily obtained from colligative properties for the inhibitor, such as the freezing point depression. For instance the activity of water in aqueous sodium chloride solutions may be obtained from Robinson and Stokes (1959, p. 476) or from any of several handbooks of chemistry and physics.

With the above data, Equation 4.21 indicates that the hydrate number n may be obtained from a measurement of the increase of the hydrate pressure with an inhibitor present at a given temperature. The fugacity may be calculated for a pure component from any of a number of thermodynamic methods given a temperature and pressure. Only in the case of a pure ideal gas (very low pressure or very high temperature) may the fugacities be replaced with the pressure itself.

It should be noted that this method contains several key assumptions, as follows:

1. The occupation of the hydrate does not change over the region of pressure and temperature considered.
2. The equilibrium constant K does not change when the inhibitor is added to the aqueous fluid, but it is only a function of temperature.
3. The activity of the hydrate phase is constant at a given temperature regardless of the other phases present.
4. The vapor presence of any component other than the hydrate former may be neglected, including any water or inhibitor present in the liquid.
5. The aqueous phase without inhibitor is pure water.

Exceptions may be found to the above assumptions and consequently the method might be expected to be more limited than the de Forcrand method presented in Section 4.6.2.1. On the other hand, the de Forcrand method requires more data. Rouher and Barduhn (1969) indicate that better results are achieved with the Miller and Strong method when NaCl solutions are in the range between 5 and 15 wt%.

Patil (1987) determined the hydrate number of simple propane hydrates to be 18.95 by the de Forcrand method; using the Miller and Strong method he obtained hydrate numbers of 19.20, 19.95, and 19.89 for NaCl solutions of 3, 5, and

10 wt%, respectively. Wilms and van Haute (1973) presented the mathematically correct version of the Miller and Strong method, which eliminates some of the above assumptions, together with the statistical thermodynamic method of the following chapter. Wilms and van Haute suggest the Miller and Strong equations to be a special case of a more rigorous method.

4.7 Summary and Relationship to Chapters Which Follow

The object of this chapter is to provide the reader with a qualitative understanding of hydrate phase equilibrium. Such an understanding implies a historical overview, which also provides successive approximations to hydrate phase equilibrium in terms of accuracy. The accuracy of three-phase prediction is given below in the order of increasing accuracy:

1. For pure components, use semilogarithmic interpolation between quadruple points Q_1 and Q_2.
2. For pure components, use Antoine's equation with constants given in Table 4.1.
3. For mixtures, use the gas gravity method.
4. For mixtures, use the K_{vsi} method, as the most accurate method of this chapter.

In the following chapter, the most accurate method available is discussed for the determination of hydrate equilibrium—that of statistical thermodynamics. The consideration of this method ties the macroscopic phase equilibrium, such as has been discussed qualitatively in the present chapter, to the microscopic structure discussed in Chapter 2.

The bridging of the microscopic and macroscopic phenomena is satisfying both from a theoretical and from a pragmatic standpoint. Mathematical bridges between the microscopic and macroscopic domains are the major focus of Chapter 6. Applications of the concepts of this chapter are also found in the final two chapters. Hydrates in the earth provide natural examples of phase equilibrium as detailed in Chapter 7. Applications to artificial hydrates and their problems in flow lines are presented in Chapter 8.

References

Austvik, T., Hustvedt, E., Meland, B., Berge, L., Lysne, D., "Tommeliten Gamma Field Hydrate Experiments," presented at *Seventh International Conference on Multiphase Production*, BHRA Group Conf. Ser. Publication 14, Cannes, June 7–9 (1995).

Bansal, V., *Kinetic Study of Clathrate Hydrates*, M.S. Thesis, T-4545, Colorado School of Mines, Golden, CO, January (1994).

Bansal, V., Christiansen, R.L., Sloan, E.D., "Influence of Guest Vapor–Liquid Critical Point on Hydrate Formation Conditions," *AIChE J.*, **39**(10), 1735 (1993).

Barrer, R., Edge, A.V.J., *Proc. R. Soc. (London)* A, **300** (1967).
Barrer, R.M., *Nature*, **183**, 463 (1959).
Barrer, R.M., Stuart, W.I., *Proc. R. Soc. (London)* A, **243**, 172 (1957).
Becke, P., Kessel, D., Rahimian, I., "Influence of Liquid Hydrocarbons on Gas Hydrate Equilibrium," SPE 25032, in *Proc. Europ. Petrol Conf. Cannes*, Nov. 16–18 (1992).
Ben-Naim, A., *Hydrophobic Interaction*, Plenum Press, New York (1980).
Berecz, E., Balla-Achs, M., *Gas Hydrates, Studies in Inorganic Chemistry*, Elsevier, New York, **411**, p. 343 (1977, English Translation 1983).
Besnard, G., Song, K.Y., Hightower, J.W., Kobayashi, R., Elliot, D., Chen, R., "New Method of Temperature-Ramping, Isobaric Experiments to Study the Hydrate Formation and Composition," in *Proc. 213th ACS National Meeting*, San Francisco, CA, April 13–17, **42**(2), 551 (1997).
Bourrie, M.S., Sloan, E.D., *Gas Proc. Assoc. Res. Rep.*, **100** (1986).
Brown, G.G., *Trans AIME*, **160**, 65 (1945).
Bucklin, R.W., Toy, K.G., Won, K.W., "Hydrate Control of Natural Gas Under Arctic Conditions Using TEG," in *Proc. Gas Conditioning Conference*, Norman, OK, (1985).
Cady, G.H., *J. Phys. Chem.*, **85**, 4437 (1983a).
Cady, G.H., *J. Chem. Ed*, **60**, 915 (1983b).
Carson, D.B., Katz, D.L., *Trans. AIME*, **146**, 150 (1942).
Circone, S., Kirby, S.H., Stern, L.A., *J. Phys. Chem. B*, **110**(16), 8232 (2006).
de Forcrand, R., *Compt. Rend*., **135**, 959 (1902).
de Roo, J.L., Peters, C.J., Lichtenthaler, R.N., Diepen, G.A.M., *AIChE J.*, **29**, 651 (1983).
Deaton, W.M., Frost, E.M., Jr., *Gas Hydrates and their Relation to the Operation of Natural-Gas Pipe Lines*, U.S. Bureau of Mines Monograph 8, p. 101 (1946).
Dickens, G.D., Quinby-Hunt, M.S., *J. Geophys. Res.*, **102**, 773 (1997).
Franks, F., in *Water: A Comprehensive Treatise* (Franks, F., ed.) Plenum Press, New York, **2**, Chapter 1 (1973).
Galloway, T.J., Ruska, W., Chappelear, P.S., Kobayashi, R., *Ind. Enq. Chem. Fundam*., **9**, 237 (1970).
Gibbs, J.W., *The Collected Works of J. Willard Gibbs*, *Thermodynamics*, Yale University Press, New Haven, CT, **I,** pp. 55–353 (1928).
Gjertsen, L., Austvik, T., Urdahl, O., in *Proc. Second International Conference on Natural Gas Hydrates* (Monfort, J.P., ed.), Toulouse, June 2–6, p. 155 (1996).
Glew, D.N., *J. Phys. Chem*., **66**, 605 (1962).
Hammerschmidt, E.G., *Ind. Eng. Chem*., **26**, 851 (1934).
Hammerschmidt, E.G., *Gas*, **15**(5), 30 (1939).
Handa, Y.P., *J. Chem. Thermo*., **18**, 891 (1986a).
Handa, Y.P., *Calorimetric Studies of Laboratory Synthesized and Naturally Occurring Gas Hydrates*, paper presented at AIChE 1986 Annual Meeting Miami Beach, Nov 2–7 (1986b).
Handa, Y.P., *J. Phys. Chem*., **94**, 2652 (1990).
Harmens, A., Sloan, E.D., *Can. J. Chem. Eng*., **68**, 151 (1990).
Holder, G.D., *Multi-Phase Equilibria in Methane–Ethane–Propane–Water Hydrate Forming Systems*, Ph.D. Thesis, University of Michigan, University Microfilms No. 77-7939, Ann Arbor, MI 48106, (1976).
Huo, Z., Hester, K., Miller, K.T., Sloan, E.D., *AIChE J.*, **49**, 1300 (2003).

Jacoby, R.H., "Vapor–Liquid Equilibrium Data for Use of Methanol in Preventing Gas Hydrates," in *Proc. Gas Hydrocarbon. Control Conference*. University of Oklahoma, Norman, OK (1953).

Jhaveri, J., Robinson, D.B., *Can. J. Chem. Eng*., **43**, 75 (1965).

Kamath, V.A., *Study of Heat Transfer Characteristics during Dissociation of Gas Hydrates in Porous Media*, Ph.D. Dissertation, University of Pittsburgh, University Microfilms No. 8417404, Ann Arbor, MI (1984).

Katz, D.L., *Trans AIME*, **160**, 140 (1945).

Katz, D.L., *J. Petrol Tech.*, **24**, 557 (1972).

Katz, D.L., Cornell, D., Kobayashi, R., Poettmann, F.H., Vary, J.A., Elenbaas, J.R., Weinaug, C.F., *Handbook of Natural Gas Engineering*, McGraw-Hill, New York, p. 802, (1959).

Knox, W.G., Hess, M., Jones, G.E., Smith, H.B., *Chem. Eng. Prog*., **57**(2), 66 (1961).

Kobayashi, R., *Vapor–Liquid Equilibrium in Binary Hydrocarbon–Water Systems*, Ph.D. Dissertation, University of Michigan, University Microfilms No. 3521, Ann Arbor, MI (1951).

Kobayashi, R., Katz, D.L., *Trans AIME*, **186**, 66 (1949).

Kobayashi, R., Katz, D.L., *Trans AIME*, **204**, 51 (1955).

Kobayashi, R., Song, K.Y., Sloan, E.D., in *Petroleum Engineering Handbook* (Bradley, H.B., ed.) Society of Petrol Eng., Richardson, TX, Chapter 25 (1987).

Koga, K., *Study of Stability and Dynamics of Clathrate Hydrates and Supercritical Fluids*, Ph.D. Thesis, Kyoto University, Japan (1995).

Koga, K., Tanaka, H., *J. Chem. Phys*., **104**, 263 (1996).

Koga, K., Tanaka, H., Nakanishi, K., *J. Chem. Phys*., **101**, 3127 (1994a).

Koga, K., Tanaka, H., Nakanishi, K., *Mol. Simul*., **12**(3–6), 241 (1994b).

Koretsky, M.D., *Engineering and Chemical Thermodynamics*, John Wiley, Hoboken, NJ, 2004.

Kuhs, W., Chazallon, B., Radaelli, P., Pauer, F., Kipfstuhl, J., in *Proc. Second International Conference on Natural Gas Hydrates* (Monfort, J.P., ed.) Toulouse, France, June 2–6, p. 9 (1996).

Loh, J., Maddox, R.N., Erbar, J.H., *Oil Gas J*., **96**(May), 16, (1983).

Makogon, T.Y., Mehta, A.P., Sloan, E.D., *J. Chem. Eng. Data*, **41**, 315 (1996).

Makogon, Y.F., *Hydrates of Natural Gas*, Moscow, Nedra, Izadatelstro, p. 208 (1974 in Russian) Transl W.J. Cieslesicz, PennWell Books, Tulsa, Oklahoma p. 237 in Russian, (1981 in English).

Mann, S.L., McClure, L.M., Poettmann, F.H., Sloan, E.D., "Vapor–Solid Equilibrium Ratios for Structure I and Structure II Natural Gas Hydrates," in *Proc. 68th Annual Gas Processing Association Convention*, San Antonio, TX, March 13–14 (1989).

McKetta, J.J., Wehe, A.H., *Petroleum Refiner*, **37**, 153 August (1958).

Mehta, A.P., *A Thermodynamic Investigation of Structure H Clathrate Hydrates*, Ph.D. Thesis, Colorado School of Mines, Golden, CO (1996).

Mehta, A.P., Ripmeester, J., "Structural Characterization of Hydrate Formation in Black Oil and Gas Condensate Systems," in *Proc. Fourth International Conference on Gas Hydrates*, Yokohama, Japan, May 19–23, 580 (2002).

Mehta, A.P., Sloan, E.D., in *Proc. Second International Conference on Natural Gas Hydrates* (Monfort, J.P., ed.), Toulouse, France, June 2–6, p. 1 (1996a).

Mehta, A.P., Sloan, E.D., "Structure H Hydrates: Implications for the Petroleum Industry," in *Proc. 1996 Annual Technical Conference*, SPE 36742, 607 Denver, CO, October 6–9 (1996b).

Menten, P.D., Parrish, W.R., Sloan, E.D., *Ind. Eng. Chem. Proc. Des. Dev*., **20**, 399 (1981).
Miller, B., Strong, E.R., *Am. Gas Assoc. Monthly*, **28**(2), 63 (1946).
Nakayama, H., Hashimoto, M., *Bull. Chem. Soc. Japan*, **53**, 2427 (1980).
Nakayama, H., Brouwer, D.H., Handa, Y.P., Klug, D.D., Tse, J.S., Ratcliffe, C.I., Zhu, X., Ripmeester, J.A., "Methanol: Clathrate Hydrate Former or Inhibitor?" in *Proc. 213th ACS National Meeting*, San Francisco, CA, April 13–17, **42**(2), 516 (1997).
Nelson, K., *Hydrocarbon Process.*, **September**, 161 (1973).
Ng, H.-J., Chen, C.-J., *Gas Proc. Assoc. Res. Rep.* **149**, March (1995).
Ng, H.-J., Robinson, D.B., *AIChE J.*, **23**, 477 (1977).
Ng, H.-J., Robinson, D.B., *Gas Proc. Assoc. Res. Rep.*, **66**, April (1983).
Nielsen, R.B., Bucklin, R.W., *Hydrocarbon Process.*, April, 71, (1983).
Nixdorf, J., Oellrich, L., in *Proc. Second International Conference on Natural Gas Hydrates* (Monfort, J.P., ed.) Toulouse, France, June 2–6, 17 (1996).
Noaker, L.J., Katz, D.L., *Trans AIME*, **201**, 237 (1954).
Olds, R.H., Sage, B.H., Lacey, W.N., *Ind. Enq. Chem*., **34**, 1223 (1942).
Patil, S.L., *Measurements of Multiphase Gas Hydrates Phase Equilibria: Effect of Inhibitors and Heavier Hydrocarbon Components*, M.S. Thesis, University of Alaska (1987).
Patwardhan, V.S., Kumar, A., *AIChE J.*, **32**, 1419 (1986).
Pieroen, A.P., *Rec. Trav. Chim*., **74**, 995 (1955).
Poettmann, F.H., *Hydrocarbon Proc*., **63**(6), 111 (1984).
Pohlman, J.W., Canuel, E.A., Chapman, N.R., Spence, G.D., Whiticar, M.J., Coffin, R.B., *Org. Geochem*., **36**, 703 (2005).
Records, J.R., Seely, D.H., Jr., *Trans AIME*, **192**, 61 (1951).
Ripmeester, J.A., Tse, J.A., Ratcliffe, C.I., Powell, B.M., *Nature*, **325**, 135 (1987).
Ripmeester, J.A., Ratcliffe, C.I., *Inclusion Compounds* (Atwood, J.L., Davies, J.E.D., et al., eds.), **5**, Oxford University Press (1991).
Roberts, O.L., Brownscombe, E.R., Howe, L.S., *Oil Gas J*., **39**(30), 37 (1940).
Roberts, O.L., Brownscombe, E.R., Howe, L.S., Ramser, H., *Petrol. Eng*., **3**, 56 (1941).
Robinson, D.B., Mehta, B.R., *J. Can. Petr. Tech*., **10**, 33 (1971).
Robinson, R.A., Stokes, R.H., *Electrolyte Solutions*, Butterworths Scientific Publications, London (1959).
Rouher, O.S., Barduhn, A.J., *Desalination*, **6**, 57 (1969).
Sassen, R., MacDonald, I.R., *Org. Geochem*., **22**(6), 1029 (1994).
Scauzillo, F.R., *Chem. Eng. Prog*., **52**, 324 (1956).
Servio, P., Englezos, P., *J. Chem. Eng. Data*, **47**, 87 (2002).
Skinner, W., Jr., *The Water Content of Natural Gas at Low Temperatures*, M.S. Thesis, University of Oklahoma, Norman, OK (1948).
Skovborg, P., Rasmussen, P., *Chem. Eng. Sci*., **49**, 1131 (1994).
Sloan, E.D., in *Proc. 63rd Annual Convention of Gas Processors Association*, **63**, 163, San Antonio, TX, March 15 (1984).
Sloan, E.D., Fleyfel, F., *Fluid Phase Equilib*., **76**, 123 (1992).
Sloan, E.D., Fleyfel, F., *Fluid Phase Equilib.*, **96**, 233 (1994).
Sloan, E.D., Khoury, F.M., Kobayashi, R., *Ind. Eng. Chem. Fundam.*, **15**, 318 (1976).
Sloan, E.D., Sparks, K.A., Johnson, J.J., Bourrie, M.S., *Fluid Phase Equilib.*, **29**, 233 (1986).
Sloan, E.D., Sparks, K.A., Johnson, J.J., *Ind. Eng. Chem. Res*., **26**, 1173 (1987).
Song, K.Y., Feneyrou, G., Fleyfel, F., Martin, R., Levois, J., Kobayashi, R., *Fluid Phase Equilib.*, **128**, 249 (1997).
Song, K.Y., Kobayashi, R., *Ind. Eng. Chem. Fund*., **21**, 391 (1982).

Song, K.Y., Kobayashi, R., *SPE Form. Eval*., December, 500 (1987).
Song, K.Y., Kobayashi, R., *Fluid Phase. Equilib.*, **95**, 281 (1994).
Sortland, L.D., Robinson, D.B., *Can. J. Chem. Eng*., **42**, 38 (1964).
Stange, E., Majeed, A., Overa, S., "Experiments and Modeling of the Multiphase Equilibrium of Inhibition of Hydrates," in *Proc. 68th Annual Gas Processors Association Conv*ention, San Antonio, TX, March 13–14, 1989.
Svartas, T.M., "Overview of Hydrate Research at Rogalands-Forskning," presented at *BHRA Conference on Operational Consequences of Hydrate Formation and Inhibition Offshore*, Cranfield, UK, November 3, (1988).
Thakore, J.L., Holder, G.D., *Ind. Eng. Chem. Res*., **26**, 462 (1987).
Tohidi, B., Danesh, A., Burgass, R., Todd, A., SPE28478, in *Proc. SPE 69th Annual Technical Conference*, New Orleans, September 25–28, 157 (1994).
Tohidi, B., Ostergaard, K.K., Danesh, A., Todd, A.C., Burgass, R.W., *Can. J. Chem. Eng*., **79**, 384 (2001).
Toplak, G.J., *Solubilities of Hydrocarbon Gas Mixtures in Distilled Water Near Hydrate Forming Conditions*, M.S. Thesis, University of Pittsburgh, PA (1989).
Townsend, F.M., Reid, L.S., *Hydrate Control in Natural Gas Systems*, Laurance Reid Associates, Inc., P.O. Box 1188, Norman, OK 73070 (1978).
Uchida, T., Hayano, I., *Rep. Govt. Chem. Ind. Res. Inst., Tokyo*, **59**, 382 (1964).
Unruh, C.H., Katz, D.L., *Trans AIME*, **186**, 83 (1949).
van der Waals, J.H., Platteeuw, J.C., "Clathrate Solutions," *Adv. Chem. Phys.*, **2**, 1 (1959a).
van der Waals, J.H., Platteeuw, J.C., *Nature*, **183**(4659), 462 (1959b).
van Hinsberg, M.G.E., Scheerboom, M.I.M., Schouten, J.A., *J. Chem. Phys*., **99**, 752 (1993).
van Hinsberg, M.G.E., Schouten, J.A., "The Phase Diagram of Nitrogen Clathrate Hydrate," *Am. Inst. Phys.*, **309**, 271 (1994).
Verma, V.K., *Gas Hydrates from Liquid Hydrocarbon–Water Systems,* Ph.D. Thesis, University of Michigan, University Microfilms No. 75-10,324, Ann Arbor, MI (1974).
Villard, P., *Compt. Rend*., **120**, 1262 (1895).
Wallqvist, A., *Chem. Phys. Lett*., **182**(3,4), 237 (1991).
Wallqvist, A., *J. Chem. Phys*., **96**, 5377 (1992).
Wierzchowski, S.A., Monson, P.A., *Ind. Eng. Chem. Res*., **45**, 424 (2006).
Wilcox, W.I., Carson, D.B., Katz, D.L., *Ind. Eng. Chem*., **33**, 662 (1941).
Wilms, D.A., van Haute, A.A., *Fourth International Symposium on Fresh Water From the Sea*, **3**, 477 (1973).
Woolridge, P.J., Richardson, H.H., Devlin, J.P., *Chem. Phys*., **87**, 4126 (1987).
Wu., B.-J., Robinson, D.B., Ng, H.-J., *J. Chem. Thermodyn*., **8**, 461 (1976).
Yamane, K. Aya, I., "Solubility of Carbon Dioxide in Hydrate Region at 30 MPa," in *Proc. International Conference on Technology for Marine Environment Preservation*, Tokyo, Sept 24–29, **2**, 911 (1995).
Yamanlar, S., Poettmann, F.R., Sloan, E.D., *Hydrocarbon Process.*, 155(September) (1991).
Yousif, M., Austvik, T., Berge, L., Lysne, D., in *Proc. Second International Conference on Natural Gas Hydrates* (Monfort, J.P., ed.) Toulouse, France, June 2–6, 291 (1996).

5 A Statistical Thermodynamic Approach to Hydrate Phase Equilibria

Introduction and Overview

The object of Chapter 4 was to provide an overview of phase equilibria concepts, which are more easily obtained through phase diagrams and the approximate, historical methods. With Chapter 4 as background, the subject of the present chapter is the phase equilibrium calculation method that is both most accurate and most comprehensive.

The statistical thermodynamic method discussed here provides a bridge between the molecular crystal structures of Chapter 2 and the macroscopic thermodynamic properties of Chapter 4. It also affords a comprehensive means of correlation and prediction of all of the hydrate equilibrium regions of the phase diagram, without separate prediction schemes for two-, three-, and four-phase regions, inhibition, and so forth as in Chapter 4. However, for a qualitative understanding of trends and an approximation (or a check) of prediction schemes in this chapter, the previous chapter is a valuable tool.

Section 5.1 presents the fundamental method as the heart of the chapter—the statistical thermodynamics approach to hydrate phase equilibria. The basic statistical thermodynamic equations are developed, and relationships to measurable, macroscopic hydrate properties are given. The parameters for the method are determined from both macroscopic (e.g., temperature and pressure) and microscopic (spectroscopic, diffraction) measurements. A Gibbs free energy calculation algorithm is given for multicomponent, multiphase systems for comparison with the methods described in Chapter 4. Finally, Section 5.1 concludes with *ab initio* modifications to the method, along with an assessment of method accuracy.

Section 5.2 shows the prediction method of phase diagrams of the major components of natural gas, namely methane, ethane, and propane hydrates and their mixtures at the common deep-ocean temperature of 277 K. Many of the commonly observed phenomena in natural gas systems are illustrated, while the power of the method is shown to go beyond that of Chapter 4, to illustrate future needs.

The method presented in this chapter serves as a link between molecular properties (e.g., cavities and their occupants as measured by diffraction and spectroscopy) and macroscopic properties (e.g., pressure, temperature, and density as measured by pressure guages, thermocouples, etc.) As such Section 5.3 includes a brief overview of molecular simulation [molecular dynamics (MD) and Monte Carlo (MC)] methods which enable calculation of macroscopic properties from microscopic parameters. Chapter 2 indicated some results of such methods for structural properties. In Section 5.3 molecular simulation is shown to predict qualitative trends (and in a few cases quantitative trends) in thermodynamic properties. Quantitative simulation of kinetic phenomena such as nucleation, while tenable in principle, is prevented by the capacity and speed of current computers; however, trends may be observed.

At the onset, it should be noted that the method presented here has been the subject of several recent theses. The reader is sure to gain additional insights from the thesis of Ballard (2002) who composed the revised method on the endpapers CD. A summary of the method is detailed in series of five publications, four by Ballard and Sloan (2002a,b; 2004a,b) and one by Jager et al. (2003). One major future direction of such calculations is indicated in Section 5.1.9 where the recent *ab initio* calculation methods of Cao (2002), Klauda (2003), and Anderson (2005) are discussed.

Since the statistical thermodynamics method is too involved for hand calculation, a computer program is provided on the CD accompanying this book. The use of the program is discussed in a preliminary way in each of the sections of the chapter, beginning in Section 5.2. A detailed User's Guide, which includes a description of the program, together with input data and illustrations, is provided in the CD which accompanies this book, and a User's Tutorial is included in Appendix A. It is recommended that the reader first try the examples in Appendix A to become familiar with the program, referring to the more comprehensive CD User's Guide as needed.

While the method of the present chapter may appear comprehensive, the reader is cautioned that the calculation is limited by the available data, as in any prediction method. For each region of phase equilibrium prediction, the limitations on both the accuracy and data availability are discussed. The methods presented are useful for interpolations between available data sets. The reader is urged to use caution for extrapolations beyond the data range. Further experiments may be required in order to appropriately bound the P–T conditions of interest.

5.1 Statistical Thermodynamics of Hydrate Equilibria

After the determination of the hydrate crystal structures in the early 1950s, it was possible to generate theories for equilibria of macroscopic properties based upon microscopic properties. With the knowledge of distinguishable cavities, each containing at most one guest particle, came the ability to describe the distribution of the guest particles via statistics (e.g., "How many ways can M indistinguishable particles be distributed in L distinguishable boxes with at most one particle per box?"). The resulting improvement in theoretical ability led to a more accurate

calculation method. Currently, the calculation of hydrate equilibria is the best exemplar of the industrial use of statistical thermodynamics on a routine basis.

The initial model was generated by Barrer and Stuart (1957), with a more accurate method by van der Waals and Platteeuw (1959), who are considered the founders of the method. In the present section the latter model is substantially expanded by Ballard (2002), as follows:

The first two of the above sections are a simplification and slight expansion of the derivation from the review article by van der Waals and Platteeuw (1959). They were written assuming that the reader has a minimal background in statistical thermodynamics on the level of an introductory text, such as that of Hill (1960), McQuarrie (1976), or Rowley (1994). The reader who does not have an interest in statistical thermodynamics may wish to review the basic assumptions in Sections 5.1.1 and 5.1.4 before skipping to the final equations and the calculation prescription in Section 5.2.

The derivation is a primary example of application of first principles in statistical thermodynamics, to link both microscopic and macroscopic domains for practical applications. For the reader's convenience, Table 5.1 gives the nomenclature used in Sections 5.1.1 and 5.1.2 as well as a listing (in parentheses) of the equations in which each term first appears.

5.1.1 Grand Canonical Partition Function for Water

To develop the model, it was necessary to make four fundamental assumptions based upon structure, stated as follows:

1. The host molecules' contribution to the free energy is independent of the occupation of the cavity. This assumption also implies that encaged molecules do not distort the cavity.
2. Each cavity can contain at most one guest molecule, which cannot diffuse from the cavity.
3. There are no interactions of the guest molecules, that is, the energy of each encaged guest molecule is independent of the number and types of other guest molecules.
4. No quantum effects are needed; classical statistics are valid.

TABLE 5.1
Nomenclature for Chapter 5

Term	Definition	First equation
A^{β}	Helmholtz free energy of empty host lattice	(5.1)
f_J	Fugacity of a molecule of type J	(5.22c)
g_J	molar Gibbs free energy of component J	(5.28)
N_{Ji}	Number of solute (guest) molecules of type J within type i cavity	(5.2)
N_{W}	Number of host (water molecules)	(5.2)
Q	canonical partition function for host lattice	(5.4)
q_{Ji}	Partition function of a J molecule in a type i cavity	(5.3)
y_k	Stability variable	(5.42)
θ_{ki}	Probability of finding a molecule of type k in a cavity of type i	(5.17)
λ_J	Absolute chemical activity of guest molecule J	(5.5b)
ν_i	Number of type i cavities per water molecule (for cavity i = S,M,L; S = 5^{12}, M = $4^3 5^6 6^3$, $\mathrm{L}_1 = 5^{12}6^2$, $\mathrm{L}_2 = 5^{12}6^4$, $\mathrm{L_H} = 5^{12}6^8$ **sI**: $\nu_{\mathrm{s}} = 1/23$, $\nu_{\mathrm{L1}} = 3/23$; **sII**: $\nu_{\mathrm{s}} = 2/17$, $\nu_{\mathrm{L2}} = 1/17$; **sH**: $\nu_{\mathrm{s}} = 3/34$, $\nu_{\mathrm{M}} = 2/34$; $\nu_{\mathrm{LH}} = 1/34$)	(5.2)
μ_J	Chemical potential of component J	(5.5a)
Ξ	Grand canonical partition function for the guest–host ensemble	(5.5)
	Subscripts and superscripts	
H	Hydrate	
i	Type of cavity	
I	Ice	
J	Type of guest molecule ($1 \leq J \leq M$)	
M	Total number of possible guest components in the mixture	
β	Property of the empty hydrate crystal	
o	Standard state	

As a convenient starting point for the model, the grand canonical partition function is developed from the canonical partition function, to incorporate the above assumptions. The canonical partition function is written as the product of three factors: the water lattice, the guest distribution within the cages, and the states of the guest molecules themselves assuming that they behave as ideal gas molecules, as follows:

Factor 1: The exponential of the empty water lattice Helmholtz free energy divided by kT, where k is Boltzmann's constant,

$$\exp(-A^{\beta}/kT) \tag{5.1}$$

Factor 2: The number of ways to distribute the indistinguishable guest molecules of type J in distinguishable cavities of type i, with an upper limit of one guest per cavity.

If we choose only one species of guest ($N_{J,i} = N_{1,i}$) and define L as the number of boxes, then we obtain the statistical permutation formula for the number of ways $N_{1,i}$ indistinguishable objects can be placed in L distinguishable boxes with at most one object per box.

$$\frac{L!}{(L - N_{1,i})!N_{1,i}!} \tag{5.2a}$$

In this case, however, there are $\nu_i N_W$ distinguishable boxes of type i and we wish to distribute $N_{J,i}$ indistinguishable objects, with no more than one object per box, so Equation 5.2a is modified to obtain the second factor in the canonical partition function as

$$\frac{(\upsilon_i N_W)!}{(\upsilon_i N_W - \sum_J N_{J,i})! \prod_J N_{J,i}!} \tag{5.2b}$$

Factor 3: The product of all individual particle partition functions, $q_{J,i}$, raised to the number of J particles in a type i cavity, $N_{J,i}$

For the third factor, the analogy is an ideal gas mixture of N_1 molecules of type 1 and N_2 molecules of type 2, so that the canonical partition function for the ideal gas mixture is

$$Q(N_1, N_2, V, T) = \frac{\mathrm{q}_1^{N_1} q_2^{N_2}}{N_1! N_2!} \tag{5.3a}$$

where the factorial product in the denominator accounts for the inability to distinguish among the molecules. In the clathrate, however, the molecules are distinguished by the cage they occupy, eliminating any need for $N_1!N_2!$ in the denominator. Thus the third product term in the canonical partition function becomes

$$\prod_J \mathrm{q}_{Ji}^{N_{Ji}} \tag{5.3}$$

Multiplying all three factors of Equations 5.1, 5.2b, and 5.3 together over type i cavities, the canonical partition function was obtained by van der Waals and Platteeuw:

$$Q = \exp\left(\frac{-A^\beta}{kT}\right) \prod_i \left[\frac{(\upsilon_i N_W)!}{(\upsilon_i N_W - \sum_J N_{J,i})! \prod_J N_{J,i}!} \prod_J q_{J,i}^{N_{J,i}} \right] \tag{5.4}$$

We must use the grand canonical partition function Ξ because N (a natural variable to Q) cannot be held constant with the insertion of guests in the hydrate. To obtain Ξ from the canonical function Q, we use the standard statistical mechanics transformation

$$\Xi = \sum_N Q \mathrm{e}^{\mu N/kT} \tag{5.4a}$$

and since the chemical potential μ is related to the absolute activity λ by

$$\mu = kT \ln \lambda \quad \text{or} \quad \lambda = \mathrm{e}^{\mu/kT} \tag{5.4b}$$

then we can multiply Equation 5.4 by the product of the activity of each molecule raised to the number of molecules of type J in type i cavities, as

$$\lambda_{\mathrm{A}}^{N_{\mathrm{A},1}}\lambda_{\mathrm{A}}^{N_{\mathrm{A},2}}\cdots\lambda_{\mathrm{B}}^{N_{\mathrm{B},1}}\lambda_{\mathrm{B}}^{N_{\mathrm{B},2}}\cdots\lambda_{\mathrm{M}}^{N_{\mathrm{M},1}} = \prod_i\prod_J \lambda_J^{N_{J,i}}$$

and sum over all values of $N_{J,i}$, to obtain the grand canonical partition function

$$\Xi = \exp\left(\frac{-A^\beta}{kT}\right)\sum_{N_{J,i}}\prod_i\left\{\frac{(\upsilon_i N_{\mathrm{W}})!}{(\upsilon_i N_{\mathrm{W}}-\sum_J N_{J,i})!\prod_J N_{J,i}!}\prod_J q_{J,i}^{N_{J,i}}\lambda_{\mathrm{J}}^{N_{J,i}}\right\} \quad (5.5)$$

Consider the summation term in Equation 5.5 for one type of cavity ($i = 1$) and for two types of guests ($J = \mathrm{A},\mathrm{B}$), for example, mixtures of C_3H_8(A) + i-C_4H_{10}(B) in $5^{12}6^4$ cavities:

$$\sum_{N_{\mathrm{A}}}\sum_{N_{\mathrm{B}}}\frac{(\upsilon_1 N_{\mathrm{W}})!}{(\upsilon_1 N_{\mathrm{W}}-N_{\mathrm{A}}-N_{\mathrm{B}})!N_{\mathrm{A}}!N_{\mathrm{B}}!}q_{\mathrm{A}}^{N_{\mathrm{A}}}q_{\mathrm{B}}^{N_{\mathrm{B}}}\lambda_{\mathrm{A}}^{N_{\mathrm{A}}}\lambda_{\mathrm{A}}^{N_{\mathrm{A}}}(1)^{(\upsilon_1 N_{\mathrm{W}}-N_{\mathrm{A}}-N_{\mathrm{B}})} \quad (5.5a)$$

with the final unity factor as the partition function for the empty cavity. Note also that the empty cavity has

$$\mu^\beta = 0, \quad \therefore\ \lambda^\beta = 1$$

Equation 5.5 may be simplified using the multinomial theorem from mathematics:

$$(x_1 + x_2 + \cdots + x_m)^N = \sum_{N=\sum_1^m n_i}\frac{N!}{n_1!n_2!\cdots n_m!}x_1^{n_1}x_2^{n_2}\cdots x_m^{n_m} \quad (5.6)$$

When we consider the analogy between Equation 5.5a and the right-hand side of Equation 5.6 we obtain, from Equation 5.5a

$$(1 + q_{\mathrm{A}}\lambda_{\mathrm{A}} + q_{\mathrm{B}}\lambda_{\mathrm{B}})^{\upsilon_1 N_{\mathrm{W}}} \quad (5.5b)$$

So we have a product of terms, such as in Equation 5.5b, one for each cavity type i. Equation 5.5 then becomes simplified to its final form

$$\Xi = \exp\left(\frac{-A^\beta}{kT}\right)\prod_i\left(1 + \sum_J q_{J,i}\lambda_J\right)^{\upsilon_i N_{\mathrm{W}}} \quad (5.7)$$

5.1.2 The Chemical Potential of Water in Hydrates

Our aim is to derive the chemical potential of water to enable phase equilibria calculations. Note that, while Equation 5.7 is the grand canonical partition function (Ξ^{guest}) and with respect to the solute (guest) molecule, it is the canonical partition function (Q^{host}) with respect to the host (water) because $\lambda^{\beta} = 1$, so that we have

$$\Xi^{\text{combined}} = Q^{\text{host}}\,\Xi^{\text{guest}}$$

or

$$kT\,\ell\text{n}\,\Xi^{\text{combined}} = kT\,\ell\text{n}Q^{\text{host}} + kT\,\ell\text{n}\,\Xi^{\text{guest}} \tag{5.8}$$

Now, using the letter "h" to denote the host, and "g" to denote the guest, each of the partition functions in Equation 5.8 can be related to their macroscopic thermodynamic properties in the usual way (see McQuarrie, 1976, p. 58) as

$$\text{d}(kT\ell\text{n}Q^{\text{h}}) = -\text{d}A^{\text{h}} = S^{\text{h}}\text{d}T + P\text{d}V^{\text{h}} - \mu_{\text{W}}^{\text{h}}\text{d}N_{\text{W}} \tag{5.9}$$

and

$$\text{d}(kT\ell\text{n}\,\Xi^{\text{g}}) = \text{d}(PV^{\text{g}}) = S^{\text{g}}\text{d}T + P\text{d}V^{\text{g}} + \sum_{J} N_J\text{d}\mu_J \tag{5.10}$$

Since entropy and volume are extensive properties, they can be combined,

$$S = S^{\text{g}} + S^{\text{h}} \quad \text{and} \quad V = V^{\text{g}} + V^{\text{h}}$$

so that adding Equations 5.9 and 5.10 results in a revised form of Equation 5.8 as

$$\text{d}(kT\ell\text{n}\,\Xi^{\text{combined}}) = S\text{d}T + P\text{d}V + \sum_{J} N_J\text{d}\mu_J - \mu_{\text{W}}\text{d}N_{\text{W}} \tag{5.11}$$

By dropping the superscript "combined," taking the left-most derivative, and using $\text{d}\mu_J = kT\text{d}\ell n\lambda_J$ on the right, we get:

$$kT\text{d}\ell\text{n}\,\Xi = (-k\ell\text{n}\,\Xi + S)\text{d}T + P\text{d}V + \sum_{J} kTN_J\text{d}\ell\text{n}\lambda_J - \mu_{\text{W}}^{\text{H}}\text{d}N_{\text{W}} \tag{5.12}$$

With the development of Equation 5.12 relating the partition function and the macroscopic properties, all of the macroscopic thermodynamic properties may be derived from Equation 5.7. For example, differentiating ln Ξ with respect to the absolute activity (λ) of J, provides the total number of guest molecules "J" over all the cavities i

$$N_J = \sum_{i} N_{J,i} = \lambda_J \left(\frac{\partial \ell\text{n}\,\Xi}{\partial \lambda_J}\right)_{T,V,N_W,\lambda_{k\neq J}} \tag{5.13}$$

In Equation 5.13 the logarithm of ln Ξ is obtained from Equation 5.7, as

$$\ell n \Xi = -\frac{A^{\beta}(T, V, N_{\mathrm{W}})}{kT} + \sum_{i} \upsilon_i N_{\mathrm{W}} \ell n \left(1 + \sum_{J} q_{J,i} \lambda_J\right) \tag{5.14}$$

to yield the total number of guest molecules N_{k} as

$$N_J = \sum_{i} \left(\frac{\upsilon_i N_{\mathrm{W}} q_{J,i} \lambda_J}{1 + \sum_J q_{J_i} \lambda_J} \right) \tag{5.15}$$

Since N_J must be a linear, homogeneous function of υ_i, the number of cavities of different types per water molecule, it follows from Equation 5.15 that $N_J = \Sigma N_{Ji}$ and

$$N_{J,i} = \frac{\upsilon_i N_{\mathrm{W}} q_{J,i} \lambda_J}{(1 + \sum_J q_{J_i} \lambda_J)} \tag{5.16}$$

Equation 5.16 may be used to determine the simple probability ($\theta_{J,i}$) of finding a molecule of type J in a cavity of type i. This value may be obtained by dividing the number of molecules of k in cavity i by the total number of cavities of type i, $\upsilon_i N_{\mathrm{W}}$

$$\theta_{J,i} = \frac{N_{J,i}}{\upsilon_i N_{\mathrm{W}}} = \frac{q_{J,i} \lambda_J}{(1 + \sum_J q_{J,i} \lambda_J)} \tag{5.17}$$

The chemical potential of the host $\mu_{\mathrm{W}}^{\mathrm{H}}$ may also be obtained from Equation 5.12 as

$$\frac{\mu_{\mathrm{W}}^{\mathrm{H}}}{kT} = -\left(\frac{\partial\, \ell n \Xi}{\partial\, N_{\mathrm{W}}} \right)_{T,V,\lambda_J}$$

so that, from Equation 5.14

$$\frac{\mu_{\mathrm{W}}^{\mathrm{H}}}{kT} = \frac{\mu_{\mathrm{W}}^{\beta}}{kT} - \sum_{i} \upsilon_i \ell n \left(1 + \sum_{J} q_{J,i} \lambda_J\right) \tag{5.18}$$

Equations 5.17 and 5.18 are important because they enable the determination of the hydrate composition and the chemical potential of the hydrated water as a function of variables (T, V, N_{W}, λ_1, λ_{M}).

Equation 5.17 may be simplified somewhat by finding expressions for the absolute activity λ_J and the individual particle partition function $q_{J,i}$ in terms of experimentally measured or fitted parameters. To achieve such a simplification, we first consider the chemical potential of an ideal gas and its relation to the particle partition function.

For an ideal gas, the canonical partition function Q may be written as

$$Q = \frac{1}{N!} q^N$$

and the ideal gas chemical potential μ is calculated by

$$\mu = -kT\left(\frac{\partial \ell \mathrm{n} Q}{\partial N}\right)_{T,V} = -kT\ell \mathrm{n}\frac{q}{N}$$

where separability may be assumed for the individual particle partition function q into a translational part and a second part containing the internal modes of energy, that is, $q = q_{\mathrm{trans}} q_{\mathrm{int}}$ with:

$$\frac{q_{\mathrm{trans}}}{N} = \left(\frac{2\pi mkT}{\mathrm{h}^2}\right)^{3/2}\frac{V}{N}$$

where the square root of the quantity in parentheses is called the mean thermal de Broglie wavelength. For an ideal gas $V/N = kT/P$, therefore

$$\mu = -kT\,\ell \mathrm{n}\left[\left(\frac{2\pi mkT}{h^2}\right)^{3/2} kT\right] - kT\ell \mathrm{n} q_{\mathrm{int}} + kT\,\ell \mathrm{n} P \tag{5.19}$$

and since the chemical potential is normally defined in reference to a standard chemical potential μ^{o} as

$$\mu = \mu^{\mathrm{o}}(T) + kT\ell \mathrm{n} P \tag{5.20}$$

the identity can be made between the standard chemical potential with the first two terms on the right of Equation 5.19 as

$$\mu^{\mathrm{o}} = -kT\,\ell \mathrm{n}\left[\left(\frac{2\pi mkT}{h^2}\right)^{3/2} kT\right] - kT\ell \mathrm{n} q_{\mathrm{int}}$$

Without the standard chemical potential, Equation 5.19 becomes in terms of absolute chemical potential ($\mu = kT\ell \mathrm{n}\lambda$),

$$\mu = kT\ell \mathrm{n}\frac{P}{kT(2pmkT/h^2)^{3/2} q_{\mathrm{int}}}$$

or for the absolute activity λ

$$\lambda = \frac{P}{kT(2\pi mkT/h^2)^{3/2} q_{\mathrm{int}}}$$

The absolute activity and the individual particle partition function may be taken into account through a constant $C_{J,i}$, defined as

$$C_{J,i} \equiv \frac{q_{J,i}\lambda_J}{P_J} = \frac{q_{J,i}}{kT(2\pi mkT/h^2)^{3/2} q_{\mathrm{int}}} \tag{5.21}$$

Note that the denominator of Equation 5.21 contains the internal portion of the particle partition function and the ideal gas contribution, so that the division indicated accounts for the nonideal gas effect. When Equation 5.21 is put into Equation 5.17, $\theta_{J,i}$, the fractional filling of cavity i by a type J molecule, is obtained:

$$\theta_{J,i} = \frac{C_{J,i}\mathrm{P}_J}{1 + \sum_J C_{J,i}P_J} \tag{5.22a}$$

For an ideal gas Equation 5.22a may be considered as elementary probability of cavity i occupation by molecule J. This is one of the most useful equations in the method of hydrate prediction, and it may also be recognized as the Langmuir isotherm. If the equation were written for one guest component J, it would contain the Langmuir constant $C_{J,i}$ as the only unknown for a given pressure and fraction of the cavities filled (or fraction of monolayer coverage).

Equation 5.21 shows that the Langmuir constant is a direct function of the particle partition function within the cavity $q_{J,i}$; in particular $C_{J,i}$ contains the nonideal gas translation term. When the fluid in equilibrium with the hydrate is a nonideal gas, the pressure of component J in Equation 5.22a is replaced with its fugacity, f_J.

With such corrections, Equation 5.22a finds many uses in the calculation of hydrate properties. The equation relies on the fitting of the Langmuir constant $C_{J,i}$ to experimental hydrate conditions. The method of relating the Langmuir constant to experimental conditions is given in Section 5.1.4.

Equation 5.22a enables the calculation of the chemical potential of water in the hydrate as a function of the fractional occupation in the cavities. Equation 5.18 provides the chemical potential of water in terms of the chemical potential in the empty hydrate, as well as the product of the individual cavity partition function and the absolute activity:

$$\frac{\mu_{\mathrm{W}}^{\mathrm{H}}}{kT} = \frac{\mu_{\mathrm{W}}^{\beta}}{kT} - \sum_i \upsilon_i \ell\mathrm{n}\left(1 + \sum_J q_{J,i}\lambda_J\right) \tag{5.18}$$

Since the final product is $q_{J,i}\lambda_J = C_{J,i}P_J$ by Equation 5.21 then

$$\frac{\mu_{\mathrm{W}}^{\mathrm{H}}}{kT} = \frac{\mu_{\mathrm{W}}^{\beta}}{kT} - \sum_i \upsilon_i \ell\mathrm{n}\left(1 + \sum_J C_{J,i}P_J\right) \tag{5.18a}$$

Now consider the logarithmic term in Equation 5.18a. It may be simplified through the use of Equation 5.22a, which relates $\theta_{J,i}$, the fractional occupation of a cavity of type i by a molecule of type J, to the Langmuir constant

$$\ell\mathrm{n}\left(1 - \sum_J \theta_{J,i}\right) = \ell\mathrm{n}\left(1 - \sum_J \frac{C_{J,i}P_J}{1 + \sum_J C_{J,i}P_J}\right)$$

or

$$\ell n\left(1-\sum_J \theta_{J,i}\right)=\ell n\left(\frac{1}{1+\sum_J C_{J,i}P_J}\right)=-\ln\left(1+\sum_J C_{J_i}P_J\right)$$

Substitution of the above equation into Equation 5.18a yields:

$$\mu_W^H=\mu_W^\beta+kT\sum_i \upsilon_i \ell n\left(1-\sum_J \theta_{J,i}\right) \tag{5.23}$$

Equation 5.23 may be used with Equation 5.22a to determine the chemical potential of water in hydrate μ_W^H, which is one of the major contributions of the model. The combination of these two equations is of vital importance to phase equilibrium calculations, since the method equates the chemical potential of a component in different phases, at constant temperature and pressure.

Equation 5.23 shows that an increased filling of the cavities causes a decrease in the value of μ_W^H so that the hydrate becomes more thermodynamically stable. In the large cavities particularly, the fractional occupation θ_{Ji} frequently approaches unity, causing the water chemical potential is to be substantially lowered because the logarithm of a small fractions $(1-\sum\theta_{Ji})$ is a large negative number.

At the other occupation extreme, if the value of $\theta_{J,i}$ were unrealistically small in Equation 5.23, the final term could be replaced by $-kT\sum\sum\upsilon_i\theta_{J,i}$. The resulting equation is van't Hoff's law:

$$\mu_W^H=\mu_W^\beta-kT\sum_i\sum_J \upsilon_i\theta_{J,i} \tag{5.23a}$$

which is used in other applications to model ideal, dilute, solid solutions (Lewis and Randall, 1923, p. 238). Thus the above limiting forms of Equation 5.23 lends mathematical credence to the hydrate solid solution concept, which is the basis of the current model as well as the Katz distribution coefficient (K_{vs_i}) method of Section 4.2.2. Equations 5.23 and 5.23a also show that hydrates are stabilized by an increase in the cavity occupation, θ_{k_i}, which lowers the chemical potential of water.

Example 5.1: Determination of Hydrate Nonstoichiometry

Cady (1983a,b) provided the below illustration of how Equations 5.22a and 5.23 may be used to determine the hydration number for seven simple hydrates of structure I.

From Chapter 2, recall that structure I has 46 water molecules in the basic crystal with 6 large ($5^{12}6^2$) cavities and 2 small (5^{12}) cavities. For ideal

sI hydrates, if all of the cavities were filled the hydration number (water molecules per guest molecule) would be $n = 46/8$. For simple hydrates, the hydration number is related to the fractional filling of the large and small cavities, θ_L, and θ_S, respectively as

$$n = \frac{46}{6\theta_L + 2\theta_S} = \frac{23}{3\theta_L + \theta_S} \tag{E5.1.1}$$

Equation 5.22a applied to each size cavity gives

$$\theta_L = \frac{C_L P}{1 + C_L P} \tag{E5.1.2a}$$

and

$$\theta_S = \frac{C_S P}{1 + C_S P} \tag{E5.1.2b}$$

Now if the formation pressure is considered for a simple hydrate at 273.15 K, we may obtain from Equation 5.23 with Davidson's (1973) suggestion that $\mu_W^H - \mu_W^\beta = -1108$ J/gmol.

$$-0.4885 = \tfrac{3}{23}\ln(1 - \theta_L) + \tfrac{1}{23}\ln(1 - \theta_S) \tag{E5.1.3}$$

Cady suggested that a value of n may be estimated at a pressure corresponding to 273.15 K for a hydrated guest using de Forcrand's method with the Clapeyron equation (Section 4.6.2.1). Equations E5.1.1 and E5.1.3 may then be solved simultaneously for θ_L and θ_S. In turn, θ_L and θ_S may be substituted into Equation E5.1.2a and b to calculate C_L and C_S. Since the values of C_L and C_S are constant at constant temperature, they may be used to determine the hydrate numbers at pressures higher than the equilibrium value, using Equations E5.1.1 and E5.1.2.

Using the above method, Cady compared the calculated hydrate numbers to his experimental values, with results as shown in Figure 5.1. The fit of the equations to the experiment seems to be remarkably good.

Example 5.2: Calculation of Hydrate Density

With values for the fractional filling of each cavity type, hydrate density may be determined based upon a unit crystal. Additional required input data are the dimensions of a unit crystal, the number of water molecules per crystal and the number of small and large cavities per unit crystal, as specified in Table 2.2. Based upon a single unit cavity, the hydrate density (ρ) may be calculated by the formula:

$$\rho = \frac{N_w \mathrm{MW}_{H_2O} + \sum_{J=1}^{C}\sum_{i=1}^{N} \theta_{iJ}\upsilon_i \mathrm{MW}_J}{N_{Ava} V_{cell}} \tag{E5.2.1}$$

where

N_w = number of water molecules per unit cell (Table 2.2)
N_{Ava} = Avagadro's number, 6.023×10^{23} molecules/mol
MW_J = molecular weight of component J
θ_{iJ} = fractional occupation of cavity i by component J (computer program)
ν_i = number of type i cavities per water molecule in unit cell (Table 2.2)
V_{cell} = volume of unit cell (dimensions in Table 2.2)
N = number of cavity types in unit cell
C = number of components in hydrate phase

Example 5.2a: Calculate the density of methane hydrate at 273.15 K

Solution

From the computer program included with this book, at 273.15 K the hydrate is predicted to have a dissociation pressure of 25.1 atm. The hydrate is predicted to be sI, with a fractional occupancy of cavities as $\theta_s = 0.870$ and $\theta_L = 0.973$. There are 46 water molecules per sI unit cell, with 2 small (5^{12}) and 6 large ($5^{12}6^2$) cavities, and the unit cell length is 12 Å on one side. The density is then calculated from Equation E5.2.1 as

$$\rho = \frac{(46 \times 18) + [(0.87 \times 2 \times 16) + (0.973 \times 6 \times 16)]}{(6.023 \times 10^{23}) \times (12.0)^3 \times (10^{-8})^3} = 0.91 \text{ g/cc} \tag{E5.2.2}$$

The above density can be compared to that calculated by Makogon (1974, p. 31) as 0.897 g/cc.

Example 5.2b: Calculate the hydrate density resulting from a gas mixture (90 mol% CH_4, 7% C_2H_6, 3% C_3H_8) at 277 K

Solution

From the computer program included with this book, at 277 K the hydrate is predicted to be sII with a dissociation pressure of 12.9 atm. The length of one side of sII is 17.3 Å, with 136 water molecules, as well as 16 small (5^{12}) and 8 large ($5^{12}6^4$) cavities per unit cell. The fractional filling of each cavity (θ_i) is given in the below table:

	CH_4	C_2H_6	C_3H_8
θ_s	0.67	0	0
θ_L	0.057	0.096	0.84
MW	16	30	44

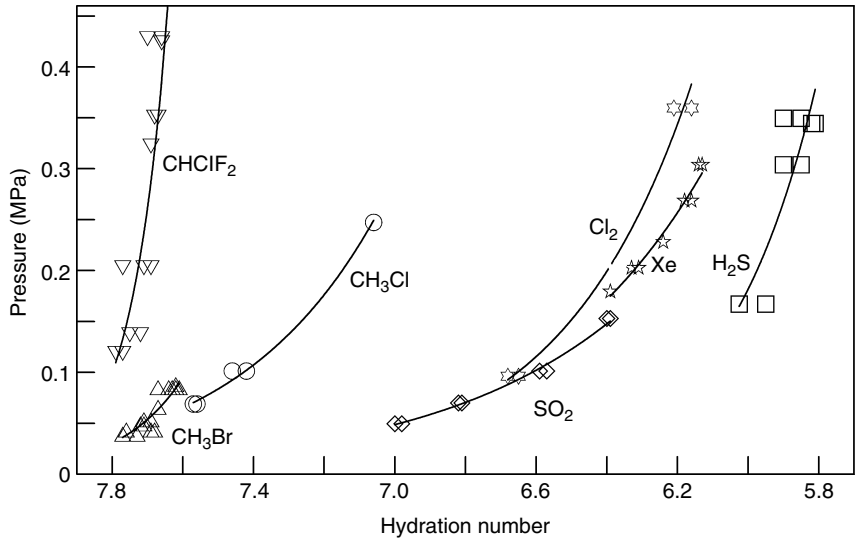

FIGURE 5.1 Change of hydration number with pressure. (Reproduced from Cady, G.H., *J. Phys. Chem.*, **85**, 4437 (1983a). With permission from the American Chemical Society.)

Using Equation E5.2.1 the density is computed as

$$\rho = [(136 \times 18) + [(0.67 \times 16 \times 16) + (0.057 \times 8 \times 16)] + [0.096 \times 8 \times 30] + [0.84 \times 8 \times 44]] \times [(6.023 \times 10^{23}) \times (17.3)^3 \times (10^{-8})^3]^{-1} = 0.94 \text{ g/cc} \quad \text{(E5.2.3)}$$

There are no measurements or calculations of this quantity for comparison.

5.1.3 The Langmuir Adsorption Analogy

In single component Langmuir adsorption, one finds many analogies to the process of guest encapsulation in the hydrate cavity, to provide a physical interpretation of guest containment. In the below listing of single component Langmuir adsorption isotherm assumptions, the analogies are readily apparent through a replacement of the words "adsorption or desorption" with "enclathration or declathration," the word "sites" should be replaced by "cavities," and the word "surface" should be replaced by "crystal unit cell." The assumptions are

1. The adsorption of gas molecules occurs at discrete sites on the surface.
2. The energy of adsorption on the surface is independent of the presence of other adsorbed molecules.

3. The maximum amount of adsorption corresponds to one molecule per site.
4. The adsorption is localized and occurs by collision of gas phase molecules with vacant sites.
5. The desorption rate depends only on the amount of adsorbed material on the surface.

To illustrate the analogy more clearly, it is necessary to consider the derivation of the Langmuir adsorption isotherm. We can incorporate the above assumptions into an equilibrium expression which equates the rate of adsorption r_{ads} to that of desorption r_{des} of gas molecules of type J. The desorption rate is directly proportional to the fraction of monolayer sites occupied Θ_J, and is expressed as

$$r_{\text{des}} = \chi' \Theta_J$$

where χ' is taken as the proportionality constant (sometimes called the desorption rate constant), which is only a function of temperature. The rate of adsorption is proportional to the product of the gas pressure P_{k} and the number of unoccupied sites $(1 - \Theta_J)$ in the equation

$$r_{\text{ads}} = \chi P_J (1 - \Theta_J)$$

At equilibrium, the above rates of adsorption and desorption are equated, and an expression is obtained for the fraction of sites occupied Θ_J, which appears identical to Equation 5.22a for simple hydrates of one component:

$$\Theta_J = \frac{\chi P_J}{\chi' + \chi P_J} = \frac{K P_J}{1 + K P_J} \tag{5.22b}$$

where the equilibrium Langmuir adsorption constant ($K \equiv \chi / \chi'$) is analogous to the Langmuir hydrate constant C_{Ji} in Equation 5.22a; both are only functions of temperature and the components (adsorbed species and site or specific cavity). One difference is that the Langmuir constant in hydrates provides for more than one type of cavity (analogous to another type of adsorption site) with the additional subscript "*i*."

Consider the physical meaning of the terms in the simple hydrate analog (Equation 5.22a) of the Langmuir Equation 5.22b above, with the pressure corrected as fugacity:

$$\theta_{J,i} = \frac{C_{J,i} f_J}{1 + C_{J,i} f_J} \tag{5.22c}$$

The fraction of the adsorbed monolayer Θ_J in (Equation 5.22b) is analogous to the fractional occupation of the cavities of type i, $\theta_{J,i}$ (Equation 5.22a). The fractional occupation of each cavity will increase as the product $(C_{Ji} f_J)$ increases. In the limit, for very large values of $C_{Ji} f_J$ the fractional occupancy approaches unity.

In other words, C_{Ji} measures the "attractiveness" of the cage for a hydrated species. At a given value of fugacity, the most strongly enclathrated component in a cavity is the component with the highest values of C_{Ji}. In Section 2.1.3.2 it was suggested that there was an optimal fit of the guest molecule within a host cavity; this optimal fit provides a higher value of the Langmuir constant.

For example, a very small molecule in a large ($5^{12}6^4$) cavity has a smaller Langmuir constant than the same molecule within a 5^{12} cavity as first shown by Holder and Manganiello (1982). In contrast, the Langmuir constant would be zero for a molecule slightly too large to fit the small cavity, but the Langmuir constant would be substantial for the same molecule within the large cavity.

Similarly, at a given value of the Langmuir constant, higher values of fugacity provide for higher fractional filling of each cavity. Loosely, fugacity may be physically interpreted as "thermodynamically corrected" pressure. Thus higher pressures provide higher fractional filling of each cavity.

However, it should be remembered that the fractional filling is a function of the product $C_{Ji}f_J$, rather than either factor in the product. Finally, in the original van der Waals and Platteeuw approach the Langmuir constants for both adsorption and enclathration were only functions of temperature for each molecule type retained at the individual site or cavity. In the modified approach below, the Langmuir constants are also a function of cage size, or the unit cell volume, which is a function of the hydrate guests, temperature, and pressure.

5.1.4 Relating the Langmuir Constant to Cell Potential Parameters

With the adsorption analogy in mind, the next object is to relate the Langmuir constants $C_{J,i}$ to experimental variables, by providing a physical interpretation. In order to consider the Langmuir constant, it is first necessary to determine the individual guest potential energy within the cavity. The force between the guest and cavity is the change in the potential energy with the guest displacement. We must first make two assumptions, in addition to the four assumptions made for the hydrate in Section 5.1.1:

1. The internal motion partition function of the guest molecule is the same as that of an ideal gas. That is, the rotational, vibrational, nuclear, and electronic energies are not significantly affected by enclathration, as supported by spectroscopic results summarized by Davidson (1971) and Davidson and Ripmeester (1984).
2. The potential energy of a guest molecule at a distance r from the cavity center is given by the spherically symmetrical potential $\varpi(r)$ proposed by Lennard-Jones and Devonshire (1932, 1938).

Assumptions (1) and (2) above are more restrictive than assumptions (1) through (4) in Section 5.1.1, in that they apply more to monatomic or spherical

molecules than for oblate or polar molecules. Prediction inaccuracies of the model for certain gases may be related to errors in these assumptions.

In this model the interactions of the guest with the nearest neighboring z_i water molecules of a spherical cage are summed in a pair-wise manner. The model obtains a function $\varpi(r)$ describing the resulting field, averaged over all positions of the molecules within the cavity. The fundamental intermolecular potential between a water molecule of the cavity wall and a solute molecule may be described by a number of intermolecular potentials.

The original work by van de Waals and Platteeuw (1959) used the Lennard-Jones 6–12 pair potential. McKoy and Sinanoglu (1963) suggested that the Kihara (1951) core potential was better for both larger and nonspherical molecules. The Kihara potential is the potential currently used, with parameters fitted to experimental hydrate dissociation data. However, it should be noted that the equations presented below are for a spherical core, and while nonspherical core work is possible, it has not been done for hydrates.

The pair potential energy Φ between the guest molecule and any water molecule is related to the force (F) each exerts on the other by, $F = -\partial\phi/\partial r$ where "r" is the molecular center distance between the two. The potential, which itself is a function of separation distance, is unique to every molecular type and is given by

$$\Phi(r) = \infty \quad \text{for } r \leq (a_g + a_w) \tag{5.24a}$$

$$\Phi(r) = 4\varepsilon \left\{ \left(\frac{\sigma}{r - 2a} \right)^{12} - \left(\frac{\sigma}{r - 2a} \right)^{6} \right\} \quad \text{for } r > (a_g + a_w) \tag{5.24b}$$

where

σ = cores distance at zero potential ($\Phi = 0$), (attraction and repulsion balance),
a = radius of the spherical core (g = guest and w = water) and
ε = maximum attractive potential (at $r = \sqrt[6]{2}\sigma$).

The Lennard-Jones–Devonshire theory (as summarized by Fowler and Guggenheim, 1952, pp. 336ff) averaged the pair potentials of Equation 5.24a and b between the solute and each water, for z_i molecules in the surface of the spherical cavity to obtain a cell potential $\varpi(r)$ of

$$\varpi(r) = 2z\varepsilon \left[\frac{\sigma^{12}}{R^{11} r} \left(\delta^{10} + \frac{a}{R} \delta^{11} \right) - \frac{\sigma^{6}}{R^{5} r} \left(\delta^{4} + \frac{a}{R} \delta^{5} \right) \right] \tag{5.25a}$$

where

$$\delta^N = \frac{1}{N} \left[\left(1 - \frac{r}{R} - \frac{a}{R} \right)^{-N} - \left(1 + \frac{r}{R} - \frac{a}{R} \right)^{-N} \right] \tag{5.25b}$$

where
$N = 4$, 5, 10, or 11, indicated in Equation 5.25a,
z = the coordination number (number of water molecules) of the cavity,
R = the free cavity radius,[1] (assuming "smeared" spherical cavity), and
r = distance of the guest molecule from the cavity center.

The spherical averaging of the potential function over all the angles of interaction with the wall enables the potential of Equation 5.25a and b) to be expressed solely in terms of distance r from the cavity center for a given guest molecule. It should be noted that the parameters ε, a, and σ are unique for every guest molecule, but they do not change in the different cavity types. On the other hand, the parameters z and R have been uniquely determined for each type cavity by x-ray diffraction data (see Table 2.1) and do not change as a function of guest molecules.

Following van der Waals and Platteeuw (1959, pp. 26ff) the individual particle partition function is related to the product of three factors: (1) the cube of the de Broglie wavelength, (2) the internal partition function, and (3) the configurational triple integral, as

$$q_{Ji} = \left(\frac{2\pi mkT}{h^2}\right)^{3/2} q_{\text{int}} \int_0^{2\pi} \int_0^{\pi} \int_0^{\text{R}} \exp\left(-\frac{\varpi\,(r)}{kT}\right) r^2 \sin\theta \, \text{d}r \, \text{d}\theta \, \text{d}\phi \quad (5.26)$$

The cavities are assumed to be spherically symmetric, which enables the elimination of the two angular portions of the triple integral, resulting in 4π. Substitution of the resulting equation into Equation 5.21 yields the final expression for the Langmuir constant in terms of the particle potential within the cavity.

$$\text{C}_{J,i} = \frac{4\pi}{kT} \int_0^{\text{R}} \exp\left(-\frac{\varpi\,(r)}{kT}\right) r^2 \, \text{d}r \quad (5.27a)$$

The evaluation of the Langmuir constant may then be determined from a minimum of experimentally fitted Kihara parameters via an integration over the cavity radius. Equation 5.27a shows the Langmuir constant to be only a function of temperature for a given component within a given cavity.

The experimentally fitted hydrate guest Kihara parameters in the cavity potential $\varpi(r)$ of Equation 5.25 are not the same as those found from second virial coefficients or viscosity data for several reasons, two of which are listed here. First, the Kihara potential itself does not adequately fit pure water virials over a wide range of temperature and pressure, and thus will not be adequate for water–hydrocarbon mixtures. Second, with the spherical Lennard-Jones–Devonshire theory the point-wise potential of water molecules is "smeared" to yield an averaged spherical shell potential, which causes the water parameters to become indistinct. As a result, the Kihara parameters for the guest within the cavity are fitted to hydrate formation properties for each component.

[1] Values given in Table 2.1, minus 1.45 Å for the free cavity radius of water to obtain R.

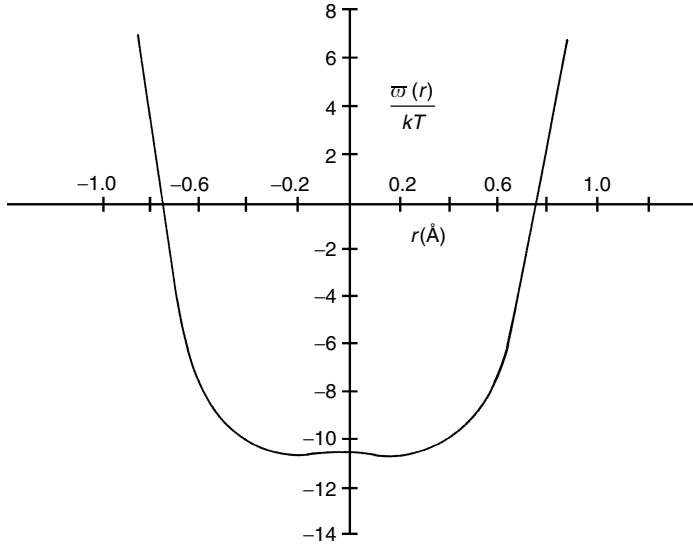

FIGURE 5.2 Typical spherically symmetrical cavity potential function between guest and cell. (Reproduced from McKoy, V., Sinanoglu, O., *J. Chem. Phys.*, **38**, 2946 (1963). With permission from the American Institute of Physics.)

A typical potential $\varpi(r)$ is shown in Figure 5.2. Note that the potential is more negative (high attraction) in the center of the cell, or at some distance from the cell wall, with high repulsion (positive values) at the cell wall. As the guest molecule approaches one wall of the cavity, it is both repulsed by that wall and attracted by the opposite wall, causing it to exist in the center. Recent work in molecular simulation suggests that smaller molecules are located in local minima away from the center, and that the repulsive portion of the potential is more important than the attraction (see the molecular simulation discussion in Section 5.3).

Equation 5.27a shows that the main contribution to the Langmuir constant comes from integrating the guest–cavity pair potential in the interior of the cells. This is a partial explanation of the reason why the final assumption (2) at the beginning of this subsection for "smeared water molecules" is a good approximation for the cavity shell; in addition the cavities are spherical, to a first approximation.

The value of fitting the Langmuir constants to simple hydrate formation data is in the prediction of mixture hydrate formation. When the formation data for the simple hydrates are adequately fitted, then mixtures of those guest components can be predicted with no adjustable parameters. Since there are only eight simple hydrate formers of natural gas which form sI and sII, but an infinite variety of mixtures, such an advantage represents a substantial savings of time and effort.

In the development of Equation 5.27a, it was assumed that the interaction between the guest and the water molecules in cage *m* could be approximated using an average cage radius. Ballard (2002) suggested another approach. He proposed

TABLE 5.2
Types of Oxygen Atoms at the Periphery of Both SI and SII Hydrate Cages and Distance of Each to the Center of the Cages

	Small cage (5^{12})		Large cage ($5^{12}6^2$)			
(a) sI ethylene oxide hydrate ($a = 12.03$ Å) (McMullan and Jeffrey, 1965)						
No. of water molecules in cage	20		24			
Average radius (Å)	3.908		4.326			
Layer type	(i)	(k)	(i)	(k)	(k)	(c)
No. of water molecules in layer	8	12	8	8	4	4
Radius (Å)	3.83	3.96	4.47	4.06	4.645	4.25

	Small cage (5^{12})			Large cage ($5^{12}6^4$)		
(b) sII tetrahydrofuran and hydrogen sulfide hydrate ($a = 17.1$ Å) (Mak and McMullan, 1965)						
No. of water molecules in cage	20		28			
Average radius (Å)	3.902		4.683			
Layer type	(a)	(e)	(g)	(e)	(g)	(g)
No. of water molecules in layer	2	6	12	4	12	12
Radius (Å)	3.748	3.845	3.956	4.729	4.715	4.635

that the interactions between the guest and water molecules can be better approximated using a "multilayered" cage, using direct single crystal diffraction data for the radii of each water molecule in the hydrate cages (Mak and McMullan, 1965; McMullan and Jeffrey, 1965). Table 5.2 lists these radii for sI and sII hydrates. Note that the cubic lattice parameter, which corresponds to these cage radii, is given for each hydrate structure. Equation 5.27b is the proposed expression for the Langmuir constant:

$$C_{J,m} = \frac{4\pi}{kT} \int_0^{R_1 - a_J} \exp\left[-\frac{\sum_n \omega_{J,n}(r)}{kT} \right] r^2 \, \mathrm{d}r \tag{5.27b}$$

where the summation is over all shells (n) in cage m, and aj is the hard core radius, subtracted from R to avoid singularities. Note that the upper limit of the integral is evaluated at R_1, which is the smallest shell in cage m. Equation 5.27a can still be used to evaluate the potential for a given layer. In the development of Equation 5.27b, it was assumed that binary interactions between the guest and the water molecules (shells) are of most importance.

The crucial change introduced in CSMGem is to make the radii of each shell functions of temperature, pressure, and composition. As the lattice expands or compresses, the cages also expand or compress. The radii of the shells are assumed to be a linear function of the cubic hydrate lattice parameter. For example, if the lattice parameter expands by 1% of its original value, each shell radius, R_n, also expands by 1% of its original value. In addition the concept of various distances from the average are included to separate a single cavity into oxygens that are

TABLE 5.3
Summary of the Equations for Fitting Simple Hydrate Formers

$$\theta_{k_i} = \frac{C_{k_i} f_k}{1 + \sum_J C_{J_i} f_J} \tag{5.22c}$$

$$\mu_W^H = g_W^\beta + RT \sum_i \upsilon_i \ln\left(1 - \sum_J \theta_{iJ}\right) + RT \ln \gamma_W^H \tag{5.28}$$

$$\varpi(r) = 2z\varepsilon\left[\frac{\sigma^{12}}{R^{11} r}\left(\delta^{10} + \frac{a}{R}\delta^{11}\right) - \frac{\sigma^6}{R^5 r}\left(\delta^4 + \frac{a}{R}\delta^5\right)\right] \tag{5.25a}$$

$$\text{where } \delta^N = \frac{1}{N}\left[\left(1 - \frac{r}{R} - \frac{a}{R}\right)^{-N} - \left(1 + \frac{r}{R} - \frac{a}{R}\right)^{-N}\right] \tag{5.25b}$$

$$C_{J,m} = \frac{4\pi}{kT}\int_0^{R_1 - a_J} \exp\left[-\frac{\sum_n \omega_{J,n}(r)}{kT}\right] r^2 \mathrm{d}r \tag{5.27b}$$

closer (or further) from the center, and sums the interaction energies over those coordination numbers.

It should be noted here that Bazant and Trout (2001) developed an ingenious mathematical method to determine the Langmuir constant for guest molecules which only fill the large cage, relating them to the calculated fluid phase fugacity and the experimentally determined change in chemical potentials in Equation 5.23, via the relations:

$$\text{For structure I large guests } C_{J,i} = \frac{\exp(23/3\Delta\mu_w^{\beta-H}/kT) - 1}{f_J} \tag{5.27c}$$

$$\text{For structure I large guests } C_{J,i} = \frac{\exp(17/1\Delta\mu_w^{\beta-H}/kT) - 1}{f_J} \tag{5.27d}$$

Using the above equations, the Langmuir constant for the large cavity occupant can be determined explicitly from the chemical potential difference and the fugacity. However, for systems in which both cavities are occupied, a second method must be used to supplement Equation 5.27c and d.

Table 5.3 summarizes the previous equations for simple hydrate formers.

5.1.5 Activity Coefficient for Water in the Hydrate

Several methods have arisen to correct the assumptions in the above van der Waals and Platteeuw model, to address the inaccuracies at the high pressures of current applications. The two most prominent modern correction methods are: (1) to use *ab initio* quantum mechanical corrections to relate to first principles as much possible, as briefly discussed in Section 5.1.9, and (2) to fit the existing

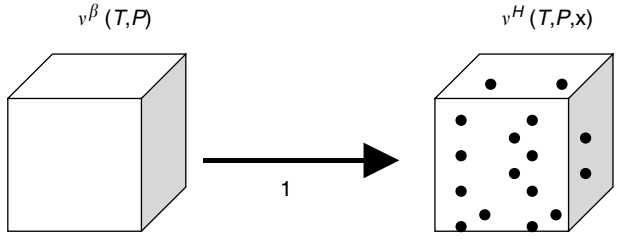

FIGURE 5.3 Filling the empty cages without distortion. Van der Waals and Platteeuw model without distortion of hydrate due to guests ($v^{\beta} = v^{H}$). Process (1) in Figure 5.3 is given by the summation term in Equation 5.23.

macroscopic (phase equilibria) and microscopic (spectroscopic) data as physically and as accurately as possible to a modified van der Waals and Platteeuw theory.

Because there is a very large phase equilibrium data base, existing over 70 years as shown in Chapter 6, and because recent spectroscopic tools (e.g., Raman, NMR, and diffraction) have provided microscopic hydrate data, the latter approach was chosen in this monograph and the accompanying computer programs. While the latter method used in this book represents a theoretical advance, it is shown to compare favorably with the existing commercial hydrate programs in Section 5.1.8.

In particular, the extension of the van der Waals and Platteeuw method addresses the first assumption listed at the beginning of Section 5.1.1—namely that encaged molecules do not distort the cavity. In the development of the statistical thermodynamic hydrate model (Equation 5.23), the free energy of water in the standard hydrate (empty hydrate lattice), g_{w}^{β}, is assumed to be known at a given temperature (T) and volume (v). Since the model was developed at constant volume, the assumption requires that the volume of the empty hydrate lattice, v^{β}, be equal to the volume of the equilibrium hydrate, v^{H}, so that the only energy change is due to occupation of the hydrate cavities, as shown in Figure 5.3.

Traditionally, the chemical potential of the standard hydrate is assumed to be at a given volume, independent of the hydrate guests. If the standard hydrate volume is not the volume of the equilibrium hydrate, there should be an energy change proportional to the difference in volume ($\Delta v^{\mathrm{H}} = v^{\mathrm{H}} - v^{\beta}$). Note that, in the development of Equation 5.23, Δv^{H} is assumed to be equal to zero (i.e., all hydrates of a given structure are at the same volume).

Equation 5.23 is considered to be an ideal solid solution model. If we choose to extend our equations from one hydrate crystal to a large number N_{A} (Avogadro's number) of crystals, we must replace the Boltzmann constant "k" with the universal gas constant R ($\equiv kN_{\mathrm{A}}$). Ballard (2002) defined the chemical potential of water in hydrates as

$$\mu_{\mathrm{W}}^{\mathrm{H}} = g_{\mathrm{W}}^{\beta} + RT \sum_{i} \upsilon_i \ln \left(1 - \sum_{J} \theta_{iJ} \right) + RT \ln \gamma_{\mathrm{W}}^{\mathrm{H}} \tag{5.28}$$

noting that the empty water chemical potential equals that of the Gibbs energy, and where the activity coefficient of water in the hydrate, γ_w^H, accounts for nonidealities due to the inclusion of the hydrate guests, which enlarge the hydrate cavities. Diffraction data show that the volume of the hydrate is a strong function of the guest(s) present in the hydrate (von Stackelberg and Jahns, 1954; Huo, 2002). Therefore, Ballard suggested that the activity coefficient be a function of the difference in volume between the hydrate and the standard hydrate, Δv^H, noting that the activity coefficient has the following property:

$$\gamma_w^H \to 1 \quad \text{as } \Delta v^H \to 0 \text{ or as } x_w^H \to 1$$

At the limit stated above, Equation 5.28 reduces to Equation 5.23 when $\Delta v^H = 0$ (i.e., $\gamma_w^H = 1$). In the strictest sense, the activity coefficient accounts for the energy change involved in taking the volume of the standard lattice to the volume of the real hydrate. That is, it will perturb the Gibbs energy of the standard lattice such as

$$\mu_w^H = g_w^\beta + \Delta g_w^\beta + RT \sum_i \upsilon_i \ln\left(1 - \sum_J \theta_{iJ}\right) \tag{5.29}$$

where the perturbation can be described as

$$\Delta g_w^\beta = \frac{\Delta g_{w0}^\beta}{RT_0} - \int_{T_0}^{T} \frac{\Delta h_w^\beta}{RT^2} dT + \int_{P_0}^{P} \frac{\Delta v^H}{RT} dP \tag{5.30}$$

Evaluating Equations 5.28 through 5.30, and assuming that the heat capacity of the hydrate is not affected in the process, Ballard proposed that the activity coefficient of water in the hydrate be expressed as

$$\ln \gamma_w^H = \frac{\Delta g_{w0}^\beta}{RT_0} + \frac{\Delta h_{w0}^\beta}{R}\left(\frac{1}{T} - \frac{1}{T_0}\right) + \int_{P_0}^{P} \frac{\Delta v^H}{RT} dP \tag{5.31}$$

where h_{w0}^β is the enthalpy of formation at reference conditions. Ballard (2002) arbitrarily defined the perturbed Gibbs energy and enthalpy of formation be linear in Δv^H; $\Delta g_{w0}^\beta = a\Delta v_0^H$, and $\Delta h_{w0}^\beta = b\Delta v_0^H$. Note that the subscript 0 refers to the volume difference at T_0 and P_0, the temperature and pressure at which the formation properties are known. This definition satisfies the above constraint on the activity coefficient—namely that it should approach unity in the limit of a pure water (hypothetical) hydrates.

Figure 5.4 illustrates the processes needed to determine the chemical potential of water in the hydrate, as given by Equation 5.28

$$g_w^\beta + RT \sum_i \upsilon_i \ln\left(1 - \sum_J \theta_{iJ}\right) + RT\gamma_w^H = \mu_w^H$$

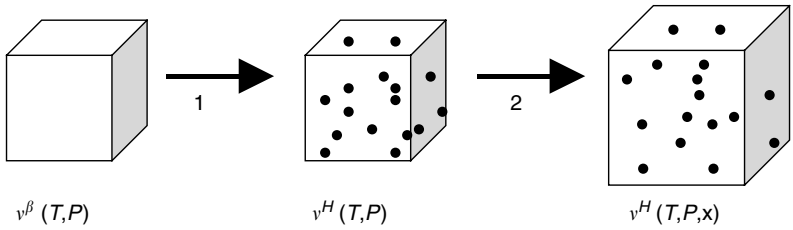

FIGURE 5.4 Corrected model allowing for distortion of hydrate due to guests ($v^{\beta} \neq v^{H}$). Process (1) in Figure 5.4 is done at constant volume and therefore, the van der Waals and Platteeuw statistical model can be used. Process (2) in Figure 5.4, the volume change of the hydrate from its standard state volume, is done at constant composition and is described by the activity coefficient in Equation 5.28.

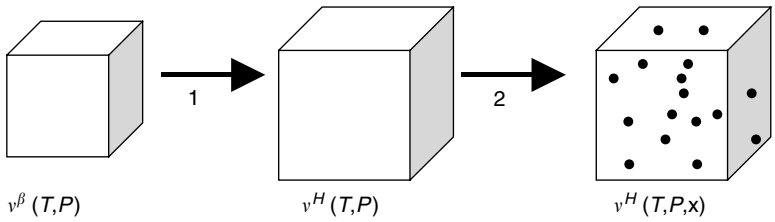

FIGURE 5.5 Alternative expression for corrected model allowing for distortion of hydrate ($v^{\beta} \neq v^{H}$). Equation 5.29 is the analogous expression for the processes shown.

Ballard (2002) noted that chemical potential is a state function and, therefore Equation 5.28 can be visualized in another path (as shown in Figure 5.5).

$$g_{\mathrm{w}}^{\beta} + \Delta g_{\mathrm{w}}^{\beta} + RT \sum_{i} \upsilon_i \ln \left(1 - \sum_{J} \theta_{iJ}\right) = \mu_{\mathrm{w}}^{\mathrm{H}}$$

In Figure 5.5, process (1) is given by Equations 5.30 and 5.31 and process (2) by the van der Waals and Platteeuw statistical model, since it is done at constant volume. Note that, since chemical potential is a state function, Figures 5.4 and 5.5 are equivalent processes.

The reader may be confused by the suggestion that the empty hydrate lattice being distorted by the addition of guests. Yet the method is pragmatically justified because it would be impossible to measure the empty lattice energies for all possible combinations of hydrate components. So we simply use methane for sI (or propane for sII, or methane + neohexane for sH) as a reference case. With these references, the deviation occurs because an empty methane lattice is not the same as an empty CO_2 or xenon lattice, and thus we try to account for that by using this activity term. This point is further discussed in Section 5.1.6.

5.1.6 Defining the Hydrate Fugacity and Reference Parameters

Ballard (2002) defined a hydrate fugacity with three major advantages:

1. The aqueous phase does not need to be present to enable hydrate calculations. Frequently, gas or condensate pipelines have no aqueous phase.
2. The properties of the empty hydrate are directly used in the model as opposed to the difference properties suggested by Parrish and Prausnitz (1972).
3. The expression for the fugacity of water in the hydrate follows the same framework as that in all other phases (i.e., aqueous, vapor or liquid, or pure solid phases).

In order to solve for thermodynamic equilibrium, the fugacity of water in the hydrate must be known. This method follows the common approach of solving for fugacity, using the standard state of the ideal gas of the pure component at 1 bar.

$$f_{\mathrm{w}}^{\mathrm{H}} = f_{\mathrm{w,o}} \exp\left[\frac{\mu_{\mathrm{w}}^{\mathrm{H}} - g_{\mathrm{w,o}}}{RT}\right] \tag{5.32}$$

where $f_{\mathrm{w,o}}$ is 1 bar, $g_{\mathrm{w,o}}$ is the Gibbs energy of pure water in the ideal gas state at 1 bar, and $\mu_{\mathrm{w,H}}$ is given by Equation 5.28. Note that the fugacity of water in the hydrate, as determined by Equation 5.32, does not require that an aqueous phase be present.

The best choice for the standard hydrate is one that is well-characterized and not too different from the real state of the system. If the standard state is well-defined, small perturbations from this standard state can be accounted for correctly. With this in mind, we turn to the three most well-known hydrates of sI, sII, and sH, namely methane, propane, and methane + neohexane. Note that the standard states for sI, sII, and sH are the empty hydrate lattices of these and not the actual hydrates. Therefore for the reference hydrates, the activity coefficients for methane, propane, and methane + neohexane hydrates will be unity.

The Gibbs energy of water in the standard state can be corrected for temperature and pressure using classical thermodynamics.

$$\frac{g_{\mathrm{w}}^{\beta}}{RT} = \frac{g_{\mathrm{w}_0}^{\beta}}{RT_0} - \int_{T_0}^{T} \frac{h_{\mathrm{w}}^{\beta}}{RT^2}\mathrm{d}T + \int_{P_0}^{P} \frac{v_{\mathrm{w}}^{\beta}}{RT}\mathrm{d}P \tag{5.33}$$

Note that $g_{w_0}^{\beta}$ is the molar Gibbs energy of formation of the standard hydrate at the reference conditions (T_0 and P_0), h_w^{β} is the molar enthalpy, and v_w^{β} is the molar

volume. These three properties are the unknowns which should be determined in order to specify the standard state hydrate.

The molar enthalpy of water in the standard hydrate can be expressed as

$$h_w^\beta = h_{w0}^\beta + \int_{T_0}^{T} c_{P_w^\beta} \mathrm{d}T \tag{5.34}$$

where h_{w0}^β is the molar enthalpy of formation of the standard hydrate at the reference conditions (T_0 and P_0) and $c_{P_w^\beta}$ is the heat capacity. The heat capacity of the standard hydrates for both sI and sII is well approximated by that of ice (Avlonitis, 1994), as is that for sH. However, the molar enthalpy of formation is not known and must be regressed to experimental data.

We define the molar volume of the standard hydrates of sI and sII as the molar volumes of methane and propane hydrate, respectively. The molar volume of these hydrates, and therefore of the standard states, is well-characterized via diffraction data (Tse, 1990; Huo, 2002). Ballard proposed the following expression for the molar volume of water in hydrates:

$$v_w^\beta = v_0 \exp[\alpha_1(T - T_0) + \alpha_2(T - T_0)^2 + \alpha_3(T - T_0)^3 - \kappa(P - P_0)] \tag{5.35}$$

The compressibility coefficient, κ, and reference volume, v_0, are solely dependent on the composition of the guest(s) in the hydrate lattice while the thermal expansion coefficients, α_1, α_2, and α_3 are solely dependent on the hydrate structure.

Note that, since all hydrates of a given structure have the same thermal expansion, the values in Table 5.4 are also the thermal expansion parameters for the standard empty hydrates.

The compositional dependence of the volume of hydrates is solely in the v_0 term. The compositional dependence was assumed to be a Langmuir type expression that accounts for a guest molecules repulsive nature with each hydrate

TABLE 5.4
Regressed Volumetric Thermal Expansion Parameters for Hydrate Volume (Divide by 3 to Get Linear Thermal Expansion Parameters)

Hydrate	α_1 (K^{-1})	α_2 (K^{-2})	α_3 (K^{-3})
sI	3.384960E–4	5.400990E–7	−4.769460E–11
sII	2.029776E–4	1.851168E–7	−1.879455E–10
sH	3.575490E–4	6.294390E–7	0

cage. The general form of the equation for v_0 is

$$v_0(x) = \left(a_0^* + \sum_i N_i \sum_J f(\theta_{iJ}) \Delta r_{iJ} \right)^3 \tag{5.36}$$

where N_i is the number cages of type i in the hydrate, Δr_{iJ} is the repulsive constant for guest molecule J in hydrate cage i, and a_0^* is denoted as the standard lattice parameter at T_0, P_0, and some $\boldsymbol{x}_0$. The standard lattice parameters for sI, sII, and sH hydrates were arbitrarily chosen to be 11.99245, 17.10000, and 11.09826 Å, respectively, such that $v_0(\vec{x})$ is that of the standard, empty hydrates (derived from data). The function, $f(\theta_{iJ})$, is defined to be

$$f(\theta_{iJ}) = \frac{(1+\eta_i)\theta_{iJ}}{1+\eta_i\theta_{iJ}} \exp[D_J - \bar{D}] \tag{5.37}$$

for the 5^{12} hydrate cage and

$$f(\theta_{iJ}) = \frac{(1+\eta_i)\theta_{iJ}}{1+\eta_i\theta_{iJ}} \tag{5.38}$$

for all other sI and sII hydrate cages ($5^{12}6^2$ and $5^{12}6^4$), where in Equations 5.37 and 5.38 η_i is the coordination number of cage i (z_i) per water molecule in the hydrate (N_i), θ_{iJ} is the fractional occupancy of component J in cage i, D_J is the molecular diameter of component J, and $\bar{D}$ is the fractional occupancy average molecular diameter of the guest molecules in the hydrate,

$$\bar{D} = \sum_J D_J \theta_{i,J}$$

Guests larger than ethane cannot fit into the small cage of sII and therefore the repulsive constants are zero. Due to the lack of sI compositional data, the repulsive constant for only one of the hydrate cages could be regressed. Due to lack of sH compositional data, the volume of sH hydrates was assumed to be independent of composition (Table 5.5).

The compressibility of a mixed hydrate (i.e., more than one guest molecule) is assumed to be of the form

$$\kappa_H = \sum_{J=1}^{C} \kappa_{J\mathrm{H}} \theta_{J\mathrm{L}} \tag{5.39}$$

where $\theta_{J\mathrm{L}}$ is the fractional occupancy of hydrate guest J in the large cage. Note that for sH hydrates, no experimental compressibility data exists. Therefore, the linear compressibility of the sH hydrate, κ_{sH}, is assumed to be 1E–7 bar^{-1}. Table 5.6 lists all compressibility parameters used in the hydrate volume model.

The standard hydrates of sI, sII, and sH were assumed to be the empty hydrates of methane, propane, and methane + neohexane, respectively. While the thermal expansion parameters are the same for the real and standard hydrates, the compressibility parameter and standard volume are not. The volumetric compressibilty of the standard hydrates of sI, sII, and sH are 3E–5, 3E–6, and 3E–7,

TABLE 5.5
Regressed Repulsive Constants and Guest Diameters for Hydrate Volume

Component	Diameter (Å)	sI small	sI large	sII small	sII large
Methane	4.247	1.7668E–2	1.0316E−2	2.0998E–3	1.1383E–2
Ethylene	4.816	0	1.5773E–2	2.3814E–3	1.3528E–2
Ethane	5.076	0	2.5154E–2	2.5097E–3	1.4973E–2
Propylene	5.522	0	2.9839E–2	0	2.1346E–2
Propane	5.745	0	0	0	2.5576E–2
n-Butane	6.336	0	0	0	3.6593E–2
i-Butane	6.306	0	0	0	3.6000E–2
i-Pentane	6.777	0	0	0	4.7632E–2
Benzene	6.272	0	0	0	3.5229E–2
Nitrogen	4.177	1.7377E–2	0	2.0652E–3	1.1295E–2
H_2S	4.308	1.7921E–2	0	2.1299E–3	1.1350E–2
CO_2	4.603	0	5.8282E–3	2.2758E–3	1.2242E–2
Xenon	4.404	1.8321E–2	0	2.1774E–3	1.1524E–2

TABLE 5.6
Regressed Linear Compressibility Parameters for Hydrate Volume (Multiply by 3 to Get Volumetric Compressibility Parameters)

Component	sI (bar^{-1})	sII (bar^{-1})
Methane	1.0E–05	5.0E–05
Ethylene	2.2E–06	2.2E–05
Ethane	1.0E–08	1.0E–07
Propylene	1.0E–07	1.0E–06
Propane	1.0E–07	1.0E–06
n-Butane	NA	1.0E–08
i-Butane	NA	1.0E–08
i-Pentane	NA	1.0E–08
Benzene	NA	1.0E–08
Nitrogen	1.1E–05	1.1E–05
H_2S	5.0E–06	1.0E–05
CO_2	1.0E–06	1.0E–05
Xenon	9.0E–06	1.0E–05

respectively. The standard volumes for each are 22.7712, 22.9456, and 24.2126 cm^3/mol, respectively. Note that the standard volumes were converted from the standard lattice parameters given earlier based on structure and corresponding number of water molecules in the hydrate lattice.

TABLE 5.7
Regressed Formation Properties of Standard Hydrates

Property	sI	sII	sH
$g^{\beta}_{w_0}$ (J/mol)	−235537.85	−235627.53	−235491.02
$h^{\beta}_{w_0}$ (J/mol)	−291758.77	−292044.10	−291979.26
A (J/cm^3)	25.74	260.00	0
B (J/cm^3)	−481.32	−68.64	0

The other regressed properties for the method are found in Tables 5.7 and 5.8. The parameters listed in this monograph are a result of a multivariate Gauss–Newton optimization by Ballard (2002) to which the reader should refer if a more detailed explanation of the method and fitted parameters is required.

Because there are a number of equations above, an equation summary is given in Table 5.9 to calculate the fugacity of water in hydrates.

5.1.7 The Gibbs Free Energy Method

This section is based on Ballard's (2002) extension of the ground-breaking work in Bishnoi's group by Gupta (1990). To calculate thermodynamic equilibrium for a closed system, three fundamental conditions must be met:

1. Temperature equilibrium of all phases,
2. Pressure equilibrium of all phases, and
3. Equality of chemical potential of a component in each phase,

all resulting from the Gibbs energy being at a minimum (Gibbs, 1928). These conditions are commonly used in developing procedures for solving for thermodynamic equilibrium. For a system of known phases, meeting the first three conditions will ensure that the Gibbs energy is at a minimum. The most common implementation of these conditions is for the two-phase system, vapor and liquid hydrocarbon, known as the vapor liquid equilibrium (VLE) flash.

The requirement that the Gibbs energy of the system must be at a minimum, at a given temperature and pressure, is a statement of the second law of thermodynamics. Meeting conditions (1) to (3) is necessary for thermodynamic equilibrium but is not sufficient for the minimization of the Gibbs energy. Baker et al. (1982) discuss this further in their development of a solution procedure for multiphase equilibrium calculations. For simple systems in which the phases present at equilibrium are known (i.e., vapor and liquid hydrocarbon), however, conditions (1) through (3) are commonly used without difficulty. When solving for thermodynamic equilibrium in a more complex system in which several phases could form, a fourth criterion, the minimum of Gibbs energy, may be used.

TABLE 5.8
Regressed Kihara Potential Parameters ("*a*" as in Original Reference)

Component	a (Å)	σ (Å)	ε/k (K)
Methane	0.3834	3.14393	155.593
Ethylene	0.4700	3.24461	180.664
Ethane	0.5651	3.24693	188.181
Propylene	0.6500	3.33039	186.082
Propane	0.6502	3.41670	192.855
n-Butane	0.9379	3.51726	197.254
i-Butane	0.8706	3.41691	198.333
i-Pentane	0.9868	3.54550	199.560
Benzene	1.2000	3.25176	223.802
2,3-Dimethyl-1-butene	1.0175	3.55376	211.924
3,3-Dimethyl-1-butene	0.7773	3.56184	253.681
Methylcyclopentane	1.0054	3.56878	229.928
Neohexane	1.0481	3.54932	229.832
2,3-Dimethylbutane	1.0790	3.57910	210.664
Cycloheptane	1.0576	3.59028	250.187
Ethylcyclopentane	1.1401	3.60425	219.083
Methylcyclohexane	1.0693	3.58776	237.989
2,2,3-Trimethylbutane	1.1288	3.59955	232.444
2,2-Dimethylpentane	1.2134	3.59989	224.609
3,3-Dimethylpentane	1.2219	3.59117	204.968
cis-1,2-Dimethylcyclohexane	1.1494	3.60555	233.510
1,1-Dimethylcyclohexane	1.1440	3.60212	246.996
Ethylcyclohexane	1.1606	3.60932	220.527
Nitrogen	0.3526	3.13512	127.426
Hydrogen sulfide	0.3600	3.10000	212.047
Carbon dioxide	0.6805	2.97638	175.405
Xenon	0.2357	3.32968	193.708

That is, if the amount of phases present at the solution is not known *a priori*, the Gibbs energy must be used to determine what phases are present.

Implementation of conditions (1) to (3) is done following a similar procedure as that of a two-phase system (Rachford and Rice, 1952). For a system with C components and π possible phases, satisfying a simple mass balance for each component in each phase results in the following objective function:

$$E_k = \sum_{i=1}^{C} \frac{z_i(x_{ik}/x_{ir} - 1)}{1 + \sum_{\substack{j=1 \\ j\neq r}}^{\pi} \alpha_j(x_{ij}/x_{ir} - 1)} = 0, \qquad k = 1, \ldots, \pi \tag{5.40}$$

where z_i is the mole fraction of component i in the feed, α_j is the molar phase fraction of phase j, and x_{ik} is the mole fraction of component i in phase k.

TABLE 5.9
Equation Summary to Determine Fugacity of Water in Hydrate

$$f_{\mathrm{w}}^{\mathrm{H}} = f_{\mathrm{w},0} \exp\left[\frac{\mu_{\mathrm{w}}^{\mathrm{H}} - g_{\mathrm{w},0}}{RT}\right] \tag{5.32}$$

where $f_{\mathrm{w},0}$ is 1 bar, $g_{\mathrm{w},0}$ is the Gibbs energy of pure water in the ideal gas state at 1 bar

$$\mu_{\mathrm{W}}^{\mathrm{H}} = g_{\mathrm{W}}^{\beta} + RT \sum_i \upsilon_i \ln\left(1 - \sum_J \theta_{iJ}\right) + RT \ln \gamma_{\mathrm{W}}^{\mathrm{H}} \tag{5.28}$$

$$\theta_{iJ} = \frac{C_{iJ} f_J}{1 + C_{iJ} f_J} \tag{5.22c}$$

$$C_{J,i} = \frac{4\pi}{kT} \int_0^{R_1 - a_J} \exp\left[-\frac{\sum_n \omega_{J,n}(r)}{kT}\right] r^2 \, \mathrm{d}r \tag{5.27b}$$

$$\varpi_{Jn}(r) = 2 z_n \varepsilon_J \left[\frac{\sigma_J^{12}}{{R_n}^{11} r}\left(\delta^{10} + \frac{a_J}{R_n}\delta^{11}\right) - \frac{\sigma_J^{6}}{{R_n}^{5} r}\left(\delta^{4} + \frac{a_J}{R_n}\delta^{5}\right)\right] \tag{5.25a}$$

$$\text{where} \quad \delta^N = \frac{1}{N}\left[\left(1 - \frac{r}{R_n} - \frac{a_J}{R_n}\right)^{-N} - \left(1 + \frac{r}{R_n} - \frac{a_J}{R_n}\right)^{-N}\right] \tag{5.25b}$$

$$\frac{g_{\mathrm{w}}^{\beta}}{RT} = \frac{g_{\mathrm{w}0}^{\beta}}{RT_0} - \int_{T_0}^{T} \frac{h_{\mathrm{w}}^{\beta}}{RT^2} \mathrm{d}T + \int_{P_0}^{P} \frac{v_{\mathrm{w}}^{\beta}}{RT} \mathrm{d}P \tag{5.33}$$

$$h_{\mathrm{w}}^{\beta} = h_{\mathrm{w}0}^{\beta} + \int_{T_0}^{T} c_{P_{\mathrm{w}}^{\beta}} \mathrm{d}T \tag{5.34}$$

$$v_{\mathrm{w}}^{\beta} = (a_0^*)^3 \exp[\alpha_1 (T - T_0) + \alpha_2 (T - T_0)^2 + \alpha_3 (T - T_0)^3 - \kappa (P - P_0)]$$

$$\ln \gamma_{\mathrm{w}}^{\mathrm{H}} = \frac{\Delta g_{\mathrm{w}0}^{\beta}}{RT_0} + \frac{\Delta h_{\mathrm{w}0}^{\beta}}{R}\left(\frac{1}{T} - \frac{1}{T_0}\right) + \int_{P_0}^{P} \frac{\Delta v^{\mathrm{H}}}{RT} \mathrm{d}P \tag{5.31}$$

$$\Delta g_{\mathrm{w}0}^{\beta} = a \Delta v_0^{\mathrm{H}} \quad \text{and} \quad \Delta h_{\mathrm{w}0}^{\beta} = b \Delta v_0^{\mathrm{H}}$$

$$\Delta v^{\mathrm{H}} = v^{\mathrm{H}} - v^{\beta}$$

$$v^{\mathrm{H}} = v_0 \exp[\alpha_1 (T - T_0) + \alpha_2 (T - T_0)^2 + \alpha_3 (T - T_0)^3 - k (P - P_0)] \tag{5.35}$$

$$v_0(\vec{x}) = \left(a_0^* + \sum_i N_i \sum_J f(\theta_{iJ}) \, \Delta r_{iJ}\right)^3 \tag{5.36}$$

$$5^{12} \text{ cages:} \quad f(\theta_{iJ}) = \frac{(1 + \eta_i)\theta_{iJ}}{1 + \eta_i \theta_{iJ}} \exp[D_J - \bar{D}] \tag{5.37}$$

$$5^{12}6^2 \text{ and } 5^{12}6^4 \text{ cages:} \quad f(\theta_{iJ}) = \frac{(1 + \eta_i)\theta_{iJ}}{1 + \eta_i \theta_{iJ}} \tag{5.38}$$

$$\kappa_{\mathrm{H}} = \sum_{J=1}^{C} \kappa_{J\mathrm{H}} \theta_{J\mathrm{L}} \tag{5.39}$$

The subscript r refers to a reference phase, which is present at thermodynamic equilibrium. Implementation of conditions (1) to (3) results in the following expression for the mole fraction ratio:

$$\frac{x_{ik}}{x_{ir}} = \frac{\phi_{ir}}{\phi_{ik}} = K_{ik} \qquad i = 1, \ldots, C \quad k = 1, \ldots, \pi \tag{5.41}$$

where K_{ik} is the distribution coefficient, and ϕ is the fugacity coefficient. Note that the definition of the distribution coefficient (Equation 5.41) is valid only for phases present at thermodynamic equilibrium. Therefore, this approach can only be used if all phases ($k = 1, \ldots, \pi$) are present. This is quite a drawback in that, for natural gases and water, the phases present at equilibrium are usually not known.

Gupta (1990) showed that, by defining the mole fraction ratio in terms of the distribution coefficient as

$$\frac{x_{ik}}{x_{ir}} = \frac{\phi_{ir}}{\phi_{ik}} e^{y_k} = K_{ik} e^{y_k} \qquad i = 1, \ldots, C \quad k = 1, \ldots, \pi \tag{5.42}$$

where y_k is defined as

$$y_k = \ln\left(\frac{f_{ik}}{f_{ir}}\right) \quad k = 1, \ldots, \pi \tag{5.43}$$

is equivalent to minimizing the Gibbs energy of the system conditional to

$$S_k = \frac{\alpha_k y_k}{\alpha_k + y_k} = 0 \quad k = 1, \ldots, \pi \tag{5.44}$$

That is, if $\alpha_k > 0$ then phase k is present and $y_k = 0$ and likewise, if $\alpha_k = 0$ then phase k is not present and $y_k \neq 0$. Note that Equation 5.44 is always satisfied for the reference phase by definition of y_k.

Replacing the mole fraction ratio in Equation 5.40 with Equation 5.42, we obtain

$$E_k = \sum_{i=1}^{C} \frac{z_i (K_{ik} e^{y_k} - 1)}{1 + \sum_{\substack{j=1 \\ j \neq r}}^{\pi} \alpha_j (K_{ij} e^{y_j} - 1)} = 0 \quad k = 1, \ldots, \pi \tag{5.45}$$

which is valid for all phases (present or not) at a solution. Equation 5.45 is used to determine the set of phase amounts, α_k, and stability variables, y_k, that satisfy thermodynamic equilibrium.

The solution procedure is split into two parts: (1) minimizing Gibbs energy by updating phase amounts and stability variables at a given set of K-values and (2) updating K-values at a given set of phase amounts and stability variables. This approach is typical in phase equilibrium problems. The Newton procedure is

used to minimize the Gibbs energy of the system at a given set of K-values (via Equation 5.45). This approach is convergent as long as the fugacity coefficients are not strong functions of composition. This is certainly the case for the fluid phases such as vapor and liquid hydrocarbon but is not necessarily true for the aqueous and hydrate phases. With proper care this approach is convergent for all systems.

The Newton method gives a correction to the phase amounts and stability variables based on the gradient of the Gibbs energy at the given set of K-values. Due to the highly nonideal behavior of the hydrate phases, all corrections are scaled such that no phase amount or stability variable is changed more than 25% of its original value. That is, the entire correction vector is scaled so as to keep the proper direction of convergence.

In the development of Equation 5.45, the composition of each phase is given as

$$x_{ik} = \frac{z_i K_{ik} e^{y_k}}{1 + \sum_{\substack{j=1 \\ j \neq r}}^{\pi} \alpha_j (K_{ij} e^{y_j} - 1)} \qquad i = 1, \ldots, C \quad k = 1, \ldots, \pi \tag{5.46}$$

Equation 5.46 is used to update the composition of each phase. With the new composition, the fugacity coefficients are calculated to get the new set of K-values. As is the case for minimizing the Gibbs energy, this approach is convergent as long as the fugacity coefficients are not strong functions of composition. Successive substitution of the composition gives linear convergence whereas Newton's method gives quadratic convergence.

Due to the highly nonideal behavior of the hydrate phases, Equation 5.46 is not used to update the hydrate composition. However, the compositions of all nonhydrate phases are determined via Equation 5.46. All composition corrections of a given phase are scaled such that no composition in that phase is changed by more than 50% of its original value. The expression for the composition of species in the hydrate follows from a simple mass balance:

$$x_{iH} = \frac{\sum_m \upsilon_m \theta_{im}}{1 + \sum_m \sum_j \upsilon_m \theta_{jm}} \tag{5.47}$$

where υ_m is the number of hydrate cages of type m per water molecule in the hydrate. This equation is used in place of Equation 5.46 to update the hydrate phase composition.

The solution procedures discussed above are implemented into the algorithm shown in Figure 5.6.

As can be seen in Figure 5.6, thermodynamic equilibrium is achieved when the Gibbs energy is at a minimum ($E_k = 0$) and the difference in the updated mole fractions and previous mole fractions (Δx_{ik}) for each phase is less than 1E–6. One of the crucial steps in obtaining a solution is creating a "good" initial estimate for the unknown variables.

Several authors have determined ideal K-values for component distribution between V–L_{hc} (DePriester, 1953; Hadden and Grayson, 1961) and V-Hydrate

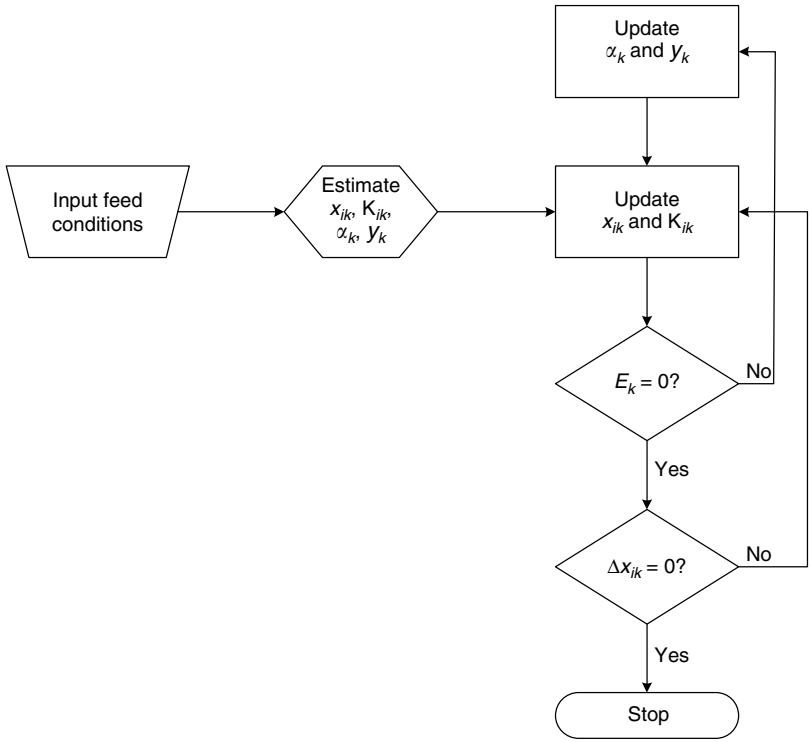

FIGURE 5.6 Algorithm to solve for thermodynamic equilibrium.

(Wilcox et al., 1941) phases. However, Ballard (2002) developed composition-independent sets of K-values to provide the initial estimate for the component distribution between all possible phases: vapor, liquid hydrocarbon, aqueous, sI hydrate, sII hydrate, sH hydrate, ice, solid NaCl, solid KCl, and solid $CaCl_2$.

The thesis of Ballard (2002) details this calculation method, which includes multiphase systems, solid phases including ice and salts, and thermodynamic inhibition. The CSMGem (the last three initials are the first letters of "Gibbs energy minimization") User's Manual, included in the CD in the endpapers, and the examples of hydrate calculation shown in the Appendix A, enable the reader to use the CD programs.

The Gibbs energy minimization method allows for calculations of the formation conditions for any phase (including the hydrate). It also allows for the calculation of phases present at any T and P (whether hydrates are present or not). Therefore, included are the options to perform all thermodynamic calculations with every phase and not just the hydrate. The types of calculations, combined with plotting capability, included in CSMGem are

1. Hydrate formation temperature and pressure (with and without inhibition)

2. Formation temperature and pressure of phases other than hydrates
3. Flashes (phase compositions/amounts) at a temperature and pressure
4. Multiphase calculations (from two to eight phases)
5. Expansion through a valve or turboexpander.

5.1.8 Accuracy of CSMGem Compared to Commercial Hydrate Programs

A comparison of predictions from CSMGem, the program included in the CD of this work, with the second edition's version (CSMHYD) and three commercial hydrate prediction programs, is given here for all recent hydrate data reported in literature. The five programs (with the last three commercial) compared in this work are

CSMGem—Colorado School of Mines (2007 edition)
CSMHYD—Colorado School of Mines (1998 edition)
DBRHydrate—DBRobinson Software Inc. (version 5.0)
Multiflash—Infochem Computer Services Ltd. (version 3.0)
PVTsim—Calsep A/S (version 11)

The comparisons are broken into two categories for hydrate formation temperatures and pressures (1) uninhibited systems, and (2) thermodynamically inhibited systems. These comparisons show the accuracy that may be expected from readily available hydrate prediction programs. A detailed comparison of the accuracy of these programs is given by Ballard and Sloan (2004b).

A series of figures follows, giving the average errors in temperature and pressure for several types of hydrates based on the following categories: (1) single guest or simple hydrates, (2) binary guest hydrates, (3) ternary guest hydrates, (4) multicomponent hydrates (natural gas hydrates), (5) hydrates in black oils (BO) and gas condensates (GC), and (6) sH hydrates. The results are given as the average error either in temperature or pressure. The average absolute error in temperature and pressure are calculated as:

$$T_{\text{Error}} = \frac{\sum_{\#\text{ data points}} |T_{\text{predicted}} - T_{\text{experimental}}|}{\#\text{ data points}} \tag{5.48}$$

$$P_{\text{Error}} = \frac{\sum_{\#\text{ data points}} |P_{\text{predicted}} - P_{\text{experimental}}|/P_{\text{experimental}}}{\#\text{ data points}} \cdot 100\% \tag{5.49}$$

and are given in Kelvin and any pressure units, respectively.

Figures 5.7 and 5.8 give the values for all available uninhibited hydrate data (listed in Chapter 6), comparing the accuracies of the five programs.

From Figures 5.7 and 5.8, it is apparent that more reliable thermodynamic data are needed, particularly for the (1) BO and GC, and (2) Natural gas systems.

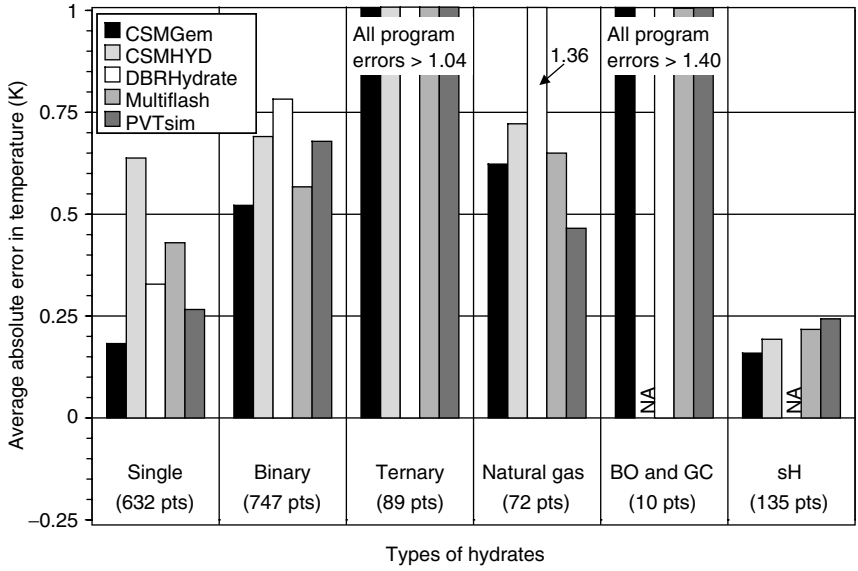

FIGURE 5.7 Incipient temperature accuracy (absolute) for uninhibited hydrate data for five programs.

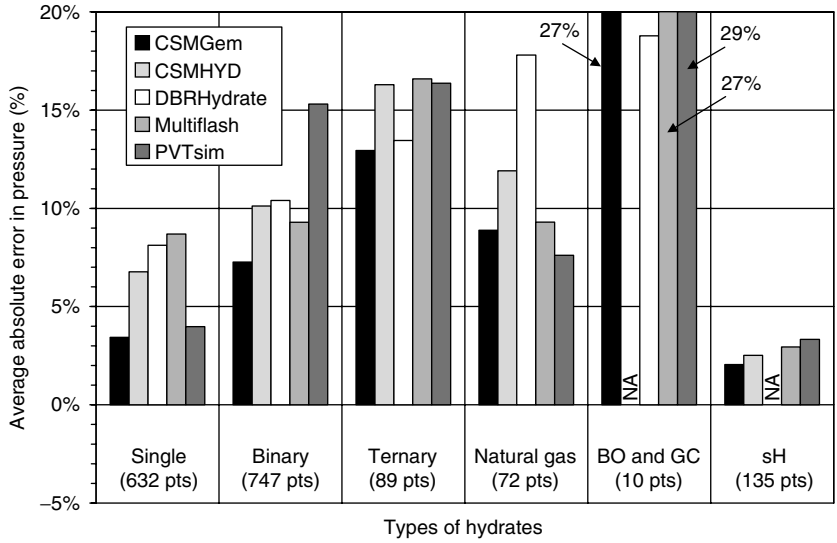

FIGURE 5.8 Incipient pressure accuracy (absolute) for uninhibited hydrate data for five programs.

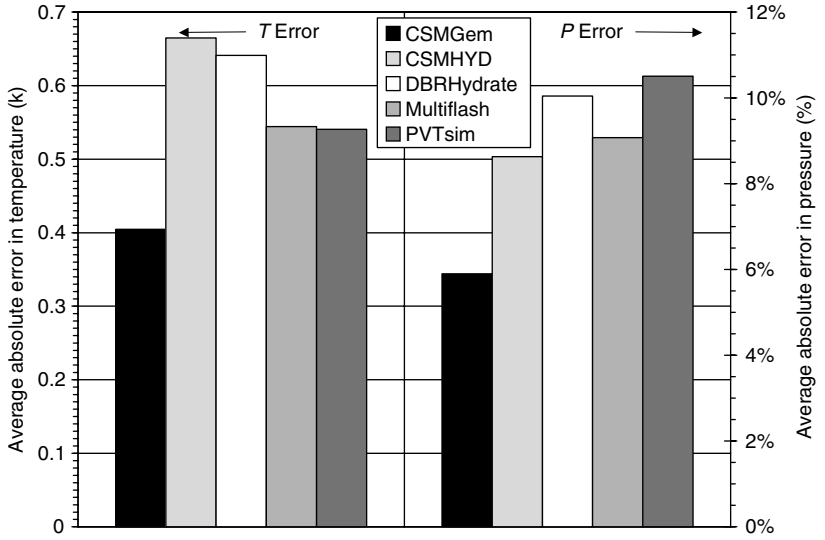

FIGURE 5.9 Uninhibited incipient hydrate T and P errors (absolute) for all hydrates (1685 pts).

Figure 5.9 suggests the rule-of-thumb that one can expect the incipient hydrate temperature and pressure to be predicted to within 0.65 K and 10% of overall pressure, respectively. These values approximate the experimental accuracy of the measurements, and suggest that it may not be practical to increase the prediction accuracy until further progress is required for measurement accuracy. Such comparisons with data suggest that hydrate phase equilibria predictions are sufficiently established to permit the state-of-the-art to turn to time dependent phenomena (Sloan, 2005).

For the second category, consider a comparison of available programs to thermodynamically inhibited incipient hydrate data, in Figures 5.10 and 5.11.

Figures 5.10 and 5.11 show that one may expect modern programs to predict the methanol- and NaCl-inhibited incipient temperature and pressure to within about 2 K and 20% in pressure, respectively. While comparisons for monoethylene glycol are not given, they might be comparable for low concentrations, such as below 30 wt% in free water. Second, the two figures show that the inaccuracies of mixtures of the two inhibitors (methanol and NaCl) are similar to that of the pure inhibitors.

5.1.9 *Ab Initio* Methods and the van der Waals and Platteeuw Method

Recently there has been a concerted effort to calculate potentials between the atoms and molecules in hydrates, using *ab initio* methods or quantum mechanics, initiated

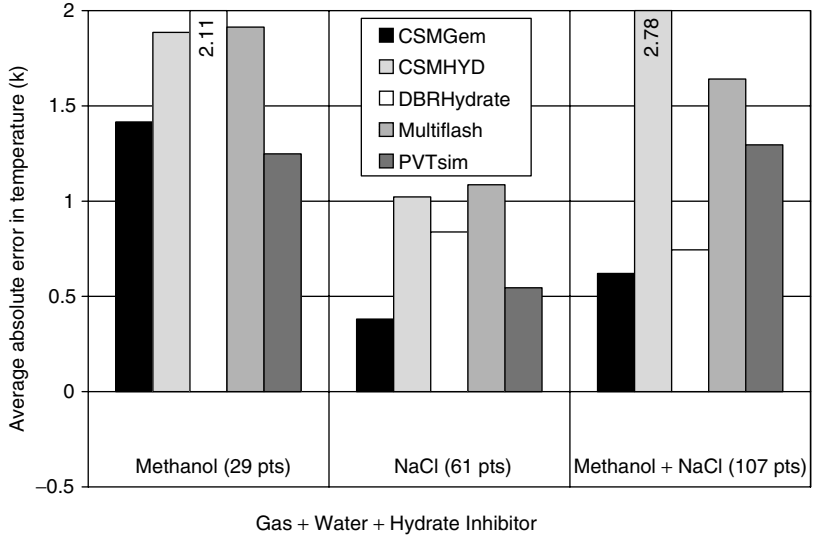

FIGURE 5.10 Hydrate formation T error (absolute) for all inhibited hydrates.

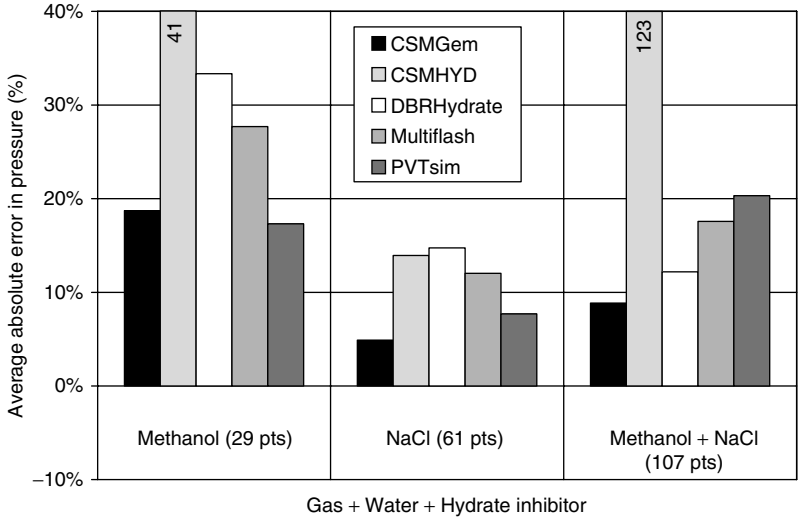

FIGURE 5.11 Hydrate formation P error (absolute) for all inhibited hydrates.

with the Schrödinger equation. These methods are enabled by greatly enhanced computing capability over the last decade. Three doctoral theses are notable in this regard (1) Cao (2002), (2) Klauda (2003), and (3) Anderson (2005); the second thesis is from the group of Sandler at the University of Delaware, and the first and last theses were developed via collaborations of Tester with the group of Trout at

the Massachusetts Institute of Technology. The thesis of Cao is considered as the fundamental *ab initio* groundwork, so only the advances of Klauda and Anderson are discussed here.

Some advantages of the *ab initio* methods are

1. Potential parameters (such as the Kihara core or Lennard-Jones potentials of the previous sections) can be calculated from a small set of fundamental, *ab initio* intermolecular energies, rather than fits of the potentials to phase equilibria and spectroscopic data.
2. Potential parameters are well-defined and do not extend over a wide range of values.
3. Nonspherical shells are readily included in generating the Langmuir constants.
4. Water molecules beyond the first shell are readily included in Langmuir constants.
5. Guest–guest interactions between cages can be easily included.
6. Critical hydrate parameters, such as cage occupancies and structural transitions can be predicted a priori, without fitting the model to spectroscopic measurements.

The above advantages remove three of the major assumptions in the van der Waals and Platteeuw model—namely Assumptions 3 and 4 in Section 5.1.1, as well as Assumption 6 in Section 5.1.4. The three theses show that, in principle, the *ab initio* methods have the potential to compose the largest improvements to the van der Waals and Platteeuw theory in the last half-century. For cases with a few components, it can be shown that *ab initio* methods represent an improvement over common methods (Anderson et al., 2005), such as the program CSMHYD, which accompanied the second, 1998 edition of this book.

However, there are several pragmatic restrictions of the *ab initio* methods for natural gas mixtures which cause them to be currently less applicable than the programs composed in Section 5.1.8, and included in the endpapers CD . Most concerns originate in the fact that computer capacity, time, and effort limit the exact application of the Schrödinger equation between all of the atoms present in the system:

1. It is only practical to calculate the interaction between the guest atoms and a partial cage, typically five or ten water molecules, and then apply some configurational procedure to account for the remainder,
2. The principle of the calculation is shown to be more accurate than previously available programs such as CSMHYD (included with the second edition of this book) using a subset of natural gas hydrate guest formers. For example Klauda (2003) calculated values for CH_4, C_2H_6, C_3H_8, N_2, and CO_2 their mixtures, but omitted n-C_4H_{10}, i-C_4H_{10}, H_2S, and all structure H formers. For hydrocarbon guests, Anderson (2005) considered only CH_4, C_2H_6, C_3H_8, and i-C_4H_{10}, without including noncombustibles, n-C_4H_{10}, or structure H formers.

3. Frequently, simple potentials such as Lennard-Jones potentials must be complicated by the inclusion of coulombic contribution parameters, as used for CO_2 and C_3H_8 by Klauda, requiring other fitting parameters.
4. The methods have yet to be extended to common thermodynamic inhibitors such as methanol or monoethylene glycol. In principal the extension is not a function of the *ab initio* methods since the thermodynamic inhibitors affect the water activity; yet this extension has not been quantified.

In sum, *ab initio* methods are beginning to fulfill their substantial promise for hydrates. For many hydrate guest components, *ab initio* methods have been shown to extend some of the most fundamental calculations from quantum mechanics to macroscopic properties, and to predict spectroscopic hydrate properties acceptably.

Yet until these methods can be extended to all common natural gas guest components and their thermodynamic inhibitors, it will be difficult to use the programs pragmatically. To date the programs have proved the *ab initio* concept from an academic perspective. While extension of *ab initio* methods to all natural gas hydrate components can be done in principle, that task awaits the generation and maintenance of a complete program.

Until more complete *ab initio* hydrate programs are available for comparison with commonly used commercial hydrate programs, such as PVTSim, Multiflash, and DBRHydrate, the use of the latter programs are likely to predominate.

5.2 Application of the Method to Analyze Systems of Methane + Ethane + Propane

Since mixtures of methane, ethane, and propane make up nearly 97 mol% of a typical natural gas mixture, the hydrate phase behavior of a natural gas mixture in contact with water will likely be approximated by that of a simple mixture of these three components in contact with water.

This chapter's statistical mechanics method was used to generate phase diagrams as illustrations of multicomponent hydrate equilibria concepts at one isotherm, 277.6 K, the most common temperature in a pipeline on the ocean floor at water depths beyond 600 m. Section 5.2.1 shows the fit if the method to single (simple) hydrates, before the extension to binary hydrate guests in Section 5.2.2. Section 5.2.3 shows the final extension to ternary mixtures of $CH_4 + C_2H_6 + C_3H_8$ and indicates an industrial application. Most of the discussion in this section was extracted from the thesis of Ballard (2002) and the paper by Ballard and Sloan (2001).

5.2.1 Pure Hydrate Phase Equilibria

Experimental data for hydrates of pure gases in contact with water are the most abundant, comprising of nearly 50% of all equilibrium hydrate-related data.

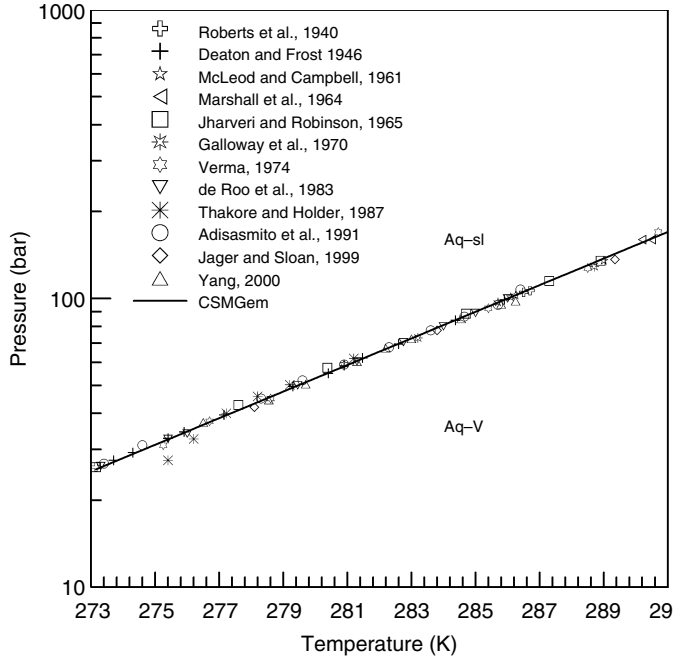

FIGURE 5.12 Pressure vs. temperature diagram for methane + water system.

Although a typical natural gas is mainly comprised of the first three normal paraffins, the phase equilibria of each component with water will differ from that of a natural gas with water. However, a comparison of predictions with data for methane, ethane, and propane simple gas hydrates is given as a basis for understanding the phase equilibria of water with binary and ternary mixtures of those gases.

Figure 5.12 is the pressure versus temperature phase diagram for the methane+ water system. Note that excess water is present so that, as hydrates form, all gas is incorporated into the hydrate phase. The phase equilibria of methane hydrates is well predicted as can be seen by a comparison of the prediction and data in Figure 5.12; note that the predicted hydrate formation pressure for methane hydrates at 277.6 K is 40.6 bar.

Figure 5.13 is the equivalent ethane + water pressure versus temperature phase diagram. Note that the Aq–sI–V line intersects the Aq–V–L_{hc} line at 287.8 K and 35 bar. Due to differences in the volume and enthalpy of the vapor and liquid hydrocarbon, the three-phase hydrate formation line changes slope at high temperature and pressure from Aq–sI–V to Aq–sI–L_{hc}, due to the intersectiion of Aq–sI–V line with the Aq–V–L_{hc} line (slightly higher than the ethane vapor pressure). Note that the hydrate formation pressure for ethane hydrates at 277.6 K is predicted to be 8.2 bar.

Figure 5.14 is the propane + water pressure versus temperature phase diagram. Note that the data are scattered along the Aq–sII–L_{hc} line due to difficulty

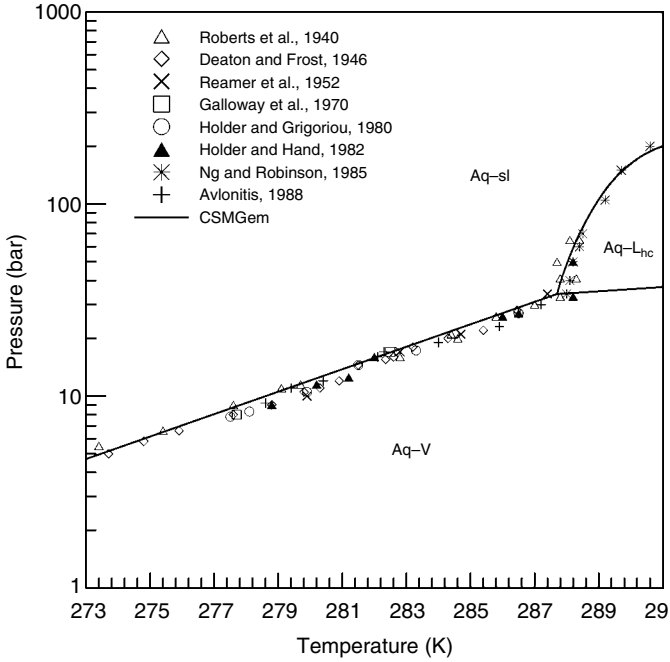

FIGURE 5.13 Pressure vs. temperature diagram for ethane + water system.

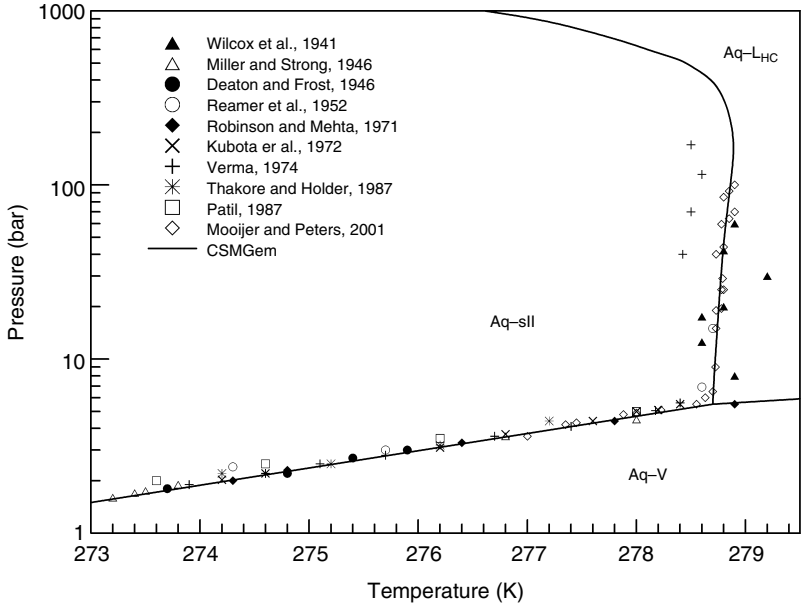

FIGURE 5.14 Pressure vs. temperature diagram for propane + water system.

measuring hydrate equilibria with three relatively incompressible phases. As with the ethane + water system in Figure 5.13, the slope of the three-phase hydrate formation line changes drastically when the Aq–sII–V line intersects the Aq–V–L_{hc} line. In fact, the Aq–sII–L_{hc} line is nearly vertical but decreases to lower temperature at high pressure. The predictions suggest "pseudo-retrograde" phenomena for the propane hydrates in which the sII hydrate is predicted to dissociate by pressurization at a constant temperature.

For example, at 278.2 K, hydrates form at a pressure of approximately 5 bar and dissociate upon pressurization at approximately 600 bar. A more detailed explanation of the pseudo-retrograde hydrate phenomena can be found in the binary hydrates section which follows. Note that the hydrate formation pressure of propane hydrates along the Aq–sII–V line at 277.6 K is predicted to be 4.3 bar.

5.2.2 Binary Hydrate Phase Equilibria

To evaluate the phase equilibria of binary gas mixtures in contact with water, consider phase diagrams showing pressure versus pseudo-binary hydrocarbon composition. Water is present in excess throughout the phase diagrams and so the compositions of each phase is relative only to the hydrocarbon content. This type of analysis is particularly useful for hydrate phase equilibria since the distribution of the guests is of most importance. This section will discuss one diagram of each binary hydrate mixture of methane, ethane, and propane at a temperature of 277.6 K.

5.2.2.1 Methane + propane hydrates

Figure 5.15 is the pseudo-binary pressure versus excess water composition diagram for the methane + propane + water system at a temperature of 277.6 K. At 277.6 K the hydrate formation pressures are 4.3 and 40.6 bar for pure propane (sII) and pure methane (sI) hydrates, respectively, as shown at the excess water composition extremes in Figure 5.15. As methane is added to pure propane, there will be a composition at which the incipient hydrate structure changes from sII to sI; as seen in the inset of Figure 5.15, this composition is predicted to be 0.9995 mole fraction methane in the vapor—a very small amount of propane added to a methane + water mixture will form sII hydrates.

As indicated in Example 4.1, note the dramatic decrease in hydrate pressure caused by a small amount of propane added to methane, due to the structure change (sI to sII). At pressures above incipient hydrate formation conditions, sII hydrates are predicted to be present throughout the entire composition range.

Of the possible binary combinations of methane, ethane, and propane, the methane + propane + water system (Figure 5.15) is the simplest.

5.2.2.2 Methane + ethane hydrates

Structural transitions (sI and sII) have been experimentally determined in the methane + ethane + water system via Raman, NMR, and diffraction between

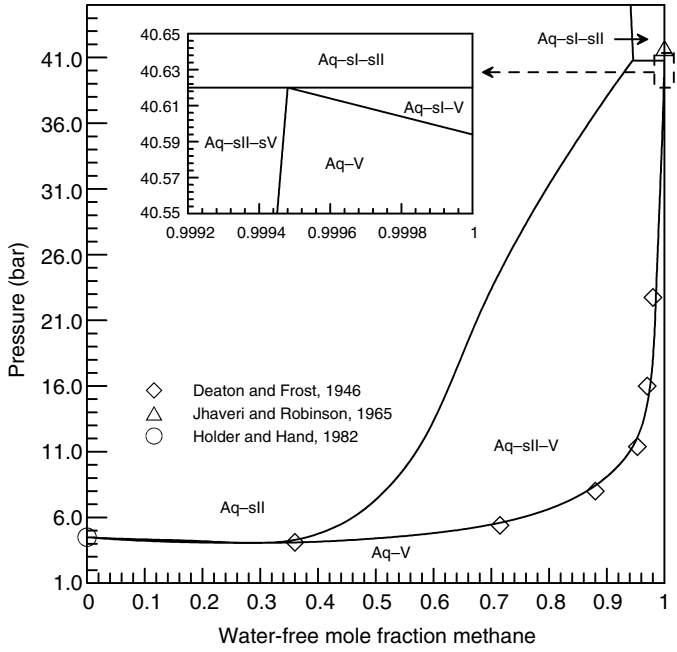

FIGURE 5.15 Pseudo-P–x diagram for methane + propane + water system at 277.6 K.

0.736 and 0.994 mole fraction methane in the vapor at a temperature of 274.2 K (Subramanian et al., 2000a,b).

Figure 5.16 is the pseudo-binary pressure versus excess water composition diagram for the methane + ethane + water system at a temperature of 277.6 K. In the diagram, pure ethane and pure methane both form sI hydrates in the presence of water at pressures of 8.2 and 40.6 bar, respectively. Note that between the compositions of 0.74 and 0.994 mole fraction methane, sII hydrates form at the incipient formation pressure. Similar to the methane + propane + water system, only a small amount of ethane added to pure methane will form sII hydrates.

At pressures well above the incipient formation pressure, sII hydrates are predicted to be present in the composition range of 0.39–0.96 mole fraction methane. Regions in which sI and sII hydrates coexist in equilibrium are predicted in Figure 5.16. A physical explanation of why this occurs is that, as hydrates form, the vapor phase composition changes. If, for example, an excess water composition of 50 mol% methane and 50 mol% ethane is fed to a fixed volume at 277.6 K, sI hydrates will initially form at approximately 11 bar. Ethane, being the larger guest, will preferentially stabilize the large cages in the sI hydrate lattice so that the excess water composition of the hydrate will contain about 24 mol% methane and 76 mol% ethane (Figure 5.16).

As pressure is increased, the amount of sI hydrate in the system relative to vapor becomes larger, enriching the vapor with methane. This can be seen by applying

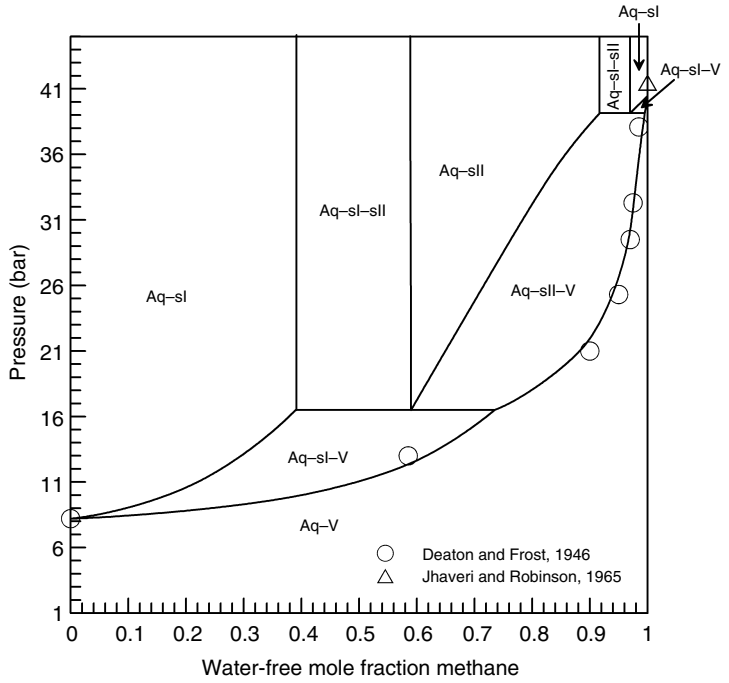

FIGURE 5.16 Pseudo-P–x diagram for methane + ethane + water system at 277.6 K.

the inverse lever rule. At 16.5 bar, the vapor composition will be approximately 74 mol% methane, which is the vapor composition at which sII hydrates will form. It is at this condition (the horizontal line) where there are four phases (Aq–sI–sII–V) in the system; by Gibbs phase rule there is one degree of freedom, which is set by the temperature of the diagram (277.6 K). Therefore, as pressure is increased for a 50/50 mixture, the remaining vapor forms sII hydrates, leaving an aqueous phase, sI, and sII hydrates in the system. A similar sI + sII region is predicted at higher concentrations of methane (91.5–96.5 mol%) in which the initial hydrate structure is sII.

Figure 5.16 clearly shows the pressure and composition dependence of hydrate structure at a constant temperature. It can be seen that the hydrate can be sI, sII, or both depending on the composition and pressure. Predictions also show that there is temperature dependence as well.

While the effect is not shown in the Figure 5.16 isotherm, Table 5.10 shows the predicted effect of temperature on incipient hydrate structure for a excess water gas mixture of 73 mol% methane and 27 mol% ethane. As temperature increases, the incipient hydrate structure changes from sII to sI to sII and back to sI.

By Gibbs' Phase Rule, if pressure and composition of one phase are specified, the temperature must also be specified to determine which hydrate structure is present for three phases. As seen from Figure 5.16, there are many regions in which sI, sII, or both are present. Without the aid of program or a hydrate phase

TABLE 5.10
Effect of Temperature on Hydrate Structure in the Methane (0.73) + Ethane (0.27) + Water (Excess) System

Temperature (K)	Incipient hydrate structure
273–275	sII
275–292	sI
292–301	sII
>301	sI

diagram, such as Figure 5.16, generated by the Gibbs energy minimization flash program, it would be difficult to determine which phases are present. Assuming that the hydrate formed at the incipient conditions prevails at higher pressures and temperatures could be a costly mistake. In many practical situations such as flow assurance in natural gas pipelines and hydrates in oceanic and permafrost regions it is essential to know what phases are present. Subramanian et al. (2000a,b) discuss the practical applications of these predictions.

5.2.2.3 Ethane + propane hydrates

Figure 5.17 shows a predicted pressure versus excess water composition plot for the ethane+propane+water system at 274 K. At 0.0 mol fraction ethane (propane+ water) sII form at approximately 2 bar, and at 1.0 mol fraction ethane (ethane + water) sI form at approximately 5 bar. At the intermediate composition of 0.78 mole fraction ethane, a quadruple point (Aq–sI–sII–V) exists in which both incipient hydrate structures are in equilibrium with vapor and aqueous phase. This point will be referred to as the *structural transition composition*: the composition at which the incipient hydrate formation structure changes from sII to sI at a given temperature.

By the Gibbs phase rule, there is only one pressure at which Aq–sI–sII–V can coexist at a given temperature. Therefore, with an increase in pressure, the free vapor phase is completely converted into either sI or sII, depending on the feed composition of ethane and propane and which hydrate structure is present as illustrated in Figure 5.17 pressures above incipient hydrate formation, phase regions are predicted to exist where both sI and sII hydrates are present.

Figure 5.17 illustrates the effect on hydrate formation when ethane and propane are combined at constant temperature. Ethane acts as an inhibitor to sII formation due to competition of ethane with propane to occupy the large cages of sII. Propane also acts as an inhibitor to sI formation when added to ethane + water. In this case, however, since propane cannot enter the sI cavities, the fugacity of ethane is lowered as propane is added, destabilizing the sI hydrate. Holder (1976) refers to this inhibiting capacity as the "antifreeze" effect.

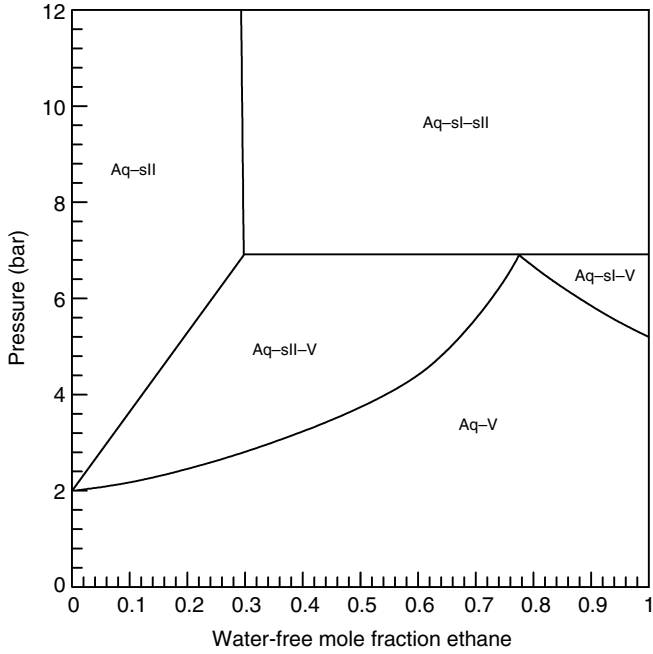

FIGURE 5.17 Pseudo-P–x diagram for ethane + propane + water system at 274 K.

As the temperature is increased to 277.6 K the pressure versus composition diagram for the ethane + propane + water system changes drastically as shown in Figure 5.18 Between 0.0 and 0.6 mole fraction of ethane, the incipient hydrate structure is sII hydrate. However, if the pressure is increased to approximately 11.45 bar, between 0.3 and 0.6 mol fraction ethane, sII is predicted to dissociate to form an Aq–V–L_{hc} region.

The pressure at which this dissociation is predicted to occur is called the *hydrate pseudo-retrograde pressure* at T. Pseudo-retrograde behavior is defined as the disappearance of a dense phase upon pressurization, which is counter-intuitive. This behavior resembles, but is not strictly the same as, vapor–liquid retrograde phenomena (de Loos, 1994).

The pseudo-retrograde pressure can be explained via evaluation of the vapor–liquid equilibria of ethane, propane, and water. The dashed line in Figure 5.18 is Aq–V–L_{hc} envelope that would form if hydrates were not present. The Aq–sII–V phase region intersects the Aq–V–L_{hc} region at the quadruple point (11.45 bar). According to Gibbs' Phase Rule there is one degree of freedom (three components, four phases), namely temperature which is set at 277.6 K. This point of intersection creates a four-phase line, Aq–sII–V–L_{hc}, in the pseudo-P–x diagram. Therefore, the pressure at which the quadruple line occurs in Figure 5.18 is unique. That is, if pressure is increased, one of the phases must disappear. In this case, the sII phase dissociates and an Aq–V–L_{hc} region remains.

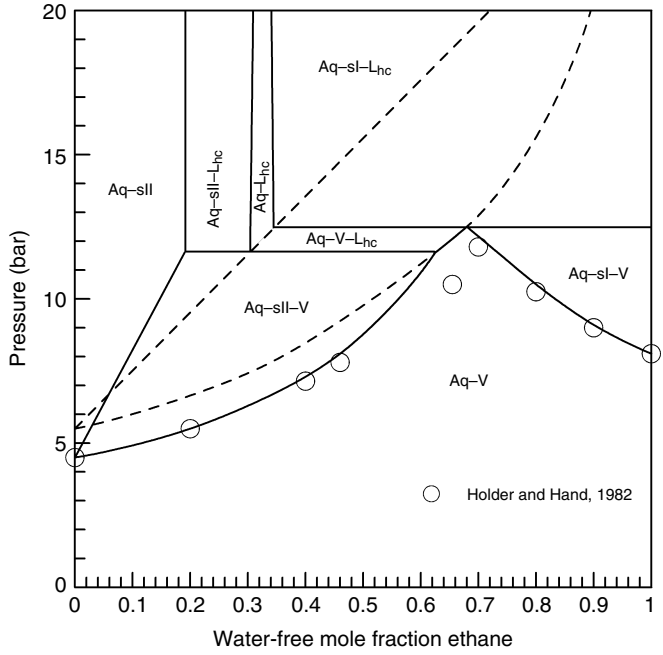

FIGURE 5.18 Pseudo-*P*–*x* diagram for ethane + propane + water system at 277.6 K.

The validity of the predictions in Figure 5.18 can be shown with a comparison of the data taken by Holder and Hand (1982) for this system. The sI and sII hydrate formation data points all compare quite well with the predictions with the exception of the point at 0.66 mole fraction ethane. Holder and Hand state that the data point at 0.66 mole fraction is sII but note that it could be at Aq–sII–V–L_{hc} conditions. The predictions in Figure 5.18 support their observation of possible four-phase conditions but suggest that the data point may be at metastable Aq–sII–V–L_{hc} conditions.

To test the predictions, experiments were carried out at the Delft University of Technology (TUD) (Ballard et al., 2001). In CSMGem, the pressure versus temperature phase diagram was generated using the model and then confirmed by experimental data. Figure 5.19 is the pressure versus temperature diagram for a 30/70 mixture of ethane and propane in contact with excess water.

Pseudo-retrograde phenomena are predicted to occur between the temperatures of 277.6 and 278.3 K. With a pressure increase of up to 5 bar, sII hydrates will dissociate at any temperature in this range. The lines are model predictions and the circles are experimental observations of hydrate dissociation obtained in the TUD laboratory. As can be seen in Figure 5.19, the TUD hydrate dissociation data do confirm the pseudo-retrograde melting. However, note that the Aq–sII–L_{hc} predictions deviate 0.2 K from the data. It is usually assumed that hydrates never dissociate with an increase in pressure. However, both measurements and

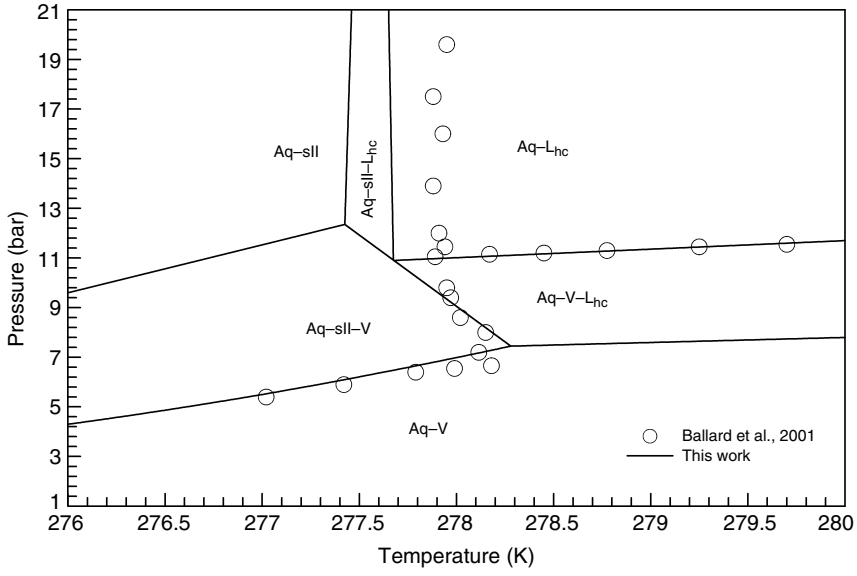

FIGURE 5.19 P versus T phase diagram for ethane (0.3) + propane (0.7) + water (excess) system with pseudo-retrograde phenomena.

predictions show, however, that for a wide excess water composition range, slight increases in pressure will result in the dissociation of sII hydrates (pseudo-retrograde dissociation) at low pressures (~7–11 bar) near a temperature of 278 K. Pseudo-retrograde hydrate behavior was also predicted in the ethane + i-butane + water and ethane + propane + decane + water systems as well (Ballard et al., 2001), but are not shown here due to space constraints.

5.2.2.4 Ternary hydrate phase equilibria and industrial application

With the phase equilibria of pure and binary hydrates discussed, the next step is to consider phase equilibria of the ternary gas mixture with water. For illustrative purposes only one pseudo-ternary phase diagram is presented at a temperature of 277.6 K and a pressure of 10.13 bar. The pseudo-ternary phase diagram is similar to true ternary phase diagrams except that water is in excess and therefore all compositions are given on a excess water basis. The pseudo-ternary phase diagrams is a composite of the phase diagrams discussed earlier: P–T diagrams for the pure hydrates and pseudo-P–x diagrams for the binary hydrates. That is, the corners represent the intersection of an isotherm and isobar in the pure hydrate P–T diagrams while the edges represent an isobar in the pseudo-P–x phase diagrams at 277.6 K.

Figure 5.20 is a pseudo-ternary phase diagram for the methane + ethane + propane + water system at a temperature and pressure of 277.6 K and 10.13 bar,

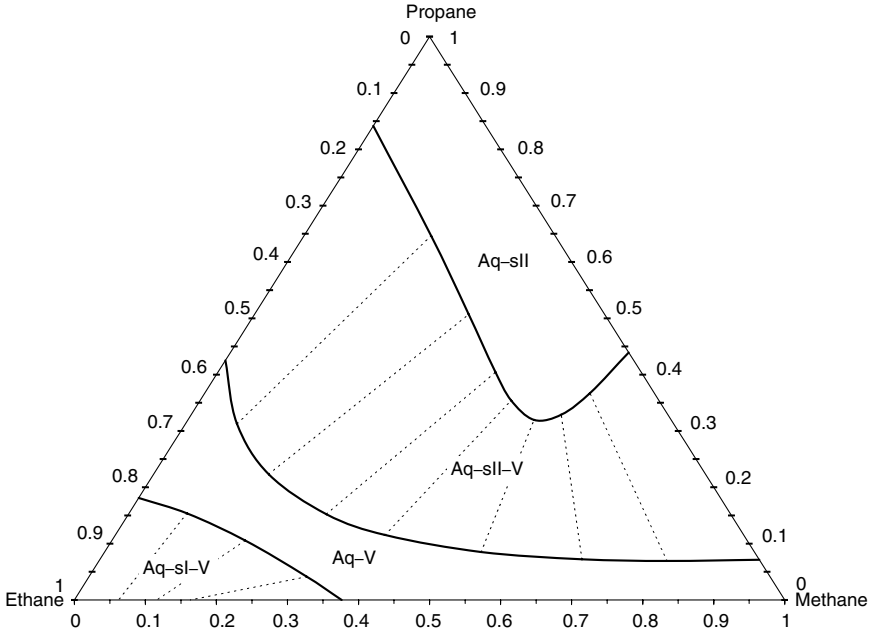

FIGURE 5.20 Pseudo-ternary diagram for methane + ethane + propane + water system at 277.6 K and 10.13 bar. Ternary diagram scales are component mole fraction.

respectively, and related to the previous binary diagrams. The ethane–propane edge of the phase diagram in Figure 5.20 can be directly compared to the pseudo-P–x phase diagram for the ethane + propane + water system in Figure 5.18 at a pressure of 10.13 bar. At 10.13 bar in Figure 5.18, the composition range for the Aq–sII phase region is between 0 and 0.16 mole fraction ethane. This is the same composition range for the Aq–sII phase region on the ethane–propane edge of Figure 5.20. Similar comparisons can be made with each edge of the pseudo-ternary phase diagram and the corresponding pseudo-P–x phase diagram (Figure 5.15 for the Methane + Propane pseudo-binary, and Figure 5.16 for the Methane + Ethane pseudo-binary)

The interior of the phase diagram in Figure 5.20 cannot be determined by a simple analysis of the pseudo- phase diagrams. Instead, an example of the procedure to determine the phase equilibria of a given excess water composition of the gas mixture is given. Suppose the excess water composition of the gas mixture is 0.3333 mole fraction for each of the three components. At a temperature and pressure of 277.6 K and 10.13 bar (Figure 5.20), respectively, the overall composition is in the center of the diagram, in the three-phase region (Aq–sII–V). The tie line (dashed line) in Figure 5.20, passing through that overall composition, gives the excess water composition (CH_4, C_2H_6, C_3H_8) of the sII hydrate (0.39, 0.19, 0.42) and vapor (0.25, 0.58, 0.17) phases. Note that, because this is a

pseudo-ternary phase diagram with excess water throughout, as is the case of the other diagrams, the composition of water in any of the phases cannot be determined.

The predicted phase diagram in Figure 5.20 indicates that sII hydrate is the predominate hydrate that forms. Propane clearly stabilizes the hydrate over a wide composition range. In Figure 5.20 four major phase regions appear from the top to the bottom of the diagram: Aq–sII, Aq–sII–V, Aq–V, and Aq–sI–V; three of those phase regions contain hydrates and encompass approximately 80% of the overall phase diagram. In other words at a temperature and pressure of 277.6 K and 10.13 bar, respectively, the likelihood of hydrate formation is large given all possible mixture compositions.

For industrial applications, determining the stable hydrate structure at a given temperature, pressure, and composition is not a simple task, even for such a simple systems as the ones discussed here. The fact that such basic mixtures of methane, ethane, propane, and water exhibit such complex phase behavior leads us to believe that industrial mixtures of ternary and multicomponent gases with water will exhibit even more complex behavior. Spectroscopic methods are candidates to observe such complex systems because, as discussed earlier, pressure and temperature measurements of the incipient hydrate structure are not enough.

Experimental work is required to confirm predictions for the majority of these systems at temperatures and pressures above the incipient conditions, and techniques such as diffraction, Raman, and NMR are well suited to do this. Spectroscopic measurements will allow hydrate model parameters to be fit to hydrate composition and structural data. Corrected model predictions can then guide areas to probe experimentally (Subramanian et al., 2000b).

The methane + ethane + propane + water system is the simplest approximation of a natural gas mixture. As shown in Figure 5.20, the phase equilibria of such a simple mixture is quite complicated at pressures above incipient hydrate formation conditions. One of the most interesting phenomenon is the coexistence of sI and sII hydrates which occurs in the interior of some pseudo-ternary phase diagrams.

Chemicals such as kinetic inhibitors or antiagglomerates are added to natural gas pipelines to prevent hydrate plugs. Kinetic inhibitors are designed to slow hydrate formation kinetics while antiagglomerants are designed to prevent hydrate particles from agglomerating. Typical natural gas hydrates are assumed to be sII and therefore these chemicals are designed to prevent sII hydrates from plugging a pipeline. Figure 5.20 suggests that if a natural gas mixture is rich in ethane, sI hydrates will form. With such a structure change it is possible that a kinetic inhibitor or antiagglomerant which may prevent the sII hydrates from plugging the pipeline may not inhibit the sI hydrates which exist at high ethane content.

5.3 Computer Simulation: Another Microscopic–Macroscopic Bridge

The major prediction method in this chapter is based on statistical thermodynamics. A statistical sampling of microscopic or molecular properties (e.g., cavities

and their filling by gas molecules) enables the prediction of properties which are macroscopic, or measurable with normal tools such as pressure guages and thermocouples. Although the derivation in Section 5.1 may be somewhat involved, the final equations are simple and are physically related to molecular phenomena.

Physical measurements are directly input to the statistical thermodynamics theory. For example three-phase hydrate formation data, and spectroscopic (Raman, NMR, and diffraction) data were used to determine optimum molecular potential parameters (ε, σ, a) for each guest, which could be used in all cavities. By fitting only a eight pure components, the theory enables predictions of engineering accuracy for an infinite number of mixtures in all regions of the phase diagram. This facility enables a substantial savings in experimental effort.

For the first three-quarters of the last century, statistical thermodynamics was the only bridge available between the molecular and the macroscopic domains. However, during the last quarter century, the availability of large, fast digital computers have enabled the use of another technique—namely computer simulation.

In computer simulation, an assembly (or ensemble) of molecules are simulated to predict macroscopic properties. Two simulation techniques have been commonly used, (1) MD and (2) MC. In Section 5.1.9 a third technique, *ab initio* quantum mechanical calculations was shown to provide interatomic potential parameters. In addition lattice dynamics (LD) has been used for the hydrate phase (Sparks and Tester, 1992; Belosludov et al., 1996; Westacott and Rodger, 1997) at considerable savings in computation. A significant LD effort is due to Tanaka and coworkers (Tanaka and Kiyohara, 1993a,b; Koga, 1995, 1994a,b; Koga and Tanaka, 1996) pointing to flaws in the van der Waals and Platteeuw (1959) model.

5.3.1 Basic Techniques of Monte Carlo and Molecular Dynamics Simulation

The overview in this section is intended to only provide a brief background for discussion of MD and MC techniques as applied to thermodynamic results. For the reader interested in MD or MC details, Table 5.11 includes a list of standard references. The LD technique, which was originally applied for low temperature solids, will not be considered in this brief overview (see the standard reference in Table 5.11). Kinetic results for molecular simulations are in Chapter 3.

As with all hydrate theory, it is important to interpret calculations at every opportunity in terms of experiments. With computer simulations, it is deceptively alluring to interpret calculations without physical validation, yet such a path can lead to false conclusions. When physical confirmation is not available, simulations should be regarded with caution. For example, at the heart of both MD and MC methods is the potential energy between individual molecules, which is itself an approximation and limits the accuracy of the simulated macroscopic properties. Such potentials should be validated in terms of their ability to predict measured properties, such as phase equilibria.

TABLE 5.11
General References for Computer Simulation Techniques

Author(s)	Title	Publisher	Date
	General		
Frenkel, D. and Smit, B.	*Understanding Molecular Simulation*	Academic Press	2001
	Molecular dynamics		
Allen, M.P. and Tildesley, D.J.	*Computer Simulation of Liquids*	Clarendon Press, Oxford	1989
Gould, H. and Toboshnik, J.	*Introduction to Computer Simulation Methods. Applications to Physical Systems, Part 1.*	Addison-Wesley	1988
Haile, J.M.	*Molecular Dynamics Simulation. Elementary Methods*	Wiley & Sons	1992
	Monte Carlo		
Gould, H. and Toboshnik, J.	*An Introduction to Computer Simulation Methods. Applications to Physical Systems, Part 2.*	Addison-Wesley	1988
Kalos, M.H. and Whitlock, P.A.	*Monte Carlo Methods,. Volume 1: Basics*	Wiley & Sons	1986
Rubinstein, R.Y.	*Simulation and the Monte Carlo Method*	Wiley & Sons	1981
	Lattice dynamics		
Horton, G.K. and Maradudin, A.A.	*Dynamical Properties of Solids, 3 Volumes*	North-Holland Amsterdam	1974

5.3.1.1 Molecular dynamics

Molecular dynamics has been used to simulate water structures, wherein an accurate water potential function is used to enable solution of Newton's equations of motion for a small (e.g., 1000–10,000) number of molecules over time. In water and water structures, the SPC (Berendsen et al., 1981) and the TIP4P (Jorgensen et al., 1983) potential models are most often used. Reanalysis of extant diffraction data by Soper et al. (1997) has called both of these potentials into question.

The integration of forces between all molecules over several thousand time-steps produces particle trajectories from which time-averaged macroscopic properties can be computed. In MD the simulation is limited by the computer storage capacity and speed, so that short-lived phenomena (100–1000 ps) are generally calculated.

Compared to MC, the MD technique is used more often, perhaps because it can calculate time-dependent phenomena and transport properties such as viscosity, thermal conductivity, and diffusivity, in addition to thermodynamic properties. However, Haile, (1992, p. 17) states a criterion for calculation of time-dependent

properties:

> the relaxation time for the phenomenon under investigation must be small enough so that one simulation generates several relaxation times

Times for molecular dynamic calculations are thus not well suited for calculation of hydrate kinetic nucleation phenomena, which can have metastability lasting hours or days, while the simulation is typically limited to 10^{-9} s.

The molecular dynamic technique has been validated for water structures through comparison of calculated properties with experimental thermodynamic water data, such as the density maximum, the high heat capacity, and diffraction patterns (Stillinger and Rahman, 1974) as well as the hydrate infrared (vibrational) spectral data by Bertie and Jacobs (1977, 1982). With acceptable comparisons of many computed and experimental properties of water structures, there is little doubt that a substance similar to water has been simulated.

Work in three laboratories comprises most of the MD hydrate studies. The pioneering works of Tse and coworkers (1983a,b, 1984, 1987) are exemplary in comparing simulation calculations to measurements, principally through macroscopic or spectroscopic techniques. The recent work of Tse et al. (1997) suggests limits to the use of infrared and Raman instruments due to enclathration changes of guest electronic and vibrational properties.

The second major study in MD was made by Rodger and coworkers (1989, 1990a,b, 1991) who considered structural stability. A third significant effort (including the aforementioned LD work) comes from Tanaka and coworkers (1993a,b; Koga et al., 1994a,b, 1996). Some conclusions from these studies are discussed in the Section 5.3.2.

Molecular dynamic studies in Holder's laboratory (Hwang, 1989; Hwang et al., 1993; Zele, 1994) have calculated Langmuir coefficients, such as in Equation 5.27 and considered the effect of guests which stretch the host lattice. Work in this laboratory concentrated on the clustering of water around guest molecules (Long and Sloan, 1993) and system behavior at the hydrate–water interface (Pratt and Sloan, 1995). Wallqvist (1991, 1992, 1994a,b) considered clustering, and the thermodynamic inhibitor methanol inside the hydrate cage.

Itoh et al. (1996) used MD to explain the CO_2 bending and stretching peaks in Raman spectra. Recently Carver et al. (1995), Kvamme et al. (1996), Makogon (1997), and Anderson (2005) used MD to model hydrate kinetic inhibitors interactions with the crystal surface.

5.3.1.2 Monte Carlo

The universal algorithm of MC methods was provided early after computers came into use by Metropolis et al. (1953). The name MC stems from a random number generator in the method, similar to that used in casinos.

In the MC method, molecules are moved randomly from an initial configuration, so that only the immediately previous configuration affects the current position. Using the individual potential (e.g., SPC or TIP4P) between

each particle, the total energy U is computed for the new configuration and compared with the previous value. If $U_{new} < U_{old}$, the move is accepted; however, if $U_{new} > U_{old}$, the change is accepted with a probability proportional to the Boltzmann distribution [exp–($\Delta U/kT$)].

In each new configuration thermodynamic properties are calculated, and accumulated in running sums, usually over a few million configurations. The space average from MC is the same as the MD time average of thermodynamic properties, confirming the Ergodic Hypothesis in statistical mechanics, that all of phase space is sampled representatively, given a large enough sample size. However, because MC techniques are limited to time-independent properties, they have not been used as extensively as molecular dynamic techniques.

As in the molecular dynamic calculations, MC calculations for water structures were first tested against experimental values. Beveridge and coworkers (Swaminathan et al., 1978) and Owicki and Scheraga (1977) obtained acceptable comparison of their calculations against experimental values for the oxygen–oxygen radial distribution function for both water and methane dissolved in water.

There are substantially fewer MC studies of hydrates than there are MD studies. The initial MC study of hydrates was by Tester et al. (1972), followed by Tse and Davidson (1982), who checked the Lennard-Jones–Devonshire spherical cell approximation for interaction of guest with the cavity. Lund (1990) and Kvamme et al. (1993) studied guest–guest interactions within the lattice. More recently Natarajan and Bishnoi (1995) have studied the technique for calculation of the Langmuir coefficients.

5.3.2 What has been Learned from Molecular Simulation?

Here we list some of the most significant applications of molecular simulation, as provided by Wierzchowski (Personal Communication, October 4, 2006) although this list is by no means exhaustive. Since the first applications of molecular simulation to hydrates by Tse, et al. (1983a,b; 1984), the tool has been widely used to interpret physical behavior. Simulation has impacted six major hydrate research areas.

1. Stability. Rodger (1990a,b,c) was first to note the utility of molecular simulation to investigate the van der Waals and Platteeuw statistical mechanical theory. The study argues the importance of repulsive forces from the guest molecules on stabilizing the hydrate water lattice. Tanaka and co-workers (Tanaka and Kiyohara, 1993a,b; Tanaka, 1994; Tanaka et al., 2004) enabled the understanding of hydrate stability via LD. The work extends over a decade, probing concepts related to non-spherical guest molecules (Tanaka, 1994), double hydrate stability (Tanaka et al., 2004), and double occupancy of cages (Tanaka, 2005).

2. Nucleation. Understanding the phenomena of nucleation is a central concept to developing a hydrate formation model. As detailed in Chapter 3, Radhakrishnan and Trout (2002) used a new simulation technique to formulate a concept of hydrate

progression from liquid to a crystal state, indicating the critical cluster diameter for CO_2 hydrate nucleation is 9.6–14.5 Å. Methane hydrate nucleation was analyzed by Baez and Clancy (1994) and Moon et al. (2003), observing formation of methane hydrate clusters.

3. Kinetic inhibitors. The advent of kinetic inhibitors stimulated simulation in molecular design (Freer and Sloan, 2000) and understanding functional groups (Carver et al., 1995). Recently, simulation was employed to screen quaternary ammonium zwitterions (Storr et al., 2004). Moreover, Anderson et al. (2005) detailed kinetic inhibitors binding energies to methane hydrates. Both studies showed a correlation between the inhibitor functional groups and the charge distribution of a hydrate surface.

4. Interfacial properties. The behavior of hydrate molecules at the surface of a hydrate is central to hydrate agglomeration and crystal growth. Rodger et al. (1996) applied simulation to investigate the stiffness and motion of molecules at the methane hydrate/methane gas interface. As a result, an intermediate region (liquid-like/hydrate-like) at the hydrate surface was identified. Almost at the same time, the interface of structure H hydrate was investigated by Pratt and Sloan (1996), detailing the translation and orientation effects of molecules at the hydrate/water interface.

5. Spectral properties. The inaugural hydrate simulations of Tse et al. (1983a,b, 1983, 1984) demonstrated the utility of MD in studying spectral properties. The tool is effective in deciphering spectra from encaged molecules, and subsequently Tse (1994) revealed three characteristic frequencies of methane vibrations (in methane hydrate) are in accord with neutron scattering data (Sears et al., 1992). Later, Itoh et al. (2000) simulated intramolecular vibrational spectra of methane, showing the stretching mode of methane and comparing with experimental findings.

6. Anomalous properties—thermal expansivity and thermal conductivity. Molecular simulation has been integral in evaluating physical behaviors of hydrate compared with ice, specifically a larger thermal expansivity (Tse, et al., 1987; Tanaka, et al., 1997) and a glasslike thermal conductivity (Tse, et al., 1983; 1984; Inoue, et al., 1996). These properties have been explained by the coupling between the water and the guest molecules.

In summary, the MD, MC, and LD (lattice dynamic) techniques are very powerful tools to investigate hydrate phenomena. Indeed, hydrate computer simulations may shortly outnumber hydrate experimental observations, because simulations are generally more accessible than experiments. However, such tools investigate phenomena which are on much smaller time and space dimensions than normally observed, outside of spectroscopy. Even with spectroscopy, the relevant peaks may be subject to some interpretation. As a result there may be several microscopic interpretations (based upon hundreds to thousands of molecules) of macroscopic phenomena which involve typically 10^{23} molecules. Such a scale-up may cause misinterpretation.

Computer simulation is best done (1) to propose experimental phenomena usually not accessible due to size or time scales, or (2) to explain experimental observation. The best simulation predictions are done jointly with experimental confirmation.

5.4 Chapter Summary and Relationship to Following Chapters

The statistical thermodynamic method and the Gibbs energy minimization presented in this chapter represents the state-of-the-art for the prediction of the following types of phase equilibria:

1. Compressible three-phases (L_W–H–V or I–H–V)
2. Incompressible three-phases (L_W–H–L_{HC})
3. Inhibition of equilibria in (1) or (2)
4. Quadruple points/lines (L_W–H–V–L_{HC} or I–L_W–H–V)
5. Two-phase (H–V or H–L_{HC}) equilibria
6. Four and five phase equilibria of structure H
7. Flash calculations
8. Expansion through a valve or turbine

The CSMGem computer program and Users Manual on the disk with this book (and the program examples in Appendix A) enables prediction of such properties using the methods of this chapter. The method has been shown to predict interesting results in the single, binary, and ternary phase diagrams of methane + ethane + propane, including retrograde phenomena, which was subsequently confirmed via experiment.

By comparing the program predictions with data, along with those of three current commercial hydrate programs, the conclusion is reached that the current state-of-the-art programs can predict the uninhibited, incipient hydrate formation temperature and pressure to within an average of 0.65 K and 10% of overall pressure, respectively. The equivalent inhibited inaccuracies for incipient temperature and pressure are 2 K and 20% in overall pressure, respectively.

The chapter also examined three molecular methods: (1) *ab initio* quantum mechanical calculations, which are typically used to get better interatomic potentials, (2) MC calculations, and (3) molecular dynamic calculations. The latter two molecular methods are most useful to probe the behavior of a small number of molecules, in which experimental capability is constrained by either space or time.

Chapter 6, which immediately follows, presents experimental methods and data for comparison with predictions in the present chapter. Such data will form the foundation for future modifications of theory in hydrate phase equilibria. However, the above thermodynamic prediction accuracies are usually satisfactory for engineering calculations, so that the state-of-the-art in hydrates is turning from thermodynamic (time-independence) to kinetics (time-dependence) phenomena,

such as those in Chapter 3. In science and engineering, kinetic prediction methods are typically an order of magnitude less accurate than thermodynamic properties, due to the additional variable of time.

Chapter 7 then considers the formation of hydrates in nature, such as in the permafrost and deep oceans of the earth. In such situations geologic time mitigates the necessity for kinetic formation effects and allows the use of thermodynamic conditions, such as those in the three-phase portions of the present chapter, for identification, exploration, and recovery.

Chapter 8 presents problems of natural gas production, transportation, and processing which are related to hydrates. Because a standard kinetic treatment method has progressed past the fledgling state in the second edition (1998), the state-of-the-art in flow assurance is turning away from thermodynamic properties which encourage hydrate avoidance, to kinetic properties which encourage a new philosophy in flow assurance—that of risk management.

References

Anderson, B., *Molecular Modeling of Clathrate-Hydrates via* Ab-Initio*, Cell Potential and Dynamic Methods*, Massachusetts Institute of Technology, MA (2005).

Anderson, B.J., Tester J.W., Borghi, G.P., Trout, B.L., *J. Am. Chem. Soc*., **127**, 17852 (2005).

Avlonitis, D., *Chem. Eng. Sci.*, **49**, 1161 (1994).

Baez, L.A., Clancy, P.A., in *(First) Int. Conf. on Natural Gas Hydrates* (Sloan, E.D., Happel, J., Hnatow, M.A., eds.), *Ann. N.Y. Acad. Sci.*, **715**, 177 (1994).

Baker, L.E., Pierce, A.C., Luks, K.D., *J. Soc. Pet. Eng*., 731 October (1982).

Ballard, A.L., *A Non-Ideal Hydrate Solid Solution Model for a Multiphase Equilibria Program*, Ph.D. Thesis, Colorado School of Mines, Golden, CO (2002).

Ballard, A.L., Jager, M.D., Nasrifar, Kh., Mooijer-van den Heuvel, M.M., Peters, C.J., Sloan, E.D., *Fluid Phase Equilib*., **185**, 77 (2001).

Ballard, A.L., Sloan, E.D., *Chem. Eng. Sci*., **56**, 6883 (2001).

Ballard, A.L., Sloan, E.D., *Fluid Phase Equilib.*, **371**, 194–197 (2002a).

Ballard, A.L., Sloan, E.D., *J. Supramol. Chem.*, **2**, 385–392 (2002b).

Ballard, A.L., Sloan, E.D., *Fluid Phase Equilib.*, **218**, 15–31 (2004a).

Ballard, A.L., Sloan, E.D., *Fluid Phase Equilib.*, **216**, 257–270 (2004b).

Barrer, R.M., Stuart, W.I., *Proc. R. Soc. (London) A*., **243**, 172 (1957).

Bazant, M.Z., Trout, B.L., *Physica A*, **300**, 139 (2001).

Belosludov, R., Grachev, E., Dyadin, Y., Belosludov, V., in *Proc. Second International Conference on Natural Gas Hydrates*, (Monfort, J.P., ed.), Toulouse, France, 2–6 June, 303 (1996).

Berendsen, J.D., Postma, J.P.M., van Gusteren, W.F., Herman, J., in *Intermolecular Forces*, (Pullman, B., ed.), Reidel, Dordrecht (1981).

Bertie, J.E., Jacobs, S.M., *Can. J. Chem*., **55,** 1777 (1977).

Bertie, J.E., Jacobs, S.M., *J. Chem. Phys*., **77,** 3230 (1982).

Cady, G.H., *J. Phys. Chem*., **85,** 4437 (1983a).

Cady, G.H., *J. Chem. Educ*., **60,** 915 (1983b).

Cao, Z., *Modeling of Gas Hydrates from First Principles*, Ph.D. Thesis, Massachusetts Institute of Technology (2002).

Carver, T.J., Drew, M.G.B., Rodger, P.M., *J. Chem. Soc. Faraday Trans*., **91**, 3449 (1995).
Davidson, D.W., *Can. J. Chem*., **49,** 1224 (1971).
Davidson, D.W., in *Water: A Comprehensive Treatise*, Plenum Press, New York, **2**, Chapter 3, 115 (1973).
Davidson, D.W., Ripmeester, J.A., in *Inclusion Compounds* (Atwood, J.L., Davies, J.E.D., MacNichol, D.D., eds.), Academic Press, **3,** Chapter 3, London, U.K. (1984).
de Loos, Th.W., *Appl. Sci.*, **273**, 89 (1994).
DePriester, C.L., *Chem. Eng. Prog. Symp. Ser.*, **49**(7), 1 (1953).
Fowler, R.H., Guggenheim, E.A., *Statistical Thermodynamics*, Cambridge University Press, Cambridge, U.K. (1952).
Freer, M.E., Sloan, E.D., *Ann. N.Y. Acad. Sci*. (Holder, G.D., Bishnoi, P.R., eds.), **912**, 651 (2000).
Gibbs, J.W., *The Collected Works of J. Willard Gibbs*, *Thermodynamics*, **I,** 55–353, Yale University Press, New Haven, Connecticut (1928).
Gupta, A.K., *Steady State Simulation of Chemical Processes*, Ph.D. Thesis, University of Calgary, Alberta (1990).
Hadden, S.T., Grayson, H.G., *Hydrocarbon Proc. Petrol. Refiner.*, **40,** 207 (1961).
Haile, J.M., *Molecular Dynamics Simulations: Elementary Methods*, John Wiley & Sons, Inc., New York (1992).
Hill, T.L., *An Introduction to Statistical Thermodynamics*, Addison-Wesley, Reading, MA (1960).
Holder, G.D., *Multi-Phase Equilibria in Methane–Ethane–Propane–Water Hydrate Forming Systems*, Ph.D. Thesis, University of Michigan, University Microfilms No. 77-7939, Ann Arbor, MI 48106 (1976).
Holder, G.D., Hand, J.H., *AIChE J*., **28,** 44 (1982).
Holder, G.D., Manganiello, D.J., *Chem. Eng. Sci*., **37**, 9 (1982).
Huo, Z., *Hydrate Phase Equilibria Measurements by X-Ray Diffraction and Raman Spectroscopy*, Ph.D. Thesis, Colorado School of Mines, Golden, CO (2002).
Hwang, M.J., *A Molecular Dynamic Simulation Study of Gas Hydrates*, Ph.D. Thesis, University of Pittsburgh, Pittsburgh, PA (1989).
Hwang, M.J., Holder, G.D., Zele, S.R., *Fluid Phase Equil*., **93**, 437 (1993).
Inoue, R., Tanaka, H., Nakanishi, K., *J. Chem. Phys*., **104**, 9569 (1996).
Itoh, H., Kawamura, K., *Ann. N.Y. Acad. Sci.* (Holder, G.D., Bishnoi, P.R., eds.), **912**, 693 (2000).
Jager, M.D., Ballard, A.L., Sloan, E.D., *Fluid Phase Equilib.*, **211**, 85–107 (2003).
Jorgensen, W.L., Chandrasekhar, J., Madura, J.D., Impey, R.W., Klein, M.L., *J. Chem. Phys*., **79**, 926 (1983).
Kihara, T., *J. Phys. Soc. Japan*, **6**, 289 (1951).
Klauda, J.B., Ab initio *Intermolecular Potentials to Predictions of Macroscopic Thermodynamic Properties and the Global Distribution of Gas Hydrates*, Ph.D. Thesis, University of Delaware, 2003.
Koga, K., *Study of Stability an Dynamics of Clathrate Hydrates and Supercritical Fluids*, Ph.D. Thesis, Kyoto University, Japan (1995).
Koga, K., Tanaka, H., *J. Chem. Phys*., **104**, 263 (1996).
Koga, K., Tanaka, H., Nakanishi, K., *J. Chem. Phys*., **101**, 3127 (1994a).
Koga, K., Tanaka, H., Nakanishi, K., *Mol. Simul*., **12**(3–6), 241 (1994b).
Kvamme, B., Juseby, G., Forrisdahl, O., in *Proc. Second International Conference on Natural Gas Hydrates*, (Monfort, J.P., ed.), Toulouse, France, June 2–6, 347 (1996).
Kvamme, B., Lund, A., Hertzberg, T., *Fluid Phase Equilib*., **90**, 15 (1993).

Lennard-Jones, J.E., Devonshire, A.F., *Proc. R. Soc*. A, **163**, 53 (1932).
Lennard-Jones, J.E., Devonshire, A.F., *Proc. R. Soc*. A, **165**, 1 (1938).
Lewis, G.N., Randall, M., *Thermodynamics*, McGraw-Hill Book Co., New York, 1923.
Lund, A., The Influences of Gas-Gas Interactions on the Stability of Gas Hydrates, Ph.D. Thesis, Norwegian Technical University.
Mak, T.C.W., McMullan, R.K., *J. Chem. Phys*., **42**, 2732 (1965).
Makogon, T.Y., *Kinetic Inhibition of Natural Gas Hydrates Formation*, Ph.D. Dissertation, Colorado School of Mines, Golden, CO (1997).
Makogon, Y.F., *Hydrates of Natural Gas*, Moscow, Nedra, Izadatelstro, p. 208 (1974 in Russian) Transl W.J. Cieslesicz, PennWell Books, Tulsa, Oklahoma p. 237 in Russian, (1981 in English).
McKoy, V., Sinanoglu, O., *J. Chem. Phys.*, **38**, 2946 (1963).
McMullan, R.K., Jeffrey, G.A., *J. Chem. Phys*., **42**, 2725 (1965).
McQuarrie, D.A., *Statistical Mechanics*, Harper & Row, New York (1976).
Metropolis, N., Riosenbluth, A.W., Rosenbluth, M.N., Teller, A.H., Teller, E., *J. Chem. Phys*., **21**, 1087 (1953).
Moon, C., Taylor, P.C., Rodger, P.M., *J. Am. Chem. Soc*., **125**, 4706 (2003).
Natarajan, V., Bishnoi P.R., *Ind. Eng. Chem. Res*., **34**, 1494 (1995).
Owicki, J.C., Scheraga, H.A., *J. Am. Chem. Soc*., **99,** 7413 (1977).
Parrish, W.R., Prausnitz, J.M., *Ind. Eng. Chem. Proc. Des & Dev*., **11**, 26 (1972).
Pratt, R.M., Sloan, E.D., *Mol. Simul*., **15**, 247 (1995).
Rachford, H.H., Rice, J.D., *J. Pet. Technol*., **4**(p. 10), **1**(p. 19), **2**(p. 3) (1952).
Radhakrishnan, R., Trout, B.L., *J. Chem. Phys*., **117**, 1786 (2002).
Rodger, P.M., *J. Phys. Chem*., **93**, 6850 (1989).
Rodger, P.M., *Chem. Br*., 1090, November (1990a).
Rodger, P.M., *J. Phys. Chem*., **94**, 6080 (1990b).
Rodger, P.M., *AIChE J.*, **37**, 1511 (1991).
Rodger, P.M., Forester, T.R., Smith, W., *Fluid Phase Equilib*., **116**, 326 (1996).
Rowley, R.L., *Statistical Mechanics for Thermophysical Property Calculations*, Prentice Hall, Englewood Cliff, NJ (1994).
Sears, V.J., Powell, B.M., Tse, J.S., Ratcliffe, C.I., Handa, Y.P., *Physica*, **B181**, 658 (1992).
Sloan, E.D., *Fluid Phase Equilib.*, **228–229C**, 67 (2005).
Soper, A.K., Bruni, F., Ricci, M.A., *J. Chem. Phys*., **106**(**1**), 247 (1997).
Sparks, K.A., Tester, J.W., *J. Phys. Chem*., **96**, 11022 (1992).
Stillinger, F.H., Rahman, A., *J. Chem. Phys*., **60**, 1545 (1974).
Storr, M.T., Taylor, P.C., Monfort, J.P., Rodger, P.M., *J. Am. Chem. Soc*., **126**, 1569 (2004).
Subramanian S., Kini, R., Dec, S.F., Sloan, E.D., *Chem. Eng. Sci*., **55**, 198 (2000a).
Subramanian, S., Ballard, A.L., Kini, R., Dec, S.F., Sloan, E.D., *Chem. Eng. Sci*., **55,** 5763 (2000b).
Swaminathan, S., Harrison, S.W., Beveridge, D.L., *J. Am. Chem. Soc*., **100**, 5705, (1978).
Tanaka, H., *J. Chem. Phys*., **101**, 10833 (1994).
Tanaka, H., Kiyohara, K., *J. Chem. Phys*., **98**, 8110 (1993a).
Tanaka, H., Kiyohara, K., *J. Chem. Phys*., **98**, 4098 (1993b).
Tanaka, H., Nakatsuka, T., Koga, K., *J. Chem. Phys*., **121**, 5488 (2004).
Tanaka, H., Tamai, Y., Koga, K., *J. Phys. Chem. B*, **101**, 6560 (1997).
Tester, J.W., Bivins, R.L., Herrick, C.C., *AIChE J.*, **18**(6), 1220 (1972).
Tse, J.S., *J. Incl. Phenom*., **8**, 25 (1990).
Tse, J.S., *Ann. N.Y. Acad. Sci.* (Sloan, E.D., Happel, J., Hnatow, M.A., eds.), **715**, 187 (1994).

Tse, J.S., Davidson, D.W., *Proc 4th Can. Perm. Conf.*, p. 329, Calgary, Alberta, March 2–6, 1981 (1982).
Tse J.S., Klein, M.L., McDonald, I.R., *J. Chem. Phys*., **78**, 2096 (1983a).
Tse, J.S., Klein, M.L., McDonald, I.R., *J. Phys. Chem*., **87**, 4198 (1983b).
Tse J.S., Klein, M.L., McDonald, I.R., *J. Chem. Phys*., **81**, 6146 (1984).
Tse, J.S., McKinnon, W.R., Marchi, M., *J. Phys. Chem*., **91**, 4188 (1987).
van der Waals, J.H., Platteeuw, J.C., *Adv. Chem. Phys.*, **2**, 1 (1959).
von Stackelberg, M., Jahns, W., *Z. Electrochem*., **58**, 162 (1954).
Wallqvist, A., *Chem. Phys. Lett*., **182**(**3, 4**), 237 (1991).
Wallqvist, A., *J. Chem. Phys*., **96**, 5377 (1992).
Wallqvist, A., in *(First) Int. Conf. on Natural Gas Hydrates, Ann. N.Y. Acad. Sci.,* (Sloan, E.D., Happel, J., Hnatow, M.A., eds.), **715**, 159, (1994a).
Wallqvist, A., in *(First) Int. Conf. on Natural Gas Hydrates, Ann. N.Y. Acad. Sci*., (Sloan, E.D., Happel, J., Hnatow, M.A., eds.), **715**, 540, (1994b).
Westacott, R.E., Rodger, P.M., "Direct Free Energy Calculations for Gas Hydrates," in *Proc. 213th ACS National Meeting*, San Francisco, CA, April 13–17, **42**(2) 539 (1997).
Wilcox, W.I., Carson, D.B., Katz, D.L., *Ind. Eng. Chem*., **33**, 662 (1941).
Zele, S.R., *Molecular Dynamics and Thermodynamic Modeling of Gas Hydrates*, Ph.D. Thesis, University of Pittsburgh, Pittsburgh, PA (1994).

6 Experimental Methods and Measurements of Hydrate Properties

Chapters 4 and 5 were concerned with the fitting and prediction of hydrate thermodynamic data. Those two chapters indicate how hydrate theoretical developments have dramatically changed over their history, particularly due to advances in knowledge of molecular structure, statistical thermodynamics, kinetics, and computing capability. Yet the powerful tools provided by all of these predictive methods are only as good as the measurements upon which they are based.

In addition to the change in the theoretical methods applied to hydrates, there have been significant advancements and widespread use of meso- and microscopic tools in hydrate research. Conversely, the typical static experimental apparatus used today to measure macroscopic properties, such as phase equilibria properties, is based on the same principles as the apparatus used by Deaton and Frost (1946). In part, this is due to the fact that the simplest apparatus is both the most elegant and reliable simulation of hydrate formation in industrial systems. In Section 6.1.1 apparatuses for the determination of hydrate thermodynamic and transport macroscopic properties are reviewed.

The traditional methods have involved experimentalists measuring the fluid phases, and predicting the hydrate phase. However, over the last 15 years there have been significant advancements in applying mesoscopic (micron-scale) and molecular-level ($\leq$ nanometer scale) tools to measure the hydrate phase. In the case of mesoscopic tools, these include laser scattering, x-ray computed tomography (CT), and electron microscopy to investigate the morphology and distribution of the hydrate phase. These and other mesoscopic tools are discussed in Section 6.2.1. On the molecular level, tools such as Raman and nuclear magnetic resonance (NMR) spectroscopy and x-ray and neutron diffraction are applied to determine the molecular properties and structure of the hydrate phase directly. These and other molecular-level tools are discussed in Section 6.2.2.

Thermodynamic data form the basis for future theoretical developments, because the data represent the physical reality and they have been painstakingly obtained. Usually a period of several months (or even years) is required to construct an experimental apparatus and, due to long metastable periods, it is not uncommon to obtain only one pressure–temperature data point per 1 or 2 days of experimental effort. Phase equilibria data are presented in Section 6.3.1 for simple hydrates (Section 6.3.1.1), binary (Section 6.3.1.2), ternary (Section 6.3.1.3),

and multicomponent (Section 6.3.1.4) gas mixtures, and systems with inhibitors (Section 6.3.1.5).

Thermal conductivity data are even more difficult to obtain. In the case of calorimetric data of heat capacity and heats of dissociation, the measurements though still reasonably challenging are aided by significant improvements in commercial calorimeters that can operate at high pressures. Thermal property data are presented in Section 6.3.2.

This chapter deals with macro-, meso-, and molecular-level thermodynamic and transport hydrate properties of natural gas and condensate components, with and without solute. The feasibility of using these tools to measure the kinetics of hydrate formation and decomposition are also briefly discussed, while the results of these measurements have been discussed in Chapter 3. The results for insoluble substances such as porous media are discussed in Chapter 7.

For quick reference, Tables 6.1 through 6.3 provide a summary of the key features, capabilities, limitations, and advantages of different experimental apparatuses for macro- (Table 6.1), meso- (Table 6.2), and molecular-level (Table 6.3) measurements of hydrate thermodynamic and kinetic properties.

6.1 Experimental Apparatuses and Methods for Macroscopic Measurements

The experimental apparatuses for hydrate phase equilibria underwent considerable evolution during the nineteenth century. During the last half century the standard methods for measuring macroscopic equilibria have not changed considerably. Table 6.1 summarizes the different macroscopic experimental methods used to study hydrate properties.

The usual protocol in obtaining phase equilibria data involves observing the hydrate phase by indirect means, such as an associated pressure decrease or temperature increase in the fluid phase. Visual observation is typically the only direct evidence of the hydrate phase. However, the need to measure the hydrate phase directly is becoming increasingly recognized, for example, macroscopic phase equilibria data and guest size may indicate a homogenous hydrate formation, while microscopic (spectroscopy/diffraction) measurements of the hydrate phase could show a very heterogeneous hydrate composition.

Section 6.1.1 deals with the evolution of the current apparatuses for the measurement of phase equilibria. Section 6.1.2 deals with the methods for measurement of macroscopic calorimetric and transport properties that relate to gas transmission, storage, and phase change due to heating and cooling.

6.1.1 Measurement Methods for Hydrate Phase Equilibria and Kinetics

In the first century after their discovery, hydrates were regarded as a scientific curiosity. Researchers worked either with gases that were highly soluble, or under conditions that enabled hydrate formation at low pressures. With the notable

TABLE 6.1
Macroscopic Experimental Methods for Studying Hydrate Properties

Method	Capabilities			Key information/ advantages
	Phase equilibria data	Kinetic data (time-dependent)	P, T[a] Limits, stirred/unstirred	
High pressure visual autoclave cell (Turner, 2005; Turner et al., 2005a)	Yes: P, T	Yes: P, T, film growth rate vs. time	Sapphire/quartz window limits: typically 5000 psi Stirred	P_{diss}, T_{diss}, gas consumption rate during growth/ decomposition, visual imaging of growth/ decomposition
High pressure "Blind" (no windows) autoclave cell	Yes: P, T	Yes: P, T vs. time	Typically 10,000 psi Stirred	P_{diss}, T_{diss}, gas consumption rate during growth/decomposition
Quartz Crystal Microbalance (QCM) in high pressure cell (Burgass et al., 2002; Mohammadi et al., 2003)	Yes: P, T (with P transducer, thermocouple in cell)	Yes: P, T vs. time	Typically 6000 psi	P_{diss}, T_{diss} Advantages: mg samples so equilibration times (hence experimental time) reduced
Cailletet (Peters et al., 1993; Jager et al., 1999)	Yes: P, T		Typically 2000 psi	Accurate P_{diss}, T_{diss}
Rocking cell (Oskarsson et al., 2005)	Yes: P, T	Yes: P, T vs. time	Typically 10,000 psi (blind cell); 5000 psi (visual cell) Stirred	P_{diss}, T_{diss}, gas consumption rate during growth/ decomposition. Typically used for LDHI testing
High pressure rheometer (Camargo et al., 2000)		Yes: P, T, viscosity vs. time	Typically 1000 psi	Viscosity changes vs. time

(Continued)

TABLE 6.1
Continued

Method	Capabilities			Key information/ advantages
	Phase equilibria data	Kinetic data (time-dependent)	*P, T*[a] Limits, stirred/unstirred	
Flow wheel (Rasch et al., 2002)		Yes: P, T vs. time, hydrate agglomeration	With plexiglass window 1450 psi, without window 2175 psi	P_{diss}, T_{diss}, gas consumption rate during growth/ decomposition, visualize agglomeration/slugging (window). Larger scale than autoclave cell. Typically used for LDHI testing
Pilot flow loop (Turner et al., 2005b)		Yes: P, T vs. time	Typically <2000 psi Shear from flow/pump	P_{diss}, T_{diss}, gas consumption rate during growth/ decomposition, visualize agglomeration/slugging (if optical window present). Larger scale than autoclave cell or flow wheel
High-pressure differential scanning calorimetry (Handa, 1986d; Le Parlouer et al., 2004; Palermo et al., 2005)	Yes: P, T	Yes: Hydrate phase vs. time	Typically up to 5800 psi, 230 to 400 K	T_{diss}, heat capacities, heat of dissociation. Emulsion stability and hydrate agglomeration

[a] If T limits not given, this is just a function of the cooling bath, cryostat being used.

TABLE 6.2
Mesoscopic Experimental Methods for Studying Hydrate Properties

Method	Capabilities			Key information/ advantages
	Phase equilibria data	Kinetic data (time-dependent)	*P, T*[a] Limits, stirred/unstirred	
Laser scattering—focused beam reflectance method, FBRM with high P cell (Clarke and Bishnoi, 2004)		Yes: *P*, *T*, particle formation (min)	1500 psi; size range: 1–1000 μm; stirred	Hydrate particle size distribution during growth/decomposition
Particle video microscope, PVM with high P cell		Yes: *P*, *T*, particle formation and agglomeration (min)	1500 psi; size range: 10–300 μm; stirred	Hydrate particle size imaging during growth/decomposition
Micromechanical force measurement apparatus (Taylor, 2006; Taylor et al., 2007)	Particle adhesive forces	Yes: Adhesive forces vs. time (min)	15 psi; >5 μm	Adhesive forces between hydrate–hydrate particles, hydrate particle-surface
Glass micromodels, in high *P* cell (Tohidi et al., 2002)	Hydrate, gas, water phase distribution	Yes: *P*, *T* hydrate phase vs. time (min)	Typically up to 5000 psi; >50 μm channels	Visual location of hydrate phase during growth

(Continued)

TABLE 6.2
Continued

Method	Capabilities			Key information/ advantages
	Phase equilibria data	Kinetic data (time-dependent)	*P*, *T*[a] Limits, stirred/unstirred	
X-ray computed tomography (CT) (Kneafsey et al., 2005)	Hydrate, water, gas phase distribution	Yes: *P*, *T*, hydrate, water vs. time (min)	Typically up to 1000 psi; microns	Density profile of hydrate plug contained in cell. Phase fractions, thermal conductivity with ITOUGH2 modeling
Scanning electron microscopy (SEM) (Stern et al., 2005)	Hydrate morphology	No	15 psi, 77 K; microns	Meso-scale imaging of hydrate morphology
Magnetic resonance imaging (MRI) (Moudrakovski et al., 2004)	Liquid, hydrate phase distribution	Yes: Hydrate conversion from ice particles or water droplets in oil (min)	Typically 3000 psi; microns	Direct visualization of droplet conversion to hydrate crystallites and hydrate shells
Infrared imaging (Long, 2003)	Hydrate phase distribution and texture		15 psi	Identify hydrate bearing zones and texture in core samples

[a] If *T* limits not given, this is just a function of the cooling bath, cryostat being used.

TABLE 6.3
Molecular-Level Experimental Methods for Studying Hydrate Properties

Method	Capabilities			Key information/ advantages
	Phase equilibria data	Kinetic data (time-dependent)	*P, T*[a] Limits	
Solid-state NMR spectroscopy (Kini et al., 2004)	Hydrate phase	Yes: hydrate phase vs. time (mins)	Typically 15 psi, or use glass bulbs up to 1000 psi	Guest occupancy, structure, structural transitions, dynamics, hydration number, hydrate formation and dissociation kinetics
Liquid-state NMR spectroscopy (Davidson and Ripmeester, 1984)		Yes: Water mobility vs. time (mins)	15 psi	Reorientation and diffusion
Raman spectroscopy with high pressure windowed cell (Sum et al., 1997; Thieu et al., 2000)	*P*, *T* and hydrate phase	Yes: *P*, *T*, hydrate phase vs. time (mins)	Typically for sapphire window <10,000 psi (for capillary tubes <60,000 psi; diamond anvil cell GPa's)	Guest occupancy ratios, structure, structural transitions
Neutron spectroscopy (Tse et al., 1997a,b)	Hydrate phase	No: Several hours	15 psi	Dynamics, lattice and guest vibrational/rotational modes
Neutron diffraction—single crystal	Hydrate phase	No: Several hours	Typically 1 atm., 20–5 K	Definitive structure determination
Neutron powder diffraction (Halpern et al., 2001)	Hydrate phase	Yes: *P*, *T*, hydrate phase vs. time (mins)	Typically <30,000 psi	Guest occupancy, structure determination, structural transitions

(Continued)

TABLE 6.3
Continued

Method	Capabilities: Phase equilibria data	Capabilities: Kinetic data (time-dependent)	Capabilities: *P, T*[a] Limits	Key information/ advantages
Small angle neutron diffraction (Koh et al., 2000)	Hydrate phase	Yes: *P*, *T*, hydrate phase vs. time (h)	Typically up to 5000 psi; Stirred	Structure factors, hydration shell structure
Small angle neutron scattering (SANS) (King et al., 2000)	Hydrate phase	No: Several hours	Typically 15 psi	Inhibitor adsorption
Single crystal x-ray (synchrotron/lab) (Udachin et al., 2001b)	Hydrate phase	No: Several hours	Typically 15 psi	Structure determination, guest occupancy
X-ray diffraction (lab/synchrotron) (Koh et al., 1996)	Hydrate phase	Yes: *P*, *T*, hydrate phase vs. time (synchr.: secs; lab: mins)	15–2000 psi; Stirred (synchrotron only)	Structure determination, structure transitions, hydrate crystal growth, decomposition, thermal expansivity
Extended x-ray fine structure spectroscopy (EXAFS, Synchrotron) (Bowron et al., 1998)	Hydrate phase	No		Hydration structure
Dielectric spectroscopy (Davidson, 1973)	Hydrate phase	No	15 psi	Dynamics, reorientation of guest molecules

[a] If *T* limits not given, this is just a function of the cooling bath, cryostat being used.

exception of Roozeboom (1884), very early workers had two concerns: (1) that hydrates of certain compounds did exist and (2) the determination of the number of water molecules associated with each gas molecule. Those research objectives, combined with a few low pressure measurements of hydrate formers, necessitated only the use of hand-blown glass apparatuses. While such apparatuses are of historic interest, they are considered costly, fragile, and unsafe to simulate industrial or *in situ* gas hydrate conditions.

Beginning in the 1880s, de Forcrand and his collaborator Villard began a 45 year study of hydrates. Using an ingenious glass apparatus, de Forcrand and Villard (1888) were able to exclude most water when H_2S formed so that the hydrate number (gas–water) for hydrogen sulfide was reduced from the previous value of $H_2S \cdot 12H_2O$ to $H_2S \cdot 7H_2O$. As indicated in Chapter 1, Villard was the first to determine hydrates of methane, ethane (1888), and propane (1890), but he was not successful in the formation of nitrogen hydrates. In order to form methane and ethane hydrates, he replaced the glass container of the Cailletet (which was not suitable for use at very high pressures) with a round metal jar, and formed hydrates of methane at 26.9 MPa and 293.4 K. Models of the Cailletet apparatus are in current use at the Technical University of Delft, Netherlands (Peters et al., 1993; Jager et al., 1999).

6.1.1.1 Principles of equilibrium apparatus development

While these early workers did not have apparatuses suitable for very high pressure, the experimentalists during the first half of the century of hydrates did prove three important principles to guide the development of succeeding apparatuses and methods:

1. *Vigorous agitation is necessary for complete water transformation*. With minor exceptions, the early results (as determined by Villard) showed that an increase in agitation caused a decrease in the number of water molecules in the hydrate.

Such agitation is necessary for three reasons:

- To provide surface renewal and exposure of liquid water to the hydrate former.
- To prevent water occlusion. Without agitation, Villard (1896) showed, for example, that nitrous oxide hydrate formation was continuous for a period longer than 15 days under a pressure of 2 MPa. Villard also determined that in previous research the ratio of water to guest molecules had been analyzed as greater than $G \cdot 6H_2O$ (Villard's Rule) due to either occlusion of water within the hydrate mass, or due to the loss of the guest component.
- Hammerschmidt (1934) added that some agitation in the form of flow fluctuations, pressure cycles, bubbling gas through water, and so on was necessary to initiate hydrate formation, in order to decrease the metastability.

2. *Hydrate dissociation is used to measure the hydrate equilibrium point*. Wroblewski (1882) was one of the first researchers to form (CO_2) hydrates, using equilibrium pressures higher than atmospheric through Joule–Thompson expansions. Cailletet (1877) found that the pressure must be increased beyond the hydrate equilibrium value and that hydrate formation results in a relaxation of the metastable pressure. With slow heating or depressurization for hydrate dissociation, however, metastability did not occur. The endpoint of hydrate dissociation was thus much more reproducible and was taken as an indication of the upper limit to formation metastability. [It is now recognized that metastability can occur on dissociation if too high a heating rate is used (Tohidi et al., 2000; Rovetto et al., 2006), or if the conditions are within the anomalous self-preservation region of 242–271 K at 0.1 MPa (see Chapter 3, Section 3.3.3)].

Half a century later, the work of Carson and Katz (1942) provided a second reason for considering the dissociation condition of the hydrate equilibrium point (see Chapter 3, Figure 3.1b for more details). Their work clearly showed the solid solution behavior of hydrates formed by gas mixtures. This result meant that hydrate preferentially encapsulated propane from a methane + propane gas mixture, so that a closed gas volume was denuded of propane (or enriched in methane) as more hydrates formed. On the other hand, upon hydrate dissociation, when the last crystal melted the initial gas composition was regained, minus a very small amount to account for solubility in the liquid phase.

3. *A rapid decrease in pressure or an increase in temperature indicates hydrate formation in a constant volume apparatus*. All of the early workers noted a concentration of the gas as it was encapsulated in the hydrate, which led to a decrease in pressure. Conversely on dissociation with heating, visual observation of the disappearance of the last hydrate crystal was accompanied by a decrease in the slope of a pressure versus temperature trace. This provided a means of obtaining higher hydrate equilibrium pressures without visual observation of crystal disappearance, simply by measuring the intersection point of the cooling and heating isochors, given as Point D in Figure 3.1b. Exothermic formation causes the temperature to increase because hydrated molecules have a lower energy of translation than those in the vapor and liquid.

The following two subsections consider the apparatuses used for most phase equilibria measurements, namely, the three-phase (L_W–H–V and I–H–V) regions, respectively. Similar equipment have been used to measure three-phase (L_W–H–L_{HC}), and four-phase (L_W–H–V–L_{HC}) conditions. For two-phase (H–L_{HC} and H–V) regions, different apparatuses have been used as discussed in Section 6.1.1.4.

6.1.1.2 Apparatuses for use above the ice point

In general, stirred autoclave cells with P, T control are used for hydrate phase equilibria measurements. Over the last 50 years, hydrate phase equilibria apparatuses have been developed with the above three principles. As a consequence of reading

Schroeder's (1927) hydrate monograph (Katz, Personal Communication, 1988), Hammerschmidt (1934) constructed a Pyrex tube flow apparatus for visual observation of simulated pipeline formations. After the gas flow stopped, slow heating enabled visual confirmation of hydrate disappearance, with measurement of temperatures and pressures. While numerous hydrate equilibria data were obtained using the above apparatus, Hammerschmidt reported a correlation rather than data, thereby inhibiting analysis of his data by others.

In 1937 Deaton and Frost constructed a static hydrate equilibrium apparatus that was to be the prototype for many others. The essential features of the apparatus are cited below and shown in Figures 6.1a,b, with a chronological

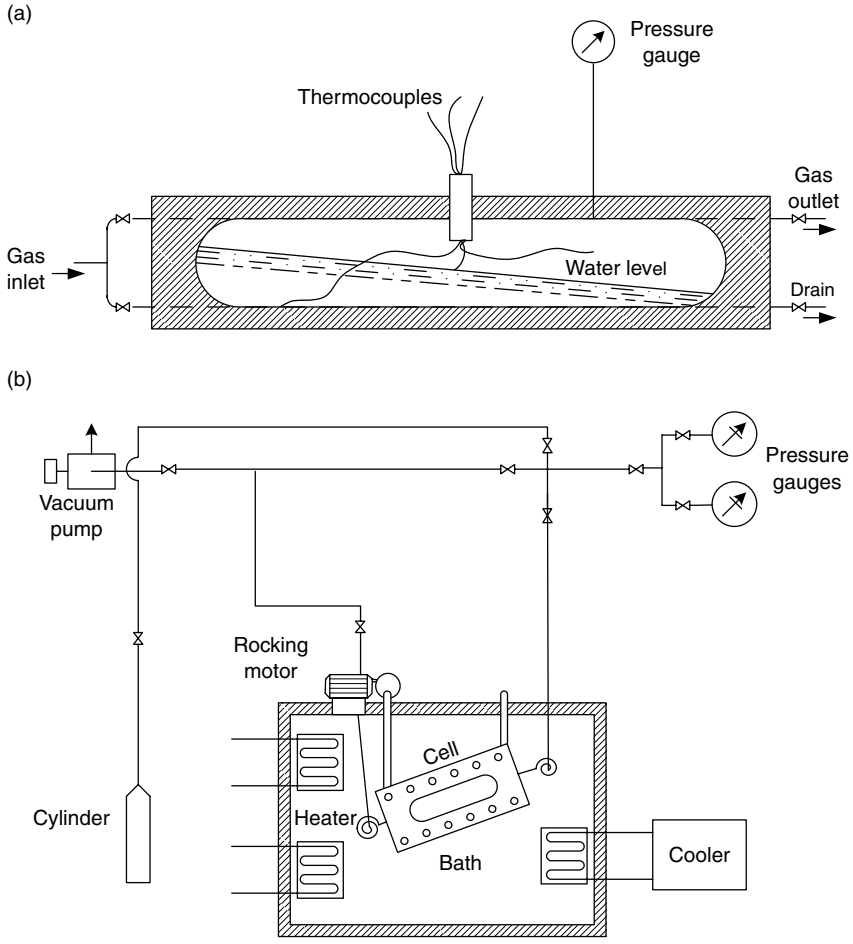

FIGURE 6.1 (a) Detail of Deaton and Frost hydrate formation equilibrium cell. (Reproduced courtesy of U.S. Bureau of Mines (Deaton and Frost, 1946).) (b) Typical rocking hydrate equilibrium apparatus.

TABLE 6.4
Development of High Pressure Visual Hydrate Cell

Date	Investigator(s)	Modification
1937	Deaton and Frost	Basic cell with options for gas flow above liquid, or sparged through liquid, option for rocking cell in thermostatted bath
1940	Roberts, Brownscombe, and Howe	Mercury (Hg) displacement of liquids, agitation
1942	Carson and Katz	Rocking hydrate cell, displacement of liquids; hydrate decomposed for composition
1952a	Reamer, Selleck, and Sage	Capillary sight glass, hydrocarbons and water over Hg; agitation
1956	Scauzillo	Cooling coils adjacent to sight glass; Hg displacement; rocking
1960	Otto and Robinson	Double window cell; rotated or agitated (after 1960)
1961	van Welie and Diepen	Hg pressurization; $P > 25$ MPa; electromagnetic agitation
1969	Andryushchenko and Vasilchenko	100 cm^3 steel-coated organic glass cylinder, magnetic agitation
1974	Y. Makogon	$P < 20$ MPa without agitation; filming capability
1974	Berecz and Balla-Achs	Single and double chamber multivibrator mixer
1980	Dharmawardhana, Parrish, and Sloan	Bronze cell, plexiglass windows, ultrasonic agitation
1981	John and Holder	Glass windowed cell without mixing used below the ice point
1983	Vysniaukas and Bishnoi	Cylinder with sight ports magnetically stirred

listing of the modifications provided in Table 6.4. Note that Table 6.4 represents only the initiation of such apparatuses in each laboratory, with a chronology of modifications. Most designs have been used by many other investigators. For example, the apparatus type designed by Carson and Katz (1942) enjoyed longevity in the University of Michigan laboratory, and was used by Holder and Hand (1982).

The salient features of the apparatus are as follows:

- The heart of the apparatus consists of a sight glass (typically 300 cm^3) for visual confirmation of hydrate formation and disappearance. Normally only 20–150 cm^3 of the cell volume contains water, with the remainder being gas and hydrate.
- The cell is enclosed in a thermostat bath but thermocouples are placed in the cell interior to measure the thermal lag between the cell and the bath.
- The pressure is usually measured with the use of Bourdon tube gauges or transducers.

- Mixing at the gas–liquid interface is provided in a variety of ways, such as by mechanical or magnetic agitators, by rotation or rocking of the cell, by bubbling gas through water in the cell, or by ultrasonic agitation.

Operation of standard static formation apparatus

With the fundamental apparatus established, normal operation above 273 K proceeds in one of three static modes:

1. In isothermal (constant temperature) operation the gas–liquid system is originally set at a pressure higher than the hydrate formation value. As hydrates are formed the temperature increases at the hydrate interface because fluid (gas and water) molecules must discharge translational energy as they are solidified. However, such energy must be dissipated through conduction or convection/agitation to the surrounding phases and bath.

Encapsulation of the gas decreases the pressure to the three-phase (L_W–H–V) condition. The system pressure may be controlled by an external reservoir for addition or withdrawal of gas, aqueous liquid, or some other fluid such as mercury. After hydrate formation, the pressure is reduced gradually, the equilibrium pressure is observed by the visual observation of hydrate crystal disappearance. Upon isothermal dissociation, the pressure will remain constant for a simple hydrate former until the hydrate phase is depleted.

2. In isobaric operation the system pressure is maintained constant, by the exchange of gas or liquid with an external reservoir. The temperature is decreased until the formation of hydrate is indicated by significant addition of gas (or liquid) from a reservoir. After hydrate formation the temperature is slowly increased (maintaining constant pressure by fluid withdrawal) until the last crystal of hydrate disappears. This point, taken as the equilibrium temperature of hydrate formation at constant pressure, may be determined by visual observation of hydrate dissociation or at a constant temperature as simple hydrates dissociate with heat input.

3. Isochoric (constant volume) operation of the hydrate formation cell is illustrated by the pressure–temperature trace of Figure 3.1b. The temperature of the closed cell is lowered from the vapor–liquid region, and isochoric cooling of the gas and liquid causes the pressure to decrease slightly. Hydrates form at the metastability limit B, causing a marked pressure decrease, ending at the three-phase (L_W–H–V) pressure and temperature. The temperature is then slowly increased to dissociate the hydrates. On a pressure–temperature plot, the hydrate dissociation point is taken as the intersection of the hydrate dissociation trace with the initial cooling trace (Point D in Figure 3.1b). This procedure is commonly used for high pressure hydrate formation, and provides an alternative to visual observation, which is the primary option in the previous two procedures.

In the mid-1940s a sight glass rupture resulted in the death of a hydrate researcher. Consequently, there was a revival of interest in non-visual means of hydrate detection, especially at high pressures. The development of

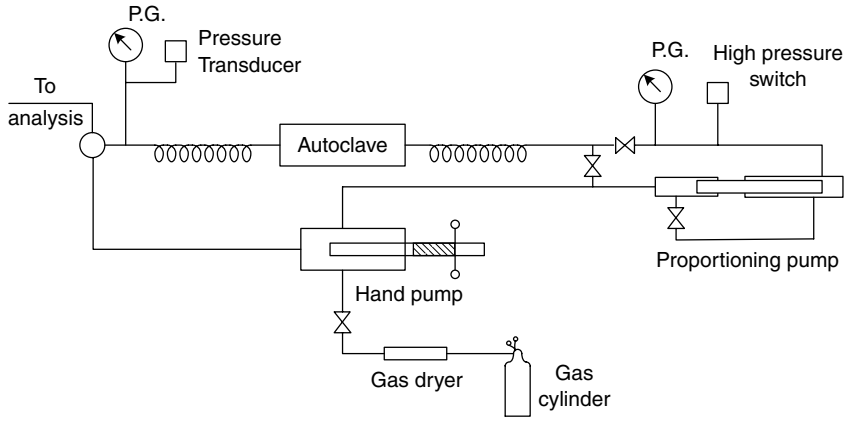

FIGURE 6.2 Kobayashi's ball mill hydrate apparatus for three-phase and for two-phase hydrate equilibria. (Reproduced, from Aoyagi, K., Song, K.Y., Kobyahshi, R., Sloan, E.D., Dharmawardhana, P.D., *Gas Proc. Assn. Res. Report*, No. 45, Julsa, OK (December 1980). With permission from the Gas Processors Association.)

the van der Waals and Platteeuw statistical theory in 1959 also rekindled interest in high pressure experimental work to complement and test the theory.

In the 1950s Kobayashi extended a series of studies he had begun with Katz at the University of Michigan. The new work represented high pressure nonvisual experimental studies that continued for half a century at Rice University. Of particular note are the high pressure studies of Kobayashi and coworkers (Marshall et al., 1964a,b; Saito et al., 1964) and the advances in the theory made by Nagata and Kobayashi (1966a,b) and Galloway et al. (1970). The apparatus consisted of a high-pressure stainless steel cylinder, which rotated about its axis. Inside the cylinder Galloway inserted stainless steel balls, suggested by Barrer and Edge (1967), to renew the surface area upon rotation, and to enable all water to be converted to hydrate. Aoyagi and Kobayashi (1978) modified the apparatus, as shown in Figure 6.2, to allow for gas recirculation through the cell in semibatch operation.

More recently, Tohidi and coworkers (Burgass et al., 2002; Mohammadi et al., 2003) have applied a novel method for measuring gas hydrate phase equilibria (L_W–H–V), which is based on a Quartz Crystal Microbalance (QCM). Figure 6.3 shows a schematic of the QCM set up and the QCM placed in a high pressure cell. The QCM consists of a thin disk of quartz sandwiched between two electrodes. The crystal will oscillate at a particular resonant frequency when an electric current is passed across the electrodes. This frequency is a function of the properties of the crystal. Any mass (from hydrate formation) attached to the surface of the crystal disk will cause a change in the resonant frequency, and hence be detected. The pressure and temperature of the system is measured using conventional methods, namely, a pressure transducer and a thermocouple in the high pressure cell.

The QCM is extremely sensitive and measures small changes in mass, that is, 1 ng mass change gives a 1 Hz frequency change (Lu and Czanderna, 1984).

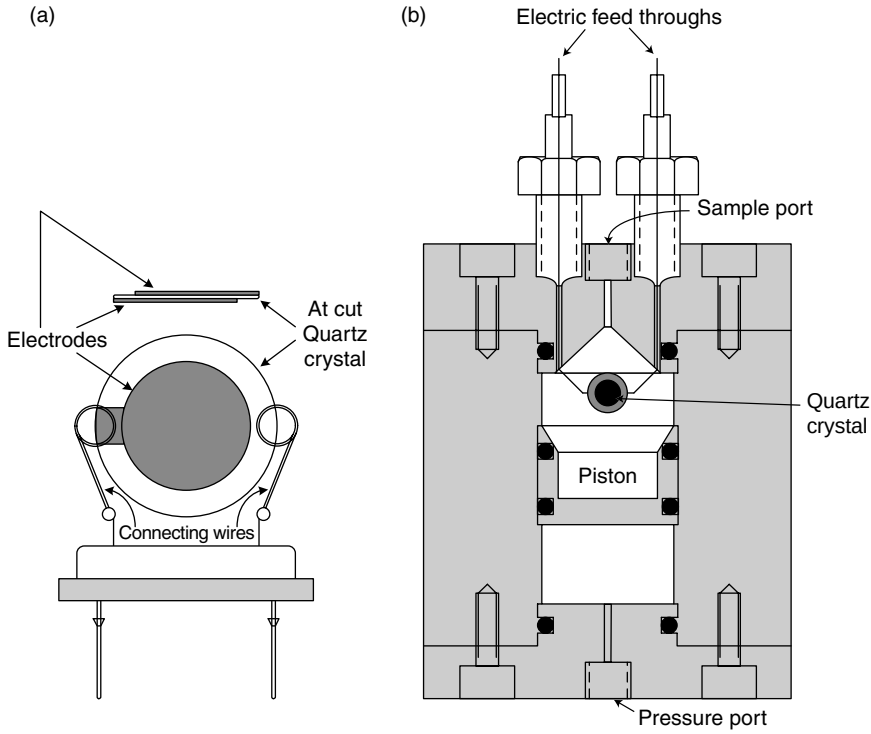

FIGURE 6.3 (a) Schematic illustration of the Quartz Crystal Microbalance (QCM), and (b) the QCM mounted within a high pressure cell. (Reproduced from Mohammadi, A.H., Tohidi, B., Burgass, R.W., *J. Chem. Eng. Data*, **48**, 612 (2003). With permission from the American Chemical Society.)

Therefore, key advantages of the QCM method are that much smaller samples (one drop of water) and hence shorter times (15 min/temperature step versus several hours for conventional methods) are required for these hydrate phase equilibria measurements. The authors applied this system to measure dissociation temperatures of gas hydrates, such as methane, nitrogen, and oxygen hydrates.

The procedure involved adding a drop of water onto the surface of the quartz crystal, and then lowering the system temperature to freeze the water. The cell was then evacuated and the gas system was introduced into the cell. The temperature and pressure conditions required for hydrate formation were then adjusted. The cell temperature was raised stepwise, and pressure and electrical parameters of the QCM were recorded at each step. The formation of a small amount of hydrate (causing a change in mass) is readily detected from the significant reduction in resonant frequency at conductance at the resonant frequency of the quartz crystal. However, the QCM method requires that hydrates adhere to the surface of the quartz crystal, and in some cases this may not occur, thereby making these measurements unfeasible.

6.1.1.3 Apparatus for use below the ice point

Hydrate experimental conditions have been defined in large part by the needs of the natural gas transportation industry, which in turn determined that experiments be done above the ice point. Below 273.15 K there is the danger of ice as a second solid phase (in addition to hydrate) to cause fouling of transmission or processing equipment. However, since the development of the statistical theory, there has been a need to fit the hydrate formation conditions of pure components below the ice point with the objective of predicting mixtures, as suggested in Chapter 5.

Because most of the upper quadruple points of the hydrocarbon hydrate formers limit the temperature range of simple hydrate formers to a few degrees above the ice point, the region below 273 K was measured to provide more extensive data. However, as recorded in Section 6.3, substantially fewer data below 273 K exist than at higher temperatures. An increasing need for hydrate phase equilibria data below the ice point is evolving as oil/gas exploration move to Arctic conditions, where typically temperatures can be well below 273 K.

Deaton and Frost (1946) suggested the same apparatus could be used for conditions below the ice point. In these experiments, gas was first bubbled through water above 273 K, to form a "honeycomb mass" of hydrate. Then free water was drained before the cell was cooled below the ice point. After the temperature was stabilized, gas was removed in small increments until a region of constant pressure was obtained, which indicated dissociation of the hydrate phase. Deaton and Frost used this procedure only for equilibria of simple hydrates, since the hydrated mass of guest mixtures was not constrained to be of uniform composition, and consequently would have decomposed at different pressures.

For glass-tube hydrate equilibria below the ice point, Barrer and coworkers (Barrer and Ruzicka, 1962a,b; Barrer and Edge, 1967) and later Falabella and Vanpee (1974) and Falabella (1975) used glass beads or stainless steel balls to provide surface renewal in a shaken glass tube. At the ice point Cady (1981, 1983a,b, 1985) was able to condense hydrates from mixtures of water and guest molecules in a visual glass apparatus. In other innovative experiments below the ice point, Holder and coworkers (Godbole, 1981; John, 1982; Kamath, 1984) performed low pressure measurements below 273.15 K using an electrobalance, a non-visual sampling cylinder, and a static sight glass, respectively.

The experiments of Hwang et al. (1990) indicated that hydrates from ice are readily formed when the sample temperature is raised just above the ice point. Stern et al. (1996) successfully converted ice to hydrates. They raised the temperature of 200–500 μm ice grains to 289 K and 31 MPa within the L_W–H–V region (beyond the almost vertical I–H–V line). Ice melted and converted all but 3% of the sample into hydrate within 8 h, as determined by x-ray diffraction. The method of Stern et al. (1996) has been widely adopted by hydrate researchers to achieve complete/near complete conversion of ice to hydrate.

At temperatures below the ice point more time is required to equilibrate the two solid phases, ice and hydrate. Byk and Fomina (1968) suggested that water molecule rearrangement is very difficult between the ice nonplanar hexagonal

structure and the hydrate planar pentagonal cage faces. Since many molecules in each structure must have some mobility to allow the transition necessary, a liquid-like structure may be required on a molecular scale. This liquid-like (quasi-liquid) layer has been more recently proposed based on neutron diffraction data to be a key part of the conversion process of ice to carbon dioxide hydrate (Henning et al., 2000).

6.1.1.4 Apparatuses for two-phase equilibria

In two-phase (H–V or H–L_{HC}) equilibria, one less phase is present than in the more common three-phase measurements; therefore, an additional intensive variable (in addition to temperature or pressure) must be measured. Typically the water concentration of the hydrocarbon fluid phase is determined; the fluid phase contains very low concentrations of water, and a special means must be used to measure minute water concentrations, such as the special chromatograph developed by Ertl et al. (1976) in Kobayashi's laboratory. Alternatively, the hydrocarbon concentration of the aqueous phase in equilibrium with hydrates is determined; these concentrations are also very low and require special techniques.

The most productive two-phase (H–V or H–L_{HC}) equilibrium apparatus was developed by Kobayashi and coworkers. The same apparatus has been used for two-phase systems such as methane + water (Sloan et al., 1976; Aoyagi and Kobayashi, 1978), methane + propane + water (Song and Kobayashi, 1982), and carbon dioxide + water (Song and Kobayashi, 1987). The basic apparatus described in Section 6.1.1.2 was used in a unique way for two-phase studies. With two-phase measurements, excess gas was used to convert all of the water to hydrate at a three-phase (L_W–H–V) line before the conditions were changed to temperature and pressures in the two-phase region. This requires very careful conditioning of the hydrate phase to prevent metastability and occlusion. Kobayashi and coworkers equilibrated the hydrate phase by using the ball-mill apparatus to convert any excess water to hydrate.

6.1.1.5 Flow loops for hydrate formation kinetics

A number of large temperature-controlled pilot flow loops have been constructed to study hydrate formation under simulated field conditions. For example, pilot flow loops have been constructed by ExxonMobil (Reed et al., 1994), Texaco (Notz, Personal Communication, 1996), Shell (Muijs et al., 1991), and l'Institut Francais du Petrole, IFP (Behar et al., 1994). The IFP loop at Solaize is 2 in. (ID; 5.1 cm) and 140 m in length, and is rated to 10 MPa (Palermo et al., 2000). ExxonMobil (Talley, Personal Communication, March 18, 2005) developed a pilot flow loop for hydrate testing and research that is 3.8 in. (ID; 9.7 cm) and 95 m in length, rated to around 10.3 MPa (see Figure 6.4a). The whole flow loop and peripheral equipment is housed in a large temperature controlled room. This flow loop has the advantage of having a particle size analyzer (focused beam reflectance method, FBRM) to monitor changes in the hydrate particle size distribution during

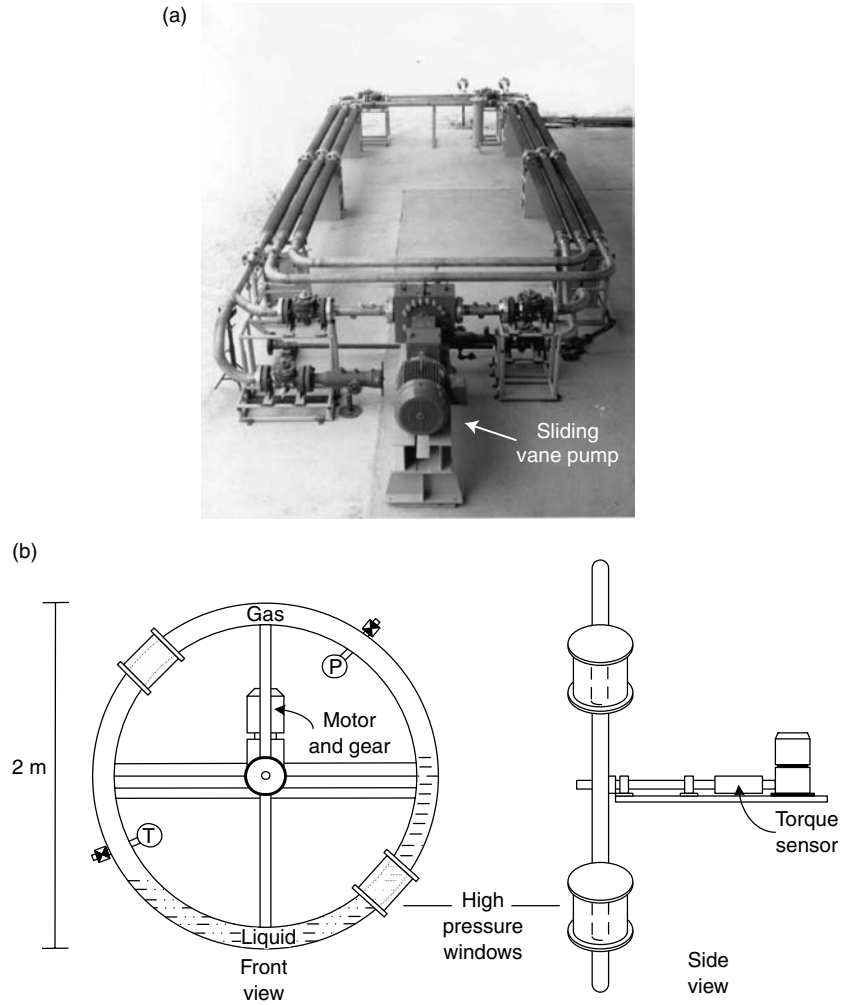

FIGURE 6.4 (a) ExxonMobil flow loop for hydrate formation, before installing the FBRM instrument, peripheral equipment and housing. (From Turner, D., *Clathrate Hydrate Formation in Water-in-Oil Dispersions*, Ph.D. Thesis, Colorado School of Mines, Golden, CO 2005. With permission.) (b) Flow wheel apparatus for hydrate formation during flow simulation. (Reproduced from Bakkeng, S.E., Fredriksen, A.E., in *Proc. First International Conference on Natural Gas Hydrates*, **715**, 502 (1994). With permission from the New York Academy of Sciences.)

hydrate formation/decomposition (see Section 6.2.1 for more details on the FBRM system). It has been suggested that the loop diameter needs to be about equal to or larger than 4 in. internal diameter in order to be able to scale-up flow results to large (e.g., at least 10 in. internal diameter) multiphase gas/oil transmission lines.

Results obtained in the Texaco flow loop (1.93 in. or 4.9 cm ID, 14 m in length, rated to 13.8 MPa) and in field tests at Werner-Bolley, Southern Wyoming

showed there was good transferability between the flow loop and field. The flow loop results indicated the most probable locations for plug formation (Matthews et al., 2000).

Another flow loop facility used to test hydrate formation is the flow loop at Tulsa University (3 in. or 7.6 cm ID, 48.8 m in length, operating at pressures up to 15.2 MPa). This flow loop can be set at different slope inclines (e.g., from 5° to 30°). The concept of using a rocking loop originated from the desire of chemical companies to scale-up their laboratory rocking cell tests on low dosage hydrate inhibitors (LDHIs) to a pilot-scale facility. However, the ability to set the flow loop at different inclines enables simulation of different field flowline geometries.

Camargo and Palermo (2002) also investigated the transferability of hydrate slurry rheology measurements obtained in the "Lyre" flow loop in Solaize (2 in. or 5.1 cm ID, 140 m long) and in a laboratory high pressure rheometer. The results showed good agreement between the two apparatuses for relative viscosity versus shear rate data. The transferability between hydrate rocking cells, a mini loop (0.5 in. or 1.3 cm ID) and a pilot-scale flow loop (4 in. or 10.2 cm ID) for screening low dosage inhibitors was examined by Talley et al. (2000). Good correlation was found between the mini loop and flow loop, although it was concluded that flow loops give different subcoolings from rocking cells.

Herri and coworkers (Fidel-Dufour et al., 2005) have developed a flow loop reactor (in Saint Etienne, France) operating at pressures of 1–10 MPa at 0–10°C. The flow section is 36.1 m long, 1.0 cm internal diameter, and has a constant slope of 4°. The unique feature of this flow loop is that the exit of the flow section is connected to a gas lift riser (10.6 m long and 1.7 cm internal diameter) in which gas coming from a separator located at the top of the column is re-injected. The gas lift is thereby able to move an emulsion or suspension slurry without any pump or mechanical system.

An alternative that is less resource-intensive than the flow loop is the flow wheel apparatus (Bakkeng and Fredriksen, 1994; Lippmann et al., 1994) shown in Figure 6.4b. The wheel (torus) is nominally a 2–5 in. (5.1–12.7 cm) pipe, 2 m in diameter that rotates at 0.3–5.0 m/s while filled with gas and less than 50 vol% liquid. Conceptually, the wheel is spun past the gas and liquid rather than the reverse. Therefore, the flow wheel apparatus does not require circulating devices such as pumps or compressors. Hydrate formation is deduced visually, or by a sharp increase in torque required to turn the wheel. Urdahl et al. (1995) and Lund et al. (1996) report good field transferability from results obtained with this apparatus. Pilot flow loops and flow wheels have been also used to simulate shut-in/start-up conditions (12 h stagnant period) and to test kinetic inhibitors (e.g., Palermo and Goodwin, 2000; Rasch et al., 2002).

6.1.2 Methods for Measurement of Thermal Properties

The number of measurements for natural gas hydrate thermal properties is several orders of magnitude lower than that for phase equilibrium properties. The experimental difficulties in thermal measurements center on the determination of

the composition of the system prior to measurement. The difficulty of system composition determination is due to two factors. First, at temperatures above the ice point, high equilibrium pressures cause decomposition when the apparatus is loaded with preformed hydrate. Second, hydrate metastability and component occlusion cause extreme difficulty in completely converting all the water to hydrate.

However, recent advances in commercially available high pressure calorimeters (e.g., by Setaram with the DSC 111, BT2-15 calorimeter, micro-DSC VII) have the potential to provide a more tractable method of obtaining thermal property data for hydrates. In particular, the problem mentioned above of incomplete conversion/decomposition of the hydrate sample during loading may be largely circumvented by using the following procedure. The gas hydrate sample is synthesized off-line and then quenched in liquid nitrogen to stabilize the hydrate at atmospheric pressure. The quenched hydrate is loaded into the high pressure DSC cell in a dry atmosphere (to avoid condensation). The sample is then pressurized with the appropriate gas system to allow any unconverted or partially decomposed hydrate to convert to hydrate [which is analogous to Handa's (1986b) method described in Section 6.1.2.1]. Another method is to add crushed ice particles into the high pressure cell and then on pressurizing the ice, freeze-thaw cycles are performed to fully convert the ice to hydrate [cf. Stern et al.'s (1996) method]. Using these methods, thermal property data at high pressures (above the ice point) have been obtained for methane hydrate by Gupta (2007).

Other attempts to avoid the experimental difficulties of measuring the thermal properties of gas hydrates have been to choose the easier route of thermal property measurements of cyclic ethers–ethylene oxide (EO) for structure I, or tetrahydrofuran (THF) for structure II. Since both compounds are totally miscible with water, liquid solutions can be made at the theoretical hydrate compositions ($EO \cdot 7.67H_2O$ or $THF \cdot 17H_2O$).

Hydrates of EO and THF may be formed at atmospheric pressure without problems of occlusion or mass transfer at temperatures of 285.7 and 277.4 K, respectively. In such measurements, the host or water contribution is correctly determined.

Table 6.5 lists the different thermal property measurements that have been performed on hydrates of cyclic ethers, other nonnatural gas components, and natural gas components.

6.1.2.1 Heat capacity and heat of dissociation methods

In a thorough review of calorimetric studies of clathrates and inclusion compounds, Parsonage and Staveley (1984) presented no direct calorimetric methods used for natural gas hydrate measurements. Instead, the heat of dissociation has been indirectly determined via the Clapeyron equation by differentiation of three-phase equilibrium pressure–temperature data. This technique is presented in detail in Section 4.6.1.

TABLE 6.5
Measurements of Hydrate Thermal Properties

Investigator(s)/date	Component	Range of experiments
Heat capacity and heat of dissociation		
Ross and Andersson (1982)	Tetrahydrofuran	C_v:100–260 K; $P < 1.5$ GPa
Leaist et al. (1982)	Ethylene oxide	ΔH and C_p: 120–260 K
	Tetrahydrofuran	ΔH and C_p: 120–260 K
Callanan and Sloan (1983)	Ethylene oxide	ΔH and C_p: 240–270 K
	Tetrahydrofuran	ΔH and C_p: 240–270 K
	Cyclopropane	C_p: 240–265 K
Handa (1984)	Tetrahydrofuran	ΔH and C_p: 100–270 K
Handa (1985)	Trimethylene oxide	ΔH and C_p: 85–270 K
Rueff et al. (1985)	Tetrahydrofuran	ΔH and C_p: 240–265 K
White and MacLean (1985)	Tetrahydrofuran	C_p: 17–261 K
Handa (1986c)	Xenon	ΔH: 273 K; C_p: 150–230 K
Handa (1986a)	Xenon and krypton	ΔH and C_p: 85–270 K
Handa (1986d)	Methane, ethane, propane	ΔH and C_p: 85–270 K
Handa (1986b)	Isobutane	ΔH and C_P: 85–270 K
Rueff et al. (1988)	Methane	ΔH: 285 K; C_p: 245–259 K
Kang et al. (2001)	Methane, Carbon dioxide, Nitrogen, Tetrahydrofuran	ΔH: 273.65
Gupta (2007)	Tetrahydrofuran	ΔH and C_p: 240–277 K
	Methane	ΔH and C_p: 243–283 K; $P \leq 20$ MPa
Thermal conductivity		
Cook and Laubitz (1981)	Ethylene oxide	Ambient freezing point
	Tetrahydrofuran	
Ross et al. (1981)	Tetrahydrofuran	100–277 K; 0.1 GPa
Ross and Andersson (1982)	Tetrahydrofuran	100–260 K; $P \leq 1.5$ GPa
Andersson and Ross (1983)	1,3-Dioxolane	100–260 K; $0.05 \leq P \leq 1.0$ GPa
	Cyclobutanone	100–260 K; $0.05 \leq P \leq 1.5$ GPa
Ashworth et al. (1985)	Tetrahydrofuran	45–160 K
Ahmad and Phillips (1987)	1,3-Dioxolane	$T < 200$ K; ambient pressure
Asher (1987)	Tetrahydrofuran	273 K; ambient pressure
Waite et al. (2005)	Tetrahydrofuran	250–270 K; ambient pressure
Waite et al. (2002)	Methane	250–293 K; 24.8 MPa
Huang and Fan (2004)	Methane	263–277 K; 6.6 MPa
Gupta et al. (2006b)	Methane	277–279 K; 4.6 MPa

However, as discussed by Barrer (1959), there is an inherent difficulty in the Clapeyron method, particularly when there is significant nonstoichiometry, as in the case for molecules that occupy the smaller cavities (see Example 5.1). Additionally, while the Clapeyron equation often provides satisfactory estimates of the heat of dissociation, no information about the hydrate heat capacity is directly determined by that equation.

The most accurate calorimetric measurements were made at the Canadian National Research Council by Handa, who modified a Setaram BT Tian-Calvet calorimeter for high pressures. In the Tian-Calvet calorimeter, the sample and reference cells are surrounded by a thermopile, allowing the heat flux to be measured directly. This device was used to measure the heat capacity and heat of dissociation between 85 and 270 K for methane, ethane, propane (Handa, 1986d), iso-butane (Handa, 1986b), and the heat of dissociation of two naturally occurring hydrates (Handa, 1988). A similarly modified BT Tian-Calvet instrument was used by Varma-Nair et al. (2006) to investigate kinetic inhibitor polymer–water interactions, and the relation of these interactions to hydrate inhibition. An abbreviated diagram of the calorimeter is provided in Figure 6.5.

Using this instrument in Figure 6.5, Handa (1986b) measured the heat input to a hydrate sample in the sample container S, relative to helium at ambient temperature and 5 kPa in reference cell R. The hydrate was externally prepared from ice in a rolling-rod mill, before a 4 g sample was loaded into the calorimeter at liquid nitrogen temperatures. For heat capacity measurements, a pressure greater than the hydrate dissociation pressure was maintained in the sample cell. By cycling

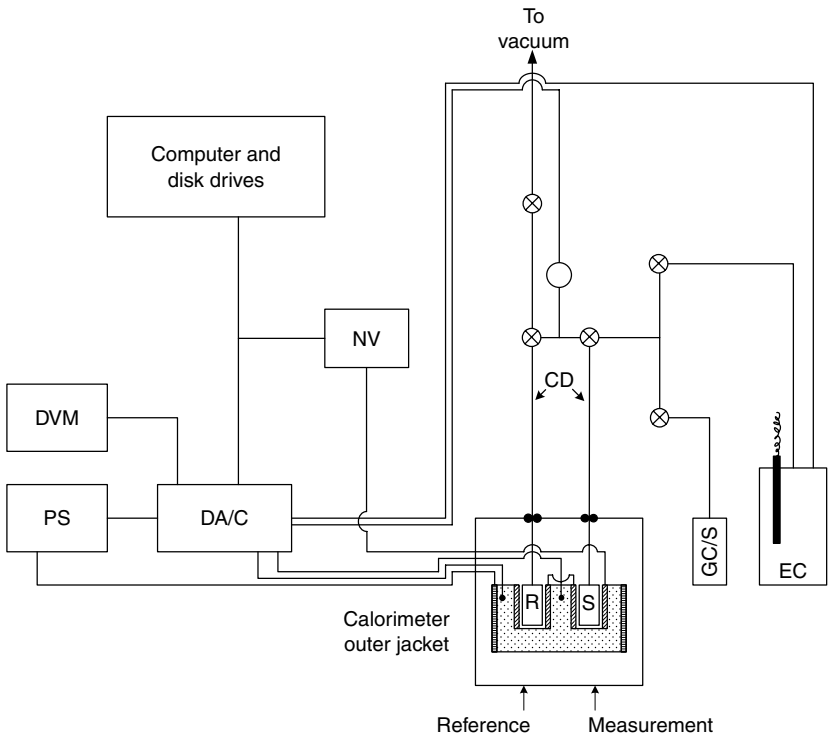

FIGURE 6.5 Schematic of Tian-Calvet calorimeter at the Canadian National Research Council. (Reproduced from Handa, Y.P., *Calorimetric Studies of Laboratory Synthesized and Naturally Occurring Gas Hydrates*, paper presented at AIChE 1986 Annual Meeting Miami Beach, November 2–7, 28 (1986b). With permission.)

the temperature around 273.15 K, Handa was able to determine the amount of ice present in the sample, and to convert most of the ice to hydrate. For hydrate dissociation measurements, the amount of gas released from the hydrates was determined by PVT analysis. Handa estimated the precision to be ±1% for all measurements; the accuracies for $C_p > 100$ K and for ΔH were ±1%, while the accuracy for $C_p < 100$ K was ±1.5%.

In the CSM laboratory, Rueff et al. (1988) used a Perkin–Elmer differential scanning calorimeter (DSC-2), with sample containers modified for high pressure, to obtain methane hydrate heat capacity (245–259 K) and heat of dissociation (285 K), which were accurate to within 20%. Rueff (1985) was able to analyze his data to account for the portion of the sample that was ice, in an extension of work done earlier (Rueff and Sloan, 1985) to measure the thermal properties of hydrates in sediments. At Rice University, Lievois (1987) developed a twin-cell heat flux calorimeter and made ΔH measurements at 278.15 and 283.15 K to within ±2.6%. More recently, at CSM a method was developed using the Setaram high pressure (heat-flux) micro-DSC VII (Gupta, 2007) to determine the heat capacity and heats of dissociation of methane hydrate at 277–283 K and at pressures of 5–20 MPa to within ±2%. See Section 6.3.2 for gas hydrate heat capacity and heats of dissociation data. Figure 6.6 shows a schematic of the heat flux DSC system. In heat flux DSC, the heat flow necessary to achieve a zero temperature difference between the reference and sample cells is measured through the thermocouples linked to each of the cells. For more details on the principles of calorimetry the reader is referred to Hohne et al. (2003) and Brown (1998).

6.1.2.2 Methods for thermal conductivity measurements

The two most common methods for thermal conductivity measurements for natural gas hydrates are the transient method and the steady-state method. Afanaseva

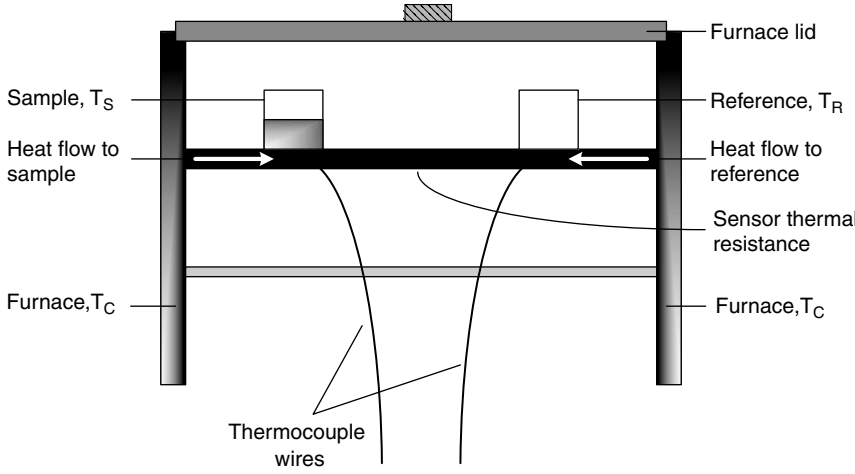

FIGURE 6.6 Schematic of a heat flux DSC System.

and Groisman (1973) first measured hydrate thermal conductivity to be the same as ice with stated accuracy to within ±10%. Stoll and Bryan (1979) first used the transient needle probe method on propane hydrates that have been compacted after formation, and showed the thermal conductivity of propane hydrate was about five times less than that of ice. The probe was modeled after the probe of von Herzen and Maxwell (1959) that had been used with marine sediments.

A slightly modified version of the probe comprised a stainless steel 20 gauge hypodermic tube containing a full length heater wire, a mid-tube thermistor, with epoxy filling the annulus. When a step power change is input to the heater, the probe temperature varies with the thermal conductivity of the material surrounding the probe. With good media contact at the probe boundary, the logarithmic increase of temperature with time gives an inverse relationship with the surrounding hydrate thermal conductivity. In the CSM laboratory the apparatus was used, and the mathematical model was refined and extended to short times by Asher (1987) for methane hydrates in sediments. The thermal conductivity accuracy was estimated to be within ±8% for this transient method.

A conventional steady-state guarded hot-plate method for thermal conductivity measurement was used by Cook and Leaist (1983). Their apparatus was used to perform an exploratory measurement of methane hydrate to within ±12%. A sample of methane hydrate was made externally, pressed, and placed in the hot-plate cell at the "Sample Disc." The lower sample heater had thermocouples contacting the top and the bottom of the sample to determine the temperature gradient.

Waite et al. (2002, 2005) have measured thermal conductivities of hydrates using von Herzen and Maxwell's (1959) needle probe method (see Figure 6.7). Waite et al. (2005) showed that THF hydrate (sII) and methane hydrate (sI) have similar thermal conductivities below 265.5 K. A novel method of determining the thermal conductivity of methane hydrate samples is to couple x-ray Computed Tomography (CT) measurements with numerical modeling using history matching of the data (Freifeld et al., 2002; Gupta et al., 2005; Moridis et al., 2005). See Section 2.2.3.1 for more details.

6.2 Measurements of the Hydrate Phase

This section will outline the developments and significance of applying mesoscopic and molecular-level methods to measure hydrate thermodynamic and kinetic properties. The characteristics of these different techniques are also listed in Tables 6.2 and 6.3.

6.2.1 Mesoscopic Measurements of the Hydrate Phase

Table 6.2 summarizes the mesoscopic methods that have been successfully applied to study hydrate properties. These are categorized as methods that provide a spatial resolution on the order of microns.

Laser scattering methods have been applied by the groups of Bishnoi and Sloan to measure changes in the hydrate particle size distribution during hydrate

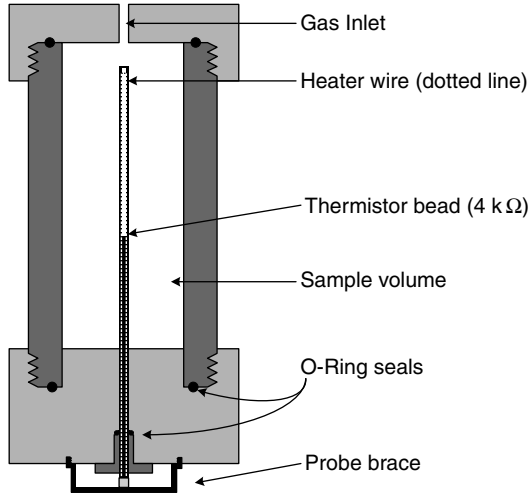

FIGURE 6.7 Schematic of the pressure vessel and needle probe system used to measure thermal conductivity. (Reproduced from Waite, W.F., deMartin, B.J., Kirby, S.H., Pinkston, J., Ruppel, C.D., *Geophys. Res. Lett.*, **29**, 2229 (2002). With permission from the American Geophysical Union.)

formation and decomposition. One recent laser scattering method that has been applied to hydrate studies is the focused beam reflectance method, FBRM (Lasentec/Mettler Toledo) (Clarke and Bishnoi, 2000, 2001a,b; Turner et al., 2005a). The FBRM probe consists of a near-infrared laser with a wavelength of 785 nm, which is housed in a cylindrical probe. The laser rotates at high velocity (2–8 m/s) and is propagated through the sapphire window mounted on the probe tip. When the laser hits a particle, it is reflected and back propagated through the sapphire window. The corresponding chord length (distance between any two points on a particle surface) is thus the product of the rotating laser velocity and the measured intersecting time of the particle (Figure 6.8). From the chord lengths, the FBRM can be used to detect hydrate formation and monitor changes in particle size during hydrate growth and decomposition.

CSM has coupled the FBRM with a second probe, the particle video microscope, PVM (Lasentec/Mettler Toledo), which consists of six illuminating near-infrared lasers (850 nm) that are transmitted into the sample. While the FBRM provides precise quantitative tracking of the chord lengths, the PVM probe provides qualitative images of the hydrate particle size and degree of agglomeration. The size range scale of hydrate particles that can be measured with the PVM probe is 10–300 μm.

A micromechanical force apparatus has been developed at CSM to measure directly the adhesive forces between hydrate particles or between a hydrate particle and a surface (Yang et al., 2004; Taylor et al., 2007). Similar micromechanical force apparatus designs have been applied to measure adhesive forces between ice particles (Hosler, 1957; Hosler and Hallgren, 1961; Fan, 2003). This apparatus

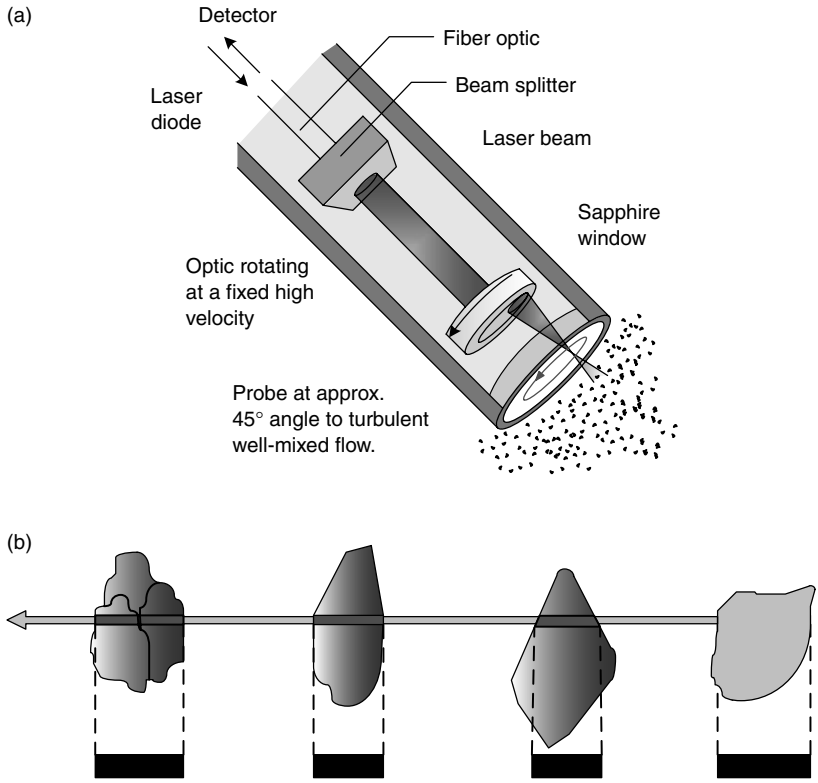

FIGURE 6.8 Schematic of the FBRM probe tip (a), and chord lengths (b). (Reproduced, with permission, from www.lasentec.com.)

consists of a stationary micromanipulator that holds a glass fiber cantilever (30 μm in diameter and 3.5 mm in length). A hydrate particle is attached to the end of the glass fiber. The other glass fiber is attached to a moving micromanipulator and also has a hydrate particle on the end of the fiber (see Figure 6.9). The cantilevers and hydrate particles are immersed in a cooled surrounding fluid, such as decane and the moving manipulator pulls off/down, and depending on the attractive force between the particles, is displaced by a distance delta from the original position. The adhesive force is given as the spring constant of the glass fiber (determined from a previous calibration) multiplied by the displacement.

A glass micromodel method has been developed to observe gas hydrate formation from the water–gas interface and water-containing dissolved gas (Tohidi et al., 2001, 2002). The glass micromodel consists of an etched glass base plate with a sealed glass cover plate (Figure 6.10). Geometric networks of pores or flow channels (width >50 μm) were etched onto the glass micromodel with hydrofluoric acid. Fluid was pumped into channels/pores through the cover plate that has an inlet and outlet. The micromodel was then placed in a vessel that was pressurized up to 40 MPa with gas (methane or carbon dioxide). The liquid water phase was dyed

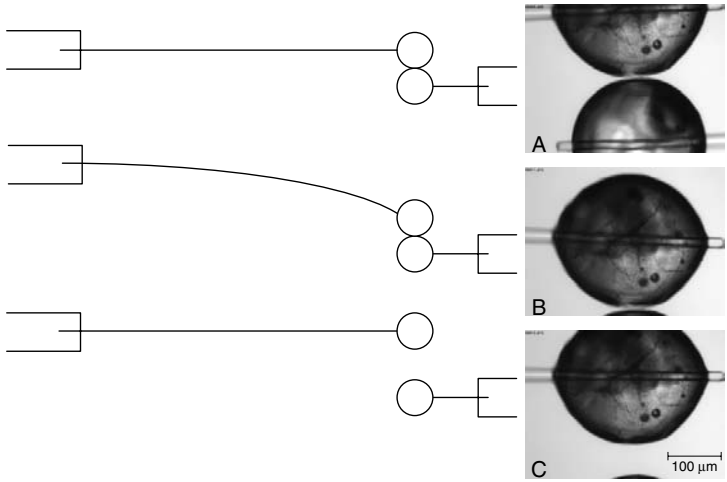

FIGURE 6.9 A schematic of the micromechanical force measurement (left) and video images of hydrate particles during each stage of the adhesive force measurement. (From Taylor, C.J., *Adhesion Force between Hydrate Particles and Macroscopic Investigation of Hydrate Film Growth at the Hydrocarbon/Water Interface*, MS Thesis, Colorado School of Mines, Golden, CO (2006). With permission.)

with methyl blue to provide increased contrast between the liquid and gas/hydrate phases (hydrates and gas exclude the dye). The pore channels were only up to 50 μm deep, and so phase changes from liquid water/gas to hydrate could be clearly observed. From these experiments, Tohidi et al. (2001, 2002) suggest that hydrate formation can occur at the liquid–gas interface, as well as from dissolved gas in water.

X-ray computed tomography (CT) measurements have been more recently applied to determine hydrate transport properties (thermal conductivity, thermal diffusivity, and permeability), and kinetic properties during hydrate core formation and dissociation (density profiling of the hydrate, gas, and water phases). The results illustrate the importance of spatially characterizing the hydrate core during transport and kinetic measurements to correctly interpret macroscopic data (P, T). For example, the heterogeneous nature of a hydrate core has been clearly illustrated using x-ray CT analysis. Figure 6.11 illustrates the use of x-ray CT analysis to obtain visual images of the density profiles of slices of a hydrate core contained in a high pressure aluminum sample cell. Therefore, the application of x-ray CT analysis to hydrate cores presents a major advance to the measurement methods used for gas hydrates (Gupta et al., 2005; Kneafsey et al., 2005). Also see Section 2.2.3.1 for more details.

Other advances in mesoscopic measurements include the application of magnetic resonance imaging (MRI) to study real-time hydrate growth from ice particles and water droplets, and particle morphology (Moudrakovski et al., 2004). Scanning electron microscopy has also been shown to be a useful tool for studying natural

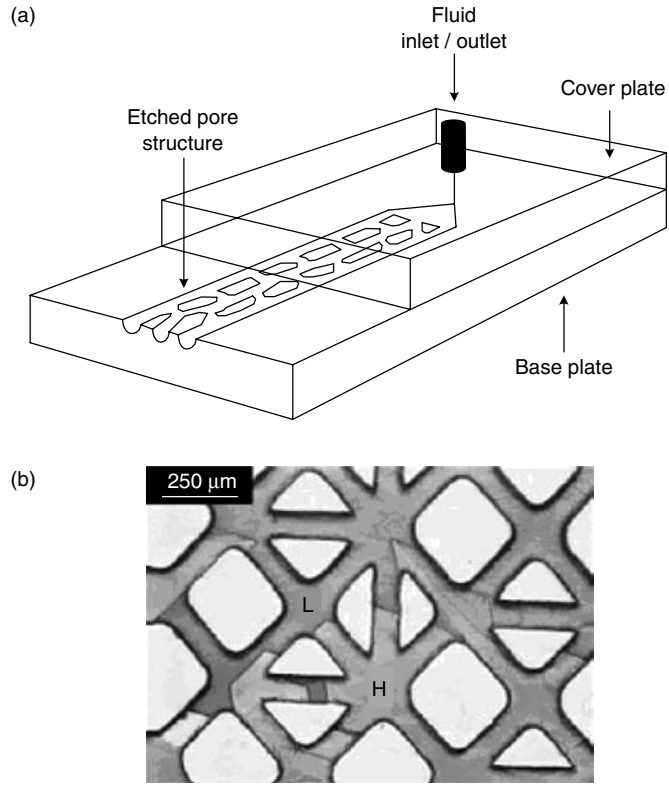

FIGURE 6.10 Schematic of the glass micromodel apparatus (a) and the micromodel pore network (b). (Reproduced from Tohidi, B., Anderson, R., Clennell, B., Yang, J., Bashir, A., Burgass, R.W., in *Proc. Fourth International Conference on Gas Hydrates*, Yokohama, Japan, May 19–23, p. 761 (2002). With permission.)

and synthetic hydrate sample morphologies (Kuhs et al., 2000; Staykova et al., 2003; Stern et al., 2005). Also see Chapter 3, Section 3.2.2.2 for more details.

6.2.2 Molecular-Level Measurements of the Hydrate Phase

Equilibrium measurements of the solid hydrate phase have been previously avoided due to experimental difficulties such as water occlusion, solid phase inhomogeneity, and measurements of solid phase concentrations. Instead, researchers have traditionally measured fluid phase properties (i.e., pressure, temperature, gas phase composition, and aqueous inhibitor concentrations) and predicted hydrate formation conditions of the solid phase using a modified van der Waals and Platteeuw (1959) theory, specified in Chapter 5.

However, over the last decade there has been a significant shift in the number of researchers recognizing the importance of implementing mesoscopic and molecular-level methods to measure the hydrate phase directly. It is clear that

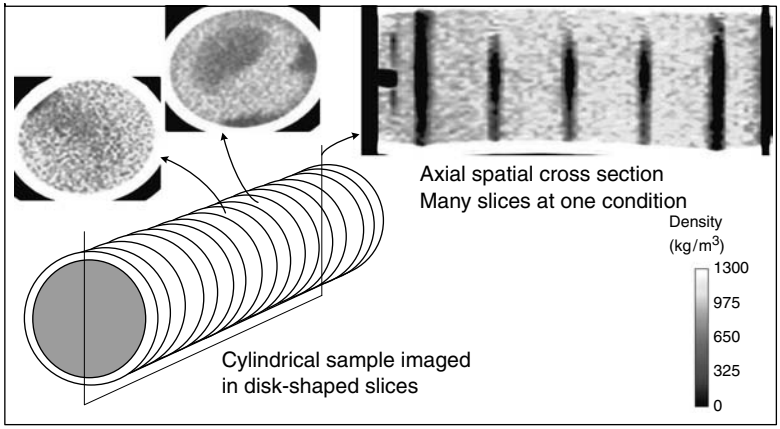

FIGURE 6.11 **(See color insert following page 390.)** Schematic of the application of x-ray CT analysis to provide density profile images of different sections of a hydrate core contained in a cylindrical high pressure aluminum cell. (From Gupta, A., *Methane Hydrate Dissociation Measurements and Modeling: The Role of Heat Transfer and Reaction Kinetics*, Ph.D. Thesis, Colorado School of Mines, Golden, CO (2007). With permission.)

prediction without molecular-level measurements of the hydrate phase does not represent the state-of-the-art for hydrate equilibria, and must be considered as a less-than-optimal solution for at least three reasons:

1. The prediction of the hydrate phase is often mistaken. For example, over four decades ago Saito et al. (1964) published gas phase measurements of hydrate equilibria for methane, argon, and nitrogen at pressures to 690 MPa. When they fit the data with the van der Waals and Platteeuw model, they made the (then common) assumption that the single guest components formed sI hydrates. In 1984, however, x-ray diffraction data (Davidson et al., 1984) proved the Holder and Manganiello (1982) prediction that argon and nitrogen formed sII as single hydrate guests. The fact that the model could be fit to (and subsequently predict) the incorrect crystal structure suggests that the model is a means of data fitting, rather than an a priori prediction technique.

Since 1987, 39 sH hydrate formers have been reported, many of which are incorrectly listed in industrially important references such as the *API Databook* (Lippert et al., 1950), where methylcyclopentane and methylcyclohexane are listed as sII formers, and the *Handbook of Natural Gas Engineering* (Katz et al., 1959), where iso-pentane and methylcyclopentane are listed as non-hydrate formers.

2. In addition to the three known natural gas hydrates, several other hydrate structures exist. Dyadin et al. (1991) found four hydrate structures and Jeffrey (1984) proposed five additional hydrate structures. These structures have yet to be confirmed in natural gas systems, although new hydrate structures have been identified using x-ray diffraction such as a tetragonal structure for bromine (Udachin et al., 1997b), a trigonal structure for dimethyl ether (Udachin et al., 2001a),

a complex hydrate structure for choline hydroxide tetra-*n*-propylammonium fluoride (Udachin and Ripmeester, 1999), and high pressure (GPa range) hydrate phases (Dyadin et al., 1999; Mao et al., 2004).

The existence of other hydrate structures is also suggested by the striking analogy of hydrate cavities to the large Buckminsterfullerene family of carbon cavities. Both types of cavities obey Euler's Rule: cavities have exactly 12 pentagonal faces and any number of hexagonal faces, except one. Hydrates have the additional restriction that cavities should fill space continuously without excessive strain on the hydrogen bonds.

With the evolution of these new structures, the possibility of forming metastable hydrate phases (Section 3.2), and the fact that different structures form at different thermodynamic conditions (pressure, temperature, composition), it is clear that macroscopic methods cannot adequately predict the hydrate structure(s) present.

3. Prediction of the hydrate phase on a laboratory scale is analogous (in vapor–liquid equilibrium) to the prediction of the liquid phase concentration given only the vapor phase concentration, temperature, and pressure. Predictions of either the liquid phase or the hydrate phase are unacceptable because all experimental errors are transferred to prediction of the unmeasured phase.

It is clear from the above that molecular-level methods are required to determine the hydrate structure. Furthermore, these methods have identified several phenomena that shift the paradigm on our understanding of clathrate hydrates, including:

1. A binary mixture of methane + ethane, which are both sI hydrate formers, can form sII hydrate as the thermodynamically stable phase (Subramanian et al., 2000).
2. Metastable crystalline phases form during hydrate formation and decomposition (Staykova and Kuhs, 2003; Schicks et al., 2006).
3. Small molecules such as hydrogen form structure II hydrate (Dyadin et al., 1999; Mao et al., 2002; Lokshin et al., 2004).
4. At high pressures (>0.5 kbar) hydrate cavities can contain more than one guest for nitrogen, methane, or hydrogen (Chazallon and Kuhs, 2002; Mao et al., 2002; Loveday et al., 2003; Lokshin et al., 2004; Mao and Mao, 2004).

Table 6.3 provides a summary of the different microscopic techniques that have been applied to hydrate studies and the type of information that can be obtained from these tools. The following discussion provides a brief overview of the application of diffraction and spectroscopy to study hydrate structure and dynamics, and formation/decomposition kinetics. For information on the principles and theory of these techniques, the reader is referred to the following texts on x-ray diffraction (Hammond, 2001), neutron scattering (Higgins and Benoit, 1996), NMR spectroscopy (Abragam, 1961; Schmidt-Rohr and Spiess, 1994), and Raman spectroscopy (Lewis and Edwards, 2001).

6.2.2.1 Diffraction methods

The classic method to obtain information on any crystal structure is via diffraction crystallography. Crystal structure information includes identification of the hydrate structure type, lattice parameters, guest occupancy, and guest position in the cavity. The earliest and most comprehensive x-ray diffraction studies were performed to define the crystal structure by von Stackelburg and coworkers (von Stackelberg, 1949, 1954; von Stackelberg and Müller, 1951a,b, 1954; von Stackelberg and Meinhold, 1954; von Stackelberg and Fruhbuss, 1954; von Stackelberg and Jahns, 1954) and confirmed by Jeffrey and coworkers (McMullan and Jeffrey, 1965; Jeffrey and McMullan, 1967; Jeffrey, 1984). More recent single crystal x-ray data were obtained for sI, sII, and sH by Udachin et al. (1997a, 2001b, 2002) and for sII by Kirchner et al. (2004). X-ray (Tse, 1987, 1990; Tse et al., 1987; Takeya et al., 2000; Udachin et al., 2001b) and neutron diffraction (Rawn et al., 2003) have been also used to determine the thermal expansion in sI, sII, sH hydrates.

It is worthwhile to note that the synchrotron x-ray facilities (e.g., ESRF in Grenoble, APS at Argonne, NSLS at Brookhaven) have significant advantages over laboratory x-ray instruments. The synchrotron x-ray source is significantly more intense than that from conventional sources. Therefore, this means the former measurements have far higher sensitivity than laboratory x-ray measurements, hence better *time resolution*, and the capability of using cells at higher pressures. The different x-ray methods available at a synchrotron source are summarized in Table 6.3. These methods range from x-ray scattering (EXAFS) to measure hydration structures or clustering during hydrate formation (Bowron et al., 1998; Montano et al., 2001) to x-ray powder diffraction for time-resolved hydrate structural studies (Koh et al., 1996; Mirinski et al., 2001).

Neutron diffraction studies have the advantage of being able to determine guest and host (both O and H/D) positions. With the difficulty of preparing single crystals of gas hydrates, most diffraction studies are performed on powder samples. Powder x-ray and neutron diffraction can be used with Rietveld analysis of the data for detailed structure determination (Rawn et al., 2003; Hester et al., 2006a).

Similar to the case of synchrotron x-ray diffraction, there are a number of different neutron scattering methods. These methods range from high resolution neutron powder diffraction for structure determination, to small angle neutron scattering, to neutron spectroscopy. Neutron powder diffraction has been applied by a number of researchers to study structural changes/transitions during hydrate formation (Halpern et al., 2001; Wang et al., 2002; Staykova and Kuhs, 2003).

Small angle neutron scattering instruments are specifically designed to examine disordered materials, such as to determine hydration structures during hydrate formation (Koh et al., 2000; Buchanan et al., 2005; Thompson et al., 2006), or to study kinetic inhibitor adsorption onto a hydrate surface (Hutter et al., 2000; King et al., 2000).

Neutron spectroscopy (also referred to as inelastic neutron scattering) has been used to measure the extent of guest–host interactions in a hydrate lattice, which help to explain the anomalous thermal behavior of hydrates (e.g., low thermal

conductivity). This work has been mostly performed by Tse and coworkers (1993, 1997a,b, 2001; Gutt et al., 2002).

6.2.2.2 Spectroscopic methods

Three main types of spectroscopy have been used to study hydrates. These are described below.

6.2.2.2.1 Solid-state NMR spectroscopy

Structure identification, quantifying relative cage occupancies. ^{1}H NMR has been used for ethane, propane, and isobutane hydrates (Davidson et al., 1977; Garg et al., 1977), while ^{2}H, ^{19}F, ^{31}P, and ^{77}Se NMR have been used for several sI guests (Collins et al., 1990). ^{13}C cross-polarization and magic angle spinning (MAS) NMR techniques have been applied to study hydrates of carbon dioxide, methane, and propane (Ripmeester and Ratcliffe, 1988, 1999; Wilson et al., 2002; Kini et al., 2004).

^{129}Xe NMR was shown to be capable of identifying ratios of xenon atoms in small and large cages (Pietrass et al., 1995; Moudrakovski et al., 2001). Subsequently, it was shown that there are unique chemical shifts for xenon in the cages of sI, sII, and sH hydrate (except for the $5^{12}6^{8}$ cage which is not occupied by xenon) as shown in Figure 6.12. ^{129}Xe is unique for NMR because, among hydrate guests, it has the largest chemical shift (100 ppm) compared to that for ^{13}C (1–5 ppm) and can be used to resolve the shape of cages (Ripmeester and Ratcliffe, 1990). Some hydrocarbon chemical shifts are given in Table 6.6.

Kinetic studies during hydrate formation and decomposition, identifying changes in hydrate structure and relative cage occupancies. Ripmeester et al. (Ripmeester and Ratcliffe, 1988; Ripmeester et al., 1994) introduced ^{1}H cross-polarization techniques to enable relaxation times compatible with hydrate kinetic measurements. Pietress et al. (1995) introduced techniques using optically polarized xenon to significantly increase the detection sensitivity to enable early stage hydrate formation to be monitored. Hyperpolarized Xe NMR has been applied to study Xe hydrate growth from ice (Moudrakovski et al., 2001). At CSM, ^{13}C MAS NMR and non-spinning (NS) NMR have been used to study growth/decomposition of hydrates of methane (Gupta et al., 2006a), methane + propane (Kini et al., 2004), and methane + ethane (Bowler et al., 2005).

Water mobility from molecular reorientation and diffusion. Evidence for the motion of the water molecules in crystal structures is typically provided by ^{1}H NMR (Davidson and Ripmeester, 1984). At very low temperatures (<50 K) molecular motion is "frozen in" so that hydrate lattices become rigid and the hydrate proton NMR analysis suggests that the first-order contribution to motion is due to reorientation of water molecules in the structure: the second-order contribution is due to translational diffusion. ^{2}H NMR has been also used to measure the reorientational rates of water and guest molecules in THF hydrate (Bach-Verges et al., 2001). Spin lattice relaxation rates (T_1) have been measured during THF hydrate

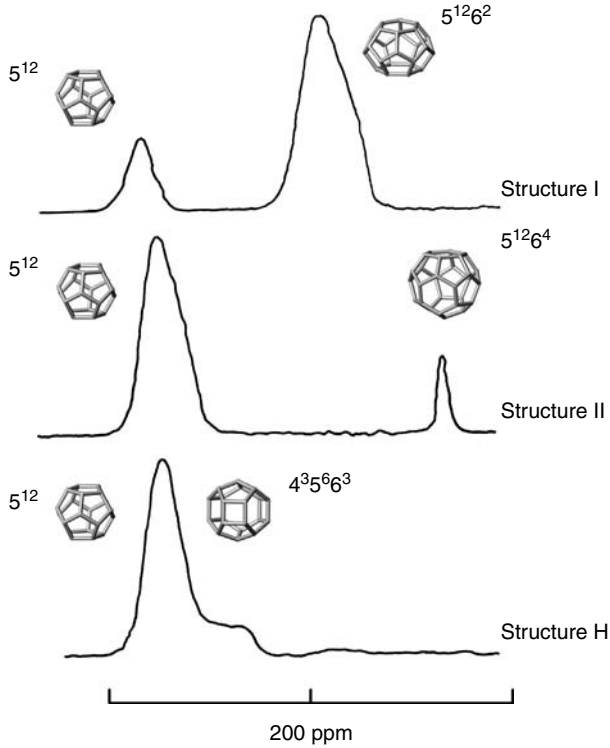

FIGURE 6.12 Determination of ratios of xenon atoms in large and small hydrate cages using ^{129}Xe NMR Spectroscopy at 77 K. (Reproduced from Ripmeester, J.A., Ratcliffe, C.I., *J. Phys. Chem.*, **94**, 8773 (1990).

formation and dissociation Gao et al. (2005). The authors suggest that close to the surface of the hydrate the liquid water is structured.

6.2.2.2.2 Infrared spectroscopy

Bertie and co-workers (Bertie et al., 1975; Bertie and Jacobs, 1978) suggested that the strength of hydrogen bonds in hydrates is very similar to that in ice. Using FTIR (Fourier transform infrared) spectroscopy for low temperature growth of hydrate from the vapor phase, Bertie and Devlin (1983), Richardson et al. (1985a,b), and Fleyfel and Devlin (1988, 1991) showed that hydrates grow from the vapor phase only when Bjerrum L-type defects (induced by ethylene oxide) propagate through the crystal body to the surface.

However, IR spectroscopy has not been widely used for hydrate studies. This is largely due to the technical problems associated with sample preparation (e.g., vapor deposition of thin films) to avoid the high IR absorptivity of water, and the difficulties of performing *in situ* and high pressure measurements. Therefore, this technique will not be further discussed here.

6.2.2.2.3 Raman spectroscopy

Raman spectroscopy has been applied for the following.

Structure identification and relative cage occupancies. The hydration number and relative cage occupation for pure components and guests were measured by Sum et al. (1997), Uchida et al. (1999), and Wilson et al. (2002). Raman guest spectra of clathrate hydrates have been measured for the three known hydrate crystal structures: sI, sII, and sH. Long (1994) previously measured the kinetic phenomena for THF hydrate. Thermodynamic sI/sII structural transitions have been studied for binary hydrate systems (Subramanian et al., 2000; Schicks et al., 2006).

Kinetic studies during hydrate formation and decomposition identifying changes in hydrate structure and relative cage occupancies. (Subramanian and Sloan, 2000; Uchida et al., 2000; Schicks et al., 2006; Gupta et al., 2006a.) Among the different laser Raman spectrometers being used to study hydrates, three main configurations are used: a macro-cell without a fiber optics probe, a macro-cell with a fiber optics probe, and a micro-cell with a confocal Raman microscope. The fiber optics probe provides more flexibility in sampling. For example, a laser Raman spectrometer equipped with a fiber optics probe has been used during successful collaborative efforts between CSM and the Monterey Bay Aquarium Research Institute (MBARI) to measure natural hydrates on the ocean floor (at ~770 m depths) in Hydrate Ridge in the Cascadia Margin (Hester et al., 2006b). The confocal Raman microscope is particularly powerful since it allows simultaneous micron-level visualization and Raman data to be collected on hydrate kinetics, as well as enabling fine control of the focus spot on the sample (Schicks et al., 2006).

The application of Raman spectroscopy becomes more challenging when samples exhibit significant fluorescence (e.g., sediment samples which are brown in color). Other difficulties occur when hydrate samples contain occluded gas (e.g., the vC–H peak for methane gas overlaps with that for methane in the small cage of structure I hydrate). In this case, care must be given to assignment of the spectra (Hester, 2007). The latter example illustrates the strength of combining Raman and NMR spectroscopy to ensure correct interpretation of the data.

In summary, spectroscopy and diffraction can provide important information about hydrates that are not accessible otherwise, namely,

- The hydration number
- Structure identification
- The relative occupancy of molecules in each cage
- Identification of metastable phases
- The kinetics of formation of various structures

NMR and Raman peak assignments for natural gas and non-natural gas hydrates are listed in Tables 6.6 through 6.8, respectively. The NMR data presented are based on the works by Ripmeester and Ratcliffe (1998, 1999) and

TABLE 6.6
List of NMR Peak Assignments for Natural Gas Hydrates

Guest molecule	Guest environment cage type	Chemical shift ppm
Methane	sI large	−6.1
	sI small	−4
	sII large	−7.7
	sII small	−3.95
Ethane	sI large	7.7
	sII large	6.5
Propane	sII large	17.7, 16.8 (18)
Iso-butane	sII large	26.6, 23.7

Note: Chemical shifts are from ^{13}C MAS NMR using tetramethylsilane as a standard at 253 K.
Chemical shifts in parentheses are from ^{13}C NS NMR.

TABLE 6.7
List of Raman Peak Assignments for Natural Gas Hydrates

		Guest environment (cm^{-1})				
Guest composition	Vibrational mode	Gas	Dissolved in water	Liquid	Cage type	Hydrate
CH_4	v1 sym C–H stretch	2917†	2911†		sI large	2905†
					sI small	2915†
					sII large	2904†
					sII small	2914†
					sH medium	2905†
					sH small	2913†
CO_2	v1 + 2v2	1266*	1274§	1280§	sI large	1276§
	v1 + 2v2	1286*				
	v1 + 2v2	1389*	1382§	1386§	sI large	1381§
	v1 + 2v2	1410*				
	v3 asym C–O stretch	2349†			sI large	2335†
	v3 asym C–O stretch				sI small	2347†
	v3 asym C–O stretch				sII small	2345†
	v2 bend CO_2	667†			sI large	660†
	v2 bend CO_2				sI small	655†
	v2 bend CO_2				sII small	655†

(Continued)

TABLE 6.7
Continued

Guest composition	Vibrational mode	Guest environment (cm^{-1}) Gas	Dissolved in water	Liquid	Cage type	Hydrate
C_2H_6	v3 sym C—C stretch	994†	1005†		sI large	1001†
	v3 sym C—C stretch				sI small	1020†
	v3 sym C—C stretch				sII large	993†
	v3 sym C—C stretch				sII small	1020†
	v1 + 2v11 C—H	2900†	2893†		sI large	2891†
	v1 + 2v11 C—H	2956†	2948†		sI large	2946†
	v1 + 2v11 C—H				sII large	2887†
	v1 + 2v11 C—H				sII large	2942†
C_2H_2	v3 C—H stretch	3289†			sI large	3261†
					sI small	3280†
					sII small	3274†
C_3H_8	v8 sym C—C stretch	871†			sII large	878†
i-C_4H_{10}	v3 sym C—C stretch	799†			sII large	812†
$CH_4 + N_2$	v1 sym C—H stretch	2918*			sI large	2905*
	v1 sym C—H stretch				sI small	2915*
	v1 sym N—N stretch	2330*			sI small	2324*
$CD_4 + C_3H_8$	v1 sym C—D stretch	2110*			sII small	2103*
	v8 sym C—C (C3) stretch	871*			sII large	878*
$CH_4 + C_7D_{14}$	v1 sym C—H stretch	2918*			sH small	2913*
$C_2H_6 + C_3D_8$	v3 sym C—C (C2) stretch				sII large	993†
	v1 + 2v11				sII large	2887†
	v1 + 2v11				sII large	2942†

[a] Raman spectra recorded at: CH_4 (g) at 298 K, 3.45 MPa, C_2H_6 (g) at 298 K, 2.07 MPa, C_2H_6 hydrate at 274 K, 1.03 MPa. sII hydrate from a C_2H_6 (65 mol%) + C_3D_8 (35 mol%) gas mixture at 274 K, 0.8 MPa. C_3H_8 vapor and hydrate at 274 K, 0.61 MPa. i-C_4H_{10} hydrate at 274 K, 0.15 MPa.

[b] The symmetric C—C stretching mode of ethane hydrate shifts by 0.5 cm^{-1} on increasing the pressure from 1.03 to 72.4 MPa (Subramanian, 2000).] Free gases when subjected to increasing pressure exhibit significant increases in the stretching mode frequencies, by 0.2–0.3 cm^{-1}/MPa.

* From Sum (1996).

† From Subramanian (2000).

§ From Nakano et al. (1998b).

TABLE 6.8
List of Raman Peak Assignments for Nonnatural Gas Hydrates

		Guest environment (cm^{-1})				
Guest composition	**Vibrational mode**	**Gas**	**Dissolved in water**	**Liquid**	**Cage type**	**Hydrate**
C_4H_8O (THF)	v12 predominantly sym C—C stretch		1036[†]	1029[†]	sI large	1036[†]
	v13 predominantly ring breathing		920[†]	915[†]	sI large	920[†]
	v14 C—O—C sym stretch		892[†]			
	v21 predominantly sym CH_2 stretch				sI large	2863[§]
	v4 predominantly sym CH_2 stretch				sI large	2883[§]
	v3 predominantly sym CH_2 stretch				sI large	2920[§]
	v19 predominantly asym CH_2 stretch				sI large	2935[§]
	v2 predominantly asym CH_2 stretch				sI large	2950[§]
	v18 asym CH_2 stretch				sI large	2989[§]
SO_2	v1 sym S—O stretch	1151.2[†]			sI large	1146[†]
	v1 sym S—O stretch				sI small	1151[†]
	v3 asym S—O stretch	1361[†]			sI large	1342[†]
	v3 asym S—O stretch				sI small	1347[†]
	v2 bending SO_2	519[†]			sI large	517[†]
	v2 bending SO_2				sI small	521[†]
$(SO_4)^{2-}$	v1 sym S—O stretch		981			
O_2	v1 sym O—O stretch	1533[‡]			sII small/ large	1546[‡]
N_2	v1 sym N—N stretch	2329[‡]			sII small/ large	2322[‡]
H_2	H—H vibron(s) (pure molecular vibration)	4124[#] 4141[#] 4152[#] 4158[#]	4125[#]		sII large sII small	4135–4155[#] 4115–4135[#]

[a] Raman spectra were recorded under the following conditions: H_2 (g) at 5 MPa, 298 K. H_2 hydrate at 234 K and 200 MPa, THF hydrate at 10–170 K.

[†] From Subramanian (2000).
[§] From Tulk et al. (1998).
[‡] From Nakahara et al. (1988).
[#] From Florusse et al. (2004). THF assignments based on Cadioli et al. (1993).

Kini (2002). The Raman data are based on the works by Sum (1996), Tulk et al. (1998), Subramanian (2000), and Hester (2007). To accompany these tables, select NMR and Raman spectra are given in Figures 6.13 through 6.19. These tables and sample spectra should serve as a useful reference to those embarking on spectroscopic measurements and analysis of clathrate hydrates.

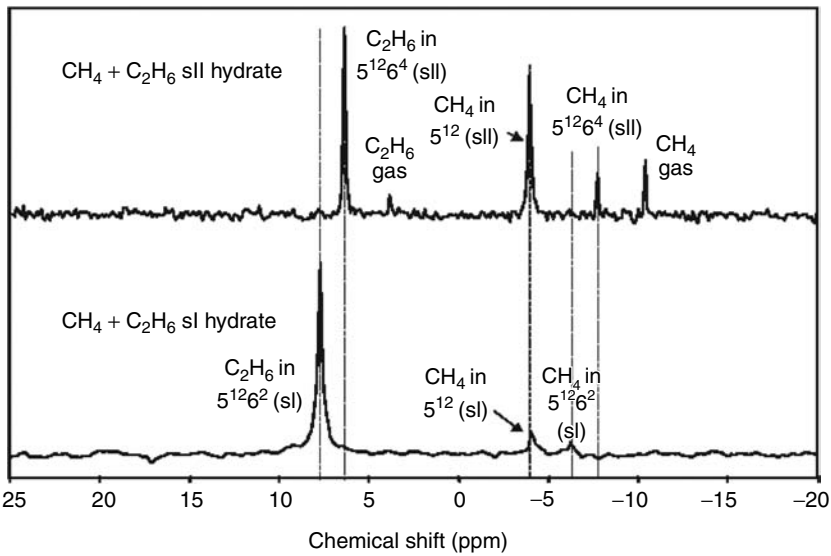

FIGURE 6.13 ^{13}C NMR spectra of sI and sII hydrates of methane + ethane. (From Kini, R.A., *NMR Studies of Methane*, *Ethane*, *and Propane Hydrates: Structure*, *Kinetics*, *and Thermodynamics*, Ph.D. Thesis, Colorado School of Mines, Golden, CO (2002). With permission.)

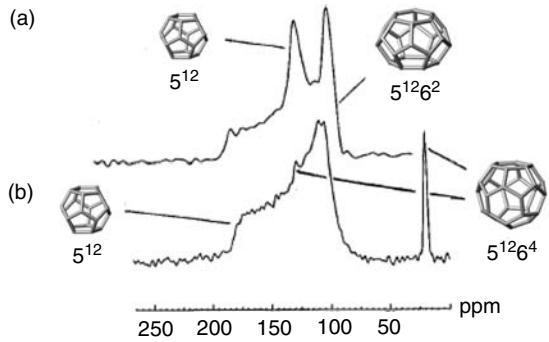

FIGURE 6.14 ^{13}C NMR spectra of (a) $^{13}CO_2$ sI hydrate, (b) $^{13}CO_2 + C_3H_8$ sII hydrate (isotropic line at 18 ppm is due to propane carbons). (From Ripmeester, J.A., and Ratcliffe, C.I., *Energy & Fuels*, **12**, 197 (1998). With permission.)

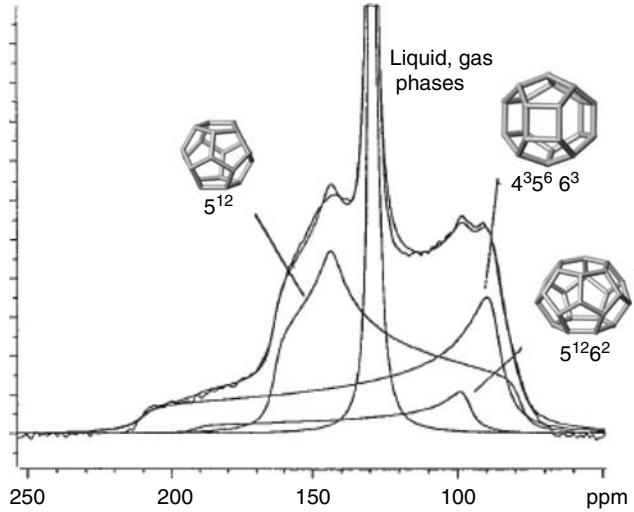

FIGURE 6.15 ^{13}C NMR spectra of $^{13}CO_2$ + neohexane sH hydrate. A small quantity of $^{13}CO_2$ sI hydrate is also present; sH small cages occupied by CO_2. (From Ripmeester, J.A., and Ratcliffe, C.I., *Energy & Fuels*, **12**, 197 (1998). With permission.)

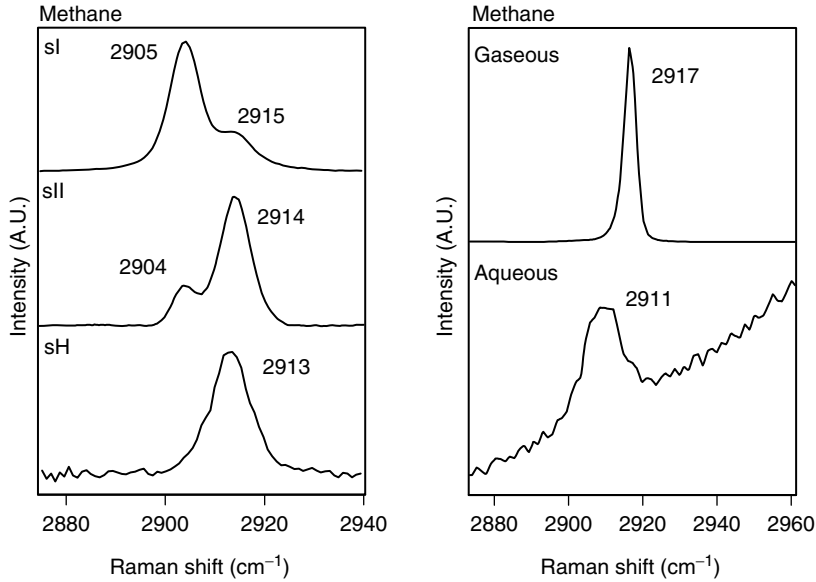

FIGURE 6.16 Raman spectra of methane in the sI, sII (formed with C_2D_6), sH (formed with C_7D_{14}), gas and aqueous phases. (Collected by Hester; Subramanian.)

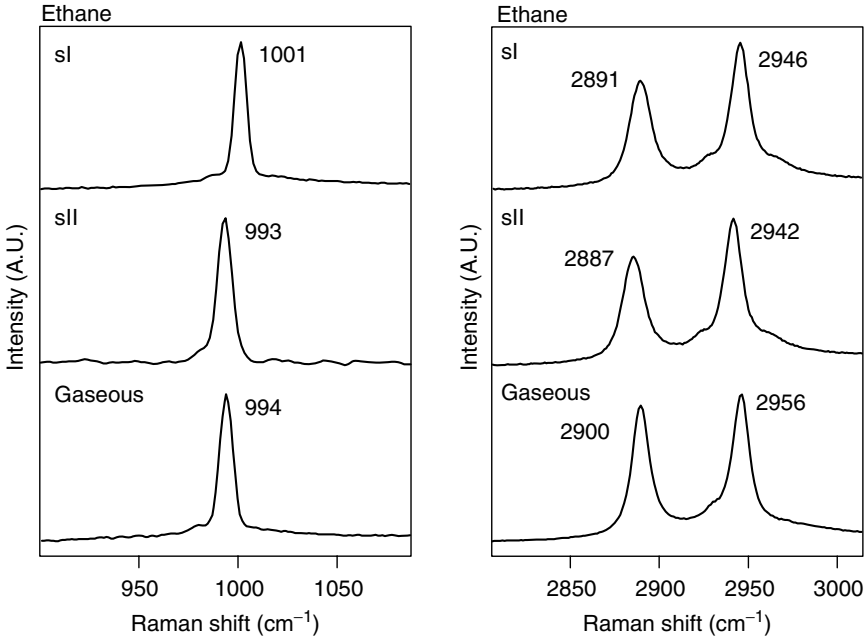

FIGURE 6.17 Raman spectra of ethane in the sI, sII (formed with CD_4), and gas phases. (Collected by Hester.)

6.3 DATA FOR NATURAL GAS HYDRATE PHASE EQUILIBRIA AND THERMAL PROPERTIES

6.3.1 Phase Equilibria Data

6.3.1.1 Equilibria of simple natural gas components

The accuracy of hydrate data has seldom been specified by experimentalists. In the following data, only a cursory effort has been made to exclude inaccurate data for simple hydrates. All three-phase data sets for simple hydrates were plotted (as logarithm pressure versus absolute temperature) to determine outliers.

In general, the data accuracy was surprisingly good. For example, while Deaton and Frost (1946, p. 13) specified that their "pure" ethane contained 2.1% propane and 0.8% methane, effects of those impurities may have counterbalanced each other; those impurities were insufficient to cause the data to fall outside the line formed by other ethane data sets. On the other hand, the simple hydrate data of Hammerschmidt (1934) for propane and isobutane all appear to be outliers on such semilogarithmic plots, because they are at temperatures much too far above the upper quadruple (Q_2) point. Obvious outlying data were excluded from this work; less obvious outliers may be determined by inspection of the plots and subsequent numerical comparisons. The data, followed by the semilogarithmic plots

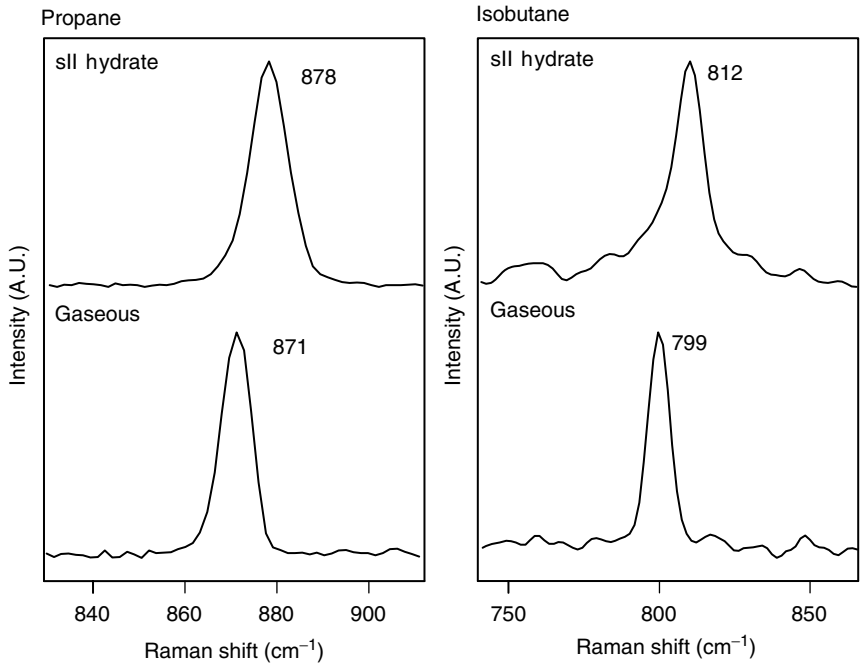

FIGURE 6.18 Raman spectra of the hydrate and gas phases of propane and iso-butane. (Collected by Subramanian.)

for each simple hydrate, are listed chronologically by compound, in the following order: methane, ethane, propane, isobutane, carbon dioxide, nitrogen, and hydrogen sulfide.

While most of the simple hydrate data consist of the three-phase and quadruple point type, the available two-phase simple hydrate data are listed for methane, ethane, propane, and carbon dioxide. Plots of these data are not suitable for comparison between data sets and are therefore not provided.

METHANE

Hydrate: Methane
Reference: Roberts et al. (1940)
Phases: I–H–V and L_W–H–V

T (K)	*P* (MPa)	Phases	*T* (K)	*P* (MPa)	Phases
259.1	1.648	I–H–V	286.5	10.63	L_W–H–V
273.2	2.641	L_W–I–H–V	286.7	10.80	L_W–H–V
280.9	5.847	L_W–H–V			

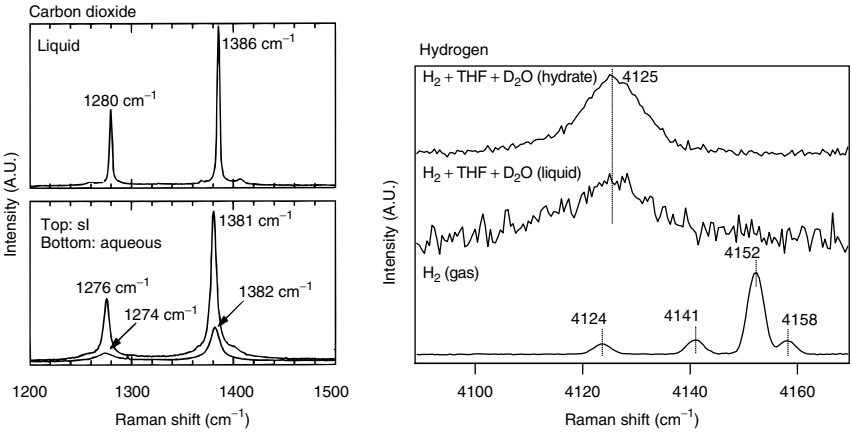

FIGURE 6.19 Raman spectra of carbon dioxide in the liquid, hydrate, and aqueous phase. (Reproduced from Nakano, S., Moritoki, M., Ohgaki, K., *J. Chem. Eng. Data*, **43**, 807 (1998b). With permission from the American Chemical Society.) and hydrogen. (Reproduced from Florusse, L.J., Peters, C.J., Schoonman, J., Hester, K.C., Koh, C.A., Dec, S.F., Marsh, K.N., Sloan, E.D., *Science*, **306**, 469 (2004).)

Hydrate: Methane
Reference: Deaton and Frost (1946)
Phases: I–H–V and L_W–H–V

I–H–V

T (K)	*P* (MPa)	*T* (K)	*P* (MPa)	*T* (K)	*P* (MPa)	*T* (K)	*P* (MPa)
262.4	1.79	266.5	2.08	268.6	2.22	270.9	2.39
264.2	1.90						

L_W–H–V

T (K)	*P* (MPa)	*T* (K)	*P* (MPa)	*T* (K)	*P* (MPa)	*T* (K)	*P* (MPa)
273.7	2.77	275.9	3.43	280.4	5.35	282.6	6.77
274.3	2.90	277.1	3.81	280.9	5.71	284.3	8.12
275.4	3.24	279.3	4.77	281.5	6.06	285.9	9.78
275.9	3.42						

Hydrate: Methane
Reference: Kobayashi and Katz (1949)
Phases: L_W–H–V

T (K)	*P* (MPa)	*T* (K)	*P* (MPa)	*T* (K)	*P* (MPa)	*T* (K)	*P* (MPa)
295.7	33.99	295.9	35.30	301.0	64.81	302.0	77.50

Hydrate: Methane
Reference: McLeod and Campbell (1961)
Phases: L_W–H–V

T (K)	*P* (MPa)	*T* (K)	*P* (MPa)	*T* (K)	*P* (MPa)	*T* (K)	*P* (MPa)
285.7	9.62	285.7	9.62	295.9	34.75	300.9	62.40
286.3	10.31	289.0	13.96	298.7	48.68	301.6	68.09
286.1	10.10	292.1	21.13				

Hydrate: Methane
Reference: Marshall et al. (1964a)
Phases: L_W–H–V

T (K)	*P* (MPa)	*T* (K)	*P* (MPa)	*T* (K)	*P* (MPa)	*T* (K)	*P* (MPa)
290.2	15.9	298.1	44.3	306.7	110.8	315.1	237.5
290.5	15.9	298.2	43.8	310.3	152.7	316.8	271.7
295.2	30.0	300.2	56.9	312.7	187.3	318.3	319.7
295.1	29.9	301.6	65.4	313.7	206.3	319.6	367.8
295.8	33.8	301.6	65.4	314.2	223.9	320.1	397.0

Hydrate: Methane
Reference: Jhaveri and Robinson (1965)
Phases: L_W–H–V

T (K)	*P* (MPa)	*T* (K)	*P* (MPa)	*T* (K)	*P* (MPa)	*T* (K)	*P* (MPa)
273.2	2.65	280.4	5.58	287.3	11.65	291.7	20.11
277.6	4.17	284.7	8.67	288.9	14.05	294.3	28.57

Hydrate: Methane
Reference: Galloway et al. (1970)
Phases: L_W–H–V

T (K)	*P* (MPa)	*T* (K)	*P* (MPa)	*T* (K)	*P* (MPa)	*T* (K)	*P* (MPa)
283.2	7.10	283.2	7.12	288.7	13.11	288.7	13.11

Hydrate: Methane
Reference: Verma (1974)
Phases: L_W–H–V

T (K)	*P* (MPa)	*T* (K)	*P* (MPa)	*T* (K)	*P* (MPa)	*T* (K)	*P* (MPa)
275.2	3.02	278.6	4.385	285.4	9.191	291.2	18.55
276.7	3.69	288.5	13.04	290.7	16.96		

Hydrate: Methane
Reference: Falabella (1975)
Phases: I–H–V

T (K)	*P* (kPa)	*T* (K)	*P* (kPa)	*T* (K)	*P* (kPa)	*T* (K)	*P* (kPa)
148.8	5.3	168.8	21.1	191.3	90.1	193.2	101.3
159.9	12.1	178.2	42.0				

Hydrate: Methane
Reference: Aoyagi et al. (1980)
Phases: V–H

T (K)	*P* (MPa)	H_2O (ppm(mol))	*T* (K)	*P* (MPa)	H_2O (ppm(mol))
240.0	3.45	12.30	260.0	3.45	78.24
240.0	6.90	5.60	260.0	6.90	39.56
240.0	10.34	2.72	260.0	10.34	24.23
250.0	3.45	32.17	270.0	3.45	178.09
250.0	6.90	15.45	270.0	6.90	94.43
250.0	10.34	8.46	270.0	10.34	64.22

Hydrate: Methane
Reference: de Roo et al. (1983)
Phases: L_W–H–V

T (K)	*P* (MPa)	*T* (K)	*P* (MPa)	*T* (K)	*P* (MPa)	*T* (K)	*P* (MPa)
273.3	2.69	279.5	5.04	282.8	7.04	285.0	9.04
275.4	3.34	281.3	6.04	284.0	8.05	286.0	10.04
276.0	3.34						

Hydrate: Methane
Reference: Thakore and Holder (1987)
Phases: L_W–H–V

T (K)	*P* (MPa)	*T* (K)	*P* (MPa)	*T* (K)	*P* (MPa)	*T* (K)	*P* (MPa)
275.4	2.87	277.2	3.90	279.2	4.90	281.2	6.10
276.2	3.37	278.2	4.50				

Hydrate: Methane
Reference: Adisasmito et al. (1991)
Phases: L_W–H–V

T (K)	*P* (MPa)	*T* (K)	*P* (MPa)	*T* (K)	*P* (MPa)	*T* (K)	*P* (MPa)
273.4	2.68	278.3	4.39	282.3	6.65	285.7	9.17
274.6	3.05	279.6	5.02	283.6	7.59	286.4	10.57
276.7	3.72	280.9	5.77	284.7	8.55		

Hydrate: Methane
Reference: Makogon and Sloan (1994)
Phases: I–H–V

T (K)	*P* (MPa)	*T* (K)	*P* (MPa)	*T* (K)	*P* (MPa)	*T* (K)	*P* (MPa)
190.2	0.08251	208.2	0.222	243.2	0.9550	262.4	1.798
198.2	0.1314	218.2	0.3571				

Hydrate: Methane at high pressure
Reference: Dyadin and Aladko (1996)
Phases: L_W–H–V

T (K)	*P* (MPa)	*T* (K)	*P* (MPa)	*T* (K)	*P* (MPa)	*T* (K)	*P* (MPa)
287.0	8	319.0	358	320.8	590	325.0	806
296.6	37	320.0	405	320.6	600	325.4	814
300.8	59	320.4	443	320.2	631	316.8m	816
303.6	84	320.4	450	321.8	642	325.2	840
307.2	117	320.8	467	320.0m	658	325.6	864
308.6	133	320.8	506	322.8	707	326.6	874
310.6	162	320.9	527	324.0	731	326.0	902
311.0	166	320.9	536	319.0m	734	326.4	956
313.8	216	320.9	548	318.6m	749	326.6	983
315.6	242	320.9	572	318.2m	784	326.8	1000
318.4	317	320.8	580	325.2	786		

m = metastable phase.

Hydrate: Methane at High Pressure
Reference: Nakano et al. (1999)
Phases: L_W–H–V

T (K)	P (MPa)	T (K)	P (MPa)
305.08	98	315.74	258
307.13	119	316.50	277
308.74	138	317.20	299
310.29	158	318.29	335
311.64	178	319.17	376
312.92	199	319.80	414
313.88	217	320.33	455
314.83	237	320.54	493

Hydrate: Methane
Reference: Nakamura et al. (2003)
Phases: L_W–H–V

T (K)	P (MPa)	ΔH (kJ/mol)	T (K)	P (MPa)	ΔH (kJ/mol)
274.25	2.92	57.1	282.23	6.53	54.2
275.25	3.22	57.2	282.73	6.88	53.7
276.22	3.55	57.1	283.25	7.25	53.3
277.24	3.92	57.1	283.74	7.65	52.6
278.24	4.33	56.9	284.26	8.10	51.8
279.23	4.79	56.4	284.76	8.55	51.1
280.24	5.31	55.9	285.25	9.03	50.3
281.24	5.89	55.1	285.78	9.54	49.7
281.73	6.20	54.6			

ΔH: Enthalpy of hydrate formation calculated from the above data using the Clapeyron equation assuming ideal hydration.

Hydrate: Methane
Reference: Mohammadi et al. (2005)
Phases: L_W–H–V

Setup	T (K) (±0.1)	P (MPa) (±0.007)
1	280.5	5.426
	283.7	7.584
	285.7	9.584
	286.4	10.342
	289.9	15.837
2	274.6	3.060
	276.2	3.446
	290.6	17.257
	293.6	25.841
	295.8	34.584
	298.3	47.863

Setup 1: 75 cm^3 equilibrium cell.
Setup 2: 650 cm^3 equilibrium rocking cell.

Hydrate: Methane
Reference: Yang et al. (2001)
Phases: L_W–H

T (K)	P (MPa)	x_{CH_4}	T (K)	P (MPa)	x_{CH_4}
278.1	5.79	0.00114	278.1	19.35	0.000960
278.1	8.12	0.00103	273.1	4.98	0.000775
278.2	8.89	0.00104	273.1	5.20	0.000751
278.2	10.44	0.00113	273.1	7.85	0.000770
278.2	11.18	0.00101	273.1	8.42	0.000776
278.1	11.53	0.00106	273.1	11.63	0.000763
278.2	13.76	0.00106	273.1	12.28	0.000752
278.1	16.02	0.00100	273.1	13.50	0.000807
278.1	16.54	0.000953	273.1	14.81	0.000765
278.1	19.29	0.000954			

x_{CH_4}: mole fraction of methane in water.

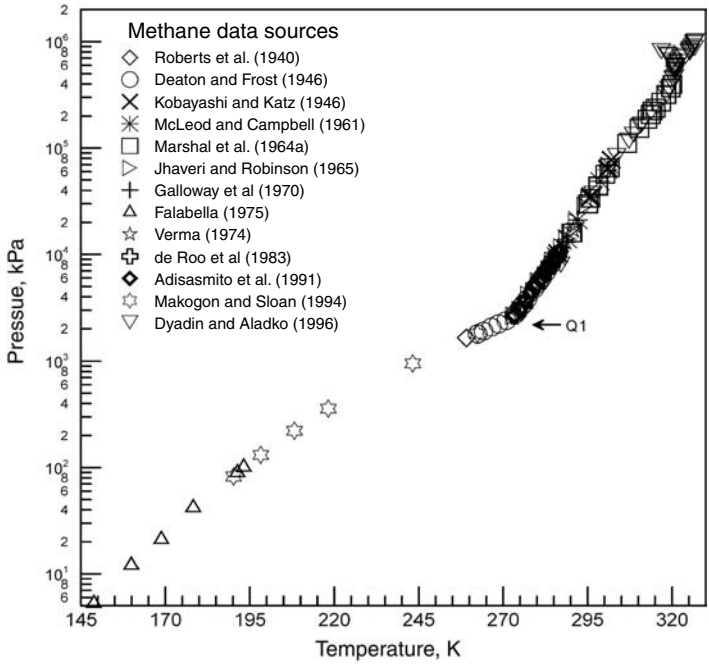

FIGURE 6.20 Three-phase data for simple hydrates of methane.

Hydrate: Methane
Reference: Yang (2000)
Phases: L_W–H

T (K)	P (MPa)	x_{CH_4} in water
276.19	50.00	0.00125
277.85	50.81	0.00150
279.85	50.98	0.00165
280.47	51.26	0.00175
276.36	101.00	0.00125
278.71	101.73	0.00150
280.11	101.88	0.00165
280.65	102.43	0.00175
276.67	127.10	0.00125
278.90	127.22	0.00150
280.39	127.35	0.00165
281.08	127.45	0.00175
276.91	143.10	0.00125

Continued

T (K)	P (MPa)	x_{CH_4} in water
279.20	143.62	0.00150
280.59	143.25	0.00165
281.65	143.24	0.00175

x_{CH_4}: mole fraction of methane in water.

Hydrate: Methane
Reference: Seo and Lee (2002)
Phases: L_W–H

T (K)	P (MPa)	x_{CH_4}	T (K)	P (MPa)	x_{CH_4}
274.15	6.00	0.001264	282.15	15.00	0.001621
278.15	6.00	0.001452	286.15	15.00	0.001826
274.15	10.00	0.001202	274.15	20.00	0.001106
278.15	10.00	0.001414	278.15	20.00	0.001322
282.15	10.00	0.001687	282.15	20.00	0.001583
274.15	15.00	0.001157	286.15	20.00	0.001799
278.15	15.00	0.001362			

x_{CH_4}: mole fraction of methane in water.

Hydrate: Methane
Reference: Servio and Englezos (2002)
Phases: L_W–H, L_W–H–V, L_W–V

T (K)	P (MPa)	x_{CH_4}	Phases	T (K)	P (MPa)	x_{CH_4}	Phases
274.35	3.5	0.001170	L_W–H	281.55	5.0	0.001524	L_W–V
275.45	3.5	0.001203	L_W–H	282.65	5.0	0.001357	L_W–V
276.25	3.5	0.001240	L_W–H–V	275.25	6.5	0.001201	L_W–H
278.65	3.5	0.001190	L_W–V	280.15	6.5	0.001567	L_W–H
280.45	3.5	0.001102	L_W–V	282.05	6.5	0.001850	L_W–H–V
274.15	5.0	0.001190	L_W–H	283.25	6.5	0.001720	L_W–V
277.35	5.0	0.001360	L_W–H	284.35	6.5	0.001681	L_W–V
279.65	5.0	0.001600	L_W–H–V				

x_{CH_4}: mole fraction of methane in water.

Hydrate: Methane
Reference: Chou, I.M. and Burruss, R.C. (Personal Communication, December 18, 2006).
Phases: L_W–H

T (K)	P (MPa)	x_{CH_4}	T (K)	P (MPa)	x_{CH_4}
278.1	5.79	0.00114	278.1	19.35	0.00096
278.1	8.12	0.00103	273.1	4.98	0.000775
278.2	8.89	0.00104	273.1	5.20	0.000751
278.2	10.44	0.00113	273.1	7.85	0.00077
278.2	11.18	0.00101	273.1	8.42	0.000776
278.1	11.53	0.00106	273.1	11.63	0.000763
278.2	13.76	0.00106	273.1	12.28	0.000752
278.1	16.02	0.00100	273.1	13.50	0.000807
278.1	16.54	0.000953	273.1	14.81	0.000765
278.1	19.29	0.000954			

x_{CH_4}: mole fraction of methane in water in the absence of a vapor phase.

Ethane

Hydrate: Ethane
Reference: Roberts et al. (1940)
Phases: I–H–V, L_W–H–V, L_W–H–$L_{C_2H_6}$

T (K)	P (kPa)	Phases	T (K)	P (kPa)	Phases
260.8	294	I–H–V	285.8	2537	L_W–H–V
260.9	290	I–H–V	287.0	3054	L_W–H–V
269.3	441	I–H–V	287.7	4909	L_W–H–L_E
273.4	545	L_W–H–V	287.8	3413	L_W–H–L_E
275.4	669	L_W–H–V	287.8	4289	L_W–H–L_E
277.6	876	L_W–H–V	288.1	3716	L_W–H–L_E
279.1	1048	L_W–H–V	288.1	6840	L_W–H–L_E
219.7	1131	L_W–H–V	288.2	4944	L_W–H–L_E
281.1	1317	L_W–H–V	288.2	5082	L_W–H–L_E
282.8	1641	L_W–H–V	288.3	4358	L_W–H–L_E
284.4	2137	L_W–H–V	288.4	6840	L_W–H–L_E
284.6	2055	L_W–H–V			

Hydrate: Ethane
Reference: Deaton and Frost (1946)
Phases: I–H–V and L_W–H–V

I–H–V

T (K)	*P* (kPa)	*T* (K)	*P* (kPa)	*T* (K)	*P* (kPa)	*T* (K)	*P* (kPa)
263.6	313	266.5	357	269.3	405	272.0	457

L_W–H–V

T (K)	*P* (kPa)	*T* (K)	*P* (kPa)	*T* (K)	*P* (kPa)	*T* (K)	*P* (kPa)
273.7	510	278.7	931	280.4	1165	283.2	1689
273.7	503	278.7	931	280.9	1255	284.3	1986
274.8	579	279.3	1007	281.5	1345	285.4	2303
275.9	662	279.8	1083	282.1	1448	285.4	2310
277.6	814	280.4	1165	282.6	1558	286.5	2730

Hydrate: Ethane
Reference: Reamer et al. (1952b)
Phases: L_W–H–V

T (K)	*P* (kPa)	*T* (K)	*P* (kPa)	*T* (K)	*P* (kPa)	*T* (K)	*P* (kPa)
279.9	972	282.8	1666	284.7	2129	287.4	3298

Hydrate: Ethane
Reference: Galloway et al. (1970)
Phases: L_W–H–V

T (K)	*P* (kPa)	*T* (K)	*P* (kPa)	*T* (K)	*P* (kPa)
277.6	814	277.7	823	282.5	1551

Hydrate: Ethane
Reference: Falabella and Vanpee (1974)
Phases: I–H–V

T (K)	*P* (kPa)	*T* (K)	*P* (kPa)	*T* (K)	*P* (kPa)	*T* (K)	*P* (kPa)
200.8	8.3	230.2	56.4	240.4	98.1	240.8	101.3
215.7	22.1						

Hydrate: Ethane
Reference: Holder and Grigoriou (1980)
Phases: L_W–H–V

T (K)	*P* (kPa)	*T* (K)	*P* (kPa)	*T* (K)	*P* (kPa)	*T* (K)	*P* (kPa)
277.5	780	279.9	1040	283.3	1660	286.5	2620
278.1	840	281.5	1380	284.5	2100		

Hydrate: Ethane
Reference: Holder and Hand (1982)
Phases: L_W–H–V

T (K)	*P* (MPa)	*T* (K)	*P* (MPa)	*T* (K)	*P* (MPa)	*T* (K)	*P* (MPa)
278.8	950	282.0	1450	286.0	2510	288.2	3360
280.2	1140	281.1	1280	286.5	2600		

Hydrate: Ethane
Reference: Ng and Robinson (1985)
Phases: L_W–H–$L_{C_2H_6}$

T (K)	*P* (MPa)	*T* (K)	*P* (MPa)	*T* (K)	*P* (MPa)	*T* (K)	*P* (MPa)
288.0	3.33	288.2	5.00	288.5	6.99	289.7	13.95
288.1	3.84	288.4	6.06	289.2	10.39	290.6	20.34

Hydrate: Ethane
Reference: Avlonitis (1988)
Phases: L_W–H–V

T (K)	*P* (MPa)	*T* (K)	*P* (MPa)	*T* (K)	*P* (MPa)	*T* (K)	*P* (MPa)
277.8	0.848	280.4	1.200	282.3	1.551	285.9	2.461
278.6	0.945	281.5	1.365	284.0	1.889	287.2	3.082
279.4	1.055	282.1	1.510				

Hydrate: Ethane
Reference: Song and Kobayashi (1994)
Phases: H–V and H–$L_{C_2H_6}$

H–V Isobar at 2.483 MPa

T (K)	$y_{H_2O} \times 10^3$	T (K)	$y_{H_2O} \times 10^3$	T (K)	$y_{H_2O} \times 10^3$
276.2	0.345	280.0	0.455	283.6	0.575

H–$L_{C_2H_6}$ Isobar at 3.45 MPa

T (K)	$x_{H_2O} \times 10^3$	T (K)	$x_{H_2O} \times 10^3$	T (K)	$x_{H_2O} \times 10^3$
281.2	0.135	271.2	0.058	240.0	0.004
276.2	0.090	260.0	0.024		

Hydrate: Ethane
Reference: Nakano et al. (1998a)
Phases: L_W–H–$L_{C_2H_6}$

T (K)	P (MPa)	T (K)	P (MPa)	T (K)	P (MPa)
290.42	19.48	293.01	39.15	295.91	61.60
290.85	23.00	293.24	40.62	296.51	67.52
291.16	25.02	293.35	41.57	297.12	71.89
291.36	26.21	293.56	42.49	297.57	77.30
291.66	28.73	293.61	43.32	297.65	77.43
291.90	30.56	293.95	45.37	297.73	78.09
292.12	31.67	294.76	51.92	298.01	82.19
292.36	33.63	295.60	59.83	298.36	83.75
292.56	34.39	295.80	60.86		

Hydrate: Ethane
Reference: Yang (2000)
Phases: L_W–H

P (MPa)	T (K)	$x_{C_2H_6}$ in water
51.0	277.31	0.0004115
101.0	277.82	0.0004115
151.0	278.46	0.0004115

Hydrate: Ethane
Reference: Morita et al. (2000)
Phases: L_W–H–$L_{C_2H_6}$

T (K)	*P* (MPa)	*T* (K)	*P* (MPa)
298.01	89	314.20	298
299.15	99	315.26	318
300.82	119	316.39	336
302.56	139	317.49	355
304.15	158	318.67	374
305.65	178	319.65	393
307.26	198	320.72	413
308.57	217	322.11	436
301.07	237	322.83	454
311.44	257	323.93	479
312.86	279		

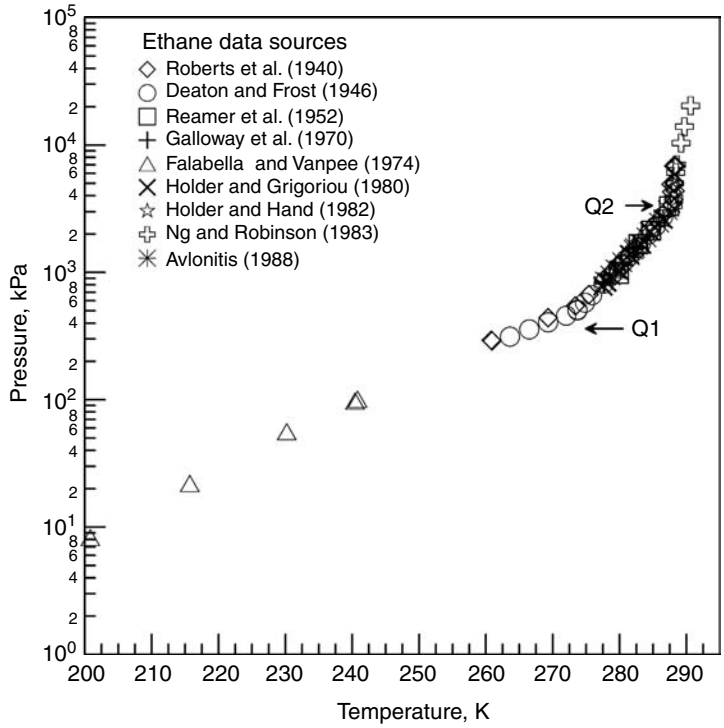

FIGURE 6.21 Three-phase data for simple hydrates of ethane.

Propane

Hydrate: Propane
Reference: Wilcox et al. (1941)
Phases: L_W–H–$L_{C_3H_8}$

T (K)	*P* (kPa)	*T* (K)	*P* (kPa)	*T* (K)	*P* (kPa)	*T* (K)	*P* (kPa)
278.9	807	278.6	1758	279.2	2902	278.9	6115
278.6	1296	278.8	2034	278.8	4247		

Hydrate: Propane
Reference: Miller and Strong (1946)
Phases: L_W–H–V

T (K)	*P* (kPa)	*T* (K)	*P* (kPa)	*T* (K)	*P* (kPa)	*T* (K)	*P* (kPa)
273.2	165	273.7	186	277.1	390	277.8	459
273.4	172	273.9	190	277.2	393	278.0	472
273.5	176	276.8	365				

Hydrate: Propane
Reference: Deaton and Frost (1946)
Phases: I–H–V and L_W–H–V

I–H–V

T (K)	*P* (kPa)	*T* (K)	*P* (kPa)	*T* (K)	*P* (kPa)	*T* (K)	*P* (kPa)
261.2	100	267.4	132	269.8	149	272.9	172
264.2	115	267.6	135	272.2	167		

L_W–H–V

T (K)	*P* (kPa)	*T* (K)	*P* (kPa)	*T* (K)	*P* (kPa)	*T* (K)	*P* (kPa)
273.7	183	274.8	232	275.9	301	277.1	386
273.7	183	275.4	270				

Hydrate: Propane
Reference: Reamer et al. (1952)
Phases: L_W–H–V and L_W–H–$L_{C_3H_8}$

L_W–H–V

T (K)	*P* (kPa)	*T* (K)	*P* (kPa)	*T* (K)	*P* (kPa)
274.3	241	275.7	305	277.2	414

L_W–H–$L_{C_3H_8}$

T (K)	*P* (kPa)	*T* (K)	*P* (kPa)	*T* (K)	*P* (kPa)
278.6	684	278.7	1477	278.8	2046

Hydrate: Propane
Reference: Robinson and Mehta (1971)
Phases: L_W–H–V

T (K)	*P* (kPa)	*T* (K)	*P* (kPa)	*T* (K)	*P* (kPa)	*T* (K)	*P* (kPa)
274.3	207	276.4	331	277.8	455	278.9	552*
274.8	241						

* = Q_2 Quadruple point (L_W–H–V–L_{C_3}).

Hydrate: Propane
Reference: Verma (1974)
Phases: L_W–H–V, L_W–H–$L_{C_3H_8}$ and L_W–H–V–$L_{C_3H_8}$

L_W–H–V, L_W–H–$L_{C_3H_8}$

T (K)	*P* (kPa)	*T* (K)	*P* (kPa)	*T* (K)	*P* (kPa)	*T* (K)	*P* (kPa)
273.9	188	275.7	288	276.7	361	278.0	512
274.6	219	276.2	322	277.4	425	278.4	562*
275.1	250						

* = L_W–H–V–L_{C_3} Quadruple point.

L_W–H–V–$L_{C_3H_8}$

T (K)	*P* (MPa)	*T* (K)	*P* (MPa)	*T* (K)	*P* (MPa)	*T* (K)	*P* (MPa)
278.42	3.87	278.5	7.03	278.6	11.3	278.5	16.8

Hydrate: Propane
Reference: Holder and Godbole (1982)
Phases: I–H–V

T (K)	*P* (kPa)	*T* (K)	*P* (kPa)	*T* (K)	*P* (kPa)	*T* (K)	*P* (kPa)
247.9	48.2	251.6	58.3	258.2	81.1	260.9	94.5
251.4	58.3	255.4	69.6	260.8	90.5	262.1	99.4

Hydrate: Propane
Reference: Kubota et al. (1984)
Phases: L_W–H–V

T (K)	*P* (MPa)	*T* (K)	*P* (MPa)	*T* (K)	*P* (MPa)	*T* (K)	*P* (MPa)
274.2	0.207	276.2	0.323	277.6	0.455	278.2	0.517
274.6	0.232	276.8	0.371	278.0	0.500	278.4	0.542
274.8	0.239						

Hydrate: Propane
Reference: Thakore and Holder (1987)
Phases: L_W–H–V

T (K)	*P* (kPa)	*T* (K)	*P* (kPa)	*T* (K)	*P* (kPa)	*T* (K)	*P* (kPa)
274.2	217	276.2	310	277.2	450	278.2	510
275.2	248						

Hydrate: Propane
Reference: Patil (1987)
Phase: L_W–H–V

T (K)	*P* (kPa)	*T* (K)	*P* (kPa)	*T* (K)	*P* (kPa)	*T* (K)	*P* (kPa)
273.6	207	276.2	338	277.2	417	278.0	510
274.6	248						

Hydrate: Propane
Reference: Song and Kobayashi (1994)
Phases: H–L_{C_3}

Isobar at 1.1 MPa

T (K)	$x_{H_2O} \times 10^3$	T (K)	$x_{H_2O} \times 10^3$	T (K)	$x_{H_2O} \times 10^3$
276.2	0.116	261.8	0.037	235.6	0.004
267.8	0.060	255.6	0.021		
264.4	0.046	246.6	0.011		

Hydrate: Propane
Reference: Mooijer-van den Heuvel et al. (2002)
Phase: L_W–H–V, L_W–H–$L_{C_3H_8}$ and Q_2

Feed composition: $x_{H_2O} = 0.9503$, $x_{C_3H_8} = 0.0407$
Q_2 at $T = 278.62$, $P = 0.6$ MPa

L_W–H–V		L_W–H–$L_{C_3H_8}$	
T (K)	P (MPa)	T (K)	P (MPa)
276.77	0.368	278.71	0.643
277.01	0.377	278.75	0.893
277.22	0.405	278.75	1.393
277.36	0.425	278.75	1.891
277.44	0.433	278.78	1.893
277.87	0.473	278.80	2.391
278.01	0.527	278.80	2.891
278.22	0.483	278.79	2.893
278.55	0.547	278.75	3.891
		278.77	3.391
		278.81	4.391
		278.79	5.892
		278.86	6.392
		278.88	6.892
		278.80	8.393
		278.84	8.893
		278.89	9.893

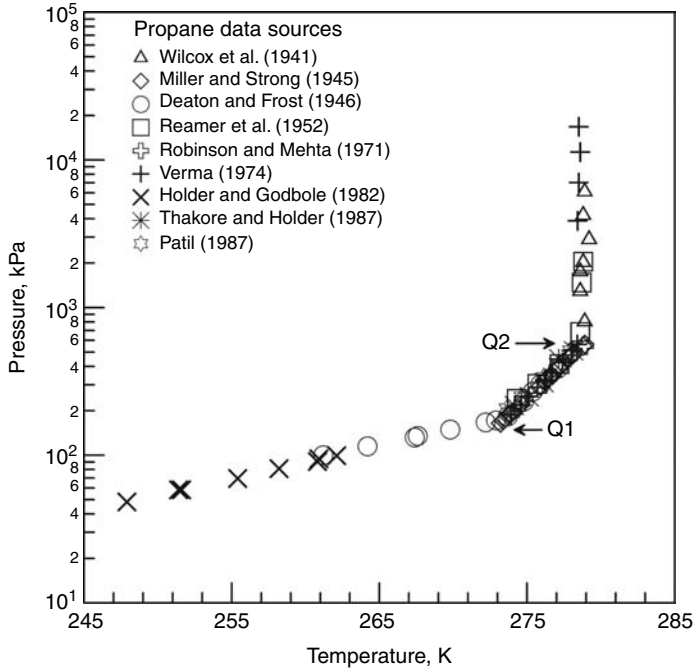

FIGURE 6.22 Three-phase data for simple hydrates of propane.

ISOBUTANE

Hydrate: Isobutane
Reference: Schneider and Farrar (1968)
Phases: L_W–H–V and I–H–V

I–H–V

T (K)	*P* (kPa)	*T* (K)	*P* (kPa)	*T* (K)	*P* (kPa)	*T* (K)	*P* (kPa)
273.1	109	272.8	109	272.3	105	271.2	95
275.1	109	272.8	102	272.2	103		

L_W–H–V

T (K)	*P* (kPa)	*T* (K)	*P* (kPa)	*T* (K)	*P* (kPa)	*T* (K)	*P* (kPa)
275.1	167	274.4	141	273.6	124	273.2	109
275.0	165	274.2	137	273.4	117	273.2	110
274.9	163	273.9	130				

Hydrate: Isobutane
Reference: Rouher and Barduhn (1969)
Phases: L_W–H–V

T (K)	*P* (kPa)	*T* (K)	*P* (kPa)	*T* (K)	*P* (kPa)	*T* (K)	*P* (kPa)
273.2	115	273.7	126	274.1	137	274.6	151
273.3	118	273.8	129	274.2	140	274.6	157
273.5	122	273.9	132	274.2	140	274.8	160
273.5	122	274.0	135	274.3	143	275.0	164
273.6	123	274.0	134	274.4	147	275.0	168
273.6	124	274.0	135	274.6	151	275.0	169

Hydrate: Isobutane
Reference: Wu et al. (1976)
Phases: L_W–H–$L_{iC_4H_{10}}$

T (K)	*P* (kPa)	*T* (K)	*P* (kPa)	*T* (K)	*P* (kPa)	*T* (K)	*P* (kPa)
275.4	226	275.4	903	275.6	5650	275.8	14270
275.4	357	275.5	2410				

Hydrate: Isobutane
Reference: Holder and Godbole (1982)
Phases: I–H–V

T (K)	*P* (kPa)	*T* (K)	*P* (kPa)	*T* (K)	*P* (kPa)	*T* (K)	*P* (kPa)
241.4	17.6	253.7	35.1	263.3	66.4	269.4	89.7
243.4	20.2	256.5	42.8	268.1	85.5	269.5	91.3
248.4	26.4	259.7	53.5				

Hydrate: Isobutane
Reference: Thakore and Holder (1987)
Phases: L_W–H–V

T (K)	*P* (kPa)	*T* (K)	*P* (kPa)
274.4	128	274.6	155

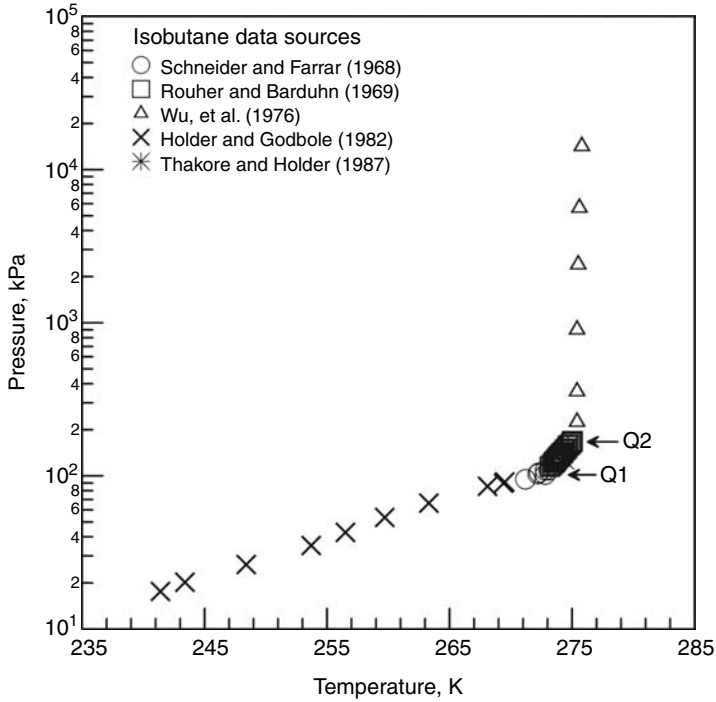

FIGURE 6.23 Three-phase data for simple hydrates of iso-butane.

CARBON DIOXIDE

Hydrate: Carbon dioxide
Reference: Deaton and Frost (1946)
Phases: L_W–H–V

T (K)	*P* (kPa)	*T* (K)	*P* (kPa)	*T* (K)	*P* (kPa)	*T* (K)	*P* (kPa)
273.7	1324	275.4	1613	278.7	2427	281.5	3530
273.7	1324	276.5	1848	278.7	2413	281.9	3709
274.3	1393	277.6	2075	279.8	2758	282.6	4130
274.3	1420	277.6	2082	279.8	2786	282.9	4323
274.3	1420	277.6	2103	280.9	3213		

Hydrate: Carbon dioxide
Reference: Unruh and Katz (1949)
Phases: L_W–H–V

T (K)	*P* (kPa)	*T* (K)	*P* (kPa)	*T* (K)	*P* (kPa)
277.2	2041	280.9	3227	283.1	4502*
279.2	2586	281.9	3689		

* = Q_2 Quadruple point (L_W–H–V–L_{CO_2}).

Hydrate: Carbon dioxide
Reference: Larson (1955)
Phases: I–H–V, L_W–H–V, and H–V–L_{CO_2}

I–H–V

T (K)	*P* (kPa)	*T* (K)	*P* (kPa)	*T* (K)	*P* (kPa)	*T* (K)	*P*(kPa)
256.8	545	268.9	924	270.7	1000	271.7	1041
264.0	752	270.0	972	271.4	1027	271.8	1048
267.4	869						

L_W–H–V

T (K)	*P* (kPa)	*T* (K)	*P* (kPa)	*T* (K)	*P* (kPa)	*T* (K)	*P* (kPa)
271.8	1048	274.4	1386	277.8	2137	280.5	3020
271.9	1048	275.0	1510	278.0	2165	280.8	3158
272.2	1089	275.1	1496	278.6	2344	281.1	3282
272.5	1110	275.7	1634	278.8	2448	281.5	3475
273.1	1200	276.0	1682	279.1	2530	281.9	3634
273.4	1234	276.2	1717	279.2	2544	282.0	3689
273.5	1241	276.5	1806	279.8	2730	282.3	3868
273.9	1317	276.9	1889	280.1	2861	283.1	4468
274.1	1351	277.2	1951	280.2	2923	283.2	4502

H–V–L_{CO_2}

T (K)	*P* (kPa)	*T* (K)	*P* (kPa)	*T* (K)	*P* (kPa)	*T* (K)	*P* (kPa)
258.8	2337	263.8	2696	272.1	3385	281.5	4316
256.5	2179	264.4	2744	273.1	3475	281.4	4302
260.2	2434	264.9	2779	274.4	3592	283.1	4489
258.5	2310	266.1	2875	275.1	3661	282.8	4454
261.2	2503	267.3	2972	276.3	3778	283.5	4523
260.1	2420	268.5	3068	277.0	3847	283.7	4558
262.5	2599	270.2	3220	278.9	4040	284.5	4640
262.5	2599	270.8	3268	279.1	4061	285.0	4695

Hydrates: Carbon dioxide
Reference: Takenouchi and Kennedy (1965)
Phases: L_W–H–L_{CO_2}

T (K)	*P* (MPa)	*T* (K)	*P* (MPa)	*T* (K)	*P* (MPa)	*T* (K)	*P* (MPa)
2832	4.500	285.2	24.30	289.2	88.10	291.6	149.30
283.6	8.500	286.2	37.20	290.2	109.50	292.2	165.10
284.2	13.00	287.2	52.20	290.6	122.00	292.7	186.20
284.6	18.20	288.2	69.60	291.2	135.30		

Hydrate: Carbon dioxide
Reference: Miller and Smythe (1970)
Phases: I–H–V

T (K)	*P* (kPa)	*T* (K)	*P* (kPa)	*T* (K)	*P* (kPa)	*T* (K)	*P* (kPa)
151.5	0.535	167.1	2.81	176.9	6.77	186.8	14.5
162.4	1.77	171.5	4.20	182.2	10.3	192.5	21.9

Hydrate: Carbon dioxide
Reference: Robinson and Mehta (1971)
Phases: L_W–H–V

T (K)	*P* (kPa)	*T* (K)	*P* (kPa)	*T* (K)	*P* (kPa)	*T* (K)	*P* (kPa)
273.9	1379	276.1	1758	280.7	3130	283.3	4468*
275.2	1558	278.9	2420	282.0	3840		

* = Quadruple point (L_W–H–V–L_{CO_2}).

Hydrate: Carbon dioxide
Reference: Ng and Robinson (1985)
Phases: L_W–H–V, L_W–H–L_{CO_2}

L_W–H–V

T (K)	*P* (MPa)	*T* (K)	*P* (MPa)	*T* (K)	*P* (MPa)
279.6	2.74	282.1	4.01	282.8	4.36

L_W–H–L_{CO_2}

T (K)	*P* (MPa)	*T* (K)	*P* (MPa)	*T* (K)	*P* (MPa)	*T* (K)	*P* (MPa)
282.9	5.03	283.1	6.47	283.6	11.98	283.9	14.36
282.9	5.62	283.2	9.01				

Hydrates: Carbon dioxide
Reference: Vlahakis et al. (1972)
Phases: L_W–H–V, H–L_{CO_2}–V

H–L_{CO_2}–V

T (K)	*P* (MPa)	*T* (K)	*P* (MPa)	*T* (K)	*P* (MPa)	*T* (K)	*P* (MPa)
263.0	2.644	269.1	3.131	275.1	3.669	281.6	4.331
264.0	2.717	269.2	3.134	275.2	3.674	282.0	4.379
264.1	2.724	270.1	3.213	275.2	3.681	282.1	4.383
264.1	2.727	270.2	3.221	277.0	3.858	283.0	4.482
264.6	2.726	271.0	3.292	277.3	3.885	283.2	4.492
265.2	2.803	271.1	3.304	278.0	3.955	283.2	4.497
265.6	2.845	271.2	3.305	278.1	3.960	283.6	4.551
266.2	2.884	272.3	3.405	278.1	3.966	284.6	4.662
266.3	2.892	273.1	3.481	278.2	3.965	285.1	4.713
267.1	2.962	273.1	3.484	279.1	4.071	287.0	4.951
267.2	2.965	273.2	3.482	281.0	4.268	288.0	5.058
267.8	3.021	274.1	3.576	281.1	4.273	288.0	5.065
268.2	3.045	274.2	3.582	281.2	4.295	288.0	5.076
268.3	3.058	27.51	3.664				

L_W–H–V

T (K)	*P* (MPa)	*T* (K)	*P* (MPa)	*T* (K)	*P* (MPa)	*T* (K)	*P* (MPa)
271.6	1.040	274.2	1.387	277.7	2.093	281.2	3.327
271.7	1.045	274.7	1.462	277.7	2.127	281.4	3.471
271.7	1.043	274.7	1.472	278.1	2.230	281.8	3.626
272.0	1.088	275.3	1.569	278.6	2.372	281.8	3.680
272.1	1.096	275.7	1.651	278.7	2.400	282.2	3.833
272.3	1.117	276.1	1.742	278.8	2.411	282.3	3.947
272.7	1.163	276.6	1.844	279.2	2.541	282.6	4.082
273.1	1.218	276.7	1.849	279.7	2.737	282.7	4.165
273.1	1.222	277.0	1.927	280.1	2.879	282.9	4.311
273.6	1.300	277.2	1.983	280.4	2.989	283.2	4.508
273.9	1.342	277.2	1.984	280.7	3.134	283.2	4.509

Hydrate: Carbon dioxide
Reference: Falabella (1975)
Phases: I–H–V

T (K)	*P* (kPa)	*T* (K)	*P* (kPa)	*T* (K)	*P* (kPa)	*T* (K)	*P* (kPa)
194.5	24.8	213.8	81.6	218.2	104.3	217.8	101.3
203.2	43.3						

Hydrate: Carbon dioxide
Reference: Song and Kobayashi (1987)
Phases: As noted

T (K)	*P* (kPa)	H_2O Mol fraction $\times 10^3$	Phases	*T* (K)	*P* (kPa)	H_2O Mol fraction $\times 10^3$	Phases
251.8	690	0.1800	V–H	290.2	4830	0.8229	V–L_W
254.2	690	0.2190	V–H	298.2	4830	1.2787	V–L_W
265.2	690	0.5570	V–I	288.7	5240	0.6400	V–L_W
294.3	690	4.3276	V–Lw	288.7	5240	1.1200	L_{CO_2}–L_W
255.2	1380	0.1142	V–H	293.4	5790	0.8999	V–L_W
258.0	1380	0.1471	V–H	293.4	5790	1.5000	L_{CO_2}–L_W
262.2	1380	0.2201	V–H	257.2	6210	0.5170	L_{CO_2}–H
271.2	1380	0.4885	V–H	263.7	6210	0.6647	L_{CO_2}–H
275.2	1380	0.6836	V–Lw	280.2	6210	1.0960	L_{CO_2}–H
273.2	2070	0.2775	V–H	299.8	6690	1.2700	V–L_W
275.7	2070	0.4368	V–H	299.8	6690	1.9541	L_{CO_2}–L_W
288.7	2070	1.0656	V–Lw	302.7	7170	1.4981	V–L_W
268.8	2070	0.2321	V–H	302.7	7170	2.1940	L_{CO_2}–L_W
260.7	2070	0.1194	V–H	304.2	7390	2.1079	3-ϕ endpt
257.2	2070	0.0890	V–H	256.2	8280	1.0890	L_{CO_2}–H
252.7	2070	0.2013	L_{CO_2}–H	265.9	8280	1.5741	L_{CO_2}–H
245.2	2070	0.1361	L_{CO_2}–H	270.2	8280	1.8695	L_{CO_2}–H
255.4	3450	0.2616	L_{CO_2}–H	286.9	8280	2.7852	L_{CO_2}–L_W
260.2	3450	0.3222	L_{CO_2}–H	298.2	8280	3.0152	L_{CO_2}–L_W
269.7	3450	0.4585	L_{CO_2}–H	256.2	10340	1.2738	L_{CO_2}–H
274.2	3450	0.2410	V–H	264.2	10340	1.6509	L_{CO_2}–H
278.7	3450	0.3794	V–H	276.2	10340	2.4687	L_{CO_2}–H
285.2	3450	0.6030	V–L_W	298.2	10340	3.3739	L_{CO_2}–L_W
293.2	3450	1.0010	V–Lw	255.4	13790	1.5091	L_{CO_2}–H
255.4	4830	0.3313	L_{CO_2}–H	260.1	13790	1.8057	L_{CO_2}–H
263.2	4830	0.4705	L_{CO_2}–H	267.7	13790	2.2043	L_{CO_2}–H
269.7	4830	0.5402	L_{CO_2}–H	275.9	13790	2.7441	L_{CO_2}–H
276.2	4830	0.7182	L_{CO_2}–H	286.3	13790	3.3627	L_{CO_2}–L_W

Hydrate: Carbon dioxide
Reference: Adisasmito et al. (1991)
Phases: L_W–H–V

T (K)	*P* (MPa)	*T* (K)	*P* (MPa)	*T* (K)	*P* (MPa)	*T* (K)	*P* (MPa)
274.3	1.42	277.6	2.11	280.6	3.12	282.1	3.81
275.5	1.63	279.1	2.55	281.5	3.51	282.9	4.37
276.8	1.90						

Hydrate: Carbon dioxide + pure water
Reference: Ohgaki et al. (1993)
Phases: L_W–H–V, H–L_W–L_{CO_2}, H–L_{CO_2}–V, L_W–L_{CO_2}–V (no hydrate)

L_W–H–V

T (K)	*P* (MPa)	*T* (K)	*P* (MPa)
273.36	1.338	278.13	2.482
274.03	1.509	278.69	2.656
274.94	1.651	278.76	2.604
276.01	1.839	279.23	3.030
276.29	1.971	279.50	3.019
276.56	1.966	280.13	3.228
276.57	2.005	280.34	3.395
276.98	2.108	280.79	3.667
277.51	2.238	281.10	4.085
273.95	1.347	279.42	2.674
275.37	1.544	281.21	3.279
276.82	1.977	281.79	3.831
277.82	2.116		
275.97	1.740	278.75	2.499
276.54	1.881	279.16	2.614
277.45	2.126	280.33	3.076
278.66	2.497		

H–L_W–L_{CO_2}

T (K)	*P* (MPa)	*T*(K)	*P* (MPa)
281.52	4.386	281.70	6.861
281.14	5.596	282.21	8.615
281.28	5.693		
283.23	4.541	283.59	8.930
283.25	6.306		

H–L_{CO_2}–V

T (K)	*P* (MPa)	*T* (K)	*P* (MPa)
274.92	3.637	278.80	4.012
275.90	3.730	279.82	4.115
276.85	3.823	280.82	4.222
277.84	3.910	281.27	4.281

Continued

L_W–L_{CO_2}–V			
T **(K)**	***P*** **(MPa)**	***T*** **(K)**	***P*** **(MPa)**
283.07	4.485	285.43	4.748
283.15	4.495	286.38	4.860
283.46	4.524	287.39	4.977
283.95	4.578	288.40	5.089
284.47	4.636	289.37	5.216

Hydrate: Carbon dioxide
Reference: Nakano et al. (1998b)
Phases: L_W–H–L_{CO_2}

T **(K)**	***P*** **(MPa)**	***T*** **(K)**	***P*** **(MPa)**
289.73	104	293.97	316
290.32	117	294.00[a]	328
290.95	138	293.99	338
291.64	158	293.92	358
292.14	177	293.77	377
292.64	197	293.57	397
293.04	218	293.35	422
293.34	237	293.13	441
293.58	257	292.82	460
293.73	276	292.45	479
293.84	296	292.14	494

[a] Maximum temperature point.

Hydrate: Carbon dioxide
Reference: Fan and Guo (1999)
Phases: As noted

Q_2 at 283.1 K and 4.65 MPa

L_W–H–V			L_{CO_2}–H–V		
T **(K)**	***P*** **(MPa)**	**Phases**	***T*** **(K)**	***P*** **(MPa)**	**Phases**
273.6	1.31	L_W–H–V	281.3	3.47	L_W–H–V
274.2	1.39	L_W–H–V	282.0	4.02	L_W–H–V
275.2	1.57	L_W–H–V	278.9	4.12	L_{CO_2}–H–V
276.4	1.81	L_W–H–V	280.7	4.23	L_{CO_2}–H–V
278.5	2.25	L_W–H–V	283.1	9.32	L_{CO_2}–H–L_W
279.2	2.52	L_W–H–V	283.2	9.43	L_{CO_2}–H–L_W
280.3	3.04	L_W–H–V	283.6	12.87	L_{CO_2}–H–L_W

Hydrate: Carbon dioxide
Reference: Fan et al. (2000)
Phases: L_W–H–V

T (K)	P (MPa)	T (K)	P (MPa)
274.7	1.50	279.7	2.78
277.5	2.03		

Hydrate: Carbon dioxide
Reference: Mooijer-van den Heuvel et al. (2001)
Phases: L_W–H–V, L_W–H–L_{CO_2} and Q_2

Overall feed composition:
$x_{H_2O} = 0.8668$, $x_{CO_2} = 0.1332$
Q_2 at 283.27 K and 4.48 MPa

L_W–H–V		L_W–H–L_{CO_2}	
T (K)	P (MPa)	T (K)	P (MPa)
276.52	1.82	283.33	5.97
277.85	1.95	283.36	7.35
278.52	2.21		
279.49	2.62		
280.44	2.88		
281.49	3.35		
281.97	3.68		
282.00	3.69		
282.45	3.85		
282.50	4.01		

Hydrate: Carbon dioxide
Reference: Zhang (2003)
Phases: L_W–H

x_{CO_2}	P (MPa)	T (K)	x_{CO_2}	P (MPa)	T (K)	x_{CO_2}	P (MPa)	T (K)
0.0199	50.582	279.3	0.0177	45.262	277.8	0.0160	50.012	276.8
0.0199	37.872	279.1	0.0177	18.002	277.2	0.0160	31.142	275.6
0.0199	23.582	277.9	0.0177	6.65	276.5	0.0160	16.472	274.0

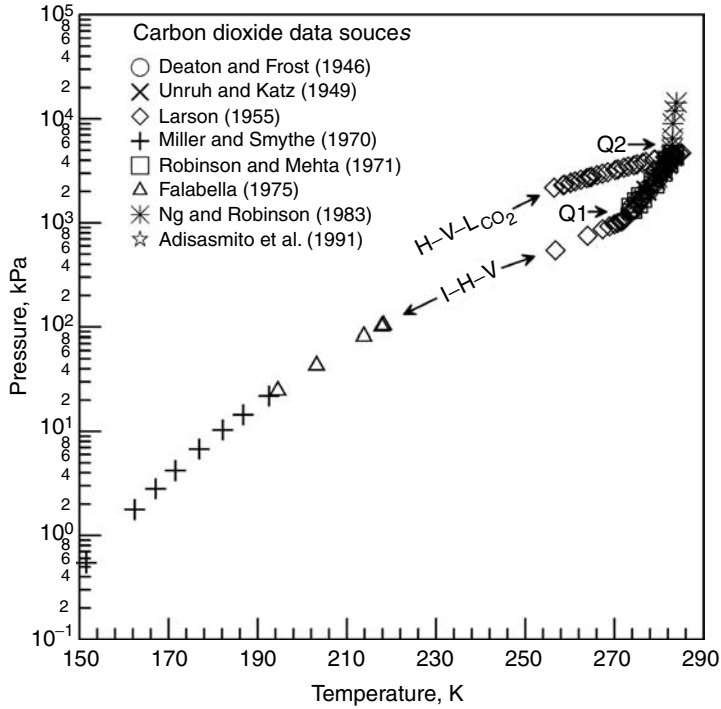

FIGURE 6.24 Three-phase data for simple hydrates of carbon dioxide.

Hydrate: Carbon dioxide
Reference: Mohammadi et al. (2005)
Phases: L_W–H–V

T **(K)** **(±0.1)**	***P*** **(MPa)** **(±0.007)**
295.8	34.584
298.3	47.863
277.5	2.048
282.2	3.840
282.5	4.020

Nitrogen

Hydrate: Nitrogen
Reference: van Cleeff and Diepen (1960)
Phases: L_W–H–V

T (K)	*P* (MPa)	*T* (K)	*P* (MPa)	*T* (K)	*P* (MPa)	*T* (K)	*P* (MPa)
272.0	14.48	274.8	19.25	279.2	29.89	285.2	55.43
272.6	15.30	275.2	19.66	279.2	30.30	286.2	61.40
272.8	15.91	275.6	20.67	280.2	33.94	287.2	67.79
273.0	15.91	275.8	21.58	281.2	37.49	287.8	71.23
273.2	16.01	276.2	22.39	281.6	38.61	288.4	74.58
273.2	16.31	276.6	23.10	282.2	41.44	289.2	81.47
273.4	16.62	277.2	24.83	283.2	45.90	290.2	89.37
274.0	17.53	278.2	27.36	284.2	50.66	290.6	92.21
274.2	17.73	278.2	27.97	284.6	52.29	291.0	95.86
274.8	19.15	278.6	28.27				

Hydrate: Nitrogen
Reference: Marshall et al. (1964a)
Phases: L_W–H–V

T (K)	*P* (MPa)	*T* (K)	*P* (MPa)	*T* (K)	*P* (MPa)	*T* (K)	*P* (MPa)
277.6	24.93	293.0	115.49	298.8	192.37	302.6	268.32
281.2	36.82	294.3	128.80	299.7	207.78	304.7	317.65
286.7	63.71	296.6	153.48	300.6	219.60	305.5	328.89
291.6	101.98	297.7	169.27				

Hydrate: Nitrogen
Reference: Jhaveri and Robinson (1965)
Phases: L_W–H–V

T (K)	*P* (MPa)	*T* (K)	*P* (MPa)	*T* (K)	*P* (MPa)	*T* (K)	*P* (MPa)
273.2	16.27	274.9	19.13	277.4	25.20	279.3	30.27
273.7	17.13	276.5	23.69	278.6	28.61	281.1	35.16

Hydrate: Nitrogen
Reference: Sugahara et al. (2002)
Phases: L_W–H–V

T (K)	*P* (MPa)	*T* (K)	*P* (MPa)	*T* (K)	*P* (MPa)
285.63	55	298.47	180	305.46	324
287.87	69	299.31	195	305.85	331
289.47	78	299.92	206	306.26	342
290.80	88	300.49	219	306.74	354
291.96	101	301.86	240	307.21	373
292.90	113	302.64	256	307.50	383
294.60	127	303.08	265	308.09	398
295.61	139	303.82	280	308.57	412
296.62	152	304.23	294	308.82	420
297.32	162	304.43	304	309.21	431
297.86	169	304.56	306	309.43	439

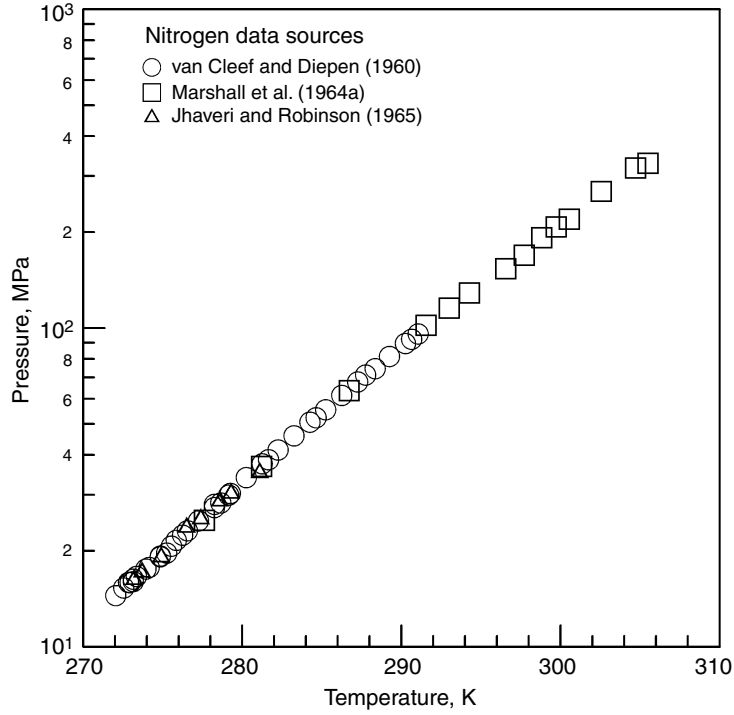

FIGURE 6.25 Three-phase data for simple hydrates of nitrogen.

Hydrate: Nitrogen
Reference: Mohammadi et al. (2003)
Phases: L_W–H–V

T (K)	*P* (kPa)
274.55	19,093
277.55	25,380
283.05	45,355

Hydrogen Sulfide

Hydrate: Hydrogen sulfide
Reference: Bond and Russell (1949)
Phases: L_W–H–V

T (K)	*P* (kPa)	*T* (K)	*P* (kPa)	*T* (K)	*P* (kPa)	*T* (K)	*P* (kPa)
283.2	310	291.2	710	299.7	1496	302.7	2241

Hydrate: Hydrogen sulfide
Reference: Selleck et al. (1952)
Phases: L_W–H–V, I–H–V, H–V–L_{H_2S}, L_W–H–L_{H_2S}

L_W–H–V

T (K)	*P* (kPa)	*T* (K)	*P* (kPa)	*T* (K)	*P* (kPa)	*T* (K)	*P* (kPa)
272.8	93 Q_1	285.2	345	295.7	1034	302.1	2068
272.8	93	288.7	499	298.5	1379	302.7	2239 Q_2
277.6	157	291.8	689	299.8	1596	302.7	2239 Q_2
283.2	280	294.3	690	300.5	1724		

Q_1 = lower Quadruple point (I–L_W–H–V).
Q_2 = upper Quadruple point (L_W–H–V–L_{H_2S}).

I–H–V

T (K)	*P* (kPa)	*T* (K)	*P* (kPa)	*T* (K)	*P* (kPa)	*T* (K)	*P* (kPa)
250.5	34	260.9	57	266.5	72	272.1	90
255.4	44	263.7	64	269.3	81	272.8	93 Q_1
258.2	50	265.3	69				

Continued

H–V–L_{H_2S}

T (K)	*P* (kPa)	*T* (K)	*P* (kPa)	*T* (K)	*P* (kPa)	*T* (K)	*P* (kPa)
259.2	689	272.3	1034	288.7	1605	299.8	2097
260.9	731	277.6	1202	291.6	1724	302.7	2239 Q_2
266.5	870	282.7	1379	294.3	1839	302.7	2239 Q_2
272.1	1027	283.2	1393	299.2	2068		

L_W–H–L_{H_2S}

T (K)	*P* (kPa)	*T* (K)	*P* (kPa)	*T* (K)	*P* (kPa)	*T* (K)	*P* (kPa)
302.7	2239 Q_2	303.4	10342	304.3	20685	304.8	27842
302.7	2239 Q_2	303.7	13790	304.3	20954	305.1	31027
302.8	3447	303.7	14190	304.6	24132	305.3	34475
303.1	6895	304.0	17237	304.8	27580	305.4	35068
303.2	7826						

Hydrates: Hydrogen sulfide
Reference: Carroll and Mather (1991)
Phases: L_{H_2S}–H–V and L_W–H–V

L_{H_2S}–H–V

T (K)	*P* (MPa)	*T* (K)	*P* (MPa)	*T* (K)	*P* (MPa)	*T* (K)	*P* (MPa)
278.0	2.03	299.7	2.09	301.0	2.13	301.4	2.18
299.0	2.05	299.8	2.09	301.1	2.15	301.6	2.20
299.1	2.06	300.1	2.09	301.2	2.17	301.6	2.22
299.4	2.08	300.4	2.12	301.2	2.15	302.6	2.24
299.6	2.08	300.8	2.11	301.4	2.17		

L_W–H–V

T (K)	*P* (MPa)	*T* (K)	*P* (MPa)	*T* (K)	*P* (MPa)	*T* (K)	*P* (MPa)
298.6	1.61	299.2	1.70	299.8	1.77	300.4	1.87
298.8	1.62	299.4	1.70	300.1	1.81	300.7	1.97
299.0	1.71	299.8	1.75	300.2	1.85	300.8	2.07
299.1	1.68						

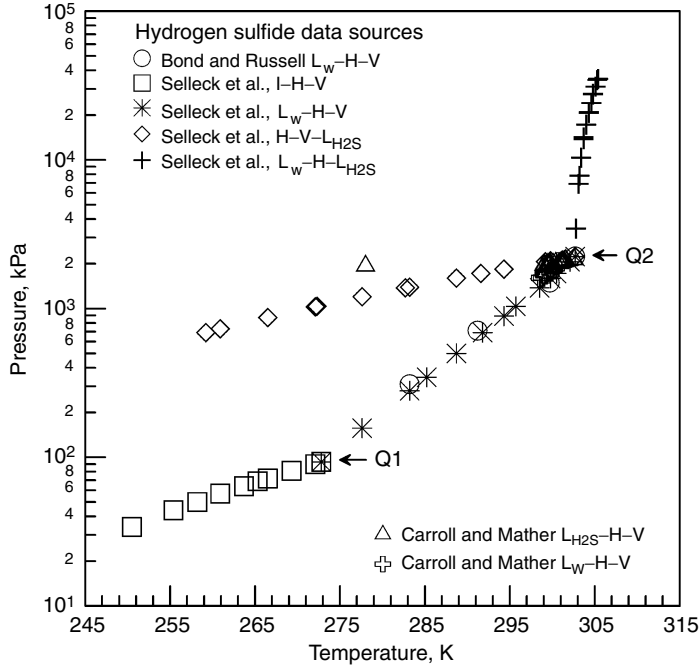

FIGURE 6.26 Three-phase data for simple hydrates of hydrogen sulfide.

6.3.1.2 Equilibria of binary guest mixtures

6.3.1.2.1 Structure I and II hydrate binary data

The phase equilibria data for binary guest mixtures are listed under the lighter component. For example, under the heading of binary guest mixtures of methane will be found data for methane + ethane, methane + propane, methane + isobutane, methane + *n*-butane, methane + nitrogen, methane + carbon dioxide, and methane + hydrogen sulfide. Concentrations are in mole percent or mole fraction in the gas phase, unless otherwise indicated.

The subsection for binary guest mixtures of ethane will thus contain no methane, only mixtures of ethane and heavier (or noncombustible) components. As an indication of consistency the data tabulations for each binary pair are followed by a semilogarithmic plot of pressure versus temperature, where there is more than one data set.

As a second means to examine binary (and higher) hydrate data, one should determine the consistency of the simple gas hydrates that compose the mixed hydrate. For example, the data for binary hydrates of methane and carbon dioxide by Berecz and Balla-Achs (1983, pp. 221ff.) show interesting new retrograde phenomena. However, a nitrogen impurity in their carbon dioxide (p. 185) may have caused a systematic deviation from the other CO_2 data sets shown in Figure 6.24, and their methane purity was only 98%, providing a simple methane hydrate data

deviation (p. 221). Because the simple hydrate data appeared quantitatively deviant they were excluded, and the resulting binary hydrate data are also suspect.

Gas impurities may have caused the systematic deviation of the Berecz and Balla-Achs $CH_4 + CO_2$ hydrate data from those of Unruh and Katz (1949) and Adisasmito et al. (1991) and for those reasons the former data are excluded.

Binary-Guest Mixtures Containing Methane and Heavier (or Noncombustible) Compounds

Hydrate: Methane + ethane
Reference: Deaton and Frost (1946)
Phases: L_W–H–V

%CH_4	*T* (K)	*P* (kPa)	%CH_4	*T* (K)	*P* (kPa)
56.4	214.8	945	95.0	283.2	4771
56.4	277.6	1289	97.1	274.8	2158
56.4	280.4	1758	97.1	277.6	2958
56.4	283.2	2434	97.1	280.4	4034
90.4	274.8	1524	97.8	274.8	2365
90.4	277.6	2096	97.8	277.6	3227
90.4	280.4	2889	97.8	280.4	4413
90.4	283.2	3965	97.8	282.6	5668
95.0	274.8	1841	97.8	283.2	6088
95.0	274.8	1841	98.8	274.8	2861
95.0	277.6	2530	98.8	277.6	3806
95.0	280.4	3447	98.8	280.4	5088

Hydrate: Methane + ethane
Reference: McLeod and Campbell (1961)
Phases: L_W–H–V

%CH_4	*T* (K)	*P* (MPa)	%CH_4	*T* (K)	*P* (MPa)
94.6	302.0	68.43	80.9	304.1	68.57
94.6	301.2	62.23	80.9	303.1	61.95
94.6	299.1	48.23	80.9	301.3	48.64
94.6	296.6	34.44	80.9	299.0	35.61
94.6	293.6	24.24	80.9	296.4	23.48
94.6	289.7	13.89	80.9	293.3	13.89
94.6	287.9	10.45	80.9	291.7	10.45
94.6	284.9	6.93	80.9	288.8	7.00

Hydrate: Methane + ethane
Reference: Holder and Grigoriou (1980)
Phases: L_W–H–V

%CH_4	*T* (K)	*P* (kPa)	%CH_4	*T* (K)	*P* (kPa)
1.6	283.9	1810	4.7	286.4	2510
1.6	285.7	2310	4.7	287.6	2990
1.6	286.6	2710	17.7	281.6	1420
1.6	287.8	3080	17.7	283.3	1770
4.7	279.4	990	17.7	284.8	2140
4.7	281.5	1340	17.7	286.2	2660
4.7	283.3	1710	17.7	287.0	3000
4.7	285.3	2170			

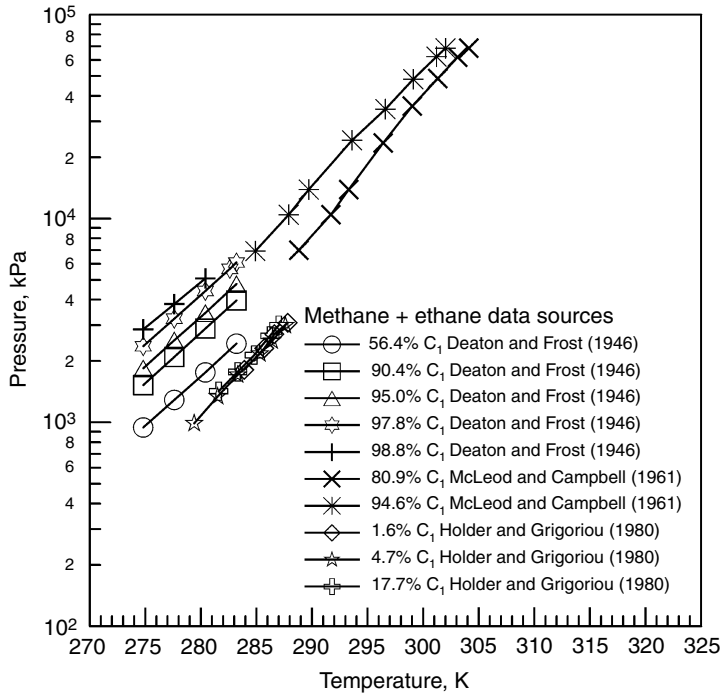

FIGURE 6.27 Methane + ethane mixture (L_W–H–V) data.

Hydrate: Methane + propane
Reference: Deaton and Frost (1946)
Phases: L_W–H–V

%CH_4	*T* (K)	*P* (kPa)	%CH_4	*T* (K)	*P* (kPa)
36.2	274.8	272	95.2	277.6	1138
36.2	277.6	436	95.2	280.4	1586
36.2	280.4	687	95.2	283.2	2227
71.2	274.8	365	97.4	274.8	1151
71.2	277.6	538	97.4	277.6	1593
71.2	280.4	800	97.4	280.4	2193
71.2	280.4	800	97.4	283.2	3013
71.2	283.2	1151	99.0	274.8	1627
88.3	274.8	552	99.0	277.6	2247
88.3	277.6	779	99.0	277.6	2255
88.3	280.4	1110	99.0	280.4	3123
88.3	283.2	1558	99.0	283.1	4358
95.2	274.8	814			

Hydrate: Methane + propane
Reference: McLeod and Campbell (1961)
Phases: L_W–H–V

%CH_4	*T* (K)	*P* (MPa)	%CH_4	*T* (K)	*P* (MPa)
96.5	290.5	6.93	96.5	290.7	6.93
96.5	303.7	62.47	94.5	293.1	7.41
96.5	304.4	68.98	94.5	292.8	7.41
96.5	299.1	34.51	94.5	300.6	34.58
96.5	296.6	20.86	94.5	302.7	48.37
96.5	301.6	48.37	94.5	304.9	62.23
96.5	303.7	62.23	94.5	298.5	23.62
96.5	294.5	13.89	94.5	296.2	13.89
96.5	293.3	10.45			

Hydrate: Methane + propane
Reference: Verma et al. (1974)
Phases: L_W–H–V and L_W–H–V–L_{HC}

L_W–H–V
23.75% CH_4

T (K)	*P* (MPa)	*T* (K)	*P* (MPa)	*T* (K)	*P* (MPa)	*T* (K)	*P* (MPa)
274.9	0.263	277.8	0.443	280.2	0.689	281.4	0.830
276.4	0.350	279.1	0.560				

37.1% CH_4

T (K)	*P* (MPa)	*T* (K)	*P* (MPa)	*T* (K)	*P* (MPa)	*T* (K)	*P* (MPa)
274.4	0.270	277.1	0.419	280.2	0.691	282.3	0.945
275.9	0.343	278.6	0.536				

L_W–H–V–L_{HC}
0.72% CH_4

T (K)	*P* (MPa)	*T* (K)	*P* (MPa)	*T* (K)	*P* (MPa)	*T* (K)	*P* (MPa)
279.6	0.66*	279.9	6.70	280.0	10.3	280.2	15.3
279.8	3.03						

0.92% CH_4

T (K)	*P* (MPa)	*T* (K)	*P* (MPa)	*T* (K)	*P* (MPa)	*T* (K)	*P* (MPa)
280.4	0.74*	280.6	3.17	280.9	11.0	281.1	15.4
280.5	1.83	280.7	6.99				

2.20% CH_4

T (K)	*P* (MPa)	*T* (K)	*P* (MPa)	*T* (K)	*P* (MPa)	*T* (K)	*P* (MPa)
282.2	0.949*	282.4	1.76	282.6	3.17	282.9	6.00

4.46% CH_4

T (K)	*P* (MPa)	*T* (K)	*P* (MPa)	*T* (K)	*P* (MPa)	*T* (K)	*P* (MPa)
284.9	1.34*	285.3	3.61	286.2	10.14	286.7	14.33
285.1	2.06	285.7	6.59				

Continued

7.80% CH_4

T (K)	*P* (MPa)	*T* (K)	*P* (MPa)	*T* (K)	*P* (MPa)	*T* (K)	*P* (MPa)
288.0	2.03*	288.3	4.80	289.3	11.50	289.8	15.34
288.0	2.81	288.7	7.36				

13.70% CH_4

T (K)	*P* (MPa)	*T* (K)	*P* (MPa)	*T* (K)	*P* (MPa)	*T* (K)	*P* (MPa)
290.2	2.71*	290.7	5.51	291.6	9.38	292.1	13.13
290.4	3.36	290.9	6.36	291.7	10.39	292.7	16.94

25.70 % CH_4

T (K)	*P* (MPa)	*T* (K)	*P* (MPa)	*T* (K)	*P* (MPa)	*T* (K)	*P* (MPa)
294.2	4.96*	294.8	7.81	296.4	13.80	297.2	17.06
294.2	5.26	295.6	10.82				

48.23% CH_4

T (K)	*P* (MPa)	*T* (K)	*P* (MPa)	*T* (K)	*P* (MPa)	*T* (K)	*P* (MPa)
297.0	8.10*	297.9	11.08	298.7	13.99	299.7	17.49
297.1	8.43						

56.35% CH_4

T (K)	*P* (MPa)	*T* (K)	*P* (MPa)	*T* (K)	*P* (MPa)	*T* (K)	*P* (MPa)
297.6	9.16*	299.0	13.18	299.7	15.38	300.2	17.41
298.1	10.43						

59.40% CH_4

T (K)	*P* (MPa)	*T* (K)	*P* (MPa)	*T* (K)	*P* (MPa)	*T* (K)	*P* (MPa)
297.6	9.38*	298.9	12.62	299.4	14.53	300.2	17.29
298.2	10.71						

65.10% CH_4

T (K)	*P* (MPa)	*T* (K)	*P* (MPa)	*T* (K)	*P* (MPa)	*T* (K)	*P* (MPa)
297.7	9.56*	298.0	10.60	298.9	13.89	300.1	17.13

* = Q_2 Quadruple point (L_W–H–V–L_{HC}).

Hydrate: Methane + propane
Reference: Song and Kobayashi (1982)
Phases: V–H

5.31 mol% propane in methane

T (K)	*P* (MPa)	H_2O mol fract ($\times 10^6$)	*T* (K)	*P* (MPa)	H_2O mol fract ($\times 10^6$)
234.2	2.07	6.86	246.2	6.89	7.03
246.2	2.07	24.28	252.1	6.89	12.25
251.7	2.07	41.54	260.0	6.89	25.42
260.1	2.07	85.20	263.2	6.89	35.78
266.5	2.07	161.99	276.2	6.89	103.70
277.2	2.07	427.28	234.2	10.34	1.15
234.2	3.45	3.47	246.2	10.34	3.75
246.2	3.45	13.85	252.1	10.34	7.33
252.1	3.45	27.50	260.1	10.34	14.67
263.2	3.45	78.76	266.5	10.34	26.75
274.7	3.45	187.89	277.6	10.34	81.15
234.2	6.89	1.92			

Hydrate: Methane + propane
Reference: Thakore and Holder (1987)
Phases: L_W–H–V

***T* = 275.15 K**

$\%CH_4$	*P* (kPa)	$\%CH_4$	*P* (kPa)	$\%CH_4$	*P* (kPa)
1.000	3370	0.420	279	0.054	245
0.903	672	0.366	279	0.046	245
0.765	424	0.352	269	0.037	245
0.727	393	0.190	245*	0.021	245
0.700	365	0.083	245	0.000	278
0.516	303	0.081	245		

***T* = 278.15 K**

$\%CH_4$	*P* (kPa)	$\%CH_4$	*P* (kPa)	$\%CH_4$	*P* (kPa)
1.000	4495	0.530	496	0.394	458
0.956	1306	0.510	489	0.390	458*
0.947	1144	0.502	479	0.030	479
0.894	848	0.468	475	0.026	480
0.768	630	0.412	479	0.000	509

* = Azeotrope point.

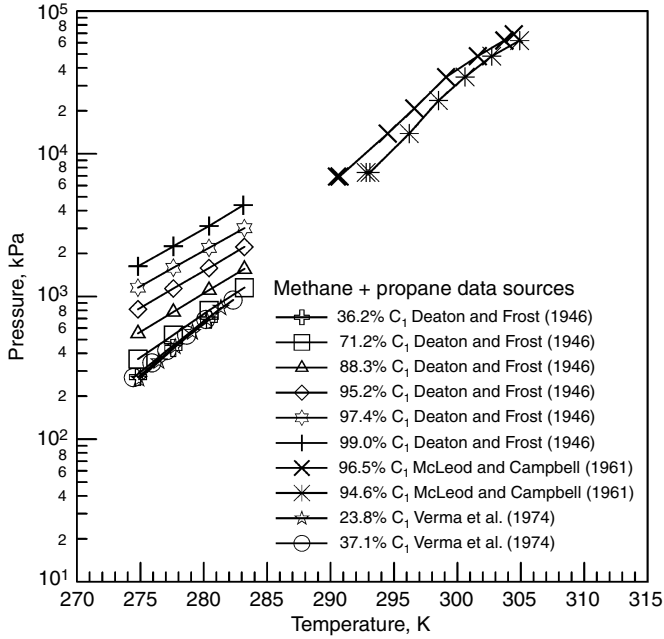

FIGURE 6.28 Methane + propane mixture (L_W–H–V) data.

Hydrate: Methane + isobutane
Reference: Deaton and Frost (1946)
Phases: L_W–H–V

%CH_4	*T* (K)	*P* (kPa)	%CH_4	*T* (K)	*P* (kPa)
98.9	274.8	1324	98.9	277.6	1841

Hydrate: Methane + isobutane
Reference: McLeod and Campbell (1961)
Phases: L_W–H–V

%CH_4	*T* (K)	*P* (MPa)	%CH_4	*T* (K)	*P* (MPa)
98.6	300.0	47.68	95.4	297.1	13.96
98.6	297.8	34.51	95.4	298.2	23.27
98.6	297.6	33.61	95.4	300.5	34.58
98.6	295.2	21.06	95.4	302.6	48.37
98.6	299.9	49.13	95.4	305.0	63.33
98.6	288.6	6.79	95.4	303.1	49.06
98.6	302.1	62.23	95.4	298.3	23.82
95.4	294.3	6.72	95.4	296.7	13.96
95.4	293.8	6.72	95.4	295.3	10.58
95.4	296.5	13.89	95.4	294.6	7.69

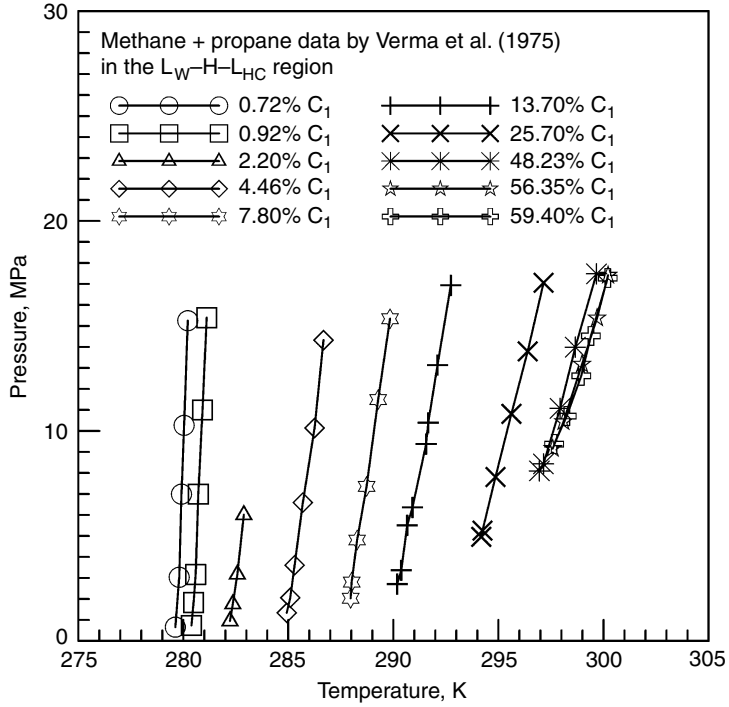

FIGURE 6.29 Methane + propane mixture (L_W–H–L_p) data.

Hydrate: Methane + isobutane
Reference: Wu et al. (1976)
Phases: L_W–H–V and L_W–H–V–L_{iC_4}

L_W–H–V

%i-C_4H_{10}	*T* (K)	*P* (kPa)	%i-C_4H_{10}	*T* (K)	*P* (kPa)
0.23	275.2	2,080	2.50	277.8	1,080
0.23	279.7	3,440	2.50	279.8	1,390
0.27	284.6	6,010	2.50	283.3	2,150
0.36	285.4	6,190	2.50	285.2	2,740
0.37	288.0	9,690	2.50	287.2	3,450
0.40	276.2	1,810	2.50	289.3	4,560
0.43	285.3	5,590	2.50	293.6	10,070
0.45	282.0	3,500	6.00	274.8	505
0.46	280.9	3,150	6.00	280.4	1,010
0.54	286.2	5,480	6.00	284.5	1,690

Continued

%i-C_4H_{10}	*T* (K)	*P* (kPa)	%i-C_4H_{10}	*T* (K)	*P* (kPa)
0.82	275.4	1,270	6.00	288.5	2,820
0.82	280.0	2,190	15.20	274.0	304
0.82	283.5	3,340	15.20	278.9	564
0.82	287.4	5,900	15.20	283.4	1,030
0.82	290.9	10,040	15.20	288.9	2,030
1.20	274.4	950	28.60	273.9	208
1.20	277.7	1,390	28.60	277.2	356
1.20	279.9	1,800	28.60	279.2	477
1.20	283.2	2,700	28.60	280.8	602
1.20	284.9	3,470	28.60	282.7	786
1.20	287.5	4,880	63.60	273.8	159
1.20	290.0	6,950	63.60	275.5	221
2.50	274.4	703	63.60	276.9	284

L_W–H–V–L_{iC_4}
(%i-C_4H_{10} = vapor phase)

%i-C_4H_{10}	*T* (K)	*P* (kPa)	%i-C_4H_{10}	*T* (K)	*P* (kPa)
65.1	277.0	254	12.2	293.2	3,990
44.5	279.6	427	12.0	293.3	4,100
31.3	282.3	703	11.2	294.8	5,560
23.8	284.7	1,030	11.0	295.3	5,760
18.2	287.5	1,540	15.0	298.0	9,990
13.8	290.8	2,700	19.8	298.6	11,570
13.5	291.5	2,970			

Mixture: Methane + isobutane
Reference: Ng and Robinson (1976a)
Phases: L_W–H–L_{iC_4}

%CH_4	*T* (K)	*P* (kPa)	%CH_4	*T* (K)	*P* (kPa)
0.1	275.4	179	15.2	288.9	1,931
0.1	275.4	226	15.2	289.0	2,441
0.1	275.4	357	15.2	289.4	3,785
0.1	275.4	903	15.2	289.9	7,129
0.1	275.6	2,406	15.2	290.5	10,577
0.1	275.7	5,653	15.2	291.2	14,073
0.1	275.8	14,251	28.4	292.9	3,792
4.3	282.2	682	28.4	293.0	4,268
4.3	282.3	1,048	28.4	293.7	6,957

(Continued)

Continued

%CH_4	T (K)	P (kPa)	%CH_4	T (K)	P (kPa)
4.3	282.7	2,179	28.4	294.8	10,439
4.3	282.9	4,474	28.4	295.0	13,866
4.3	283.3	8,233	42.5	295.9	6,619
4.3	283.9	14,024	42.5	296.4	8,784
8.7	286.4	1,338	42.5	297.2	11,321
8.7	266.5	1,744	42.5	297.9	14,093
8.7	286.8	3,958	64.7	298.1	10,204
8.7	287.2	6,902	64.7	298.4	11,232
8.7	287.8	11,197	64.7	298.7	12,528
8.7	288.4	14,231	64.7	299.3	14,548

Hydrate: Methane + isobutane
Reference: Thakore and Holder (1987)
Phases: L_W–H–V

$T = 274.35$ K

%CH_4	P (kPa)	%CH_4	P (kPa)	%CH_4	P (kPa)
100.0	3099	31.3	156	7.3	131
94.9	841	17.2	136	6.6	129
91.9	461	15.0	134	5.6	129
79.2	268	12.4	133	5.1	129
72.5	234	9.1	132	4.8	127
63.2	210	8.6	131	3.6	129
50.0	180	7.6	131	0.0	128

Hydrate: Methane + *n*-butane
Reference: Deaton and Frost (1946)
Phases: L_W–H–V

%CH_4	T (K)	P (kPa)	%CH_4	T (K)	P (kPa)
97.4	274.8	2048	97.5	274.8	2165
97.4	277.6	2875	99.2	274.8	3075
97.4	280.4	4061	99.2	277.6	4075

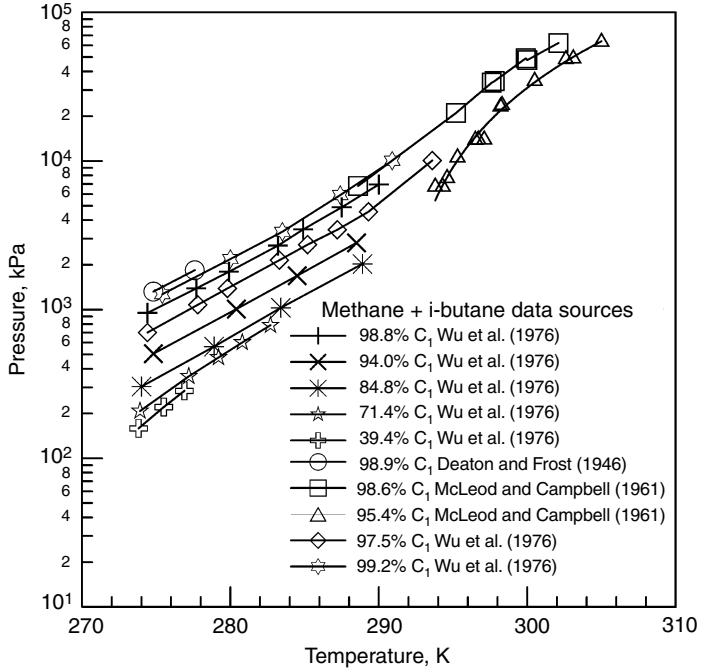

FIGURE 6.30 Methane + iso-butane mixture (L_W–H–V) data.

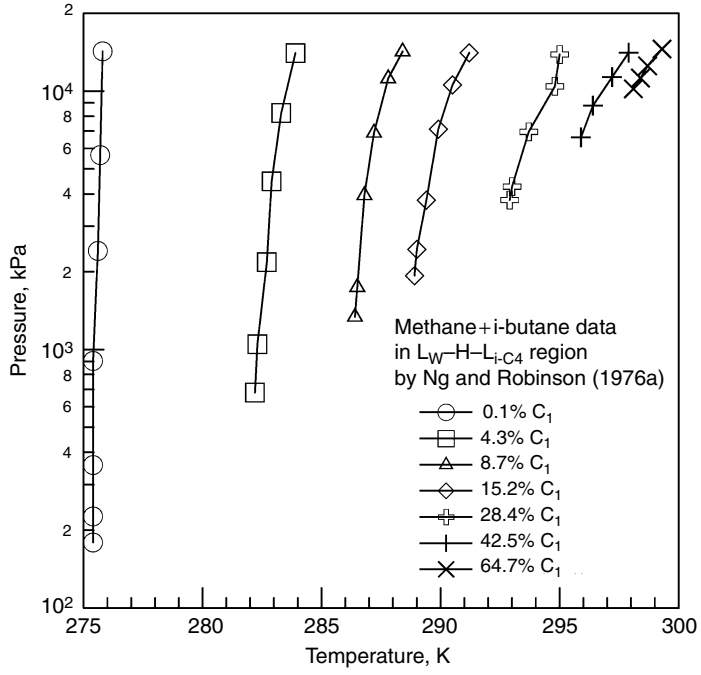

FIGURE 6.31 Methane + iso-butane mixture (L_W–H–L_{iC_4}) data.

Hydrate: Methane + *n*-butane
Reference: McLeod and Campbell (1961)
Phases: L_W–H–V

%CH_4	*T* (K)	*P* (MPa)	%CH_4	*T* (K)	*P* (MPa)
97.4	285.0	7.69	94.7	295.1	34.16
97.4	287.7	12.45	94.7	297.9	48.23
97.4	295.7	34.58	94.7	300.1	61.61
97.4	301.1	65.95	94.7	301.1	68.43
97.4	286.3	10.45	94.7	290.3	17.96
97.4	285.7	9.07	94.7	288.8	13.89
97.4	282.5	5.76	94.7	287.6	10.65
94.7	287.5	10.65	94.7	286.6	8.69
94.7	292.4	23.89	94.7	285.3	7.00

Hydrate: Methane + *n*-butane
Reference: Ng and Robinson (1976b)
Phases: L_W–H–V

%*n*-C_4H_{10}	*T* (K)	*P* (MPa)	%*n*-C_4H_{10}	*T* (K)	*P* (MPa)
1.64	276.0	2.48	2.48	284.75	7.47
1.64	279.4	3.82	2.48	286.40	10.40
1.64	283.4	6.65	3.91	276.91	2.15
1.64	286.1	10.08	3.91	279.74	3.14
1.64	287.4	12.06	3.91	283.12	5.09
1.64	288.5	13.72	3.91	285.95	8.16
2.48	276.4	2.30	3.91	287.55	11.05
2.48	279.7	3.59	5.82	277.99	2.05
2.48	282.4	5.13	5.82	281.43	3.29

Hydrate: Methane + *n*-butane
Reference: John and Holder (1982b)
Phases: L_W–H–V, I–H–V–$L_{n\text{-}C_4H_{10}}$, L_W–H–V–$L_{n\text{-}C_4H_{10}}$

I–H–V

%*n*-C_4H_{10}	*T* (K)	*P* (kPa)	%*n*-C_4H_{10}	*T* (K)	*P* (kPa)
0.4	251.2	1267	4.2	262.2	846
0.7	251.2	1011	6.3	262.2	715
1.1	251.2	805	9.3	262.2	639
1.8	251.2	680	12.6	262.2	570*

Continued

I–H–V

%*n*-C_4H_{10}	*T* (K)	*P* (kPa)	%*n*-C_4H_{10}	*T* (K)	*P* (kPa)
3.8	251.2	522	0.55	268.2	2204
5.0	251.2	474	0.75	268.2	1963
5.9	251.2	446	1.15	268.2	1728
8.8	251.2	391	1.50	268.2	1563
13.3	251.2	336*	2.30	268.2	1342
0.5	256.2	1480	3.15	268.2	1232
0.6	256.2	1246	3.40	268.2	1177
1.0	256.2	1067	5.20	268.2	1011
1.5	256.2	901	6.80	268.2	915
2.0	256.2	818	7.80	268.2	880
3.2	256.2	680	11.00	268.2	784*
4.5	256.2	605	0.80	273.1	2611
6.5	256.2	536	0.95	273.1	2446
10.0	256.2	460	1.20	273.1	2335
11.4	256.2	446	1.40	273.1	2142
12.8	256.2	432*	1.95	273.1	1894
0.5	262.2	1784	2.75	273.1	1618
0.9	262.2	1529	4.10	273.1	1384
1.2	262.2	1356	6.60	273.1	1136
2.0	262.2	1108	10.10	273.1	1011*
2.9	262.2	970			

* = Q_1 Quadruple point (I–H–V–$L_{n\text{-}C_4}$).

I–H–V–$L_{n\text{-}C_4H_{10}}$

T (K)	*P* (kPa)	*T* (K)	*P* (kPa)	*T* (K)	*P* (kPa)	*T* (K)	*P* (kPa)
255.3	417.1	259.9	524.0	264.5	661.9	270.3	875.6
256.1	430.9	260.8	544.7	255.1	682.6	271.0	903.2
257.2	458.5	261.9	575.7	265.9	710.2	271.7	937.7
258.0	479.2	263.6	620.5	269.1	813.6	272.5	979.0
259.0	499.9	263.9	634.0	269.2	827.4		

L_W–H–V–$L_{n\text{-}C_4H_{10}}$

T (K)	*P* (kPa)	*T* (K)	*P* (kPa)	*T* (K)	*P* (kPa)	*T* (K)	*P* (kPa)
273.3	1046.0	274.3	1177.0	275.9	1504.0	276.8	1722.0
273.8	1073.0	275.1	1342.0				

Hydrate: Methane + *n*-butane
Reference: Ng and Robinson (1977)
Phases: L_W–H–$L_{n\text{-}C_4H_{10}}$

			$\%CH_4$ in $L_{n\text{-}C_4H_{10}}$		
$\%CH_4$	T (K)	P (MPa)	$\%CH_4$	T (K)	P (MPa)
8.7	275.0	1.24*	21.8	282.7	9.05
8.7	275.6	3.41	21.8	283.4	12.13
8.7	275.7	6.01	21.8	283.3	12.34
8.7	276.3	10.06	42.4	285.9	6.62*
8.7	276.7	12.82	42.4	286.1	7.78
15.7	279.4	2.39*	42.4	286.4	9.09
15.7	279.4	2.96	42.4	286.9	10.92
15.7	279.5	3.61	42.4	287.0	12.16
15.7	279.8	4.27	42.4	287.4	13.82
15.7	280.0	6.76	50.1	287.4	8.83*
15.7	280.6	9.09	50.1	287.5	9.85
15.7	281.1	12.44	50.1	287.8	10.75
21.8	281.8	3.45*	50.1	288.2	12.47
21.8	282.1	5.23	50.1	288.5	13.82
21.8	282.4	6.75			

* = Q_2 Quadruple point (L_W–H–V–$L_{n\text{-}C_4H_{10}}$).

Hydrate: Methane + nitrogen
Reference: Jhaveri and Robinson (1965)
Phases: L_W–H–V

$\%CH_4$	T (K)	P (MPa)	$\%CH_4$	T (K)	P (MPa)
87.3	282.8	7.40	50.25	291.8	33.19
87.3	284.6	9.31	27.2	273.2	7.96
87.3	287.7	14.52	27.2	277.1	10.16
87.3	289.5	17.11	27.2	280.0	12.64
87.3	290.4	17.49	27.2	282.9	17.04
87.3	291.0	19.53	27.2	283.2	17.50
87.3	291.5	19.99	27.2	285.1	20.72
87.3	292.9	22.94	27.2	286.8	25.15
87.3	293.4	24.66	27.2	288.0	28.49

Continued

%CH_4	T (K)	P (MPa)	%CH_4	T (K)	P (MPa)
87.3	295.2	31.31	24.0	273.2	8.62
73.1	273.2	3.90	24.0	274.6	9.15
73.1	283.3	8.95	24.0	278.8	12.96
73.1	286.8	13.22	24.0	282.1	17.44
73.1	289.9	19.55	24.0	285.1	24.34
73.1	292.3	25.99	24.0	287.6	31.99
73.1	294.4	34.33	24.0	289.1	35.96
50.25	273.2	4.96	10.8	273.2	12.55
50.25	277.2	6.13	10.8	277.2	15.86
50.25	279.7	7.77	10.8	279.1	19.39
50.25	282.3	10.49	10.8	280.9	22.52
50.25	287.3	17.90	10.8	282.1	25.82
50.25	289.8	24.99	10.8	283.2	28.79

(Continued)

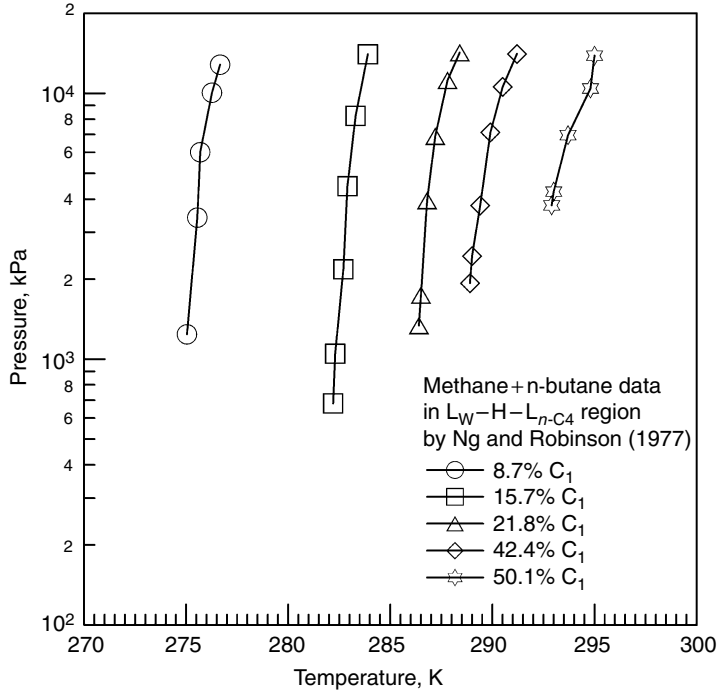

FIGURE 6.32 Methane + n-butane mixture (L_W–H–$L_{n-C_4H_{10}}$) data.

Continued

Isothermal *P–z–y* Data (*z* = hydrate mol fraction)

273.2 K			277.4 K			279.8 K		
***P* (MPa)**	y_{N_2}	z_{N_2}	***P* (MPa)**	y_{N_2}	z_{N_2}	***P* (MPa)**	y_{N_2}	z_{N_2}
2.64	0.00	0.00	13.32	0.925	0.81	25.18	1.00	1.00
3.62	0.16	0.065	14.59	0.94	0.86	5.14	0.00	0.00
4.31	0.31	0.098	16.21	1.00	1.00	7.14	0.35	0.091
5.35	0.53	0.20	3.86	0.00	0.00	8.37	0.46	0.224
6.55	0.645	0.35	5.20	0.44	0.18	15.55	0.75	0.55
7.75	0.725	0.425	8.11	0.63	0.31	20.67	0.84	0.68
10.64	0.815	0.62	10.34	0.74	0.47	25.23	0.914	0.802
11.65	0.88	0.71	12.06	0.78	0.56	32.42	1.00	1.00
12.77	0.90	0.765						

z_{N_2} = Mol fraction nitrogen in hydrate phase.
y_{N_2} = Mol fraction nitrogen in vapor phase.

Hydrate: Methane + nitrogen
Reference: Mei et al. (1996a)
Phases: L_W–H–V

89.26 mol% CH_4

***T* (K)**	***P* (MPa)**	***T* (K)**	***P* (MPa)**
273.7	2.99	279.2	5.24
274.8	3.31	281.2	6.58
275.6	3.73	283.2	8.12
277.1	4.36	285.3	10.1

Hydrate: Methane + carbon dioxide
Reference: Unruh and Katz (1949)
Phases: L_W–H–V

$\%CH_4^*$	***T* (K)**	***P* (MPa)**	$\%CH_4^*$	***T* (K)**	***P* (MPa)**
66.0	277.0	2.84	91.5	278.4	3.95
70.0	278.9	3.46	93.0	281.0	5.10
64.0	278.9	3.43	94.5	283.8	6.89
68.0	280.9	4.24	29.0	279.6	3.00
72.0	282.9	5.17	39.0	282.2	4.27
77.0	284.7	6.47	48.0	283.8	5.27
40.0	275.5	1.99	59.0	285.5	6.89
56.0	279.2	3.08	59.0	285.7	7.00
87.5	276.4	3.20			

* = Vapor composition calculated in reference.

Hydrate: Methane + carbon dioxide
Reference: Adisasmito et al. (1991)
Phases: L_W–H–V

$\%CO_2$	T (K)	P (MPa)	$\%CO_2$	T (K)	P (MPa)
10.0	273.7	2.52	40.0	280.7	4.03
9.0	275.8	3.10	39.0	283.1	5.43
8.0	277.8	3.83	39.0	285.1	6.94
8.0	280.2	4.91	39.0	287.4	9.78
8.0	283.2	6.80	50.0	275.6	1.99
8.0	285.1	8.40	47.0	278.5	2.98
9.0	287.2	10.76	40.0	280.9	4.14
14.0	274.6	2.59	41.0	281.8	4.47
13.0	276.9	3.24	44.0	285.1	6.84
13.0	279.1	4.18	45.0	287.4	9.59
13.0	281.6	5.38	73.0	274.6	1.66
13.0	284.0	7.17	70.0	276.4	2.08
12.0	286.1	9.24	68.0	278.2	2.58
13.0	287.4	10.95	68.0	280.2	3.28
25.0	273.8	2.12	67.0	282.0	4.12
22.0	279.4	3.96	79.0	273.7	1.45
22.0	283.4	6.23	78.0	275.9	1.88
21.0	285.2	7.75	76.0	277.8	2.37
25.0	287.6	10.44	75.0	279.6	2.97
44.0	273.7	1.81	74.0	281.6	3.79
42.0	276.9	2.63	85.0	282.7	4.37

Hydrate: Methane + carbon dioxide
Reference: Ohgaki et al. (1996)
Phases: L_W–H–V

$T = 280.3$ K

P (MPa)	z_{CO_2}	y_{CO_2}	P (MPa)	z_{CO_2}	y_{CO_2}
3.04	1.00	1.000	4.22	0.44	0.241
3.24	0.84	0.683	4.31	0.39	0.215
3.38	0.80	0.585	4.32	0.36	0.217
3.60	0.67	0.488	4.34	0.37	0.203
3.64	0.69	0.450	4.37	0.35	0.203
3.67	0.68	0.448	4.37	0.36	0.183
3.71	0.61	0.429	4.44	0.36	0.179
3.77	0.60	0.384	4.50	0.35	0.169
3.86	0.59	0.357	4.57	0.32	0.144

(Continued)

Continued

P (MPa)	z_{CO_2}	y_{CO_2}	P (MPa)	z_{CO_2}	y_{CO_2}
3.98	0.53	0.302	4.58	0.32	0.141
4.00	0.52	0.310	4.63	0.29	0.143
4.01	0.55	0.311	4.75	0.24	0.104
4.06	0.51	0.288	4.85	0.23	0.090
4.07	0.52	0.293	4.99	0.16	0.065
4.15	0.47	0.268	5.46	0.00	0.000
4.20	0.45	0.245			

Mole fraction of CO_2 in vapor, y_{CO_2} measured directly; calculated mole fraction of CO_2 in hydrate phase, z_{CO_2}

Hydrate: Methane + carbon dioxide
Reference: Fan and Guo (1999)
Phases: L_W–H–V

3.46% CH_4

T (K)	P (MPa)	T (K)	P (MPa)
273.5	1.10	277.9	2.05
273.6	1.16	280.4	3.00
273.7	1.20	281.7	3.73
277.2	1.95	282.3	4.80
277.6	1.94		

Hydrate: Methane + carbon dioxide
Reference: Seo et al. (2001a) and Seo and Lee (2001b)
Phases: H–V, L_W–H–V, L_W–H–V–L_{CO_2}

H–V

%CO_2 (in vapor)	%CO_2 (in hydrate)	T (K)	P (MPa)	%CO_2 (in vapor)	%CO_2 (in hydrate)	T (K)	P (MPa)
28.44	91.51	273.06	2.0	64.11	98.08	277.46	2.6
40.25	93.63	274.06	2.0	83.39	99.35	278.06	2.6
60.76	98.15	275.36	2.0	13.25	64.72	276.56	3.5
79.44	99.65	276.26	2.0	25.23	73.34	277.56	3.5
12.93	66.18	273.76	2.6	41.91	88.99	278.96	3.5
23.44	84.68	274.86	2.6	61.13	95.23	279.86	3.5
41.46	92.72	276.26	2.6	83.44	99.3	280.46	3.5

Continued

L_W–H–V

%CO_2 (loading)	%CO_2 (in vapor)	*T* (K)	*P* (MPa)	%CO_2 (loading)	%CO_2 (in vapor)	*T* (K)	*P* (MPa)
	40.67	272.66	1.5		78.43	278.26	2.6
60.0	61.69	273.56	1.5	100.0	100.00	279.16	2.6
	90.41	274.36	1.5	0.0	0.00	276.16	3.5
100.0	100.00	274.76	1.5	20.0	20.09	278.06	3.5
20.0	26.34	273.56	2.0		42.65	279.26	3.5
	33.75	274.36	2.0	60.0	60.87	280.16	3.5
60.0	56.48	275.86	2.0		76.17	280.76	3.5
	79.54	276.56	2.0	100.0	100.00	281.46	3.5
100.0	100.00	277.16	2.0	0.0	0.00	279.60	5.0
0.0	0.00	273.16	2.6	20.0	19.71	281.46	5.0
20.0	18.54	275.36	2.6		40.89	282.56	5.0
	39.72	276.76	2.6	100.0	59.89	283.26	5.0
60.0	61.95	277.96	2.6		80.52	283.56	5.0

%CO_2 (in vapor)	*T* (K)	*P* (MPa)	%CO_2 (in vapor)	*T* (K)	*P* (MPa)
Q_2: L_W–H–V–L_{CO_2} (Seo et al., 2001a)					
82.50	285.56	6.72	94.83	283.86	4.93
89.93	284.56	5.56	100.00	283.32	4.53
Q_2: L_W–H–V–L_{CO_2} (Seo and Lee 2001b)					
100.00	283.32	4.12	83.56	285.03	6.22
94.04	283.86	4.93	79.74	285.76	7.251
89.13	284.39	5.50			

Hydrate: Methane + carbon dioxide
Reference: Hachikubo et al. (2002)
Phases: L_W–H–V

%CO_2	*T* (K)	*P* (MPa)
100	273.93	1.349
100	276.80	1.806
100	278.05	2.204
100	263.17	0.774
100	268.11	0.921
100	271.23	1.029
100	277.78	2.187
0	268.4	2.324
0	271.28	2.527

(Continued)

Continued

$\%CO_2$	T (K)	P (MPa)
77	271.25	1.271
50	271.41	1.434
25	271.37	2.022

Hydrate: Methane + hydrogen sulfide
Reference: Noaker and Katz (1954)
Phases: L_W–H–V

$\%CH_4^*$	T (K)	P (MPa)	$\%CH_4^*$	T (K)	P (MPa)
91.77/93.0	288.7	4.83	96.22/96.10	276.5	2.03
90.49/91.0	284.3	2.59	99.0	278.4	3.24
93.7	282.3	3.03	98.96	282.3	4.62
93.5	287.1	4.79	98.89/98.94	284.8	6.69
93.0	290.1	6.79	78.0	287.6	2.10
94.27/93.5	279.3	2.21	80.20/79.0	295.4	5.07
93.40/93.0	290.1	6.38	78.60/78.0	279.8	1.03
97.0	278.7	2.83	90.5	281.5	2.07
96.9	282.9	4.27	89.0	287.3	3.59
97.08/97.05	287.6	6.65	88.50/88.50	292.1	6.00

* If two values of vapor composition are provided the first was measured and the second calculated; if only one value of vapor composition is given, it was calculated in the reference.

Binary Guest Mixture Containing Ethane and Heavier (or Noncombustible) Compounds

Hydrate: Ethane + propane
Reference: Holder and Hand (1982)
Phases: L_W–H–V and L_W–H–L_{HC}

L_W–H–L_E

$\%C_3H_8$	T (K)	P (kPa)	$\%C_3H_8$	T (K)	P (kPa)
16.8	278.1	910*	43.5	280.2	5180
16.8	278.1	1440	43.5	280.6	6550
16.8	278.2	1550	68.9	284.3	2230*
16.8	278.3	2560	68.9	284.3	2900
16.8	278.6	2790	68.9	284.4	5580
43.5	279.9	1470*	68.9	284.5	7280
43.5	279.9	2300			

* = Q_2 Quadruple point (L_W–H–V–L_{HC}).

Continued

L_W–H–V

%C_3H_8	T (K)	P (kPa)	%C_3H_8	T (K)	P (kPa)
72.0	277.9	660	32.2	281.1	1630
72.0	276.9	530	27.1	273.4	490
72.0	276.5	460	27.1	273.9	540
55.7	275.9	50	27.1	274.3	610
55.7	276.4	570	27.1	274.6	600
55.7	276.7	610	27.1	275.3	770
55.7	277.0	650	27.1	275.6	870
55.7	277.4	720	27.1	275.8	920
54.1	275.8	500	26.0	274.5	630
54.1	276.4	590	26.0	274.7	690
54.1	277.0	660	26.0	275.2	790
54.1	277.6	770	26.0	276.4	940
54.1	278.0	850	26.0	277.1	1020
34.2	273.9	440	26.0	277.7	1120
34.2	274.2	470	18.6	273.1	540
34.2	275.1	590	18.6	273.8	640
34.2	275.8	690	18.6	273.8	640
34.2	276.2	830	18.6	274.3	660
34.2	276.3	850	18.6	274.7	710
34.2	276.5	870	18.6	276.8	940
34.2	277.6	1060	18.6	278.9	1210
32.2	275.6	750	18.6	279.6	1300
32.2	276.1	870	15.0	275.7	740
32.2	277.1	1140	15.0	277.2	900
32.2	277.2	1160	15.0	280.6	1370
32.2	277.9	1220	14.3	279.7	1190
32.2	278.6	1300	14.3	280.2	1300
32.2	279.4	1430	14.3	282.1	1670
32.2	280.4	1560	14.3	283.2	2030
32.2	280.6	1610	14.3	283.3	2020

Hydrates: Ethane + propane
Reference: Song and Kobayashi (1994)
Phases: L_{HC}–H

Isobaric Data at 3.447 MPa

Liquid phase %C_2H_6	T (K)	H_2O mol fract ($\times 10^4$)	Liquid phase %C_2H_6	T (K)	H_2O mol fract ($\times 10^4$)
0.5	276.8	1.13	0.75	264.5	0.400
0.5	267.0	0.532	0.75	262.6	0.345

(Continued)

Continued

Liquid phase $\%C_2H_6$	T (K)	H_2O mol fract ($\times 10^4$)	Liquid phase $\%C_2H_6$	T (K)	H_2O mol fract ($\times 10^4$)
0.5	260.4	0.296	0.75	261.1	0.311
0.5	255.9	0.214	0.895	277.9	1.076
0.75	277.9	1.101	0.895	266.8	0.465
0.75	275.9	0.980	0.895	263.4	0.346
0.75	269.6	0.611	0.895	257.7	0.226

Hydrates: Ethane + carbon dioxide
Reference: Adisasmito and Sloan (1992)
Phases: L_W–H–V

$\%CO_2$	T (K)	P (kPa)	$\%CO_2$	T (K)	P (kPa)
22.0	273.7	565.4	60.2	284.4	2833.7
20.2	275.6	696.4	80.7	274.2	1041.1
18.9	277.5	868.7	83.6	276.0	1344.5
19.3	279.3	1089.4	83.3	277.5	1613.4
24.6	281.1	1406.5	82.1	279.4	1958.1
25.6	282.9	1751.3	81.7	281.0	2406.3
31.7	285.1	2392.5	81.9	283.0	3150.9
42.8	276.5	854.9	81.4	284.6	3785.2
41.7	278.4	1075.6	93.4	273.9	1199.7
40.6	280.2	1351.4	93.2	275.6	1482.4
40.0	282.0	1716.8	92.6	277.6	1847.8
40.2	283.8	2185.6	92.4	279.2	2220.1
38.9	285.8	2826.8	92.3	281.2	2833.7
39.8	287.8	3826.6	96.5	273.7	1241.1
63.9	273.5	779.1	96.2	275.2	1482.4
62.8	274.8	889.4	96.1	276.7	1758.2
63.0	276.8	1123.8	95.5	278.6	2220.1
62.9	278.7	1420.3	95.7	280.6	2854.4
62.1	280.7	1806.4	96.6	281.8	3357.7
59.9	282.6	2240.8	96.7	283.1	4081.7

Hydrate: Ethane + carbon dioxide
Reference: Fan and Guo (1999)
Phases: L_W–H–V

5.31 mol% Ethane

T (K)	P (MPa)	T (K)	P (MPa)
276.0	1.58	281.6	3.31
278.2	2.07	282.7	3.90
280.4	2.84		

Binary Guest Mixtures Containing Propane and Heavier (or Noncombustible) Components

Hydrate: Propane + isobutane
Reference: Kamath and Holder (1984)
Phases: I–H–V

$\%C_3H_8$	*T* (K)	*P* (kPa)	$\%C_3H_8$	*T* (K)	*P* (kPa)
0.0	272.1	101.3	90.7	272.2	149.43
12.5	272.2	108.2	90.9	272.2	149.24
12.6	272.2	108.5	95.8	272.1	152.04
50.7	272.2	124.0	95.8	272.1	152.13
50.5	272.2	124.6	95.9	272.2	153.70
49.8	272.2	130.0	100.0	272.1	171.32
81.0	272.1	137.1			

Hydrate: Propane + isobutane
Reference: Paranjpe et al. (1987)
Phases: L_W–H–V–L_{HC}

$\%C_3H_8$ = vapor composition

$\%C_3H_8$	*T* (K)	*P* (kPa)	$\%C_3H_8$	*T* (K)	*P* (kPa)
11.2	275.25	213.0	48.8	276.65	365.4
27.1	275.85	282.7	65.3	277.15	426.1
47.5	276.55	355.1	79.4	277.85	490.0

Hydrate: Propane + *n*-butane
Reference: Kamath and Holder (1984)
Phases: I–H–V

$\%C_3H_8$	*T* (K)	*P* (kPa)	$\%C_3H_8$	*T* (K)	*P* (kPa)
90.3	260.15	110.10	83.5	248.15	69.03
90.3	257.85	99.26	83.5	245.85	66.76
90.3	254.35	83.86	83.5	242.45	59.59
90.3	248.65	67.09	70.0	253.75	97.16
90.3	245.05	61.23	70.0	250.95	85.86
90.3	242.05	49.20	70.0	245.65	70.07
83.5	250.55	76.36	70.0	241.85	55.38
83.5	249.55	73.37	70.0	238.25	46.90

Hydrate: Propane + *n*-butane
Reference: Paranjpe et al. (1987)
Phases: I–H–V, L_W–H–V, L_W–H–V–$L_{n\text{-}C4}$, I–H–V–$L_{n\text{-}C4}$

I–H–V (%C_3H_8 = vapor composition)

%C_3H_8	*T* (K)	*P* (kPa)	%C_3H_8	*T* (K)	*P* (kPa)
86.4	271.2	153.1	80.3	271.2	191.7
87.9	271.2	170.9	76.0	271.2	204.1
86.1	271.2	177.9	67.6	271.2	217.9

L_W–H–V

%C_3H_8	*T* (K)	*P* (kPa)	%C_3H_8	*T* (K)	*P* (kPa)
99.6	275.2	269.6	81.7	274.2	269.6
92.4	275.2	281.3	100.0	273.2	169.6
89.4	275.2	302.0	96.9	273.2	171.7
87.3	275.2	308.9	95.3	273.2	177.9
88.0	275.2	317.2	93.8	273.2	183.4
86.3	275.2	339.2	89.5	273.2	193.1
100.0	274.2	219.3	86.4	273.2	208.2
96.1	274.2	228.2	82.8	273.2	220.6
93.3	274.2	240.6	78.8	273.2	227.5
90.6	274.2	244.8	72.5	273.2	244.1

I–H–V–$L_{n\text{-}C4}$

%C_3H_8	*T* (K)	*P* (kPa)	%C_3H_8	*T* (K)	*P* (kPa)
64.9	273.0	215.1	64.9	267.4	174.4
67.4	271.0	211.7	63.9	266.8	168.2
67.3	270.0	201.3	64.8	264.0	157.9
62.1	269.6	184.8	66.5	262.0	146.2
66.5	269.0	192.4	65.1	260.6	133.8

L_W–H–V–$L_{n\text{-}C4}$

%C_3H_8	*T* (K)	*P* (kPa)	C_3H_8	*T* (K)	*P* (kPa)
92.6	277.85	511.6	81.6	275.2	324.1
84.6	276.65	399.2	71.0	273.6	242.7

Mixture: Propane + nitrogen
Reference: Ng et al. (1977, 1978)
Phases: L_W–H–V, L_W–H–V–L_{C_3}, L_W–H–L_{C_3}

L_W–H–V (%C_3H_8 = vapor composition)

%C_3H_8	*T* (K)	*P* (MPa)	%C_3H_8	*T* (K)	*P* (MPa)
0.94	275.3	4.59	13.00	281.5	2.74
0.94	279.6	8.16	13.00	283.2	3.54
0.94	283.0	13.68	13.00	286.2	5.54
0.94	284.3	18.09	28.30	274.6	0.569
2.51	276.3	3.03	28.30	277.0	0.889
2.51	279.3	4.51	28.30	279.2	1.31
2.51	282.7	7.35	28.30	280.8	1.72
2.51	287.1	13.64	54.20	274.2	0.332
6.18	274.5	1.72	54.20	276.8	0.570
6.18	278.3	2.85	54.20	280.3	1.19
6.18	283.0	5.50	75.00	274.5	0.256
6.18	287.0	9.47	75.00	275.9	0.359
6.18	289.2	13.71	75.00	277.4	0.517
13.00	275.1	1.10	75.00	278.7	0.676
13.00	278.4	1.72			

L_W–H–V–L_{C_3} (%C_3H_8 = vapor composition)

%C_3H_8	*T* (K)	*P* (MPa)	%C_3H_8	*T* (K)	*P* (MPa)
71.1	279.0	0.76	18.8	289.6	8.58
47.7	281.2	1.54	21.3	292.3	13.37
26.5	283.2	2.88	21.6	292.3	13.51
22.9	284.6	3.68	23.0	293.0	14.92
18.8	288.0	6.37	23.7	293.8	16.99

L_W–H–L_{C_3} (%C_3H_8 = liquid composition)

%C_3H_8	*T* (K)	*P* (MPa)	%C_3H_8	*T* (K)	*P* (MPa)
99.0	280.1	1.17	89.6	287.4	5.83
99.0	280.1	1.98	89.6	287.9	8.14
99.0	280.3	5.65	89.6	288.5	11.06
99.0	280.6	9.39	89.6	288.8	12.82

(Continued)

Continued

%C_3H_8	*T* (K)	*P* (MPa)	%C_3H_8	*T* (K)	*P* (MPa)
99.0	280.9	13.89	88.6	287.7	6.17
96.8	282.7	2.34	88.6	288.0	7.34
96.8	282.8	2.85	88.6	288.2	8.20
96.8	283.2	7.10	88.6	288.4	9.11
96.8	283.7	10.44	83.1	289.8	8.86
93.5	285.2	4.08	83.1	290.0	9.82
93.5	285.5	5.16	83.1	290.5	11.25
93.5	286.1	8.41	83.1	290.9	13.29
93.5	286.3	11.55	83.1	291.3	15.31
93.5	286.7	13.33			

Hydrate: Propane + carbon dioxide
Reference: Robinson and Mehta (1971)
Phases: L_W–H–V

%C_3H_8 = vapor composition

%C_3H_8	*T* (K)	*P* (kPa)	%C_3H_8	*T* (K)	*P* (kPa)
5.5	284.83	4268	25.0	283.8	1917
6.0	276.3	1151	25.0	280.2	979
7.0	273.8	814	26.0	281.8	1303
8.0	283.7	3179	42.0	283.7	1655
8.0	281.7	2186	42.2	275.7	414
8.0	273.9	676	47.5	278.6	689
9.0	283.5	3034	48.0	281.1	1069
9.0	280.4	1772	60.0	279.7	793
9.0	278.9	1455	60.0	274.8	324
10.0	278.3	1255	61.0	276.4	434
13.0	280.9	1572	63.0	279.6	752
13.0	273.8	517	65.0	278.3	579
14.0	279.4	1207	72.0	275.2	303
15.0	275.4	827	82.0	279.1	593
15.0	276.5	758	83.0	278.2	503
16.0	286.2	3378	83.0	279.1	641
21.0	274.0	359	84.0	277.8	476
23.0	278.1	710	86.0	276.0	338
24.0	277.4	655			

Hydrate: Propane + carbon dioxide
Reference: Adisasmito and Sloan (1992)
Phases: L_W–H–V

$\%CO_2$	*T* (K)	*P* (kPa)	$\%CO_2$	*T* (K)	*P* (kPa)
9.9	273.7	220.6	91.2	278.2	1337.6
43.5	273.7	262.0	92.9	278.2	1537.5
60.2	273.7	337.8	94.7	278.2	2164.9
71.0	273.7	406.8	95.4	278.2	2440.7
84.2	273.7	489.5	97.0	278.2	2344.2
88.5	273.7	592.9	98.7	278.2	2227.0
90.8	273.7	655.0	30.0	280.4	930.8
93.3	273.7	717.1	49.7	280.4	965.3
94.4	273.7	848.1	74.0	280.4	1020.4
95.3	273.7	985.9	80.1	280.4	1123.8
96.3	273.7	1261.7	89.1	280.4	1640.9
97.1	273.7	1406.5	91.1	280.4	1999.5
98.5	273.7	1358.3	92.4	280.4	2316.6
32.7	275.9	351.6	94.0	280.4	2999.2
65.0	275.9	448.2	95.4	280.4	3109.5
74.8	275.9	551.6	96.5	280.4	3033.7
86.0	275.9	737.7	98.7	280.4	2909.6
92.2	275.9	917.0	35.0	282.0	1248.3
93.7	275.9	999.7	57.7	282.0	1317.2
95.1	275.9	1268.6	79.4	282.0	1510.3
95.8	275.9	1634.1	85.2	282.0	1800.0
96.8	275.9	1799.5	88.5	282.0	2206.9
97.1	275.9	1771.9	90.8	282.0	2779.3
99.0	275.9	1682.3	92.0	282.0	3186.2
35.7	278.2	551.6	92.8	282.0	3800.0
63.4	278.2	717.1	95.2	282.0	3820.7
81.1	278.2	965.3	97.0	282.0	3724.1
			98.7	282.0	3641.4

Binary Guest Mixtures Containing Isobutane and/or *n*-Butane

Hydrates: Isobutane + *n*-butane
Reference: Godbole (1981)
Phases: L_W–H–V

$\%i\text{-}C_4H_{10}$	*T* (K)	*P* (kPa)	$\%i\text{-}C_4H_{10}$	*T* (K)	*P* (kPa)
0.77	267.3	68.8	0.748	265.3	80.8
0.77	261.1	56.2	0.748	263.4	73.2
0.835	264.3	63.2			

Hydrates: Isobutane + carbon dioxide
Reference: Adisasmito and Sloan (1992)
Phases: L_W–H–V

$\%CO_2$	T (K)	P (kPa)	$\%CO_2$	T (K)	P (kPa)
20.7	273.7	144.8	79.0	277.6	537.8
52.8	273.7	165.5	85.2	277.6	641.2
66.6	273.7	206.8	94.2	277.6	958.4
77.5	273.7	275.8	96.6	277.6	1337.6
84.3	273.7	344.7	97.5	277.6	1792.6
89.3	273.7	427.5	98.2	277.6	2123.6
94.2	273.7	565.4	99.0	277.6	2082.2
96.7	273.7	744.6	62.5	279.3	517.1
97.7	273.7	937.7	71.9	279.3	551.6
98.3	273.7	1137.6	82.4	279.3	696.4
98.6	273.7	1358.3	88.0	279.3	841.2
99.3	273.7	1323.8	93.5	279.3	1151.4
30.8	275.9	262.0	95.4	279.3	1468.6
42.3	275.9	275.8	96.5	279.3	1840.9
58.8	275.9	303.4	97.1	279.3	2137.4
72.8	275.9	358.3	97.6	279.3	2564.8
85.4	275.9	496.4	98.4	279.3	2606.2
91.9	275.9	634.3	99.6	279.3	2558.0
94.4	275.9	744.6	79.1	280.9	875.6
95.4	275.9	827.4	85.2	280.9	1054.9
96.6	275.9	999.7	91.8	280.9	1523.7
97.4	275.9	1234.2	94.1	280.9	1799.5
98.3	275.9	1723.7	95.3	280.9	2033.9
99.0	275.9	1703.0	96.1	280.9	2316.6
54.0	277.6	413.7	97.3	280.9	3178.5
66.1	277.6	441.3	97.9	280.9	3171.6

Hydrates: *n*-Butane + carbon dioxide
Reference: Adisasmito and Sloan (1992)
Phases: L_W–H–V

$\%CO_2$	T (K)	P (kPa)	$\%CO_2$	T (K)	P (kPa)
92.3	273.7	1137.9	94.4	277.0	1917.2
93.9	273.7	1206.9	95.2	277.0	1993.1
95.5	273.7	1317.2	96.8	277.0	2082.8
97.7	273.7	1351.7	98.0	277.0	2041.4
98.4	273.7	1337.9	98.8	277.0	2013.8
99.2	273.7	1324.1	99.4	277.0	1993.1
93.0	275.4	1462.1	96.2	278.2	2400.0
94.8	275.4	1586.2	97.5	278.2	2372.4
97.3	275.4	1675.9	98.5	278.2	2331.0
98.0	275.4	1655.2	99.1	278.2	2303.4
99.2	275.4	1620.7			

Binary Guest Mixtures Containing Nitrogen and Carbon Dioxide

Hydrate: Nitrogen + carbon dioxide
Reference: Fan and Guo (1999)
Phases: L_W–H–V

mol% N_2	T (K)	P (MPa)
3.48	273.1	1.22
3.48	274.6	1.54
3.48	278.3	2.42
3.48	279.4	2.89
3.48	280.2	2.95
9.01	273.4	1.37
9.01	274.1	1.53
9.01	276.7	1.89
9.01	279.1	3.09

Hydrate: Nitrogen + carbon dioxide
Reference: Kang et al. (2001)
Phases: L_W–H–V

x_{CO_2} (loading)	T (K)	P (MPa)	x_{CO_2} (loading)	T (K)	P (MPa)
0.9659	274.95	1.565	0.1761	272.85	7.240
	277.45	2.060		274.05	8.120
	280.25	2.900		277.45	10.650
	282.55	4.000		278.65	11.748
	283.55	5.115		280.55	14.220
0.7780	274.00	2.000	0.1159	274.25	11.020
	276.15	2.600		275.65	13.870
	280.65	4.225		277.60	18.100
	283.45	6.450		278.95	22.230
	284.25	7.445			
0.4815	273.75	3.195	0.0063	273.95	14.085
	276.00	4.257		274.55	15.400
	279.00	5.867		277.00	20.680
	281.00	7.449		278.25	24.120
	282.00	8.975			

Hydrate: Nitrogen + carbon dioxide
Reference: Kang et al. (2001)
Phases: H–V

T (K)	P (MPa)	x_{CO_2} (vapor)	x_{CO_2} (hydrate)
274	1.394	1.0000	1.0000
	1.769	0.8205	0.9850
	2.354	0.5999	0.9517
	2.835	0.5048	0.9301
	3.560	0.3994	0.9001
	7.235	0.2057	0.5836
	11.200	0.1159	0.3426
	14.928	0.0498	0.1793
	17.926	0.0000	0.0000
277	1.953	1.0000	1.0000
	2.600	0.8491	0.9782
	3.377	0.5867	0.9455
	5.233	0.3899	0.8867
	11.980	0.1761	0.5400
	15.500	0.1159	0.3526
	19.174	0.0663	0.1928
	24.041	0.0000	0.0000
280	2.801	1.0000	1.0000
	3.600	0.8520	0.9765
	4.233	0.6999	0.9612
	5.068	0.5917	0.9432
	8.275	0.3924	0.8641
	14.974	0.2510	0.6400
	20.753	0.1709	0.4500
	26.690	0.0905	0.2217
	32.308	0.0000	0.0000

6.3.1.2.2 Structure H hydrate data (binary, multicomponent, inhibited)

With few exceptions (as indicated in the table), all structure H equilibria data were obtained with methane as the small component. Also because there were always four phases present (L_W–H–V–L_{HC}) with three components (including water) the Gibbs Phase Rule provides for only one composition of each phase which satisfies the equilibrium conditions. Consequently all data were taken without measurement of any phase composition, and only the equilibrium temperature and pressure of the four phases are reported. Due to the paucity of structure H data, included here are one binary including nitrogen and three structure H systems with inhibitor. Such systems clearly illustrate the need for more structure H data.

Hydrates: Methane + large hydrocarbon component
References: Given in table
Phases: L_W–H(sH)–V–L_{HC}

Large component	*T* (K)	*P* (MPa)	Reference
Isopentane	275.2	2.654	Mehta and Sloan (1993)
	276.2	2.978	
	277.8	3.640	
	279.0	4.150	
Isopentane	274.0	2.241	Hütz and Englezos (1995)
	276.2	2.955	
	277.4	3.501	
Neopentane	276.6	0.400	Tohidi et al. (1997a)
	282.9	1.014	
	286.0	1.593	
	289.9	2.944	
	292.8	4.861	
Neohexane	276.0	1.598	Mehta and Sloan (1993)
	278.0	2.028	
	279.2	2.391	
	282.2	3.339	
Neohexane	285.4	5.22	Thomas and Behar (1994)
	288.2	7.51	
Neohexane	275.0	1.415	Hütz and Englezos (1995)
	276.8	1.805	
	279.9	2.601	
	282.8	3.750	
Neohexane	244.8	0.332	T. Makogon et al. (1996)
	251.4	0.447	
	258.8	0.626	
	274.0	1.241	
Neohexane	254.40	0.509	Ohmura et al. (2005)
	255.90	0.548	
	257.85	0.597	
	258.85	0.623	
	260.85	0.678	
	263.35	0.751	
	267.35	0.882	
	269.65	0.966	
	271.35	1.025	
	272.85	1.095	

(Continued)

Continued

Large component	*T* (K)	*P* (MPa)	Reference
2,3-Dimethylbutane	275.9	2.078	Mehta and Sloan (1994a)
	277.4	2.482	
	279.2	3.088	
	280.8	3.795	
2,3-Dimethylbutane	282.6	4.95	Thomas and Behar (1994)
	286.4	8.19	
2,2,3-Trimethylbutane	275.6	1.475	Mehta and Sloan (1994a)
	277.4	1.840	
	279.5	2.247	
	280.9	2.702	
2,2,3-Trimethylbutane	288.0	5.94	Thomas and Behar (1994)
	289.4	7.55	
2,2-Dimethylpentane	275.9	3.287	Mehta and Sloan (1994a)
	277.4	3.819	
	279.2	4.556	
	280.31	5.140	
	281.34	5.832	
	282.2	6.195	
	282.8	6.691	
2,2-Dimethylpentane	286.6	3.79	Thomas and Behar (1994)
	288.2	5.70	
	290.0	7.15	
3,3-Dimethylpentane	274.8	1.734	Mehta and Sloan (1994a)
	277.0	2.264	
	279.2	3.009	
	281.3	3.930	
3,3-Dimethylpentane	280.6	3.62	Thomas and Behar (1994)
	283.6	5.42	
	286.4	7.28	
Methylcyclopentane	276.5	2.199	Mehta and Sloan (1994a)
	277.8	2.578	
	279.5	3.195	
	280.8	3.812	

Continued

Large component	*T* (K)	*P* (MPa)	Reference
Methylcyclopentane	279.2	3.22	Thomas and Behar (1994)
	281.3	3.94	
	282.6	4.70	
	284.8	6.14	
	286.0	7.44	
	287.2	8.69	
	287.8	10.01	
Methylcyclopentane	278.2	2.635	Danesh et al. (1994)
	278.6	2.937	
	279.0	2.965	
	279.7	3.289	
	280.35	3.737	
	282.2	4.606	
	283.0	4.999	
	283.2	5.295	
	285.2	6.653	
	287.0	8.625	
Methylcyclopentane	274.28	1.75	Makino et al. (2004)
	275.25	1.98	
	276.20	2.22	
	277.08	2.48	
	277.99	2.77	
	278.88	3.08	
	279.78	3.47	
	280.67	3.88	
	281.48	4.29	
	282.27	4.75	
	283.06	5.25	
	283.86	5.79	
	284.66	6.44	
	285.43	7.12	
	286.21	7.92	
	286.77	8.57	
	287.40	9.34	
Methylcyclohexane	275.6	1.599	Mehta and Sloan (1994b)
	277.6	2.137	
	279.4	2.688	
	281.2	3.357	

(Continued)

Continued

Large component	*T* (K)	*P* (MPa)	Reference
Methylcyclohexane	280.2	3.0	Becke et al. (1992)
	280.6	3.2	
	285.6	6.0	
	289.6	10.2	
	290.4	11.2	
Methylcyclohexane	282.6	3.99	Thomas and Behar (1994)
	284.2	4.62	
	286.45	6.47	
	287.4	7.61	
	289.2	8.82	
	290.25	10.5	
Methylcyclohexane	277.1	2.041	Tohidi et al. (1996a)
	279.9	2.951	
	282.2	3.937	
	283.4	4.606	
	287.1	7.391	
Methylcyclohexane	279.48	2.65	Mooijer-van den Heuvel et al. (2000)
	280.49	2.93	
	281.43	3.17	
	282.42	3.87	
	283.39	4.37	
	284.44	4.81	
	284.95	5.20	
	285.44	5.50	
	285.95	5.96	
	286.49	6.34	
	286.96	6.75	
	287.46	7.34	
	288.40	8.33	
	288.97	9.13	
Methylcyclohexane	274.09	1.42	Nakamura et al. (2003)
	274.78	1.54	
	275.28	1.66	
	275.79	1.75	
	276.26	1.87	
	276.79	1.99	
	277.26	2.11	
	277.80	2.25	
	278.30	2.39	
	279.25	2.70	
	280.26	3.05	
	281.27	3.45	

Continued

Large component	*T* (K)	*P* (MPa)	Reference
Methylcyclohexane	282.28	3.90	Nakamura et al. (2003)
	283.29	4.43	
	284.30	5.03	
	285.29	5.72	
	286.28	6.50	
	287.25	7.42	
	288.29	8.48	
Methylcyclohexane	251.50	0.519	Ohmura et al. (2005)
	253.15	0.559	
	255.70	0.619	
	258.10	0.686	
	261.00	0.774	
	264.00	0.873	
	267.00	0.984	
	269.05	1.063	
	271.00	1.145	
	272.60	1.213	
cis-1,2-Dimethylcyclohexane	275.8	1.871	Mehta and Sloan (1994a)
	277.4	2.237	
	279.4	2.816	
	281.0	3.433	
cis-1,2-Dimethylcyclohexane	282.0	4.00	Thomas and Behar (1995)
	284.4	5.29	
	286.2	6.81	
	287.4	7.63	
	288.8	9.67	
	290.0	11.32	
cis-1,2-Dimethylcyclohexane	274.18	1.57	Nakamura et al. (2003)
	274.65	1.67	
	275.25	1.80	
	276.22	2.03	
	277.18	2.29	
	278.14	2.57	
	279.10	2.89	
	280.10	3.28	
	281.58	3.93	
	283.04	4.71	
	284.53	5.66	
	285.99	6.83	
	286.93	7.75	
	287.96	8.89	

(Continued)

Continued

Large component	*T* (K)	*P* (MPa)	Reference
2,3-Dimethyl-1-butene	275.7	2.530	Mehta and Sloan (1994a)
	277.8	3.275	
	279.53	4.088	
	280.78	4.805	
3,3-Dimethyl-1-butane	276.2	2.016	Mehta and Sloan (1994a)
	277.6	2.423	
	279.2	2.933	
	281.42	3.871	
3,3-Dimethyl-1-butyne	275.8	2.851	Mehta (1996)
	276.9	3.216	
	278.4	3.878	
	278.9	4.133	
	279.6	4.567	
Cyclopentane*	282.8	0.157	Tohidi et al. (1997a)
	283.8	0.237	
	285.5	0.372	
	289.1	0.869	
	291.7	1.462	
	294.4	2.082	
	300.5	5.426	
Cyclohexane*	283.5	2.68	Mooijer-van den Heuvel et al. (2000)
	285.51	3.61	
	287.48	4.82	
	289.49	6.49	
	291.48	8.70	
	293.46	11.66	
Cycloheptene	275.1	2.106	Mehta and Sloan (1994a)
	277.7	2.671	
	279.2	3.051	
	281.0	3.809	
cis-Cyclooctene	276.9	2.082	Mehta and Sloan (1994a)
	278.5	2.562	
	280.0	3.009	
	281.3	3.561	
Adamantane	275.1	1.779	Lederhos et al. (1992)
	276.9	2.165	
	278.4	2.510	
	280.2	3.001	

* sII not sH

Continued

Large component	*T* (K)	*P* (MPa)	Reference
Adamantane	275.2	1.790	Hütz and Englezos (1995)
	275.9	1.941	
	277.6	2.300	
	279.1	2.709	
Ethylcyclopentane	280.2	3.59	Thomas and Behar (1995)
	281.2	4.02	
	283.2	5.16	
	284.8	6.39	
	286.4	7.93	
	287.4	9.13	
1,1-Dimethylcyclohexane	280.2	2.00	Thomas and Behar (1995)
	281.0	2.34	
	282.4	2.82	
	283.6	3.34	
	285.8	4.30	
	287.8	5.51	
	288.8	6.06	
	290.6	7.53	
	291.8	9.07	
	292.6	10.13	
	293.2	11.53	
1,1-Dimethylcyclohexane	274.67	1.07	Hara et al. (2005)
	276.67	1.37	
	278.65	1.76	
	280.63	2.19	
	282.61	2.90	
	284.57	3.74	
	286.53	4.75	
	288.51	6.08	
	289.31	6.77	
cis-1,4-Dimethylcyclohexane	274.13	1.62	Nakamura et al. (2004)
	274.75	1.76	
	275.30	1.88	
	275.98	2.03	
	276.79	2.24	
	277.55	2.46	
	278.57	2.79	
	279.53	3.14	

(Continued)

Continued

Large component	*T* (K)	*P* (MPa)	Reference
cis-1,4-Dimethylcyclohexane	280.50	3.53	Nakamura et al. (2004)
	281.44	3.93	
	281.97	4.22	
	282.45	4.45	
	283.43	5.01	
	284.30	5.62	
	285.30	6.32	
	285.72	6.78	
	286.15	7.16	
	286.97	8.04	
	287.49	8.53	
	287.95	9.13	
Ethylcyclohexane	283.6	6.3	Thomas and Behar (1995)
	286.0	8.9	
Cycloheptane	281.4	3.39	Thomas and Behar (1995)
	284.1	4.62	
	285.0	5.15	
	286.8	6.54	
	288.2	7.79	
	289.2	9.15	
	290.4	10.93	
Cyclooctane	282.4	4.21	Thomas and Behar (1995)
	284.4	5.36	
	285.8	6.29	
	286.4	6.63	
	287.4	7.55	
	289.0	9.65	
	290.4	11.65	
Cyclooctane	274.08	1.60	Makino et al. (2004)
	275.16	1.84	
	276.17	2.03	
	277.15	2.29	
	278.00	2.53	
	278.83	2.79	
	279.78	3.14	
	280.96	3.57	
	282.13	4.13	
	283.07	4.64	
	284.11	5.28	
	284.90	5.83	
	285.90	6.59	

Continued

Large component	*T* (K)	*P* (MPa)	Reference
Cyclooctane	286.91	7.50	Makino et al. (2004)
	287.87	8.53	
	288.13	8.84	
	288.57	9.33	
tert-Butyl methyl ether	274.6	1.85	Hütz and Englezos (1995)
	277.5	2.55	
	280.8	3.95	
	284.1	5.90	
tert-Butyl methyl ether	252.85	0.652	Ohmura et al. (2005)
	256.35	0.731	
	259.84	0.836	
	263.25	0.947	
	266.65	1.07	
	269.85	1.203	
	270.85	1.252	

Hydrate: Propane + methylcyclohexane
Reference: Mooijer-van den Heuvel et al. (2002)
Phase: L_W–H*–V–L_{HC}, L_W–H*–L_{HC}, and Q(L_W–H*–V–L_{HC})
Overall feed composition: $x_{H_2O} = 0.9100$, $x_{C_3H_8} = 0.0502$, $x_{MCH} = 0.0398$

Q(L_W–H–V–L_{HC}) at $T = 276.50$, $P = 0.200$ MPa

L_W–H–V–L_{HC}		L_W–H–L_{HC}	
T (K)	*P* (MPa)	*T* (K)	*P* (MPa)
274.52	0.139	276.71	0.647
275.04	0.158	276.91	0.897
275.46	0.163	277.13	1.147
275.51	0.164	277.19	1.396
275.76	0.167	277.33	1.896
276.05	0.185	277.12	2.396
		277.19	2.396
		277.05	2.893
		277.09	3.893
		277.05	4.893
		277.09	5.893
		277.07	6.893
		277.04	7.893

* Probably sII (not sH), no structure confirmation done

Hydrate: Propane + cyclohexane
Reference: Mooijer-van den Heuvel et al. (2002)
Phase: L_W–H*–V–L_{HC}, L_W–H*–L_{HC}, and Q(L_W–H*–V–L_{HC})
Overall feed composition: $x_{H_2O} = 0.8987$, $x_{C_3H_8} = 0.0503$, $x_{CH} = 0.0510$

Q(L_W–H–V–L_{HC}) at $T = 276.05$, $P = 0.172$ MPa

L_W–H–V–L_{HC}		L_W–H–L_{HC}	
T **(K)**	***P*** **(MPa)**	***T*** **(K)**	***P*** **(MPa)**
274.52	0.146	276.04	0.545
274.98	0.151	276.03	0.645
274.52	0.157	276.09	0.895
275.33	0.157	276.13	1.145
275.67	0.164	276.17	1.395
275.81	0.168	276.26	1.642
274.98	0.172	276.18	2.392
275.51	0.174	276.32	2.893
276.10	0.175	276.32	3.893
275.50	0.185	276.38	4.893
		276.43	5.893
		276.46	6.893
		276.53	7.893
		276.61	8.893
		276.61	9.893

* Probably sII (not sH), no structure confirmation done

Hydrate: Carbon dioxide + methylcyclohexane
Reference: Mooijer-van den Heuvel et al. (2001)
Phases: L_W–H–V–L_{MCH}, L_W–H–L_{CO_2}–L_{MCH}, and Quadruple point Q_2
Overall feed compositon: $x_{H_2O} = 0.7488$, $x_{CO_2} = 0.1257$, $x_{MCH} = 0.1255$

Q_2 at 280.22 K and 2.89 MPa

L_W–H–V–L_{MCH}		L_W–H–L_{CO_2}–L_{MCH}	
T **(K)**	***P*** **(MPa)**	***T*** **(K)**	***P*** **(MPa)**
277.06	1.86	280.24	2.90
277.22	1.89	280.24	3.39
277.29	1.91	280.25	3.89
277.33	1.94	280.30	4.89
277.36	1.91	280.31	4.39
277.59	2.00	280.43	5.40
277.77	2.05	280.46	6.39

Continued

L_W–H–V–L_{MCH}		L_W–H–L_{CO_2}–L_{MCH}	
T **(K)**	***P*** **(MPa)**	***T*** **(K)**	***P*** **(MPa)**
277.99	2.10	280.47	6.39
278.18	2.15	280.50	5.89
278.35	2.22	280.53	6.89
278.63	2.26	280.63	8.39
278.85	2.32	280.68	7.39
279.07	2.44	280.70	7.89
279.37	2.53	280.76	8.89
279.49	2.59	280.81	9.39
279.61	2.58	280.84	10.39
279.74	2.64	280.84	9.89
279.79	2.69	280.89	10.39
279.84	2.71	280.94	11.39
279.99	2.76	280.99	10.89
280.15	2.78		

Hydrates: Natural gas + methylcyclohexane
Reference: Tohidi et al. (2001)
Phases: L_W–H–V–L_{HC}
Composition (mol%) of natural gas: 4.99% N_2; 1.12% CO_2; 86.36% CH_4; 5.43% C_2H_6; 1.49% C_3H_8; 0.18% i-C_4H_{10}; 0.31% n-C_4H_{10}; 0.06% i-C_5H_{12}; 0.06% n-C_5H_{12}; <0.01% C_6^+

L_W–H–V–L_{HC} Conditions of Gas Mixture with Methylcyclohexane (MCH)

Natural gas (NG)		**NG + 21.9 mol% MCH**		**NG + 37.2% MCH**		**NG + 49.3% MCH**	
T **(K)**	***P*** **(MPa)**	***T*** **(K)**	***P*** **(MPa)**	***T*** **(K)**	***P*** **(MPa)**	***T*** **(K)**	***P*** **(MPa)**
276.15	1.269	278.75	2.103	279.75	3.089	280.6	3.468
283.35	3.054	280.85	2.875	282.05	4.089	284.0	5.357
284.15	3.337	283.75	4.316	284.95	6.109	286.5	7.543
285.65	4.075	287.65	7.377	287.95	9.308	290.8	13.79
286.25	4.688	290.05	11.04	289.65	12.34		
290.05	7.619						
291.05	8.705						

Hydrates: Nitrogen + methylcyclopentane (MCP) or methylcyclohexane (MCH)
Reference: Danesh et al. 1994 (MCP); Tohidi et al. 1996a (MCH)
Phases: L_W–H(sH)–V–L_{HC}

T (K)	*P* (MPa)	*T* (K)	*P* (MPa)
	Methylcyclopentane		
274.2	7.770	281.0	18.216
276.2	9.997	282.0	20.422
278.2	12.769	285.8	30.709
	Methylcyclohexane		
276.4	8.805	283.7	20.843
279.2	12.473		

Hydrates: Nitrogen + cyclopentane; nitrogen + neopentane
Reference: Tohidi et al. (1997a)
Phases: L_W–H–V–L_{HC}

Nitrogen + cyclopentane*		Nitrogen + neopentane	
T (K)	*P* (MPa)	*T* (K)	*P* (MPa)
282.9	0.647	278.9	2.303
284.3	1.282	282.5	4.337
286.6	2.117	287.8	9.708
289.1	3.496	281.3	15.775

* sII not sH

Hydrates: Methane + nitrogen + (methylcyclohexane or methylcyclopentane)
Reference: Tohidi et al. (1996a)
Phases: L_W–H(sH)–V–L_{HC}
Feed compositions: methylcyclohexane = 16.05 mol% CH_4, 23.17% N_2, 3.79% MCH, 56.99% H_2O; methylcyclopentane = 9.65 mol% CH_4, 12.38% N_2, 7.21% MCP, 70.76% H_2O

Continued

Methylcyclohexane		Methylcyclopentane	
***T* (K)**	***P* (MPa)**	***T* (K)**	***P* (MPa)**
279.4	5.178	278.0	5.495
282.3	7.577	280.9	8.122
286.1	12.328	284.8	13.872

Hydrates: Methane + large component + NaCl
References: Hütz and Englezos (1995)
Phases: L_W–H(sH)–V–L_{HC}

Large component	wt% NaCl	*T* (K)	*P* (MPa)
Isopentane	10	271.2	2.61
		272.6	3.16
		275.8	4.90
2,2-Dimethylbutane	12	272.4	2.06
		273.0	2.31
		276.1	3.35
		279.0	4.95
		281.2	6.55
tert-Butyl methyl ether	12	270.4	2.325
		274.4	3.601
		277.0	4.925
		279.4	6.96

Hydrates: Carbon dioxide + cyclohexane
Reference: Mooijer-van den Heuvel et al. (2001)
Phases: L_W–H*–V–L_{CH}, L_W–H*–L_{CO_2}–L_{CH}, and Quadruple point Q_2
Overall feed composition: $x_{H_2O} = 0.7122$, $x_{CO_2} = 0.1095$, $x_{CH} = 0.1783$

Q_2 at 280.03 K and 2.65 MPa

L_W–H–V–L_{CH}		L_W–H–L_{CO_2}–L_{CH}	
***T* (K)**	***P* (MPa)**	***T* (K)**	***P* (MPa)**
274.97	0.90	280.32	3.40
275.49	1.03	280.34	4.40

(Continued)

* Probably sII (not sH), no structure confirmation done

Continued

L_W–H–V–L_{CH}		L_W–H–L_{CO_2}–L_{CH}	
T **(K)**	***P*** **(MPa)**	***T*** **(K)**	***P*** **(MPa)**
275.97	1.13	280.91	7.40
276.51	1.26	281.03	8.40
276.97	1.41	281.09	9.40
277.49	1.55	281.23	10.40
278.03	1.77		
278.94	2.41		
279.22	2.49		
279.44	2.53		
279.80	2.55		

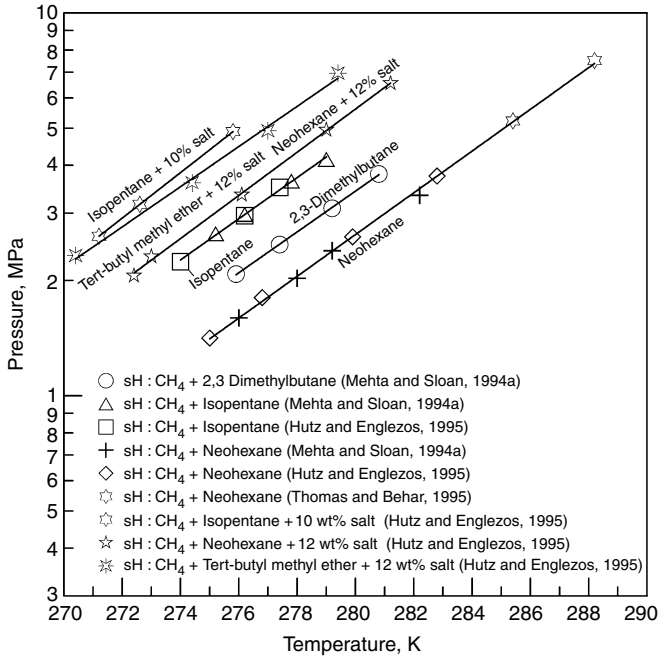

FIGURE 6.33 Data for structure H hydrates of methane with isopentane, neohexane, 2,3-dimethylbutane, and sodium chloride inhibition of hydrates of methane with isopentane, neohexane, and tert-butyl methyl ether.

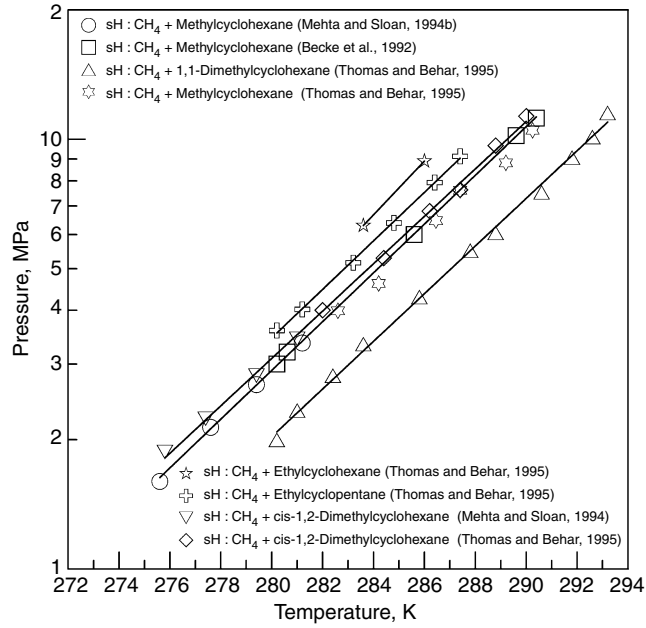

FIGURE 6.34 Data for structure H hydrates of methane with methylcyclohexane, 1,1-dimethylcyclohexane, cis-1,2-dimethylcyclohexane, and ethylcyclohexane.

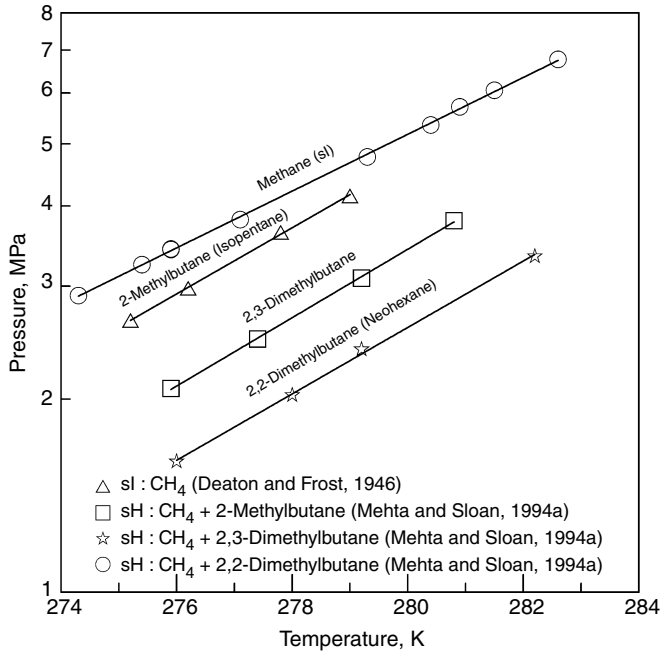

FIGURE 6.35 Data for structure H hydrates of methane with 2-methylbutane, 2,2-dimethylbutane, and 2,3-dimethylbutane.

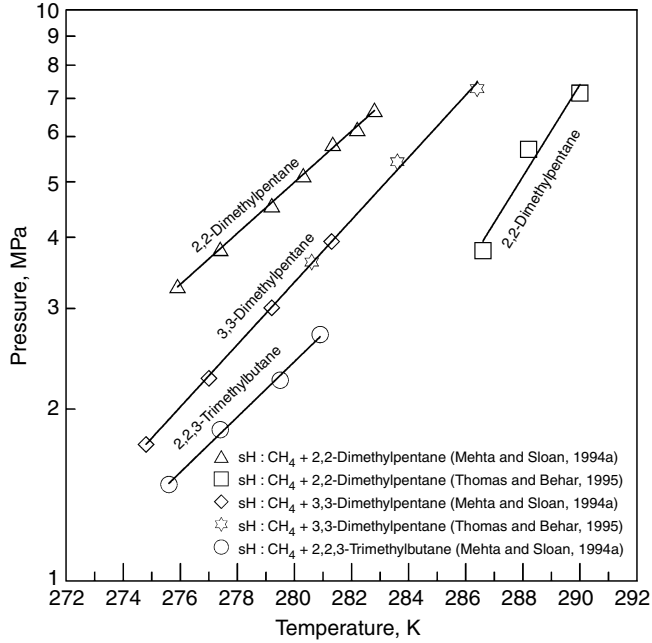

FIGURE 6.36 Data for structure H hydrates of methane with 2,2-dimethylpentane, 3,3-dimethylpentane, and 2,2,3-trimethylbutane.

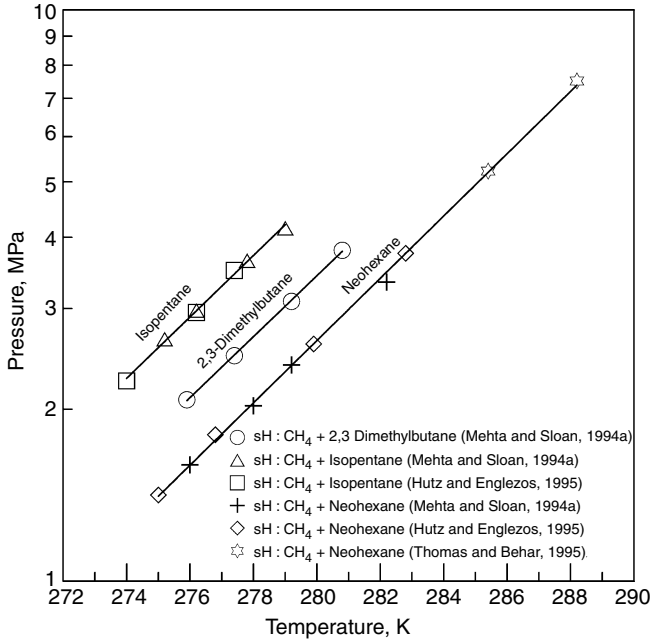

FIGURE 6.37 Data for structure H hydrates of methane with 2,3-dimethylbutane, isopentane, and neohexane.

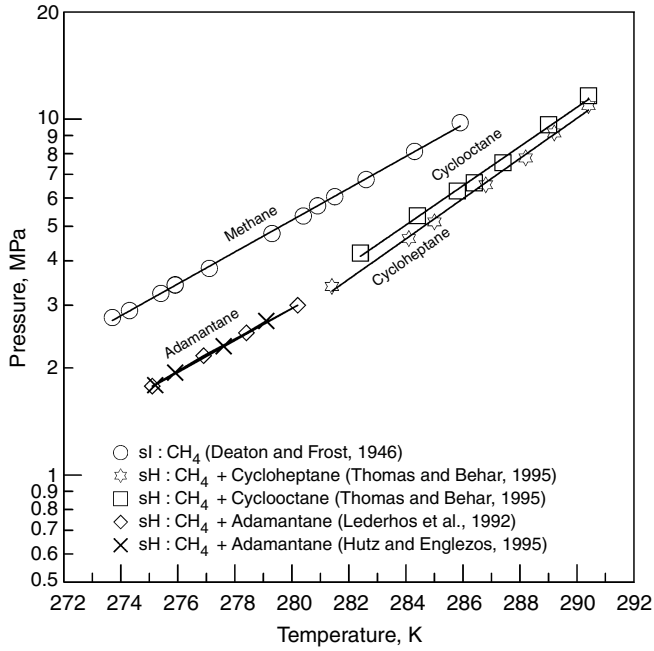

FIGURE 6.38 Data for structure H hydrates of methane with cycloheptane, cyclooctane, and adamantane.

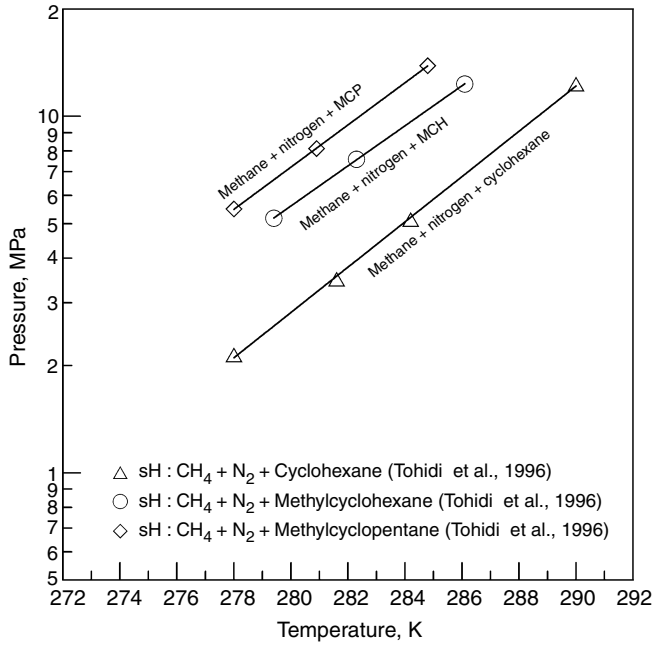

FIGURE 6.39 Data for structure H hydrates of methane + nitrogen with cyclohexane, methylcyclopentane, and methylcyclohexane.

6.3.1.3 Equilibria of ternary guest mixtures

Due to the diversity of gas compositions for ternary guest systems, duplicate data sets have not been obtained by various investigators. The variety of gas compositions make plots of the data meaningless, except for self-consistency within an individual investigation. Consequently plots of ternary (and higher) guest data sets are not provided. Frequently such plots are given in the original reference with the data set. Compositions are given in mol fractions or mol percent unless otherwise stated.

Hydrate: Methane + ethane + propane
Reference: Holder and Hand (1982)
Phases: L_W–H–V–L_{HC} (compositions are mol fractions in the L_{HC} phase)

$$x_{C1}/(x_{C1} + x_{C3}) = 0.0$$

x_{C_2}	T (K)	P (kPa)	x_{C_2}	T (K)	P (kPa)
0.168	278.1	900	NM	278.6	1300
NM	278.1	970	NM	279.4	1430
0.280	277.8	1080	NM	280.4	1560
NM	278.2	700	NM	280.6	1610
0.435	279.9	1480	NM	281.1	1630
0.523	281.8	1740	1.00	288.3	3330
0.689	284.3	2230			

NM = not measured.

$$x_{C1}/(x_{C1} + x_{C3}) = 0.0255$$

x_{C_2}	T (K)	P (kPa)	x_{C_2}	T (K)	P (kPa)
0.000	282.8	1030	0.716	284.8	2320
0.189	281.7	1240	0.799	286.1	2730
0.314	280.1	1580	1.000	288.3	3330
0.517	282.8	2020			

Continued

$$x_{C1}/(x_{C1} + x_{C3}) = 0.051$$

x_{C_2}	T (K)	P (kPa)	x_{C_2}	T (K)	P (kPa)
0.082	284.9	1500	0.549	283.7	2180
0.181	284.2	1610	0.726	285.7	2730
0.231	283.5	1680	1.000	288.3	3330

$$x_{C1}/(x_{C1} + x_{C3}) = 0.092$$

x_{C_2}	T (K)	P (kPa)	x_{C_2}	T (K)	P (kPa)
0.054	287.4	2120	0.506	283.8	2380
0.148	286.9	2170	0.616	285.1	2570
0.212	285.7	2210	0.677	285.9	2820
0.365	284.9	2280	1.000	288.3	3330

Hydrate: Methane + ethane + propane
Reference: Mooijer-van den Heuvel (2004; pp. 91, 244–245)
Phases: L_W–H(I + II)–V, L_W–H–V–L_{HC}, L_W–H(II)–V, L_W–H(I + II)–V, L_W–H(I + II)–L_{HC}, and L_W–H(I)–L_{HC} (Phase diagram is complex—see reference)
Overall composition: $x_{H_2O} = 0.938$, $y_{C_3H_6} = 0.501$

L_W–H(I + II)–V		L_W–H(II)–V–L_{HC}		L_W–H(II)–V	
T (K)	P (MPa)	T (K)	P (MPa)	T (K)	P (MPa)
277.59	1.13	277.91	1.15	277.06	0.81
277.78	1.09	277.93	1.15	277.90	0.81
277.80	1.17	277.98	1.01	277.96	0.86
277.86	1.00	278.05	1.05	278.03	0.86
		278.06	0.95	278.12	0.96
		278.06	1.01	278.18	0.91
		278.14	0.96		
		278.19	0.96		
		278.21	0.91		

(Continued)

Continued

L_W–H(I + II)–V		L_W–H(I + II)–L_{HC}		L_W–H(I)–L_{HC}	
T **(K)**	***P*** **(MPa)**	***T*** **(K)**	***P*** **(MPa)**	***T*** **(K)**	***P*** **(MPa)**
276.66	1.12	277.70	3.40	281.64	1.90
276.99	1.11	277.43	5.40	281.68	2.40
277.34	1.17	277.61	5.40	281.71	2.90
				281.92	3.40
				281.94	3.90
				282.07	3.90
				282.18	4.40
				282.27	4.90
				282.30	5.40
				282.44	5.90
				282.47	6.90
				282.52	6.40
				282.73	7.40
				282.77	7.90
				283.05	8.40
				283.16	9.40
				283.17	8.40
				283.41	8.90
				283.47	9.90
				283.91	11.40
				283.98	10.40
				284.22	11.90

Hydrate: Methane + ethane + propane
Reference: Mooijer-van den Heuvel (2004; pp. 90, 244)
Phases: L_W–H(II)–V–L_{HC}, L_W–H(II)–L_{HC}, and L_W–H(II)–V (Phase diagram is complex—see reference)
Overall composition: $x_{H_2O} = 0.938$, $y_{C_2H_6} = 0.299$

L_W–H(II)–V–L_{HC}		L_W–H(II)–L_{HC}		L_W–H(II)–V	
T **(K)**	***P*** **(MPa)**	***T*** **(K)**	***P*** **(MPa)**	***T*** **(K)**	***P*** **(MPa)**
277.96	0.97	277.88	1.39	277.03	0.54
277.97	0.93	277.89	1.74	277.43	0.58
278.01	0.86	277.89	2.14	277.78	0.63
278.13	0.72	277.91	2.54	277.99	0.66
278.15	0.80	277.91	1.19	278.17	0.67
		277.92	2.34		
		277.92	1.59		
		277.92	1.14		
		277.96	1.94		

Hydrate: Methane + propane + isobutane
Reference: Paranjpe et al. (1987)
Phases: L_W–H–V–L_{HC}

		Mol Fraction in Vapor		
T **(K)**	***P*** **(kPa)**	CH_4	C_3H_8	i-C_4H_{10}
276.2	220.6	0.261	0.000	0.739
276.2	248.2	0.155	0.106	0.739
276.2	262.0	0.123	0.194	0.683
276.2	303.4	0.000	0.369	0.631
279.2	398.0	0.511	0.000	0.489
279.2	458.5	0.201	0.085	0.714
279.2	495.0	0.092	0.279	0.629
279.2	543.3	0.128	0.542	0.330
279.2	576.4	0.128	0.737	0.135
279.2	606.7	0.102	0.851	0.047
279.2	674.0	0.010	0.990	0.000
281.2	585.1	0.620	0.000	0.380
281.2	621.9	0.242	0.071	0.687
281.2	668.8	0.187	0.393	0.420
281.2	723.9	0.150	0.569	0.281
281.2	773.6	0.126	0.814	0.060
281.2	832.0	0.030	0.970	0.000

Hydrate: Methane + propane + n-butane
Reference: Paranjpe et al. (1987)
Phases: I–H–V–L_{HC} and L_W–H–V–L_{HC}

		Mol Fraction in Vapor		
T **(K)**	***P*** **(kPa)**	CH_4	C_3H_8	n-C_4H_{10}
268.2	181.4	0.000	0.660	0.340
268.2	216.5	0.349	0.407	0.244
268.2	270.3	0.736	0.082	0.182
268.2	362.7	0.840	0.027	0.127
268.2	784.0	0.890	0.000	0.110
275.2	315.8	0.000	0.834	0.166
275.2	478.5	0.327	0.258	0.415
275.2	523.4	0.922	0.051	0.027
275.2	551.6	0.935	0.012	0.053
275.2	1330.7	0.921	0.000	0.079
281.2	821.9	0.111	0.889	0.000
281.2	1048.0	0.686	0.206	0.108
281.2	1206.6	0.836	0.090	0.074
281.2	1834.0	0.942	0.018	0.040
281.2	2643.8	0.965	0.005	0.031
281.2	3441.0	0.985	0.000	0.015

Hydrate: Methane + propane + *n*-decane
Reference: Verma (1974)
Phases: L_W–H–L_{HC} and L_W–H–V–L_{HC} (compositions for hydrocarbon liquid phase)

L_W–H–L_{HC}

T (K)	*P* (kPa)	%CH_4	%C_3H_8	%$C_{10}H_{22}$
287.5	2,875	14.51	27.09	58.4
287.8	4,544	14.51	27.09	58.4
288.1	6,888	14.51	27.09	58.4
288.7	10,225	14.51	27.09	58.4
289.2	13,707	14.51	27.09	58.4

L_W–H–V–L_{HC}

T (K)	*P* (kPa)	%CH_4	%C_3H_8	%$C_{10}H_{22}$
278.3	539	0.00	96.55	3.45
278.2	525	0.00	94.88	5.12
277.9	501	0.00	91.81	8.19
277.4	443	0.00	80.71	19.29
277.5	465	0.00	80.32	19.68
276.7	391	0.00	72.16	27.84
276.1	343	0.00	63.45	36.55
275.0	269	0.00	49.90	50.10
288.5	2,241	10.32	74.47	15.21
286.2	1,806	8.26	59.76	31.97
283.9	1,338	6.41	46.40	47.19
281.4	1,014	5.01	32.55	59.44
278.8	758	3.92	27.91	68.17
296.0	7,122	33.64	57.19	9.17
295.1	6,585	29.38	51.10	19.52
293.8	5,702	25.78	45.55	28.68
292.2	4,826	22.39	39.91	37.70
290.6	3,951	19.32	34.87	45.81
289.2	3,427	17.01	31.06	51.93
287.5	2,875	14.51	27.09	58.40
297.8	11,597	44.66	38.46	16.88
296.3	11,370	42.74	24.93	32.33
294.0	8,763	34.95	20.48	44.58
291.7	6,764	29.09	17.08	53.83
289.5	5,426	24.68	14.51	60.82
287.4	4,344	20.75	12.23	67.02
297.9	15,031*	72.08	25.72	2.20

Continued

T (K)	*P* (kPa)	%CH_4	%C_3H_8	%$C_{10}H_{22}$
298.2	16,886	59.53	21.01	19.46
297.7	16,251	53.41	19.00	25.59
296.3	12,763	45.37	16.20	38.42
294.3	10,336	39.44	14.07	46.49
291.5	7,936	32.86	11.74	55.40
288.9	6,019	26.83	9.68	63.53
286.7	4,847	22.72	8.19	69.09
297.2	21,788*	86.60	8.60	4.80
292.9	13,121	55.42	5.62	38.96
288.7	8,019	41.00	4.02	54.98
285.9	5,868	32.12	3.16	64.71
282.2	4,302	25.36	2.50	72.14
279.2	3,151	19.36	1.90	78.74
295.4	31,027*	91.50	0.00	8.50
290.4	17,079	58.48	0.00	41.5
285.2	9,350	42.47	0.00	57.53
282.9	7,116	34.52	0.00	65.48
278.9	4,702	26.90	0.00	73.10

* = Quadruple-cum-critical point.

Hydrate: Methane + carbon dioxide + hydrogen sulfide
Reference: Robinson and Hutton (1967)
Phases: L_W–H–V

T (K)	*P* (MPa)	%CH_4	%CO_2	%H_2S	*T* (K)	*P* (MPa)	%CH_4	%CO_2	%H_2S
281.1	1.675	78.5	13.9	7.6	279.2	1.475	68.6	24.9	6.5
282.5	2.275	80.3	13.0	6.7	282.1	2.034	69.9	24.1	6.0
286.6	3.868	81.0	13.0	6.0	284.0	2.771	70.5	23.5	6.0
287.3	4.558	82.0	12.6	5.4	286.4	3.744	71.5	22.8	5.7
289.4	5.888	82.0	12.6	5.4	288.4	4.930	72.5	22.0	5.5
290.8	6.881	82.0	12.6	5.4	290.0	6.185	72.5	22.0	5.5
292.2	8.653	82.0	12.5	5.5	290.9	7.550	72.5	22.0	5.5
292.9	9.632	82.0	12.6	5.4	293.0	11.225	72.0	22.3	5.7
293.6	10.790	82.0	12.6	5.4	293.7	12.011	72.3	22.2	5.5
294.7	12.341	82.5	12.1	5.4	287.4	2.020	69.9	12.7	17.4
295.6	14.079	82.0	12.6	5.4	289.9	2.648	70.0	12.3	16.7
296.4	15.707	82.0	12.6	5.4	291.5	3.330	72.0	12.0	16.0
284.2	1.903	81.0	11.8	7.2	293.3	4.392	72.0	12.0	16.0
285.4	2.765	81.0	11.8	7.2	294.7	5.123	72.0	12.0	16.0
289.1	4.254	80.0	12.0	8.0	295.4	6.495	71.1	11.9	17.0
290.4	4.978	80.0	12.0	8.0	296.5	7.384	70.8	12.1	17.1
292.1	5.943	80.0	12.0	8.0	297.6	8.405	72.5	11.9	15.6
293.1	6.984	81.6	11.1	7.3	297.6	8.005	68.8	13.6	17.6
294.0	7.529	83.9	9.4	6.7					

Hydrate: Methane + carbon dioxide + hydrogen sulfide
Reference: Sun et al. (2003)
Phases: L_W–H–V

Gas	$\%CO_2$	$\%H_2S$
I	7.40	4.95
II	10.77	6.78
III	7.16	9.93
IV	7.31	14.98
V	6.81	17.71
VI	7.00	26.62

Gas I

T (K)	*P* (MPa)	*T* (K)	*P* (MPa)
274.2	1.044	286.2	5.121
277.2	1.58	288.2	6.358
280.2	2.352	289.2	7.212
282.2	3.126	290.2	8.220
284.2	3.964		

Gas II

T (K)	*P* (MPa)	*T* (K)	*P* (MPa)
276.2	1.114	287.2	4.570
278.2	1.385	288.2	4.890
280.2	1.815	289.2	6.110
282.2	2.265	290.2	6.862
284.2	3.110	290.9	7.650
286.2	4.065	291.2	8.024

Gas III

T (K)	*P* (MPa)	*T* (K)	*P* (MPa)
278.2	1.192	289.7	4.930
282.2	1.932	291.2	5.868
284.2	2.460	292.2	6.630
286.2	3.303	293.2	7.916
288.2	4.212		

Continued

Gas IV

T (K)	*P* (MPa)	*T* (K)	*P* (MPa)
277.2	0.646	291.2	4.070
280.2	1.020	293.2	5.270
283.2	1.428	294.7	6.698
286.2	2.080	295.7	7.910
289.2	3.164		

Gas V

T (K)	*P* (MPa)	*T* (K)	*P* (MPa)
282.2	0.950	294.2	5.314
284.2	1.244	295.2	6.310
286.2	1.670	295.8	6.880
288.2	2.368	296.6	7.825
290.2	3.080	297.2	8.680
292.2	4.008		

Gas VI

T (K)	*P* (MPa)	*T* (K)	*P* (MPa)
281.2	0.582	295.2	3.910
284.2	0.786	296.7	5.030
287.2	1.160	298.2	6.562
290.2	1.788	299.7	8.080
293.2	2.688		

Hydrates: Methane + nitrogen + cyclohexane
Reference: Tohidi et al. (1996a)
Phases: L_W–H–V
Feed composition (mol fraction): 0.1336 CH_4; 0.1409 N_2; 0.0464 c-C_6H_{12}; 0.6791 H_2O

T (K)	*P* (MPa)	*T* (K)	*P* (MPa)
278.0	2.144	284.2	5.137
281.6	3.496	290.0	12.321

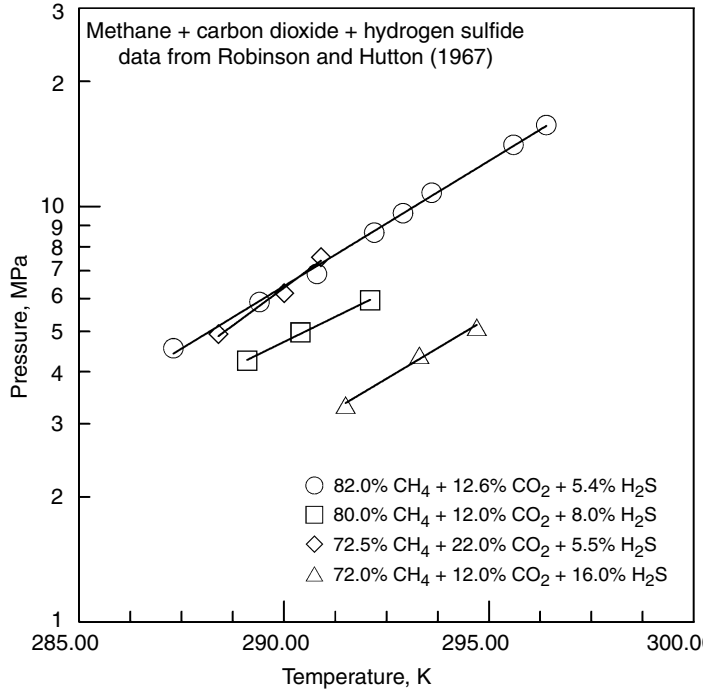

FIGURE 6.40 Methane + carbon dioxide + hydrogen sulfide mixture (L_W–H–V) data.

6.3.1.4 Equilibria of multicomponent guest mixtures

Hydrate: Methane + ethane + propane + 2-methylpropane
Reference: Mei et al. (1998)
Phases: L_W–H–V

T (K)	*P* (MPa)	%CH_4 (mol%)	%C_2H_6 (mol%)	%C_3H_8 (mol%)	%2-Methylpropane (mol%)
273.5	0.92	97.25	1.42	1.08	0.25
275.0	1.15	97.25	1.42	1.08	0.25
276.6	1.36	97.25	1.42	1.08	0.25
277.7	1.50	97.25	1.42	1.08	0.25
278.8	1.63	97.25	1.42	1.08	0.25
279.7	1.87	97.25	1.42	1.08	0.25
280.9	2.24	97.25	1.42	1.08	0.25
281.9	2.67	97.25	1.42	1.08	0.25

Hydrate: Natural gases
Reference: Wilcox et al. (1941)
Phases: L_W–H–V

Compositions of Gases

Gas	%N_2	%CO_2	%CH_4	%C_2H_6	%C_3H_8	%i-C_4H_{10}	%n-C_4H_{10}	%C_5H_{12}
B	0.64		86.41	6.47	3.57	0.99	1.14	0.78
C	0.43	0.51	93.20	4.25	1.61			
D			88.36*	6.82	2.54	0.38	0.89	1.01

* = Includes nitrogen of unspecified amount.

Phase Equilibrium Data
Gas B

T (K)	*P* (MPa)	*T* (K)	*P* (MPa)	*T* (K)	*P* (MPa)	*T* (K)	*P* (MPa)
278.8	1.255	292.2	6.964	295.1	12.27	297.1	20.68
282.9	1.924	294.1	9.680	296.1	16.84	298.3	27.32
288.7	4.123						

Gas C

T (K)	*P* (MPa)	*T* (K)	*P* (MPa)	*T* (K)	*P* (MPa)	*T* (K)	*P* (MPa)
277.7	1.600	289.2	6.964	292.1	10.501	293.3	14.13
283.9	3.392						

Gas C (second series)

T (K)	*P* (MPa)	*T* (K)	*P* (MPa)	*T* (K)	*P* (MPa)	*T* (K)	*P* (MPa)
279.1	1.924	290.3	8.136	295.0	20.264	296.7	27.50
281.8	2.648	291.2	9.481	294.3	17.16	295.6	22.99
286.7	4.820	293.3	13.780				

Gas D

T (K)	*P* (MPa)	*T* (K)	*P* (MPa)	*T* (K)	*P* (MPa)	*T* (K)	*P* (MPa)
276.8	1.207	284.9	3.516	291.2	8.205	293.2	12.00
281.6	2.186	288.7	5.447				

Gas D (second series)

T (K)	*P* (MPa)	*T* (K)	*P* (MPa)	*T* (K)	*P* (MPa)	*T* (K)	*P* (MPa)
289.2	6.171	293.9	14.07	296.9	26.55	295.9	22.55
292.1	9.308	295.0	18.20				

Hydrate: Natural gases
Reference: Deaton and Frost (1946)
Phases: L_W–H–V

Compositions of Gases (mol%)

Gas	CO_2	H_2S	N_2	CH_4	C_2H_6	C_3H_8	C_4H_{10}
A	0.20		7.7	65.4	12.7	10.3	3.7
B	0.20		1.1	87.9	4.4	4.9	1.5
C	0.20		9.4	78.4	6.0	3.6	2.4
D	0.30		9.5	79.4	5.8	3.6	1.4
E	3.25	0.25	1.1	87.8	4.0	2.1	1.5
F	0.40		0.3	91.0	3.2	2.0	3.1
G			1.0	90.8	3.0	2.1	3.2
H	0.20		14.3	75.2	5.9	3.3	1.1
I			3.4	88.5	4.3	2.0	1.7
J	0.9		1.2	90.6	3.8	1.5	2.0
K	0.8		25.0	67.4	3.7	1.9	1.2
L	0.6		0.2	96.5	0.9	1.8	

Phase Equilibrium Data

Gas A

T (K)	*P* (kPa)	*T* (K)	*P* (kPa)	*T* (K)	*P* (kPa)	*T* (K)	*P* (kPa)
274.8	627	285.9	2571	290.1	4296	292.6	6302
280.3	1262	288.7	3592	291.5	5364	294.0	8536
283.2	1806						

Gas B

T (K)	*P* (kPa)	*T* (K)	*P* (kPa)	*T* (K)	*P* (kPa)	*T* (K)	*P* (kPa)
273.7	600	280.4	1338	283.7	2089	285.9	2668
275.4	738	282.6	1779	284.3	2248	286.5	2861
277.6	993						

Gas C

T (K)	*P* (kPa)	*T* (K)	*P* (kPa)	*T* (K)	*P* (kPa)	*T* (K)	*P* (kPa)
273.7	724	275.9	903	277.6	1172	279.8	1462
274.8	807	276.5	972	278.2	1241	283.2	2213

Gas D

T (K)	*P* (kPa)	*T* (K)	*P* (kPa)	*T* (K)	*P* (kPa)	*T* (K)	*P* (kPa)
273.7	752	276.5	1089	280.4	1675	282.1	2096
274.8	883	278.7	1400				

Continued

Gas E

T (K)	*P* (kPa)	*T* (K)	*P* (kPa)	*T* (K)	*P* (kPa)	*T* (K)	*P* (kPa)
275.4	945	280.3	1717	285.9	3454	289.3	5254

Gas F

T (K)	*P* (kPa)	*T* (K)	*P* (kPa)	*T* (K)	*P* (kPa)	*T* (K)	*P* (kPa)
273.7	765	280.4	1731	288.7	4909	292.1	8653
277.6	1241	285.9	3461	288.7	4895	292.7	9391
280.4	1731						

Gas G

T (K)	*P* (kPa)	*T* (K)	*P* (kPa)	*T* (K)	*P* (kPa)	*T* (K)	*P* (kPa)
273.7	758	280.4	1723	288.7	5033	291.5	7729
277.6	1234	285.9	3468	288.7	5033		

Gas H

T (K)	*P* (kPa)	*T* (K)	*P* (kPa)	*T* (K)	*P* (kPa)	*T* (K)	*P* (kPa)
274.2	758	277.6	1255	280.4	1758	282.1	2131
275.4	945						

Gas I

T (K)	*P* (kPa)	*T* (K)	*P* (kPa)	*T* (K)	*P* (kPa)	*T* (K)	*P* (kPa)
273.7	793	275.3	972	277.6	1310	280.4	1813

Gas J

T (K)	*P* (kPa)	*T* (K)	*P* (kPa)	*T* (K)	*P* (kPa)	*T* (K)	*P* (kPa)
273.7	883	277.6	1455	285.9	4034	287.6	5068
274.3	952	280.4	2027	285.9	4027	288.2	5433
274.8	1020	280.4	1993	285.9	4054	288.7	5812
274.8	1027	280.4	2006	286.5	4364	289.8	6985
275.9	1172	283.2	2841	287.1	4675	290.9	8384
277.6	1441	285.4	3765	287.1	4682		

Gas K

T (K)	*P* (kPa)	*T* (K)	*P* (kPa)	*T* (K)	*P* (kPa)	*T* (K)	*P* (kPa)
274.3	1069	277.6	1607	283.2	3165	286.0	4592
275.4	1220	280.4	2248				

(Continued)

Continued

Gas L

T (K)	*P* (kPa)	*T* (K)	*P* (kPa)	*T* (K)	*P* (kPa)	*T* (K)	*P* (kPa)
273.7	1,262	277.6	2,027	283.2	4,047	289.8	10,329
274.8	1,427	280.4	2,855	287.7	7,425	289.8	10,439
274.8	1,420						

Hydrate: Natural gases
Reference: Kobayashi et al. (1951)
Phases: L_W–H–V

Compositions of Gases (mol%)

Gas	N_2	CH_4	C_2H_6	C_3H_8	i-C_4H_{10}	n-C_4H_{10}	C_5H_{12}	C_6H_{14}
Hugoton	15.0	73.29	6.70	3.90	0.36	0.55	0.20	0.00
Michigan	6.8	79.64	9.38	3.22	0.18	0.58	0.15	0.05

Phase Equilibrium Data
Hugoton Gas

T (K)	*P* (MPa)	*T* (K)	*P* (MPa)	*T* (K)	*P* (MPa)	*T* (K)	*P* (MPa)
281.6	1.765	287.7	3.847	288.9	4.461	290.9	5.833
283.9	2.517						

Michigan Gas

T (K)	*P* (MPa)	*T* (K)	*P* (MPa)	*T* (K)	*P* (MPa)	*T* (K)	*P* (MPa)
283.3	2.186	287.2	3.578	289.4	4.613	291.0	5.661
285.7	2.930						

Hydrate: Gas composition 90.6% CH_4; 6.6% C_2H_6; 1.8% C_3H_8; 0.5% i-C_4H_{10}; 0.5% n-C_4H_{10}
Reference: McLeod and Campbell (1961)
Phases: L_W–H–V

T (K)	*P* (MPa)	*T* (K)	*P* (MPa)	*T* (K)	*P* (MPa)	*T* (K)	*P* (MPa)
293.6	13.55	300.0	41.34	303.1	62.85	298.6	33.75
297.5	27.68	301.7	52.16	295.8	20.24		

Hydrates: Three natural gases
Reference: Lapin and Cinnamon (1969)
Phases: L_W–H–V

Compositions of Gases

Gas	%N_2	%CH_4	%C_2H_6	%C_3H_8	%n-C_4H_{10}	%n-C_5H_{12}	%n-C_6H_{14}
1	1.70	72.78	14.50	7.63	2.65	0.63	0.11
2	1.58	67.69	13.50	14.10	2.45	0.58	0.10
3	1.47	62.49	12.47	20.62	2.26	0.58	0.11

Formation Temperature at 4.207 MPa

Gas 1	Gas 2	Gas 3
288.75	289.85	289.85

Hydrate: Five natural gases with carbon dioxide
Reference: Adisasmito and Sloan (1992)
Phases: L_W–H–V

Composition (mol %)

Gas	%CO_2	%CH_4	%C_2H_6	%C_3H_8	%i-C_4H_{10}	%n-C_4H_{10}
A	0.00	76.62	11.99	6.91	1.82	2.66
B	31.40	52.55	8.12	4.74	1.31	1.88
C	66.85	24.42	3.99	3.07	0.75	0.92
D	83.15	12.38	1.96	1.66	0.37	0.48
E	89.62	7.86	1.13	0.86	0.20	0.33

Hydrate Equilibria

Gas	*T* (K)	*P* (MPa)	Gas	*T* (K)	*P* (MPa)	Gas	*T* (K)	*P* (MPa)
A	273.7	496.6	B	282.0	1682.8	D	279.3	2565.5
A	276.5	703.4	C	273.7	758.6	D	282.0	3510.3
A	279.3	986.2	C	276.5	1089.7	E	273.7	1337.9
A	282.0	1413.8	C	279.3	1565.5	E	276.5	1841.4
B	273.7	593.1	C	282.0	2227.6	E	279.3	2531.0
B	276.5	841.4	D	273.7	1365.5	E	282.0	3469.0
B	279.3	1220.7	D	276.5	1869.0			

Hydrate: Natural gas (0.90% N_2; 0.22% CO_2; 85.24% CH_4; 7.68% C_2H_6; 3.31% C_3H_8; 1.19% i-C_4H_{10}; 0.85% n-C_4H_{10}; 0.30% i-C_5H_{12}; 0.31% n-C_5H_{12})
References: Tohidi et al. (1997b)
Phases: L_W–H–V

***T* (K)**	***P* (MPa)**	***T* (K)**	***P* (MPa)**
279.1	1.317	288.1	3.930
281.9	1.772	290.1	4.881
283.3	2.062	291.5	6.088
283.5	2.110	292.9	7.619
285.3	2.606	294.8	11.769

Hydrate: Processed natural gas with hydrate structural transition
Reference: Jager and Sloan (2002)
Phases: L_W–H–V
Gas composition: 97.53 mol% CH_4; 0.8797% C_2H_6; 0.1397% C_3H_8; 0.0149% i-C_4H_{10}; 0.0248% n-C_4H_{10}; 0.0180% i-C_5H_{12}; 0.0203% n-C_5H_{12}; 0.0222% C_6H_{14}; 0.0126% C_7H_{16}; 0.9303% N_2; 0.4100% CO_2

Processed natural gas (PNG) + H_2O			**PNG + H_2O+ 6 mol% NaCl**		
***T* (K)**	***P* (MPa)**	**Structure**	***T* (K)**	***P* (MPa)**	**Structure**
278.8	3.83	II	268.0	3.68	II
283.6	6.71	II	274.4	7.21	II
285.8	8.43	II	279.1	13.95	II
287.2	11.16	II	282.1	22.38	II/I(?)
287.2	10.50	I	283.9	28.59	I(?)
287.5	11.81	II/I	284.3	31.12	I
287.9	12.29	II/I	284.7	32.33	I
288.7	13.51	I	285.2	34.70	I
290.4	16.67	I	286.5	42.25	I
292.8	23.48	I	288.0	50.71	I
294.6	29.83	I	289.2	57.28	I
295.8	34.25	I			
297.3	41.92	I			
298.5	48.51	I			
299.5	54.67	I			
300.4	60.87	I			
301.3	68.23	I			

Hydrate: Hydrate denuding of CH_4 and C_3H_8 from condensates or crudes
Reference: Verma et al. (1974)
Phases: L_W–H–V–L_{HC}

Initial Properties of Condensates and Crude

Property	Prudhoe Bay condensate	Ray Field condensate	North slope crude
Molec Wt	136	110	260
Spec Grav	0.75	0.73	0.932

Properties before and after Hydrate Formation

	Liquid composition			Hydrate composition		Quadruple	
	%CH_4	%C_3H_8	%Cond	%CH_4	%C_3H_8	*T* (K)	*P* (MPa)
Prudhoe Bay condensate							
Initial	32.2	18.2	49.6	N/A		293.9	6.825
Final	21.2	19.6	59.2	92.5	7.5	291.3	4.875
Ray Field condensate[a]							
Initial	49.2	16.2	34.6	N/A		297.2	15.27
Final	46.1	13.1	40.8	64.8*	35.2*	295.4	13.66
North slope crude oil							
Initial	32.8	14.5	52.7	N/A		296.7	10.17
Final	17.0	14.2	68.8	85.9	14.1	290.5	6.41

* Calculated by material balance.

Hydrate: Natural gases, hexane, decane, and crude oils
Reference: Holder (1976)
Phases: L_W–H–V–L_{HC}

Overall mol% of Hydrocarbon Components

Expt	CH_4	C_2H_6	C_3H_8	CO_2	n-C_6H_{14}	c-C_6H_{12}	n-$C_{10}H_{22}$	MWcrude = 320
I	45.51	1.82	1.44			31.87		19.36
II	64.16	3.65	2.48	0.62	11.10		9.57	8.42

(Continued)

Continued

Experiment I		Experiment II	
T **(K)**	***P*** **(MPa)**	***T*** **(K)**	***P*** **(MPa)**
285.9	8.412	289.0	8.688
286.3	8.826	289.2	8.908
288.1	9.998	289.4	9.412
288.4	10.204	289.9	10.025
288.7	10.342	290.6	10.770
288.8	10.928	290.8	10.722
289.2	11.308	291.5	10.963
289.9	11.997		
290.3	12.893		

Hydrate: Natural gas liquids
Reference: Ng and Robinson (1976a)
Phases: L_W–H–L_{HC} and L_W–H–V–L_{HC}

Composition of Liquids in mol%

Gas composition	I	II	III	IV	V	VI
Nitrogen	0.3	0.2	0.2			
Methane		2.2	21.9			
Ethane	31.3	30.6	24.7	23.4	21.5	17.0
Propane	51.5	50.8	40.8	30.4	48.9	38.6
Isobutane	16.9	16.2	12.4	19.6	23.8	18.9
n-Pentane				26.6		
Carbon dioxide					5.8	25.5

Phase Equilibrium

Gas I		Gas II		Gas III	
T **(K)**	***P*** **(kPa)**	***T*** **(K)**	***P*** **(kPa)**	***T*** **(K)**	***P*** **(kPa)**
277.7	1,158*	281.2	1,565	291.7	4,799*
277.7	1,186	281.2	1,620	291.8	5,240
277.7	1,462	281.3	2,461	292.1	5,902
277.7	2,234	281.4	3,813	292.5	7,212
277.7	4,523	281.7	6,102	293.2	9,797
277.8	7,074	281.9	8,232	293.9	13,623
277.8	9,714	282.2	11,224		

Continued

Gas IV		Gas V		Gas VI	
T **(K)**	***P*** **(kPa)**	***T*** **(K)**	***P*** **(kPa)**	***T*** **(K)**	***P*** **(kPa)**
274.8	689*	280.1	1,207	283.9	2,344*
274.8	1,730	280.1	1,351	284.0	2,496
275.1	4,054	280.1	1,427	284.2	3,316
275.3	6,964	280.1	2,399	284.6	5,130
275.6	11,893	280.2	3,689	284.9	8,163
		280.4	6,129	285.7	14,700
		280.7	9,377		
		280.9	14,403		

* = L_W–H–V–L_{HC}.

Hydrate: Natural gases
References: Aoyagi and Kobayashi (1978)
Phases: V–H

Compositions

Gas	%CH_4	%C_2H_6	%C_3H_8	%CO_2
I	75.02	7.95	3.99	13.04
II	87.06	7.96	3.88	1.10

T **(K)**	***P*** **(MPa)**	H_2O ppm (mol)	***T*** **(K)**	***P*** **(MPa)**	H_2O ppm (mol)
Gas I					
267.1	4.499	98.9	249.0	4.499	20.6
267.1	5.857	87.1	249.8	12.078	18.4
267.1	12.068	63.0	243.2	4.479	10.5
260.9	4.458	58.8	243.7	5.847	10.3
261.2	5.836	56.7	243.2	12.048	10.5
260.9	12.048	41.6	237.2	12.088	4.52
251.8	5.857	25.2	233.9	12.068	2.50
Gas II					
277.6	0.345	18.0	260.9	3.445	63.0
277.6	0.445	52.0	249.8	10.345	10.0
260.9	0.345	8.4	249.8	3.445	19.7

Hydrate: Gas liquids and condensate
Reference: Ng et al. (1987a)
Phases: As noted

Composition of Hydrocarbon Liquids

	A	B	C	D
Concentration, mol%				
Nitrogen	0.00	0.04	0.16	0.64
Methane	2.49	12.48	26.19	73.03
Carbon dioxide	0.48	12.01	2.10	3.11
Ethane	4.22	8.88	8.27	8.04
Propane	8.63	10.57	7.50	4.28
Isobutane	2.85	2.14	1.83	0.73
n-Butane	7.02	5.63	4.05	1.50
Isopentane	3.39	1.74	1.85	0.54
n-Pentane	4.59	2.85	2.45	0.60
Hexanes plus	66.33	53.66	45.60	7.53
Mol.Wt.	123.0	113.0	90.2	32.4
Saturation pressure (MPa) at Ts	0.71*	4.34*	8.95*	43.94**
Ts (K)	281.15	310.95	310.95	416.15

* = Bubble point temperature.
** = Retrograde dew point pressure.

Liquid A

T (K)	*P* (MPa)	Phases	*T* (K)	*P* (MPa)	Phases
273.8	0.64	L_W–H–V–L_{HC}(V = 0)	274.8	15.95	L_W–H–L_{HC}
274.0	5.27	L_W–H–L_{HC}	275.75	20.78	L_W–H–L_{HC}
274.4	10.34	L_W–H–L_{HC}			

Liquid B

T (K)	*P* (MPa)	Phases	*T* (K)	*P* (MPa)	Phases
279.6	1.52	L_W–H–V–L_{HC}	286.8	12.00	L_W–H–L_{HC}
286.2	3.54	L_W–H–V–L_{HC}(V = 0)	288.4	20.00	L_W–H–L_{HC}

Liquid C

T (K)	*P* (MPa)	Phases	*T* (K)	*P* (MPa)	Phases
287.0	4.00	L_W–H–V–L_{HC}	291.8	12.00	L_W–H–L_{HC}
291.4	7.74	L_W–H–V–L_{HC}(V = 0)	293.0	20.00	L_W–H–L_{HC}

Continued

Liquid D

T (K)	*P* (MPa)	Phases	*T* (K)	*P* (MPa)	Phases
290.8	6.01	L_W–H–V–L_{HC}	295.0	15.01	L_W–H–V–L_{HC}
293.8	11.07	L_W–H–V–L_{HC}	296.2	9.99	L_W–H–V–L_{HC}

Hydrate: Alaskan West Sak Crude
Reference: Paranjpe et al. (1988)
Phases: L_W–H–V–L_{HC}

Live West Sak Crude Composition

Composition	mol%	Composition	mol%	Composition	mol%
CO_2	0.016	C_7	0.016	C_{15}	1.944
N_2	0.032	C_8	0.008	C_{16}	1.795
C_1	38.333	C_9	0.823	C_{17}	1.570
C_2	0.857	C_{10}	1.496	C_{18}	1.795
C_3	0.359	C_{11}	1.720	C_{19}	2.468
C_4	0.179	C_{12}	1.346	C_{20}	2.841
C_5	0.064	C_{13}	1.496	C_{21}^+	39.037
C_6	0.200	C_{14}	1.795	Avg mol wt C_{21}	455

West Sak Crude PVT Properties

Pressure MPa	GOR SCF/STB	Density g/cc	Viscosity cp	Pressure MPa	GOR SCF/STB	Density g/cc	Viscosity cp
11.65	210	0.902	35.4	4.93	93	0.917	68.4
10.34	188	0.905	40.0	3.45	68	0.920	82.5
8.96	165	0.908	45.2	2.07	42	0.923	102.1
7.58	141	0.911	51.2	0.69	15	0.927	127.6
6.21	117	0.914	58.5				

Analysis of West Sak Separator Gas at 2.16 MPa and 291.5 K

Composition	mol%	Composition	mol%	Composition	mol%
H_2S	0.00	C_2	0.24	i-C_5	0.03
CO_2	0.02	C_3	0.31	n-C_5	0.03
N_2	0.16	i-C_4	0.07	C_6	0.02
C_1	98.33	n-C_4	0.12	C_6^+	0.02

(Continued)

Continued

Constant Composition Expansion for West Sak Crude at 299.8 K

Pressure MPa	Rel Liq Vol	Pressure MPa	Rel Liq Vol	Pressure MPa	Rel Liq Vol
11.75	1.00	8.68	0.934	4.87	0.762
9.98	0.974	7.04	0.878	4.10	0.685
9.46	0.954	6.26	0.844	3.17	0.6054

Rel Liq Vol = (Vol of Liq)/(Vol of Liq at Bub Pt Press).

Saturation Pressures of West Sak Crude

T (K)	*P* (MPa)	*T* (K)	*P* (MPa)	*T* (K)	*P* (MPa)	*T* (K)	*P* (MPa)
299.8	11.75	310.9	14.12	366.5	16.24	394.3	17.20

L_W–H–V–L_{HC} Data for West Sak Crude

T (K)	*P* (MPa)	*T* (K)	*P* (MPa)	*T* (K)	*P* (MPa)
279.8	5.36	281.6	6.38	282.4	7.03
280.8	6.03	282.0	6.79	284.0	8.30

Hydrate: Crude oil
Reference: Avlonitis (1988)
Phases: L_W–H–V–L_{HC}

Characterization of Crude Oil

Composition	mol%	Composition	mol%	Composition	mol%
N_2	0.61	C_3H_8	8.06	n-C_5H_{12}	2.57
CO_2	2.01	i-C_4H_{10}	1.34	n-C_6H_{14}	3.15
CH_4	35.6	n-C_4H_{10}	4.26	C_7^+	31.26
C_2H_6	9.90	i-C_5H_{12}	1.28		

Note: The i = C_7^+ fraction is characterized by $T_C = 770$ K, $P_C = 103.42$ kPa, $\omega = 0.690$ and Equation-of-State δij interaction constants for the Soave equation of $\delta_{C1} = 0.055$; $\delta_{C2} = 0.030$; $\delta_{N2} = 0.150$; $\delta_{CO_2} = 0.120$.

Continued

L_W–H–V–L_{HC} Data

T (K)	*P* (MPa)	*T* (K)	*P* (MPa)	*T* (K)	*P* (MPa)	*T* (K)	*P* (MPa)
280.2	1.26	283.6	2.18	288.2	4.59	290.6	5.73
280.2	1.43	284.6	2.63	289.6	5.14	292.4	8.032
283.0	2.08	285.8	3.189				

6.3.1.5 Equilibria with inhibitors

The phase equilibria data for hydrates with inhibitors are presented below. As in previous results, data plots are provided for those systems which have been considered by more than one investigation, as a first order means of data evaluation. Individual investigators usually include plots of their data in the original reference. Unless otherwise indicated the mass concentration of the inhibitor in the aqueous phase is included in the column marked "wt%," hydrocarbon/CO_2/H_2S/N_2 concentrations are mol% in vapor unless otherwise indicated.

Simple methane hydrates with inhibitors

Hydrate: Methane with methanol
Reference: Ng and Robinson (1985)
Phases: L_W–H–V

wt%	*T* (K)	*P* (MPa)	wt%	*T* (K)	*P* (MPa)	wt%	*T* (K)	*P* (MPa)
10.0	266.2	2.14	10.0	283.7	13.3	20.0	270.1	5.61
10.0	271.2	3.41	10.01	286.4	18.8	20.0	273.6	8.41
10.0	275.9	5.63	20.0	263.3	2.83	20.0	277.6	13.30
10.0	280.3	9.07	20.0	267.5	4.20	20.0	280.2	18.75

Hydrate: Methane with methanol
Reference: Robinson and Ng (1986)
Phases: L_W–H–V

wt%	*T* (K)	*P* (MPa)	wt%	*T* (K)	*P* (MPa)	wt%	*T* (K)	*P* (MPa)
35	250.9	2.38	35	267.8	13.68	50	240.1	2.95
35	256.3	3.69	35	268.5	17.22	50	247.4	7.24
35	260.3	6.81	35	270.1	20.51	50	250.4	10.54
35	264.6	10.16	50	233.1	1.47	50	255.3	16.98

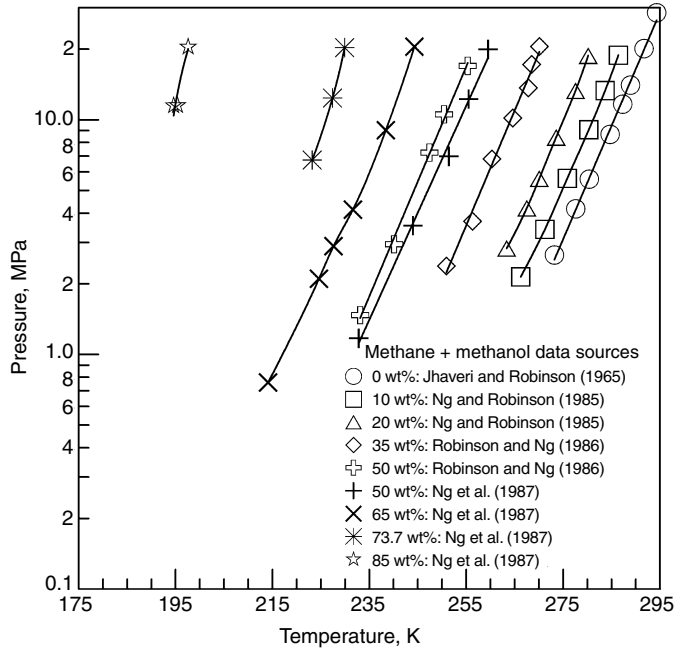

FIGURE 6.41 Methanol inhibition of simple methane hydrates.

Hydrate: Methane with methanol
Reference: Ng et al. (1987b)
Phases: L_W–H–V

wt%	*T* (K)	*P* (MPa)	wt%	*T* (K)	*P* (MPa)	wt%	*T* (K)	*P* (MPa)
50.0	232.8	1.17	65.0	224.6	2.10	73.7	227.4	12.37
50.0	244.0	3.54	65.0	227.6	2.89	73.7	229.9	20.30
50.0	251.4	6.98	65.0	231.6	4.14	85.0	194.6	11.49
50.0	255.5	12.26	65.0	238.4	9.03	85.0	195.4	11.51
50.0	259.5	19.93	65.0	244.3	20.49	85.0	197.6	20.42
65.0	214.1	0.76	73.7	223.2	6.73			

Hydrate: Methane with ethylene glycol
Reference: Robinson and Ng (1986)
Phases: L_W–H–V

wt%	*T* (K)	*P* (MPa)	wt%	*T* (K)	*P* (MPa)	wt%	*T* (K)	*P* (MPa)
10	270.2	2.42	30	267.6	3.77	30	279.9	16.38
10	273.5	3.40	30	269.7	4.93	50	263.4	9.89
10	280.2	6.53	30	274.4	7.86	50	266.3	14.08
10	287.1	15.6	30	280.1	16.14	50	266.5	15.24

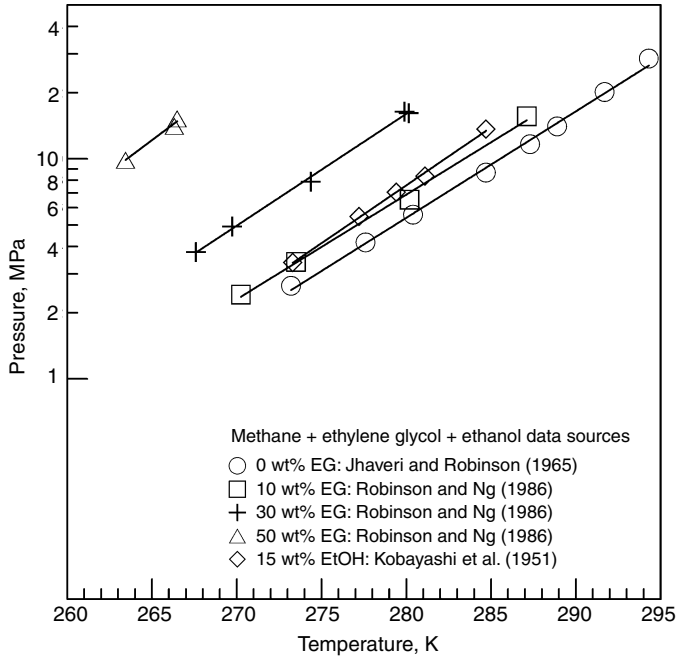

FIGURE 6.42 Ethanol and ethylene glycol inhibition of simple methane hydrates.

Hydrate: Methane with triethylene glycol
Reference: Ross and Toczylkin (1992)
Phases: L_W–H–V

wt%	*T* (K)	*P* (MPa)	wt%	*T* (K)	*P* (MPa)	wt%	*T* (K)	*P* (MPa)
10	274.6	3.17	20.2	275.0	4.37	40.0	274.5	7.27
10	276.0	3.87	20.2	276.0	4.97	40.0	276.0	9.87
10	278.0	4.77	20.2	278.0	6.32	40.0	278.0	15.27
10	283.0	8.02	20.2	283.0	11.32	40.0	280.5	23.02
10	288.0	14.72	20.2	288.0	21.62	40.0	283.0	35.17
10	293.0	25.57	20.2	293.0	39.87			

Hydrate: Methane with 15 wt% ethanol solution
Reference: Kobayashi et al. (1951)
Phases: L_W–H–V

wt%	*T* (K)	*P* (MPa)	wt%	*T* (K)	*P* (MPa)	wt%	*T* (K)	*P* (MPa)
15	273.3	3.38	15	279.4	7.06	15	284.7	13.67
15	277.2	5.47	15	281.1	8.36			

Hydrate: Methane with sodium chloride solution
Reference: Kobayashi et al. (1951)
Phases: L_W–H–V

wt%	*T* (K)	*P* (MPa)	wt%	*T* (K)	*P* (MPa)	wt%	*T* (K)	*P* (MPa)
10	270.0	2.59	10	278.6	6.38	20	272.3	6.18
10	271.0	2.80	10	282.1	10.03	20	272.3	7.19
10	272.7	3.58	10	284.3	13.42	20	275.7	11.09
10	274.5	3.65	20	265.9	3.78	20	276.4	10.82
10	276.9	4.89	20	267.8	4.63	20	276.3	13.66

Hydrate: Methane with sodium chloride solutions
Reference: de Roo et al. (1983)
Phases: L_W–H–V

mol fraction NaCl	*T* (K)	*P* (MPa)	mol fraction NaCl	*T* (K)	*P* (MPa)	mol fraction NaCl	*T* (K)	*P* (MPa)
0.0394	268.3	2.69	0.0598	268.8	4.26	0.0778	271.2	8.83
0.0394	271.0	3.53	0.0598	272.0	6.12	0.0778	272.8	11.00
0.0394	273.2	4.50	0.0598	275.0	8.57	0.0891	263.0	4.78
0.0394	274.8	5.29	0.0778	261.8	2.94	0.0891	264.6	5.78
0.0394	275.9	5.98	0.0778	264.4	4.06	0.0891	266.2	7.11
0.0394	278.0	7.55	0.0778	266.4	5.05	0.0891	267.6	8.36
0.0598	263.4	2.39	0.0778	268.2	6.12	0.0891	268.6	9.55
0.0598	265.8	3.13	0.0778	269.4	7.05			

Hydrate: Methane and potassium formate
Reference: Fadnes et al. (1998)
Phases: L_W–H–V

wt% HCOOK	*T* (K)	*P* (MPa)
0	285.45	10
0	285.75	10
10	283.15	10
10	289.55	20
10	288.15	20
20	278.35	9.6
20	278.55	10
20	283.65	20
30	272.75	10
30	277.05	20

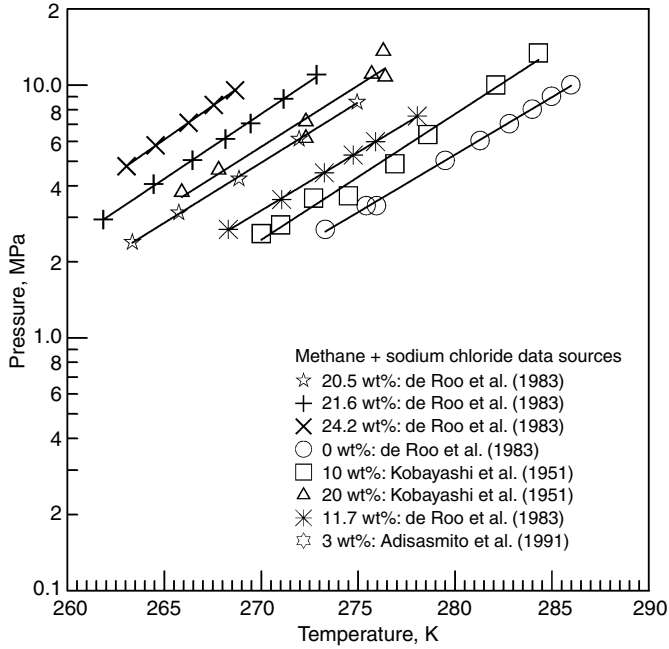

FIGURE 6.43 Sodium chloride inhibition of simple methane hydrates.

Hydrate: Methane and single and mixed electrolytes
Reference: Dholabhai et al. (1991)
Phases: L_W–H–V

Compositions of Aqueous Solutions

Solution ID	wt% NaCl	wt% KCl	wt% $CaCl_2$	Molality
Na3	3.00	0	0	0.5287
Na3K3	3.00	3.00	0	0.7939
Na5K5	5.00	5.01	0	1.6975
Na5K10	5.00	9.98	0	2.5809
Na5K15	5.00	15.00	0	3.5869
Na10K12	10.01	12.00	0	4.2591
Na15K8	14.99	7.99	0	4.7189
Na3Ca3	3.00	0	3.00	1.2651
Na6Ca3	6.00	0	3.00	1.7221
Na10Ca3	10.00	0	3.00	2.7422
Na10Ca6	9, 97	0	5.98	3.6321
Na3Ca10	3.00	0	10.00	3.1770
Na6Ca10	6.00	0	10.00	3.9019
SEA*	2.394	0.069	0.115	NA

* = SEA also contains 0.401 wt% Na_2SO_4, 0.009 wt% NaF, 0.011 wt% KBr, 0.508 wt% $MgCl_2$, and 0.002 wt% $SrCl_2$.

(Continued)

Continued

L_W–H–V Phase Equilibrium Results

Solution ID	*T* (K)	*P* (MPa)	Solution ID	*T* (K)	*P* (MPa)
Na3	274.4	3.243	Na15K8	270.2	7.049
	276.5	3.993		266.3	4.400
	278.3	4.807		264.4	3.614
	279.4	5.361		272.1	8.839
	272.7	2.754			
	277.2	4.303	Na3Ca3	274.1	3.584
				277.1	4.874
Na3K3	277.2	4.746		281.8	8.159
	279.2	5.857		270.4	2.504
	275.2	3.873			
	271.4	2.704	Na6Ca3	274.1	4.189
	273.0	3.192		277.0	5.679
	276.2	4.346		280.1	7.839
	277.7	5.106		271.3	3.134
Na5K5	272.23	3.464	Na10Ca3	274.3	5.399
	270.3	2.829		272.2	4.339
	274.2	4.215		269.4	3.214
	276.3	5.169		277.3	7.444
	272.2	3.439			
	281.5	9.379	Na10Ca6	274.2	6.779
	279.4	7.340		266.0	2.819
				269.3	3.939
Na5K10	272.1	4.174		274.3	6.899
	267.5	2.569			
	279.0	9.046	Na3Ca10	277.0	7.159
	276.4	6.764		279.7	9.664
				274.2	5.189
Na5K15	272.2	5.564		268.8	3.019
	269.2	4.014			
	266.3	2.914	Na6Ca10	274.1	6.739
	276.2	8.689		277.1	9.514
				270.8	4.699
Na10K12	272.2	7.144		268.6	3.689
	269.4	5.144			
	266.3	3.689	SEA	277.0	4.364
	264.6	2.989		279.0	5.424
	274.2	8.819		281.2	6.659
				283.9	9.064

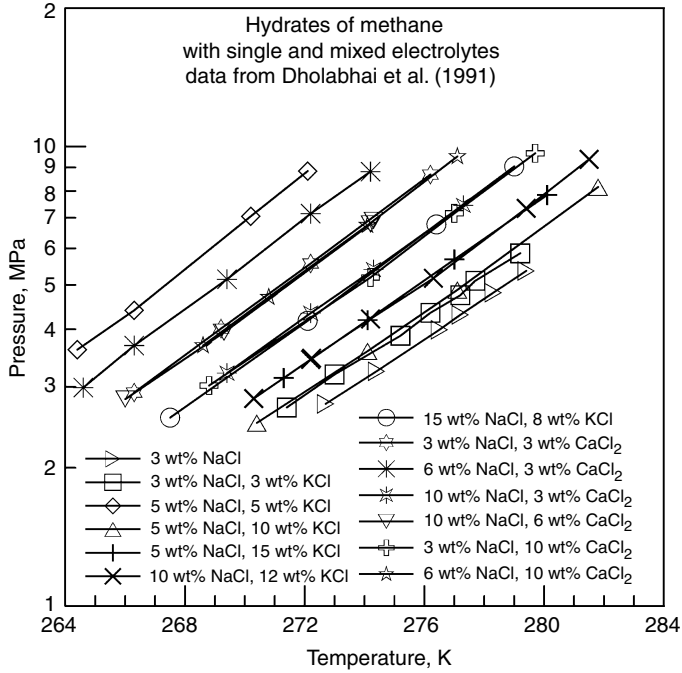

FIGURE 6.44 Inhibition of simple methane hydrates with single and mixed electrolytes.

Hydrate: Methane + ethylene glycol (EG) + sodium chloride (NaCl)
References: Eichholz et al. (2004)
Phases: L_W–H–V

EG mass %	NaCl mass %[a]	T (K)	P_{exp} (MPa)	T^b (K)	P_b (MPa)
19.16	0	266.5	2.136	266.1	2.108
		272.6	3.815	272.6	3.769
		279.5	8.620	279.8	8.574
5.77	3.77	271.1	2.811	271	2.777
		274.5	3.968	274.6	3.932
		277.9	5.491	277.9	5.471
		282.2	8.109	281.1	8.076
15.36	3.77	267.1	2.392	267.1	2.353
		270.8	3.735	270.8	3.706
		274.3	5.314	274.4	5.264
		279.4	9.558	279.5	9.531
23.88	3.77	262.8	2.264	262.8	2.231
		266.6	3.308	266.7	3.291
		270.3	5.055	270.3	5.032
		276.1	9.489	276	9.450

(Continued)

Continued

EG mass %	NaCl mass %[a]	T (K)	P_{exp} (MPa)	T^b (K)	P_b (MPa)
3.77	15.67	264.9	2.772	264.9	2.732
		268.4	4.191	268.5	4.142
		272.2	6.384	272.2	6.345
12.07	15.01	263.6	3.497	263.5	3.448
		267.0	5.156	267.0	5.120
		270.6	7.690	270.5	7.637

[a] On wet basis (used without drying).
[b] Data denote the no hydrate point.

P_{exp}: equilibrium pressure data.
P_b: pressure where hydrates were not stable.

Hydrate: Methane + ethylene glycol (EG) + salt (NaCl, KCl, or $CaCl_2$)
References: Masoudi et al. (2004, 2005)
Phases: L_W–H–V

Salt	Salt concentration wt%	EG concentration wt%	Hydrate conditions T (K)	Hydrate conditions P (MPa)
NaCl	15.0	21.3	262.3	5.068
			268.4	11.431
			274.3	27.758
			277.9	46.698
	12.0	30.8	262.4	6.957
			267.3	13.610
			270.5	22.946
			275.2	46.691
KCl	10.0	23.0	265.5	4.164
			273.4	10.356
			279.1	22.760
			283.9	44.513
	8.0	35.0	259.3	3.930
			267.0	9.935
			273.0	23.442
			277.6	45.050
$CaCl_2$	15.0	21.3	269.4	4.027
			277.6	10.756
			283.1	22.918
			287.8	43.864

Continued

Salt	Salt concentration wt%	EG concentration wt%	Hydrate conditions	
			T **(K)**	***P*** **(MPa)**
$CaCl_2$	15.3	13.4	265.1	3.971
			272.7	9.804
			279.5	25.090
			283.6	45.436
	18.0	14.0	261.5	3.907
			268.9	9.404
			275.2	22.994
			279.6	44.843
	14.0	26.0	261.6	4.675
			268.1	9.942
			273.5	22.801
			277.9	43.347

Hydrate: Methane with aqueous glycerol
Reference: Ng and Robinson (1994)
Phases: L_W–H–V

wt% glycerol	***T*** **(K)**	***P*** **(MPa)**	wt% glycerol	***T*** **(K)**	***P*** **(MPa)**
25.0	273.8	4.39	50.0	264.2	4.53
	278.0	6.91		267.8	6.65
	283.0	12.41		273.4	13.81
	286.2	20.53		276.2	20.53

Simple Ethane Hydrates with Inhibitors

Hydrate: Ethane with methanol
Reference: Ng and Robinson (1985)
Phases: L_W–H–V, L_W–H–V–$L_{C_2H_6}$, L_W–H–$L_{C_2H_6}$

L_W–H–V

wt%	***T*** **(K)**	***P*** **(MPa)**	wt%	***T*** **(K)**	***P*** **(MPa)**
10	268.3	0.417	20	263.5	0.550
16	272.1	0.731	20	264.9	0.614

(Continued)

Continued

wt%	*T* (K)	*P* (MPa)	wt%	*T* (K)	*P* (MPa)
10	276.0	1.160	20	267.7	0.869
10	278.4	1.630	20	268.8	1.030
10	280.4	2.160	20	271.8	1.520
10	281.4	2.800	20	274.1	2.060
10	281.9	2.820			

L_W–H–$L_{C_2H_6}$

wt%	*T* (K)	*P* (MPa)	wt%	*T* (K)	*P* (MPa)
10	282.2	2.91*	10	283.6	13.76
10	282.0	3.99	10	284.4	20.20
10	282.4	4.22	20	275.7	2.65*
10	282.0	5.65	20	276.3	5.89
10	282.0	6.59	20	277.0	10.03
10	282.7	7.30	20	277.8	15.12
10	282.9	10.36	20	278.6	20.40

* = L_W–H–V–$L_{C_2H_6}$.

Hydrate: Ethane with methanol
Reference: Ng et al. (1985a)
Phases: L_W–H–V, L_W–H–V–$L_{C_2H_6}$, L_W–H–$L_{C_2H_6}$

L_W–H–V

wt%	*T* (K)	*P* (MPa)	wt%	*T* (K)	*P* (MPa)
35	252.6	0.502	50	237.5	0.423
35	257.1	0.758	50	242.0	0.592
35	260.1	1.050	50	246.1	0.786
35	262.2	1.48	50	249.8	1.007

L_W–H–$L_{C_2H_6}$

wt%	*T* (K)	*P* (MPa)	wt%	*T* (K)	*P* (MPa)
35	264.7	1.937*	50	252.8	1.441*
35	265.5	4.095	50	252.9	3.820
35	265.9	7.695	50	253.7	7.074
35	267.1	13.93	50	254.6	13.89
35	268.4	20.18	50	255.5	20.35

* = L_W–H–V–$L_{C_2H_6}$.

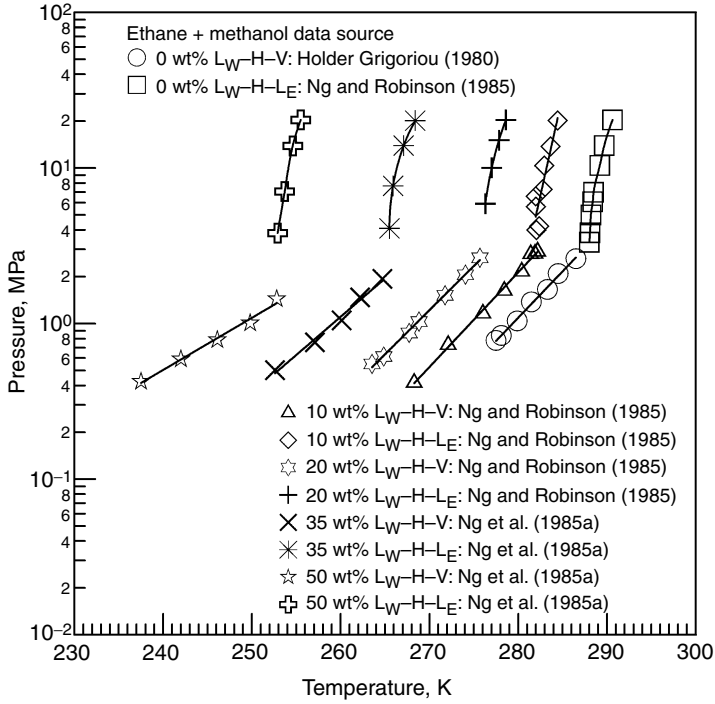

FIGURE 6.45 Methanol inhibition of simple ethane hydrates.

Hydrate: Ethane with triethylene glycol
Reference: Ross and Toczylkin (1992)
Phases: L_W–H–V and L_W–H–LC_2H_6

wt%	*T* (K)	*P* (MPa)	wt%	*T* (K)	*P* (MPa)	wt%	*T* (K)	*P* (MPa)
10	277.0	1.00	20.0	273.7	0.79	40.0	275.0	1.97
10	282.0	1.80	20.0	276.5	1.29	40.0	275.8	2.30
10	286.3	3.72*	20.0	278.0	1.54	40.0	277.9	3.30*
10	289.0	23.27*	20.0	283.0	2.63	40.0	281.7	20.77*
			20.0	285.5	9.72*	40.0	283.0	33.57*
			20.0	288.0	28.27*			
			20.0	289.0	36.27*			

* = L_W–H–$L_{C_2H_6}$.

Hydrate: Ethane + NaCl
References: Tohidi et al. (1993)
Phases: L_W–H–V

wt% NaCl	*T* (K)	*P* (MPa)
10	273.7	0.883
	276.0	1.165
	277.6	1.455
	278.8	1.737
	280.4	2.165
15	272.7	1.082
	274.1	1.386
	277.1	2.151
20	266.2	0.689
	269.2	1.117
	271.2	1.469
	271.4	1.524

Simple Propane Hydrates with Inhibitors

Hydrate: Propane with methanol
Reference: Ng and Robinson (1985)
Phases: L_W–H–V, L_W–H–$L_{C_3H_8}$

L_W–H–V

wt%	*T* (K)	*P* (MPa)	wt%	*T* (K)	*P* (MPa)
5.00	272.1	0.234	10.39	269.2	0.228
5.00	272.6	0.259	10.39	270.9	0.360
5.00	273.3	0.316	10.39	271.0	0.352
5.00	274.2	0.405	10.39	271.6	0.415
5.00	274.8	0.468	10.39	271.8	0.434
10.39	268.3	0.185			

L_W–H–$L_{C_3H_8}$

wt%	*T* (K)	*P* (MPa)	wt%	*T* (K)	*P* (MPa)
5.00	275.0	0.794	10.39	272.1	0.984
5.00	275.1	1.720	10.39	272.1	2.737
5.00	275.0	6.340	10.39	272.1	6.510

Hydrate: Propane with methanol
Reference: Ng and Robinson (1984)
Phases: L_W–H–V, L_W–H–$L_{C_3H_8}$

L_W–H–V

wt%	*T* (K)	*P* (MPa)	wt%	*T* (K)	*P* (MPa)
35	248.0	0.137	50	229.7	0.090
35	250.2	0.207			

L_W–H–$L_{C_3H_8}$

wt%	*T* (K)	*P* (MPa)	wt%	*T* (K)	*P* (MPa)
35	250.6	0.876	50	229.9	1.970
35	251.1	6.090	50	229.3	7.830
35	251.0	9.770	50	229.3	19.710
35	251.3	20.38			

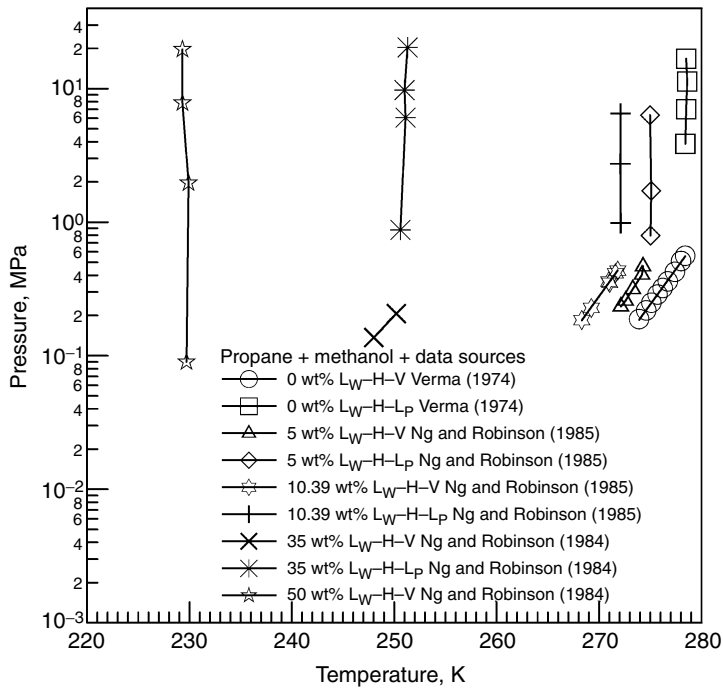

FIGURE 6.46 Methanol inhibition of simple propane hydrates.

Hydrate: Propane with sodium chloride
Reference: Kobayashi et al. (1951)
Phases: L_W–H–V

wt%	*T* (K)	*P* (MPa)	wt%	*T* (K)	*P* (MPa)
10	268.3	0.122	10	272.4	0.370
10	269.7	0.170	10	272.8	0.479
10	271.8	0.278	10	273.0	1.118
10	272.0	0.309	10	273.1	1.911

Hydrate: Propane with sodium chloride
Reference: Patil (1987)
Phases: L_W–H–V

wt%	*T* (K)	*P* (kPa)	wt%	*T* (K)	*P* (kPa)
3.0	272.2	179	5.0	274.4	324
3.0	274.2	290	5.0	275.6	448
3.0	275.4	366	10.0	270.8	191
3.0	276.2	455	10.0	272.2	259
5.0	271.2	185	10.0	273.6	355
5.0	272.6	241	10.0	274.6	450

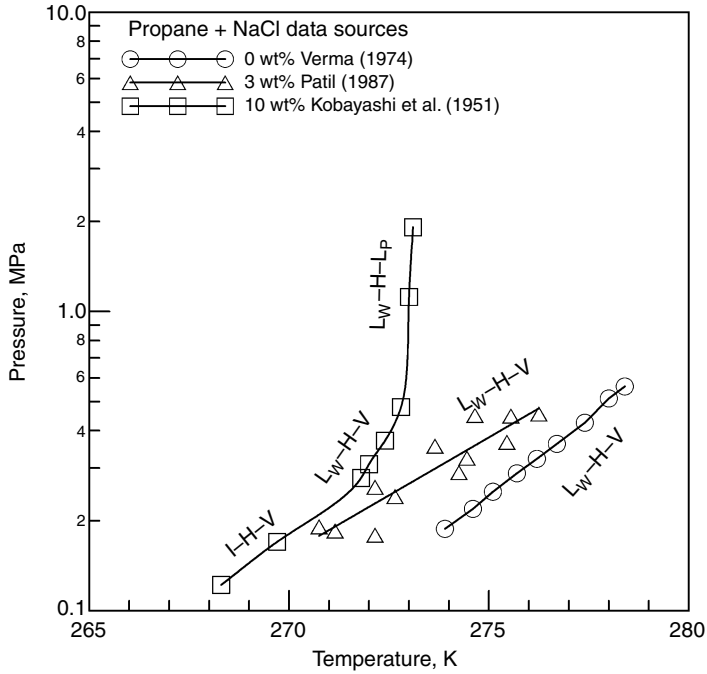

FIGURE 6.47 Sodium chloride inhibition of simple propane hydrates.

Hydrate: Propane and single and mixed electrolytes
Reference: Englezos and Ngan (1993)
Phases: L_W–H–V

Electrolyte (wt%)					
$CaCl_2 \cdot 2H_2O$	NaCl	KCl	$CaCl_2$	*T* (K)	*P* (MPa)
15.00	0	0	0	268.7	0.205
				269.8	0.270
				270.3	0.317
				271.1	0.376
				271.7	0.412
7.5	7.5	0	0	265.9	0.172
				266.4	0.186
				267.6	0.248
				268.5	0.312
				269.4	0.385
				269.8	0.418
0	7.5	7.5	0	265.2	0.157
				266.2	0.206
				267.4	0.259
				268.5	0.321
				269.0	0.372
0	0	7.5	7.5	266.3	0.181
				266.9	0.206
				267.5	0.230
				268.1	0.263
				268.6	0.294
				269.5	0.370
				270.1	0.432
0	7.5	7.5	5.0	261.9	0.172
				262.3	0.192
				262.8	0.214
				263.4	0.249
				263.6	0.267
				264.2	0.286
				264.4	0.303
				264.5	0.303
				265.1	0.342
				265.2	0.352

Hydrate: Propane with single salts of NaCl, KCl, $CaCl_2$
Reference: Tohidi et al. (1993)
Phases: L_W–H–V

Salt	wt%	*T* (K)	*P* (MPa)	Salt	wt%	*T* (K)	*P* (MPa)
NaCl	3.1	273.2	0.221	KCl	15.0	269.0	0.221
		273.8	0.248			269.8	0.269
		274.6	0.303			270.4	0.324
		275.4	0.365			270.6	0.345
		276.0	0.414			271.2	0.393
NaCl	10.0	270.0	0.241	KCl	20.0	266.4	0.228
		270.8	0.283			266.8	0.262
		271.6	0.359			267.2	0.290
		272.2	0.421			267.4	0.310
		272.8	0.531*			267.6	0.338
NaCl	15.0	266.2	0.221	$CaCl_2$	7.5	271.6	0.234
		266.8	0.241			272.0	0.269
		267.4	0.290			272.8	0.317
		268.2	0.379			273.6	0.379
		268.6	0.455*			274.2	0.427
NaCl	20.0	261.0	0.200	$CaCl_2$	11.3	269.6	0.248
		261.6	0.228			270.0	0.283
		262.6	0.283			270.6	0.324
		263.0	0.331			271.4	0.372
KCl	10.0	271.0	0.228	$CaCl_2$	15.2	266.4	0.234
		271.8	0.283			267.0	0.262
		272.6	0.331			267.2	0.303
		273.0	0.379			267.8	0.345
		273.4	0.421			268.0	0.359

* = L_W–H–V–$L_{C_3H_8}$.

Hydrate: Propane with single and salts of NaCl, KCl, $CaCl_2$
Reference: Tohidi et al. (1994a)
Phases: L_W–H–V and phase fractions

Salt	Original wt% salt	*T* (K)	*P* (MPa)	C_3H_8 mol%	wt% salt in H_2O	Hydrate phase fraction
$CaCl_2$	7.274	272.2	0.317	3.248	8.533	0.163
$CaCl_2$	11.343	269.4	0.310	3.639	12.265	0.088
$CaCl_2$	15.121	266.0	0.324	3.783	16.346	0.089
NaCl	3.078	273.2	0.255	2.968	3.914	0.226

Continued

Salt	Original wt% salt	T (K)	P (MPa)	C_3H_8 mol%	wt% salt in H_2O	Hydrate phase fraction
NaCl	20.03	260.0	0.283	3.646	21.324	0.080
KCl	9.976	270.8	0.290	3.834	12.245	0.210
KCl	15.067	268.6	0.296	4.777	16.829	0.125
NaCl	4.820	271.15	0.324	2.940	5.589	0.154
$CaCl_2$	3.710				4.301	
NaCl	5.109	270.2	0.296	3.107	5.863	0.148
KCl	5.109				5.863	

Hydrate: Propane + (mixed salts and two North Sea brines)
References: Tohidi et al. (1997b)
Phases: L_W–H–V

Composition of North Sea Brine and Forties Formation Water

Salt	North Sea brine wt%	Forties formation H_2O wt%
NaCl	2.354	6.993
$CaCl_2$	0.116	0.735
$MgCl_2$	0.524	0.186
KCl	0.086	0.066
Na_2SO_4	0.428	—
$SrCl_2$	—	0.099
$BaCl_2$	—	0.036

Hydrate Dissociation Conditions with Salts

Salt (wt%)	T (K)	P (MPa)	Salt	T (K)	P (MPa)
5.0% NaCl	270.4	0.234	North Sea brine	272.7	0.234
+ 5.0% KCl	270.9	0.269		273.7	0.269
	272.4	0.379		274.3	0.296
	272.8	0.441		274.8	0.324
				275.0	0.352
4.9% NaCl	270.9	0.234		275.9	0.427
+ 3.8% $CaCl_2$	271.4	0.290			
	272.2	0.331	Forties formation	270.6	0.241
	272.6	0.379	H_2O	271.2	0.269
	273.5	0.441		271.8	0.317
				272.9	0.393
				273.5	0.448

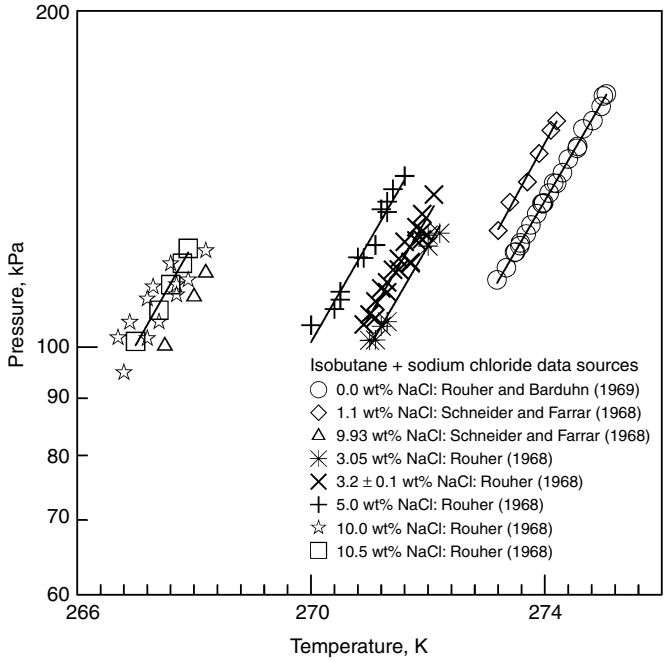

FIGURE 6.48 Sodium chloride inhibition of simple isobutane hydrates.

SIMPLE ISOBUTANE HYDRATES WITH INHIBITORS

Hydrate: Isobutane with sodium chloride
Reference: Schneider and Farrar (1968)
Phases: L_W–H–V

NaCl (wt%)	*T* (K)	*P* (kPa)	NaCl (wt%)	*T* (K)	*P* (kPa)
1.10	273.2	127.2	1.08	274.2	159.5
1.10	273.4	134.8	9.93	268.2	116.6
1.10	273.7	140.6	9.93	268.0	111.0
1.09	273.9	149.1	9.93	267.5	100.3
1.10	274.1	156.4			

Hydrate: Isobutane with sodium chloride
Reference: Rouher (1968)
Phases: L_W–H–V

NaCl (wt%)	*T* (K)	*P* (kPa)	NaCl (wt%)	*T* (K)	*P* (kPa)
5.00	270.5	110.3	3.05*	271.7	119.2
5.00	270.8	120.3	3.05*	271.8	124.6
5.00	271.1	123.5	3.05*	271.9	124.9
5.00	271.3	135.0	3.05*	271.9	127.0

Continued

NaCl (wt%)	*T* (K)	*P* (kPa)	NaCl (wt%)	*T* (K)	*P* (kPa)
5.00	270.0	104.6	3.32*	271.0	101.4
5.00	270.4	108.2	3.32*	271.2	104.4
5.00	270.5	112.1	3.32*	272.0	126.0
5.00	270.9	120.2	3.27*	271.1	101.5
5.00	271.1	123.4	3.21*	272.0	123.2
5.00	271.2	132.9	3.16*	271.3	105.4
5.00	271.3	132.1	3.16*	272.2	126.5
5.00	271.4	138.5	10.0	266.7	102.0
5.00	271.6	142.3	10.0	266.9	105.3
3.05*	270.9	104.8	10.0	267.2	110.5
3.05*	271.0	107.0	10.0	267.3	113.3
3.05*	271.1	109.9	10.0	267.6	118.8
3.05*	271.2	112.9	10.0	266.8	94.9
3.05*	271.3	114.3	10.0	267.2	101.8
3.05*	271.4	117.3	10.0	267.4	105.4
3.05*	271.5	120.0	10.0	267.7	113.8
3.05*	271.6	124.3	10.0	267.7	111.4
3.05*	271.8	128.1	10.0	267.9	114.9
3.05*	271.9	131.6	10.0	268.2	122.0
3.05*	272.1	137.0	10.55	267.0	101.2
3.05*	271.1	106.2	10.55	267.4	107.9
3.05*	271.3	112.0	10.5	267.6	113.8
3.05*	271.5	117.4	10.5	267.8	118.9
3.05*	271.7	118.9	10.5	267.9	122.6

* = Sea water with 3.05 wt% NaCl equivalent activity.

Simple Carbon Dioxide Hydrate with Inhibitors

Hydrate: Carbon dioxide with hydrogen chloride
Reference: Larson (1955)
Phases: L_W–H–V

HCl	*T* (K)	*P* (kPa)	HCl	*T* (K)	*P* (kPa)
0.1 N	274.2	1379	0.5 N	281.0	3716
0.1 N	278.5	2351	0.5 N	282.0	4371Q_2
0.1 N	282.2	3916	1.0 N	273.5	1565
0.1 N	283.1	4489Q_2	1.0 N	276.6	2262
0.5 N	272.6	1310	1.0 N	278.5	2903
0.5 N	277.0	2172	1.0 N	281.2	4289Q_2

Q_2 = Inhibited upper quadruple point (L_W–H–V–L_{CO_2}).

Hydrate: Carbon dioxide with sodium hydroxide
Reference: Larson (1955)
Phases: L_W–H–V

NaOH	*T* (K)	*P* (kPa)	NaOH	*T* (K)	*P* (kPa)
0.1 N	273.5	1324	0.5 N	279.0	2868
0.1 N	276.3	1834	0.5 N	281.0	3827
0.1 N	279.1	2592	0.5 N	282.0	$4378Q_2$
0.1 N	282.2	3923	1.0 N	273.9	1600
0.1 N	283.0	$4482Q_2$	1.0 N	276.6	2220
0.5 N	273.3	1393	1.0 N	279.6	3358
0.5 N	276.3	2000	1.0 N	281.3	$4296Q_2$

Q_2 = Inhibited upper quadruple point (L_W–H–V–L_{CO_2})

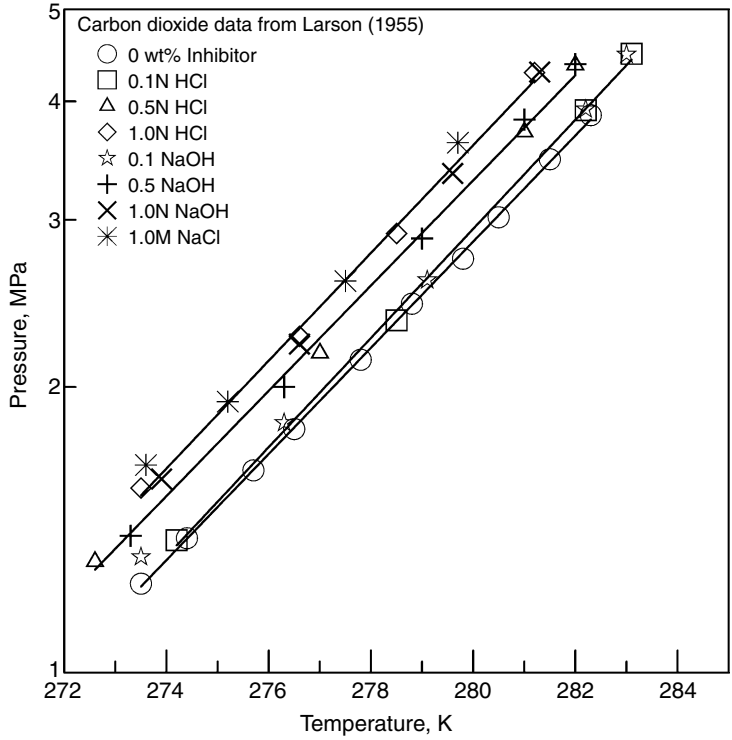

FIGURE 6.49 Acid, base, and salt inhibition of simple carbon dioxide hydrates.

Hydrate: Carbon dioxide with sodium chloride
Reference: Larson (1955)
Phases: L_W–H–V

NaCl	*T* (K)	*P* (kPa)	NaCl	*T* (K)	*P* (kPa)
1.0 M	273.6	1655	1.0 M	277.5	2586
1.0 M	275.2	1931	1.0 M	279.7	3619

Hydrate: Carbon dioxide and sodium chloride
Reference: Vlahakis et al. (1972)
Phases: L_W–H–V

wt% NaCl	*T* (K)	*P* (MPa)	wt% NaCl	*T* (K)	*P* (MPa)
5.42	276.1	2.297	5.949	278.2	3.072
5.28	277.2	2.596	5.632	278.7	3.222
5.30	279.2	3.371	5.568	279.2	3.438
4.865	279.6	3.468	10.17	271.6	1.735
5.37	280.0	2.877	10.33	272.6	2.024
5.27	275.9	2.158	10.30	273.2	2.095
5.72	276.4	2.333	10.31	274.2	2.384
5.76	277.0	2.534	10.50	274.7	2.651
5.80	277.5	2.795	10.30	275.2	2.786
5.545	277.9	2.886	10.46	275.7	3.040
5.445	278.6	3.231	10.26	276.2	3.185
5.45	279.3	3.530	10.37	276.7	3.434
5.53	279.7	3.727	10.27	277.2	3.619
4.79	271.6	1.319	10.21	277.4	3.767
5.215	272.1	1.398	10.59	268.2	1.189
5.375	272.6	1.502	10.55	269.1	1.339
5.26	273.1	1.589	10.38	270.1	1.488
5.385	273.6	1.709	10.22	271.1	1.648
4.665	274.1	1.737	10.25	272.2	1.919
5.715	274.6	1.927	10.22	273.7	2.261
4.81	275.3	2.018	10.20	274.5	2.488
5.875	280.4	4.227	10.32	275.3	2.892
5.871	273.2	1.653	10.30	275.4	2.878
5.917	274.2	1.865	10.19	276.3	3.233
5.834	275.1	2.056	10.29	276.5	3.333
5.764	276.2	2.355	10.16	276.9	3.454
6.132	276.6	2.555	10.41	277.0	3.567
5.733	277.2	2.675	10.20	277.2	3.681
5.860	277.7	2.899			

Hydrate: Carbon dioxide with methanol
Reference: Ng and Robinson (1985)
Phases: L_W–H–V, L_W–H–L_{CO_2}

L_W–H–V

wt%	*T* (K)	*P* (MPa)	wt%	*T* (K)	*P* (MPa)
10.00	269.5	1.59	20.02	264.5	1.83
10.00	269.6	1.58	20.02	265.2	1.98
10.00	271.3	2.06	20.02	266.4	2.21
10.00	273.8	2.89	20.02	267.2	2.53
10.00	273.8	2.85	20.02	268.1	2.74
10.00	274.9	3.48	20.02	268.9	2.94
20.02	264.0	1.59			

L_W–H–L_{CO_2}

wt%	*T* (K)	*P* (MPa)	wt%	*T* (K)	*P* (MPa)
10.00	276.0	4.60	20.02	270.1	7.68
10.00	276.8	7.23	20.02	270.5	11.27
10.00	277.4	10.09	20.02	270.7	11.40
10.00	278.1	13.98	20.02	271.6	15.89
20.02	269.1	3.34	20.02	271.8	16.09
20.02	269.6	5.50			

Hydrate: Carbon dioxide with methanol
Reference: Robinson and Ng (1986)
Phases: L_W–H–V, L_W–H–L_{CO_2}

wt%	*T* (K)	*P* (MPa)	wt%	*T* (K)	*P* (MPa)
L_W–V–H					
35	242.0	0.379	50	232.6	0.496
35	247.6	0.724	50	235.5	0.676
35	250.1	1.030	50	241.3	1.310
35	252.4	1.390			
35	255.1	1.770			
L_W–H–L_{CO_2}					
35	256.9	2.18	50	241.1	8.83
35	257.5	2.87	50	241.8	12.36
35	257.8	5.91	50	241.3	14.62
35	257.9	6.87	50	241.1	19.53
35	258.0	13.34			
35	258.5	20.70			

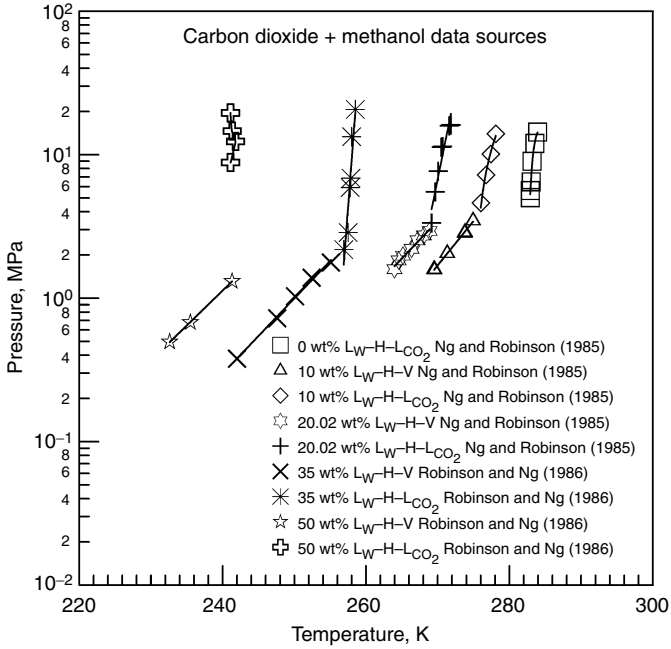

FIGURE 6.50 Methanol inhibition of simple carbon dioxide hydrates.

Hydrate: Carbon dioxide + seawater
Reference: Ohgaki et al. (1993)
Phases: L_W–H–V, H–L_W–L_{CO_2}, L_W–L_{CO_2}–V (no hydrate)

***T* (K)**	***P* (MPa)**	***T* (K)**	***P* (MPa)**
H–L_W–V			
T-cycle method, formation			
273.87	1.710	278.79	3.165
273.95	1.711	279.67	3.537
275.57	2.095	279.74	3.549
275.66	2.103	280.08	3.970
277.43	2.652	280.36	3.980
277.48	2.654		
T-cycle method, dissociation			
274.75	1.730	280.42	3.561
276.57	2.121	281.28	4.014
278.34	2.677	281.46	4.020
279.68	3.182		

(Continued)

Continued

T (K)	*P* (MPa)	*T* (K)	*P* (MPa)
T-cycle method, stationary point			
273.78	1.59	279.73	3.426
275.56	1.945	280.03	3.625
277.47	2.532	280.36	3.743
278.70	2.986		
$H–L_W–L_{CO_2}$			
T-cycle method, formation			
280.57	4.891		
T-cycle method, dissociation			
282.01	5.436		
$H–L_{CO_2}–V$			
First freezing point method			
279.62	4.1494		
$L_W–L_{CO_2}–V$			
First freezing point method			
281.59	4.361		
282.56	4.464		
283.52	4.573		
284.15	4.681		

For T-cycle methods, refer to the description given in Section 6.3.1.1. Ohgaki et al. (1993).

Hydrate: Carbon dioxide and single and mixed electrolytes
Reference: Dholabhai et al. (1993c)
Phases: L_W–H–V

Composition of Aqueous Solutions

Solution ID	wt% NaCl	wt% KCl	wt% $CaCl_2$	Solution ID	wt% NaCl	wt% KCl	wt% $CaCl_2$
Na3-1	3.00	0	0	Na5-1	5.00	0	0
Na3-2	3.02	0	0	Na5-2	5.00	0	0
Na3-3	3.02	0	0				
Na10-1	10.02	0	0	Na15	15.00	0	0
Na10-2	10.0	0	0				
Na20	20.03	0	0	K3	0	3.00	0
K5	0	5.01	0	K10	0	10.02	0
K15	0	14.97	0	Ca3	0	0	3.03
Ca5	0	0	5.02	Ca10	0	0	9.99
Ca15	0	0	14.97	Ca20	0	0	19.96
Na3K3	3.01	3.02	0	Na5K5	5.00	5.01	0
Na7K10	6.99	10.00	0	Na15K5	15.01	5.03	0
Na15K5	15.01	5.03	0	Na3Ca3	3.03	0	3.03
Na2Ca8	2.02	0	8.00	Na8Ca2	8.01	0	2.03
Na5Ca15	5.02	0	14.7	Na15Ca5	15.01	0	5.03

Continued

Solution ID	*T* (K)	*P* (MPa)	Solution ID	*T* (K)	*P* (MPa)	Solution ID	*T* (K)	*P* (MPa)
Pure H_2O	273.8	1.340	Na3-1	279.0	2.955	Na3-2	273.2	1.434
	275.5	1.640		277.0	2.309	Na3-3	280.9	3.907
	277.1	1.985		275.2	1.837			
	279.0	2.52		272.2	1.304			
Na5-1	278.0	3.004	Na10-1	277.2	3.781	Na15	273.0	3.239
	275.0	2.016		277.0	3.671		271.0	2.469
	273.0	1.597	Na10-2	276.1	3.155		268.2	1.703
	271.2	1.306		276.1	3.149		265.4	1.212
Na5-2	278.0	3.766		274.1	2.409			
				271.0	1.656			
				268.0	1.162			
Na20	266.8	2.63	K3	281.1	3.834	K5	280.5	3.905
	265.3	2.208		280.0	3.233		280.4	3.861
	263.3	1.606		278.7	2.760		279.4	3.324
				276.8	2.154		278.6	2.960
				274.6	1.654		276.0	2.129
				272.7	1.326		274.1	1.700
							272.1	1.325
K10	277.9	3.485	K15	269.0	1.415	Ca3	275.5	1.827
	276.3	2.807		272.2	2.095		272.6	1.302
	273.1	1.848		274.6	2.901		278.2	2.529
	269.0	1.130		276.0	3.575		280.9	3.702
Ca5	278.2	2.805	Ca10	270.8	1.511	Ca15	273.2	3.221
	280.1	3.657		268.0	1.102		270.1	2.138
	275.1	1.872		274.0	2.198		267.4	1.497
	271.1	1.184		277.3	3.460		263.4	0.960
				277.9	3.824			
Ca20	266.6	2.690	Na3K3	279.9	3.976	Na5K5	270.0	1.347
	264.6	2.052		279.3	3.573		271.7	1.660
	262.0	1.504		276.1	2.317		274.1	2.258
	259.2	1.051		274.0	1.814		277.3	3.432
				271.5	1.326			
Na7K10	267.6	1.482	Na15K5	262.9	1.218	Na3Ca3	279.2	3.595
	270.5	2.180		266.3	1.872		277.3	2.738
	273.1	3.044		268.2	2.388		275.7	2.227
	274.1	3.455		269.8	3.050		271.8	1.375
							271.0	1.258
Na8Ca2	267.8	1.086	Na2Ca8	277.5	3.697	Na5Ca15	267.3	2.935
	271.1	1.623		276.3	3.101		266.3	2.490
	273.2	2.112		272.7	1.909		264.1	1.878
	276.0	3.089		267.8	1.053		261.1	1.288
							259.2	1.042
Na15Ca5	267.4	2.665	SEA	274.6	1.688			
	265.7	2.112		275.9	2.001			
	263.5	1.609		277.9	2.556			
	259.0	0.909		281.1	4.072			
				272.1	1.288			

Hydrate: Carbon dioxide with 25 wt% glycerol
Reference: Ng and Robinson (1994)
Phases: L_W–H–V and L_W–H–L_{CO_2}

Phases	*T* (K)	*P* (MPa)	Phases	*T* (K)	*P* (MPa)
L_W–H–V	269.6	1.48	L_W–H–L_{CO_2}	277.2	8.47
L_W–H–V	274.4	2.83		278.8	20.67
L_W–H–V	276.8	3.96			

Hydrate: Carbon dioxide with glycerol
Reference: Breland and Englezos (1996)
Phases: L_W–H–V

wt%	*T* (K)	*P* (MPa)	wt%	*T* (K)	*P* (MPa)	wt%	*T* (K)	*P* (MPa)
10	272.3	1.391	20	270.4	1.502	30	270.1	2.030
10	274.6	1.786	20	270.6	1.556	30	270.6	2.096
10	276.1	2.191	20	272.3	1.776	30	271.4	2.340
10	277.7	2.640	20	273.6	2.096	30	272.3	2.651
10	278.4	2.942	20	274.1	2.281	30	273.2	2.981
10	279.3	3.345	20	275.5	2.721			
			20	276.2	3.001			
			20	277.1	3.556			

Hydrate: Carbon dioxide + sodium chloride or potassium chloride
References: Tohidi et al. (1997b)
Phases: L_W–H–V

wt%	*T* (K)	*P* (MPa)
10% NaCl	273.2	2.151
	276.0	3.151
	271.9	1.862
	276.1	3.227
20% NaCl	263.2	1.517
	266.5	2.248
	267.2	2.489
	268.8	3.116
10% KCl	273.5	1.937
	275.2	2.517
	276.9	3.047
	278.4	3.613

Hydrate: Carbon dioxide with methanol and monoethylene glycol
Reference: Fan et al. (2000)
Phases: L_W–H–V

wt% inhibitor	*T* (K)	*P* (MPa)	wt% inhibitor	*T* (K)	*P* (MPa)
10% MeOH	271.6	1.74	10% MEG	270.9	1.15
	273.8	2.35	273.1		1.74
				275.8	2.40
				278.3	3.20

Simple Hydrogen Sulfide Hydrates with Inhibitors

Hydrate: Hydrogen sulfide with methanol
Reference: Bond and Russell (1949)
Phases: L_W–H–V

wt%	*T* (K)	*P* (kPa)	wt%	*T* (K)	*P* (kPa)
16.5	273.2	275.80	16.5	290.1	1496.20
16.5	283.2	730.86			

Hydrate: Hydrogen sulfide with methanol
Reference: Ng and Robinson (1985)
Phases: L_W–H–V, L_W–H–V–L_{H_2S}, L_W–H–L_{H_2S}

wt%	*T* (K)	*P* (MPa)	wt%	*T* (K)	*P* (MPa)
L_W–H–V					
10.0	265.7	0.068	10.0	285.4	0.541
10.0	267.5	0.084	10.0	291.8	1.080
10.0	273.0	0.148	20.0	271.8	0.221
10.0	278.9	0.270	20.0	281.2	0.593
L_W–H–L_{H_2S}					
10.0	297.5	1.90*	20.0	291.1	1.63*
10.0	297.7	3.85	20.0	291.7	3.09
10.0	298.8	7.23	20.0	292.6	7.29
10.0	299.1	10.35	20.0	293.6	10.46
10.0	299.5	14.71	20.0	293.5	14.57
10.0	299.5	18.16	20.0	294.2	18.26

* = L_W–H–V–L_{H_2S}.

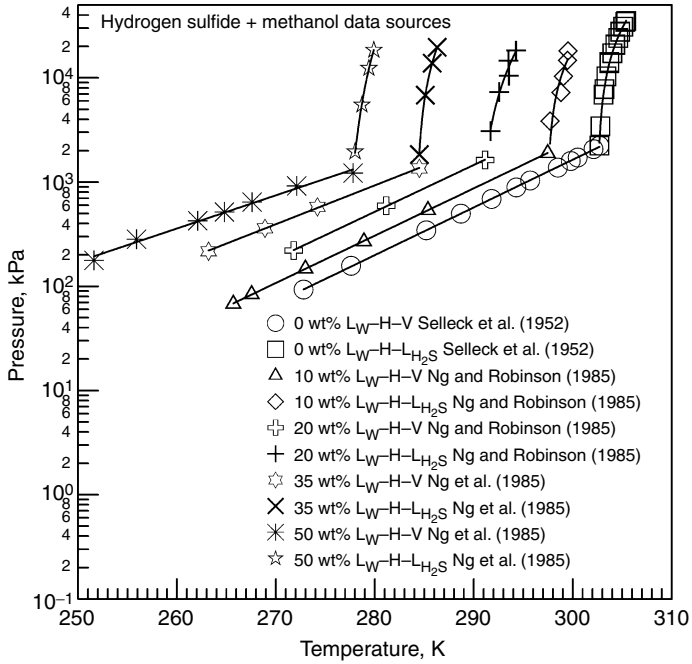

FIGURE 6.51 Methanol inhibition of simple hydrogen sulfide hydrates.

Hydrate: Hydrogen sulfide with methanol
Reference: Ng et al. (1985b)
Phases: L_W–H–V, L_W–H–V–L_{H_2S}, L_W–H–L_{H_2S}

wt%	*T* (K)	*P* (MPa)	wt%	*T* (K)	*P* (MPa)
L_W–V–H					
35	263.2	0.217	50	255.9	0.283
35	268.9	0.361	50	262.1	0.426
35	274.2	0.579	50	264.8	0.517
35	284.5	1.351	50	267.6	0.642
50	251.6	0.177	50	272.1	0.920
50	277.8	1.220*			
L_W–H–L_{H_2S}					
35	284.5	1.834	50	278.0	1.951
35	285.1	6.812	50	278.7	5.516
35	285.8	13.84	50	279.4	12.36
35	286.3	19.65	50	279.9	18.48

* = L_W–H–V–L_{H_2S}.

Hydrate: Hydrogen sulfide with sodium chloride
Reference: Bond and Russell (1949)
Phases: L_W–H–V

wt%	*T* (K)	*P* (kPa)	wt%	*T* (K)	*P* (kPa)
10.0	274.8	206.8	26.4	276.2	668.8
10.0	287.1	648.1	26.4	278.2	1020.4
10.0	294.8	1875.0	26.4	280.2	1303.1
26.4	269.2	420.6	26.4	280.2	1447.9

Hydrate: Hydrogen sulfide with calcium chloride
Reference: Bond and Russell (1949)
Phases: L_W–H–V

wt%	*T* (K)	*P* (kPa)	wt%	*T* (K)	*P* (kPa)
10.0	274.8	172.4	21.1	277.2	655.0
10.0	288.4	724.0	21.1	281.2	917.0
10.0	295.4	1896.0	21.1	284.2	1489.0
21.1	271.7	365.4	21.1	284.3	1565.0
			36.0	265.4	882.55

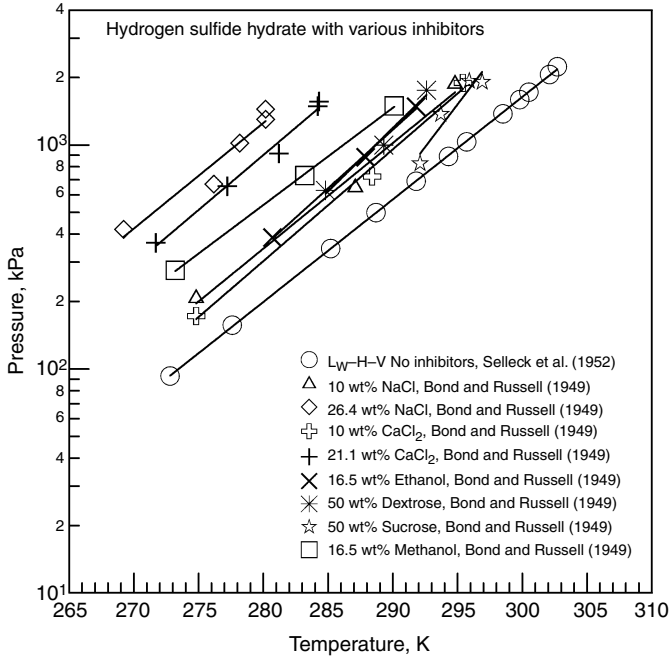

FIGURE 6.52 Simple hydrogen sulfide hydrates with various inhibitors.

Hydrate: Hydrogen sulfide with ethanol
Reference: Bond and Russell (1949)
Phases: L_W–H–V

wt%	*T* (K)	*P* (kPa)	wt%	*T* (K)	*P* (kPa)
16.5	280.7	386.12	16.5	291.8	1482.4
16.5	287.9	882.55			

Hydrate: Hydrogen sulfide with dextrose
Reference: Bond and Russell (1949)
Phases: L_W–H–V

wt%	*T* (K)	*P* (kPa)	wt%	*T* (K)	*P* (kPa)
50.0	284.8	627.4	50.0	292.6	1758.2
50.0	289.3	999.8			

Hydrate: Hydrogen sulfide with sucrose
Reference: Bond and Russell (1949)
Phases: L_W–H–V

wt%	*T* (K)	*P* (kPa)	wt%	*T* (K)	*P* (kPa)
50.0	292.1	827.4	50.0	295.9	1930.6
50.0	293.7	1372.1	50.0	295.9	1909.9

Binary Mixtures of Methane + Ethane with Inhibitors

Hydrate: 89.51 mol% methane and 10.49% ethane with methanol
Reference: Ng and Robinson (1983)
Phases: L_W–H–V

wt%	*T* (K)	*P* (MPa)	wt%	*T* (K)	*P* (MPa)
10.02	268.7	1.40	20.01	263.9	1.49
10.02	270.9	1.78	20.01	267.0	2.11
10.02	273.6	2.32	20.01	272.3	3.76
10.02	277.1	3.28	20.01	275.2	5.49
10.02	280.4	4.78	20.01	278.1	8.34
10.02	284.9	8.42	20.01	281.3	13.22
10.02	287.5	13.21	20.01	283.61	19.1
10.02	289.4	18.89			

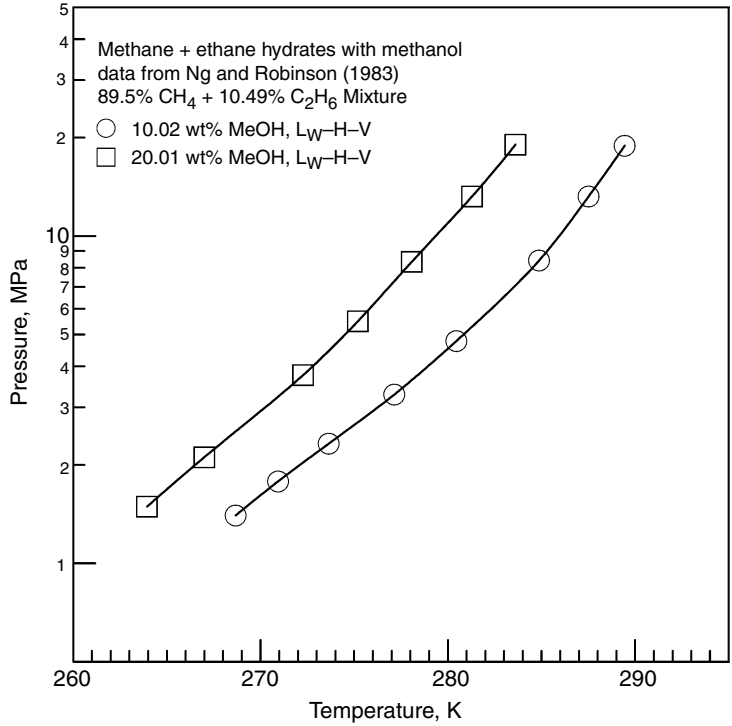

FIGURE 6.53 Methanol inhibition of methane + ethane hydrates.

BINARY MIXTURES OF METHANE + PROPANE WITH INHIBITORS

Hydrate: 95.01 mol% methane and 4.99% propane with methanol
Reference: Ng and Robinson (1983)
Phases: L_W–H–V

wt%	*T* (K)	*P* (MPa)	wt%	*T* (K)	*P* (MPa)
10.0	265.5	0.532	20.0	265.2	0.938
10.0	270.1	0.903	20.0	270.5	1.772
10.0	274.5	1.544	20.0	275.7	3.144
10.0	280.4	3.006	20.0	281.9	6.846
10.0	286.9	6.950	20.0	286.5	14.100
10.0	291.2	13.831			

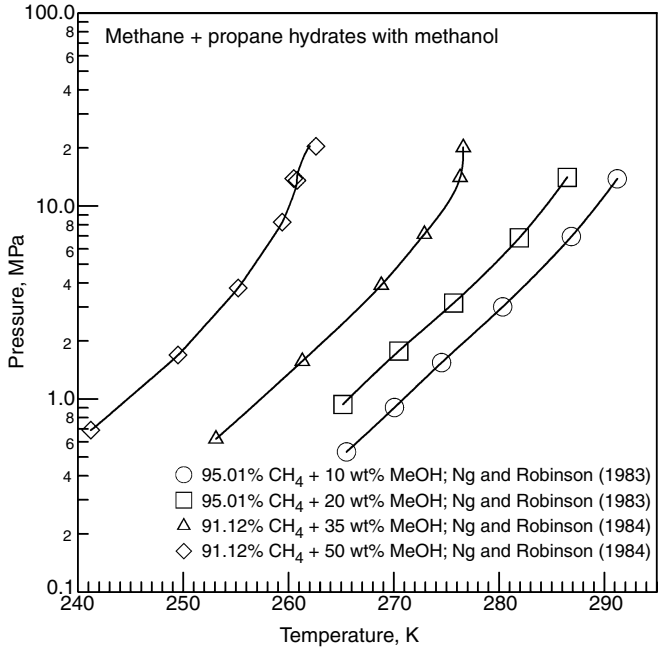

FIGURE 6.54 Methanol inhibition of methane + propane hydrates.

Hydrate: 91.12 mol% methane and 8.88% propane with methanol
Reference: Ng and Robinson (1984)
Phases: L_W–H–V

wt%	*T* (K)	*P* (MPa)	wt%	*T* (K)	*P* (MPa)
35	253.1	0.621	50	249.5	1.690
35	261.3	1.570	50	255.2	3.760
35	268.8	3.890	50	259.4	8.240
35	272.9	7.150	50	260.8	13.580
35	276.3	14.070	50	260.5	13.860
35	276.6	20.110	50	262.6	20.420
50	241.2	0.689			

Hydrate: 88.13 mol% methane + 11.87% propane with methanol and ethylene glycol
Reference: Song and Kobayashi (1989)
Phases: L_W–H–V

Inhibitor (wt%)	*T* (K)	*P* (MPa)	*T* (K)	*P* (MPa)
Methanol (7.0 wt%)	278.5	0.824	295.3	10.717
	286.8	2.735	295.4	10.742
	288.9	3.677	297.6	17.979
	292.4	6.314		

Continued

Inhibitor (wt%)	*T* (K)	*P* (MPa)	*T* (K)	*P* (MPa)
Methanol (15.0 wt%)	276.9	1.365	289.1	12.664
	281.9	3.732	289.8	17.834
	288.6	12.640		
Methanol (35.0 wt%)	281.3	0.980	280.2	11.198
	274.2	2.345	280.5	13.831
	277.0	5.561		
Ethylene glycol (5.0 wt%)	282.2	1.230	296.6	10.260
	288.8	3.168	298.2	15.640
	293.8	6.246		
Ethylene glycol (25.0 wt%)	279.6	1.944	289.6	8.092
	285.2	3.725	291.4	13.331
	288.6	5.420		
Ethylene glycol (40.0 wt%)	276.2	1.051	283.2	8.106
	283.5	5.294	283.6	10.941
	283.2	7.212	284.1	13.305
	282.8	8.099		
Ethylene glycol (50.0 wt%)	273.2	2.359	279.8	9.069
	277.2	3.966	280.8	14.883
	279.2	7.379	280.8	17.441

Binary Mixtures of Methane + Nitrogen with Inhibitors

Hydrate: Methane + Nitrogen + (single and mixed salts)
References: Mei et al. (1996a)
Phases: L_W–H–V

Vapor Phase is 89.26% CH_4 + 10.74% N_2

Salt (wt%)	*T* (K)	*P* (MPa)	Salt (wt%)	*T* (K)	*P* (MPa)
Pure water	273.7	2.99	$NaHCO_3$ (5%)	271.0	2.45
	274.8	3.31		273.2	3.16
	275.6	3.73		275.5	4.15
	277.1	4.36		278.0	5.34
	279.2	5.24		279.8	6.83
	281.2	6.58		282.3	8.62
	283.2	8.12		283.7	10.31
	285.3	10.10		285.4	12.57
NaCl (5%)	271.2	3.08	$MgCl_2$ (5%)	271.3	2.71
	272.7	3.44		273.4	3.34
	274.3	4.12		276.3	4.45
	275.8	4.90		279.7	6.50
	277.4	5.99		282.8	9.18
	279.8	7.88		285.2	11.82
	282.3	9.97			
	284.5	12.68			

(Continued)

Continued

Salt (wt%)	*T* (K)	*P* (MPa)	Salt (wt%)	*T* (K)	*P* (MPa)
NaCl (10%)	272.7	4.33	$MgCl_2$ (10%)	270.3	2.54
	274.0	5.04		271.9	2.96
	274.9	5.68		273.6	3.57
	276.4	6.67		275.7	4.58
	278.0	7.64		278.2	5.91
	279.4	8.75		280.4	7.55
	280.4	9.82		282.5	9.38
	281.6	11.41		285.2	12.33
$NaHCO_3$ (3%)	269.8	2.05	$CaCl_2$ (10%) +	269.9	3.72
	272.1	2.62	NaCl (10%)	271.6	4.40
	273.2	3.00		273.0	5.14
	275.8	3.98		273.9	5.71
	278.1	5.02		276.0	7.09
	280.4	6.48		277.9	8.92
	283.0	8.54		279.8	11.16
	285.8	11.31	NaCl (5%) +	270.2	2.41
NaCl (5%) +	272.1	3.44	$MgCl_2$ (5%) +	272.2	3.05
$MgCl_2$ (5%)	274.5	4.38	$CaCl_2$ (5%)	273.5	3.82
	277.3	5.54		275.1	4.88
	278.8	6.32		276.9	6.30
	280.6	7.71		278.1	7.36
	282.8	9.63		279.3	8.75
	285.2	12.26		280.4	10.09
NaCl (5%) +	268.1	2.40	NaCl (5%) +	269.2	2.53
$NaHCO_3$ (3%)	271.1	3.24	KCl (5%) +	270.6	2.53
	273.1	3.89	$CaCl_2$ (3%) +	272.1	3.72
	275.3	4.92	$MgCl_2$ (3%)	273.5	4.48
	277.9	6.32		275.0	5.62
	279.2	7.23		276.5	6.95
	281.1	8.76		278.0	8.56
	283.2	10.79		279.4	10.49
$CaCl_2$ (10%) +	269.6	3.16			
$MgCl_2$ (5%)	271.6	3.91			
	273.9	5.01			
	275.4	5.82			
	277.0	6.97			
	278.7	8.10			
	280.2	9.61			
	281.8	11.34			

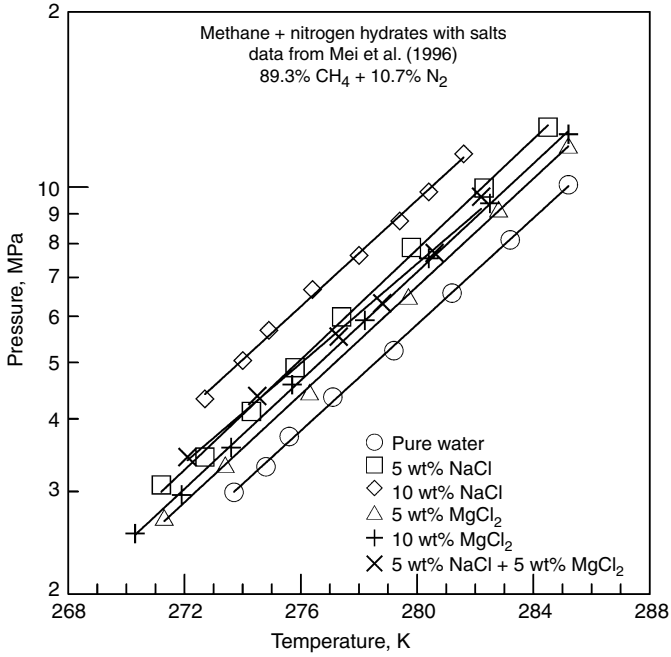

FIGURE 6.55 Inhibition of methane + nitrogen hydrates with sodium chloride and magnesium chloride.

BINARY MIXTURES OF METHANE + CARBON DIOXIDE WITH INHIBITORS

Hydrate: 90.09 mol% methane and 9.91% carbon dioxide with methanol
Reference: Ng and Robinson (1983)
Phases: L_W–H–V

wt%	*T* (K)	*P* (MPa)	wt%	*T* (K)	*P* (MPa)
10.0	265.4	1.49	10.0	287.0	18.95
10.0	265.4	1.50	20.0	263.4	2.76
10.0	268.7	2.16	20.0	263.6	2.81
10.0	268.7	2.18	20.0	267.0	4.12
10.0	271.2	2.92	20.0	267.1	4.21
10.0	271.2	2.92	20.0	267.1	4.27
10.0	275.5	4.91	20.0	272.9	6.98
10.0	275.5	4.93	20.0	273.2	7.03
10.0	280.6	8.98	20.0	280.1	14.36
10.0	280.7	9.05	20.0	280.1	14.40
10.0	285.2	15.28	20.0	282.2	19.00
10.0	285.2	15.29	20.0	282.1	19.01
10.0	286.8	18.66			

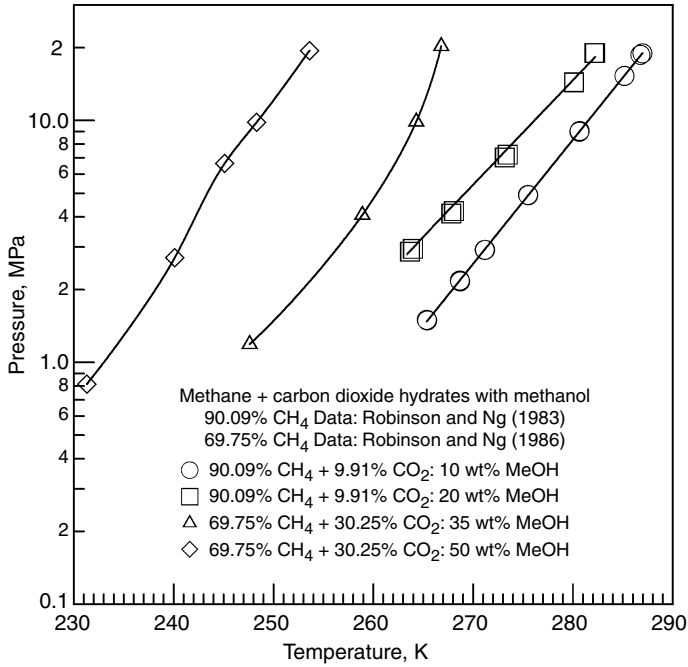

FIGURE 6.56 Methanol inhibition of methane + carbon dioxide hydrates.

Hydrate: 69.75 mol% methane and 30.25% carbon dioxide with methanol
Reference: Robinson and Ng (1986)
Phases: L_W–H–V

wt%	*T* (K)	*P* (MPa)	wt%	*T* (K)	*P* (MPa)
35	247.6	1.190	50	240.1	2.710
35	258.9	4.070	50	245.1	6.640
35	264.3	9.890	50	248.3	9.830
35	266.8	20.270	50	253.6	19.430
50	231.3	0.814			

Hydrate: Methane + carbon dioxide and single and mixed electrolytes
Reference: Dholabhai and Bishnoi (1994)
Phases: L_W–H–V

Composition of Aqueous Solutions

Solution ID	wt% NaCl	wt% KCl	wt% $CaCl_2$	Molality
Na5	5.02	0	0	0.9044
Na10	9.99	0	0	1.8992
Na15	15.00	0	0	3.0197

Continued

Solution ID	wt% NaCl	wt% KCl	wt% $CaCl_2$	Molality
Na20-1	20.00	0	0	4.2779
Na20-2	20.01	0	0	4.2806
K5	0	5.00	0	0.7060
K10	0	10.00	0	1.4904
K15	0	15.01	0	2.3690
Ca10	0	0	9.91	2.9733
Ca15	0	0	15.00	4.7699
Ca20	0	0	20.00	6.7574
Na5K10	5.00	10.00	0	2.5847
Na10K5	10.00	5.00	0	2.8022
K10Ca5	0	10.00	5.00	3.1681
Na5Ca10	5.01	0	10.00	4.1890
Na10Ca10	10.0	0	10.00	5.5176
Na10Ca10	10.17	0	5.08	3.6736
Na6K5Ca4-1	6.01	5.00	3.99	3.2677
Na6K5Ca4-2	6.00	5.00	4.00	3.2689

Hydrate Formation Conditions (Initial Gas Composition = 80 mol% CH_4 + 20% CO_2)

Solution	*T* (K)	*P* (MPa)	%CO_2	*T* (K)	*P* (MPa)	%CO_2
H_2O	277.6	3.41	15.3	274.1	2.36	16.4
	281.5	5.14	16.7	284.8	7.53	17.9
Na5	282.0	6.98	17.7	275.0	3.26	16.1
	279.2	5.08	17.2	271.6	2.30	15.2
Na10	279.0	6.56	17.4	276.1	4.66	19.4
	272.1	3.10	16.1	268.5	2.03	19.3
Na15	277.2	7.31	18.9	273.1	4.40	19.8
	269.1	2.88	19.4	264.8	1.86	17.3
	276.8	7.37	18.2			
Na20-1	270.4	5.42	19.3	267.5	3.85	19.8
	262.0	2.12	19.1			
Na20-2	274.3	9.15	19.9			
K5	271.4	2.04	19.7	275.0	2.96	19.8
	278.8	4.46	19.8	282.0	6.43	19.8
K10	275.9	3.94	19.6	272.2	2.59	19.8
	269.2	1.83	19.7	279.0	5.56	19.8
K15	267.0	1.89	18.4	272.7	3.45	19.5
	270.1	2.62	19.0	277.1	5.63	19.7

(Continued)

Continued

Solution	*T* (K)	*P* (MPa)	%CO_2	*T* (K)	*P* (MPa)	%CO_2
Ca10	268.6	1.96	18.7	272.0	2.80	19.4
	276.0	4.32	19.7	279.1	6.08	19.7
Ca15	273.1	4.61	19.0	266.6	1.88	19.6
	269.1	3.00	19.7	276.9	7.09	19.7
Ca20	263.8	2.89	19.8	267.6	4.30	19.8
	271.3	7.24	19.9	273.7	9.46	19.9
Na5Ca10	273.7	5.04	19.4	265.5	2.06	19.7
	269.4	3.12	19.8	276.7	7.14	19.9
K10Ca5	265.1	1.65	19.8	269.4	2.46	19.8
	274.8	4.60	19.9	281.6	10.61	19.9
Na5K10	269.3	2.59	19.2	275.2	4.99	19.7
	281.3	10.41	19.8	265.1	1.66	20.3
Na10Ca5	275.1	6.07	19.5	269.2	3.10	20.0
	265.5	2.11	20.1	278.7	9.71	19.4
Na6K5Ca4-1	275.1	5.23	19.9	269.0	2.67	19.9
	278.2	7.65	19.7	265.5	1.85	20.3

Hydrate Formation Conditions (Initial Gas Composition = 50 mol% CH_4 + 50% CO_2)

Solution ID	*T* (K)	*P* (MPa)	% CO_2	*T* (K)	*P* (MPa)	% CO_2
Na10Ca10	268.1	3.53	48.6	270.8	5.16	49.4
	264.1	2.15	49.7	268.2	3.52	49.7
Na10K5	275.5	4.59	46.5	268.0	1.82	49.8
	271.6	2.78	49.5	265.8	1.38	50.0
Na6K5Ca4-2	275.5	4.46	47.5	266.0	1.45	48.1
	271.9	2.80	50.0	268.1	1.81	49.6

Hydrate: Methane + carbon dioxide with 9.45 wt% sodium chloride
Reference: Fan and Guo (1999)
Phases: L_W–H–V

5.02% CH_4

T (K)	*P* (MPa)	*T* (K)	*P* (MPa)
267.9	1.24	274.1	2.43
271.0	1.76	275.1	2.85
273.3	2.22	277.4	3.75
273.5	2.35		

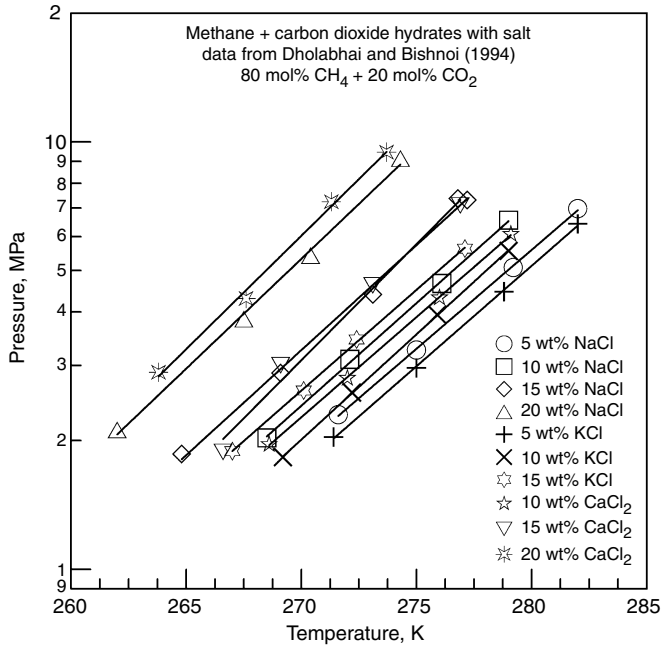

FIGURE 6.57 Inhibition of methane + carbon dioxide hydrates with salts.

Hydrate: Methane + carbon dioxide with 10 wt% monoethylene glycol
Reference: Fan et al. (2000)
Phases: L_W–H–V

3.48 mol% CH_4

T (K)	*P* (MPa)	*T* (K)	*P* (MPa)
268.7	1.14	274.2	2.26
271.3	1.60	278.0	3.22

BINARY MIXTURES OF METHANE + HYDROGEN SULFIDE WITH INHIBITORS

Hydrate: Methane and hydrogen sulfide with 20 wt% methanol
Reference: Ng et al. (1985a)
Phases: L_W–H–V

CH_4	H_2S	*T* (K)	*P* (MPa)	CH_4	H_2S	*T* (K)	*P* (MPa)
0.896	0.104	264.5	0.945	0.780	0.220	287.0	11.670
0.897	0.103	271.8	2.130	0.741	0.259	290.3	18.710
0.837	0.163	281.4	5.750				

Binary Mixtures of Ethane + Carbon Dioxide with Inhibitors

Hydrate: 75% ethane and 25 mol% carbon dioxide with methanol
Reference: Ng et al. (1985b)
Phases: L_W–H–V, L_W–H–V–L_{MIX}, L_W–H–L_{MIX}

L_W–H–V

wt%	*T* (K)	*P* (MPa)	wt%	*T* (K)	*P* (MPa)
20	266.4	0.738	35	266.8	2.110
20	271.1	1.400	50	237.0	0.319
20	275.3	2.689	50	242.1	0.494
35	251.4	0.422	50	248.4	0.862
35	256.9	0.724	50	251.5	1.172
35	260.2	0.993	50	254.3	1.593
35	263.9	1.586	50	255.3	1.800

L_W–H–V–L_{MIX}

wt%	*T* (K)	*P* (MPa)	wt%	*T* (K)	*P* (MPa)
20	276.9	3.523	50	255.5	1.855
35	267.8	2.627	50	255.8	2.096
35	268.1	2.806			

L_W–H–L_{MIX}

wt%	*T* (K)	*P* (MPa)	wt%	*T* (K)	*P* (MPa)
20	277.1	4.254	35	270.4	13.960
20	278.3	9.080	35	271.6	20.170
20	279.3	14.470	50	256.5	3.999
20	280.5	20.770	50	257.9	8.267
35	268.6	4.192	50	259.4	15.010
35	269.2	6.998	50	260.6	20.420

Hydrate: Ethane + carbon dioxide with 10 wt% sodium chloride
Reference: Fan and Guo (1999)
Phases: L_W–H–V

5.31 mol% C_2H_6

T (K)	*P* (MPa)	*T* (K)	*P* (MPa)
269.1	1.17	272.9	1.88
270.9	1.50	274.2	2.30

Hydrate: Ethane + carbon dioxide with 10.6 wt% monoethylene glycol
Reference: Fan et al. (2000)
Phases: L_W–H–V

5.31 mol% C_2H_6

T (K)	*P* (MPa)	*T* (K)	*P* (MPa)
269.1	0.85	274.9	1.82
271.0	1.03	276.4	2.31
272.9	1.31		

Binary Mixtures of Propane + *n*-Butane with Inhibitors

Hydrate: Propane + *n*-butane with sodium chloride
Reference: Paranjpe et al. (1987)
Phases: L_W–H–V and L_W–H–V–L_{HC}

L_W–H–V

wt% NaCl	mol% C_3H_8	*T* (K)	*P* (MPa)	wt% NaCl	mol% C_3H_8	*T* (K)	*P* (MPa)
3.0	0.999	275.2	350.3	5.0	0.984	273.2	299.2
3.0	0.955	275.2	373.7	5.0	0.952	273.2	307.3
3.0	0.906	275.2	391.6	5.0	0.927	273.2	317.2
3.0	0.997	273.2	224.8	5.0	0.894	273.2	330.9
3.0	0.921	273.2	246.8	5.0	0.906	273.2	336.5
3.0	0.854	273.2	273.7	5.0	0.981	272.2	242.7
3.0	1.000	272.2	197.2	5.0	0.930	272.2	255.1
3.0	0.964	272.2	209.6	5.0	0.905	272.2	262.7
3.0	0.833	272.2	221.3	5.0	0.878	272.2	272.3
3.0	0.826	272.2	238.6				

L_W–H–V–L_{HC}

wt% NaCl	mol% C_3H_8	*T* (K)	*P* (MPa)	wt% NaCl	mol% C_3H_8	*T* (K)	*P* (MPa)
3.0	NA	275.2	373.7	5.0	NA	274.2	412.3
3.0	NA	274.2	332.3	5.0	NA	273.2	350.3
3.0	NA	273.2	281.3	5.0	NA	272.2	284.1
3.0	NA	272.2	241.3	5.0	NA	271.2	241.3
3.0	NA	271.3	214.4	5.0	NA	270.2	209.6

Binary Mixtures of Nitrogen + Carbon Dioxide with Inhibitors

Hydrate: Nitrogen + carbon dioxide with 9.41 wt% sodium chloride
Reference: Fan and Guo (1999)
Phases: L_W–H–V

9.01 mol% N_2

$\%CO_2$	*T* (K)	*P* (MPa)	$\%CO_2$	*T* (K)	*P* (MPa)
90.99	266.9	1.12	90.99	272.9	2.03
90.99	269.3	1.40	90.99	275.0	2.89
90.99	271.7	1.72	90.99	276.2	3.16
90.99	271.8	1.74			

Hydrate: Nitrogen + carbon dioxide with monoethylene glycol
Reference: Fan et al. (2000)
Phases: L_W–H–V

mol% CO_2		*T* (K)	*P* (MPa)	mol% CO_2		*T* (K)	*P* (MPa)
96.52	10 wt% MEG	268.9	1.00	90.99	13.01 wt% MEG	267.2	0.93
96.52		272.1	1.35	90.99		267.9	1.03
96.52		273.4	1.62	90.99		270.2	1.20
96.52		276.1	2.49	90.99		271.9	1.76
				90.99		273.7	2.15
				90.99		274.2	2.49
				90.99		275.3	2.80
				90.99		276.5	3.39

Ternary and Multicomponent Mixtures with Inhibitors

Hydrate: Methane + carbon dioxide + hydrogen sulfide with methanol
Reference: Ng et al. (1985b)
Phases: L_W–V–H

MeOH wt%	CH_4	CO_2	H_2S	*T* (K)	*P* (MPa)
10	0.7647	0.1639	0.0714	264.9	0.556
10	0.7648	0.1654	0.0698	267.7	0.734
10	0.6980	0.2059	0.0961	275.7	1.411
10	0.6941	0.1998	0.1061	280.9	2.237
10	0.6635	0.2167	0.1198	285.6	3.900

Continued

MeOH wt%	CH_4	CO_2	H_2S	*T* (K)	*P* (MPa)
10	0.6106	0.2350	0.1544	291.0	6.546
20	0.6938	0.2161	0.0901	267.5	1.072
20	0.6463	0.2334	0.1209	273.5	1.627
20	0.6263	0.2338	0.1399	277.8	2.455
20	0.6119	0.2408	0.1473	280.7	3.344
20	0.6060	0.2408	0.1532	283.6	4.909
20	0.5873	0.2434	0.1693	285.7	6.705
20	0.5924	0.2470	0.1606	284.5	5.634
20	0.5320	0.1988	0.2642	270.0	0.575

Hydrate: Quaternary gas mixture with single; mixed salts; methanol; salts + methanol inhibitors
Reference: Mei et al. (1998)
Phases: L_W–H–V
Methane + Ethane + Propane + 2-Methylpropane

Gas Composition

Composition	mol%	Composition	mol%
CH_4	97.25	C_3H_8	1.08
C_2H_6	1.42	*n*-C_4H_{10}	0.25

Sol wt%	*T* (K)	*P* (MPa)	Sol wt%	*T* (K)	*P* (MPa)
10% NaCl	267.1	0.81	10% MeOH	266.8	0.61
	269.2	1.01		269.0	0.79
	271.0	1.30		271.2	1.00
	273.4	1.66		273.2	1.03
	275.5	2.12		275.4	1.68
	277.6	2.66		277.5	2.14
	277.7	2.68		279.5	2.71
	279.8	3.43	20% MeOH	264.5	0.74
10% KCl	269.1	0.78		266.0	1.20
	271.3	0.97		268.6	1.51
	273.3	1.25		270.6	1.91
	275.6	1.81		272.8	2.48
	277.7	2.26		275.4	3.40
	279.8	2.81		277.6	4.50

(Continued)

Continued

Sol wt%	*T* (K)	*P* (MPa)	Sol wt%	*T* (K)	*P* (MPa)
10% $CaCl_2$	266.7	0.63	30% MeOH	262.6	1.60
	269.2	0.88		264.7	1.97
	271.1	1.14		266.9	2.24
	273.5	1.44		267.9	2.56
	275.4	1.88		268.9	2.85
	277.4	2.48		270.2	3.20
	279.7	3.34	10% NaCl + 20% MeOH	260.8	1.70
2% NaCl + 0.5% $CaCl_2$ + 0.5% KCl	270.9	0.60		262.4	2.06
	273.2	0.93		264	2.56
	275.2	1.20		265.5	3.06
	277.4	1.60		267.5	3.98
	279.2	2.06		269	4.96
	281.2	2.75	10% KCl + 20% MeOH	264.6	1.80
10% KCl + 10% MeOH	266.5	1.16		266.6	2.50
	269.3	1.42		268.6	3.46
	270.9	1.84		271.3	5.53
	273.4	2.67		273.4	7.76
	275.5	3.47		275.5	11.18
	277.5	4.61	10% $CaCl_2$ + 20% MeOH	264.5	1.47
	279.5	6.03		266.1	2.05
10% NaCl + 10% MeOH	264.7	1.05		267.6	2.66
	267.0	1.40		269.1	3.44
	269.0	1.78		270.7	4.34
	271.0	2.47		272.4	5.89
	273.4	3.18	2% NaCl + 0.5% $CaCl_2$ + 0.5% KCl + 10% MeOH	268.6	0.78
	275.4	3.98		271.3	1.18
	277.5	4.90		276.4	2.48
10% $CaCl_2$ + 10% MeOH	267.0	1.10		278.9	3.46
	273.8	1.66		281.5	4.69
	269.0	1.58	2% NaCl + 0.5% $CaCl_2$ + 0.5% KCl + 20% MeOH	266.5	1.47
	270.8	1.84		270.7	2.57
	273.5	2.57		272.9	3.40
	275.5	3.42		274.8	4.52
	277.5	4.43		268.7	1.96
	279.4	5.95		276.9	5.92
				279	7.88

Hydrate: Quaternary gas mixture with 10 wt% monoethylene glycol (mol% gas composition: 88.53% CO_2 + 6.83% CH_4 + 0.38% C_2H_6 + 4.26% N_2)
Reference: Fan et al. (2000)
Phases: L_W–H–V

T (K)	*P* (MPa)	*T* (K)	*P* (MPa)
268.8	0.80	276.4	2.41
270.7	1.16	278.1	2.85
274.4	1.82	279.3	3.50

Hydrate: Synthetic natural gas mixture with methanol
Reference: Ng and Robinson (1983)
Phases: L_W–H–V

Gas Composition

Composition	mol%	Composition	mol%	Composition	mol%
N_2	7.00	C_2H_6	4.67	*n*-C_4H_{10}	0.93
CH_4	84.13	C_3H_8	2.34	*n*-C_5H_{12}	0.93

wt%	*T* (K)	*P* (MPa)	wt%	*T* (K)	*P* (MPa)	wt%	*T* (K)	*P* (MPa)
10.0	267.7	0.90	10.0	288.6	17.19	20.0	275.0	4.66
10.0	273.5	1.80	10.0	288.9	18.82	20.0	279.2	8.92
10.0	279.2	3.57	20.0	264.8	1.26	20.0	281.4	13.73
10.0	283.5	6.78	20.0	270.0	2.38	20.0	283.3	18.82
10.0	286.3	10.86						

Hydrate: Synthetic natural gas mixture containing carbon dioxide with methanol
Reference: Ng and Robinson (1983)
Phases: L_W–H–V

Gas composition

Composition	mol%	Composition	mol%	Composition	mol%
N_2	5.96	C_3H_8	1.94	*n*-C_5H_{12}	0.79
CH_4	71.60	*n*-C_4H_{10}	0.79	CO_2	14.19
C_2H_6	4.73				

(Continued)

Continued

wt%	*T* (K)	*P* (MPa)	wt%	*T* (K)	*P* (MPa)	wt%	*T* (K)	*P* (MPa)
10.0	268.3	1.04	10.0	286.5	13.91	20.0	276.3	6.94
10.0	271.0	1.46	10.0	287.7	17.44	20.0	278.0	9.53
10.0	276.6	2.76	10.0	288.3	19.03	20.0	278.8	12.14
10.0	281.5	5.52	20.0	264.4	1.41	20.0	279.5	15.04
10.0	283.9	8.42	20.0	270.4	2.83	20.0	280.3	16.75
10.0	285.0	10.73	20.0	274.1	4.77	20.0	281.0	19.15

Hydrate: Seven-component mixture with methanol
Reference: Robinson and Ng (1986)
Phases: L_W–H–V, L_W–H–V–L_{HC}, L_W–H–L_{HC}

Composition	mol%	Composition	mol%	Composition	mol%	Composition	mol%
N_2	5.26	CH_4	73.90	C_3H_8	2.02	*n*-C_5H_{10}	0.80
CO_2	13.37	C_2H_6	3.85	*n*-C_4H_{10}	0.80		

L_W–H–V

wt%	*T* (K)	*P* (MPa)	wt%	*T* (K)	*P* (MPa)
35	244.9	0.362	35	248.2	0.600

L_W–H–V–L_{HC}

wt%	*T* (K)	*P* (MPa)	wt%	*T* (K)	*P* (MPa)
35	256.1	1.390	50	234.4	0.518
35	262.6	3.610	50	241.5	1.410
35	266.8	7.290	50	250.1	3.450
			50	254.5	7.250
35	269.9	13.82	50	256.3	13.57
35	273.1	20.35	50	256.8	14.22
			50	258.5	20.28

Hydrate: Gas liquid and condensate with methanol and ethylene glycol
Reference: Ng et al. (1987a)

Composition of Hydrocarbon Liquids (mol%)

Component	Gas C	Gas D
Nitrogen	0.16	0.64
Methane	26.19	73.03
Carbon dioxide	2.10	3.11
Ethane	8.27	8.04
Propane	7.50	4.28
Isobutane	1.83	0.73
n-Butane	4.05	1.50
Isopentane	1.85	0.54
n-Pentane	2.45	0.60
Hexanes plus	45.60	7.53
Mol.Wt.	90.2	32.4
Satn. *P* (MPa) at Ts	8.95[B]	43.94[R]
Ts(K)	310.95	416.15

B = Bubble point pressure.
R = Retrograde dew point pressure.

Liquid C

Sol (wt%)	*T* (K)	*P* (MPa)	Phases	Sol (wt%)	*T* (K)	*P* (MPa)	Phases
13% MeOH	281.0	3.91	L_W–H–V–L_{HC}	20% MEG	281.2	3.94	L_W–H–V–L_{HC}
	285.8	7.40	L_W–H–V–L_{HC}		285.6	7.37	L_W–H–V–L_{HC}
	286.2	12.00	L_W–H–L_{HC}		286.4	12.00	L_W–H–L_{HC}
	287.6	20.00	L_W–H–L_{HC}		287.8	20.00	L_W–H–L_{HC}
24% MeOH	275.2	4.02	L_W–H–V–L_{HC}	39% MEG	274.4	4.08	L_W–H–V–L_{HC}
	278.8	6.97	L_W–H–V–L_{HC}		278.4	6.92	L_W–H–V–L_{HC}
	279.0	11.99	L_W–H–L_{HC}		278.8	12.06	L_W–H–L_{HC}
	280.4	19.99	L_W–H–L_{HC}		280.0	19.99	L_W–H–L_{HC}

(Continued)

Continued

Liquid D

Aqueous solution wt%	*T* (K)	*P* (MPa)	Phases
16% MeOH	283.2	6.00	L_W–H–V–L_{HC}
	286.4	11.03	L_W–H–V–L_{HC}
	288.0	15.01	L_W–H–V–L_{HC}
	288.95	19.99	L_W–H–V–L_{HC}
29% MeOH	276.0	6.03	L_W–H–V–L_{HC}
	278.8	10.99	L_W–H–V–L_{HC}
	280.0	14.97	L_W–H–V–L_{HC}
	281.6	20.00	L_W–H–V–L_{HC}

Hydrate: Lean gas and rich gas with methanol
Reference: Ng et al. (1987b)
Phases: L_W–H–V–L_{LG}, L_W–H–L_{LG}, L_W–H–V–L_{RG}, L_W–H–L_{RG}

Mol Fraction

Component	Lean gas	Rich gas
CH_4	0.9351	0.8999
C_2H_6	0.0458	0.0631
C_3H_8	0.0131	0.0240
i-C_4H_{10}	0.0010	0.0030
n-C_4H_{10}	0.0020	0.0050
i-C_5H_{12}	0 0010	0.0010
n-C_5H_{12}	0.0010	0.0010
n-C_6H_{14}	0.0010	0.0030

Lean Gas
L_W–H–V–L_{LG}

wt%	*T* (K)	*P* (MPa)	wt%	*T* (K)	*P* (MPa)
65.0	225.8	0.66	73.7	229.2	2.90
65.0	235.0	1.61	73.7	235.1	5.79
65.0	244.4	4.25	85.0	199.8	2.08
73.7	221.9	1.37	85.0	204.4	4.63

Continued

L_W–H–L_{LG}

wt%	*T* (K)	*P* (MPa)	wt%	*T* (K)	*P* (MPa)
65.0	248.9	10.29	73.7	237.2	20.07
65.0	250.4	19.75	85.0	205.8	11.34
73.7	236.4	9.51	85.0	206.8	20.37
73.7	235.9	10.17			

Rich Gas
L_W–H–V–L_{RG}

wt%	*T* (K)	*P* (MPa)	wt%	*T* (K)	*P* (MPa)
65.0	229.4	0.77	73.7	228.9	
65.0	238.2	1.70	73.7	236.4	
65.0	46.0	4.28	785.0	198.1	
73.7	218.2	0.76	85.0	207.4	

L_W–H–L_{RG}

wt%	*T* (K)	*P* (MPa)	wt%	*T* (K)	*P* (MPa)
65.0	250.0	10.54	73.7	238.6	
65.0	251.2	20.17	85.0	211.1	
73.7	237.7	10.23	85.0	212.4	

Hydrate: Gas mixture with calcium chloride (0.1% N_2, 1.8% CO_2, 80.5% CH_4, 10.3% C_2H_6, 5% C_3H_8, 4.3% C_4H_{10})
Reference: Ng and Robinson (1994)
Phases: L_W–H–V

wt% $CaCl_2$	*T* (K)	*P* (MPa)	wt% $CaCl_2$	*T* (K)	*P* (MPa)
0	289.6	5.0	23.0	274.0	5.0
	299.8	30.0		282.0	30.0
	304.6	60.0		285.8	60.0
7.0	287.2	5.0	31.0	255.2	3.8
	292.0	11.5		259.4	11.5
	296.6	30.0		261.8	20.8
	301.6	60.0			
15.0	283.0	5.0	33.0	252.6	6.5
	290.8	30.0		255.6	14.3
	296.0	60.0		256.4	20.8

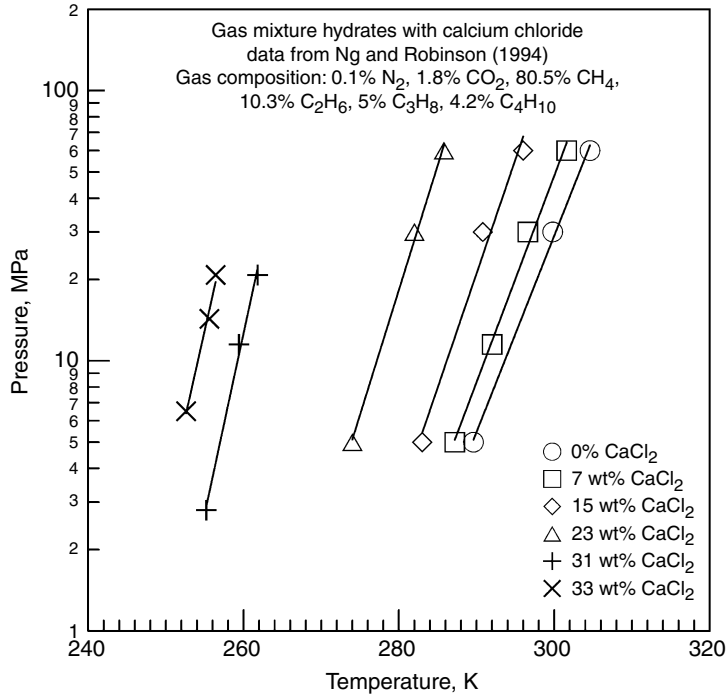

FIGURE 6.58 Calcium chloride inhibition of a multicomponent gas mixture.

Hydrate: Reservoir fluid with methanol and formation water
Reference: Ng and Robinson (1994)
Phases: L_W–H–V–L_{HC} and L_W–H–L_{HC}
Reservoir fluid: 1.05 mol% CO_2, 0.29% N_2, 61.07% CH_4, 4.58% C_2H_6, 3.16% C_3H_8, 1.98% C_4H_{10}, 1.35% C_5H_{12}, 1.92% C_6H_{14}, 24.6% $C_7H_{16}^+$
Fraction concentrations: CH_4 (60 mol%), $C_7H_{16}^+$ (25 mol%)
Salt content of formation water = 3 wt%

Formation water			**20 wt% MeOH/80% formation H_2O**		
***T* (K)**	***P* (MPa)**	**Phases**	***T* (K)**	***P* (MPa)**	**Phases**
280.2	2.48	L_W–H–V–L_{HC}	272.6	3.10	L_W–H–V–L_{HC}
288.2	7.47	L_W–H–V–L_{HC}	279.0	7.65	L_W–H–V–L_{HC}
294.0	20.6	L_W–H–V–L_{HC}	284.0	20.7	L_W–H–V–L_{HC}
298.9	44.0	L_W–H–L_{HC}	288.2	43.2	L_W–H–L_{HC}

Hydrate: Natural gas and condensate in distilled and saline water and in methanol
Reference: Tohidi et al. (1994a, 1995b, 1996b)
Phases: L_W–H–V and phase fractions

Composition of Mixture, Condensate, and Salt Water

Component	Gas mixture	Gas condensate	Forties Formation H_2O salt concentration (wt%)	
CH_4	85.93	73.9	NaCl	6.993
C_2H_6	6.75	7.50	$CaCl_2$	0.735
C_3H_8	3.13	4.08	$MgCl_2$	0.186
i-C_4H_{10}	0.71	0.61	KCl	0.066
n-C_4H_{10}	0.88	1.58	$SrCl_2$	0.099
i-C_5H_{12}		0.50	$BaCl_2$	0.036
n-C_5H_{12}	0.57	0.74		
C_6H_{14}		0.89		
$C_7H_{16}^+$		7.19		
CO_2	1.31	2.38		
N_2	0.72	0.58		

Hydrate Formation Conditions

Gas mixture				Gas condensate			
Distilled water		Forties Formation H_2O		Distilled water		30.5 wt% MeOH	
T **(K)**	***P*** **(MPa)**	***T*** **(K)**	***P*** **(MPa)**	***T*** **(K)**	***P*** **(MPa)**	***T*** **(K)**	***P*** **(MPa)**
280.5	1.634	277.5	1.613	277.3	0.993	262.4	1.151
283.9	2.468	281.8	2.916	277.6	1.082	264.4	1.627
287.8	3.916	286.8	5.681	278.2	1.207	267.2	2.268
				278.8	1.289	269.4	2.923
				279.4	1.386	271.2	3.723
				280.6	1.620	271.8	3.944
				281.2	1.758	272.2	4.185
				281.8	1.924		
				283.4	2.289		
				284.4	2.558		
				286.0	3.096		

(Continued)

Continued

Phase Fractions, Compositions, and Temperature and Pressure

	Gas mixture				Gas condensate	
	Pure water		Forties Formation H_2O		Pure water	30 wt% MeOH
Phase	**284.8 K 3.591 MPa**		**284.5 K 5.366 MPa**		**283.3 K 2.85 MPa**	**270.2 K 4.027 MPa**
mol H_2O/ mol gas	5.029		4.987		13.354	3.632
N_2	*	*	*	*	0.65	0.96
CO_2	1.68	0.37	1.28		1.76	1.99
CH_4	88.57	67.89	87.43	69.9	86.46	86.88
C_2H_6	6.47	8.63	6.47	8.54	7.29	6.92
C_3H_8	1.67	17.29	3.04	16.69	2.03	1.94
i-C_4H_{10}	0.29	4.54	0.40	3.73	0.21	0.20
n-C_4H_{10}	0.80	1.28	0.85	1.14	0.69	0.41
i-C_5H_{12}					0.13	0.05
n-C_5H_{12}	0.52	0.14			0.15	0.08
$C_6H_{14}^+$					0.63	0.44
MeOH						0.13
Vapor%	14.85		15.06			
Hydrate%	11.63 (calc'd)		9.96 (calc'd)			
Water%	73.52		74.98			
mol gas in hydrate	0.022		0.019			
mol% vapor					5.30	13.68
mol H_2O converted to hydrate					0.042	0.048

* = Vapor phase composition on a nitrogen-free and water-free basis.

Hydrate: Natural gas and black oil with synthetic salts and North Sea brines
References: Tohidi et al. (1997b)
Phases: L_W–H–V and L_W–H–V–L_{HC}

Component	Black oil MW = 131.8 mol%	Specific gravity at 60°F/60°F	Composition of gas mixture
N_2			0.84
CO_2			0.25

Continued

Component	Black oil MW = 131.8 mol%	Specific gravity at 60°F/60°F	Composition of gas mixture
CH_4	23.96		85.47
C_2H_6	3.98		7.72
C_3H_8	5.65		3.30
i-C_4H_{10}	2.00		0.81
n-C_4H_{10}	4.12		1.01
i-C_5H_{12}	2.09		0.30
n-C_5H_{12}	2.89		0.30
C_6's	4.10	0.666	
C_7's	6.25	0.714	
C_8's	6.55	0.738	
C_9's	5.20	0.761	
C_{10}'s	4.06	0.776	
C_{11}'s	3.31	0.790	
C_{12}'s	2.64	0.801	
C_{13}'s	2.36	0.815	
C_{14}'s	2.18	0.831	
C_{15}'s	1.95	0.837	
C_{16}'s	1.61	0.844	
C_{17}'s	1.28	0.849	
C_{18}'s	1.27	0.856	
C_{19}'s	1.05	0.863	
C_{20}^+	11.50	0.947	

Composition of North Sea Brine and Forties Formation Water

Salt	North Sea brine wt%	Forties Formation H_2O wt%
NaCl	2.354	6.993
$CaCl_2$	0.116	0.735
$MgCl_2$	0.524	0.186
KCl	0.086	0.066
Na_2SO_4	0.428	—
$SrCl_2$	—	0.099
$BaCl_2$	—	0.036

(Continued)

Continued

Hydrate Formation from Natural Gas with Mixed Salt Inhibitors

T (K)	*P* (MPa)	*T* (K)	*P* (MPa)
	10 wt% NaCl		
275.8	1.427	283.8	3.558
281.0	2.217	291.0	13.155
	2.87 wt% NaCl + 2.87% KCl + 2.89% $CaCl_2$		
278.4	1.682	288.7	5.192
282.3	2.496	290.2	6.964
284.7	3.516	292.6	13.224
	5.55 wt% NaCl + 1.85% KCl + 1.85% $CaCl_2$		
276.8	1.413	287.7	5.364
280.4	2.124	289.2	6.964
283.0	2.979	291.0	10.342
285.7	4.199	291.9	13.066
287.2	5.171		
	North Sea brine		
2788	1.434	288.3	4.730
281.7	1.937	291.0	6.957
283.6	2.620	293.6	10.632
286.0	3.468		
	Forties Formation water		
275.3	1.165	283.0	2.923
278.0	1.586	286.7	4.309
280.6	2.151	290.0	6.943

Hydrate Formation from Black Oil with Mixed Salt Inhibitors

T (K)	*P* (MPa)	*T* (K)	*P* (MPa)
	Distilled water		
275.0	0.779	282.3	2.193
276.6	0.958	282.9	2.379
277.7	1.082	283.6	2.599
277.8	1.158	284.6	3.075
278.7	1.310	285.4	3.427
279.9	1.531		
	6.01 wt% NaCl + 1.49% $CaCl_2$ + 0.19% $MgCl_2$		
276.1	1.296	280.3	2.723
278.4	2.041		
	8.46 wt% NaCl + 3.04% $CaCl_2$ + 0.87% $MgCl_2$		
270.9	1.055	275.9	2.103
272.2	1.289	277.0	2.461
274.0	1.737	277.8	3.130

Continued

T (K)	*P* (MPa)	*T* (K)	*P* (MPa)
Forties Formation water			
274.9	1.165	282.0	3.447
278.5	1.924	284.3	4.868
Forties Formation H_2O + 8.67 wt% methanol			
270.9	1.255	277.8	3.392
274.5	2.075	281.1	5.330

Hydrate: Gas, condensate with distilled water, salty water, and methanol
Reference: Tohidi et al. (1994b)
Phases: L_W–H–V and L_W–H–L_{HC} with inhibitors

Composition of Gas and Gas Condensate

Component	Gas (mol%)	Gas condensate (mol%)
CH_4	85.93	73.9
C_2H_6	6.75	7.50
C_3H_8	3.13	4.08
i-C_4H_{10}	0.71	0.61
n-C_4H_{10}	0.88	1.58
i-C_5H_{12}	—	0.50
n-C_5H_{12}	0.57	0.74
C_6H_{14}	—	0.89
$C_7H_{16}^+$	—	7.19
CO_2	1.31	2.38
N_2	0.72	0.58

Composition of Forties Formation (Salt) Water

Salt	NaCl	$CaCl_2$	$MgCl_2$	KCl	$SrCl_2$	$BaCl_2$
Concentration wt%	6.993	0.735	0.186	0.066	0.099	0.036

Hydrate Conditions for Gas in Pure Water and Forties Formation (Salt) Water

Distilled water		Forties formation water	
T (K)	*P* (MPa)	*T* (K)	*P* (MPa)
280.5	1.634	277.5	1.613
283.9	2.468	281.8	2.916
287.8	3.916	286.8	5.681

(Continued)

Continued

Hydrate Conditions for Condensate in Pure Water and 30.5 wt% Methanol

Distilled water		30.5 wt% methanol	
T **(K)**	***P*** **(MPa)**	***T*** **(K)**	***P*** **(MPa)**
277.25	0.993	262.35	1.151
277.65	1.082	264.35	1.627
278.25	1.207	267.25	2.268
278.75	1.289	269.35	2.923
279.45	1.386	271.25	3.723
280.55	1.620	271.75	3.944
281.25	1.758	272.15	4.185
281.85	1.924		
283.35	2.289		
284.35	2.558		
285.95	3.096		

Compositions for Gas in Pure Water and Forties Formation (Salt) Water

	With distilled water at 284.8 K and 5.03 MPa. Init mol H_2O/mol gas = 5.03		With Forties water at water at 284.5 K and 5.366 MPa. Init mol H_2O/mol gas = 4.99	
Component	**Vapor mol%**	**Hydrate mol%**	**Vapor mol%**	**Hydrate mol%**
CH_4	88.57	67.89	87.43	69.9
C_2H_6	6.47	8.63	6.47	8.54
C_3H_8	1.67	17.29	3.04	16.69
i-C_4H_{10}	0.29	4.54	0.40	3.73
n-C_4H_{10}	0.80	1.28	0.85	1.14
n-C_5H_{12}	0.52	—	0.53	0.0
CO_2	1.68	0.37	1.28	—
Phase	**Amount of each phase (mol%) at equilibrium**			
Vapor	14.85		15.06	
Hydrate	11.63		9.96	
Water	73.52		74.98*	
Mol gas released from hydrate	0.022		0.019	

* As a result of hydrate formation, salt concentration in the free water phases increased to 8.9 wt% from an initial value of 8.1 wt%.

Continued

Vapor Compositions and Moles of Water Converted to Hydrate for Gas Condensate

Component	With distilled water at 283.25 K and 2.85 MPa. mol H_2O/mol condensate = 13.354 vapor mol%	With water/methanol at 270.2 K and 4.027 MPa. mol H_2O/mol condensate = 3.632 vapor mol%
CO_2	1.76	1.99
N_2	0.65	0.96
CH_4	86.46	86.88
C_2H_6	7.29	6.92
C_3H_8	2.03	1.94
i-C_4H_{10}	0.21	0.20
n-C_4H_{10}	0.69	0.41
i-C_5H_{12}	0.13	0.05
n-C_5H_{12}	0.15	0.08
C_6H_{14}+	0.63	0.44
Methanol	—	0.13
H_2O	—	—
Mol% vapor	5.30	13.68
Mol of H_2O converted to hydrates	0.042	0.048

Hydrate: Near critical natural fluid with distilled water, salty water, and methanol
Reference: Tohidi et al. (2001a)
Phases: L_W–H–V–L_{HC} with inhibitors

Composition of Synthetic Formation Water

Salt	NaCl	$CaCl_2$	$MgCl_2$	KCl	$SrCl_2$	$BaCl_2$
Concentration, wt%	12.06	1.04	0.12	0.56	0.04	0.01

Composition of Original Near Critical Fluid, and Liquid Compositions and Vapor Phase Amounts from High and Medium Pressure Separators

Component	Original fluid mol%	Specific gravity at 288.7 K	Composition of separator liquid at 298.1 K and 17.189 MPa, mol%	Composition of separator liquid at 298.0 K and 4.089 MPa, mol%
N_2	0.36		0.38	0.37
CO_2	0.27		0.28	0.27

(Continued)

Continued

Component	Original fluid mol%	Specific gravity at 288.7 K	Composition of separator liquid at 298.1 K and 17.189 MPa, mol%	Composition of separator liquid at 298.0 K and 4.089 MPa, mol%
CH_4	68.73		50.04	16.79
C_2H_6	9.88		10.23	9.23
C_3H_8	4.22		5.43	7.70
i-C_4H_{10}	0.48		0.69	1.14
n-C_4H_{10}	1.49		2.26	3.96
i-C_5H_{12}	0.32		0.53	0.99
n-C_5H_{12}	0.86		1.48	2.82
C_6's	1.00	0.670	1.88	3.66
C_7's	2.02	0.724	4.11	8.10
C_8's	2.33	0.758	4.93	9.74
C_9's	1.78	0.774	3.83	7.58
C_{10}'s	1.25	0.783	2.78	5.51
C_{11}'s	0.89	0.784	1.98	3.93
C_{12}'s	0.64	0.798	1.42	2.83
C_{13}'s	0.52	0.814	1.16	2.30
C_{14}'s	0.65	0.823	1.45	2.87
C_{15}'s	0.48	0.835	1.07	2.12
C_{16}'s	0.36	0.843	0.80	1.59
C_{17}'s	0.24	0.840	0.53	1.06
C_{18}'s	0.25	0.841	0.56	1.10
C_{19}'s	0.20	0.850	0.44	0.88
C_{20}^+	0.78	0.868	1.74	3.46
Vapor mol fraction	NA		0.55	0.50

Hydrate Dissociation Conditions for Near Critical Fluid with Distilled Water, Salt Formation Water, and Methanol

Distilled water		Formation water		10.41 wt% methanol	
T **(K)**	***P*** **(MPa)**	***T*** **(K)**	***P*** **(MPa)**	***T*** **(K)**	***P*** **(MPa)**
277.2	1.069	276.2	2.103	276.3	5.330
280.4	1.627	281.3	4.137	280.7	11.349
284.5	2.772	285.2	7.805	283.6	24.256
288.4	4.702	287.8	13.914		

Continued

Dissociation Conditions of Liquids from the High Pressure and Medium Pressure Separators, in the Presence of Distilled Water, Flashed to below Conditions

298.1 K, 17.18 MPa high pressure liquid feed separator		298.0 K, 4.089 MPa medium pressure liquid feed separator	
T **(K)**	***P*** **(MPa)**	***T*** **(K)**	***P*** **(MPa)**
278.4	1.193	279.7	1.400
283.8	2.510	283.3	2.275
289.3	6.095	287.2	3.944
		287.7*	11.721

* For this run only no vapor phase was present and the dissociation was observed visually.

6.3.2 Thermal Property Data

In this section the hydrate data for heat capacity and enthalpy of dissociation are presented. The other thermal properties such as thermal conductivity and thermal expansion are presented in Chapter 2 with their analogs for ice.

6.3.2.1 Heat capacity and heat of dissociation

Since there is a paucity of data, the data for the heat capacity and enthalpy of dissociation are presented by investigation without discrimination, other than the accuracy statements presented in Section 6.1.2. The reader is also referred to Section 4.6.1 for a discussion of heat of dissociation values.

Compounds: Methane, ethane, and propane
Reference: Handa (1986a)
Properties: Molar heat capacity and enthalpy of dissociation

Constant Pressure Heat Capacity J/(K · mol)

T **(K)**	CH_4 6.0 H_2O	$C_2H_6 \cdot 7.67\ H_2O$	$C_3H_8 \cdot 17.0\ H_2O$
85	107.7	149.6	281.7
90	112.1	156.0	294.0
100	121.4	167.2	318.8
110	131.5	177.2	342.0

(Continued)

Continued

T (K)	CH_4 6.0 H_2O	$C_2H_6 \cdot 7.67\ H_2O$	$C_3H_8 \cdot 17.0\ H_2O$
120	140.3	188.6	366.5
130	149.0	199.4	392.4
140	156.8	210.0	415.9
150	164.2	219.6	437.6
160	171.1	229.0	459.3
170	178.6	237.9	481.0
180	186.3	248.2	502.4
190	194.1	259.1	524.8
200	201.4	269.2	548.3
210	209.8	277.4	573.5
220	219.3	292.8	599.5
230	225.9	301.7	617.7
240	233.7	310.9	644.0
250	240.4	323.0	674.4
260	248.4	337.8	710.2
270	257.6		

		ΔH (kJ/mol gas)	
Compound	***T* (K) range**	**H ↔ I + G**	**H ↔ L + G**
CH_4	160–210	18.13 ± 0.27	54.19 ± 0.28
C_2H_6	190–250	25.70 ± 0.37	71.80 ± 0.38
C_3H_8	210–260	27.00 ± 0.33	129.2 ± 0.4

Compounds: Isobutane and two naturally occurring hydrates
Reference: Handa (1986b, 1988)
Properties: Enthalpy of dissociation

Composition of Naturally Occurring Hydrates (mol%)

Composition	Gulf of Mexico	Mid-America trench
CH_4	66.0	99.93
C_2H_6	2.9	0.01
C_3H_8	14.7	0.01
i-C_4H_{10}	3.7	0.05
n-C_4H_{10}	0.08	
neo-C_5H_{12}	0.13	

Continued

Composition	Gulf of Mexico	Mid-America trench
i-C_5H_{12}	0.01	
cy-C_5H_{12}	0.01	
CO_2	7.8	
H_2S	0.49	
N_2	4.0	
wt% Sdmnt	7.4	0.764

Standard Molar Enthalpy of Dissociation ΔH′

Hydrate sample	H ↔ I + G	H ↔ L + G
Isobutane	18.13 ± 0.27 (KJ/mol)	54.19 ± 0.28 (KJ/mol)
Gulf of Mexico	27.8 (J/g)	33.1 (J/g)
Assumption	all water = hydrate	20% water = ice
Mid-America trench	17.5 (kJ/mol)	(19.2 mass% water as ice)

Compound: Methane
Reference: Lievois (1987)
Property: Enthalpy of dissociation

T (K)	ΔH (J/gmol CH_4)
278.2	57,739
278.2	57,358
278.2	57,697
283.2	52,798
283.2	53,610

Compound: Methane
Reference: Rueff et al. (1988)
Property: Constant volume heat capacity and enthalpy of dissociation

T (K)	Cv (J/g-K)	*T* (K)	ΔH (J/g)
245	1.62	285	429.66
255	1.56		
255	1.61		
256	1.70		
257	1.66		
259	1.61		

Compound: Methane, carbon dioxide, nitrogen, carbon dioxide + nitrogen, carbon dioxide + nitrogen + tetrahydrofuran
Reference: Kang et al. (2001)
Property: Enthalpy of dissociation

Guest(s)	ΔH/kJmol^{-1}	Hydrate composition
CH_4	56.84 ± 0.89	$n = 6.38$
CO_2	65.22 ± 1.03	$n = 7.23$
N_2	65.81 ± 1.04	$n = 5.94$
$0.17CO_2 + 0.83N_2$	64.59 ± 1.02	$x = 5.43, y = 1.89$
$0.70CO_2 + 0.30N_2$	63.41 ± 1.00	$x = 7.08, y = 0.25$
$0.17CO_2 + 0.83N_2$ with $0.01C_4H_8O + 0.99H_2O$	109.01 ± 1.72	$x = 2.96, y = 9.47, z = 11.39$
$0.17CO_2 + 0.83N_2$ with $0.03C_4H_8O + 0.97H_2O$	118.94 ± 1.87	$x = 2.35, y = 7.42, z = 12.53$
$0.70CO_2 + 0.30N_2$ with $0.01C_4H_8O + 0.99H_2O$	107.18 ± 1.69	$x = 9.97, y = 2.58, z = 10.94$
$0.70CO_2 + 0.30N_2$ with $0.03C_4H_8O + 0.97H_2O$	113.66 ± 1.79	$x = 8.11, y = 2.19, z = 13.16$

Enthalpies of dissociation for pure and mixed gases were measured three times and average values reported above. $G \cdot nH_2O$: n is the number of water molecules in the unit cell and G is the pure guest. $xCO_2 \cdot yN_2 \cdot 46H_2O$: x and y are the calculated numbers of CO_2 and N_2 molecules, respectively, in sI. $xCO_2 \cdot yN_2 \cdot zC_4H_8O \cdot 136H_2O$: x, y, and z are the calculated numbers of CO_2, N_2, and THF molecules, respectively, in sII [THF = C_4H_8O].

Compound: Methane
Reference: Gupta (2007)
Property: Constant volume heat capacity and enthalpy of dissociation

T_{onset}/K	P/MPa	$\Delta H_d \pm 11.72$ (J/gm-hydrate)	$\Delta H_d \pm 13.3$ (J/gm-water)	$\Delta H_d \pm 1.45$ (kJ/mol-gas)
280.60	5.5	442.21	508.29	54.90
285.65	9.8	420.60	483.45	52.21
288.15	12.8	433.96	498.80	53.87
288.45	13.2	428.58	492.62	53.20
289.85	15.0	455.01	523.00	56.48
292.16	18.5	441.39	507.35	54.79
291.65	19.3	448.02	514.97	55.62

Continued

T/K	*P*/MPa	Cp (J/gm hydrate/K)	*T*/K	*P*/MPa	Cp (J/gm hydrate/K)
247.91	20.00	1.797	266.57	20.00	1.947
250.58	20.00	1.827	278.61	20.00	2.082
253.24	20.00	1.850	280.11	20.00	2.132
255.91	20.00	1.870	281.61	20.00	2.172
258.57	20.00	1.883	283.11	20.00	2.217
261.24	20.00	1.898	284.61	20.00	2.281
263.90	20.00	1.904			

6.4 Summary and Relationship to Chapters that Follow

The object of this chapter is to provide an overview of the experimental methods, the phase equilibria data, and the thermal property data available on hydrates since Hammerschmidt (1934) on hydrates in natural gas systems. The tabulations and figures illustrate that more data are needed, particularly for phase equilibria mixtures of noncombustible components, structure H components, and for thermal property data.

Chapters 7 and 8 consider two applications of the data in this chapter and the correlation methods of Chapters 4 and 5. Chapter 7 considers the impact of hydrate on energy, climate, and geohazards in the earth, as examples of phase equilibria and thermal property data application. In Chapter 8, applications caused by hydrates in gas processing and production are described.

References

Abragam, A., *The Principles of Nuclear Magnetic Resonance*, Oxford University Press, New York (1961).

Adisasmito, S., Frank, R.J., Sloan, E.D., *J. Chem. Eng. Data*, **36**, 68 (1991).

Adisasmito, S., Sloan, E.D., *J. Chem. Eng. Data*, **37**, 343 (1992).

Afanaseva, L.D., Groisman, A.G., *Siberian Branch of the USSR Academy of Science*, **100**, 103 (1973).

Ahmad, N., Phillips, W.A., *Solid State Commun.*, **63**, 167 (1987).

Andersson, P., Ross, R.G., *J. Phys. Chem: Solid State Phys.*, **16**, 1423 (1983).

Andryushchenko, F.K., Vasilchenko, V.P., *Gasov. Prom.*, 10 (1969).

Aoyagi, K., Kobayashi, R., in *Proc. 57th Annual Convention*, *Gas Processors Association*, New Orleans, LA, March 20–22, 3 (1978).

Aoyagi, K., Song, K.Y., Kobyahshi, R., Sloan, E.D., Dharmawardhana, P.B., *Gas Proc. Assn. Res. Report*, No. 45, Tulsa, OK (December 1980).

Asher, G.B., *Development of a Computerized Thermal Conductivity Measurement System Utilizing the Transient Needle Probe Technique: An Application to Hydrates in Porous Media*, Dissertation, Colorado School of Mines, Golden, CO (1987).

Ashworth, T., Johnson, L.R., Lai, L.P., *High Temperatures-High Pressures*, **17**, 413 (1985).

Avlonitis, D., *Multiphase Equilibria in Oil-Water Hydrate Forming Systems*, M.Sc. Thesis, Heriot-Watt University, Edinburgh, Scotland (1988).

Bach-Verges, M., Kitchin, S.J., Harris, K.D.M., Zugic, M., Koh, C.A., *J. Phys. Chem. B*, **105**, 2699 (2001).

Bakkeng, S.E., Fredriksen, A.E., in *Proc. First International Conference on Natural Gas Hydrates*, *Ann. N.Y. Acad. Sci.* (Sloan, E.D., Happel, J., et al., eds.), **715**, 502 (1994).

Barrer, R.M., *Nature*, **183**, 463 (1959).

Barrer, R.M., Edge, A.V.J., *Proc. R. Soc. London*, **A300**, 1 (1967).

Barrer, R.M., Ruzicka, D.J., *Trans. Faraday Soc.*, **58**, 2253 (1962a).

Barrer, R.M., Ruzicka, D.J., *Trans. Faraday Soc.*, **58**, 2262 (1962b).

Becke, P., Kessel, D., Rahimian, I., Influence of Liquid Hydrocarbons on Gas Hydrate Equilibrium, SPE 25032, *Proc. European Petroleum Conference*, Cannes, November 16–18 (1992).

Behar, E., Delion, A.S., Sugier, A., Thomas, M., in *Proc. First International Conference on Natural Gas Hydrates*, *Ann. N.Y. Acad. Sci.* (Sloan, E.D., Happel, J., et al., eds.), **715**, 94 (1994).

Berecz, E., Balla-Achs, M., In *Research Report No. 37 (185-XL-1-1974, OGIL) NME* (Tech. Univ. Heavy Ind.), Miskolc (1974).

Berecz, E., Balla-Achs, M., *Gas Hydrates*, *Studies in Inorganic Chemistry* 411, Elsevier, New York, p. 343 (1977, English Translation (1983)).

Bertie, J.E., Bates, F.E., Hendricksen, D.K., *Can. J. Chem.*, **53**, 71 (1975).

Bertie, J.E., Devlin, J.P., *J. Chem. Phys.*, **78**, 6340 (1983).

Bertie, J.E., Jacobs, S.M., *J. Chem. Phys.*, **69**, 4105 (1978).

Bond, D.C., Russell, N.B., *Trans AIME*, **179**, 192 (1949).

Bowler, K., Stadterman, L.L., Creek, J.L., Koh, C.A., Sloan, E.D., Dec, S.F., in *Proc. Fifth International Conference on Gas Hydrates*, Trondheim, Norway, June 13–16, Paper 5030 (2005).

Bowron, D.T., Filipponi, A., Roberts, M.A., Finney, J.L., *Phys. Rev. Lett.*, **81**, 4164 (1998).

Breland, E., Englezos, P., *J. Chem. Eng. Data*, **41(1)**, 11 (1996).

Brown, M., *Handbook of Thermal Analysis and Calorimetry*, **1**, Elsevier, Amsterdam (1998).

Buchanan, P., Soper, A.K., Westacott, R.E., Creek, J.L., Koh, C.A., *J. Chem. Phys.*, **123**, 164507 (2005).

Burgass, R.W., Tohidi, B., Danesh, A., Todd, A.C., in *Proc. Fourth International Conference on Gas Hydrates*, Yokohama, Japan, May 19–23, 380 (2002).

Byk, S.S., Fomina, V.I., *Russ. Chem. Rev.*, **37**, 469 (1968).

Cadioli, B., Gallinella, E., Coulombeau, C., Jobic, H., Berthier, G., *J. Phys. Chem.*, **97**, 7844 (1993).

Cady, G.H., *J. Phys. Chem.*, **85**, 3225 (1981).

Cady, G.H., *J. Phys. Chem.*, **87**, 4437 (1983a).

Cady, G.H., *J. Chem. Ed.*, **60**, 915 (1983b).

Cady, G.H., *J. Phys. Chem.*, **89**, 3302 (1985).

Cailletet, L., *Compt. Rend.*, **85**, 851 (1877).

Callanan, J.E., Sloan, E.D., in *Proc. International Gas Research Conference*, London, June 13–16, 1012 (1983).

Camargo, R., Palermo, T., in *Proc. Fourth International Conference on Gas Hydrates*, Yokohama, Japan, May 19–23, 880 (2002).

Camargo, R., Palermo, T., Sinquin, A., Glenat, P., in *Proc. Gas Hydrates: Challenges for the Future*, *Ann. N.Y. Acad. Sci*. (Holder, G.D., Bishnoi, P.R., eds.), **912**, 906 (2000).

Carroll, J.J., Mather, A.E., *Can. J. Chem. Eng.*, **69**, 1206 (1991).

Carson, D.B., Katz, D.L., *Trans. AIME*, **146**, 150 (1942).
Chazallon, B., Kuhs, W.F., *J. Chem. Phys.*, **117**, 308 (2002).
Clarke, M., Bishnoi, P.R., in *Gas Hydrates: Challenges for the Future*, *Ann. N.Y. Acad. Sci.* (Holder, G.D., Bishnoi, P.R., eds.), **912**, 556 (2000).
Clarke, M., Bishnoi, P.R., *Can. J. Chem. Eng.*, **79**, 143 (2001a).
Clarke, M.A., Bishnoi, P.R., *Chem. Eng. Sci.*, **56**, 4715 (2001b).
Clarke, M.A., Bishnoi, P.R., *Chem. Eng. Sci.*, **59**, 2983 (2004).
Collins, M.J., Ratcliffe, C.I., Ripmeester, J.A., *J. Phys. Chem.*, **94**, 157 (1990).
Cook, J.G., Laubitz, M.J., in *Proc. 17th International Thermal Conductivity Conference*, Gaithersburg, MD, June 26, 13 (1981).
Cook, J.G., Leaist, D.G., *Geophys. Res. Lett.*, **10**, 397 (1983).
Danesh, A., Tohidi, B., Burgass, R.W., Todd, A.C., *Trans. IChemE.*, **72(A)**, 197 (1994).
Davidson, D.W., *Clathrate Hydrates*, Plenum, New York (1973).
Davidson, D.W., Garg, S.K., Gough, S.R., Hawkins, R.E., Ripmeester, J.A., *Can. J. Chem.*, **55**, 3641 (1977).
Davidson, D.W., Handa, Y.P., Ratcliffe, C.I., Tse, J.S., Powell, B.M., *Nature*, **311**, 142 (1984).
Davidson, D.W., Ripmeester, J.A., *Inclusion Compounds*, Chapter 3 (Atwood, J.L., Davies, J.E.D., et al., eds.) Academic Press, London, 3, p. 69 (1984).
de Forcrand, R., Villard, P., *Compt. Rendu.*, **106**, 849 (1888).
de Roo, J.L., Peters, C.J., Lichtenthaler, R.N., Diepen, G.A.M., *AIChE J.*, **29**, 651 (1983).
Deaton, W.M., Frost, E.M., *Oil Gas J.*, **36**, 75 (1937).
Deaton, W.M., Frost, E.M., Jr., *Gas Hydrates and Their Relation to the Operation of Natural-Gas Pipe Lines*, U.S. Bureau of Mines Monograph 8, p. 101 (1946).
Dharmawardhana, P.B., Parrish, W.R., Sloan, E.D., *Ind. Eng. Chem. Fundam.*, **19**, 410 (1980).
Dholabhai, P.D., Bishnoi, P.R., *J. Chem. Eng. Data*, **39**, 191 (1994).
Dholabhai, P.D., Englezoa, P., Kalogerakis, N., Bishnoi, P.R., *Can. J. Chem. Eng.*, **69**, 800 (1991).
Dyadin, Y., Aladko, E., in *Proc. Second International Conference on Natural Gas Hydrates* (Monfort, J.P., ed.), Toulouse, June 2–6, p. 67 (1996).
Dyadin, Y.A., Bondaryuk, I.V., Zhurko, F.V., in *Inclusion Compounds, Inorganics and Physical Aspects of Inclusion* (Atwood, J.L., Davies, J.E.D., et al., eds.), Oxford University Press, 5, Chapter 7, p. 213 (1991).
Dyadin, Y.A., Larionov, E.G., Aladko, E.Y., Manakov, A.Y., Zhurko, F.V., Mikina, T.V., Komarov, V.Y., Grachev, E.V., *J. Struct. Chem.*, **40**, 790 (1999).
Eichholz, C., Majumdar, A., Clarke, M.A., Oellrich, L.R., Bishnoi, P.R., *J. Chem. Eng. Data*, **49**, 847 (2004).
Englezos, P., Ngan, Y.T., *J. Chem. Eng. Data*, **38**, 250 (1993).
Ertl, H., Khoury, F., Sloan, D., Kobayashi, R., *Chemie Ingenieur Technik*, **48**, 811 (1976).
Fadnes, F.H., Jakobsen, T., Bylov, M., Holst, A., Downs, J.D., in *Proc. 1998 SPE European Petroleum Conference*, SPE 50688, The Hague, The Netherlands, October 20–22, p. 497 (1998).
Falabella, B.J., *A Study of Natural Gas Hydrates*, Ph.D. Thesis, University of Massachusetts, University Microfilms, No. 76-5849, Ann Arbor, MI (1975).
Falabella, B.J., Vanpee, M., *I & EC Fundamentals*, **13**, 228 (1974).
Fan, S.-S., *Powder Technol.*, **131**, 105 (2003).
Fan, S.-S., Chen, G.-J., Ma, Q.-L., Guo, T.-M., *Chem. Eng. J.*, **3595**, 1 (2000).
Fan, S.-S., Guo, T.-M., *J. Chem. Eng. Data*, **44**, 829 (1999).

Fidel-Dufour, A., Gruy, F., Herri, J.M., in *Proc. Fifth International Conference on Gas Hydrates*, Trondheim, Norway, June 13–16, Paper 1044 (2005).
Fleyfel, F., Devlin, J.P., *J. Phys. Chem.*, **92**, 631 (1988).
Fleyfel, F., Devlin, J.P., *J. Phys. Chem.*, **95**, 3811 (1991).
Florusse, L.J., Peters, C.J., Schoonman, J., Hester, K.C., Koh, C.A., Dec, S.F., Marsh, K.N., Sloan, E.D., *Science*, **306**, 469 (2004).
Freifeld, B.M., Kneafsey, T.J., Tomutsa, L., Stern, L., Kirby, S., in *Proc. Fourth International Conference on Gas Hydrates*, Yokohama, Japan, May 19–23, 750 (2002).
Galloway, T.J., Ruska, W., Chappelear, P.S., Kobayashi, R., *Ind. Enq. Chem. Fundam.*, **9**, 237 (1970).
Gao, S., Chapman, W., House, W., in *Proc. Fifth International Conference on Gas Hydrates*, Trondheim, Norway, June 13–16, Paper 1039 (2005).
Garg, S.K., Majid, Y.A., Ripmeester, J.A., Davidson, D.W., *Mol. Phys.*, **33**, 729 (1977).
Godbole, S.P., *Dissociation Pressures of Propane and I-Butane Hydrates Below the Ice Point*, M.S. Thesis, University of Pittsburgh, PA (1981).
Gupta, A., *Methane Hydrate Dissociation Measurements and Modeling: The Role of Heat Transfer and Reaction Kinetics*, Ph.D. Thesis, Colorado School of Mines, Golden, CO (2007).
Gupta, A., Dec, S.F., Koh, C.A., Sloan, E.D., *J. Phys. Chem. C*, **111**, 2341 (2007).
Gupta, A., Kneafsey, T.J., Moridis, G.J., Seol, Y., Kowalsky, M.B., Sloan, E.D., *J. Phys. Chem. B*, **110**, 16384 (2006b).
Gupta, A., Sloan, E.D., Kneafsey, T.J., Tomutsa, L., Moridis, G., in *Proc. Fifth International Conference on Gas Hydrates*, Trondheim, Norway, June 13–16, Paper 2004 (2005).
Gutt, C., Baumert, J., Press, W., Tse, J.S., Janssen, S., *J. Chem. Phys.*, **116**, 3795 (2002).
Hachikubo, A., Miyamoto, A., Hyakutake, K., Abe, K., Shoji, H., in *Proc. Fourth International Conference on Gas Hydrates* (Mori, Y.H., ed.), Yokohama, May 19–23, p. 357 (2002).
Halpern, Y., Thieu, V., Henning, R.W., Wang, X.P., Schultz, A.J., *J. Am. Chem. Soc.*, **123**, 12826 (2001).
Hammerschmidt, E.G., *Ind. Eng. Chem.*, **26**, 851 (1934).
Hammond, C., *The Basics of Crystallography and Diffraction (International Union of Crystallography Texts on Crystallography)*, 2nd Edition, Oxford University Press, Oxford, UK (2001).
Handa, Y.P., *Can. J. Chem.*, **62**, 1659 (1984).
Handa, Y.P., *Can. J. Chem.*, **63**, 68 (1985).
Handa, Y.P., *J. Chem. Thermodyn.*, **18**, 891 (1986a).
Handa, Y.P., *Calorimetric Studies of Laboratory Synthesized and Naturally Occurring Gas Hydrates*, paper presented at AIChE 1986 Annual Meeting Miami Beach, November 2–7, 28 (1986b).
Handa, Y.P., *J. Phys. Chem.*, **90**, 5497 (1986c).
Handa, Y.P., *J. Chem. Thermodyn.*, **18**, 915 (1986d).
Handa, Y.P., *Ind. Eng. Chem. Res.*, **27**, 872 (1988).
Hara, T., Hashimoto, S., Sugahara, T., Ohgaki, K., *Chem. Eng. Sci.*, **60**, 3117 (2005).
Henning, R.W., Schultz, A.J., Thieu, V., Halpern, Y., *J. Phys. Chem. A*, **104**, 5066 (2000).
Hester, K.C., *Probing Hydrate Stability and Structural Characterization of Both Natural and Synthetic Clathrate Hydrates*, Ph.D. Thesis, Colorado School of Mines, Golden, CO (2007).

Hester, K.C., Strobel, T.A., Huq, A., Schultz, A.J., Sloan, E.D., Koh, C.A., *J. Phys. Chem. B*, **110**, 14024 (2006a).

Hester, K.C., White, S.N., Peltzer, E.T., Brewer, P.G., Sloan, E.D., *Mar. Chem.*, **98**, 304 (2006b).

Higgins, J.S., Benoit, H.C., *Polymers and Neutron Scattering*, Clarendon Press, Oxford (1996).

Hohne, G.W.H., Hemminger, W.F., Flammersheim, H.-J., *Differential Scanning Calorimetry*, 2nd Edition, Springer, Berlin (2003).

Holder, G.D., *Multi-Phase Equilibria in Methane-Ethane-Propane-Water Hydrate Forming Systems*, Ph.D. Thesis, University of Michigan, University Microfilms No. 77-7939, Ann Arbor, MI 48106 (1976)

Holder, G.D., Godbole, S.P., *AIChE J.*, **28**, 930 (1982)

Holder, G.D., Grigoriou, G.C., *J. Chem. Thermodyn*., **12**, 1093 (1980).

Holder, G.D., Hand, J.H., *AIChE J.*, **28**, 44 (1982).

Holder, G.D., Manganiello, D.J., *Chem. Eng. Sci.*, **37**, 9 (1982).

Hosler, C.L., *J. Meteorol.*, **14**, 415 (1957).

Hosler, C.L., Hallgren, R.E., *Discussions Faraday Soc.*, **30**, 200 (1961).

Huang, D., Fan, S., *J. Chem. Eng. Data*, **49**, 1479 (2004).

Hutter, J.L., King, H.E., Jr., Lin, M.Y., *Macromolecules*, **33**, 2670 (2000).

Hütz, U., Englezos, P., "Measurement of Structure H Hydrate Phase Equilbrium and Effect of Electrolytes," in *Proc. 7th International Conference on Fluid Properties and Phase Equilibria for Chemical Process Design* (1995).

Hwang, M.J., Wright, D.A., Kapur, A., Holder, G.D., *An Experimental Study of Crystallizaton and Crystal Growth of Methane Hydrates from Melting of Ice*, 103 (1990).

Jager, M.D., de Deugd, R.M., Peters, C.J., de Swaan Arons, J., Sloan, E.D., *Fluid Phase Equilib.*, **165**, 209 (1999).

Jager, M.D., Sloan, E.D., in *Proc. Fourth International Conference on Gas Hydrates* (Mori, Y.H., ed.), Yokohama, May 19–23, p. 575 (2002).

Jeffrey, G.A., *Inclusion Compounds* (Atwood, J.L., Davies, J.E.D., et al., eds), Academic Press, London, 1, p. 135 (1984).

Jeffrey, G.A., McMullan, R.K., *Prog. Inorg. Chem.*, **8**, 43 (1967).

Jhaveri, J., Robinson, D.B., *Can. J. Chem Eng*., **43**, 75 (1965).

John, V.T., *Improved Predictions of Gas Hydrate Phase Equilibria*, Ph.D. Thesis, University of Pittsburgh, Pittsburgh, PA (1982).

John, V.T., Holder, G.D., *J. Phys. Chem.*, **85**, 1811 (1981).

John, V.T., Holder, G.D., *J. Chem. Eng. Data*, **27**, 18 (1982b).

Kamath, V.A., *Study of Heat Transfer Characteristics during Dissociation of Gas Hydrates in Porous Media*, Ph.D. Dissertation, University of Pittsburgh, PA (1984).

Kamath, V.A., Holder, G.D., *Chem. Eng. Sci.*, **16**, 399 (1984).

Kang, S.-P., Lee, H., Ryu, B.-J., *J. Chem. Thermodyn*., **33**, 513 (2001).

Katz, D.L., Cornell, D., Kobayashi, R., Poettmann, F.H., Vary, J.A., Elenbaas, J.R., Weinaug, C.F., *Handbook of Natural Gas Engineering*, McGraw-Hill, New York, p. 802 (1959).

King, H.E., Jr., Hutter, J.L., Lin, M.Y., Sun, T., *J. Chem. Phys.*, **112**, 2523 (2000).

Kini, R., Dec, S.F., Sloan, E.D., *J. Phys. Chem. A*, **108**, 9550 (2004).

Kini, R.A., *NMR Studies of Methane, Ethane, and Propane Hydrates: Structure, Kinetics, and Thermodynamics*, Ph.D. Thesis, Colorado School of Mines, Golden, CO (2002).

Kirchner, M.T., Boese, R., Billups, W.E., Norman, L.R., *J. Am. Chem. Soc.*, **126**, 9407 (2004).

Kneafsey, T.J., Tomutsa, L., Moridis, G.J., Seol, Y., Freifeld, B., Taylor, C.E., Gupta, A., in *Proc. Fifth International Conf. on Gas Hydrates*, Trondheim, Norway, June 13–16, Paper 1033 (2005).

Kobayashi, R., Katz, D.L., *Trans AIME*, **186**, 66 (1949).

Kobayashi, R., Withrow, H.J., Williams, G.B., Katz, D.L., *Proc. NGAA*, 1951, 27 (1951).

Koh, C.A., Savidge, J.L., Tang, C.C., *J. Phys. Chem.*, **100**, 6412 (1996).

Koh, C.A., Wisbey, R.P., Wu, X.P., Westacott, R.E., Soper, A.K., *J. Chem. Phys.*, **113**, 6390 (2000).

Kubota, H., Shimizu, K., Tanaka, Y., Makita, T., *J. Chem. Eng. Japan*, **17**, 423 (1984).

Kuhs, W.F., Klapproth, A., F., G., Techmer, K., Heinrichs, T., *Geophys. Res. Lett.*, **27**, 2929 (2000).

Lapin, A., Cinnamon, S.J., "Problem of Hydrate Formation in Natural Gas Systems," in *Proc. Liquid Natural Gas: Its Production, Handling, and Use*, London, p. 198, 3/25–28 (1969).

Larson, S.D., *Phase Studies of the Two-Component Carbon Dioxide-Water System, Involving the Carbon Dioxide Hydrate*, University of Illinois, Urbana, IL (1955).

Le Parlouer, P., Dalmazzone, C., Herzhaft, B., Rousseau, L., Mathonat, C., *J. Therm. Anal. Calorimetry*, **78**, 165 (2004).

Leaist, D.G., Murray, J.J., Post, M.L., Davidson, D.W., *J. Phys. Chem.*, **86**, 4175 (1982).

Lederhos, J.P., Mehta, A.P., Nyberg, G.B., Warn, K.J., Sloan, E.D., *AIChE J.*, **38**, 1045 (1992).

Lewis, I.R., Edwards, H.G.M., *Handbook of Raman Spectroscopy—-From the Research Laboratory to the Process Line*, Marcel Dekker, Inc., New York (2001).

Lievois, J.S., *Development of an Automated, High Pressure Heat Flux Calorimeter and Its Application to Measure the Heat of Dissociation of Methane Hydrate*, Ph.D. Thesis, Rice University, TX (1987).

Lippert, E.L., Palmer, H.A., Blankenship, F.F., in *Proc. Oklahoma Academy of Science*, **31**, 115 (1950).

Lippmann, D., Kessel, D., Rahimian, I., in *Proc. First International Conference on Natural Gas Hydrates*, *Ann. N.Y. Acad. Sci.* (Sloan, E.D., Happel, J., Hnatow, M., eds.), **715**, 525 (1994).

Lokshin, K.A., Zhao, Y.S., He, D.W., Mao, W.L., Mao, H.K., Hemley, R.J., Lobanov, M.V., Greenblatt, M., *Phys. Rev. Lett.*, **93**, 125503 (2004).

Long, J.P., *Gas Hydrate Formation Mechanism and Kinetic Inhibition*, Ph.D. Thesis, Colorado School of Mines, Golden, CO (1994).

Long, P., "Phase II Core Handling and Core Analysis—IR Imaging of Cores," *ChevronTexaco JIP Workshop*, Winchester, CO, September 30–October 1 (2003).

Loveday, J.S., Nelmes, R.J., Klug, D.D., Tse, J.S., Desgreniers, S., *Can. J. Phys.*, **81**, 539 (2003).

Lu, C., Czanderna, A.W., *Applications of Piezoelectric Quartz Crystal Microbalances*, Elsevier, Amsterdam (1984).

Lund, A., Urdahl, O., Kirkhorn, S.S., *Chem. Eng. Sci.*, **51**, 3449 (1996).

Makino, T., Nakamura, T., Sugahara, T., Ohgaki, K., *Fluid Phase Equilib.*, **218**, 235 (2004).

Makogon, T.Y., Mehta, A.P., Sloan, E.D., *J. Chem. Eng. Data*, **41**, 315 (1996).

Makogon, T.Y., Sloan, E.D., *J. Chem. Eng. Data*, **39**, 351 (1994).

Makogan, Y.F., *Hydrates of Natural Gas, Moscow, Nedra, Izadatelstro*, PennWell Books, Tulsa, Oklahoma, p. 237 in Russian (1981 in English) (1974).

Mao, H.K., Mao, W.L., *Proc. Natl. Acad. Sci. U.S.A.*, **101**, 708 (2004).
Mao, W.L., Mao, H.K., Goncharov, A.F., Struzhkin, V.V., Guo, Q.Z., Hu, J.Z., Shu, J.F., Hemley, R.J., Somayazulu, M., Zhao, Y.S., *Science*, **297**, 2247 (2002).
Marshall, D.R., Saito, S., Kobayashi, R., *AIChE J.*, **10**, 202 (1964a).
Marshall, D.R., Saito, S., Kobayaski, R., *AIChE J.*, **10**, 723 (1964b).
Masoudi, R., Tohidi, B., Danesh, A., Todd, A.C., *Fluid Phase Equilib.*, **215**, 163 (2004).
Masoudi, R., Tohidi, B., Danesh, A., Todd, A.C., Anderson, R., Burgass, R.W., Yang, J., *Chem. Eng. Sci.*, **60**, 4213 (2005).
Matthews, P., Notz, P., Widener, M., in *Proc. Gas Hydrates: Challenges for the Future*, *Ann. N.Y. Acad. Sci.* (Holder, G.D., Bishnoi, P.R., eds.), **912**, 330 (2000).
McLeod, H.O., Campbell, J.M., *J. Petl Tech*., **222**, 590 (1961).
McMullan, R.K., Jeffrey, G.A., *J. Chem. Phys.*, **42**, 2725 (1965).
Mehta, A.P., Sloan, E.D., *J. Chem. Eng. Data*, **38**, 580 (1993).
Mehta, A.P., Sloan, E.D., *J. Chem. Eng. Data*, **39**, 887 (1994a).
Mehta, A.P., Sloan, E.D., *AIChE J.*, **40**, 312 (1994b).
Mehta, A.P., *A Thermodynamic Investigation of Structure H Clathrate Hydrates*, Ph.D. Thesis, Colorado School of Mines, Golden, CO (1996).
Mei, D.-H., Liao, J., Yang, J.-T., Guo, T.-M., *Ind. Eng. Chem. Res.*, **35**, 4342 (1996a).
Mei, D.-H., Liao, J., Yang, J.-Y., Guo, T.-M., *J. Chem. Eng. Data*, **43**, 178 (1998).
Miller, B., Strong, E.R., *Am. Gas Assoc. Monthly*, **28**, 63 (1946).
Miller, S.L., Smythe, W.D., *Science*, **170**, 531 (1970).
Mirinski, D.S., Manakov, A.Y., Larionova, E.G., Kurnosov, A.V., Ancharov, A.I., Dyadin, Y.A., Tolochko, B.P., Sheromov, M.A., *Nucl. Inst. Meth. Phys. Res. Sec. a- Accel. Spectr. Det. Assoc. Equip.*, **470**, 114 (2001).
Mohammadi, A.H., Anderson, R., Tohidi, B., *AIChE J.*, **51**, 1 (2005).
Mohammadi, A.H., Tohidi, B., Burgass, R.W., *J. Chem. Eng. Data*, **48**, 612 (2003).
Montano, P.A., Linton, J., Thieu, V., Halpern, Y., *J. Synchrotron Rad.*, **8**, 972 (2001).
Mooijer-van den Heuvel, M.M., *Phase Behaviour and Structural Aspects of Ternary Clathrate Hydrate Systems*, Dissertation, Technische Universiteit Delft, p. 260 (2004).
Mooijer-van den Heuvel, M.M., Peters, C.J., de Swaan Arons, J., *Fluid Phase Equilib.*, **172**, 73 (2000).
Mooijer-van den Heuvel, M.M., Peters, C.J., de Swaan Arons, J., *Fluid Phase Equilib.*, **193**, 245 (2002).
Mooijer-van den Heuvel, M.M., Witteman, R., Peters, C.J., *Fluid Phase Equilib.*, **182**, 97 (2001).
Moridis, G.J., Seol, Y., Kneafsey, T.J., in *Proc. Fifth International Conference on Gas Hydrates*, Trondheim, Norway, June 13–16, Paper 1004 (2005).
Morita, K., Nakano, S., Ohgaki, K., *Fluid Phase Equilib.*, **169**, 167 (2000).
Moudrakovski, I.L., McLaurin, G.E., Ratcliffe, C.I., Ripmeester, J.A., *J. Phys. Chem. B*, **108**, 17591 (2004).
Moudrakovski, I.L., Sanchez, A.A., Ratcliffe, C.I., Ripmeester, J.A., *J. Phys. Chem. B*, **105**, 12338 (2001).
Muijs, H.M., Anselme, M.J., Beers, N.C.M., Van Os, N.M., Kind, C.E., *European Patent Application*, 91.0619 (1991).
Nagata, I., Kobayashi, R., *I & EC Fundam.*, **5**, 344 (1966a).
Nagata, I., Kobayashi, R., *I & EC Fundam.*, **5**, 466 (1966b).
Nakahara, J., Shigesato, Y., Higashi, A., Hondo, T., Langway, C.C., *Philosophical Magazine B*, **57**, 421 (1988).

Nakamura, T., Makino, T., Sugahara, T., Ohgaki, K., *Chem. Eng. Sci*., **58**, 269 (2003).
Nakamura, T., Sugahara, T., Ohgaki, K., *J. Chem. Eng. Data*, **49**, 99 (2004).
Nakano, S., Moritoki, M., Ohgaki, K., *J. Chem. Eng. Data*, **43**, 807 (1998b).
Nakano, S., Moritoki, M., Ohgaki, K., *J. Chem. Eng. Data*, **44**, 254 (1999).
Nakano, S., Yamamoto, K., Ohgaki, K., *Proc. Instn. Mech. Engnrs*, **212**, 159 (1998a).
Ng, H.-J., Petrunia, J.P., Robinson, D.B., *Fluid Phase Equilib.*, **1**, 283 (1977).
Ng, H.-J., Petrunia, J.P., Robinson, D.B., *Fluid Phase Equilib.*, **1**, 77 (1978).
Ng, H.-J., Chen, C.-J., Robinson, D.B., in *Gas Processors Association Research Report 87*, March (1985a).
Ng, H.-J., Chen, C.-J., Robinson, D.B., in *Gas Processors Association Research Report 92*, September (1985b).
Ng, H.-J., Chen, C.-J., Saeterstad, T., *Fluid Phase Equilib.*, **36**, 99 (1987a).
Ng, H.-J., Chen, C.-J., Robinson, D.B., in *Gas Processors Association Research Report 106*, April (1987b).
Ng, H.-J., Robinson, D.B., *Ind. Eng. Chem. Fundam*., **15**, 293 (1976a).
Ng, H.-J., Robinson, D.B., *AIChE J.*, **22**, 656 (1976b).
Ng, H.-J., Robinson, D.B., *AIChE J.*, **23**, 477 (1977).
Ng, H.-J., Robinson, D.B., in *Gas Processors Association Research Report 66*, April (1983).
Ng, H.-J., Robinson, D.B., in *Gas Processors Association Research Report 74*, March (1984).
Ng, H.-J., Robinson, D.B., *Fluid Phase Equilib.*, **21**, 145 (1985).
Ng, H.-J., Robinson, D.B., in *Proc. First International Conference on Natural Gas Hydrates*, *Ann. N.Y. Acad. Sci.* (Sloan, E.D., Happel, J., et al., eds.), **715**, 450 (1994).
Noaker, L.J., Katz, D.L., *Trans. AIME*, **201**, 237 (1954).
Ohgaki, K., Makihara, Y., Takano, K., *J. Chem. Eng. Jpn.*, **26**, 558 (1993).
Ohgaki, K.,Takano, K., Sangawa, H., Matsubara, T., Nakano, S., *J. Chem. Eng. Jpn.*, **29**, 478 (1996).
Ohmura, R., Matsuda, S., Uchida, T., Ebinuma, T., Narita, H., *J. Chem. Eng. Data*, **50**, 993 (2005).
Oskarsson, H., Uneback, I., Navarrette, R.C., Hellsten, M., Lund, A., Hjarbo, W., in *Proc. Fifth International Conference on Gas Hydrates*, Trondheim, Norway, June 13–16, Paper 4024 (2005).
Otto, F.D., Robinson, D.B., *AIChE J.*, **6**, 602 (1960).
Palermo, T., Argo, C., Goodwin, S., Henderson, A., in *Proc. Gas Hydrates: Challenges for the Future*, *Ann. N.Y. Acad. Sci*. (Holder, G.D., Bishnoi, P.R., eds.), **912**, 355 (2000).
Palermo, T., Arla, D., Borregales, M., Dalmazzone, C., Rousseau, L., in *Proc. Fifth International Conference on Gas Hydrates*, Trondheim, Norway, June 13–16, Paper 1050 (2005).
Palermo, T., Goodwin, S., in *Proc. Gas Hydrates: Challenges for the Future*, *Ann. N.Y. Acad. Sci*. (Holder, G.D., Bishnoi, P.R., eds.), **912**, 339 (2000).
Paranjpe, S.G., Patil, S.L., Kamath, V.A., Godbole, S.P., in *Proc. 62nd SPE Annual Conference 379, SPE 16871*, Dallas, TX, September 27–30 (1987).
Paranjpe, S.G., Patil, S.L., Kamath, V.A., Godbole, S.P., "*Hydrate Formation in Crude Oils and Phase Behavior of Hydrates in Mixtures of Methane, Propane, Isobutane, and n-Butane*," paper presented at the Third Chemical Congress of North America, Toronto, June 5–10 (1988).
Parsonage, N.G., Staveley, L.A.K., in *Inclusion Compounds* (Atwood, J.L., Davies, J.E.D., et al., eds.), Academic Press, London, 3, 1 (1984).

Patil, S.L., *Measurements of Multiphase Gas Hydrates Phase Equilibria: Effect of Inhibitors and Heavier Hydrocarbon Components*, M.S. Thesis, University of Alaska, Anchorage, AL (1987).
Peters, C.J., de Roo, J.L., de Swaan Arons, J., *Fluid Phase Equilib.*, **85**, 30 (1993).
Pietrass, T., Gaede, H.C., Bifone, A., Pines, A., Ripmeester, J.A., *J. Am. Chem. Soc.*, **117**, 7520 (1995).
Rasch, A., Mikalsen, A., Austvik, T., Gjertsen, L.H., Li, X., in *Proc. Fourth International Conference on Gas Hydrates*, Yokohama, May 19–23, 927 (2002).
Rawn, C.J., Rondinone, A.J., Chakoumakos, B.C., Circone, S., Stern, L.A., Kirby, S.H., Ishii, Y., *Can. J. Phys.*, **81**, 431 (2003).
Reamer, H.H., Selleck, F.T., Sage, B.H., *Pet. Trans. AIME*, **195**, 197 (1952a).
Reamer, H.H. Selleck, F.T., Sage, B.H., *J. Petrol Tech.*, **4**, 197 (1952b).
Reed, R.L., Kelley, L.R., Neumann, D.L., Oelfke, R.H., Young, W.D., in *Proc. First International Conference on Natural Gas Hydrates*, *Ann. N.Y. Acad. Sci*. (Sloan, E.D., Happel, J., et al., eds.), **715**, 430 (1994).
Richardson, H.H., Wooldridge, P.J., Devlin, J.P., *J. Phys. Chem.*, **89**, 3552 (1985a).
Richardson, H.H., Wooldrige, P.J., Devlin, J.P., *J. Chem. Phys.*, **83**, 4387 (1985b).
Ripmeester, J.A., Ratcliffe, C.I., *J. Phys. Chem.*, **92**, 337 (1988).
Ripmeester, J.A., Ratcliffe, C.I., *J. Phys. Chem.*, **94**, 8773 (1990).
Ripmeester, J.A., Ratcliffe, C.I., *Energy & Fuels*, **12**, 197 (1998).
Ripmeester, J., Ratcliffe, C., *J. Struct. Chem.*, **40**, 654 (1999).
Ripmeester, J.A., Ratcliffe, C.I., Klug, D.D., Tse, J.S., in *Proc. First International Conference on Natural Gas Hydrates*, *Ann. N.Y. Acad. Sci*. (Sloan, E.D., Happel, J., et al., eds.), **715**, 161 (1994).
Ripmeester, J.A., Ratcliffe, C.I., Tse, J.S., *J. Chem. Soc. Faraday Trans. I*, **84**, 3731 (1988).
Roberts, O.L., Brownscombe, E.R., Howe, L.S., *Oil Gas J.*, **39**, 37 (1940).
Robinson, D.B., Hutton, J.M., *J. Can. Pet. Tech*., **6**, 6 (1967).
Robinson, D.B., Mehta, B.R., *J. Can. Pet. Tech*., **10**, 33 (1971).
Robinson, D.B., Ng, H.-J., *Hydrocarbon Process.*, 95 (December 1976).
Robinson, D.B., Ng, H.-J., *J. Can. Pet. Tech.*, **25**, (1986).
Roozeboom, H.W.B., *Rec. Trav. Chem. Pays-Bas*, **3**, 26 (1884).
Ross, M.J., Toczylkin, L.S., *J. Chem. Eng. Data*, **37**, 488 (1992).
Ross, R.G., Andersson, P., *Can. J. Chem.*, **60**, 881 (1982).
Ross, R.G., Andersson, P., Backstrom, G., *Nature*, **290**, 322 (1981).
Rouher, O.S., *The* n-*Butane and Iso-Butane Hydrates*, M.S. Thesis, Syracuse University, June (1968).
Rouher, O.S., Barduhn, A.J., *Desalination*, **6**, 57 (1969).
Rovetto, L.R., Strobel, T.A., Koh, C.A., Sloan, E.D., *Fluid Phase Equilib.*, **247**, 84 (2006).
Rueff, R.M., *The Heat Capacity and Heat of Dissociation of Methane Hydrates: A New Approach*, Dissertation, Colorado School of Mines, Golden, CO (1985).
Rueff, R.M., Sloan, E.D., *Ind. Eng. Chem. Process Des. Dev.*, **24**, 882 (1985).
Rueff, R.M., Sloan, E.D., Yesavage, V.F., *AIChE J.*, **34**, 1468 (1988).
Saito, S., Marshall, D.R., Kobayashi, R., *AIChE J.*, **10**, 734 (1964).
Scauzillo, F.R., *Chem. Eng. Prog*, **52**, 324 (1956).
Schicks, J.M., Naumann, R., Erzinger, J., Hester, K.C., Koh, C.A., Sloan, E.D., *J. Phys. Chem. B*, **110**, 11468 (2006).
Schmidt-Rohr, K., Spiess, H.W., *Multidimensional Solid-State NMR and Polymers*, Academic Press, New York (1994).

Schneider, G.R., Farrar, J., *U.S. Dept. of Interior*, *Res. Dev. Report No 292*, p. 37 (January 1968).
Schroeder, W., *Die Geschichte Der Gas Hydrate, Sammlung*, F. Enke, Stuttgart, 98 (1927).
Selleck, F.T., Carmichael, L.T., Sage, B.H., *Ind. Eng. Chem*., **44**, 2219 (1952).
Seo, Y.-T., Lee, H., Yoon, J.-H., *J. Chem. Eng. Data*, **46**, 381 (2001a).
Seo, Y.-T., Lee, H., *J. Phys. Chem. B*., **105**, 10084 (2001b).
Seo, Y., Lee, H., *Geophys. Res. Lett.*, **29**, 85 (2002).
Servio, P., Englezos, P., *J. Chem. Eng. Data*, **47**, 87 (2002).
Sloan, E.D., Khoury, F.M., Kobayashi, R., *Ind. Eng. Chem. Fundam.*, **15**, 318 (1976).
Song, K.Y., Kobayashi, R., *Ind. Eng. Chem. Fundam*, **21**, 391 (1982).
Song, K.Y., Kobayashi, R., *SPE Formation Evaluation*, 500 (December 1987).
Song, K.Y., Kobayashi, R., *Fluid Phase Equilib.*, **47**, 295 (1989).
Song, K.Y., Kobayashi, R., *Fluid Phase Equilib.*, **95**, 281 (1994).
Staykova, D.K., Kuhs, *J. Phys. Chem. B*, **107**, 10299 (2003).
Staykova, D.K., Kuhs, W.F., Salamatin, A.N., Hansen, T., *J. Phys. Chem. B*, **107**, 10299 (2003).
Stern, L., Coircone, S., Kirby, S., Durham, W., in *Proc. Fifth International Conference on Gas Hydrates*, Trondheim, Norway, June 13–16, Paper 1046 (2005).
Stern, L.A., Kirby, S.H., Durham, W.B., *Science*, **273**, 1843 (1996).
Stoll, R.D., Bryan, G.M., *J. Geophys. Res.*, **84**, 1629 (1979).
Subramanian, S., *Measurements of Clathrate Hydrates Containing Methane and Ethane Using Raman Spectroscopy*, Ph.D. Thesis, Colorado School of Mines, Golden, CO (2000).
Subramanian, S., Ballard, A.K.R., Dec, S.F., Sloan, E.D., *Chem. Eng. Sci.*, **55**, 5763 (2000).
Subramanian, S., Sloan, E.D., in *Proc. Gas Hydrates: Challenges for the Future*, *Ann. N.Y. Acad. Sci.* (Holder, G.D., Bishnoi, P.R., eds.), **912**, 583 (2000).
Sugahara, K., Tanaka, Y., Sugahara, T., Ohgaki, K., *J. Supramol. Chem.* **2**, 365 (2002).
Sum, A., *Measurements of Clathrate Hydrate Properties Via Raman Spectroscopy*, M.S. Thesis, Colorado School of Mines, Golden, CO (1996).
Sum, A.K., Burruss, R.C., Sloan, E.D., *J. Phys. Chem. B*, **101**, 7371 (1997).
Sun, C.-Y., Chen, G.-J., Lin, W., Guo, T.-M., *J. Chem. Eng. Data*, **48**, 600 (2003).
Takenouchi, S., Kennedy, G.C., *J. Geol.*, **73**, 383 (1965).
Takeya, S.N.H., Matsuyama, T., Hondoh, T., Lipenkov, V., *J. Phys. Chem.*, **104**, 668 (2000).
Talley, L., Mitchell, G., Oelfke, R., in *Proc. Gas Hydrates: Challenges for the Future*, *Ann. N.Y. Acad. Sci.* (Holder, G.D., Bishnoi, P.R., eds.), **912**, 314 (2000).
Taylor, C.J., *Adhesion Force between Hydrate Particles and Macroscopic Investigation of Hydrate Film Growth at the Hydrocarbon/Water Interface*, MS Thesis, Colorado School of Mines, Golden, CO (2006).
Taylor, C.J., Dieker, L.D., Miller, K.T., Koh, C.A., Sloan, E.D., *J. Colloid Interface Sci.*, **305**, 255 (2007).
Thakore, J.L., Holder, G.D., *Ind. Eng Chem. Res*., **26**, 462 (1987).
Thieu, V., Subramanian, S., Colgate, S.O., Sloan, E.D., Jr., in *Proc. Gas Hydrates*: *Challenges for the Future*, *Ann. N.Y. Acad. Sci.* (Holder, G.D., Bishnoi, P.R., eds.), **912**, 983 (2000).
Thomas, M., Behar, E., *Proc. 73rd Gas Processors Association Convention*, New Orleans, LA, March 7–9 (1995).
Thompson, H., Soper, A.K., Buchanan, P., Aldiwan, N., Creek, J.L., Koh, C.A., *J. Chem. Phys.*, **124**, 164508 (2006).

Tohidi, B., Anderson, R., Clennell, M.B., Burgass, R.W., Biderkab, A.B., *Geology*, **29**, 867 (2001).

Tohidi, B., Anderson, R., Clennell, B., Yang, J., Bashir, A., Burgass, R.W., in *Proc. Fourth International Conference on Gas Hydrates*, Yokohama, Japan, May 19–23, p. 761 (2002).

Tohidi, B., Burgass, R., Danesh, A., Todd, A., SPE26701, *Proc. SPE Offshore European Conference*, Aberdeen, September 7–10, p. 255 (1993).

Tohidi, B., Burgass, R., Danesh, A., Todd, A., in *Proc. First International Conference on Natural Gas Hydrates*, *Ann. N.Y. Acad. Sci.* (Sloan, E.D., Happel, J., et al., eds.), **715**, 532 (1994a).

Tohidi, B., Burgass, R.W., Danesh, A., Østergaard, K.K., Todd, A.C., in *Proc. Gas Hydrates: Challenges for the Future*, *Ann. N.Y. Acad. Sci.* (Holder, G.D., Bishnoi, P.R., eds.), **912**, 924 (2000).

Tohidi, B., Danesh, A., Burgass, R., Todd, A., SPE28478, *Proc. SPE 69th Annual Technical Conference*, New Orleans, LA, September 25–28, p. 157 (1994b).

Tohidi, B., Danesh, A., Burgass, R., Todd, A., in *Proc. Second International Conference on Natural Gas Hydrates* (Monfort, J.P., ed.), Toulouse, 2–6 June, p. 109 (1996a).

Tohidi, B., Danesh, A., Østergaard, K., Todd, A., in *Proc. Second International Conference on Natural Gas Hydrates* (Monfort, J.P., ed.), Toulouse, 2–6 June, p. 229 (1996b).

Tohidi, B., Danesh, A., Todd, A., *Chem. Eng. Res. Des*., **73**, 464 (1995b).

Tohidi, B., Danesh, A., Todd, A., Burgass, R.W., Østergaard, K.K., *Fluid Phase Equilib.*, **138**, 241 (1997a).

Tohidi, B., Danesh, A., Todd, A.C., Burgass, R.W., *Chem. Eng. Sci.*, **52**, 3257 (1997b).

Tohidi, B., Østergaard, K., Danesh, A., Todd, A., Burgass, R.W., *Can. J. Chem. Eng.*, **79**, 384 (2001a).

Tse, J.S., *J. De Physique*, **48**, 543 (1987).

Tse, J.S., *J. Inclusion Phenom. Mol. Recognition Chem.*, **8**, 25 (1990).

Tse, J.S., McKinnon, W.R., Marchi, M., *J. Phys. Chem.*, **91**, 4188 (1987).

Tse, J.S., Powell, B.M., Sears, V.F., Handa, Y.P., *Chem. Phys. Lett.*, **215**, 383 (1993).

Tse, J.S., Ratcliffe, C.I., Powell, B.M., Sears, V.F., Handa, Y.P., *J. Phys. Chem. A*, **101**, 4491 (1997a).

Tse, J.S., Shpakov, V.P., Belosludov, V.R., Trouw, F., Handa, Y.P., Press, W., *Europhys. Lett.*, **54**, 354 (2001).

Tse, J.S., Shpakov, V.P., Murashov, V.V., Belosludov, V.R., *J. Chem. Phys.*, **107**, 9271 (1997b).

Tulk, C.A., Klug, D.D., Ripmeester, J.A., *J. Phys. Chem. A*, **102**, 8734 (1998).

Turner, D., *Clathrate Hydrate Formation in Water-in-Oil Dispersions*, Ph.D. Thesis, Colorado School of Mines, Golden, CO (2005).

Turner, D., Boxall, J., Yang, S., Kleehammer, Koh, C., MIller, K., Sloan, E.D., Xu, Z., Matthews, P., Talley, L., in *Proc. Fifth International Conference on Gas Hydrates*, Trondheim, Norway, June 13–16, Paper 4018 (2005b).

Turner, D.J., Kleehammer, D.M., Miller, K.T., Koh, C.A., Sloan, E.D., Talley, L.D., in *Proc. Fifth International Conference on Gas Hydrates*, Trondheim, Norway, June 13–16, Paper 4004 (2005a).

Uchida, T., Ebinuma, T., Narita, H., *J. Cryst. Growth*, **217**, 189 (2000).

Uchida, T., Hirano, T., Ebinuma, T., Narita, H., Gohara, K., Mae, S., *AIChE J.*, **45**, 2641 (1999).

Udachin, K., Ratcliffe, C.I., Enright, G.D., Ripmeester, J.A., *Supramol. Chemistry*, **8**, 173 (1997a).

Udachin, K.A., Enright, G.D., Ratcliffe, C.I., Ripmeester, J.A., *J. Am. Chem. Soc.*, **119**, 11481 (1997b).
Udachin, K.A., Ratcliffe, C.I., Ripmeester, J.A., *Angew. Chem. Int. Ed.*, **40**, 1303 (2001a).
Udachin, K.A., Ratcliffe, C.I., Ripmeester, J.A., *J. Phys. Chem. B*, **105**, 4200 (2001b).
Udachin, K.A., Ratcliffe, C.I., Ripmeester, J.A., in *Proc. Fourth International Conference on Gas Hydrates*, Yokohama, Japan, May 19–23, p. 19 (2002).
Udachin, K.A., Ripmeester, J.A., *Nature*, **397**, 420 (1999).
Unruh, C.H., Katz, D.L., *Trans. AIME*, **186**, 83 (1949).
Urdahl, O., Lund, A., Mork, P., Nilsen, T.-N., *Chem. Eng. Sci.*, **50**, 863 (1995).
van Cleeff, A., Diepen, G.A.M., *Rec. Trav. Chim.*, **79**, 582 (1960).
van der Waals, J.H., Platteeuw, J.C., *Adv. Chem. Phys.*, II, 1 (1959).
Varma-Nair, M., Costello, C.A., Colle, K.S., King, H.E., *J. Appl. Polymer Sci.*, **103**, 2642 (2006).
Verma, V.K., *Gas Hydrates from Liquid Hydrocarbon–Water Systems*, Ph.D. Thesis, University of Michigan, University Microfilms No. 75-10,324, Ann Arbor, MI (1974).
Verma, V.K., Hand, J.H., Katz, D.L., in *Gas Hydrates from Liquid Hydrocarbons Methane–Propane–Water System*, *AIChE-VTG Joint Meeting*, Munich, September, p. 106 (1975).
Villard, M., *Compt. Rend.*, **123**, 337 (1896).
Villard, P., *Compt. Rend.*, **107**, 395 (1888).
Villard, P., *Compt. Rend.*, **111**, 302 (1890).
Vlahakis, J.G., Chen, H.-S., Suwandi, M.S., Barduhn, A.J., *The Growth Rate of Ice Crystals: Properties of Carbon dioxide Hydrates*, *A Review of Properties of 51 Gas Hydrates*, Syracuse U. Research and Development Report 830, prepared for US Department of the Interior, November (1972).
von Herzen, R.P., Maxwell, A.E., *J. Geophys. Res.*, **64**, 1557 (1959).
von Stackelberg, M., *Naturwiss*, **36**, 359 (1949).
von Stackelberg, M., *Z. Elektrochem.*, **58**, 104 (1954).
von Stackelberg, M., Fruhbuss, H., *Z. Elektrochem.*, **58**, 99 (1954).
von Stackelberg, M., Jahns, W., *Z. Elektrochem.*, **58**, 162 (1954).
von Stackelberg, M., Meinhold, W., *Z. Elektrochem.* **58**, 40 (1954).
von Stackelberg, M., Muller, H.R., *Naturwiss*, **38**, 456 (1951a).
von Stackelberg, M., Muller, H.R., *J. Chem. Phys.*, **19**, 1319 (1951b).
von Stackelberg, M., Muller, H.R., *Z. Elektrochem.*, **58**, 25 (1954).
Waite, W.F., De Martin, B.J., Kirby, S.H., Pinkston, J., Ruppel, C.D., *Geophys. Res. Lett.*, **29**, 2229 (2002).
Waite, W.F., Gilbert, L.Y., Winters, W.J., Mason, D.H., in *Proc. Fifth International Conference on Gas Hydrates*, Trondheim, Norway, June 13–16, Paper 5042 (2005).
Wang, X.P., Schultz, A.J., Halpern, Y., *J. Phys. Chem. A*, **106**, 7304 (2002).
White, M.A., MacLean, M.T., *J. Phys. Chem.*, **89**, 1380 (1985).
Wilcox, W.I., Carson, D.B., Katz, D.L., *Ind. Eng. Chem.*, **33**, 662 (1941).
Wilson, L.D., Tulk, C.A., Ripmeester, J.A., in *Proc. Fourth International Conference on Gas Hydrates*, Yokohama, Japan, May 19–23, 614 (2002).
Wroblewski, S.V., *Compt. Rend.*, **94**, 1355 (1882).
Wu, B.-J., Robinson, D.B., Ng, H.-J., *J. Chem. Thermodyn.*, **8**, 461 (1976).
Yang, S.O., *Measurements and Prediction of Phase Equilibria for Water + Natural Gas Components in Hydrate-Forming Conditions*, Ph.D. Thesis, Korea University, December (2000).

Yang, S.O., Cho, S.H., Lee, H., Lee, C.S., *Fluid Phase Equilib*., **185**, 53 (2001).
Yang, S.O., Kleehammer, D.M., Huo, Z., Sloan, E.D., Miller, K.T., *J. Colloid Interface Sci.*, **277**, 335 (2004).
Zhang, Y., *Formation of Hydrate from Single-Phase Aqueous Solutions*, M.S. Thesis, University of Pittsburgh, PA (2003).

7 Hydrates in the Earth

Introduction and Overview

Only since 1965 has mankind recognized that the formation of *in situ* hydrates in the geosphere predated their artificial formation (ca. 1800) by millions of years. In addition to their age, it appears that hydrates in nature are ubiquitous, with some probability of occurrence wherever methane and water are in close proximity at low temperature and elevated pressures.

Because hydrates concentrate methane [at standard temperature and pressure (STP)] by as much as a factor of 164, and because less than 15% of the recovered energy is required for dissociation, hydrate reservoirs have been considered as a substantial future energy resource. While the total amount of hydrated gas is under some dispute, researchers in both the eastern (Makogon, 1988b) and western (Klauda and Sandler, 2005) hemispheres agree that the total amount of gas in this solid form may surpass the total conventional gas reserve, by an order of magnitude. Hydrates in the earth provide two additional applications, namely, (1) causes of current and ancient climate change and (2) geological hazards.

However, because there has been an overwhelming amount of information generated over the last decade on this topic, it may be well to provide an initial, conceptual overview or "reader's guide" to this chapter alone, to structure the information. These eight concepts for hydrates in nature are considered, each in a chapter section as

7.1: The paradigm is changing: from assessment of amount to production of gas.
7.2: Ocean sediments with hydrates typically contain low amounts of biogenic methane.
7.3: Sediment lithology and fluid flow are major controls on hydrate deposition.
7.4: Remote methods enable an estimation of the extent of a hydrated reservoir.
7.5: Drilling logs and coring provide improved assessments of hydrated gas amounts.
7.6: Hydrate reservoir models indicate key variables for methane production.
7.7: Future hydrated gas production trends are from the permafrost to the ocean.
7.8: Hydrates play a part in climate change and geohazards.

Examples of these eight concepts are illustrated in four field case studies, the first two for assessment, and the second two for production: (1) Blake Bahama Ridge, (2) Hydrate Ridge, (3) Messoyakha, and (4) Mallik 2002. In choosing only four case studies for this chapter, the authors were restricted to regions with the broadest applications, in which many research groups have worked, reasoning for a consensus perspective, rather than that of a few groups. For example, interesting perspectives for hydrates in the Gulf of Mexico have evolved from excellent studies by Sassen, et al.; Roberts, et al.; and Paull et al. (all in Paull and Dillon, 2001) but as typical in emerging knowledge areas, several competing perspectives exist regarding the hydrate amounts and assessment. However, even with the consensus which exists in the following examples, the conceptual pictures are certain to be corrected in the future by more knowledgeable writers.

Several excellent volumes have been published over the last decade on hydrates in nature, to further guide the reader: The summaries below are in addition to individual ocean cruises and wells, to which the authors refer in the chapter,

1. *Hydrates of Hydrocarbons*, by Y.F. Makogon, 1997.
2. The *Proceedings of the International Gas Hydrate Conferences* contain state-of-the-art descriptions of hydrates, at three year intervals:
   - The first conference (New Paltz, New York, USA, 1993), edited by E.D. Sloan, J. Happel, and M.A. Hnatow, contains 61 papers by 130 authors.
   - The second conference (Toulouse, France, 1996), edited by J.-P. Monfort, contains 87 papers by 195 authors.
   - The third conference (Salt Lake City, Utah, USA, 1999), edited by G.D. Holder and P.R. Bishnoi, contains 104 papers by 258 authors.
   - The fourth conference (Yokohama, Japan, 2002), edited by Y.H. Mori, contains 204 papers by 500 authors.
   - The fifth conference (Trondheim, Norway, 2005), edited by T. Austvik, contains 247 papers by 683 authors.
3. *Gas Hydrates: Relevance to World Margin Stability and Climate Change*, edited by J.-P. Henriet and J. Minert, 1998.
4. *Submarine Gas Hydrates*, by G.D. Ginsburg and V.A. Soloviev, 1998.
5. *Natural Gas Hydrates: Occurrence*, *Distribution and Detection*, edited by C.K. Paull, and W.P. Dillon, 2001.
6. *Natural Gas Hydrates in Oceanic and Polar Environments*, edited by M.D. Max, 2003.
7. *Methane Hydrates in Quaternary Climate Change: The Clathrate Gun Hypothesis*, by J.P. Kennett, G. Cannariato, I.L. Hendy, R.J. Behl, 2003.
8. *Advances in the Study of Gas Hydrates*, edited by C.E. Taylor and J.T. Kwan, 2004.
9. *Economic Geology of Natural Gas Hydrates*, edited by A.H. Johnson, M.D. Max, and W.P. Dillon, 2006.

The above books represent years of effort by the authors/editors. For a conceptual picture of hydrates in nature, let us return to an exposition of the eight principles listed earlier.

7.1 The Paradigm is Changing from Assessment of Amount to Production of Gas

Makogon (1965) announced the presence of gas hydrates in the permafrost regions of the Soviet Union. Since that time there have been two extreme views of *in situ* hydrate reserves. In one view, they have been ignored, presumably because they were considered to be too dispersed and difficult to recover, relative to the conventional supply of gas. In the other view, they were thought to be pervasive in all regions of the earth with permafrost (23% of the land mass) and in thermodynamically stable regions of the oceans (90% of the oceans areal extent). With further exploration and production of gas from a hydrate reservoir, a third, more realistic estimate of the hydrate resource has evolved, as the basis for this chapter.

7.1.1 Extent of the Occurrence of *In Situ* Gas Hydrates

Knowledge of the occurrence of *in situ* gas hydrates is very incomplete, and is obtained from both indirect and direct evidence. For the most irrefutable evidence, there have been 23 locations where hydrate samples have been recovered, 3 in permafrost and 20 in ocean environments. In permafrost regions, hydrate evidence is limited to drillings and associated well logs, whereas the sonic reflection method is relatively inexpensive but much less direct and much less reliable means of sensing hydrate on oceanic continental margins. Economics is the determining factor promoting increasing interest in the larger, oceanic hydrate reservoirs.

Table 7.1 lists the estimates of natural gas in hydrates in the geosphere's gas hydrate stability zone (GHSZ). These estimates range from the maximum values of Trofimuk et al. (1973), who apparently assumed that hydrates could occur wherever satisfactory temperatures and pressures exist, to the minimum values of Soloviev (2002) who considered more limiting factors such as availability of methane, limited porosity, and percentages of organic matter, thermal history of various regions, and so on. All estimates of natural gas hydrates are not well defined, and therefore somewhat speculative. However, even the most conservative estimates suggest very large amounts of gas in hydrated form.

Table 7.1 illustrates that as man learns more about hydrates in the environment, estimates of the amount of hydrates decrease. As shown in Figure 7.1, this resulted in a steady reduction in the estimate of hydrated gas, since the initial estimates of 3053×10^{15} m^3 methane (STP) in by Trofimuk et al. (1973). The overwhelming size of this number may be realized by comparison to 1×10^{15} m^3, which is the energy consumption of the United States for 1000 years at the current rate. In Figure 7.1, it should be noted that all of the estimates (except the estimate of Klauda and Sandler [2005]) were done in approximately the same way—a limited

TABLE 7.1
Estimates of *In Situ* Methane Hydrates

Year	CH_4 amount 10^{15} m^3 STP	Citations
1973	3053	Trofimuk et al.
1977	1135	Trofimuk et al.
1982	1573	Cherskiy et al.
1981	120	Trofimuk et al.
1981	301	McIver
1974/1981	15	Makogon
1982	15	Trofimuk et al.
1988	40	Kvenvolden and Claypool
1988	20	Kvenvolden
1990	20	MacDonald
1994	26.4	Gornitz and Fung
1995	45.4	Harvey and Huang
1995	1	Ginsburg and Soloviev
1996	6.8	Holbrook et al.
1997	15	Makogon
2002	0.2	Soloviev
2004	2.5	Milkov
2005	120	Klauda and Sandler

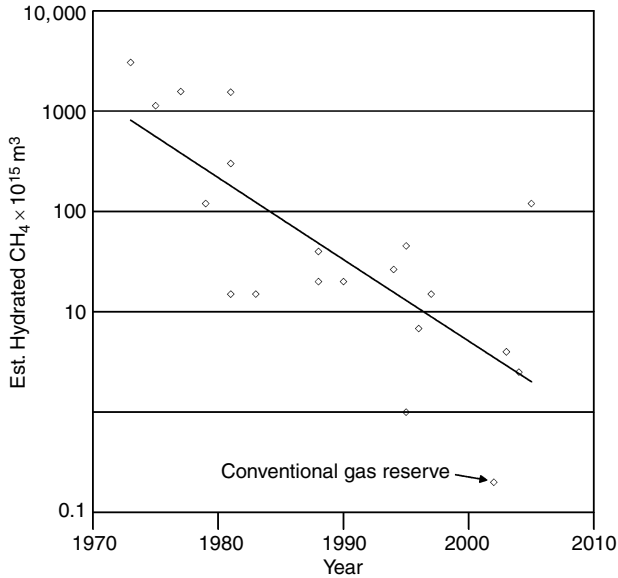

FIGURE 7.1 Estimates of amount of hydrated gas have generally decreased with time. Note the logarithmic scale of the ordinate.

amount of fairly well-known geological data on a local scale was extrapolated to a global level.

The Klauda and Sandler (2005) model is state-of-the-art as discussed in detail in Section 7.2.3.2.1 on hydrate formation. The model represents a singular advance because it alone enables prediction of 68 of the 71 occurrences of hydrates, with explanations for the three exceptions. The large amount of hydrates predicted by Klauda and Sandler includes both very deep hydrates and very dispersed hydrates, many of which are not accounted for by the other models or discovered by sampling due to dissociation. When only continental hydrates are considered, Klauda and Sandler predict 4.4×10^{16} m^3 (STP) of gas in hydrates, an estimate larger than those of Kvenvolden (1988) or Makogon (1997).

For simplicity, only estimates over the last decade are presented in Table 7.2, with assumptions or notable aspects that discriminate between the various models. Note that all estimates are comparatively large relative to estimates of the conventional gas reserve of 0.15×10^{15} m^3 methane (STP) (Radler, 2000).

Even the most conservative estimates of gas in hydrates in Table 7.1 indicate their enormous energy potential. Kvenvolden (1988) indicated that the 10,000 Gt (1 Gt = 10^{15} g) carbon or 1.8×10^{16} m^3 of methane in hydrates may surpass the available, recoverable conventional methane by two orders of magnitude, or a factor of two larger than the methane equivalent of the total of all fossil fuel

TABLE 7.2
Assumptions in Models of the Last Decade of Hydrated Gas Amounts

Model	Estimated amount × 10^{15} m^3 CH_4	Assumptions or notable aspects
Harvey and Huang (1995)	23	1. Limited to 250–3000 m H_2O depth 2. Interpolated seafloor temperature 3. Required >0.5 wt% organic carbon 4. Reduced area arbitrarily by 25% 5. 2.5–10% pore volume filling
Dickens (2001)	4.9–25	1. GHSZ is represented by Atlantic margin 2. Isobath of 1 km used for span of global margins 3. All continental margins contain hydrates 4. Hydrated pore space is 1–5%
Milkov (2004)	3	1. Same approach as Dickens (above) with exceptions 2. Only 20% of GHSZ contains hydrates 3. Predicts overall (not local) amounts 4. 1.2% of pore volume occupied
Klauda and Sandler (2005)	120	1. New thermomodel with pores and salt for GHSZ 2. Measured seafloor T and organic carbon content 3. Methanogenesis model matched to Blake-Bahama Ridge data 4. Global average of 3.4% of pore volume filled 5. Can predict 68 of 71 local hydrate sites

deposits. He noted, based on Bolin (1983) and Moore and Bolin (1987), that global carbon cycle amounts were as follows: fossil fuel deposits (5,000 Gt), terrestrial soil, detritus, and peat (1960 Gt), marine dissolved materials (980 Gt), terrestrial biota (830 Gt), the atmosphere (3.6 Gt), and marine biota (3 Gt). Relative to hydrates, the only larger pool of inorganic and organic carbon is that disseminated in sediments and rocks (20,000,000 Gt), which is unrecoverable as an energy resource.

Ginsburg and Soloviev (1995) and Milkov (2004) suggested that hydrates may be two orders of magnitude less than the previous consensus. They suggested that both the high contents of sediments and the concept of continuous regional distribution were overstated in past estimates. However, even with more conservative estimates, they indicated that the gas content in hydrates was 10^{15} m^3, accurate to one order of magnitude. It was difficult to reconcile the original Ginsburg and Soloviev (1995) local hypothesis with a continuous distribution shown by bottom simulating reflectors (BSRs), so modifications were made to account for both diffusion and water migration (Ginsburg and Soloviev, 1997; Soloviev and Ginsburg, 1997).

A second concern for the large estimates of methane in hydrate results from the Leg 164 drilling by Holbrook et al. (1996) who suggest downscaling the estimates in Table 7.1 by as much as a factor of three. However, even if such errors are real, the amount of gas in hydrates remains enormous. Ginsburg and Soloviev note that most resource estimates in Table 7.1 rely upon the equation $Q = S \times h \times K \times Z \times E$, where Q = gas content (m^3), S = hydrate area (m^2), h = hydrate thickness (m), K = sediment porosity (%), Z = fractional pore filling, and E = gas expansion (164 vol. gas/vol. hydrate).

The most detailed method of U.S. hydrate resource estimation has been by Collett (1995, 1996). He assigned probabilities to 12 different factors to estimate the hydrate resources within the United States at 9×10^{15} m^3 of gas. Collett (1995) notes the high degree of uncertainty places the above mean value between the 95% probability level (3×10^{15} m^3) and the 5% probability level (19×10^{15} m^3). However, in the United States, the mean hydrate value indicates 300 times more hydrated gas than the gas in the total remaining recoverable conventional reserves.

After concluding that the hydrated reserves are enormous, a second major point is that the amount of hydrates in the ocean surpasses that in the permafrost by two orders of magnitude. This oceanic amount is larger than would be expected, even though the oceans comprise 70% of the earth's surface, while the permafrost (regions with the land hydrates) comprise only 23% of the earth's land mass. In the relative hydrate amounts in the ocean and permafrost (Table 7.3), note that the estimates of the oceanic hydrate reserves are so large that a 1% error in ocean approximations could encompass the entire permafrost hydrate reserves. It should be noted that methane accumulates to form hydrates in continental margin sediments for the following two reasons: (1) the flux of organic carbon to the seafloor is the greatest and (2) the sedimentation rates are the highest (Dillon and Max, 2001).

The major difficulty in considering hydrates as actual reserves stems from the solid, dispersed character of the hydrates in locations that are difficult to

TABLE 7.3
Estimates of Relative Hydrated Methane in the Permafrost and the Ocean

Permafrost hydrated methane (10^{14} m^3)	Oceanic hydrated methane (10^{16} m^3)	References
0.57	0.5–2.5	Trofimuk et al. (1977)
0.31	0.31	McIver (1981)
340	760	Dobrynin et al. (1981)
l.0	1.0	Makogon (1988)
7.4	2.1	MacDonald (1990)

access, such as permafrost and deep oceans. The most recent estimate (Klauda and Sandler, 2005) determined that there is a global average value of 3.4% of the pore space filled, compared to the common a priori assumption of an overall global value of 5%.

Due to this low pore filling and long formation times, hydrates should be considered a nonrenewable resource from which the recovery of gas is much more difficult than that from a normal gas reservoir. In addition, while an energy balance of the dissociation of pure hydrates is highly favorable, hydrates may be sparsely dispersed in sediment so economic recovery will be problematic. However, before turning to the production of gas from hydrates, consider first the locations of hydrate reserves, and requirements for formation.

Kvenvolden (Personal Communication, November 28, 2005) compiled 89 hydrate sites shown in Figure 7.2, with a complete listing in Tables 7.4 and 7.5. In those locations hydrates were either:

1. Recovered as samples (23 locations),
2. Inferred from BSRs (63 locations), decrease in pore water chlorinity (11 locations), well logs (5 locations), and slumps (5 locations), or
3. Interpreted from geologic settings (6 locations).

In the above hydrate evidence, some locations are double-listed because they had more than one piece of evidence. It is interesting that 63 BSR locations provide the most evidence for hydrates—a factor of almost 3 larger than the 23 sample locations with the most irrefutable evidence. As will be demonstrated later in the Blake-Bahama Ridge and Hydrate Ridge Case Studies and Section 7.4.2, BSR evidence is not totally reliable, but provides a first approximation of hydrated subsurface depth and area extent.

The hydrates-in-nature paradigm is currently changing. The above tables and quantity estimates indicate that much of the natural gas containing hydrates is in the ocean bottom, and while production of gas from such deep-lying hydrates is now too expensive, it is likely that in the near future mankind will need to

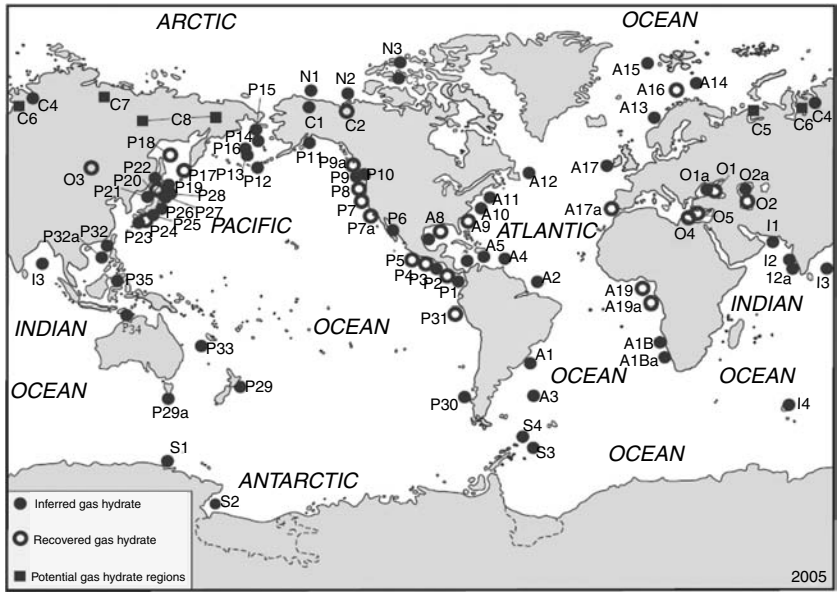

FIGURE 7.2 Inferred (63), Recovered (23), and Potential (5) hydrate locations in the World. (Courtesy of K. Kvenvolden, Personal Communication November 28, 2005.)

tap that fuel source to meet growing energy demands. However, the conceptual paradigm is changing from assessment of the energy resource, as in the two initial case studies of the Blake-Bahama Ridge and Hydrate Ridge, to the conceptual proof of energy production from hydrates, as shown in the two case studies of the Messoyakha field and the Mallik 2002 field, with all four case studies given at the chapter conclusion. The next step will be extended production testing in permafrost-associated hydrates.

This paragraph summarizes the preceding first principle of hydrates in nature. Very large amounts of hydrated methane exist in nature, perhaps, as much as twice that of all other fossil fuels combined. Such a large resource finds major applications in energy, climate, and geohazards. Of the two geologic types of reservoirs, the amount of hydrates in the ocean overshadows that in the permafrost, by two orders of magnitude. Except for anecdotal instances, hydrates are distributed in very low concentrations over very large areas. The reader should be cautioned that it is very unlikely that any reservoirs similar to the Blake Ridge (see Case Study 1) will ever be exploited. Kleinberg (Personal Communication, July 27, 2006) cautions, "There will be windmills on the roofs of Charleston before the Blake Ridge is drilled for gas." Hydrated reservoirs should be considered as a nonrenewable resource, because they require geologic times to accumulate,as will be demonstrated in the remainder of this chapter. The hydrate paradigm is changing—moving from locating and quantifying amounts of hydrates in reservoirs to conceptual production and production testing.

TABLE 7.4
Summary of Known and Inferred Subaquatic Gas-Hydrate Occurrences in Atlantic Ocean, Polar Oceans, Continents, and in Inland Seas and Lakes

Designation	Location offshore	Evidence	References
Atlantic ocean			
A1	(Pelotas Basin)	BSR	Fontana and Mussemeci (1994)
A2	Brazil (Amazon Fan)	BSR	Manley and Flood (1988)
A3	Argentina (Central Argentine Basin)	BSR	Manley and Flood (1988)
A4	Barbados (Barbados Ridge)	BSR	Ladd et al. (1982)
A5	Southern Caribbean Sea	BSR	Ladd et al. (1984)
A6	Panama and Colombia (Colombia Basin)	BSR	Shipley et al. (1979)
A7	Gulf of Mexico (off Mexico, western area)	BSR	Shipley et al. (1979)
A8	(off USA, northern area)	Samples	Brooks et al. (1985, 1986); Sassen and MacDonald (1994, 1997a,b)
A9	Southeastern USA (Blake-Bahama Ridge)	BSR	Markl et al. (1970); Shipley et al. (1979)
		Slumps	Carpenter (1981); Dillon et al. (1996)
	(DSDP Leg 76)	Samples	Kvenvolden and Barnard (1983)
		$<Cl^-$	Jenden and Gieskes (1983)
	(ODP Leg 164)	BSR	Holbrook et al. (1996)
	(ODP Leg 164)	Samples	Paull et al. (1996)
A10	Eastern USA (Carolina Trough)	BSR	Dillon and Paull (1983)
A11	Eastern USA (Continental Rise)	BSR	Tucholke et al. (1977); Dillon et al. (1993, 1995)
A12	Newfoundland, Canada (Laborador Shelf)	BSR	Taylor et al. (1979)
A13	Norway (Storegga Slide)	BSR	Bugge et al. (1987); Mienert et al. (1998)
		Slumps	Jansen et al. (1987); Bugge et al. (1987)
		$<Cl^-$	Hesse and Harrison (1981)
	(ODP Leg 104)	CH_4, $<Cl^-$	Kvenvolden et al. (1989)

(Continued)

TABLE 7.4
Continued

Designation	Location offshore	Evidence	References
A14	(Barents Sea)	BSR	Andreassen et al. (1990)
A15	(off Svalbard)	BSR	Posewang and Mienert (1999)
A16	(Haakon-Mosby mud volcano)	Samples	Ginsburg et al. (1999)
A17	Ireland (Porcupine Basin)	Geophysics	Henriet et al. (1998)
A17a	Spain (Gulf of Cadiz)	Sample	Mazurenko et al. (2002)
A18	Africa (S.W. Africa)	Slumps	Summerhayes et al. (1979)
A18a	South Africa (S.W. continental margin)	BSR	Ben-Avraham et al. (2002)
A19	Nigeria (continental slope)	Samples	Brooks et al. (1994)
A19a	Congo/Angola (Congo–Angola Basin)	Samples	Charlou et al. (2004)
North (Arctic)			
N1	Alaska (Beaufort Sea)	BSR	Grantz and Dinter (1980); Kvenvolden and Grantz (1990)
		Slumps	Kayen and Lee (1991)
N2	Canada (Beaufort Sea)	Logs	Weaver and Stewart (1982)
N3	Canada (Sverdrup Basin)	Logs	Judge (1982)
South (Antarctic)			
S1	Antarctica (Wilkes Land Margin)	BSR	Kvenvolden et al. (1987)
S2	(Ross Sea)	CH_4	McIver (1975)
		$<Cl^-$	Mann and Gieskes (1975)
S3	(Weddell Sea)	BSR	Lonsdale (1990)
S4	(South Shetland margin)	BSR	Lodolo et al. (1993)

Other (inland seas and lakes)			
O1	Black Sea, Russia	Samples	Yefremova and Zhizhchenko (1974); Ginsburg et al. (1990)
O1a	Black Sea, Russia	BSR	Zillmer et al. (2005)
O2	Caspian Sea, Russia	Samples	Yefremova and Gritchina (1981); Ginsburg et al. (1992)
O2a	Caspian Sea, Russia	BSR	Diaconescu et al. (2004)
O3	Lake Baikal, Russia	BSR	Hutchinson et al. (1991)
		Samples	Kus'min et al. (1998)
O4	Mediterranean Sea (ODP Leg 160)	$<Cl^-$, CH_4	DeLange and Brumsack (1998)
O5	Turkey (Kula mud volcano)	Sample	Woodside et al. (1998)
Continental			
C1	Alaska (North Slope)	Logs	Collett (1993)
		PCS	Summary by Collett (1993)
C2	Canada (Mackenzie Delta)	Logs	Bily and Dick (1974)
		Samples	Dallimore et al. (1999)
C3	(Arctic Islands)	Logs	Davidson et al. (1978); Judge (1982)
C4	Russia (Messoyakah Field)	CH_4	Makogon et al. (1972)
C5	(Timan-Pechora Province)	Interpretation	Cherskiy et al. (1982)
C6	(Western Siberian Platform)	Interpretation	Cherskiy et al. (1982)
C7	(Eastern Siberian Craton)	Interpretation	Cherskiy et al. (1982)
C8	(Northeast Siberia)	Interpretation	Cherskiy et al. (1982)

Note: BSR, Bottom-Simulating Reflection; $<Cl^-$, Low Chloride Content of Pore Water; CH_4, High Methane Content; Logs, Well-Log Response; PCS, Pressure Core Sample; Geophysical, Seismic Evidence of Past Occurrence of Gas Hydrate.

Source: From Kvenvolden, Personal Communication, November 28, 2005.

TABLE 7.5
Summary of Known and Inferred Subaquatic Gas–Hydrate Occurrences in the Pacific and Indian Oceans

Designation	Location offshore	Evidence	References
Pacific ocean			
P1	Panama	BSR	Shipley et al. (1979)
P2	Costa Rica (Middle America Trench)	BSR	Shipley et al. (1979)
	(DSDP Leg 84)	Samples	Kvenvolden and McDonald (1985)
	(ODP Leg 170)	Samples	Shipboard Scientific Party (1997)
P3	Nicaragua (Middle America Trench)	BSR	Shipley et al. (1979)
P4	Guatemala (Middle America Trench)	BSR	Shipley et al. (1979)
	(DSDP Leg 67)	Samples	Harrison and Curiale (1982)
		$<Cl^-$	Hesse and Harrison (1981); Harrison et al. (1982)
	(DSDP Leg 84)	Samples	Kvenvolden and McDonald (1985)
		Logs	Kvenvolden and McDonald (1985)
		$<Cl^-$	Hesse et al. (1985)
P5	Mexico (Middle America Trench)	BSR	Shipley et al. (1979)
	(DSDP Leg 66)	Samples	Shipley and Didyk (1982)
P6	Mexico (Gulf of California, Guaymas Basin)	BSR	Lonsdale (1985)
P7	California, USA (Eel River Basin)	BSR	Field and Kvenvolden (1985)
		Samples	Brooks et al. (1991)
P7a	(Santa Monica Basin)	Samples	Normark et al. (2003)
P8	Oregon, USA (Cascadia Basin)	BSR	Moore et al. (1992)
	(ODP Leg 146)	Samples	Whiticar et al. (1995); Kastner et al. (1998)
	(Hydrate Ridge)	Samples	Suess et al. (1999a,b)
P9	Canada (Cascadia Basin)	BSR	Davis et al. (1990); Hyndman and Spence (1992)
P9a	Northern Cascadia Margin	Samples	Pohlman et al. (2005)
P10	(Fjords of British Columbia)	Slumps	Bornhold and Prior (1989)
P11	Alaska, USA (Eastern Aleutian Trench)	BSR	Kvenvolden and von Huene (1985)
P12	Alaska, USA (Middle Aleutian Trench)	BSR	McCarthy et al. (1984)
		$<Cl^-$	Hesse and Harrison (1981)
P13	Bering Sea (Alaska, USA)	VAMPs	Scholl and Cooper (1978)

TABLE 7.5
Continued

Designation	Location offshore	Evidence	References
P14	(USA, Bering Sea Shelf)	BSR	Hammond and Gaither (1983)
P15	(USA/Russia, Navarin Margin)	BSR	Carlson et al. (1985)
P16	Russia (Shirshov Ridge)	BSR	Saltykova et al. (1987)
P17	Okhotsk Sea (Paramushir Island, Russia)	Samples	Zonenshayn et al. (1987)
P18	(Sahkalin Island, Russia)	Samples	Ginsburg et al. (1993)
P19	(Off Abashiri, Kitami-Yamato Mount, Japan)	BSR	Matsumoto et al. (1994); Sato (1994)
P20	Japan, Japan Sea (DSDP Leg 57)	$<Cl^-$	Moore and Gieskes (1980)
	(Okushiri Ridge) (ODP Leg 127)	Sample	Shipboard Scientific Party (1990)
		BSR	Kuramoto and Okamura (1995)
P21	(Western Tsugaru Basin)	BSR	Sato (1994)
P22	(Tatar Trough)	BSR	Sato (1994)
P23	Japan, Nankai Trough (off eastern Miyazaki)	BSR	Aoki et al. (1983); Tamano et al. (1984)
P24	(off southern Shikoku)	BSR	Shipboard Scientific Party (1991)
	(ODP Leg 131)	Sample	Shipboard Scientific Party (1991)
P25	(Muroto Trough)	BSR	Sato (1994); Matsumoto et al. (1994)
P26	(Kumano-nada off Omaezaki Cape)	BSR	Okuda (1995); Gas Epoch (1995)
		CH_4, $<Cl^-$	JNOC press release (2000)
P27	Japan, Offshore Chiba Basin	BSR	Arato et al. (1995)
P28	Japan, Kuril Trench (off Tokachi/Hidaka)	BSR	Sato (1994)
P29	New Zealand (Hikurangi Trough)	BSR	Katz (1981)
P29a	Tasmania (South Tasman Rise)	BSR	Stagg et al. (2000)
P30	Chile (Peru–Chile Trench)	BSR	Cande et al. (1987)
		CH_4, $<Cl^-$	Froelich et al. (1995)
P31	Peru (Peru–Chile Trench)	BSR	Miller et al. (1991)
	(ODP Leg 112)	Samples	Kvenvolden and Kastner (1990)
P32	Taiwan (South China Sea)	BSR	Chi et al. (1998)
P32a	South China Sea	BSR	Wu et al. (2005)
P33	Australia (Tasman Sea, Lord Howe Rise)	BSR	Exon et al. (1998)
P34	(Timor Trough)	CH_4	McKirdy and Cook (1980)
P35	Indonesia (Celebes Sea)	BSR	Neben et al. (1998)
Indian Ocean			
I1	Oman (Gulf of Oman, Makran Margin)	BSR	White (1979)
I2	India (Arabian Sea)	BSR	Veerayya et al. (1998)

(Continued)

TABLE 7.5
Continued

Designation	Location offshore	Evidence	References
I2a	(Western continental margin)	BSR	Rao et al. (2001)
I3	(Bay of Bengal)	BSR	Rastogi et al. (1999)
I4	Kerguelen Plateau (Labuan Basin)	BSR	Stagg et al. (2000) P29a

Note: BSR, Bottom simulating reflection; $<Cl^-$, low chloride content of pore water; CH_4, high methane content; VAMPs, velocity amplitude pulldowns; Logs, well-log response.

Source: From Kvenvolden, Personal Communication, November 28, 2005.

7.2 Sediments with Hydrates Typically Have Low Contents of Biogenic Methane

The rule of thumb in the title is shown in the following six points, which comprise the subsections of 7.2:

1. As a heuristic, methane availability limits hydrate formation in reserves. Of the two sources of methane (biogenic and thermogenic) in natural hydrates, most of the gas is biogenic, that is, from bacterially generated methane, with anecdotal exceptions.
2. Hydrates result from two types of reservoirs: (1) the large majority of cases are for slow flux or in-place generation of methane dissolved in water, as shown in the case study of the Blake Bahama Ridge and (2) fast fluxes of dissolved and free gas from deeper in the earth, as shown in the Hydrate Ridge case study, with other examples being the Black and Okhotsk Seas. Exceptions to this rule of thumb are shown via thermogenic gas examples from the Gulf of Mexico, Barkley Canyon and the Caspian Sea, which also have fast fluxes.
3. The biogenic methane is generated from anaerobic degradation, accompanied by a sulfate–methane interface (SMI), which can be used to determine the upper boundary of hydrate formation depth (Paull et al., 2005).
4. Another heuristic (Roberts, 2001) is that intermediate fluxes of gas result in hydrates, while very fast fluxes result in mud volcanoes and very slow fluxes result in mineralization, or carbonates.
5. With anecdotal exceptions, the hydrate content is usually low, typically averaging 3.5% of pore volume.
6. Current hydrated gas estimates are made for biogenic gas associated with in-place generation that tends to be more uniformly distributed. We have no general factual data about the extent of hydrate distribution in the vicinity of submarine seepages (Ginsburg and Soloviev, 1998, p. 165).

After the section summary in the preceding six statements, let us consider the evidence for such judgments. Methane availability is one of the most critical issues controlling the occurrence of natural gas hydrates (Xu and Ruppel, 1999). In the thermodynamic regime of temperature and pressure in the ocean or permafrost, water is seldom the limiting chemical; therefore several of the markers of hydrate formation are related to the generation of methane. The origins of the gases in hydrate are mostly biogenic but there is anecdotal evidence of thermogenic gases, as in the Gulf of Mexico and Caspian Sea. Kvenvolden and Lorenson (2001) state that more than 99% of the hydrates on earth contain methane formed by biogenic processes. We will consider the gas source (Section 7.2.1), before qualitative hydrate formation (Section 7.2.2) and the mechanism (Section 7.2.3) is investigated.

7.2.1 Generation of Gases for Hydrate Formation

For details of methane hydrates *in situ* geochemistry beyond the overview in this section, the reader is referred to the review by Kvenvolden (1995). While they are not typical in hydrates, thermogenic gases are more common in normal natural gas reservoirs, and thermogenic generation has been reviewed thoroughly in a number of references (see for example, Hunt, 1979, 163 ff.). The thermogenic gases are produced by a catagenesis process characterized by high temperatures (>450 K), producing relatively large amounts of ethane and higher hydrocarbons. However, because biogenic gases dominate in hydrates, organic diagenesis will be briefly reviewed, with its low temperature mechanism.

The words "organic diagenesis" (sometimes called bacterial methanogenesis) are used to denote the low temperature, biogenic conversion of organic matter to methane, which is subsequently transformed to hydrate. Organic diagenesis is usually enhanced by high values of the clastic/organic flux to the seafloor. Kvenvolden (1985a) suggested sedimentation rates between 30 m/10^6 yr and 300 m/10^6 yr are necessary for hydrate formation. Collett (1996) and Klauda and Sandler (2005) assign probabilities of zero to hydrate formation if the total organic carbon (TOC) present is less than 0.5% and 0.4%, respectively. Collett assigns a probability of unity if the TOC is greater than 2%, as an upper bound.

The following discussion is derived almost entirely from the classic review of organic diagenesis by Hesse (1986). He modified the work of Claypool and Kaplan (1974), to suggest six stages (diagrammed in Figure 7.3) through which organic matter passes in anaerobic sediments. At each stage the change in the standard Gibbs free energy of reaction is more negative (favorable) than the reaction mechanism of the stages above it.

In stage one of Figure 7.3 the organic matter (containing carbon, nitrogen, and phosphorus in the ratio 106:16:1) is oxidized by dissolved oxygen. With somewhat deeper sediments, the organic matter is reduced in the second stage by nitrates, primarily in the form of nitric acid. More typically, oceans are anaerobic where hydrates are found, and follow the systems on the right of Figure 7.3. However, from the third stage onward, both the ventilated basin (on the left of Figure 7.3)

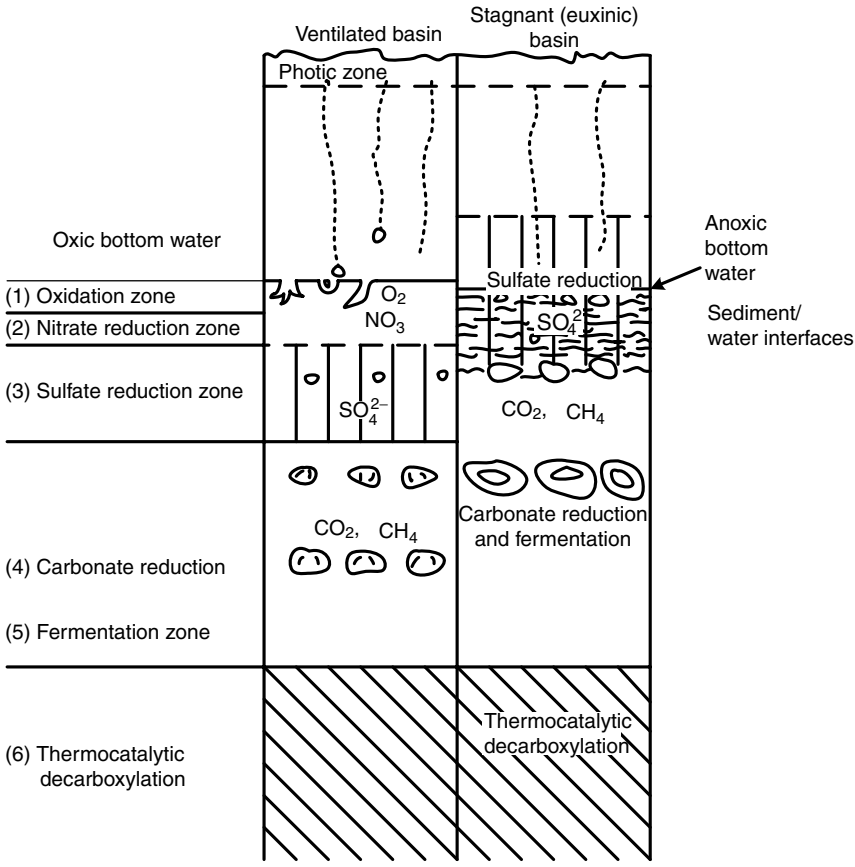

FIGURE 7.3 Stages of organic matter oxidation in anoxic sediments. (Reproduced from Hesse, R., *Geosci. Can.*, **14**, 165 (1986). With permission from the Geological Association of Canada.)

and anaerobic or anoxic basins (on the right) follow similar mechanisms. The third stage is characterized by sulfate ion reduction. Immediately below is the fourth stage of carbonate reduction, which generates methane for hydrate formation. Whiticar et al. (1986) demonstrated that methane is generated by microbial reduction of CO_2 after the sulfate has been reduced. Without giving the complete carbonate mechanism, the overall reaction for the production of methane from an organic is

$$(CH_2O)_{106}(NH_3)_{16}(H_3PO_4) \rightarrow 53CO_2 + 53CH_4 + 16NH_3 + H_3PO_4 \quad (7.1)$$

Below the stage of methane production is the fermentation (fifth) stage, followed by the sixth, thermocatalytic stage at still greater depths. The initial five stages require the presence of bacteria; below stage five, bacterial activity ceases

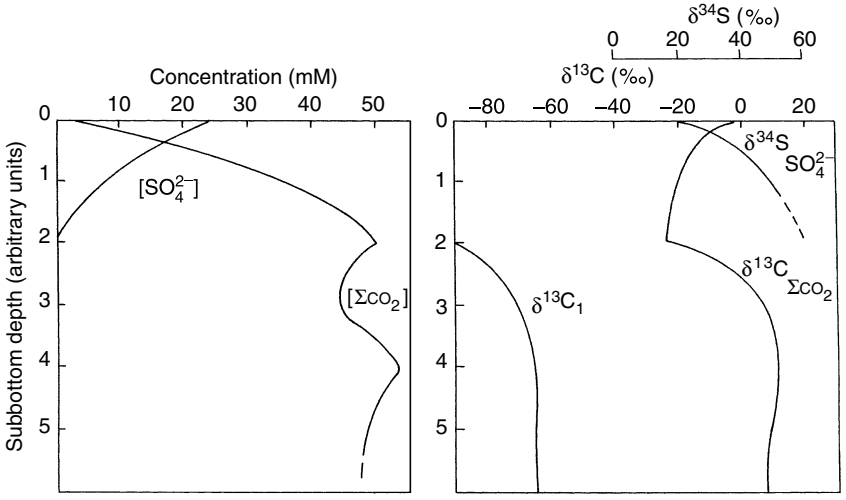

FIGURE 7.4 Generalized profiles of concentration and isotope ratio changes for dissolved sulfate and carbon species in anoxic marine sediments. Depth scale is arbitrary with depth units ranging from 10^{-1} to 10^{2} m. (Reproduced from Claypool, G.E., Kvenvolden, K.A., *Ann. Rev. Earth Planet Sci.*, **11**, 299 (1983). With permission from Annual Reviews, Inc.)

and the more usual thermocatalytic reactions begin, which are associated with hydrocarbon production. The main chemical species released to the pore water from the microbial breakdown of organic matter are the carbonate species listed as ΣCO_2, which include CO_2, H_2CO_3, HCO_3^-, and CO_3^{2-} as shown in Figure 7.4.

Carbonates are generated in all of the zones, but they are consumed only below the third stage. After the depletion of more than 80% of the sulfate, the components of ΣCO_2 become oxidants, leading to the production of methane. It is possible to distinguish between the CO_2 produced and the CO_2 consumed, determining the extent of carbon isotopic fractionation, particularly associated with the methane production in stage four.

The way of discriminating gas source is via the isotope ^{13}C, which is distributed through sediments of all geological ages; the ^{13}C difference in mass relative to ^{12}C is brought about through fractionation by both biological and physical processes. The fractionation is measured relative to a standard sample of Pee Dee Belemnite (PDB), with the units of parts per thousand (‰). The ratio difference (δ) of ^{13}C to ^{12}C may be measured spectrometrically, and is defined by

$$\delta^{13}C \equiv \left[\frac{[^{13}C]/[^{12}C]_{\text{sample}}}{[^{13}C]/[^{12}C]_{\text{PDB}}} - 1 \right] \times 10^3 \tag{7.2}$$

Methane formed by biogenic processes ranges in $\delta^{13}C$ from about $-60‰$ to $-85‰$, while methane from thermogenic processes ranges from $-25‰$ to $-55‰$ (Hunt 1979, p. 25).

During the first three stages of organic matter decomposition in Figure 7.3, negligible carbon isotopic fractionation occurs. However, in the fourth stage, methane generated from carbonates has an isotopic composition that is about 70‰ lighter than the carbon of the parent material (Hesse, 1986). The residual CO_2 consequently becomes enriched in $\delta^{13}C$ reaching positive values as high as +15–25‰.

Figure 7.4 shows the reduction in sulfates and the corresponding growth of both the parent carbonates and the offspring methane with subbottom depth. The methane production is parallel but lower in isotope production than the carbonates. In Figure 7.4 the sulfur isotope ($\delta^{34}S$) content is defined in an identical manner to Equation 7.2 with the replacement of the fraction $^{13}C/^{12}C$ by $^{34}S/^{32}S$ in both the numerator and the denominator, using Cañon Diablo meteoritic troilite as a standard. The $\delta^{34}S$ value increases from 20–60‰ before substantial biogenic methane is produced.

A second heuristic differentiating biogenic and thermogenic gas is the ratio of methane to heavier hydrocarbons. Biogenic gas typically has values greater than 10^3 for the ratio of methane to the sum of ethane and propane $[C_1/(C_2 + C_3)]$ while for thermogenic gas this ratio is usually less than 100 (Bernard et al., 1976). Figure 7.5 is a plot of the ratio of $C_1/(C_2 + C_3)$ against isotopic composition for

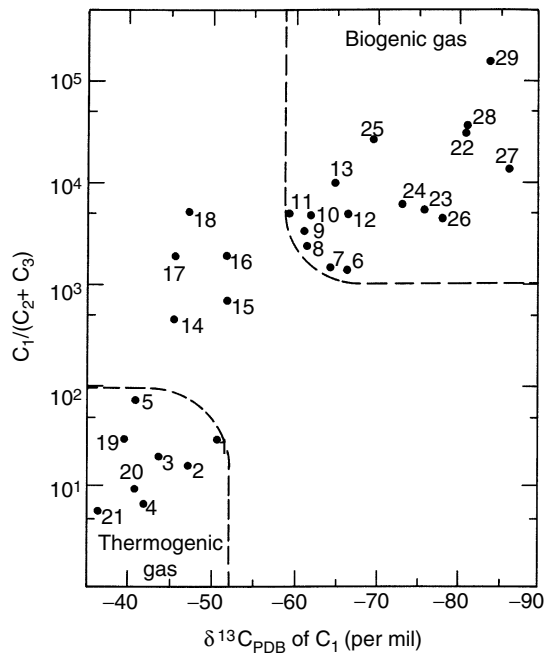

FIGURE 7.5 Plot of $C_1/(C_2 + C_3)$ against isotopic composition of C_1 to distinguish biogenic and thermogenic gas. (Reproduced from Claypool, G.E., Kvenvolden, K.A., *Ann Rev Earth Planet. Sci.*, **11**, 299 (1983). With permission.)

TABLE 7.6
Gas Characteristics of Gulf of Mexico and Caspian Sea Hydrate Samples

	δ^{13} C	Composition of gas, mol%						
Site	CH_4	C_1	C_2	C_3	i-C_4	n-C_4	CO_2	$\frac{C_1}{C_2+C_3}$
Biogenic hydrate samples								
Orca Basin	−71.3	99.1	0.34	0.28			0.24	159
Garden Banks-388	−70.4	99.5	0.12				0.26	829
Green Canyon-257	−69.2	99.7					0.26	>1000
Green Canyon-320	−66.5	99.7	0.08				0.12	1246
Thermogenic gas hydrates								
Green Canyon-184	−44.6	70.9	4.7	15.6	4.4	0.3	4.1	3.2
Green Canyon-204	−56.5	61.9	9.2	22.8	4.5	1.3	0.2	1.9
Green Canyon-234	−43.2	74.3	4.0	13.0	3.2	0.86	4.6	4.4
Mississippi Canyon	−48.2	93.4	1.2	1.3			4.0	37.4
Buzdag (Caspian)	−44.8	74.7	17.4	2.4	0.4	1.1	3.6	3.77
Buzdag (Caspian)	n.a.	76.0	19.3	2.4	0.6	0.3	1.2	3.50
Elm (Caspian)	−56.0	95.3	0.6	1.6	1.7	n.d.	0.9	43.3
Elm (Caspian)	n.a.	81.4	15.3	1.6	0.2	0.7	0.8	4.81

Source: From Brooks, J.M., et al., *Org. Geochem.*, **10,** 221, 1986, Ginsburg, G.D., Soloviev, V.A., *Bull. Geol. Soc of Denmark*, Copenhagen, **41**, 95, 1994. With permission.

several gas seep samples as a principal means to distinguish the gas source. Note in Figure 7.5 that samples 14 through 18 are derived from mixtures of thermogenic and biogenic gases.

Table 7.6 quantifies the isotope and composition differences for biogenic and thermogenic hydrate samples in the Gulf of Mexico (Brooks et al., 1986), as well as for thermogenic hydrates from the Caspian Sea (Ginsburg and Soloviev, 1994). Note that there is usually between 1 mol% and 20% propane in thermogenic hydrates, compared against propane's relative absence in biogenic hydrates. These amounts are consistent with the phase equilibrium heuristics of Chapter 4 which suggest that propane should be concentrated in the hydrate phase. One would not expect a small (e.g., ppm) propane concentration in hydrates for a thermogenic gas.

7.2.2 The SMI, the Hydrate Upper Boundary, and the SMI Rule-of-Ten

As shown in the discussion accompanying Figure 7.4, sulfate is reduced before methane is generated in the diagenesis process. At the subsediment SMI, sulfate from the seawater above, and methane from the dissolved (or free) gas below, are consumed to produce carbonate and hydrogen sulfide. The anaerobic reaction for

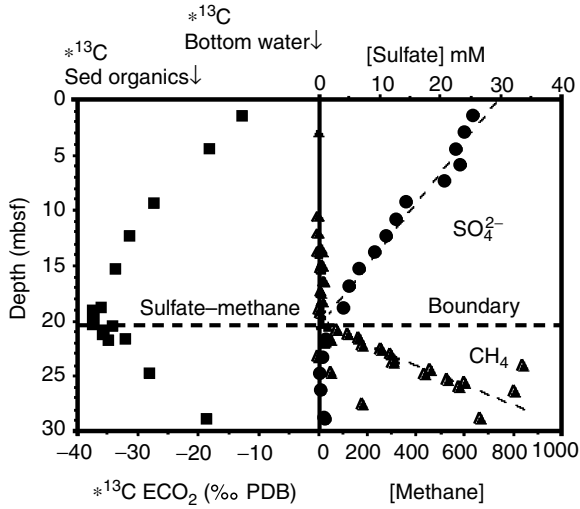

FIGURE 7.6 Samples from ODP Leg 164 Hole 994 at Blake Bahama Ridge, showing the sub-bottom reduction in sulfate until the depth of the Sulfate–Methane Interface (SMI), and the increase in methane concentrations below the SMI. (Paull, Personal Communication, October 25, 2001.)

the consumption of methane and sulfate resulting in the production of carbonates for subsea ridges, chimneys, or chemoherms, and hydrogen sulfide as a substrate for chemosynthetic communities (see the Hydrate Ridge case study) is

$$CH_4 + SO_4^{2-} \rightarrow CO_3^{2-} + H_2S + H_2O \tag{7.3}$$

As one of many examples of the relative sulfate and methane concentrations with depth, Paull et al. (1996) measured samples (Figure 7.6) from the Blake-Bahama Ridge ODP Leg 164 hole 994.

Recently, based upon 435 samples on 25 long cores (up to 37 m) in the Gulf of Mexico and multiple samples in the Blake-Bahama Ridge, Paull et al. (2005) offered the following rule of thumb, which might be called the SMI Rule of 10: the methane concentration is insufficient to form hydrates, until a depth of a factor of10 times the SMI depth. For example, at Blake-Bahama Ridge, the average SMI was at 20 mbsf and the top of the hydrate zone was at 200 mbsf. Similarly in the Gulf of Mexico west of the Mississippi Canyon, the average SMI is at 12 mbsf so hydrates should be stable beginning at 120 mbsf in those locations. Figure 7.6 shows the concentration changes of sulfate, methane, and carbonates around the SMI (Paull et al., 1996). As with all rules of thumb, there are exceptions to the general case, particularly where the methane flux is very high, such as at the Hydrate Ridge where hydrates appear in the uppermost 25 m, and in the Gulf of Mexico sites that have surface hydrate outcrops, indicating fast flows.

For the average case, however, the SMI Rule of 10 can bound the top of the hydrate zone, when the gas flux is small enough to reduce a significant amount of sulfate. Ten times the depth of the SMI is the approximate initiation depth for hydrate formation. This new and largely unrecognized heuristic provides a convenient upper bound to hydrates in sediments just as, in the next section, the lower bound of hydrate stability will be shown to be the intersection of the phase boundary and the geothermal gradient, also complemented in Section 7.4 by the Bottom Simulating Reflector (BSR). Another suggestion is that the tenfold depth of the SMI may coincide with the gas solubility required to form hydrates in seawater, as indicated at the conclusion of Section 7.4.

7.2.3 Mechanisms for Generation of Hydrates

Methane, either from biogenic or thermogenic sources, combines with water in sediments to form hydrates. While biogenic gas in the majority of the cases is in the ocean (Dillon and Max, 2000), in the northern Gulf of Mexico, Brooks (Personal Communication, June 29, 1988) estimated that approximately equal numbers of hydrate samples were recovered from each type of gas source. Due to the high temperature requirements for its production, thermogenic gas must migrate along sediment faults from its source at depth to the cooler hydrate stability region.

Thermogenic gas migration occurs via channels and faults (e.g., salt diapirs) that are common to regions such as the Gulf of Mexico or mud volcanoes in the Caspian Sea (Ginsburg and Soloviev, 1994). Thermogenic, massive hydrates are associated with faults in fine-grained sediments rather than biogenic, dispersed hydrates in course-grained rocks, as shown, for example, in the ODP Leg 146 results (Westbrook et al., 1994) and in the gas hydrate samples database (Booth et al., 1996).

Thermogenic gas hydrates associated with faults are generally more localized than biogenic hydrates which are normally indicated by widespread BSRs. Consequently, hydrate resource estimates (Collett, 1995; Kvenvolden, 1995) are based principally on biogenic gas properties and phase equilibria. Thermogenic hydrates are considered to be anecdotal in nature, due to their association with faults that act as conduits for deeper gas. Paull et al. (2005) suggest that such conduits cause thermogenic hydrates to be localized in the pathway vicinity, rather than be dispersed over wide areas, and that such localization may be responsible in the Gulf of Mexico for the lack of BSRs discussed in Section 7.4.

For Prudhoe Bay permafrost hydrates, Collett et al. (1988) suggested that thermogenic gas migrated along faults from deeper regions, where it was mixed with biogenic gas and either directly converted to gas hydrate or first concentrated in existing structural/stratigraphic traps, and later converted to hydrate.

Similarly, if channels are available, biogenic gas may migrate to regions within the hydrate stability envelope. Most of the gas was of biogenic origin in the hydrate core recovered from the Northwest Eileen State Well Number 2, one of the first wells to recover hydrates (Collett, 1983). The biogenic source is likely to predominate for hydrates in permafrost (Kvenvolden, Personal Communication,

October 19, 1988), in addition to biogenic dominance in ocean hydrates (Dillon and Max, 2000), with sporadic mixtures of biogenic and thermogenic gas in Alaska, Russia, offshore Canada, and the Gulf of Mexico. It is possible to have both means (in place generation and fast fluxes) of supplying biogenic gas, indicated by Kvenvolden et al. (1984) and Kvenvolden and Claypool (1985) at DSDP Site 570 in the Middle America Trench.

7.2.3.1 Hydrate formation in the two-phase region

Because free gas (or gas-saturated water) is less dense than either water or sediments, it will percolate upward into the region of hydrate stability. Kvenvolden suggested that a minimum residual methane concentration of 10 mL/L of wet sediment was necessary for hydrate formation. The upward gas motion may be sealed by a relatively impermeable layer of sediment, such as an upper dolomite layer (Finley and Krason, 1986a) or the upper siltstone sequence, as in the North Slope of Alaska (Collett et al., 1988). Alternatively, permafrost or hydrate itself may act as an upper gas seal. These seals can also provide traps for free gas that has exsolved from solution, and the seals can subsequently act to provide sites for hydrate formation from the free gas.

In addition the extensive hydrate exploration experience of Collett (Personal Communication, May 25, 2006) suggests that the container can control the amount of hydrate present. For example, when the container is relatively porous, grain-supported sand, the hydrate content can be high (as much as 70–80% of the pore volume). However, for low porosity shales the content may be much lower (e.g., 3% of the pore volume).

Hydrate formation from free gas will likely initiate at a gas–liquid interface, as observed in the laboratory experiments of Chapter 6. As indicated in Chapter 3, either initial hydrate formation or a solid phase can serve as nucleation sites for additional formation from the gas and aqueous liquid phases. However, most geochemists (Claypool and Kaplan, 1974; Finley et al., 1987, etc.) suggest hydrates form from gas (either at equilibrium or supersaturated) dissolved in the liquid phase, without a free gas.

Using innovative experiments, Tohidi and coworkers (2001) and Anderson et al. (2001) have shown that hydrates can be formed in artificial glass pores from saturated water, without a free gas phase. They found that with significant subcooling the amount of hydrate formation was proportional to the gas solubility; carbon dioxide formed more hydrates from a saturated solution than did methane. Further, the maximum amount of methane hydrate formation was fairly low—about 3% of the pore volume—a value consistent with the amount of hydrates in sediment.

While hydrate formation from a saturated water phase may be possible, substantial accumulation will require geologic-like times because the concentration of dissolved gas in water is extremely low—only $0.5–2.5 \times 10^{-3}$ methane mole fraction in water and brines at depths from 300 to 5000 m (Hunt, 1979). The concentration of gas in the hydrate (one molecule of gas per six molecules of water)

is much higher than the methane solubility in water (2.5×10^{-3} mol fraction methane) at typical ocean hydrate conditions.

However, as shown in the phase diagrams and accompanying discussion in Chapter 4, hydrate stability is thermodynamically possible in equilibration with only saturated seawater. In the following section it is shown that Klauda and Sandler (2005) calculated the period for hydrate formation to be very long (1–10 million years). Similarly Rempel (1994) provided a model for the formation and accumulation of hydrates, using a moving boundary mathematical technique similar to the Yousif et al. (1988) model. Rempel's model predicts a time period required of 2×10^5 years for a 1% accumulation of hydrates. Xu and Ruppel (1999) showed the time to be greater than 1×10^6 years to generate a substantial hydrate mass using only diffusive fluxes.

Booth et al. (1996) compiled the data for all recovered hydrate samples and determined that 70% of the recovered samples were in the two-phase region, that is, at pressures higher (or temperatures lower) than the three-phase boundary, as shown in Figure 7.7. This result gives validity to the suggestion that

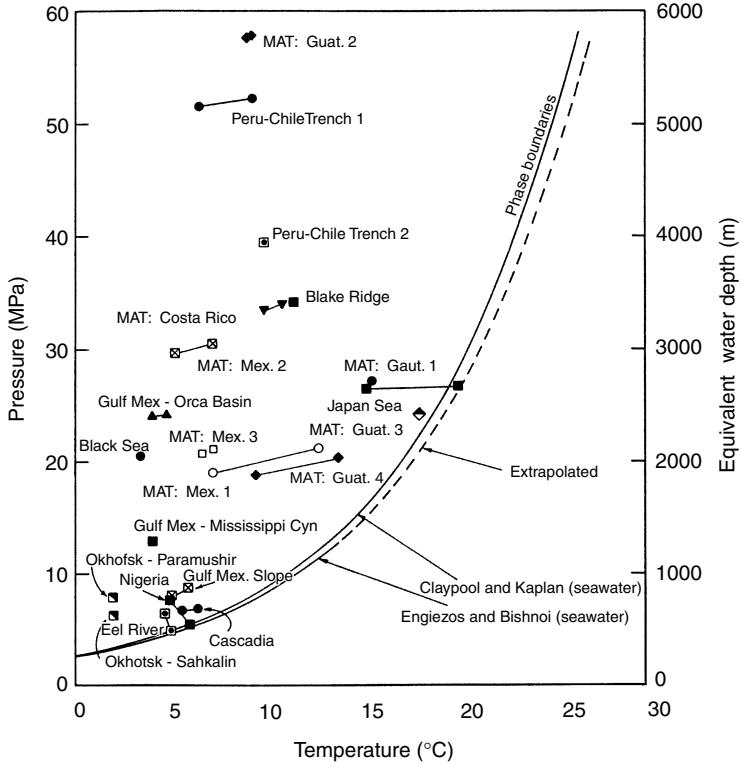

FIGURE 7.7 Compilation of data for recovered hydrate samples in relation to the three-phase boundary. (Courtesy of Booth et al., 1996.)

hydrates form from methane-saturated water. It is unlikely that 70% of the recovered hydrates formed at the three-phase line and then moved into the two-phase region. The two-phase hydrate formation mechanism is discussed further in Section 7.2.3.2.3.

More importantly, the result of Booth et al. also suggests that only massive hydrate samples can survive the trip from the bottom of the ocean to ship deck. For example, if the massive MAT: Guatemala 2 sample (topmost in Figure 7.7) were recovered at constant pressure, the temperature would need to rise more than 16°C before the sample reached the three-phase line, where dissociation would begin. This result is consistent not only with laboratory determinations for dispersed hydrates (Kumar et al., 2004; Paull et al., 2005; Wright and Dallimore, 2005) but also shows the parallel of recovered core dissociation with radial dissociation due to depressurization in pipelines, modified for sediment content (Davies and Sloan, 2006).

This requirement for a large increase in temperature below the phase boundary may have enabled the MAT: Gautamala 2 sample to survive the trip from seafloor to shipboard. However, upon recovery and heating of smaller, more dispersed *in situ* samples at the three-phase condition, dissociation will begin almost immediately, so that the sample may not survive nonpressurized recovery. In contrast to small hydrates, massive hydrates are aided in slow dissociation by a low surface to volume ratio, together with the protective formation of an ice layer by the dissociated water (Yakushev and Istomin, 1991; Gudmundsson and Parlaktuna, 1992).

The smaller dispersed hydrates, which are considered more pervasive, may be heated to the three-phase boundary more readily due to the high surface to volume ratio of small particles. Small particles may decompose before they are recovered, as suggested by Paull et al. (2005) and by Klauda and Sandler (2005). Thus the amount of hydrates may be underestimated via the method of gas evolution from nonpressurized cores. Much of the dispersed hydrates may have dissociated on the trip from the seafloor to shipboard (Paull et al., 2005).

7.2.3.2 Models for *in situ* hydrate formation

Based upon an overview of several years of research sponsored by the U.S. Department of Energy, R.D. Malone (1985) suggested that hydrates occur in four types, each of which is depicted in Figure 7.8:

1. The first type of hydrate is finely disseminated. Due to their disseminated nature, these hydrates may dissociate rapidly, frequently within the time span of a core's trip from the seafloor to shipboard, leaving residual traces of pore water freshening, or low temperatures, because of the endothermic heat of dissociation. As discussed in this section, disseminated hydrates represent the large majority of hydrates in the ocean.

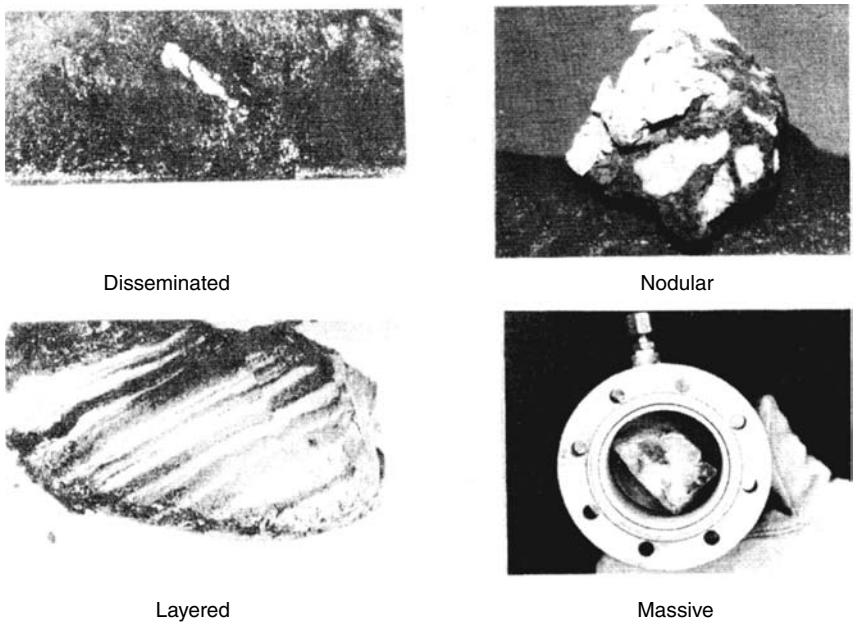

FIGURE 7.8 Photographs of four types of hydrates. (R.D. Malone, courtesy of W.F. Lawson, U.S. Department of Energy, 1988.)

2. Nodular hydrates up to 5 cm in diameter may occur, such as found in the Green Canyon Gulf of Mexico; the gas in these hydrates may be of thermogenic origin that migrated from depth.
3. Layered hydrates are separated by thin layers of sediments, such as cores recovered from the Blake-Bahama Ridge. Such hydrates probably occur both offshore and in permafrost regions.
4. Massive hydrates, such as the one recovered from Site 570 of DSDP Leg 84 off the MAT, may be as thick as 3–4 m and contain more than 95% hydrate. While there is some question as to whether this sample is of biogenic origin (Kvenvolden and Claypool, 1985) or thermogenic origin (Finley and Krason, 1986a), it appears that much of the gas migrated to the hydrate site, and either formed along a fault, or pushed aside sediments as the massive hydrate grew, using the pressure of crystallization indicated by Torres et al. (2004) and Sassen et al. (2004).

Brooks et al. (1985) suggested that since most Gulf of Mexico hydrates were found to be biogenic, if disseminated, and thermogenic, if more massive. Thermohydrates may have a greater supply of gas through faults and diapirs. They note, however, that hydrate formation is influenced by a number of other factors, among which are sediment texture, formation of authigenic carbonate rubble, and shallow faulting and fracturing of the sediments.

Figure 7.9 (from Roberts, 2001) gives an overview mechanism of hydrate formation in the Gulf of Mexico as a function of the flux of methane through sediments:

1. Low gas fluxes result in mineralization, such as carbonate mounds, cones, and chimneys, with very localized and poorly developed chemosynthetic communities, and highly biodegraded hydrocarbons.
2. Moderate gas fluxes result in gas hydrate mounds, dense diverse chemosynthetic communities, (Beggiatoa, tube worms, clams), and moderately degraded hydrocarbons.
3. Rapid gas fluxes result in mud volcanoes and vents, localized bacterial mats and clams, and nonbiodegraded hydrocarbons.

Such a summary overview for the Gulf of Mexico, also finds a clear example in the case study of Hydrate Ridge. While Roberts provided a qualitative summary of the three ranges of gas fluxes, his conceptual picture evolved from a career of field experiments, serves as a basis for quantification, such as in the following models.

There are three current models of hydrate formation in the literature: (1) *in situ* formation from biogenic methane, (2) formation from free (perhaps recycled) gas traveling upward, and (3) formation by upward mobile water which exsolves the gas used for hydrate formation. Each model is discussed briefly in Sections 7.2.3.2.1–7.2.3.2.3.

7.2.3.2.1 Hydrate formation by in-place biogenic methane

Kvenvolden and Barnard (1983) and Brooks et al. (1985) followed the Claypool and Kaplan (1974) suggestion that free methane can be generated in place using the diagenetic mechanism indicated above. Brooks et al. (1987) indicate that twice the methane solubility amount can be achieved by *in situ* production.

However, other researchers suggest that considerably less methane can be generated by *in situ* hydrate production. Hyndman and Davis (1992) indicated that an unaccountably high concentration of gas was required for hydrate formation. Minshull et al. (1994), Paull et al. (1994), and Klauda and Sandler (2005) suggest that for in-place formation, under the best conditions the maximum amount of hydrate that can fill the sediments is 3%.

Hydrate generation by in-place diagenesis is thought to produce the most uniform layers and may be responsible for uniform seismic responses, such as BSRs (Ginsburg and Soloviev, 1998, p. 151). However, as shown in Section 7.4.2, BSRs are only a first-order tool for hydrate prospecting and have a substantial number of false indications, both positive and negative. Consider the conceptual picture of in-place hydrate formation. Carbon-containing components fall to the bottom of the ocean and are buried. The diagenesis occurs producing methane below the SMI. Finally hydrates form with the produced biogenic methane. The process is very slow, because the temperature is very low (typically 277 K) relative to most man-made chemical reactions.

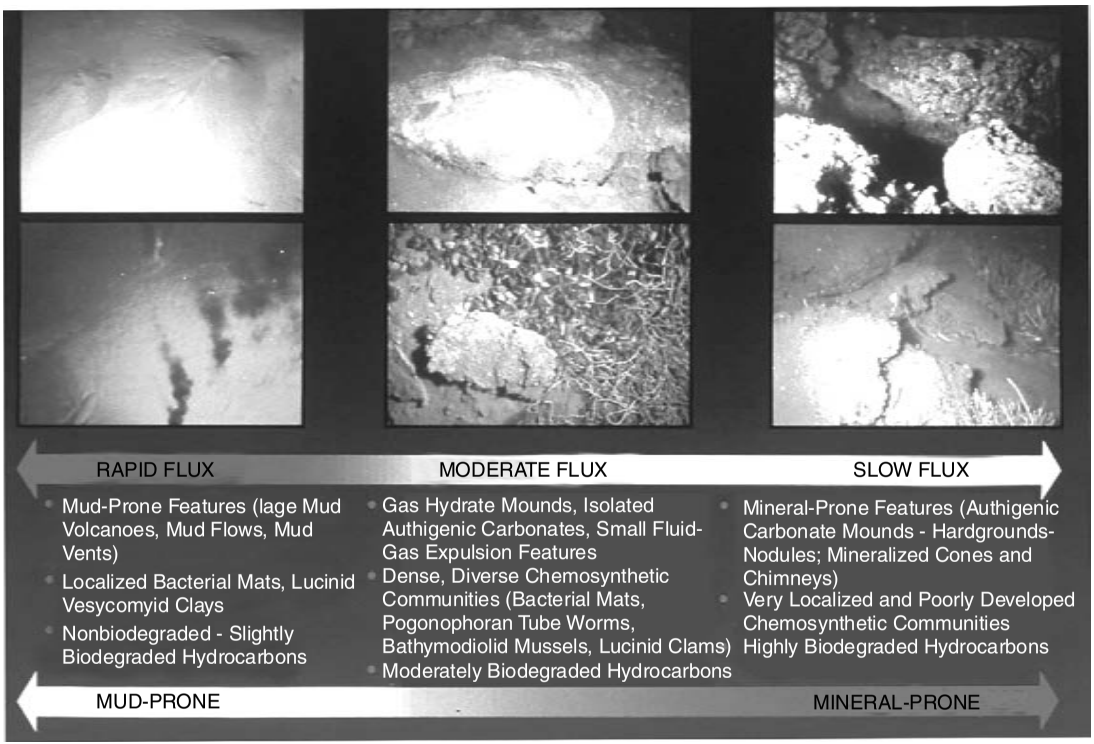

FIGURE 7.9 **(See color insert following page 390.)** Qualitative relationships between fluid fluxes and geologic–biologic response. Each picture has a field of view 3–4 m across. (From Roberts, H.H., in *Natural Gas Hydrates: Occurrence, Distribution and Detection*, (Paull, C.K., Dillon, W.P., eds.) p. 145. American Geophysical Union, Washington, DC (2001). With permission.)

Consider the recent model of Klauda and Sandler (2005) for in-place hydrate formation. Their hydrated gas estimate [120×10^{15} m^3 methane (STP)] was made using a different method from those of all preceding estimates. First a new *ab initio* thermodynamic model was generated to include effects of pores and salt. Then measured local temperatures and gradients in each of the world's oceans were used to determine the intersection of the geothermal gradient with the phase boundary, without restriction to depth. Measured local organic sediment contents were also used to serve as input to the methanogenesis mass transfer model of Davie and Buffett (2001, 2003), which was matched to the Blake-Bahama Ridge data of ODP Leg 164 to determine a minimum organic content of >0.4 wt% carbon was required and that a global pore volume average of 3.4% of hydrate existed.

The above summary suggests that hydrates were generated *in situ*, by the decomposition of organic matter. It is interesting to note that the model of Klauda and Sandler (2005) provides local estimates that sum to a large global value of 1.2×10^{17} m^3 methane (STP) but that estimate includes very deep hydrates, as well as dispersed small concentrations of hydrates that may dissociate during core recovery. When only continental margins are considered (as with the geoscience models) Klauda and Sandler reduce the estimate to 4.4×10^{16} m^3 methane (STP), more comparable to other recent estimates.

The Klauda and Sandler model can be used to predict the uniformly distributed hydrates that form in place on the seafloor with a resulting BSR, rather than those associated with rapid convective fluxes, which tend to be associated with faults, and thus more anecdotal in nature. Klauda and Sandler note that their model can be used to predict 68 of 71 local occurrences where hydrates have been found around the world, and explain the three exceptions. The ability to predict hydrate occurrences is a significant step in model verification.

7.2.3.2.2 Hydrate formation by migration of free gas

Paull et al. (1994) and Minshull et al. (1994) proposed models dealing with hydrate formation by the upward migration of free gas. The rudiments of the model suggest that free gas from below the hydrates migrates through fissures or permeable sediments and forms hydrates at nucleation/growth sites. Gas may come from either free biogenic gas or from dissociated hydrates.

Paull et al. (1994) provided a model for hydrate formation from free and recycled gas, as shown in Figure 7.10. In this model, the base of the gas hydrate stability (BGHS) field moves upward with progressive burial/subsidence through times 1, 2, and 3. Shown in Figure 7.10 at time 2, the former BGHS has been displaced upward, leading to decomposing hydrates. As hydrates decompose, the methane solubility limit is surpassed, so that so-called recycled rising gas bubbles permeate fissures in the overlying hydrate stability layer. At time 3 a higher gas stability zone and layer is achieved.

Two independent experiments have formed hydrates from free gas bubbles at the ocean bottom. Sassen and McDonald (1997) in the Gulf of Mexico and Brewer et al. (1997) off California have performed undersea experiments to show that hydrates readily form from artificial methane and carbon dioxide in sea water.

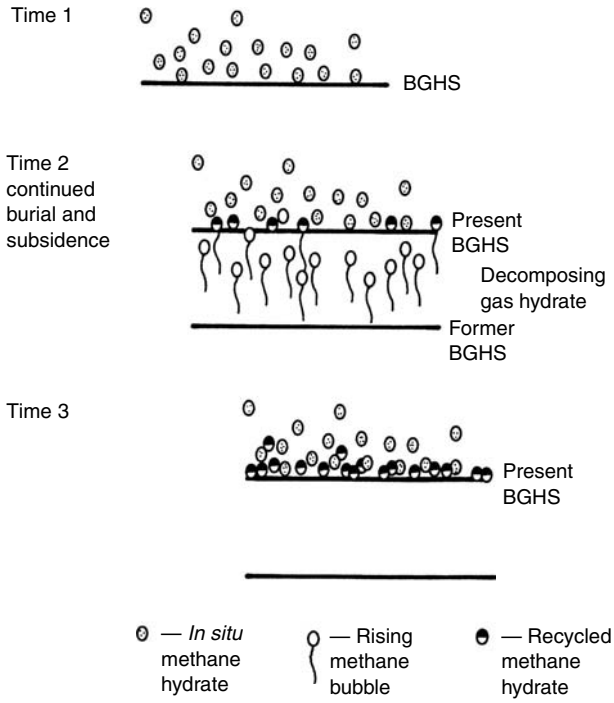

FIGURE 7.10 Proposed model of hydrate formation by upward migration and recycling of gas. (Reproduced from Paull, C.K., Ussler, W., Borowski, W.S., in *Proc. First International Conference on Natural Gas Hydrates*, **715**, 392 (1994). With permission from the New York Academy of Sciences.)

7.2.3.2.3 Hydrate formation from gas dissolution of rising water

Hyndman and Davis (1992) proposed that as methane-unsaturated water rises, it becomes saturated at lower pressures. As the saturated (or supersaturated) water passes through the phase stability zone, hydrate formation occurs without a free gas zone. This model results in a maximum hydrate concentration at the three-phase (BSR) boundary with a successively lower hydrate amounts above the BSR as was shown to be the case in Cascadia Margin ODP Drill Sites 889 and 890 by Hyndman et al. (1996).

From Chapters 4, 5 and 6 thermodynamic data and predictions, the maximum methane concentration (solubility) occurs in the aqueous liquid at equilibrium with hydrates. In order for methane to exsolve the liquid, the solubility must change rapidly as the water rises with corresponding decreases in pressure and temperature. Solubility calculations (Handa, 1990) indicate a change in methane concentration too gradual to account for a significant hydrate amount. Solubility data are needed at conditions of hydrate formation, in order to confirm this model. Preliminary solubility data are available from Besnard et al. (1997).

Rempel (1994) provided a model for the formation and accumulation of hydrates, using a moving boundary mathematical technique similar to the

Yousif et al. (1988) model. Rempel's model predicts a hydrate volume fraction of less than 1%, with a time period required of 2×10^5 years for a 1% accumulation of hydrates.

Xu and Ruppel (1999) solved the coupled mass, heat, and momentum equations of change, for methane and methane-saturated fluxes from below into the hydrate stability region. They show that frequently methane is the critical, limiting factor for hydrate formation in the ocean. That is, the pressure–temperature envelope of the Section 7.4.1 only represents an outer bound of where hydrates might occur, and the hydrate occurrence is usually less, controlled by methane availability as shown in Section 7.4.3. Further their model indicates the fluid flow (called advection or convection) in the amount of approximately 1.5 mm/yr (rather than diffusion alone) is necessary to produce significant amount of oceanic hydrates.

7.3 Sediment Lithology and Fluid Flow are Major Controls on Hydrate Deposition

In a recent ocean hydrate formation state-of-the-art summary, Tréhu et al. (2006) listed the effects of fluid flow and sediment lithology. Ocean hydrate deposits are distributed on a spectrum between two types in ocean sediments: (1) focused high flux (FHF) gas hydrates, and (2) distributed low flux (DLF) gas hydrates. In FHF hydrates the gas comes from a large sediment volume channeled through a high-permeability sand to the point of hydrate formation, and these hydrates are typically in the upper tens of meters of the sediment. In contrast, the DLF hydrates are generated near where the hydrates are formed, and fluid flow is responsible for movement of the gas within the gas hydrate occurrence zone (GHOZ).

Table 7.7 contrasts FHF and DLF hydrates. It should be emphasized that both hydrates are end-member types with the frequent occurrence of mixed types. For example, while Table 7.7 typifies Blake Ridge as DLF hydrates and Barkley Canyon as FHF hydrates, there is often a mixture of both types as shown in the Leg 204 study in the Cascadia Margin. As a second example, while the Gulf of Mexico is normally known for FHF hydrate deposits, Hutchinson et al. (2004) provide evidence for some elements that have DLF characteristics.

7.4 Remote Methods Enable an Estimation of the Extent of a Hydrated Reservoir

In addition to the thermodynamic and kinetic models shown above, which use parameters such as temperature, pressure, and carbon content, three initial detection tools enable initial estimates of hydrates in an ocean geologic setting: (1) the thermodynamic pressure–temperature stability data of Chapters 5 and 6, combined with the geothermal gradient, determine the maximum stability depth, (2) seismic methods such as BSR provide tentative assessments of the area and the maximum depth (lower boundary) of hydrate formation, and (3) methane solubility that determines the top and bottom stability within the P–T region of item (1). These are considered in Sections 7.4.1, 7.4.2, and 7.4.3, respectively.

TABLE 7.7
Two End-Member Hydrate Deposits

FHF gas hydrates	DLF gas hydrates
Rich, localized hydrate deposits	Broadly distributed, lean hydrate deposits
Related to mounds, vents, pockmarks	Related to dispersed, low concentrations
CH_4/H_2O from kilometers below seafloor	CH_4 generated near hydrate deposit
High-permeability conduits	Low-permeability flow
Frequently are deposited in sands	Frequently are deposited in shales
Forming flow rapid: convective and diffusive	Forming flow is slow; frequently diffusive
Form within tens of meters of mud line	Form deeper in occurrence zone GHOZ
Represent a small amount of hydrates	Represent the majority of hydrate
Not normally predicted by models	Frequently modeled
Can be massive gas hydrates	Hydrates dispersed less than—5% of pore volume
Found by seafloor imaging and protrusions	Found by BSR and GHOZ zones
Can be structure I, II, or H hydrates	Usually structure I, biogenic gas hydrates
Can have complex fauna with them	Usually associated with shales, not fauna
Represented by Barkley Canyon hydrates	Represented by Blake Ridge hydrates

7.4.1 The Hydrate Pressure–Temperature Stability Envelope

There are four requirements for generation of natural gas hydrates: (1) low temperature, (2) high pressure, (3) the availability of methane or other small nonpolar molecules, and (4) the availability of water. Without any one of these four criteria, hydrates will not be stable. As indicated in both the previous section and in Section 7.4.3, the third criteria for hydrate stability—namely methane availability—is the most critical issue controlling the occurrence of natural gas hydrates. Water is ubiquitous in nature so it seldom limits hydrate formation. However, the first two criteria are considered here as an initial means of determining the extent of a hydrated reservoir.

Figures 7.11a,b are arbitrary examples of the depths of hydrate phase stability in permafrost and in oceans, respectively. In each figure the dashed lines represent the geothermal gradients as a function of depth. The slopes of the dashed lines are discontinuous both at the base of the permafrost and the water–sediment interface, where changes in thermal conductivity cause new thermal gradients. The solid lines were drawn from the methane hydrate P–T phase equilibrium data, with the pressure converted to depth assuming hydrostatic conditions in both the water and sediment. In each diagram the intersections of the solid (phase boundary) and dashed (geothermal gradient) lines provide the lower depth boundary of the hydrate stability fields.

In Figure 7.11a, it is important to note that in the region between the three-phase line and the geothermal gradient, hydrates are stable with only one other phase. The second phase is in excess—in most cases, liquid water containing

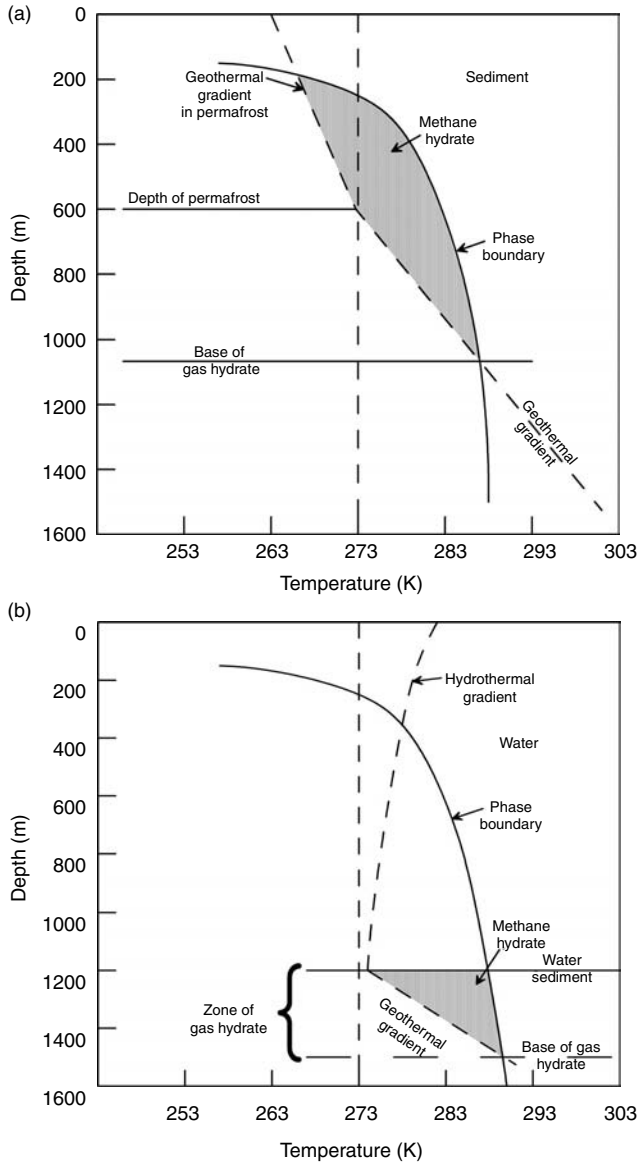

FIGURE 7.11 Envelopes of methane hydrate stability (a) in Permafrost and (b) in Ocean sediment. (Reproduced from Kvenvolden, K.A., *Chem. Geol.*, **71**, 41 (1988). With permission from Elsevier Science Publishers.)

dissolved methane. Once hydrates are initiated, further nucleation can occur in the two-phase region with increases in pressure, decreases in temperature, or addition of methane as determined by the solubility limits. Quantitative two-phase P–T-solubility conditions are provided in Chapter 6.

In Figure 7.11b one would not expect hydrates to be stable in the region above the seafloor sediment due to an absence of means to concentrate gas in water and a means of retaining the hydrates, because hydrate density (sp. gr. 0.9) is less than that of seawater. In both Figures 7.11a,b, a small addition of heavier natural gas components, such as ethane, propane, or isobutane, will cause the hydrate stability depth to increase due to a displacement of the phase boundary line away from the geothermal gradient. In neither case, however, have hydrates been found at depths greater than about 2000 m below the surface, due to the high temperatures resulting from the geothermal gradient.

For methane hydrate, the minimum water depth is 381 m in freshwater and upto 436 m in seawater, respectively, at 277 K. In the world's oceans at water depths greater than 600 m, the temperature is typically uniform at 277 K, due to the density maximum in seawater. Lower bottom water temperature exceptions can be found with strong subbottom currents from Antarctic and Arctic environments such as the north of Norway or Russia. Methane-phase equilibrium data in Chapter 6, indicate that 3.81 MPa are required to stabilize methane hydrates at 277.1 K. Using the rule of thumb 1 MPa = 100 m water, hydrates in pure water would be stable at depths greater than 381 m.

At a sea salt concentration totaling 3.5 wt%, using the thermodynamic data of Dholabhai et al. (1991) in Chapter 6, a pressure of 4.364 MPa (a minimum seawater depth of 436 m—about 55 m deeper than in pure water) is required to stabilize hydrates at 277 K. Further corrections to the phase boundary are required considering effects of (1) hydrocarbons other than methane, (2) salt concentrations other than 3.5 wt%, and (3) sediment pores or capillary pressure, as indicated in Chapter 5.

Two final points should be made regarding the hydrate pressure–temperature limits shown in Figures 7.11a,b. The intersection of the phase boundary with the geothermal gradient limits the lower stability depth of hydrates. In Section 7.4.2, it will be shown that this intersection usually coincides with the BSR, an approximate exploration tool, which is caused by a seismic velocity decrease from hydrates above, to gas below the reflector.

Second, the hydrates at the lower stability depth are the most easily dissociated because they are at the phase boundary. At some constant depth, above the lower intersection of the two lines, the hydrates (along with their encasing sediments) that exist at the geothermal gradient must be heated to the phase boundary resulting in a loss of recovery efficiency, due to the requirement of heating the hydrated sediment before dissociation.

Example: What Fraction of Hydrate Reserves are Economical to Recover for Energy?

If we assume that the temperatures and pressures of the hydrate samples in Figure 7.7 are representative of worldwide hydrate reservoirs, we can use the principles of Figure 7.11 to estimate what fraction of hydrated reservoirs

are economical for energy recovery. At 100% efficiency, the energy obtained from the gas, as measured by the heat of combustion, must equal to or be greater than the sensible energy to bring the hydrates from the geothermal line to the phase boundary in Figure 7.11, and the energy of dissociation. This can be expressed as enthalpy (energy corrected for pressure and volume).

$$\Delta H^{\text{combustion}} = \Delta H^{\text{sensible}} + \Delta H^{\text{dissociation}} \tag{7.4}$$

The values in Equation 7.4 may be calculated, assuming that hydrates occupy 3% of the typical pore volume of 30%, as determined by field studies. Using Equation 7.4 one may perform the following calculation (Gupta, A.R., Personal Communication, January 13, 2006):

Assumptions

1. Basis: 1 m^3 of reservoir of 30% porosity, with 3% of the pore volume as hydrates
2. Volume of rock in 1 m^3 with 30% porosity = 0.7 m^3
3. Volume of hydrates (seawater) in 1 m^3 of reservoir = 0.009 m^3_{hydrate}, (0.291 m^3_{seawater})
4. Only hydrates and seawater exist in the pore volume
5. Heat of methane combustion = 37,250 kJ/m^3 of gas
6. Heat of hydrate dissociation = 368,803 kJ/m^3 of hydrate
7. Heat capacity of hydrate, seawater, and rock is 2500, 4180, 2240 kJ/m^3 K, respectively

Step 1: Calculate the energy gained from combustion ($\Delta H^{\text{combustion}}$ in Equation 7.4)

$$\frac{37{,}250\ \text{kJ}}{\text{m}^3\ \text{gas}} \times \frac{170\ \text{m}^3\text{gas}}{\text{m}^3\ \text{hydrate}} \times \frac{0.009\ \text{m}^3\ \text{hydrate}}{\text{m}^3\ \text{reservior}} = 56{,}992.5 \frac{\text{kJ}}{\text{m}^3\ \text{reservoir}}$$

Step 2: Calculate the energy required to dissociate hydrate

(2a) Calculate the sensible heat required to move reservoir to three-phase temperature at constant pressure ($\Delta H^{\text{sensible}}$ in Equation 7.4), that is,

$$= \left(\frac{0.7\ \text{m}^3\ \text{rock}}{\text{m}^3\ \text{reservior}} \times \frac{2240\ \text{kJ}}{\text{m}^3\ \text{rock-K}} + \frac{0.291\ \text{m}^3\ \text{water}}{\text{m}^3\ \text{reservior}} \times \frac{4180\ \text{kJ}}{\text{m}^3\ \text{water-K}} + \frac{0.009\ \text{m}^3\ \text{hydrate}}{\text{m}^3\ \text{reservior}} \times \frac{2500\ \text{kJ}}{\text{m}^3\ \text{hydrate-K}} \right) \times (T_{\text{eqm}} - T_{\text{sys}})$$

$$= \left(\frac{2806.88\ \text{kJ}}{\text{m}^3\ \text{reservior}} \right) \times (T_{\text{eqm}} - T_{\text{sys}})$$

(2b) Calculate the energy of hydrate dissociation ($\Delta H^{\text{dissociation}}$ in Equation 7.4), that is,

$$\frac{368{,}803\ \text{kJ}}{\text{m}^3\ \text{hydrate}} \times \frac{0.009\ \text{m}^3\ \text{hydrate}}{\text{m}^3\ \text{reservior}} = 3{,}319.22 \frac{\text{kJ}}{\text{m}^3\ \text{reservior}}$$

Total heat input to dissociate hydrate

$$= \left(\frac{2{,}806.88\ \text{kJ}}{\text{m}^3\ \text{reservior}}\right) \times (T_{\text{eqm}} - T_{\text{sys}}) + \left(\frac{3{,}319.22\ \text{kJ}}{\text{m}^3\ \text{reservior}}\right)$$

At breakeven point:
Heat input = Heat output

$$\left(\frac{2{,}806.88\ \text{kJ}}{\text{m}^3\ \text{reservior}}\right) \times (T_{\text{eqm}} - T_{\text{sys}}) + \left(\frac{3{,}319.22\ \text{kJ}}{\text{m}^3\ \text{reservior}}\right) = \left(\frac{5{,}6992.5\ \text{kJ}}{\text{m}^3\ \text{reservior}}\right)$$

$$(T_{\text{eqm}} - T_{\text{sys}}) = 19.09\ \text{K}$$

The example shows that if such hydrates are further than 19 K from the phase boundary, it will never be economical to recover the hydrated methane to use for energy. This subcooling is greater than almost all of the recovered hydrate samples shown in Figure 7.7.

7.4.2 Seismic Velocity Techniques and Bottom Simulating Reflections

Seismic velocity techniques for hydrate detection have two components: (1) translation of seismic signals to velocity and (2) translation between velocity and detection of hydrates. The first component is beyond the scope of this monograph. However, a brief consideration will be given to advances in translating velocity to the detection of hydrates.

For hydrates in ocean sediments, the technology for detecting the BSR was determined in 1953 with the development of a precision ocean depth recorder (Hamblin, 1985, p. 11). In this technique a sonic wave penetrates (and is reflected from) the ocean floor, with the time recorded for the return of the reflected wave to the source. Velocity contrasts beneath the ocean floor mark a change in material density, such as would be obtained by hydrate-filled sediments overlying a gas. BSRs related to hydrates are normally taken as indications of velocity contrasts between velocity in hydrated sediments and a gas, marked by a sharp decrease in sonic compressional velocity (Vp) and a sharp increase in shear velocity (Vs) (Ecker et al., 1996).

Hyndman and Spence (1992) indicated that about one-third of the pore space should be filled with hydrate to give a BSR impedance contrast at the Cascadia

Margin; the sediments contain 15–20% (volume) hydrate. This 33% of the total might be taken as a maximum for the hydrate indicated by a BSR. Hyndman and Davis (1992) indicated that the *V*p decrease (1) suggested a gradational boundary with the thickest hydrate at the BSR and lesser hydrate concentrations above the BSR and (2) that the BSR did not require a gas layer beneath the hydrate.

Andreassen (1995) used the amplitude versus offset (AVO) technique to determine the phases at the BSR interface. The classical AVO technique, as stated by Ostrander (1984), measures the angle-dependent P-wave ratio amplitude (reflected to incident). Andreassen and coworkers determined that usually gas is just below the hydrate layer.

While the AVO technique can be used to determine the phases at the BSR interface, Nur and coworkers (Dvorkin and Nur, 1992; Ecker et al., 1996) used AVO to determine that hydrates were usually located away from grain contacts, only partially filling the pore space. That is, in theory, hydrates typically do not cement the grains of unconsolidated sediment, when reflections are weak and permeability is low.

Figure 7.12a shows the most famous BSR related to hydrates, in the Blake-Bahama Ridge. Sediments associated with this reflector have been drilled on two ODP voyages, the more recent (Leg 164) in December 1995. Figure 7.12b illustrates velocity of the wave in the sediment (at the arrow in 7.12a) as a function of depth. Table 7.8 shows the areal extent of many of the BSR's cited in the hydrate locations of Table 7.4.

Ginsburg and Soloviev (1998, pp. 150–151) state that the BSR is the most widely used indirect indication of gas hydrates. "The most important evidence of the hydrate caused nature of the BSR is the coincidence of temperature and pressure calculated at it's depth with the equilibrium temperatures and pressure of gas hydrate stability . . . . The association with the base of the hydrate stability zone is beyond question."

Paull et al. (1996) summarized requirements for a BSR as the following:

1. Subbottom depths that parallel the ocean floor, varying with water depth in accordance with the phase diagram.
2. Anomalously high seismic velocities ($V_p > 2.0$ km/s) directly above the BSR.
3. Polarity reversals at the BSR, lower velocities than seawater (<1500 m/s) beneath the BSR perhaps indicating free gas.
4. Blanking or transparent zone above the BSR with a very low impedance contrast.
5. High reflectivity in a zone as much as several hundred meters beneath the BSR.

While the BSR was originally considered as a means of obtaining the areal extent of hydrate, a classic article by Lee et al. (1993) provided a method to determine the amount of hydrate, assuming that the porosity of the sediment is known. Waveform inversion techniques proposed by Minshull and coworkers

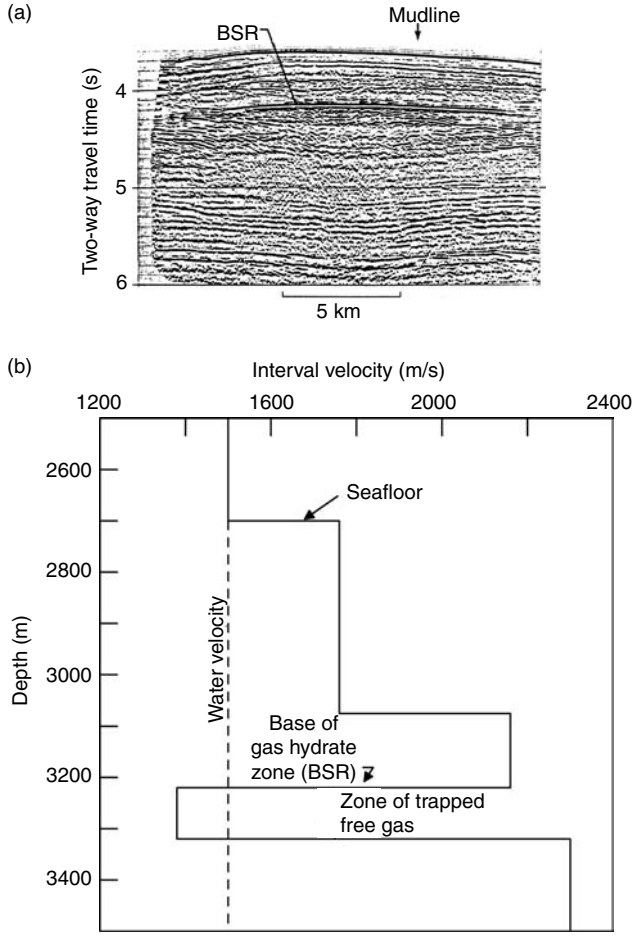

FIGURE 7.12 (a) Bottom simulating reflector for hydrate deposit in Blake-Bahama Ridge. (b) Velocity analysis at location of arrow of BSR in (a). (Reproduced courtesy of U.S. Geological Survey, Dillon and Paull, 1983.)

(1994, 1996), Singh and Minshull, 1994), Hyndman and coworkers (1996) and Yuan et al. (1996) represent significant improvements. All models are reviewed and compared by Lee et al. (1996) who proposed a new, weighted equation to determine the hydrate amount. It should be noted that BSRs are also useful in determining heat flows through sediments, as shown by Yamano and Uyeda (1990) for the Peru BSR and by Hyndman et al. (1992) for the Cascadia Margin BSR.

Table 7.8 suggests that hydrates are commonly found in the oceans, yet care must be exercised, because BSRs are not reliable as sole indicators of hydrates. For example, Finley and Krason (1986a) indicate Sites 490, 498, 565, and 570 on DSDP Leg 84 in the MAT where hydrates were recovered without BSRs present. Conversely, BSRs existed beneath Sites 496 and 569, yet no hydrates were

TABLE 7.8
Ocean Gas Hydrate Bottom Simulating Reflector (BSR) Extent

Number in Figure 7.2 and Table 7.4	Location	Extent and reference area/depth
P1	Pacific Ocean off Panama	4,500 km^2 poor BSR data 250–550 m subbottom depth Krason and Ciesnik (1986a)
P2 and P3	MAT off Costa Rica and Nicaragua	14,000 km^2 variable quality BSR data 600 m subbottom depth Finley and Krason (1986a)
P4	MAT off Guatemala	23,000 km^2 variable quality BSR data 0–450 m depth Finley and Krason (1986a)
P5	MAT off Mexico	19,000 km^2 variable quality BSR data 0–640 m subbottom depth Finley and Krason (1986a)
P7	Eel River Basin off California	3,000 km^2 200 m subbottom depth Krason and Ciesnik (1986b)
P31	Peru–Chile Trench off Peru	Areal BSR extent not available 350–570 m subbottom depth
A6	Colombia Basin off Panama and Colombia	30,000 km^2 60–200 m subbottom depth Finley and Krason (1986b)
A7	W. Gulf of Mexico off Mexico	8,000 km^2 good BSR data 100–600 m subbottom depth Krason et al. (1985)
A9	Blake outer Ridge off SE USA	31,000 km^2 good BSR data 22,000 km^2 acceptable BSR data 245 m subbottom depth at Site (533) Krason and Ridley (1985a)
A11	Baltimore Canyon off E. USA	12,600 km^2 good BSR data 19,150 km^2 acceptable BSR 450–600 m subbottom depth Krason and Ridley (1985b)
A12	Labrador Shelf off Newfoundland	$<$100 km^2 poor BSR data 20–600 m subbottom depth Krason and Rudloff (1985)
N1	Beaufort Sea off Alaska	Areal BSR extent not available 100–800 m subbottom depth Grantz et al. (1976)
A13	Continent Slope off W. Norway	Not available
I1	Makran Margin, Gulf of Oman	Undetermined area 350–700 m subbottom depth White (1979)

TABLE 7.8
Continued

Number in Figure 7.2 and Table 7.4	Location	Extent and reference area/depth
P9	Cascadia Margin off Vancouver	30 km wide band, 300 m subbottom Hyndman and Spence (1992); Yuan et al. (1996)
P8	Cascadia Margin off Oregon	73 m subbottom depth; undefined area Westbrook et al. (1994)

recovered by coring to within 200 m (vertical) of the BSR. Similarly at Site 994 of Leg 164, hydrates were recovered without a BSR indication. Since 1998 we have come to realize that the BSR absence may be caused in places where methane supply limits hydrate formation (Xu and Ruppel, 1999) or by localized hydrates along a channel or diapir such as in the Gulf of Mexico (Paull et al., 2005).

However, as indicated by Kleinberg (2006) there is the need for a much better prospecting tool than the BSR, due to reliability issues. First, very little gas is required to produce a strong seismic reflector (Domenico, 1977). Second, an apparently continuous reflector does not imply a continuous gas-saturated zone. It is now well established by high resolution seismic techniques that BSRs that appear continuous in conventional marine seismic can actually be because of discontinuous patches of gas (Wood et al., 2002; and Dai et al., 2004). As a final example, the recent drilling of a BSR off the west coast of India failed because the BSR was caused by a carbonate deposit, rather than hydrates (Collett, T., Personal Communication, November 6, 2006).

In addition to BSRs and the intersections of the geothermal gradients with the hydrate phase boundary, the transport and kinetic tools discussed in the Section 7.2 [e.g., Xu and Ruppel (1999), Davie and Buffett (2001, 2003) or most recently Klauda and Sandler (2005)] can be used as first-order predictions of where hydrates exist.

Johnson (Personal Communication, March 6, 2006) suggests that hydrate indications by BSRs have been superseded by other, more reliable geological factors, "The key elements of commercial gas hydrate prospects are (1) reservoir quality sands, (2) sufficient gas flux, and (3) the GHSZ. Where all three are together commercial accumulations are likely. If any one is missing, there will be no prospect. A BSR will help identify the phase boundary, but has little other value."

7.4.3 Methane Solubility Further Limits the Hydrate Occurrence

Since, as indicated by Johnson, the availability of methane may control the stability of hydrates, a second reason that hydrates may not exist at the bottom of the *P–T*

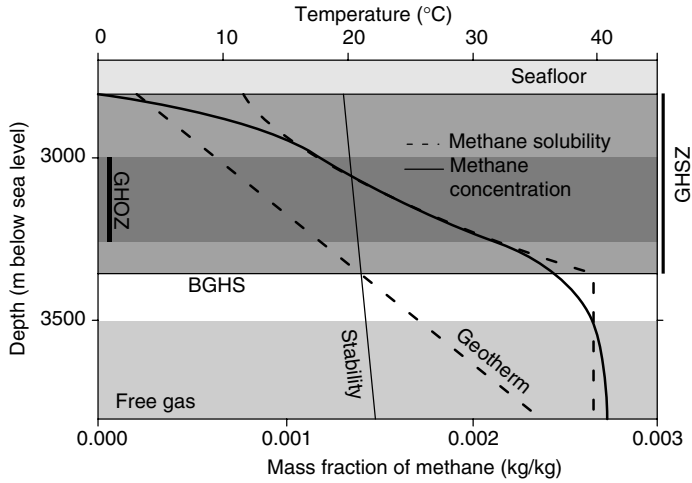

FIGURE 7.13 Methane solubility imposes a narrower limit than the *P–T* stability region for hydrate depth.

stability zone is due to methane solubility. In fact Tréhu et al. (2004a, 2006) suggest that the GHSZ defined by the *P–T* field, be considerably narrower, defined by the methane solubility to be the GHOZ.

As shown in Figure 7.13 the pressure and temperature limits to the hydrate stability exists from the seafloor (because hydrates are less dense than seawater) to the intersection of the geotherm (BGHS). The solubility limit, however, imposes a further depth restriction because the methane concentration must equal the solubility limit to be in equilibrium with hydrates. It is assumed that the sediment provides sufficient nucleation sites so that there is no methane metastability, so hydrate forms in the narrow depth region where methane concentration lies atop the methane solubility line. As illustrated in the Leg 311 case study, the GHOZ is always smaller than the GHSZ.

7.5 Drilling Logs and/Coring Provide Improved Assessments of Hydrated Gas Amounts

After the above initial remote assessments, the more expensive methods of drilling and coring enable refinement of estimation of reservoir hydrate content. Logging tools such as caliper, gamma ray, density, resistivity, and neutron porosity determine the hydrate depth, and to some extent the concentration. To this suite of drilling logs, nuclear magnetic resonance (NMR) spectroscopy has recently proved a valuable addition. Secondary tools, such as infrared (IR) temperature sensing, gas evolution from cores, pore water chlorinity decrease, and computed tomography (CT) of cores, provide two important parameters for the extent of hydrates—namely the extent and concentration of the hydrate reservoir. The SMI and methane solubility zone, both notable additions to the core tool suite, enable

estimation of the top hydrate boundary, as discussed in Sections 7.2.2 and 7.4.3, respectively. Third, it has recently proved possible to perform hydrate assessments at the seafloor, using Raman spectroscopy for assessing hydrate amounts and concentrations. Let us consider the three types of assessment tools.

7.5.1 Open Hole Well Logs

The most recent well log summaries for hydrates is that by Anderson et al. (2005) and the log summary in the Mallik 2002 case study by Collett et al. (2005). While a brief overview is presented below and exemplified in the Mallik 2002 case study, the reader interested in details is encouraged to review the above two documents for a thorough exposition of hydrate open hole well logging.

Collett (1983) and Collett and Ehlig-Economides (1983) studied the logs of 125 wells in the Prudhoe Bay region, to find 102 hydrate occurrences in 32 wells. The analyses of other permafrost wells were based upon the logs of a known hydrate well, the Northwest Eileen State Well Number Two, in which ARCO/Exxon recovered hydrate cores in 1972. Other studies on the effects of hydrates in wells and logs in the permafrost are by Weaver and Stewart (1982), Collett et al. (1984), Kamath and Godbole (1987), Mathews (1986), Collett (1992), Prensky (1995), with the most recent review of hydrate well logs in by Anderson et al. (2005).

In general, all studies indicated difficulty in distinguishing hydrates based on single logs, particularly within the permafrost interval. It is difficult to distinguish hydrates from ice based upon well logs and thus hydrates within permafrost depth boundaries are seldom assessed. To have some confidence in hydrate determination, it is necessary to consider a suite of logs. Figure 7.14 shows that the simultaneous log responses corroborate hydrate interpretations. Table 7.9 provides a summary of the individual responses of well logs to the presence of hydrates, again illustrating the fact that hydrates are difficult to distinguish from ice. The drilling mud log is the most responsive to hydrates, but its response may not be very different from a log for free gas. NMR logs, the most exciting new log development, is discussed briefly below.

Nuclear magnetic resonance logging presents a new and efficient means of hydrate detection. Dallimore and Collett (2005, p. 21) summarize the NMR method as follows:

> Kleinberg et al. (2005) and Takayama et al. (2005) show that NMR-log measurement of sediment porosity, combined with density-log measurement of porosity, is the simplest and possibly the most reliable means of obtaining accurate gas hydrate saturations. Because of the short NMR relaxation times of the water molecules in gas hydrate, they are not discriminated by the NMR logging tool, and the *in situ* gas hydrates would be assumed to be part of the solid matrix. Thus the NMR-calculated "porosity" in a gas-hydrate-bearing sediment is apparently lower than the actual porosity. With an independent source of accurate *in situ* porosities, such as the density-log measurements, it is possible to accurately estimate gas hydrates saturations by comparing the apparent NMR-derived porosities with the actual reservoir porosities . . . . Collett and Lee (2005) conclude that at relatively low gas

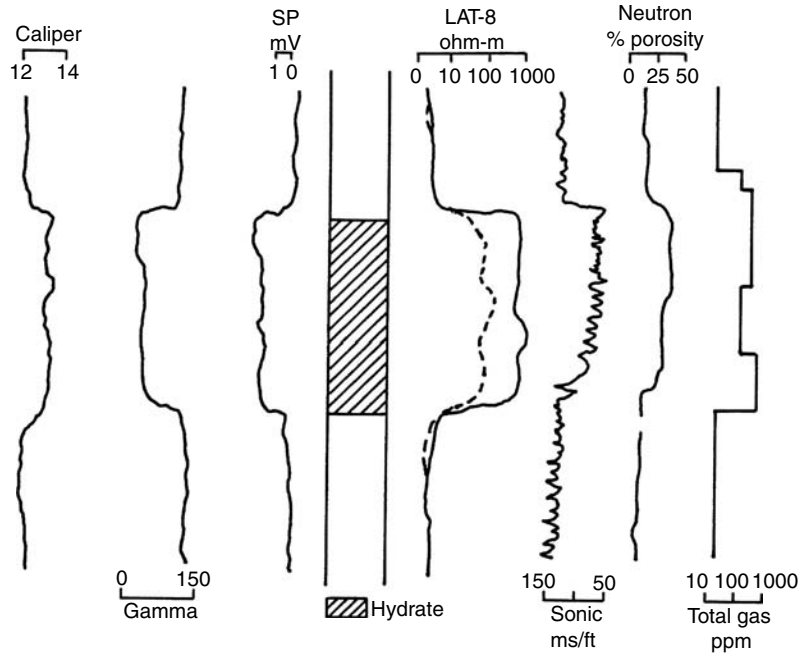

FIGURE 7.14 Typical well log responses to hydrates in permafrost. (Reproduced from Collett, T.S., *Detection and Evaluation of Natural Gas Hydrates from Well Longs*, Prudhoe Bay, U. Alaska, Anchorage (1983). With permission.)

hydrate saturations in shale-bearing sections, the electrical-resistivity derived gas hydrate saturations are sometimes greater than the NMR-density derived gas hydrate saturations. The cause of this difference is unclear at this time.

The Mallik case study (Figures 7.36 and 7.37) provides the best example of well logs in a permafrost hydrate reservoir, followed closely by the Leg 204 (Figures 7.26 and 7.27) example for ocean hydrates. All four of the case studies for field hydrates have associated logs.

7.5.2 Evidence of Hydrates in Cores

There are two types of cores—pressurized, as in the HYACE coring tool developed by Amman et al. (1996) and extended by Schulteiss et al. (2006) to HYACINTH, and the unpressurized coring tools that are more typical of ocean-field experiments. It is important to note the distinction because, while pressurized cores frequently fail due to pressure incontinence, when they function well, they preserve the hydrated core in a much better state than nonpressurized cores, which give unambiguous results only for nonvolatile components such as chloride and sulfates.

When a nonpressurized core is obtained, the trip frequently requires more than 45 min, between the original cored position and the recovery site on the

TABLE 7.9
Summary of Well Log Responses to Hydrates

Type of log	Response to hydrates
Mud log	The dissociation of hydrates causes a significant increase of gas in the drilling mud, which is encountered at the top of the well. Cold or dense drilling fluids may suppress dissociation resulting in lower gas
Dual induction	In the shallow penetration log, a higher resistivity is obtained relative to a free gas zone due to hydrate dissociation. This is a very tricky interpretation problem with Rw changing, and gas and hydrate both being insulators. The deep induction log shows high resistivity and mimics an ice-bearing reservoir. However, this log is confounded by Rw changing, and by gas and hydrate both being insulators
Spontaneous potential	Compared to a free gas bearing zone, the spontaneous potential log is less negative, but similar to that of ice
Caliper log	An oversized drill hole is indicated by hydrate dissociation. This may also occur with ice in the permafrost. However, as noted by Kleinberg (Personal Communication, July 20, 2006) "In some circumstances, hydrates can be a good cement (until it dissociates), and strengthen the unconsolidated host sediment"
Acoustic transit time	The acoustic wave time decreases relative to either water or free gas; however, the acoustic transit time for hydrates is like ice-bearing sediments. See Section 7.4.2 for BSR and AVO in ocean applications
Neutron porosity	For the neutron log, the hydrate response is nearly the same as liquid water. Hydrate is 6% higher than fresh water, somewhat more than that for salt water. Both differences are swamped by the clay effect
Density	The density decrease apparent in hydrates is very small but may be distinguished from the density of water but not from ice density. However, this is a fine difference, and it should be used with the suite of other logs
NMR	The NMR tool senses porosity including water; the porosity without water is determined by another tool (e.g., density), so the amount of hydrates is obtained by difference. See discussion in paragraph starting 'NMR logging . . .'
Drilling rate	The drilling rate also decreases in the hydrate region relative to that in a fluid-saturated sediment, but not significantly different from that of ice

Source: Modified from Collett (1983).

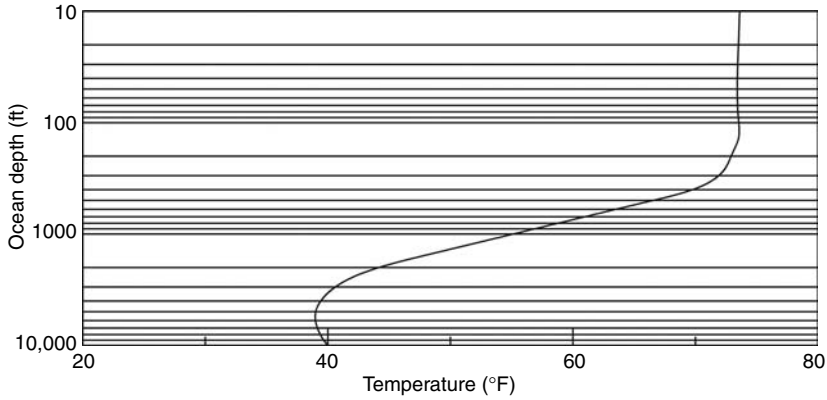

FIGURE 7.15 Gulf of Mexico ocean temperature vs. depth. (From Churgin J., Halminski, S.J., *Key to Oceanographic Records Documentation #2*, *Gulf of Mexico*, Natl Oceanographic Data Center, Washington, DC, 1974. With permission.)

ship or drill site. During this trip time, hydrate dissociates and gas evolves from the nonpressurized core as the core is removed through warmer waters. A typical ocean thermal gradient in the Gulf of Mexico is shown in Figure 7.15, indicating that at most ocean depths below 4000 ft, the water temperature is approximately 40°F, while the ocean-air surface temperature is considerably warmer.

Even when the nonpressurized core is at the surface or aboard the ship, hydrates continue to dissociate, and gas evolves, requiring the drilling of holes in the core liner to relieve the pressure for safety considerations, as shown in Figure 7.16. Because hydrates dissociate in nonpressurized cores, the endothermic heat of dissociation (Chapter 4) causes low temperatures (typically $-1.5°C$) in the cores, which is used as an IR signal of dissociated hydrates in cores. Even with the low temperatures, however, because gas has evolved during the trip to the surface, many dispersed hydrates will completely dissociate before arriving at the surface.

Consequently, gas evolution at the surface cannot be reliably measured for hydrate dissociation. However, it is possible to predict nonpressurized core hydrate dissociation during this trip (Davies and Sloan, 2006) as a function of the depth–temperature–time profile during the coring. The model for nonpressurized core dissociation is modified from CSMPlug (in the book's endpapers) for hydrate plug dissociation in flowlines.

The above discussion suggests two of the common ways of quantifying hydrates in cores: (1) low core temperatures as sensed by IR imaging (Ford et al., 2003) and (2) gas evolution from pressurized core sampling systems (Pettigrew, 1992). A third method of sensing hydrates is by the use of chlorinity, which may be reliable because unlike the previous two methods, it does not depend upon the volatility of gas evolution from nonpressurized cores, nor the time–temperature history of the water surrounding the core.

Recall from Chapter 2 that hydrates exclude all ions on formation. The ions form strong Coulombic bonds with water resulting in effective radii that cause

FIGURE 7.16 Shipboard drilling of gas pressure relief holes in hydrate nonpressurized core liner to accommodate gas hydrate dissociation. (Courtest F. Rack, May 5, 2004.)

them to be both too large and too polar for hydrate cage guests; in addition, ions provide competition with clathrates for the available water molecules. Therefore, hydrates formed in salt water are depleted in chloride ions, while the water around recently formed hydrates is enriched in salt concentration.

When hydrates dissociate on core retrieval, the melting hydrates provide water that is lower in chlorinity than the surrounding seawater. *In situ* hydrates content can be determined by measuring the degree of prewater dilution relative to a baseline assumed to represent the *in situ* pore water Cl^- concentration prior to gas hydrate dissociation (Hesse and Harrison, 1981; Egeberg and Dickens, 1999).

In the following southern Hydrate Ridge Leg 204 case study, Tréhu et al. (2004) compared estimates of hydrate fractions by the three methods, relative to the hydrate fractions estimated by resistivity at bit (RAB) logs. All four results consistently indicate that, at depths greater than the crest of the ridge, the average gas hydrate content is generally $<2\%$ of the pore space. Such numbers are typical of oceanic hydrates.

As in Section 7.4.3, Tréhu et al. (2004a) distinguish between the GHSZ and the GHOZ with the former always greater than the latter. The difference between these two values implies that the BSR and thermodynamic stability region are necessary for the GHSZ, but not sufficient for hydrate determinations in the GHOZ, which may be limited by methane availability, stratigraphy, or other factors.

A fourth rapidly evolving hydrated core method that is just coming into use is that of portable CT scanning, which applies x-ray imaging techniques to hydrate cores at the surface. This method was developed and calibrated by Freifeld et al. (2002) at the USA Lawrence Berkeley National Laboratory; it is evolving into frequent use to determine the hydrate content of cores.

When cores are obtained, after shipboard measurements they are preserved in liquid nitrogen (Tulk et al., 1999) and transported to laboratories, where they

are thoroughly studied using diffraction (Eaton et al., 2005), scanning electron microscopy (Genov et al., 2004; Stern et al., 2005; McGrail et al, 2005), and Raman and NMR spectroscopy (Ripmeester et al., 2005) with the last two being a comprehensive reference.

7.5.3 Combining Laboratory and Field Experiments

The above experimental work is bifurcated into those in the field and the laboratory. This bifurcation requires resolving the question of how the laboratory experimental results are representative of hydrates in nature. In resolving this question, the work of Brewer, Paull, Peltzer, Ussler, and colleagues at the Monterey Bay Aquarium Research Institute (MBARI) has been exemplary. MBARI has both the goal and resources to perform high quality laboratory experiments subsea, so that core retrieval and possible damage (for example) is not a concern. Their work has been notable for generating ocean scientific knowledge and educating the public about the ocean. In particular, MBARI excels in areas of subsea use of hydrate NMR and Raman spectroscopy (Kleinberg et al., 2003; Hester et al., 2005, respectively), methane and CO_2 hydrate formation and storage (Rehder et al., 2003), and ocean geochemistry (Paull et al., 2005). It is clear that MBARI's efforts are moving ocean science towards quantification.

The above suite of hydrate sensing tools (thermodynamics, geothermal gradients, kinetics, BSRs, lithology and fluid flow, logging and coring tools, and subsea tools) has enabled an assessment of where hydrates may exist worldwide. On the basis of the data provided by these tools, hydrate formation models such as that of Klauda and Sandler (2005) enable our prediction of hydrate formation sites in nature—notably the *a priori* prediction of 68 of the 71 sites at which hydrates have been indicated.

Currently in the state-of-the art, hydrate experiments and modeling are synergistic partners, with the experiments serving as a calibration for models, and the model suggesting new experiments. After reliable models are generated, the models are always more cost effective than laboratory and field experiments.

In the first principle in this chapter, it was indicated that the state-of-the-art was moving away from *in situ* hydrate assessment, to hydrate production. In the next section we turn to hydrate production models, which are calibrated by a number of costly field and laboratory experiments.

Most natural hydrates are in the ocean environment. As a state-of-the-art summary of ocean hydrates, Tréhu et al. (2006) list six major lessons learned during the decade from 1996 to 2006:

1. Lithology may exercise a primary control of hydrate deposition, resulting from permeability, faults, and traps.
2. Gas hydrate is distributed heterogeneously and can fill pore space between sediments grains, or displace grains to form lenses and nodules. Hydrates form preferentially in coarse-grained sands.

3. New remote sensing tools are needed to supplement a BSR indication of hydrates. Gas hydrates can form without a BSR indication.
4. Multiple proxies are required to determine hydrate distributions. Of particular note are the new tools for laboratory imaging (IR, CT, and x-ray), logging while drilling, pressure coring and physical testing under pressure.
5. There are two end-members of hydrates, FHF and DLF. Although it is possible to typify hydrate deposits as predominately one end-member, most deposits contain elements of both end-members.
6. Acceptable geological assessment of hydrates require integration of information from several fields of geology, geophysics, and geochemistry.

7.6 Hydrate Reservoir Models Indicate Key Variables for Methane Production

Experiments, both in the field and laboratory, are very expensive. Models of methane production from hydrate can save substantial expense of time, effort, and capital. This section of Chapter 7 gives guidelines from the models for hydrate dissociation.

One might consider the rationale for models, as one of three analogs of the real hydrated reservoir situation:

1. A field test, such as the Mallik 2002 case study, is perhaps the best analog of hydrate dissociation in a reservoir. However, the Mallik 2002 project cost many man years and approximately US$22,000,000. Even with such a large cost, there was still concern about the data obtained, and how representative the transient data would be for long-term production.
2. A laboratory experiment typically requires months to plan and costs approximately US$50,000–300,000. There is less certainty here than in the field tests, but also less expense.
3. A mathematical model of the hydrate reservoir typically requires several minutes to days to execute and costs typically US$10–100. Even with these low costs, unless the model is based upon extensive laboratory and field data, the model will have the weakest link of the three methods to physical reality.

Progressing from each of the above levels to the next saves 2–3 orders of magnitude in financial and time expense. So, for example, if one wished to perform a sensitivity study of methane production rate response to reservoir permeability or hydrate saturation, it is many orders of magnitude easier to do so via a model, than via a field test.

Before summarizing the models, however, consider as background the three common means of hydrate dissociation from Makogon (1997), shown in

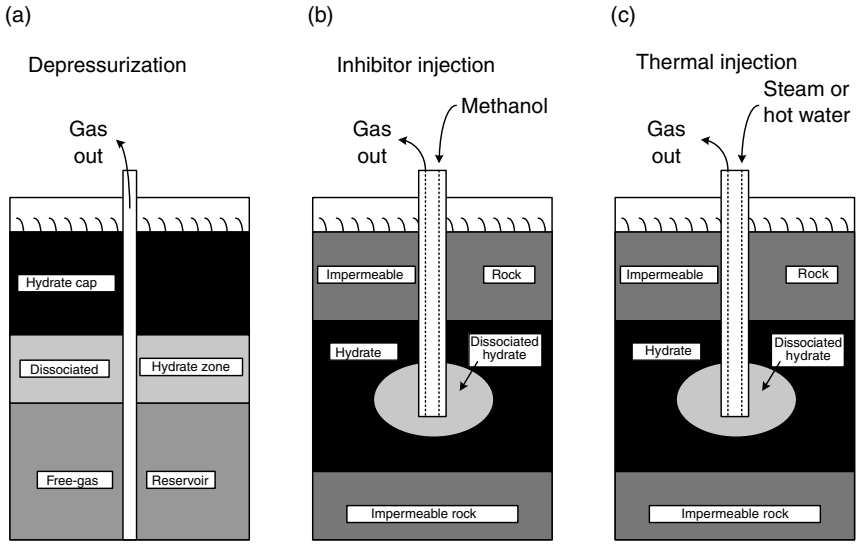

FIGURE 7.17 The three common means of hydrate dissociation. (From Makogon, Y.F., *Hydrates of Hydrocarbons*, PennWell Publishing Co., Tulsa, 1997. With permission.)

Figure 7.17. In Figure 7.17a, the depressurization method shows that drilling through an overlying hydrate reservoir into free gas allows normal production of gas to depressurize the gas reservoir, which is replenished by gas from dissociating hydrates; this method is illustrated in the Messoyakha case study at the end of the chapter. In Figure 7.17b, the inhibitor injection method is shown to dissociate hydrates via injecting methanol or brine into the wellhead; this was used for a short time at Messoyakha, but quickly abandoned due to the short-lived results. In Figure 7.17c, the thermal stimulation method is shown to increase the temperature of the hydrate reservoir to dissociate the hydrates; the thermal stimulation method is illustrated, combined with the pressure reduction method, in the Mallik 2002 case study.

Relative to our phase equilibrium study in Chapters 4 and 5, the above three techniques are illustrated on the phase diagram of Figure 7.18, as $\Delta T = 0$, $\Delta P = 0$, and 10% methanol, for depressurization, thermal stimulation, and inhibitor injection, respectively. Additional explanation is given in the figure caption.

The above discussion demonstrates two principles for hydrate dissociation: (1) hydrates will not occur outside the thermodynamic restrictions of the phase equilibria, that is, hydrates require the appropriate temperature, pressure, as shown in the area to the left of the lines in Figure 7.18, as well as methane and water and (2) when hydrates are dissociated, even at constant temperature as shown in Figure 7.18, heat must flow from the surrounding media to the hydrates, causing a cooling. This last point is also intuitive, because gas and water molecules from dissociated hydrates have more energy than they do in nondissociated hydrates. Thus energy must flow to the hydrate surface in order to dissociate it.

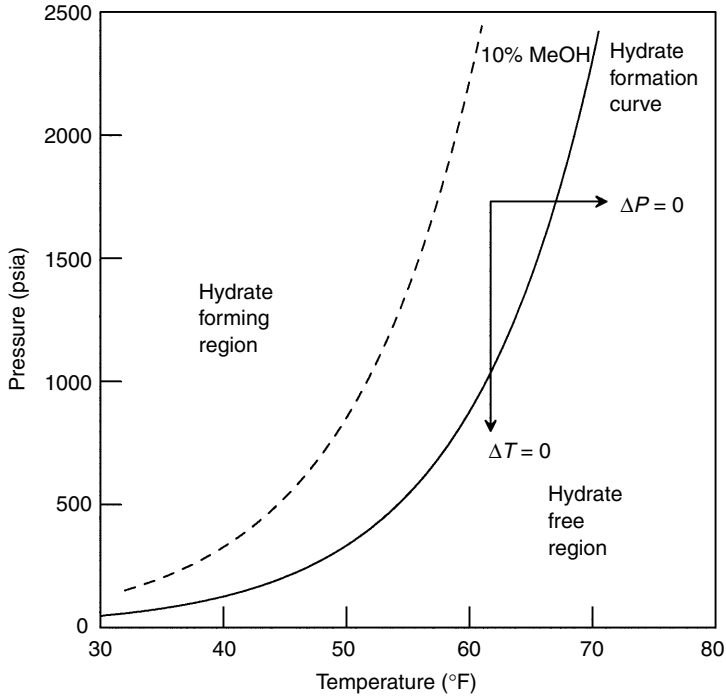

FIGURE 7.18 A phase diagram showing the three common hydrate dissociation techniques, relative to the initial sample condition (intersection of horizontal and vertical arrows). Depressurization is shown as $\Delta T = 0$; thermal stimulation as $\Delta P = 0$; inhibitor injection is represented by displacing the solid hydrate formation curve to the dashed curve, via injection of 10 wt% methanol in the free water phase.

As additional background for modeling hydrate dissociation, it should be noted that there are three commonly cited classes of hydrate reservoirs in the permafrost, following the definition of Moridis and Collett (2004):

Class 1—hydrate layer underlain by two-phase zone of mobile gas and water
Class 2—hydrate layer underlain by one-phase zone of mobile water
Class 3—hydrate layer with absence of underlying zones of mobile fluids

In every hydrate dissociation process, three phenomena exist: (1) heat transfer to the hydrate–fluid interface, (2) the kinetic dissociation of hydrates, and (3) the flow of fluids (gas and water) away from the hydrate interface. The models are classified according to each of these three phenomena in Table 7.10, modified from a recent review of hydrate models, by the laboratory of Pooladi-Darvish (Hong, 2003).

TABLE 7.10
Summary of Hydrate Dissociation Models Since 1982

	Heat transfer		Fluid flow			Solution
Model	**Conduction**	**Convection**	**Gas**	**Water**	**Kinetics**	**Method**
Holder and Angert (1982)	X		X			Numerical
Burshears et al. (1986)	X		X	X		Numerical
Jamaludin et al. (1989)	X				X	Numerical
Selim and Sloan (1989)	X	X	X			Analytical
Yousif and Sloan (1991)			X	X	X	Numerical
Makogon (1997)	X	X	X	X		Analytical
Tsypkin (2000)	X	X	X	X		Analytical
Masuda et al. (2002)	X	X	X	X	X	Numerical
Moridis et al. (2002)	X	X	X	X	X	Numerical
Pooladi-Darvish et al. (2003)	X	X	X	X	X	Numerical

As indicated in Table 7.10, only in the last decade have models considered all three phenomena of heat transfer, fluid flow, and hydrate dissociation kinetics. The rightmost column in Table 7.10 indicates whether the model has an exact solution (analytical) or an approximate (numerical) solution. Analytic models can be used to show the mechanisms for dissociation. For example, a thorough analytical study (Hong and Pooladi-Darvish, 2005) suggested that (1) convective heat transfer was not important, (2) in order for kinetics to be important, the kinetic rate constant would have to be reduced by more than 2–3 orders of magnitude, and (3) fluid flow will almost never control hydrate dissociation rates. Instead conductive heat flow controls hydrate dissociation.

Numerical models such as the one by Moridis et al. (2005) are more sophisticated, and are subject to space- and time-discretization errors; so numerical models must be compared to some standard, such as a physical measurement, or perhaps an analytical model.

While economy of space prevents detailing the various models here, it is worthwhile to provide outcomes, based upon the model sensitivity studies. These results summarize the recent work by Pooladi-Darvish and coworkers (2005) and Moridis and coworkers (2005), and the economic studies by Howe et al. (2004) and by Hancock et al. (2005a,b):

1. Of the three common means to dissociate hydrates, depressurization is the most economical.
2. Most economical for dissociation by depressurization is the sub-permafrost reservoir in which hydrates overly a free gas, with impermeable boundaries both at the top of the hydrate layer, and at the bottom of the free gas layer.
3. The sediment setting will control the target to some degree. Hydrate deposits in sandy ocean sediments (e.g., the Gulf of Mexico) likely

contain larger hydrate amounts relative to the silty/clay sediments characteristic of the majority of hydrate reservoirs (e.g., the Blake Bahama Ridge).
4. Proximity to the phase boundary, and the need to supply energy to dissociate the hydrates, will control the rate of dissociation and thus the economics. Because conductive heat transfer controls hydrate dissociation, hydrates closer (in temperature and pressure) to the phase boundary will be most economical to dissociate. Heat transfer limitations indicate that high surface areas (thin layers) are most economical.
5. High hydrate concentrations can lead to drastic reductions in effective permeability, thus limiting the areal extent of depressurization.
6. Pore size is not important until pores are small, less than 100 nm, but salt concentration has a major effect.
7. More data are needed on which to base the models. In the field, long-term production tests are needed to eliminate transient phenomena for validation of the reservoir models. In the laboratory more data are needed for permeability, conductivity, hydrate kinetics, and for determining the transition between heat-, mass-, and kinetic-controlled dissociation.
8. The models for the above reservoir conditions indicate that economical hydrate production can be achieved at a gas cost of US$9 per MMBTUs in 2005 economics.

7.7 Future Hydrated Gas Production Trends are from the Permafrost to the Ocean

The discussion in Section 7.6 is not intended to imply that the three methods of depressurization, thermal stimulation, and inhibitor injection are the only means of hydrate dissociation. Because the hydrate science is available as indicated in the earlier chapters of this book, the application of that science to recovery from hydrates is an exercise for the innovative engineer. Novel ideas such as fire flooding (Halleck et al., 1982), burial of nuclear wastes (Malone, 1985, p. 27), and the use of electromagnetic heating (Islam, 1994) are only three innovative ways of dissociating hydrates, but none have been tried. However, in this portion of the chapter, it is intended to describe trends for dissociating hydrates in several kinds of reservoirs, as an indication of the future.

The state-of-the-art for hydrated energy is in transition—moving from assessment of the location and extent of hydrate concentrations, to the proof of concept for long-term production, first from the permafrost, and then from the ocean. One projection of the way forward in hydrated energy recovery is the following:

1. The 2002 Mallik well provided an indisputable proof of the concept—namely, it is possible to in transient testing to recover energy from permafrost hydrates upon dissociation.
2. Other permafrost-associated hydrate wells should be drilled in 2007–2008 to move beyond the proof of concept, to a proof of long-term

production, eliminating the transient phenomena in the 2002 Mallik three-day tests. Many suggest the Messoyakha Field provided proof of long-term production (Makogon, 1988), but while all agree that hydrates played a part at Messoyakha, the exact role of hydrates is under some scientific dispute (Collett and Ginsburg, 1998).

3. The technology developed in the Mallik production test should be transferred to recover hydrates from the "sweet spots" of high concentrations in the ocean, such as at Barkley Canyon or the Gulf of Mexico.
4. An engineering breakthrough is required for the final step—recovery of hydrates in dispersed concentration (usually around 3.5 vol% in 30% porosity) in the deep ocean (>500 m water depth), which may prove problematic.

Consider the above four steps in some detail:

1. The 2002 Mallik well provided a proof of the concept—namely, that it is possible to recover energy from permafrost hydrates upon dissociation.

This important work was a major advance in technology—moving the state-of-the-art from the identification of hydrate reserves, to the recovery of energy from those reserves. The 2002 Mallik proof of concept (see case study 4) is a cornerstone upon which future energy recovery from hydrates will be built. In addition, the work is validated by a wide diversity of credible scientific organizations and is scientifically established beyond doubt in the Geological Survey of Canada (GSC) Bulletin 585 (Dallimore and Collett, Eds. 2005), which includes more than 65 reviewed, technical publications on Mallik 2002. In essence, a gas flare was generated over a short period to prove the concept of energy evolution from hydrates, combining depressurization and thermal stimulation.

2. Other permafrost-associated hydrate wells should be drilled in 2007–2008, to move beyond the proof of concept, to a proof of production, eliminating the transient phenomena in the 2002 Mallik three-day tests.

Because field tests are so expensive it is important to validate prediction models to obviate future tests, with a minimum of reliable data. However, the three-day Mallik 2002 test contained too many transient phenomena to be modeled accurately. Instead a new 3–6 month production test that eliminates transients should be carried out at a site such as Mallik 2002, to enable modeling of production via state-of-the-art work such as Moridis' LBNL model for energy production from hydrates. Once the model is refined by production data, cost savings of several orders of magnitude can be realized, to reliably predict the outcome of future tests.

3. The technology developed in the Mallik production test should be transferred to recover hydrates from the "sweet spots" of high concentrations in the ocean, such as at Barkley Canyon or the Gulf of Mexico.

The amount of ocean-hydrated energy is so large that the likely error in its estimate, is greater than all of the hydrated energy in the permafrost. Thus, because of its size, the ocean hydrated energy will be the ultimate target. However, it is not possible to produce oceanic hydrates initially because they are generally too

dispersed—typically less than 3.5% of pore volume, in sediments that have less than 30% porosity.

Leg 204 at Hydrate Ridge (Tréhu et al., 2004b) and the following IODP Leg 311 showed that it is possible to access "sweet spots" in the ocean for the potential recovery of hydrates, such as those close to the surface at the crest of Hydrate Ridge. These higher concentrations will be the first ocean targets for hydrate recovery. Similarly, in the Gulf of Mexico, sandy sediments provide higher porosities, and the sandy sediment pore volume filling can be much higher than the 3.5% cited for a worldwide average.

It can be argued that, if it is not possible to recover oceanic hydrates at high concentrations, it will be impossible to recover hydrates at lower concentrations in the ocean. Thus, success in the Gulf of Mexico, at Hydrate Ridge, or in a similar setting is vital to the energy recovery from more dispersed, deeper hydrates.

4. An engineering breakthrough is required for the final step—recovery of hydrates in dispersed concentration (typically 3.5 vol% in 30% porosity) in the deep ocean (>500 m water depth) to use science and engineering, but most importantly previous experience, to produce hydrates efficiently from very dispersed resources in sediments. Probably not much new science will be needed for this step; rather an engineering breakthrough will be necessary.

This area of hydrated gas recovery is of very active international interest, due to its energy impact. However, because of thermodynamic and practical constraints (Moridis and Sloan, 2006) recovery of energy from low concentration (3% of pore volume) may be problematic. Clearly energy is a major driver of technology, and technology in turn is largely responsible for national economic success (Economides and Oligney, 2000; Bernstein, 2004; Sachs, 2005).

7.8 Hydrates Play a Part in Climate Change and Geohazards

Because hydrates are so widely distributed in most of the world's ocean continental shelves, it seems logical to inquire how hydrates may have impacted the other components in the earth—for example, the climate. Dickens et al. (1995), Dickens (2003) and Kaiho et al. (1996) indicate that an ancient, massive ocean methane hydrate dissociation explains a 4–8°C temperature rise over a brief geologic time interval (10^3 years) called the Late Paleocene Thermal Maximum (LPTM) that occurred 55.5 million years ago. This is documented in deep ocean drilling samples as a prominent negative carbon isotope excursion ($\delta^{13}C$ of $-2.5‰$) in all ocean sediments, in fossil tooth enamel, and in carbonates and organic sediments in terrestrial sequences. This $\delta^{13}C$ reduction in the ocean and the recovery over the ensuing 200×10^3 years (see Figure 7.19a) is consistent with pronounced dissolution of calcium carbonate in the deep sea sediment deposited during the LPTM, shown in Figure 7.19b.

The evolution of a large amount (1.12×10^{18} g of CH_4) of methane from hydrates is the only plausible hypothesis that has been offered to explain this environmental perturbation. The abnormal $\delta^{13}C$ isotope indicates that source

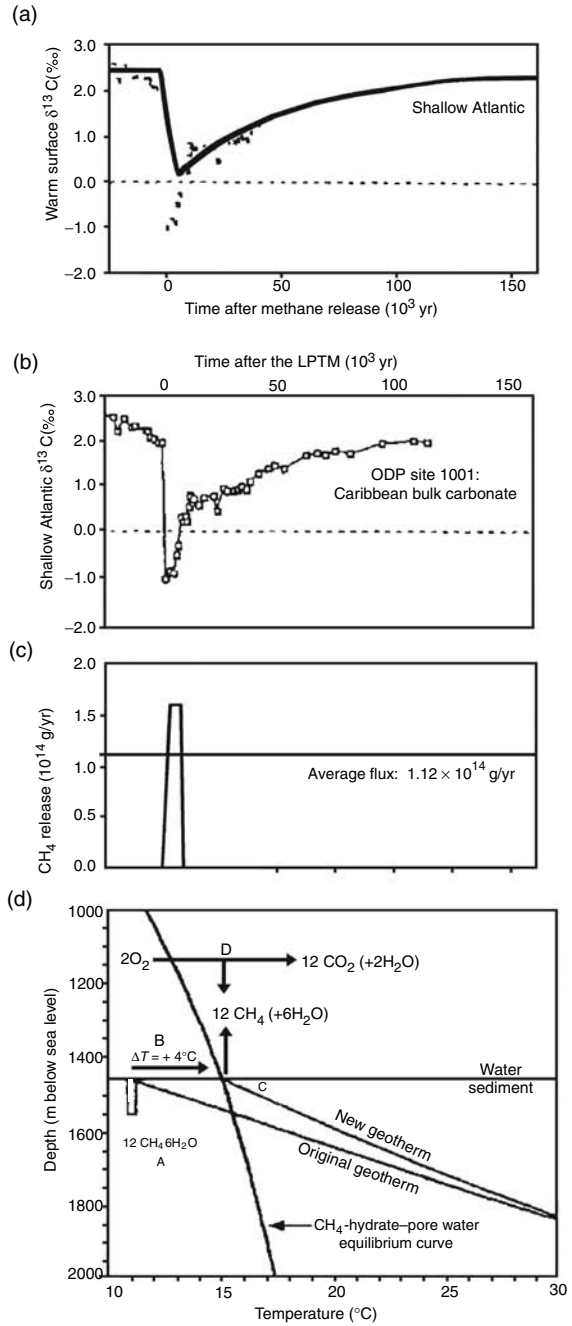

FIGURE 7.19 Temperature (a) bulk carbonate (b), methane release (c), and change in geotherm (d) with time and temperature associated with the LPTM. (Reproduced from Dickens, G.R., *Nature*, **401**, 752 (1999). Copyright with permission from Macmillan Publishers Ltd.)

was external to the normal ocean-atmospheric-biomass carbon pool. Figure 7.19c shows a rapid evolution of methane from hydrates, which is hypothesized to be oxidized to CO_2 greatly enriched in $\delta^{12}C$ (Dickens et al., 1995; Thomas and Shackleton, 1996).

Figure 7.19d shows the hydrate equilibrium curve as a function of depth and temperature in the ocean. Hydrates are only stable between equilibrium line and the original geotherm to the left of the curved line, at depths below the sediment surface, shown by the small vertical rectangle at A. If the ocean were warmed by 4°C, the hydrates between the original geotherm and the equilibrium curve would melt, as the new geotherm was established. The warming from the original to the new geotherm would result in methane expulsion to the environment, where it would be oxidized to CO_2, resulting in significant further warming. It was hypothesized that the resulting CO_2 was reabsorbed by the ocean over the ensuing 200×10^3 years.

Dickens (1999) cautions that in modern times a similar reoccurrence is prevented by deeper oceans than in ancient times. However, the importance of the LPTM perturbation is that it is the only analog available in the geological record for understanding how the global carbon cycle and other systems is related to a rapid, massive input of fossil fuel such as that which may be occurring in modern industrial times.

A monograph by Kennett et al. (2003) thoroughly documents evidence for Late Quaternary climate change by hydrates, commonly called "The Hydrate Gun Hypothesis." The concept is that, as little as 15,000 years ago, methane from hydrates caused significant global warming. The data and summary in the monograph by Kennett et al. is the most thorough source for extending the theory to more modern times (the Late Quaternary). However, there is a considerable controversy concerning the validity of the hypothesis, and Kennett et al. (2005) appeal for more data to validate their hypothesis.

In a review of the Kennett et al. monograph, Dickens (2003) generally concurs with the hypothesis, but criticizes it on the grounds that the monograph "perpetuates the common-misconception that present-day methane hydrates are stable. These systems may be in a steady state, but they must be viewed as dynamic with large . . . carbon fluxes to and from the ocean, even at present day." The question of climate change is the current focus of much research, for example, in the Hydrate Ridge case study by Boetius and Suess (2004), who conclude that location may not be contributing much methane to climate change.

In closing the discussion on hydrate-related climate change, it should be noted that seafloor hydrate dissociation is also directly related to slumping of sediments on the seafloor. Significant ocean hydrated sediment slumps can jeopardize the foundation of subsea structures such as platforms, manifolds, and pipelines. The single incident off the Carolina coast shown in Figure 7.20 occurred about 15,000 years ago (Dillon, et al., 2001) and increased the extant earth's atmospheric methane as much as 4%. The interested reader is referred to the recent monograph by Paull and Dillon (2001) on this topic. It should be noted that subsea subsidence was the major focus of a U.S. Department of Energy, Joint Industry Project in 2005 in the Gulf of Mexico (Boswell, 2006).

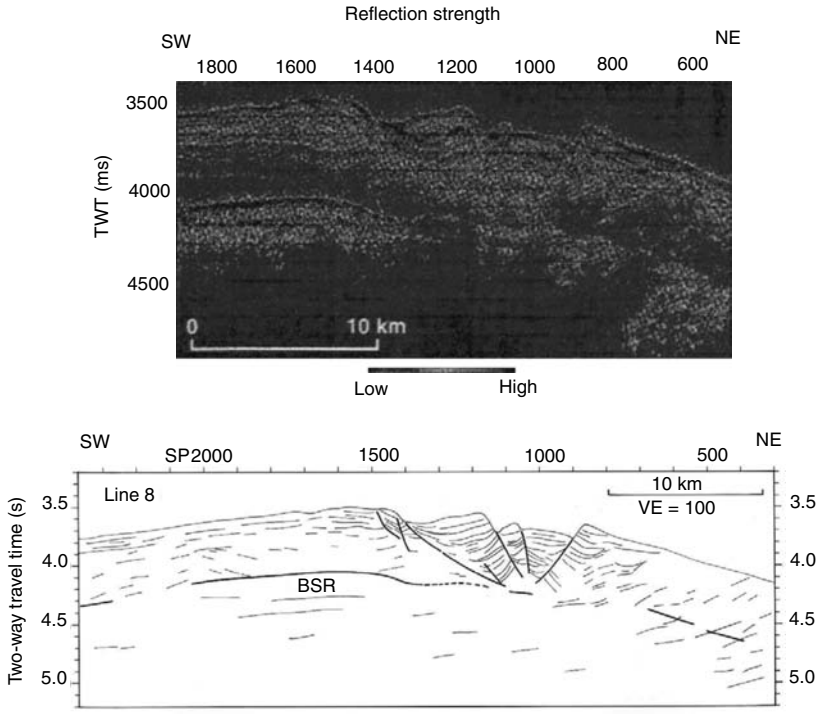

FIGURE 7.20 (See color insert following page 390.) Seafloor slump in the Blake-Bahama Ridge shown in both seismic (top) and cartoon (bottom) relief. (From Dillon, W.P., Nealon, J.W., Taylor, M.H., Lee, M.W., Drury, R.M., Anton, C.H., *Natural Gas Hydrates: Occurrence, Distribution, and Detection*, (Paull, C.K., Dillon, W.P., eds.) American Geophysical Union Monograph, 124, p. 41, Washington DC (2001). With permission.) Note the bottom simulating reflector parallel to the ocean bottom, except in the middle section where it appears a seafloor eruption has occurred.

This chapter's preceding eight principles of hydrates in nature find application in the following four field case studies. The first two (Blake-Bahama Ridge and Hydrate Ridge) illustrate the geoscience fundamentals of locating and assessing hydrate formation in ocean deposits. The final two case studies (Messoyakha and Mallik 2002) deal with production of energy from permafrost hydrate reservoirs, which are a necessary prelude to recovery of energy from ocean hydrates.

7.8.1 Case Study 1: Leg 164 in the Blake-Bahama Ridge (Hydrate Assessment)

The discussion in this section is exerpted from Leg 164 Scientific Party Report. The Ocean Drilling Program (ODP) Leg 164, represented a drilling effort in late

1995 to understand the amounts of gas associated with the famous Blake-Bahama Ridge BSR (see Figures 7.12a,b) that was known since the late 1960s (Markl et al., 1970). Samples indicating the presence of hydrates were obtained earlier in this BSR vicinity at Deep Sea Drilling Project (DSDP) Leg 11, Site 102, 103 (Ewing and Hollister, 1972) and Leg 76, Site 553 (Kvenvolden and Barnard, 1983). Figure 7.21a gives the location of earlier sites, as well as those of Leg 164 (Sites 991 through 997).

On ODP Leg 164, three sites were drilled below the base of hydrate stability over a short distance (9.6 km) in the same stratigraphic interval. Figure 7.21b shows the three Leg 164 holes: Site 994 without a BSR, Site 995 with a weak BSR, and

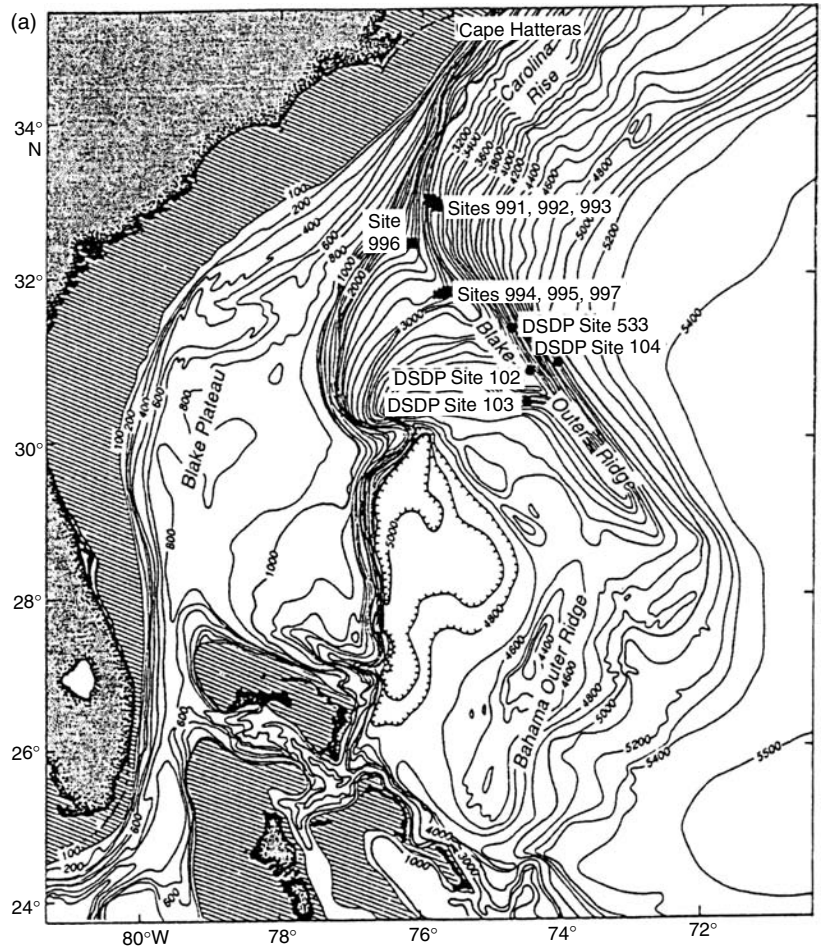

FIGURE 7.21a Map showing the location of Leg 164 in the Blake-Bahama Ridge (Sites 991 through 997). (Paull et al., 1996.)

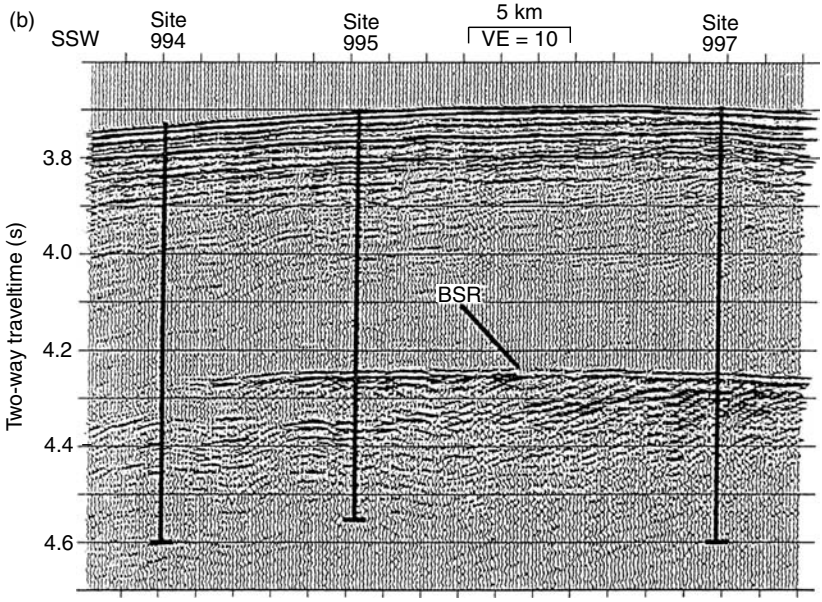

FIGURE 7.21b Bottom simulting reflector for the Three Leg 164 Holes at Blake-Bahama Ridge. (Paull C.K., et al., Leg 164 Scientific Party, in *Gas Hydrates—Relevance to World Margin Stability and Climatic Change*, The Geological Society, London, Special Publication, 1998. With permission.)

Site 997 with a strong BSR on the ridge crest. Site 996 was drilled some distance away from the BSR, to investigate migration in a fault zone where methane was leaking from the rise.

7.8.1.1 Site 994

Hydrates were indicated by both direct evidence [nodules at 259 m below seafloor (mbsf) in 994C, and a piece <1 cm^3 in 994D at 261 mbsf] and indirect evidence (low chloride values and logs that show dramatic changes in P-wave velocity and electrical resistivity). As shown in Figure 7.22a the chloride anomalies and the electrical resistivity and sonic velocity logs indicate significant changes just below 220 mbsf where the hydrate samples were recovered, and at the base of the BSR, 420 mbsf.

The hydrate recovered consisted of methane ($\sim$99%), with minor to trace amounts of carbon dioxide (1.22%), ethane (86 ppmv), propane (2 ppmv), with a volumetric ratio of methane to water of 154. The chlorinity concentration (57.2 mM) of water collected indicated that the sample was a mixture of 10% pore water and 90% freshwater. The gas:water ratio exceeded 170, higher than any previously reported for *in situ* hydrates. The C_1/C_2 ratio was 11,500, compared to a headspace value three times lower; however, both gas ratios indicate biogenic gas.

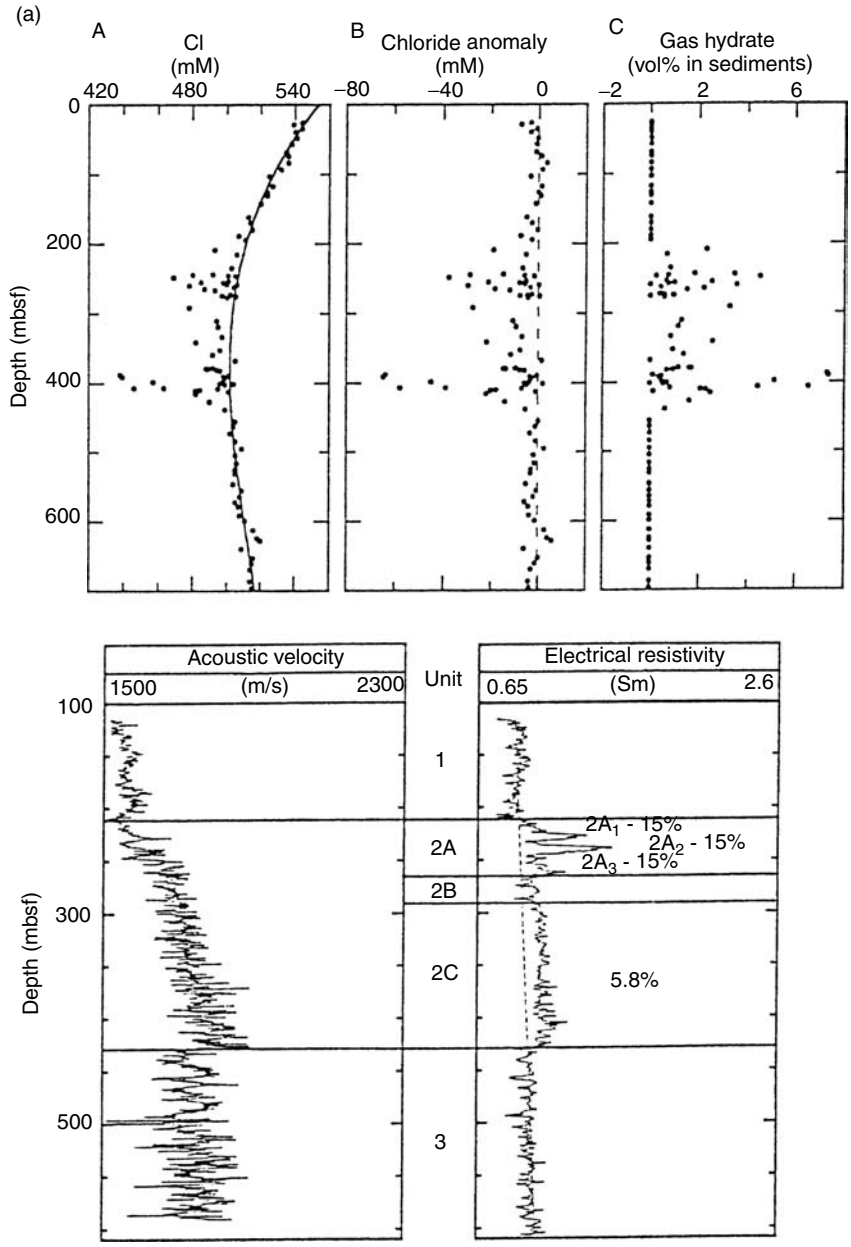

FIGURE 7.22a Chloride anomalies and acoustic and resistivity logs for Blake-Bahama Ridge site 994. (Paul et al., 1996. With permission.)

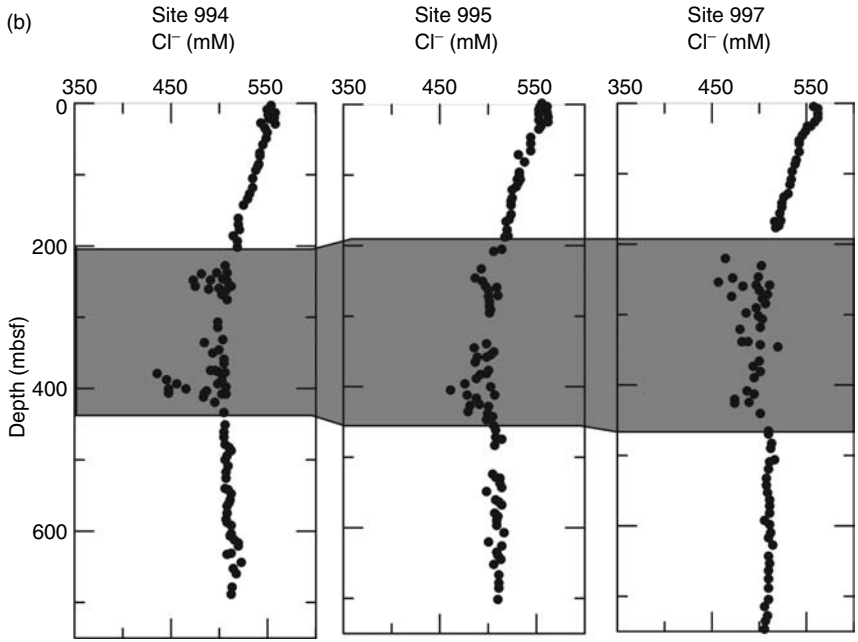

FIGURE 7.22b Similar chlorinity anomalies for Blake Bahama Ride Sites 994, 995, and 997. (From Paull, C.K., Lorenson, T.D., Boroworski, W.S., Ussler, W., Olsen, K., Rodriguez, N.M., Wehner, H., in *Proc. Ocean Drilling Program, Scientific Results*, **164**, 67 (1996). With permission.)

In addition at Site 994 recovered cores were very gassy, and recovery below 190 mbsf was poor, as a result of vigorous degassing. The average geothermal gradient (35.4°C/km) intersected the hydrate stability phase line about 50 m below the other hydrate indicators. The reason for this discrepancy is unclear, but it should be noted that a similar discrepancy was noted at the Cascadia Margin in ODP Leg 146 (Hovland et al., 1995). Some possible reasons for this discrepancy are considered after the Site 997 discussion.

Core temperatures upon recovery on the catwalk were variable. Small areas of low temperatures (6–8°C versus other parts of the core at 11–13°C) were interpreted as indicating areas where endothermic hydrate decomposition decreased the core temperature. Cores evolved large amounts of gas, which was considered responsible for low core recovery—from a norm of >80% to 20–60% in the hydrate region.

The estimated amount of hydrate by chloride anomalies had a mean value of 1.3 ± 1.8 vol%, ranging to as high as 7%; however, these values may be minimum because the baseline may have been lower than the actual interstitial water chlorinities. The logging tools indicate the presence of as much as 2.9 vol% hydrate, ranging as high as 9.5%. Recovered pieces of hydrate were concentrated in zones from 2 to 10 cm thick. However, most of the hydrate was disseminated

as fine-grained crystals in clay and claystone pore spaces. All inferred hydrates occurred well above the phase-equilibria base of the hydrate zone.

7.8.1.2 Site 995

Although a strong BSR occurred at 440 ± 10 mbsf, at Site 995 samples of hydrate were not recovered. Instead a suite of chemical, thermal, and log indicators suggested that hydrate was present in a significant section, but hydrate was so fine-grained that it had dissociated prior to inspection. The sediment physical properties at Site 995 were coincident with those at Site 994, without differences that could account for changes in the strength of the BSR between the two sites.

The logs at Site 995 indicate a material of increased resistivity and acoustic velocity, but similar density. The 450 mbsf boundary depth detected by logs coincides with the BSR. A zone of anomalously low chloride values (as low as 466 mM between 195 and 440 mbsf) was coincident with that found at Site 994, indicating that sites 3 km apart possessed similar vertical distributions of hydrate.

Low chlorinity zones were coincident with zones of anomalously low recovered core temperatures on the ship catwalk. For example, while some of the background core temperatures were at 10–12°C, cores in suspected hydrate regions had temperatures as low as 1°C, perhaps caused by endothermic dissociation of hydrate. The extrapolated geothermal gradient of 33.5°C/km yielded a temperature of 18.3°C at the BSR (440 mbsf), well within the temperature stability field of methane hydrate.

The concentrations of gases in the core voids were measured, with C_1/C_2 ratios from approximately 1,200 to 39,000 indicating biogenic sources. Concentrations of propane through heptane were usually below 10 ppmv, and the concentration of carbon dioxide varied widely from 0% to 20% of the free gas.

Hydrate inferred at Site 995 existed as fine-grain, pore-filling accumulations that were widely dispersed in host sediments rather than as concentrated nodules large enough to survive the coring/recovery process. Gas voids and expansions were noted in several core samples, and the amount of methane recovered exceeded that expected from methane saturation of the interstitial waters at *in situ* pressures.

Although no hydrate was recovered from Site 995, the interstitial-water chlorinity anomalies, anomalously cold temperature in recovered cores, and log data all indicate that gas hydrates occurred between 1 and 4 vol% in sediments from 195 to 450 mbsf, with some intervals containing as much as 10 vol% hydrate. However, Paull et al. (1998) noted that these are probably minimum values because the baseline chlorinity might be lower than actual *in situ* interstitial water chlorinities.

In Site 995, as in Site 994, there is a discrepancy between the inferred lowest hydrate level (450 mbsf) and the experimentally predicted base of the stability zone (541–577 mbsf). Possible reasons for this discrepancy are discussed after the Site 997 discussion.

7.8.1.3 Site 997

Site 997 was drilled at the crest of the Blake-Bahama Ridge (where the strongest BSR occurs) at 450 mbsf. One large solid piece of gas hydrate was recovered from approximately 331 mbsf at a suspected small fault plane. However, the presence of more disseminated hydrates was inferred over a zone from approximately 180 to 450 mbsf. It was indicated that gas hydrate development may be extensive at this location, possibly acting as a means of sealing with permeability and porosity reduction.

Hydrate was inferred by low temperature observations, interstitial-water low chloride values, and velocity and resistivity logs. Most of the indirect indicators were very similar to those in the earlier Sites 994 and 995. Increases in resistivity (by 0.2 Ωm) and acoustic velocity (by 0.2 km/s) were marked in the hydrate region. In some cases, the temperature ($-2.1°C$) was less than the ice point due to endothermic hydrate dissociation.

The hydrate produced gas of 98.43% CH_4 and 1.57% CO_2. Ethane and propane were at 196 and 3.8 ppmv, respectively, and the C_1/C_2 ratio (4936) was between the ratios of gas in the headspace (1880) and free gas (6748). All above indicators suggested the gas was biogenic. However, microscopically visible oil occurred from approximately 500–620 mbsf, which suggested migration of some oil and gas, when coupled with the occurrence of higher molecular weight hydrocarbons.

Similar to Sites 994 and 995 , six indicators of hydrate were present: (1) large gas exsolution from cores, (2) high methane sediment concentration, (3) BSRs, (4) low interstitial-water chlorinity, (5) low core temperatures (although IR technology was introduced just after this hydrate leg), and (6) P-wave velocity logs and resistivity logs. As in Sites 994 and 995, there was a discrepancy between the indicated base of the inferred hydrate zone (452 mbsf) and the phase-equilibria stability zone (491 to 524 mbsf).

The estimated volume of hydrate via chlorinity had a mean value of 2.4 ± 2.7 vol% ranging as high as 13.6 vol%; again these are minimum values, perhaps caused by a low baseline. Logging tools indicated that hydrate occupied approximately 4 vol% of bulk sediments, ranging as high as approximately 11 vol%.

7.8.1.4 Common features

At all three sites, the six indirect indicators were found as listed in the Site 997 discussion. The similarity of the indicators in the three sites is exemplified by the chlorinity anomalies in the hydrate regions of Figure 7.22b. There is a minimum of approximately 1.4 vol%, 1.7% and 2.1% gas hydrate at Sites 994, 995, and 997, respectively assuming a low chlorinity baseline, and a sediment porosity of 50%. The amount of gas hydrate appears to increase from the ridge flank (Site 994) to the ridge crest (Site 997) with various indicators shown in Table 7.11.

At all three sites many direct and indirect evidences indicated the base of the hydrate to be at 450 ± 10 mbsf. However, there was a discrepancy between hydrate signals and the phase boundary. The temperature gradient indicated

TABLE 7.11
Fraction of Bulk Sediment as Hydrates at Leg 164 Sites

Detection means	Bulk hydrate volume
Chlorinity	1–2% (minimum) as high as 12%
Log suite	8%
Acoustic VSP	6–7%

that the boundary should have been significantly lower (at 490–570 m) than observed.

Paull et al. (1998) cited four possible reasons for the above discrepancy:

1. The inferred base is a fossil depth reflecting conditions during a previous sea level stand or bottom water temperature regime.
2. Experimental (P–T) data do not adequately characterize hydrates, particularly in fine-grained sediments. Clennell et al. (1999) used surface effects to explain this discrepancy. Inhibition by localized salt could also explain this discrepancy.
3. Gas hydrate existed below 450 ± 10 mbsf, but was undetected.
4. The hydrate depth is limited by the gas supply as suggested by Xu and Ruppel (1999).

In all samples there was a large (10 vol%) amount of gas below the hydrates and as much as 50% water, so three phases were present in all cases. However, most of the hydrates were recovered in disseminated form—that is, they had decomposed by the time the core barrel reached the deck. In two instances (Sites 994 and 997) samples of hydrates were recovered.

7.8.2 Case Study 2: Hydrate Ridge (Hydrate Assessment)

Hydrate Ridge is one of the best-studied convergent ocean margin with intense fluid flow and large-scale gas hydrate deposits. Due to the significant amount of hydrate found both at the seafloor surface and in deeper sediments, this site has provided an effective ocean laboratory to study hydrates in a marine environment. The following four research groups have performed extensive studies of the hydrate environment at Hydrate Ridge:

1. Geomar studied the habitat of hydrates and chemosynthetic communities for over two decades (see the review by Boetius and Suess, 2004).
2. The ODP devoted ODP Leg 204 to the study of hydrates (Milkov et al., 2003; Torres et al., 2004; Tréhu et al., 2004a,b; Claypool et al., 2006).

IODP Expedition 311 was also at this site, but articles are just being published as this book goes to press.

3. Scripps Institute of Oceanography and others laid the groundwork for Leg 204 through hydrate work in Sites 889 and 892 on ODP Leg 146 (Kastner et al., 1995, ODP Leg 146 Scientific Party). Controlled source electromagnetics at Hydrate Ridge was done by a different Scripps group (Weitemeyer et al., 2006).
4. The MBARI (Brewer, Paull, Peltzer, Ussler, and colleagues) have pioneered subsea science using remote operated vehicles (ROVs)—particularly the use of spectroscopic equipment to quantify hydrate measurements, especially with Raman subsea deployment at southern Hydrate Ridge (Hester et al., 2005), to supplement the NMR spectroscopy with MBARI (Kleinberg et al., 2003) in Monterey Canyon waters.

From the above studies has come a composite picture of hydrate formation at Hydrate Ridge, with particular emphasis on the southern summit. While a composite picture is attempted in the following few pages, the interested reader will turn to the above review articles for a detailed expansion.

Hydrate Ridge is located 80 km west of Newport, Oregon on the second accretionary ridge of the Cascadia subduction of the Juan de Fuca Plate and the North American Plate. The northern summit is in 600 m of water depth with an area of 0.4 km^2, while the southern peak is in 800 m of water with an area of 0.8 km^2.

The methane from hydrates has a stable isotopic signature of $-65‰$ $\delta^{13}C$, showing its biogenic origin, although infrequently there is as much as 10% contribution from thermogenic gas (Claypool et al., 2006). Boetius and Suess (2004) estimated the amount of methane in hydrates at North and South Hydrate Ridge at 0.5 and 1.7×10^{10} mol CH_4 respectively. They assumed that (1) 50% of summit has hydrates in 10% of sediment volume down to the bottom of the stability zone and (2) methane hydrates occupy 50% of pore space, to obtain an average hydrate content of 2.5% of the pore volume in the GHSZ. Tréhu et al. (2004b) estimated that the average hydrate content is less than 2% of pore volume within the GHSZ. However, Tréhu comments (Personal Communication, January 8, 2006) that there is a large amount of heterogeneity, so that a single average number can be misleading.

In this summary, we will concentrate on the southern Hydrate Ridge summit, which appears to be the most interesting due to the higher concentrations of hydrates. In Leg 204 (Tréhu et al., 2004b) southern Hydrate Ridge sites were chosen to complement ODP Site 892 on Leg 146, where there was an anomalously shallow BSR (Kastner et al., 1995). At the southern summit, there are three strong reflections, resulting from gas-charged, coarse-grained sediments. There are three groupings of nine Leg 204 sites drilled on southern Hydrate Ridge as shown in Figure 7.23:

1. Sites 1244–1247 characterize the flank
2. Sites 1248–1250 characterize the ridge crest with active venting

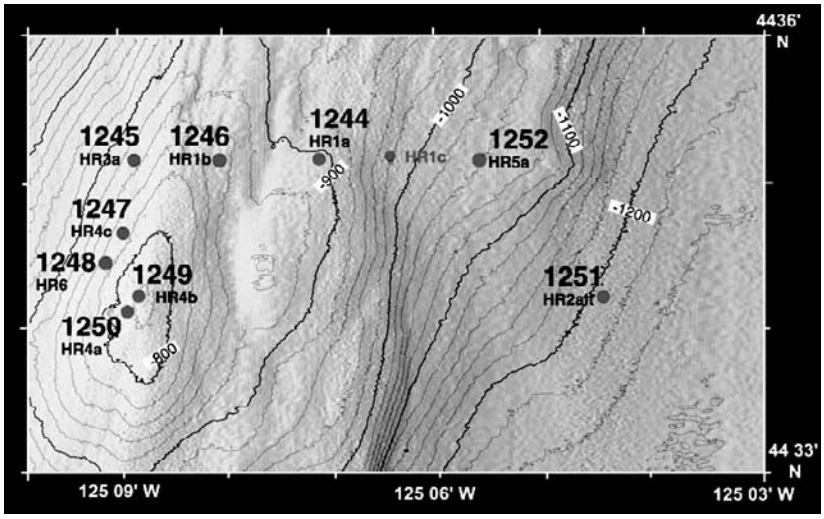

FIGURE 7.23 The location of the Leg 204 drilling sites on southern Hydrate Ridge. Note that sites 1249 and 1250 are at the summit. (From Tréhu, A.M., Long, P.E., Torres, M.E., Bohrmann, G., Rack, F.R., Collett, T.S., Goldberg, D.S., et al., *Earth Planet. Sci. Lett.*, **222**, 845 (2004b). With permission from Elsevier.)

3. Sites 1251 and 1252 deal with the slope basin to the east with rapid sedimentation

At the southern Hydrate Ridge summit, hydrate is deposited in two regions: (1) the first region with hydrates in 30–40% of the pore volume, extends from the surface to approximately 25 m below the seafloor and (2) a deeper region with much less hydrate (averaging less than 2–4% of pore volume) beginning approximately 25 mbsf to the BSR at a depth of approximately 115 mbsf.

Both Tréhu et al. (2004b) and Boetius and Suess (2004) suggest that emission of methane bubbles is much more effective at producing the observed phenomena than flow of dissolved methane through sediment–water interface. Most of the dissolved methane is consumed in the sediments by methanotropic communities. Torres et al. show that a free gas phase is required to produce the high hydrate concentration and high salinities observed at shallow depth near the summit. Tréhu (2004a) provides a mechanism to feed gas at saturation, that overtakes the amount of water locally available to form hydrates. Milkov and Xu (2005) have suggested alternative, salinity-based models for free gas migration. Torres et al. (2004) provide a rebuttal to Milkov and Xu's critique, but the details of how gas gets from the base of the stability zone to the seafloor remain poorly constrained.

7.8.2.1 Near surface hydrates: the chemosynthetic community and chemoherms

As a case study of rapid gas fluxes with hydrate formation, the work of Geomar [reviewed by Boetius and Suess (2004)] has provided an understanding of the

intertwined life of the chemosynthetic communities and gas hydrates. Over two decades this work has effectively provided insight into the nature of cold gas seeps, with surface microorganisms effectively acting as markers of hydrates.

The study of Hydrate Ridge by multiple teams of scientists, both at Geomar, and in ODP Legs 146 and 204 (Torres et al., 2004; Tréhu et al., 2004b), provide an illustration that has analogs in other parts of the world, for example, the Gulf of Mexico, intensively studied by Sassen and MacDonald (1994, 1997a,b) and Sassen et al. (2004). At Hydrate Ridge, cold seeps have enabled determination of the reaction sequence of anaerobic oxidation of methane (AOM), with visual determination of hydrates near the seafloor surface.

It is well known that the AOM process involves a transfer of electrons from methane to sulfate, producing bicarbonate and sulfide in equimolar amounts, which in-turn react with hydronium and calcium ions in the water, to produce the overall reaction:

$$CH_4 + SO_4^{2-} + Ca^{2+} \leftrightarrow CaCO_3 + H_2S + H_2O \tag{7.5}$$

The first product ($CaCO_3$) of reaction (7.5) produces chemoherms, or chimney-like carbonate structures, up to 40 m high on the seafloor. However, understanding the interactive role of H_2S, the second reaction product, with the microorganisms mediating AOM was more recent, awaiting the joint participation of microbiologists, geochemists, and geologists studying cold seeps and gas hydrate deposits.

In Figure 7.24, structure I hydrates underlie bacterial mats of giant sulfide-oxidizing bacteria (*Beggiatoa*) and fields of *Calyptogena* clams that have sulfide oxidizing bacteria in their gills. Both the sulfide concentration and rate of sulfide flux determines the species present and the location close to the hydrate deposits. Distribution is mainly related to sulfide fluxes regulated by the supply of methane (electron donor) from below and sulfate (electron acceptor) from above, for the AOM, mediated by consortia of methanotrophic archaea, and sulfate reducing bacteria.

Sahling et al. (2002) indicate that the diffusive sulfide fluxes limit the growths that are classified into:

1. Beggiatoa at the mudline with a sulfide flux of 23 ± 13 mol/m^{2}yr
2. Calyptogena clams at the mudline with a sulfide flux of 6.6 ± 2.4 mol/m^{2}yr
3. Acharax at 5 to -30 cm below seafloor, with a sulfide flux of 0.05 ± 0.05 mol/m^{2}yr

These different settings have fluid flow rates varying over four orders of magnitude.

Boetius and Suess (2004) note that clams, mussels, and tubeworms have distinct adaptations to obtain oxygen from the seawater and sulfide from the sediments. If fluid flow is reduced so that sulfide does not reach the seafloor, these communities are replaced by specially adapted faunas, such as Acharax, that are

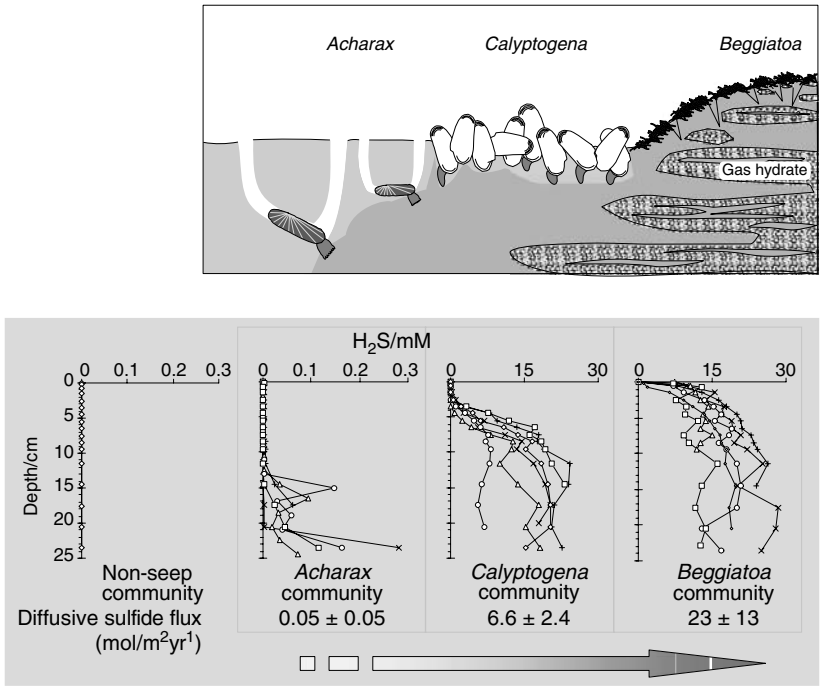

FIGURE 7.24 Chemo-synthetic species above their H_2S concentrations and fluxes. Note that *Beggiatoa* and *Calyptogena* overlie the hydrate deposits. (From Sahling, H., et al., *Marine Ecol. Prog. Ser.*, **231**, 121 (2002). With permission.)

able to burrow more deeply into the sediments to obtain sulfide. Members of the deep-sea community invade seeps to use the seep fauna, or seep structures as a habitat, as in the case of ice worms (Fisher et al., 2000).

The biologically active surface (to 10 cm depth) has a methane flux that varies between 1 and 100 mmC/m^2 per day. The hydrate results from free gas and gas dissolved in water. Two types of hydrate fabric result: (1) porous hydrates, from accumulation of bubbles of free gas and (2) massive hydrates, with twice the density of porous hydrates (0.9 g/L versus 0.4 g/L). In the recent Raman spectroscopy, southern Hydrate Ridge experiments by the MBARI (Hester et al., 2005), the near-surface hydrate Raman specta contained significant amounts of free gas as well as hydrates, with only a trace of hydrogen sulfide in the methane gas.

Another way of considering the hydrates at Hydrate Ridge relates to the SMI concept of Paull, indicated in Section 7.2.2. At Hydrate Ridge, hydrates near the surface (up to a few meters) are related to rapid methane flux from below, perhaps with contributions from dissociated hydrates. While these hydrates relate to the SMI, as indicated in reaction (7.5), the methane comes from below, and the

near-surface methane hydrate concentration is not indicative of the entire Hydrate Ridge reserve.

Below the SMI to a submudline level ten times the depth of the SMI, hydrates are not found because the methane concentration is too low to produce hydrates. It should be noted that this Rule of 10 is perhaps related to methane solubility limit in the liquid phase. Even though the deeper hydrate layers have a lesser concentration, due to the larger volume, the deeper hydrate amounts represent the largest in the reservoir, and cause the total reservoir concentration to be estimated at 2.5% of pore volume.

7.8.2.2 Deeper hydrates at Southern Hydrate Ridge: characterization and assessment

Even with the high concentrations of the near-surface hydrates, the deeper (>20 m) hydrate deposits contain most of the gas in the hydrated reservoir. This deeper hydrated gas is mostly biogenic, with anecdotal incidents of 10% thermogenic gas.

Figure 7.25 shows the position of five Leg 204 drill sites. The off-summit Site 1245 intersects an unusual horizon marked "A" extending from about 1600 to 1400 m (although not shown here, this fault does extend to the summit). This silty sand horizon is important because its porosity and permeability allows for rapid

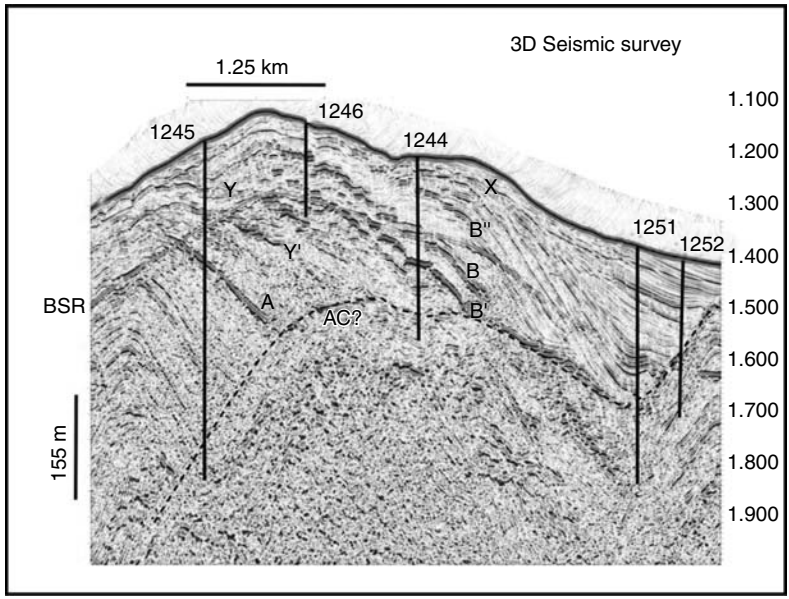

FIGURE 7.25 The position of five off-summit drill sites at southern Hydrate Ridge. Note the under-thrust sediments of the accretionary complex labeled AC. The reflections labeled A, B, and B′ result from gas-charged, coarse-grained sediments. (From Tréhu, A.M., et al., *Earth Planet Sci. Lett.*, **222**, 845 (2004b). With permission from Elsevier.)

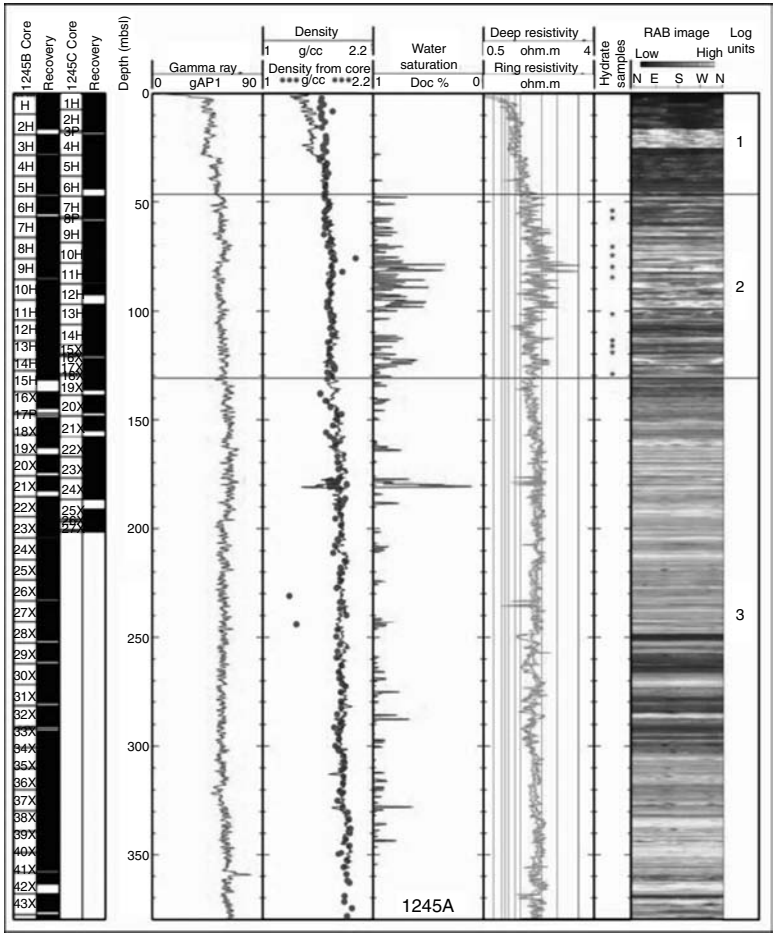

FIGURE 7.26 (See color insert following page 390.) Site 1245A southern Hydrate Ridge Flank logs (gamma ray, density, Resistivity at Bit, and Archie water saturation). (T.S. Collett, Personal Communication, November 18, 2005, Leg 204, Scientific Party, 2005)

migration of free gas and methane-saturated fluids from depth. Horizon A acts as a restricted pipeline to transport lighter fluids from depth to the summit.

Sediment stratigraphy controls the hydrate distribution at Hydrate Ridge. The methane-rich migration pathway of Horizon A provides enriched hydrate formation relative to other sediments. In Figure 7.26, the remote sensing logs (gamma ray, density, RAB, and Archie water saturation) are most sensitive to hydrates.

7.8.2.3 Logs and remote sensing

In the well logs of Figure 7.26 for Site 1245A note the log responses (e.g., the high water content indicated by the resistivity) indicative of hydrates between the two

black horizontal lines where the hydrate saturation ranges between 10% and 80% of pore volume. The high water content means low hydrate saturation. Hydrate saturation is typically around 10–15%. The maximum concentration is 60%, and then only at two spikes. Around 70 m a fine-clay porosity restricts the hydrate saturation to 10–20% of pore volume, while further down at around 175 m, the more porous/permeable silt (associated with Horizon A in Figure 7.25) provides for hydrate occupation of up to 60–80% of pore volume.

The subtleties of the well logs for hydrate detection at Site 1245A for the southern Hydrate Ridge flank can be contrasted with the more prominent hydrate indications at Hydrate Ridge crest, through the well logs data of Figure 7.27. In the figure, note particularly the region between 20 and 50 mbsf, where three logs

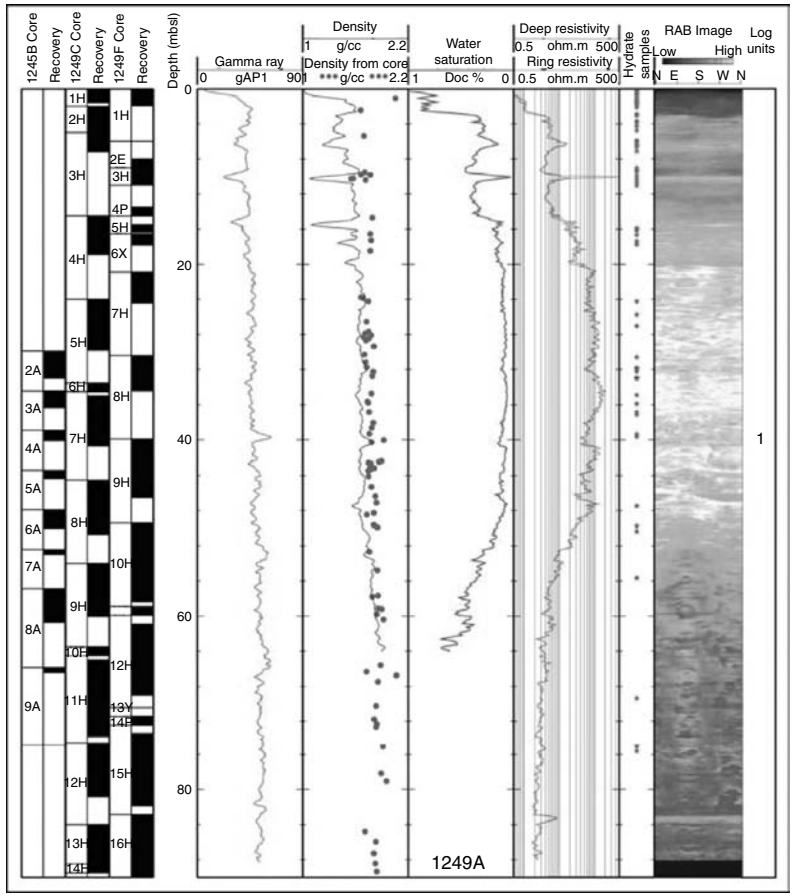

FIGURE 7.27 (See color insert following page 390.) Site 1249A southern Hydrate Ridge crest remote sensing logs (gamma ray, density, RAB, and Archie water saturation). (T.S. Collett, Personal Communication, November 18, 2005, Leg 204 Scientific Party, 2005.)

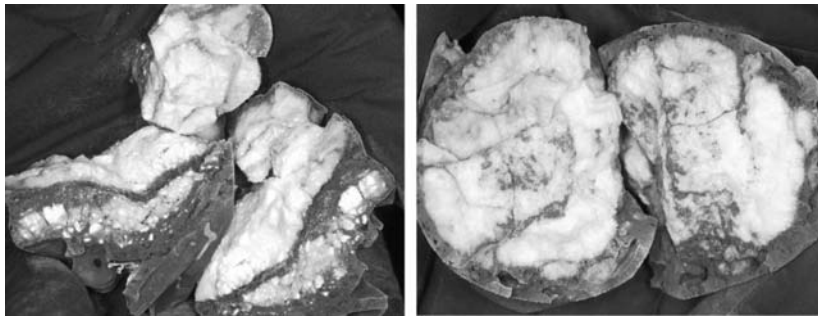

FIGURE 7.28 Site 1249F southern Hydrate Ridge crest recovered hydrate cores. (T.S. Collett, Personal Communication, November 18, 2005, Leg 204 Scientific Party, 2005.)

(water saturation, resistivity, and the lighter sections of RAB) provide a combined remote sensing image of hydrate occurrence. Visual evidence of massive recovered hydrates at the same Site 1249F, are shown in Figure 7.28 confirming the log.

In combination, these logs give further evidence of gas migration from the ridge flank (in Figure 7.26 of Site 1245A, at 70 and 175 mbsf) to the ridge summit (in Figure 7.27 of Site 1249A at 20–50 mbsf).

7.8.2.4 Coring and direct evidence

Tréhu et al. (2004b) compared hydrate estimates from RAB such as those shown in Figures 7.26 and 7.27, with more direct hydrate evidence from cores of the following three types:

1. Infrared (IR) sensing of the cores gave reduced temperatures (ΔT) as a result of endothermic heats of hydrate dissociation. These temperature indications were taken as linearly related to the amounts of hydrate present.
2. Hydrated-methane evolution from the pressure core sampler (PCS) was far beyond the normal gas solubility in the core waters, and provided an estimate of hydrate amounts.
3. Reduction in chlorinity resulted from hydrate dissociation upon retrieval, and the amount of the reduction can be used to estimate hydrate amount (Torres et al., 2004). It should be noted that an accurate method was determined for the chlorinity baseline decrease, due to the deposit of ions within the shale, and the expulsion of fresh water from the shale, due to overpressure.

Tréhu et al. (2004b) distinguish between the GHSZ defined as the region from the BSR to the mudline, and the GHOZ, a thinner zone, defined as the region

TABLE 7.12
Hydrate Amount Estimates (% Pore Volume) Via Four Techniques

Estimated method→ Site/BSR(m)↓	ΔT GHOZ/GHSZ	PCS GHOZ/GHSZ	Chlorinity GHOZ/GHSZ	RAB GHOZ/GHSZ Hole A at site	Overall GHOZ/GHSZ
1245B/134	3.8/1.9	NA	3.0/2.0	3.1/1.9	2.74/1.74
1247B/130	1.9/1.5	2.6/1.3	1.5/0.8	2.0/1.6	2.74/1.74
1250C/114	2.6	0.7	4.3	26/5	NA
1251B/200	9.4	1.6/1.2	0.5/0.5	1.2/1.0	2.48/2.00

from the BSR and the shallowest occurrence of hydrate based on one of the three indicators above.

Table 7.12 compares the hydrate amounts (as percent of pore space) estimated by the above three techniques, to that from the RAB for the GHOZ and GHSZ. Below the surficial hydrates mentioned earlier, for a few tens of meters below the mudline, the methane concentration is not sufficient for hydrate formation. One possible reason for the discrepancy in the values of GHOZ and GHSZ is "Paull's Rule of 10," which relates hydrate depth to ten times the SMI, as discussed in Section 7.2.2. As mentioned this Rule of 10 may be related to methane solubility.

In the formation model of the above hydrate concentrations, Torres et al. (2004) indicate that the pressure of hydrate crystallization can exceed the overburden pressure. This can occur at shallow subseafloor depth, to cause massive hydrate deposits such as those shown in Figure 7.28, if hydrates do not promptly cement the grains. This finding is similar to that observed by Sassen and coworkers in the Gulf of Mexico (Personal Communication, November 10, 2005). Torres and coworkers also suggest that methane dissolved in water alone is insufficient to cause the noted hydrate concentrations—there must be additional free gas present.

Linke et al. (2005) provide macroscopic evidence of free gas in recovered cores, but it might be argued that such gas could evolve from dissociated hydrates. However, in recent MBARI ROV Raman spectroscopy deployment at the crest of southern Hydrate Ridge, Hester et al. (2005) presents spectroscopic evidence for free gas associated with hydrates at the seafloor. An earlier paper by Bohrmann et al. (2002) suggested hydrates act as an enclosure to free gas, as does the observations of bubble streaming from the seafloor (Heeschen et al., 2003). This "Bubble-wrap" mechanism finds an analogy in hydrate formation in pipelines, shown in Chapter 8, and some cross-technology applications.

7.8.2.5 The lessons of Hydrate Ridge

Because this site is one of the most extensively studied in the world, the lessons from it are important to summarize for future seafloor hydrate exploration:

1. The cold seeps of methane migration along the geologic faults or permeable stratigraphic horizons provide concentrations in excess of

methane solubility, resulting in two types of hydrate communities:
   (a) Surface hydrates have an evolved synergism between hydrates, chemoherms, and chemosynthetic communities. These communities provide visual hydrate prospecting tools for high (30–40% of pore volume) surface hydrate amounts. In these communities the free gas affects hydrate fabric and morphology.
   (b) Deeper hydrates extend from 20 to 200 mbsf, in which the pressure of crystallization may exceed that on the seafloor to provide massive amounts of hydrates. The concentration of these deeper hydrates is less than 2% of pore volume, but the overall hydrate amounts in the deep deposits far exceed the surficial hydrates.
2. Well logs from Hydrate Ridge indicated acceptably consistent estimates of hydrate occurrence, particularly water saturation, and RAB. Hydrate concentration data from logging tools have been confirmed and quantified by more direct core methods of IR sensing of temperature, gas evolution, and chlorinity decrease.
3. There are deeper zones of stratigraphically controlled hydrates that can contain up to 20% of pore space, when averaged over zones 10 m thick.
4. The cold seeps at Hydrate Ridge, cause this site to be labeled a "sweet spot" of high hydrate concentration, relative to others such as the Blake-Bahama Ridge (ODP Leg 164) example that may be more representative of hydrate deposits in the world. Tréhu et al. (2004a) estimate $1.5–2 \times 10^8$ m^3(STP) of methane for the summit deposit, on the basis of the drilling and seismic data, which also define the limits of the deposit. Tréhu (Personal Communication, January 8, 2006) indicated that this amount is comparable to a small gas field, not economical unless facilities are already in place.

7.8.3 Case Study 3: Messoyakha (Hydrate Production in Permafrost)

The Messoyakha gas hydrate field is the first exemplar for gas production from hydrate in the permafrost. Hydrates were produced from this field semicontinuously for over 17 years. The field is located in the northeast of western Siberia, close to the junction of the Messoyakha River and the Yenisei River, 250 km west of the town of Norilsk, as shown in Figure 7.29.

Figure 7.30 provides a cross section of the field, showing the hydrate deposit overlying the free gas zone. The depth–temperature plot of Figure 7.31 from Sheshukov (1972) shows the hydrate layer to extend to the intersection of the 281 K geotherm, later determined to be closer to 283 K by Makogon (1988). The gas in the hydrate zone is both in the free and in the hydrated state. Makogon (1988) provided summary information regarding the properties of the field, as tabulated in Table 7.13. Krason and Finley (1992) provided an additional summary.

A suite of well logs from Well Number 136 of the Messoyakha field is presented in Figure 7.32 by Sapir et al. (1973). The Soviet work indicated the need to use a

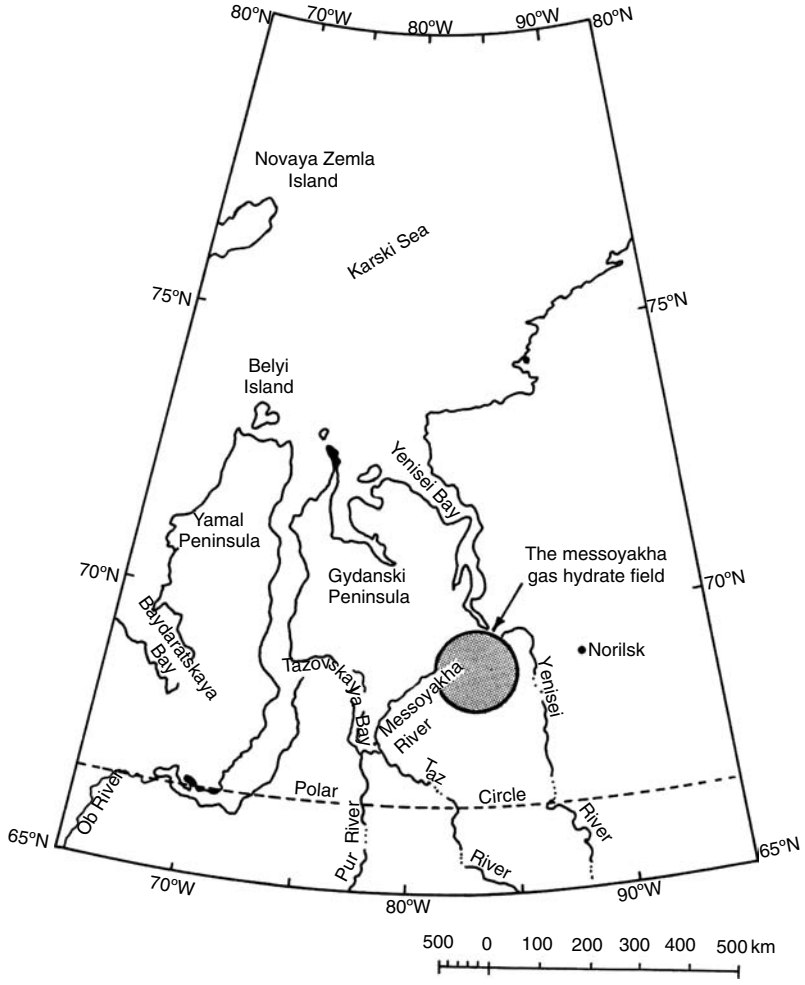

FIGURE 7.29 Location of Messoyakha gas hydrate field. (Reproduced courtesy of U.S. Dept. of Energy (Krason and Ciesnik, 1985).)

suite of well logs rather than a single log to indicate hydrates, similar to the later findings in the Western hemisphere as previously discussed in Section 7.5.

The Messoyakha field has been produced through both inhibitor injection and depressurization, as well as combinations of the two. The inhibitor injection tests, presented in Table 7.14 from the combined results by Sumetz (1974) and Makogon (1981, p. 174), frequently gave dramatic short-term increases in production rates, due to hydrate dissociation in the vicinity of each injected well bore. In the table, methanol and mixtures of methanol and calcium chloride were injected under pressure, using a "cement aggregate." For long-term dissociation of hydrates, depressurization was used.

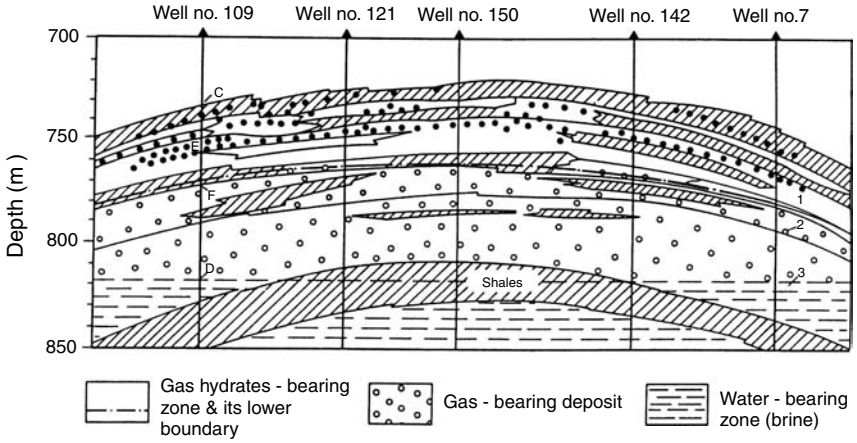

FIGURE 7.30 Cross section of Messoyakha field with hydrates overlying gas. (Reproduced from Makogon, Y.F., "Natural Gas Hydrates: The State of Study in the USSR and Perspectives for Its Use," paper presented at the *Third Chemical Congress of North America*, Toronto, Canada, June 5–10 (1988). With Permission.)

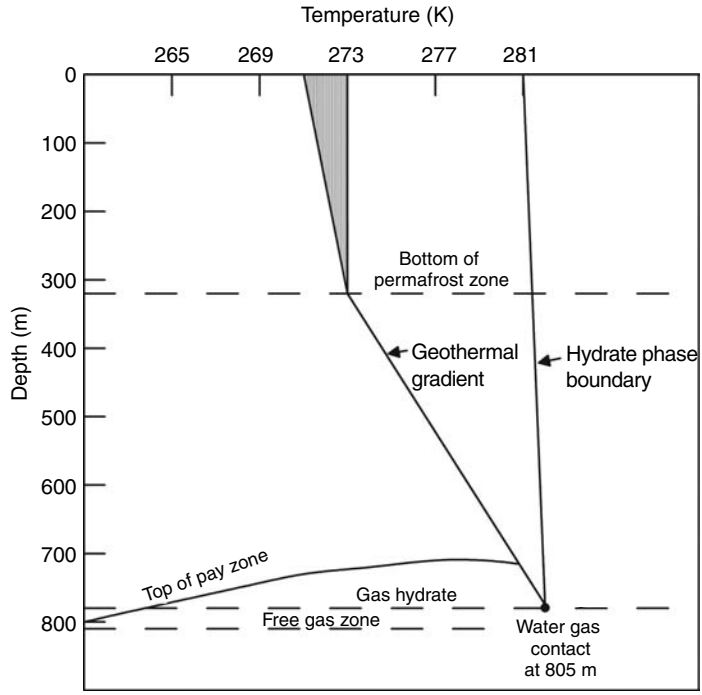

FIGURE 7.31 Gas hydrate stability envelope at Messoyakha. (Reproduced courtesy of U.S. Dept. of Energy (Sheshukov, 1972).)

TABLE 7.13
Properties of Messoyakha Gas Hydrate Field

Area of the pay zone	12.5 km
Thickness of the pay zone	84 m
Open porosity	16–38% (average 25%)
Residual water saturation	29–50% (average 40%)
Initial reservoir pressure	7.8 MPa
Reservoir temperature range	281–285 K
Reservoir water salinity	<1.5 wt%
Water-free gas composition	98.6% CH_4
	0.1% C_2H_6
	0.1% $C_3H_8^+$
	0.5% CO_2
	0.7% N_2

Source: After Makogon,Y.F., "Natural Gas Hydrates: The State of Study in the USSR and Perspectives for Its Use," paper presented at the *Third Chemical Congress of North America*, Toronto, Canada, 1988. With permission.

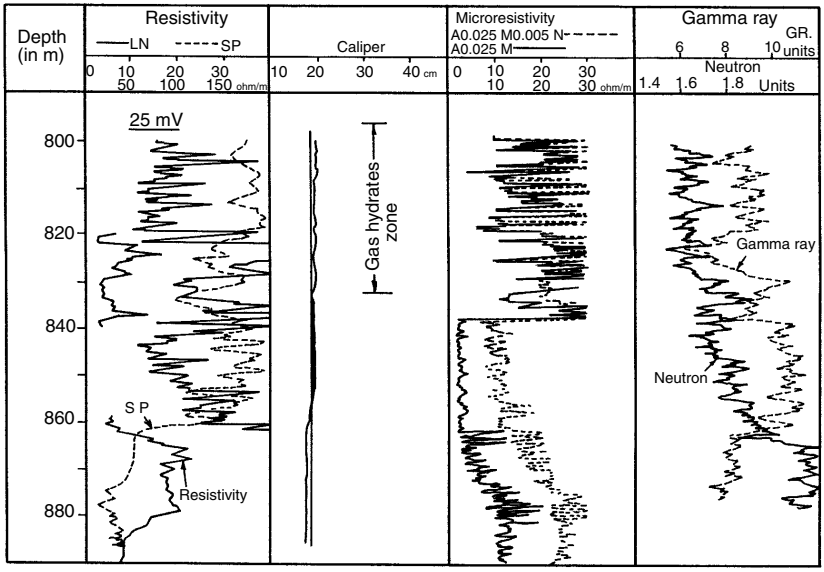

FIGURE 7.32 Well Logs from Well Number 136 at Messoyakha. (Reproduced Courtesy of U.S. Dept. of Energy (Sapir, et al., 1973).)

TABLE 7.14
Test Results from Inhibitor Injection in the Messoyakha Field

Well no.	Type of inhibitor	Volume of inhibitor m^3	Gas flow before treatment 1000 m^3/day	Gas flow after treatment 1000 m^3/day
2	96 wt% methanol	3.5	Expected results not achieved	
129	96 wt% methanol	3.5	30	150
131	96 wt% methanol	3.0	175	275
133	Methanol	Unknown	25	50
			50	50
			100	150
			150	200
138	Mixture 10% MeOH 90 vol% of 30 wt% $CaCl_2$	4.8	200	300
139	Mix of Well 138	2.8		
141	Mix of Well 138	4.8	150	200
142	Methanol	Unknown	5	50
			10	100
			25	150
			50	200

Source: From Sumetz, V.I., *Gaz. Prom.*, 2, 24, 1974 and Makogon, Y.F., *Hydrates of Natural Gas*, Moscow, Nedra, Izadatelstro, (1974 in Russian) Transl. J. Cieslesicz, PennWell Books, Tulsa, Oklahoma, 237pp., 1981. With permission.

Makogon (1988) indicates that of all the complex studies obtained during the 19 years of the production life of the Messoyakha field, the most informative results came from an analysis of the reservoir pressure change as a function of the gas withdrawal rate. A diagram showing pressure and gas production as a function of time is shown in Figure 7.33, with the accompanying pressure–temperature relationship in Figures 7.34a,b. While Figure 7.34a may represent the measured pressure–temperature values (Makogon, 1988) far away from the hydrate, Poettmann (Personal Communication, July 20, 1988) suggested that the values in the neighborhood of the hydrate interface are better represented by Figure 7.34b, for reasons given below. The combination of these three figures represents a classic study in slow depressurization, done via the production of the free gas reservoir over a period of years.

In Figure 7.34 the following initial points are used (with C,D,E,F corresponding to letters on Well No. 109 in the reservoir diagram of Figure 7.30): AB = hydrate equilibrium line; C = temperature at the top of the pay zone; D = temperature at a level of gas and water contact; E average gas–hydrate temperature; F = temperature at boundary surface between gas and gas–hydrate reserves; H = beginning dissociation pressure for gas hydrates.

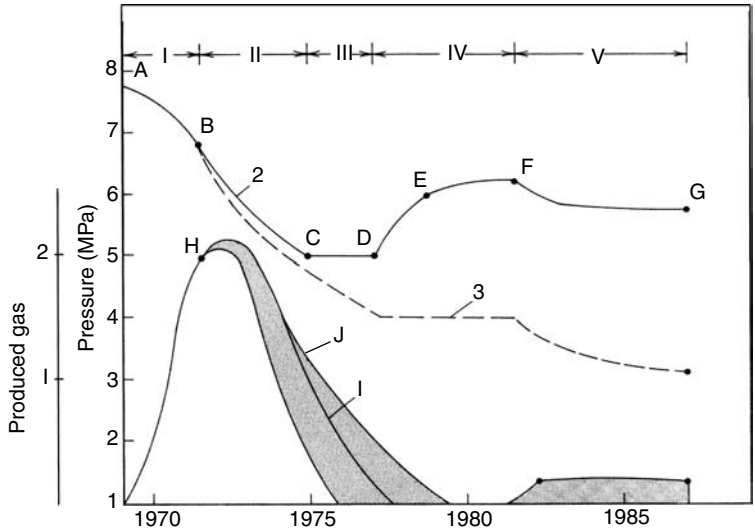

FIGURE 7.33 Pressure (upper curves) without hydrates (dashed) and with hydrates (solid) as a function of time; Produced gas (lower curves) both with and without hydrates. See text for labels. (Reproduced from Makogon, Y.F., "Natural Gas Hydrates: The State of Study in the USSR and Perspectives for Its Use," paper presented at the *Third Chemical Congress of North America*, Toronto, Canada, June 5–10 (1988). With Permission.)

As the production of the field was begun from 1969 to mid-1971, the pressure decreased from E to just above the hydrate dissociation point at H in Figures 7.33 and 7.34a,b. During this period, only free gas was produced because the pressure was above the hydrate equilibrium value.

When the pressure reached the hydrate equilibrium value at point H, the hydrates began to dissociate, adding the shaded portion to the gas production curve at the lower half of Figure 7.33. The top half of Figure 7.33 shows the reservoir pressure was maintained at a higher value (solid line 2) than the expected pressure (dashed line 3) due to the addition of gas to the reservoir by the hydrates. After point H in Figure 7.34a, Makogon (1988) indicated that the pressure away from the hydrate decreased below the equilibrium value, with a slight decrease in temperature. The pressure at the hydrate interface in Figure 7.34b, however, should not deviate from the equilibrium line, unless all of the hydrates were dissociated. Consequently, the pressure and temperature at the hydrate interface decreased along the equilibrium curve as the reservoir was depressurized. Between the third and sixth year of the field development there was probably a pressure drop between the hydrate interface, from H to L in Figure 7.34b, and the measured pressure from H to L in Figure 7.34a, due to the flow of gas in porous media.

As the Messoyakha reservoir attained the pressure at point L, the average pressure stabilized for 2 years to point M, indicating that the volume of gas recovered was replenished by the gas liberated from the hydrate. The difference between

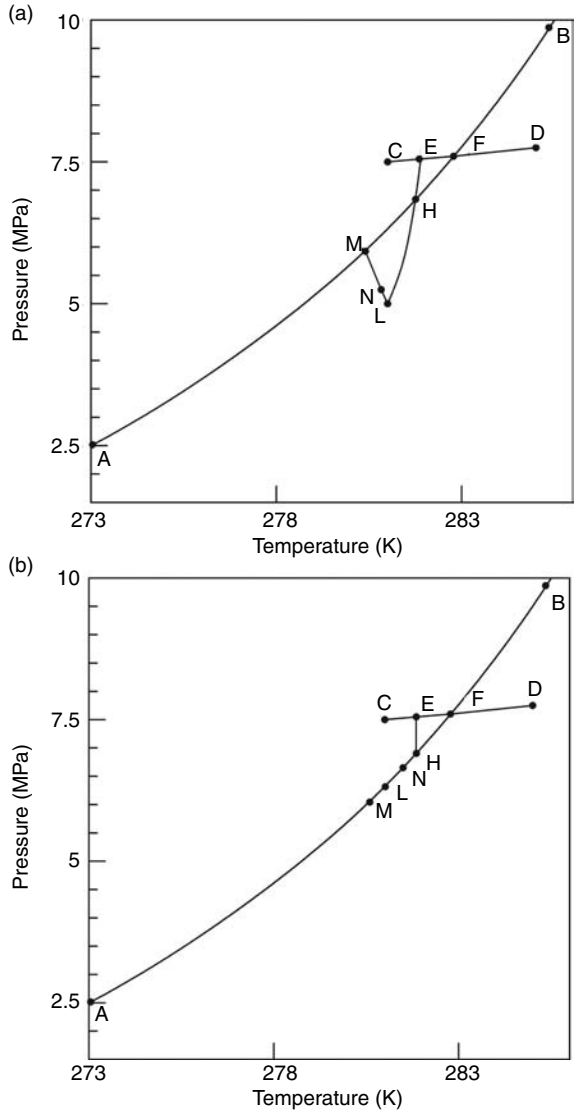

FIGURE 7.34 Messoyakha pressure and temperature with hydrate production (top) away from hydrate face (Makogon, 1988), (bottom) hypothesized at hydrate face (Poettmann, Personal Communication, July 20, 1988).

curves I and J in Figure 7.33 indicates that the total gas produced (curve I) was slightly less than the gas liberated (curve J) by the hydrates. During this period, from the seventh to the eighth year of the life of the reservoir, the pressure away from the hydrate face in Figure 7.34a rose slightly (L→M), compensated by a corresponding pressure decrease at the hydrate face in Figure 7.34b.

At point M, the reservoir was shut in, while other higher pressure reservoirs were produced (Makogon, 1988). During that period, the average pressure of the reservoir began to rise from point M to point N in Figure 7.34b. The difference between curves I and J in Figure 7.33 indicates that gas continued to be liberated by the hydrate until the reservoir pressure was uniform in mid-1981. As the average gas pressure approached the equilibrium value, the amount of gas produced decreased exponentially. Makogon indicated that the temperature of the reservoir tended to be restored to its original value, after a period of time. The equilibrium pressure itself rose slightly as the high reservoir heat capacity increased the temperature of the hydrate mass.

Since 1982 there has only been a modest production of the Messoyakha reservoir. The amount of gas withdrawn has been equivalent to the amount of gas liberated from the hydrate. The total amount of gas liberated from hydrates thus far has amounted to 36% of the total gas withdrawn from the field. It is noted further that the position of the gas–water interface did not change over the 17-year period of the production of the field.

7.8.4 Case Study 4: Mallik 2002 (Hydrate Production in Permafrost)

For readers who wish more Mallik 2002 details than the present, a brief overview is referred to the 63-paper compilation in the GSC Bulletin 585 (Dallimore and Collett, 2005) that includes a CD of manuscripts, an interactive-data viewer CD, and expanded charts and maps.

While the Messoyakhan well was an engineering production application from hydrates, the Mallik 2002 well provided the first scientifically documented evidence that gas could be produced from hydrates. It may be suggested that this concept had been shown before at Messoyakha (Makogon, 1988), however, while there is widespread agreement that hydrates did play some part in Messoyakhan production, some authors (e.g., Collett and Ginsburg, 1998) have suggested that a detailed understanding of the role of hydrates in Messoyakhan production is unclear.

Another perspective relating Messoyakha to Mallik 2002 is that applications drive research, as suggested in the preface. That is, the engineering production of hydrates in the Messoyakha field over the decade of the 1970s provided an impetus for further research with scientifically enhanced tests at Mallik 2002, which were not feasible at the time of Messoyakhan production. Consider only three differences of many:

1. At Messoyakha, production from gas hydrates began substantially about 2 years after the initial depressurization of the gas reservoir underlying hydrates, as shown in Figure 7.33. As indicated below, the Mallik 5L-38 site was chosen because the presence of hydrates had been validated there twice before (Mallik L-38 in 1972 and Mallik 2L-38 in 1998). Yet the Mallik site had no BSR because only a few meters of free gas underlay the hydrates, making Messoyakha-like depressurization problematic. However, in any short-term production testing, it is

impractical to wait for 2 years before obtaining results from hydrate dissociation by depressurization

2. Many scientists were involved to document the Mallik effort. In contrast to a relatively small number of engineers at Messoyakha, the Mallik 2002 well had 265 scientists and engineers who participated from six different entities [Japan National Oil Corporation (JNOC), GSC, BP–Chevron–Burlington joint-venture, the International Continental Scientific Drilling Program (ICDP) based at GFZ (GeoForschungsZentrum-Potsdam), the Indian National Gas Hydrate Program (NGHP), and the United States (Department of Energy and United States Geological Survey)].

3. Many modern scientific tools were applied to Mallik that were not available at the time of Messoyakha. For example, well logs had advanced substantially so that it was possible to determine, for example, the porosity, permeability, and hydrate saturation of the sediments at Mallik, which were not available at Messoyakha. In addition, reservoir models for hydrate production could be based upon well-constrained Mallik 2002 production data, such as pressure stimulation tests over constrained well intervals or thermal stimulation tests.

After the differences between the two production sites, it is important to list the two major accomplishments of Mallik 2002:

1. Gas was immediately produced from hydrates via controlled depressurization and thermal stimulation tests, without question regarding the gas source.
2. Data were obtained to calibrate well logs and gas hydrate production simulators.

The above two accomplishments are milestones in the knowledge development of hydrates in nature. It is now beyond question that gas can be produced from hydrates, and that data from such production can be accurately modeled. However, because only a few days were spent proving the concept, the transient results prevented the unambiguous long-term modeling of hydrate production, as shown in the sections that follow. As one result of this work, it appears to be important to provide a longer production test, to enable the long-term projection of gas production from hydrates.

7.8.4.1 Background of the Mallik 2002 well

In the Mallik L-38 (ca. 69°27′ latitude, 134°40′ longitude) well drilled in 1972, Bily and Dick (1974) provided one of the first permafrost hydrate descriptions, from a MacKenzie Delta well site on Richard's Island bordering the Beaufort Sea in Canada. In 1998 the JAPEX/JNOC/GSC 2L-38 well at the same site found core and well-log evidence for hydrates from 900 to 1100 m with *in situ* porosities of 35% and hydrate concentrations often in excess of 80% of the pore volume. The documentation of the 2L-38 well is provided in a compilation of 31 technical papers in GSC Bulletin 544 (Dallimore et al., 1999).

7.8.4.2 Overview of the Mallik 2002 well

When in 2002, the Japanese National Hydrate Program wanted evidence of the conceptual production of gas from hydrates, they chose the proven Mallik site, so it was natural to join with the Canadian Geological Survey. Over the course of the project, a team of 265 scientists/engineers joined the effort, with six major sponsoring entities, as indicated in the introduction.

The Mallik 2002 drilling program was conducted from December 25, 2001 until March 14, 2002, with the completion of two observation wells (3L-38 and 4L-38) drilled to 1188 m depth, coplanar with the 5L-38 main well, drilled to 1166 m. Well logs were obtained from 885 to 1151 m in 5L-38 (Collett et al., 2005). Forty-eight wireline cores were obtained (Dallimore and Collett, p. 82, 2005), three successful pressure stimulation tests (Hancock et al., 2005a) were performed over 0.5 m intervals, and a thermal stimulation test (Hancock et al., 2005b) was done over a 13 m reservoir interval.

In three zones 110 m of gas hydrate bearing strata were observed: (1) 892–930 m in which thermal stimulation was done for hydrate dissociation; (2) 942–993 m in which two successful pressure stimulation tests were performed over a 0.5 m interval, and (3) 1070–1107 m also with a successful pressure stimulation test. The average porosity was 29.3% over the hydrate interval and the average hydrate saturation was 47% of pore volume, with a bimodal distribution of hydrate saturations within the GHSZ. The lateral continuity in the area of the three historical wells (L-38, 2L-38, and 5L-38) indicated there is 5.39×10^7 m^3 of hydrated gas in place over an area of 10,000 m^2.

While a number of important results (e.g., well logs, coring methods, etc.) were determined in the Mallik 2002 test for future hydrate applications, this overview will concentrate on two major outcomes in the test itself: (1) proving the concept of gas production from hydrates and (2) modeling the gas production. The gas was principally of thermogenic origin, migrating from deeper in the earth, with low number of methanogens in the sediment (Colwell et al., 2005). In the cores, hydrates averaged about 40–50% of core volume, mostly in a pore-filling habit, as shown by sonic velocities and the new technique of magnetic resonance logging (Kleinberg, et al., 2005). The frozen mechanical strength of the cores at $-30°C$ was 22 MPa, decreasing to 6 MPa at 5°C. The sediments of the three hydrate zones of are briefly characterized as follows:

The Zone A (892–930 m) sand had uniform porosity of 32–38% with hydrates preferentially occupying the larger sediment pores and visible hydrate coatings on sand grains. The permeability of hydrate-free sand ranged from 100 to 1000 mD, but with hydrates present the permeability became as low as 0.1 mD. This region had very high hydrate saturations, frequently attaining values of 80% of pore volume.

Zone B (942–993 m) had interbedded silt and sand, with porosities between 30% and 40%, and hydrates occupying 40–80% of pore volumes. Without hydrates, the clay permeability was as high as 1 mD but with hydrates the sand permeability reduced to 0.01–0.1 mD.

Zone C (1070–1107 m) consisted of sandy silt of 30–40% porosities and hydrate saturations of 80–90% of pore volumes. With hydrates in sand, the permeability ranged from 0.01 to 0.1 mD, becoming less than 0.1 mD in silt.

The depths of the pressure stimulation and thermal stimulation experiments are superimposed on the methane phase equilibria—geothermal gradient diagram shown in Figure 7.35 (Wright et al., 2005). Without a BSR, the geothermal gradient

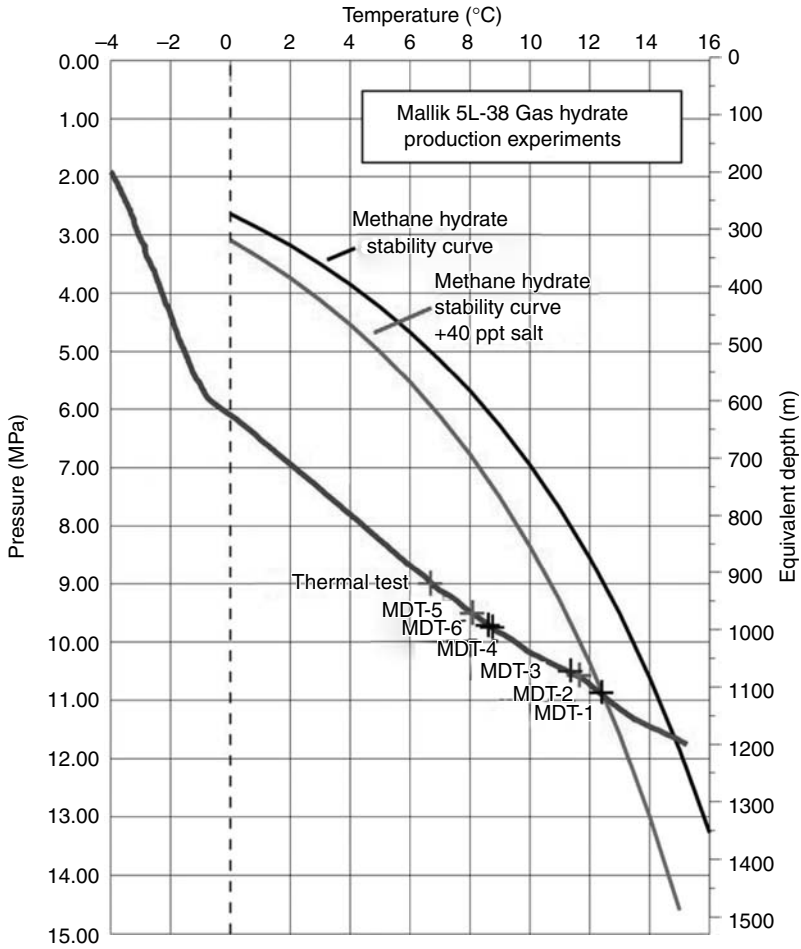

FIGURE 7.35 Mallik 2002 geothermal gradient and hydrate stability curve for pure water and water containing 40 ppt salt. Note the depths of the thermal stimulation test and the six pressure stimulation (MCT) tests. (From Wright, J.F., et al., in *Scientific Results from the Mallik 2002 Gas Hydrate Production Research Well Program*, Mackenzie Delta, Northwest Territories, Canada, Geological Survey of Canada Bulletin 585, including CD (2005). With permission.)

must be combined with the phase equilibrium line. Equilibrium data in Figure 7.35 are in Chapter 6, with prediction methods of Chapter 5 and the prediction methods of CSMGem on the disk in the Appendix of this book. These results confirm the suggestion of Wright et al. (2005) that when hydrates increase the salt in the remaining reservoir water, the sharp phase equilibrium boundary becomes displaced over a region from 0 to 45 ppt of salt concentration.

7.8.4.3 Well logs in Mallik 2002

Figure 7.36 shows the common well logs in the Mallik test Well 2L-38. Note the suite of wells confirming hydrates in the shaded region from about 900 to 1100 m, provide reinforcing evidence of gas hydrates.

In addition to the above suite of well logs, the newest type of log was obtained via NMR (here called CMR) as shown in Figure 7.37. In this new method, the capillary, clay-bound, and free water (on the right) as determined by the NMR log, are subtracted from the total porosity as determined by the density tool (not shown) to obtain the hydrate saturation in the middle column.

7.8.4.4 Pressure stimulation tests in the 5L-38 well

There were three successful Modular Formation Dynamics Tester (MDT) tests that provided two important pieces of information: (1) evidence of hydrates through the reservoir response to pressure simulation and (2) geomechanical/geothermal measurements at pressure production interval.

To illustrate the hydrate dissociation pressure response, consider the evidence for hydrates from one pressure stimulation test (MDT-2) at 1090 m depth in hydrate Zone C. Figure 7.38 (Hancock et al., 2005b). In this test 0.5 m of wells were temporarily sealed at the top and bottom of the section, before the well was perforated. In the figure three pressure stimulation tests were performed over the first 8 h, with pressure responses shown by the lower line:

1. About 30 min into the test, gas was removed for 8 min to reduce the pressure, then for 25 min the pressure increased as reservoir hydrates dissociated, flowing gas into the well.
2. Similarly at 1.2 h the pressure was drawn down for 37 min, and dissociating hydrates replenished the pressure over the next 69 min. The response time for the pressures can be modeled as indications of reservoir permeability, determined to range from 0.001 to 0.1 mD.
3. Just before 3 h into the test, the pressure was drawn down for 16 min, and gas from dissociating hydrates replenished the pressure over the next 190 min, until about 6.25 h into the test.

Between 7 and 8 h into the test, the flow was reversed and well fluids were pumped into the reservoir to cause three microfracture sequences. Finally just before 9 h in Figure 7.38, the interval was flowed for 21 min, and the pressure

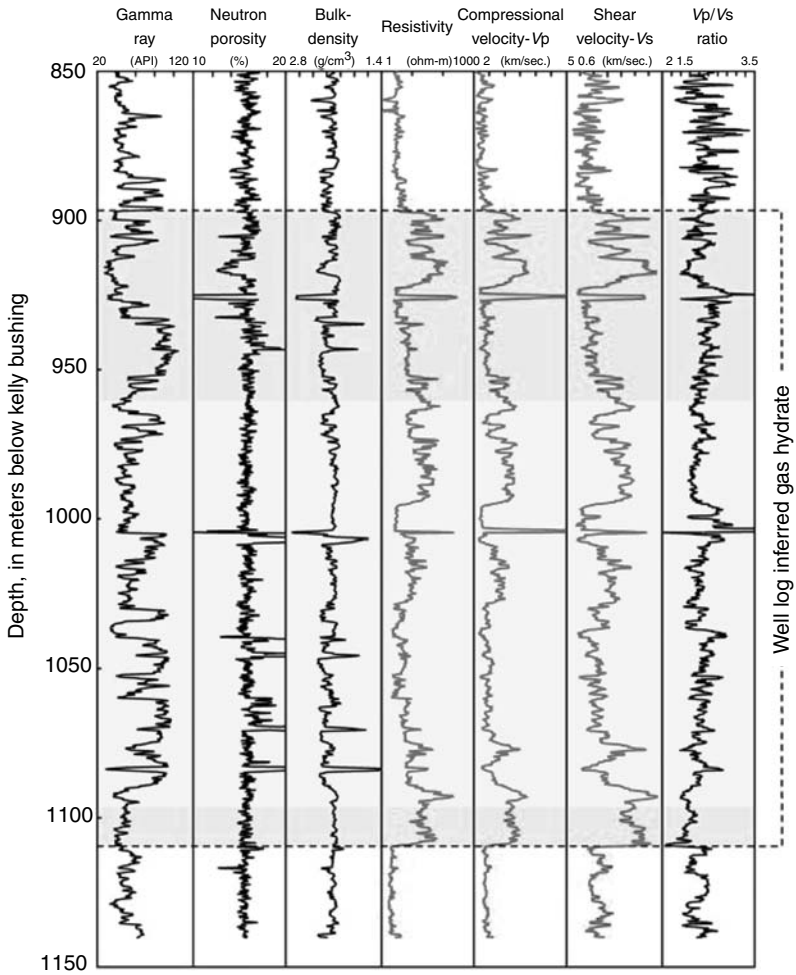

FIGURE 7.36 Well logs from Mallik 2L-38 showing inferred gas hydrates. (From Collett, T.S., et al., in *Scientific Results from the Mallik 2002 Gas Hydrate Production Research Well Program*, Mackenzie Delta, Northwest Territories, Canada, Geological Survey of Canada Bulletin 585, including CD (2005). With permission.)

rebuilt over the next 76 min, to determine the permeability increase due to the previous microfractures.

7.8.4.5 The Thermal stimulation test in Mallik 5L-38

A thermal stimulation test was performed on hydrates in Zone A, with well flow blockers above and below the interval between 907 and 920 m depth. The well was perforated over the 13 m length and hot brine was pumped down the circulation

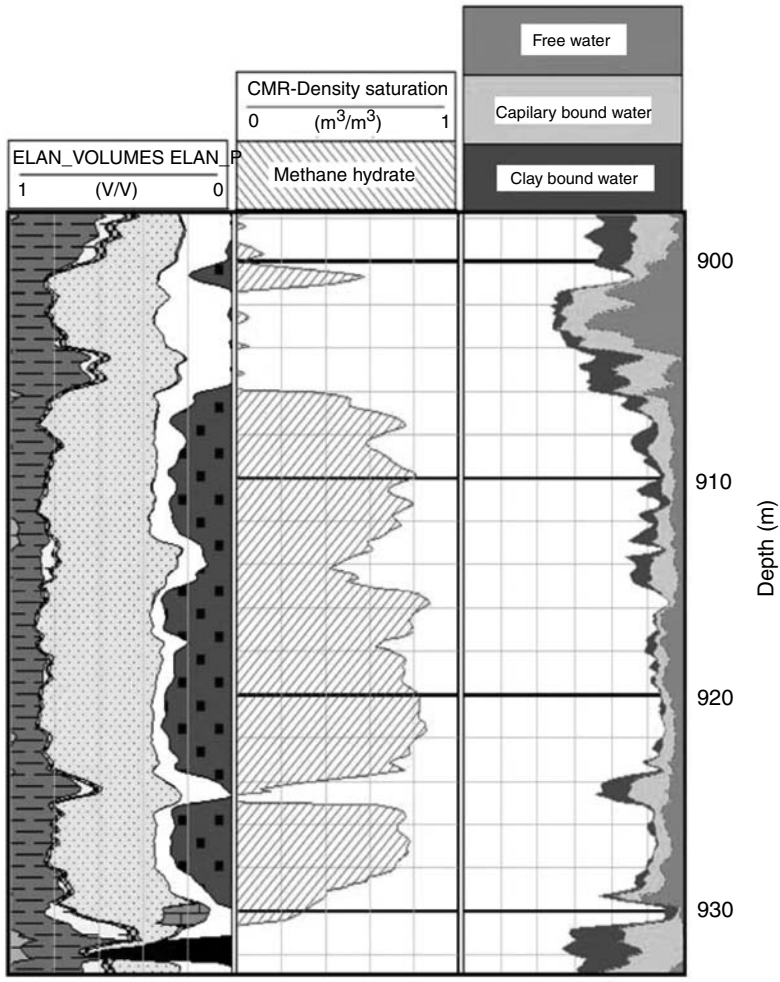

FIGURE 7.37 (See color insert following page 390.) 5L-38 CMR logs showing hydrate extent at depths between 900 and 930 m. Note that hydrates are obtained by the difference (middle column) between the total porosity as determined by density (not shown), and the capillary, clay-bound and free water determined by NMR.

string, returning in the outer tubing. In this way the 13 m of the reservoir was increased to above 50°C, as shown in Figure 7.39 (Hancock et al., 2005b). The resulting gas was handled at the wellhead by the process shown in Figure 7.40 (Hancock et al., 2005b) and sent to flare.

Over the interval of the test, the gas saturation averaged about 70% of pore volume, as shown in Figure 7.41 (Hancock et al., 2005b), and the permeability average was about 0.1 mD, indicated in Figure 7.42 (Hancock et al., 2005b). The Mallik Scientific Party (Dallimore and Collett, 2005) emphasized that the test was not designed as a conventional industrial-style test, but one to show the

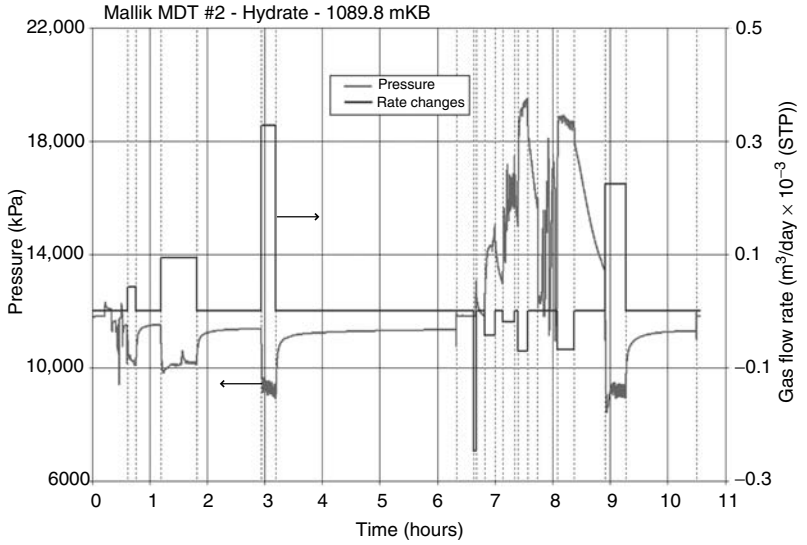

FIGURE 7.38 Mallik 2002 pressure stimulation test 2 at 1090 m, showing the initial three flow and shut-in sequences, 3 fractures sequences, and a final flow and shut in sequence. (From Hancock, S.H., et al., in *Scientific Results from the Mallik 2002 Gas Hydrate Production Research Well Program*, Mackenzie Delta, Northwest Territories, Canada, Geological Survey of Canada Bulletin 585, including CD (2005b). With permission.)

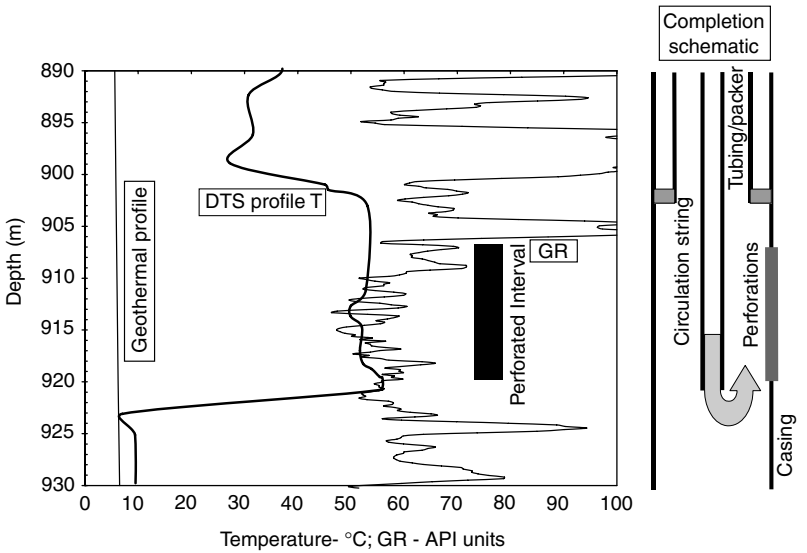

FIGURE 7.39 The Mallik 5L-38 thermal stimulation test. Note the geothermal profile (leftmost line) and reservoir temperature profile (middle line). (From Hancock, S.H., et al., in *Scientific Results from the Mallik 2002 Gas Hydrate Production Research Well Program*, Mackenzie Delta, Northwest Territories, Canada, Geological Survey of Canada Bulletin 585, including CD (2005b). With permission.)

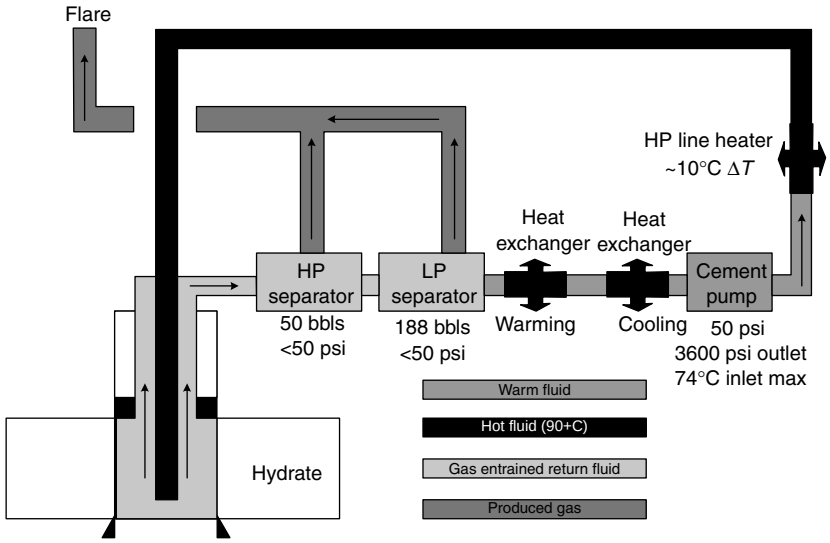

FIGURE 7.40 Mallik 5L-38 process flow diagram for well-head handling of gases and recirculating brine during thermal test. (From Hancock, S.H., et al., in *Scientific Results from the Mallik 2002 Gas Hydrate Production Research Well Program*, Mackenzie Delta, Northwest Territories, Canada, Geological Survey of Canada Bulletin 585, including CD (2005b). With permission.)

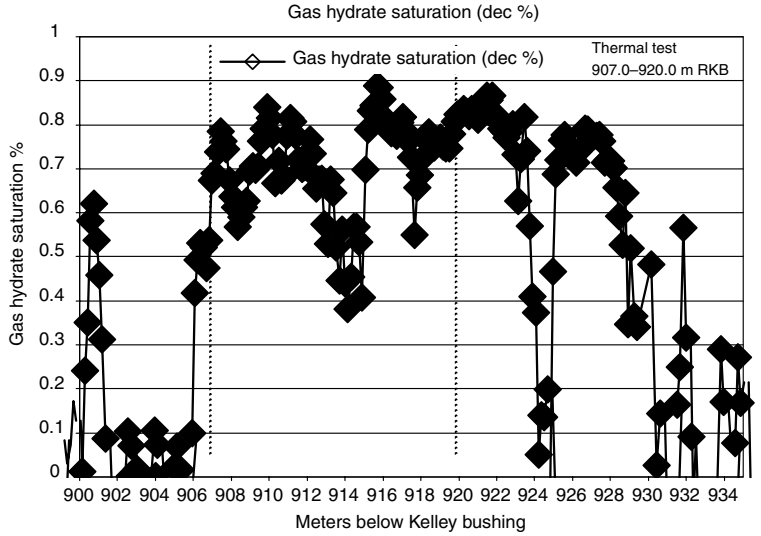

FIGURE 7.41 Mallik 5L-38 gas hydrate saturations at point of thermal stimulation test. (From Hancock, S.H., et al., in *Scientific Results from the Mallik 2002 Gas Hydrate Production Research Well Program*, Mackenzie Delta, Northwest Territories, Canada, Geological Survey of Canada Bulletin 585, including CD (2005b). With permission.)

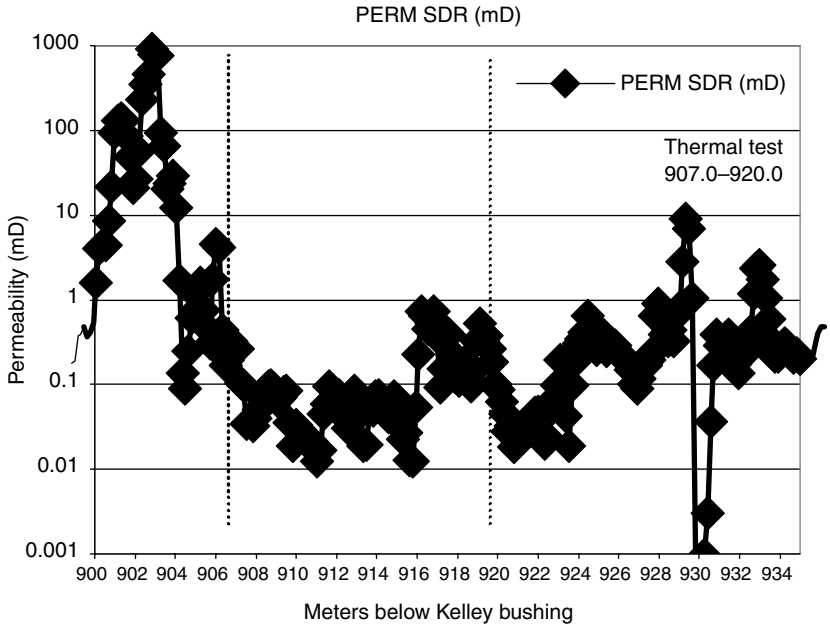

FIGURE 7.42 Mallik 5L-38 gas hydrate sediment permeability at point of thermal stimulation test. (From Hancock, S.H., et al., in *Scientific Results from the Mallik 2002 Gas Hydrate Production Research Well Program*, Mackenzie Delta, Northwest Territories, Canada, Geological Survey of Canada Bulletin 585, including CD (2005b). With permission.)

concept of producing gas from reservoir hydrates, and to provide calibration data for modeling. Figure 7.43 (Hancock et al., 2005b) shows the gas produced from the thermal stimulation test as a function of time. A total of 468 SCM was produced during the 125 h of the test, with another 48 m^3 produced during the test shutdown. Figure 7.44 (Dallimore and Collett, 2005) is a picture of flared gas from the thermal hydrate production test.

7.8.4.6 Modeling gas production from hydrates

Three models were used to fit the Mallik 2002 production data, and to extrapolate the results for long-term gas production: (1) the Kurihara et al. (2005) model, frequently called the JOE (Japan Oil Engineering Co., Ltd.) model, which was fit to the thermal stimulation and one pressure-stimulation test, (2) the Moridis et al. (2005) model, labeled LBNL (Lawrence Berkeley National Laboratory), which was used to model the thermal stimulation test, and (3) the Hong and Pooladi-Darvish (2005) model, which was used to predict production from first principles, rather than to fit data of the production itself.

In the LBNL model for the thermal test, initially shown as part of Figure 7.43 and repeated here in Figure 7.45 it is shown that heat-transfer-limited hydrate

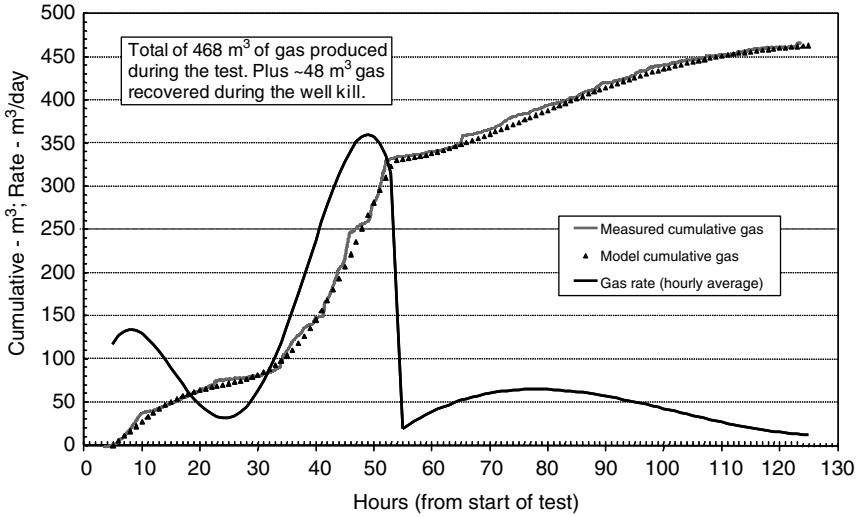

FIGURE 7.43 Mallik 5L-38 gas production on thermal test. (From Hancock, S.H., et al., in *Scientific Results from the Mallik 2002 Gas Hydrate Production Research Well Program*, Mackenzie Delta, Northwest Territories, Canada, Geological Survey of Canada Bulletin 585, including CD (2005b). With permission.)

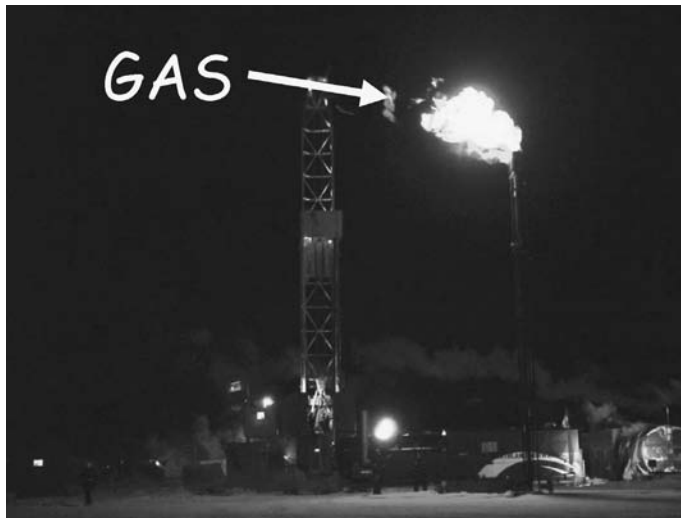

FIGURE 7.44 Flared gas from Mallik 5L-38 thermal stimulation test.

dissociation (marked "Simulation–Equilibrium" in the figure), rather than the kinetics of hydrate dissociation. The progress of the thermal wave to the hydrate interface was limited by a low hydrate thermal conductivity, so that hydrate kinetics were insignificant. The results of Figure 7.45 appear to match the data equally well,

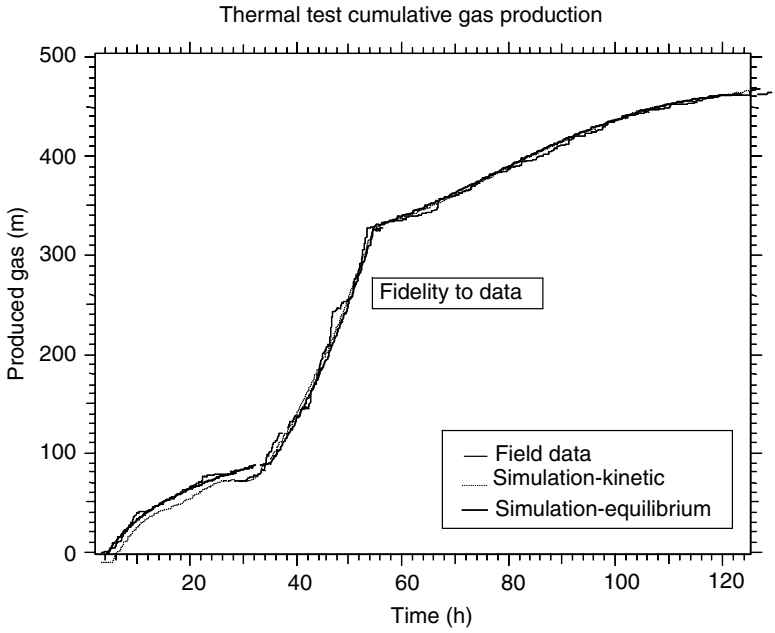

FIGURE 7.45 Cumulative gas production from Mallik 5L thermal test using LBNL heat transfer limited and kinetic dissociation models (Moridis et al., 2005).

whether hydrate kinetics are included or not. This result is confirmed in Hong's thesis (2003, p. 188) which indicates that the hydrate dissociation rate constant would have to be reduced by five orders of magnitude in order for hydrate kinetics to significantly limit the dissociation rate.

Consider the ten year cumulative gas production prediction of the JOE model shown in Figure 7.46 (note the logarithmic scale of both axes). From the figure it is clear that hot water circulation alone will not be productive for a period after 0.02 years, due to the low thermal conductivity of the hydrates and sediments. However, depressurization does appear to be a favorable production mechanism, comparing favorably to hot water circulation with reduce bottom hole pressure, or partial hot water injection.

Finally, it is important to note that, while both the JOE and LBNL model fit the Mallik production data acceptably, as shown in Table 7.15 both extrapolate to significantly different long-term production values, perhaps due to the short-term and transient nature of the Mallik production test.

Two things should be noted from Table 7.15: (1) while both the JOE and LBNL models fit the short-term Mallik 2002 data, the variation in predicted gas production varies from a factor of 3.7 to 290 and (2) the long-term gas production varies between 0.9 and 325 m^3/day.

While the above production rates are somewhat encouraging, the variation in the prediction provides impetus for longer-range testing, to eliminate the transient

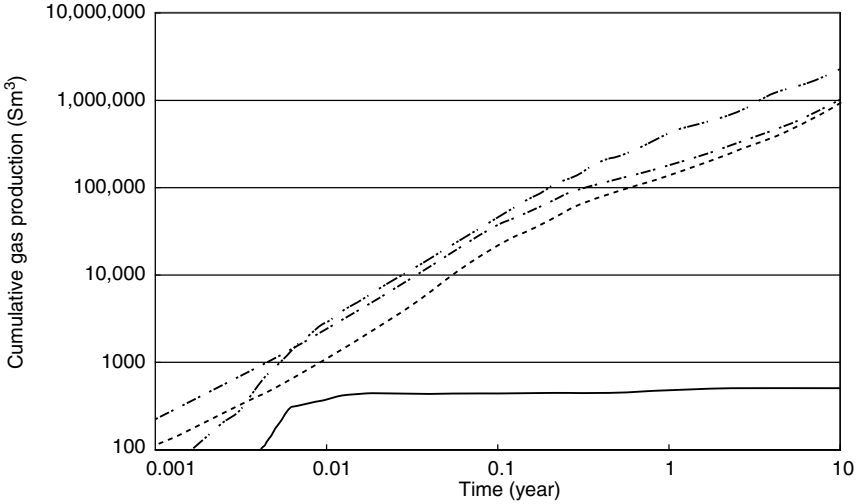

FIGURE 7.46 Cumulative gas production at Mallik 5l-38. Lowest line: hot water circulation. Second lowest line: depressurization. Third lowest line: hot water circulation with reduced BHP. Top line: partial hot water injection (Kurihara et al., 2005).

TABLE 7.15
Hydrated Gas Production Predictions of JOE and LBNL Models

Type test/model	Test period	JOE prediction, m^3	LBNL prediction, m^3
Depressurization (no heating) with 2.2 Mpa = bottom hole flow pressure	3 years	290,000	1,000
Depressurization with heating	5 days	500	1,850
	3 years	356,000	71,867

phenomena inherent in Mallik 2002, and provide a more fundamental basis for modeling.

7.9 SUMMARY

The hydrates-in-nature paradigm is currently changing from reservoir assessment to production from the most likely reservoirs. However, most of the methane-containing hydrates are in low concentrations (<3.5 vol%) in the ocean bottom. While production of gas from such lean, deep-lying hydrates is now too expensive, mankind is currently poised to produce hydrates, first from hydrates overlying gas in permafrost, then in the near future we will produce gas from "sweet spots" of high concentrations in the ocean, near where the distribution infrastructure exists.

With the hydrate technology from permafrost and ocean sweet spots in hand, it is likely that one day mankind will need to tap the leaner hydrate fuel source to meet growing energy demands.

References

Amann, H.-J, et al., ODP Leg 164 Shipboard Scientific Party, Explanatory Notes, in *Proc. Ocean Drilling Programme. Initial Reports*, **164**, 13 (1996).

Anderson, B.I., Collett, T.S., Lewis, R.E., Dubourg, I., in *Proc. SPWLA 46th Annual Logging Symposium*, New Orleans, LA, June 26–29, 2005.

Anderson, R., Biderkab, A.-B., Tohidi, B., Clennell, M.B., in *Proc. 63rd European Association of Geoscientist and Engineering Conference and Technical Expedition*, Amsterdam, June 1–15 (2001).

Andreassen, K., *Seismic Reflections Associated with Submarine Gas Hydrates*, Dr. Scient. Thesis, University of Tromso, Norway (1995).

Andreassen, K., Hogstad, K., Berteussen, K.A., *First Break*, **8**, 235 (1990).

Aoki, Y., Tamano, T., Kato, S., *Am. Assoc. Pet. Geol. Memoir*, **34**, 309 (1983).

Arato, H., Akai, G., Uchiyama, S., Kudo, T., Sekiguchi, K., *BSRs Recognized within the Offshore Chiba Basin*, Abstract, Spring Meeting, Japanese Association for Petroleum Technology (1995).

Austvik, T., (ed.) in *Proc. 5th International Conference on Natural Gas Hydrates*, (4 volumes and CD) Trondheim, Norway, June 13–16 (2005).

Ben-Avraham, Z., Smith, G., Reshef, M., Jungslager, E., *Geology*, **30**, 927 (2002).

Bernard, B.B., Brooks, J.M., Sackett, W.M., *Earth. Planet. Sci. Lett*., **31**, 48 (1976).

Bernstein, W., *The Birth of Plenty*, McGraw-Hill Co., New York (2004).

Besnard, G., Song, K.Y., Hightower, J.W., Kobayashi, R., Elliot, D., Chen, R., in *Proc. 213th ACS National Meeting*, San Francisco, CA, April 13–17, **42**(2), 551 (1997).

Bily, C., Dick, J.W.L., *Bull. Can. Pet. Geol.*, **22**, 320 (1974).

Boetius, A., Suess, E., *Chem. Geol*., **205**, 291 (2004).

Bohrmann, G., Suess, E., Greinert, J., Teicheret, B., Nahr, T., in *Proc. Fourth International Conference on Gas Hydrates* (Mori. Y.H., ed.), Yokohama, May 19–23, 18 (2002).

Bolin, B., in *Oceanography: The Present and Future* (P.G. Brewer, ed.), Springer-Verlag, NY, pp. 305–326 (1983).

Booth, J.S., Rowe, M..M., Fischer, K.M., "*Offshore Gas Hydrate Sample Database*" USGS Open-file Report 96-272, June 1996.

Bornhold, B.D., Prior, D.B., *GeoMarine Lett.*, **9**, 135 (1989).

Boswell, R., *An Interagency Roadmap for Methane Hydrate Research and Development*, http://www.fe.doe.gov/programs/oilgas/publications/methane_hydrates/mh_interagency_plan.pdf, July (2006).

Brewer, P.G., Orr, F.M., Friederich, G., Kvenvolden, Orange, D.L., in *Proc. 213th ACS National Meeting*, San Francisco, CA, April 13–17, **42**(2), 475 (1997).

Brooks, J.M., Anderson, A.L., Sassen, R., MacDonald, I.R., Kennicutt II, M.C., Guinasso, Jr., N.L., *Ann. N.Y. Acad. Sci.*, **715**, 318 (1994).

Brooks, J.M., Cox, H.B., Bryant, W.R., Kennicutt, M.C., Mann R.G., McDonald, T.J., *Org. Geochem.*, **10**, 221 (1986).

Brooks, J.M., Field, M.E., Kennicutt, M.C., *Mar. Geol.*, **96**, 103 (1991).

Brooks, J.M., Jeffrey, A.W.A., McDonald, T.J., Pflaum, R.C., *Initial Reports of Deep Sea Drilling Project* (von Huene, R., Auboin, J. et al., eds.), Washington, U.S. Govt Printing Office **LXXXIV**, 699 (1985).

Brooks, J.M., Kennicutt, M.C., Bidigare, R.R., Wade, T.L., Powell, E.N., Denoux, G.J., Fay, R.R., Childress, J.J., Fisher, C.R., Rossman, I., Boland, G., *EOS*, *Trans. Am. Geophys. Union*, **68**(18), 498 (1987).

Bugge, T., Befring, S., Belderson, R.H., Eidvin, T., Jansen, E., Kenyon, N.H., Holtedahl, H., Sejrup, H.P., *Geo-Marine Lett.*, **7**, 191 (1987).

Burshears, M., O'Brien, T.J., Malone, R.D., "A MultiPhase Multi-Dimensional, Variable Composition Simulation of Gas Production from a Conventional Gas Reservoir in Contact with Hydrates," in *Proc. SPE Unconventional Gas Technology Symposium*, SPE 15246, Louisville, KY, May 18–21, (1986).

Cande, S.C., Leslie, R.B., Parra, J.C., Hobart, M., *J. Geophys. Res.*, **92**(B1), 495 (1987).

Carlson, P.R., Golan-Bac, M., Karl, H.A., Kvenvolden, K.A., *Am. Assoc. Pet. Geol. Bull.* **69**, 422 (1985).

Carpenter, G., *Geo-Marine Lett.*, **1**, 29 (1981).

Charlou, J.L., Donval, J.P., Fouquet, Y., Ondreas, H., Knoery, J., Cochonat, P., Levaché, D., Poirier, Y., Jean-Baptiste, P., Fourré, E., Chazallon, B., and the ZAIROV Leg 2 Scientific Party, *Chem. Geol.*, **205**, 405 (2004).

Cherskiy, N.V., Tsaarev, V.P., Nikitin, S.P., *Petrol. Geol.*, **21**, 65 (1982).

Chi, W-C., Reed, D.L., Liu, C-S, Lundberg, N., *Terrestrial, Atmos. Oceanic Sci.*, **9**, 779 (1998).

Churgin, J., Halminski, S.J., *Key to Oceanographic Records Documentation #2*, *Gulf of Mexico*, National Oceanographic Data Center, Washington, DC (1974).

Claypool, G.E., Kaplan, I.R., *Natural Gases in Marine Sediments* (Kaplan, I.R., ed.), Plenum Press, New York, **3**, 99 (1974).

Claypool, G.E., Kvenvolden, K.A., *Ann. Rev. Earth Planet. Sci.*, **11**, 299 (1983).

Claypool, G.E., Milkov, A.V., Lee, Y.-J., Torres, M.E., Borowski, W.S., Tomaru, H., in *Proc. ODP Scientific Results Leg 204* (Tréhu, A.M., Bohrmann, G., et al., eds.), College Station, TX, **113** (2006).

Clennell, B., Hovland, M., Booth, J.S., Henry, P., Winter, W.J., *J. Geophys. Res.*, **104**(22), 985 (1999).

Collett, T.S., Detection and Evaluation of Natural Gas Hydrates from Well Longs, Prudhoe Bay, U. Alaska, Anchorage, AL (1983).

Collett, T.S., *Well Log Evaluation of Natural Gas Hydrates*, USGS Open-File Report 92-381 (1992).

Collett, T.S., *Am. Assoc. Pet. Geol. Bull.*, **77**, 793 (1993).

Collett, T.S., *1995 National Assessment of U.S. Oil and Gas Resources* (on CD-ROM) (Gautier, D.L., Goldton, G.L., et al., eds.), USGS (1995).

Collett, T.S., in *Proc. 2nd International Conference on Natural Gas Hydrates* (Monfort, J.P., ed.), Toulouse, France, June 2–6, 499 (1996).

Collett, T.S., Bird, K.J., Kvenvolden, K.A., Magoon, L.B., *Geologic Interrelations Relative to Gas Hydrates Within the North Slope of Alaska*, Final Report DE-AI21-83MC20422, U.S. Department of Energy, (1988).

Collett, T.S., Ehlig-Economides, C., "Detection and Evaluation of the *In-Situ* Natural Gas Hydrates in the North Slope Region, Alaska," SPE 11673, in *Proc. 1983 SPE California Regional Meeting*, March 23–25 (1983).

Collett, T.S., Ginsburg, G.D., *Int. J. Offshore Polar Eng.*, **8**, 22 (1998).

Collett, T.S., Godbole, S.P., Ehlig2-Economomides, C., in *Proc. 35th Annual Meeting of Canadian Institute of Mining*, Calgary, Canada, June 10–12 (1984).

Collett, T.S., Lee, M.W., in *Scientific Results from the Mallik 2002 Gas Hydrate Production Research Well Program*, Mackenzie Delta, Northwest Territories, Canada (Dallimore, S.R., Collett, T.S., eds.), Geological Survey of Canada Bulletin 585, including CD, p. 112 (2005).

Collett, T.S., Lewis, R.E., Dallimore, S.R., in *Scientific Results from the Mallik 2002 Gas Hydrate Production Research Well Program*, Mackenzie Delta, Northwest Territories, Canada (Dallimore, S.R., Collett, T.S., eds.), Geological Survey of Canada Bulletin 585, including CD, p. 111 (2005).

Colwell, F.S., Nunoura, T., Delwiche, M.F., Boyd, S., Bolton, R., Reed, D.W., Takai, K., Lehman, R.M., Horikoshi, K., Dlias, D.A., Phelps, T.J., in *Scientific Results from the Mallik 2002 Gas Hydrate Production Research Well Program*, Mackenzie Delta, Northwest Territories, Canada (Dallimore, S.R., Collett, T.S., eds.), Geological Survey of Canada Bulletin 585, including CD, p. 102 (2005).Dai, J., Xu, H., Snyder, F., Dutta, N., *Leading Edge*, **23**, 60 (2004).

Dallimore, S.R., Collett, T.S., (eds.), in *Scientific Results from the Mallik 2002 Gas Hydrate Production Research Well Program*, Mackenzie Delta, Northwest Territories, Canada, Geological Survey of Canada Bulletin 585, including CD (2005).

Dallimore, S.R., Uchida, T., Collett, T.S., *Geol. Sur. Can. Bull.,* **544**, 403 (1999).

Davidson, D.W., El-Defrawy, M.K., Fuglem, M.O., Judge, A.S., in *Proc. Third International Conference on Permafrost*, **1**, 938, Calgary, Alberta, March 15 (1978).

Davie, M.K., Buffett, B.A., *J. Geophys. Res*., **106**, 497 (2001).

Davie, M.K., Buffett, B.A., *J. Geophys. Res*., **108**(B10), 2495 (2003).

Davies, S.R., Sloan, E.D., "Predictions of the Dissociation of Hydrate in Sediment Samples with Numerical Heat Transfer Models Based on Fourier's Law" presented at the *16th Symposium on Thermophysical Properties* (http://symp16.boulder.nist.gov/) Boulder, CO, July 30–August 4 (2006).

Davis, E.E., Hyndman, R.D., Villinger, H., *J Geophys. Res*., **95**(B6), 8869 (1990).

DeLange, G.J., Brumsack, H.-J., *Gas Hydrates—Relevance to World Margin Stability and Climatic Change* (Henriet, J.-P., Mienert, J., eds.), The Geological Society, London, Special Publication, **137**, p. 167 (1998).

Dholabhai, P.D., Englezoa, P., Kalogerakis, N., Bishnoi, P.R., *Can. J. Chem. Eng*., **69**, 800 (1991).

Diaconescu, C.C., Kieckhefer, R.M., Knapp, J.H., *Mar. Pet. Geol.*, **18**, 209 (2001).

Dickens, G.R., *Nature*, **401**, 752 (1999).

Dickens, G.R., *Organ. Geochem*., **32**, 1179 (2001).

Dickens, G.R., *Science*, **299**, 1017 (2003).

Dickens, G.R., O'Neil, J.R., Rea, D.K., Owen, R.M., *Paleoceanography*, **10**, 965 (1995).

Dillon, W.P., Danforth, W.W., Hutchinson, D.R., Drury, R.M., Taylor, M.H., Booth, J.S., *Gas Hydrates—Relevance to World Margin Stability and Climatic Change* (Henriet, J.-P., Mienert, J., eds.), The Geological Society, London, Special Publication, **137**, p. 293 (1998).

Dillon, W.P., Fehlhaber, K., Coleman, D.F., Lee, M.W., Hutchinson, D.R., *U.S. Geological Survey*, *Miscellaneous Field Studies Map*, *MF 2268*, 2 sheets (1995).

Dillon, W.P., Hutchinson, D.R., Drury, M., in *Proc. Ocean Drilling Program Initial Reports*, (Paull, C.K., Matsumoto, R., et al., eds.), **164**, p. 47 (1996).

Dillon, W.P., Lee, M.W., Fehlhaber, K., Coleman, D.G., *The Future of Energy Gases*, *U.S. Geological Survey*, *Professional Paper 1570*, pp. 313–330 (1993).

Dillon, W.P., Max, M.D., *Natural Gas Hydrate in Oceanic and Polar Environments* (Max, M.D., ed.), Kluwer Academic Publishers, Dordrecht, 61 (2000).

Dillon, W.P., Max, M.D., in *Proc. 33rd Offshore Technical Conf*erence, Houston, TX, OTC 13034, 30 April–3 May (2001).

Dillon, W.P., Nealon, J.W., Taylor, M.H., Lee, M.W., Drury,R.M., Anton, C.H., *Natural Gas Hydrates: Occurrence*, *Distribution and Detection* (Paull, C.K., Dillon, W.P., eds.), Geophysical Monograph 124, American Geophysical Union, Washington, DC, p. 211, (2001).

Dobrynin, V.M., Korotajev, Yu, P., Plyuschev, D.V., in *Long Term Energy Resources* (Meyer, R.G., ed.), Pitman, Boston, MA, 727 (1981).

Domenico, S.N., *Geophysics*, **65**, 565 (1977).

Dvorkin, J., Nur, A., *The Future of Energy Gases USGS Prof. Paper No 1570*, 293 (1992).

Eaton, M.K., Hester, K.C., Sloan, E.D., in *Scientific Results from the Mallik 2002 Gas Hydrate Production Research Well Program*, Mackenzie Delta, Northwest Territories, Canada (Dallimore, S.R., Collett, T.S., eds.), Geological Survey of Canada Bulletin 585, including CD, p. 107 (2005).

Ecker, C., Lumley, D., Dvorkin, J., Nur, A., in *Proc. Second International Conference on Natural Gas Hydrates* (Monfort, J.P., ed.), Toulouse, France, June 2–6, 491 (1996).

Economides, M., Oligney, R., *The Color of Oil*, Round Oak Publishing, Katy, TX (2000).

Edeberg, P.K., Dickens, G.R., *Chem. Geol.*, **153**, 53 (1999).

Ewing, J.I., Hollister, C.D., *Initial Rep. Deep Sea Drilling Project*, **11**, 951 (1972).

Exon, N.F., Dickens, G.R., Auzende, J-M., Lafoy, Y., Symonds, P.A., Van de Beuque, S., *Pet. Explor. Soc. Aust. J.*, **26**, 148 (1998).

Field, M.E., Kvenvolden, K.A., *Geology*, **13**, 517 (1985).

Finley, P., Krason, J., *Geological Evolution and Analysis of Confirmed or Suspected Gas Hydrate Localities: Basin Analysis*, *Formation and Stability of Gas Hydrates in the Middle America Trench*, U.S. Department of Energy, DOE/MC/21181-1950, **9** (1986a).

Finley, P., Krason, J., *Geological Evolution and Analysis of Confirmed or Suspected Gas Hydrate Localities: Basin Analysis*, *Formation and Stability of Gas Hydrates of the Colombia Basin*, U.S. Department of Energy, DOE/MC/21181-1950, **7** (1986b).

Finley, P.D., Krason, J., Dominic, K., *Am. Assoc. Pet. Geol. Bull.*, **71**(5), 555 (1987).

Fisher, C.R., MacDonald, I.R., Sassen, R., Young, C.M., Macko, S.A., Hourdez, S., Carney, R.S., Joye, S., McMullin E., *Naturwissenschaften*, **87**, 184 (2000).

Fontana, R.L., Mussemeci, A., in *Proc. First International Conference on Natural Gas Hydrates*, *Ann. N.Y. Acad. Sci.* (Sloan, E.D., Happel, J., et al., eds.), **715**, 106 (1994).

Ford, K.H., Naehr, T.H., Skilbeck, C.G., in *Proc. ODP Initial Reports*, Ocean Drilling Program (D'Hondt, S.L., Miller, B.B. et al., eds.), College Station, TX, **201**, 1 (2003).

Freifeld, B.M., Kneafsey, T.J., Tomutsa, L., Stern, L.A., Kirby, S.H., in *Proc. Fourth International Conference on Gas Hydrates* (Mori, Y.H., ed.), Yokohama, May 19–23, 750 (2002).

Froelich, P.N., Kvenvolden, K.A., Torres, M.E., Waseda, A., Didyk, B.M., Lorenson, T.D., in *Proc. Ocean Drilling Program*, *Scientific Results*, **141**, 279 (1995).

Gas Epoch, *Gas Epoch*, **8**, 18 (1995).

Genov, G., Kuhs, W.F., Staykova, D.K., Goreshnik, E., Salamatin, A.N., *Am. Mineral.*, **89**(8–9), 1228 (2004).

Ginsburg, G.D., Guseynov, R.A., Dadashev, A.A., Ivanova, G.A., Kazantsev, S.A., Soloviev, V.A., Telepnev, E.V., Askeri-Nasirov, P. Ye., Yesikov, A.A., Mal'tseva, V.I., Mashirov, G. Yu., Shabayeva, I. Yu., *Int. Geol. Rev*., **43**, 765 (1992).

Ginsburg, G.D., Kremlev, A.N., Grigor'ev, M.N., Larkin, G.V., Pavlenkin, A.D., Saltykova, N.A., *Geologiya I Geofizika*, **31**(3), 10 (1990).

Ginsburg, G.D., Milkov, A.V., Soloviev, V.A., Egorov, A.V., Cherdashev, G.A., Vogt, P.R., Crane K., Lorenson, T.D., Khutorskoy, M.D., *Geo-Marine Lett.*, **19**, 57 (1999).

Ginsburg, G.D., Soloviev, V.A., *Bull. Geol. Soc. Denmark*, Copenhagen, **41**, 95 (1994).

Ginsburg, G.D., Soloviev, V.A., in *Proc. 27th Annual Offshore Technology Conference*, Houston, OTC 7693, May 1–4, 513 (1995).

Ginsburg, G.D., Soloviev, V.A., *Mar. Geol.*, **137**, 49 (1997).

Ginsburg, G.D., Soloviev, V.A., *Submarine Gas Hydrates*, VNIIOkeangeologgia, St. Petersburg (1998).

Ginsburg, G.D., Soloviev, V.A., Cranston, R.E., Lorenson, T.D., Kvenvolden, K.A., *Geo-Marine Lett.*, **13**, 41 (1993).

Gornitz, V., Fung, I., *Global Biogeochem. Cycles*, **8**, 335 (1994).

Grantz, A., Boucher, G., Whitney, O.T., *U.S. Geol. Surv. Circ.* **733**, 17 (1976).

Grantz, A., Dinter, D.A., *Oil Gas J.* **78**(18), 304 (1980).

Gudmundsson, J.-S., Parlaktuna, M., "Storage of Natural Gas at Refrigerated Conditions," in *AIChE Spring National Meeting*, New Orleans, LA, March 15 (1992).

Halleck, P.M., Byrer, C.W., McGuire, P.L., Judge, A.S., Corlett, R.C., Barraclough, B., in *Proc. Methane Hydrate Workshop*, Morgantown, WV, Mar 29–30, 63 (1982).

Hamblin, W.K., *The Earth's Dynamic Systems*, Macmillan, New York (1985).

Hammond, R.D., Gaither, J.R., *Geophysics*, **48**, 590 (1983).

Hancock, S.H., Dallimore, S.R., Collett, T.S., Carle, D., Weatherill, B., Satoh, T., Inoue, T., in *Scientific Results from the Mallik 2002 Gas Hydrate Production Research Well Program*, Mackenzie Delta, Northwest Territories, Canada (Dallimore, S.R., Collett, T.S., eds.), Geological Survey of Canada Bulletin 585, including CD, p. 134 (2005a).

Hancock, S.H., Collett, T.S., Dallimore, S.R., Satoh, T., Inoue, T., Huenges, E., Henninges, J., Weatherill, B., in *Scientific Results from the Mallik 2002 Gas Hydrate Production Research Well Program*, Mackenzie Delta, Northwest Territories, Canada (Dallimore, S.R., Collett, T.S., eds.), Geological Survey of Canada Bulletin 585, including CD, p. 135 (2005b).

Handa, Y.P., *J. Phys. Chem*., **94**, 2652 (1990).

Harrison, W.E., Curiale, J.A., *Initial Rep. Deep Sea Drilling Project*, **67**, 591 (1982).

Harrison, W.E., Hesse, R., Gieskes, J.M., *Initial Rep. Deep Sea Drilling Project*, **67**, 603 (1982).

Harvey, L.D.D., Huang, Z., *J. Geophys. Res*., **100D2**, 2905 (1995).

Heeschen, K.U., Tréhu, A.M., Collier, R.W., Suess, E., Rehder, G., *Geophys. Res. Lett.*, **30**(12), 1643 (2003).

Henriet, J.P., De Mol, B., Pillen, S., Vanneste, M., Van Rooij, D., Versteeg, W., Croker, P.F., Shannon, P.M., Unnithan, V., Bouriak, S., Chachkine, P., and The Porcupine—Beligica 97 Shipboard Party, *Nature*, **391**, 648 (1998).

Henriet, J.-P., Minert, J., (eds.), *Gas Hydrates: Relevance to World Margin Stability and Climate Change*, Geological Society of London, Special Publication, 137 (1998).

Hesse, R., *Geosci. Can.*, **14**(3), 165 (1986).
Hesse, R., Harrison, W.E., *Earth. Plan. Sci. Lett.*, **55**, 453 (1981).
Hesse, R., Lebel, J., Gieskes, J.M., *Initial Rep. Deep Sea Drilling Project*, **84**, 727 (1985).
Hester, K.C., White, S.N., Peltzer, E.T., Brewer, P.G., Sloan, E.D., *Mar. Chem.*, **98**, 304 (2005).
Holbrook, W.S., Hoskins, H., Wood, W.T., Stephen, R.A., Lizarralde, D., and Leg 164 Science Party, *Science*, **273**, 1840 (1996).
Holder, G.D., Angert, P.F., in *Proc. Soc. Petr. Enq. Meet*., SPE 11105, New Orleans, LA, September 26–29 (1982).
Holder, G.D., Bishnoi, P.R., *Gas Hydrates: Challenges for the Future*, *Ann. N.Y. Acad. Sci*., **912**, (2000).
Hong, H., *Modeling of Gas Production from Hydrates in Porous Media*, M.Sc. Thesis, University of Calgary, Alberta, Canada, p. 267 (2003).
Hong, H., Pooladi-Darvish, M., in *Scientific Results from the Mallik 2002 Gas Hydrate Production Research Well Program*, Mackenzie Delta, Northwest Territories, Canada, (Dallimore, S.R., Collett, T.S., eds.), Geological Survey of Canada Bulletin 585, including CD, p. 138 (2005).
Hong, H., Pooladi-Darvish, M., *J. Can. Pet. Technol*., **44**(11), 39 (2005).
Hovland, M., Lysne, D., Whiticar, M., in *Proc. Ocean Drill Program*, *Leg 146* (Carson, B., Westbrook, G.K., et al., eds.), **146**(1), 151 (1995).
Howe, S.J., Nanchary, N.R., Patil, S.L., Ogbe, D.O., Chukwu, G.A., Hunter, R.B., Wilson, S.J., in *Proc. Hedburg Conference on Gas Hydrates: Energy Resource Potential and Associated Geologic Hazards*, Vancouver, BC, September 12–16 (2004).
Hunt, J.M., *Petroleum Geochemistry and Geology*, W.H. Freeman, San Francisco, CA (1979).
Hutchinson, D.R., Golmshtok, A.J., Scholz, C.A., Moore, T.C., Lee, M.W., Kuzmin, M., *Trans. Am. Geophys. Union,* **72**(17, Supplement), 307 (1991).
Hutchinson, D.R., Ruppel, C.D., Pohlman, G., Hart, P.E., Dugan, B., Snyder, F., Coffin, R.B., "An integrated geological, geophysical, and geochemical analysis of subsurface gas hydrates in the Northern Gulf of Mexico," in *Proc. of Gas Hydrates: Energy Resources Potential and Associated Geologic Hazards*, American Association of Petroleum Geologists Hedberg Conference, Sepetmeber 12–16, 2004, Vancouver, Canada, Available at http://www.searchanddiscovery.net/documents/abstracts/2005hedburg-_vancouver/extended/Hutchinson/hutchinson.htm.
Hyndman, R.D., Davis, E.E., *J. Geophys. Res*., **97**(B5), 7025 (1992).
Hyndman, R.D., Foucher, J.P., Yamano, M., Fisher, A., and Sci Team of ODP leg 131, *Earth Planet Sci. Lett.*, **109**, 289 (1992).
Hyndman, R.D., Spence, G.D., *J. Geophys. Res.*, **97**(B5), 6683 (1992).
Hyndman, R.D., Spence, G.D., Yuan, T., Desmons, B., in *Proc. Second International Conference on Natural Gas Hydrates* (Monfort, J.P., ed.), Toulouse, France, June 2–6, 485 (1996).
Islam, M.R., *J. Pet. Sci. Eng.*, **11**, 267 (1994).
Jamaluddin, A.K.M., Kalogerakis, N., Bishnoi, P.R., *Pet. Soc. Can. Inst. Mining*, **89**, 5 (1989).
Jansen, E., Befring, S., Bugge, T., Eidvin, T., Hotedahl, G., Sejrup, H.P., *Mar. Geol.*, **78**, 77 (1987).
Jenden, P.D., Gieskes, J.M., *Initial Rep. Deep Sea Drilling Project* (Sheridan, R.E., Gradstein, F., et al., eds.), US Government Printing Office, **76**, 453 (1983).

JNOC press release, Proof of the methane-hydrate-containing layer in the national wildcat, "Nankai Trough," based on the National Domestic Petroleum Exploration Program, Japan National Oil Corporation, January 20 (2000).

Judge, A.S, in *Proc. Fourth Canadian Permafrost Conference 1981*, 320, Calgary, Alberta, March 15 (1982).

Kaiho, K., Arinobu, T., Ishiwatari, R., Morgans, H.E.G., Okada, H., Takeda, N., Taxaki, K., Zhou, G., Kajiwara, Y., Matsumoto, R., Hirai, A., Niitsuma, N., Wada, H., *Paleoceanography*, **11**, 447 (1996).

Kamath, V.A., Godbole, S.P., *J. Pet. Tech.*, **39**, 1379 (1987).

Kastner, M., Kvenvolden, K.A., Lorenson, T.D., *Earth Planet. Sci. Lett.*, **156**, 173 (1998).

Kastner, M., Kvenvolden, K.A., Whiticar, M.J., Camerlenghi, A., Lorenson, T.D., in *Proc. Ocean Drill Program*, *Leg 146* (Carson, B., Westbrook, G.K., et al., eds.), **146**(1), 175 (1995).

Katz, H.R., *J. Pet. Geol.*, **3**, 315 (1981).

Kayen, R.E., Lee, H.J., *Mar. Geotechnol.*, **10**, 125 (1991).

Kennett, J.P., Cannariato, G., Hendy, I.L., Behl, R.J., *Methane Hydrates in Quaternary Climate Change: The Clathrate Gun Hypothesis*, The American Geophysical Union, Washington, DC, (2003).

Kennett, J.P., Hill, T.M., Behl, R.J., in *Proc. Fifth International Conference Gas Hydrates*, (Austvik, T., ed.), (paper 3008), 4 volumes and CD, Trondheim, Norway, June 13–15, 759 (2005).

Klauda, J.B., Sandler, S.I., *Energy and Fuels*, **19**, 469 (2005).

Kleinberg, R.L., *New Techniques in Sediment Core Analysis*, Geological Society of London, Special Publication (Rothwell, R.G., ed.), **267**, 179 (2006).

Kleinberg, R.L., Brewer, P.G., Malby, G., Peltzer, E.T., Friederich, G., Yesinowski, J., Flaum, C., *J. Geophys. Res*., 108:B3, doi:10.1029/2001JB0000919 (2003).

Kleinberg, R.L., Flaum, C., Collett, T.S, in *Scientific Results from the Mallik 2002 Gas Hydrate Production Research Well Program*, Mackenzie Delta, Northwest Territories, Canada (Dallimore, S.R., Collett, T.S., eds.), Geological Survey of Canada Bulletin 585, including CD, p. 114 (2005).

Krason, J., Ciesnik, M., *Geological Evolution and Analysis of Confirmed or Suspected Gas Hydrate Localities: Gas Hydrates in the Russian Literature*, U.S. Department of Energy, DOE/MC/21181-1950, **5** (1985).

Krason, J., Ciesnik, M., *Geological Evolution and Analysis of Confirmed or Suspected Gas Hydrate Localities: Basin Analysis*, *Formation and Stability of Gas Hydrates in the Panama Basin*, U.S. Department of Energy, DOE/MC/21181-1950, **6** (1986a).

Krason, J., Ciesnik, M., *Geological Evolution and Analysis of Confirmed or Suspected Gas Hydrate Localities: Basin Analysis*,*Formation and Stability of Gas Hydrates in the Northern California Offshore*, U.S. Department of Energy, DOE/MC/21181-1950, **8** (1986b).

Krason, J., Finley, P.D., *Structural Traps VII.* (*AAPG Treatise Petrol Geol Atlas of Oil and Gas Fields*), 197 (Beaumont E.A., Foster, N.H., eds.), AAPG, Tulsa, OK (1992).

Krason, J., Finley, P.D., Rudloff, B., *Geological Evolution and Analysis of Confirmed or Suspected Gas Hydrate Localities: Basin Analysis*,*Formation and Stability of Gas Hydrates in the Western Gulf of Mexico*, U.S. Department of Energy, DOE/MC/211811950, **3** (1985).

Krason, J., Ridley, W.I., *Geological Evolution and Analysis of Confirmed or Suspected Gas Hydrate Localities: Blake-Bahama Outer Ridge-U.S. East Coast*, U.S. Department of Energy, DOE/MC/21181-1950, **1** (1985a).

Krason, J., Ridley, W.I., *Geological Evolution and Analysis of Confirmed or Suspected Gas Hydrate Localities: Baltimore Canyon Trough and Environs U.S. East Coast*, U.S. Department of Energy, DOE/MC/21181-1950, **2** (1985b).

Krason, J., Rudloff, B., *Geological Evolution and Analysis of Confirmed or Suspected Gas Hydrate Localities: Offshore of Newfoundland and Labrador*, U.S. Department of Energy, DOE/MC/21181-1950, **4** (1985).

Kumar, P., Turner, D., Sloan, E.D., *J. Geophys. Res.*, **109**, B01207 (2004).

Kuramoto, S., Okamura, I., *Geol. Surv. Jpn.*, 28 (1995).

Kurihara, M., Funatsu, K., Kusaka, K., Yasuda, M., Dallimore, S.R., Collett, T.S., Hancock, S.H., in *Scientific Results from the Mallik 2002 Gas Hydrate Production Research Well Program*, Mackenzie Delta, Northwest Territories, Canada (Dallimore, S.R., Collett, T.S., eds.), Geological Survey of Canada Bulletin 585, including CD, p. 139 (2005).

Kus'min, M.I., Kalmychkov, G.V., Geletii, R.F., Gnilusha, V.A., Goreglyad, A.V., Khakhaev, B.N., Pevzner, L.A., Kawai, T., Yoshida, N., Duchkov, A.D., Ponomarchuk, V.A., Kontorovich, A.E., Abazhin, N.M., Makhov, G.A., Dyadin, Yu. A., Kuznetsov, F.A., Larionov, E.G., Manakov, A.Yu., Smolyakov, B.S., Mandel'baum, M.M., Zheleznyakov, N.K., *Doklady Akademii Nauk*, **362**, 541 (1998) [Translation in *Doklady Earth Sciences*, **362**, 1029 1998].

Kvenvolden, K.A., *Mar. Pet. Geol*., **2**, 65 (1985a).

Kvenvolden, K.A., *Chem. Geol*., **71**, 41 (1988).

Kvenvolden, K.A., *Org. Geochem*., **23**, 997 (1995).

Kvenvolden, K.A., Barnard, L.A., *Initial Reports DSDP* (Sheridan, R.E., Gradstein, F., et al., eds.), U.S. Government Printing Office, Washington, DC, **76**, 353 (1983).

Kvenvolden, K.A., Claypool, G.E., in *Proc.Unconventional Gas Recovery: Gas Hydrates Peer Review Session*, Bethesda, MD., April 24–25, (1985).

Kvenvolden, K.A., Claypool, G.E., *U.S. Geological Survey Open File Report 88-216*, p. 50 (1988).

Kvenvolden, K.A., Claypool, G.E., Threlkeld, C.N., Sloan, E.D., *Org. Geochem*., **6**, 703 (1984).

Kvenvolden, K.A., Golan-Bac, M., McDonald, T.J., Pflaum, R.C., Brooks, J.M., in *Proc. Ocean Drilling Program*, *Scientific Results*, **104**, 319 (1989).

Kvenvolden, K.A., Golan-Bac, M., Rapp, J.B., *Circum-Pacific Council on Energy and Mineral Resources*, *Earth Science Series 5A*, 205 (1987).

Kvenvolden, K.A. Grantz, A., in *The Geology of North America*, 50, *The Arctic Ocean Region*, Geological Society of America, 539 (1990).

Kvenvolden, K.A., Kastner, M., in *Proc. Ocean Drilling Program*, *Scientific Results*, **112**, 517 (1990).

Kvenvolden, K.A., Lorenson, T.D., in *Natural Gas Hydrates: Occurrence*,*Distribution and Detection* (Paull C.K., Dillon, W.P., eds.), Geophysical Monograph 124, American Geophysical Union, Washington, DC, 3 (2001).

Kvenvolden, K.A., McDonald, T.J., *Initial Rep. Deep Sea Drilling Project*, **84**, 667 (1985).

Kvenvolden K.A., von Huene, R., *Circum-Pacific Council on Energy and Minerals*, *Earth Science* Series, **1**, 31 (1985).

Ladd, J., Westbrook, G., Lewis, S., *Lamont-Doherty Geological Observatory Yearbook 1981–1982*, **8**, 17, Columbia University Thesis, NY (1982).

Ladd, J.W., Truchan, M., Talwqni, M., Stoffa, P.L., Buhl, P., Houtz, R., Mauffret, A., Westbrook, G., in *The Geological Society of America Memoir 162* (Bonini W.E., Hargraves, R.B., et al., eds.), 153, Geol. Soc of America, Washington, DC (1984).

Lee, M.W., Hutchinson, D.R., Collett, T.S., Dillon, W.P., *J. Geophys. Res*., **101B9**(20), 347 (1996).
Lee, M.W., Hutchinson, D.R., Dillon, W.P., Miller, J.J., Agena, W.F., Swift, B.A., *Mar. Pet. Geol.*, **10**, 493 (1993).
Linke, P., Wallmann, K., Suess, E., Hensen, C., Rehder, G., *Earth Plan. Sci. Lett.*, **235**, 79 (2005).
Lodolo, E., Camerlenghi, A., Brancolini, G., *Antarctic Sci.*, **5**, 207 (1993).
Lonsdale, M.J., in *Proc. Ocean Drilling Program*, *Scientific Results*, **113**, 27 (1990).
Lonsdale P., *Am. Assoc. Pet. Geol. Bull.*, **69**, 1160 (1985).
Lorenson, T.D., Collett, T.S., in *Proc. Ocean Drilling Program*, *Scientific Results*, **164**, 37 (1999).
MacDonald, G.J., *Climatic Changes*, **16**, 247 (1990).
Makogon, Y.F., *Gazov. Promst*., **5**, 14 (1965).
Makogon, Y.F., *Hydrates of Natural Gas*, Moscow, Nedra, Izadatelstro, (1974 in Russian) Transl. J. Cieslesicz, PennWell Books, Tulsa, Oklahoma, p. 237 (1981).
Makogon, Y.F., "Natural Gas Hydrates: The State of Study in the USSR and Perspectives for Its Use," paper presented at the *Third Chemical Congress of North America*, Toronto, Canada, June 5–10 (1988).
Makogon, Y.F., *Hydrates of Hydrocarbons*, PennWell Publshing Co., Tulsa, OK, p. 482 (1997).
Makogon, Yu. F., Trebin, F.A., Trofimuk, A.A., Tsarev, V.P., Cherskiy, N.V., *Doklady Akademii Nauk SSSR*, **196**, 203 (1971) [Translation in Doklady-Earth Science Section, **196**, 197 (1972)].
Malone, R.D., *Gas Hydrates Topical Report*, DOE/METC/SP-218, U.S. Department of Energy, April (1985).
Manley, P.L., Flood, R.D., *AAPG Bull.*, **72**, 912 (1988).
Mann, R., Gieskes, J., *Initial Rep. Deep Sea Drilling Project*, **28**, 805 (1975).
Markl, R.G., Bryan, G.M., Ewing, J.I., *J. Geophys. Res*., **75**, 4539 (1970).
Masuda, Y., Kurihara, M., Ohuchi, H., Sato, T., in *Proc. Fourth International Conference on Gas Hydrates* (Mori, Y.H., ed.), Yokohama, May 19–23, 40 (2002).
Mathews, M.A., *The Log Analyst*, p. 26, May–June (1986).
Matsumoto, R., Okuda, Y., Aoki, Y., *Methane Hydrate*, Nikkei Science Publishers, Tokyo (1994).
Max, M.D., (ed.), *Natural Gas Hydrate: in Oceanic and Permafrost Environments*, Kluwer Academic Publishers, London, 2nd Ed., p. 422 (2003).
Max, M.D., Johnson, A.H., Dillon, W.P., *Economic Geology of Natural Gas Hydrate*, Springer, New York, p. 338 (2006).
Mazurenko, L.L., Soloviev, V.A., Belenkaya, I., Ivanov, M.K., Pinheiro, L.M., *Terra Nova*, **14**, 321 (2002).
McCarthy, J., Stevenson, A.J., Scholl, D.W., Vallier, T.L., *Mar. Pet. Geol.*, **1**, 151 (1984).
McGrail, B.P., Young, J.S., Martin, P.F., Alexander, M.L., in *Scientific Results from the Mallik 2002 Gas Hydrate Production Research Well Program*, Mackenzie Delta, Northwest Territories, Canada (Dallimore, S.R., Collett, T.S., eds.), Geological Survey of Canada Bulletin 585, including CD , p. 110 (2005).
McIver, R.D., *Initial Reports*, *Deep Sea Drilling Project*, **28**, 815 (1975).
McIver, R.D., *Long-Term Energy Resources* (Meyer, R.F., Olson, J.C., eds.), Pitman, Boston, **1**, 713 (1981).
McKirdy, D.M., Cook, P.J., *Am. Assoc. Pet. Geol. Bull.*, **64**, 2118 (1980).

Mienert, J., Posewang, J. Baumann, M., *Gas Hydrates—Relevance to World Margin Stability and Climatic Change* (Henriet, J.-P., Mienert, J., eds.), The Geological Society, London, Special Publication 137, p. 275 (1998).

Milkov, A.V. *Earth Sci. Rev.*, **66**(3–4), 183 (2004).

Milkov, A.V., Claypool, G.E., Lee, Y.-J., Diekens, G.R., Xu, W., Borowski, W.S., and ODP Leg 204 Science Party, *Geology*, **31**(10), 833 (2003).

Milkov, A.V., Xu, W., *Earth Planet Sci. Lett.*, **239**, 162 (2004).

Miller, J.J., Lee, M.W., von Huene, R., *Am. Assoc. Pet. Geol. Bull.*, **75**, 910 (1991).

Minshull, T., Singh, S., Pecher, I., Korenaga, J., Yuan, T., in *Proc. 2nd International Conference on Natural Gas Hydrates* (Monfort, J.P., ed.), Toulouse, France, June 2–6, 517 (1996).

Minshull, T.A., Singh, S.C., Westbrook, G.K., *J. Geophys. Res.*, **99**(B3), 4715 (1994).

Monfort, J.P., (ed.), in *Proc. 2nd International Conference on Natural Gas Hydrates*, Toulouse, France, June 2–6 (1996).

Moore, B., Bolin, B., Oceanus, **29**, 9 (1989).

Moore, G.W., Gieskes, J.M., *Initial Reports*, *Deep Sea Drilling Project* 56, **57**(2), 1269 (1980).

Moore, J.C., Brown, K.M., Horath, F., Cochrane, G., MacKay, M., Moore, G., *Philosophical Transactions Royal Society of London Series A*, **335**, 275 (1992).

Mori, Y.H., in *Proc. Fourth International Conference on Natural Gas Hydrates* (2 volumes and CD) Yokohama, May 19–23 (2002).

Moridis, G.J., Collett, T.S., in *Recent Advances in the Study of Gas Hydrates* (Taylor, C., Kwan, J. eds.), Kluwer Academic Publishers, MA, p. 75 (2004).

Moridis, G.J., Collett, T.S., Dallimore, S.R., Inoue, T., Mroz, T., in *Scientific Results from the Mallik 2002 Gas Hydrate Production Research Well Program*, Mackenzie Delta, Northwest Territories, Canada (Dallimore, S.R., Collett, T.S., eds.), Geological Survey of Canada Bulletin 585, including CD, p. 140 (2005).

Moridis, G.J., Collett, T.S., Dallimore, S.R., Satoh, T., Hancock, S., Weatherill, B., in *Proc. of Fourth International Conference on Gas Hydrates* (Mori, Y.H., ed.), Yokohama, May 19–23, p. 239 (2002).

Moridis, G.J., Sloan, E.D., "Gas Production Potential of Disperse Low-Saturation Hydrate Accumulations in Oceanic Sediments," *Energy Conversion and Management Journal*, accepted (2006), also as LBNL Report 61446, August 2006.

Neben, S., Hinz, K., Beiersdorf, H., in *Gas Hydrates—Relevance to World Margin Stability and Climatic Change* (Henriet, J.-P., Mienert, J., eds.), The Geological Society, London, Special Publication 137, p. 255 (1998).

Normark, W.R., Hein, J.R., Powell, C.L., Lorenson, T.D., Lee, H.J., Edwards, B.D., *EOS*, *Trans. AGU*, 84(46), *Fall Meeting Suppl.*, *Abstract OS51B08555*, **F845** (2003).

Okuda, Y., in *Proc. of Thermal Engineering Symposium of July 7, 1995; Japan Association of Mechanical Engineering*, Tokyo, Japan, 5 (1995).

Ostrander, W.J., *Geophysics*, **49**, 1637 (1984).

Paull, C.K., Borowski, W.S., Rodriguez, N.M., and the ODP Leg 164 Shipboard Scientific Party, in *Gas Hydrates—Relevance to World Margin Stability and Climatic Change* (Henriet, J.-P., Mienert, J. eds.), The Geological Society, London, Special Publication 137, p. 153 (1998).

Paull, C.K., Dillon, W.P., *Natural Gas Hydrates: Occurrence*, *Distribution and Detection*, American Geophysical Union Monograph 124 (2001).

Paull, C.K., Lorenson, T.D., Boroworski, W.S., Ussler, W., Olsen, K., Rodriguez, N.M., Wehner, H., in *Proc. Ocean Drilling Program*, *Scientific Results*, **164**, 67 (1996).

Paull, C.K., Ussler, W., Borowski, W.S., in *(First) International Conference on Natural Gas Hydrates*, *Ann. N.Y. Acad. Sci*. (Sloan, E.D., Happel, J., et al., eds.), **715**, 392 (1994).

Paull, C.K., Ussler, W., Lorenson, T., Winters, W., Dougherty, J., *Geo-Mar. Lett.* **25**(5), 273, Nov. DOI:10.1007/s00367-005-0001-3 (2005).

Pettigrew, T.L., *The Design and Operation of a Wireline Pressure Core Sampler*, ODP Tech Note 17 (1992).

Pohlman, J.W., Canuel, E.A., Chapman, N.R., Spence, G.D., Whiticar, M.J., Coffin, R.B., *Org. Geochem.*, **36**, 703 (2005).

Pooladi-Darvish, M., Hong, H., Bishnoi, P.R., *J. Can. Pet. Technol*., **42**(11), 45 (2003).

Posewang, J., Mienert, J., *Geo-Mar. Lett.*, **19**, 150 (1999).

Prensky, S., in *SPWLA 36th Annual Logging Symp*osium, June 26–29 (1995).

Radler, M., *Oil Gas J*., **98**(51), 121 (2000).

Rao, Y.H., Subrahmanyam, C., Rastogi, A., Deka, B., *Geo-Mar. Lett.*, **21**, 1 (2001).

Rastogi, A., Deka, B., Budhiraja, I.L., Agarfwal, G.C., *Mar.Geores. Geotechnol.*, **17**, 49 (1999).

Rehder, G., Kirby, S.H., Durhan, W.B., Stern, L.A., Peltzer, E.T., Pinkston, J., Brewer, P.G., *Geochim. Cosmochim. Acta*, **68**, 285 doi:10.1016/j.gca.2003.07.001 (2003).

Rempel, A., *Theoretical and Experimental Investigations into the Formation and Accumulation of Gas Hydrates*, M.S. Thesis, University of British Columbia, Vancouver, B.C., Canada (1994).

Ripmeester, J.A., Lu, H., Moudrakovski, I.L., Dutrisac, R., Wilson, L.D., Wright, F., Dallimore, S.R., in *Scientific Results from the Mallik 2002 Gas Hydrate Production Research Well Program*, Mackenzie Delta, Northwest Territories, Canada (Dallimore, S.R., Collett, T.S., eds.), Geological Survey of Canada Bulletin 585, including CD, p. 110 (2005).

Roberts, H.H., in *Natural Gas Hydrates: Occurrence*, *Distribution and Detection* (Paull C.K., Dillon, W.P., eds.), Geophysical Monograph 124, American Geophysical Union, Washington, DC, p. 145 (2001).

Sachs, J.D., *The End of Poverty*, Penguin Press, New York (2005).

Sahling, H., Rickert, D., Lee, R.W., Linke, P., Suess, E., *Mar. Ecol. Prog. Ser*., **231**, 121 (2002).

Saltykova, N.A., Soloviev, V.A., Pavlenkin, A.D., *Sevmorgeologia*, *Lenigrad*, 119 (1987).

Sapir, M.H., Khramenkov, E.N., Yefremov, I.D., Ginzburg, G.D., Beniaminovich, A.E., Lenda, S.M., Koslova, V.I., *Geol. Nefti i Gaza*, **6**, 26 (1973).

Sassen, R., MacDonald, I.R., *Org. Geochem*., **22**(6), 1029 (1994).

Sassen, R., MacDonald, I.R., *Org. Geochem.*, **26**, 289 (1997a).

Sassen, R., MacDonald, I.R., "Thermogenic Gas Hydrates, Gulf of Mexico Continental Slope," in *Proc. 213th ACS National Meeting*, San Francisco, CA, April 13–17, **42**(2), 472 (1997b).

Sassen, R., Roberts, H., Milkov, A., DeFreitas, D., Lanoil, B., Zhang, C., *Chem. Geol.*, **205**, 195 (2004).

Sato, M., *The Earth Monthly*, **16**, 533 (1994).

Scholl, D.W., Cooper, A.K., *Am. Assoc. Pet. Geol. Bull.,* **62**, 2481 (1978).

Schulteiss, P., Holland, M., Roberts, J., Druce, M., Humphrey, G. and the Shipboard Scientific Party of IODP Leg 311 nad NGHP Exp 1. "X-ray Images of Gas Hydrates Within Deep Sea Marine Sedciment, Retrieved and Analyzed Using HYACINTH Pressure Coring Systems," Poster at *American Geophysical Union Annual Meeting*, San Francisco, CA, December 14, 2006.

Selim, M.S., Sloan, E.D., *AIChE J.*, **35**, 1049 (1989).
Sheshukov, N.L., *Gazov. Delo*., **6,** 8 (1972).
Shipboard Scientific Party, Site 796, in *Proc. Ocean Drilling Program*, *Initial Reports*, **127**, 247 (1990).
Shipboard Scientific Party, Site 808, in *Proc. Ocean Drilling Program*, *Initial Reports*, **131**, 71 (1991).
Shipboard Scientific Party, Site 1041, in *Proc. Ocean Drilling Program*, *Initial Reports*, **170**, 153 (1997).
Shipley, T.H., Didyk, B.M., *Initial Reports*, *Deep Sea Drilling Project*, **66**, 547 (1982).
Shipley, T.H., Houston, M.H., Buffler, R.T., Shaub, F.J., McMillen, K.J., Ladd, J.W., Worzel, J.L., *American Association of Petroleum Geologists Bulletin*, **63**, 2204 (1979).
Singh, S.C., Minshull, T.A., *J. Geophys. Res*., **99B12**, 24, 221 (1994)
Sloan, E.D., Happel, J., Hnatow, M.A., (eds), in *International Conference on Natural Gas Hydrates*, *Ann. N.Y. Acad. Sci.*, **715** (1994).
Soloviev, V.A., *Russian Geol. Geophys.*, **43**(7), 648 (2002).
Soloviev, V.A., Ginsburg, G.D., *Mar. Geol.*, **137**, 59 (1997).
Stagg, H.M.J., Symonds, P.A., Exon, N.F., Auzende, J-M., Dickens, G.R., Van de Beuque, S., in G.R. Wood (compiler), *Second Sprigg Symposium*, *Abstracts*, *Geological Society of Australia*, **60**, 69 (2000).
Stern, L.A., Kirby, S.H., Durham, W.B., in *Scientific Results from the Mallik 2002 Gas Hydrate Production Research Well Program*, Mackenzie Delta, Northwest Territories, Canada (Dallimore, S.R., Collett, T.S., eds.), Geological Survey of Canada Bulletin 585, including CD, p. 109 (2005).
Suess, E., Bohrman, G., Greinert, J., Lausch, E., *Sci. Am.*, **281**(5), 76l (1999b).
Suess, E., Torres, M.E., Bohrmann, G., Collier, R.W., Greinert, J., Linke, P., Rehder, G., Tréhu, A., Wallmann, K., Winckler, G., Zuleger, E., *Earth Planet. Sci. Lett.*, **170**, 1 (1999a).
Sumetz, V.I., *Gaz. Prom*., **2,** 24 (1974).
Summerhayes, C.P., Bornhold, B.D., Embley, R.W., *Mar. Geol.*, **31**, 265 (1979).
Takayama, T., Nishi, M., Uchida, T., Akihisa, K., Sawamure, F., Ochiai, K., in *Scientific Results from the Mallik 2002 Gas Hydrate Production Research Well Program*, Mackenzie Delta, Northwest Territories, Canada (Dallimore, S.R., Collett, T.S., eds.), Geological Survey of Canada Bulletin 585, including CD, p. 115 (2005).
Tamano T, Toba, T., Aoki, Y., in *Proc. 11th World Petroleum Congress*, Wiley, New York, **2**, 135 (1984).
Taylor, A.E., Wetmiller, R.J., Judge, A.S., in W. Denner (ed.), *Symposium on Research in the Labrador Coastal and Offshore Region*, Memorial University of Newfoundland, p. 91 (1979).
Taylor, C.E., Kwan, J.T. (eds.), *Advances in the Study of Gas Hydrates*, Springer, New York, p. 225 (2004).
Thomas, E., Shackleton, N.J., *Correlation of the Early Paleogene in Northwest Europe* (Knox, R.O., Corfield, R.M., et al., eds.), Geological Society (London) Special Publication 101, p. 401 (1996).
Tohidi, B., Anderson, R., Clennell, M.B., Burgess, R.W., Biderkab, A.-B., *Geology*, **29**(9), 867 (2001).
Torres, M.E., Wallmann, K., Tréhu, A.M., Bohrmann, G., Borowski, W.S., Tomaru, H., *Earth Planet. Sci. Lett*., **226**, 225 (2004).

Torres, M.E., Wallmann, K., Tréhu, A.M., Bohrmann, G., Borowski, W.S., Tomaru, H., *Earth Planetary Sci. Lett*., **239**, 168 (2005).

Tréhu, A.M., Glemings, P.B., Bangs, N.L., Chevallier, J., Gracia, E., Johnson, J.E., Liu, C.-S., Liu, X., Riedel, M., Torres, M.E., *Geophys. Res. Lett.*, **31**, L23310, doi:10.1029/2004GL021286 (2004a).

Tréhu, A.M., Long, P.E., Torres, M.E., Bohrmann, G., Rack, F.R., Collett, T.S., Goldberg, D.S., et al., *Earth Planet. Sci. Lett*, **222**, 845 (2004b).

Tréhu, A.M., Ruppel, C., Holland, M., Dickens, G.R., Torres, M.E., Collett, T.S., Goldberg, D.S., Riedel, M., Schultheiss, P., *Oceanography*, **19**(4), 124 (2006).

Trofimuk, A.A., Cherskiy, N.V., Lebedev, V.S., Semin V.I., et al., *Geol. Geofiz*., **2**, 3 (1973).

Trofimuk, A.A., Cherskiy, N.V., Tsarev, V.P., *Future Supply of Nature-Made Petroleum and Gas* (Meyer, R.F., ed.), Pergamon Press, New York, 919 (1977).

Trofimuk, A.A., Cherskii, N.V., Tsarev, V.P., Nikitin, S.P., *Geologiva i Geofizika*, **23**, 3 (1982).

Trofimuk, A.A., Makogon, Y.F., Tolkachev, M.V., *Geologiia Nefti i Gaza*, **10**, 15 (1981).

Tsypkin, G.G., *Gas Hydrates: Challenges for the Future*, *Ann. N.Y. Acad. Sci*. (Holder, G.D., Bishnoi, P.R., eds.), **912**, p. 428 (2000).

Tucholke, B.F., Bryan, G.M., Ewing, J.I., *Am. Assoc. Pet. Geol. Bull*., **61**, 698 (1977).

Tulk, C.A., Wright, J.F., Ratcliffe, C.I., Ripmeester, J.A., in *Geological Survey of Canada Bulletin 544* (Dallimore, S.R., Uchida, T., et al., eds.), p. 263 (1999).

Veerayya, M., Karisiddaiah, S.M., Vora, K.H., Wagle, B.G., Almeida, R., in *Gas Hydrates—Relevance to World Margin Stability and Climatic Change* (Henriet, J.-P., Mienert, J., eds.), The Geological Society, London, Special Publication 137, p. 239 (1998).

Weaver, J.S., Stewart, J.M., in Roger J.E. Brown Memorial Volume, in *Proc. Fourth Canadian Permafrost Conference*, **1981**, 312 (1982).

Weitemeyer, K., Constable, S., Key, K., *The Leading Edge*, **25**, 629 (2006).

Westbrook, G.K., Carson, B., Musgrave, R.J., et al., Scientific Drilling Project in *Proc. Ocean Drilling Program Leg 146*, **146**(1), 301 (1994).

White, R.S., *Planet. Sci. Lett.*, **42**, 114 (1979).

Whiticar, M.J., Faber, E., Schoell, M., *Geochim. Cosmochim Acta*, **50**, 693 (1986).

Whiticar, M.J., Hovland, M., Kastner, M., Sample, J.C., in *Proc. Ocean Drilling Program, Scientific Results*, **146**(1), 385 (1995).

Wood, W.T., Gettrust, J.F., Chapman, N.R., Spence, G.D., Hyndman, R.D., *Nature*, **420**, 656 (2002).

Woodside, J.M., Ivanov, M.K., Limonov, A.F., and Shipboard Scientists of the Anaxiprobe Expeditions, in *Gas Hydrates—Relevance to World Margin Stability and Climatic Change* (Henriet, J.-P., Mienert, J., eds.), The Geological Society, London, Special Publication 137, p. 177 (1998).

Wright, J.F., Dallimore, S.D., in *Proc. Fifth International Conference Gas Hydrates* (Austvik, T., ed.) (paper 5039), 4 volumes and CD, Trondheim, Norway, June 13–15, p. 1699 (2005).

Wright, J.F., Dallimore, S.D., Nixon, F.M., Dchesne, C., in *Scientific Results from the Mallik 2002 Gas Hydrate Production Research Well Program*, Mackenzie Delta, Northwest Territories, Canada (Dallimore, S.R., Collett, T.S., eds.), Geological Survey of Canada Bulletin 585, including CD, p. 92 (2005).

Wu, S., Zhang, G., Huang, Y., Liang, J., Wong, H.K., *Marine and Petroleum Geology*, **22**, 403 (2005).

Xu, W., Ruppel, C., *J. Geophys. Res*., **104**, 5,081 (1999).
Yakushev, V.S., Istomin,V.A., "Gas Hydrates Self-Preservation Effect," presented at the *IPC-91 Symposium*, Sapporo, Japan, September (1991).
Yamano, M., Uyeda, S., in *Proc. ODP. Sci. Results* (Suess, E., von Huene, R., et al., eds.), **112**, p. 653 (1990).
Yefremova, A.G., Gritchina, N.D., *Geologiya Nefti i Gaza*, **2**, 32 (1981).
Yefremova, A.G., Zhizhchenko, B.P., *Doklady Akademii Nauk SSSR*, **214**, 1179 (1974).
Yousif, M.H., Abass, H., Selim, M.S., Sloan, E.D., SPE 18320, in *Proc. 63rd Annual Technical Conference of SPE*, Houston, TX, October 2–5 (1988).
Yousif, M.H, Sloan, E.D., in *SPE Reserve Engineering*, 452, November (1991).
Yuan, T., Hyndman, R.D., Spence, G.D., Desmons, B., *J. Geophys. Res*., **101**, 13655 (1996).
Zillmer, M., Flueh, E.R., Petersen, J., *Geophys. J. Int.*, **161**, 662 (2005).
Zonenshayn, L.P., Murdmaa, I.O., Baranov, B.V., Kusnetsov, A.P., Kuzin, V.S., Kuz'min, M.I., Avdeyko, G.P., et al., *Oceanology*, **27**, 795 (1987).

8 Hydrates in Production, Processing, and Transportation

Introduction

The objective of this chapter is provide an overview of how solid masses of hydrates (plugs) form, means of preventing and encouraging plug formation, and means of dissociating plugs once they have formed.

Unlike the other portions of the book, for example, the thermodynamic calculation methods in Chapters 4 and 5, in this chapter, conceptual pictures indicate how phenomena occur, based upon hydrate research and industrial practice. Particularly emphasized are those that have evolved during the last decade. For those who wish to do prevention calculations, several practical engineering guides are available. The engineering books by Kidnay and Parrish (2006), Carroll (2003), Makogon (1997), and Sloan (2000) prescribe hydrate calculations for the practicing engineer.

Because most of the industrial hydrate concerns have been in flow assurance, that application is emphasized. However, the concepts apply to other uses, such as gas processing and hydrated gas transport. In Section 8.1 beginning with several typical case studies of hydrate plug formation, we conclude with a conceptual overview of hydrate formation in both oil- and gas-dominated systems. Section 8.2 considers hydrate plug prevention, before considering plug remediation in Section 8.3. Then, and perhaps most important, hydrate safety is considered in Section 8.4, together with a computer program CSMPlug (on the book's CD) that provides the sole chapter exception, to enable calculations of plug remediation and safety considerations. Finally, Section 8.5 discusses concepts of gas storage and transportation.

Below are six important points to realize in this chapter:

1. Hydrate plugs and their dissociation can have major economic and safety impacts on flowline operation.
2. While the past methods of preventing hydrate plugs have been to use avoidance with thermodynamic inhibitors such as methanol or glycols, our new understanding of how plugs form, allows us to propose economic risk management (kinetics) to avoid hydrate formation. These concepts differ in type for oil-dominated and gas-dominated systems.
3. New, low dosage hydrate inhibitors (LDHIs) are being commonly used in the industry, based upon the kinetics of hydrate formation.

4. We can predict plug dissociation using two-sided dissociation.
5. The safety implications of plug dissociation are sometimes life-threatening, and should be an important concern.
6. It is possible to store and transport gas in hydrated form.

8.1 How do Hydrate Plugs Form in Industrial Equipment?

Considering hydrate formation and prevention, the physical conditions necessary for hydrates are

1. A hydrate guest molecule
2. Water
3. The correct conditions of temperature and pressure—usually low temperature and high pressure

Without any one of the above conditions, hydrates will not form. However, removing some of the above conditions may be impractical:

1. To remove the guest molecule (e.g., methane) may be to remove the reason for the process.
2. To use an insufficient gas pressure (typically less than 225 psia or 1.5 MPa) may decrease the energy density to a point that it is not economical.

However, it is practical to use the other thermodynamic prevention conditions:

1. Frequently the system is heated to keep it above the hydrate formation temperature at the system pressure.
2. Frequently the system has both the free water and vaporized water removed, by separation and drying the remaining gas with triethylene glycol or molecular sieves.

A second, indirect way of removing the free water is by injecting an inhibitor (typically alcohol or glycol) so that much of the free water is hydrogen bonded to the inhibitor. This reduces the water activity so that lower temperatures and higher pressures are required to form hydrates with the lower concentration of nonhydrogen bonded water, as shown in the first case study below.

In a 1999 survey of 110 energy companies, flow assurance was listed as the major technical problem in offshore development (Welling and Associates, 1999). On September 24, 2003, in a Flow Assurance Forum, Professor James Brill (2003) discussed the need for a new academic discipline called “Flow Assurance.” Such a question, presented to an audience of 289 flow assurance engineers, would not have been considered in 1993, when the flow assurance community totaled a few dozen people.

Yet the statement of Professor Brill's question indicates the importance of flow assurance, particularly related to hydrates, waxes, scale, corrosion, and asphaltenes, in decreasing order of importance. In the Gulf of Mexico, for example, hydrates are considered to be the largest problem by an order of magnitude relative to the others.

Hydrate plugs do not occur in normal flowline operation due to design, but plugs are the result of three types of abnormal flowline operation:

1. When the water phase is uninhibited, as when excess water is produced, dehydrator failure, or when inhibitor injection is lost, for example, due to inhibitor umbilical failure or inhibitor pump failure.
2. Upon start-ups following emergency shut-ins, due to system component failure and recovery, such as compressor failure, without the opportunity to take inhibition steps.
3. When cooling occurs with flow across a restriction, such as in the flow of a wet gas through a choke or valve in a fuel gas line.

8.1.1 Case Study 1: Hydrate Prevention in a Deepwater Gas Pipeline

Notz (1994) noted that almost all of Texaco's efforts concerning natural gas hydrates dealt with the prevention of hydrate formation in production and transportation systems. He presented Figure 8.1 from Texaco's hydrate prevention program in a 50 mile deepwater gas pipeline, using a phase diagram similar to those discussed with Figure 4.2.

Figure 8.1 shows the pressure and temperature of fluids in a flowline at various points along the ocean floor, predicted by a multiphase flow prediction program. As a unit mass of fluid traverses the pipeline, the pressure drops normally due to friction losses associated with fluid flow. However, the temperature decrease is more interesting.

At water depths greater than 4000 ft, the ocean floor temperature is amazingly uniform at temperatures of 36–40°F. The ocean thus provides an infinite cooling medium for the warm fluids from the reservoir. In the case shown in Figure 8.1 at low pipeline distance (e.g., 7 miles) the flowing unit mass retains some residual energy (high T and high P) from the hot reservoir.

The ocean cools the fluids as they flow, including both produced water (here assumed to be salt-free) and condensed water that is always salt-free. At about 9 miles the flowing hydrocarbons and water enter the hydrate region (to the left of the line marked "hydrate formation curve"), remaining in the uninhibited hydrate envelope until mile 45. Such a distance may represent several days of residence time for the water phase (which flows slower than the hydrocarbon phases) so that hydrates would undoubtedly form, were no inhibition steps taken.

In Figure 8.1, by mile 30 the gas in the pipeline has cooled to within a few degrees of the ocean floor temperature, so that approximately 23 wt% methanol in the free water phase is required to prevent hydrate formation and subsequent

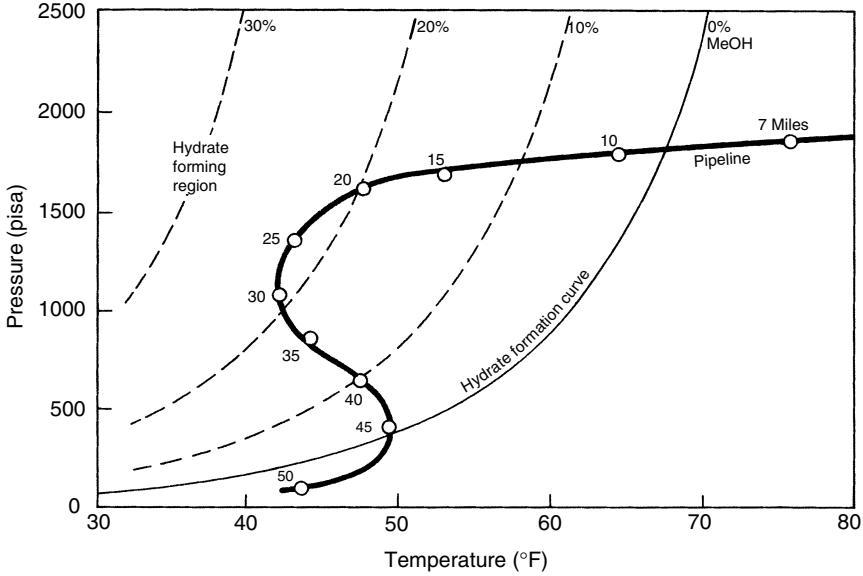

FIGURE 8.1 Typical offshore flowline system with intrusion into hydrate region. (From Notz, P.K., in *(First) International Conference on Natural Gas Hydrates*, *Ann. N.Y. Acad. Sci.*, **715**, 425, 1994. With permission.)

pipeline blockage. Methanol injection facilities are not available at the needed points (9–45 miles) along the pipeline. Instead methanol is vaporized into the pipeline at some convenient upstream point, such as a subsea well-head so that in excess of 23 wt% methanol will be present in the free water phase over the entire pipeline length.

As vaporized methanol flows along the pipeline shown in Figure 8.1, it partitions into any produced water, along with water condensed from the gas. Hydrate inhibition occurs in the free water, usually at water accumulations with some change in geometry (e.g., a riser, bend, or pipeline dip along an ocean floor depression) or some nucleation site (e.g., sand, weld slag, etc.).

Hydrate inhibition occurs in the aqueous liquid, rather than in the vapor or hydrocarbon liquid phases. While a significant portion of the methanol partitions into the water phase, a significant amount of methanol either remains with the vapor or partitions into any liquid hydrocarbon phase. Although the methanol mole fraction in the vapor or liquid hydrocarbon may be low relative to the water phase, the large amounts (phase fractions) of vapor and liquid phases will cause a substantial amount of inhibitor loss.

In Figure 8.1 Notz notes that the gas begins to warm (from mile 30 to mile 45) with shallower, warmer water conditions. From mile 45 to mile 50, however, a second cooling trend is observed due to Joule–Thomson expansion. The methanol exiting the pipeline in the vapor, aqueous, and condensate phases is usually not recovered, due to the expense of separation.

Note that regular methanol (or monoethylene glycol) injection is used only with gas-dominated systems. In oil-dominated systems the higher liquid heat capacity allows the system to retain reservoir heat, so that insulation maintains sufficient temperatures to prevent hydrate formation. Thermodynamic inhibitor is normally only injected for planned shutdowns in oil-dominated systems.

8.1.2 Case Study 2: Hydrates Prevention via Combination of Methods

As a summary of the thermodynamic hydrate prevention methods, consider the steps taken to prohibit hydrates in the Dog Lake Field export pipeline in Louisiana, by Todd et al. (1996) of Texaco. During the winter months hydrates formed in the line, which traverses land and shallow water (a marsh).

Hydrate formation conditions, shown in Figure 8.2 are calculated via the methods of Chapters 4 and 5 with 0, 10 and 20 wt% methanol in the water phase. The Dog Lake gas composition is: 92.1 mol% methane, 3.68% ethane, 1.732% propane, 0.452% *i*-butane, 0.452% *n*-butane, 0.177% *i*-pentane, 0.114% *n*-pentane, 0.112% hexane, 0.051% heptane, 0.029% octane, 0.517% nitrogen, 0.574% carbon dioxide.

The pipeline pressure and temperature, calculated using PIPEPHASE®, were superimposed on the hydrate formation curve shown in Figure 8.3. Gas leaves

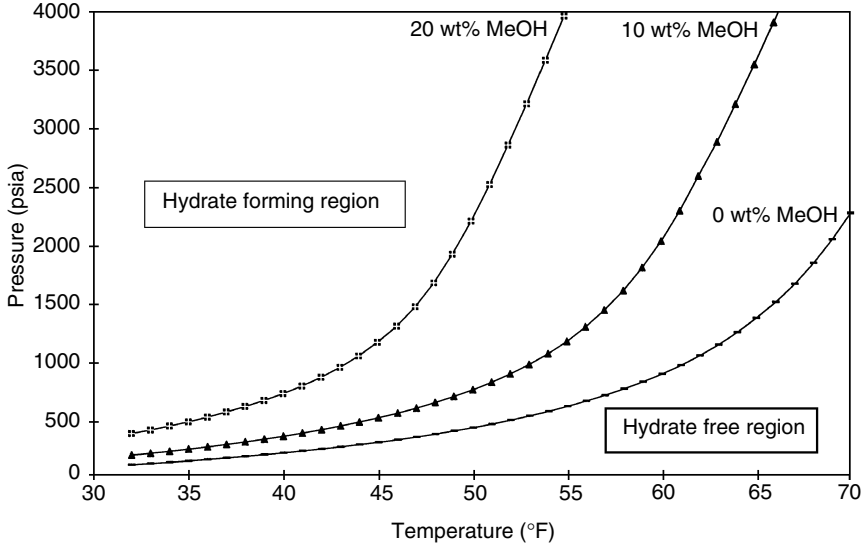

FIGURE 8.2 Dog Lake gas hydrate formation curves with methanol in free water phase. (From Todd, J.L., et al., *Reliabilty Engineering—Gas Freezing and Hydrates*, Texaco Company Hydrate Handbook (1996). With permission.)

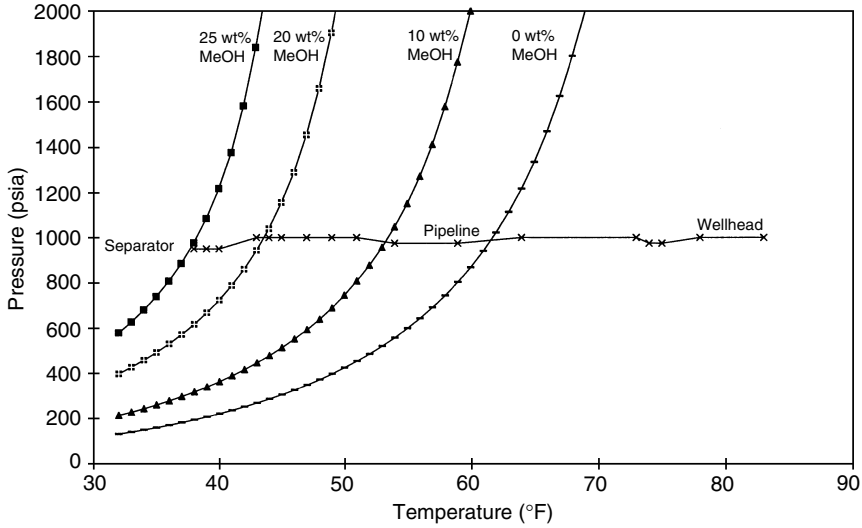

FIGURE 8.3 Normal Dog Lake flowline conditions indicating the need for methanol. (From Todd, J.L., et al., *Reliabilty Engineering—Gas Freezing and Hydrates*, Texaco Company Hydrate Handbook (1996). With permission.)

the wellhead at 1000 psia and 85°F, far from hydrate forming conditions. As the gas moves down the pipeline, it is cooled toward ambient temperatures. Once the temperature reaches approximately 62°F, hydrates will form, so methanol must be added to avoid blockage. The figure shows pipeline conditions and the hydrate formation curves for various concentrations of methanol, indicating that 25 wt% methanol in the free water phase is needed to inhibit hydrates.

Despite large quantities of methanol injection for hydrate prevention, 110 hydrate incidents occurred in the Dog Lake line during the winter of 1995–1996 at a remediation cost of $323,732, not counting lost production. Combinations of four alternative hydrate prevention methods were considered: (1) burying the pipeline, (2) heating the gas at the wellhead, (3) insulating the pipeline, and (4) methanol addition. The first three methods were intended to maintain sufficiently high temperatures to prevent hydrate formation, while the last method effectively inhibited free water, via hydrogen bonding with methanol. The details of each prevention measure are considered below.

8.1.2.1 Burying the pipeline

Portions of the Dog Lake pipeline were built over a stretch of marsh. The exposure to winter ambient temperatures caused rapid reductions in the gas temperature. Burying the pipeline would protect it from low environmental temperatures due to the higher earth temperatures. Figure 8.4 shows the increase in the pipeline

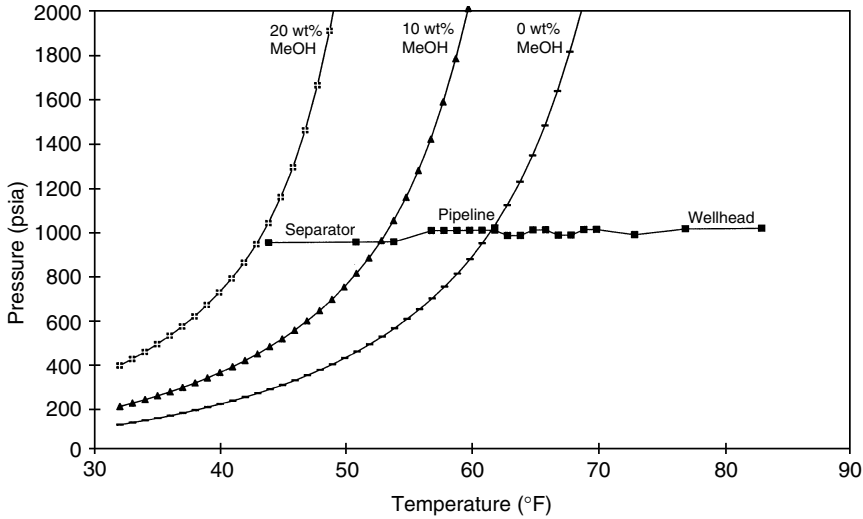

FIGURE 8.4 Dog Lake line burial increased the discharge temperature and reduced the amount of methanol. (From Todd, J.L., et al., *Reliabilty Engineering—Gas Freezing and Hydrates*, Texaco Company Hydrate Handbook (1996). With permission.)

discharge temperature after the exposed areas were buried, relative to the exposed line in Figure 8.3. With pipeline burial, the need for methanol in the water phase was reduced from 25 wt% (Figure 8.3) to less than 20 wt% (Figure 8.4).

8.1.2.2 Line burial with wellhead heat addition

Line heaters could be installed at the wellhead to increase the inlet gas temperature from 85°F to 125°F. Figure 8.5 shows the pipeline temperature increase caused by the combined prevention methods of burial and wellhead heating. Use of these two methods permitted the methanol concentration in the free water phase to be reduced to approximately 14 wt% to prevent hydrate formation in the line. It should, however, be noted that heating may increase the amount of corrosion in the line.

8.1.2.3 Burial, heat addition, and insulation

In addition to line burial and the addition of heat at the wellhead, insulation of exposed areas near the wellhead maintained higher pipeline temperatures, thereby reducing the amount of methanol needed for hydrate inhibition. Figure 8.6 displays the temperature increase in the buried and heated pipeline when exposed pipes were insulated. A combination of the methods causes the pipeline fluid to be outside the hydrate formation region (to the right of the curve marked 0 wt% MeOH), and methanol addition is no longer needed.

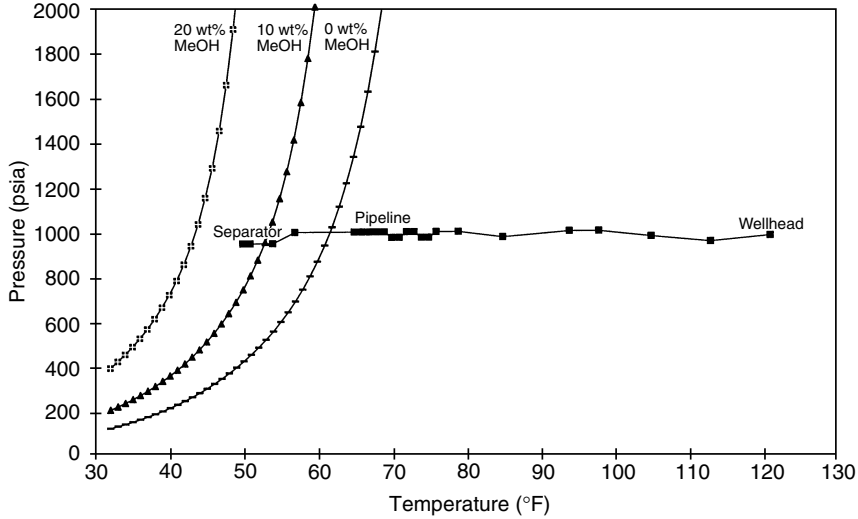

FIGURE 8.5 Dog Lake line burial and inlet heating reduces the need for methanol. (From Todd, J.L., et al., *Reliabilty Engineering—Gas Freezing and Hydrates*, Texaco Company Hydrate Handbook (1996). With permission.)

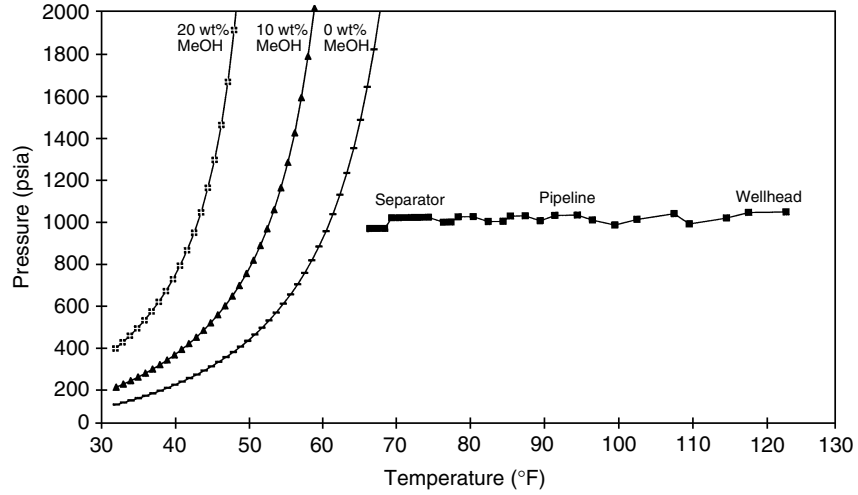

FIGURE 8.6 Dog Lake line burial, inlet heating, and insulation removes system from hydrate region. (From Todd, J.L., et al., *Reliabilty Engineering—Gas Freezing and Hydrates*, Texaco Company Hydrate Handbook (1996). With permission.)

8.1.2.4 Methanol addition alternative

Continued methanol injection could be done at a cost of approximately $1.50–2.00 per gallon during the 1996–1997 winter. Since methanol recovery is problematic,

methanol is normally considered an operating cost. In addition, refineries have put restrictions on methanol concentrations in condensate and this further decreases the economics of methanol injection.

This case study illustrates how combinations of pipeline burial, insulation, heating, and methanol injection can be used to prevent hydrates. The selection of the hydrate prevention scheme(s) is then a matter of balancing capital against operating costs.

8.1.3 Case Study 3: Hydrate Formation via Expansion through Valves or Restrictions

When water-wet gas expands rapidly through a valve, orifice or other restriction, hydrates form due to rapid gas cooling caused by adiabatic (Joule–Thomson) expansion. Hydrate formation with rapid expansion from a wet line commonly occurs in fuel gas or instrument gas lines. Hydrate formation with high pressure drops can occur in well testing, start-up, and gas lift operations, even when the initial temperature is high, if the pressure drop is very large.

Figure 8.1 shows the pressure and temperature of a pipeline production stream during normal flow with entry into the hydrate formation region. If the gas expands more rapidly, the normal pipeline cooling curve of Figure 8.1 will take on a much steeper slope, but the hydrate formation line remains the same. Two rapid Joule–Thomson expansion curves for a 0.6 gravity gas are shown in Figure 8.7. Intersections of the gas expansion curves with the hydrate formation line (bounding the shaded area) limits the expansion discharge pressures from two different high initial pressure/temperature conditions.

In Figure 8.7, the curves determine the restriction downstream pressure at which hydrate blockages will form for a given upstream pressure and temperature. Gas A expands from 2000 psia and 110°F until it strikes the hydrate formation curve at 700 psia (and 54°F), so 700 psia represents the limit to hydrate-free expansion. Gas B expands from 1800 psia (120°F) to intersect the hydrate formation curve at a limiting pressure of 270 psia (39°F). In expansion processes while the upstream temperature and pressure are known, the discharge temperature is almost never known, but the discharge pressure is normally set by a downstream vessel or pressure drop.

Cooling curves such as the two in Figure 8.7 were determined for constant enthalpy (or Joule–Thomson) expansions, obtained from the First Law of Thermodynamics for a system flowing at steady-state, neglecting kinetic and potential energy changes:

$$\Delta H = Q + W_s \tag{8.1}$$

where ΔH is the enthalpy difference across the restriction (downstream–upstream), while Q represents the heat added, and W_s is shaft work done at the restriction. Restrictions (e.g., valves or orifices) have no shaft work, and because rapid flow

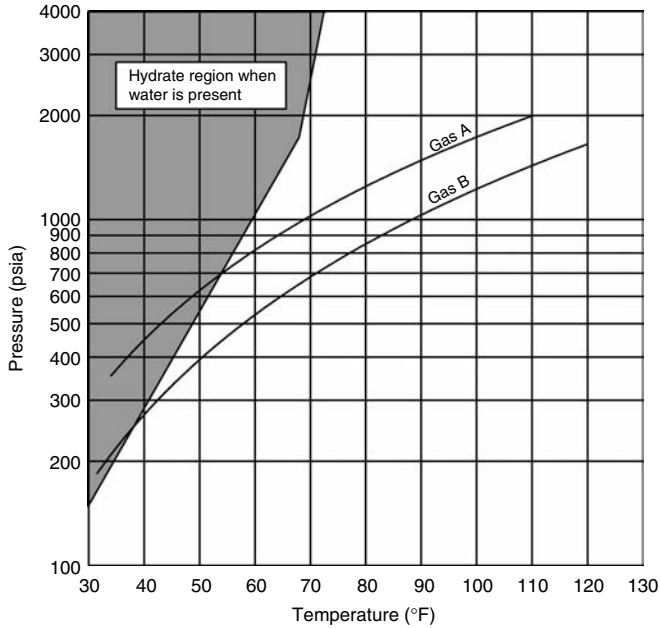

FIGURE 8.7 Expansion of two gases into the hydrate formation region. (From Katz, D.L., *Trans AIME*, **160**, 140 (1945). With permission.)

approximates adiabatic operation (limited heat transfer); both W_s and Q are zero, resulting in constant enthalpy ($\Delta H = 0$) operation on expansion.

Due to the constant enthalpy requirement, rapid gas expansion with pressure lowering normally results in cooling. Because of the constraint that the enthalpy (roughly a flow-corrected energy) must be equal on both sides of the valve, a lower pressure gas (higher enthalpy) downstream of the valve, must be compensated by a lower temperature (lower enthalpy). So Figure 8.7 for fluid expansion through a valve has a steeper slope than normal flow along a pipeline (Figure 8.1) that has heat transfer (Q) with the surroundings, which are typically around 40°F.

To prevent hydrate formation in expansion on the downstream side of a valve, the most common method is to inject methanol or glycol before the value, removing the hydrate formation (shaded) region to the left of Figure 8.7 from the expansion conditions. Alternatives include heating the inlet gas or limiting the downstream pressure.

In concluding this case study, it should be recalled that Section 4.2.1.1 provides the hand calculation limits to Joule–Thomson expansion, through Figures 4.7 through 4.9. The computer program CSMGem on the CD supplied with this book also provides a method for calculation of expansion limits, as shown in the User's Examples in Appendix A, and in the User's Guide found on the CD accompanying this volume.

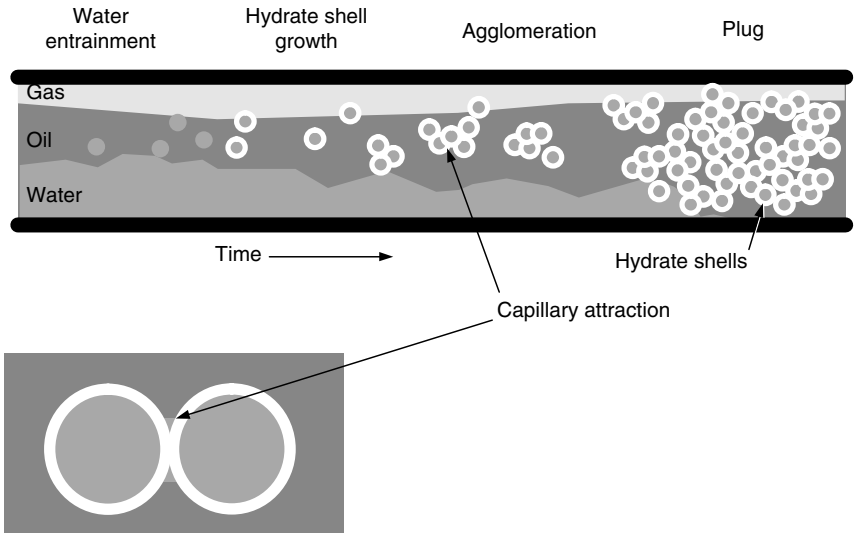

FIGURE 8.8 (See color insert following page 390.) Plug formation via aggregation in an oil-dominated system. (From Turner, D.J., *Clathrate Hydrate Formation in Water-in-Oil Dispersions*, Ph.D. Thesis, Colorado School of Mines, Golden, CO (2004). With permission.)

8.1.4 Conceptual Overview: Hydrate Plug Formation in Oil-Dominated Systems

Figure 8.8 gives a conceptual figure of hydrate formation in an oil-dominated pipeline. This figure is an extension of the hypothesis originally proposed by Norsk Hydro (Lingelem et al., 1994) and has gained some acceptance in the industry.

In Figure 8.8 six steps are involved in hydrate plug formation:

1. The water phase is emulsified within the oil phase. Usually the oil phase fraction is much greater than the water phase fraction, so the large majority of oil production involves a water within oil (W/O) emulsion. The water droplet size is typically tens of microns (μm).
2. A thin (perhaps smaller than 6 μm thick) hydrate shell grows around the water droplets, from small gas molecules dissolved in the oil phase. Initially this hydrate shell is extremely malleable, so much so the hydrate-encrusted droplet will extrude through screens, for example.
3. While they are malleable, these hydrate shells form a diffusional barrier between the hydrocarbon and water phases. The shells do not usually become very thick, except at long times—periods of days.
4. Capillary forces of attraction cause the hydrate-encrusted droplets to agglomerate. These capillary forces are a strong function of temperature; at low temperatures the forces decrease between the particles, as measured by Taylor (2006).

5. As the hydrated particles agglomerate, the effective viscosity increases dramatically, and spikes in the flowline pressure drop occur with time, indicating agglomeration and breakage of hydrate masses. Finally the agglomerate becomes sufficiently large to increase the pressure drop so that flow is stopped. This point is normally taken as a hydrate plug, causing flow to be shut in.
6. As the plug sits for a longer period of time, the masses anneal and the plug becomes more solid-like, with less flexibility. That is, both intra- and interparticle growth occurs. This annealing process is not shown in Figure 8.8.

The simplified conceptual picture in Figure 8.8 has important implications for flow assurance. For example, the model's implication is that hydrate agglomeration (not the kinetics of shell growth) is the limiting factor in plug formation. If one could determine a means of preventing agglomeration, such as antiagglomerants (AAs) (Mehta, et al., 2003) or cold flow (Wolden, et al., 2005), one could allow the hydrates to form and flow without obstructing the pipeline. There is significant evidence that such situations normally occur in flowlines in Brazil (Palermo et al., 2004), where natural AAs exist in oils.

8.1.5 Conceptual Overview: Hydrate Formation in Gas-Dominated Systems

Hydrate formation in a gas-dominated system is thought to differ significantly from formation in oil-dominated systems. In gas systems, there is much less liquid (both hydrocarbon and water), so that the W/O emulsion concept may not apply. Instead a concept may apply as shown in Figure 8.9.

The bottom portion of Figure 8.9 gives the concept of hydrate formation in a gas-dominated system, while the top portion shows the line pressure (note the semi-logarithmic scale) before a hydrate plug point as a function of time in the pipeline, upstream of a water/hydrate accumulation, corresponding to the lower conceptual portions of the figure. The bottom conceptual picture is a second extension of a picture originally proposed by Lingelem et al. (1994). The pressure data shown were obtained just before the location of hydrate formation at the Werner–Bolley gas line in Wyoming by Hatton and Kruka (2002).

Figure 8.9 suggests five steps for hydrate formation in a gas-dominated line:

1. Water in the pipeline (at Point A) is due to both produced water, and condensed water from the gas.
2. Hydrates originally form at the walls of the pipe (Point B) via vapor deposition and/or splashing of water with subsequent conversions. The wall is the radial point of lowest temperature, and consequently the point of hydrate deposition due to heat transfer with the outside environment, which is at a lower temperature than the gas.

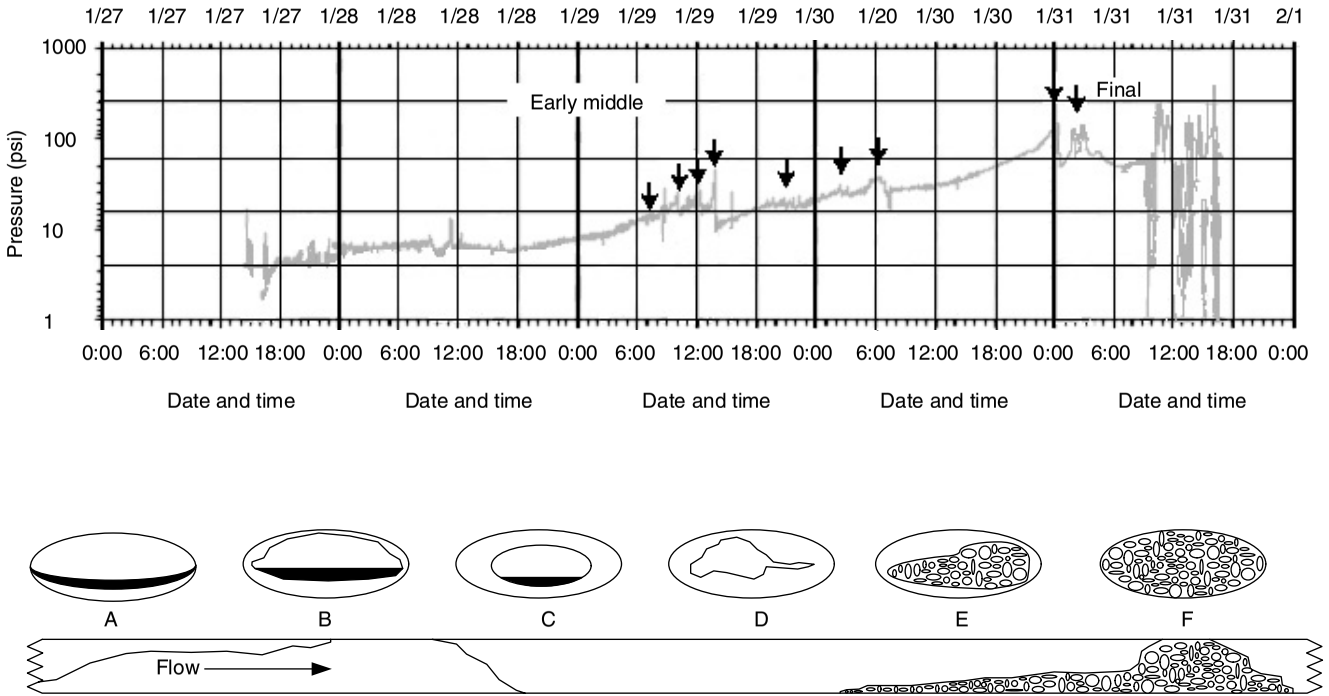

FIGURE 8.9 Hydrate blockage formation (bottom) and corresponding pressure buildup (top) in a gas-dominated pipeline (upper figure From Hatton, G.J., Kruka, V.R., *Hydrate Blockage Formation—Analysis of Werner Bolley Field Test Data*, DeepStar CTR 5209-1, 2002; lower figure modified from Lingelem, M.N., et al., in *(First) International Conference on Natural Gas Hydrates*, *Ann. N.Y. Acad. Sci.*, **715**, 75 (1994). With permission.)

3. As the hydrate deposition on the wall becomes thicker (Point C), narrowing of the flow channel occurs. The deposition forms irregularly (Point D) so that a nonconcentric annulus increases the pipeline pressure drop. Steps 1–3 are in the stages of hydrate plug formation marked "early" in the top of Figure 8.9, with a gradual upstream pressure increase.
4. At Point E in the bottom of Figure 8.9, the hydrate wall deposit can no longer bear the stress imposed by a combination of the fluid passing by together with the hydrate deposit weight, and hydrate sloughs from the wall. These sloughs are marked by a decrease in the upstream pressure, at each of the arrows in the top of Figure 8.9 in the portion marked "middle."
5. As the sloughed particles travel downstream, they bridge across the flow channel (Point F) to form a plug, with the corresponding upstream pressure spikes as shown in the "final" period of the top of Figure 8.9.

The above simplified picture has important implications for flow assurance in gas lines, as shown by the gas line operation in the case studies of Section 8.2.

8.2 How are Hydrate Plug Formations Prevented?

The five studies of hydrate formation given in Section 8.1 are of two types. The first three case studies show thermodynamic (time-independent) methods to prevent plug formation. However, the second type provides a closer, mechanistic look at the physical kinetics (time-dependent) hydrate formation and agglomeration. A goal of this section is to show how these two methods provide two different methods of plug prevention.

Avoidance of the hydrate formation thermodynamic conditions of temperature, pressure, or inhibitor concentration, makes it impossible for plugs to form. The calculations of thermodynamic conditions can be made with acceptable accuracy. Using the methods presented in Chapters 4 and 5 along with the CD program CSMGem provided with this book, the temperature, pressure, and inhibitor concentrations can be calculated respectively, to within 2°F, 10% in pressure and 3% of inhibitor concentration. Since the discovery of hydrate flowline plugs in 1934, such thermodynamic methods have served to provide the major method of flow assurance.

However, as mankind has exhausted the most accessible hydrocarbon supplies, more severe conditions (e.g., higher pressures, lower temperatures, and higher acid gas contents) caused thermodynamic prevention means to be less acceptable economically. The following two case studies illustrate the fact that thermodynamic inhibition is becoming very expensive.

8.2.1 Case Study 4: Thermodynamic Inhibition Canyon Express and Ormen Lange Flowlines

1. At start-up in September 2002, the Canyon Express development in the Gulf of Mexico was the world's deepest, with the three field locations in

6500–7200 ft of sea water (Hare and Case, 2003). Due to the extreme depth, large amounts of methanol injection necessitated an unusual distillation methanol recovery. Without methanol recovery, the Canyon Express maximum design of 1000 BPD of water production requires 1 million dollars of methanol injection (at U.S.$1/gal methanol) every 16 days.

2. The Ormen Lange gas field (Wilson et al., 2004), offshore of northern-Norway, when it commences production in 2016, will have two unusual features: (1) flow of fluids uphill against a seabed gradient of 26% and (2) an unusual ocean bottom temperature of 30°F due to subsea currents. Typical deepwater temperatures are around 40°F (well above 32°F, the freezing point of water), and such a low temperature at Ormen Lange means that any water produced could form ice, as well as hydrates. Extra precautions, must be taken because an ice plug is much more problematic to remove than a hydrate plug (which can be removed by depressurization). The estimated maximum monoethylene glycol injection needed is 26,500 ft^3/d, with a capacity of 53,000 ft^3/d. As a result, when the Ormen Lange inhibition system is first charged, the amount of monoethylene glycol will require 67% of the world's annual production capacity (Wilson, Personal Communication, March 15, 2004).

The above two examples serve to illustrate that more severe conditions of gas recovery require large expense in thermodynamic inhibitors. The high pressure and high water production at Canyon Express and the steeply upward sloping lines and subfreezing temperatures of Ormen Lange are harbingers of more severe conditions in the future. There are some cases in which the cost of hydrate inhibitors determine the project viability.

A fair question is, "If industry always recovers from infrequent blockages, what is the economic incentive to justify the risk of very infrequent blockages?" The answer is complex, including technical disciplines, statistics, economics, and risk management.

Forty-six case studies of hydrate plug formation and remediation are recorded in *Hydrate Engineering* (Sloan, 2000). In every case, hydrate plugs were remediated. In addition, a rule of thumb is that most of the offshore flowline shut-ins are less than the 10 h "no touch" time, which requires no antihydrate operation before restart (J.E. Chitwood, Personal Communication, August 1, 2003). However, hydrate prevention methods are very expensive, as shown in the above Canyon Express and Ormen Lange examples, or in the fact that deepwater insulation costs are typically U.S.$1 million per kilometer of flowline.

In the future, economic risk evaluation will guide the hydrate-plugging prevention philosophy. It is important to note that phase equilibria thermodynamics provide the current paradigm of hydrate avoidance, but risk management is in the domain of time-dependent phenomena or physical hydrate kinetics. The experience base with hydrate plugs and their remediation impacts the economic need for large amounts of insulation and/or thermodynamic inhibitors.

While accurate thermodynamic predictions (as in Chapters 4 and 5) enable avoidance via use of inhibitors such as methanol, risk management is enabled by operating experience and by kinetic predictions. Hydrate thermodynamic predictions can provide avoidance techniques, but kinetic predictions are required to provide techniques of risk management.

Lacking an acceptable hydrate kinetics model, however, the leaders in deepwater multiphase flow operations have moved to risk evaluation technology, again using the engineering method of using the best technology, past operating experiences, and taking small risks in new designs. There are several examples to illustrate risk evaluation or kinetics in flowline design: (1) hydrate kinetic inhibitors, (2) antiagglomerants, and (3) hydrate plug dissociation. The use of each of the three methods is affected by the time-wise kinetics of hydrate formation and dissociation. Each is discussed in examples that follow.

An operating example of time-dependence is presented as an industrial finding, pointing out the need for hydrate kinetics.

8.2.2 Case Study 5: Under-Inhibition by Methanol in a Gas Line

Flow assurance engineers for a major energy company (Mehta et al., 2003) indicate that for a two year periods, one of their offshore gas flowlines operated well inside the hydrate formation region. The problem arose from increased water production (to >1000 BPD) over the field life, with limited methanol delivery. Their approach was to inject as much methanol as possible, in the knowledge that they were under-inhibiting the system. Due to under-inhibition, there was a gradual increase in the pressure drop (ΔP) in the line over a period of about 2 weeks, indicating a hydrate build-up on the walls.

Upon increase of ΔP over two weeks, gas production was gradually reduced, while continuing to inject methanol at the same (maximum) rate as before. By reducing gas (and thus the water) production, the methanol concentration increased. A higher methanol concentration melted hydrate that had formed in the line. After allowing the high concentration methanol to sweep the hydrates for some time, the pressure drop returned to normal and production was gradually ramped to its original gas rate. The 2 week cycle then was repeated.

This strategy was successful in extending the field life by almost 2 years. This is one key example of the risk management philosophy, enabled by operating experience on the platform. The hydrate plug prevention technique in this case study is time-dependent and should be contrasted with thermodynamic (time-independent) inhibition methods in Case Study 4 of Canyon Express and Ormen Lange.

While accurate thermodynamic predictions enable avoidance via use of thermodynamic inhibitors such as methanol or glycol, hydrates risk management is enabled by experience in the form of experiments, both in the field and in the laboratory. This is because, as indicated in Chapter 3, there is no comprehensive, predictive hydrate kinetic theory that can be accurately invoked at high hydrate

concentrations. The very best work in hydrate kinetics comes from the laboratory of Bishnoi over the last three decades. However, that work was confined to low hydrate concentrations, due to the need to eliminate confounding heat and mass transfer phenomena. In pipelines and other processes, heat and mass transport phenomena can commonly limit hydrate formation more than kinetics.

The following sections present three examples of kinetic phenomena: (1) kinetic inhibitors, (2) antiagglomerants (AAs), and (3) hydrate plug remediation. These kinetic phenomena were determined by field and laboratory observations. They also point to the need for a comprehensive kinetics theory, from which hydrate nucleation and growth can be predicted for industrial utility.

As shown in Chapter 3 and in Figure 8.8, the three steps to hydrate plug formation are (1) nucleation of hydrate films, (2) growth of hydrate films around water droplets or along the wall, and (3) agglomeration of hydrated particles to form plugs. Kinetic hydrate inhibitors (KHIs, also known as KIs) and AAs, both falling under the general nomenclature of low dosage hydrate inhibitors (LDHIs), which are typically lower in concentration than 1 wt%, provide chemical approaches to all three of the plug formation mechanisms. While kinetic inhibitors focus on the first two means of prevention, AAs deal with the third means. It should be noted that in addition to the chemical means of hydrate plug prevention, there are flow means of doing so, but this evolving technology is not discussed here.

A major thrust of the research on LDHIs is driven by concern for the environment—for chemicals with high biodegradability. The Norwegian Pollution Authority requires that all new chemicals used offshore must have a biodegradability of higher than 60%, while British environmental authorities require a biodegradability of greater than 20% for new offshore chemicals. For example, although kinetic inhibitors such as those based on PVCap (see description below) and water-soluble polymers have low toxicity, neither kinetic inhibitors nor AAs can be used in the Norwegian sector of the North Sea, while normal PVCap has a biodegradability below the British requirements. Grafted polymers have been developed to help increase the biodegradability of the kinetic inhibitor polymer (Maximilian et al., 2005). In other places in the world where restrictions are not so stringent, kinetic inhibitors and AAs have wider use.

8.2.3 Kinetic Hydrate Inhibition

Kinetic inhibitors are low molecular weight polymers dissolved in a carrier solvent and injected into the water phase in pipelines. These inhibitors bond to the hydrate surface and prevent plug formation for a period longer than the free water residence time in a pipeline. Liquid hydrocarbons may or may not be present for this prevention method to be effective. Water and small hydrate crystals are removed at a platform or onshore. Kinetic inhibitors are limited at long times, low temperatures, and high pressures because with sufficient time, the crystal growth is significant enough to cause line plugs.

However, there is a limit to the effectiveness of the inhibitors, commonly taken to be a subcooling (ΔT = temperature below the equilibrium temperature)

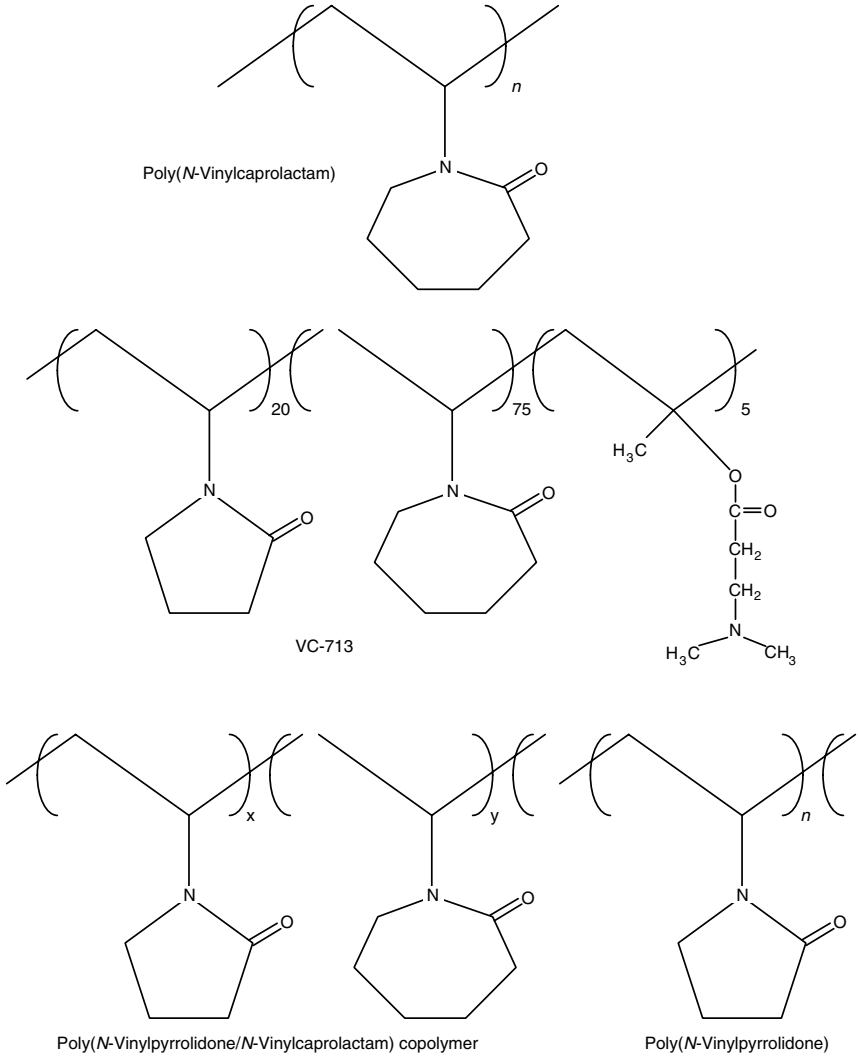

FIGURE 8.10 Hydrate kinetic inhibitors. Unless indicated, every angle is the location of a carbon atom and the appropriate number of hydrogens.

of 20°F. These kinetic inhibitors have been shown to be active at significantly lower concentrations than thermodynamic inhibitors, that is, about 0.5–2.0 wt% versus 40–60 wt%.

Examples of kinetic inhibitor chemicals are shown in Figure 8.10. In the figure, each inhibitor is shown with a polyethylene backbone, from which a pendant group (typically a ring compound with an amide [–N–C═O] linkage) is suspended. There are several types of kinetic inhibitors, and due to proprietary

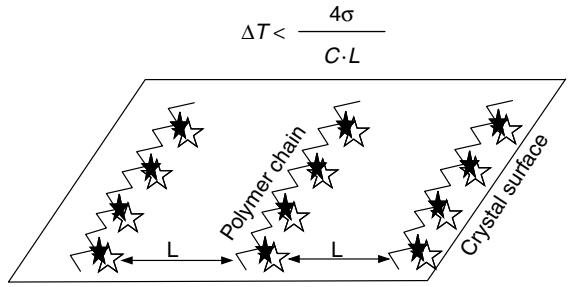

FIGURE 8.11 One mechanism for kinetic inhibition $\Delta T \leq 4\sigma / C \cdot L$.

concerns, only a few in the literature are discussed to show the principles involved. The reader is referred to the review by Kelland (2006) for a more detailed overview.

The definitive hydrate kinetic inhibition mechanism is not yet available. Some work suggests that the mechanism is to prevent hydrate nucleation (Kelland, 2006). However, a significant amount of evidence suggests that hydrate kinetic inhibitors inhibit the growth (Larsen et al., 1996). However, this apparent conflict is due to the definition of the size at which crystal nucleation stops and growth begins. To resolve this confusion, one may consider growth to occur after the critical nucleus size is achieved.

As indicated in Figure 8.11, the subcooling ΔT is directly proportional to the liquid-crystal surface tension (σ), but inversely proportional to the length (L) between polymer strands; C is a constant. If the amount of polymer adsorption increases, the distance L between the polymer strands decrease, resulting in an increased subcooling ΔT performance. Conversely, if the amount of inhibitor adsorption decreases (due to depletion by multiple small hydrate crystals) the distance L between polymer strands increases, resulting in a smaller subcooling ΔT.

Initial field tests of kinetic inhibitors were reported by ARCO (Bloys et al., 1995) and Texaco (Notz et al., 1995). Bloys reported the effectiveness of 0.3–0.4 wt% VC-713 in a 17-day test in a North Sea pipeline. Other large field applications, include BP's West Sole/Hyde 69 km wet gas pipeline where the maximum subcooling was 8°C (Argo et al., 1997; Philips 1997), the BP operated Eastern Trough Area Project (ETAP) in the British Sector of the North Sea (Philips 1997; Palermo et al., 2000) where the subcooling was 6–8°C. In the latter ETAP application, kinetic inhibitors replacing methanol were used. A similar method was used by Elf (now Total) to replace methanol in an onshore multiphase transportation line (Leporcher 1998; Kelland 2006). More recently, PVCap kinetic inhibitors have been applied in Qatar involving about 100–120 tn of PVCap per year, representing the largest applications of kinetic inhibitors in the world.

It should be noted here that, while PVP was one of the first kinetic inhibitors discovered, it is one of the weakest kinetic inhibitors available.

Examples of the use of modern kinetic inhibitors are given by Fu (2002) and Kelland (2006). Perhaps the best kinetic inhibitor copolymer was developed by ExxonMobil (Talley, Personal Communication, February 20, 2006) as the *N*-methyl-*N*-vinylacetamide: polyisopropyl-methacrylamide 1:1 low molecular weight copolymer (VIMA:IPMA 1:1) that can provide a subcooling of up to 22–23°C. However, the use of VIMA:IPMA is determined by availability and cost. Table 8.1 summarizes the development of kinetic inhibitors in chronological order, a qualitative ranking of these inhibitors is also given. Much of this historical development of kinetic inhibitors has been excerpted from the recent review of LDHIs by Kelland (2006).

In his review of LDHIs, Kelland shows that kinetic inhibitors are well-established tools for hydrate prevention, with the following three points:

1. Low molecular weight PVCap-based products with added synergists were the best kinetic inhibitors for structure II hydrates on the market in 2005, and these inhibitors can provide 48 h of inhibition at a subcooling of 13°C.
2. In 2005, 40–50 applications of kinetic inhibitors operated worldwide, with the largest applications in the North Sea and Qatar Applications.
3. In 2000 the sales of PVCap-based polymers were 300–500 tn per year.

8.2.3.1 Antiagglomerant means of preventing hydrate plugs

As shown in Figure 8.8, in oil-dominated systems there are three ways to prevent hydrate plug formation: (1) prevent particle nucleation, (2) prevent particle growth, and (3) prevent agglomeration of particles so that plugs will not form. AAs prevent the latter aggregation stages that lead to plugging.

AAs are surface active agents that reduce particle adhesion. The AA method was begun by Behar, Sugier, and coworkers at l'Institut Francais du Petrole in 1987 (Behar et al., 1988). Chemicals effective as AAs are surfactants that typically provide a relatively stable water-in-oil emulsion. The developments by l'Institut Francais du Petrole were followed by Shell with surfactants of alkylarylsulfonic acid and its salts (Muijs et al., 1991) and alkyl glycocides (Reynhout et al., 1993). In Bishnoi's laboratory, Kalogerakis et al. (1993) showed that some surfactants increased the agglomeration tendency, counter to the desired effect. Many of these first chemicals, as well as surfactants and polymers were shown to be ineffective through testing by Urdahl et al. (1995).

Figure 8.12 shows the macroscopic method of AAs. In the top portion of the figure, hydrates are agglomerated into a plug, analogous to that in the far right of Figure 8.8. In the lower portion of the figure, the hydrate particles are dispersed in the hydrocarbon liquid, so that they will continue to flow.

There are two types of AAs: (1) the French Petroleum Institute (IFP) type that provides a special kind of water-in-oil emulsion so that on hydrate formation, the emulsion will not agglomerate and (2) the Shell type that have hydrate-philic head group(s) and long hydrophobic tail(s). Because the IFP-type of AA still awaits a

TABLE 8.1
Chronology of Kinetic Inhibitor Developments

Kinetic hydrate inhibitor (KHI)			
Brief name	**Chemical name**	**Research group (reference)**	**ΔT sub (°C)**
PVP	Poly-*N*-vinylpyrrolidone	CSM (Long et al., 1994)	5
HEC	Hydroxyethylcellulose	CSM (Long et al., 1994)	
PVCap	Poly-*N*-vinylcaprolactam	CSM (Long et al., 1994)	8–9
Graffix VC-713	Terpolymer of vinycaprolactam (VCap), vinylpyrollidone (VP), and dimethlyaminoethyl methacrylate	CSM (Sloan, 1995a,b)	8–9
Polyelectrolytes		CSM (Sloan, 1995a,b)	
Polyether block copolymers		CSM (Sloan, 1995a,b)	
Polyvinylamides	For example, poly(*N*-methyl-*N*-vinyl acetamide)	CSM (Sloan, 1995a,b)	
Polyalkylacrylamides	For example, polyethylacrylamide	CSM (Sloan, 1995a,b)	
Polyalkyloxazolines	For example, polyethyloxazoline	CSM (Sloan, 1995a,b)	
AFPs	Antifreeze proteins (from winter flounder)	BP/Shell (Edwards, 1994)	
AGGPs	Antifreeze glycoproteins (from winter flounder)	BP/Shell (Edwards, 1994)	
Butylated PVP	Butylated poly-*N*-vinylpyrrolidone	Shell (Anselme et al., 1993)	
Amino acids	Tyrosines and related chemicals	BP (Duncan et al., 1993)	
Threshold inhibitor blends	For example, polyvinylcaprolactam + tetrabutylammonium bromide, or + tetrapentylammonium bromide	BP (Duncan et al., 1996)	<10
Polyamino acids	Poly-L-proline (related to fish antifreeze protein)	RF (Rogaland Research)	
VIMA:VCap 1:1	*N*-methyl-*N*-vinylacetamide:vinylcaprolactam 1:1 copolymer	RF/Exxon (Colle et al., 1996, 1999)	10–11
VCap:vinyl imidazole		RF	

(Continued)

TABLE 8.1
Continued

Kinetic hydrate inhibitor (KHI)			
Brief name	**Chemical name**	**Research group (reference)**	**Δ*T* sub (°C)**
Ring-opened polyethyloxazoline	Contains ethylamide groups in repeating unit of polyethyloxazoline	RF	
Polymer-containing amide groups	For example, polyalkylacrylamides, polydialkylacrylamides, polyvinylamides, polyallylamides, polymaleimides, polymers of cycliciminoethers and polyalkyloxazolines, and amides and esters of *N*-acyldehydroalannine	Exxon (Colle et al., 1996)	
PolyAP and Poly-iPAm	Acrylamide polymers—polyacryloylpyrrolidene (polyAP) best, followed by polydiethylacrylamide, then polyisopropylacrylamide (poly-iPAm)	Exxon (Colle et al., 1996)	
PolyVIMA	Poly-*N*-methyl-*N*-vinylacetamide	Exxon (Colle et al., 1996)	
Copolymers of VIMA with other alkylamide polymers	For example, 1:1 VIMA:iPMA (isopropylmethacrylamide) copolymer gave 4°C higher subcooling than polyiPMAM	Exxon (Talley and Oelfke, 1997)	~13.5
Ring-closed oxazaline polymers		Exxon	
VIMA:vinyl butyrate copolymer		Exxon	
Alkyl acrylate:VP copolymers	For example, butyl acrylate:vinyl pyrrolidone copolymers	RF/Nippon Shokubai (NS) (Namba et al., 1996)	
Surfactants as synergists with KHI polymers	For example, butyl sulfate, sodium valerate, zwitterionics, such as butyldimethylammonium butylene sulfonate, and *N*-dodecylpyrrolidone	Exxon (Colle et al., 1996)	
KHI blends of TBAB and VCap polymers		BP/Clariant	10
Small alcohols and glycol ethers (3–5 C's) as synergists for VC polymers	For example, butyl glycol ether (BGE) synergist (and solvent) of PVCap	ISP	
Modified AMPS polymers with 5-carbon tail	Modified acrylamidopropylsulfonic acid polymers; homopolymer of monomer	Exxon (Pfeiffer et al., 1999)	
Modified AMPS monomer with VCap	Copolymers of modified acrylamidopropylsulfonic acid monomer with vinylcaprolactam	Exxon (Pfeiffer et al., 1999)	

Acrylamide:AMPS copolymers		IFP (Sinquin et al., 1998)	
Polymers with at least one N containing monomer	Dimethylaminomethylacrylate monomer	IFP (Sinquin et al., 1998)	
AP:VCap copolymer		RF	
Synergistic 2:1 blend of 90/10 iPA/AMPS:PVCap		NS/RF (Kelland et al., 2000)	12
TBAO and TPAO with PVCap	Tributylamine oxides and tripentylamine oxides	Clariant (Klug et al., 1998)	
VIMA: IPMA 1:1 low MWt copolymer (oligomer)		Exxon (Talley and Oelfke, 1997)	11
PVCap oligomer		CSM	
PVCap oligomer	MWt 1500 gave best activity	ISP/BP (Bakeev et al., 2000, 2001, 2002)	
Copolymers of VCap	Containing small amounts of comonomer: dimethylaminoethylacrylate or *N*-(3-dimethylaminopropyl)methacrylamide	ISP (Thieu et al., 2002)	
VCap:vinyl pyridine copolymers		ISP (Bakeev et al., 2001)	
Polyoxyalkylenediamines as synergists for VCap polymers		ISP (Bakeev et al., 2000)/BJ Unichem	
Hybranes	Hyper-branched polyesteramides	Shell (Klomp, 2001)	
Polyesteramide KHIs with PVCap as synergist	Typical polyesteramide made from di-2-propanolamine, hexahydrophthalic anhydride and bis-(dimethylaminopropyl)imine. Synergists: polyethyleneimine reacted with formaldehyde and caprolactam giving polymers with pendant caprolactam rings; *N*-methyl butylamine reacted with formaldehyde and polyacrylamide	Baker Petrolite (Rivers and Crosby, 2004)	
Amidated maleic anhydride copolymers with ether carboxamine surfactant synergists		Clariant	
PVCap (low MW) with synergists		ISP/Nalco (Fu et al., 2002)	
Low MW lactam-based polymer		BASF (Neubecker, 2006)	
Water-soluble vinyl lactam copolymers	For example, 80:20 VP:butyl acrylate	BASF (Angel et al., 2004, 2005)	

(Continued)

TABLE 8.1
Continued

Kinetic hydrate inhibitor (KHI)			
Brief name	**Chemical name**	**Research group (reference)**	**Δ*T* sub (°C)**
VCap:alkyl(methyl)acrylate ester copolymers	Copolymers contain short-chain alkyl methacrylates, such as methyl methacrylate	Clariant (Dahlmann et al., 2004)	
PEO (high MW) as synergist for PVCap	Poly(ethylene oxide)	Lee and Englezos, (2005)	
PolyIPMA	Poly isopropylmethacrylamide	Exxon/Mitsubishi (Toyama and Seye, 2002)/ISP (Thieu, 2002)	
Polymers with bimodal MWt distribution	Synthesized from single polymerization or by mixing two polymers with unequal MWt distributions. Polymer is polyIPMA, as well as PVCap and other polymers	ExxonMobil (Colle et al., 2005)	24
Polymeric emulsifier mixed with nonionic nonpolymeric coemulsifier			12
Polyalkoxylated amines	Alkoxylation with, for example, propylene oxide (PO). Preferred amine is triethanolamine, or ammonia and other alkanolamines used; amine can also be quaternized; Best example is triethanol with 14.9 PO units	Akzo Nobel (Burgazli et al., 2003)	
Derivatives of poly(vinyl alcohol) by reaction with aldehydes	Contains vinyl ester acetal functionalities besides some unreacted vinyl alcohol monomer units. Preferred aldehyde is butyraldehyde	Kurarau Specialties Europe (Dahlman et al., 2004)	
Grafted polymers	Backbone, for example, polyalkylene glycol, polyalkyl-eneimine, polyether, or polyurethane, and active functional side groups made from grafting VP or VCap to backbone using radical initiators	BASF (Maximilion et al., 2005)	
Polyquaternaries with pendant TBA groups	TBA (tributylammonium groups)	RF/Stavanger U (Kelland, 2006)	

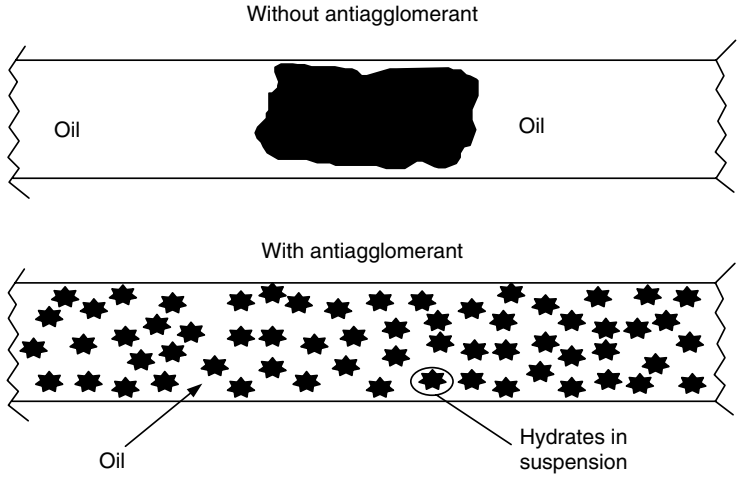

FIGURE 8.12 The macroscopic mechanism of hydrate antiagglomerant slurries.

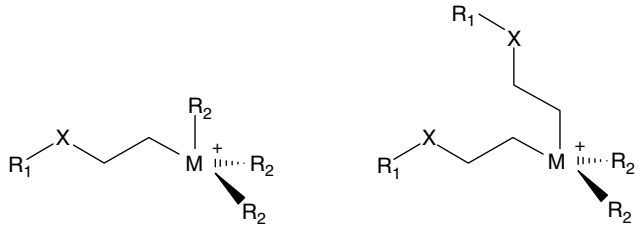

FIGURE 8.13 The two Shell-types of antiagglomerant. On the left is the water-soluble type, with one branch (R_1) containing 8–18 carbons. On the right is the oil-soluble type with two branches (R_1) with 8–18 carbons. The central atom is nitrogen or phosphorus, and the shorter branches (R_2) are butyl- or pentyl-groups.

field trial (Kelland, 2006) we will concentrate here on the Shell-type AA, which can be further categorized as (1) water soluble, with one long hydrocarbon tail or (2) oil soluble, with two long hydrocarbon tails. Both of these types are shown in Figure 8.13.

A typical water soluble Shell-type AA is a quaternary ammonium salt (QAS), in which two or three of the four ammonium branches are short (e.g., a butyl compound that might be a candidate for inclusion within hydrate cavities) and one or two branch(es) are much longer (e.g., C8 to C18) so that it might be soluble within the oil phase. The mechanism of AAs is uncertain at this time, but some educated guesses can be given, which evolve from the chemical structure of AAs.

The butyl-ammonium end of the AA is very attractive to water and to hydrates, so that it remains firmly attached either to the water droplet, or to the hydrate phase after the water droplet conversion. The other, long carbon end of the AA has the

function of stabilizing the QAS in the liquid hydrocarbon, using the physical chemistry principle of "like dissolves like." So the attachment of one end of the AA to the hydrate with the other end dissolved in the hydrocarbon liquid turns the spherical hydrate shells in Figure 8.8 to spheres with protruding strands of chemicals.

These long protruding chemical strands provide separation of the hydrate particles, so that agglomeration does not occur for the suspension in the oil phase. As measured by Yang et al. (2004) and by Taylor (2006), without such prevention the capillary forces between the hydrate particles are very strong, and can lead to large hydrate masses.

In antiagglomeration, since the prevention method relies on emulsified water/hydrates, a condensed hydrocarbon is required (Mehta et al., 2003). The solid phase loading cannot exceed 50 volume% of the liquid hydrocarbon phase to prevent high viscosity associated with compacted slurry flow. The emulsion is broken and water is removed onshore or at a platform.

The oil-soluble Shell-type AA may behave similarly, but with two long-chain hydrocarbon tails to maintain solubility in the oil phase. However, of the two categories of Shell-type AAs, the water-soluble type has had the widest use. With the above broad-brush, conceptual picture of AAs, it is clear that further definition should be done for refinement of the AA mechanism.

8.2.4 Case Study 6: AAs are a Major Hydrate Plug Prevention Tool

Mehta et al. (2003) review the shortcomings of traditional thermodynamic inhibitors, and the use of the new LDHIs, which are based upon kinetic principles, and are typically applied in concentrations less than 1 wt%. They note that the new KHIs have an upper subcooling limitation of approximately 20°F, while deepwater developments often have subcooling requirements of 35–40°F.

In addition, Mehta et al. present a case study of Shell's Popeye field use of a new AA inhibitor in a gas condensate line, with the following points:

1. The AA works by emulsifying hydrates in the hydrocarbon liquid. Hydrates are carried as a nonagglomerated slurry, without viscosity increase for up to 50% water cuts.
2. The AA limit to water cut (volume of water per volume of oil) is approximately 60%.
3. In the field case study, the AA effectively inhibited hydrate formation, with no significant downstream problems.
4. Flowlines are continuously treated with AA before shut-in, eliminating the need for instantaneous corrective actions (e.g., flowline depressurization) on shut-in.
5. The volume reduction of injected inhibitor can be reduced by a factor of 25 relative to methanol, allowing less topside storage space, easier transportation, and smaller umbilicals.

6. The AA eliminates methanol discharge in overboard water and export lines.
7. CAPEX savings are particularly appealing with the use of AAs for new projects, but OPEX savings may justify retrofits of existing projects.

Table 8.2 summarizes the chronological development of AAs. As of April 1, 2004, AAs were used in 17 gas and oil fields in the Gulf of Mexico, with prospects for rapid expansion. However, as of this writing, kinetic inhibitors are predominantly used in LDHI work.

8.3 How is a Hydrate Plug Dissociated?

This section provides a qualitative understanding of CSMPlug, the plug dissociation program which accompanies this book and is illustrated in Appendix B. Sometimes a hydrate plug does form, with the consequences of blocking fluid flow. When a flowline plugs, the usual responses are

1. Locate the plug to determine its position and length
2. Carefully evaluate the safety concerns of plug removal (please read the following section to determine the major safety implications imposed by hydrate plugs)
3. Evaluate the methods of plug removal, of which there are four types:
   a. Hydraulic methods such as depressurization
   b. Chemical methods such as injection of inhibitors or reactive chemicals that generate heat (Freitas et al., 2002)
   c. Thermal methods that involve direct electrical heating (Davies et al., 2006)
   d. Mechanical methods with coiled tubing, drilling, etc.

The below concepts are an extension of those in Chapter 3 of *Hydrate Engineering* (Sloan, 2000). Details of the model can be found in the work by Davies et al. (2006). Here, only the first, most-common method of depressurization is treated conceptually.

From both a safety and technical standpoint, the preferred method to dissociate hydrate plugs is to depressurize from both sides. Depressurization is particularly difficult when the liquid head on the hydrate plug is greater than the dissociation pressure, as in mountainous terrain or in very deepwater, in which case electrical heating may be used (Davies et al., 2006), a method not considered here.

When a hydrate plug occurs in a pipeline at temperatures above the ice point, the pressure–temperature conditions are illustrated in Figure 8.14. To the left of the three phase (L_W–H–V) line hydrates can form, while to the right only fluids can exist. Because the lowest ground burial temperatures or ocean temperatures (39°F) are usually above 32°F, ice formation (which will also block flows) is not a normal

TABLE 8.2
Chronology of Antiagglomerant Developments

AA inhibitors

Brief name	Chemical name	Research group (reference)
IFP dispersant additives	Diethanolamides	IFP (Sugier et al., 1989)
IFP dispersant additives	Dioctylsulfosuccinates	IFP (Sugier et al., 1989)
IFP dispersant additives	Sorbitans	IFP (Sugier et al., 1989)
IFP dispersant additives	Ethoxylated polyols	IFP (Sugier et al., 1989)
IFP dispersant additives	Ethoxylated amines	IFP (Sugier et al., 1989)
Polymeric surfactants	Based on polyalkenyl succinic anhydride	IFP (Sugier et al., 1989)
Alkylarylsulfonates	Surfactant	Shell (Muijs et al., 1991)
Alkyl glucosides	Surfactant	Shell (Reynhout et al., 1993)
TBAB, a QAS	Tetrabutylammonium bromide-quaternary ammonium surfactants	Shell (Klomp et al., 1995)
TPAB, a QAS	Tetrapentylammonium bromide-quaternary ammonium surfactants	Shell (Klomp et al., 1995)
Water soluble single-tail QAS	For example, tributylammonium or tripentylammonium (better) headgroup	Shell US
QAS	Quaternary ammonium surfactants - $\geq$2 *n*-butyl, *n*-pentyl, isopentyl groups	Shell (Klomp et al., 1995)
QAS	Replacing 1 or 2 small alkyl groups with long hydrophobic tail (8–18 carbon atoms)	Shell (Klomp et al., 1995)
Polyalkoxylates	Polypropoxylates	RF
Polyalkoxylate amine	Polyalkoxylate amine, MW 6000	Akzo Nobel
Planteren 600 CPUS	An alkyl glucoside	RF
Polymeric emulsifiers	Polyglycol derivatives of polyalkyenylsuccinic anhydride	IFP (Behar, 1994)
Twin-tailed QAS	Tetraalkylammonium salts with two tails, such as dicocoyldibutylammonium bromide	Shell/Akzo Nobel (Klomp and Reijnhart, 1996)
Twin-tailed QAS	Diesters of dibutyldiethanolammonium halides and 2 mol alkyl carboxylic acid (optimum 12–14 carbons)	Shell/Akzo Nobel (Klomp and Reijnhart, 1996)
Polymeric surfactants, for example, Emulfip 102b	50% solution of polymerized fatty acids and amides in rapeseed oil	IFP/EUCHARIS (Palermo et al., 1997)

Polyetherpolyamine and polyetherdiamines	Polyetherpolyamines and polyetherdiamines (particularly of the oxypropylene type)	BJ Unichem (Pakulski, 1998, 2001)
Polyetherpolyamine	Quaternized polyetherpolyamines reacted with a long-chain alkyl bromide	BJ Unichem (Pakulski, 2001)
Span sorbitan surfactant		CSM (Huo et al., 2001)
Monotail surfactants with caprolactam headgroup and polymeric surfactants based on VC oligomer or *N*,*N*-dialkylacrylamides with alkyl thioether end groups	Dodecyl-2-(2-caprolactamyl) ethanamide	CSM (Huo et al., 2001)
Oil soluble twin-tailed QAS	*N*-butyl diethanolamine and methyl or ethyl branch added to ethylene spacer groups between ester groups and quaternary N atom	Shell (Klomp, 1999)
Monomeric surfactants with alkylamide or dialkylamide groups in head	For example, groups mostly carbonylpyrollidone and isopropylamide goups performed well in KHI polymers	RF/NS (Kelland, 2000)
Hybranes	Hyper-branched polyesteramides	Shell (Klomp, 2001)
VCap:alkyl(methyl)acrylate ester copolymers	Copolymers contain long-chain alkyl methacrylates, such as oleyl methacrylate	Clariant (Dahlmann, 2004)
Water-soluble quaternary AA (onium compound)	Formulated with amine salt containing alkyl or hydroxylalkyl groups (1–3 carbons) or ammonium salt, and optionally a solvent	Baker Petrolite (Przbylinski and Rivers, 2003)
QAS phase separation		Shell (Blytas and Kruka, 2001)
QAS detoxified	Addition of anionic polymers or anionic surfactants	Baker Petrolite (Rivers et al., 2004)
Ion pair mixture	QAS + anionic, nonionic, or amphoteric compound, for example, dodecylbenzenesulfonic acid (DDBSA) + quaternary ammonium compound (with appendages <6 carbons)	Baker Petrolite (Crosby et al., 2005)
Hydrophobic oil-soluble block copolymers	Emulsion AA (Emulfip 102b, IPE202b), for example, made from polyalkenylsuccinic anhydride with monoether of poly(ethylene glycol); typical block copolymer is made from styrene/ethylene/propylene	IFP (Gateau et al., 2004)
QAS	Quaternary center with butyl or pentyl groups	Nalco (Cowie et al., 2003)
QAS	QAS with ether spacer group between quaternary N atom and long alkyl tail	Goldschmidt (Milburn and Sitz, 2002)
QAS	Alkylaminoalkyl mono- and diesters; *N*,*N*′-dialkylaminoalkylether carboxylates; alkylaminoalkyl/alkoxy monoesters	Clariant (Dahlmann, 2004)
Amine oxides and betaine surfactants		Champion Tech. (Panchalingham et al., 2005a,b,c,d,e)

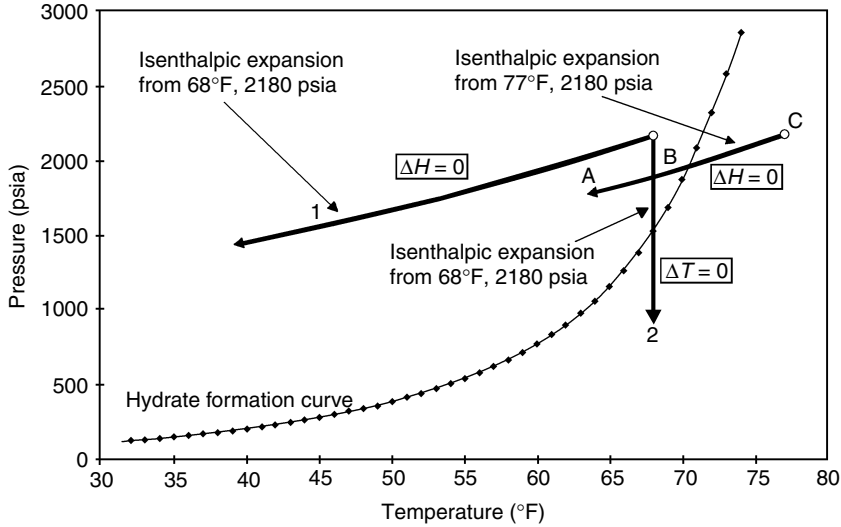

FIGURE 8.14 Temperature changes as a result of depressurization (1) isenthalpic rapid expansion as through a valve, and (2) very slow depressurization, as in a large-volume pipeline. Note that for the rightmost case, a fluid system can be expanded into the hydrate region, as calculated by the methods in Section 4.2.1.1 and the programs of CSMGem on the CD accompanying this book.

operating concern. When hydrates form, flow is blocked so that the plug temperature rapidly decreases to the surroundings temperature at the pipeline pressure. Figure 8.14 shows the rapid depressurization of a pipeline hydrate plug to Point A causes it to proceed further into the two-phase (H–V) region, with an excess gas phase, so that the liquid water has converted to hydrate.

When a hydrate plug occurs in a pipeline at temperatures above the ice point, the three conditions (sufficient temperature, pressure, and composition) exist for hydrate formation. When hydrates form, flow is blocked so that the plug temperature rapidly decreases to the surroundings temperature at the pipeline pressure.

Pressure reduction is accompanied at the hydrate interface by a temperature decrease to the equilibrium temperature. Normally the pipeline cannot be depressured sufficiently rapidly for Joule–Thomson (isenthalpic) cooling to lower the temperature; this would occur through a restriction such as a valve. If the pressure is reduced slowly, a vertical isothermal depressurization ($\Delta T = 0$) results. Usually an intermediate pressure reduction rate causes the hydrate interfacial temperature to be significantly less than the surroundings, causing heat influx from the surroundings to melt hydrates from the pipe boundary inward.

With rapid extreme pressure reduction, the hydrate equilibrium temperature can decrease below 32°F for a methane hydrate depressurized to atmospheric

pressure. In this case the water from the dissociated hydrate buffers the temperature reduction to around 0°C, by converting to ice below the solid–liquid line. If ice formation occurs with hydrate dissociation, then the question arises, "How will the ice plug dissociation rate compare to the hydrate dissociation rate in an ocean pipeline?"

Recent experiments and modeling suggests that blockages are most efficiently removed when the line is depressurized to the fullest extent, as rapidly as possible. When ice forms, it normally has a lower temperature and higher thermal diffusivity than hydrates, resulting in a rate increase of heat transfer into the pipe.

During 1994–1997 field studies, over 20 hydrate plugs were systematically formed and removed from a 6 in. North Sea line in the Tommeliten Gamma field. In both laboratory and field studies these plugs were found to be very porous (>50%) and permeable. Porous, permeable hydrates easily transmit gas pressure while still acting to prevent liquid flow in the pipeline. When the pressure was decreased at both ends of a highly porous hydrate plug, the pressure decreased throughout the entire plug to a constant value. The dissociation temperature at the hydrate front is determined by the pipeline pressure and by the buffering capacity of the water fusion to ice.

Pipeline depressurization reduces the hydrate temperature below the temperature of the surroundings. Heat flows radially into the pipe, causing dissociation first at the pipe wall as shown in Figure 8.15. In the figure three laboratory hydrate plugs are shown after three separate experiments—after 1, 2, and 3 h of dissociation (Peters, 1999). Radial hydrate dissociation controls plug removal, because the pipe diameter (typically less than 2 ft) is at least an order of magnitude less than the length of a hydrate plug (frequently more than 50 ft) in a pipeline.

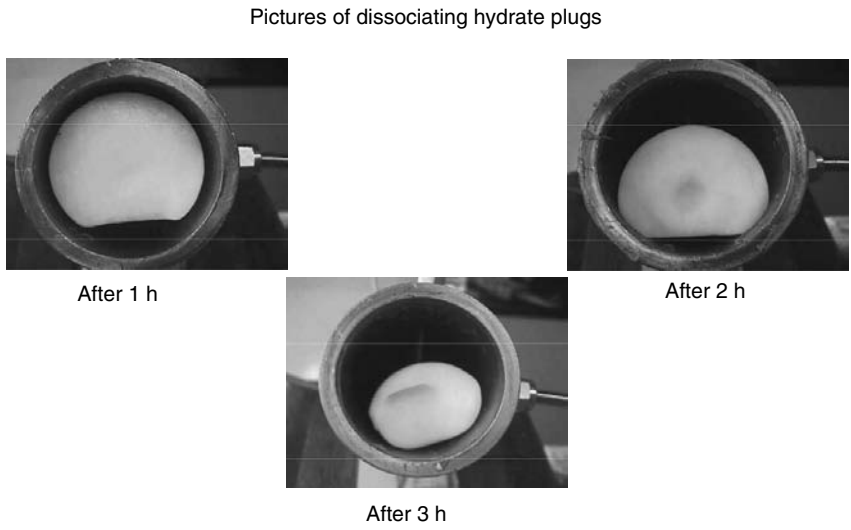

FIGURE 8.15 Hydrate plug radial dissociation in three experiments.

The radial dissociation concept is in contrast to previous longitudinal dissociation concepts of nonporous hydrates, in which depressurization from both ends was supposed to result in dissociation progressing from the plug ends toward the middle (Yousif et al., 1990). As shown in Figure 8.15 when the temperature of the hydrate is lower than that of the surroundings, heat flows radially into the plug, causing dissociation along the entire length. Of course, some plug dissociation occurs at the ends, but due to much smaller dimensions, the radial dissociation (which occurs simultaneously along the plug length) controls blockage removal.

A close inspection of the first photo (1 h) in Figure 8.15 shows the periphery of the first plug has a different morphology than its inner section. This is because, when hydrates dissociate, the energy is drawn from the phase with the highest thermal diffusivity—the water phase from the melted hydrate. That is, the hydrate converts to a peripheral ice plug, and the ice plug subsequently converts to water. The problem of hydrate plug dissociation is two moving boundaries, the inner, hydrate + ice boundary, and the outer, ice + water boundary. The water has a higher thermal diffusivity than gas and caused the flat spot at the bottom of the plugs in Figure 8.15. However, water cannot be seen in the figure, because it flowed out of the horizontal pipe, once it was opened to the atmosphere in each of the three photos.

Because hydrate plug detachment occurs first at the pipe wall, a partially dissociated plug will move down the pipeline when the line is restarted with a pressure gradient, only to result in a later plug at a pipeline bend, depression, or other obstruction. The second plug blockage can be more compact than the first, for example, if there is substantial momentum on impact at the bend. In extreme cases the plug can act as a projectile, which may result in severe safety problems as indicated in the following section. As a result, methanol is used to dissociate the plug, when the annulus is sufficient to allow flow around the plug.

The concepts are similar for both onshore and subsea pipelines. In the above conceptual picture, it is assumed that the pipeline wall temperature is constant at 39°F. If a line is insulated, hydrate dissociation becomes much more difficult because the insulation that prevented heat loss from the pipe in normal operation will prevent heat influx to the pipe for hydrate dissociation. Alternatively, if the pipe is buried, the pipe wall temperature will be greater than 39°F and the system may be insulated by the ground.

Austvik et al. (1997) noted some exceptions to radial dissociation, particularly for plugs of low porosity/permeability or for very long plugs. As shown by Berge et al. (1998) hydrate plugs consolidate after plug formation, causing porosity and permeability to decrease considerably. The amount of water converted to hydrate is very low, often as low as 2–4%, due to the thin hydrate films shown in Figure 8.8. Hydrate plugs should be dissociated as soon as possible to take advantage of higher porosity, permeability, and lower fractions of hydrate.

Hydrate depressurization. Hydrate depressurization must always be done very carefully. The two methods of dissociation are from both sides of the plug(s),

or from one side of a plug(s). There are two reasons for the preferred method of two-sided hydrate plug dissociation:

1. For a single plug, dissociation from both sides eliminates the safety concern of having a projectile in the pipeline. As indicated in the next section this is a major safety concern. Sometimes plug dissociation can cause projectiles that damage equipment and in the extreme, can cause a loss of life. It should be noted, however, that sometimes gas trapped between two plugs can cause risks, even for two-sided dissociation, as indicated in Section 8.4 on Safety.
2. Two-sided dissociation eliminates the Joule–Thomson cooling that may stabilize the downstream end of the plug. With radial dissociation along the plug, two-sided dissociation is more than twice as fast as single-sided dissociation.

For the above reasons, the upstream portion of a hydrate plug should be dissociated through a second production line, if available. If this is impossible, depressurization through an umbilical for injecting inhibitors at the wellhead may be possible; in this case provision should be made for removing or bypassing any check valve that may be in the service line at the wellhead. In extreme cases, where the line cannot be depressurized due to a high liquid head on the plug, it may be possible to use electrical heating to dissociate the plug, as indicated by Davies et al. (2006) and as practiced on the Nakika gas field operated by BP, but designed by Shell.

Two-sided dissociation is almost always the method of choice for the flow assurance engineer. Many of the concerns with single-sided plug dissociation are discussed by Davies et al. (2006). The program CSMPlug and a User's Manual are provided on the CD in the endpapers of this book. Appendix B contains a set of User's examples to enable the engineer: (1) to estimate the time for two-sided dissociation, (2) to estimate the time required for (very careful) single-sided dissociation, and (3) to estimate the safety concerns of the hydrate, such as velocity and plug displacement.

8.3.1 Case Study 7: Gulf of Mexico Plug Removal in Gas Export Line

A hydrate blockage in the export line from Shell's Bullwinkle platform in the Green Canyon Block 65 to the Boxe platform was reported in DeepStar Report A208-1 (Mentor Subsea, 1996, p. 52). The 12 in., 39,000 ft line was not insulated. The seawater temperature was 50°F at the base of the platform in 1,400 ft of water. Gas gravity was 0.7 and the flow rate was 140 MMscf/d at an inlet pressure of 800 psi.

Gas hydrates formed during a restart after the platform was shut down due to a hurricane. During the shut-in period the gas dehydrator partially filled with water. After production restarted, since the dehydrator was not cleaned properly, it was not dehydrating gas as designed and wet gas entered the export line, causing

water condensation and hydrate formation. A complete hydrate blockage formed in less than 1 h, just past the base of the export riser at a low spot.

To remove the blockage, the line was depressured on both sides of the plug. Then methanol was circulated into the line to accelerate the hydrate dissociation rate. After complete removal of the hydrates, the dehydrator was cleaned, inspected and restarted properly. The entire remedial operation required 36 h to complete. The major cost was the lost production time.

8.4 Safety and Hydrate Plug Removal

There are many examples of line rupture, sometimes accompanied by loss of life, attributed to the formation of hydrate plugs. Hydrate safety problems are caused by three characteristics:

1. Hydrate density is similar to ice, and upstream pressure can propel a dislodged hydrate plug at high velocity. In 1997 DeepStar Wyoming field tests, plugs ranged from 25 to 200 ft with velocities between 60 and 270 ft/s. Such velocities and masses provide sufficient momentum to cause two types of failure at a pipeline restriction (orifice), obstruction (flange or valve), or sharp change in direction (bend, elbow, or tee) as shown in Figure 8.16. First, hydrate impact can fracture the pipe, and second, extreme plug momentum and gas compression can cause pipe rupture downstream of the hydrate path.
2. Hydrates can form either single or multiple plugs, with no method to predict that will occur. High differential pressures can be trapped between plugs, even when the discharge end of plugs are depressurized.
3. Hydrates contain 164 volumes (STP) of gas per volume of hydrate. When hydrate plugs are dissociated by heating, any confinement causes rapid

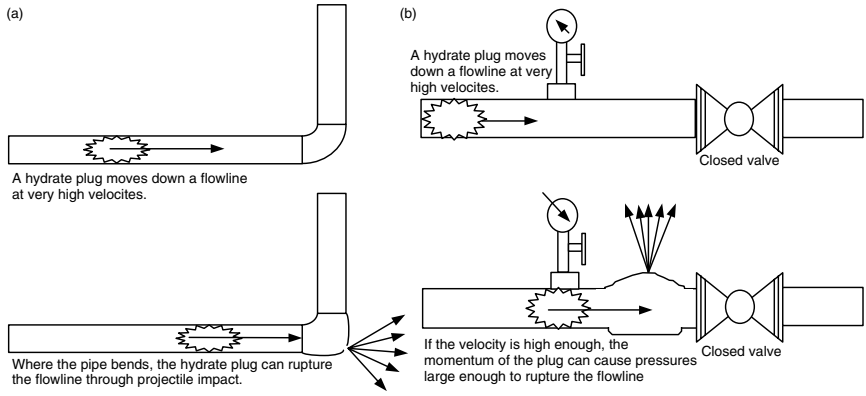

Figure 8.16 Two ways a plug can rupture a pipe: (at left) via momentum impact of high velocity projectile at a pipeline bend, and (at right) via a combination of plug momentum and gas compression at a pipeline obstruction.

gas pressure increases. However, heating is not an option within buried pipe due to the difficulty of plug location and economics of heating an inaccessible pipeline.

When a plug is depressured using a high differential pressure, the dislodged plug can be a very dangerous projectile, as the below case study indicates (from Mobil's Kent and Coolen, 1992).

The first chapter of Sloan (2000) is devoted to hydrate safety principles, showing several types of safety problems associated with a hydrate plug. Here only one precautionary example is given.

8.4.1 Case Study 8: Hydrate Plug Incident Resulting in Loss of Life

At a major energy company in Alberta, a foreman and operator were attempting to clear a hydrate plug in an outlying sour gas flowline. They had bled down the pressure in the distant end from the wellhead. They were standing near the line when the line failed, probably from the impact of a moving hydrate mass. A large piece of pipe struck the foreman and the operator summoned help. An air ambulance was deployed; however, the foreman was declared dead on arrival at the hospital. No preexisting pipe defects were found.

The *Canadian Association of Petroleum Producers Hydrate Guidelines* (King et al., 1994) suggest three safety concerns in dealing with hydrate blockages:

- Always assume multiple hydrate plugs; there may be pressure between the plugs.
- Attempting to move ice (hydrate) plugs can rupture pipes and vessels.
- While heating a plug is not normally an option for a buried pipeline, any heating should always be done from the end of a plug to release the gas, rather than heating the plug middle.

The above case study warns that hydrates can be hazardous to personnel and to equipment. Yet hydrate plugs can be safely dissociated with the use of CSMPlug and User's Manual on the CD in the endpapers of this book, with the User's Guide Examples in Appendix B. The safety option of this program and process should be considered first, so that the potential for overpressurization and eruption can be considered.

In ocean drilling, hydrated sediment cores are often obtained. Because the cores frequently traverse warm waters for periods of about 1 h, hydrated cores dissociate and release gas, to yield higher pressures. When core liners are retrieved on the deck of a drilling vessel, frequently the warm weather can cause additional hydrate dissolution, resulting in further pressure increases. The modeling of this dissociation has been done by Wright et al. (2005) and by Davies et al. (2006).

To counteract these shipboard safety problems, several steps are taken such as drilling through core liners to relieve the pressure, or placing wooden barriers at

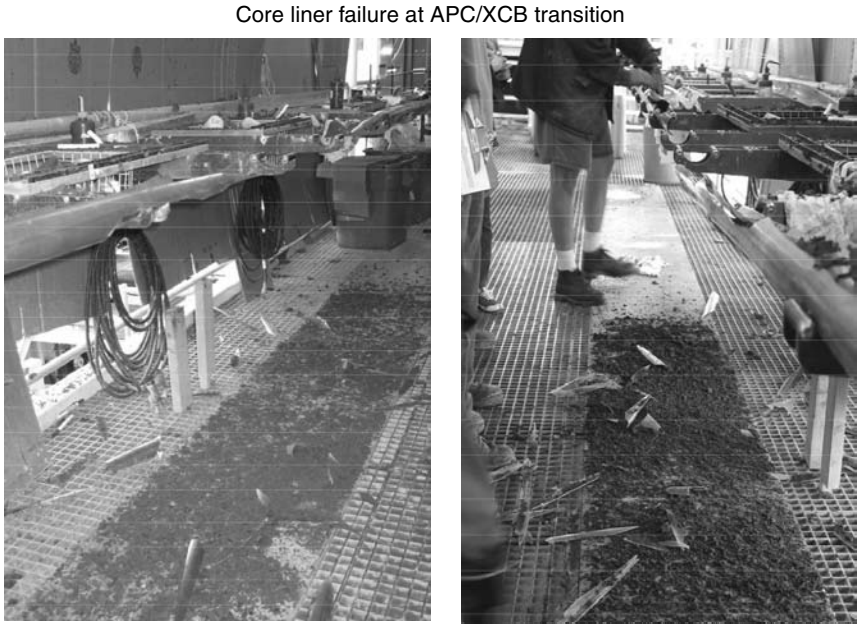

FIGURE 8.17 Core liner failures due to hydrate gas release on ship board.

the open end of cores. Nevertheless, with these cautions, exploding core liners can occur, as shown by Figure 8.17. These examples point to the need for a hydrate core safety manual, whose basis is in experiment.

8.5 APPLICATIONS TO GAS TRANSPORT AND STORAGE

It is estimated that about 70% of the total gas reserve is either too far from an existing pipeline or too small to justify a liquefaction facility. Gudmundsson and Borrehaug (1996, 2000) suggested that it is economically feasible to transport stranded gas in hydrated form. In the fourth international hydrate conference Mitsui Shipbuilding (Nakajima et al., 2002) show that work in conjunction with the Japan Maritime Research Institute (Shirota et al., 2002) provides a basis for extending the basic concept by Gudmundsson and Borrehaug to ship stranded gas.

For storage and transportation the self-preservation phenomenon of Section 3.3.3 could be an important phenomenon due to its requirements of decreased amounts of refrigeration. Recall that the self-preservation phenomenon was described as: "Self-preservation" consists of a short rapid dissociation phase with a release of 5–20 vol% of the total methane in the hydrate sample. During this gas release, adiabatic cooling of methane as well as general heat absorption occur, resulting in a drop in temperature of between 3 and 7 K relative to the temperature of the external cooling bath. After this rapid dissociation phase, the methane hydrate remains "metastably preserved for up to 24 h." It is thought that

this phenomena is associated with an ice coating that prevents rapid dissociation, aided by ice defect propagation (Kuhs et al, 2004).

Frequently, hydrates become important in natural gas storage in salt caverns for peak shaving, or seasonal or diurnal volume averaging delivery of gases. The work by deRoo et al. (1983) discusses this process, regarding hydrate formation in high salt concentration, with their data provided in Chapter 6 on methane hydrate inhibited by sodium chloride.

8.6 Summary of Hydrates in Flow Assurance and Transportation

As the energy industry produces from more hostile environments, such as the ultra-deepwater and the arctic, flow assurance problems will increase. Associated higher pressures, colder temperatures, and higher concentrations of acid gases will cause hydrates to be a larger concern, frequently impacted economically by the high cost of thermodynamic inhibitors at high concentration, so that LDHIs will be more commonly used.

The industrial flow assurance paradigm is shifting from avoidance, enabled by thermodynamic inhibition, to risk management, enabled by application of kinetics. Examples of time-dependent flow assurance phenomena are kinetic inhibitors, AAs, plug dissociation, and electrical heating of pipelines for plug dissociation. Research support will move from thermodynamics, which is currently acceptably accurate for engineering applications, to time-dependent kinetics.

The current chapter shows the application of mainly thermodynamic calculations, which have their basis in Chapters 4 and 5. However, as indicated in Chapter 3, a fundamental kinetic model, separated from heat and mass transfer phenomena, has yet to be established, particularly at high concentrations to extend the measurements pioneered in the laboratory of Bishnoi during the last three decades. The generation of such a time-dependent growth model and its application is one of the major remaining hydrate challenges.

References

Angel, M., Neubecker, K., Stein, S., WO Patent Application 04/042190 (2004).

Angel, M., Stein, S., Neubecker, K., US Patent 6878788 (2005).

Anselme, M.J., Reijnhout, M.J., Klomp, U.C., WO Patent Application 93/25798 (1993).

Argo, C.B., Blaine, R.A., Osborne, C.G., Priestly, I.C., in *Proc. SPE International Symposium on Oilfield Chemistry*, SPE 37255 Houston, TX, February (2007).

Austvik, T., Hustvedt, E., Gjertsen, L.H., Urdahl, O., in *Proc. 75th GPA Annual Convention*, p. 205 (1997).

Bakeev, K., Chuang, J.-C., Drzewinski, M.A., Graham, D.E., US Patent 6117929 (2000).

Bakeev, K., Harris, K., Argo, C.B., Drzewinski, M.A., Graham, D.E., US Patent 6451892 (2002).

Bakeev, K., Myers, R., Chuang, J.-C., Winkler, T., Krauss, A., US Patent 6242518 (2001).

Behar, E., in *Gas Hydrate Seminar*, Trondheim, Norway, June (1994).

Behar, E., Sugier, A., Rojey A., "*Hydrate Formation and Inhibition in Multiphase Flow*," presented at BHRA Conference Operation consequences of Hydrate Formation and Inhibition Offshore, Cranfield, UK, November 3 (1988).

Berge, L.I., Gjertsen, L.H., Lysne, D., *Chem. Eng. Sci*., **53**(9), 1631 (1998).

Bloys, B., Lacey, C., Lynch, P., in *Proc. 27th Annual OTC*, OTC 7772, Houston, TX, May 1–4 (1995).

Blytas, G.C., Kruka, V.R., International Patent Application WO 01/36895 (2001).

BP/Clariant, Internal unpublished reports, cited in Kelland, pp. 831, 834 (2006).

Brill, J.E., in *Flow Assurance as a Discipline*, *Flow Assurance 2003*, Galveston, Texas, September 23–25 (2003).

Burgazli, C.R., Navarrete, R.C., Mead, S.L., in *Proc. Canadian International Petroleum Conference*, Paper 2003-070, Calgary, Alberta, Canada, June 10–12 (2003).

Carroll, J.J., *Natural Gas Hydrates: A Guide for Engineers*, Gulf Professional Publishing, Houston, TX (2003).

Colle, K.S., Costello, C.A., Talley, L.D., Longo, J.M., Oelfke, R.H., Berluche, E., WO Patent Applications, 96/08672, 96/41784 and 96/41834 (1996).

Colle, K.S., Oelfke, R.H., Kelland, M.A., U.S. Patent Applications 58746560 (1999).

Colle, K.S., Talley, L.D., Longo, J.M., World Patent Application WO 2005/005567 (2005).

Cowie, L., Shero, W., Singleton, N., Byrne, N., Kauffman, L., *Deepwater Technology*, Gulf Publishing Co, p. 39 (2003).

Crosby, D.L., Rivers, G.T., Frostman, L.M., US Patent Application 2005/0261529 (2005).

Dahlmann, U., Feustel, M., Kayser, C., Morschchaeuser, R., US Patent Application 2004/00030206 (2004).

Davies, S.R., Selim, M.S., Sloan, E.D., Bollavaram, P., Peters, D.J., Hydrate Plug Dissociation, *AIChE J.*, **52**(12), 4016–4027 (2006).

de Roo, J.L., Peters, C.J., Lichtenthaler, R.N., Diepen, G.A.M., *AIChE J.*, **29,** 651 (1983).

Duncan, S., Edwards, A.R., Osborne, C.G., European Patent Application 0536950 A1 (1993).

Duncan, S., Edwards, A.R., Osborne, C.G., WO Patent Applications 96/04462, 96/29501, 96/29502 (1996).

Edwards, A.R., in *(First) International Conference on Natural Gas Hydrates*, *Ann. NY Acad. Sci.* (Sloan, E.D., Happel, J., et al., eds.), **715**, 543 (1994).

Freitas, A.M., Lobao, D., Anselmo C., Cardoso, C.B., in *Offshore Technology Conference Proceedings*, OTC 14257 Houston, TX, May (2002).

Fu, B., *Special Publication—Royal Society of Chemistry, Chemistry in the Oil Industry VII*, p. 264 (2002).

Gateau, P., Sinquin, A., Beunat, V., Vilagines, R., US Patent Application 2004/0162456 (2004).

Gudmundsson, J., Borrehaug, A., in *Proc. Second International Conference on Natural Gas Hydrates* (Monfort, J.P., ed.), Toulouse, France, June 2–6, p. 415 (1996).

Gudmundsson, J., Borrehaug, A., in *Proc. Third International Conference on Natural Gas Hydrates*, Salt Lake City, Utah, U.S.A., July 18–22, 1999; *Ann. NY Acad. Sci.* (Holder, G.D., Bishnoi, P.R., eds.), **912**, 403 (2000).

Hare, S., Case, R., Canyon Express Commissioning and Start-up Experience, in *Offshore Technology Conference Proceedings*, OTC15097, Houston, TX, May 6 (2003).

Hatton, G.J., Kruka, V.R., *Hydrate Blockage Formation—Analysis of Werner Bolley Field Test Data*, DeepStar CTR 5209-1 (2002).

Huo, Z., Freer, E., Lamar, M., Sannigrahi, B., Knauss, D.M., Sloan, E.D., *Chem. Eng. Sci*., **56**, 4979 (2001).

ISP, Internal unpublished reports, cited in Kelland, 834 (2006).
Kalogerakis, N., Jamaluddin, A.K.M., Dhloabhai, P.D., Bishnoi, P.R., in *Proc. SPE International Symposium on Oilfield Chemistry*, SPE25188, New Orleans, LA, March 2–5, 375 (1993).
Katz, D.L., *Trans. AIME*, **160**, 140 (1945).
Kelland, M.A., *Energy Fuels*, **20**(3), 825 (2006).
Kelland, M.A., Svartaas, T.M., Ovsthus, T.M., in *Proc. Third International Conference on Natural Gas Hydrates*, Salt Lake City, Utah, U.S.A., July 18–22, 1999; *Ann. NY Acad. Sci*. (Holder, G.D., Bishnoi, P.R. eds.), **912**, 281 (2000).
Kent, R.P., Coolen, M.E., *Hydrates in Natural Gas Lines*, Mobil Internal Report (1992).
Kidnay, A.J., Parrish, W.R., *Fundamentals of Natural Gas Processing*, Taylor and Francis, Boca Raton, FL (2006).
King, R., et al., *Canadian Association of Petroleum Producers Hydrate Guidelines*, Canadian Association of Petroleum Producers, Calgary, Alberta, Canada (1994).
Klomp, U.C., WO Patent Application 99/13197 (1999).
Klomp, U.C., WO Patent Application 01/77270 (2001).
Klomp, U.C., Kruka, V.C., Reijnhart, R., WO Patent Application 95/17579 (1995).
Klomp, U.C., Reijnhart, R., WO Patent Application 96/34177 (1996).
Klug, P., Feustel, M., Frenz, V., WO Patent Application 98/22557 and 98/03615 (1998).
Kuhs, W.F., Genov, G., Stalkova, D.K., Hansen, T., *Phys. Chem. Chem. Phys.*, **6**, 4917 (2004).
Larsen, R., Makogon, T., Knight, C., Sloan, E.D., in *Proc. Second International Conference on Natural Gas Hydrates* (Monfort, J.P., ed.), Toulouse, France, June 2–6, p. 163 (1996).
Lee, D.J., Englezos, P., in *Proc Fifth International Conference on Gas Hydrates* (Austvik, T., ed.), Trondheim, Norway, June 13–16, p. 44 (2005).
Leporcher, E.M., Fourest, J.M., Labes Carrier, C., Lompre, M., in *Proc. 1998 SPE European Petroleum Conference*, SPE 50-683, The Hague, The Netherlands, October 20–22 (1998).
Lingelem, M.N., Majeed, A.I., Stange, E., in *(First) International Conference on Natural Gas Hydrates*, *Ann. NY Acad. Sci*. (Sloan, E.D., Happel, J., et al., eds.), **715**, 75 (1994).
Long, J., Lederhos, J., Sum, A., Christiansen, R., Sloan, E.D., "Kinetic Inhibitors of Natural Gas Hydrates," in *Proc. 73rd Annual Convention of Gas Processors Association*, New Orleans, LA, March 7–9, p. 85 (1994).
Makogon, Y.F., *Hydrates of Hydrocarbons*, PennWell Books, Tulsa, OK (1997).
Maximilian, A., Neubecker, K., Sanner, A., US Patent 6867262 (2005).
Mehta, A.P., Hebert, P.B., Cadena, E.R., Weatherman, J.P., *SPE Prod. Facil*., 73 (2003).
Mentor Subsea, *Methods to Clear Blocked Flowlines*, DeepStar CTR A208-1 (1996).
Milburn, C.R., Sitz, G.M., US Patent 644852 B1 (2002).
Muijs, H.M., Anselme, M. J., Beers, N.C.M., Van Os, N.M., Kind, C.E., Patent Application, Nr. 91.0619 (1991).
Nakajima, Y., Takaoki, T., Ohgaki, K., Ota, S., in *Proc. Fourth International Conference on Gas Hydrates* (Mori, Y.H., ed.), Yokohama, Japan, May 19–23, 987 (2002).
Namba, T., Fujii, Y., Saeki, R., Kobayashi, H., WO Patent Application 96/38492 and 96/37584 (1996).
Neubecker, K., Personal communication in 2005 to M.Kelland, cited in Kelland, p. 828 (2006).

Notz, P.K., in *(First) International Conference on Natural Gas Hydrates*, Annals of New York Academy of Sciences (Sloan, E.D., Happel, J., et al., eds.), **715**, 425 (1994).

Notz, P.K., Bumbgartner, S.B., Schaneman, B.D., Todd, J.L., in *Proc. 27th Ann OTC*, OTC 7777, Houston, TX, May 1–4 (1995).

Pakulski, M. European Patent Application 57458 (1998).

Pakulski, M. US Patent Application 6331508 (2001).

Palermo, T., Argo, C.B., Goodwin, S.P., Henderson, A., in *Proc. Third International Conference on Natural Gas Hydrates*, Salt Lake City, Utah, July 18–22, 1999; *Ann. NY Acad. Sci*. (Holder, G.D., Bishnoi, P.R., eds.), **912**, 355 (2000).

Palermo, T., Mussumeci, A., Leporcher, E., in *Proc. Offshore Technology Conference*, OTC 16681, Houston, TX, May 3–8 (2004).

Palermo, T., Sinquin, A., Dhulesia, H., Fourest, J.M., in *Proc. of Multiphase 1997*, BHR Group, p. 133 (1997).

Panchalingham, V., Rudel, M.G., Bodnar, S.H., US Patent Application 20050081714 (2005a).

Panchalingham, V., Rudel, M.G., Bodnar, S.H., US Patent Application 20050081432 (2005b).

Panchalingham, V., Rudel, M.G., Bodnar, S.H., US Patent Application 20050085396 (2005c).

Panchalingham, V., Rudel, M.G., Bodnar, S.H., US Patent Application 20050085675 (2005d).

Panchalingham, V., Rudel, M.G., Bodnar, S.H., US Patent Application 20050085676 (2005e).

Peters, D.J., *A Study of Hydrate Dissociation in Flowlines by the Method of Two-Sided Depressurization: Experiment and Model*, M.S. Thesis, Colorado School of Mines, Golden, CO (1999).

Pfeiffer, D.G., Costello, C.A, Talley, L.D., Wright, P.J., WO Patent Application 99/64718 (1999).

Philips, N.J., in *Proc. 8th International Oilfield Chemical Symposium* Geilo, Norway, March (1997).

Przbylinski, J.L., Rivers, G.T., US Patent 6596911 B2 (2003).

Reijnhout, M.J., Kind, C.E., Klomp, U.C., European Patent Application, 0 526 929 AL (1993).

Reynhout, M.J., Anselme, M.J., Beers, N.C.M., Van Os, N.M., Kind, C.E., Patent Application Nr. 91.0619 (1993).

Rivers, G.T., Crosby, D.L., US Patent Application 2004/0110998 (2004) WO Patent Application 2004/22909 (2004).

Rivers, G.T., Downs, H.H., US Patent Application 20040144732 (2004).

Rivers, G.T., Frostman, L.M., Pryzbyliski, J.L., McMahon, J.A., US Patent Application 2003146173 (2003).

Rogalands Research Unpublished Report of Early 1990s, cited in Kelland, p. 825 (2006).

Rogalands Research Unpublished Reports of 1995, cited in Kelland, p. 832 (2006).

Shirota, H., Aya, I., Namie, S., Bollavaram, P., Turner, D., Sloan, E.D., in *Proc. Fourth International Conference on Gas Hydrates* (Mori, Y.H., ed.), Yokohama, Japan, May 19–23, p. 972 (2002).

Sinquin, A., Vellyh, M., Durand, J.P., European Patent Application 789132 (1998).

Sloan, E.D., U.S. Patent 5,420,370, May 30 (1995a).

Sloan, E.D., U.S. Patent 5,432,292, July 11 (1995b).

Sloan, E.D., *Hydrate Engineering*, Monograph 21, Society of Petroleum Engineers, Richardson, TX (2000).

Sugier, A., Bourgmayer, P., Behar, E., Freund, E., European Patent Applications 323307, 323774 (1989).

Talley, L.D., Oelfke, R.H., WO Patent Application 97/07320 (1997).

Taylor, C.J., *Adhesion Force between Hydrate Particles and Macroscopic Investigation of Hydrate Film Growth at the Hydrocarbon/Water Interface*, M.Sc. Thesis, Colorado School of Mines, Golden, CO (2006).

Thieu, V., Bakeev, K., Shih, J.S., US Patent 6359047 (2002).

Todd, J.L., et al., *Reliabilty Engineering—Gas Freezing and Hydrates*, Texaco Company Hydrate Handbook, New Orleans, LA (1996).

Toyama, M., Seye, M., World Patent Application WO 02/10318 (2002).

Turner, D.J., *Clathrate Hydrate Formation in Water-in-Oil Dispersions*, Ph.D. Thesis, Colorado School of Mines, Golden, CO (2004).

Urdahl, O., Lund, A., Mork, P., Nilsen, T.-N., *Chem. Eng. Sci*., **50**, 863 (1995).

Welling and Associates 1999 Survey, cited by Macintosh, N., "Flow Assurance Still Leading Concern Among Producers," *Offshore*, October (2000).

Wilson, A., Overaa, S.J., Holm, H., *Offshore Technology Conference*, OTC 1655, Houston, TX, May 3–6 (2004).

Wolden, M., Lund, A., Oza, N., Makogon, T., Argo, C.B., Larsen, R., in *Proc. Fifth International Conf. on Gas Hydrates* (Austvik, T., ed.), paper 4002 (5 volumes and CD), Trondheim, Norway, June 13–16, p. 1101 (2005).

Wright, J.F., Dallimore, S.D., Nixon, F.M., Dchesne, C., in *Scientific Results from the Mallik 2002 Gas Hydrate Production Research Well Program*, Mackenzie Delta, Northwest Territories, Canada (Dallimore, S.R., Collett, T.S., eds.), Geological Survey of Canada Bulletin 585, including CD, p. 92 (2005).

Yang, S.O., Kleehammer, D.M., Huo, Z., Sloan, E.D., Miller, K.T., *J. Colloid Interf. Sci.*, **277**, 335 (2004).

Yousif, M.H., Li, P.M., Selim, M.S., Sloan, E.D., *J. Inclus. Phenom. Mol.*, **8**, 71 (1990).

Appendix A: CSMGem Example Problems

A.1 Introduction

The Center for Hydrate Research has been conducting hydrate experiments for over 30 years in efforts to improve flow assurance strategies. The first statistical thermodynamic model for hydrates was developed in 1959 and involved many assumptions, including the assumption that volume is constant. This model predicted hydrate formation temperatures and pressures reasonably well at temperatures near the ice point and at low pressures. However, as industry moves to deeper waters, there is a need for a hydrate model that can predict hydrate formation at higher temperatures and pressures.

The new hydrate model relaxes the constant volume assumption. This model, coupled with the models for aqueous, vapor, liquid hydrocarbon, ice, and solid salt phases, is the basis of CSMGem. CSMGem can calculate multiphase equilibria at any given temperature and pressure using an algorithm based on Gibbs energy minimization. CSMGem is tailored specifically to the hydrocarbon industry in that the models used are regressed in temperature and pressure ranges typically found in subsea pipelines (i.e., temperatures above the ice-point and pressures up to 15,000 psia).

Phase equilibria can be calculated for the following conditions:

- Incipient hydrate formation temperature at a fixed pressure
- Incipient hydrate formation pressure at a fixed temperature
- Fixed temperature and pressure
- Fixed temperature and specified phase fraction (i.e., dew and bubble points)
- Fixed pressure and specified phase fraction (i.e., dew and bubble points)
- Expansion through a valve (i.e., fixed pressure and enthalpy)
- Expansion through a turboexpander (i.e., fixed pressure and entropy)

CSMGem can also plot phase boundaries when used in conjunction with MS Excel.

Please see the "Read me" statement on the CD for installing the program. Also note a complete user's guide on the CD.

The authors acknowledge the Center for Hydrate Research Consortium members for the funding and data required for the development of CSMGem. Consortium members include: BP, Chevron, ConocoPhillips, ExxonMobil, Halliburton, Petrobas, Schlumberger, Shell, Statoil.

A.2 Example Problems

The following example problems are all performed with a given natural gas mixture and will be saved as "Feed.csm." The natural gas selected for the problems has the following composition:

Methane	0.9033
Ethane	0.0519
Propane	0.0140
n-Butane	0.0031
i-Butane	0.0022
n-Pentane	0.0005
i-Pentane	0.0007
n-Hexane	0.0002
Nitrogen	0.0206
Carbon dioxide	0.0035
Water	10 mol% of gas mixture

Note: The temperature and pressure of hydrate formation is slightly dependent on the amount of water in the feed. However, this is of more concern when alcohols are present due to partitioning. It is recommended to use approximately 10 mol% of water relative to the gas mixture.

A.3 Setting up the Natural Gas Example

To perform calculations with the above gas mixture do the following:

1. Open the Components Selection menu, check the above components and then press OK button
2. Feed menu opens automatically. Change the feed units to "mole fraction". Input the above composition with the exception of water (Figure A.1)
3. Click on Aqueous Phase Calculator
4. Input "10" into Amount box for Water and select "mol% Feed + Water"
5. Press OK button
6. Open Units menu and select Fahrenheit and psia for the T and P units, respectively

A.4 Incipient Hydrate Formation Conditions

The objective next is to determine the hydrate formation pressure at a given temperature (35°F). To perform this calculation, do the following:

1. Open Incipient Hydrate Formation form and select Hydrate Formation P at given T
2. Input "35" into Temperature box
3. Press Calculate button

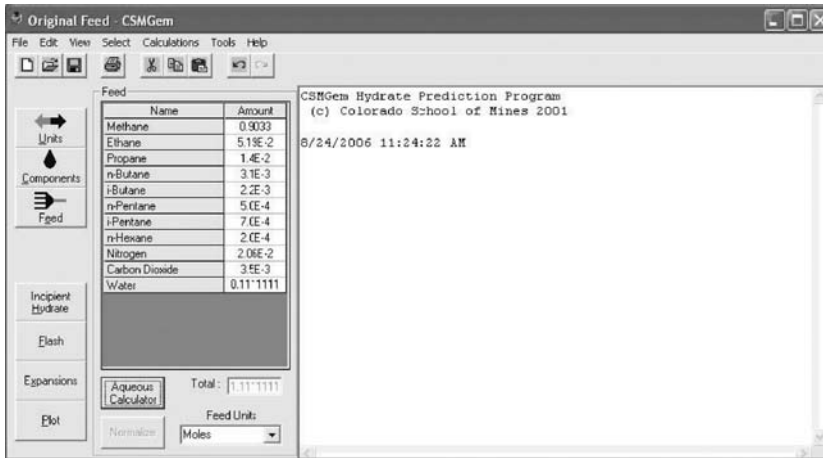

FIGURE A.1 Layout of feed screen for fluid composition input.

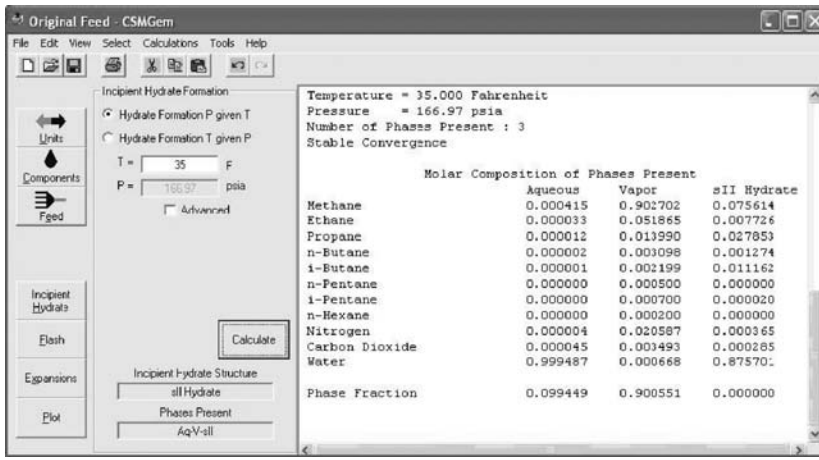

FIGURE A.2 Layout for "hydrate formation P given T" calculation.

CSMGem predicts sII hydrate to form at a pressure of 166.97 psia (Figure A.2). *Note*: If Advanced box is checked, the output for sI and sH hydrates is "$P > P$ sII." This simply means that the calculation was only performed for sII and that it was internally determined that sI and sH were not stable.

The next objective is to determine the hydrate formation temperature at a given pressure (200 psia). To perform this calculation, do the following:

1. Open Incipient Hydrate Formation form and select Hydrate Formation T at given P
2. Input "200" into Pressure box
3. Press Calculate button

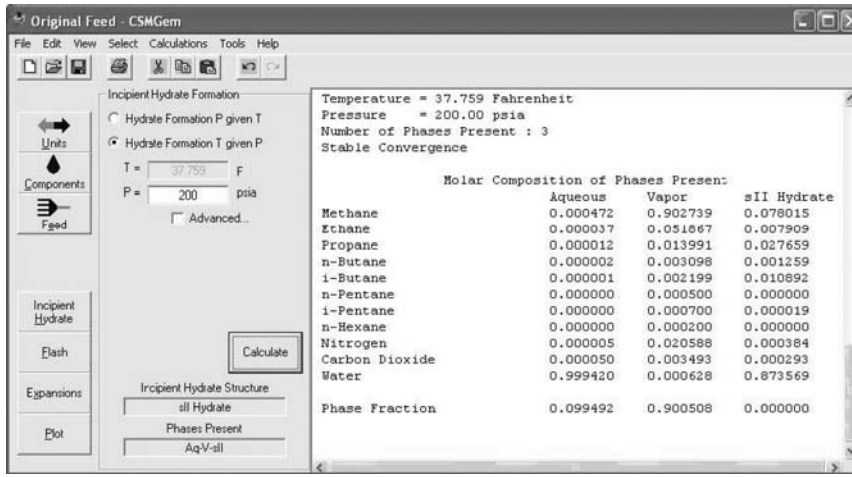

FIGURE A.3 Layout for "hydrate formation T given P" calculation.

CSMGem predicts sII hydrate to form at a temperature of 37.759°F (Figure A.3).
Note: If the Advanced box is checked, the output for sI and sH hydrates is "$T < T$ sII." This simply means that the calculation was only performed for sII and that it was internally determined that sI and sH were not stable.

A.5 PLOTTING A 2-PHASE VLE CURVE

We will create a water-free 2-Phase VLE envelope next. Because the bounds for this calculation are automatically set, we only need to open the Plot form and select the "2-Phase VLE" option and press the Plot button to create the plot:

1. Open Plot form, found in the bottom left corner of the interface
2. Select "2-Phase VLE" option
3. Press Plot button

Depending on the speed of your computer, it may take some time to calculate the envelope and open the plotting tool (especially if you are using MS Excel). The final plot should look like Figure A.4.

A.6 ADDING HYDRATE INHIBITOR

1. Add methanol (MeOH) to components list
2. Go to "Aqueous Calculator" form under the "Feed" menu
3. Add a mass ratio of 0.1 g methanol/g water (see Figure A.5).

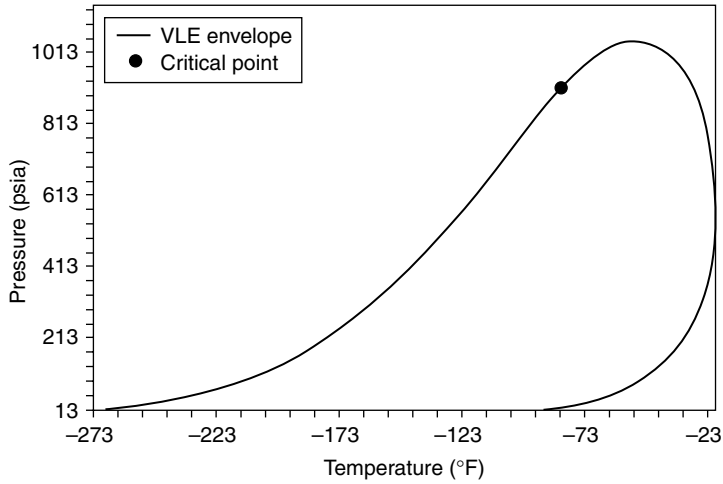

FIGURE A.4 Output for "2-Phase VLE."

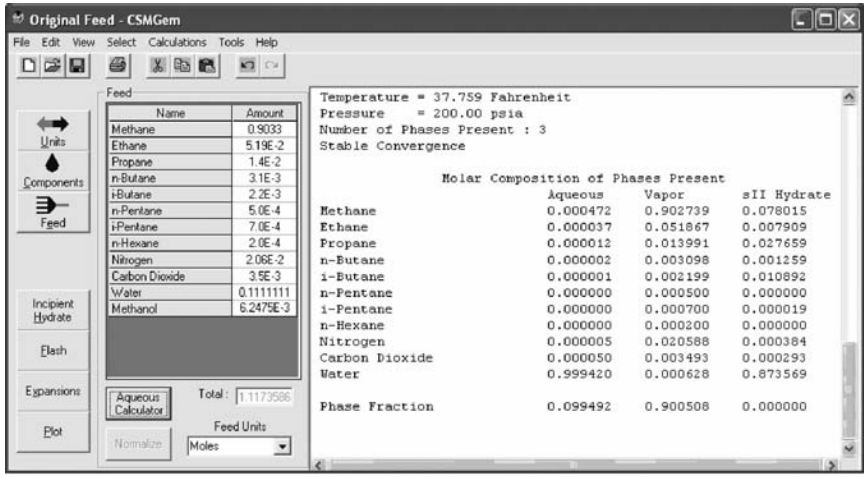

FIGURE A.5 Components list with methanol concentration at 0.1 g/g water.

What is the new equilibrium pressure at 35°F?
What is the new equilibrium temperature at 200 psia?

4. Increase the methanol concentration to a mass ratio of 0.5 g methanol/g water

What is the new equilibrium pressure at 35°F?
What is the new equilibrium temperature at 200 psia?

A.7 Adding Hydrate Inhibitor Solutions

Methanol mass ratio of 0.1:

The new equilibrium pressure at 35°F is: 253.67 psia.
The new equilibrium temperature at 200 psia is: 31.383°F.

Methanol mass ratio of 0.5:

The new equilibrium pressure at 35°F is: 2104.1 psia.
The new equilibrium temperature at 200 psia is: 7.78°F.

A.8 Expansion Across a Valve

Determine the temperature downstream of a choke valve:

1. Click on "Expansions" option
2. Select "Valve"
3. Enter an inlet pressure of 3500 psia and temperature of 65°F (see Figure A.6)
4. Enter an outlet pressure of 3250 psia
5. Check the "initial guess" box and set this to "1F". Press the Calculate button

What is the outlet temperature?
What is the new temperature if the outlet pressure is reduced to 3100 psia?
Hint: You may need to use an initial guess to get the iteration to converge (try 50°F).

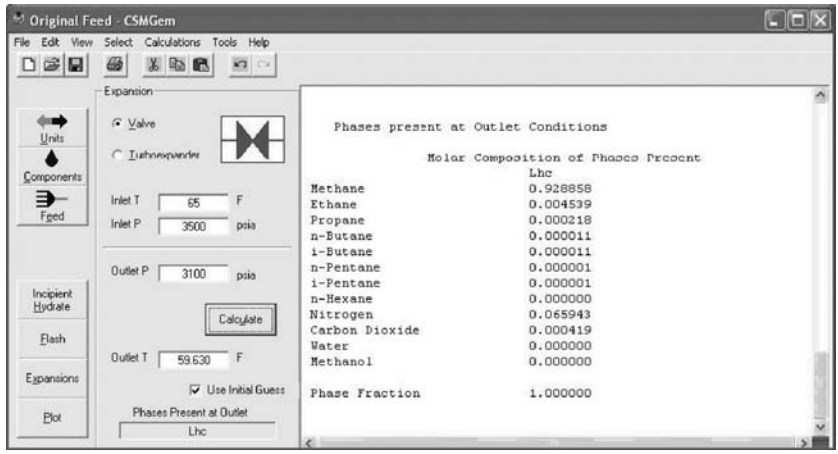

Figure A.6 Layout for expansion across a valve.

A.9 Expansion Across a Valve Solutions

Outlet temperature is 61.81°F when the outlet pressure is 3250 psia.
The outlet temperature is 59.63°F when the outlet pressure is 3100 psia.

A.10 Real Life Situation

Using the initial composition above, answer the following question from a real life situation. Make sure to remove methanol for the first part of the question.

A subsea well head is at 2000 psia and 85°F. A choke valve is to be installed to regulate the downstream pressure:

1. What is the maximum pressure drop that can be sustained without danger of hydrate formation?
2. What is the temperature at this pressure?
3. What is the maximum pressure drop with a 10 wt% (0.1 g/g water) methanol addition?

Isenthalpic expansion and "10 mol% feed + water" can be assumed.

Use the Plot tab on CSMGem to plot the isenthalpic expansion curve using MS Excel. Save this data under a different file name before continuing to plot-phase boundaries. The file will be overwritten if the name is not changed.

Use the Plot tab on CSMGem (add # intervals required) to plot the sII phase boundaries with and without methanol using MS Excel. After combining the calculated data, the final plot should look like Figure A.7. The solutions are the intersection of the expansion line and sII phase boundary lines.

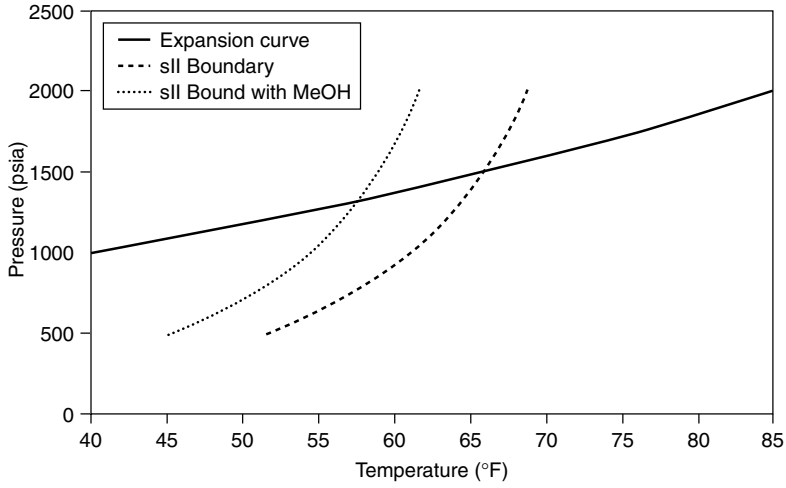

Figure A.7 Phase diagram for hydrate formation.

Downstream conditions at equilibrium point:

Without methanol: Temperature = 66°F; Pressure = 1480 psia.
With methanol: Temperature = 57°F; Pressure = 1320 psia.

Appendix B: CSMPlug Example Problems

B.1 Introduction

This tutorial will guide the user through some sample problems to familiarize them with the features of CSMPlug. The following sample problems will be illustrated:

- One-sided dissociation (1SD)
- Two-sided dissociation (2SD)
- Safety simulator
- Electrical heating

Please see the "Read me" statement on the CD for installing the program. Also note a complete user's guide on the CD.

The authors acknowledge the DeepStar members for the funding and data required for the development of CSMPlug. DeepStar Members: Anadarko, BP, Chevron Corporation, ENI/Agip, Kerr-McGee, Marathon, Petrobras, Statoil, Total.

B.2 Example Problem for One-Sided Dissociation

Figure B.1 shows the layout of the one-sided form in CSMPlug by selecting the 1SD tab. Inputs to the model are upstream and downstream temperature and pressure, equilibrium pressure, hydrate structure, plug porosity, permeability, diameter of the pipeline, and plug length. Input details are given by placing the mouse at each input box.

A 30 ft hydrate blockage occurs in a 12 in. diameter un-insulated pipeline. The upstream and downstream pressures are 780 and 180 psia, respectively. The Structure II equilibrium pressure is 200 psia (from CSMGem at the ambient temperature).

The temperature of the seabed is known to be 42°F, but the downstream end of the pipeline will be colder than this (38°F) due to Joule–Thompson cooling when it is vented. A porosity of 0.5 and a permeability of 0.01 mD are default values. An annulus spacing of 0.1 is required for pressure flow communication.

Using this information, what is the dissociation time until flow and pressure communication can be re-established?

FIGURE B.1 Layout of the 1SD tab in CSMPlug with default values.

Inputting these values and then clicking the "Calculate" button gives these results in the output boxes: flow restart time and phases present during dissociation. Simulation runtime increases substantially for large values of:

1. Pipe diameter
2. Upstream pressure
3. Plug length
4. Annulus spacing

Runtime also increases for small values of:

1. Plug porosity and
2. Heat transfer coefficient

Note: To calculate without a heat transfer coefficient, outside the pipe enter a "–" in the input box.

B.3 1SD SOLUTIONS

The input parameters required for running this calculation are:

1. Upstream temperature: 42°F
2. Downstream temperature: 38°F

3. Hydrate structure: sII
4. Porosity: 0.5 (default)
5. Diameter of the pipe: 12 in.
6. Heat transfer coefficient: −Btu/h ft^2 °F
7. Upstream pressure: 780 psia
8. Downstream pressure: 180 psia
9. Equilibrium pressure: 200 psia
10. Permeability: 0.01 mD (default)
11. Plug length: 30 ft
12. Annulus spacing: 0.1

Restart time: 38.03 h.

B.4 Example Problem for Two-Sided Dissociation

Figure B.2 shows the layout of CSMPlug for a 2SD calculation. Inputs to the model are ambient and dissociation temperature, hydrate structure, plug porosity, and the pipeline diameter. Selecting the default values option on the 2SD tab or from the defaults pull down menu will enter the default values. The default values for the parameters can be seen in Figure B.2.

An sII hydrate blockage occurs in an 18-in. diameter insulated pipeline. The seabed temperature is known to be 41°F. The heat transfer coefficient is known to be 4 Btu/h ft^2°F. The default values for the hydrate dissociation temperature and plug porosity will be used.

What is the time required to fully dissociate (hydrate and ice phases dissociated) the plug?

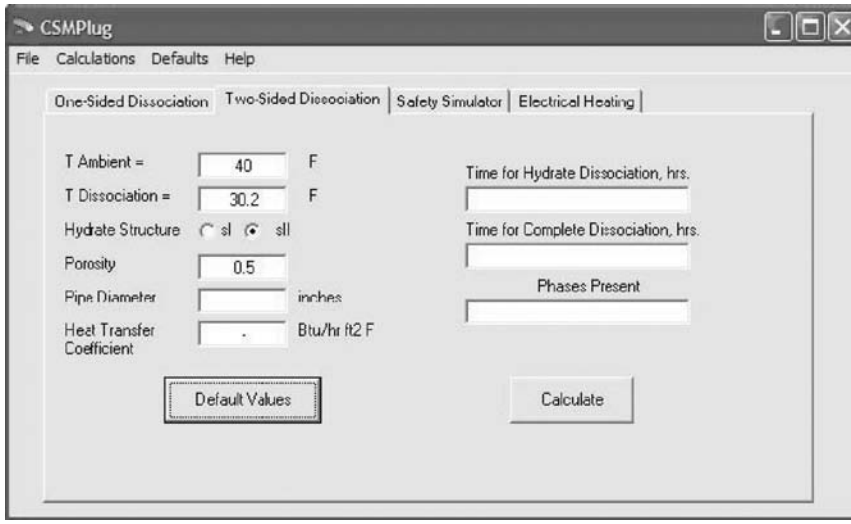

Figure B.2 Layout of the 2SD tab in CSMPlug with default values.

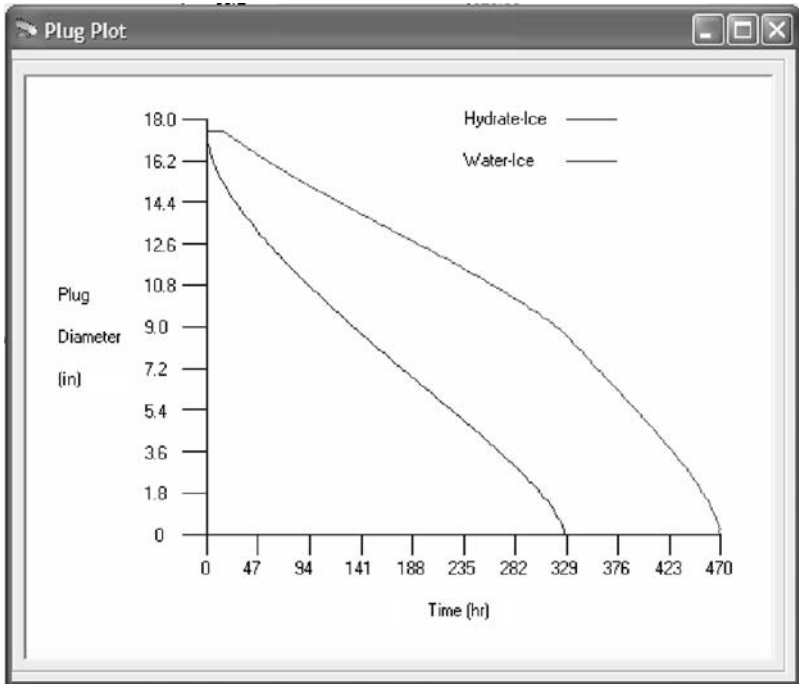

FIGURE B.3 Diameter of the hydrate core and hydrate ice plug as a function of time.

Inputting the values into the respective text boxes, and clicking the "Calculate" button, gives the result for 2SD. The calculation can be stopped if it is taking too long. The results are shown in the output boxes labeled: Time for Hydrate Dissociation and Time for Complete Dissociation (hydrate and ice). The phases present are W–H–I as well as the vapor phase, but only W–H–I phase should be listed?

The presence of insulation slows the dissociation as it reduces heat transfer from the sea to the plug. To calculate without a heat transfer coefficient, enter a "−" into the input box.

A figure similar to Figure B.3 is displayed once the run is complete. The figure shows the water–ice and ice–hydrate interface positions as a function of time. This plot can be used to determine the time when the pipeline can be restarted or when methanol can be flowed based upon the annulus spacing available.

The time for the annulus spacing to achieve 2 in. can be determined by opening the file "two.dat" (see below) in Excel and looking at the time for the diameter of the ice phase to reach 14 in.

CSMPlug automatically plots relevant data, but the data can be viewed in Excel by (1) loading Excel, (2) clicking File, Open, (3) changing the dropdown box titled "File Type" at the bottom of the window to "All Files," then (4) going to C:\Program Files\CSMPlug Version 2.1\two.dat or to the file where you installed

the CSMPlug program. Use Excel to plot a graph of the diameter versus time for the hydrate core and the ice-hydrate plug.

B.5 2SD Solution

For this calculation the inputs required were:

1. Ambient temperature: 41°F
2. Dissociation temperature: 30.20°F
3. Hydrate structure: sII
4. Porosity: 0.5
5. Pipe diameter: 18 in.
6. Heat transfer coefficient: 4 Btu/h ft^2 °F
7. Time to dissociate hydrate phase: 327 h
8. Time to dissociate ice phase: 470 h
9. Time before methanol can be flowed (a 2-in. wide annulus is required): 136 h

B.6 Example Problem for Safety Simulator

A hydrate plug has been formed in a 4-in. diameter gas condensate pipeline. The plug length is 30 ft, and the plug is located at 5660 ft from the pipeline inlet. The downstream length is 9750 ft. The upstream pressure is 550 psia, and the downstream pressure is 50 psia. The pipeline burst pressure is 5000 psia. Assume a porosity of 0. Find the maximum plug velocity and final position of the plug. Run the simulation for 100 s. Figure B.4 shows the layout of CSMPlug for the safety simulator tab.

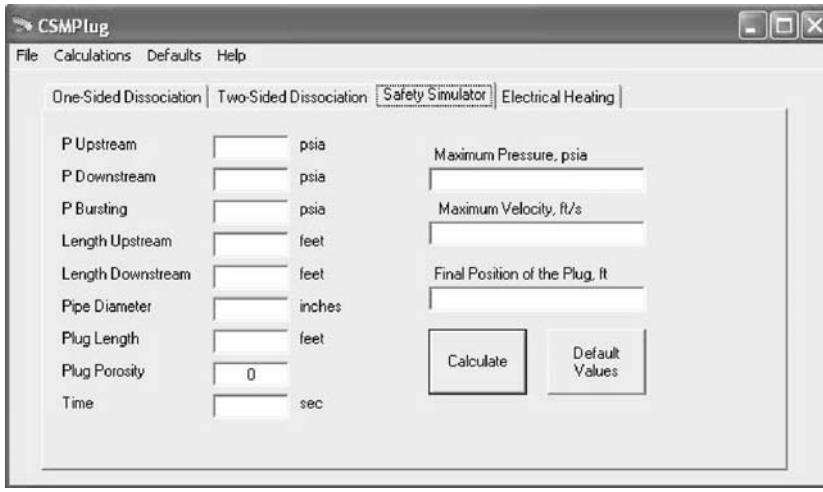

Figure B.4 Layout of the safety simulator tab in CSMPlug.

What is the maximum pressure in the system, the maximum plug velocity, and the final position of the plug?

B.7 Safety Simulator Solutions

The values that should have been entered for the calculation were:

1. *P* upstream: 550 psia
2. *P* downstream: 50 psia
3. *P* bursting: 5000 psia
4. Distance upstream: 5660 ft
5. Distance downstream: 9750 ft
6. Pipe diameter: 4 in.
7. Plug length: 30 ft
8. Plug porosity: 0
9. Time: 100 s

Inputting the above values and clicking the "Calculate" button give the result in the text boxes—maximum pressure, maximum velocity, and final position of the front end of the plug (Figure B.5). A file is created called "safe.dat" with details on the plug position (ft), the velocity (ft/s), and the upstream and downstream pressures (psia). If bursting pressure is exceeded, the program asks you to input values for safe operating conditions. This can be accomplished by increasing downstream pressure, bursting pressure, downstream distance, plug porosity, or by decreasing upstream pressure or distance.

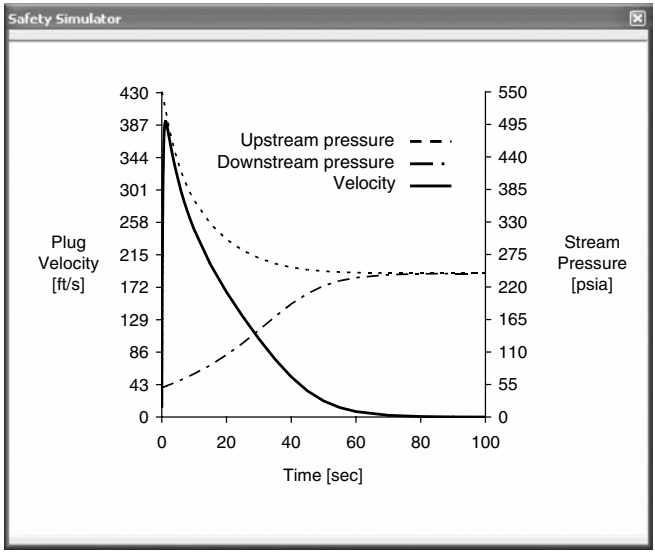

Figure B.5 Results from the safety simulator in CSMPlug.

Maximum pressure: 550 psia
Maximum velocity: 391.85 ft/s
Final position of the plug: 13,468.94 ft

Note: The final position of the plug is 13,500 ft from the wellhead.

B.8 Example Problem for Electrical Heating

Figure B.6 shows the layout of CSMPlug for an electrical heating calculation. Inputs to the model are ambient temperature, dissociation temperature, hydrate structure, plug porosity, heat input per unit length, and the pipeline internal diameter. Selecting the default values option on the heating tab or from the defaults pull-down menu will automatically replace the dissociation temperature, ambient temperature, and porosity with the default values. These default values can be seen in Figure B.6.

A hydrate blockage occurs in a 12-in. electrically heated pipeline. The hydrate dissociation temperature is known to be 58°F. The seabed temperature is 40°F. The heat input per unit length is 30 W/m. Assume the plug porosity is 0.5 and that the hydrate plug is structure II.

What is the complete dissociation time?

B.9 Electrical Heating Solutions

The values that should have been entered for the calculation were:

1. Dissociation temperature: 58°F
2. Ambient temperature: 40°F
3. Hydrate structure: sII

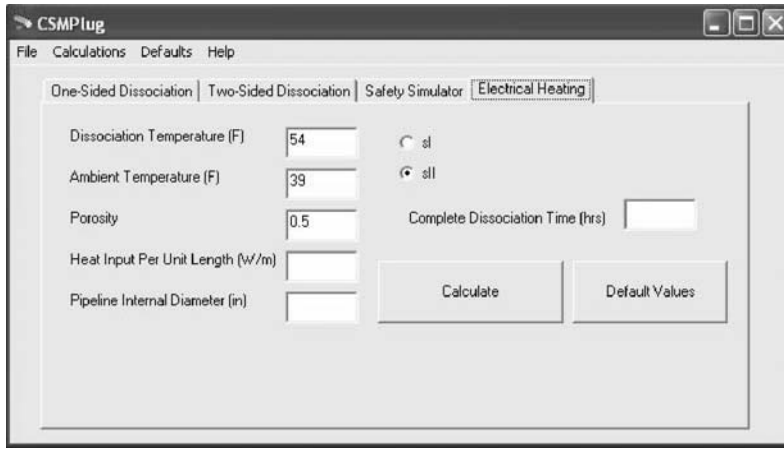

Figure B.6 Layout of the heating tab in CSMPlug with default values.

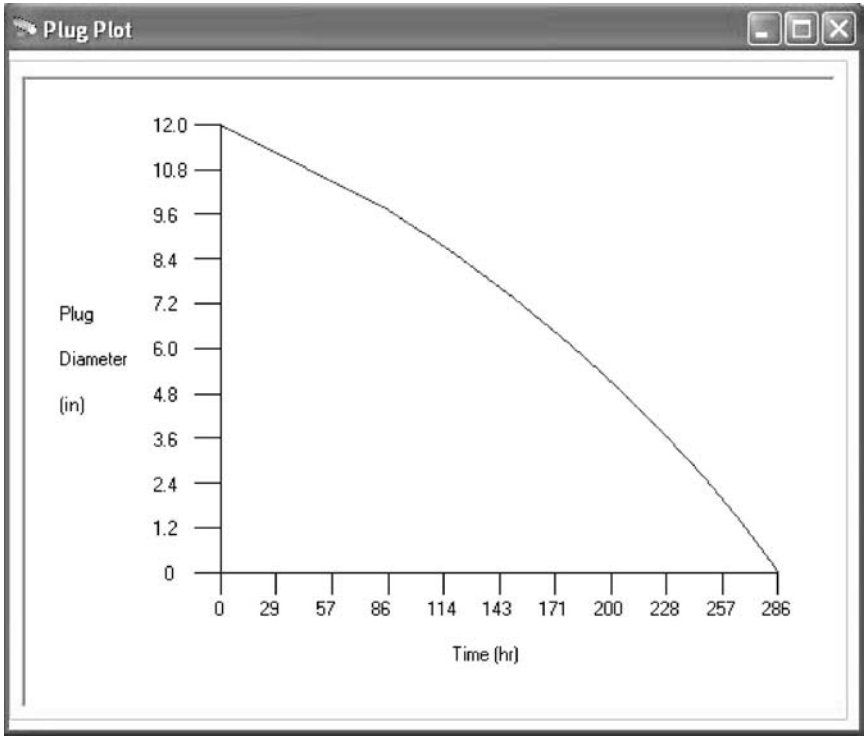

FIGURE B.7 A typical plot of plug diameter vs. time.

4. Porosity: 0.5
5. Heat input per unit length: 30 W/m
6. Pipe diameter: 12 in.

Inputting these values into the respective text boxes, and clicking the "Calculate" button gives the result for final dissociation time. The result is shown in the output box labeled: Complete Dissociation Time (h). A graph is also automatically plotted of plug diameter versus time (Figure B.7). The values of the plug diameter in inches and the corresponding dissociation time in hours are also automatically written to "heat.dat" located in the CSMPlug directory. These values can be copied into a spreadsheet program and used in flow simulation calculations or to predict when the given annulus spacing exists.

Dissociation time: 286 h.

CSMPlug is capable of predicting hydrate dissociation for three scenarios: two-sided depressurisation, one-sided depressurisation and electrical heating. Predictions are most sensitive to the plug porosity and in the case of the one-sided depressurisation model, plug permeability. The model should be used to perform

a sensitivity analysis on these parameters in order to determine the best and worst case dissociation times, prior to dissociating a plug. The default values in the program were chosen to represent a worst case scenario.

CSMPlug can predict the total dissociation time by two-sided depressurisation, and by evenly applied radial heat input to an accuracy of 10%, provided accurate plug properties are known. Predictions from the one-sided depressurisation module are less accurate than those of the other modules, but are within an order of magnitude of those observed; dissociation times for laboratory scale hydrates are typically over predicted but industrial hydrates are under predicted.

The key assumptions are:

1. The hydrate plug dissociates radially
2. The hydrate dissociation is in the heat transfer limited regime
3. The plug is immersed in water
4. Heat transfer resistance in the hydrate phase is neglected

The models were validated on laboratory scale hydrates made from powdered ice, with diameters between 1 and 1.9 inches and lengths between 8 and 36 inches. The one-sided depressurisation module has had limited experimental validation due to problems creating a laboratory scale plug with a low permeability. CSM Plug has been used to model published field data for Tommelieten[1] (970 psi, 40°F, 6″ ID) and the Genesis[2] pipeline (1600 psi, 42°F, 10″ ID). Predictions were within an order of magnitude of those observed. The discrepancies are due to the high gas fraction of these pipelines.

1. Berge L., Gjertsen L. and Lysne D. *The Importance of Porosity and Permeability for Dissociation of Hydrate Plugs in Pipes*. Proc. 2nd International Conference on Gas Hydrates, pp 533–540, Toulouse, 1996.
2. Kashou S. et al *GOM Export Gas Pipeline, Hydrate Plug Detection and Removal*. Offshore Technology Conference, OTC 16691, Houston, 2004

Index

A

B

C

D

E

F

G

H

I

J

K

L

M

N

O

P

Q

R

S

T

U

V

W

X

Y

Z

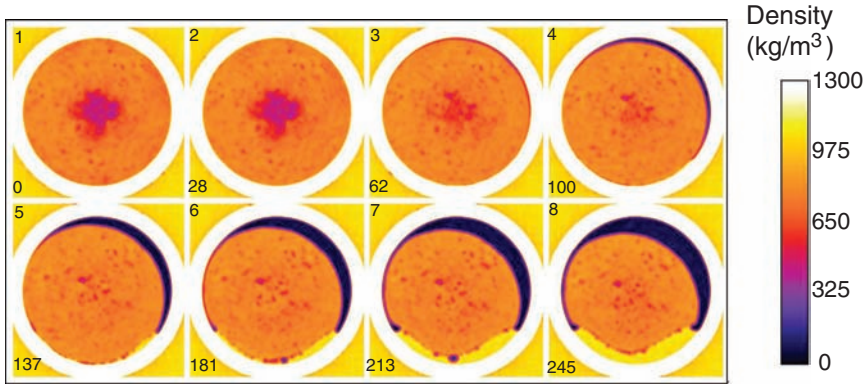

COLOR FIGURE 3.35 X-ray CT imaging shows radial dissociation of a hydrate core. Image number 1–8 (top number on each image) recorded over 0–245 min (bottom number on each image). The cell pressure was decreased from 4.65 to 3.0 MPa over 248 min. The hydrate core temperature decreased from 277 to 274 K with time, following the three-phase methane hydrate equilibrium line. (From Gupta, A., *Methane Hydrate Dissociation Measurements and Modeling: The Role of Heat Transfer and Reaction Kinetics*, Ph.D. Thesis Colorado School of Mines, Golden, CO (2007). With permission.)

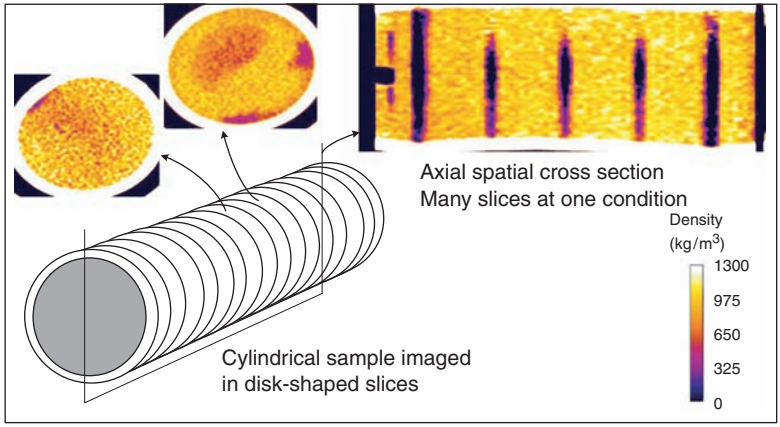

COLOR FIGURE 6.11 Schematic of the application of x-ray CT analysis to provide density profile images of different sections of a hydrate core contained in a cylindrical high pressure aluminum cell. (From Gupta, A., *Methane Hydrate Dissociation Measurements and Modeling: The Role of Heat Transfer and Reaction Kinetics*, Ph.D. Thesis, Colorado School of Mines, Golden, CO (2007). With permission.)

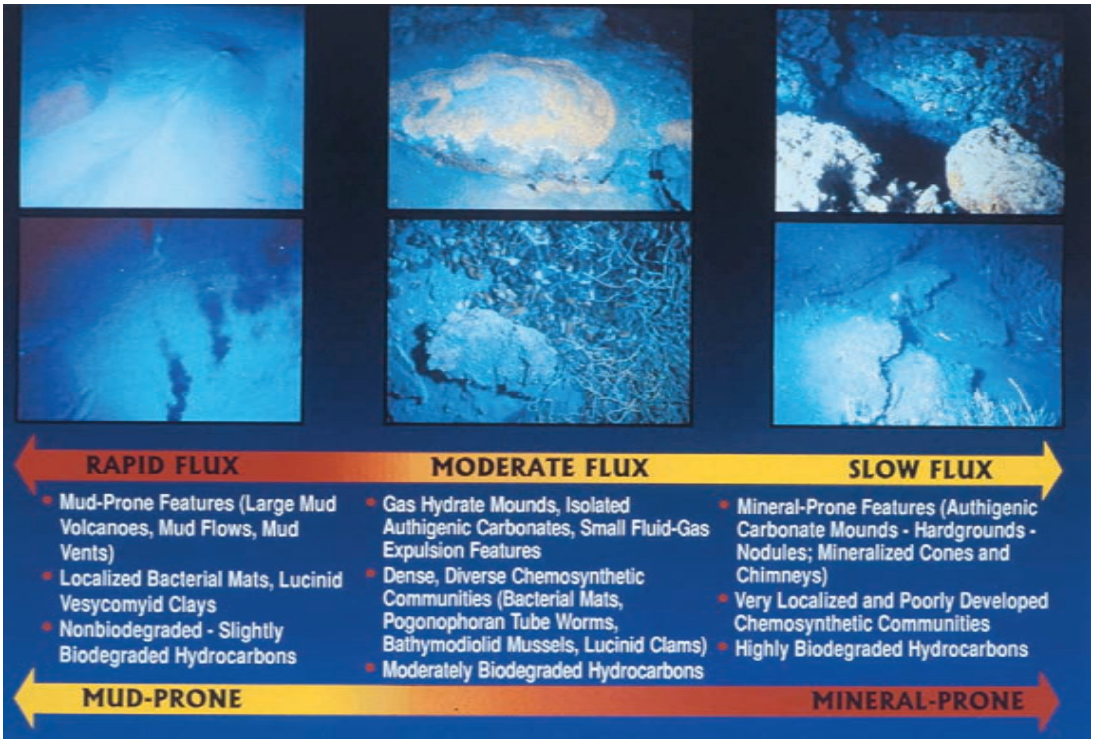

COLOR FIGURE 7.9 Qualitative relationships between fluid fluxes and geologic–biologic response. Each picture has a field of view 3–4 m across. (From Roberts, H.H., in *Natural Gas Hydrates: Occurrence, Distribution and Detection*, (Paull, C.K., Dillon, W.P., eds.) p. 145. American Geophysical Union, Washington, DC (2001). With permission.)

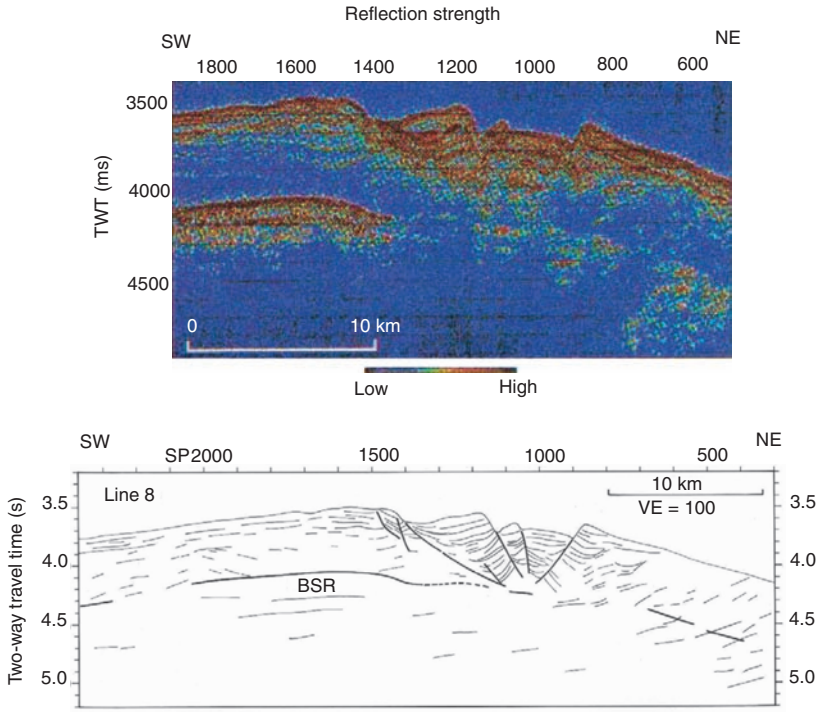

COLOR FIGURE 7.20 Seafloor slump in the Blake-Bahama Ridge shown in both seismic (top) and cartoon (bottom) relief. (From Dillon, W.P., Nealon, J.W., Taylor, M.H., Lee, M.W., Drury, R.M., Anton, C.H., *Natural Gas Hydrates: Occurrence, Distribution, and Detection*, (Paull, C.K., Dillon, W.P., eds.) American Geophysical Union Monograph, 124, p. 41, Washington DC (2001). With permission.) Note the bottom simulating reflector parallel to the ocean bottom, except in the middle section where it appears a seafloor eruption has occurred.

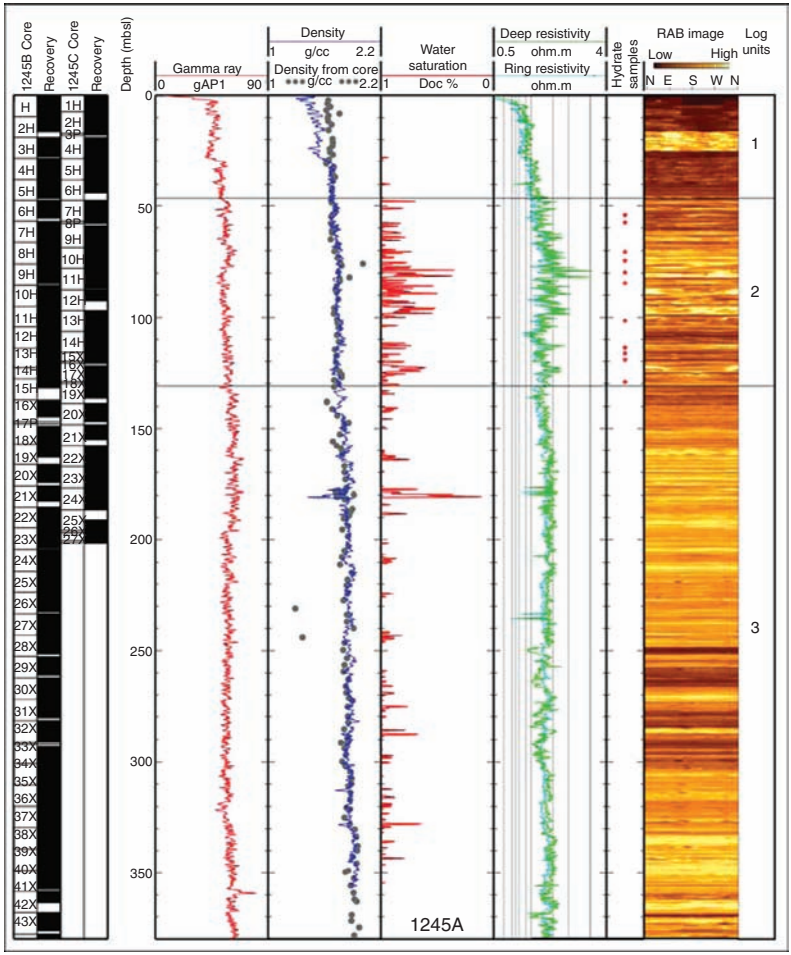

COLOR FIGURE 7.26 Site 1245A southern Hydrate Ridge Flank logs (gamma ray, density, Resistivity at Bit, and Archie water saturation). (T.S. Collett, Personal Communication, November 18, 2005, Leg 204, Scientific Party, 2005.)

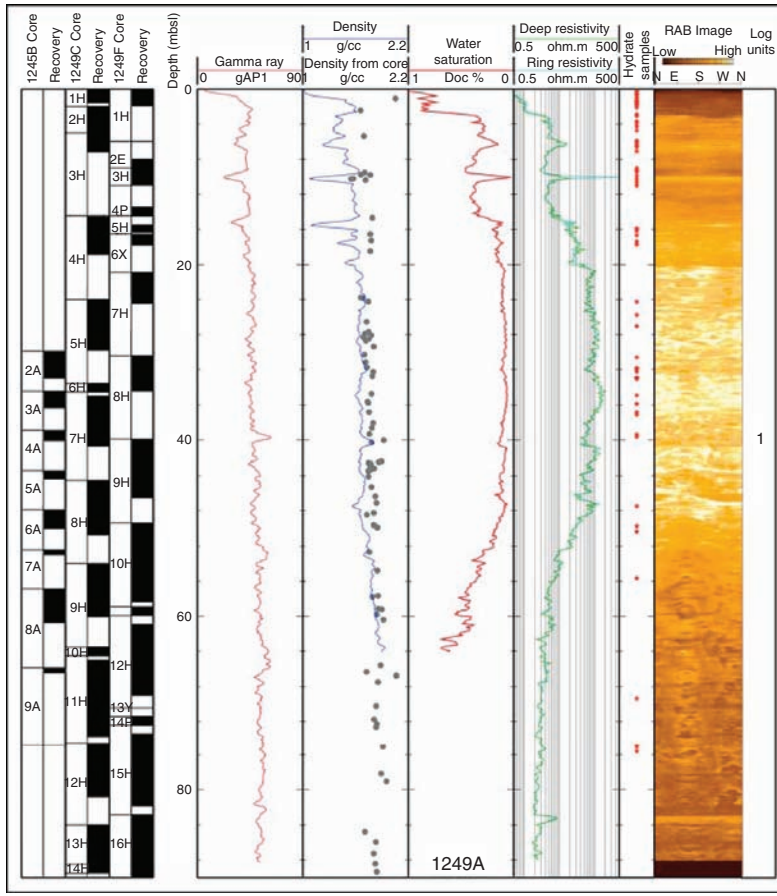

COLOR FIGURE 7.27 Site 1249A southern Hydrate Ridge crest remote sensing logs (gamma ray, density, RAB, and Archie water saturation). (T.S. Collett, Personal Communication, November 18, 2005, Leg 204 Scientific Party, 2005.)

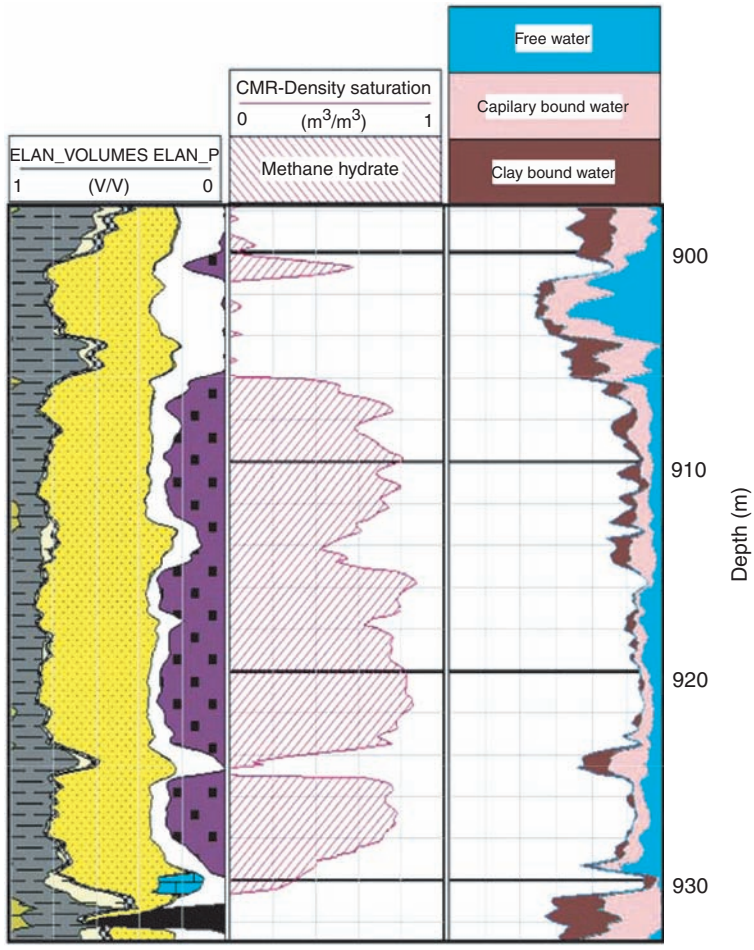

COLOR FIGURE 7.37 5L-38 CMR logs showing hydrate extent at depths between 900 and 930 m. Note that hydrates are obtained by the difference (middle column) between the total porosity as determined by density (not shown), and the capillary, clay-bound and free water determined by NMR.

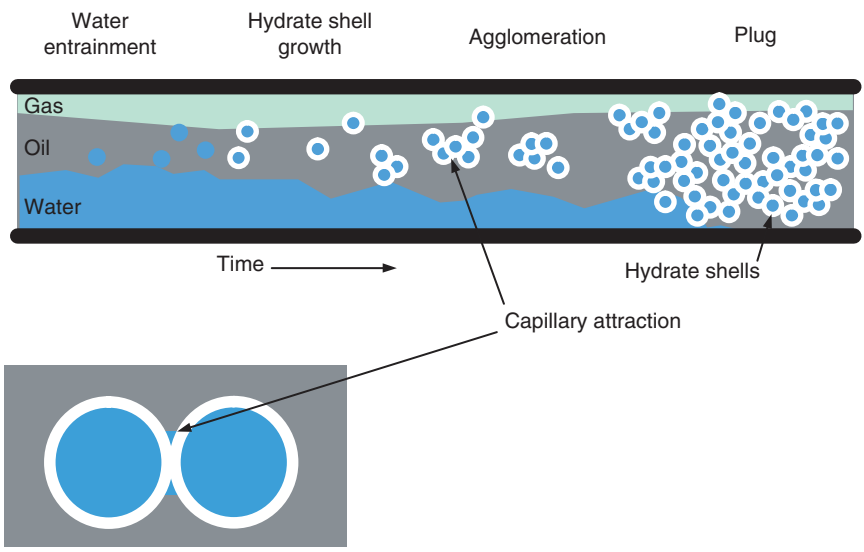

COLOR FIGURE 8.8 Plug formation via aggregation in an oil-dominated system. (From Turner, D.J., *Clathrate Hydrate Formation in Water-in-Oil Dispersions*, Ph.D. Thesis, Colorado School of Mines, Golden, CO (2004). With permission.)

Hydrate research has expanded substantially over the past decade, resulting in more than 4,000 hydrate-related publications. Collating this vast amount of information into one source, **Clathrate Hydrates of Natural Gases, Third Edition** presents a thoroughly updated, authoritative, and comprehensive description of all major aspects of natural gas clathrate hydrates.

What's New in the Third Edition?

This new edition of a bestseller offers updated information on the clathrate hydrate compounds discovered in the past decade, provides a balance between experimental and theoretical perspectives, and incorporates two software programs on the accompanying CD-ROM. It also presents case studies on low dosage hydrate inhibitor prevention and hydrate drilling in nature, phase equilibrium data and kinetic models, and descriptions of the paradigm change in flow assurance to risk management. Other new material discusses the paradigm transition from hydrate reservoir assessment to reservoir production and summarizes the *in situ* conditions for hydrates in the permafrost and oceans.

Features

- Provides a historical perspective of natural gas clathrate hydrates existing from 1790 to 2006
- Illustrates the transition in flow assurance from thermodynamics to kinetics, which resulted from the study of more sophisticated, time-dependent phenomena
- Discusses the structural and physical properties of natural gas hydrates and compares these properties between different hydrate structures and ice
- Describes natural gas hydrate production, transportation, processing, and environmental concerns including methods for prevention and dissociation
- Includes the software programs CSMGem, which supplies the most recent thermodynamic predictions, and CSMPlug, which provides the time required for hydrate plug removal from a pipeline

Cover: The top photograph is a hydrate plug in a Campos Basin slugcatcher, courtesy of Petrobras; the lower photograph is of a 2 m × 2 m hydrate mound in Barkley Canyon, courtesy of MBARI, the Monterey Bay Aquarium Research Institute.

9078

ISBN 0-8493-9078-8

CRC Press
Taylor & Francis Group
an informa business
www.taylorandfrancisgroup.com

6000 Broken Sound Parkway, NW
Suite 300, Boca Raton, FL 33487
270 Madison Avenue
New York, NY 10016
2 Park Square, Milton Park
Abingdon, Oxon OX14 4RN, UK

www.crcpress.com